AD-A041 848 GENERAL ELECTRIC CO CINCINNATI OHIO AIRCRAFT ENGINE GROUP F/G 14/2
HIGH VELOCITY JET NOISE SOURCE LOCATION AND REDUCTION. TASK 1. --ETC(U)
FEB 77 C T SAVELL, E J STRINGAS DOT-OS-30034
UNCLASSIFIED R77AEG187 FAA-RD-76-79-1 NL

1 OF 7
ADA041 848



1 OF
ADA041 848



AD A041848

REPORT NO. FAA-RD-76-79,I

HIGH VELOCITY JET NOISE SOURCE LOCATION AND REDUCTION

TASK I - ACTIVATION OF FACILITIES AND VALIDATION OF SOURCE LOCATION TECHNIQUES

DDC
RECEIVED
JUL 21 1977
C

FEBRUARY 22, 1977
FINAL REPORT

Document is available to the U.S. public through the National Technical Information Service, Springfield, Virginia 22161.

Prepared for

U.S. DEPARTMENT OF TRANSPORTATION
FEDERAL AVIATION ADMINISTRATION
Systems Research & Development Service
Washington, D.C. 20590

AD No. _____
DDC FILE COPY

NOTICE

This document is disseminated under the sponsorship of the Department of Transportation in the interest of information exchange. The United States Government assumes no liability for its contents or use thereof.

1. Report No. FAA-RD-76-79-1	2. Government Accession No.	3. Recipient's Catalog No.
4. Title and Subtitle: HIGH VELOCITY JET NOISE SOURCE LOCATION AND REDUCTION. TASK 1, ACTIVATION OF FACILITIES AND VALIDATION OF SOURCE LOCATION TECHNIQUES		5. Report Date: February 22, 1977 6. Performing Organization Code
7. Author(s): C.T. Savell (Task 1 Technical Director and Editor) et.al E.J. Stringas (Technical Project Manager)		8. Performing Organization Report No. R77AEG187 10. Work Unit No.
9. Performing Organization Name and Address: General Electric Company Advanced Engineering & Technology Program Department Aircraft Engine Group Cincinnati, Ohio 45215		11. Contract or Grant No. DOT-OS-30034 13. Type of Report and Period Covered: Final Report, August 1973 – March 1976
12. Sponsoring Agency Name and Address: U.S. Department of Transportation, Federal Aviation Administration Systems Research and Development Service Washington, D.C. 20590		14. Sponsoring Agency Code: ARD-550

15. Supplementary Notes: This report is in partial fulfillment of the subject program. Related documents to be issued in the course of the program include final reports of the following tasks: Task 2 - Theoretical Developments & Basic Experiments; Task 3 - Experimental Investigation of Suppression Principles; Task 4 - Development & Evaluation of Techniques for "Inflight" Investigation; Task 5 - Investigation of "Inflight" Aero-Acoustic Effects; Task 6 - Noise Abatement Nozzle Design Guide.

16. Abstract

This report summarizes the results of Task 1 as conducted under the subject program. The intent of this 29-month effort was to check out candidate test facilities and noise source location techniques to ensure that the best possible jet noise data over the full range of conditions (velocities ranging from 600 fps to 3000 fps with the best instrumentation are obtained.

The facilities activated and validated included:

- Two anechoic facilities; the University of Southern California in Los Angeles, California, and the University of British Columbia in Vancouver, Canada;
- Two outdoor scale-model jet noise facilities; the General Electric Jet Exhaust Noise Outdoor Test Stand in Evendale, Ohio, and the General Electric Corporate Research and Development Center Hot Jet Noise Facility at Schenectady, New York;
- One large-scale engine outdoor test stand; a super suppressed J79 engine at the General Electric Facility at Edwards Air Force Flight Test Center, California;
- One aerodynamic performance facility; the FluiDyne Engineering Corporation Aerodynamic Laboratory at Medicine Lake, Minnesota; (Replaced for Task 3 of this program by NASA-Lewis 8 x 6-foot Wind Tunnel).
- The GE Anechoic Jet Noise Test Facility, (Reported in Task 1, Supplement, FAA-RD-76-79, Ia).

Numerous noise source location techniques were subjected to a preliminary screening study from which three techniques: the in-jet to far-field correlation approach, the hole-in-the-wall, and ellipsoidal mirror were selected and carried through an experimental demonstration stage. Based on the results from this phase of the activity, the ellipsoidal mirror microphone technique was recommended for use in subsequent program tasks.

17. Key Words (Suggested by Author(s))	18. Distribution Statement
Acoustic facility certification, air attenuation, electronic noise floor, ground reflection corrections, circular nozzle jet noise, acoustic probes, "hole in the wall", ellipsoidal mirror microphone, laser velocimeter	Document is available to the public through the National Technical Information Service, Springfield, Virginia

19. Security Classif. (of this report)	20. Security Classif. (of this page)	21. No. of Pages	22. Price*
UNCLASSIFIED	UNCLASSIFIED	671	

* For sale by the National Technical Information Service, Springfield, Virginia 22151

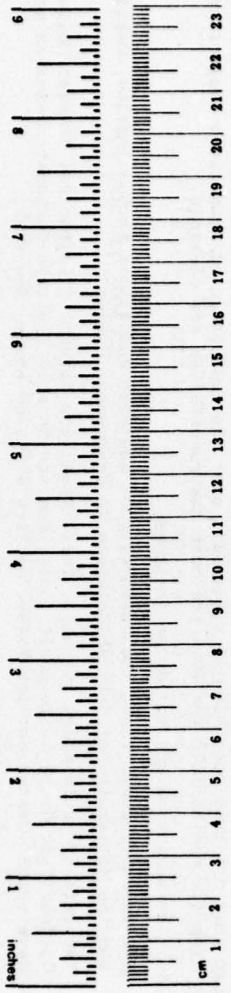
403468

METRIC CONVERSION FACTORS

Approximate Conversions to Metric Measures

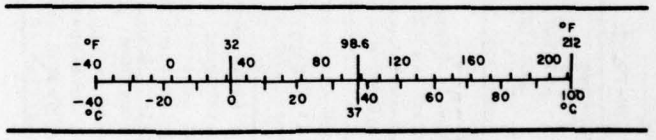
Symbol	When You Know	Multiply by	To Find	Symbol
	LENGTH			
in	inches	*2.5	centimeters	cm
ft	feet	30	centimeters	cm
yd	yards	0.9	meters	m
mi	miles	1.6	kilometers	km
	AREA			
in^2	square inches	6.5	square centimeters	cm^2
ft^2	square feet	0.09	square meters	m^2
yd^2	square yards	0.8	square meters	m^2
mi^2	square miles	2.6	square kilometers	km^2
	acres	0.4	hectares	ha
	MASS (weight)			
oz	ounces	28	grams	g
lb	pounds	0.45	kilograms	kg
	short tons (2000 lb)	0.9	tonnes	t
	VOLUME			
tsp	teaspoons	5	milliliters	ml
Tbsp	tablespoons	15	milliliters	ml
fl oz	fluid ounces	30	milliliters	ml
c	cups	0.24	liters	l
pt	pints	0.47	liters	l
qt	quarts	0.95	liters	l
gal	gallons	3.8	liters	l
ft^3	cubic feet	0.03	cubic meters	m^3
yd^3	cubic yards	0.76	cubic meters	m^3
	TEMPERATURE (exact)			
°F	Fahrenheit temperature	5/9 (after subtracting 32)	Celsius temperature	°C

*1 in = 2.54 (exactly). For other exact conversions and more detailed tables, see NBS Misc. Publ. 286, Units of Weights and Measures, Price $2.25, SD Catalog No. C13.10:286.



Approximate Conversions from Metric Measures

Symbol	When You Know	Multiply by	To Find	Symbol
	LENGTH			
mm	millimeters	0.04	inches	in
cm	centimeters	0.4	inches	in
m	meters	3.3	feet	ft
m	meters	1.1	yards	yd
km	kilometers	0.6	miles	mi
	AREA			
cm^2	square centimeters	0.16	square inches	in^2
m^2	square meters	1.2	square yards	yd^2
km^2	square kilometers	0.4	square miles	mi^2
ha	hectares (10,000 m^2)	2.5	acres	
	MASS (weight)			
g	grams	0.035	ounces	oz
kg	kilograms	2.2	pounds	lb
t	tonnes (1000 kg)	1.1	short tons	
	VOLUME			
ml	milliliters	0.03	fluid ounces	fl oz
l	liters	2.1	pints	pt
l	liters	1.06	quarts	qt
l	liters	0.26	gallons	gal
m^3	cubic meters	35	cubic feet	ft^3
m^3	cubic meters	1.3	cubic yards	yd^3
	TEMPERATURE (exact)			
°C	Celsius temperature	9/5 (then add 32)	Fahrenheit temperature	°F



PREFACE

This report describes the work performed under Task 1 of the DOT/FAA High Velocity Jet Noise Source Location and Reduction Program (Contract DOT-OS-30034). The objectives of the contract were:

- Investigation of the aerodynamic and acoustic mechanisms of various jet noise suppressors, including scaling effects.
- Analytical and experimental studies of the acoustic source distribution in such suppressors, including identification of source location, nature and strength, and noise reduction potential.
- Investigation of inflight effects on the aerodynamic and acoustic performance of these suppressors.

The results of these investigations lead to the preparation of a design guide report for predicting the overall characteristics of suppressor concepts from models to full-scale static, to inflight conditions, as well as quantitative and qualitative prediction of the phenomena involved.

The work effort in this program was organized under the following major Tasks, each of which is reported in a separate Final Report:

Task 1 - Activation of Facilities and Validation of Source Location Techniques.

Task 2 - Theoretical Developments and Basic Experiments.

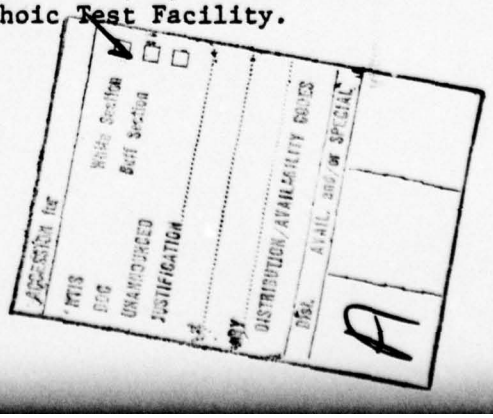
Task 3 - Experimental Investigation of Suppression Principles.

Task 4 - Development and Evaluation of Techniques for "Inflight" Investigation.

Task 5 - Investigation of "Inflight" Aero-Acoustic Effects on Suppressed Exhausts.

Task 6 - Preparation of Noise Abatement Nozzle Design Guide Report.

Task 1, the subject of the present report (FAA-RD-76-79,I), was formulated to investigate candidate test facilities and noise source location techniques (including their accuracies and limitations) in order to assure that data acquired later under this, and future programs, would be properly validated. A supplement to this report, FAA-RD-76-79,Ia, covers certification of the General Electric Jet Noise Anechoic Test Facility.



Task 2 was a theoretical effort complemented by theory verification experiments which extended across the entire contract period of performance. Task 3 represented a substantial contract effort to gather various test data on a wide range of high velocity jet nozzle suppressors. These data, intended to help identify several "optimum" nozzles for "inflight" testing under Task 5, provide an extensive high quality data bank useful to preparation of the Task 6 design guide, as well as to future studies.

Task 4 was similar to Task 1, except that it dealt with the specific test facility requirements, measurement techniques, and analytical methods necessary to evaluate the "inflight" noise characteristics of simple and complex suppressor nozzles. This effort provided the capability to conduct the "flight" effects test program of Task 5.

TABLE OF CONTENTS

Section		Page
1.0	SUMMARY AND CONCLUSIONS	1
	1.1 Facilities	1
	1.2 Source Location Techniques	3
2.0	INTRODUCTION	5
	2.1 General Objectives	5
	2.2 Facility Validation	5
	2.3 Noise Source Measurement Techniques	7
	2.4 Report Organization	8
3.0	ACTIVATION OF FACILITIES	9
	3.1 Introduction	9
	3.2 University of Southern California Anechoic Room	9
	3.2.1 Anechoic Chamber	9
	3.2.2 Jet Facilities	13
	3.2.2.1 Compressor and Pressure Vessels	13
	3.2.2.2 Pressure Reducing Valve and Regulator	13
	3.2.2.3 Electrical Heater	17
	3.2.2.4 Settling Chamber and Nozzles	17
	3.2.2.5 Recording Acquisition System	17
	3.2.3 Acoustic Data Acquisition System	19
	3.2.4 Data Reduction System	19
	3.3 University of British Columbia Anechoic Room	19
	3.3.1 Anechoic Chamber	22
	3.3.2 Jet Noise Facility	25
	3.3.3 Data Acquisition and Reduction Systems	29
	3.4 General Electric JENOTS Scale Model Acoustic Test Facility	30
	3.4.1 The Acoustic Arena	30
	3.4.2 Jet Facility	33
	3.4.2.1 Air Supply System	33
	3.4.2.2 Fuel System	35
	3.4.2.3 Burner System	36
	3.4.2.4 Domestic Water System	38
	3.4.2.5 Coannular Flow JENOTS Facility	38
	3.4.3 Aerodynamic Instrumentation and Data Acquisition	42
	3.4.3.1 Airflow	42
	3.4.3.2 Fuel Flow	42
	3.4.3.3 Tunnel Temperature	42

TABLE OF CONTENTS (Continued)

Section		Page
	3.4.3.4 Tunnel Pressure	44
	3.4.3.5 Cooling Water	44
	3.4.3.6 Meteorological Data	44
	3.4.3.7 Digital Data Acquisition System	44
	3.4.4 Acoustic Data Acquisition and Reduction	45
	3.4.4.1 Data Acquisition	45
	3.4.4.2 Data Reduction	48
3.5	General Electric/CR&DC Hot Jet Noise Facility	50
	3.5.1 The Acoustic Arena	50
	3.5.2 Jet Facility	53
	3.5.3 Data Acqusition and Reduction System	53
3.6	J79 Engine Installation at GE/EFTC	55
	3.6.1 The Acoustic Arena	55
	3.6.2 Jet Facility	60
	3.6.2.1 Turbine Exhaust Suppressor	60
	3.6.2.2 Inlet Suppressor	60
	3.6.2.3 Casing Radiation Suppressor	68
	3.6.3 Aero Data Acquisition System and Data Reduction	68
	3.6.4 Acoustic Data Acquisition	73
	3.6.5 Acoustic Data Processing	73
3.7	FluiDyne Engineering Corporation's Medicine Lake Aerodynamic Laboratory	75
	3.7.1 Facility Description	78
	3.7.2 Channel 7 Description	78
	3.7.3 Channel 11 Description	78
	3.7.4 Force Balance Calibration	80
3.8	NASA-Lewis 8 X 6 foot Wind Tunnel	81
	3.8.1 Facility Description	81
3.9	Summary	87
4.0	ESTABLISHMENT OF UNCONTAMINATED JET NOISE	89
4.1	Statistical Analysis	91
4.2	General Environmental Effects	94
4.3	Air Attenuation Corrections: Accuracy and Precision	96
	4.3.1 Statistical Analysis	100
	4.3.2 General Environmental Effects	100
	4.3.3 Numerical Results	104

TABLE OF CONTENTS (Continued)

Section		Page
	4.4 Aero Instrumentation Accuracy	111
	4.4.1 Variance Equations	116
	4.4.2 Results	117
	4.5 Acoustic Measurement Errors	120
	4.5.1 Fundamentals of Electronic System Functions	124
	4.5.2 Sensitivity and Frequency Response Measurement	125
	4.6 Electronic Noise Floor	126
	4.6.1 Theoretical Prediction of the Floor	127
	4.6.2 Calculation of the Noise Floor at JENOTS	128
	4.6.3 Electronic Noise Floor Spectra	136
	4.6.4 Electronic Noise at Other Facilities	152
	4.7 Ambient Environmental Noise	152
	4.8 Facility Piping Noise	160
	4.9 Combustion and Heater Noise	160
	4.10 Turbomachinery Noise from J79 Engine	169
	4.11 Mechanical Radiated Noise	175
	4.12 Summary	186
5.0	CORRECTIONS TO A FREE-FIELD ENVIRONMENT	187
	5.1 Location of the Measurement Arc	187
	5.2 Ground Reflections	199
	5.3 Ground Reflection Theory	199
	5.4 Distributed Source Effects on Ground Reflection Index	206
	5.4.1 Analysis	211
	5.4.2 Parametric Study	217
	5.5 JENOTS Ground Reflection Corrections	217
	5.5.1 Microphone Height Change	217
	5.5.2 Determination of the Phase Factor	224
	5.5.3 Determination of the Reflection Coefficient	240
	5.5.4 JENOTS Ground Reflection Correction Factors	245
	5.5.5 A Check for Smoothness: Tests with a Fiberglass Ground	245

TABLE OF CONTENTS (Continued)

Section		Page
	5.6 CR&DC Ground Reflection Corrections	252
	5.7 J79/EFTC Ground Reflection Corrections	268
	5.7.1 Two Microphone Philosophy	268
	5.7.2 Ground Impedance Measurement	271
	5.8 Precision and Accuracy of the Ground Reflection Corrections	272
	5.9 Reflections in the Anechoic Rooms	282
	5.10 Other Reflections at JENOTS	286
	5.11 Additional Reflections at CR&DC	286
	5.12 Spurious Reflections at 150° and 160° with J79/EFTC	291
	5.13 Inverse Square Law at USC	291
	5.14 Inverse Square Law at UBC	296
	5.15 Inverse Square Law at JENOTS	296
	5.16 Inverse Square Law at CR&DC	301
	5.17 Inverse Square Law Tests at GE/EFTC	306
	5.18 Summary	313
6.0	CERTIFICATION OF THE FACILITIES	314
	6.1 "Referee" Data Presentation	314
	6.2 Certification at USC	328
	6.3 Certification at UBC	344
	6.4 Certification of the JENOTS Facility	344
	6.5 Certification at CR&DC	376
	6.6 Certification of the J79 Engine at GE/EFTC	386
	6.7 Aerodynamic Measurement Accuracy at FluiDyne	398
	6.8 Data Quality Assurance for NASA-Lewis Wind Tunnel	398
	6.9 Summary	409
7.0	ANALYSIS OF VARIANCE - OVERALL PRECISION OF ACOUSTIC MEASUREMENTS	411
	7.1 Introduction	411
	7.2 Type of Error	411

TABLE OF CONTENTS (Continued)

Section			Page
	7.3	Calculation of the Precision Error	413
	7.4	Effect of the Tape Recorder	425
	7.5	OASPL Precision Estimate	425
8.0	NOISE SOURCE LOCATION TECHNIQUES		440
	8.1	General Survey and Classification	441
		8.1.1 Near Field Surveys	441
		8.1.2 Triangulation and Plane Image Technique	444
		8.1.3 Hole-in-the-Wall Technique	450
		8.1.4 Directional Microphones	450
		8.1.5 Correction Techniques with In-Jet Measurements	452
		8.1.5.1 Cross Correlation of Turbulent Velocity Measurements Within the Jet	452
		8.1.5.2 Cross Correlation of Jet Turbulence with Far-Field Acoustic Measurements	454
		8.1.5.3 Cross Correlation of Jet Pressure and Far-Field Pressure Measurements	455
		8.1.5.4 Coherence of Spectral Lines	459
		8.1.5.5 Noninvasive Measurements	460
	8.2	The Feasibility Study	460
		8.2.1 Near Field Surveys	461
		8.2.2 Plane Image Versus Hole in the Wall	463
		8.2.3 Directional Microphones	463
		8.2.4 Correlation Techniques	464
		8.2.4.1 Two Point or Causality Correlations	464
		8.2.4.2 Velocity or Pressure	465
		8.2.4.3 Choice of Sensor for In-Jet Measurement	465
		8.2.5 Summary	468
	8.3	Optimum Acoustic Probe Shape Study	469
		8.3.1 Desired Measurement	469
		8.3.2 Relative Magnitude of Probe Signal Contaminants	472
		8.3.3 Design of a Low Noise Probe	477
		8.3.3.1 Surface Pressure Distributions	477

TABLE OF CONTENTS (Continued)

Section		Page
	8.3.3.2 Two-Hole Probes	478
	8.3.3.3 Comparison with Rackl's Probe	490
	8.3.3.4 Dipole-Radiated Noise from the Cylindrical Probes	490
	8.3.4 Conclusions and Recommendations	490
8.4	Laser Velocimeter Developments for Noise Source Location	495
	8.4.1 Basic LV Mean and Turbulent Velocity Measurements	495
	8.4.2 LV-Measured Turbulence Spectra	497
	8.4.3 In-Jet/Far-Field Cross-Correlation Measurements	506
	8.4.3.1 Acoustic Theory and General Approach	506
	8.4.3.2 The Random Sample Correlation Estimator	507
	8.4.3.3 Simulation Experiments	515
	8.4.4 Cross-Correlation Experiments with General Electric's Laser Velocimeter	518
	8.4.4.1 Experimental Arrangement and Test Conditions	518
	8.4.4.2 Discussion of Results	518
	8.4.5 Conclusions	530
8.5	Laser Shadowgraph Causality Correlation	530
	8.5.1 The Density Laplacian as a Source Term	531
	8.5.2 Laser Shadowgraph	533
	8.5.3 Two-Dimensional Approximation of Source Term	538
	8.5.4 Calibration	540
	8.5.4.1 Calibrator Theory	540
	8.5.4.2 Practical Difficulties	544
	8.5.5 Jet Noise Surveys	546
	8.5.6 Conclusions and Recommendations	550
8.6	Hole in the Wall	551
	8.6.1 Design and Calibration	553
	8.6.2 Source Location Measurements	558
	8.6.3 Conclusions and Recommendations	567
8.7	Ellipsoidal Mirror Microphones	567
	8.7.1 Operating Principles	567
	8.7.2 Mirror Designs	575
	8.7.3 Calibration of Mirrors	577
	8.7.4 Jet Noise Source Location Mapping at JENOTS	590
	8.7.5 A Test for Integral Closure	597
	8.7.6 Loss of Resolution Due to the "Window Function"	597
	8.7.7 Source of Error	604
	8.7.8 Summary	605

TABLE OF CONTENTS (Concluded)

Section		Page
9.0	CONCLUSIONS AND RECOMMENDATIONS	606
	9.1 Conclusions	606
	9.1.1 Activation of Facilities	606
	9.1.2 Noise Source Location Techniques	608
	9.2 Recommendations for Future Work	609
	APPENDIX - GE AIR ATTENUATION MODEL	611
	REFERENCES	627

LIST OF ILLUSTRATIONS

Figure		Page
3-1	Jet Noise Research Facilities at USC.	10
3-2	Interior of USC Anechoic Chamber.	11
3-3	Schematic Diagram Showing Arrangement of Microphones for Far Field Measurements at USC.	12
3-4	USC Compressor and Pressure Vessels.	14
3-5	Details of USC Valve Disc.	15
3-6	Compressor and Control Valve at USC.	16
3-7	Schematic Diagram Showing Settling Chamber and a Subsonic Nozzle at USC.	18
3-8	The USC Data Acquisition and Reduction Systems.	21
3-9	Aeroacoustic Facility at Department of Mechanical Engineering (UBC).	23
3-10	Microphone Locations Relative to Point Source for Free Field Calibrations (UBC).	24
3-11	UBC Anechoic Chamber in Vancouver, B.C., Canada.	26
3-12	Piping Layout for UBC Air Supply System.	27
3-13	UBC Settling Chamber and Conical Nozzle.	28
3-14	Schematic of JENOTS Facility.	31
3-15	JENOTS Test Facility in Evendale, Ohio.	32
3-16	Building 401 Central Air Supply System for the JENOTS and Anechoic Chamber Facilities at General Electric Plant, Evendale, Ohio.	34
3-17	Schematic of JENOTS Single-Jet Main Air Pipe and Burner System.	37
3-18	Schematic of Coannular-Flow JENOTS Facility.	39

LIST OF ILLUSTRATIONS (Continued)

Figure		Page
3-19	JENOTS Coannular Facility in Evendale, Ohio.	40
3-20	JENOTS Coannular Plenum Chamber.	41
3-21	JENOTS Control Panel.	43
3-22	JENOTS Data Acquisition System.	46
3-23	Data Reduction System.	49
3-24	CR&DC Hot Jet Noise Facility.	51
3-25	Acoustic Arena at GE CR&DC Hot Jet Facility.	52
3-26	Burner-Muffler Construction (CR&DC).	54
3-27	Edwards Flight Test Center "North Site" After Grading.	56
3-28	Schematic of the GE/EFTC Sound Field.	57
3-29	GE/EFTC Oiled Sound Field.	58
3-30	Acoustic Arena of the J-79 at GE/EFTC Showing Two-Microphone Setup.	59
3-31	J79 Engine Cross Section.	61
3-32	J79 Engine Stackup.	62
3-33	Unshielded View of J79 Engine Installation at GE/EFTC.	63
3-34	Turbine Exhaust Suppressor for the J79 Engine.	64
3-35	Treated Exhaust Suppressor Trays for the J79 Engine.	65
3-36	Turbine Exhaust Suppressor Assembly for J79 Engine.	66
3-37	J79 Inlet Suppressor Schematic.	67
3-38	View of J79 Bellmouth Showing Inlet Instrumentation.	69
3-39	Shielded View of Casing Radiation Suppressor Box for the J79 Engine.	70
3-40	End View of Casing Radiation Suppression Box.	71

LIST OF ILLUSTRATIONS (Continued)

Figure		Page
3-41	Shielded View of J79 Engine Installation at EFTC.	72
3-42	Sketch of Acoustic Data Acquisition Equipment at GE/EFTC.	74
3-43	GE/EFTC Acoustic Data Processing System.	76
3-44	Fluidyne Engineering Corporation's Aerodynamic Facilities.	77
3-45	FluiDyne Engineering Corporation's Static Nozzle Test Facilities.	79
3-46	NASA Lewis 6 x 8 Foot Supersonic Wind Tunnel Aerodynamic Cycle.	82
3-47	Operating Characteristics of NASA Lewis 6 x 8-Foot Supersonic Wind Tunnel.	83
3-48	Model Installed in 6 x 8 Foot Supersonic Wind Tunnel.	88
4-1	Montage of Possible Contaminants to Acoustic Measurements.	90
4-2	Background Noise Corrections for Sound Level Measurements.	92
4-3	Variance of the Background Noise Correction.	95
4-4	Representative Ambient Temperature and Relative Humidity at GE/EFTC.	97
4-5	Representative Wind Velocity and Percent of Precipitation at GE/EFTC.	98
4-6	Average Test Days per Week Based on Acceptable Environmental Conditions for Acoustic Testing.	99
4-7	Comparison of Air Attenuation Models at 50% Relative Humidity and Temperature = 68° F.	101
4-8	Atmospheric Attenuation Variance at 500 Hz.	105
4-9	Atmospheric Attenuation Variance at 1000 Hz.	106
4-10	Atmospheric Attenuation Variance at 5000 Hz.	107

Figure		Page
4-11	Atmospheric Attenuation Variance at 10,000 Hz.	108
4-12	Atmospheric Attenuation Variance at 20,000 Hz.	109
4-13	Atmospheric Attenuation Variance at 80,000 Hz.	110
4-14	Air Attenuation Accuracy During J79 Certification Testing at GE/EFTC.	112
4-15	Aero Calibration of Inlet Total Pressure Rake.	113
4-16	Aero Calibration of Plane 7 Static Taps.	114
4-17	Aero Calibration of Exhaust Total Pressure Rake.	115
4-18	Variance in PWL Due to Variances in Nozzle Exit and Ambient Pressures and Temperatures.	118
4-19	Variance in PWL Due to Variances in Nozzle Exit and Ambient Pressures and Temperatures - Constant σ_{PWL} Contours.	119
4-20	Variance in PWL Due to Variances in Nozzle Exit and Ambient Pressures and Temperatures in Low-Velocity Range.	121
4-21	Variance in PWL Due to Variances in Nozzle Exit and Ambient Pressures and Temperatures in Low-Velocity Range - Constant σ_{PWL} Contours.	122
4-22	Sound Level Variance Due to Aero Measurement Errors with the J79 Engine at GE/EFTC.	123
4-23	Open-Circuit rms Voltage Produced by Thermal Agitation in the Real Component of the Impedance of a Parallel Resistor and Condenser.	129
4-24	RMS Noise Voltage Produced by a 640-AA Condenser Microphone in Bands 1 Cycle Wide as a Function of Frequency with Two Different Load Resistors.	130
4-25	Predicted Electronic Noise Floor of the JENOTS Microphone System with the Wideband Group II Tape Recorder and Locked Vernier Amplifier.	132

LIST OF ILLUSTRATIONS (Continued)

Figure		Page
4-26	Predicted Electronic Noise Floor of the JENOTS Microphone System with the Wideband Group II Tape Recorder and B&K 4133 Microphone Vernier Coupler Set to Give Maximum Output of 124 dB at +10 Gain Setting.	133
4-27	Predicted Electronic Noise Floor of the JENOTS Microphone System with the Wideband Group II Tape Recorder and B&K 4135 Microphone Vernier Coupler Set to Give Maximum Output of 124 dB at +20 Gain Setting.	134
4-28	Predicted Electronic Noise Floor with Various Microphone Cathode Followers on the Wideband Group I Recorder and Locked Vernier Amplifier.	135
4-29	Relative Dynamic Range of Measured Data at a Fixed Gain Setting Above the Noise Floor.	137
4-30	Summary of Dynamic Range Capability with Various System Combinations.	138
4-31	Electronic Noise Floor Spectra of the 80° Microphone System with Shorted Cathode Follower.	139
4-32	Electronic Noise Floor Spectra of the 90° Microphone System with Shorted Cathode Follower.	140
4-33	Electronic Noise Floor Spectra of the 100° Microphone System with Shorted Cathode Follower.	141
4-34	Electronic Noise Floor Spectra of the 110° Microphone System with Shorted Cathode Follower.	142
4-35	Electronic Noise Floor Spectra of the 120° Microphone System with Shorted Cathode Follower.	143
4-36	Electronic Noise Floor Spectra of the 130° Microphone System with Shorted Cathode Follower.	144
4-37	Variability of the Electronic Noise Floor with Time (130° System).	146
4-38	Electronic Noise Floor Spectra of the 30° System with Microphone Covered by Piston Phone.	147

LIST OF ILLUSTRATIONS (Continued)

Figure		Page
4-39	Electronic Noise Floor Spectra of the 60° System with Microphone Covered by Piston Phone.	148
4-40	Electronic Noise Floor Spectra of the 90° System with Microphone Covered by Piston Phone.	149
4-41	Electronic Noise Floor Spectra of the 120° System with Microphone Covered by Piston Phone.	150
4-42	Electronic Noise Floor Spectra of the 150° System with Microphone Covered by Piston Phone.	151
4-43	Comparison of Jet Noise of a 2-inch Jet at M_j = 0.69 and θ = 90° with Electronic and Acoustic Background Noise at USC.	153
4-44	1/3-Octave Spectra of Jet Noise with Nozzle-off Noise at Equivalent Flow Rates at UBC (θ = 90°).	154
4-45	Comparison of Narrowband Spectra With and Without On-Line Filters at GE/EFTC.	155
4-46	Example of 1/3-Octave Data Before and After Noise Flow Corrections at GE/EFTC.	156
4-47	Comparison of JENOTS Ambient Noise Levels with Low Velocity Jet Spectra.	157
4-48	Facility Noise Comparisons at CR&DC.	158
4-49	Comparison of the Ambient Noise Level with Recorded Jet Noise at GE/EFTC.	159
4-50	Comparison of JENOTS Potential Noise Contaminates with the Jet Noise Level.	161
4-51	Normalized Power Spectra for Two Cold Subsonic Jets at USC.	162
4-52	UBC Comparison of OASPL at 90° for Jet Nozzle On and Off.	163
4-53	Airflow Contamination from the USC Facility at Low Velocities with a Cold Jet.	164

LIST OF ILLUSTRATIONS (Continued)

Figure		Page
4-54	Airflow Contamination from the UBC Facility at Low Velocities with a Cold Jet.	165
4-55	Airflow Contamination from the JENOTS Facility at Low Velocities with a Cold Jet.	166
4-56	Airflow and Core Noise Contamination from the J79 Engine at Low Jet Velocities.	167
4-57	J79 Turbomachinery Noise Suppressor Performance.	168
4-58	Velocity Dependence of the Normalized Overall Sound Pressure Level at 90° for the JENOTS Dual-Flow Installation.	170
4-59	Velocity Dependence of Normalized Overall Sound Pressure Level at 90° for the JENOTS Single-Flow Installation.	171
4-60	Narrowband of 60° (MIC-A) High Microphone at GE/EFTC.	172
4-61	Narrowband of 60° (MIC-B) Low Microphone at GE/EFTC.	173
4-62	Height of Tone Above 40 Hz Broadband Level to Add 1 dB to 1/3-Octave Band Level.	174
4-63	1/3-Octave Band Composite Spectra of the 70° Station at Idle Speed for a Conical Nozzle at GE/EFTC.	181
4-64	Velocity Dependence of Normalized Overall Sound Pressure Level at 90° for the J79 at GE/EFTC.	182
4-65	Near field MIC Setup at GE/EFTC.	183
4-66	Narrowband of Near-Field Microphone No. 2 at GE/EFTC.	184
4-67	Narrowband of Near-Field Microphone No. 3 at GE/EFTC.	185
5-1	General Behavior of Sound with Distance from a Source.	188
5-2	Variation of Pressure Fluctuation with Distance from Jet, Starting at 4 Diameters Downstream in the Jet and Proceeding at Right Angles to the Jet Axis at UBC.	189
5-3	Arrangement of Cable and Microphone for Spherical Divergence Test at USC.	191

LIST OF ILLUSTRATIONS (Continued)

Figure		Page
5-4	Intensity-Distance Plots with a 2-inch Cold Jet, $M_j = 0.85$, $\theta_I = 70°$ at USC.	192
5-5	Intensity-Distance Plots with a 2-inch Cold Jet, $M_j = 0.85$, $\theta_I = 90°$ at USC.	193
5-6	Intensity-Distance Plots with a 2-inch Cold Jet, $M_j = 0.85$, $\theta_I = 120°$ at USC.	194
5-7	Intensity-Distance Plots with a 2-inch Cold Jet, $M_j = 0.85$, $\theta_I = 150°$ at USC.	195
5-8	Intensity-Distance Plots with a 2-inch Cold Jet, $M_j = 0.85$, $\theta_I = 152°$ at USC.	196
5-9	Intensity-Distance Plots with a 2-inch Cold Jet, $M_j = 0.85$, $\theta_I = 153°$ at USC.	197
5-10	Intensity-Distance Plots with a 1-inch Cold Jet, $M_j = 0.85$, $\theta_I = 153°$ at USC.	198
5-11	Sound Field Geometry.	201
5-12	Working Curve for Calculating Null Frequency.	202
5-13	Theoretical Reflection Indices (1/3-Octave Bands) (Point Source over a Reflecting Surface).	203
5-14	Effect of Varying Phase on the Reflection Pattern.	207
5-15	Effect of Varying Coefficient of Reflection on the Reflection Pattern.	208
5-16	Schematic of Typical Jet Plume Source Distribution and Associated Frequency Distribution.	209
5-17	Geometry and Notation for Analysis of Ground Reflection Effects.	210
5-18	Normalized Jet Plume Source Strength Distribution.	212
5-19	Reflection Index Correction Due to Distributed Source Location for $\theta_I = 30°$ Angle at JENOTS.	218
5-20	Reflection Index Correction Due to Distributed Source Location for $\theta_I = 60°$ Angle at JENOTS.	219

LIST OF ILLUSTRATIONS (Continued)

Figure		Page
5-21	Reflection Index Correction Due to Distributed Source Location for θ_I = 90° Angle at JENOTS.	220
5-22	Reflection Index Correction Due to Distributed Source Location for θ_I = 120° Angle at JENOTS.	221
5-23	Reflection Index Correction Due to Distributed Source Location for θ_I = 160° Angle at JENOTS.	222
5-24	JENOTS Facility Operational Limit Lines for Less Than 1 dB Correction to Ground Reflection Index.	223
5-25	Comparison of 90° Microphone Narrowband Spectra of Jet Noise with Different Microphone Heights at JENOTS.	225
5-26	Elevation Projection of 15.93-foot Microphone Arc at JENOTS.	226
5-27	Altec Driver.	229
5-28	Sound Field Set Up for Altec Driver and Spark Test at JENOTS.	230
5-29	10-Hz Narrowband of White Noise Signal from Altec Driver at JENOTS.	231
5-30	Two-Hz Narrowband of Sweep Oscillator Signal from Altec Driver at JENOTS.	232
5-31	Spark Source.	233
5-32	Closeup of Spark Gap.	234
5-33	Spark Waveforms from Lab Test.	235
5-34	20-Hz Narrowband of 90° Far-Field (40 foot) Conic Nozzle Data (4.64-inch Diameter Cold Jet) at JENOTS.	237
5-35	20-Hz Narrowband of 90° Far-Field (40 foot) Dual-Flow Suppressor Data (V_{jp} = 2080 fps, V_{js} = 400 fps) at JENOTS.	238
5-36	Variation of Ground Phase Factor with Frequency at JENOTS.	239

LIST OF ILLUSTRATIONS (Continued)

Figure		Page
5-37	Working Curve to Calculate Reflection Coefficient, Q, from Difference Between Adjacent Peaks and Nulls.	243
5-38	Variation of Ground Reflection Coefficient with Frequency at JENOTS.	244
5-39	Variation of Energy Scattering Coefficient with Frequency.	246
5-40	JENOTS Test Facility in Evendale, Ohio.	248
5-41	Fiberglass Ground Treatment at JENOTS.	249
5-42	Elevation View of Reflection Paths at JENOTS.	250
5-43	Owens-Corning Fiberglass R-19 Nominal 6-in. Thick.	251
5-44	Prediction of Reflection Coefficient and Phase Factor Based on Experimental Data.	253
5-45	Prediction of Reflection Correction Index for JENOTS.	254
5-46	Comparison of Corrected Hard Ground Data to Data Taken with Fiberglass Bats at θ_I = 30° at JENOTS.	255
5-47	Comparison of Corrected Hard Ground Data to Data Taken with Fiberglass Bats at θ_I = 40° at JENOTS.	256
5-48	Comparison of Corrected Hard Ground Data to Data Taken with Fiberglass Bats at θ_I = 50° at JENOTS.	257
5-49	Comparison of Corrected Hard Ground Data to Data Taken with Fiberglass Bats at θ_I = 60° at JENOTS.	258
5-50	Comparison of Corrected Hard Ground Data to Data Taken with Fiberglass Bats at θ_I = 70° at JENOTS.	259
5-51	Comparison of Corrected Hard Ground Data to Data Taken with Fiberglass Bats at θ_I = 80° at JENOTS.	260
5-52	Comparison of Corrected Hard Ground Data to Data Taken with Fiberglass Bats at θ_I = 90° at JENOTS.	261
5-53	Comparison of Corrected Hard Ground Data to Data Taken with Fiberglass Bats at θ_I = 100° at JENOTS.	262
5-54	Comparison of Corrected Hard Ground Data to Data Taken with Fiberglass Bats at θ_I = 110° at JENOTS.	263

LIST OF ILLUSTRATIONS (Continued)

Figure		Page
5-55	Comparison of Corrected Hard Ground Data to Data Taken with Fiberglass Bats at θ_I = 140° at JENOTS.	264
5-56	Comparison of Corrected Hard Ground Data to Data Taken with Fiberglass Bats at θ_I = 150° at JENOTS.	265
5-57	Comparison of Corrected Hard Ground Data to Data Taken with Fiberglass Bats at θ_I = 160° at JENOTS.	266
5-58	Ground Reflection Corrections for Different Ground Treatments at CR&DC.	267
5-59	Ground Reflection Corrections, ΔdB, for Different Radii.	269
5-60	Acoustic Arena of the J79 at GE/EFTC Showing Two Microphone Setup.	270
5-61	Phase Factor Versus Frequency at GE/EFTC.	277
5-62	Coefficient of Reflection Versus Frequency at GE/EFTC.	278
5-63	Empirical Matching of High and Low Microphone Data at GE/EFTC.	279
5-64	Ground Reflection Precision Error at JENOTS.	283
5-65	Ground Reflection Precision Error at GE/CR&DC.	284
5-66	Ground Reflection Precision Error at GE/EFTC.	285
5-67	Peak OASPL Spectra for Conic Baseline at JENOTS.	287
5-68	JENOTS Microphone Mount.	288
5-69	Schematic of JENOTS Facility.	289
5-70	GE CR&DC Hot Jet Facility in Schenectady, New York.	290
5-71	Boom-Microphone Separation Effect at GE CR&DC.	292
5-72	Saddle-Microphone Separation Effect at GE CR&DC.	293
5-73	Unknown Spurious Reflection in the θ_I = 160° Microphone Data at GE/EFTC.	294

LIST OF ILLUSTRATIONS (Continued)

Figure		Page
5-74	Free Field Characteristics of Anechoic Chamber at USC.	295
5-75	Departure of Sound Pressure Levels from Free Field Conditions at USC.	297
5-76	Point Source Used for Spherical Divergence Tests at UBC.	298
5-77	UBC Free Field Calibration at UBC.	299
5-78	JENOTS Setup for Inverse Square Law Test.	300
5-79	JENOTS Inverse Square Law at Low Frequencies Using Microphone and Speaker at 12-inch Height.	302
5-80	JENOTS Inverse Square Law at Intermediate Frequencies Using Microphone and Speaker at 55-inch Height.	303
5-81	JENOTS Inverse Square Law at High Frequencies Using Jet Source and Microphone at 55-inch Height.	304
5-82	Variance in JENOTS Data from Inverse Square Law Line.	305
5-83	Spherical Divergence Tests at GE/CR&DC (Loudspeaker Acoustic Source).	307
5-84	Speaker Setup for Inverse Square Law Test at GE/EFTC.	308
5-85	Microphone Setup for Speaker Test at GE/EFTC.	309
5-86	Inverse Square Law at GE/EFTC.	310
5-87	High Frequency Speaker Results at GE/EFTC.	311
5-88	Standard Deviation of Speaker Data from Inverse Square Law at GE/EFTC.	312
6-1	Aerodynamic Test Domain for Referee Data.	316
6-2	Variation of Overall Power with Lighthill's Parameter for Referee Data.	317
6-3	Jet Density Exponent Vs. Jet Velocity.	318
6-4	Variation of Density Correction Factor with Jet Velocity and Temperature.	319

LIST OF ILLUSTRATIONS (Continued)

Figure		Page
6-5	Variation of Normalized Overall Power with Jet Velocity for the Referee Data.	320
6-6	Velocity Dependence of Normalized Overall Sound Pressure Level at 90° for the Referee Data.	322
6-7	Normalized Power Spectra for the Cold Jet Referee Data	323
6-8	Normalized Power Spectra for Lockheed and NGTE Data at 1260° R.	324
6-9	Normalized 90° SPL Spectra for the Cold Jet Referee Data.	325
6-10	Normalized 90° SPL Spectra for Lockheed and NGTE at 1260° R.	326
6-11	SPL Spectra at 90° for Cold and 1260° R Referee Data.	327
6-12	Domain of Operation of the USC Anechoic Chamber Jet.	329
6-13	Diagram Showing Contour of Subsonic Nozzle at USC.	330
6-14	Schematic Diagram Showing Contraction Section and Nozzle Contour at USC.	331
6-15	Variation of Overall Power with Lighthill's Parameter for the USC Data.	332
6-16	Variation of Normalized Overall Power with Jet Velocity at USC.	333
6-17	Velocity Dependence of Normalized Overall Sound Pressure Level at 90° for the USC Data.	334
6-18	Normalized Power Spectra for Two Cold Subsonic Jets at USC.	335
6-19	PWL Strouhal Spectra for Different Diameter Jets at USC.	336
6-20	PWL Frequency Spectra Variation with Cold Subsonic 2-inch Diameter Jets at USC.	337

LIST OF ILLUSTRATIONS (Continued)

Figure		Page
6-21	Normalized Power Spectra for Subsonic Heated Jets at USC.	338
6-22	Normalized Power Spectra for 1-inch Cold and Hot Supercritical Jets at USC.	339
6-23	SPL Spectra at 90° for 2-inch Cold Subsonic Jets at USC.	340
6-24	SPL Spectra at 90° for Various Diameter Cold Jets at USC.	341
6-25	SPL Spectra at 90° for 1-inch Hot Subsonic Jets at USC.	342
6-26	SPL Spectra at 90° for 1-inch Supercritical Jets at USC.	343
6-27	Domain of Operation of the UBC Anechoic Chamber Jet.	345
6-28	Schematic of Contoured Nozzle Used in Jet Noise Validation at UBC.	346
6-29	Shape of Nozzle Used at UBC.	347
6-30	Variation of Overall Power with Lighthill's Parameter for the UBC Data.	348
6-31	Variation of Normalized Overall Power with Jet Velocity for the UBC Data.	349
6-32	Velocity Dependence of Normalized Overall Sound Pressure Level at 90° for the UBC Data.	350
6-33	Normalized Power Spectra for Cold Subsonic Jets at UBC.	351
6-34	Normalized SPL Spectra at 90° for Subsonic Cold Jets at UBC.	352
6-35	Shape of the 5.7-inch-Diameter Convergent Nozzle at JENOTS.	353
6-36	Shape of the 4.31-inch-Diameter Convergent Nozzle at JENOTS.	354

LIST OF ILLUSTRATIONS (Continued)

Figure		Page
6-37	Shape of the 3.56-inch-Diameter Convergent Nozzle at JENOTS.	355
6-38	Shape of the 3.588-inch-Diameter Nozzle at JENOTS.	356
6-39	Shape of the 4.64-inch-Diameter, Baseline Coannular-Coplanar Nozzle at JENOTS.	357
6-40	Shape of Converging/Diverging (M = 1.55) Nozzle at JENOTS.	358
6-41	Domain of Aerodynamic Operation for JENOTS.	360
6-42	Variation of Overall Power Spectra with Lighthill's Parameter for JENOTS.	361
6-43	Variation of Normalized Overall Power with Jet Velocity for JENOTS.	362
6-44	Velocity Dependence of Normalized Overall Sound Pressure Level at 90° for the JENOTS Data.	363
6-45	ΔSPL Spectra Correlation at 90° with a Cold (650° R) and 1260° R Subsonic Jet at JENOTS.	364
6-46	ΔSPL Spectra at 90° for Subsonic ($V_j \sim$ 1000 ft/sec) Heated Jets at JENOTS.	365
6-47	Normalized Power Spectra for Subsonic Cold (500° R) Jet at JENOTS.	366
6-48	Normalized SPL Spectra at 90° for Subsonic Cold (500° R) Jets at JENOTS.	367
6-49	Normalized Power Spectra at JENOTS with Jets Heated to 1000° R.	368
6-50	Normalized 90° SPL Spectra at JENOTS with Jets Heated to 1000° R.	369
6-51	Normalized Power Spectra for Subsonic Jets at JENOTS Heated to 1260° R.	370

LIST OF ILLUSTRATIONS (Continued)

Figure		Page
6-52	Normalized SPL Spectra at 90° for Subsonic Jets at JENOTS Heated to 1260° R.	371
6-53	Normalized Power Spectra at JENOTS with Jets Heated to 1500° R.	372
6-54	Normalized 90° SPL Spectra at JENOTS with Jets Heated to 1500° R.	373
6-55	Normalized Power Spectra at JENOTS with Jets Heated to 2350° R.	374
6-56	Normalized 90° SPL Spectra with Jets Heated to 2350° R.	375
6-57	Certification Nozzle at CR&DC (D = 1 and 2 inches).	377
6-58	Domain of Operation for GE/CR&DC.	378
6-59	Variation of Overall Power with Lighthill's Parameter for the GE/CR&DC Data.	379
6-60	Variation of Normalized Overall Power with Jet Velocity for the GE/CR&DC Data.	380
6-61	Velocity Dependence of Normalized OASPL at 90° for the GE/CR&DC Data.	381
6-62	Normalized Power Spectra for Cold Subsonic Jets at GE/CR&DC.	382
6-63	Normalized SPL Spectra at 90° for Subsonic Cold Jets at GE/CR&DC.	383
6-64	Normalized Power Spectra, $T_{T_j} \sim 1500°$ R at GE/CR&DC.	384
6-65	Normalized Power Spectra, $T_{T_j} \sim 1900°$ R at GE/CR&DC.	385
6-66	Effect of Jet Heating at $V_j \sim 1000$ fps at GE/CR&DC.	387
6-67	Effect of Jet Heating at $V_j \sim 1500$ fps at GE/CR&DC.	388
6-68	Acoustic Certification Conic Nozzle at GE/EFTC.	389
6-69	Operation Domain of the J79 at GE/EFTC.	390

LIST OF ILLUSTRATIONS (Continued)

Figure		Page
6-70	Variation of Overall Power with Lighthill's Parameter for the J79 at GE/EFTC.	391
6-71	Variation of Normalized Overall Power with Jet Velocity for the J79 at GE/EFTC.	392
6-72	Velocity Dependence of Normalized Overall Sound Pressure Level at 90° for the J79 at GE/EFTC.	393
6-73	Normalized Power Spectra for the J79 Operating Line at GE/EFTC.	394
6-74	Normalized 90° SPL Spectra for the J79 Operating Line at GE/EFTC.	395
6-75	Normalized 60° SPL Spectra for the J79 Operating Line at GE/EFTC.	396
6-76	Normalized 120° SPL Spectra for the J79 Operating Line at GE/EFTC.	397
6-77	ΔSPL Spectra at 90° from the Inlet on the J79 Operating Line at GE/EFTC.	399
6-78	ΔSPL Spectra at 120° from the Inlet on the J79 Operating Line at GE/EFTC.	400
6-79	FluiDyne ASME Nozzle.	401
6-80	Channel 7 ASME Test Results for a 4.5-inch-Diameter Nozzle at FluiDyne.	403
6-81	Channel 11 ASME Test Results for a 5.5-inch-Diameter Cold Nozzle at FluiDyne.	404
6-82	Channel 11 ASME Test Results for a 2.5-inch-Diameter Hot Nozzle at FluiDyne.	405
6-83	ASME Test Results for 5.5-inch Cold and 2.5-inch Hot Nozzles at FluiDyne.	406
6-84	Supersonic Tunnel Association (STA) Nozzle Efficiency.	408

LIST OF ILLUSTRATIONS (Continued)

Figure		Page
7-1	Comparisons of Two Test Cases to the Microphone Noise Floor, Ambient Noise and Noise at JENOTS.	420
7-2	Test Spectra at GE/EFTC Compared to Microphone and Ambient Noise Levels.	421
7-3	Comparison of Two Test Cases to the Flow Noise, Ambient Noise and Microphone Noise Floor at GE/CR&DC.	422
7-4	Test Spectra at USC Compared to Microphone Noise Floor Level.	423
7-5	Test Spectra at UBC Compared to Flow Noise and the Microphone Noise Floor.	424
7-6	Standard Deviation of Data at JENOTS.	426
7-7	Standard Deviation of Data at GE/EFTC.	427
7-8	Standard Deviation of Data at GE/CR&DC.	428
7-9	Standard Deviation of Data at USC.	429
7-10	Standard Deviation of Data at UBC.	430
7-11	Effect of Wideband Group I Tape Recorder Noise Floor on Two Test Cases at JENOTS.	431
7-12	Effect of Wideband Group II Tape Recorder Noise Floor on Two Test Cases of JENOTS.	432
7-13	Effect of Tape Recorder Noise Floor on Two Test Spectra at GE/EFTC.	433
7-14	Effect of Tape Recorder Noise Floor on Two Test Spectra at GE/CR&DC.	434
7-15	Effect of Tape Recorder Noise Floor on Two Test Spectra at USC.	435
8-1	Source Location from Sound Pressure Level Contours.	442
8-2	Experimental Arrangement for Source Location by Traversing Microphone.	443

LIST OF ILLUSTRATIONS (Continued)

Figure		Page
8-3	Experimental Arrangement for Correlator Sound Source Study.	445
8-4	Coordinate System for the Image Technique.	447
8-5	Cross-Correlation of the Plane Surface Pressure and Far Field Pressure.	449
8-6	Experimental Arrangement for Source Location by the Shielding Method.	451
8-7	Comparison of Parabolic and Ellipsoidal Mirror Designs.	453
8-8	Cause Effect Correlation Experiment Showing Contamination Due to Dipole Radiation from Conventional Cylindrical Probe.	456
8-9	C_p Variation for Foil-Type Probe as a Function of Inclination Angle.	457
8-10	Geometry of Foil-Type Pressure Probe which Minimizes Interaction Errors in Plane of Foil.	458
8-11	Source Frequency Distribution in the Jet.	462
8-12	Acoustic Probe Contamination.	470
8-13	Variation of Pressure Fluctuation with Distance from Jet, Starting at 4 Diameters Downstream in the Jet and Proceeding at Right Angles to the Jet Axis.	473
8-14	Fundamental Error Mechanisms for Conventional Stem Design.	475
8-15	Single-Hole Cylindrical Probes.	479
8-16	Surface Pressure Response at M = 0.3 and Pitch = 0′ Angle for Various Single-Hole Cylindrical Probes.	480
8-17	Two-Hole Cylindrical Probe.	481
8-18	Engineering Sketch of Probe Cross Section.	482
8-19	Two-Hole Cylindrical and Rackl-Type Probes.	483

LIST OF ILLUSTRATIONS (Continued)

Figure		Page
8-20	Surface Pressure Response to Flow Mach Number, Yaw and Pitch Angle Variations for Probe 8.	485
8-21	Measured Maximum Surface Pressure for Various Two-Hole Cylindrical Probes at M = 0.4 and Pitch = 0°.	486
8-22	Comparison of Surface Pressure Response for Various Two-Hole Cylindrical Probes at M = 0.4 and Pitch = 0°.	487
8-23	Surface Pressure Response to Yaw and Pitch Angles at M = 0.2 for Probe 10.	488
8-24	Surface Pressure Response to Yaw and Pitch Angles at M = 0.4 for Two-Hole Cylindrical Probes Nos. 8, 10, and 10M.	489
8-25	Velocity Vector Direction Change in a 40-Chute Nozzle.	491
8-26	Surface Pressure Response to Yaw and Pitch Angles at M = 0.4 for Rackl-Type Probes Nos. 14, 15, and 16.	492
8-27	Surface Pressure Response to Yaw and Pitch Angles at M = 0.4 for Rackl-Type Probes Nos. 14 and 15.	493
8-28	Probe Noise Radiation at M = 0.4.	494
8-29	Schematic of Laser Velocity Measurements.	496
8-20	Comparisons of LV Measurements with Hot Film/Hot Wire Measurements for an Ambient Subsonic Jet.	498
8-31	LV Measurements of Mean Velocity and Turbulent Velocity Decay for a Shock-Free, High Velocity, High Temperature Jet.	499
8-32	LV-Measured Normalized Radial Mean Velocity Profiles for Shock-Free and Shock-Flow, High Velocity, High Temperature Jet.	500
8-33	LV-Measured Normalized Radial Turbulence Velocity Profiles.	501
8-34	LV-Measured Influence of Jet Velocity on Exit Plan Turbulence.	502

LIST OF ILLUSTRATIONS (Continued)

Figure		Page
8-35	LV-Measured Mean Velocity and Turbulence Intensity on Centerline for a High Velocity, High Temperature Jet.	503
8-36	Model for Sampling Process for LV Spectra.	504
8-37	LV-Measured Axial Turbulent Velocity Spectra for Ambient and Heated Jets.	505
8-38	Schematic of Sampling Scheme.	509
8-39	Bias Error in Derivative Estimate as a Function of Cutoff Frequency.	512
8-40	Influence of Window Function to Improve Stability of Second Derivative.	513
8-41	Schematic of System Used to Generate Simulated Data.	516
8-42	Simulation Specifications.	517
8-43	Analysis of Simulated Data, N = 20,000 Samples.	519
8-44	Analysis of Simulated Data, N = 100,000 Samples.	520
8-45	Analysis of Simulated Data, N = 500,000 Samples.	521
8-46	General Arrangement for LV to Far-Field Acoustic Cross-Correlation Experiments.	522
8-47	Test Arrangement Showing Microphone Slightly out of Plane for LV Far-Field Acoustic Cross-Correlation Experiments.	523
8-48	LV-Measured Normalized Cross Corelation of In-Jet Velocity to Far-Field Acoustic (180,000 Samples).	525
8-49	LV-Measured Cross-Power Spectrum.	527
8-50	Expected Shape of Cross Correlation and Cross-Power Spectrum without Ground Reflection.	528
8-51	Cross Spectra of Final Correlation Files.	529
8-52	Principle of Shadowgraph Detection.	535

Figure		Page
8-53	DC Voltage at Photodetector Output as a Function of Incident Light Intensity.	537
8-54	Sketch of Shadowgraph System.	539
8-55	Calibration Apparatus.	541
8-56	Photograph of Calibration Apparatus.	542
8-57	Photograph of Photodetector and Optics.	542
8-58	Calibration Apparatus Frequency Responses.	545
8-59	Schlieren and Shadowgraph Principles.	547
8-60	Photograph of Shadowgraph System with Calibration Apparatus Mounted.	548
8-61	Photograph of Shadowgraph System Mounted on Traversing Gear.	548
8-62	Typical Cross Correlation Records.	549
8-63	Acoustic Leakage and Nonclosure of Source Distribution.	552
8-64	"Hole-in-the-Wall" Experimental Apparatus.	554
8-65	Interaction Noise - Aperture Alone.	555
8-66	Strouhal Number of Peak Interaction Noise.	556
8-67	Effect of Axial Location of Aperture.	557
8-68	Power Spectra as a Function of Aperture Location, 1-inch Jet.	559
8-69	Decrease of Measured Acoustic Power with Aperture Location.	560
8-70	Axial Source Distribution (Percent OAPWL/X/D).	561
8-71	Decrease of Measured Acoustic Power, at Various Strouhal Numbers, with Aperture Location.	562

LIST OF ILLUSTRATIONS (Continued)

Figure		Page
8-72	Axial Source Distribution at Various Strouhal Numbers, 1-inch Jet.	563
8-73	Power Spectra as a Function of Aperture Location, 2-inch Jet.	564
8-74	Axial Source Distribution at Various Strouhal Numbers, 2-inch Jet.	565
8-75	Frequency Distribution of Jet Noise Sources with the GE Hole in the Wall.	566
8-76	Ellipsoidal Mirror Geometry.	568
8-77	Diffraction in the Ellipsoidal Mirror.	571
8-78	Fraunhaufer Diffraction Patterns for a Slot and Hole.	573
8-79	14-inch-Diameter Deep-Dish EM with 10.66-inch Working Distance.	578
8-80	18-inch-Diameter Shallow-Dish EM with 9-foot Working Distance.	579
8-81	36-inch-Diameter Deep-Dish EM with 15-foot Working Distance.	580
8-82	Altec Driver.	582
8-83	Resolution Window Width (3 dB Down) for 14-inch Ellipsoidal Mirror.	583
8-84	Gain of 14-inch Ellipsoidal Mirror.	584
8-85	18-inch Ellipsoidal Mirror Mounted on Rotary Actuator.	585
8-86	18-inch Relfector.	586
8-87	Resolution Volume of the Mirrors.	587
8-88	Gain of the Ellipsoidal Mirrors.	588
8-89	Ellipsoidal Microphone Installation at JENOTS.	589

LIST OF ILLUSTRATIONS (Concluded)

Figure		Page
8-90	Test Setup for Ellipsoidal Surveys.	591
8-91	Typical Mirror Surveys with a Convergent Nozzle Cold Jet.	592
8-92	Ellipsoidal Mirror Frequency Spectra.	594
8-93	Energy Distribution in the Jet from Ellipsoidal Mirror Surveys.	595
8-94	Frequency Distribution of Source Location in the Jet from EM Survey.	596
8-95	Generalized Source Distribution in a Supersonic Cold Jet from EM Survey.	598
8-96	Generalized Source Distribution in a Sonic Jet from EM Surveys.	599
8-97	Generalized Source Distribution in a Subsonic Cold Jet from EM Surveys.	600
8-98	Integral Closure Test of the Ellipsoidal Mirror.	601
8-99	Schematic Representation of Resolution Window Problem.	602
A-1	JENOTS Data - SPL Spectra FSDR Program Calculation.	612
A-2	JENOTS Data - PWL Spectra FSDR Program Calculation.	613
A-3	Revised Atmospheric Correction Factors.	614
A-4	Revised Atmospheric Absorption.	615
A-5	Atmospheric Attenuation Factors.	616
A-6	Total Absorption of Sound in Air as a Function of Frequency.	617

LIST OF TABLES

Table		Page
1-I.	Summary of Certified Facility Characteristics.	2
3-I.	Summary of Acoustic Data Acquisitions Systems.	20
4-I.	J79-15 Engine Noise Components.	176
4-II.	J79-15 Engine Noise Component Frequency Spectrum for Idle Speed.	177
5-I.	JENOTS Ground Reflection Corrections.	247
5-II.	Low Microphone Ground Reflection Corrections (J79 at EFTC).	273
5-III.	High Microphone Ground Reflection Corrections (J79 at EFTC).	275
5-IV.	Empirical Ground Reflection Corrections to J79 Data.	280
6-I.	FluiDyne Aero Facility Accuracies.	402
6-II.	Summary of Certified Facility Characteristics.	410
7-I.	Intermediate Standard Deviations at JENOTS.	414
7-II.	Intermediate Standard Deviations at GE/EFTC.	415
7-III.	Intermediate Standard Deviations at GE/CR&DC.	416
7-IV.	Intermediate Standard Deviations at USC.	417
7-V.	Intermediate Standard Deviations at UBC.	418
7-VI.	Comparison of Test Site Arc Radius and Nozzle Diameter.	419
7-VII.	Contamination from a Wideband Group II Tape Recorder at JENOTS.	436
7-VIII.	Contamination from a Wideband Group I Tape Recorder at JENOTS.	437
7-IX.	Contamination from an Intermediate Band Tape Recorder Noise Floor at USC.	438
7-X.	Standard Deviation of Test Case OASPL at Five Test Sites.	439

LIST OF TABLES (Concluded)

Table		Page
8-I.	Comparative Merits of Noninvasive Probe Systems.	466
8-II.	Experimental Study of Ellipsoidal Mirrors.	576
8-III.	Design Parameters of Ellipsoidal Mirrors.	581
8-IV.	Comparison of Measured and Estimated Window Size.	590
A-I.	Listing of the "GE" Air Attenuating Correction Computer Program.	618
A-II.	Summary of Ambient Conditions During Certification Testing of the Facilities.	622

1.0 SUMMARY AND CONCLUSIONS

This report contains the results of the Task 1 effort under Contract DOT-OS-30034 involving the activation of model jet test facilities and of a full-scale engine test stand to explore high speed jet acoustic and flow phenomena. The effort also involved the validation of techniques for establishing the noise source distribution in a jet plume.

1.1 FACILITIES

The facilities certified are summarized in Table 1-I. Documenting the facility information gathered in Task 1 provides assurance that any jet noise data recorded in subsequent program tasks will be acoustically clean, and represent uncontaminated jet noise. These pure jet noise results can thus be utilized with confidence to verify any or all postulated aero-acoustic analytical prediction techniques as well as to permit comparative evaluation of quantitative differences in acoustic and aerodynamic performance effectiveness among noise abatement nozzles.

The scale-model acoustic test facilities can deliver "pure" uncontaminated jet noise over the velocity range (600 to 3000 fps) and frequency range (400 to 80,000 Hz) of interest. The standard deviation of the data about its mean falls within ± 3 dB from 800 Hz to 20 kHz and less than ± 4 dB from 20 kHz to 80 kHz.

A J79 turbojet engine was activated along with an acoustic test site at Edwards Flight Test Center (EFTC), California, as the full-scale test stand. Turbomachinery noise contaminated the jet noise data near the engine idle power setting resulting in a useful jet noise testing range from an exhaust velocity of 750 fps to maximum power exhaust velocity of 2150 fps. The standard deviation of the precision error at this full-scale test site was less than ± 2 dB from 50 Hz to 1250 Hz, less than ± 3 dB from 1600 Hz to 10 kHz and less than ± 3.75 dB from 12.5 kHz to 20 kHz.

The two most serious contaminants are the lack of proper air attenuation corrections at high frequency and the electronic floor noise. Both of these effects can be significant above 20 kHz. The exact relationships for the air attenuation model at high frequency are yet unknown, so a bias in the correction factors is possible. Electronic noise floor limits encountered with the "peaky" spectra near the jet axis can be improved by utilizing high pass filters and two microphone setups. Corrections for electronic noise floor on final spectral shape should be analyzed with air attenuation removed using an appropriate air absorption model.

The accuracy of the aerodynamic instrumentation at the acoustic facilities was excellent. A statistical study of the variance showed that significant variability is possible only at low velocity, high temperature conditions and, therefore, of no consequence in the realm of actual engine operating conditions.

Table 1-I. Summary of Certified Facility Characteristics.

Facility/Item	USC	UBC	GE/JENOTS (Coannular and Single Flow) Primary	GE/JENOTS (Coannular) Secondary	GE/CR&DC	GE/EFTC- J79A	FluiDyne - Channels 7, 12, 13, and 11	NASA Lewis 8 ft x 6 ft Wind Tunnel
• Application	Orderly Structure (Task 2)	Laser Shadowgraph (Task 1); Lip Noise (Task 2)	EM Verification (Task 1) Lip Noise (Task 2), Baseline and Suppressed Nozzles (Task 3 and 4)	EM Verification (Task 1) Lip Noise (Task 2), Baseline and Suppressed Nozzles (Task 3 and 4)	Hole-in-the-Wall (Task 1) Basic Experiments in Support of Theoretical Developments (Task 2)	Acoustic Scaling Demonstration (Task 3)	Replaced by NASA Lewis Facility	Thrust and Flow Measurements (Task 3, 4 and 5)
• Nozzle Diameter Range, inches	1 and 2	~3/4	2 to 6	~12	1 and 2	20.84	8	5
• Max. Weight Flow, lbm/sec	~3.5	~0.28	~80	~50	8	160	40	30
• Jet Velocity Range Certified, fps	600 to 1750	600 to 1050	600 to 3000	600 to 1050	600 to 1900	750 to 2150	Velocities Corresponding to Pressure Ratios up to 4.0	Velocities Corresponding to Pressure Ratios in excess of 4.0
• Jet Total Temperature Certified, °R	540 to 1040	540	540 to 2500	540	540 to 1900	1000 to 1600 per Operating Line	540 to 1700	540
• Thrust Measurement Capability	No	No	No	No	No	Yes	Yes	Yes
• Acoustic Arena	Anechoic	Anechoic	Outdoor Cement Pad to 20 feet, Crushed Rock From 20 ft to 40 ft	Outdoor Cement Pad to 20 feet, Crushed Rock From 20 ft to 40 ft	Outdoor Foam Covered Pad	Outdoor Packed Desert Sand	N/A	N/A
• Microphone Arc Radius, ft	7.5	10	40	40	9	160	N/A	N/A
• Microphone Distributed Angle from Inlet, Degrees	10 Microphones from 70° to 160° Staggered Intervals	1 Moving Microphone from 80° to 180°	14 Microphones Every 10° from 20° to 160°	14 Microphones Every 10° from 20° to 160°	12 Microphones Every 10° From 50° to 160°	26 Microphones (2 per Angle) Every 10° From 40° to 160°.	N/A	N/A
• Microphone Height Above Ground, ft	N/A	N/A	15.91	15.91	6 to 15, Function of Azimuthal Position of Boom	2 and 12	N/A	N/A
• Nozzle Centerline Above Ground, ft	N/A	N/A	4.58	4.58	6	12	N/A	N/A
• Certified 1/3-OB Frequency Range, Hz	315 to 80,000	315 to 80,000	400 to 80,000	400 to 80,000	315 to 40,000	50 to 20,000	N/A	N/A
• Precision OASPL Max./Min. at 90°, σ ± dB	0.32/0.30	0.29/0.27	0.53/0.41	0.53/0.41	0.35/0.32	0.38/0.37	N/A	N/A
• Frequency Range Precision	400 Hz: 3.75 dB 500 Hz: 2.75 dB 6.30 kHz to 10 kHz: 1.25 dB	200 Hz to 1000 Hz: <1 dB 1000 Hz to 63 kHz: 1.25 dB 80 kHz: 1.75 dB	200 Hz to 630 Hz: 3 to 3.75 dB 800 Hz to 63 kHz: <3 dB 80 kHz: 3.75 dB	200 Hz to 630 Hz: 3 to 3.75 dB 800 Hz to 63 kHz: <3 dB 80 kHz: 3.75 dB	400 Hz to 630 Hz: <3 dB 800 Hz to 40 kHz: <3 dB	50 Hz to 1250 Hz: <3 dB 1600 Hz to 10 kHz: <3 dB 12.5 kHz to 20 kHz: 3.75 dB	N/A	N/A

Contamination from ambient background noise was insignificant. Facility related noise from flow piping, valves, and combustors or heaters (and turbomachinery on the J79) was effectively eliminated through the use of acoustically-treated mufflers.

All of the test facilities have measurement arc radii greater than 50 nozzle diameters, considered a minimum based on experimental results to date, and all facilities exhibited inverse square law characteristics (6 dB decrease for each doubling of distance, with a nominal variance of ±1 dB).

Classical ground reflection theory was modified to account for non-anechoic ground impedance, jet scattering, and distributed jet noise source effects for the General Electric Jet Exhaust Noise Outdoor Test Stand (JENOTS) and the EFTC/J79 outdoor facility. Effective free field was attained at GE/JENOTS by placing the microphones to a given height so that the first ground null was below the lowest frequency of interest and then applying corrections from the aforementioned modified classical ground reflection theory. The J79 turbojet setup at GE/EFTC utilized two microphones to reconstruct a "composite spectra" after the respective microphone spectra were corrected by the modified reflection theory.

The precision errors introduced by the ground reflections were only significant at frequencies around the first few cancellation nulls where the spectra was rapidly changing with frequency.

Round nozzle noise spectra obtained from the facilities were found to be in substantial agreement with acknowledged "referee" data from several sources, thereby validating the facilities as well as the data acquisition capabilities and correction techniques.

Aerodynamic performance testing at either the FluiDyne Engineering Corporation or the NASA Lewis 6 x 8 foot wind tunnel facilities were determined to result in very high quality data.

1.2 SOURCE LOCATION TECHNIQUES

A screening study of potential noise source location techniques resulted in experimental investigations of four techniques: (1) optimum-shaped probe stems (point source information), (2) laser shadowgraph causality correlations (point source information), (3) "hole-in-the-wall" isolation technique (essentially slice of jet information), and (4) ellipsoidal mirror microphone (essentially slice of jet information). A fifth technique using laser velocimeter causality correlations (point source information) was investigated under a separate DOT/USAF sponsored program (USAF Contract F33615-73-C-2031).

Acoustic probes were found to have a domain of operation limited to jet Mach numbers below 0.7 (~ 1000 fps) and to jet total temperatures below 1000° R (uncooled) or 1600° R (cooled), as well as to turbulence angle swings (velocity vector variations) not exceeding 15°. The laser shadowgraph method produced only qualitative results because of unwanted Schlieren type behavior

in the optical system. The "hole-in-the-wall" gave reasonable results, but its applicability is limited by the need of asymmetric apertures when using noncircular (2D) and suppressor nozzles.

Both the ellipsoidal mirror microphone and the "hole-in-the-wall" methods were found to give acceptable macroscopic source distribution information. However, the inherent simplicity and flexibility of the ellipsoidal mirror microphone made it the prime choice for future noise source mapping on subsequent program tasks.

Comparison of ellipsoidal mirror microphone data with other investigator's data and techniques showed good agreement at the peak level versus distance recorded at each one-third octave frequency (within 3 dB). Pseudo-sound oscillations indicative of the jet near field did not permit acquisition of valid data below 1000 Hz, however, for the mirror design selected for the Task 1 study. The mirror also exhibited a loss of resolution due to the diffraction "window function."

A new "deep dish" mirror with a longer working distance was designed and fabricated to permit good data acquisition down to about 400 Hz. A numerical relaxation technique was adapted and implemented as part of the data reduction computer program to remove the diffraction "window function" effects from the mirror data. These improvements were utilized in subsequent program Tasks 3 and 5.

The results of the Task 1 facility activation and noise source location technique evaluation give the assurance that data acquired in this and future programs will accurately represent the acoustic mechanisms associated with jet noise suppressor nozzles.

2.0 INTRODUCTION

2.1 GENERAL OBJECTIVES

The cornerstone to the success of any test program is the accuracy of the test facilities and instrumentation. To ensure the best possible data over the full range of conditions with the best available instrumentation, a detailed checkout of the proposed test facilities and source location techniques was instituted in Task 1 of the DOT High Velocity Jet Noise Source Location and Reduction Contract (DOT-OS-30034). The detailed work plan, Task 1 (Reference 1) had the following specific objectives:

1. Activate the test facilities required for future testing, making the necessary modifications to give data within the required performance domain in terms of jet velocity and total temperature.

2. Classify and document the limitations of each test facility as to its ability to produce pure jet noise within the frequency range of interest. Make the necessary modifications to minimize contaminating effects. When facility modifications are deemed too expensive to undertake, determine necessary correction factors to the data.

3. Explore and establish the relative potential noise source measurement techniques. Demonstrate several pertinent methods to determine the range of application and relative quantitative error experienced with each technique.

2.2 FACILITY VALIDATION

The original General Electric program plan for carrying out the testing portions of the entire DOT Contract (Reference 2) identified five acoustic facilities and one aerodynamic facility for activation and certification in Task 1. The list was composed of:

- Two anechoic rooms; the University of British Columbia (UBC) in Vancouver, British Columbia, Canada, and at the University of Southern California (USC) in Los Angeles, California, respectively, for small-scale specialized testing of noise source mechanisms.

- Two outdoor scale-model facilities; at the General Electric Jet Exhaust Noise Outdoor Test Stand (JENOTS) in Evendale, Ohio, and the General Electric Corporate Research and Development Center (CR&DC) Outdoor Jet Facility in Schenectady, New York, for basic suppression principle and parametric concept testing.

- One large scale engine outdoor test facility utilizing the J79 engine at the General Electric Facility at Edwards Air Force Base Flight Test Center (GE/EFTC) for acoustic testing.

- The FluiDyne Engineering Corporation at Medicine Lake, Minnesota, to perform static aerodynamic performance testing.

This report contains a detailed description of the above facilities and certification as to their accuracy.

The method of approach for certifying and validating the various test facilities and source location/measurement techniques was outlined in Reference 3. In compliance with the detailed work plan, each of the test facilities was investigated as to its capability in delivering a "clean" jet sufficiently free of internal noise to enable proper evaluation of the data. In particular, each facility was studied as to its relative cleanliness from the following points of view:

1. Pure jet noise: Contamination due to:

   - Air Compressors
   - Burners
   - Turbomachinery (J79 only)
   - External background noise

2. Free field environment: The effect on the data as effected by:

   - Ground reflection and refraction
   - Obstruction reflection and reverberation
   - Environmental effects

3. Certification testing: The resulting jet acoustic signals were normalized to remove scaling effects and compared with classical data and semiempirical laws.

The accuracy of the acoustic measurement at each facility was determined throughout the test frequency and operation domain. The goal of Task 1 was to obtain an accuracy less than ± 3 dB standard deviation from the lower frequency of interest to 20 kHz and within ± 5 dB from 20 kHz to 80 kHz. The resulting variation in the overall level was required to be within ± 2 dB. These objectives were easily obtained and much tighter tolerance bands have been determined for each of the facilities.

Near the end of the Task 1 effort, a redirection in the overall program plan eliminated the University of Southern California anechoic room and FluiDyne Engineering Corporation facility from further consideration. General Electric's construction of a large anechoic facility was adapted for some of the subsequent scale-model suppressor testing in the program. The aerodynamic and thrust measurements of models previously planned to be made at FluiDyne were now planned to be conducted in the NASA Lewis 6 x 8 foot wind tunnel. This change in direction occurred after activation

and validation of the USC anechoic room and FluiDyne Aero facility had already been completed, so this work is also included in the present document. A discussion of the NASA Lewis 8 x 6 foot wind tunnel data accuracy assessment is included in this report. A supplementary report on the certification of the General Electric anechoic facility was issued as a companion document to this Task 1 report (FAA-RD-76-79, Ia).

Activation/certification of methods of flight simulation were carried out under Task 4 of this program, "Development/Evaluation of Techniques for Inflight Investigation." Task 4 verification activity included a series of controlled flyover tests (F106, Lear Jet aircraft, moving-frame (Bertin Aerotrain), and fixed frame (JENOTS free jet) tests on various unsuppressed and suppressed exhaust systems. The results of Task 4 are available in the Task 4 Final Report (FAA-RD-76-79, IV).

2.3 NOISE SOURCE MEASUREMENT TECHNIQUES

Numerous methods have been proposed for measuring the distribution of jet noise sources in the exhaust plume including:

- Hole-in-the-wall
- Parabolic or spherical mirrors
- Two mirror techniques
- Acoustic lens
- Infrared readings from the jet
- Equal intensity contours
- Two-point (in-jet - in-jet) cross correlations
- In-jet far-field cross correlations
- Microphone array
- Ellipsoidal mirror
- Plane image technique
- Pressure gradient microphone
- Acoustic watt meter

All of these methods were subjected to a screening study which identified (1) hole-in-the-wall, (2) ellipsoidal mirror, and (3) in-jet - far-field correlations as the most promising candidates to be carried through

an experimental/demonstration stage to determine the validity and range of application of each. The study resulted in recommending the use of the ellipsoidal mirror for subsequent tasks.

The point noise source location experiments conducted under the USAF/DOT Supersonic Jet Exhaust Noise Program (Contract F33613-73-C-2031) indicated that some degree of success was attained in cross-correlating in-jet velocity squared (from the laser-velocimeter) and far-field acoustic pressure. Subsequent work verified these observations. General Electric independently sponsored another area of noise source location development work, e.g., the two-point (in-jet - in-jet) cross-correlation technique, which was subsequently demonstrated during the Task 3 test program.

2.4 REPORT ORGANIZATION

This report is organized as follows:

- Section 3.0 describes all the facilities studied in Task 1.
- Section 4.0 describes the methods used to establish the relative acoustic cleanliness of the measured jet noise.
- Section 5.0 describes the approaches used to ensure free-field data.
- Section 6.0 shows the results of certification testing and comparison with classical data and laws.
- Section 7.0 presents acoustic measurement precision from the various test facilities.
- Section 8.0 describes the validation of the various source location techniques.
- Section 9.0 states the conclusions and recommendations.
- An Appendix to air attenuation corrections presented in Section 4.0

3.0 ACTIVATION OF FACILITIES

3.1 INTRODUCTION

All of the acoustic test facilities identified for use on the High Velocity Jet Noise Source Location and Reduction Program required some degree of modification to meet the specifications for the contract. In the case of UBC, CR&DC, and J79 engine at EFTC either completely new facilities were constructed or existing ones totally refurbished, whereas at JENOTS and USC, only minor modifications were required. The Fluidyne facility and the NASA Lewis 8 x 6 foot wind tunnel met all the aerodynamic requirements, and no modifications were required.

3.2 UNIVERSITY OF SOUTHERN CALIFORNIA ANECHOIC ROOM

The acoustic laboratory was established in 1970 under DOT grant number DOT-OS-000002. It is located in the north wing of the Vivian Hall of Engineering on the campus of the University of Southern California, Los Angeles.

As shown in Figure 3-1, the facility consists of an anechoic chamber, a blow-down type jet arrangement with an electrical heater for hot jet experiments. Certification of the facility was conducted in the August 1973 to August 1974 time period. A report of this work is found in Reference 3.

3.2.1 Anechoic Chamber

The anechoic chamber was manufactured by Eckel Industries, Inc. It has a working space measuring 20 feet 4 inches x 15 feet 8 inches x 11 feet 11 inches, and is "floated" on vibration isolators. The walls are constructed of 4-inch-thick Eckoustic Type H panels with 18-gauge JP galvanized steel facings on both sides and fiberous glass packing. The interior of the room is equipped with glass fiber wedges which have a "depth" of 16-1/2 inches designed for a low frequency cutoff of 150 Hz. A 4 x 4 foot opening and a baffled venting duct has been provided for free passage of air to the outside of the room. At the end of the venting duct, an exhaust fan has been installed to help ventilate the chamber after a hot jet experiment. A picture of the interior of the room is shown in Figure 3-2. Jet noise is carried out at a distance of about 90 inches from the nozzle exit. Ten B&K microphones are mounted on a curved pipe forming an arc centered at the nozzle exit as shown in Figure 3-2. These microphones were arranged at different angles from the jet axis, as depicted in Figure 3-3. The closest approach of the microphone to the wedge tips occurs at the 90° station where a 20-inch distance is obtained, as shown on Figure 3-3. For hot jet experiments, a thermocouple is placed at the 160° microphone position (20° from jet exhaust) to ensure that the room temperature does not rise above the

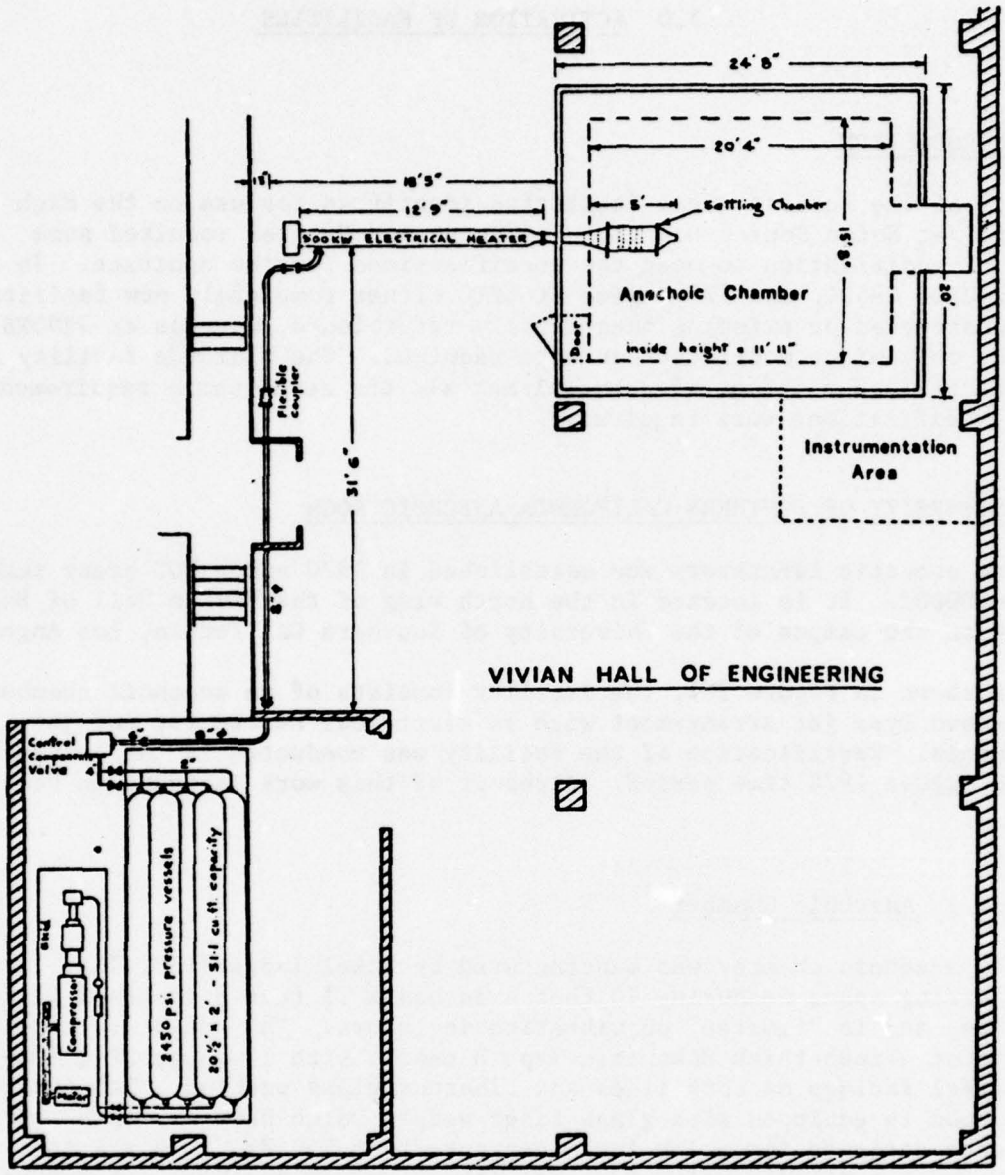
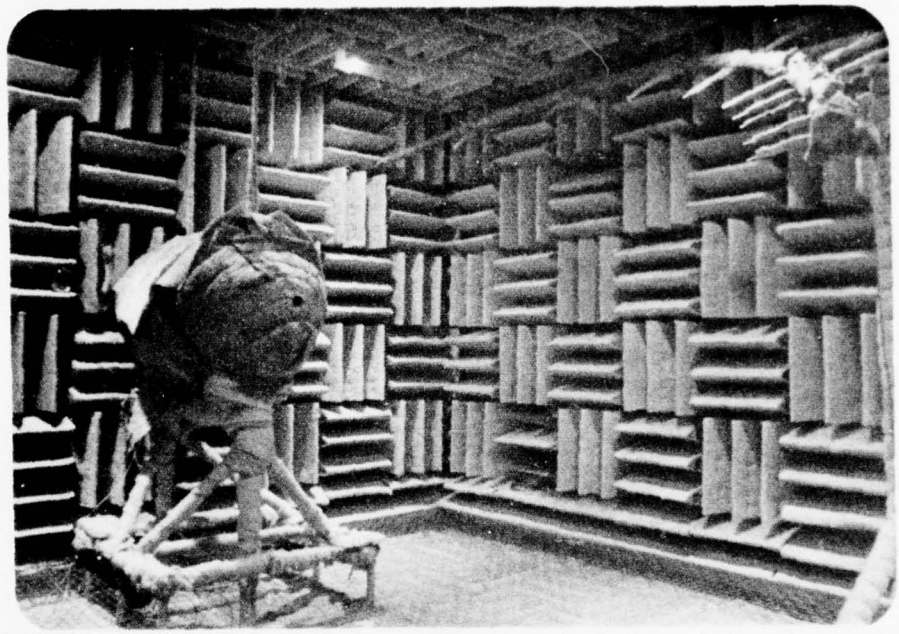


Figure 3-1. Jet Noise Research Facilities at USC.



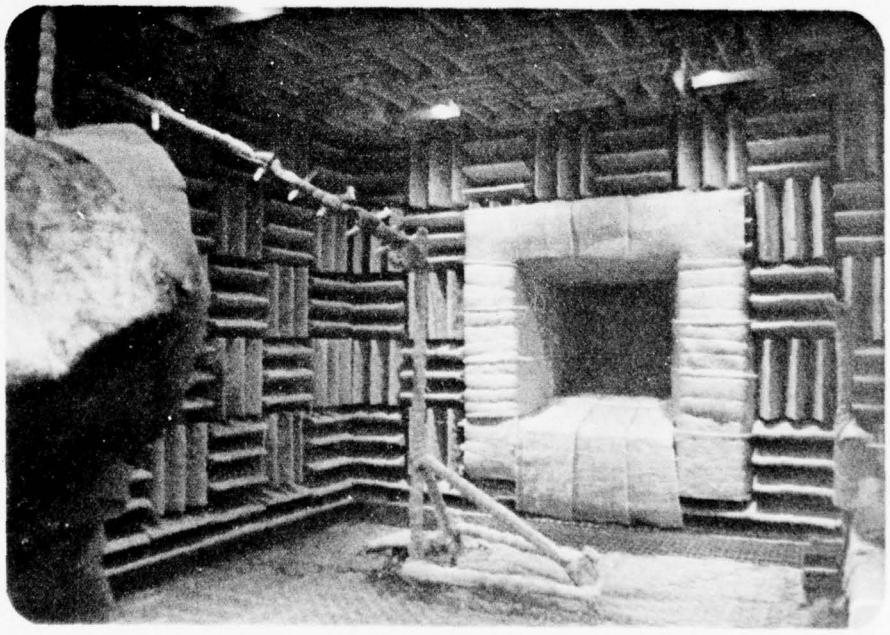


Figure 3-2. Interior of USC Anechoic Chamber.

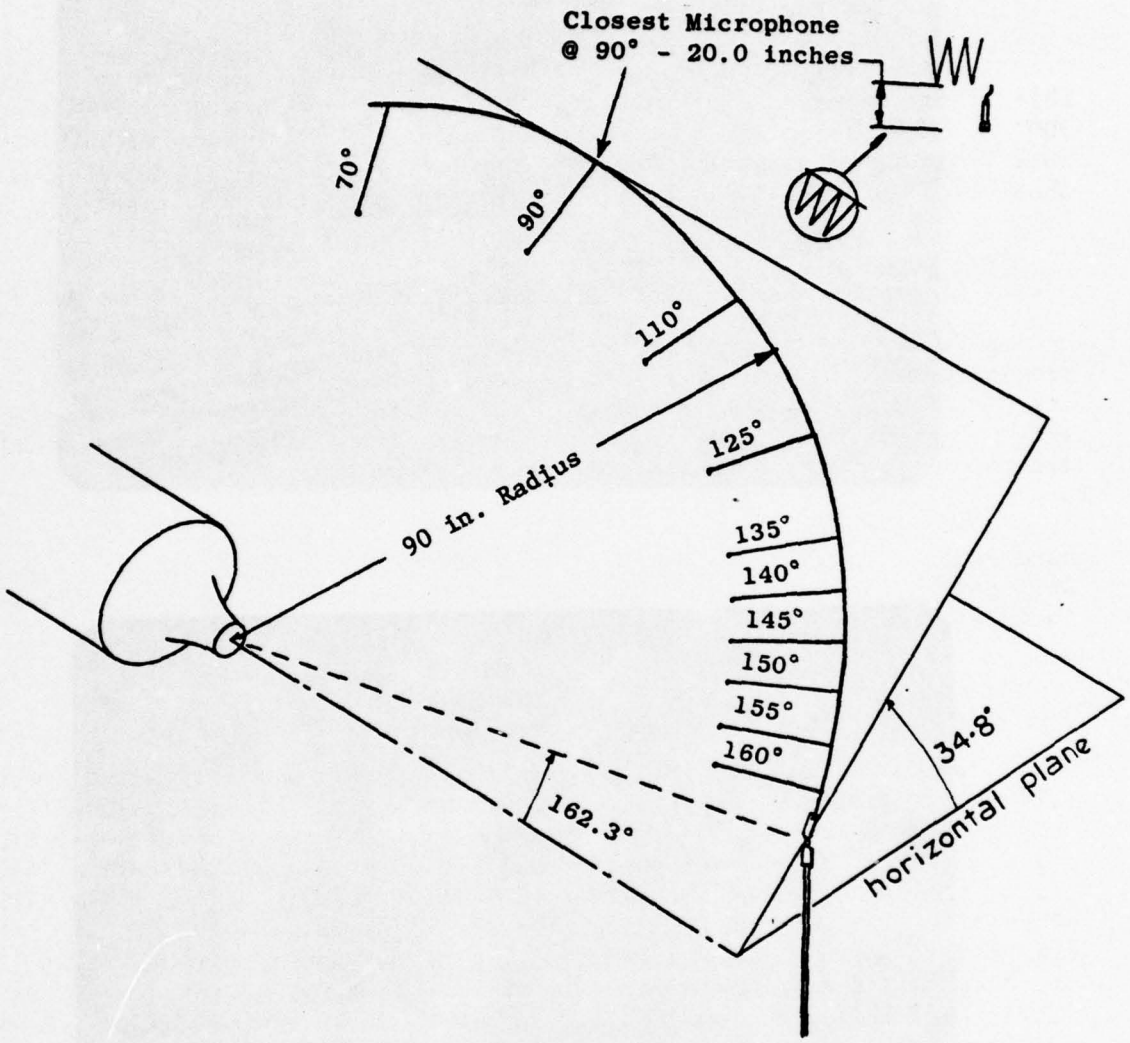


Figure 3-3. Schematic Diagram Showing Arrangement of Microphones for Far Field Measurements at USC.

tolerance limit of the microphone system. Depending on the Mach numbers of the runs, either 1/8-, or 1/2-inch microphones were chosen to give the best signal-to-noise frequency limits.

3.2.2 Jet Facilities

The jet facilities belong to the intermittently operating class capable of providing cold or hot jet flows up to a stagnation temperature of 900° F. The system can provide a maximum mass flow rate of 6.8 lbm/sec up to a 7-minute running time for cold flow. A schematic of the layout is shown in Figure 3-1. The system consists of the following items.

3.2.2.1 Compressor and Pressure Vessels

A 75 HP - 2500 psi - 142 cfm Chicago pneumatic water-cooled air compressor with a mechanical filter and a chemical dehydration system provides dry air with a dewpoint of -48° F. The compressor is mounted on a concrete skid, as shown in Figure 3-4, in a room at some distance from the chamber, and is not operated during tests.

There are five 2450 psi - 51.1 ft^3 capacity United States Steel pressure vessels, each measuring 20 feet 6 inches long and 2 feet in diameter. They can be connected in combinations of two and three, or five, together, as shown in Figure 3-4.

3.2.2.2 Pressure Reducing Valve and Regulator

The control valve of the present system is a "state-of-the-art" low self-noise "drag" valve by Control Component, Inc., of Irvine, California. Utilizing a patented multiple disk technique, the valve divides the incoming flow stream into a series of smaller flow streams. Each small flow stream is then directed through an individual passage containing a series of right-angle turns to effect the necessary pressure drop. To complete the valve trim, a predetermined grouping of the disks, with multiple flow passages etched onto their faces are stacked and positioned around the valve plug. The one used in the present system is a 4-inch inlet and 6-inch outlet angle valve. Figure 3-5 shows the outlet face of these stacked discs, and Figure 3-6 shows its location in the system.

This low noise valve has made it possible to study jet noise down to fairly low Mach numbers, as reported in Reference 4.

Because of the nonlinear characteristics of this special valve, considerable difficulties were experienced in regulating it. After some experimenting, it is now possible to regulate the settling-chamber pressure to within ±3%. The regulator used is a Honeywell's batch air-0-line controller model RY 704P1-P1-(93).

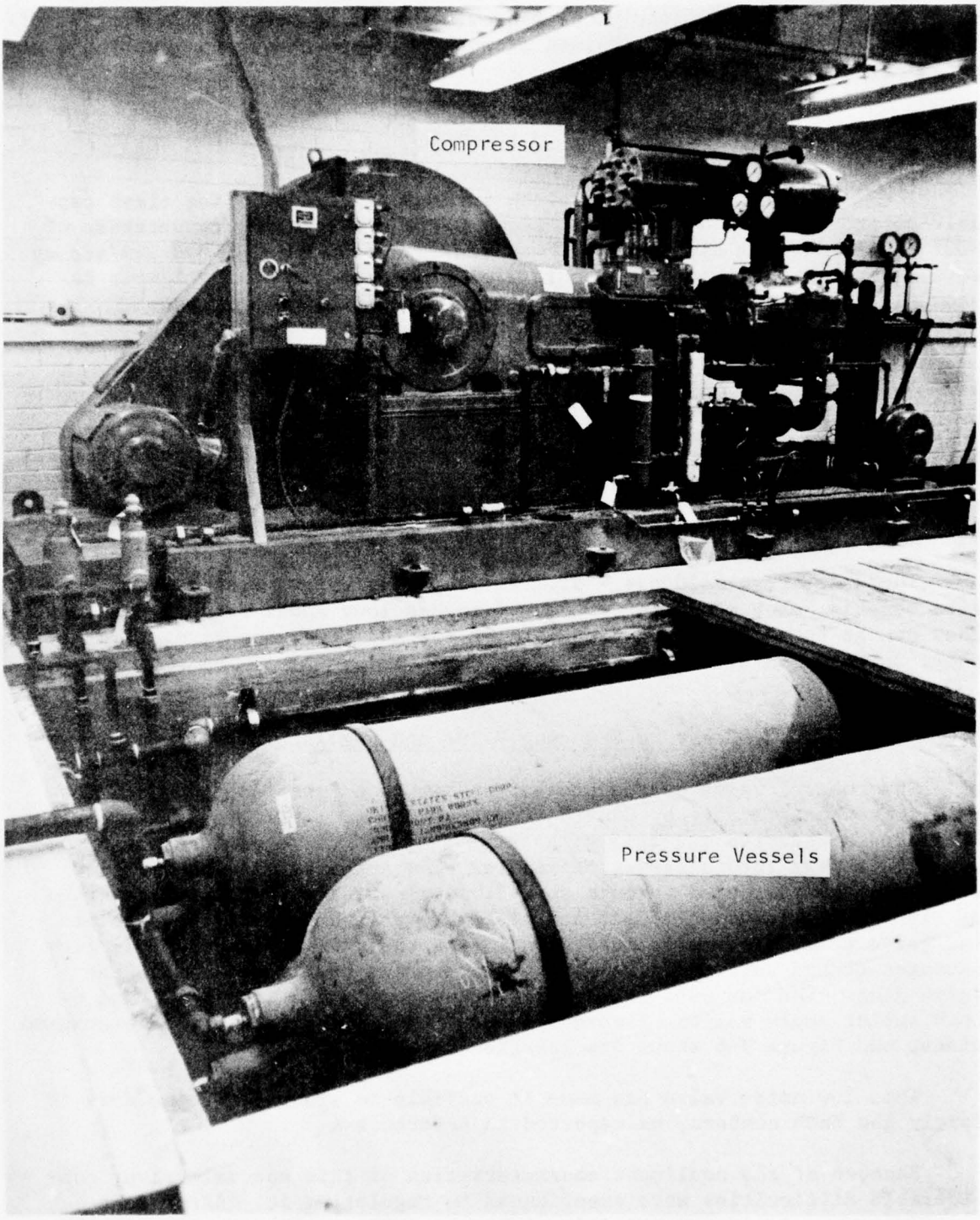


Figure 3-4. USC Compressor and Pressure Vessels.

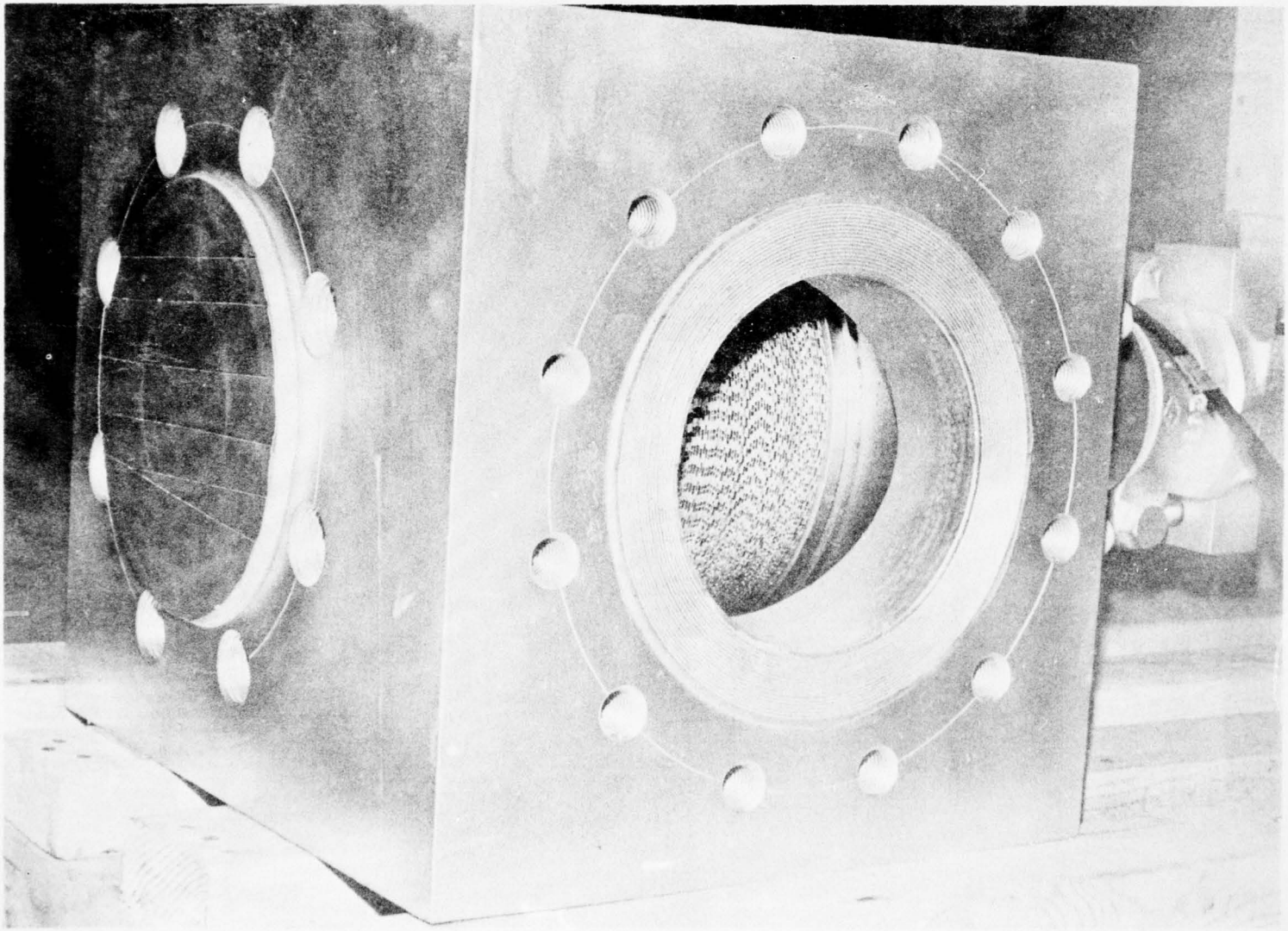


Figure 3-5. Details of USC Valve Disc.

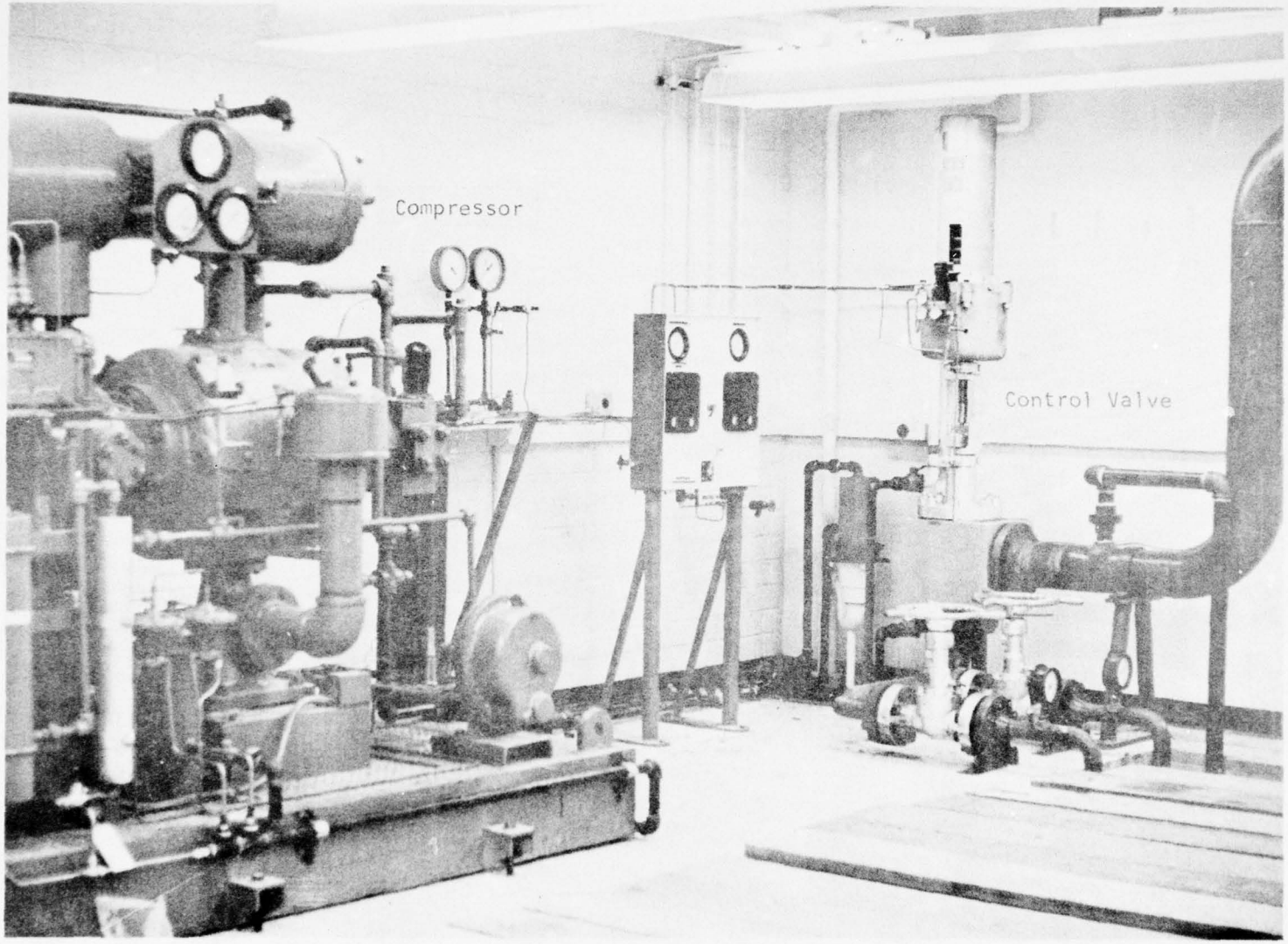


Figure 3-6. Compressor and Control Valve at USC.

3.2.2.3 Electrical Heater

The electrical heater is a 500-kilowatt Hynes Radi-Fin heater utilizing 480-volt, 3-phase 60-Hz electric power. It is capable of providing a stagnation temperature of 900° F for M = 2.5, 1-inch-diameter supersonic jet. The heater is 12-3/4 inch OD x 15 foot long constructed of 304 stainless steel.

The heater is controlled and regulated by a 500-kVA SCR power control unit made by Crydom Controls.

The heater is installed immediately after the settling chamber, and is anchored at the joint with the settling chamber. The other end of the heater is free for thermal expansion. A flexible coupler has been installed in the piping system to accommodate such expansion as shown in Figure 3-1.

The piping connecting the control valve and the heater is 8 inches in diameter and is about 40 feet long.

3.2.2.4 Settling Chamber and Nozzles

Figure 3-7 shows a schematic drawing of the settling chamber and a subsonic nozzle. It is designed for a maximum pressure of 250 psi at maximum temperature of 900° F, and consists of a rapid expansion cone followed by a 3-foot straight section of 18 inches in diameter. To prevent separation in the expansion cone, three screens of appropriate mesh sizes are installed at the designed locations. Five fine screens and a layer of steel wool are installed in the settling chamber section to reduce turbulence in the flow. As a result, the turbulence intensity measured inside the settling chamber just before the contraction is about 0.4%. This level would further be reduced by the contraction.

3.2.2.5 Recording Equipment

During any experiment, the settling chamber pressure was monitored by means of a Validyne Model DP 15TL pressure transducer located at a wall top halfway between the last screen and the nozzle contraction as shown in Figure 3-7. The chamber pressure was recorded on the HP Model 3955 tape recorder and displaced on the Gould Brush Model 220 chart recorder. The Validyne pressure transducer has a changeable diaphragm for different pressure ranges (±1, ±5, ±20, ±75, and ±250 psig) and has an accuracy of 0.5%. The settling chamber stagnation temperature was monitored at the same plane as the pressure measurement by means of a calibrated thermocouple whose output was also recorded on the Gould Brush chart recorder.

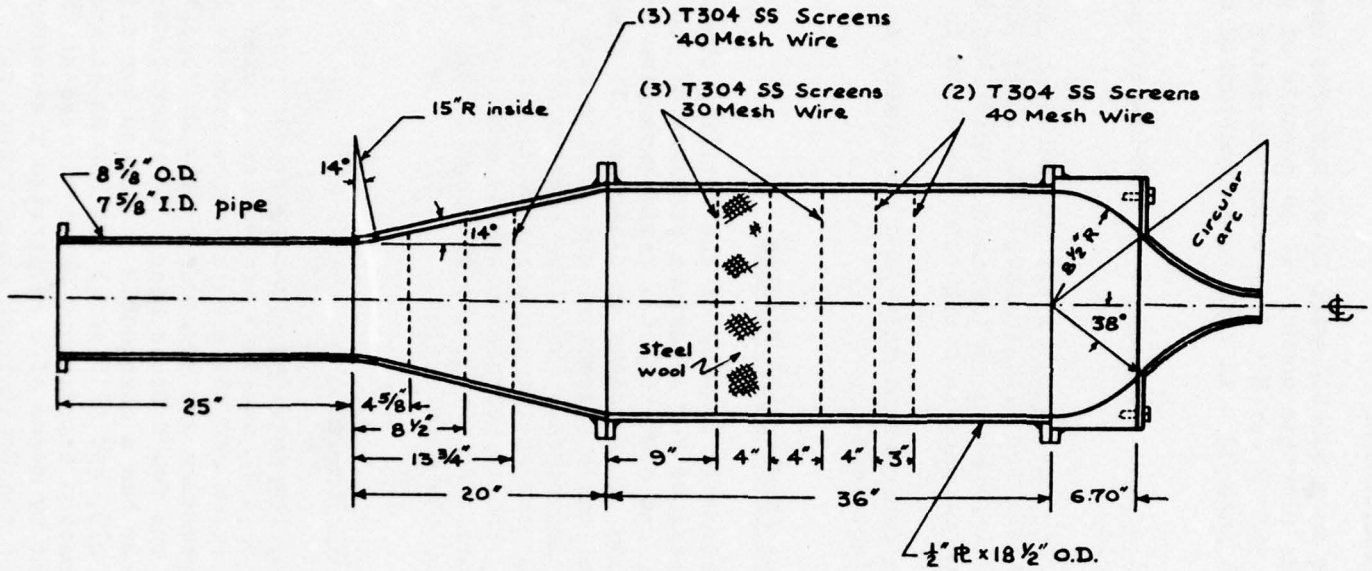


Figure 3-7. Schematic Diagram Showing Settling Chamber and a Subsonic Nozzle at USC.

3.2.3 Acoustic Data Acquisition System

Table 3-I gives a list of the instrumentation used for acoustic data acquisition. A schematic of the system arrangement is shown in Figure 3-8(a).

Before any acoustic measurements were made, sinusoidal signals at a number of selected frequencies were recorded on tape first for obtaining the frequency response of the recorder and data reduction system. To calibrate the whole system, including the microphone, the B&K 4220 pistonphone was used and the signal was recorded on tape with proper setting of the amplifier gain and input sensitivity of the tape recorder. These settings were left unchanged for the actual data recording.

During recording, both recording and instantaneous playback signals were monitored on the oscilloscope.

A square pulse train was also recorded on a separate channel of the tape recorder so that the same segment of the recorded acoustic signal would be used in obtaining the spectra from different microphones.

3.2.4 Data Reduction System

The recorded acoustic signals were analyzed in narrow frequency bands by means of a General Radio 1900-a wave analyzer which has a frequency range of 20 Hz to 54 kHz and three selectable nominal bandwidths of 3, 10, and 50 Hz. Using a type speed reduction of 2 and a bandwidth of 50 Hz, an equivalent 100 Hz bandwidth spectrum could be obtained from 160 Hz to 80 kHz. The 1/3-octave center frequencies were chosen as the center frequencies of analysis so that the equivalent 1/3-octave spectrum could be calculated from the narrow band spectrum fairly readily.

To obtain a true mean square value of the acoustic signals, the wave analyzer was used only as a filter. The filter signal was first squared by means of a 0.5% accuracy multiplier (Model 428 K, by Analog Devices) and averaged using a true integrator of our design. The integration time limit was 3 seconds in real time. This combination gives a confidence limit of 95% that the spectrum will be accurate to within ±1/2 dB.

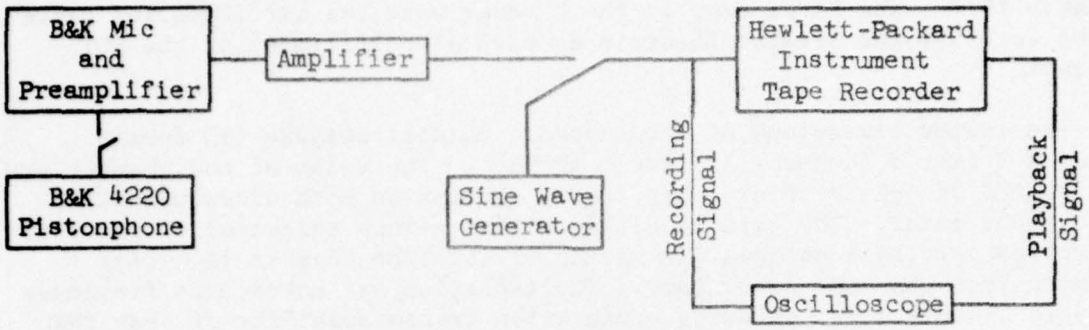
A schematic diagram of the arrangement of instrumentations for the data reduction system is shown in Figure 3-8(b).

3.3 UNIVERSITY OF BRITISH COLUMBIA ANECHOIC ROOM

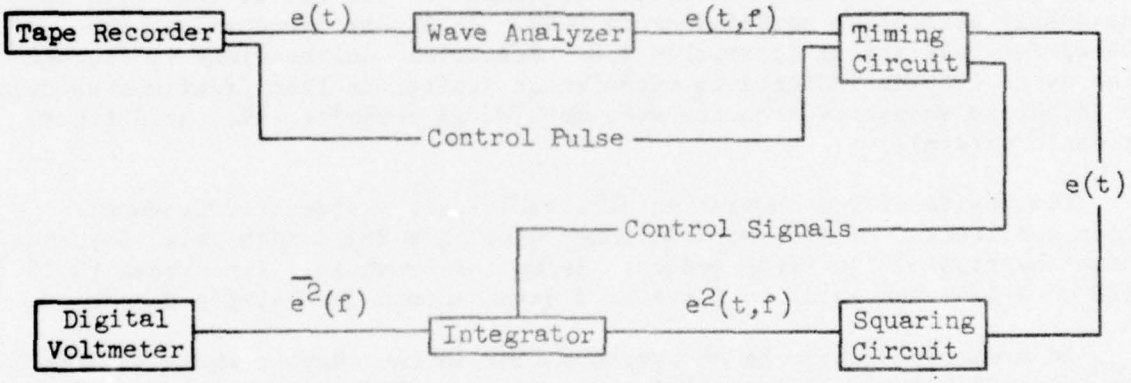
The aeroacoustic facilities at UBC were constructed under Canadian government funds. They are located in the Mechanical Engineering Laboratory Annex on the Campus of the University of British Columbia in Vancouver, British Columbia, Canada. Certification of the facility is reported in Reference 4.

Table 3-I. Summary of Acoustic Data Acquisition Systems.

	USC	UBC	JENOTS	CR&DC	J79
Microphones	4133 4135 4138	4145 4133 4135 4136 4138	4133 4135 4138	4133	4133
Preamplifiers	B&K 222 (11 channels)	N/A	Random 10 dB	Encore -30 to +60	B&K 2615, 2801 power supply- 6 dB attenuation.
Amplifiers	7 channel B&K 2 channel PAR 211	B&K 2606	Random Variable Gain	GR 1566 59 dB in 1 dB Steps	Attenuator Amplifier (GE put together)
Recorders	HP 3955 14 channel, direct Intermediate Band @ 30 ips	N/A	Sangemo Saber IV 28 channel, FM WB Group I @ 60 ips	Sangemo Saber IV 28 channel, FM WB Group II @ 30 ips or WB Group I @ 60 ips	Ampex FR100 28 channels FM-Intermediate Band @ 60 ips
Calibration Equipment	B&K 4220 B&K UA0033 Electrostatic Actuator	B&K 4220 P/P B&K 1024 R/G Wavetek 101 R/G	B&K 4220	B&K 4220	B&K 4220 HP 8057A
Playback recorder	HP 3955 with 2X reduction in tape speed	N/A	Honeywell CEC 3700B	Sangemo Saber IV	Record Electronics "Genesco"
Analyzer	GR 1900-A Narrowband Analyzer	B&K 2107 Narrowband B&K 1614 1/3 octave	GR 1921 B&K 1612	GR 1921 HP 2100	GR 1921 FS UA500
Computer			GEPAC 30	HP 2100	Honeywell H 316



a) Data Acquisition System



b) Data Reduction System

Figure 3-8. The USC Data Acquisition and Reduction Systems.

3.3.1 Anechoic Chamber

Construction of the anechoic room, shown in Figure 3-9, was completed in early 1974. The first test in the chamber were the certification tests of the facility for General Electric as partial fulfillment of the DOT Contract.

The inside dimensions of the anechoic chamber measure (13 feet 6 inches x 8 feet 5 inches x 15 feet 6 inches). The walls of the chamber are constructed of 4-inch-thick Z-bar frame, covered on both sides with 18-gauge sheet metal. The core is filled with a 4-inch thickness of semirigid fiberglass, giving a nominal STC rating of 45. The chamber is spring isolated from the main laboratory. The isolation has a resonant frequency of approximately 1 Hz, ensuring a vibration transmissibility of less than 0.01, for floor frequencies above 10 Hz. Inside, a fiberglass wedge treatment of 24-inch effective depth on the walls, floor, and ceiling renders the chamber anechoic down to about 150 Hz.

The wedges installed in the chamber were supplied by Eckel Industries (Canada) Ltd. They are the Eckel-Type EW Wedge (2400 Series) made of semirigid fiberglass, and encased in a protective No. 2 mesh of 19-gauge galvanized hardwire cloth. The wedge tips are covered with a strip of fine fiberglass cloth which overlaps the points by 2 inches, to prevent feathering. Installed on an Eckel-supplied grid system, the wedges have an effective depth of 24 inches, and base dimensions of approximately 8 x 24 inches. This yields a certified lower cutoff frequency of 150 Hz; at this frequency the energy absorption coefficient is 0.99. At higher frequencies, the absorption coefficient approaches 1.0. Free-field calibrations at frequencies up to 100 kHz indicate no significant deviations from freefield behavior (as might be suspected from the wire-mesh wedge covering, wire grid floor, or catch screen).

The inside of the chamber is accessible over a standard wire-mesh floor constructed of 1/8-inch tensioned wire on a 2-1/4-inch grid, 6-inches above the tips of the floor wedges. Below this mesh is a finer mesh (0.75 wire on a 1/4-inch grid) to serve as a catch screen for falling debris.

In order that there be no pressure rise in the chamber while running the jet, 625 holes of 1/4-inch diameter were drilled through the anechoic chamber door on a 1-inch grid pattern in a position centered on the downstream extension at the jet axis. This gives an area ratio of approximately 60, resulting in very low velocities through the door even at the maximum flow rate. The long holes pass through the fiberglass core and the fiberglass wedges on the inside of the door so that acoustic attenuation across the door is not significantly altered, except at very low frequencies.

There are two microphone booms with integral cables inside the chamber, one of which is centered over the jet exit plane, as shown in Figure 3-10. At a 10-foot microphone radius, this boom can sweep from 180° to 80° (0° to 100° relative to the jet axis), without obstruction. Over this range of

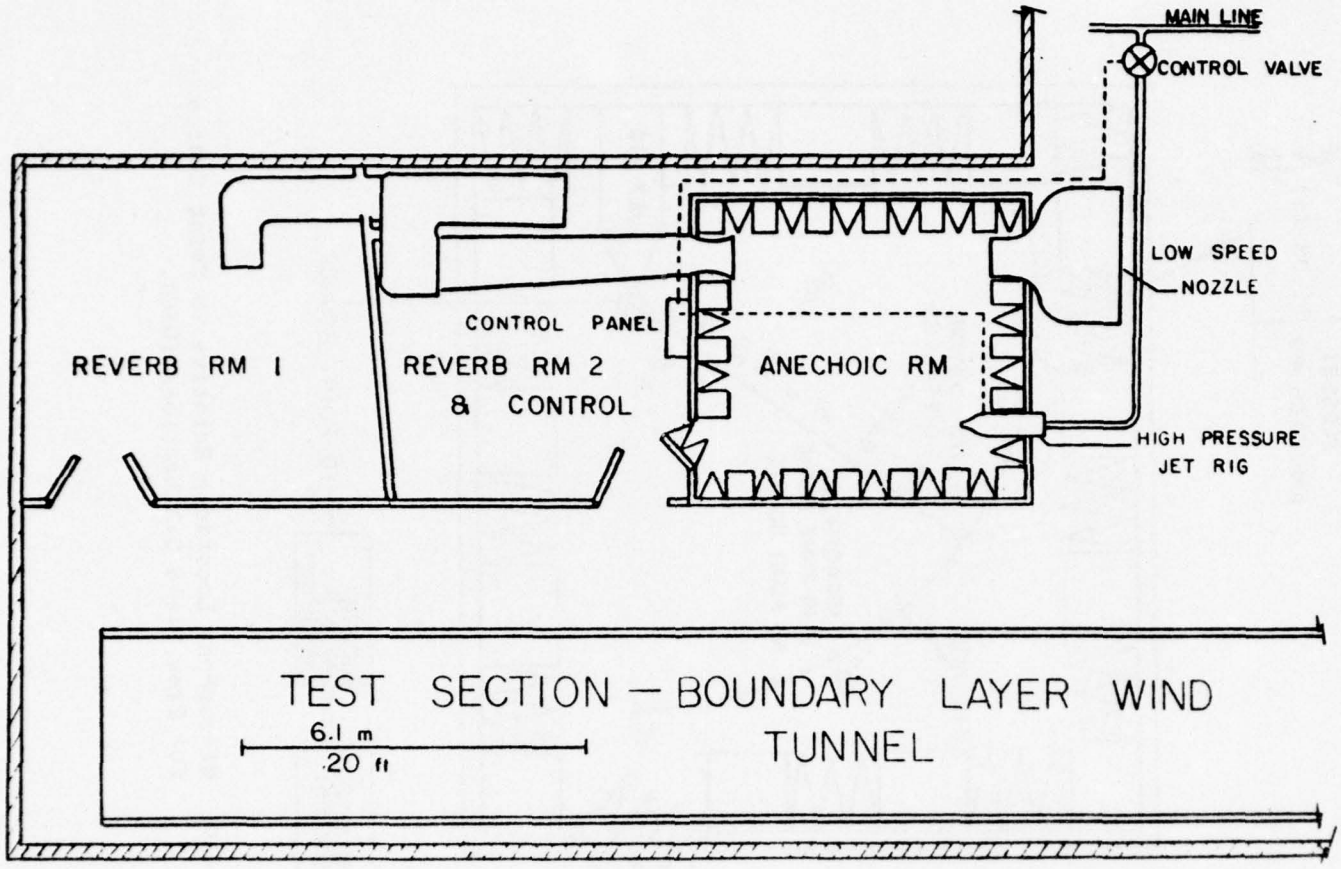


Figure 3-9. Aeroacoustic Facility at Department of Mechanical Engineering (UBC).

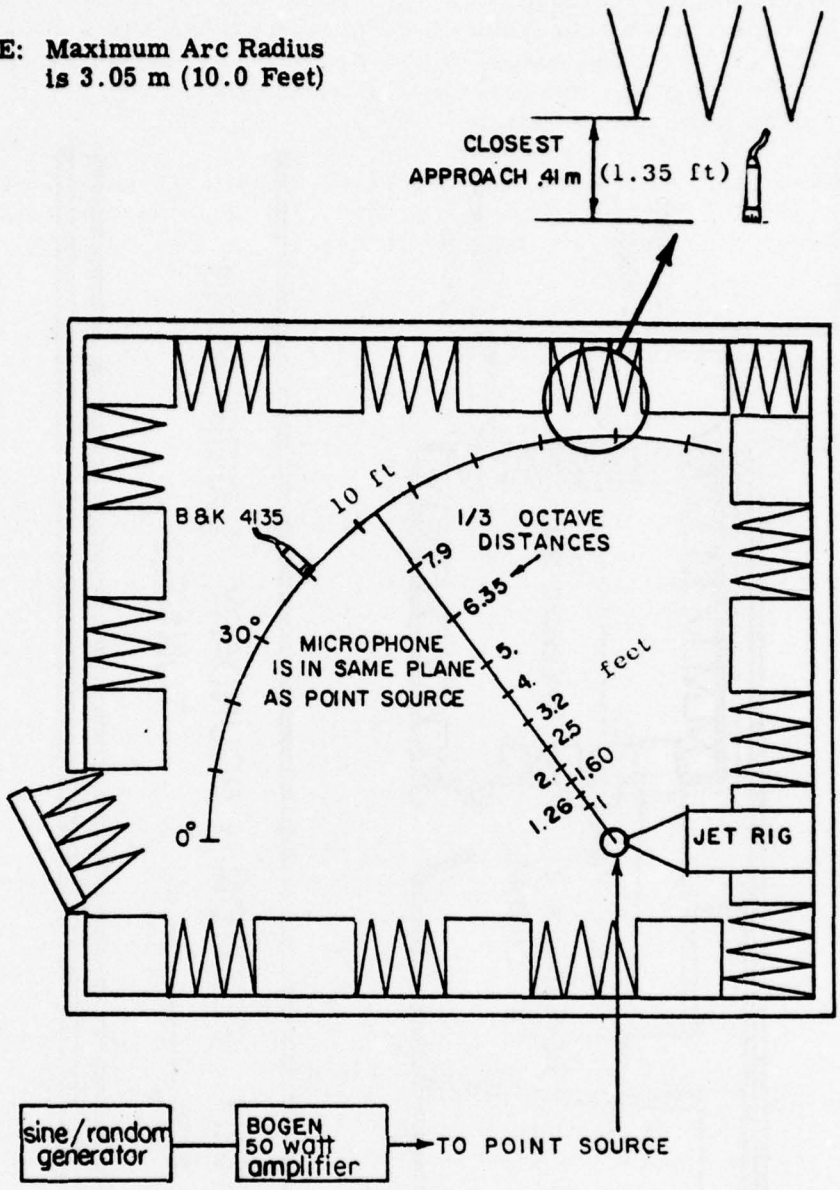


Figure 3-10. Microphone Locations Relative to Point Source for Free Field Calibrations (UBC).

angles, the microphone cartridge is always more than 16 inches from the nearest wedge tips. A shorter boom of 5-foot length allows a backward arc angle up to 60° (120° to jet axis), while preserving the same wedge tip clearance. In the future, both booms will be automatically controlled and monitored from outside the chamber.

Microphone cables or other electrical services exit the chamber through a special panel with built-in Bruel and Kjaer 7-lead connectors and BNC 2-lead connectors. The pressure tap from the jet plenum also exits through this panel.

A view of the inside of the chamber showing the nozzle system is shown in Figure 3-11.

3.3.2 Jet Noise Facility

The primary air supply for the jet noise facility is a Quincy Northwest Model 260 rotary screw air compressor which is rated at a nominal capacity of (268 scfm) at 100 psi delivery pressure. Connected directly to the compressor is a 500-gallon air receiver. An automatic mercury switch on the receiver controls the compressor to keep the receiver pressure at 100 psi ± 5% (or any lower set-point).

Figure 3-12 shows the piping layout from the compressor to the jet rig. Approximately 200 feet of 1-1/2-inch-diameter copper pipe connects the compressor to the tap-off point in the main line. For accurate pressure control a Fisher valve actuator type 667 is used in conjunction with a Taylor proportional-type controller series 440R. The controller is mounted in the instrumentation area, near the door of the anechoic chamber. The valve positioner is moved either on automatic or manual command to maintain the desired stagnation pressure in the jet settling chamber.

Because of early indications that the Fisher control valve was generating excessive noise, a large in-line silencer (6.3 inch diameter x 5.6 feet long) was installed near the valve discharge as shown in Figure 3-12. The silencer contains a lining of 2-inch-thick fiberglass with flow resistant covering. The connection between silencer and settling chamber is made with a 6 m length of 8 cm rubber steam hose (rated at 200 psi pressure).

The jet rig itself (as shown in Figure 3-13) consists of a cylindrical silencer plenum 4-foot long by 10-inch diameter, to which a variety of nozzles may be attached. The exit diameter of the nozzles used in this study is 0.787 inches. This diameter just enables achievement of sustained sonic flow with the available compressor. The large plenum area ensures a maximum approach velocity of less than 10 fps even when the nozzle is choked.

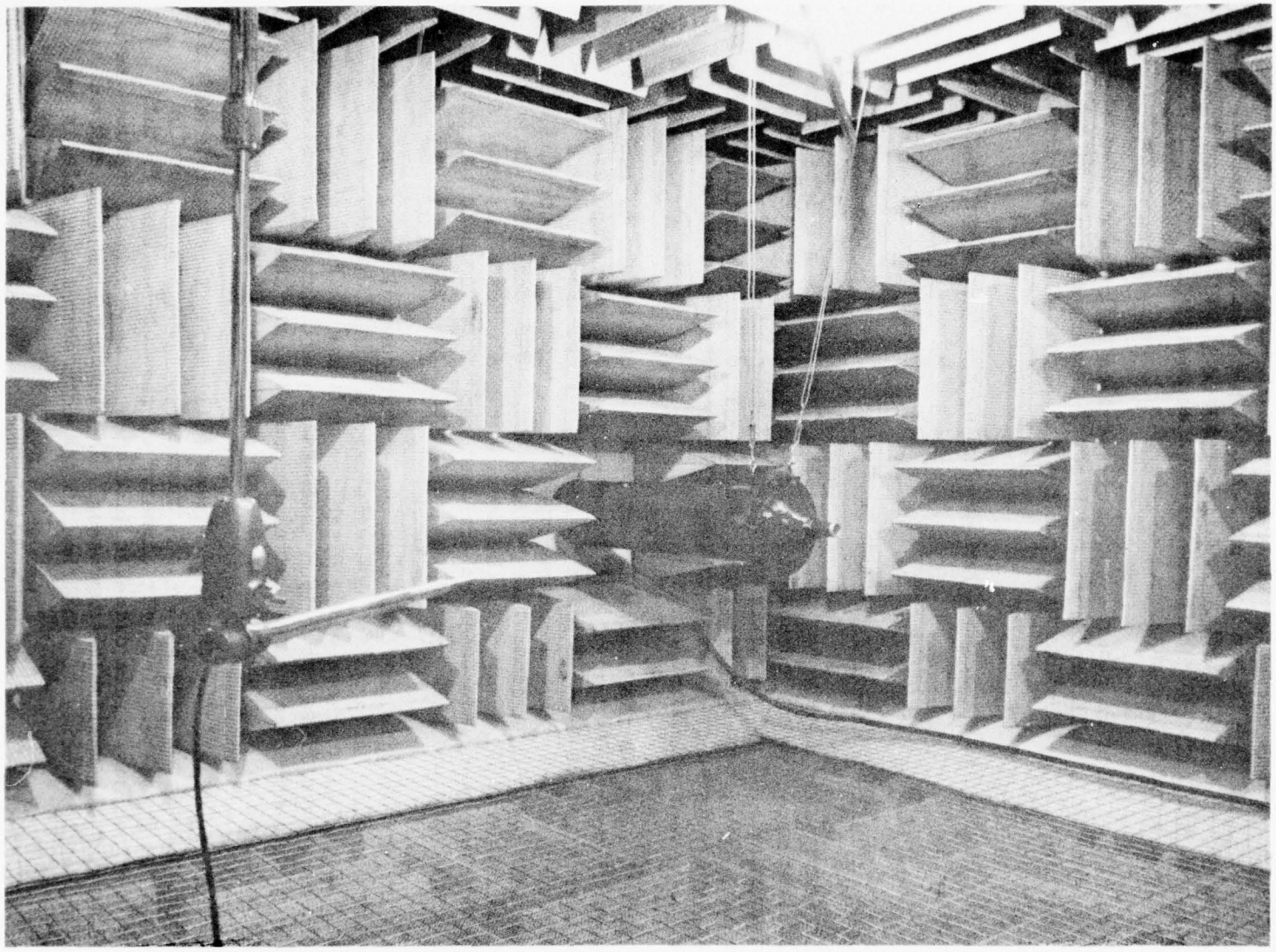


Figure 3-11. UBC Anechoic Chamber in Vancouver, B.C., Canada.

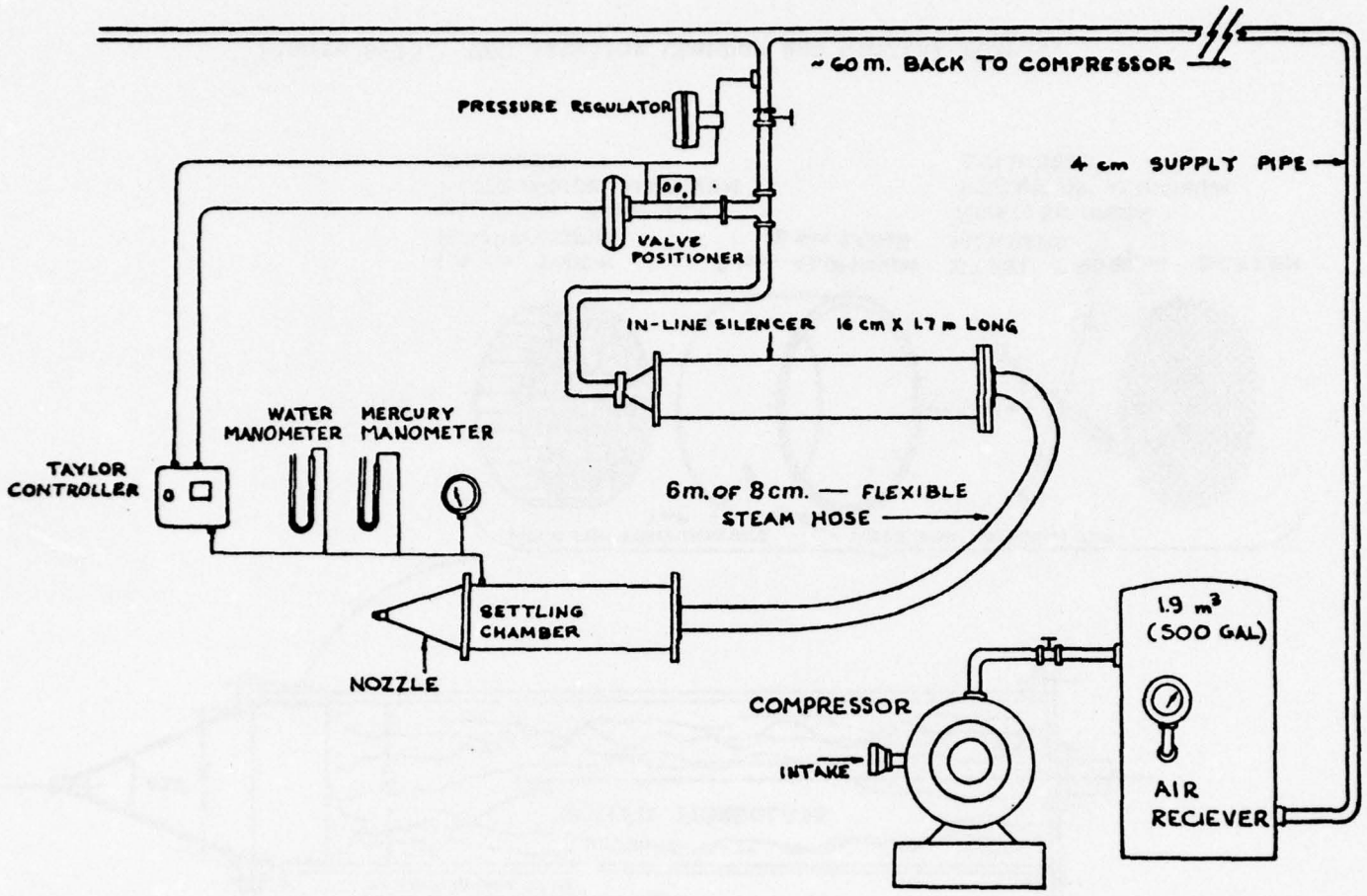


Figure 3-12. Piping Layout for UBC Air Supply System.

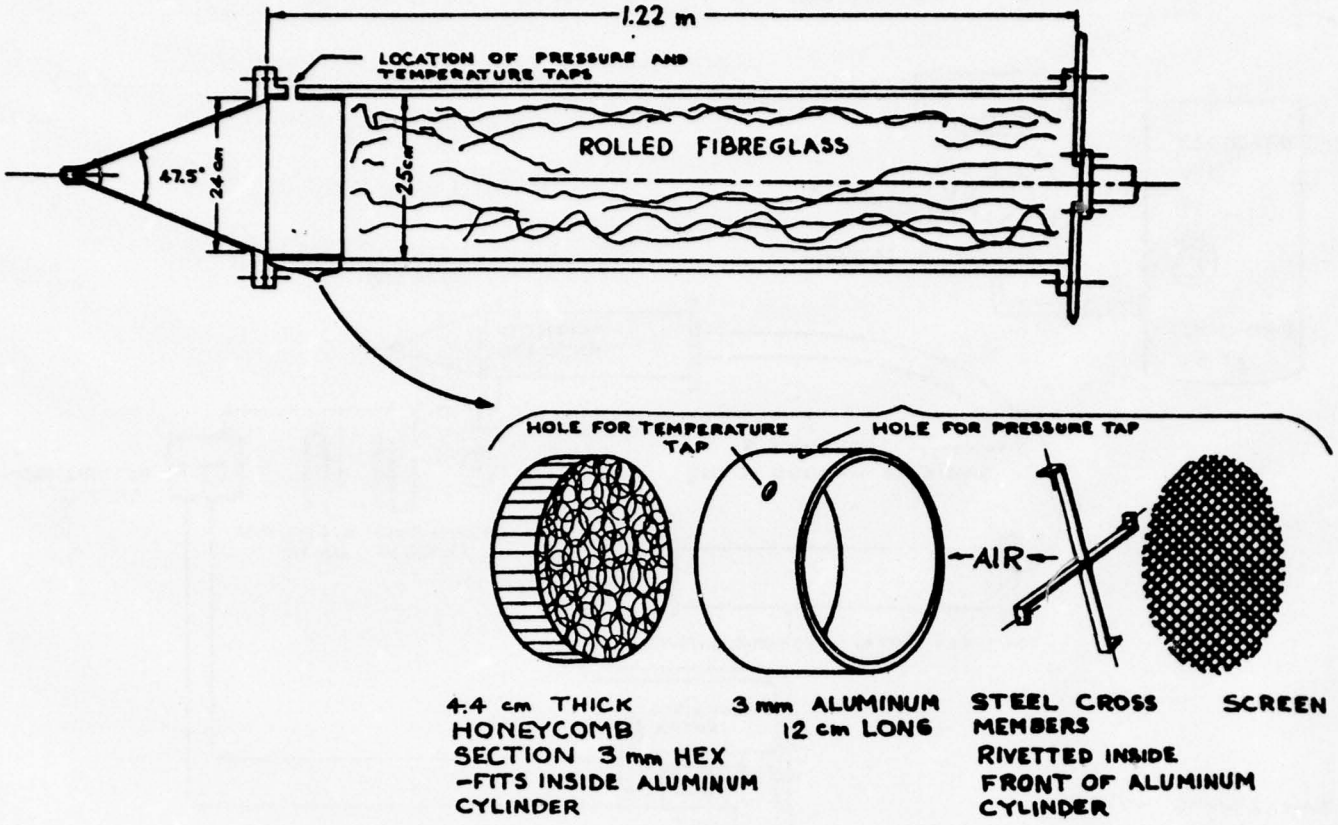


Figure 3-13. UBC Settling Chamber and Conical Nozzle.

In order to compound the effectiveness of the upstream silencer, most of the jet plenum is filled with a rolled fiberglass plug. Immediately upstream of the nozzle, a section of screen and aluminum honeycomb is used to straighten the flow. The steel cross supports shown in Figure 3-13 are primarily to keep the fiberglass plug from blowing out at high Mach numbers. Stagnation temperature and pressure rakes were inserted through holes in the aluminum sleeves just downstream of the honeycomb, as shown in Figure 3-13.

To monitor the jet plenum pressure at low velocities ($0.26 \approx M_j \leq 0.4$), a 45-inch water manometer is used. At the lowest test point ($M_j = 0.26$), the deflection is about 50 cm H_2O. The reading accuracy is 2 mm giving a corresponding 0.4% accuracy in the pressure measurement. For higher jet condition ($M_j > 0.4$), 73-inch mercury manometer is used. At $M_j \approx 0.52$, the deflection is about 15.4 cm of Hg and the reading accuracy is again about 2 mm, which corresponds to a 1.3% pressure variation. A 0 to 100 psi Bourdon gauge is also connected in parallel as a quick-check instrument on the pressure reading.

3.3.3 Data Acquisition and Reduction Systems

Since most of the equipment listed in Table 3-I is manufactured by Bruel and Kjaer, detailed specifications are not given herein but are available for each item from Bruel and Kjaer literature.

- Microphones - four Bruel and Kjaer microphone types are available (4133, 4135, 4136, and 4138). The Type 4135 microphone was used for most measurements in the current validation program. For the jet noise certification measurements, the grid cap was removed, giving a uniform free-field-corrected frequency response to 80 kHz (within ± 1 dB). For the lower Mach number runs ($M_j < 0.5$), however, the 1/2-inch microphone 4133 was used instead, because of its lower electronic noise threshold. Unfortunately, the 40 kHz upper frequency limit of the 4133 imposes some penalty.

- Voltage amplification - Bruel and Kjaer type 2606 precision measuring amplifier, 2 units available.

- Spectrum analysis - 2 units Bruel and Kjaer type 2107 constant-percentage bandwidth frequency analyzer. These units cover the frequency range 20 Hz - 20,000 Hz. The smallest bandwidth is 6% of the center frequency.

  - 1 unit Bruel and Kjaer type 1614 1/3-octave or 1-octave band pass filter. This unit has a frequency range 2 Hz - 160 kHz. Both types, 1614 and 2107, can be synchronized to the Bruel and Kjaer type 2305 level recorder for automatic recording of spectrograms.

- Correlation computer - The signal correlator is a SAICOR/Honeywell Model SA143A with 2000 units of precomputational delay, and 400-point time base. This unit exhibits excellent resolution, and wide dynamic range.

- Recording equipment - Two tape recording units are available:

  - Bruel and Kjaer type 2204 with all accessories.

  - General Radio Model 1565a.

  These units, however, are not normally used and the data is reduced on line.

- Calibration equipment - Bruel and Kjaer type 1024 sine-random generator which will give wide and narrow random noise and sine sweep over the frequency range 20 Hz - 20 kHz.

  - Wavetek waveform generator model 101 is capable of generating frequencies between 0.01 Hz and 1000 kHz.

3.4 GENERAL ELECTRIC JENOTS SCALE MODEL ACOUSTIC TEST FACILITY

The JENOTS (Jet Engine Noise Outdoor Test Stand) has been under continuous development since its establishment in the late 1950's for early turbojet noise and suppressor studies. It is located at the north end of the Evendale Ohio, General Electric plant remote from the main factory area or engine test cells. Certification of the Facility is reported in Reference 5.

3.4.1 The Acoustic Arena

The sound field is shown in Figures 3-14 and 3-15. It consists of 14 microphones arranged on 10° intervals around a 40-foot arc from 30° to 160°, centered at the nozzle discharge plane centerline. The microphones are elevated 16 feet above the ground on specially designed "goosenock" mounts to minimize the influence of reflections.

The ground plane is composed of concrete to approximately a 20-foot radius from the nozzle exit, then crushed rock to a 40-foot radius. A grassy field exists beyond the acoustic arena. Specially designed acoustic barriers are located approximately 60 feet from the sound field to protect the neighboring community from the high sound levels. These barriers are designed such that there are no measurable reflections back into the sound-field. On both the single-flow and dual-flow configurations, the nozzle centerline is 55 inches above the ground.

The acoustic and aerodynamic control room is located in Building 315, approximately 100 feet from the sound field.

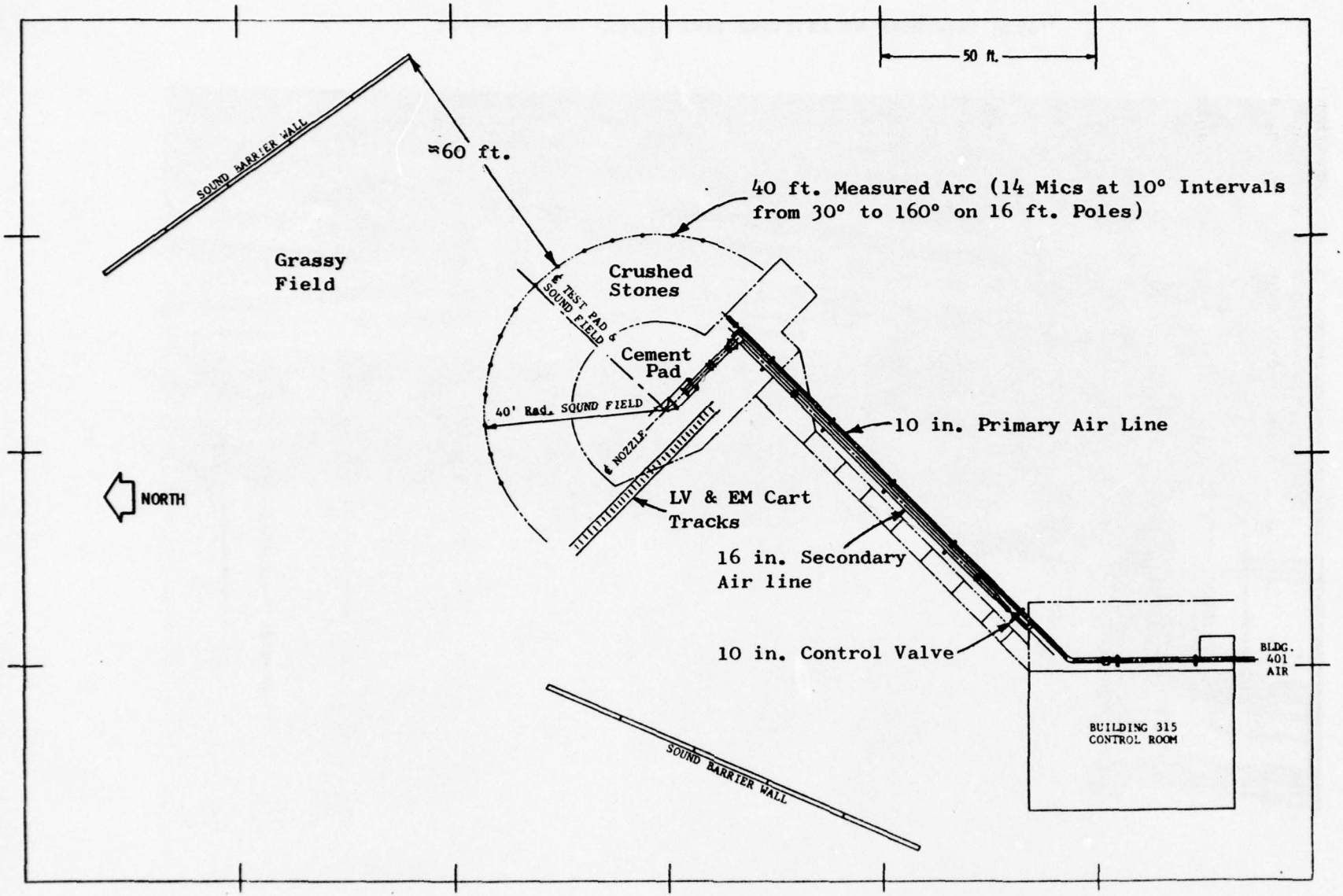


Figure 3-14. Schematic of JENOTS Facility.

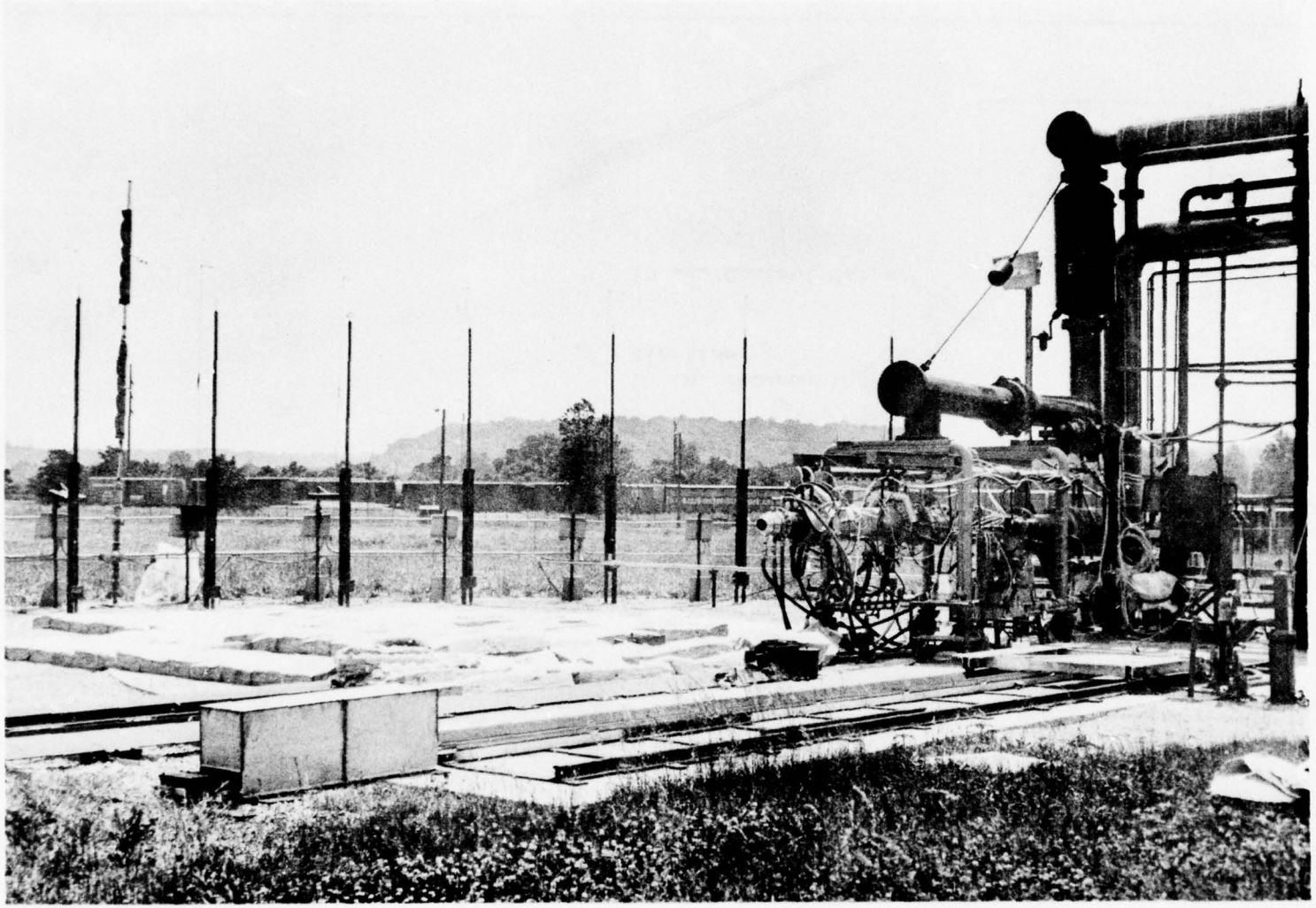


Figure 3-15. JENOTS Test Facility in Evendale, Ohio.

3.4.2 Jet Facility

The JENOTS facility is capable of operation either as a single- or coannular-flow system, through interchangeable burner and acoustically treated plenum sections. In the single-flow mode, for clean operation from low through highly supersonic jet velocity, the system consists of a preburner and afterburner capable of operating up to 6 inch diameter nozzles to pressure ratios of 4:1 and temperatures of 3000° R. In the coannular-flow mode, the afterburner is replaced by an acoustically treated core/fan plenum chamber. The core flow is fed by the same pipe/preburner system that supplied the single jet facility and is capable of operating to 1600° R. The fan flow is supplied from a separate cold flow system and is independently controlled from the core stream.

3.4.2.1 Air Supply System

Three types of air are available for the JENOTS facility. They are as follows:

- Central Air Supply
- Shop Air
- Instrument Air (filtered)

Compressor Boost (C/B) air is used to augment required air flows.

Central Air Supply System - The Central Air Supply System, Figure 3-16, is the basic air supply system for the Evendale component test complex. It continuously provides up to 100 lb/sec of airflow at pressures up to 300 psig. The Central Air Supply System consists of an arrangement of five multistage centrifugal compressors driven by synchronous motors through speed-increasing gears. Operation flexibility is obtained by the ability to stage the compressors in series or in parallel, in various combinations, for a wide range of pressures and flows, or for use as exhausters.

Test air is supplied to the JENOTS test stand through a 10-inch air line which connects to the Central Air Supply 14-inch air line. The shutoff valve for the JENOTS facility is a remotely controlled 250-pound, 10-inch Kennedy gate valve located opposite Building 315, as shown in Figure 3-14. The airflow in the 10-inch line is controlled and adjusted by two pairs of valves, each pair connected in parallel. In each case, a 4-inch plug valve is in parallel with an 8-inch butterfly valve. The 4-inch valves serve as the fine adjustment, while the coarse adjustment is set with the 8-inch orifice pressure and orifice ΔP. The 4-inch plug valve features a regulator for automatic pressure control. The pair of valves downstream of the orifice are used for flow rate control.

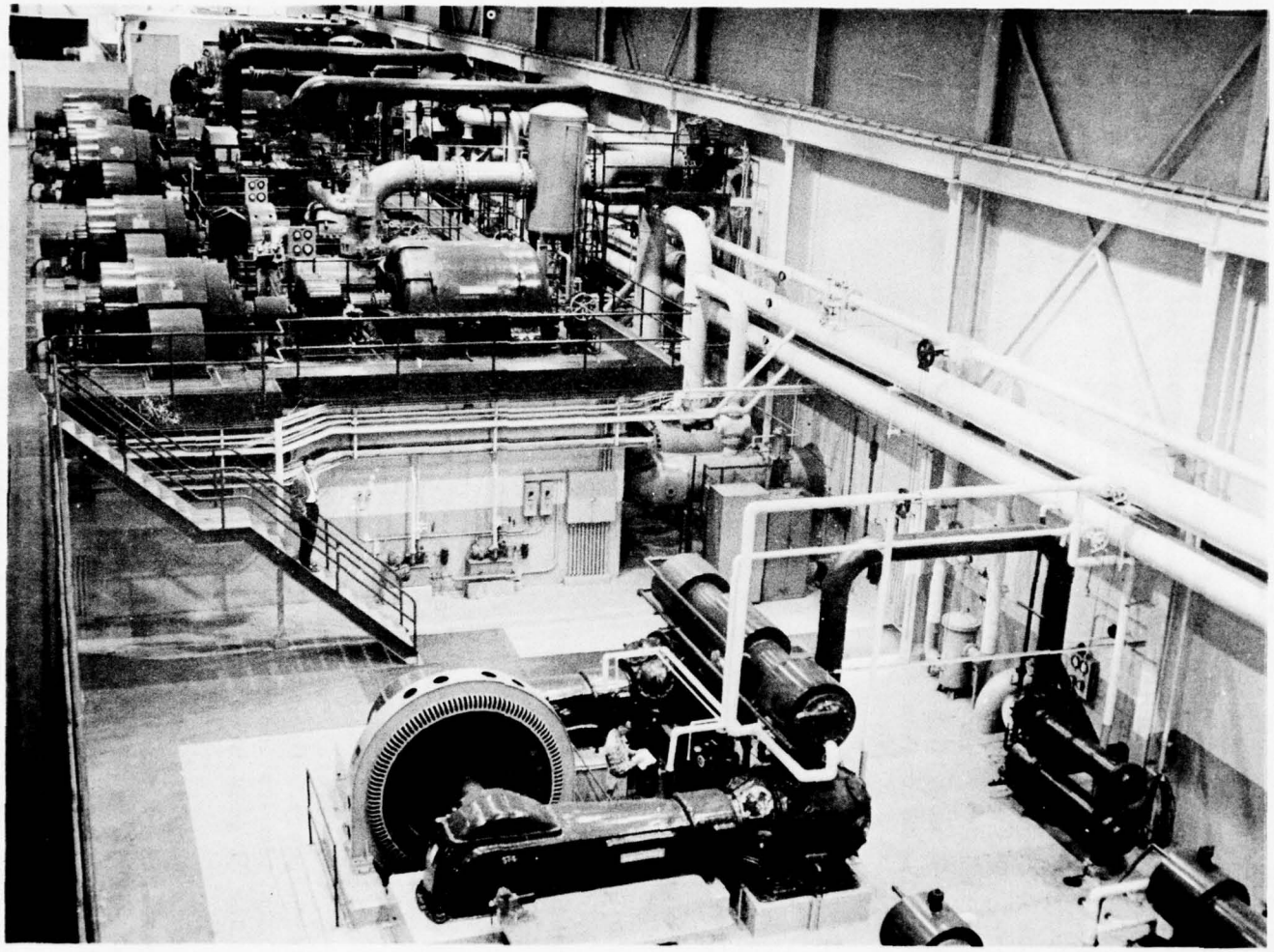


Figure 3-16. Building 401 Central Air Supply System for the JENOTS and Anechoic Chamber Facilities at General Electric Plant, Evendale, Ohio.

The main airflow is measured by a Daniels square edge orifice 5.000-inches in diameter with $\beta = 0.499$. The orifice is mounted in a quick-change, orifice plate holder. The inside diameter of the main air line is 10.020-inches.

The 10-inch air line has a blow-down leg prior to the burners. A manually operated 6-inch gate valve is mounted on the 6-inch blowdown pipe. The air pressure limitation in this section is 300 psig at ambient temperature.

Shop Air - A 4-inch shop air line crossover provides for use of shop air through the 10-inch air line. It features a 4-inch regulator-controlled, pneumatic-operated gate valve mounted on the crossover. A rupture disk assembly is mounted on the crossover to prevent high pressure air from leaking upstream in the shop air line. Pressure is limited to 125 psi by the rupture disk.

Secondary Air - A 4-inch secondary air line is connected to the primary 10-inch line between the orifice and the upstream control valves. It contains 4-inch, 300 lb Daniels pressure-tapped mounting flanges, with Meriam square edge orifice plates of different sizes.

C/B Air - Compressor boost (C/B) air may be used in any of the systems previously described. It is usually used in conjunction with shop air in the 10-inch line to augment pressure and airflow in meeting test requirements.

Instrument Air - The instrument air system consists of a 3/4-inch line connecting to the instrument air supply. The instrument air line runs to the test stand where it is used for operating air and fuel control valves and shutoff solenoids for JP-4, H_2, and N_2. Instrument air is also conducted to the control room through a 1/2-inch line for operating panel loaders, temperature controllers, and pressure transducers used with the signal digital data acquisition system.

3.4.2.2 Fuel System

The fuel system provides JP-4 from a fuel supply up to maximum of 5000 lb/hr at 1000 psi. Hydrogen is available from a 12-bottle rack and is used primarily for burner ignitors. Nitrogen obtained from a 9275 ft^3 capacity nitrogen trailer is used for purging the hydrogen and JP-4 lines.

JP-4 fuel is drawn from a 4000-gallon fuel supply. A 1-1/2-inch pipe connects to the fuel line and runs to the JENOTS facility fuel pad just opposite the northeast corner of Building 315.

At the fuel pad, a pumping, cooling, filtering, and bypass function operation is performed. The pumping unit is designed to bypass fuel during low fuel demand, yet provides up to a maximum of 5000 lb/hr at 1000 psi to the test pad when required.

From the fuel pad, fuel arrives at the test stand where it goes through an automatic cutoff valve that is controlled by the facility cooling water pressure. The valve remains open while the facility cools outlet water to a 3/4-inch stainless steel pipe and connects to two filters connected in parallel followed by two chromel-alumel (CA) thermocouples (T/C) for fuel temperature measurement at the test pad. After the T/C's, a flowmeter is mounted in the line to measure total flow. From this point, the fuel line divides into four units. These units consists of the preburner, afterburner "pilot", afterburner "local", and afterburner "fill" fuel systems. Mounted on each unit, in order, are a manual shutoff valve, a flowmeter, and a fuel control valve. In the case of the preburner, the fuel line is divided into the small and large slot subsystems, with each branch having its own control valve. Figure 3-17 is a schematic of the burner systems on the single-jet JENOTS stand.

Using combinations of these units, a wide range of temperatures and air-flows can be obtained while keeping a stable and uniform burner condition. The control valves can be fitted with several available inner bodies (trim size) depending on the required range of operation. In addition to the automatic fuel shutoff valve, operating on cooling water pressure, the system has other safety features.

The fuel pad contains a relief valve set for 1000 psig, and a thermoswitch that stops the fuel pump if fuel temperature exceeds 140° F. The fuel control valve for the preburner is equipped with an API over and under temperature shutoff. The afterburner "local" fuel control valve is connected to an API overtemperature shutoff.

3.4.2.3 Burner System

The burner system consists of a preburner (P/B) and afterburner (A/B) mounted in the main air pipe as shown in Figure 3-17.

Preburner - A J-73 large and small-slot fuel nozzle and J-47 burner "can" are used for the JENOTS preburner. A large- and small-slot fuel supply line, each with its own control valve, is available to the preburner. An ignitor torch is used for lighting the preburner. A spark plug is utilized to ignite a mixture of hydrogen and air in the torch tube.

Afterburner - The afterburner consists of the afterburner (A/B) ignitor torch, A/B pilot, and two sets of A/B spray bars. The ignitor torch is a 1/2-inch stainless steel tube housing, an AC spark plug ignitor, and inlets for the H_2, N_2 purge and air supply line using instrument air. The A/B pilot is made up of a simplex fuel nozzle, a swirl cup, and a "V" gutter flame holder. The eight A/B spray bars are mounted between the pilot and ignitor torch and use both "local" and "fill" fuel systems. The dual spray bars are used when high airflows (above 11 pps) are required.

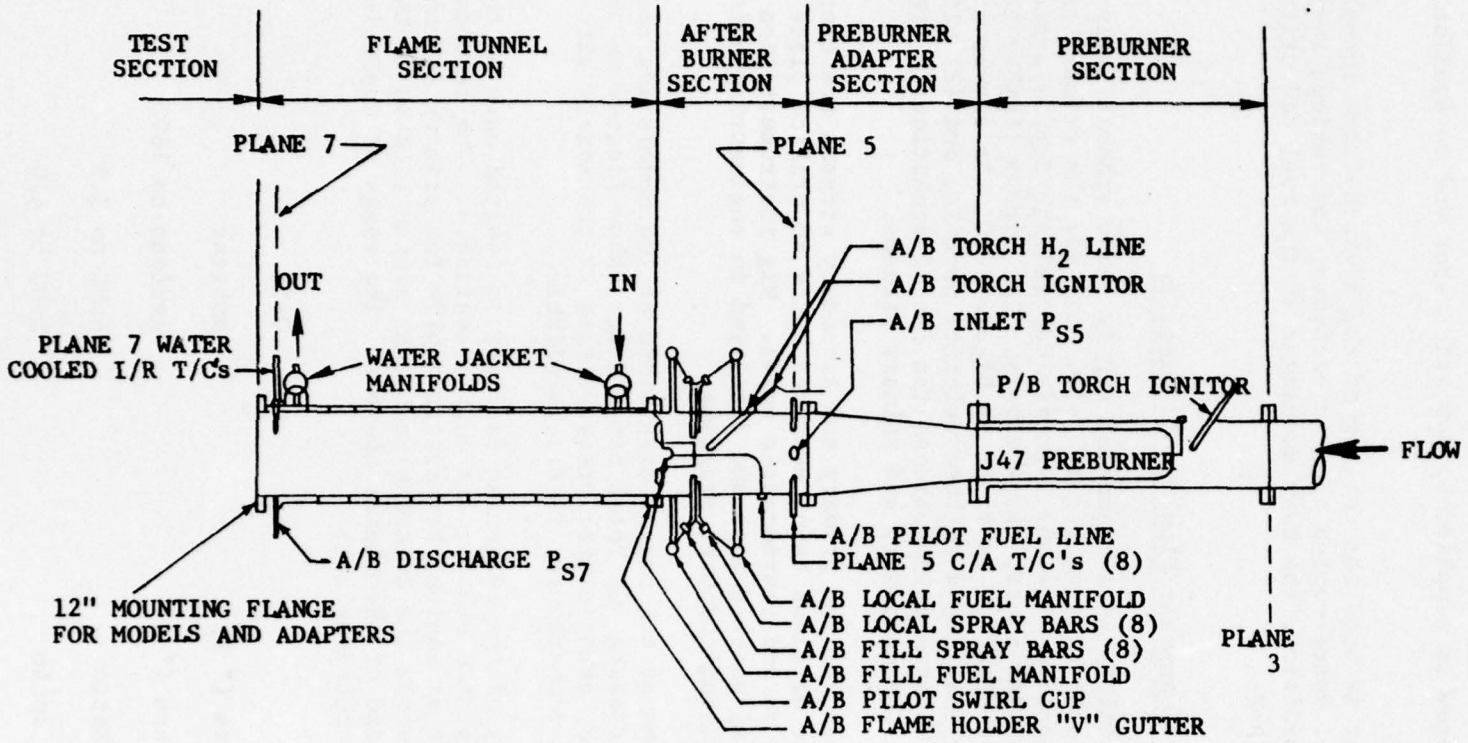


Figure 3-17. Schematic of JENOTS Single-Jet Main Air Pipe and Burner System.

3.4.2.4 Domestic Water System

The water system is supplied by domestic water and is available up to 60 psi at 300 gpm.

Domestic water is used for cooling of the 12-inch flame tunnel, the plane 7, IR probes, water-cooled adapter sections, and various test configurations. In addition, the heat exchanger at the fuel pad utilized the domestic water supply.

3.4.2.5 Coannular Flow JENOTS Facility

The JENOTS facility as a coannular rig is shown schematically in Figure 3-18 and pictorially in Figure 3-19. Air for the primary and secondary streams is supplied from the Evendale Central Air Supply system through 10-inch and 16-inch air lines, respectively. The plenum chamber to which the test models are attached is shown in Figure 3-20. It serves a two-fold purpose: (1) gives the flow a uniform velocity profile, and (2) eliminates any high frequency system noise through the use of acoustically treated baffles located in the secondary and primary streams.

Flow conditions for the primary and secondary streams are controlled separately with the airflows being measured using an orifice plate system coupled with pressure and thermocouple rakes. Rig instrumentation data are converted to digital punched tape and displayed in engineering units through the use of time-sharing computer programs.

Flow conditions at the nozzle exit plane of the models are set through the use of total pressure and total temperature rakes located on the model. An alternate method, using static pressure taps at the nozzle exit plane and preburner exit temperature, is also available.

The capability of the coannular facility is limited only by the baffle system inside the plenum and the air supply available. The secondary stream will exhaust at ambient temperature while the primary stream may be heated to 1600° R using the existing preburner system located in the primary air supply line ahead of the plenum chamber. The range of conditions under which the facility operates are:

Bypass Ratio	0-15
Fan Temperature (° R)	ambient
Core Temperature (° R)	ambient to 1600
Fan Pressure Ratio	1.05 to 3.5
Core Pressure Ratio	1.05 to 4.0

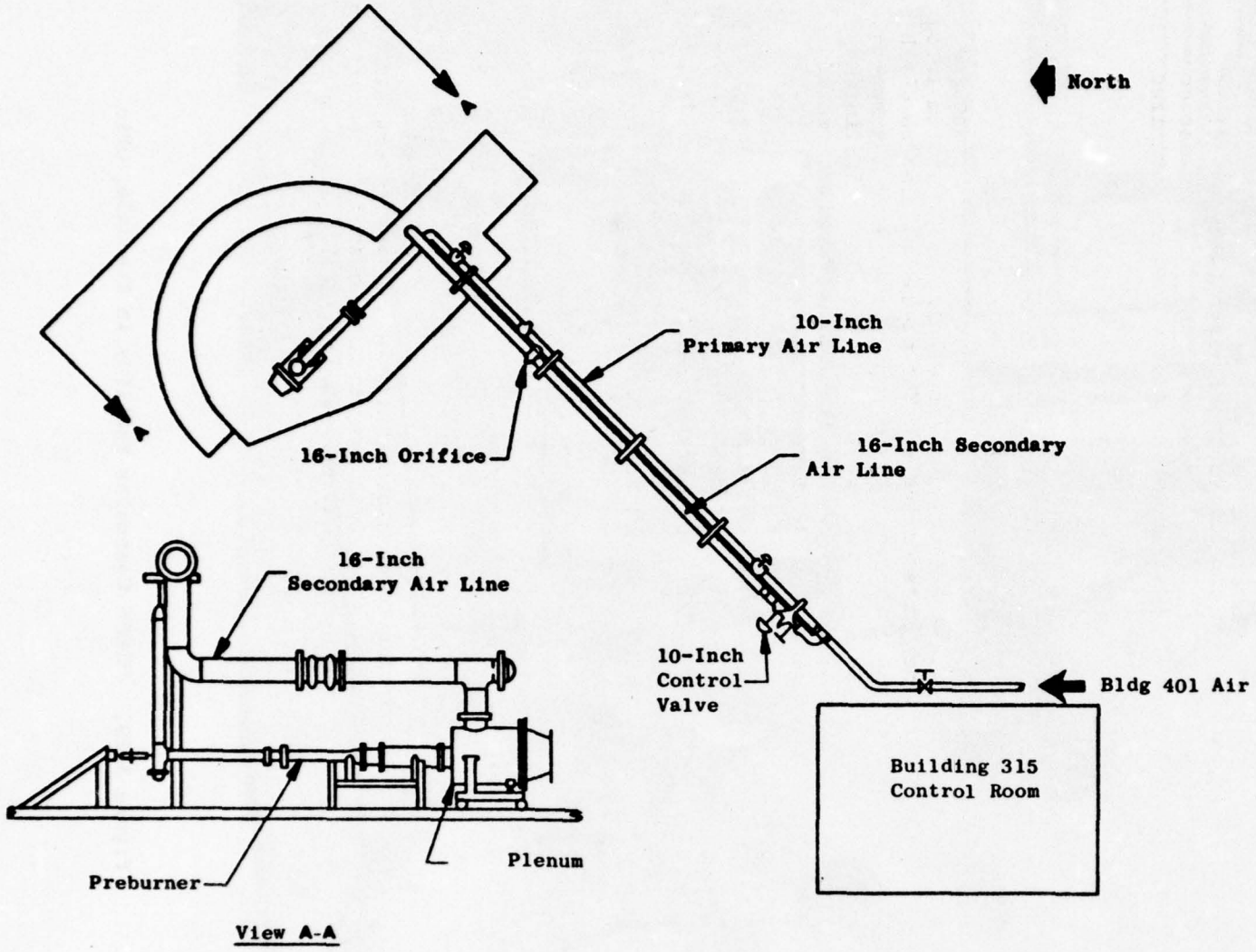


Figure 3-18. Schematic of Coannular-Flow JENOTS Facility.

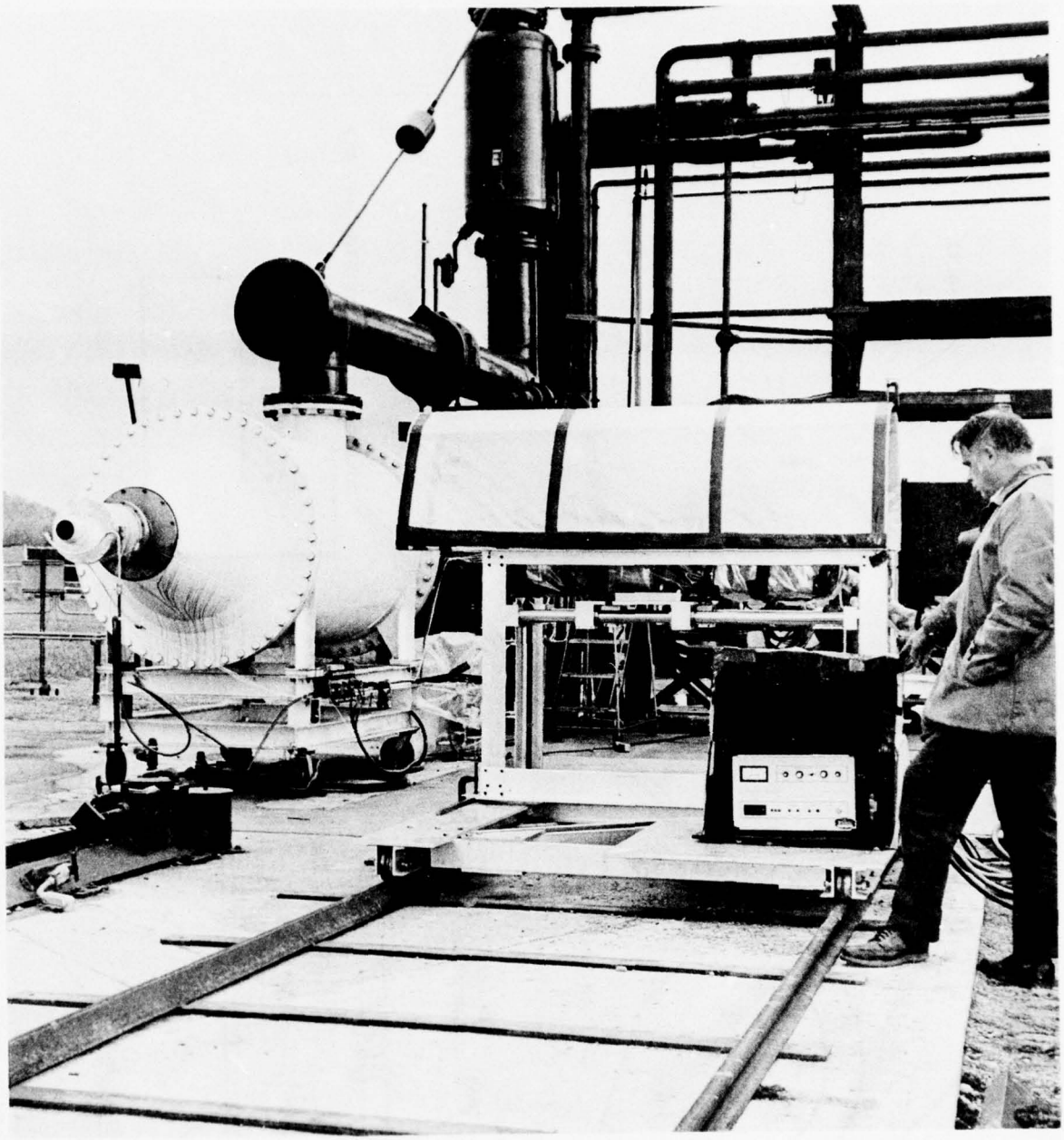


Figure 3-19. JENOTS Coannular Facility in Evendale, Ohio.

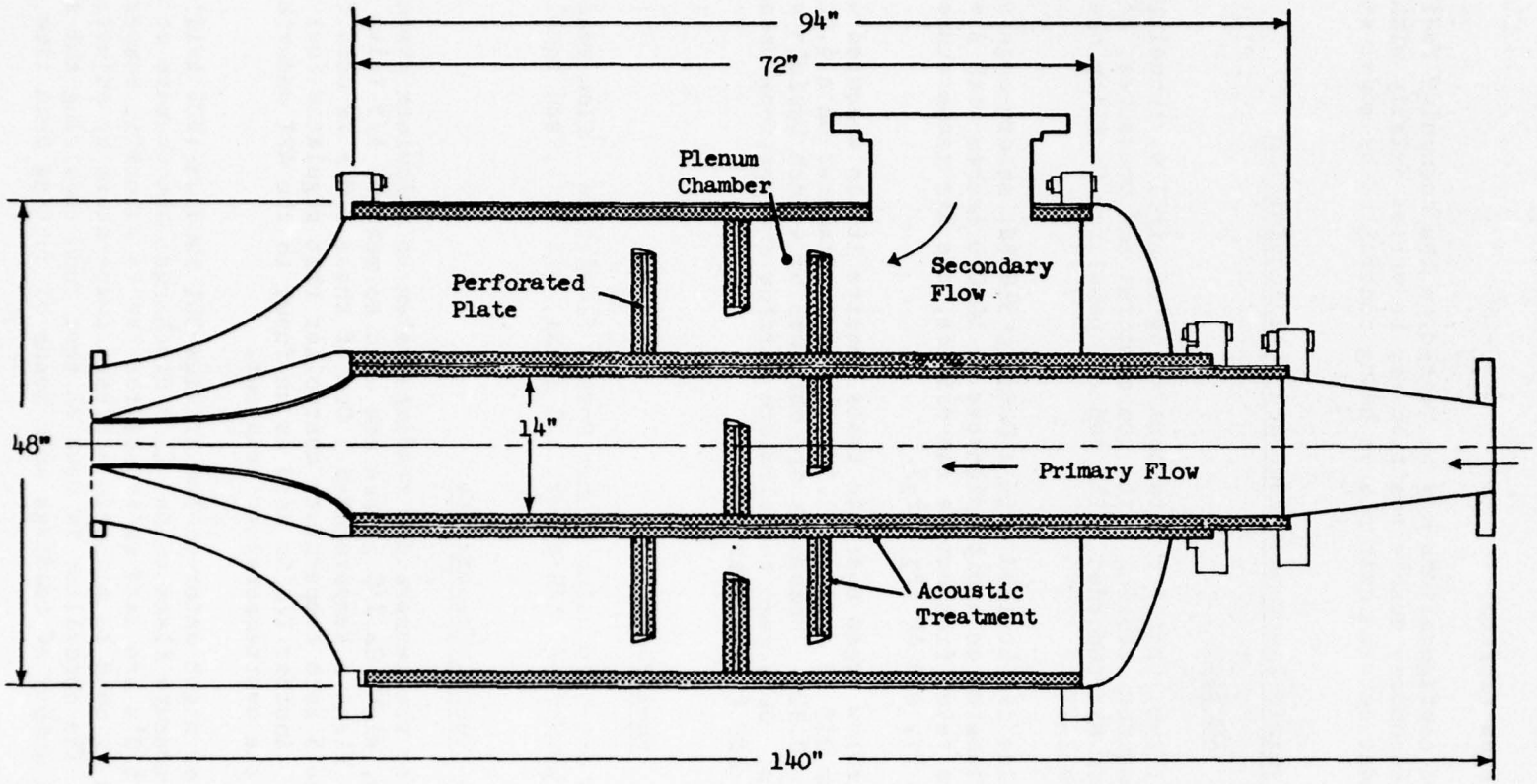


Figure 3-20. JENOTS Coannular Plenum Chamber.

Fan Weight Flow (lb/sec)	0-50
Core Weight Flow (lb/sec)	0-30

Various model configurations may be tested on the coannular facility. Both primary and secondary nozzle position may be varied axially with the maximum displacement between exit planes being controlled by model size.

3.4.3 Aerodynamic Instrumentation and Data Acquisition

3.4.3.1 Airflow

For each test run, facility data consisting of airflow, tunnel temperatures and pressures, cooling water temperatures and pressures, and meteorological data are recorded. The control panel for facility operation is shown in Figure 3-21.

Primary airflow is obtained with a Daniels 316 SS, square-edge orifice 5.000 inches in diameter on a pipe diameter of 10.020 inches with β = 0.499. Using data taken from across the orifice, the air temperatures, upstream pressure P_1, and ΔP ($P_1 - P_2$).

Secondary airflow (when specific tests require it) is measured with a square-edge Meriam 316 SS orifice, 1.250-inches in diameter on a 4.026-inch pipe with β = 0.310. Pressures are obtained by 4-inch Daniels orifice flange static taps. Data used to calculate airflow are upstream pressure, ΔP, and secondary air line temperature.

3.4.3.2 Fuel Flow

Fuel flow is obtained using Fisher Porter flowmeters. Flow readings are taken of the preburner, A/B pilot, A/B local, A/B fill, and total flow.

3.4.3.3 Tunnel Temperature

In addition to the temperature readings taken to calculate primary and secondary airflow, eight CA T/C probes are used to measure A/B inlet (preburner discharge) Plane 5 temperatures. One of these T/C's is used for input to the Plane 5 auto temperature controller that regulates fuel flow to the preburner. Another T/C is used as an input to the API undertemperature and one for the overtemperature trip-out.

Another set of eight water-cooled iridium-50% rhodium/100% iridium (IR) T/C's is used to measure flame tunnel (A/B discharge) temperature at Plane 7. Two of these T/C's are used as inputs for the T_7 automatic temperature controller, which is used to maintain a preset temperature by adjusting A/B local fuel flow. The controller is used on test runs requiring the same T_7 temperature for a number of readings as a means of cutting down time for

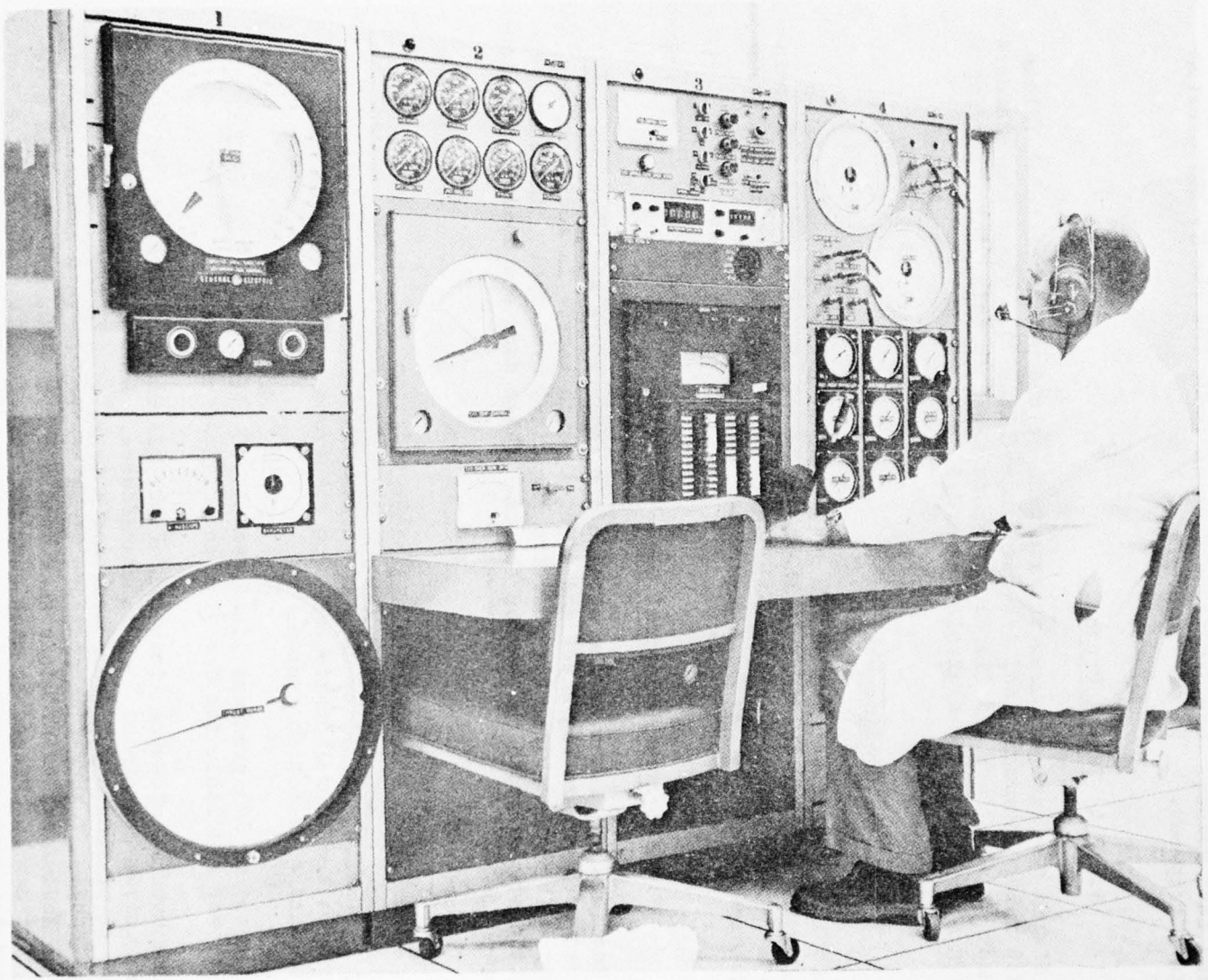


Figure 3-21. JENOTS Control Panel.

setting test points. One T/C is used as an input for the T_7 API overtemperature trip-out.

3.4.3.4 Tunnel Pressure

Static pressure measurements are made at the preburner inlet (Plane 3), A/6 inlet (Plane 5), and A/B discharge (Plane 7). These measurements are made on a Wallace and Tiernan pressure gage, in psia, for recording on the log sheets, and are digitally recorded.

3.4.3.5 Cooling Water

Cooling water pressure at the inlet and outlet is measured with a pressure transmitter and read in the cell remote pressure gauge. Temperatures are measured using chromel-aluminum T/C's and read out on the Brown potentiometer.

3.4.3.6 Meteorological Data

Readings are taken of the outside air temperature and pressure and recorded both on the log sheet and digital punch tape. In addition, wet and dry bulb temperatures for relative humidity, wind speed, and wind direction are recorded on the log sheets. These data are used in correlating sound data.

3.4.3.7 Digital Data Acquisition System

All the above facility data and additional pressure and temperatures for various test model instrumentation requirements are recorded on a digital data acquisition system.

A total of 125 pressure lines, 96 CA T/C circuits, and 21 IR T/C circuits are available for use with the digital system.

One hundred pressure lines out of the 125 connect to a bank of 8 scanner valves containing 25-psia transducers. Each scanner valve can measure 11 pressures per transducer for a total of 88 pressures in the 0 - 25 psia range. Twenty-five pressure lines are routed to a cabinet containing five individual transducers that handle 0, 50, 100, and 500 psia pressures, but can be changed to meet specific requirements. The eight scanners are used for measuring model pressures, while the individual transducers measure facility airflow data.

The CA T/C's are used to measure main airflow temperature and various skin temperatures on the models. The IR T/C's are used to measure flame tunnel temperature. These signals are then fed into an automatic switching unit in an ordered manner and conducted through digital amplifiers to a digital printer and a digital punch. The printer stamps respective digital position numbers and parameters, in "counts", on a ribbon paper that can be correlated, with the aid of a "hook-up" sheet, to readings in engineering units. The punch unit perforates a digital punch tape, which is used for inputting the time-sharing teletype system for processing to engineering units and calculations.

3.4.4 Acoustic Data Acquisition and Reduction

3.4.4.1 Data Acquisition System

The acoustic data collection system at JENOTS is shown schematically in Figure 3-22, while Table 3-I lists the key components. It is composed of a B&K microphone/cathode follower powered and conditioned by a B&K 2801 power supply, followed by three feet of line to a specially designed 10-dB, fixed-gain preamplifier which drive 150 feet of cable terminating at the variable-gain differential input amplifiers to the Sangemo Saber IV tape recorder. The signal is recorded on tape for future playback in the data reduction room.

The most commonly used microphones are the B&K 4135, 1/4-inch (without grid caps) and the B&K 4133, 1/2-inch (with grid caps) free-field microphones. These free-field microphones are designed such that the microphone diaphragm resonance is overdamped in such a way that the normal incidence free-field pressure increase is compensated by the decrease of pressure sensitivity of the microphone cartridge.

The cathode follower used most often is the B&K 2615 preamplifier although B&K 2619 is also used. The purpose of the cathode follower is to give a very high input impedance with small load to the microphone and a low output impedance allowing the connection of long cables between the preamplifier and relatively low impedance amplifiers in the circuit. The B&K 2619 uses a field effect transistor to give higher input impedance and lower inherent noise than Type B&K 2615. The cathode follower also supplies the microphone with a 200 volt polarization from the power supply.

The B&K 2801 power supply is operated in the direct-output mode to avoid sensitivity loss. The frequency response of the various preamplifiers is not influenced by the power supply when used in this position. This power supply does have optional 50-ohm and 200-ohm transformer outputs for use in eliminating amplifier oscillation and dampening RC resonance. The JENOTS systems, however, are free of such problems due to the unloading of the power supply by the preamplifier.

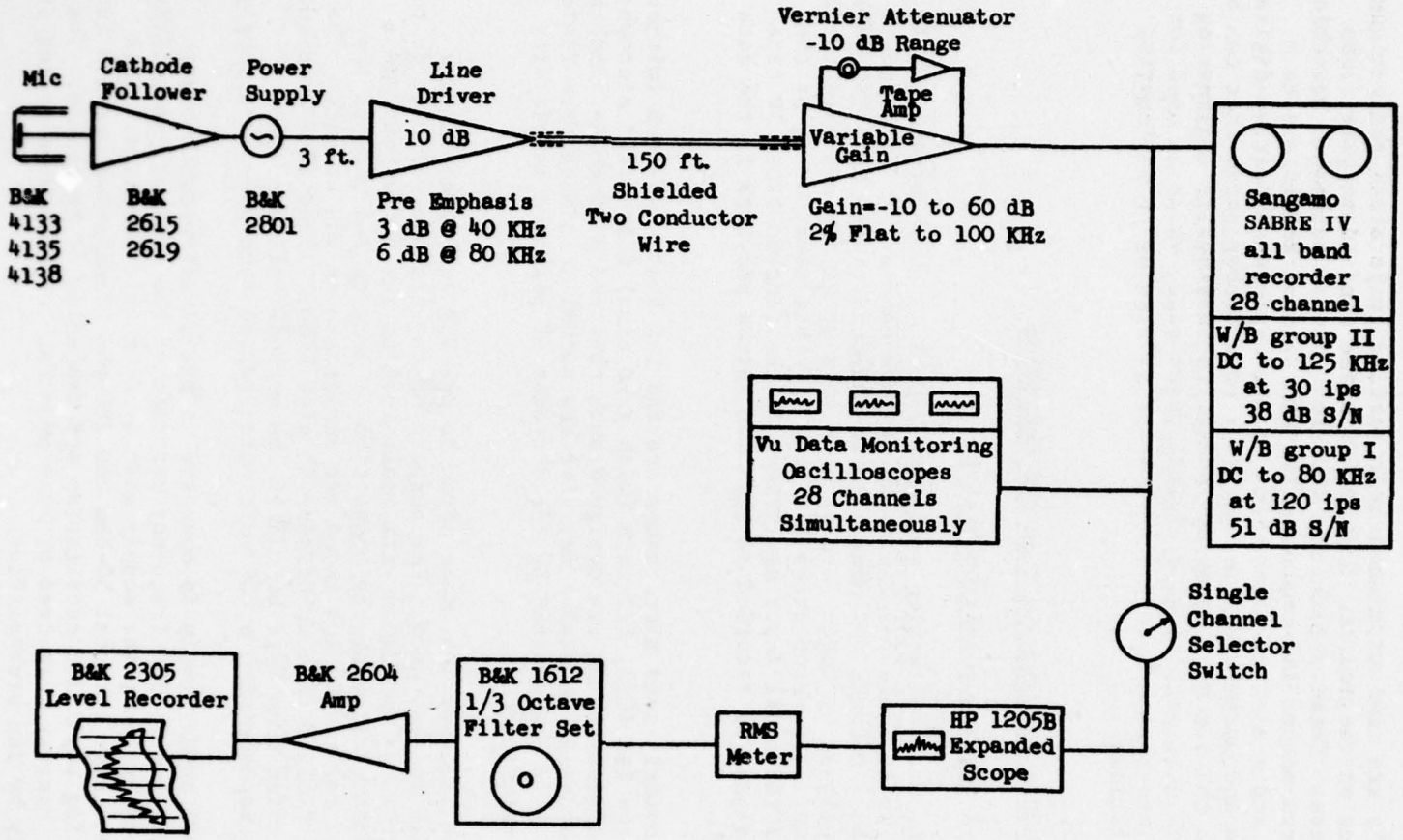


Figure 3-22. JENOTS Data Acquisition System.

Three feet from the output of the power supply is a fixed 10-dB amplifier for driving the signal to the tape recorder amplifier. The amplifier was designed by the General Electric AEG Electronic Instrumentation Group and built from high quality components by Random Electronics, a Cincinnati firm. In anticipation of the low sound levels experienced at high frequency, the circuitry was designed with a frequency response that "pre-emphasized" the high frequency signals such that it has a 3 dB increase at 40 Hz and an additional 3 dB between 40 Hz to 80 Hz. This feature is optional and can easily be removed if one expects high levels at high frequency, and desires a flat frequency response throughout the spectra.

Two conductor shielded wire was chosen for the 150 feet of lead from the line driver to the tape recorder amplifier. This design was favored over the conventional coaxial cable because of the susceptibility of the coaxial cable towards pick up of stray signals, such as radio stations. The two-conductor shielded wire is also more rugged than the coaxial and lasts longer giving lower maintenance and replacement cycles. The cable introduces an effective 0.0458 μf capacitance to the circuit.

The amplifier at the tape recorder was designed by GE and built by Random Electronics. It has a variable gain from -10 dB to +60 dB. The amplifier delivers a 4-volt peak-to-peak signal to the tape recorder electronics at the normal calibration signal level. This setting will allow a 6 dB over range without distortion. The amplifiers are flat within 5% from 5 Hz to 100 Hz. Each amplifier has an adjustable vernier attenuator which can give any desired measure of attenuation between 0 and 10 dB. During test calibration, this vernier is usually adjusted to make the 124 dB piston phone calibration signal the full-scale (1.4 V/rms) input to the tape recorder. The 10 dB steps in the tape recorder amplifier then directly correspond to 10 dB steps in OASPL from 124 dB. The vernier can be moved to the fixed position, in which case, the signal goes directly into the 10 dB step tape recorder amplifier. The output of each amplifier channel has a V-Data Monitoring oscilloscope for continual inspection of all signals for any clipping or deterioration of the signal due to excessive crest factor (Peak Value/rms).

The Sangemo Sabre IV, 4930 magnetic tape recorder/reproducer has IRIG wideband and RM wideband Group I and Group II capability. In normal JENOTS operation all data is recorded on one inch in Wideband Group II at 30 inch/sec, having a flat frequency response in excess of 100 kHz when used in conjunction with the B&K 4135 microphone. The voice channel is recorded direct.

The JENOTS recorder was modified to record 28 tracks and to improve its signal-to-noise dynamic range from the normal 32 dB to 39 dB overall frequencies. This lower noise floor was obtained by individual channel tuning by the Sangemo Electric Company at the factory. Playback capability of two data channels + voice for on site data investigation is also available.

3.4.4.2 Data Reduction

On-line data reduction and monitoring capability is available in the JENOTS control room. As shown in Figure 3-22, a single-channel selector switch can route any microphone signal parallel to the tape recorder for expanded waveform presentation on an HP1205 B oscilloscope. Overall sound level of the selected channel can be read out on a calibrated rms meter. The signal can then be passed through a B&K 1612 band pass filter set, amplified by a B&K 2604 amplifier and recorded on a B&K 2305 level recorder. The filter set can be dialed to 1/3-octave frequencies from 12.5 Hz to 40 kHz, octave frequencies from 16 Hz to 31.5 kHz, or linear, "A", "B", and "C" weighted networks from 20 Hz to 45 kHz.

Standard data reduction is conducted in the General Electric AEG Instrumentation and Data Room (IDR). As shown in Figure 3-23, the data tapes are played back on a CEC3700B tape deck with electronics capable of reproducing signal characteristics within the specifications indicated for Wideband Group I and Group II. An automatic shuttling control is incorporated in the system. In normal operation, a tone is inserted on the recorder and the time slot designed for the data analysis. Tape control automatically shuttles the tape initiating an integration start signal to the analyzer at the tone as the tape moves in its forward motion. This motion continues until an integration complete is received from the analyzer, at which time the tape direction is reversed and, at the tone, the tape restarts in the forward direction advancing channel to be analyzed until all the channels have been processed. A time code generator is also utilized to signal tape position of the readings, as directed by the computer program control. After each total reading is completed, the number of tape channels at each point is advanced to the next reading.

All 1/3-octave analysis is performed on a General Radio 1921 1/3-octave analyzer. Normal integration time is set for 32 seconds to ensure good iteration for the low frequency content. The analyzer has a 1/3-octave filter set for 12.5 Hz to 100 kHz and has a rated accuracy of ± 1/4 dB in each band. Each data channel is passed through an interface to the GEPAC 30 computer where the data is corrected for the freqency response of the microphone and the data acquisition system; corrected to Standard day (59° F, 70% RH) atmospheric attenuation conditions, per SAE ARP866 Standards; and processed to calculate the perceived noise level and OASPL from the spectra. The output of the computer is passed to a Terminet 300 console where the corrected SPL's can be punched out on paper tape and printed out on sheets for "quick look" analysis. For calculation of acoustic power, corrections for ground reflections to free field, scaling to other nozzle sizes, or extrapolations to different far-field distances, the data is sent to the Honeywell 6000 computer for data processing. This step can either be accomplished by storing the SPL's on punched paper tape and/or transmitting via direct time-share link to the 6000 computer through a 1200 Band Modem. In the 6000 computer, the data are processed through the Full-Scale Data Reduction (FSDR) Program where the appropriate calculations are performed. The data print out is accomplished on a high speed, "remote" terminal. A magnetic tape can be written for Calcomp plotting of the data.

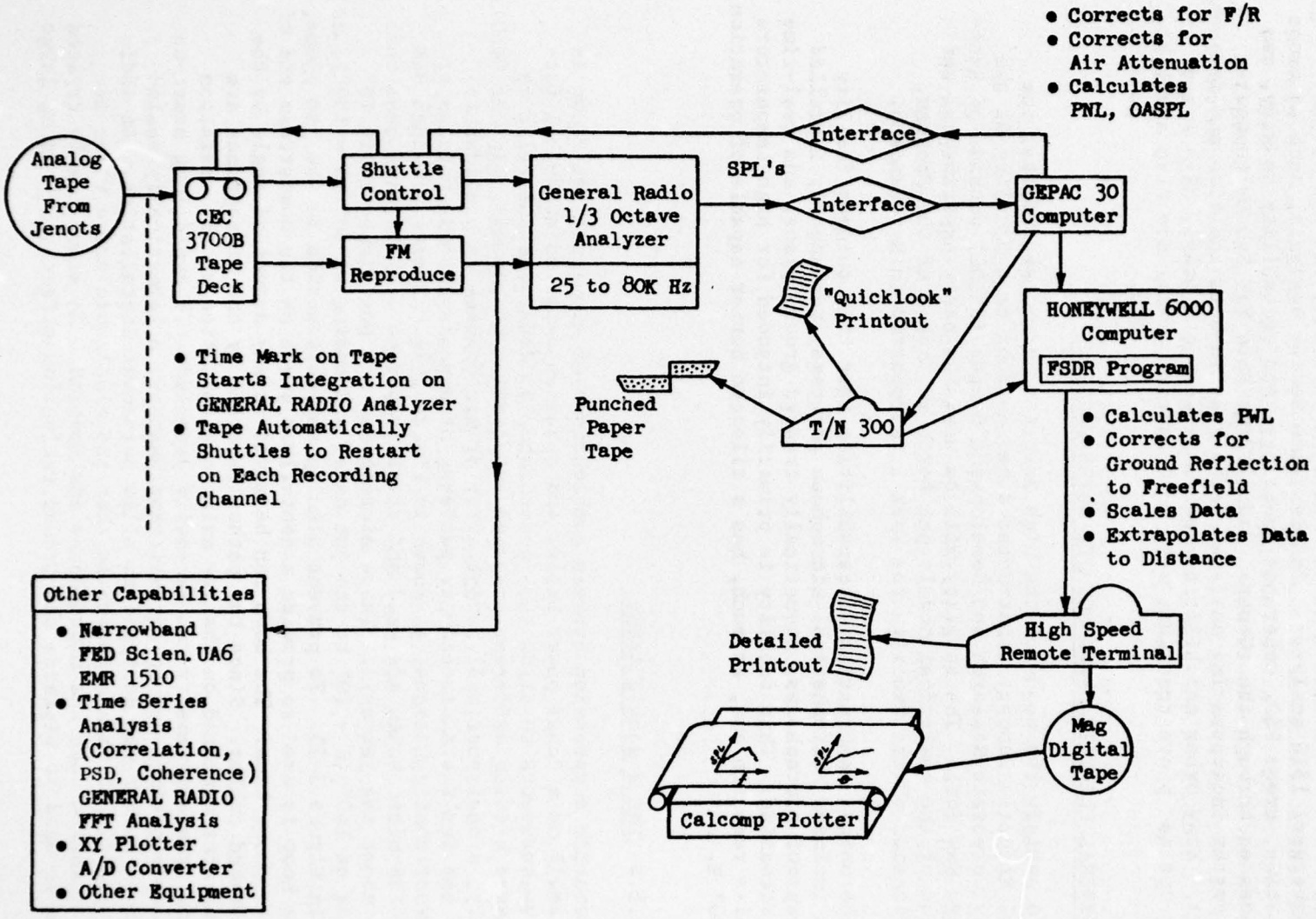


Figure 3-23. Data Reduction System.

Other data reduction techniques are available in IDR. Constant narrow-band spectra can be reduced on the Federal Scientific UA6 or the EMR (Schlumberger) 1510 analyzer. Complex Time Series Analysis, such as cross correlation, cross PSD, coherence functions, and probability density, can be processed through the (General Radio) Time Data FFT System (computer based system incorporating analysis techniques in both the time and frequency domain). Many other capabilities such as tracking filters, high speed "Fiber Optics" plots transient wave form capture, etc., are also available.

3.5 GENERAL ELECTRIC/CR&DC HOT JET NOISE FACILITY

To satisfy the needs of the High Velocity Jet Noise Program, the General Electric Company constructed a new outdoor test facility at the company Corporate Research and Development Center (CR&DC) outside of Schenectady, New York. The facility will be used for basic experimental verification of the analytical models set forth in Task 2 of the Program. Certification of the facility for Task 1 is reported in Reference 6.

The unique combination of capabilities that this outdoor facility offers includes hemispherical microphone coverage, permanently installed weatherproof microphones, acoustically treated ground plane, and real-time data processing. This facility is primarily intended for high temperature jet noise research and, as such, has a silenced burner capable of operation to 2200° R.

3.5.1 The Acoustic Arena

Acoustic suppression between combinations of elemental jet flows is quite small on a total power basis, and requires detailed azimuthal far-field measurements to allow the investigator to determine the relative importance between different proposed suppression mechanisms. In the CR&D facility, a hemispherically swept array of microphones is provided to survey the far-field directivity patterns of nonaxisymmetric nozzles or suppressor configurations, as shown in Figure 3-24. Twelve 1/2-inch B&K Model 4133 microphones are used and are attached to a traversing boom that pivots about the jet axis. These microphones are positioned every 10° starting at 160° (θ = 20° to the jet axis) and ending at 50° (θ = 130°), as shown in Figure 3-25. To prevent placing any obstruction in the jet plume, a large hoop is used to provide a centerless pivot on the downstream end of the microphone boom. The boom can be moved to any azimuthal angle by the two overhead cables. Since the paths traversed by the microphones are circular arcs centered on the jet axis, any deviation of the radiation patterns from axisymmetry can be easily detected. To avoid long start-up and shut-down times due to intermittent weather, a hermetically sealed microphone holder was designed to allow permanent installation. An additional benefit of this approach is that the electronic noise floor is easily measured when the microphones are covered. An acoustically treated surface is used to minimize the ground reflection effects. By using large



Figure 3-24. CR&DC Hot Jet Noise Facility.

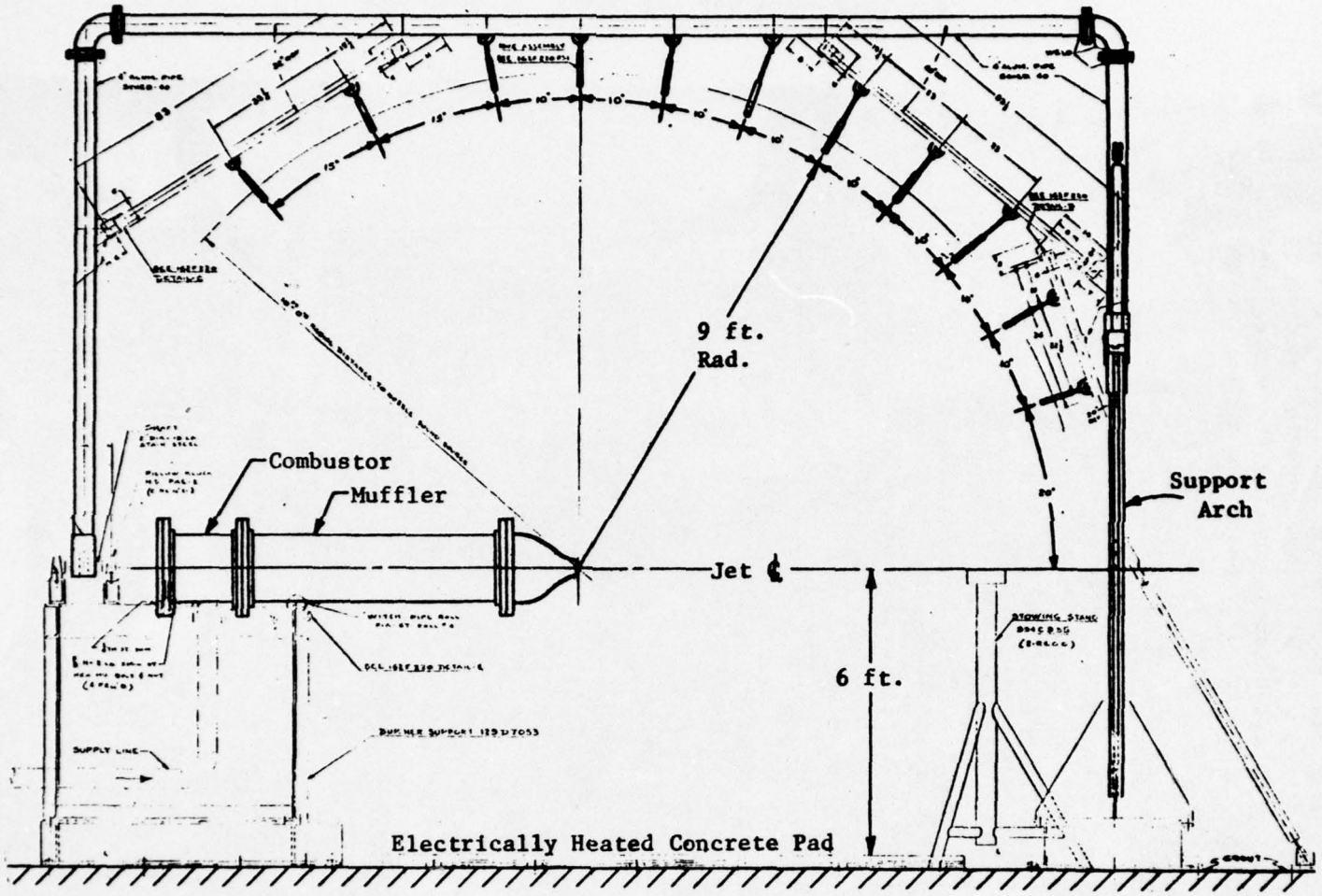


Figure 3-25. Acoustic Arena at GE CR&DC Hot Jet Facility.

sheets of acoustical foam, significant reduction of the ground reflection pattern can be obtained with a minimal time required to lay down and take up the coverings. To allow testing during the winter months, the 30 x 28 foot concrete pad is electrically heated to remove ice and snow.

3.5.2 Jet Facility

To provide the heated air for the high temperature tests, two heaters are used. A large natural gas-fired heat exchanger preheats the air to about 400° F and this warm air is fed into the burner end of the combustor-muffler through a 4-inch pipe, as can be seen on Figure 3-26. Two small JP4 combustors are used to provide the remainder of the heat addition. To prevent combustion noise from contaminating the jet noise downstream of the burners, acoustically treated baffles are used to prevent a see-through path, and the wall of the plenum is lined with two inches of Kaowool and faced with a 1/8-inch-thick perforated sheet (45% porosity) of Hastelloy X. A layout of this muffled burner is shown on Figure 3-26. To date, the burner has been operated to 2000° R with no thermal damage.

The jet total temperature and pressure are monitored using wall static taps and a thermocouple in the low velocity plenum upstream of the nozzle contraction, as shown in Figure 3-26.

3.5.3 Data Acquisition and Reduction System

Data acquisition is controlled by an HP 2100 series minicomputer that obtains the acoustic signals from a GR 1921 real-time 1/3-octave band analyzer and samples the temperatures and pressure signals. By the use of a scanning multichannel amplifier, GR 1566, each microphone signal is sequentially analyzed, and the signal level of each 1/3-octave band (100 Hz to either 40 kHz or 80 kHz depending on the type microphone utilized) is stored on magnetic tape (see Table 3-I for complete listing). For operational monitoring, a three-dimensional plot of SPL, 1/3-octave frequency, and acoustic angle from each microphone is displayed on an oscilloscope as the microphone array is sampled. For backup and when longer averaging times are necessary, the acoustic signals are recorded simultaneously on a Sangemo Sabre IV, Wideband, Group II tape recorder. After all the signals have been accumulated, the computer corrects the data for nonuniform response of the microphone cartridge. Using these corrected values of the sound pressure levels for each microphone, the 1/3-octave band acoustic power levels and the overall acoustic power level are computed. The raw and calculated data is then stored on magnetic tape.

While the computer is processing the acoustic data, simultaneous measurement and calculation of all the pertinent parameters for determination of the nozzle exit conditions and ambient conditions are also carried out and recorded on magnetic tape. Since all the pertinent data exists on one magnetic tape, the acoustic information is readily normalized immediately following the test on the minicomputer.

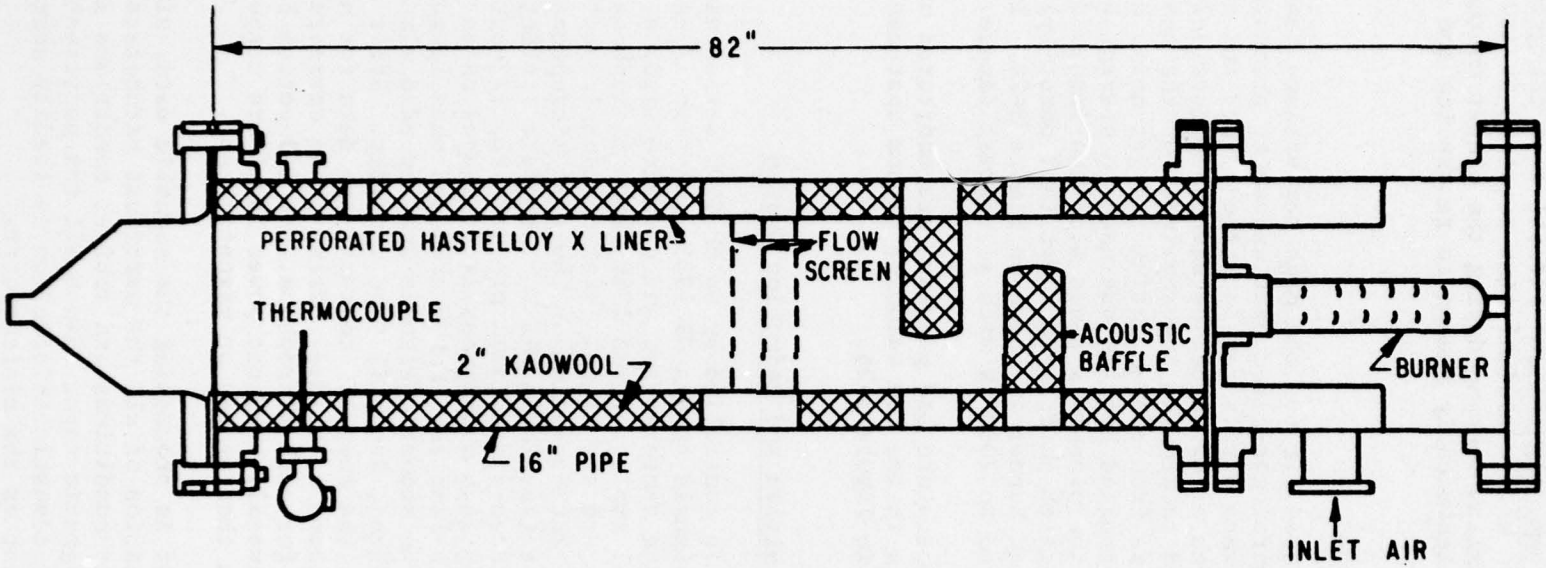


Figure 3-26. Burner-Muffler Construction (CR&DC).

3.6 J79 ENGINE INSTALLATION AT GE/EFTC

To obtain full-scale (effective nozzle diameter = 20.84 inches) jet noise data, the J79-15 engine was installed on the General Electric Edwards Flight Test Center Testing Facility (GE/EFTC). GE/EFTC is located at Edwards Air Force Base in Southern California's Mojave Desert. An existing outdoor test site with its thrust measuring table, referred to as "the North Site", was chosen as the prime location due to the absence of surrounding buildings and obstructions. The Task 1 certification of the facility is found in Reference 7.

3.6.1 The Acoustic Arena

Before acoustic testing could be conducted on the North Site, the following preparations to the surrounding ground were seen as desirable and implemented:

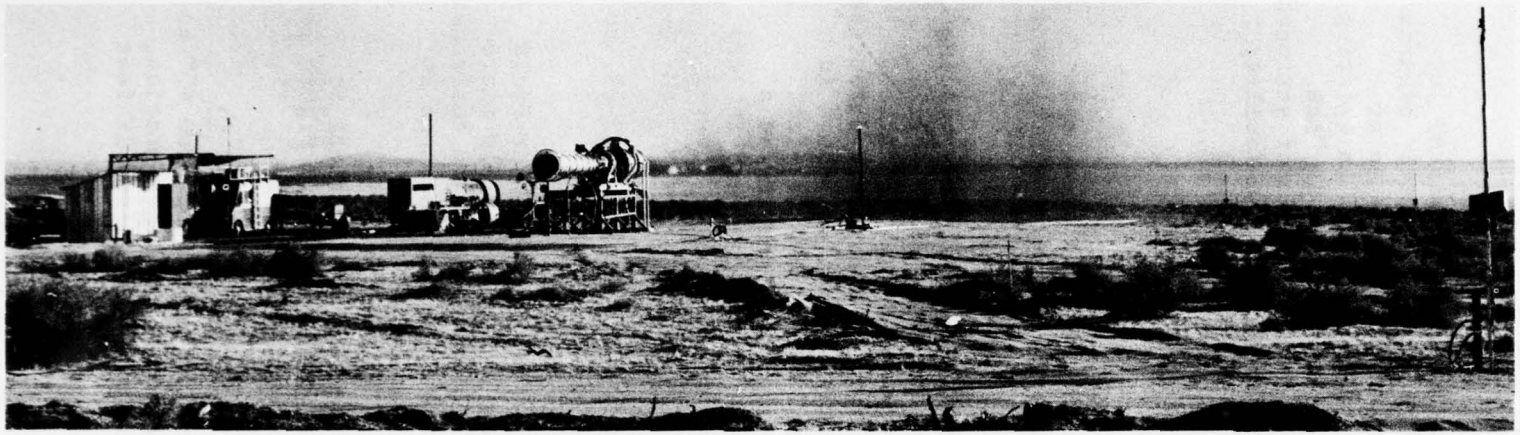
- Grading of the existing site, shown in Figure 3-27a, surrounding the thrust pad to obtain a smooth acoustic arena which still would provide water drainage during adverse weather conditions. Therefore, the ground was gradually sloped in a downward direction to obtain a -0.3-foot elevation at a 160-foot radius, shown in the inset of Figure 3-28. Between the 160-foot and 170-foot radii the terrain slopes down another -0.3 foot serving as a trench to carry off rain water. Between this trench and the dry lake bed (elevation -4.2 ft), the terrain is sparsely covered with desert brush.

- Oiling and packing of the new test site, shown in Figure 3-29, to prevent desert sand from shifting during wind storms.

- Installation of underground transmission cables for: far-field microphone stations (36 individual lines), and near-field microphone stations (20 individual lines). These cables were collected in a submerged junction box, the location of which is shown in Figure 3-28.

- Installation of junction boxes containing AC power outlets to provide line voltage to the microphone power supplies. Figure 3-27(b) shows a view of the test site as used during 1974.

The sound field used during exhaust nozzle tests consisted of 13 microphone stations distributed around a 160-foot arc extending from 40° to 160° (engine inlet plane referenced) in 10° increments. At each station, two microphones were erected to approximate heights of 2 feet and 12 feet above the ground, as shown in Figure 3-30.



Edwards Flight Test Center "North Site" Before Grading.

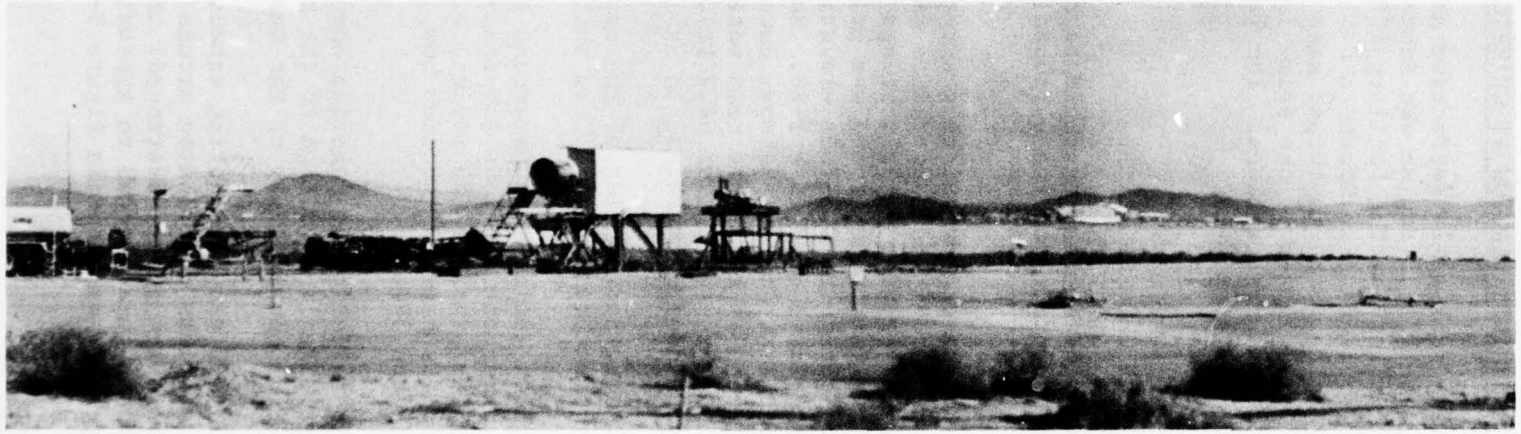


Figure 3-27. Edwards Flight Test Center "North Site" After Grading.

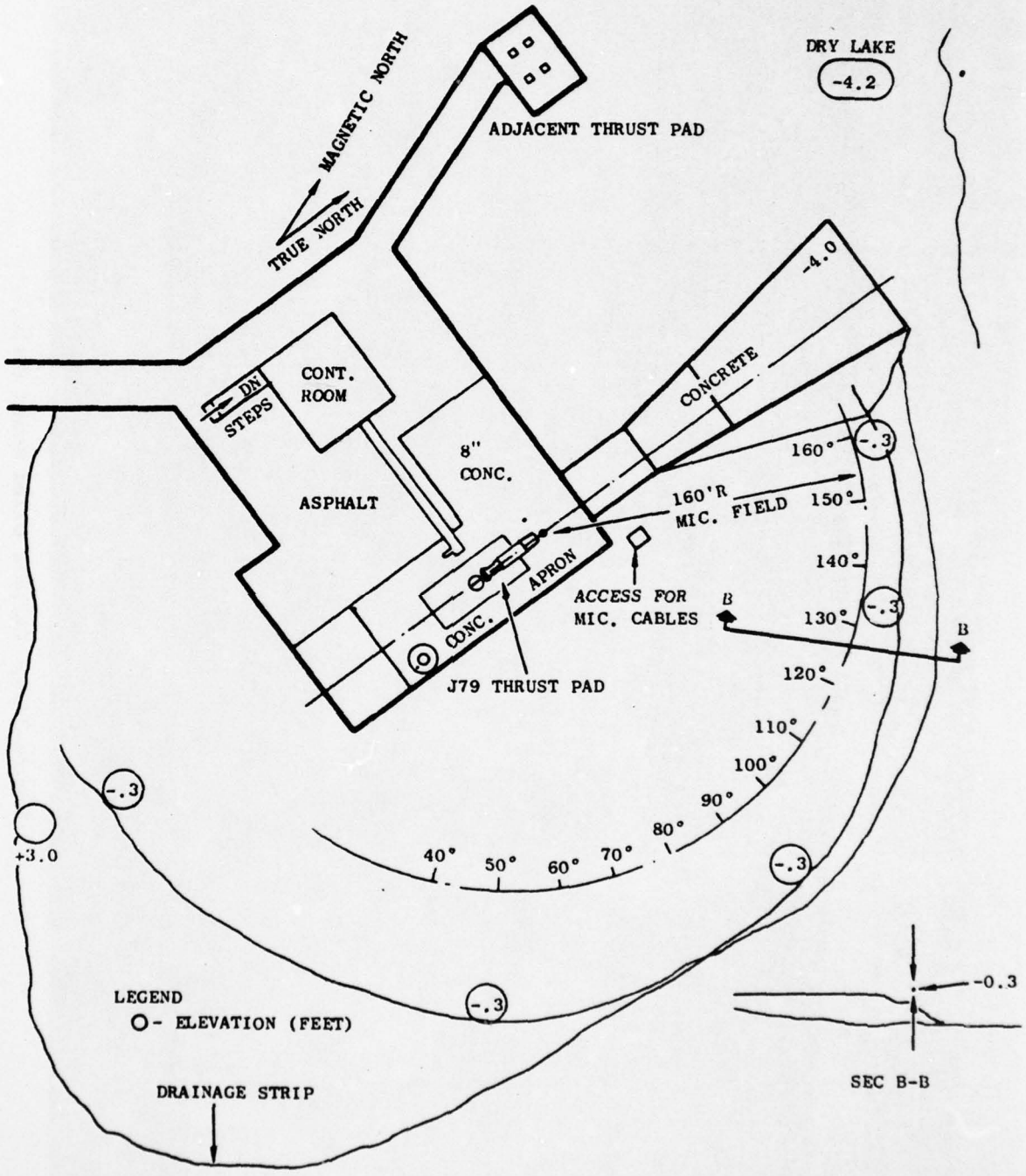
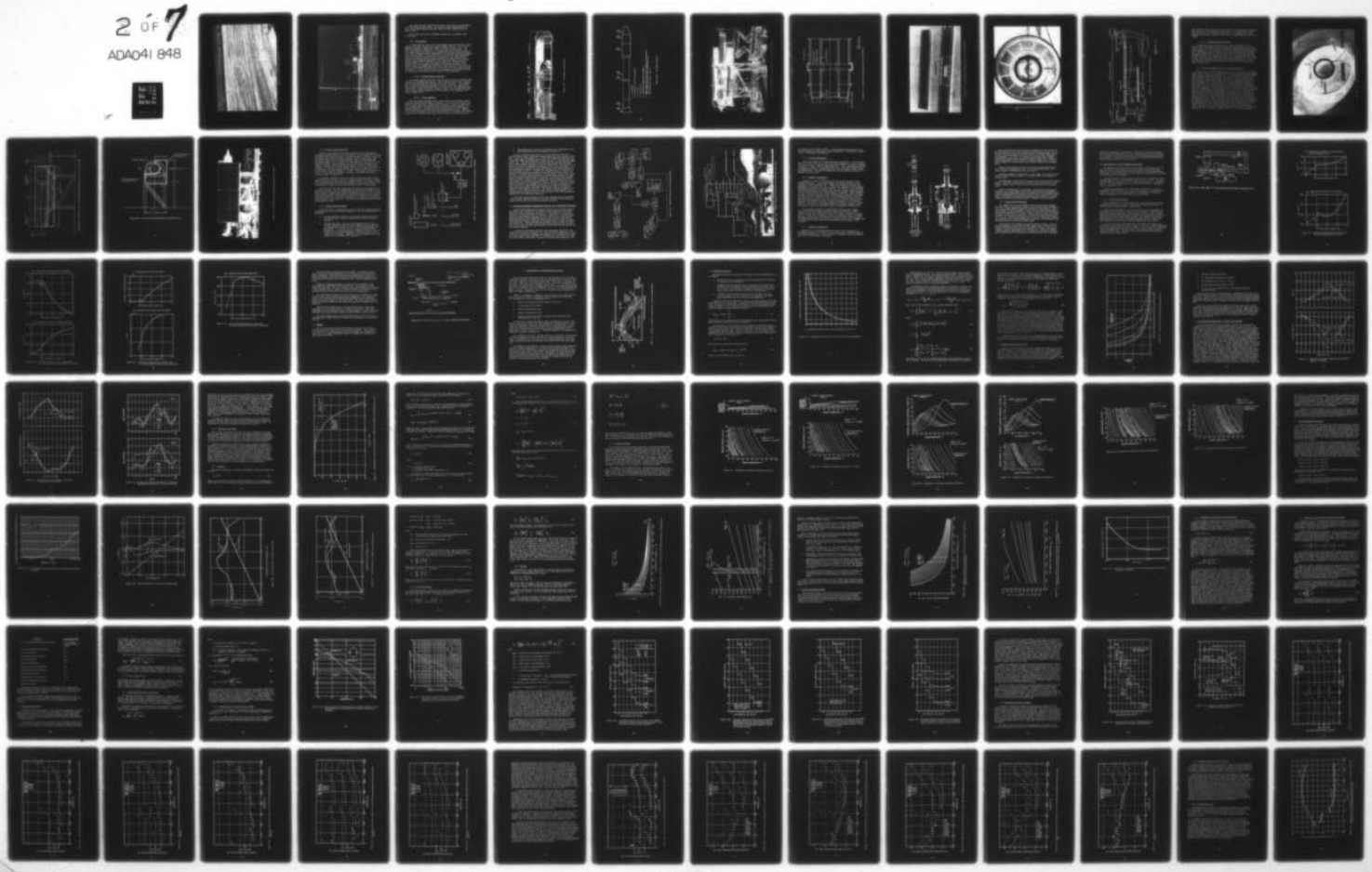


Figure 3-28. Schematic of the GE/EFTC Sound Field.

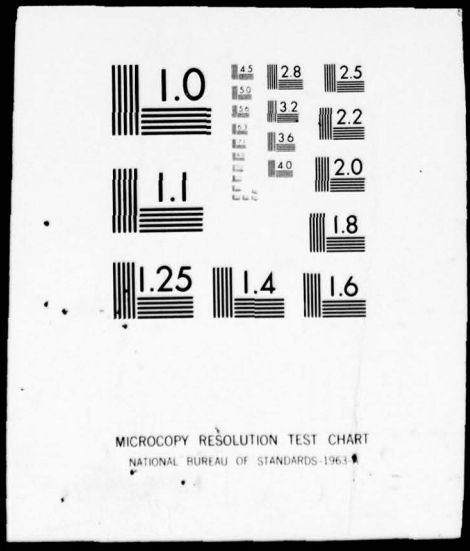
AD-A041 848 GENERAL ELECTRIC CO CINCINNATI OHIO AIRCRAFT ENGINE GROUP F/G 14/2
HIGH VELOCITY JET NOISE SOURCE LOCATION AND REDUCTION. TASK 1. --ETC(U)
FEB 77 C T SAVELL, E J STRINGAS DOT-OS-30034
UNCLASSIFIED R77AEG187 FAA-RD-76-79-1 NL

2 OF 7
ADA041 848



2 OF 7

ADA041 848



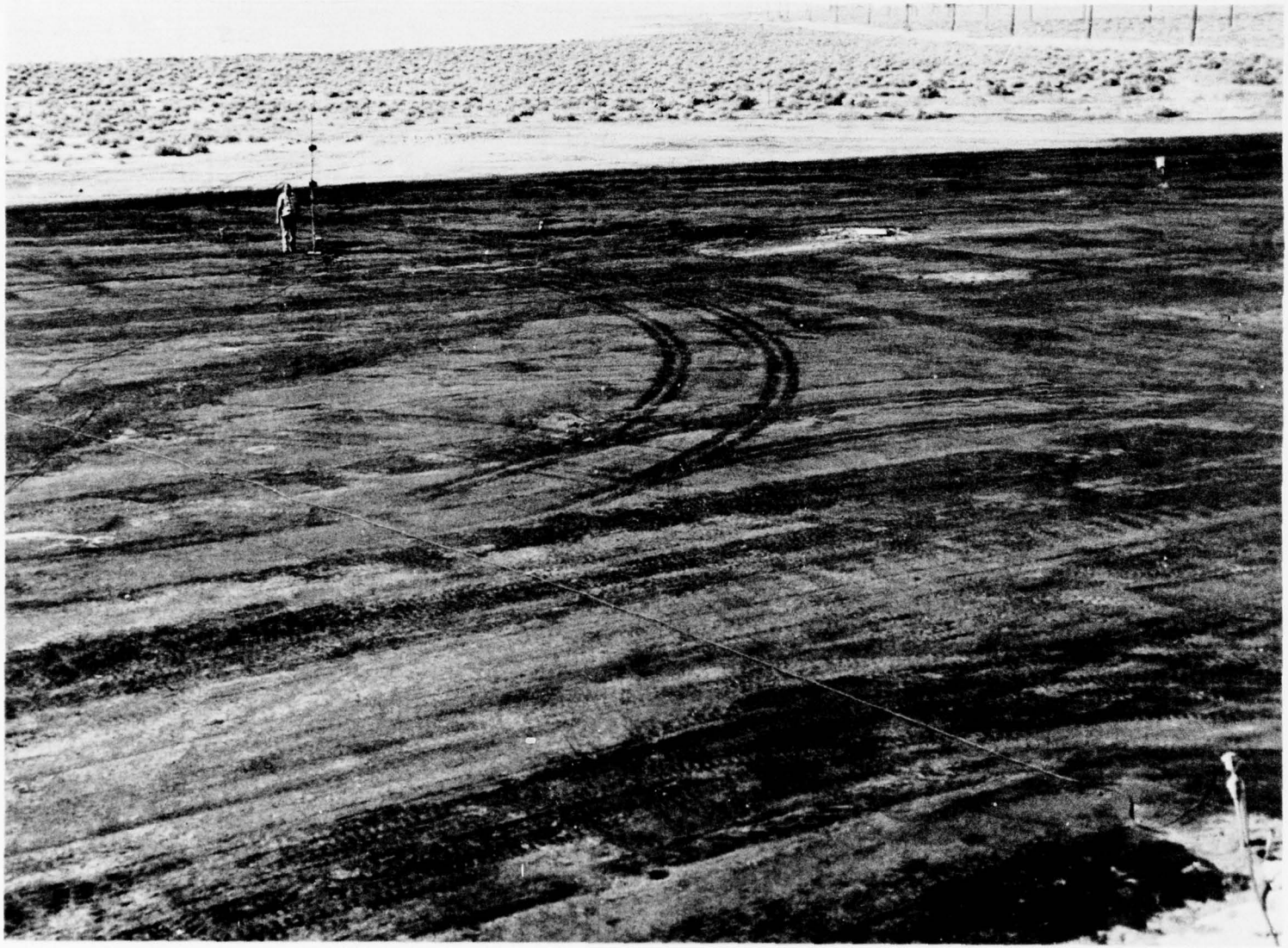


Figure 3-29. GE/EFTC Oiled Sound Field.

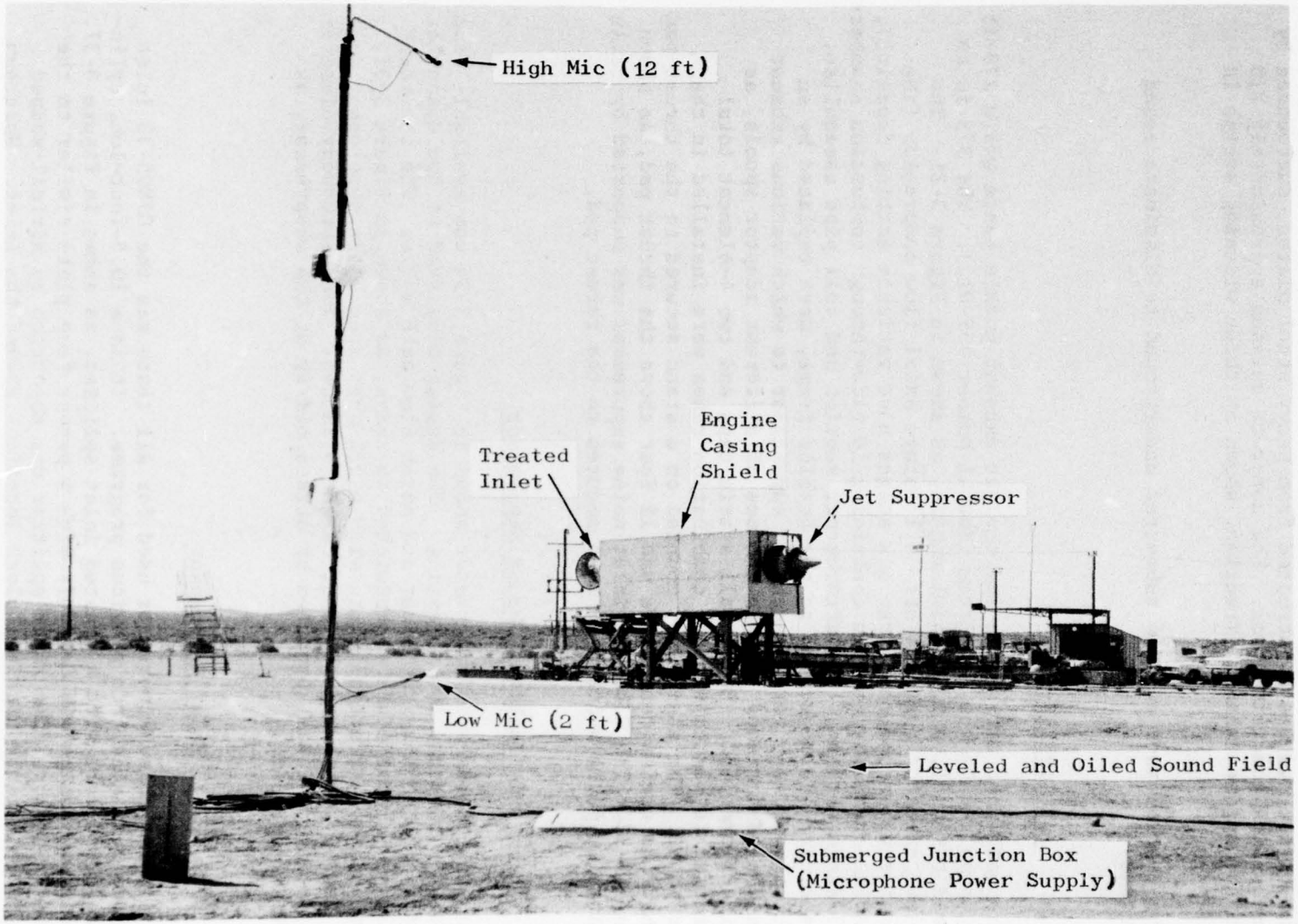


Figure 3-30. Acoustic Arena of the J-79 at GE/EFTC Showing Two-Microphone Setup.

The thrust pad was constructed from heavy steel plates, surrounded by an 8-inch-thick concrete apron. The concrete extends approximately 210 feet in the engine exhaust direction, shown as three widening strips in Figure 3-28.

The control room was 3/4 submerged underground to eliminate sound reflections.

3.6.2 Jet Facility

The noise and air source for the jet exhaust nozzle tests was a J79-15 engine, supplied by the Air Force (Serial Number 439-012). The J79 is an augmented turbojet, single-spool engine, as shown in Figure 3-31. The basic gas generator consists of: a 17-stage axial flow compressor (the inlet guide vanes and the first six stages have variable setting capacity), a coannular combustor section containing 10 flow-through combustion chambers, and a 3-stage turbine. The afterburner section and tail pipe assemblies, which are normally connected to the turbine frame, were replaced by an acoustically treated turbine exhaust suppressor to which various exhaust nozzles can be fastened through the use of different adaptor spools, as shown in Figure 3-32. Eight wall static taps and two 4-element total pressure and total temperature combination rakes were installed in the adaptor spool. The engine was mounted on a stand secured to the thrust pad such that the engine centerline was 12 feet above the thrust pad, as shown in Figure 3-33. The CJ805-23 inlet noise suppressor was supported by rails and hydraulic jacks which were also secured to the thrust pad.

3.6.2.1 Turbine Exhaust Suppressor

The turbine exhaust suppressor shown in Figure 3-34 was available from previous J79 turbomachinery testing. The design consisted of two coannular treated spools forming the inner and outer flow path walls. The treatment was 1.3-inch-thick Cerafelt sandwiched in trays, as shown in Figure 3-35, and enclosed by perforated plate with a 23% open area. The suppressor duct length was 54 inches and the duct height 9 inches. The centerbody diameter was 18 inches, and was supported by struts midway of the suppressor, as shown in Figure 3-36.

3.6.2.2 Inlet Suppressor

The inlet noise suppressor used for all tests was the CJ805-23 inlet suppressor available from previous programs. It is a 10.5-foot-long cylindrically lined duct with a treated inlet splitter, as shown in Figure 3-37. The treatment design was Cerafelt with a porous face plate similar to the exhaust suppressor. The inlet splitter was supported by airfoil-shaped struts placed at the cardinal clock locations around the inlet. Upstream of the inlet suppressor, a 27-inch-long calibrated J79 bellmouth was attached containing four thermocouples, also at the cardinal clock positions, and

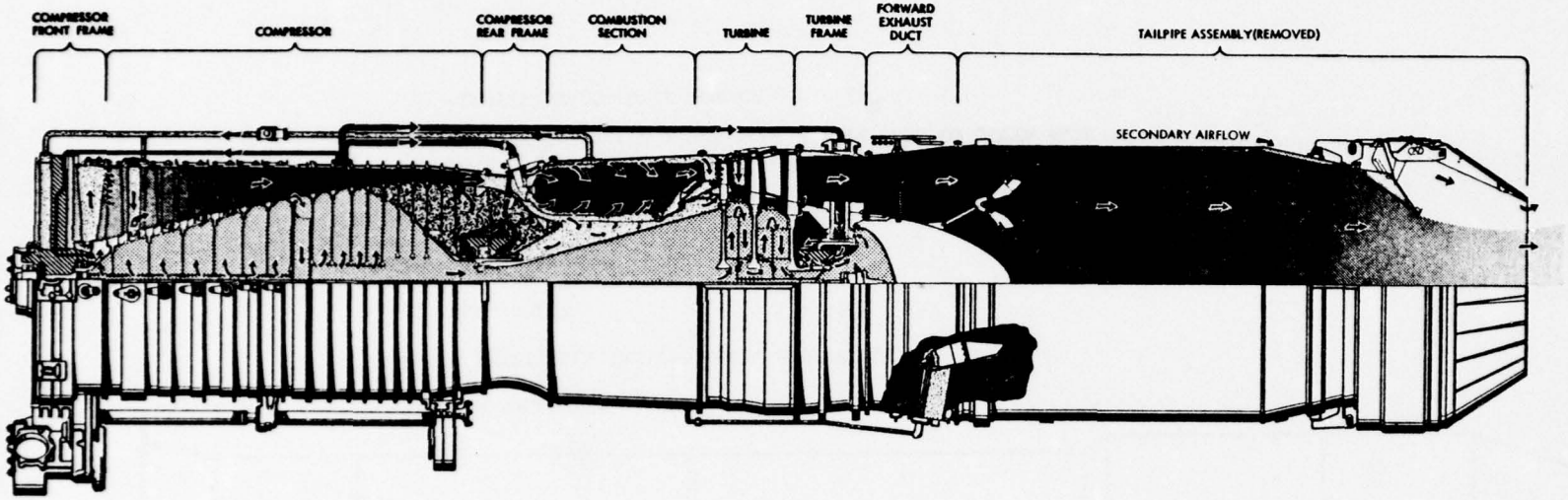
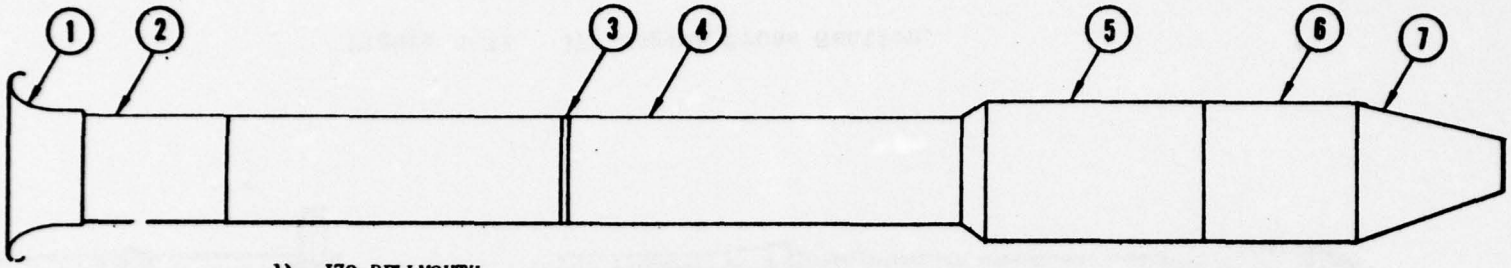


Figure 3-31. J79 Engine Cross Section.



1) J79 BELLMOUTH

2) ACOUSTICALLY TREATED INLET SUPPRESSOR

3) SLIP JOINT

4) J79-15 ENGINE

5) ACOUSTICALLY TREATED EXHAUST SUPPRESSOR

6) NOZZLE ADAPTER SPOOL INCLUDING TWO 4 ELEMENT Pt-Tt COMBINATION EXHAUST RAKES AND EIGHT WALL STATIC TAPS ON OUTER WALL

7) CERTIFICATION CONIC NOZZLE: 338 IN^2

Figure 3-32. J79 Engine Stackup.

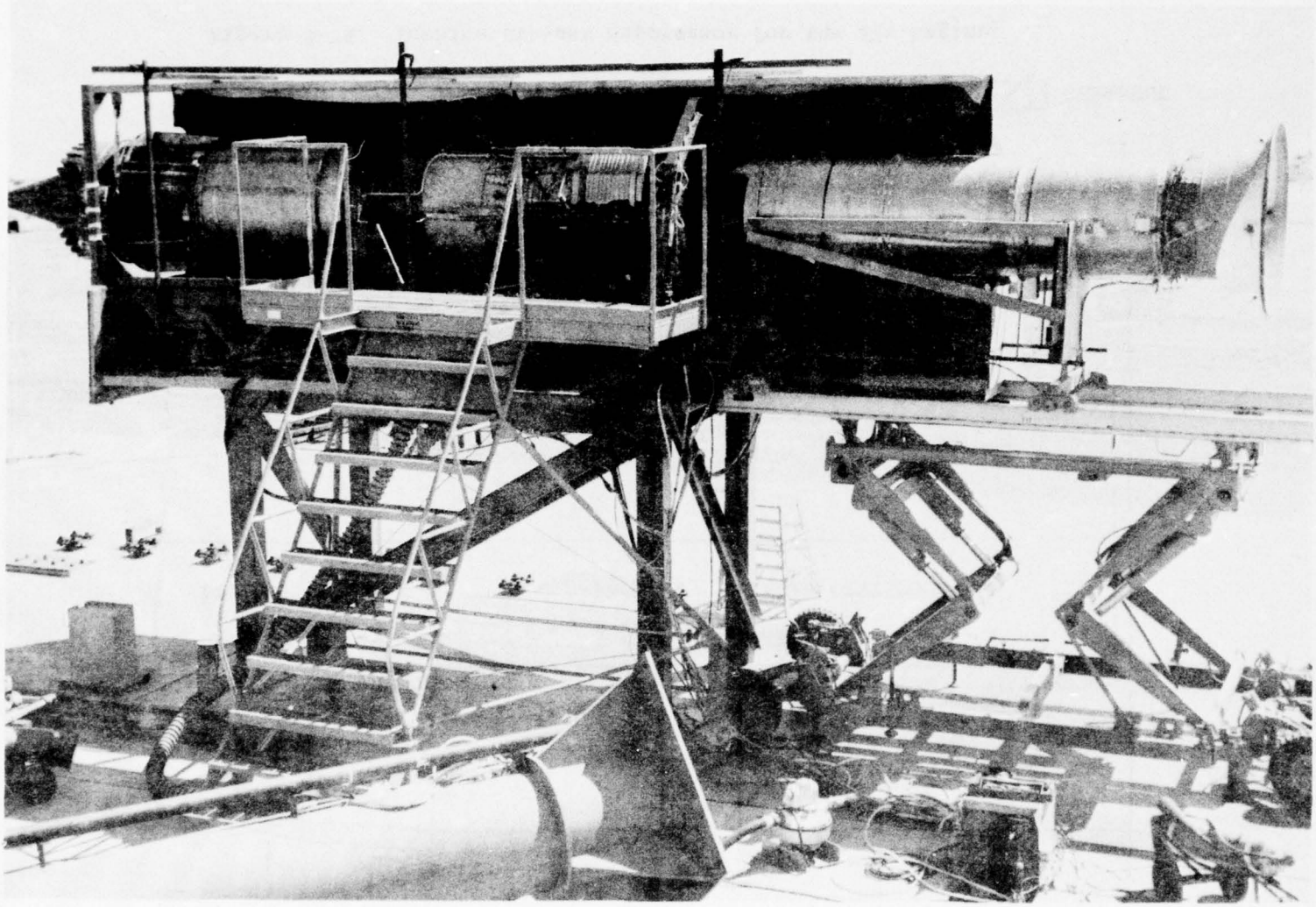


Figure 3-33. Unshielded View of J79 Engine Installation at GE/EFTC.

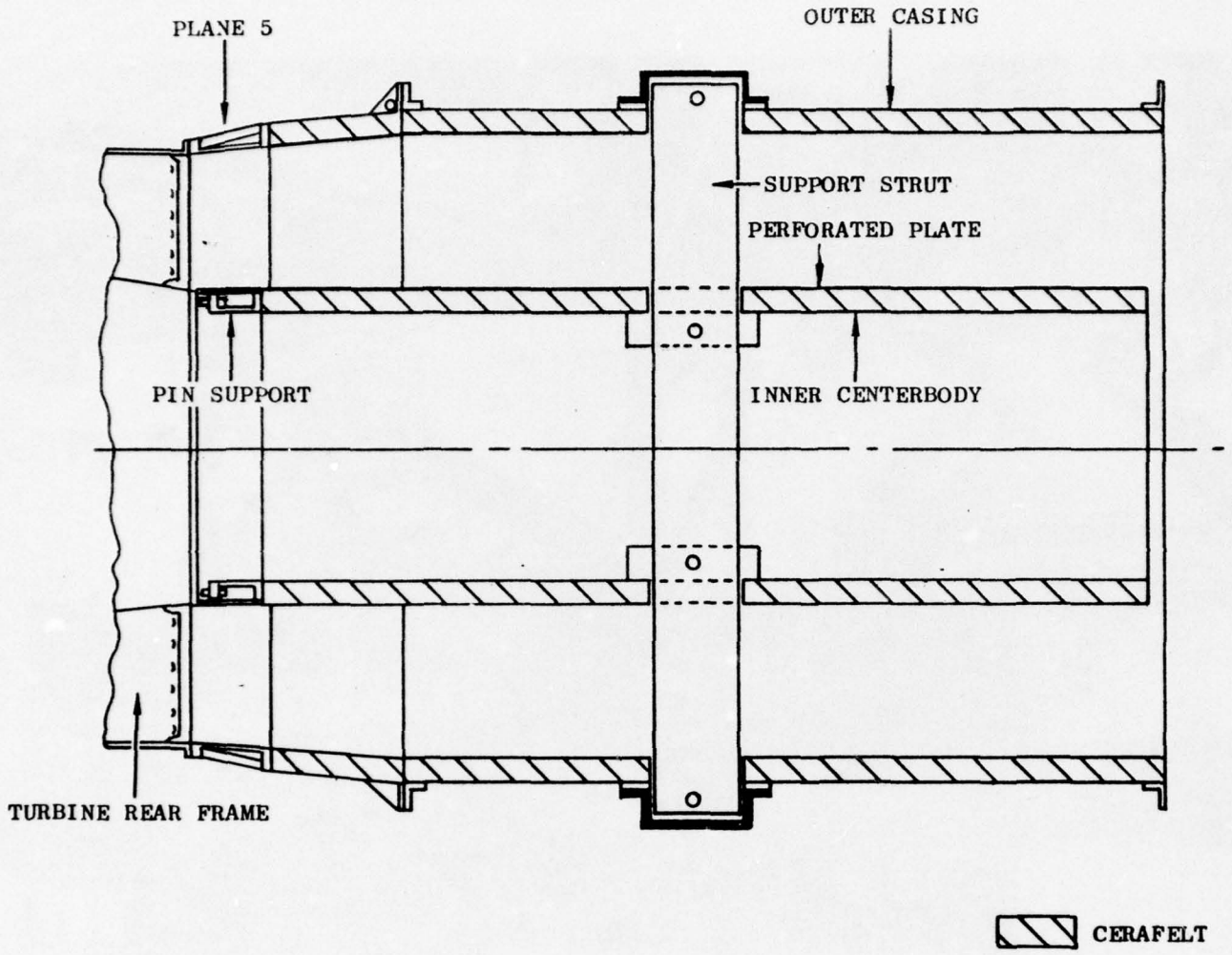


Figure 3-34. Turbine Exhaust Suppressor for the J79 Engine.

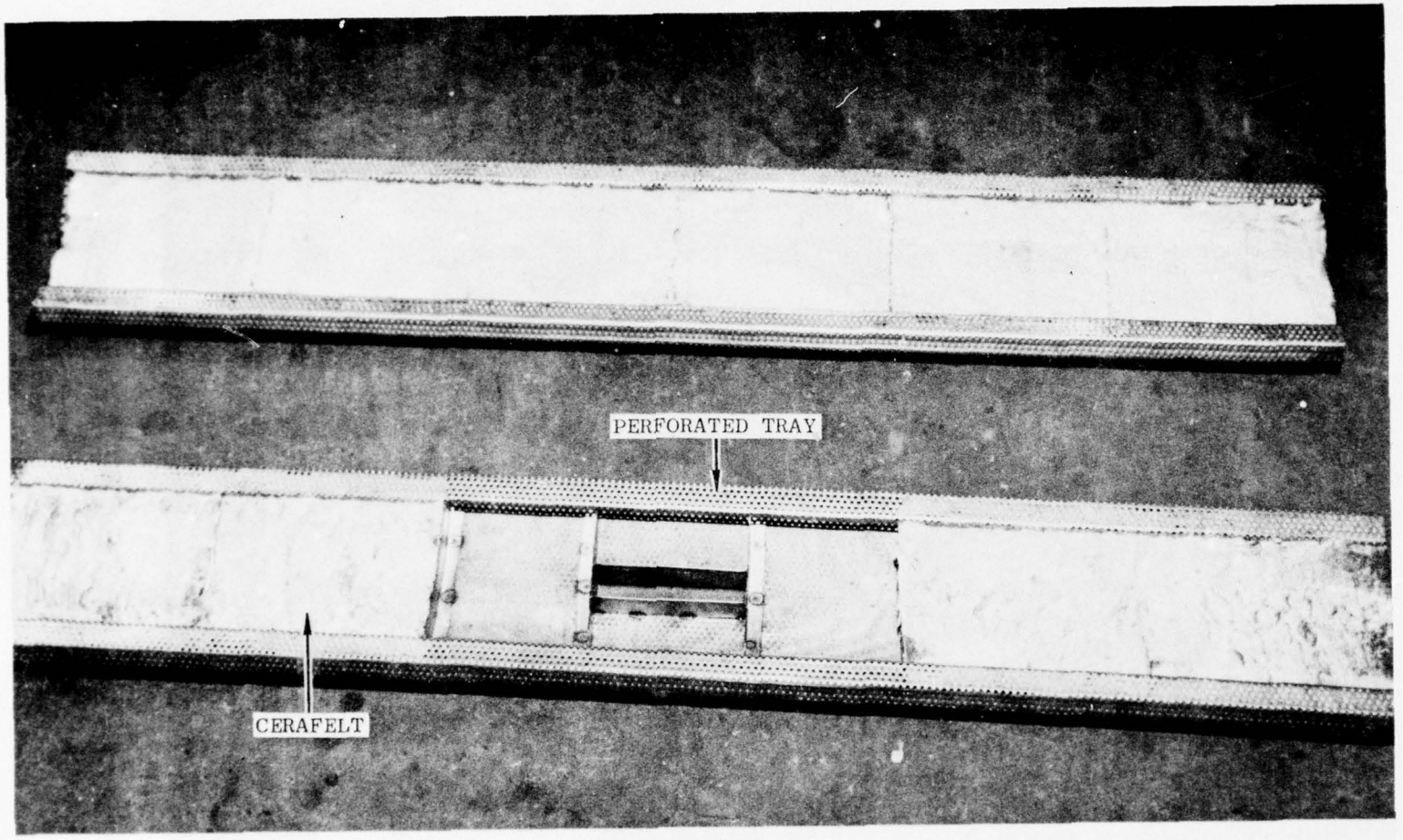


Figure 3-35. Treated Exhaust Suppressor Trays for the J79 Engine.

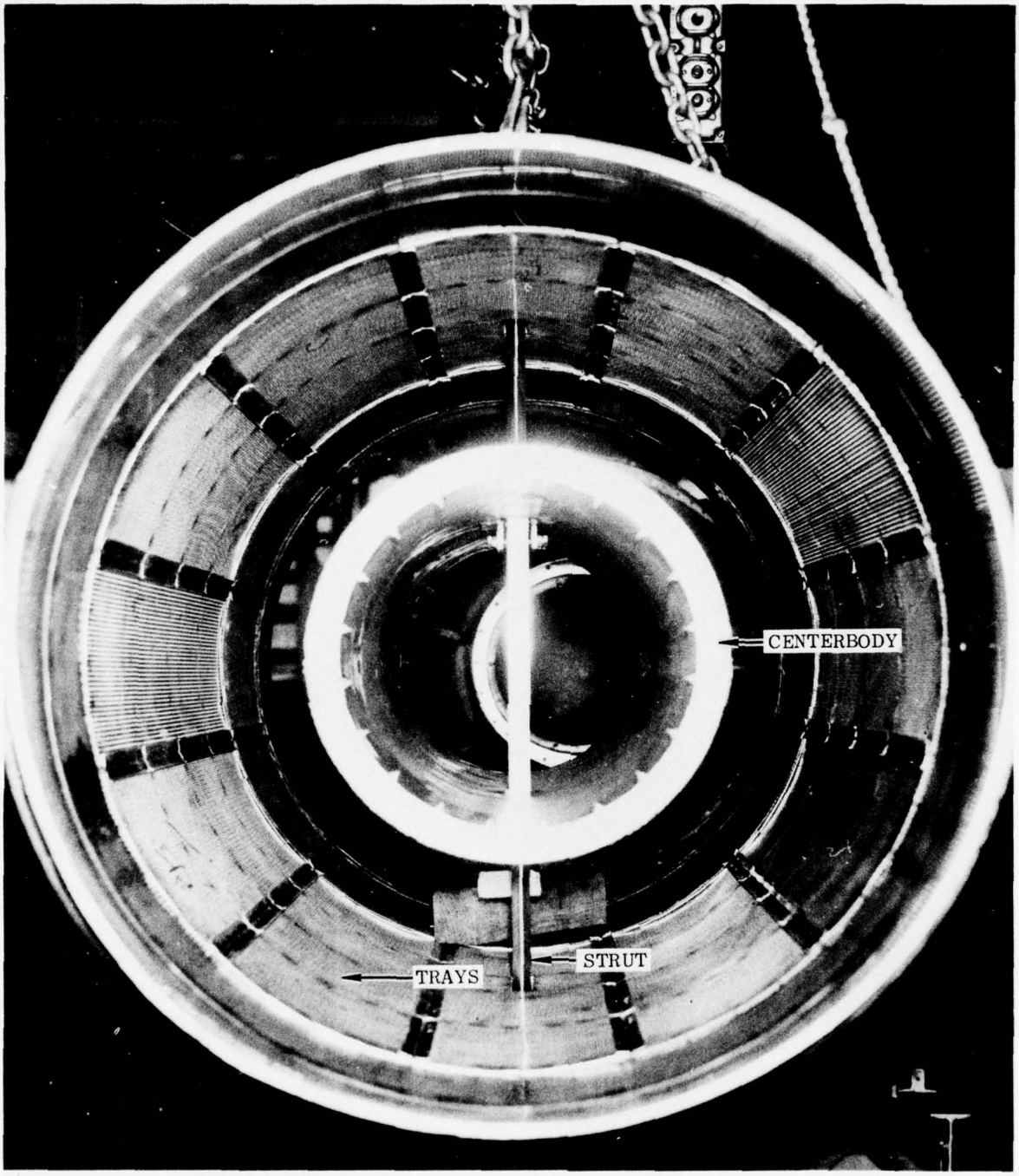


Figure 3-36. Turbine Exhaust Suppressor Assembly for J79 Engine.

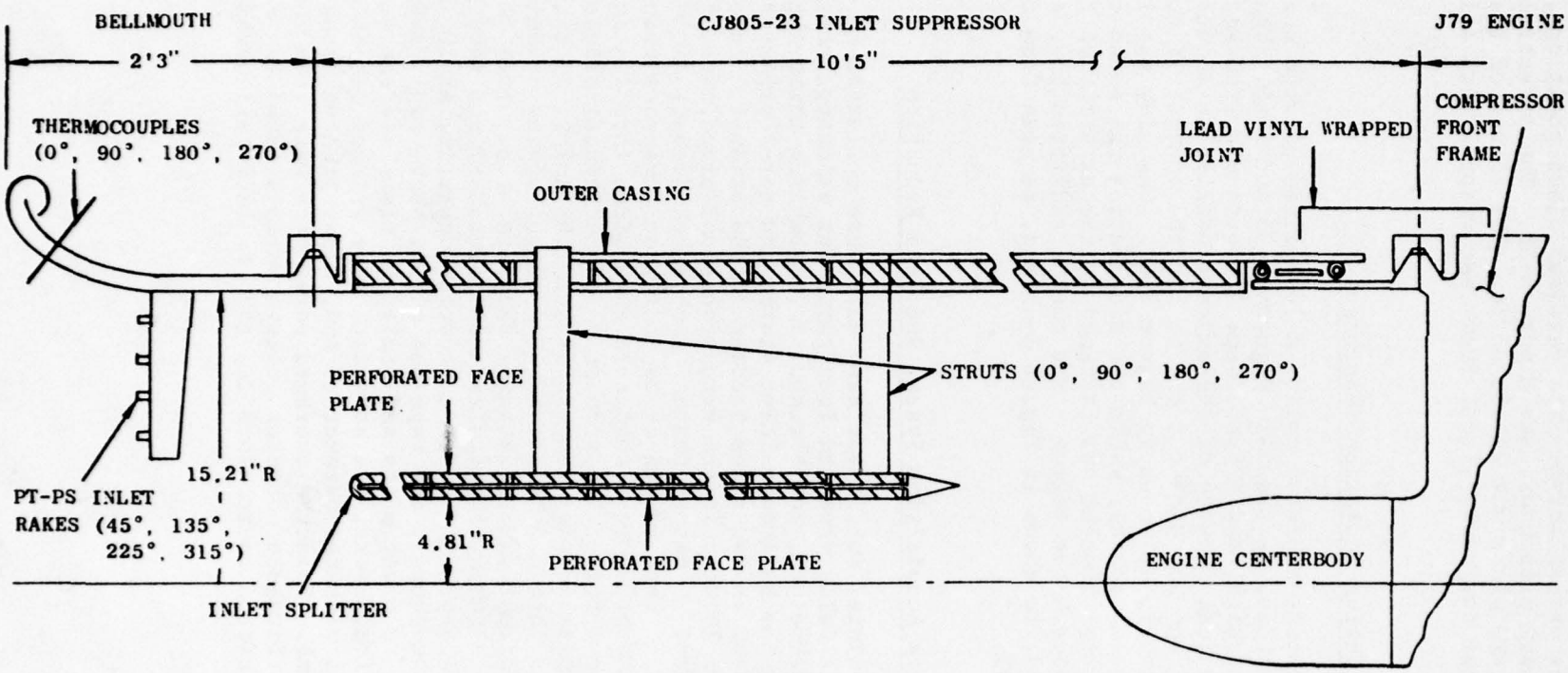


Figure 3-37. J79 Inlet Suppressor Schematic.

four 4-element rakes offset between the cardinal clock positions, measuring inlet static and total pressures, see Figure 3-38. The effective inlet area at the inlet rake plane was 719.63 sq in. The flange of the inlet suppressor and engine compressor front frame was wrapped with a lead vinyl blanket.

3.6.2.3 Casing Radiation Suppressor

To eliminate casing-radiated noise, a lead-lined plywood box was fitted around the engine, as shown in Figures 3-39 and 3-40. The box was 22 feet long, 8 feet high, and 4 feet deep, and extended from midway of the inlet suppressor to just forward of the exhaust nozzle, as shown in Figure 3-39. The sides of the box were cut out to fit the contour of the inlet and exhaust suppressors, as shown in Figure 3-40. One side was left open to permit access to the engine, while the side facing the sound field was closed. The lead vinyl blanket was fastened on the exterior of the box and on the inside underneath the engine. The casing radiation box, as seen from the sound field, is shown in Figure 3-41 and, as seen from the open side, in Figure 3-33.

3.6.3 Aero Data Acquisition System and Data Reduction

For all test points, sufficient aero data were collected to determine inlet airflow, ideal fully expanded isentropic jet velocity, nozzle pressure ratio, exit gas temperature, and thrust. To accomplish this, the instrumentation signals from the bellmouth inlet static and total pressures, the total pressures sensed on two rakes located in the extension spool piece, and wall static taps located in the extension spool piece, were fed into four transducer heads. Other pressures, such as compressor discharge static pressure, etc., were hooked up to individual pressure transducers. The output of all the pressure transducers were wired into a scannivalve, which could complete a full-cycle scan of these individual pressures in 4.8 seconds. Thermocouples sensing temperatures in the inlet, turbine discharge, etc., were connected into a CATS block. The output of the scannivalve together with some direct instrumentation readouts, e.g., fuel flow, rpm, etc., were fed into a PCM System (pulse code modulator) and recorded on magnetic tape via an Ampex FR-100 tape recorder operating at 30 inch/sec. In the data reduction center, the tape was played back, amplified, and, via a computer, decoded to count units and scaled to translate the measurements into engineering units. Next, the aero data were printed out on a 10 per second basis for all measured parameters and, also, printed using a 30 second averaging time. Selected averaged parameters were then used as input to an aero performance computer program which printed the as-measured, calculated, and corrected to standard day (59° F, 14.7 psi) parameters.

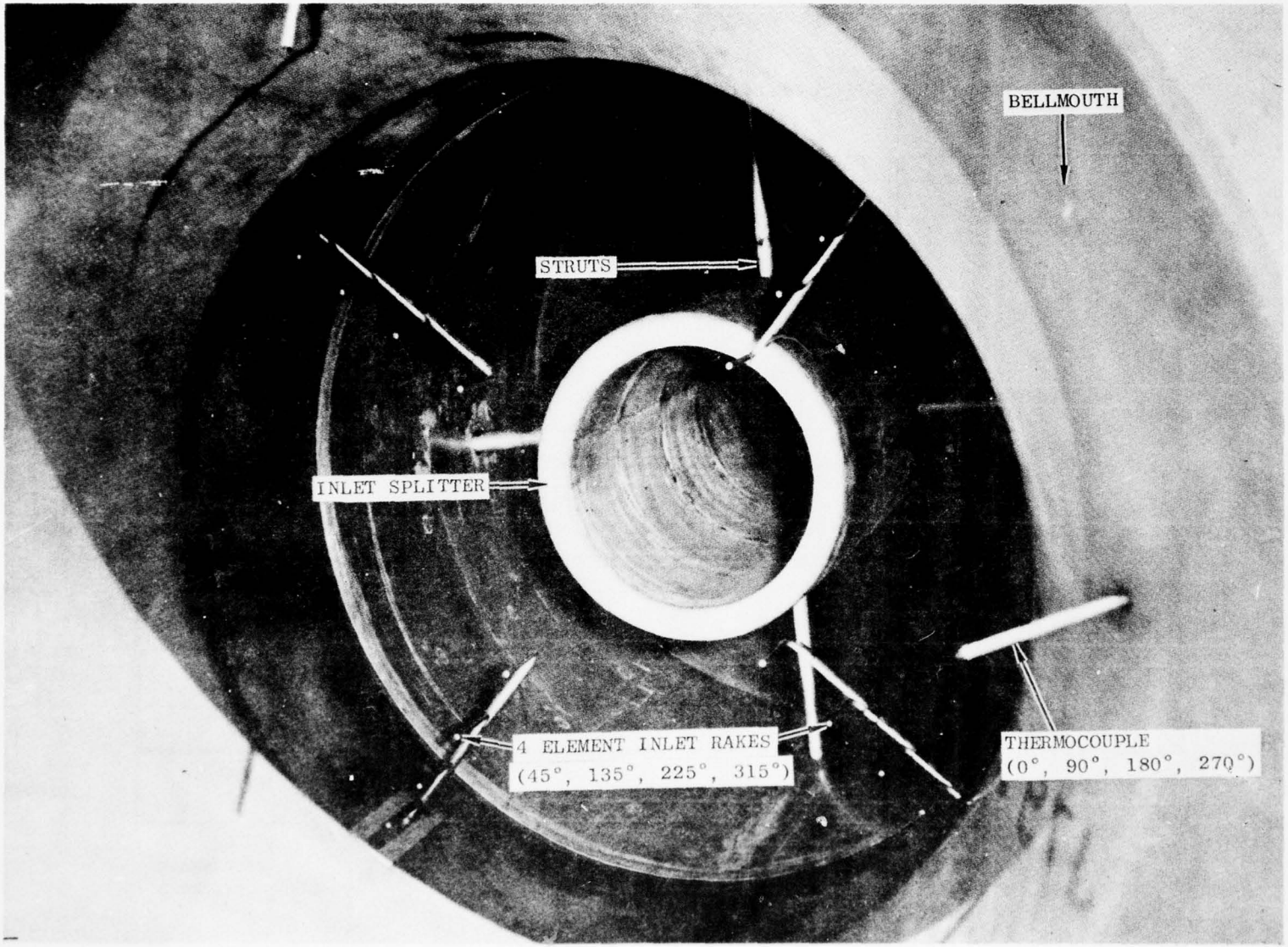


Figure 3-38. View of J79 Bellmouth Showing Inlet Instrumentation.

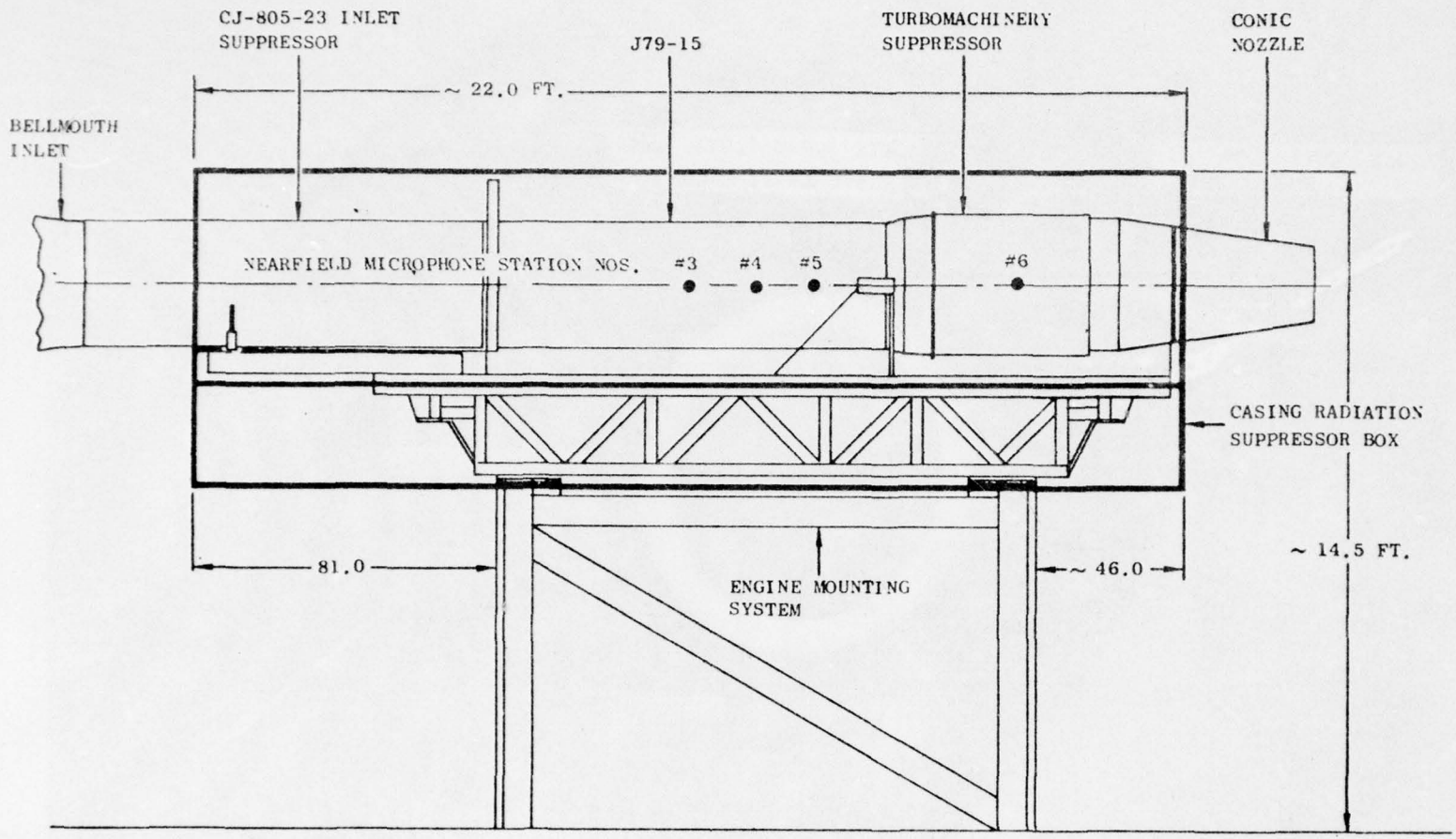


Figure 3-39. Shielded View of Casing Radiation Suppressor Box for the J79 Engine.

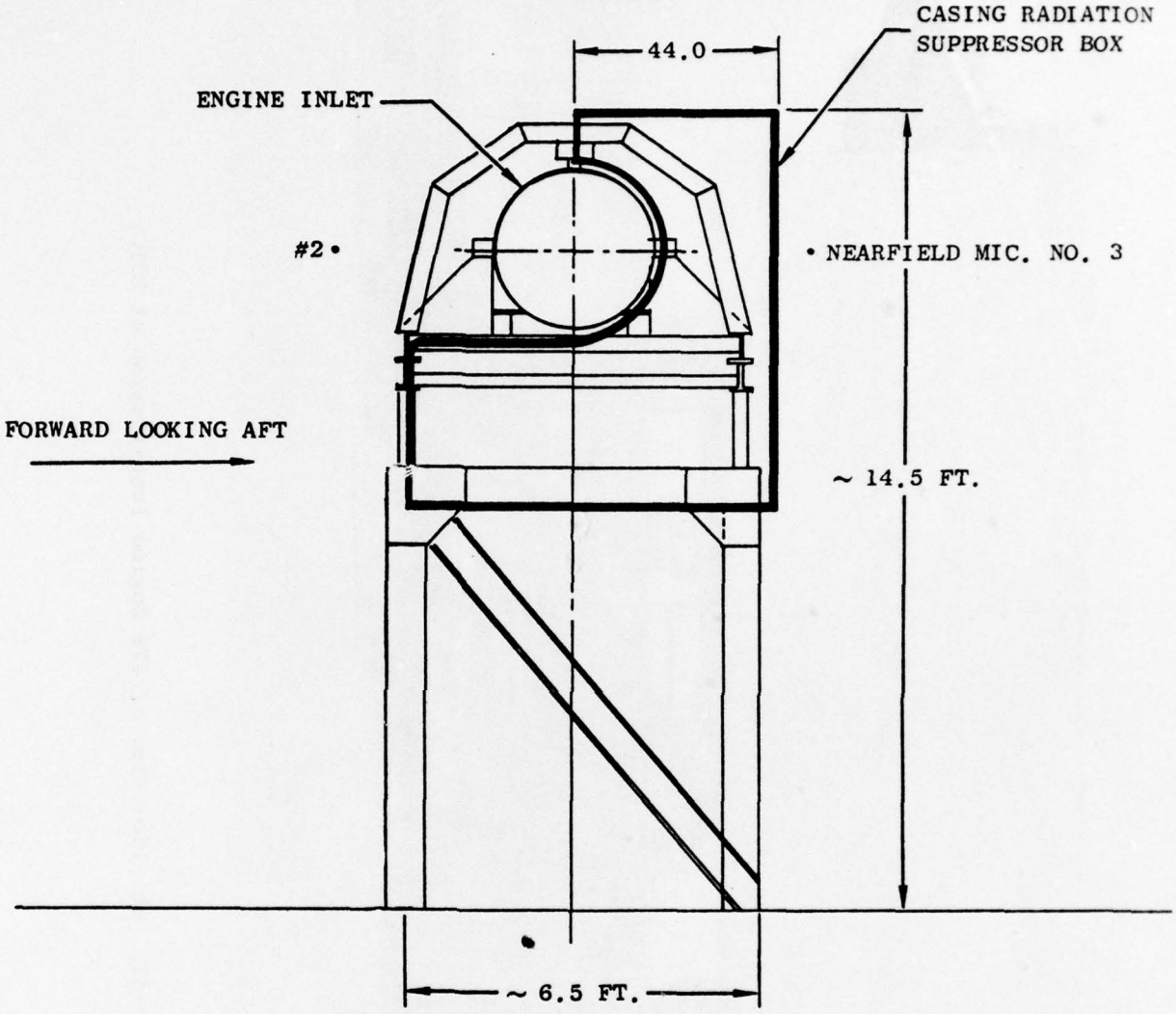


Figure 3-40. End View of Casing Radiation Suppression Box.

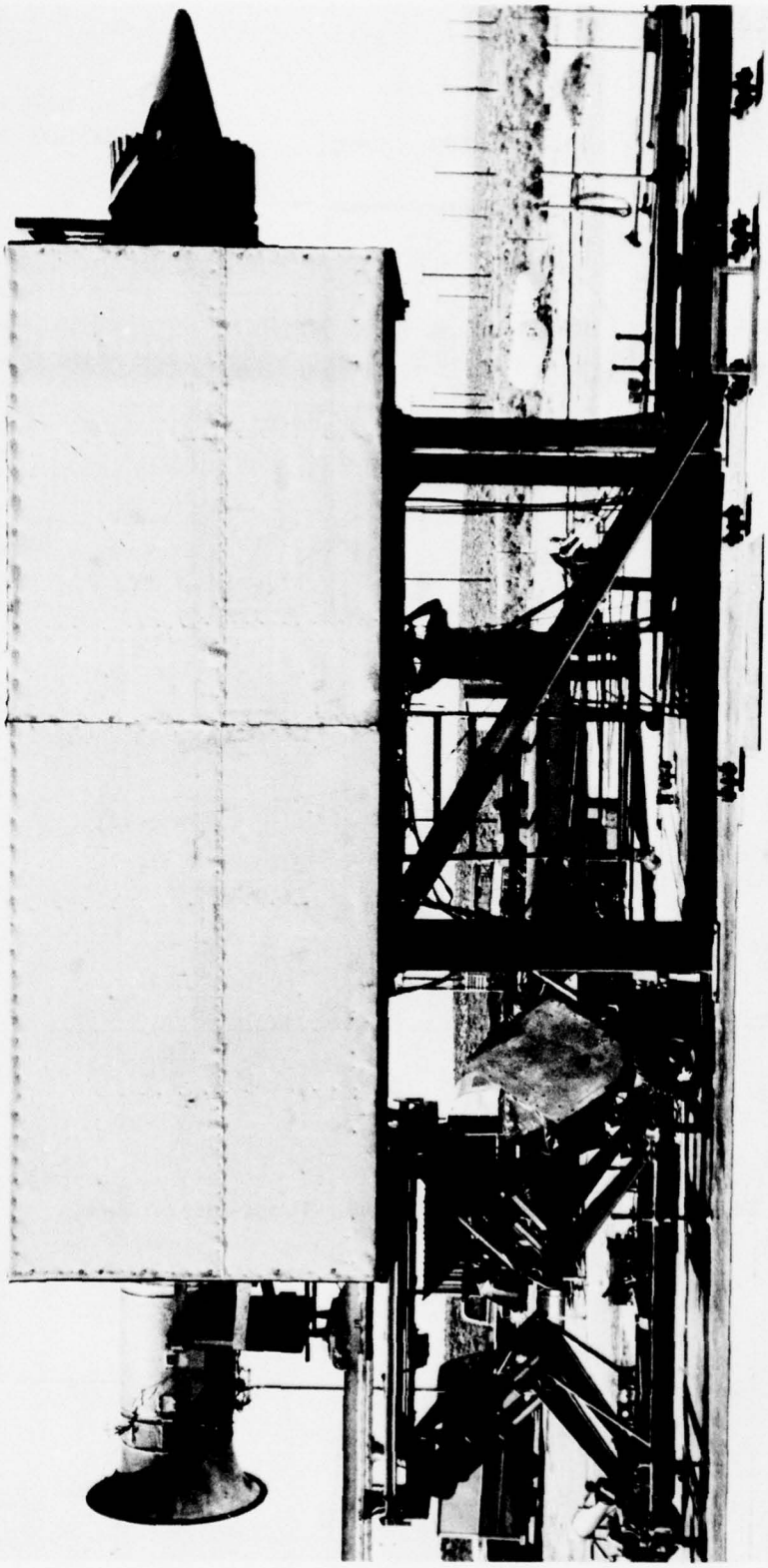


Figure 3-41. Shielded View of J79 Engine Installation at EFTC.

3.6.4 Acoustic Data Acquisition

Acoustic data acquisition was made through the use of Bruel-Kjaer microphone systems attached to vertical poles. Two microphones per station were used on the 160-foot radius: one high microphone, called A, which was at engine centerline, and a low microphone, called B, which was 2 feet above the ground. The far-field microphones were 1/2-inch Model 4133 cartridges screwed on to a cathode follower, Model 2615 (see Table 3-I for complete listing). Each microphone was operated from a Microphone Power Supply, Type 2801, which provided the necessary voltage to the cathode follower. The output of the microphone was fed via a signal amplifier onto the magnetic tape using an Ampex FR-100 tape recorder, operating at 60 in./sec with a carrier frequency of 108 kHz. Each signal was monitored by an oscilloscope and rms voltmeter. A sketch of this data acquisition system is shown in Figure 3-42.

A frequency response of each data channel (without microphone head) was performed by inserting a Hewlett - Packard Model 8057A Pseudo - Random Pink Noise Generator signal into each cathode follower; the signal of which was preserved on tape for response determination (pink noise contains all frequencies of interest and has equal energy in each 1/3-octave band).

Each day's acoustic data acquisition was started and finished with a system calibration. This was accomplished by inserting a B&K piston phone, type 4220, on each microphone head and recording its signal output on tape. Any microphone voltage output found to deviate more than ± 1.5 dB, with the piston phone applied, from laboratory microphone calibration was replaced. All data points were recorded for a minimum of 1.5 minutes to allow enough sample length for data reduction. No acoustic data were taken above 10 mph or during gusty winds.

3.6.5 Acoustic Data Processing

In this section, a description is given of the data reduction process, instrumentation, and the corrections applied to the tape recorded data for obtaining:

- "As measured data", which is the recorded (raw) data corrected for the nonlinear frequency response of the data acquisition equipment.

- "Standard day data", which is the as-measured data to which humidity absorption corrections were added to obtain sound data at standard day conditions of 59° F, 70% relative humidity per SAE ARP 866. To do this, the test humidity conditions were determined, for each data point, by reading the wet and dry bulb temperature on an Assman Hygrometer, which was placed in the vicinity of the engine. Temperature records together with other relevant test information were compiled.

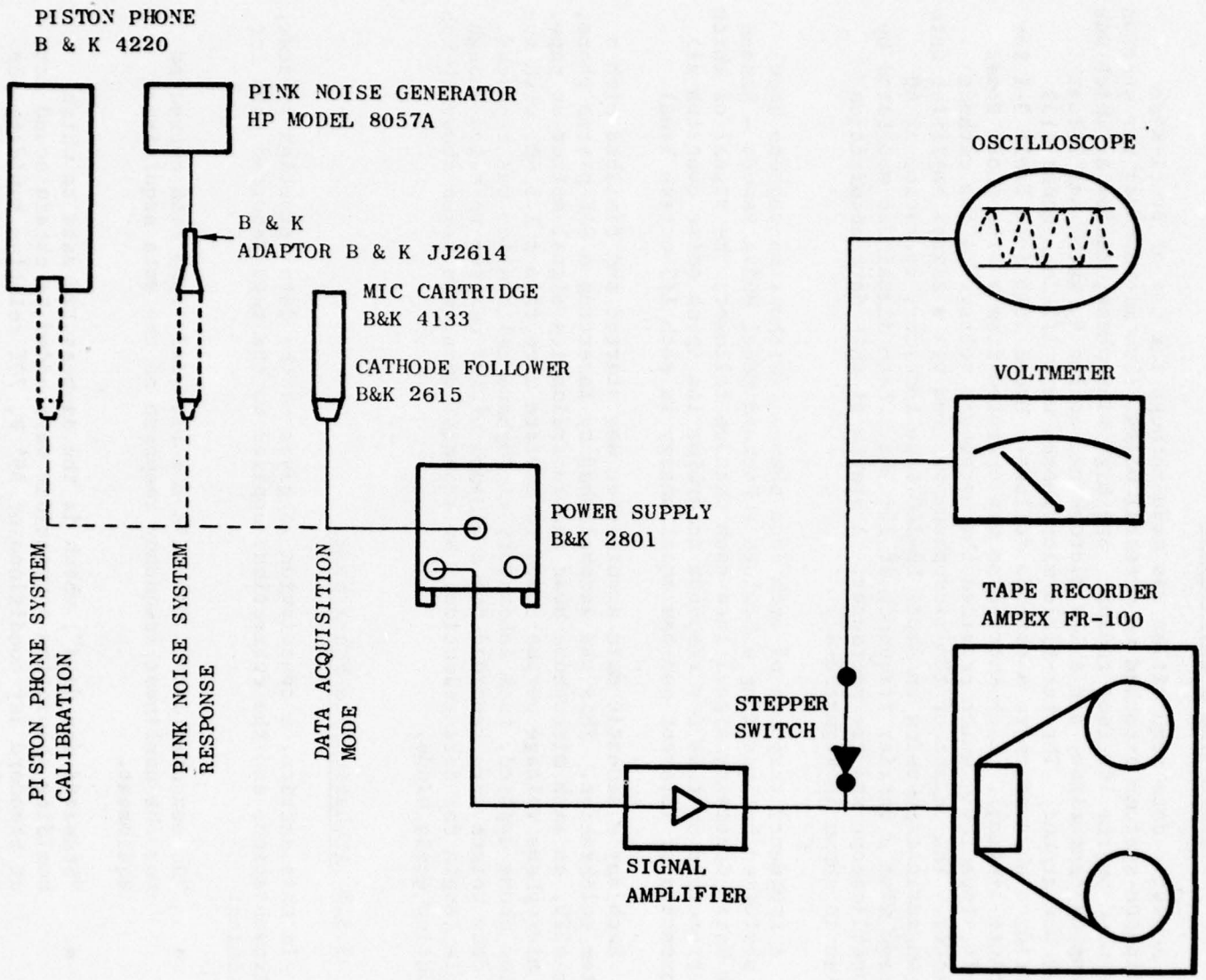


Figure 3-42. Sketch of Acoustic Data Acquisition Equipment at GE/EFTC.

- "Free-field data", which is the standard data corrected for test site characteristics, as discussed in Section 5.0.

To obtain 1/3-octave band spectra, the data reduction started by playing back the speed tapes into a General Radio Real Time Analyzer, Model 1921. These data were sampled over a 32-second integration time, with all frequencies sampled simultaneously through the use of a tape marking signal (time code). The same portion of the data tape was shuttled back and forth for all data channels (microphone stations) and analyzed by the General Radio 1/3-octave band analyzer, as shown in Figure 3-43. The output of the analyzer went into a Honeywell H-316 computer (A-D conversion) which, in turn, generated a computer formated tape (digital tape) that contained the 1/3-octave band raw data. To obtain the as-measured data, the total frequency response system corrections of each data channel were added to the raw data. To obtain these corrections, the frequency response tape recording of the pink noise was analyzed by the General Radio analyzer for each channel through the same process as the data, as described above (shown on right hand side of Figure 3-42), yielding pink noise response levels for each channel and 1/3-octave band of interest. These were fed into the XDS computer where they were normalized to the 250 Hz band to obtain the necessary corrections. The response correction for the pink noise generator itself and the microphone cartridge response were added to provide the complete system response correction. The system correction breakdown was printed out on a hard copy and on punched cards and added together with other nonsystem correction factors to the raw data to provide the measured, standard day, and free-field sound data.

Narrowband spectrum analysis of the tape recorded data was performed using a Federal Scientific Ubiquitous Spectrum Analyzer, Model UA-500, in conjunction with an X-Y plotter for tracing the results.

3.7 FLUIDYNE ENGINEERING CORPORATION'S MEDICINE LAKE AERODYNAMIC LABORATORY

The FluiDyne Engineering Corporation maintains and operates extensive aerodynamic test facilities at its Medicine Lake, Minnesota, home office, which are used by Government and industry. The majority of the studies performed in these facilities are related to propulsion system performance, mostly to engine exhaust systems aft of the turbine exit. During the 20 years FluiDyne has been conducting studies, they have developed special measurement systems and techniques which uniquely apply to their corporate test facilities. These techniques and equipment are continually reviewed and updated to be consistent with new test requirements so that the experiments they conduct and the resulting data are as controlled and accurate as are produced anywhere.

A schematic of FluiDyne's Medicine Lake Aerodynamic Laboratory test facilities is included as Figure 3-44. Each facility is designed to create uniform and controlled aerodynamic environments for the models being tested. An extreme range of flow properties is available with pressures up to 5000 psi, flow rates of 300 lb/sec, 10 microns of vacuum, Mach numbers up to 14,

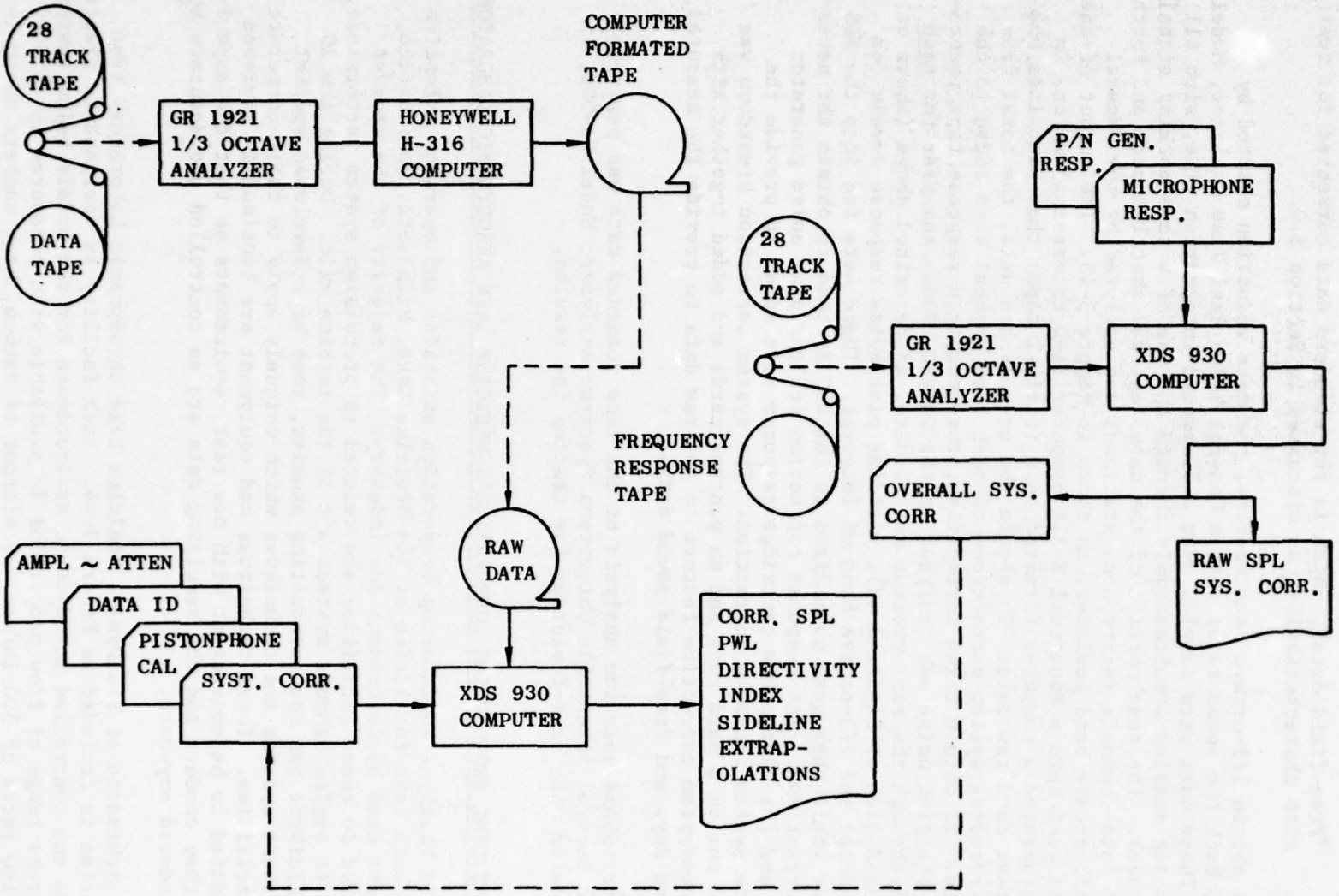


Figure 3-43. GE/EFTC Acoustic Data Processing System.

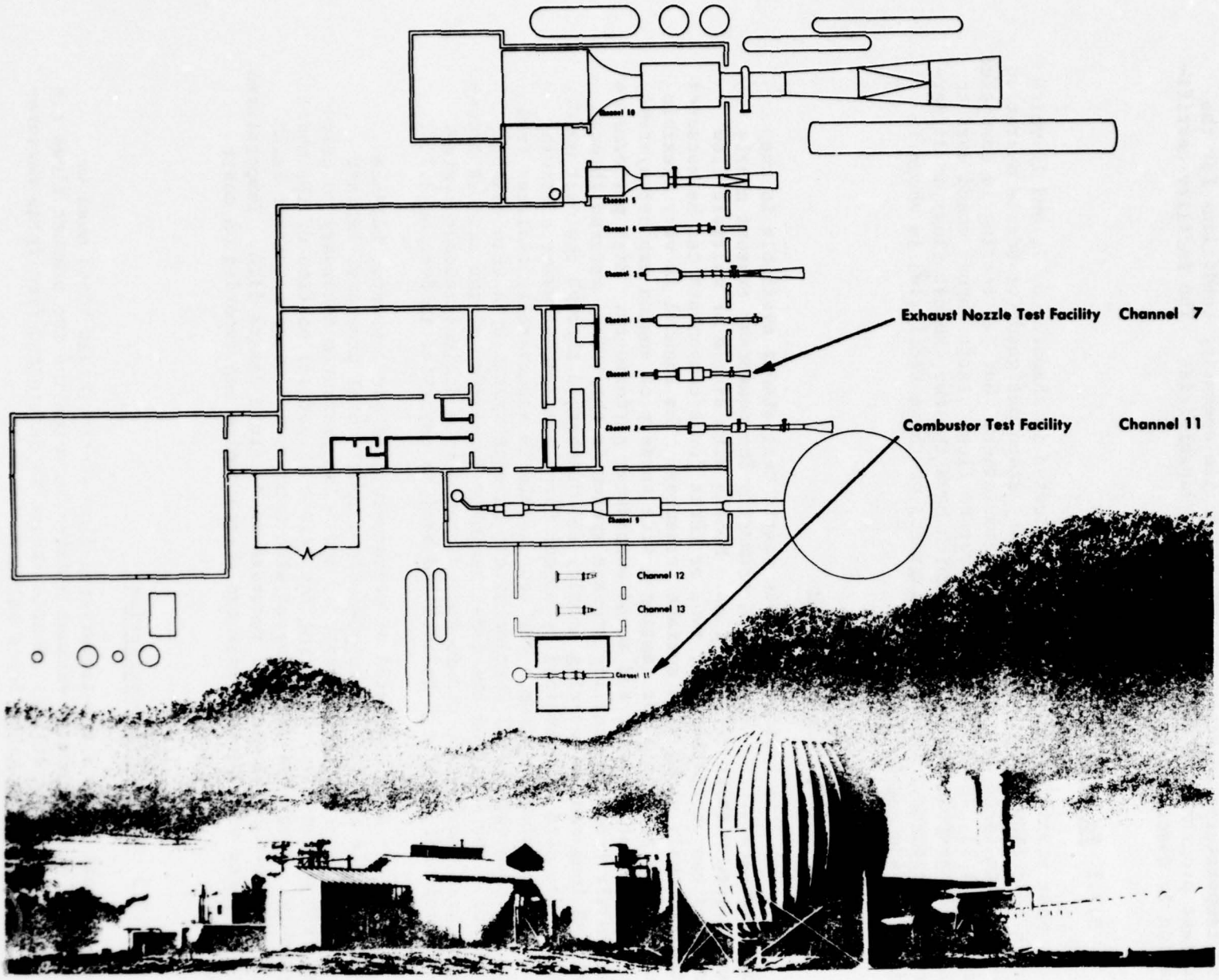


Figure 3-44. FluiDyne Engineering Corporation's Aerodynamic Facilities.

and temperatures as high as 4000° F. Nozzle operating conditions for the current program were well with FluiDyne capabilities. The facility certification is described in Reference 8.

3.7.1 Facility Description

Most static model jet testing conducted in channels 6, 7, and 12 which are a cold flow, free jet, static thrust stand designed for nozzle operation over a wide range of pressure ratio simulation. Hot jet testing is conducted in channel 11, which is a two temperature flow, static thrust stand used to determine performance of nozzles which have the two exhaust flows at different temperatures. The basic arrangement of these facilities is shown in Figures 3-45a and 3-45b.

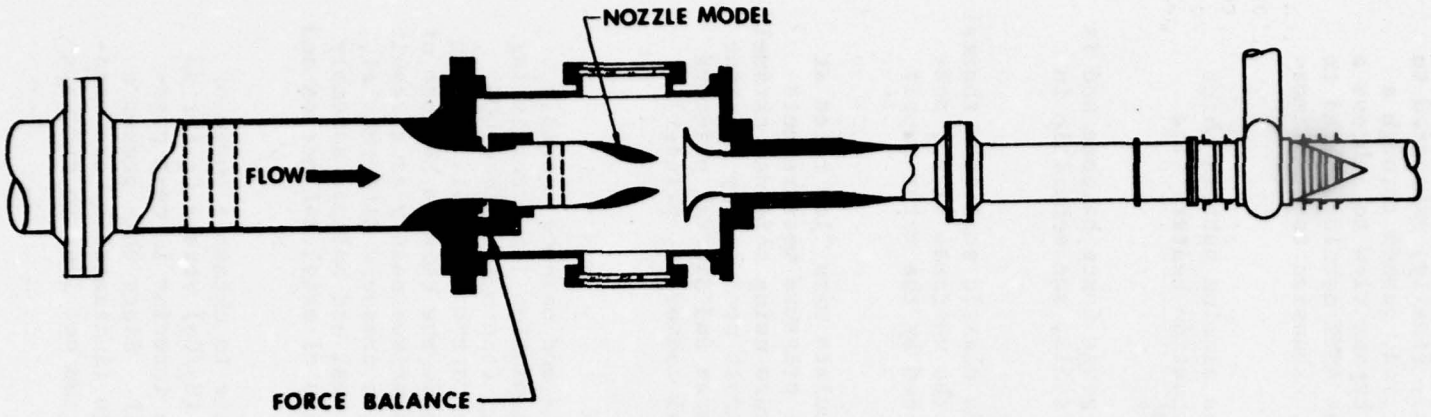
3.7.2 Channel 7 Description

Channel 7 is typical of three static test stands available in the FluiDyne Laboratory. It is used primarily for measuring exhaust nozzle performance without external flow. Models with single or multiple flow passages can be tested; one, two, or three force components can be measured simultaneously along with surface pressures. The channel is very flexible and quickly adaptable for testing a wide variety of engine exhaust systems, such as thrust reverser and sound suppressor performance. High performance driven air from the facility storage system is throttled, metered through an ASME long-radius metering nozzle, and discharged through the test model. The thrust data are obtained by direct force measurement using a strain gage force balance system. The test nozzle is structurally isolated from the upstream (grounded) portion of the balance system by a thin elastic membrane. The force on the model assembly downstream of the seal is transmitted via the balance strain gage elements to a digital readout system. Calibration of the force balance and seal is described in Section 3.7.4.

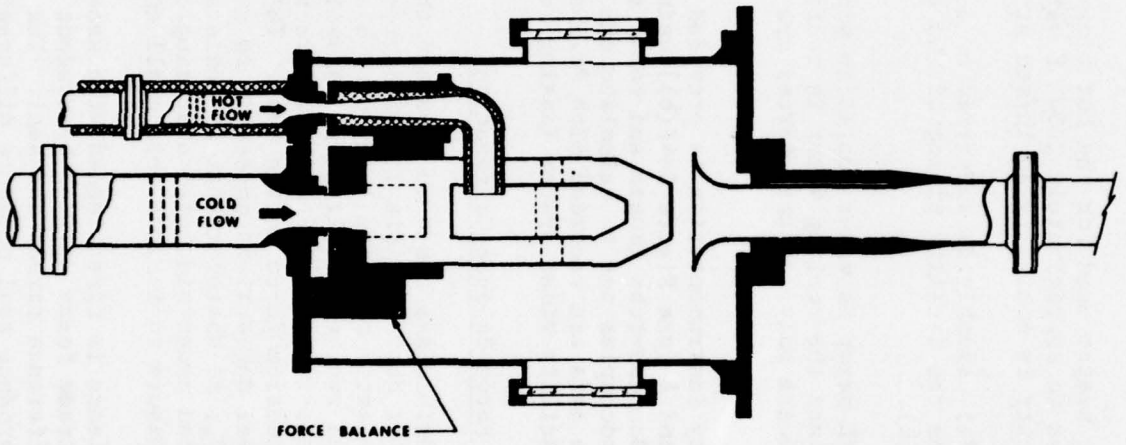
The test data consisted of measurements of airflow rate, balance force, nozzle surface static pressures, model total pressure, ambient pressure, meter total temperature, and inlet pressures necessary to calculate the stream thrust entering the metric (floating) portion of the model assembly. Pressures are measured with mercury and water manometer banks and Bourdon-tube gauges, and recorded on Polaroid camera film. Temperatures are measured with iron/ constantan thermocouples and recorded on chart recorders.

3.7.3 Channel 11 Description

Channel 11 is a two-temperature-flow static thrust stand used to determine performance of exhaust nozzles in which the two exhaust flows are at different temperatures. Nozzle thrust is determined from force measurement with a strain gauge force balance.



(a) Channels 7, 12 and 13.



(b) Channel 11.

Figure 3-45. FluiDyne Engineering Corporation's Static Nozzle Test Facilities.

The airflows for both the cold and hot passages of a test nozzle are obtained from the facility high pressure, dry-air storage system. Air for the cold passage is throttled, metered through a long-radius ASME nozzle, ducted to the cold passage of the test nozzle, and, finally, exhausted to the atmosphere. Air for the hot passage is throttled, passed through a regenerative storage heater, mixed with unheated bypass flow to achieve a desired temperature, metered through a long-radius ASME nozzle, ducted to the hot passage of the test nozzle, and, finally, exhausted to the atmosphere.

The air heater used for the hot flow contains alumina pebbles which are preheated to approximately 1250° F with a combustion heater. The heater capacity is nominally 40 lb/sec at 1200° F.

The model assembly is supported by a strain gauge force balance and is isolated from the facility piping of two elastic seals, see schematic in Figure 3-45(b).

The ASME meter is water cooled to protect the elastic seal from thermal effects. Since the cooling water is confined to the upstream (i.e., non-metric) hardware only, no tare forces are introduced by the water supply lines.

Facility instrumentation is provided to calculate mass flow rates at Stations 1 and 4 [see Figure 3-45(b)] using total pressure measurements from Heise Bourdon-tube gauges and total temperature using shielded chromel/alumel thermocouples and to calculate the exit thrust produced by the test nozzle. The data are recorded with Polaroid cameras and digital printers using the facility video system (analog to digital converter, printer).

3.7.4 Force Balance Calibration

The flexible seal used to separate the nozzle and balance assembly from the inlet duct is a simple, pressure-tight expansion joint consisting of a thin, elastic membrane lying over a small gap (approximately 0.006 inch) between two metal cylinders. A small force carryover exists between the grounded structure and the structure which loads the balance because of the finite tension force in the seal. This force arises mainly as a result of radial seal deflections necessary to support the pressure differential, $\Delta P_3 = P_3 - P_a$, at whatever seal gap exists. The seal and balance assembly are calibrated under simulated operating conditions of axial deflection and internal pressure to include this small effect.

The balance is first loaded with known weights to obtain a curve of axial downstream force divided by readout signal (H_2/C_2) versus C_2 for no pressure difference across the seal. The balance interior is next pressurized to produce seal pressure differentials, ΔP. Since this pressure loading produces a downstream force on the balance (indicated by the readout), upstream loads (L) are applied to decrease the net load to simulate

actual test conditions of load and ΔP. The sum of the indicated flexure load and the reverse load must equal the downstream pressure load, $\Delta P(A_3 + \Delta A)$. Since H_2, L, ΔP, and A_3 are known, the effective seal area (ΔA) may be calculated. Plotting of ΔA as a function of balance output and differential pressure completes the calibration.

3.8 NASA LEWIS 8 x 6 FOOT SUPERSONIC WIND TUNNEL

As discussed in Section 2.0, an overall program redirection near the end of the Task 1 effort resulted in the decision to utilize the wind tunnel facilities of NASA Lewis rather than those of FluiDyne Engineering Corporation. A short description of this NASA Lewis wind tunnel is included for completeness of information.

The NASA Lewis 8 x 6 foot supersonic wind tunnel is capable of attaining test section flow in a Mach number range from 0.36 to 2.0. The change in Mach number is continuous up to 1.3 and in increments of 0.1 between 1.3 and 2.0. The tunnel may be operated in either of two modes: aerodynamic cycle or propulsion cycle.

During the aerodynamic cycle, the tunnel is operated as a closed system with dry air added only as required to maintain the desired tunnel conditions. This cycle is used primarily for aerodynamic flow studies where contaminants are not introduced into the airstream.

3.8.1 Facility Description

Major components of the NASA Lewis 8 x 6 foot supersonic wind tunnel (Figure 3-46) are an air dryer, a compressor, a flexible-wall nozzle, a test section, an acoustic muffler, and a cooler.

Operating characteristics of the tunnel for both the aerodynamic and propulsion cycles are given in Figure 3-47 (a through g), which show the test section total temperature, total pressure, static pressure, dynamic pressure, altitude, Reynolds number, and mass flow versus the test section Mach number over the tunnel operating range. The discontinuity between Mach 0.50 and 0.55 is caused by varying compressor speeds to avoid over pressurization of the balance chamber surrounding the test section.

The test section is 8 feet high and 6 feet wide with parallel side walls for a total length of 23 feet 6 inches. For 2 feet 3 inches downstream of the test section, the side walls diverge to 6 feet 4 inches to compensate for the blockage of the transonic strut. The top and bottom plates are parallel to each other. The walls and top and bottom plates are made of 1.00-inch-thick stainless steel.

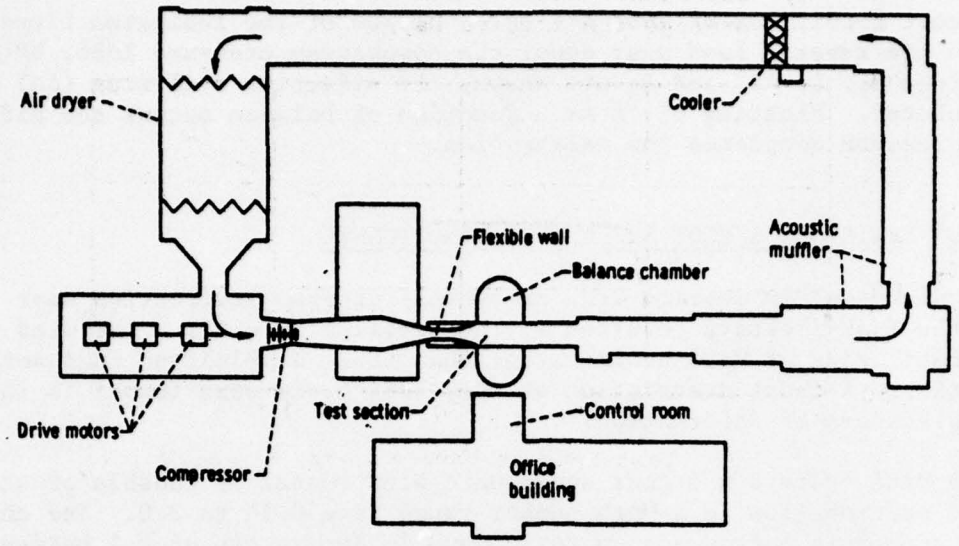
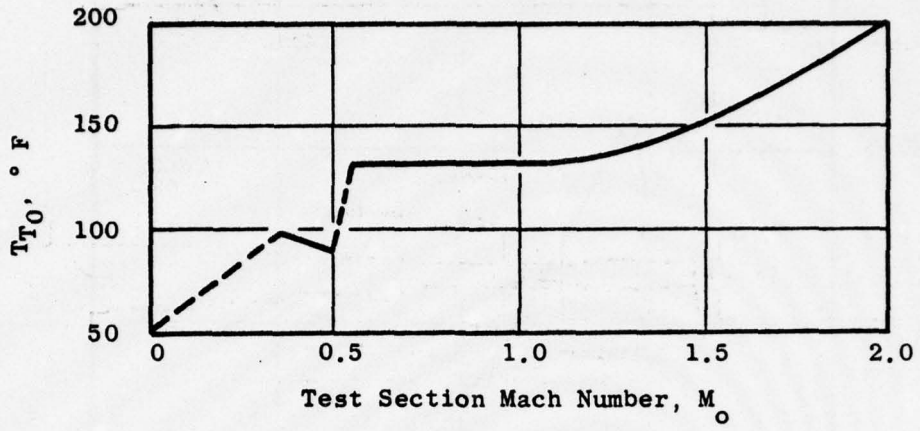


Figure 3-46. NASA Lewis 6 X 8 Foot Supersonic Wind Tunnel Aerodynamic Cycle.

(a) Supersonic Wind Tunnel Total Temperature. Average Temperature Day.



(b) Supersonic Wind Tunnel Total Pressure.

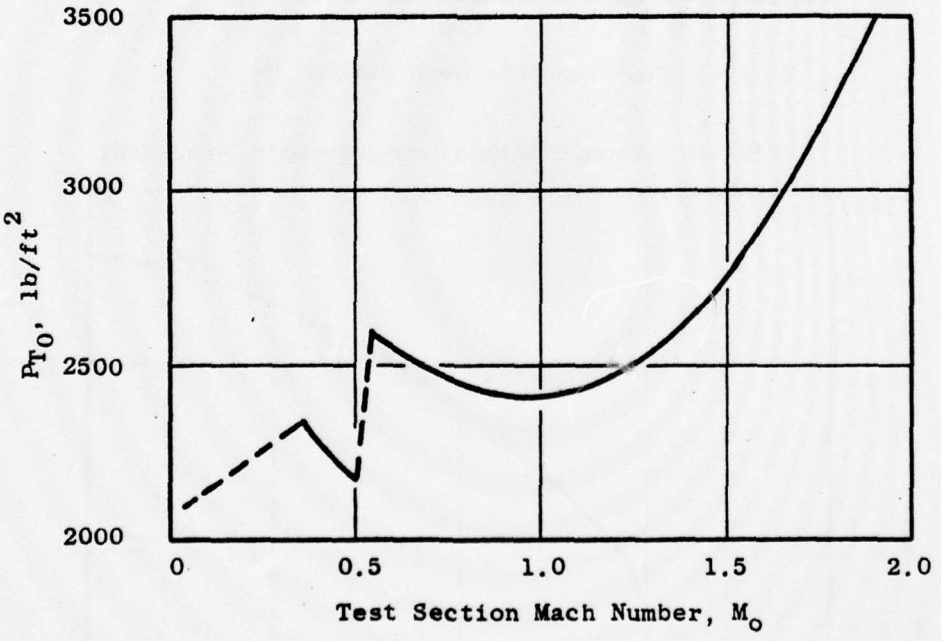
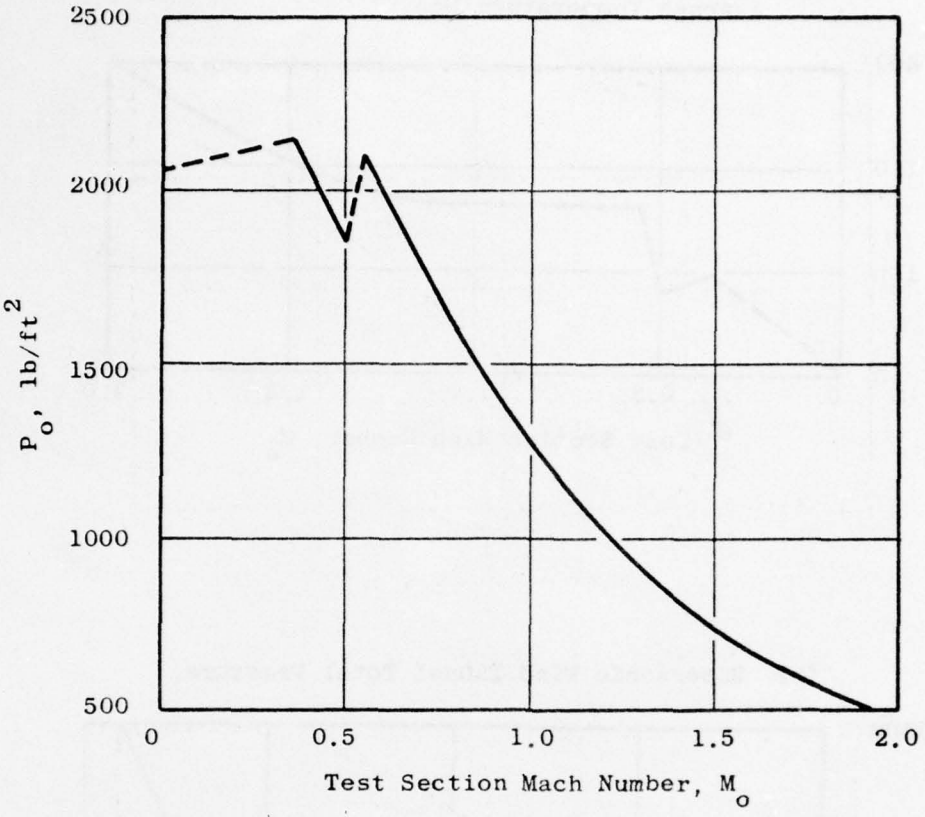


Figure 3-47. Operating Characteristics of NASA Lewis 6 x 8 Foot Supersonic Wind Tunnel.

(c) Supersonic Wind Tunnel Static Pressure.



(d) Supersonic Wind Tunnel Dynamic Pressure.

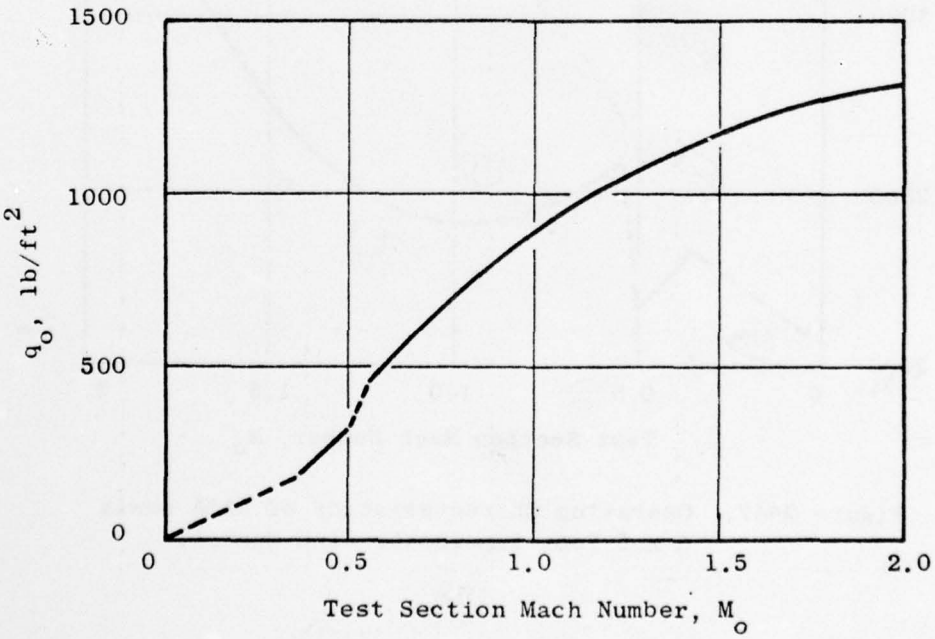
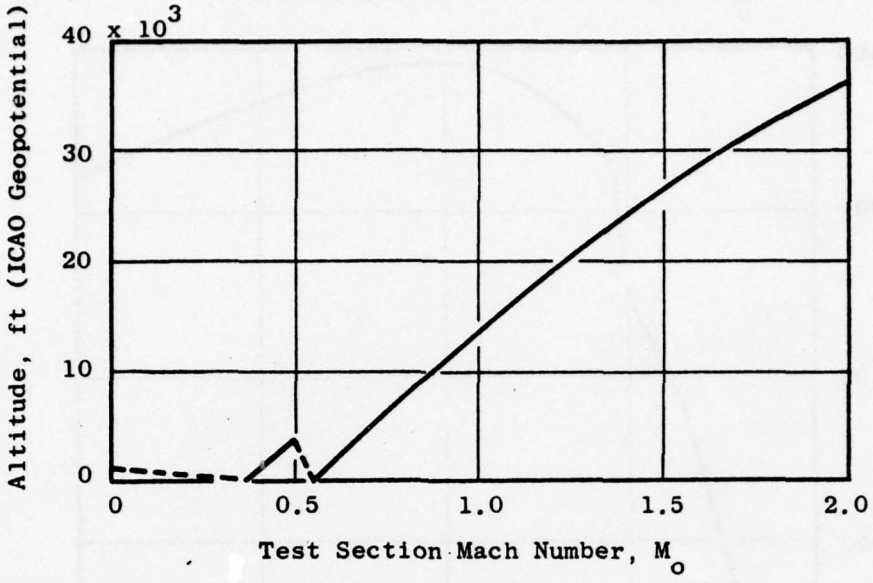


Figure 3-47. Operating Characteristics of NASA Lewis 6 x 8 Foot Supersonic Wind Tunnel (Continued).

(e) Supersonic Wind Tunnel Altitude



(f) Supersonic Wind Tunnel Reynolds Number.

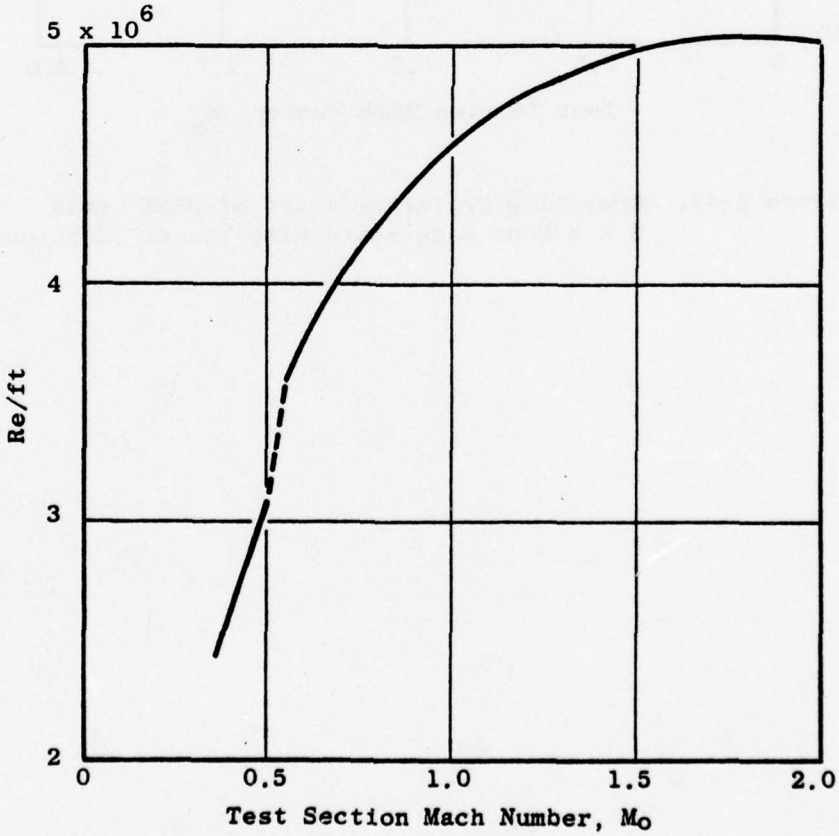


Figure 3-47. Operating Characteristics of NASA Lewis 6 x 8 Foot Supersonic Wind Tunnel (Continued).

(g) Supersonic Wind Tunnel Mass Flow.

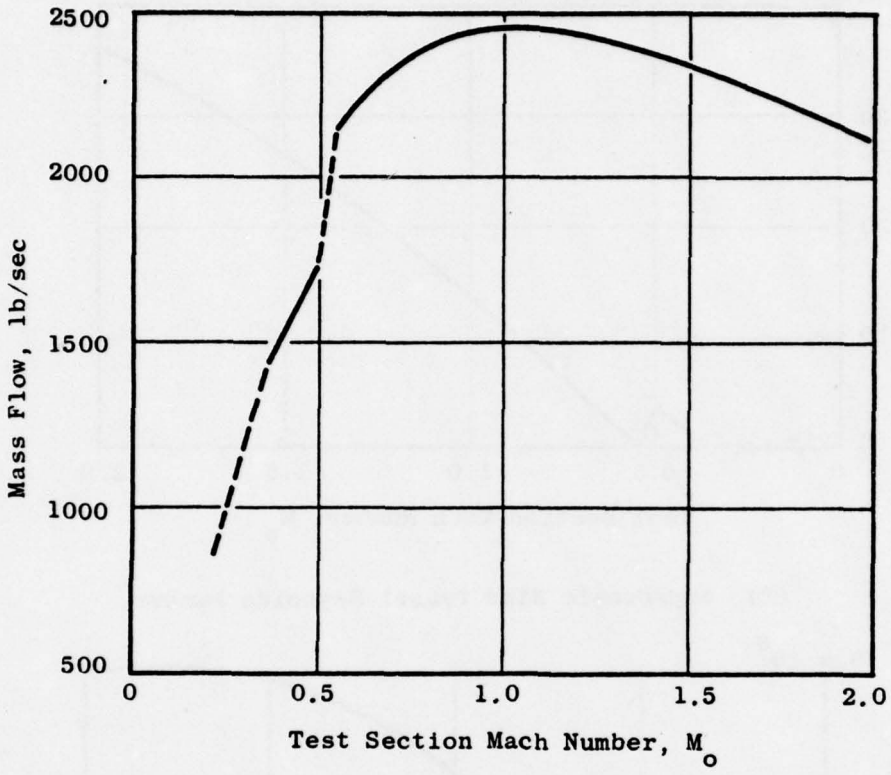


Figure 3-47. Operating Characteristics of NASA Lewis 6 x 8 Foot Supersonic Wind Tunnel (Concluded).

The test section is perforated on four sides. Perforations start 9 feet 1 inch from the upstream end of the test section and extend 14 feet 5 inches downstream. These perforations provide approximately 6 percent porosity; however, this can be reduced and varied along the length of the test section by selective use of inserts in the 1.0-inch-diameter perforations.

Models are installed through an access door in the bottom of the tunnel diffuser downstream of the test section. The opening is 16 feet long and 6 feet wide. Two 2-ton overhead cranes are provided in the ceiling of the diffuser section. Models, on special dollies, are lifted into the diffuser section and rolled to the test section for installation.

The top and bottom plates of the test section are removable for installation of small model supports and auxiliary apparatus. The opening may vary up to 10 feet long by 12 inches wide depending upon the selection of insert plates and location in the test section. The tunnel insert plates cannot be altered; therefore, new inserts are required if modifications are necessary.

Typical model installations in the wind-tunnel employ single-strut mountings (0° or 30° swept struts), as shown in Figure 3-48. The model suppressors for the performance tests are approximately 8 inches in diameter. Transition sections are used to adapt the model nozzles to the facility.

The thrust-minus-drag data are determined with the direct force-and-flow-measuring systems, which are located just downstream of the transition sections.

3.9 SUMMARY

Each of the test facilities offers unique capability for the High Velocity Jet Noise Source Location and Reduction Program. They represent a cross section of capabilities that give the Program the flexibility to carry out the necessary fundamental research on suppression mechanisms of high velocity jet noise.

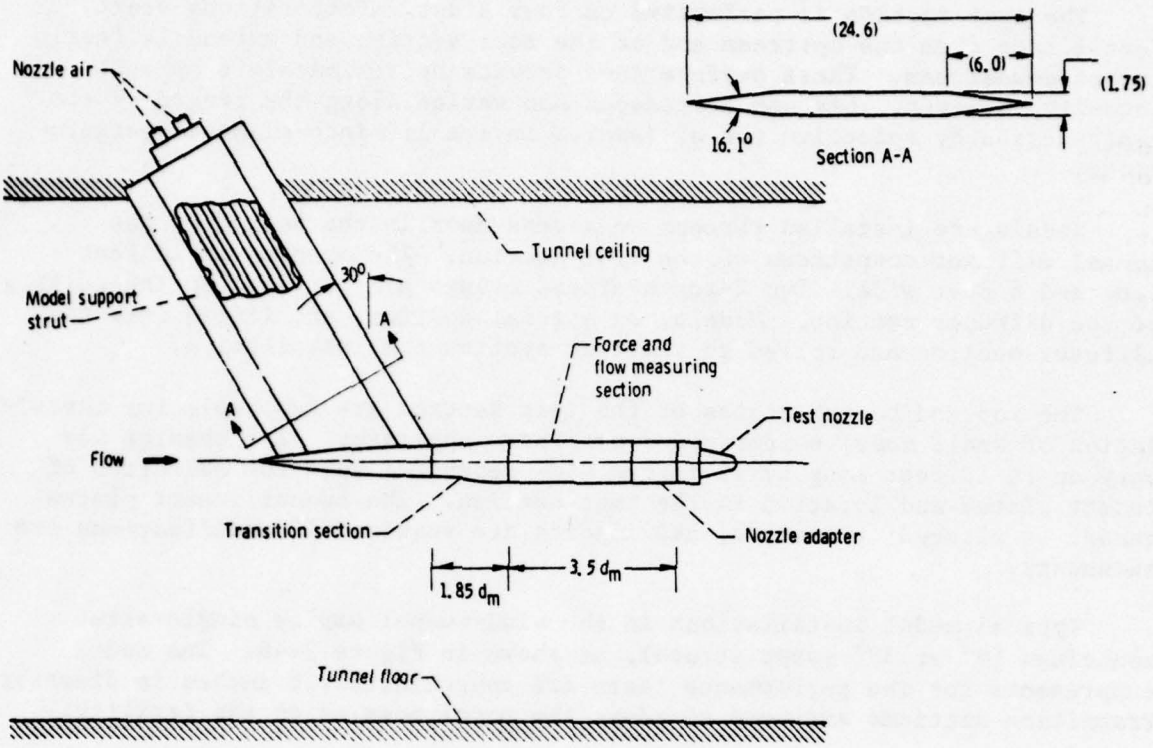


Figure 3-48. Model Installed in 6 X 8 Foot Supersonic Wind Tunnel.

4.0 ESTABLISHMENT OF UNCONTAMINATED JET NOISE

The task of certifying each of the test facilities as to its acoustic cleanliness involves a statistical study of the measurement error and correction error contained in the final sound pressure level used to represent the jet noise. There are two terms which are used to describe the deviation of data from its expected value: precision and accuracy. In a statistical sense precision is concerned with the random scatter of the data when comparing the mean of the data with a particular sample. Accuracy is a term describing the amount of bias or systematic error in a data population when comparing the mean to a fixed or known value.

Figure 4-1 represents a montage of error sources which contaminate the pure jet noise and result in significant loss of accuracy and precision. Such biasing errors include contamination from:

- General environmental effects (winds, rain, etc.)
- Air attenuation variations
- Acoustic measurement errors
- Ambient environmental noise
- Facility related noise such as piping noise, combustor noise, turbomachinery noise, etc.

A distinction is made here between these contaminants of the jet noise and that error which results when the measurements are being made in a nonfreefield environment, such as in the presence of a ground plane. In such cases, the signature is modified further by the reflections and reverberations due to obstructions in the acoustic arena and additional error is experienced as shown in Figure 4-1. A detailed analysis of the nonfreefield effects is included in Section 5.0.

One contaminate of "pure" jet noise which is not evaluated in this study is the noise generated by flow separation off nozzle surfaces. This noise source is considered to be part of the total spectra generated by the individual suppressor design and therefore is not removed from the noise signature.

The problem is then defined. Given an acoustic facility which generates a typical frequency spectrum, such as shown by the symbols on Figure 4-1, make the necessary modification or establish appropriate correction factors to the data so the facility will produce the desired jet noise spectra indicated by the dashed line on Figure 4-1. Furthermore, the precision of the final corrected sound pressure level with frequency will exhibit specific standard deviations from the lowest frequency of interest to 80 kHz, as indicated by the precision band on the figure.

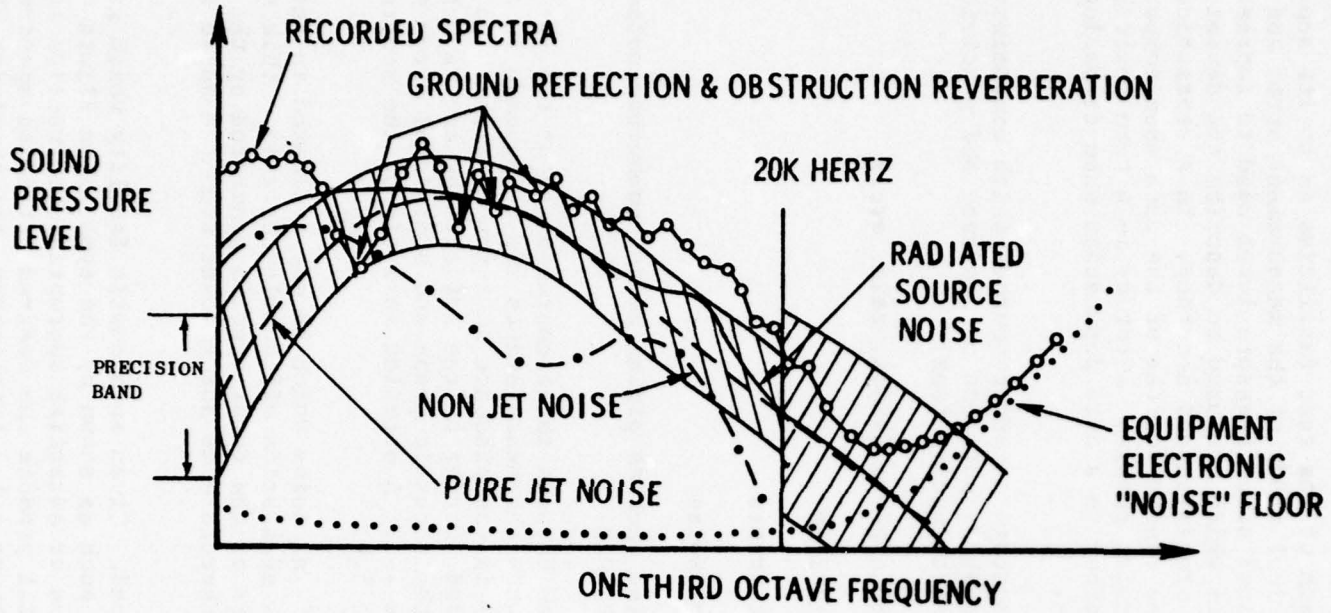


Figure 4-1. Montage of Possible Contaminants to Acoustic Measurements.

4.1 STATISTICAL ANALYSIS

The method of approach utilized to eliminate jet noise contamination is as follows:

1. Improve the facility design and institute changes which eliminate or minimize the contamination.

2. Establish that the contamination is insignificant by direct measurement of the extraneous noise source relative to the jet noise or, if this is not possible, by subjective evaluation of the measured noise spectra in terms of jet noise characteristics.

3. If steps (1) and (2) still produce accuracy errors, or if the facility change would be too extensive to undertake, then appropriate correction factors to the data are determined.

Correction factors are specified in one of two ways depending on how the modification of the signal arose. In cases where the measured acoustic pressure is adjusted or attenuated by a multiplier, such as by microphone system frequency response or air attenuation coefficients, the adjustment to the spectra is made by constant adders as follows:

$$SPL_{jet} = SPL_M + \sum_{i=1}^{K} \Delta_i \qquad (1)$$

where SPL_{jet} is the idealized pure free-field jet noise, and SPL_M is the measured jet noise containing various contaminates.

Alternatively, if the measured acoustic pressure is modified from the desired jet noise due to the addition of extraneous sources, such as ambient noise, electronic noise floor, facility noise, etc., and the level of the contaminating source is known, then Δ_i in Equation (1) is a variable which is determined by the calculated difference δ_i between the measured SPL_M and the known contamination level SPL_i, viz

$$\delta_i = SPL_M - SPL_i \qquad (2)$$

The relation for logarithmic addition gives:

$$SPL_{jet} = SPL_M + 10 \log_{10} (1 - 10^{\delta_i/10}) \qquad (3)$$

Figure 4-2 shows variation of Δ_i with δ_i.

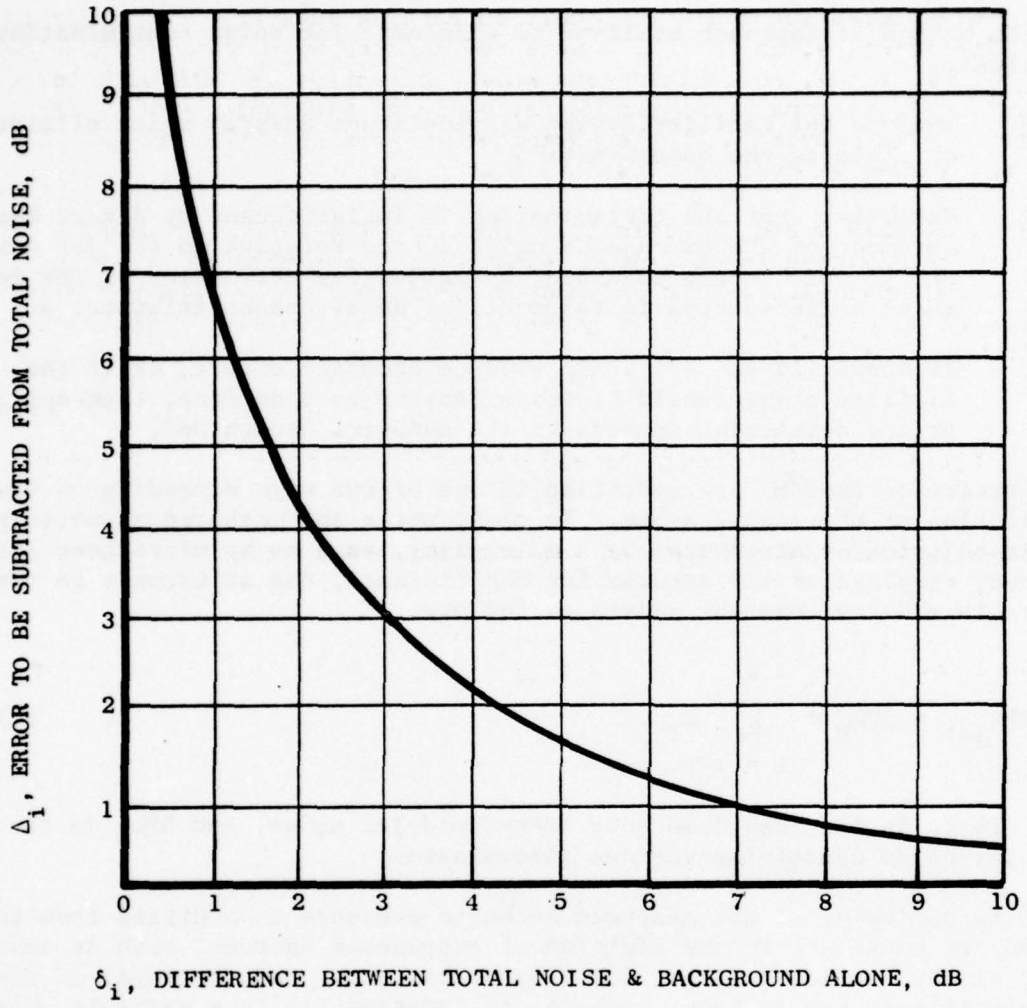


Figure 4-2. Background Noise Corrections for Sound Level Measurements.

Using equation (1) and (3), the pure jet noise spectra can be pulled from a contaminated spectra. The question remains however: "How accurate is this?" Specifically, if one has a measured spectra with an associated tolerance σ_M, ($SPL_M \pm \sigma_M$), and either some known correction factors with tolerance $\sigma\Delta_i$ ($\Delta_i \pm \sigma\Delta_i$), or some known contaminating level with tolerance σ_i ($SPLi \pm \sigma_i$), what is the precision of the corrected spectra ($SPL_{jet} \pm \sigma_{jet}$)? To obtain the answer we turn to classical statistics.

In References 9 and 10, Berrettoni develops the method of partial derivatives for calculating the standard deviation. The method is based on a Taylor series expansion of the calculated function $f(x_i)$ in the vicinity of the expected value a_i. It can be generalized to the case of k independent variables x_i (i = 1, 2, --- k) as:

$$f(x_i) = f(a_i) + \frac{\partial f(a_1 \ldots a_K)}{\partial x_1} (x_i - a_1) + \cdots\cdots + \frac{\partial f(a_1 \ldots a_K)}{\partial x_K} (x_K - a_K) + R_2 \quad (4)$$

which when carried through for the variance expression gives

$$\sigma_f^2 = \sum_{i=1}^{K} \left[\left(\frac{\partial f}{\partial x_i} \right)^2 \sigma_i^2 + \sum_{j=i+1}^{K} 2 \frac{\partial f}{\partial x_i} \frac{\partial f}{\partial x_j} \rho_{ij} \sigma_i \sigma_j \right] \quad (5)$$

where

$$\sigma_f^2 = \sum_{\ell=1}^{N} \left[\frac{f(x_{i\ell} \cdots x_{k\ell}) - f(a_1 \cdots a_K)}{N} \right]^2 \quad (6)$$

$$\sigma_i^2 = \sum_{\ell=1}^{N} \frac{(x_{i\ell} - a_i)^2}{N} \quad (7)$$

$$\rho_{ij} = \frac{\sum_{\ell=1}^{N} (x_{i\ell} - a_i)(x_{j\ell} - a_j)}{\left[\sum_{\ell=1}^{N} (x_{i\ell} - a_i)^2 \sum_{\ell=1}^{N} (x_{j\ell} - a_j)^2 \right]^{1/2}} \quad (8)$$

The terms σ_f and σ_i are the standard deviations of the parameters f and x_i over N samples. The term ρ_{ij} is the Pearsonian coefficient of correlation

which takes into account those corrections that are interdependent. In the case where the variable x_i are mutually independent, thereby uncorrelated, then $\rho_{ij} = 0$. In the case of jet noise contamination, we assume that all the forces are unrelated and uncorrelated, so, in the case of constant Δ_i, Equation (1) gives:

$$\sigma_{jet} = \sqrt{\sum_{i=1}^{K} \left(\frac{\partial SPL_{jet}}{\partial \Delta_i}\right)^2 \sigma_{\Delta_i}^2 + \left(\frac{\partial SPL_{jet}}{\partial SPL_M}\right)^2 \sigma_M^2} = \sqrt{\sum_{i=1}^{K} \sigma_{\Delta_i}^2 + \sigma_M^2} \quad (9)$$

and the value of $\sigma\Delta_i$ is determined directly. In the case that a fixed contaminant level, SPL_i, and the associated variance, σ_i^2 is given, σ_{jet} is calculated from Equation (3) using Equation (5), as follows;

$$\sigma_{jet} = \frac{\sqrt{(10^{-\delta_i/5})\ \sigma_i^2 + \sigma_M^2}}{(1 - 10^{-\delta i/10})} \quad (10)$$

Figure 4-3 shows Equation (10) plotted in terms of δ_i, σ_{jet}/σ_M. From Figures 4-2 and 4-3, one can obtain the magnitude and variance of a correction factor. For example, if we knew the measured spectra within ± 1 dB ($\sigma_M = \pm 1$) and the contaminating noise floor within ± 5 dB ($\sigma_i = \pm 5$) and they were separated by 10 dB, then the correction factor would be $\Delta = 0.5$, and the precision of the new spectra would be $\sigma_{jet} = \pm 1.24$ dB. At $\delta i = 3$ dB we get a correction factor of Δi 3 dB and a variance of the new spectra of $\sigma_{jet} = \pm 5.4$ dB. The exercise displays that when the noise floor is far below the measured spectra, the accuracy of the corrected spectra approaches the accuracy of the measured spectra (which could be obtained from Equation 10 with $\delta_i \to \infty$). On the other hand, when the actual jet SPL is the same level as the noise floor or less, then the accuracy of the correction becomes exceedingly poor (in Equation 10, $\sigma_{jet} \to \infty$ as $\sigma_i \to 0$).

Armed with the above relations for determining the accuracy and precision of any correction factors, we will now investigate the relative cleanliness of each of the test facilities in terms of potential contaminants.

4.2 GENERAL ENVIRONMENTAL EFFECTS

Adverse weather conditions can have a significant effect on test data recorded outdoors. The influence of winds, temperature gradients, snow, rain, etc. are difficult to assess qualitatively, let alone measure quantitatively. References 11, 12, and 13 describe some techniques to estimate their influence. Anechoic facilities, such as those at USC and UBC, of course, are free of this problem but the outdoor facilities at JENOTS, CR&DC, and EFTC all limit testing to the following environmental windows.

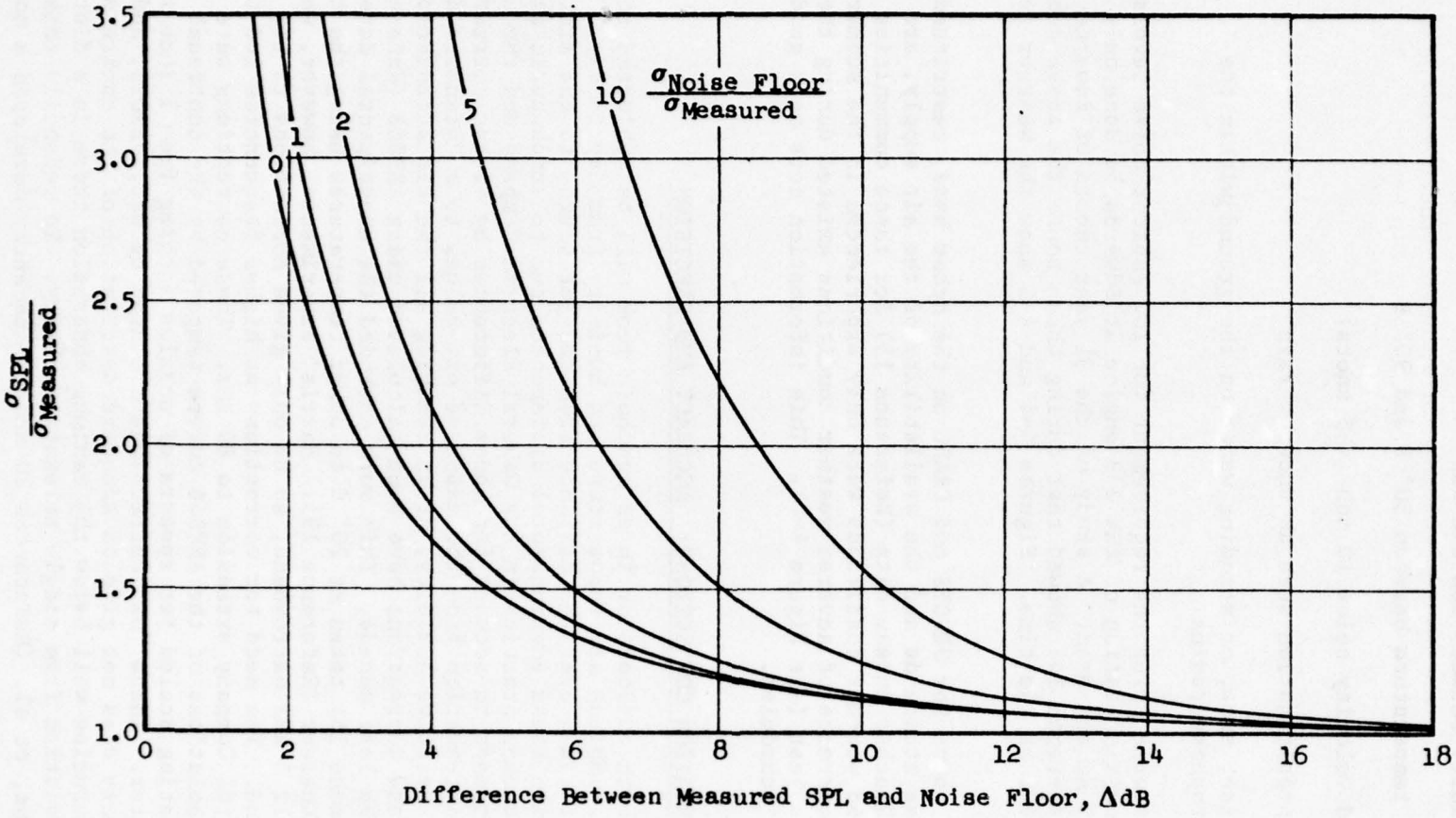


Figure 4-3. Variance of the Background Noise Correction.

1. Humidity between 30% and 90%

2. Air temperature between 30° F and 90° F

3. Wind velocity below 10 mph (< 5 knots)

4. No precipitation such as snow or rain

5. No ice, snow, or standing water on the ground within the microphone radius

These criteria, plus the requirement for low ambient noise levels, dictated that acoustic testing of the J79 engine at Edwards be done only between the hours of 3 am and 8 am. A study of the 31 year record of Edwards weather conditions (Reference 14) showed that during these hours the above conditions would be met 99% of the time. Figures 4-4 and 4-5 show the weather record at EFTC.

The test hours for JENOTS and CR&DC on the other hand, restricted by community noise standards and the availability of the air supply, are from 8 am to 6 pm. Weather Bureau data (Reference 15) for these communities indicated that good weather conditions were only experienced in the summer months and a high occurrence of adverse weather conditions existed during the remainder of the year (see Figure 4-6). This information acts as a guide in planning test schedules.

4.3 AIR ATTENUATION CORRECTIONS: ACCURACY AND PRECISION

Testing both outdoors or in an anechoic room will be subjected to changes in the ambient air temperature and humidity from day to day. The attenuation of sound over the distance from the jet source to the microphone will change with these environmental differences due to atmospheric absorption. It is common practice in the General Electric Company and throughout industry to attempt to account for these differences by either correcting the data for air attenuation from the measured day values to a "standard day" of 59° F and 70% relative humidity, or by removing all the air attenuation from the data. These corrections have been calculated using ARP866 (References 16 and 17) for the last decade. This work extended the experimental data of Harris (Reference 18) taken at 20° C to other temperatures using the theoretical work of Knesner (Reference 19). Harris' experiments, however, were only performed to 12.5 kHz narrowband, so he only gives corrections to the 8 kHz 1/3-octave band. The need for corrections at higher frequencies led to a General Electric Company extension to 80 kHz. These corrections were developed by extrapolations of the ARP866 curves tempered by the continual experience of comparing scaled jet spectra of nozzles ranging from 1 inch to 4 feet in diameter. These "GE" corrections are used by USC, JENOTS, and EFTC. Knesner's theory does not give an adequate description of the entire problem since at frequencies well below the maximum absorption there is a distinct systematic deviation from single relaxation theory. To reconcile this discrepancy, Evans, et al. (References 20 and 21) recently developed a model for

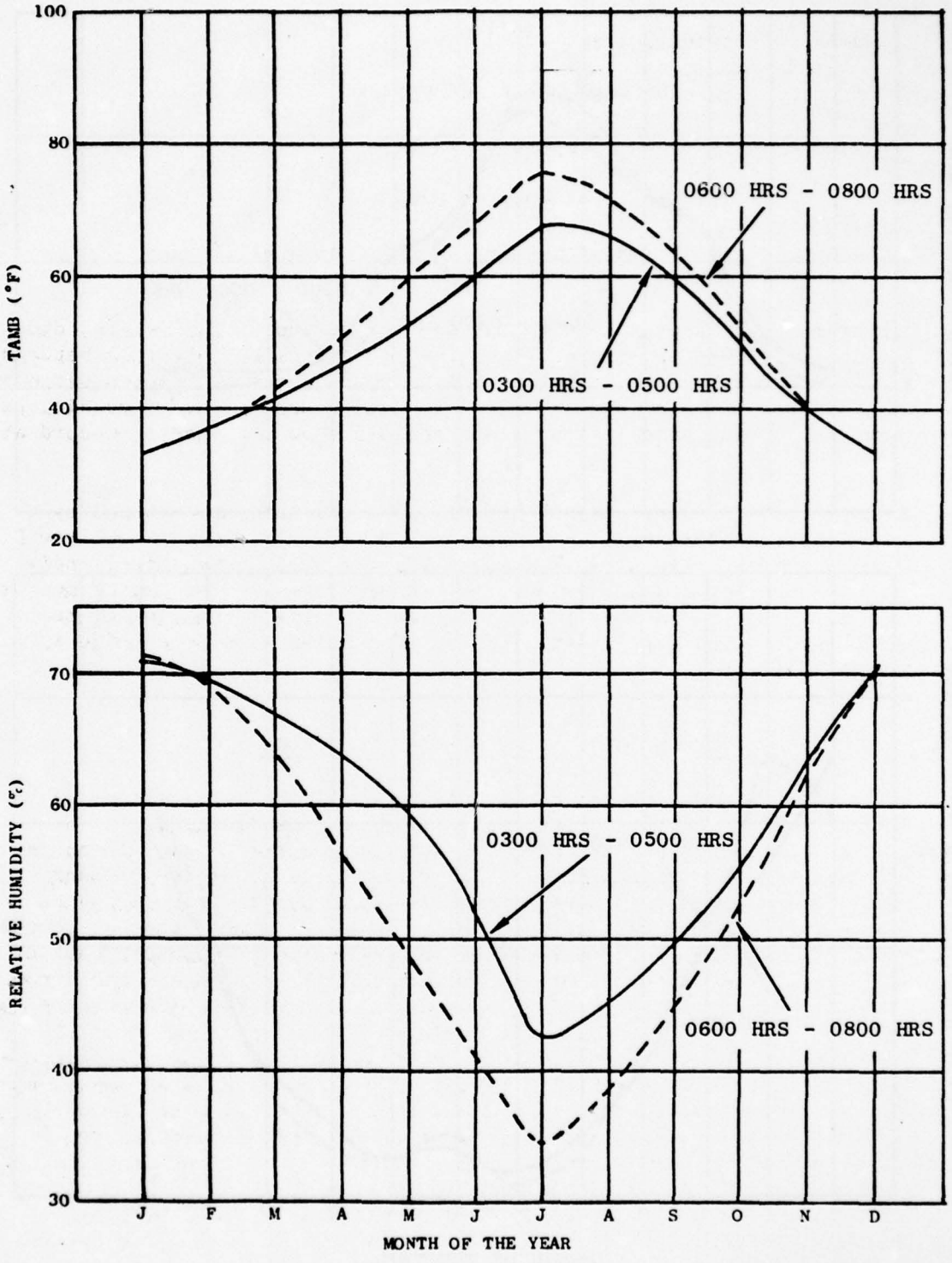


Figure 4-4. Representative Ambient Temperature and Relative Humidity at GE/EFTC.

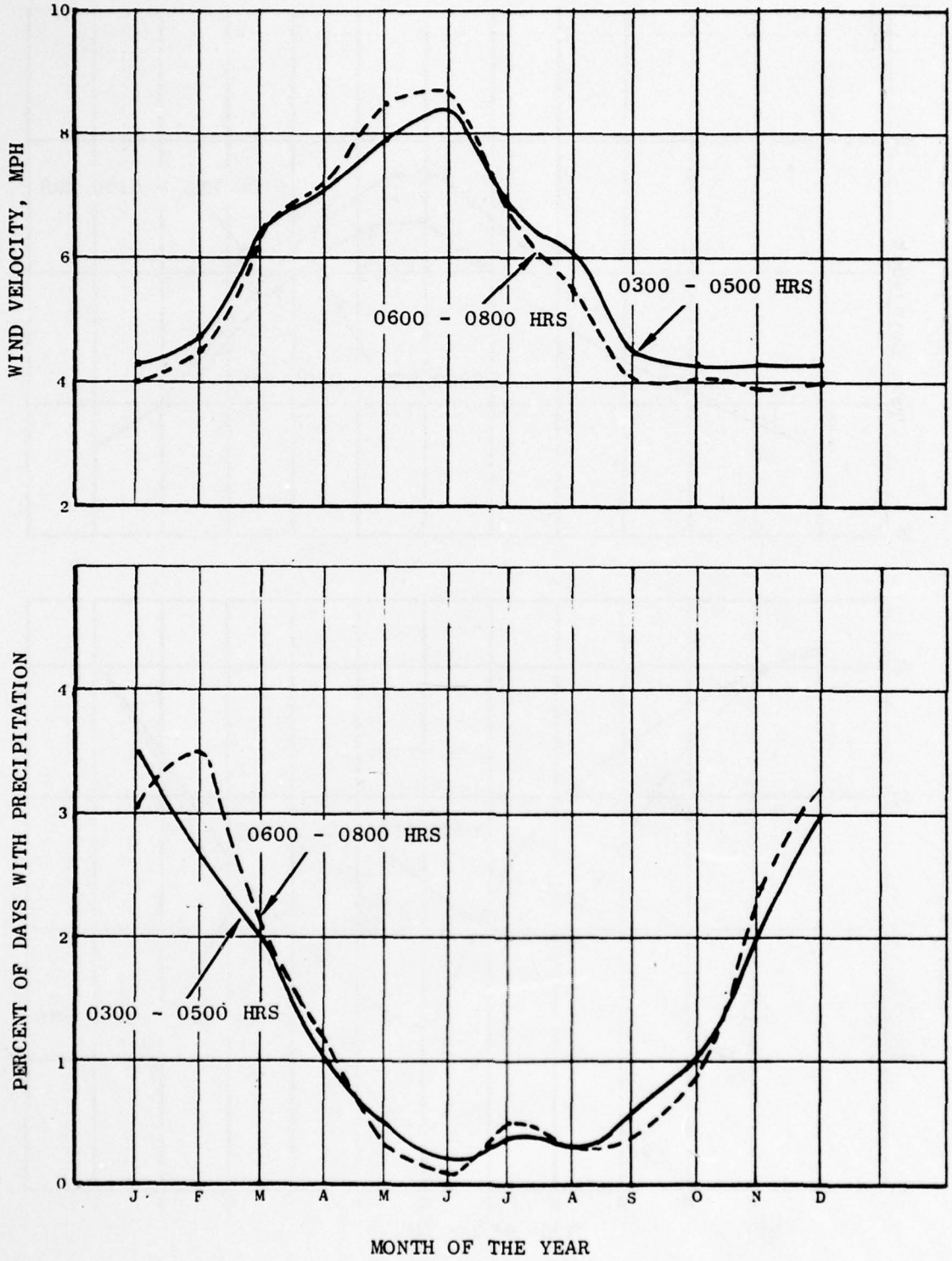


Figure 4-5. Representative Wind Velocity and Percent of Precipitation at GE/EFTC.

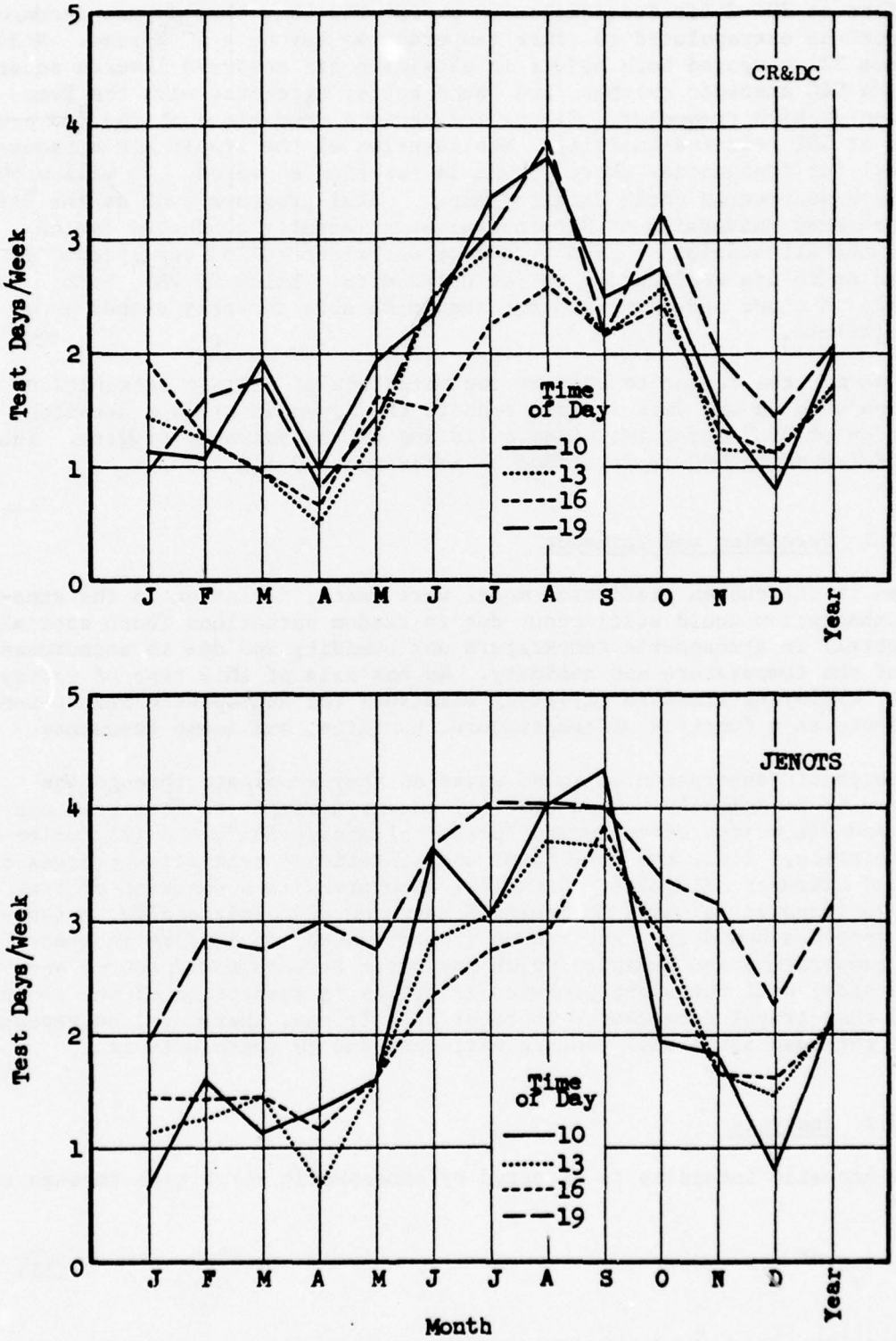


Figure 4-6. Average Test Days per Week Based on Acceptable Environmental Conditions for Acoustic Testing.

predictions at 20° C for frequencies up to 100 kHz, but they do not recommend their model be extrapolated to other temperatures beyond a 5° spread. Siddon (Reference 22) compared both models in obtaining his measured inverse square law in the UBC anechoic chamber, and found better agreement with the Evans prediction at high frequency. Figure 4-7 shows a comparison of the two predictions at 50% relative humidity. The question of the proper air attenuation model for frequencies above 20 kHz is far from answered. It will probably remain unanswered until detailed experimental programs such as the NASA Lewis sponsored University of Mississippi work recently conducted (which measured the attenuation at high frequency under controlled conditions) is evaluated as to its application to jet noise data. Below 20 kHz, both models are in close agreement and one should be able to apply either model with confidence.

To permit the reader to extract the magnitude of the air attenuation correction used on the data in this report, the Appendix gives a detailed description of "GE" model including a listing of the computer program. The Evans model used by UBC is described in References 20 and 21.

4.3.1 Precision and Variance

Even if the chosen prediction model were exact, variation in the atmospheric absorption would still occur due to random variations (both spatial and temporal) in atmospheric temperature and humidity and due to measurement errors of the temperature and humidity. An analysis of this type of variance was made, employing standard empirical relations for atmospheric absorption coefficients as a function of temperature, humidity, and sound frequency.

Atmospheric absorption of sound waves as they propagate through the atmosphere is principally caused by: (1) energy dissipation from heat conduction and viscosity, often termed "classical absorption"; and (2) "molecular absorption," i.e., the rotational and vibrational relaxation process of oxygen and nitrogen molecules. Classical absorption is a function of frequency and temperature while molecular absorption is, additionally, a function of absolute humidity. Any random (uncorrelated) variations in atmospheric temperature and humidity which may occur between sound source and sound recorder will therefore produce variations in absorption of the sound waves as they travel from source to recorder. It can, therefore, be expected that the recorded sound will contain variances due to these effects.

4.3.2 Analysis

The acoustic intensity is affected by atmospheric absorption through the relation

$$I = I_o e^{-\alpha r} \qquad (11)$$

where I_o is the acoustic intensity wihtout absorption, α is the absorption coefficient, and r is the distance along the acoustic wave path influenced by

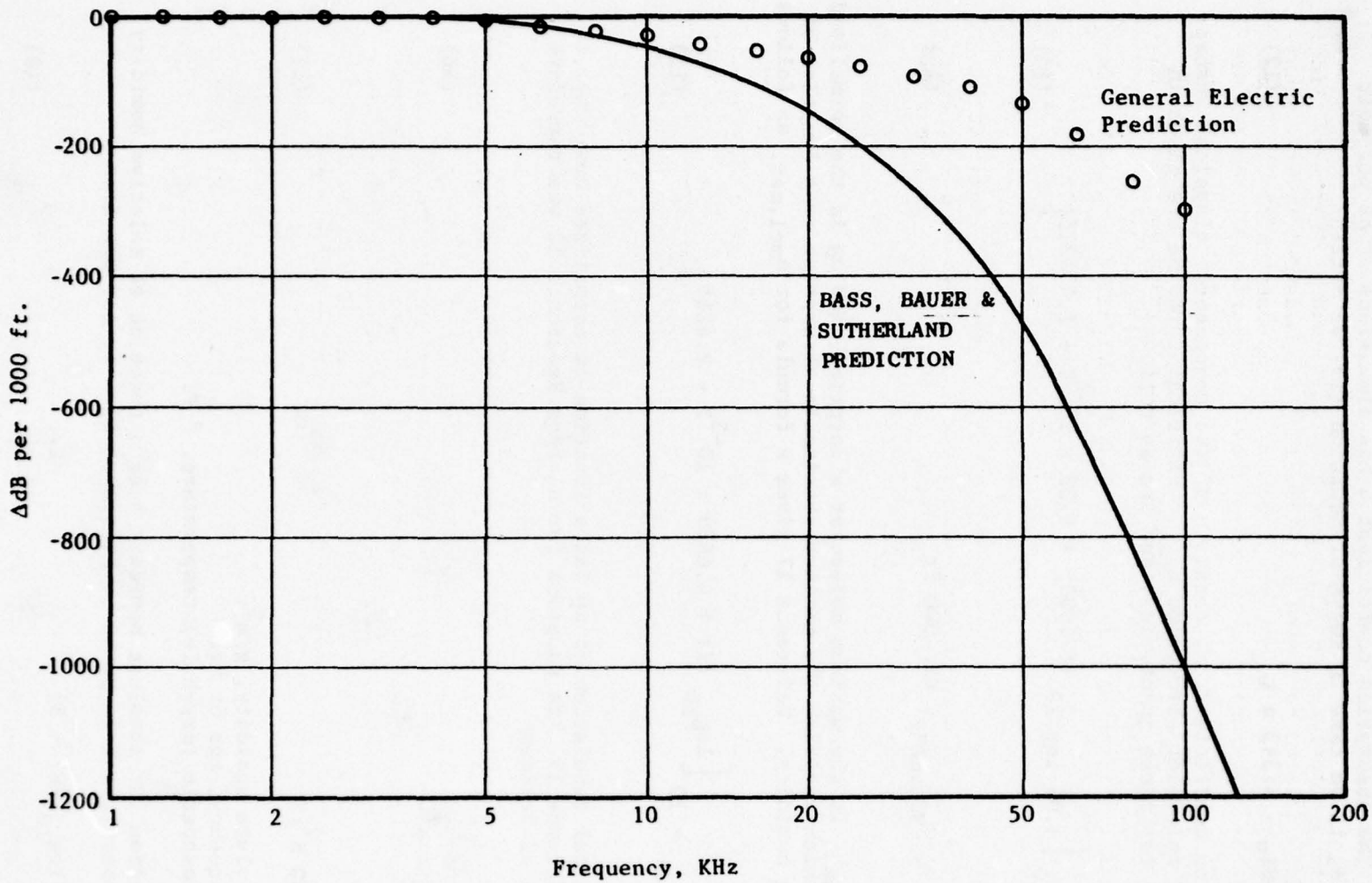


Figure 4-7. Comparison of Air Attenuation Models at 50% Relative Humidity and Temperature = 68° F.

absorption. The absorption coefficient α has dimensions of dB per unit length, since, if we take 10 $\log_{10}$ of Equation (11) we obtain

$$SPL = SPL_o - 4.343\ \alpha\ r \tag{12}$$

The absorption coefficient, α, consists of two components: classical absorption α_{cl} and molecular absorption α_{mol}. Empirical formulae are given in Reference 17 for these quantities, and are as follows:

$$\alpha_{cl} = 10^{\left[2.05 \log 10\ (f/1000) + 6.33 \times 10^{-4} T - 1.435325\right]} \tag{13}$$

$$\alpha_{MOL} = \alpha_N\ \alpha_{MOL,MAX.},\ \text{dB/1000 ft} \tag{14}$$

where $\alpha_{mol,max.}$ is the maximum molecular absorption, and α_N is the normalized absorption which modifies the maximum attainable absorption as a function of the existing humidity. Reference 17 gives a formula for $\alpha_{mol,max.}$ as follows:

$$\alpha_{MOL,MAX.} = 10^{\left[\log_{10}(f) + 4.6833 \times 10^{-3} T - 2.4215\right]} \tag{15}$$

Only a numerical tabulation of α_N (as a function of normalized humidity) is given in Reference 17. An equation for α_N from Reference 12 was therefore used, and is as follows:

$$\alpha_N = \frac{2x}{1 + x^2} \tag{16}$$

where

$$x = 1000\ h^2/f \tag{17}$$

and h = absolute humidity, g/m^3,
f = frequency, cps or Hz.
T = atmoshperic (dry-bulb) temperature, ° F.

An equation for absolute humidity h as a function of relative humidity (RH) and temperature T is given in Reference 17. It has the form

$$h = 10^{[\log_{10}(RH) - B]} \tag{18}$$

where

$$B = b_0 + b_1 T + b_2 T^2 + b_3 T^3 \tag{19}$$

The root-mean-square variance in α, assuming that variance in T and h are statistically independent, is given by the following using Equation (5):

$$\sigma\alpha = \left[\left(\frac{\partial\alpha}{\partial T}\right)^2 \sigma T^2 + \left(\frac{\partial\alpha}{\partial h}\right)^2 \sigma h^2\right]^{1/2}$$

$$\alpha = \alpha_{cl} + \alpha_{mol}$$

$$\alpha_{cl} = \alpha_{cl}(f,T) \tag{20}$$

$$\alpha_{mol} = \alpha_{mol}(f,T,h)$$

$$\sigma\alpha = \left\{\left[\left(\frac{\partial\alpha_{cl}}{\partial T}\right)^2 + \left(\frac{\partial\alpha_{mol}}{\partial T}\right)^2 (\sigma T)^2 + \left(\frac{\partial\alpha_{mol}}{\partial h}\right)^2 (\sigma h)^2\right\}^{1/2}$$

From Equations (17-19), the derivatives required in Equation (20) can be evaluated, and are as follows:

$$\frac{\partial\alpha_{cl}}{\partial T} = [\log_e 10]\,[6.33 \times 10^{-4}]\alpha_{cl}$$

$$\frac{\partial\alpha_{mol}}{\partial T} = \alpha_N \frac{\partial\alpha_{mol,max.}}{\partial T} \tag{21}$$

$$\frac{\partial\alpha_{mol,max.}}{\partial T} = [\log_e 10]\,[4.6833 \times 10^{-3}]\alpha_{mol,max.}$$

$$\frac{\partial \alpha_{mol}}{\partial h} = \alpha_{mol,max.} \frac{\partial \alpha}{\partial h} N$$

$$\frac{\partial \alpha}{\partial h} N = \frac{\partial \alpha}{\partial x} N \frac{\partial x}{\partial h} \qquad (21) \text{ (cont'd)}$$

$$\frac{\partial \alpha}{\partial x} N = \frac{2(1 - x^2)}{(1 + x^2)^2}$$

$$\frac{\partial x}{\partial h} = 2000 \frac{h}{f} = 2 \frac{x}{h}$$

Thus, given any combination of f, T, and RH, the expected variance in atmospheric absorption, $\Delta\alpha$ in ΔdB/1000 foot, can be computed using Equations (12-21). The variance (rms variation) in h and T for the particular experimental facility being evaluated are additional required input.

4.3.3 Numerical Results

The procedure just described was employed to evaluate the atmospheric absorption variance which can be expected at the various facilities. The computations were performed for sample frequencies of 100, 500, 1,000, 5,000, 10,000, 20,000, and 80,000 Hz. The temperature was varied from 0 to 100° F, and relative humidity was varied from 30 to 90%, for each frequency. The variance in ambient temperature was assumed to be $\Delta T \approx 5°$ F. The variance in Δ absolute humidity was assumed to be ~1.5 g/m^3, then ambient temperature and humidity were systematically varied over the above ranges, and $\Delta\alpha$ was computed. From these calculations, contours of constant $\Delta\alpha$ were generated on a plot of RH (ordinate) versus T (absissa). These contour plots are presented in Figures 4-8 through 4-13 for each of the frequencies quoted.

For example, at the JENOTS facility, the microphone arc radius is 40 feet. If we adopt the criterion that the variance in absorption should be no greater than 1 dB, the maximum acceptable variance is then 25 dB per 1000 feet. The contours of 25 dB/1000 feet shown in Figures 4-11 through 4-13 indicate the boundaries of operation (T and RH) where acceptable variances

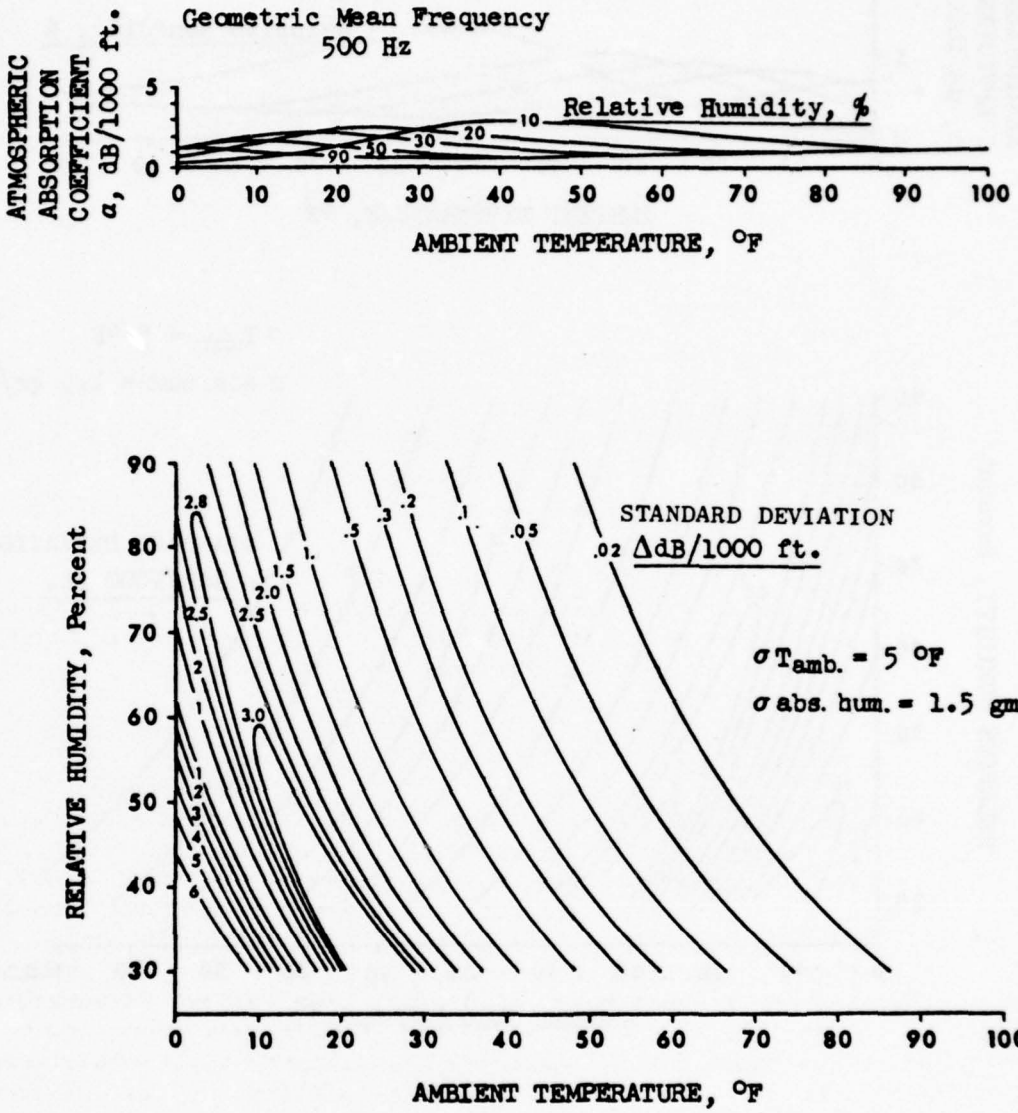


Figure 4-8. Atmospheric Attenuation Variance at 500 Hz.

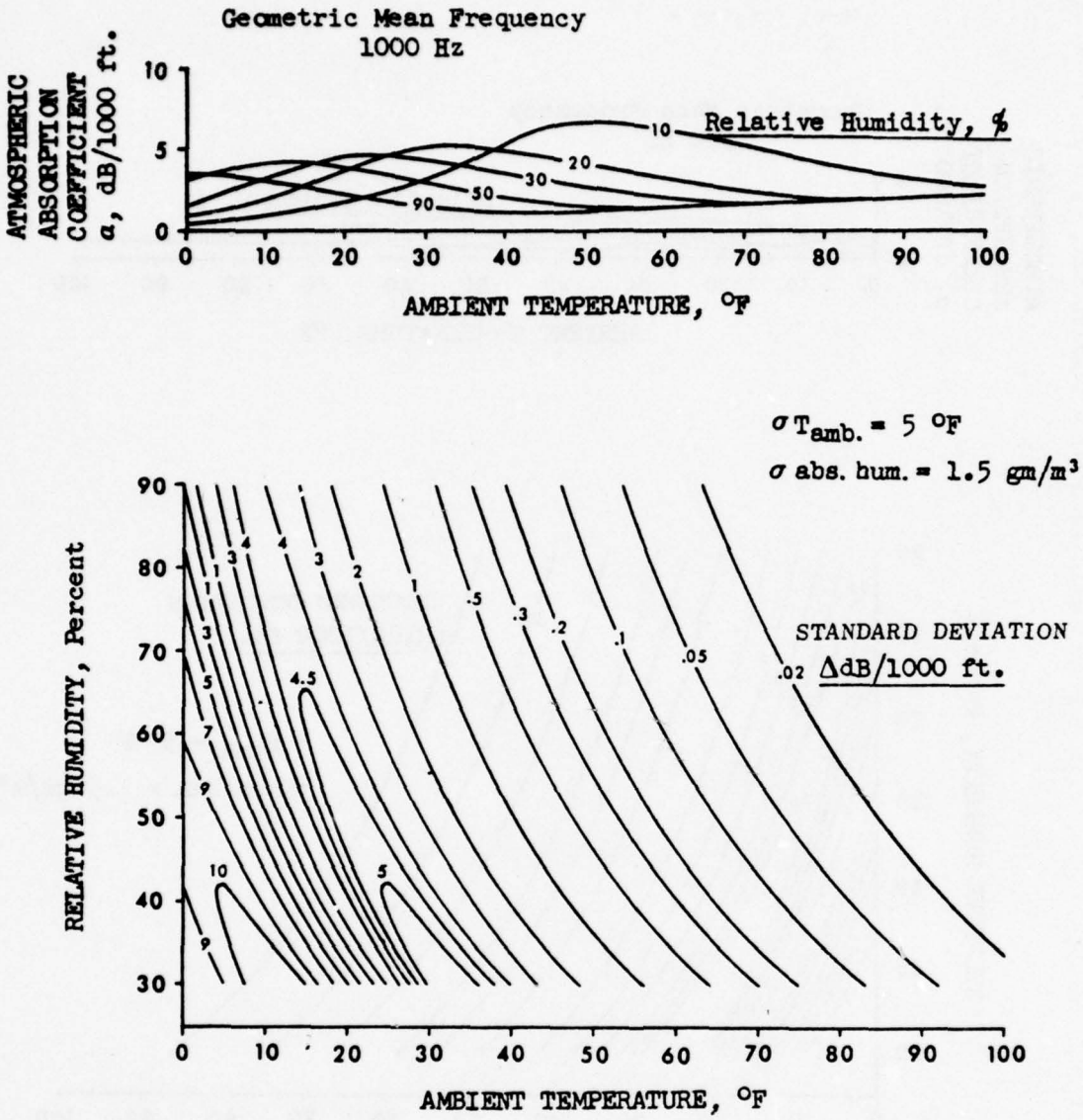


Figure 4-9. Atmospheric Attenuation Variance at 1000 Hz.

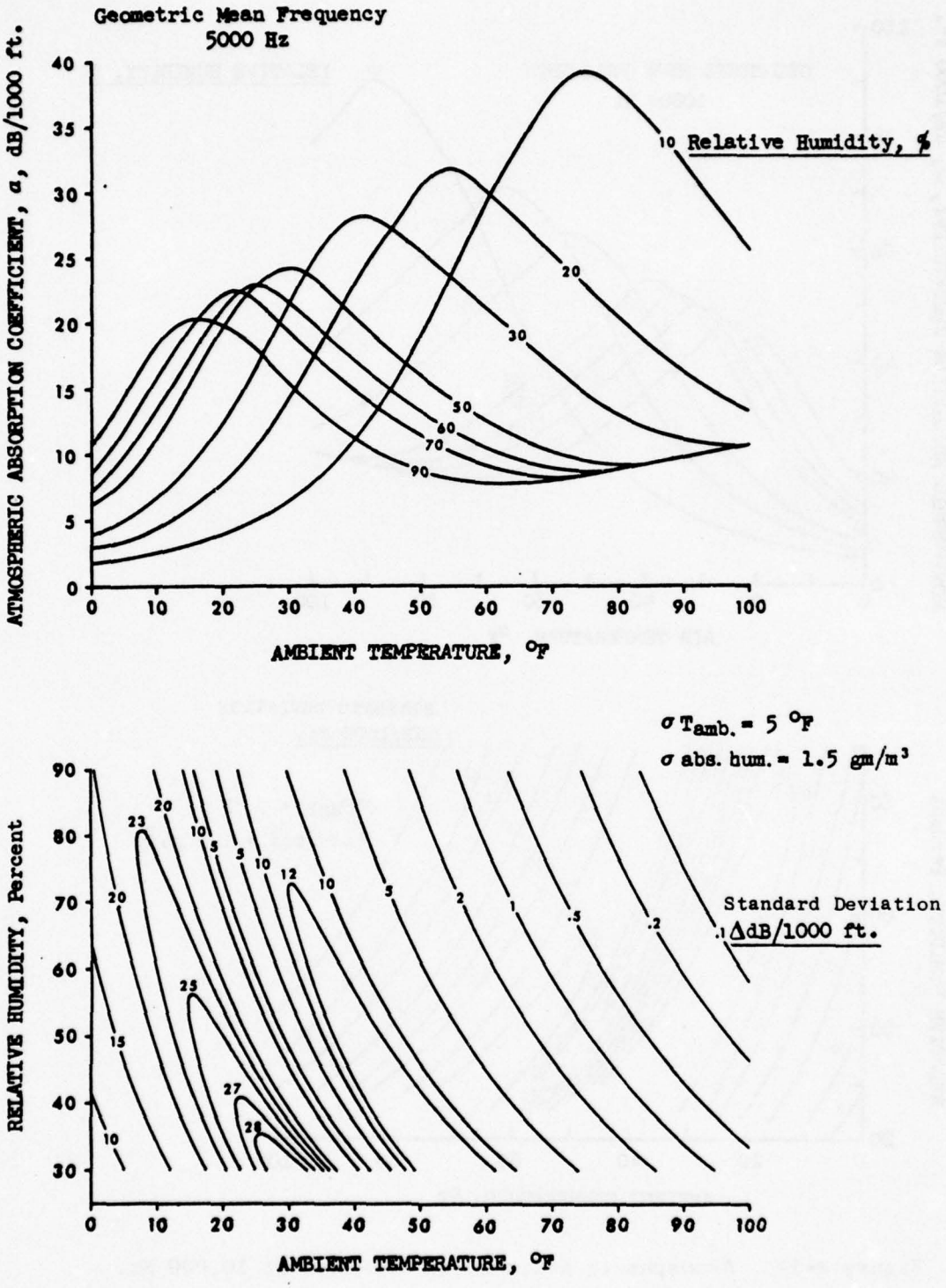


Figure 4-10. Atmospheric Attenuation Variance at 5000 Hz.

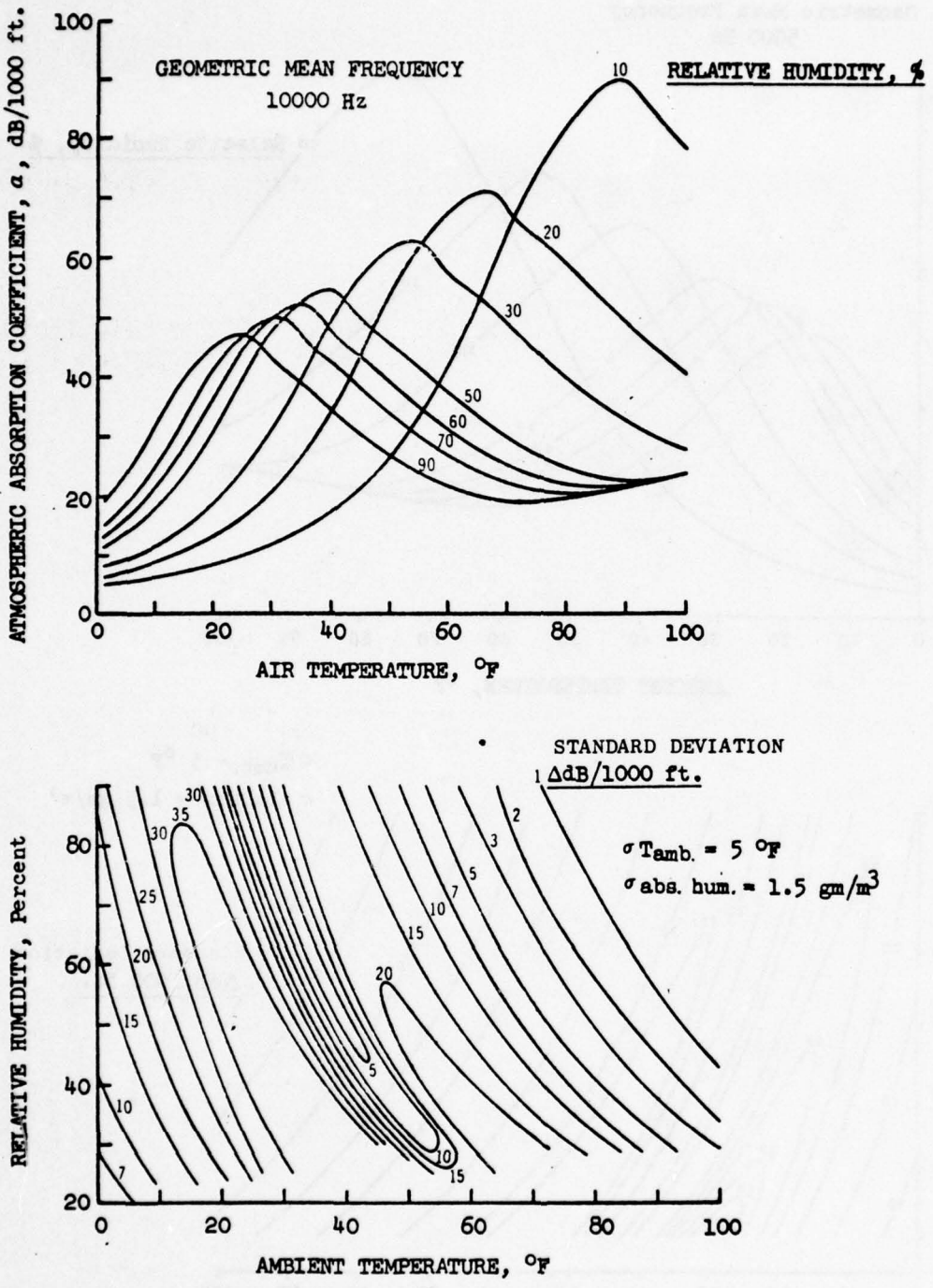


Figure 4-11. Atmospheric Attenuation Variance at 10,000 Hz.

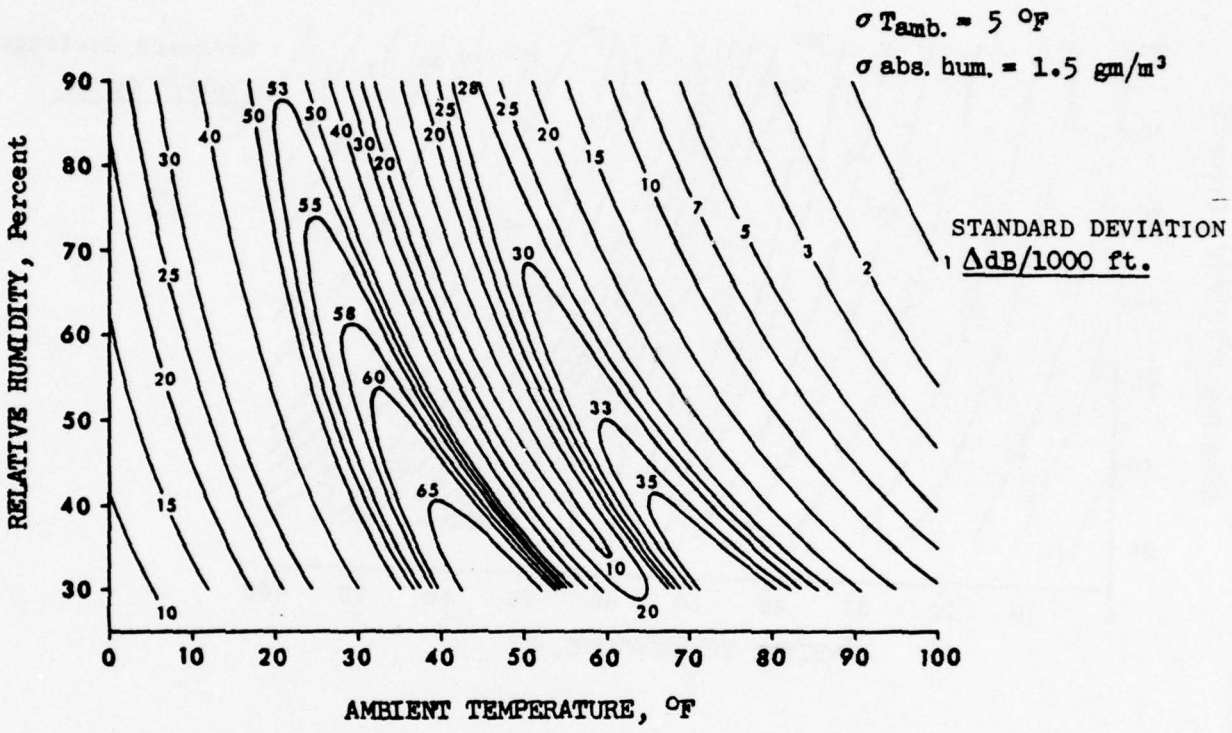


Figure 4-12. Atmospheric Attenuation Variance at 20,000 Hz.

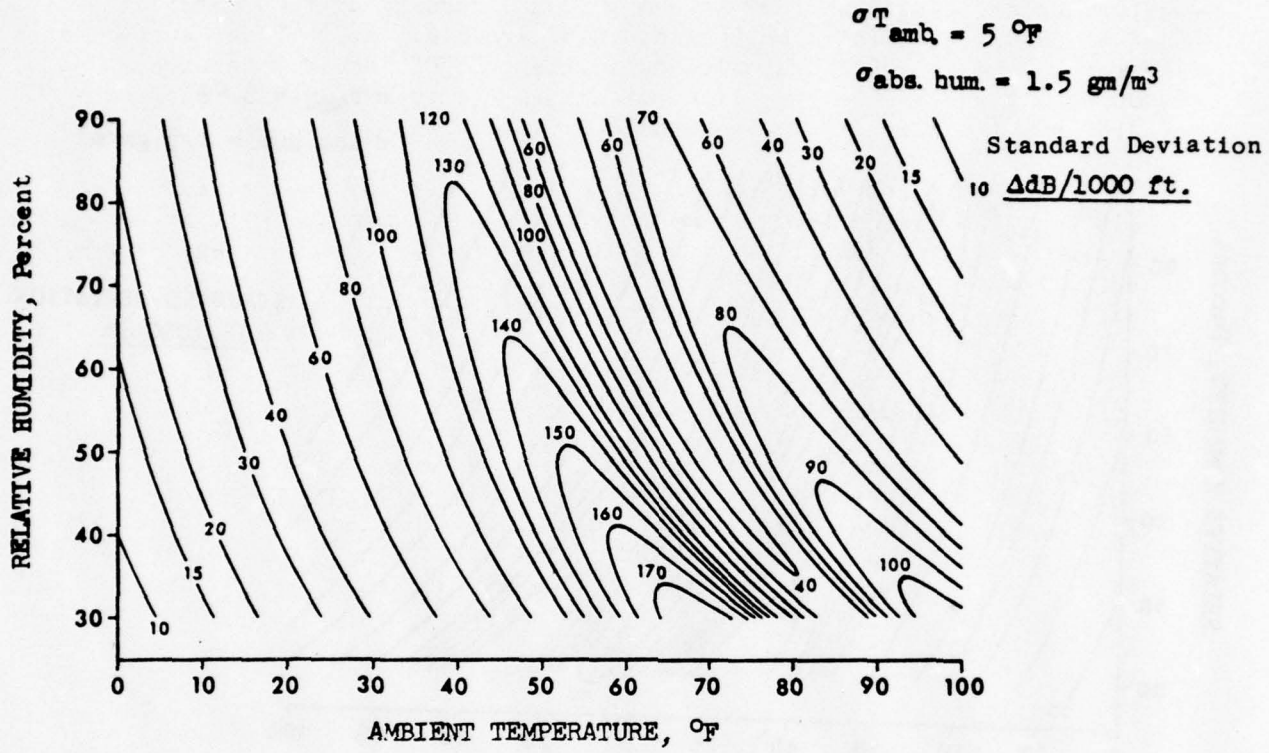


Figure 4-13. Atmospheric Attenuation Variance at 80,000 Hz.

are achievable. Examination of Figures 4-8 through 4-13 shows that any test point in the range of $0 \leq T \leq 100°$ F and $10 \leq RH \leq 90\%$ meets this criterion for frequencies less than 5000 Hz. A 5000 Hz, running at temperatures below 40° F and below humidities of 50% should be avoided. At 5000 Hz, running at temperatures below 40° F and below humidities of 50% should be avoided. At 10,000 Hz and above, the criterion for minimum acceptance is not straightforward, and is generally dealt with individually.

At Edwards, a required variance of 0.75 dB over 160 feet gives 4.7 dB over 1000 feet. So the acceptable temperature and humidity range is small. Using a typical test day from Figure 4-11 representing the coverage experienced during certification testing of the J79, one obtains the variance of the air attenuation model with frequency shown in Figure 4-14.

4.4 AERO INSTRUMENTATION ACCURACY

Another parameter which influences the measured sound pressure level is the ability to accurately set the aerodynamic jet velocity and total temperature. An error in these parameters would lead to misinterpretation of the data, and will cause disagreement when comparing levels obtained from various facilities. Assuming, however, that all biasing accuracy errors have been removed and the mean aerodynamic values are properly calculated, there will still be variance in the sound level due to uncontrollable variations in the measurement instrumentation of the ambient temperatures and pressures over the time of the reading.

To further evaluate the variance in the sound pressure levels, the calibration and measurement accuracies of the major components in the aero data acquisition system (such as the pressure transducers, thermocouples, and electronic tachometer) were examined. Figures 4-15 through 4-17 show typical calibration curves for the transducers which were used to measure inlet total pressure PT2, exhaust total pressure PT7, and exhaust static pressure PS7, on the J79 engine tests. The calibration curves depict the exerted pressure, their equivalent digital counts, and the pressure error in percent of full scale. From these figures, the following maximum variances were established:

$$\text{Variance in PT2} - \sigma_{PT2} = 0.002\ PT2$$

$$\text{Variance in PT7} - \sigma_{PT7} = 0.002\ PT7$$

$$\text{Variance in PS7} - \sigma_{PS7} = 0.0025\ PS7$$

The variance in the exhaust temperature as measured by thermocouples was estimated to be less than 1% or,

$$\text{Variance in TT7} - \sigma_{TT7} = 0.01\ TT7$$

Similar estimates were made for the scale-model facilities where wall static pressure taps upstream of the nozzle are used to calculate the jet total pressure. In this case one obtains

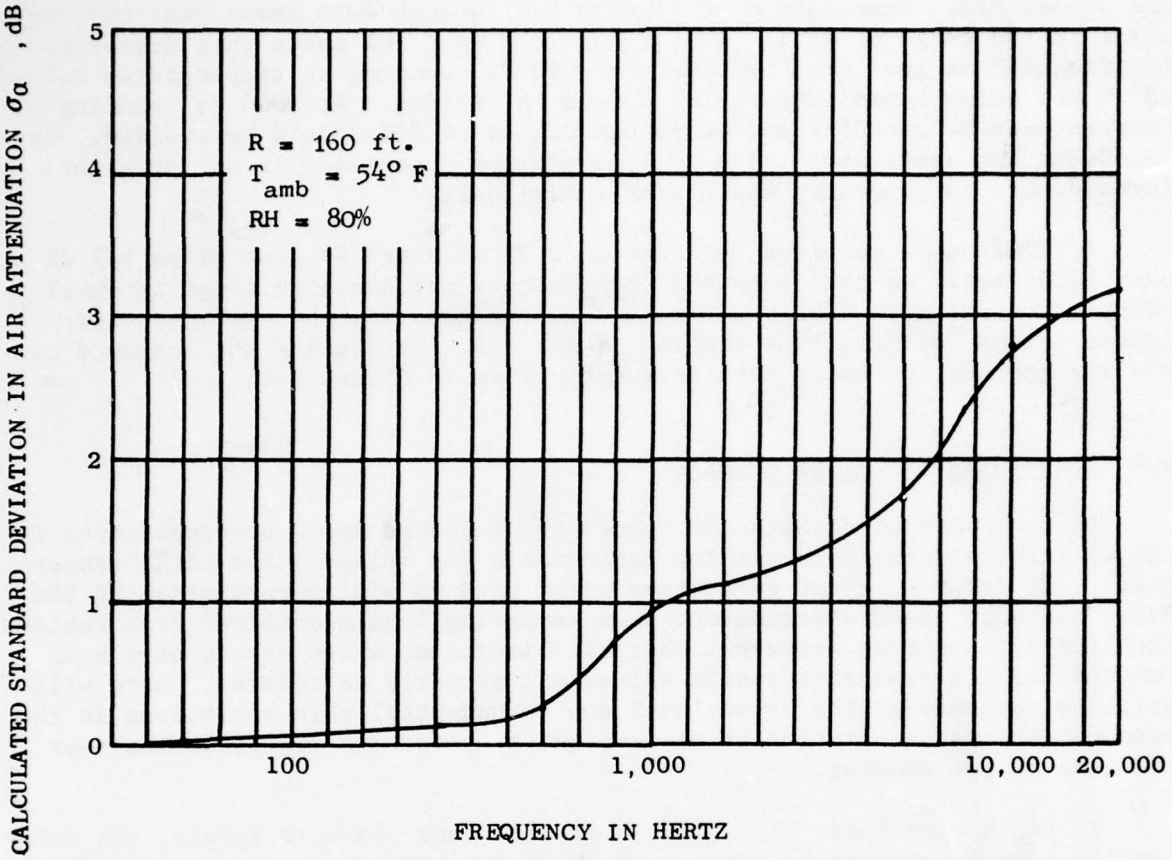


Figure 4-14. Air Attenuation Accuracy During J79 Certification Testing at GE/EFTC.

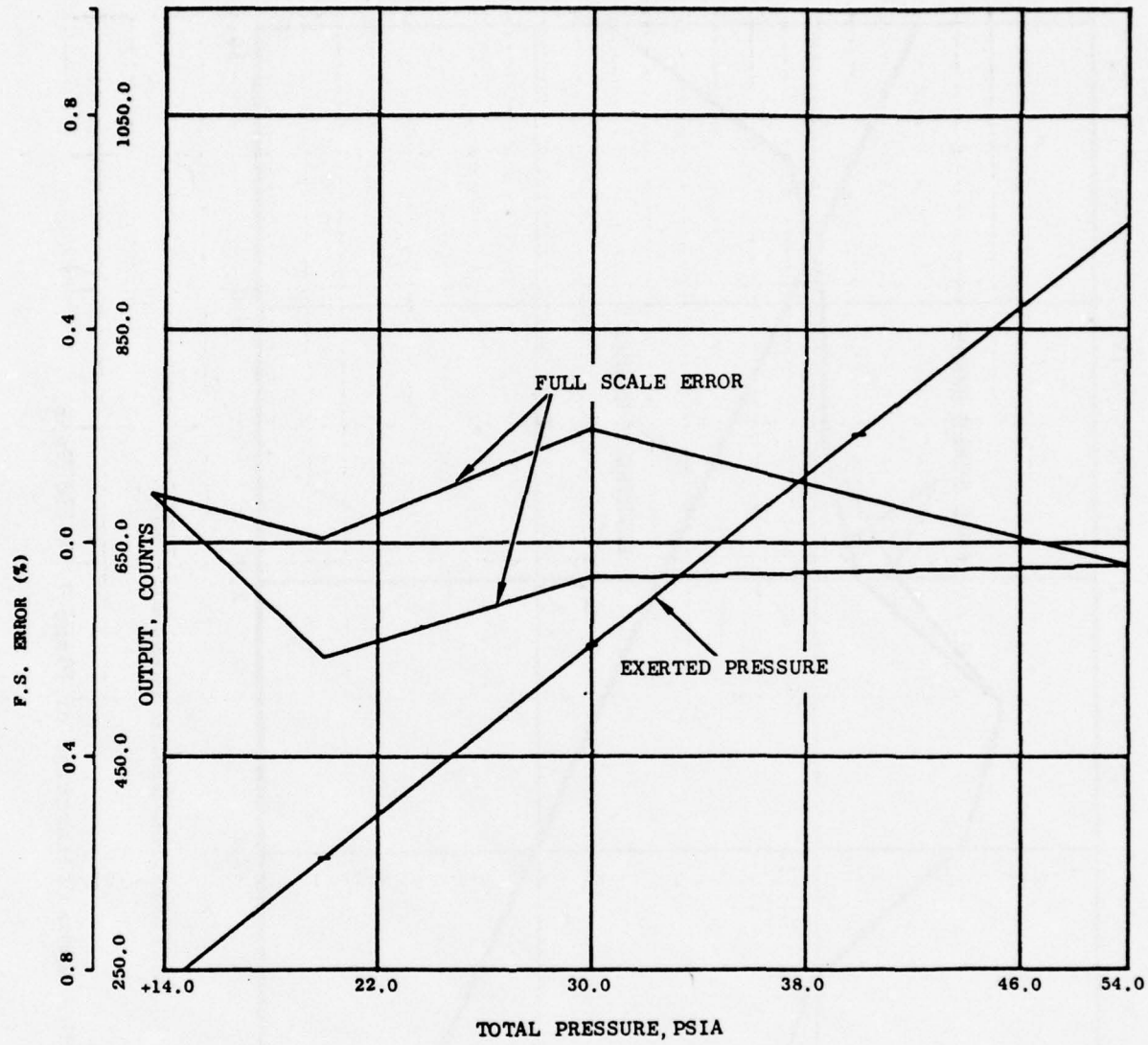


Figure 4-15. Aero Calibration of Inlet Total Pressure Rake.

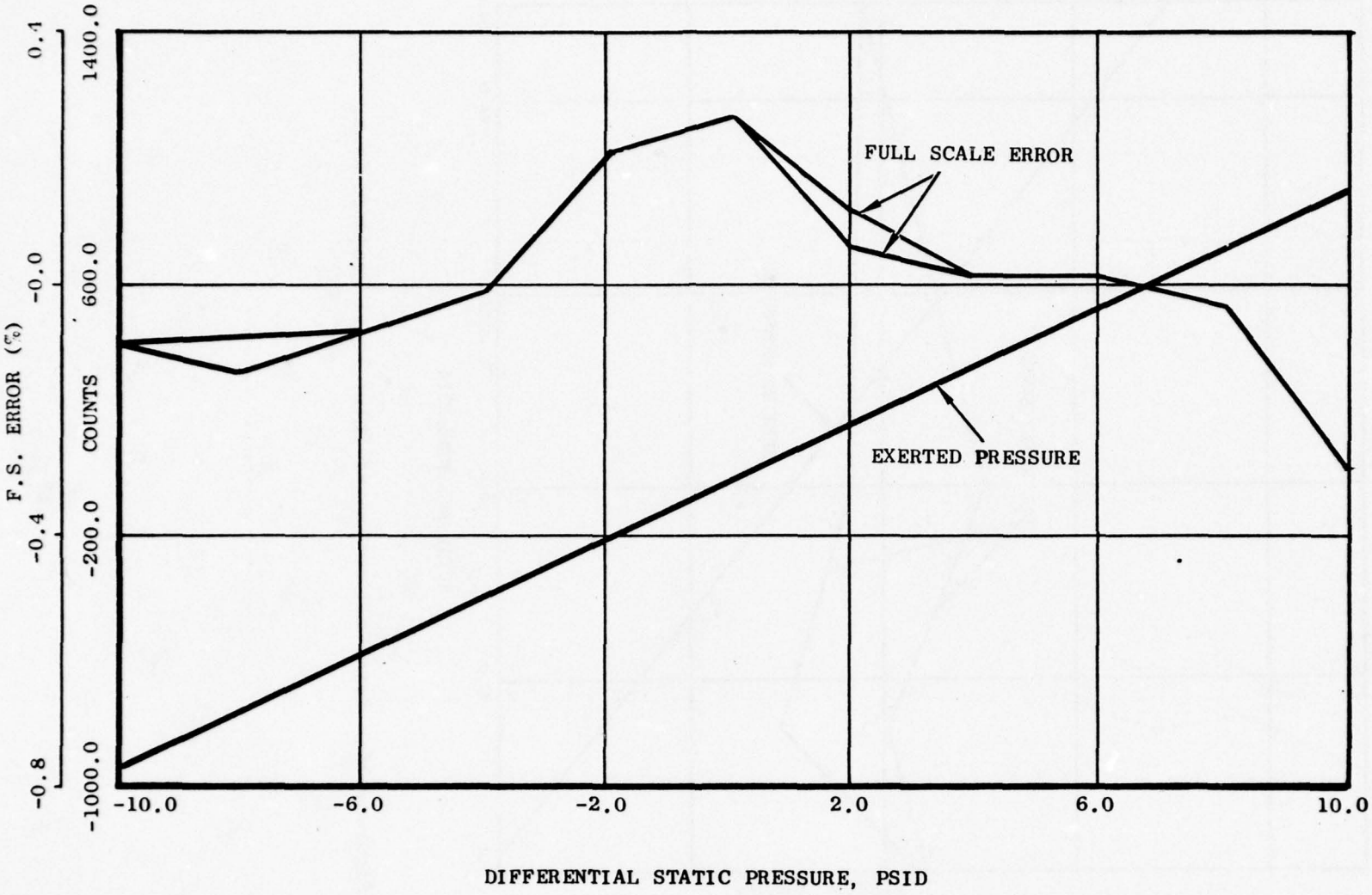


Figure 4-16. Aero Calibration of Plane 7 Static Taps.

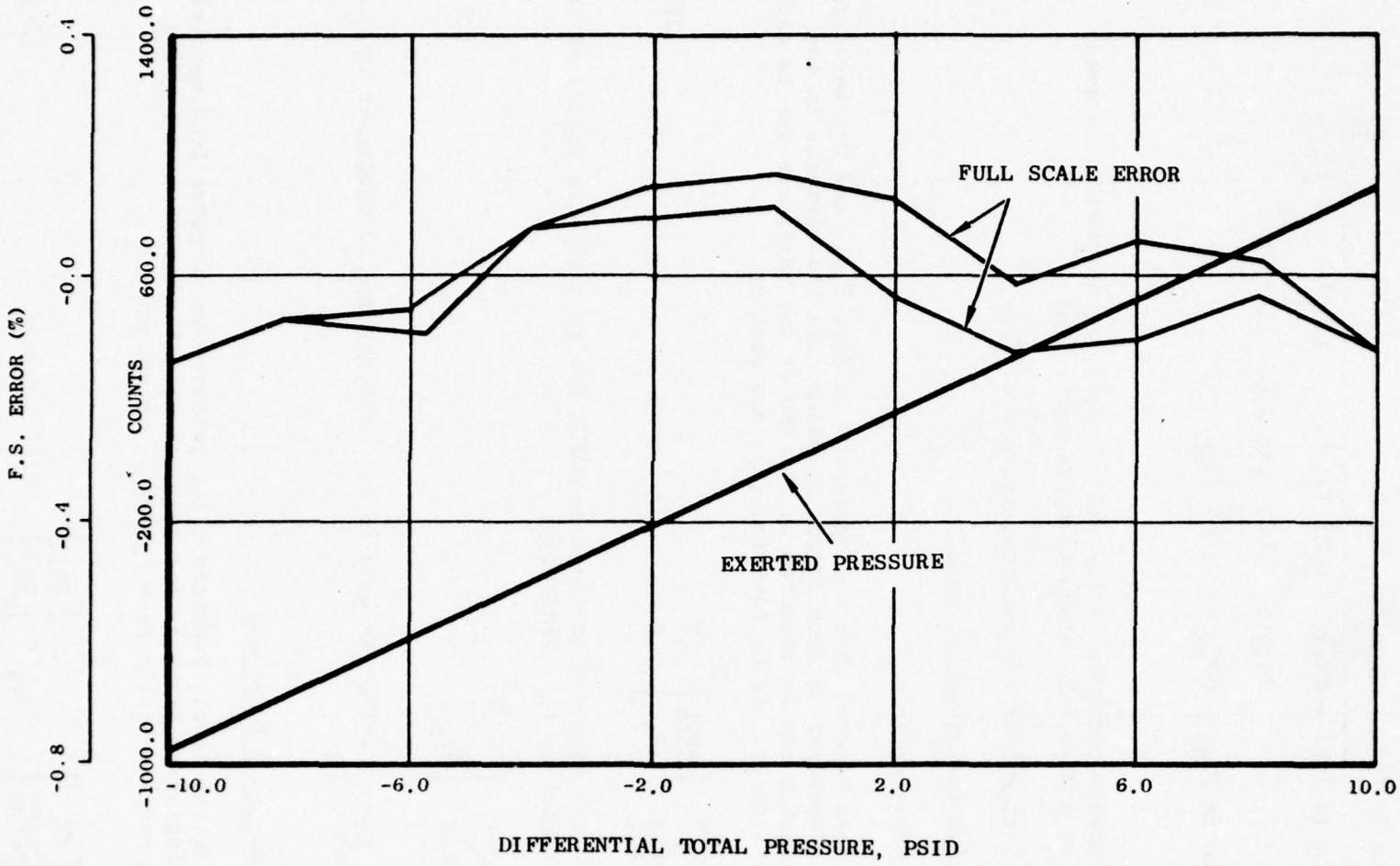


Figure 4-17. Aero Calibration of Exhaust Total Pressure Rake.

Variance in P_{S7} - $\sigma_{PS7} = 0.01\ P_{S7}$

Variance in T_{T8} - $\sigma T_{T8} = 0.01\ T_{T8}$, $T_{T8} \geq 1500°$ R

$\sigma T_{T8} = 0.005\ T_{T8}$, $T_{T8} < 1500°$ R

Variance in P_{amb} - $\sigma P_{amb} = 0.005\ P_{amb}$

where:

P_{S7} = Nozzle upstream plenum static pressure, assumed to be equal to nozzle exit stagnation pressure, pisa

T_{T8} = Nozzle exit stagnation temperature, ° R

P_{amb} = Ambient pressure, psia

σ_x = Variance in x

It was also assumed that the variances in P_{S7}, P_{amb}, and T_{T8} were statistically independent of each other, in which case the variance in any dependent variable can be computed as the rms of the variances due to each parameter separately. Using Equation (5), one obtains

$$\sigma^2_{PWL} = \sum_{n=1}^{\infty} \left[\frac{\partial PWL}{\partial x_n}\right]^2 \sigma^2_n \tag{22}$$

where σ_{PWL} is the expected variance in OAPWL due to variances in all of the independent variables σ_n. Similarly,

$$\sigma^2_{V_j} = \sum_{n=1}^{\infty} \left[\frac{\partial V_j}{\partial x_n}\right]^2 \sigma^2_n \tag{23}$$

where σ_{V_j} is the expected variance in jet velocity due to variances in independent variables σ_n.

4.4.1 Variance Equations

Utilizing the ideal, isentropic jet velocity as computed from measured jet nozzle stagnation pressure and temperature and ambient pressure, and denoting the pressure ratio $Pr = P_{S7}/P_{amb}$, we can write

$$\sigma^2_{V_j} = \left[\frac{\partial V_j}{\partial T_{T8}}\right]^2 \sigma^2_{T_{T8}} + \left[\frac{\partial V_j}{\partial Pr}\right]^2 \sigma^2_{Pr} \tag{24}$$

$$\sigma^2_{Pr} = \left[\frac{\partial Pr}{\partial P_{S7}}\right]^2 \sigma^2_{P_{S7}} + \left[\frac{\partial Pr}{\partial P_{amb}}\right]^2 \sigma^2_{P_{amb}} \qquad (25)$$

From the modified Lighthill (see Reference 23) similarity relation for jet noise, the OAPWL variance can be evaluated; thus

$$\sigma^2_{PWL} = \left[\frac{\partial PWL}{\partial V_j}\right]^2 \sigma^2_{V_j} + \left[\frac{\partial PWL}{\partial T_{T8}}\right]^2 \sigma^2_{T_{T8}} \qquad (26)$$

It was further assumed that ρ_{jet}/ρ_{amb} could be approximated by T_{amb}/T_{T8}, and that variances in T_{amb} were neglibible. For low jet velocities, this approximation is reasonable; but for high jet velocities, jet static temperature (i.e. T_8) must be utilized. Thus, a secondary effect of jet velocity is implied which may be important when computing variances, especially at the higher velocities. This effect was not included in the results to be presented herein. Also, the density exponent ω is a function of jet velocity, and this variation is not known to a sufficient degree of confidence such that its influence on variances could effectively be assessed. Experiments (Reference 23) indicate that ω varies from -1 to +2 as V_j goes from ~200 to 3000 fps. Sample numerical calculations were done with $\omega = 0$ and $\omega = 2$, over a range of $1000 < V_j < 3000°$ R, and the maximum difference in σ_{PWL} results were found to be only 0.03 dB, so remaining results were done with $\omega = 0$.

4.4.2 Results

Calculations of σ_{PWL} were performed, using the previously discussed assumptions for σP_{S7}, σT_{T8}, σP_{amb}, and $\omega = 0$. The ranges of velocity and temperatures investigated were as follows:

$$500 \leq V_j \leq 3000 \text{ fps}$$

$$500 \leq T_{T8} \leq 2500 \text{ ° R}$$

Results are shown in Figure 4-18 as a function of parametric variations in T_{T8} and V_j, for $V_j \geq 1000$ fps, and $T_{T8} > 1050°$ R. From these results, a contour plot (Figure 4-19) of constant σ_{PWL} lines was constructed.

Figure 4-18 indicates that the maximum variance in PWL (as a result of variances in V_j) is about ± 1.5 dB, occurring at high temperatures and low velocities.

It may be noted from Figure 4-18 that, for high velocity levels, the PWL variance is relatively insensitive to jet stagnation temperature level. Further, the PWL variance decreases with increasing jet velocity (T_{T8}

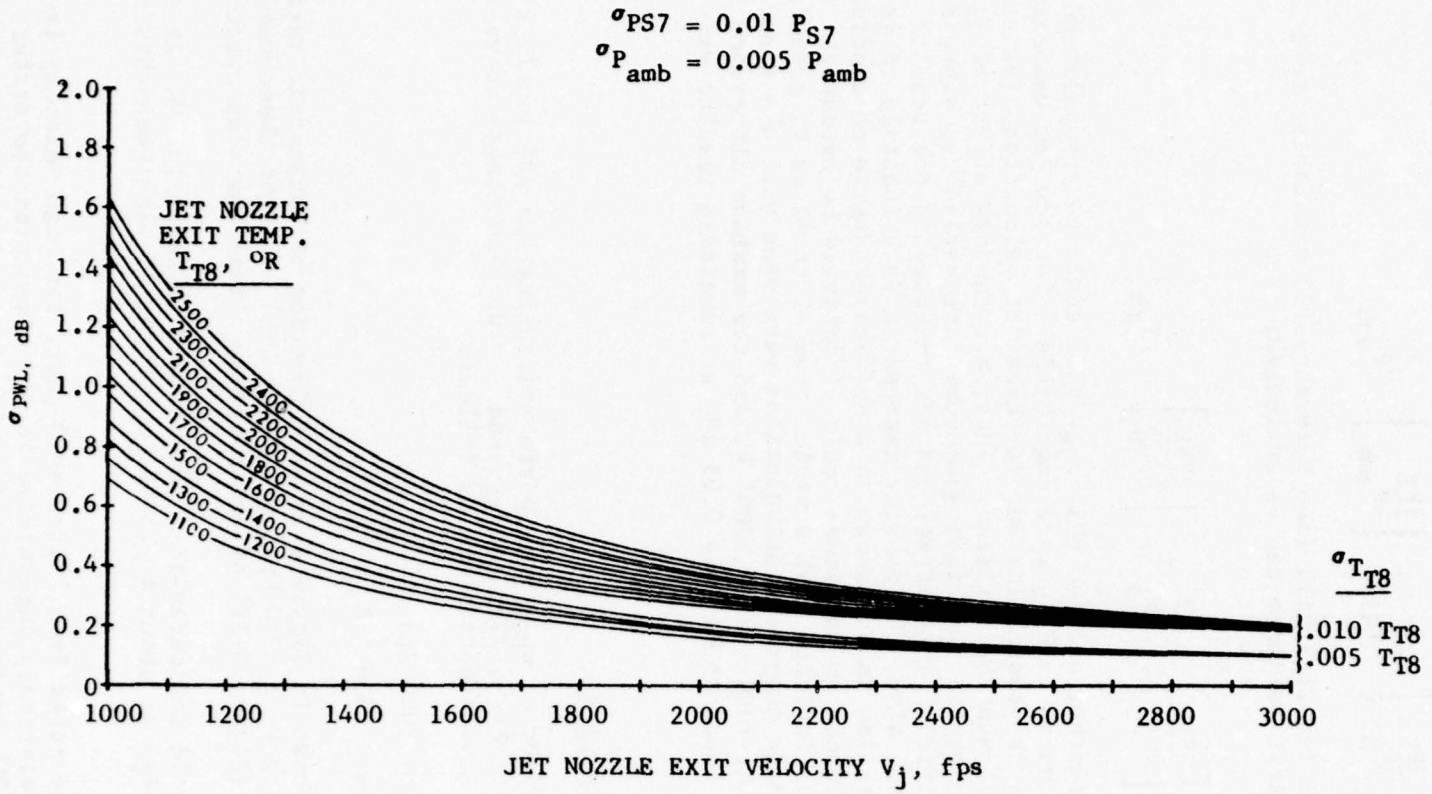


Figure 4-18. Variance in PWL Due to Variances in Nozzle Exit and Ambient Pressures and Temperatures.

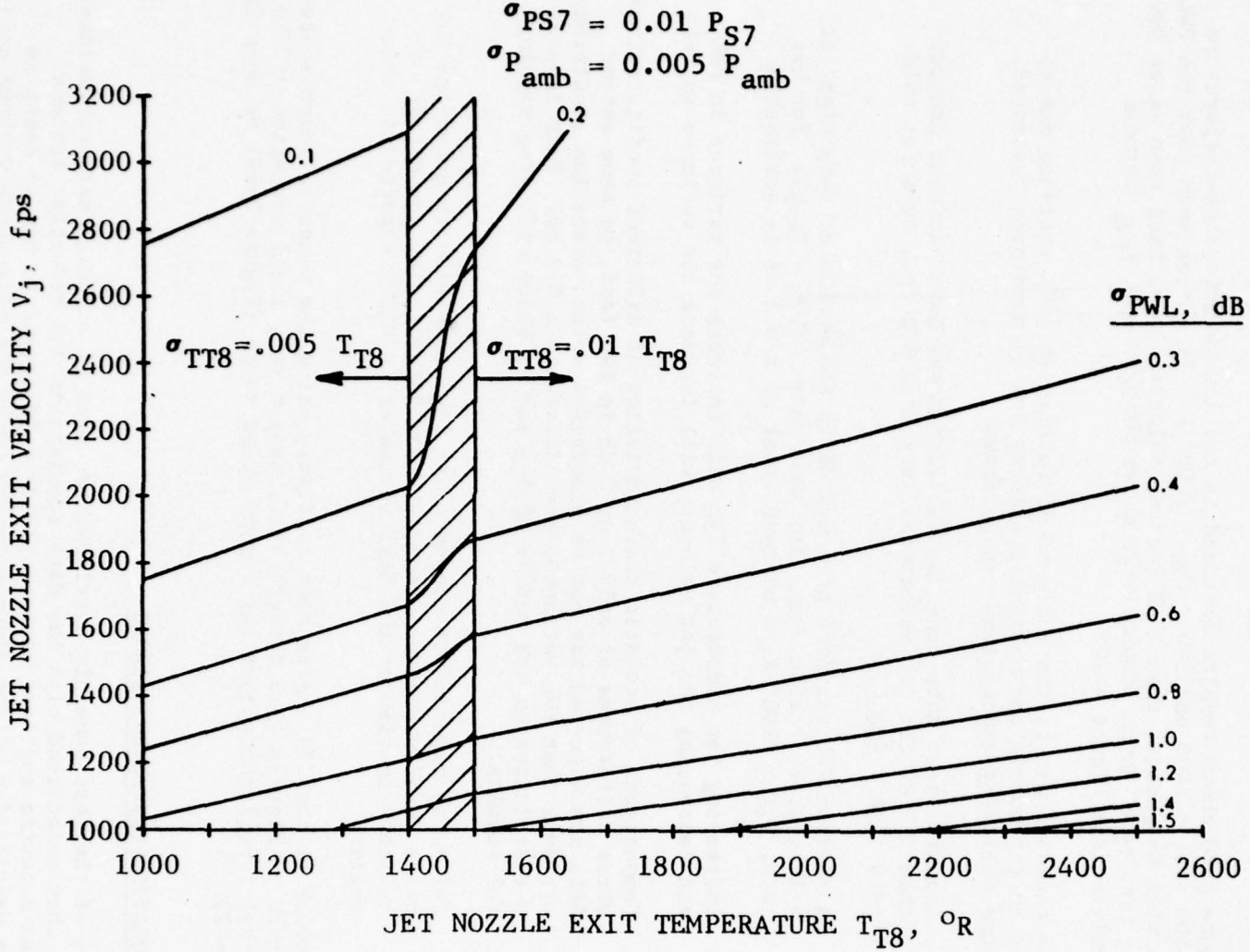


Figure 4-19. Variance in PWL Due to Variances in Nozzle Exit and Ambient Pressures and Temperatures - Constant σ_{PWL} Contours.

constant), reaching a minimum "Floor" level variance which apparently is governed by the σT_{T8} variance assumed.

Figure 4-20 shows results obtained in the low-velocity/low-temperature regime, $500 < V_j < 1000$ and $500 < T_{T8} < 2000°$ R. It can be seen that the PWL variance will be greater than 1 dB for any velocity level less than about 600 fps, even for "cold" jets. Figure 4-21 shows the constant σ_{PWL} contour lines derived from Figure 4-20.

From the analysis of the scale-model facilities, PWL variance due to variances in jet nozzle and ambient pressures and temperatures presented herein, the following conclusions can be drawn:

1. Acoustic test data from the facilities may have variance greater than ± 1 dB for jet velocities less than 600 fps, even for cold jets ($T_{T8} \approx T_{Tamb}$).

2. A minimum PWL variance of ± 0.1 dB is achievable at very high jet velocity, $V_j > 2500$ fps, for cold jets ($T_{T8} \approx T_{amb}$). For hot jets, $T_{T8} \geq 1500°$ R, a minimum level of ± 0.2 dB is achievable.

3. Increasing jet temperature T_{T8} will increase the variance in PWL, and decreasing the jet velocity will increase the variance in PWL.

4. Comparisons of acoustic characteristics of different configurations where differences of only 2 or 3 dB in PWL (and, to some extent SPL) are expected may not be meaningful unless operating conditions are such that PWL variances are limited to ± 0.5 dB. This imposes a restriction on the matrix of T_{T8} and V_j which will give meaningful results.

5. Jet noise experiments conducted at low velocities to determine jet noise density exponent dependence on jet velocity may not be reliable in view of the high variances in OAPWL expected in this regime.

A study of the J79 engine test facility, using the measured instrumentation errors in Figures 4-15 through 4-17, gave a very small variation of the sound level (σ_{PWL}) throughout the engine speed range (Figure 6-69) as seen in Figure 4-22.

4.5 ACOUSTIC MEASUREMENT ERRORS

One of the most commonly overlooked sources of acoustic data contamination is that associated with the data acquisition and reduction systems. Often the acoustic engineer accepts the data delivered to him as being an accurate description of the signals picked up by the microphone without consideration of the limitations of the electronic equipment which collected, recorded, and reduced his data.

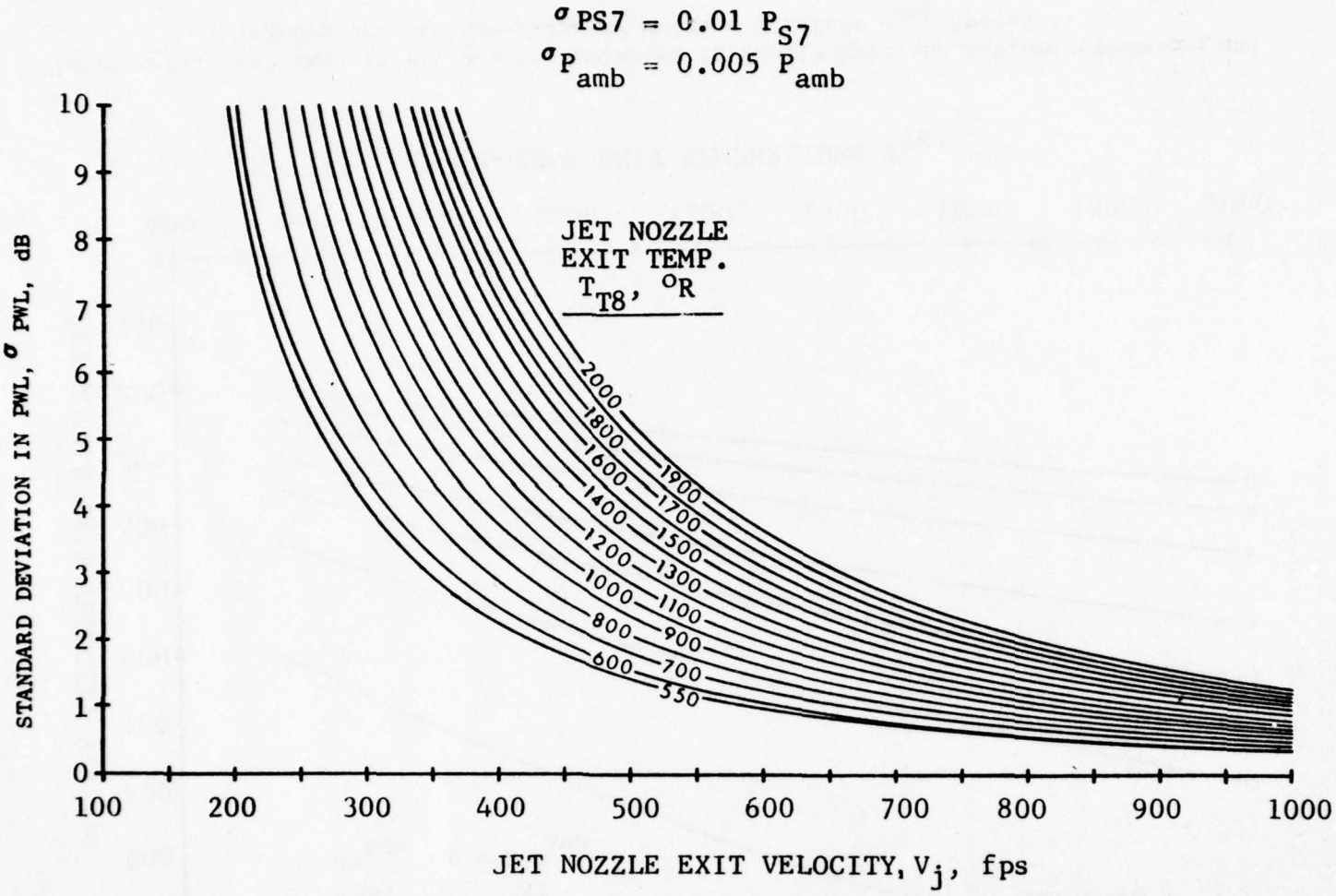


Figure 4-20. Variance in PWL Due to Variances in Nozzle Exit and Ambient Pressures and Temperature in Low-Velocity Range.

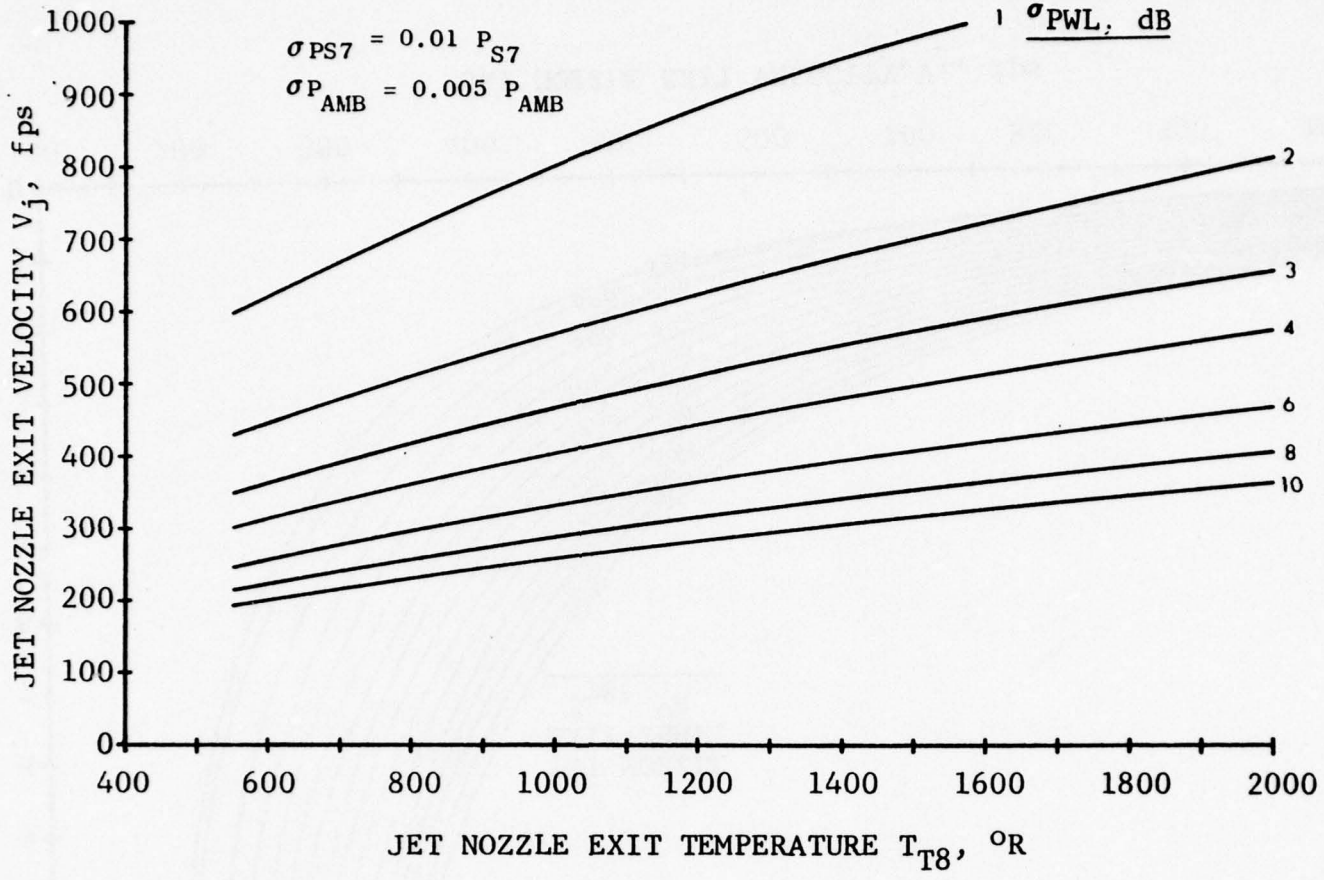


Figure 4-21. Variance in PWL Due to Variances in Nozzle Exit and Ambient Pressures and Temperatures in Low-Velocity Range - Constant σ_{PWL} Contours.

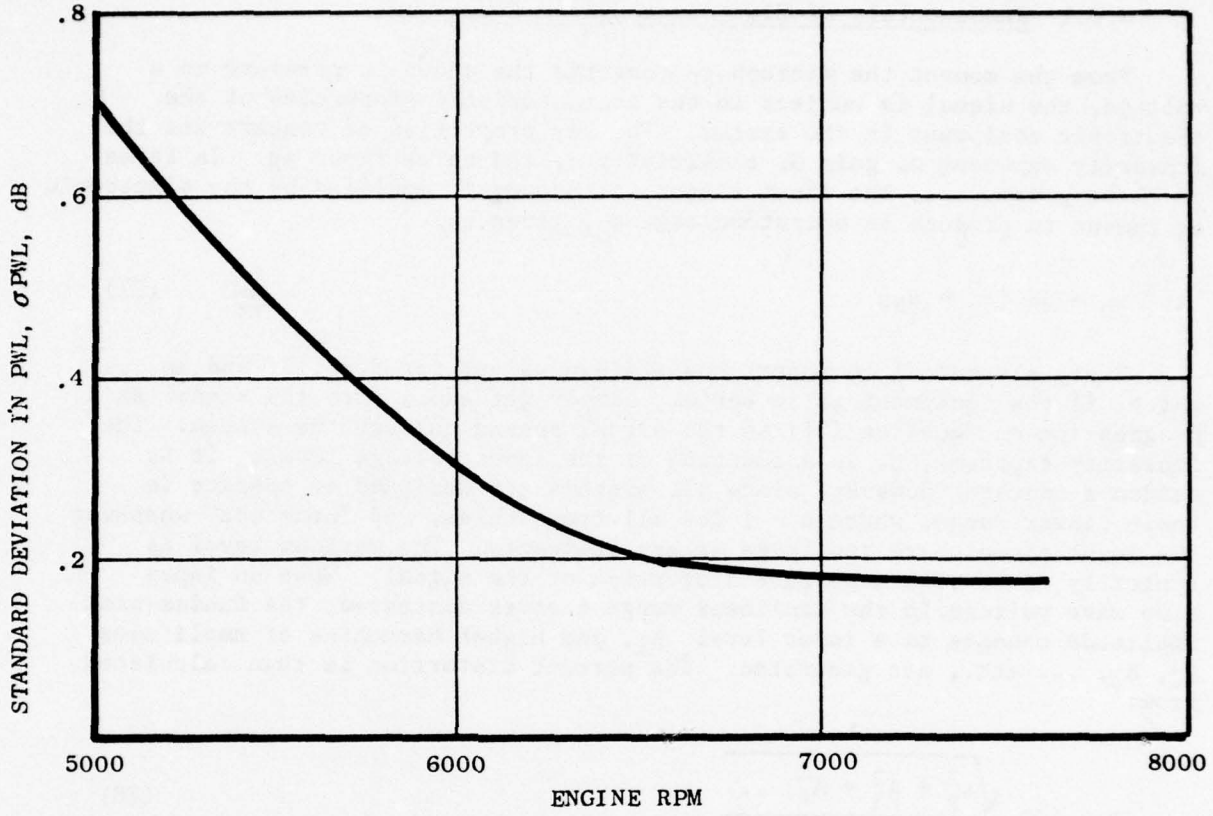


Figure 4-22. Sound Level Variance Due to Aero Measurement Errors with the J79 Engine at GE/EFTC.

4.5.1 Fundamentals of Electronic System Functions

From the moment the microphone converts the acoustic pressure to a voltage, the signal is subject to the characteristic properties of the electronic equipment in the system. The key properties of concern are the linearity exponent n, gain G, sensitivity S, and noise floor e_N. In terms of these parameters, the input signal voltage e_I is modified by the electronic equipment to produce an output voltage e_o, given by:

$$e_o = GS\ [e_I^n + e_N] \tag{27}$$

Every electrical component has its own values for N, G, S, and e_N which, if the equipment is in series, simply get added into the signal as a progression on Equation (27) as the signal passes through the system. The linearity exponent, n, is a function of the input voltage level. It is seldom a concern, however, since all systems are designed to operate in their linear range, where n = 1 for all frequencies, and "peak out" whenever the input signals are too large at any frequency. The maximum level is typically rated with a percent distortion of the signal. When an input sine wave voltage in the nonlinear range becomes distorted, the fundamental amplitude changes to a lower level, A_1, and higher harmonics of amplitudes A_2, A_3, ... etc., are generated. The percent distortion is then calculated from:

$$D = 100\ \frac{\sqrt{A_2^2 + A_3^2 + A_4^2, \ \ldots}}{A_1}\ , \ \% \tag{28}$$

The component sensitivity, S (transmission loss), and gain, G, are both seen as multipliers to the input voltage and can easily be lumped together as a single parameter. The distinction between the two terms is that the sensitivity is the inherent response of a system to the input which varies with frequency. The term "gain" on the other hand is used to refer to a constant multiplier which is purposely inserted into the system to enhance the signal. The gain is (hopefully) independent of frequency. The frequency distribution of the sensitivity is obtained by performing a frequency response of the system. Known calibrated electric signals, such as: (1) a constant amplitude sine wave sweep; (2) constant level, constant bandwidth broadband noise (white noise); or (3) constant level, percent bandwidth broadband noise (pink noise); are fed into the component from a signal generator. The output distribution shows the frequency response of the system. These response curves are assumed to be independent of the amplitude of the voltage. It is good practice however to use an applied voltage from the signal generator which approximates the expected voltage from the microphone. The absolute level of the sensitivity (transmission loss) or gain at any frequency is measured by inserting a known amplitude input voltage and measuring the output. Although the electronic noise floor and sensitivity vary with frequency, most equipment specifications only give the overall rms values which include all frequencies.

4.5.2 Sensitivity and Frequency Response Measurements

In general, the whole recording and reproduction process is calibrated by two distinct methods: one being the insertion of signal characteristics and specific frequencies, and the second being the insertion of a known pink noise signal. This end-to-end calibration dictates the correction characteristics for both amplitude and frequency.

A random signal generator is typically used for the signal source. The calibration is accomplished by removing the microphone cartridge and connecting the output of the signal generator to the cathode follower. The data is recorded on tape and processed like sound data. The resulting 1/3-octave spectra is normalized at the 250-Hz, 1/3-octave level and the resulting set of ΔdB's represent the system corrections.

$$\Delta = 10 \log_{10} \left[\lim_{T \to \infty} \int_0^T e_o^2 \, dt \Big/ \int_0^T e_I^2 \, dt \right] \sim 20 \log S$$

As a verification test in data reduction, the pink noise characteristics are inserted at playback full-scale level and 50 dB down from the level, with specific attention paid to the amplitude in each 1/3-octave band. Any deterioration is readily indicated by this technique, especially deterioration of the noise floor. The operators have limits of inspection on these signals and perform system adjustments to ensure high data quality at all times.

Frequency response calibration charts are supplied with each microphone cartridge. The error on frequency response is less than 0.2 dB up to 10 kHz and 0.5 dB at higher frequencies (Reference 24). The combination of the microphone response and the system response represents the corrections applied to the data. Before and after each acoustic test, a 124 dB piston phone calibration signal is recorded at 250 Hz using a B & K 4220 piston phone. Any microphone voltage output found to deviate more than ± 1.5 dB from the laboratory sensitivity rating is replaced.

The accuracy of the acoustic data recording system can be calculated from the tolerance of each independent component in the system. Since these tolerances are independent of each other, the estimated variance of the sound level can be computed as the rms of the variances due to each component separately, using

$$\sigma_{SL} = \sqrt{\sum_{n=1}^{\infty} \sigma_n^2} \qquad (29)$$

where σ_{SL} = the estimated variance in sound level due to the variances in all of the independent components obtained or derived from the respective manufacturer, with specifications as follows (3σ tolerances):

Component	3σ Tolerance (±dB)
B & K Microphone Cartridge Calibration:	0.2 to 10 kHz 0.5 from 10 kHz to 20 kHz
B & K Cathode Follower Amplifier	0.2
B & K Piston Phone	0.2
General Radio Noise Generator	0.5
B & K Power Supply	0.09
Random 6 dB Amplifier	0.2
Random Variable-Gain Amplifier	0.2
Sangemo Sabre IV Tape Recorder	0.5
CFC 3700 B Tape Deck	0.5
General Radio 1/3-OB Analyzer	0.25
Honeywell 6000 Series Computer	0
GEPAC 300 Computer	0

Substituting the above values in the equation for the sound level variance yields an estimated variance (3σ tolerance) of ± 1 dB below 10 kHz and ± 1.1 dB above 10 kHz, for the sound level due to the acoustic data recording instrumentation at JENOTS.

The USC CR&DC and GE/EFTC systems have comparable accuracy. The University of British Columbia system is more accurate due to the fact they reduce data on line and eliminate the errors associated with the tape recorder.

4.6 ELECTRONIC NOISE FLOOR

Electronic Noise floor appears in all facilities particularly at angles near the jet axis where the spectra is very peaky. All electronic instruments generate small amounts of low energy electrical noise, even those designed with special low-noise electrical components such as microphone cartridges, pre- and final-stage amplifiers, tape recorders, and data reduction instrumentation.

The instantaneous electronic noise floor, e_N, in Equation (30) is seen to be an additive voltage to the input which varies in value as a function of frequency. Low frequency noise floors are caused by 60 cycles, DC drift,

low frequency surge, "part wander" in components such as amplifiers, and by tape flutter and WOW in tape recorders. High frequency noise floors are caused by thermal effects such as Brownian movement, Schottky noise, electronic bombardment, and "popcorn" noise of differential amplifiers. Tape recorders are limited by the percent deviation in their carrier tone. Microphone cartridge floors are generally limited by the physical inability of the diaphram to respond to low amplitude pressures, although the associated cathode follower floor is experienced before this is ever realized.

The floor level is always expressed in terms of its rms value, given by

$$e_{Nrms} = \sqrt{\lim_{T\to\infty} \int_0^T (e_{N_{TOTAL}})^2 \, dt} \tag{30}$$

The general spectral shape of e_{Nrms} with frequency is a complex matter to predict but can easily be measured by recording the levels present without an input voltage. When a nearly fixed input voltage is used, the instrument can be rated in terms of its dynamic range or signal to noise ratio given by

$$DR = 20 \log_{10} (e_{Nrms}/e_{Irms}) \tag{31}$$

Such ratings are typically used with tape recorders. Noise floors are also often quoted from an "A weighted scale," which allows the high and low frequency levels to be disregarded. These specifications can be used as a guide to where a system might experience trouble. Exact levels, as a function of frequency, required a complete system calibration.

4.6.1 Theoretical Prediction of the Floor

The voltage noise floor of a microphone system is composed of three parts: that from the electric resistance measured with the diaphragm blocked; that from the motional component of the resistance due to the real part of the mechanical resistance; and that from the motional component of the resistance due to the real part of the acoustic admittance.

Schottky[22], Johnson and Llewellyn[26], and Beranek[27] have discussed this problem. Mathematically, the electrical self noise in the frequency band f_1 to f_2 is given by

$$e_N = \sqrt{4kT \int_{f_1}^{f_2} R(f)df} \tag{32}$$

where

k = Boltzman Gas Constant = 1.37×10^{-23} Joule/° K

T = Absolute Temperature (° K)

$R(f)$ = Resistive component of the electrical impedance (ohms), in general a function of frequency

At a temperature of 73° F, this expression becomes

$$e_N = \frac{1.27 \times 10^{-10}}{\sqrt{2\pi C}} \sqrt{\text{Tan}^{-1}(2\pi f_2 RC) - \text{Tan}^{-1}(2\pi f_1 RC)} \qquad (33)$$

For a typical RC circuit

$$R(f) = \frac{R}{1 + (2\pi f RC)^2} \qquad (34)$$

So

$$e_N = 1.27 \times 10^{-10} \sqrt{\int_{f_1}^{f_2} R(f)\,df} \qquad (35)$$

For the frequency range f_1 = 20 Hz to f_2 = 10 kHz, the overall (rms) level of the noise floor is plotted for three values of resistance, R, and for a capacitance, C range of 0.1 to 1000 μf in Figure 4-23. The equivalent 1 Hz bandwidth frequency spectra is shown in Figure 4-24. At high frequency, the narrowband level is seen from Equations (33) and (34) to fall off as 1/f. In 1/3-octave band, this would result in a constant level floor. Many electrical components can be described in terms of an effective RC network, so Figures 4-23 and 4-24 would be appropriate.

4.6.2 Calculation of the Noise Floor at JENOTS

To illustrate the degree of contamination and the characteristics of electronic noise, the composition of the floor experienced at JENOTS was calculated.

Given the nominal values for noise floor quoted in the equipment specifications, one can predict the expected noise floor on tape. Using the JENOTS system shown in Figure 3-18 and Equations (31) and (33) gives

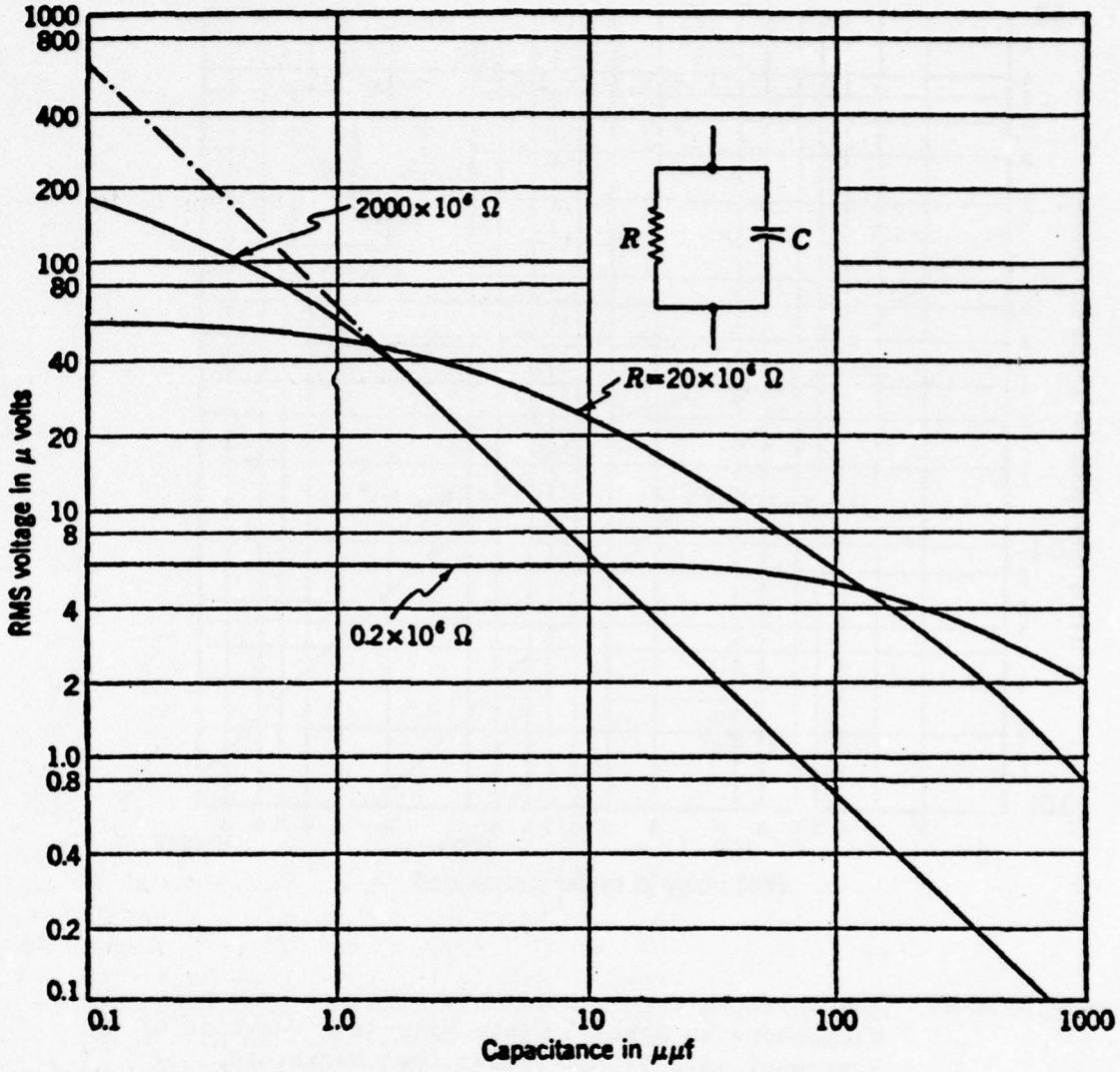


Figure 4-23. Open-Circuit rms Voltage Produced by Thermal Agitation in the Real Component of the Impedance of a Parallel Resistor and Condenser.

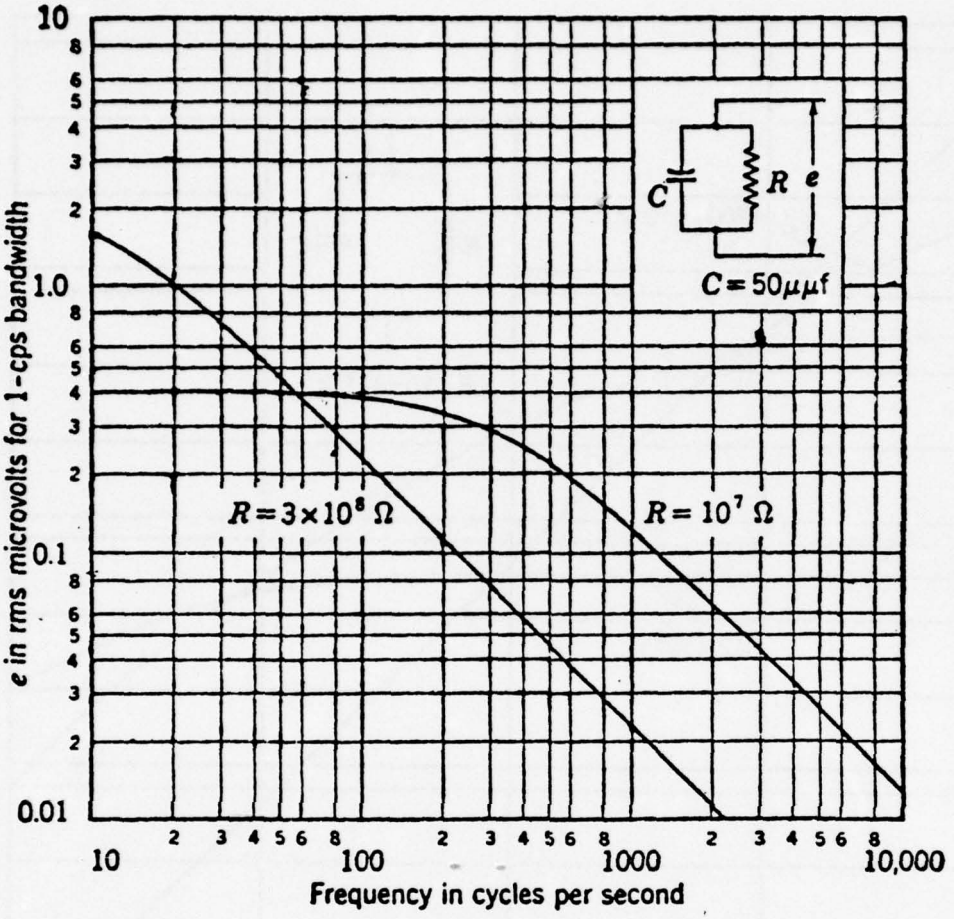


Figure 4-24. RMS Noise Voltage Produced by a 640-AA Condenser Microphone in Bands 1 Cycle Wide as a Function of Frequency with Two Different Load Resistors.

$$e_N = \left\{ \left[\left(e_{M+P}^2 + e_{PS}^2 + e_{LD}^2 \right) 10 + e_{TA}^2 \right] 10^{\frac{G+V}{10}} + e_{TR}^2 \right\}^{1/2} \qquad (36)$$

where

e_{M+P} = noise floor of microphone and preamp, 20 - 60 μV

e_{PS} = noise floor of power supply, 30 μV

e_{LD} = noise floor of line driver, 30 μV

e_{TA} = noise floor of tape amplifier, 50 μV

e_{TR} = noise floor of tape recorder, 38 dB

G = the tape recorder gain

V = vernier gain = $20 \log_{10} K - G_{cal.}$, 9 dB for B&K 4133 and 4135 mic. 4.5 dB for B&K 4138 mic.

K = microphone sensitivity, mv/μbar

The effective sound level of this noise floor is calculated from

$$OASPL_{eff} = 20 \log_{10} Ke_N - 10 - G - V + 74 \qquad (37)$$

This equation is plotted in Figure 4-25 for the fixed vernier, and in Figures 4-26 and 4-27 for the case when the vernier is adjusted to give a full-scale voltage to the tape recorder with the piston phone for the B&K 4133 and 4135 microphones, respectively. In all cases, one sees that the tape recorder 38 dB dynamic range is the limiting floor at most gain settings used for jet noise work. This floor can be improved by converting the tape recorder to the wideband Group I and recording at 120 in./sec. With this setup, the frequency response is DC to 80 kHz and the dynamic range is 51 dB. Of course, four times as much magnetic tape is required for the same amount of data. This may well be worth the expense, however, in cases where noise floor contamination is a serious problem, such as when measuring jet spectra close to the jet axis where the spectra is extremely peaky; or when very large tones occur, driving the broadband noise into the electronic floor. Figure 4-28 shows the predicted floors with gain setting in the wideband Group I configuration with the vernier in the fixed position.

Significant noise floor improvement is observed in Figure 4-28 when the FET 2619 preamplifier is used instead of the 2615 cathode follower on the 4135 and 4138 microphones. This improvement is the result of the high input impedance and lower capacitance of the 2619. Practically speaking, however, the 2615 is a much more rugged instrument and is less susceptible to failure. Nevertheless, where noise floor may be a problem such as with the 1/8-inch 4138 microphone on the ellipsoidal mirror, the 2619 should be used.

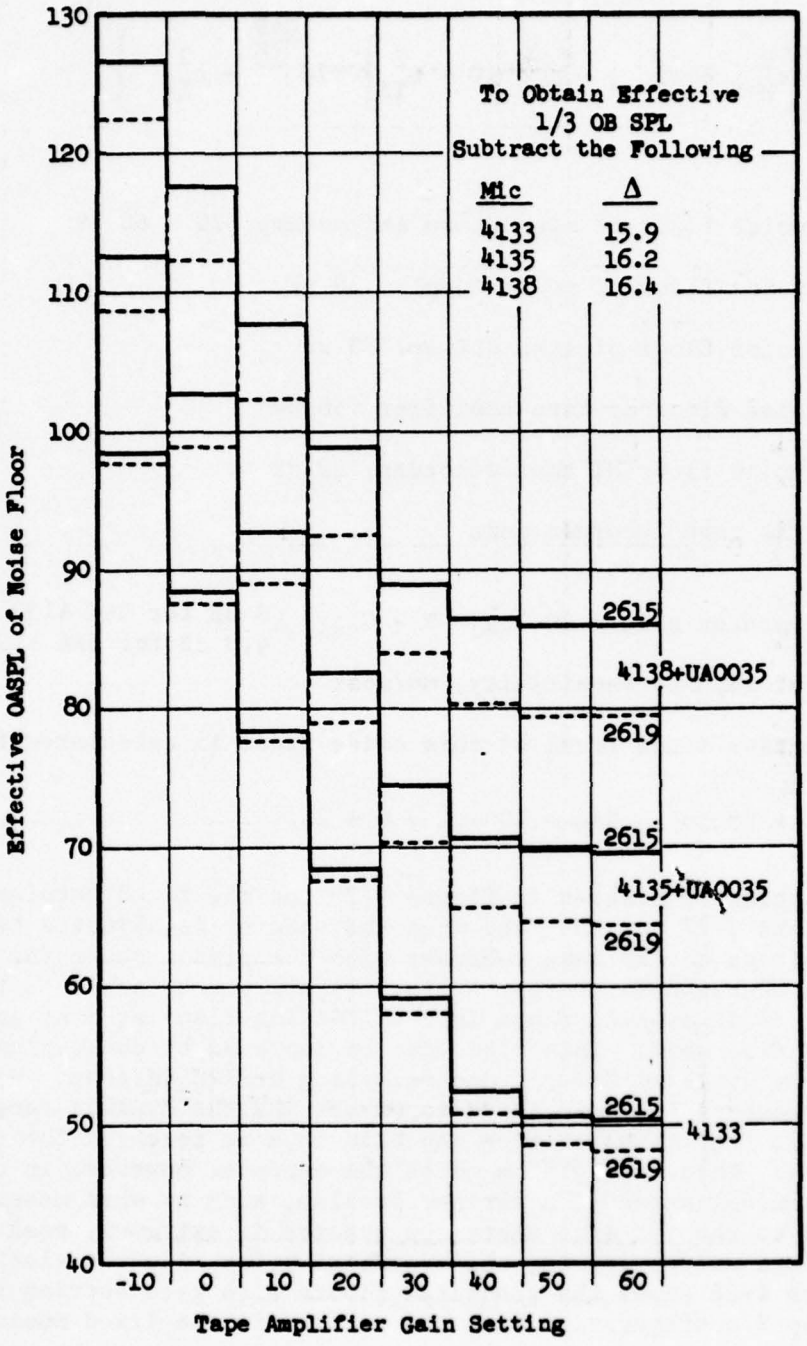


Figure 4-25. Predicted Electronic Noise Floor of the JENOTS Microphone System with the Wideband Group II Tape Recorder and Locked Vernier Amplifier.

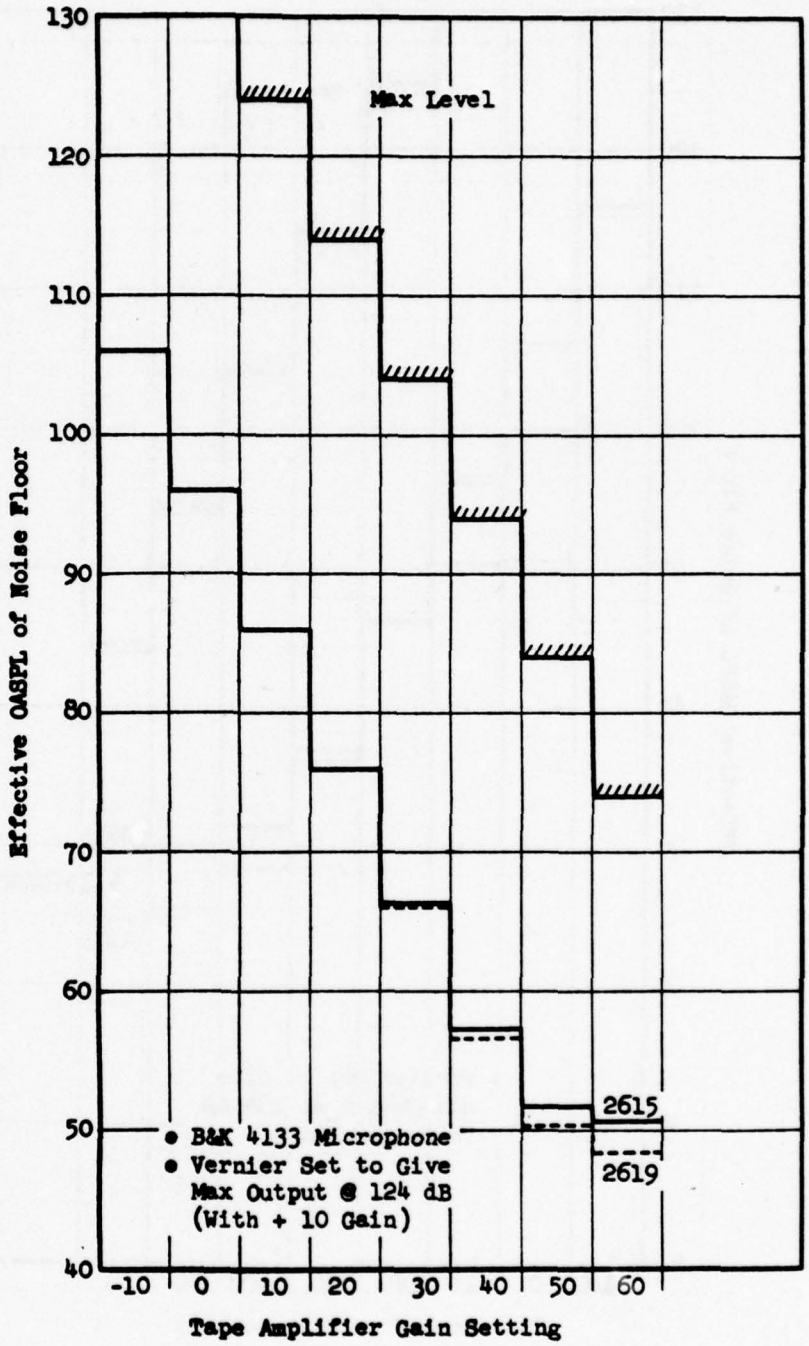


Figure 4-26. Predicted Electronic Noise Floor of the JENOTS Microphone System with the Wideband Group II Tape Recorder and B&K 4133 Microphone Vernier Coupler Set to Give Maximum Output of 124 dB at +10 Gain Setting.

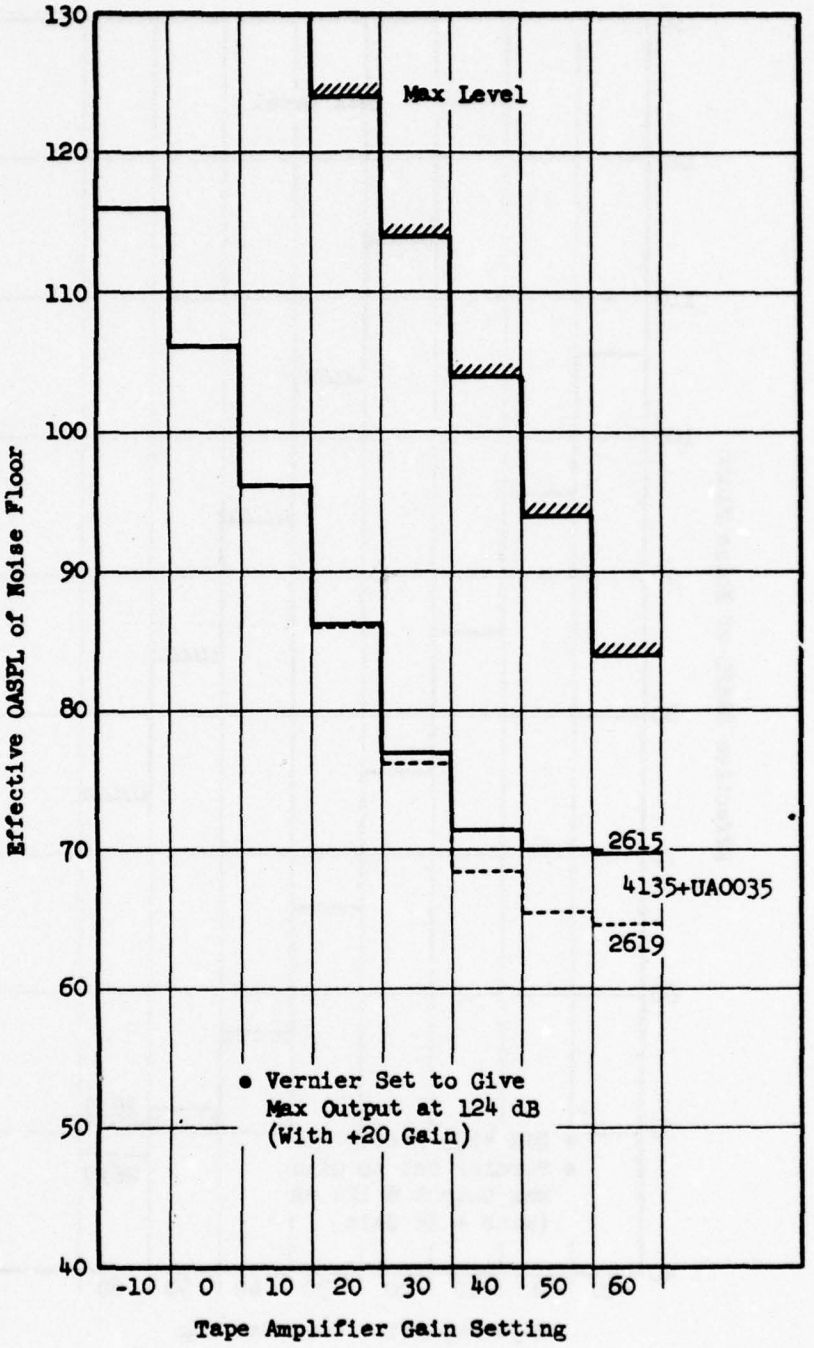


Figure 4-27. Predicted Electronic Noise Floor of the JENOTS Microphone System with the Wideband Group II Tape Recorder and B&K 4135 Microphone Vernier Coupler Set to Give Maximum Output of 124 dB at +20 Gain Setting.

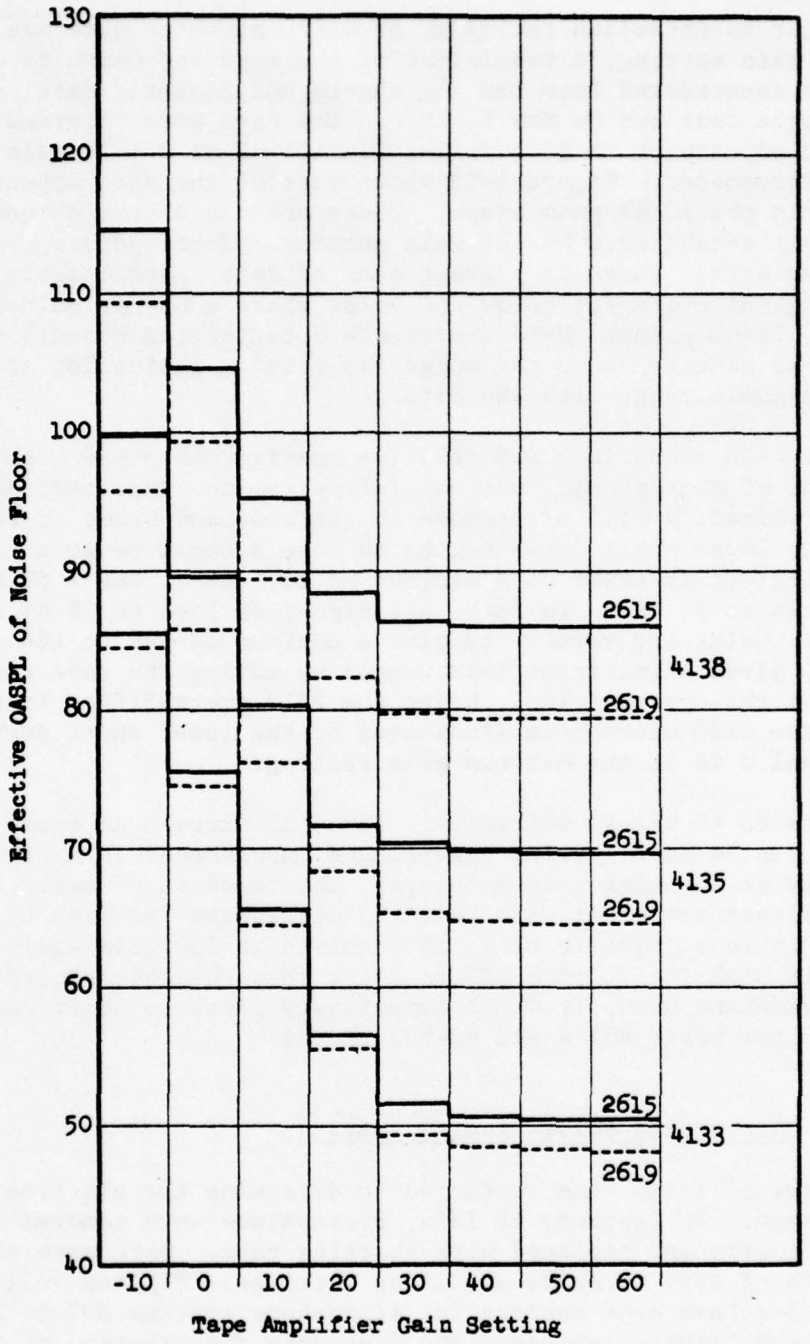


Figure 4-28. Predicted Electronic Noise Floor with Various Microphone Cathode Followers on the Wideband Group I Recorder and Locked Vernier Amplifier.

In order to establish the range of OASPL at which data are taken at any particular gain setting, a tabulation of the measured OASPL at each gain setting was constructed from the log sheets and acoustic data, using a typical conical nozzle test run on May 9, 1974. The data were recorded on tape using the vernier adjustment to give full-scale 124 dB at a + 20 gain setting with B&K 4135 microphones. Figure 4-29 shows most of the data appears to be contained within the 10 dB gain steps. There are one or two points beyond the maximum level established by the gain setting. These points most probably have clipped data. There is a great deal of data, particularly at the +10 gain setting which are far below the point where a higher gain should have been used. These points would experience deteriorated dynamic range. The height of the circles above the noise floor is an indication of the relative available dynamic range with the data.

Figure 4-30 summarizes the relative benefits obtained with the various combinations of microphones, cathode followers, and tape recorders. With the vernier fixed, a 2615 microphone on the wideband Group II recorder (indicated by the lower small dots) begins to lose dynamic range at a jet OASPL of 133. The falloff is rapid to a minimum of 10.5 dB at the + 60 dB gain (jet OASPL from 84 to 94 dB). In fact, all signal is lost at 72 dB in this configuration. Using the vernier to give a maximum output at 124 dB (lower solid line) gives significant improvement by moving the tape recorder noise further from the system noise. Using the 2619 preamplifier instead of the 2615 with the 4135 microphone (indicated by the lower short dashes) provides an additional 5 dB at the maximum gain setting.

If data to 40 kHz is sufficient, the 4133 microphone (indicated by the long dash) can be used, giving significant improvement in dynamic range, particularly at the high gain settings. The benefits of using a 2619 cathode follower are minor with the 4133 microphone (as seen by the upper dots). If improved dynamic range is required at low gain settings where the jet noise is high (OASPL from 100 to 144), then the tape recorder can be converted to wideband Group I, which immediately gives an additional 13 dB (as seen by the upper solid and dashed lines).

4.6.3 Electronic Noise Floor Spectra

A number of tests were conducted to determine the electronic floor spectral shape. In February of 1974, microphones were removed from the cathode followers and replaced with shorting caps. Data were then recorded for a series of tape recorder amplifier settings. Figures 4-31 through 4-36 show the 1/3-octave band spectra for microphone systems 80° to 130°, respectively. These figures represent the frequency distribution of the electronic noise floor for the JENOTS electronic system. A relative SPL scale is used because the cathode followers were capped with a dead short so the effect of the microphone capacitance is not in the system and absolute levels would be misleading.

The spectra have three distinct characteristics. The first is the relatively constant level from 50 Hz to 400 Hz and from 1600 Hz to 10 kHz

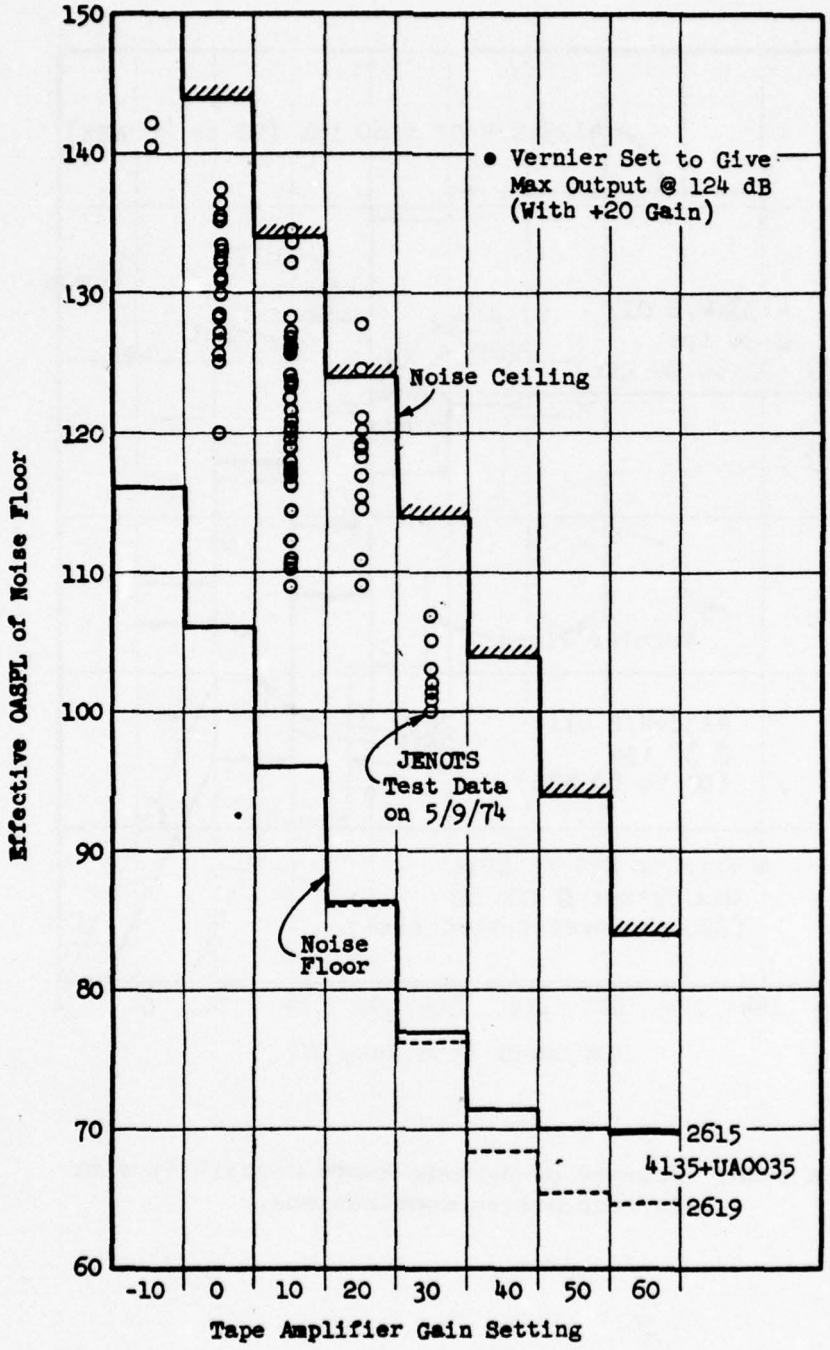


Figure 4-29. Relative Dynamic Range of Measured Data at a Fixed Gain Setting Above the Noise Floor.

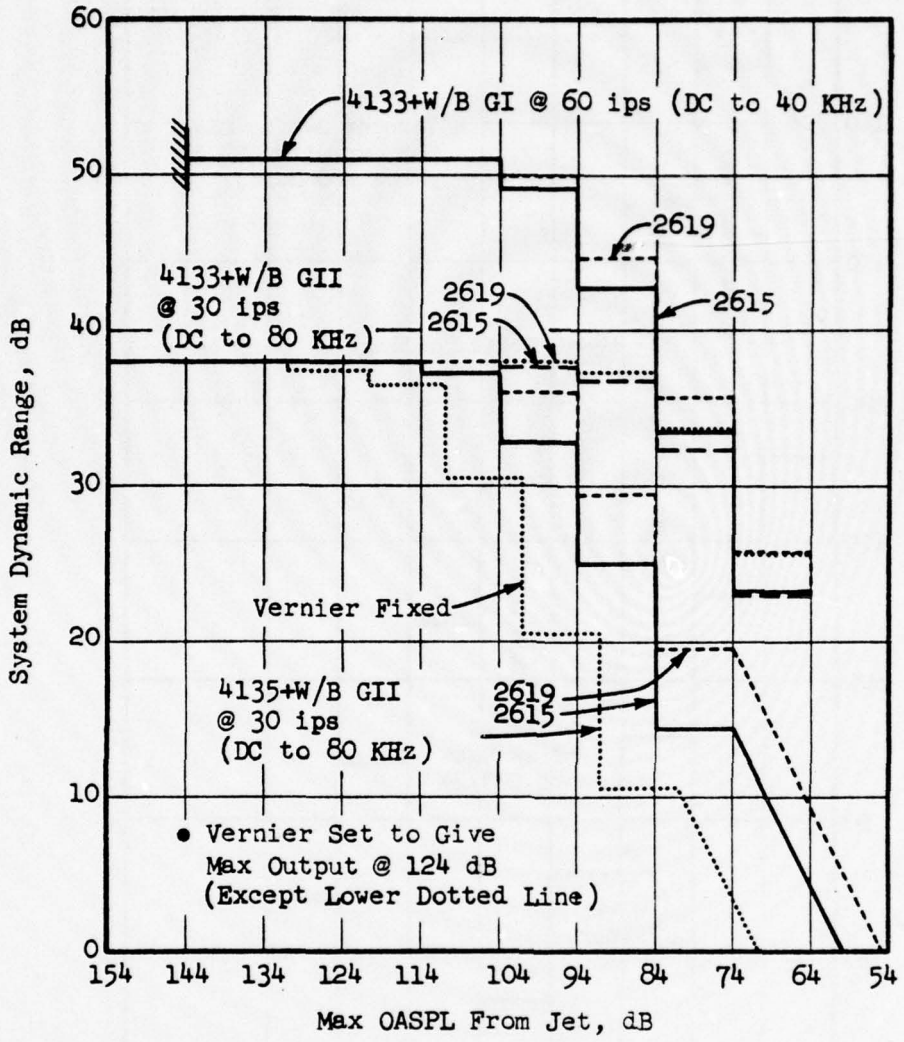


Figure 4-30. Summary of Dynamic Range Capability with Various System Combinations.

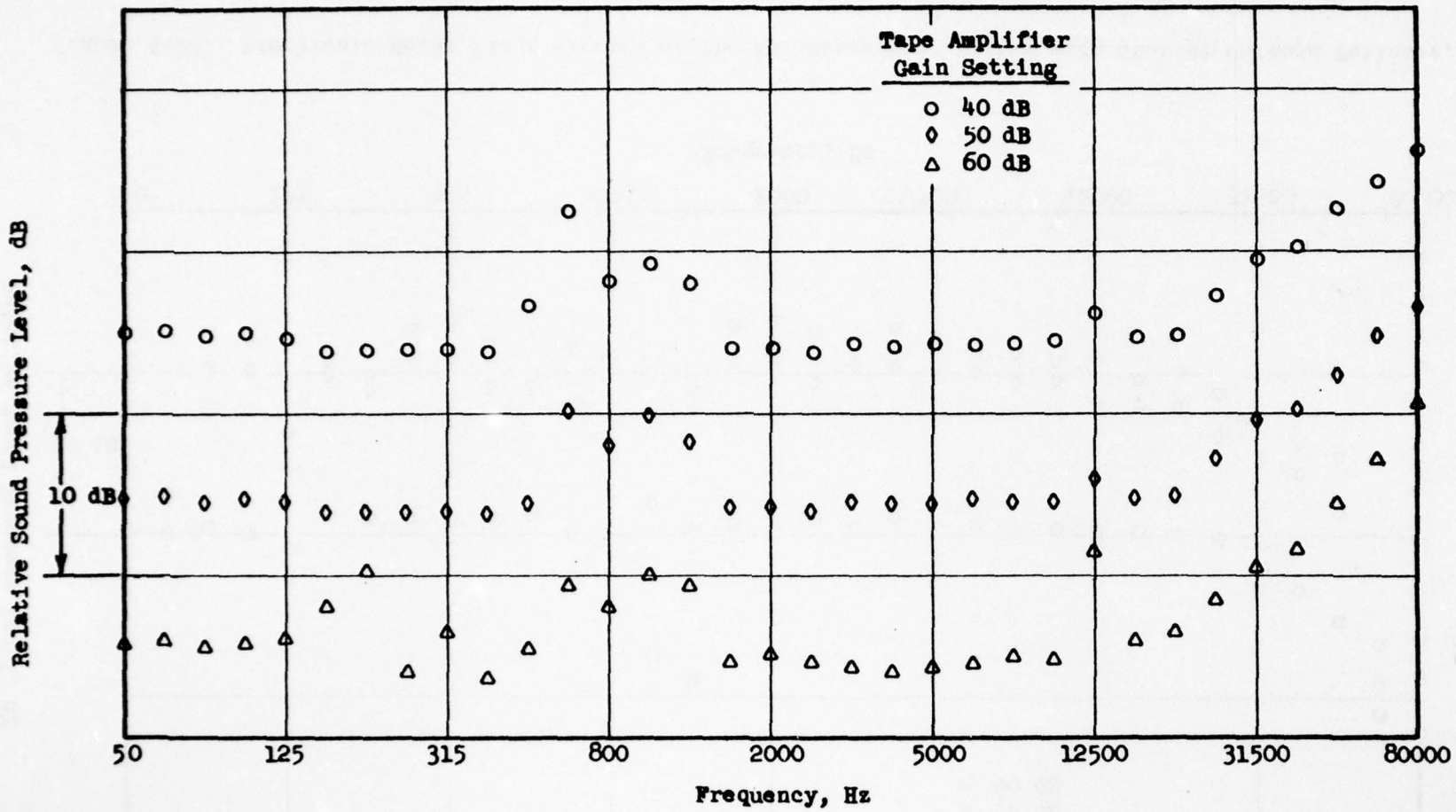


Figure 4-31. Electronic Noise Floor Spectra of the 80° Microphone System with Shorted Cathode Follower.

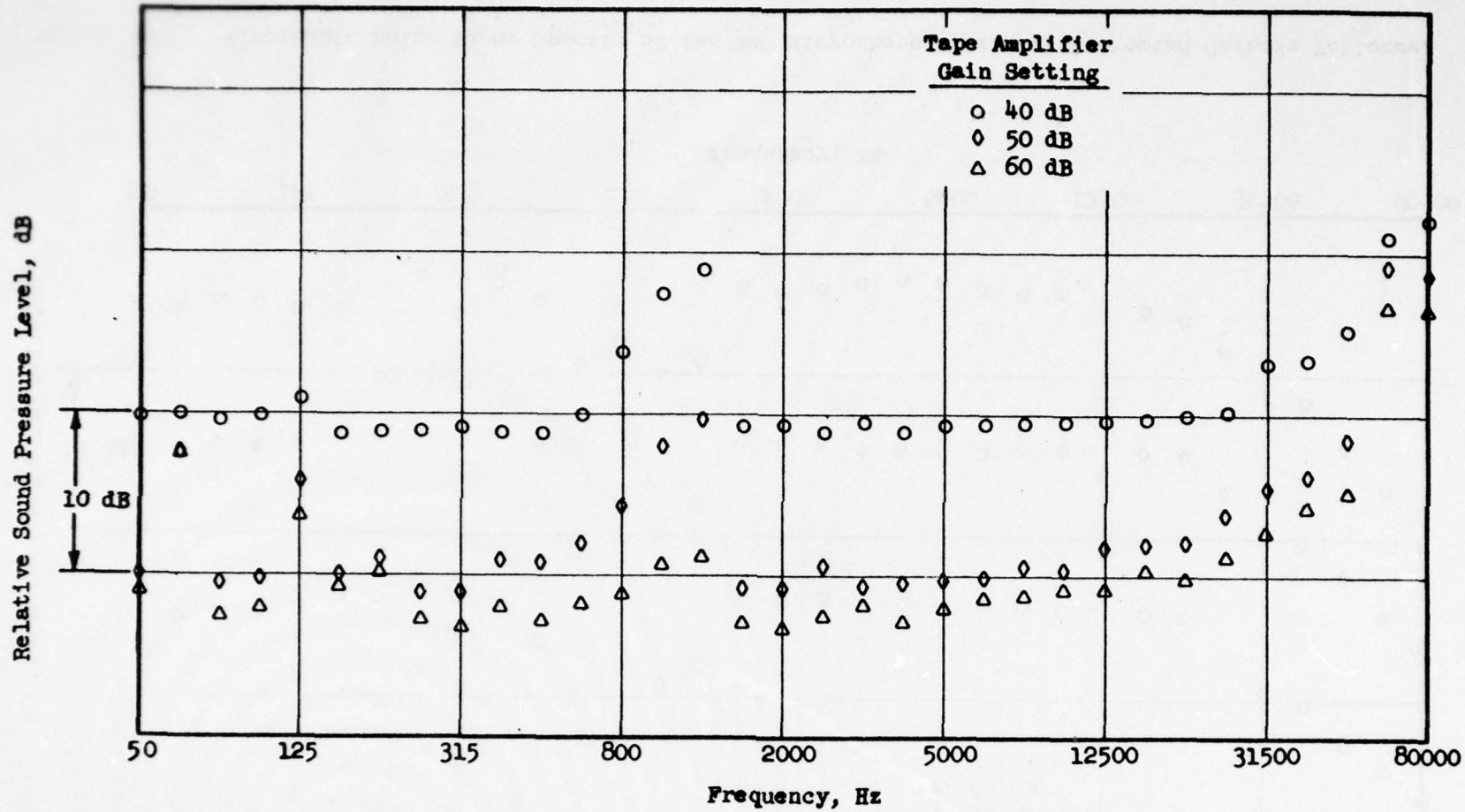


Figure 4-32. Electronic Noise Floor Spectra of the 90° Microphone System with Shorted Cathode Follower.

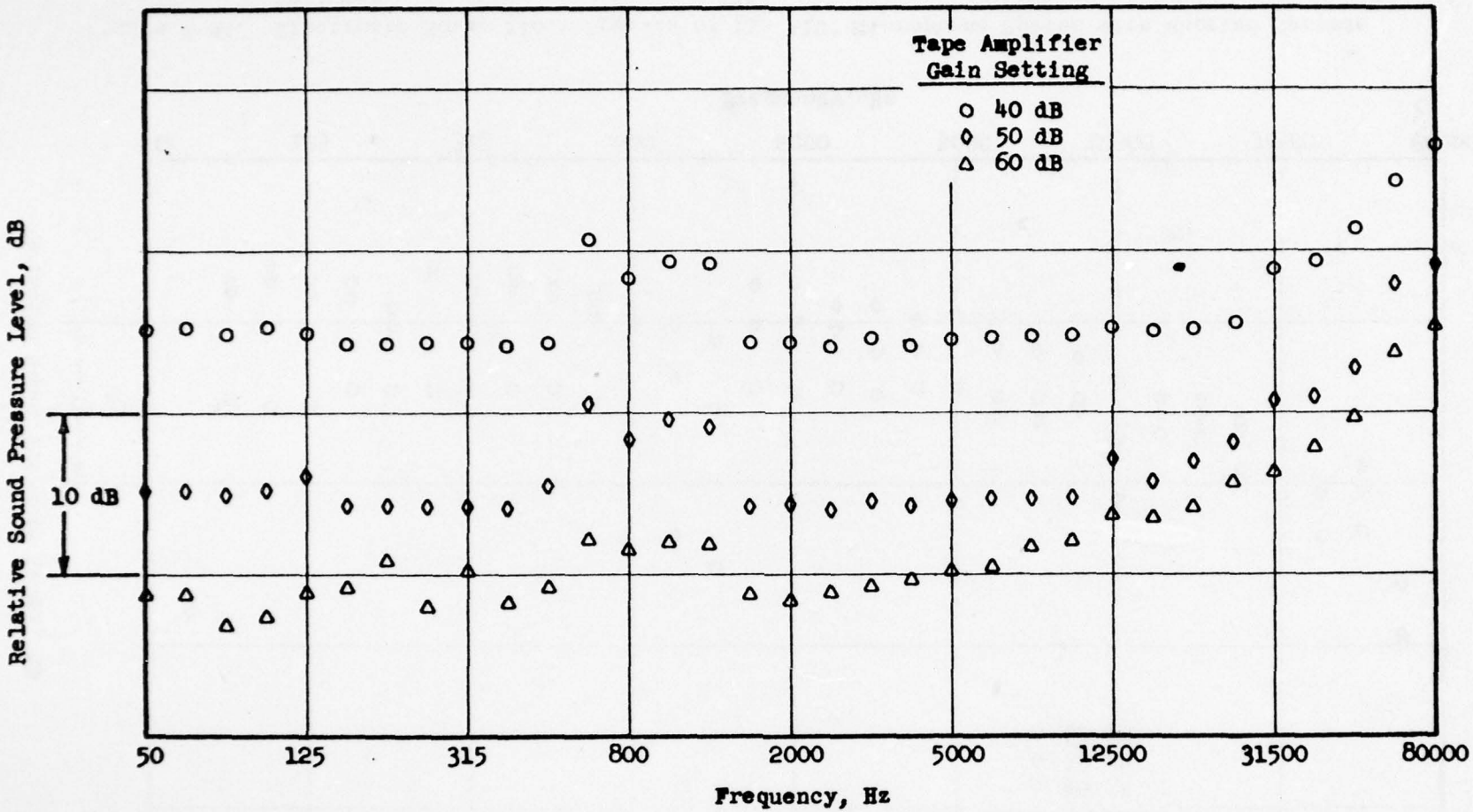


Figure 4-33. Electronic Noise Floor Spectra of the 100° Microphone System with Shorted Cathode Follower.

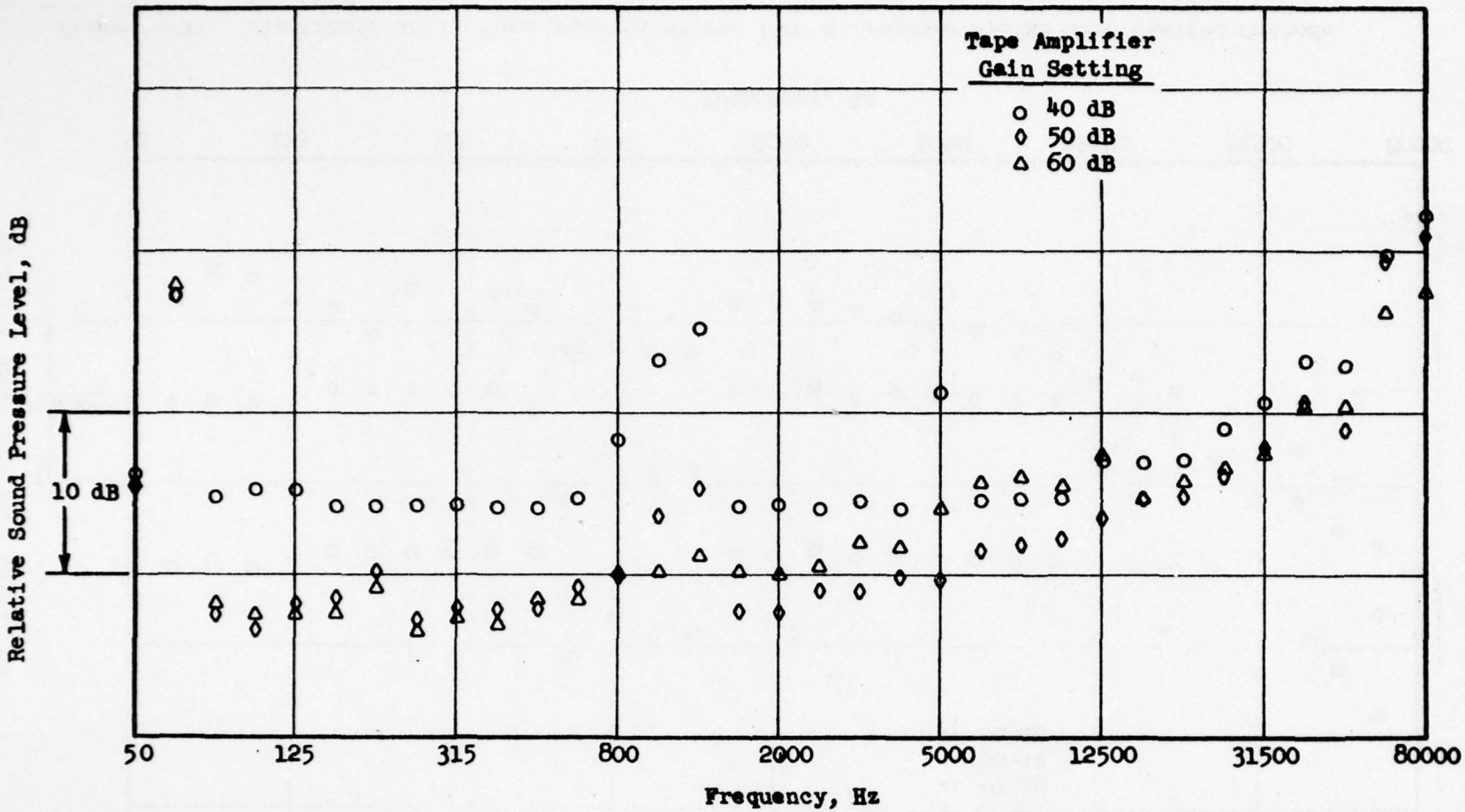


Figure 4-34. Electronic Noise Floor Spectra of the 110° Microphone System with Shorted Cathode Follower.

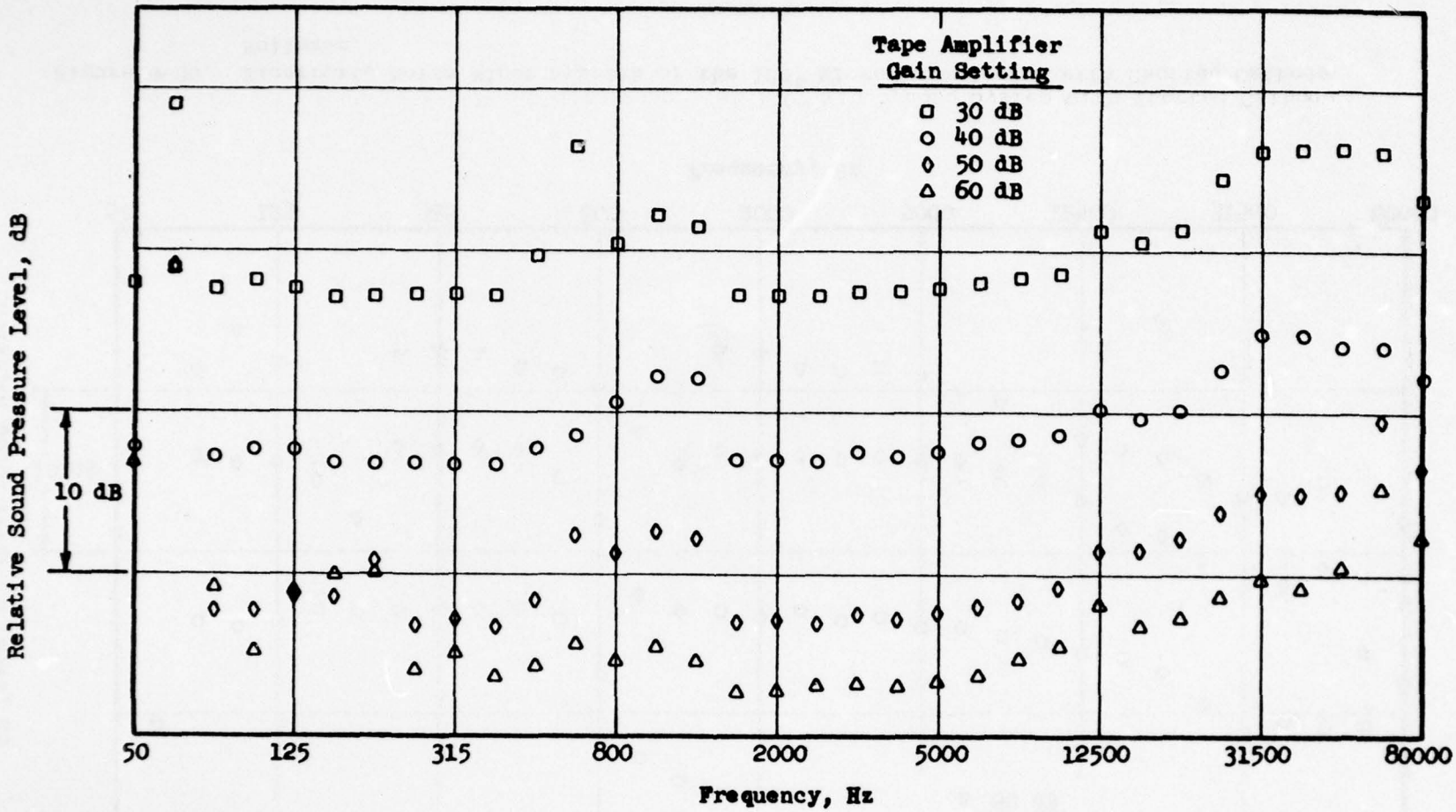


Figure 4-35. Electronic Noise Floor Spectra of the 120° Microphone System with Shorted Cathode Follower.

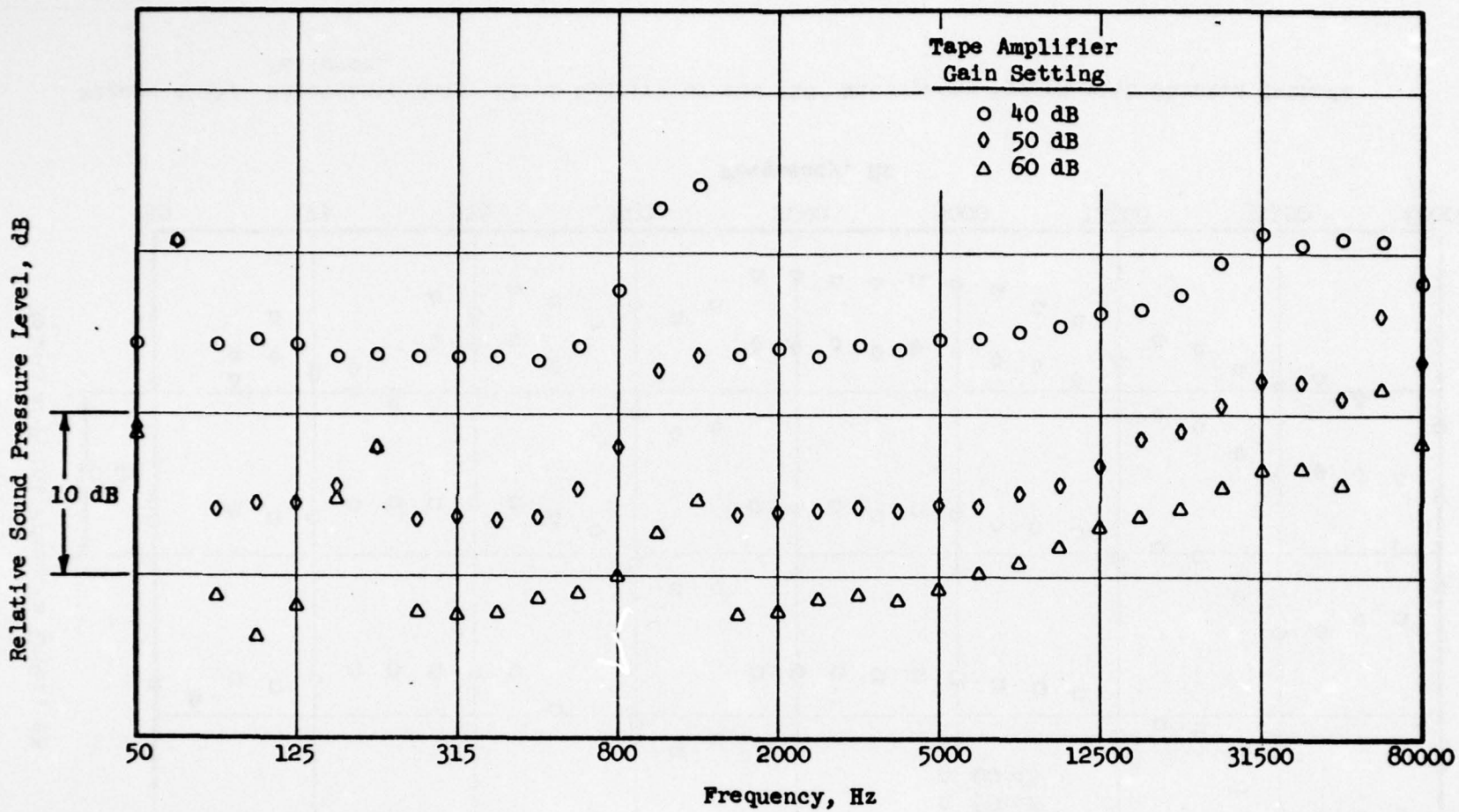


Figure 4-36. Electronic Noise Floor Spectra of the 130° Microphone System with Shorted Cathode Follower.

(except at high gain setting), which would indicate a 1/f drop off on a narrowband as expected from a simple RC network from Equation (37). The fact that this flat region shifts uniformly with the 10 dB gain steps and vanishes at the highest setting indicates that this portion of the spectra is associated with the tape recorder electronics. The second characteristic is the peculiar peaking occurring in the bands from 500 Hz to 1250 Hz. Comparing the various plots, it can be seen that the frequency content of the peaking is the same with all the microphone systems, but the shape of the spectra distortion is drastically different from one plot to the next. The fact that the shape is maintained and shifted uniformly with amplifier gain; and that it tends to "sink into the mud" at the highest gain, implies that the phenomenon is associated with the tape recorder electronics. The third spectral characteristic is the 6 dB per octave ramp occurring at high frequency, starting at about 20 kHz. The fact that the ramp shifts uniformly with gain changes indicates that it is from the tape recorder.

At the highest gain settings, an additional ramp is uncovered which is seen to shift to a lower frequency as the gains increased. Of the three sources, the cathode follower is the noisiest. As the amplifier gain is increased to 60 dB, this system noise overtakes the tape recorder noise as the dominant source. At the highest setting, a multitude of tones, such as 60 cycles and its harmonics, create a humpy spectral appearance. Each microphone system appears to experience the tradeoff between tape recorder noise and system noise at a different point. Figure 4-31, for example, shows the 80° microphone system has minimal system noise even at the 60 dB gain. Figure 4-34 on the other hand, shows the 110° system to have significant system noise even at the 40 dB gain setting.

A study into the variability of the noise floor over the course of one day was also conducted. Figure 4-37 shows the variability of the data collected at different times for three gain settings of 50, and five gain settings of 60. Most of the data scatter is seen to occur at the high frequency, near the midfrequency hump and with the low frequency tones.

A similar test was conducted nearly a year later in January of 1975. This time, B&K 4135 1/4-inch microphones were left on the cathode follower, and the microphones were covered by the piston phone calibration device in the off position during data collection. In this configuration, the capacitance of the microphone is properly accounted for in the generated electronic noise, so an absolute level is plotted. Figures 4-38 through 4-42 show the results for the 30°, 60°, 90°, 120°, and 150° microphone stations, respectively. The spectra shapes are similar to the February 1974 data, displaying the high frequency ramp, midfrequency spike, and flat spectra between 1600 Hz and where the ramp curl up occurs. The low frequency portion of the spectra is apparently dominated by ambient acoustic signals which are leaking into the piston phone calibration device.

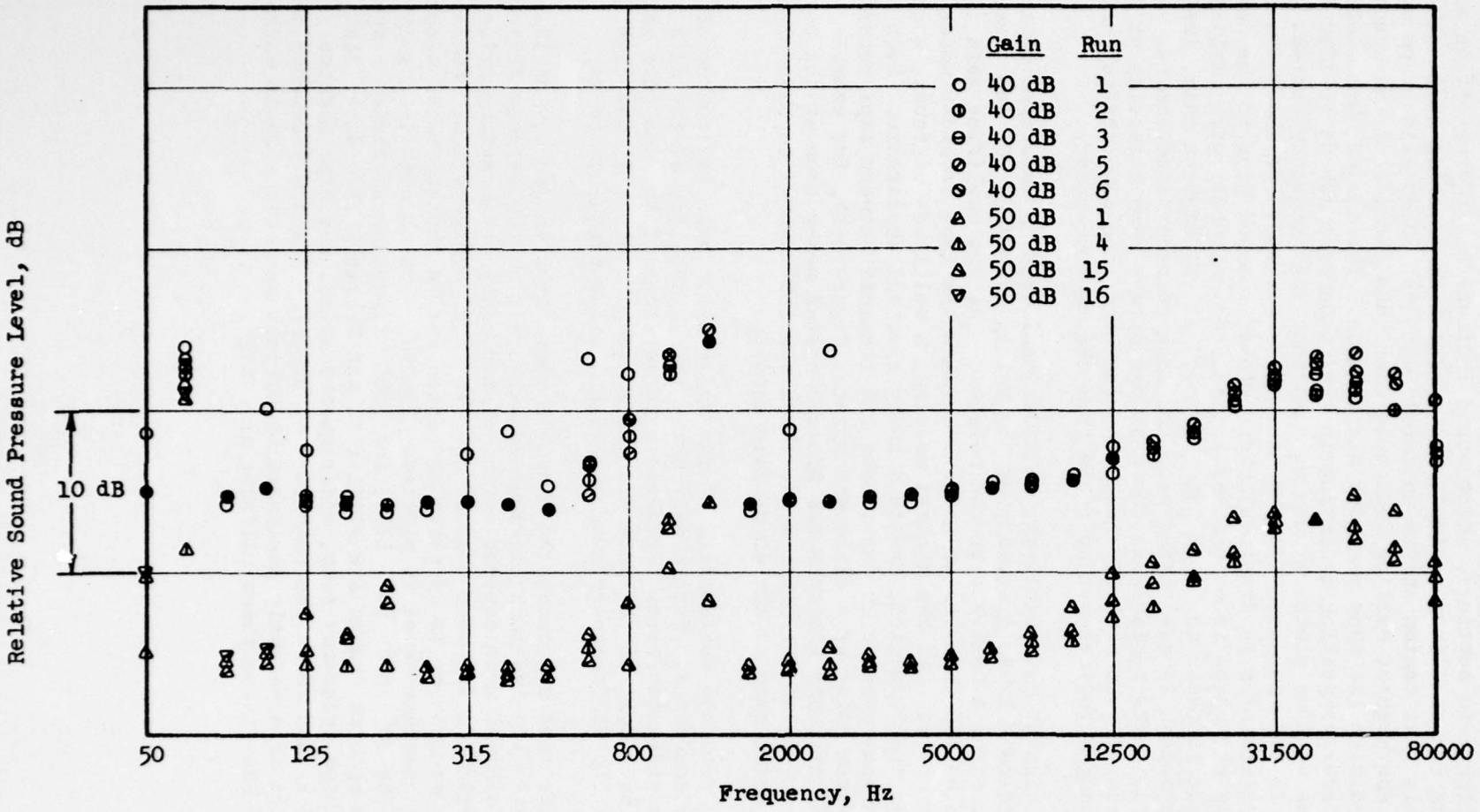


Figure 4-37. Variability of the Electronic Noise Floor with Time (120° System).

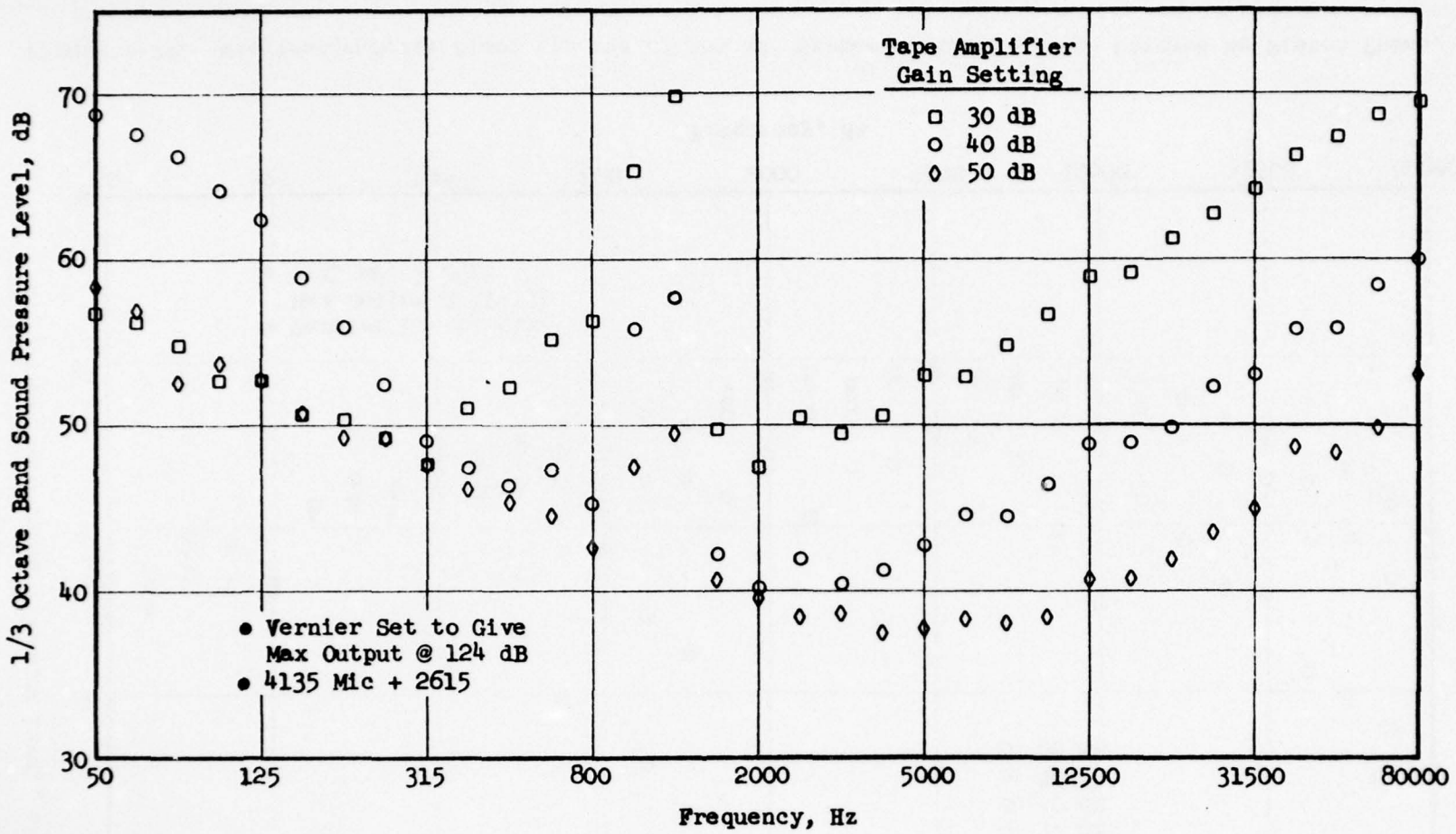


Figure 4-38. Electronic Noise Floor Spectra of the 30° System with Microphone Covered by Piston Phone.

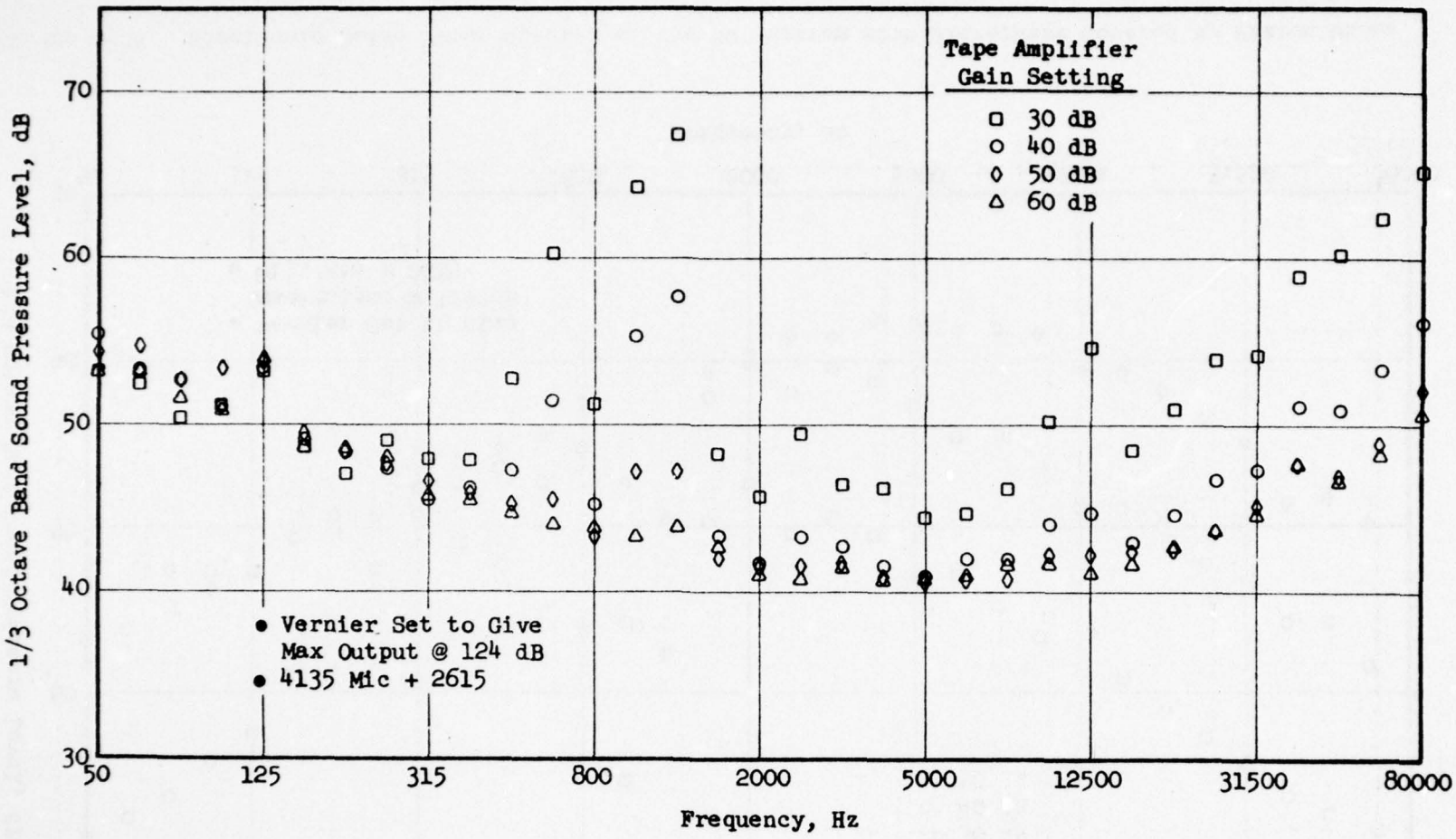


Figure 4-39. Electronic Noise Floor Spectra of the 60° System with Microphone Covered by Piston Phone.

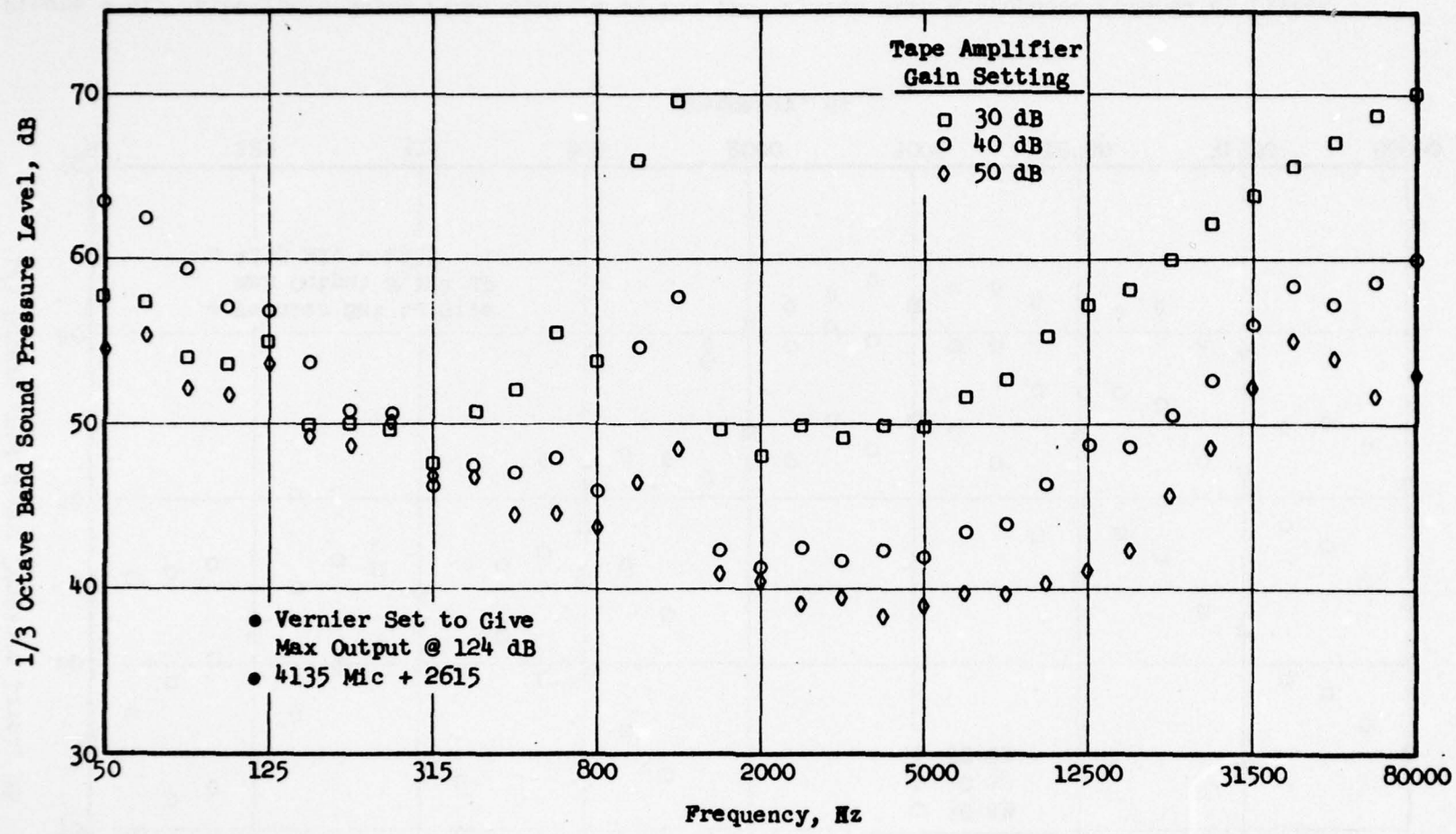


Figure 4-40. Electronic Noise Floor Spectra of the 90° System with Micrpohone Covered by Piston Phone.

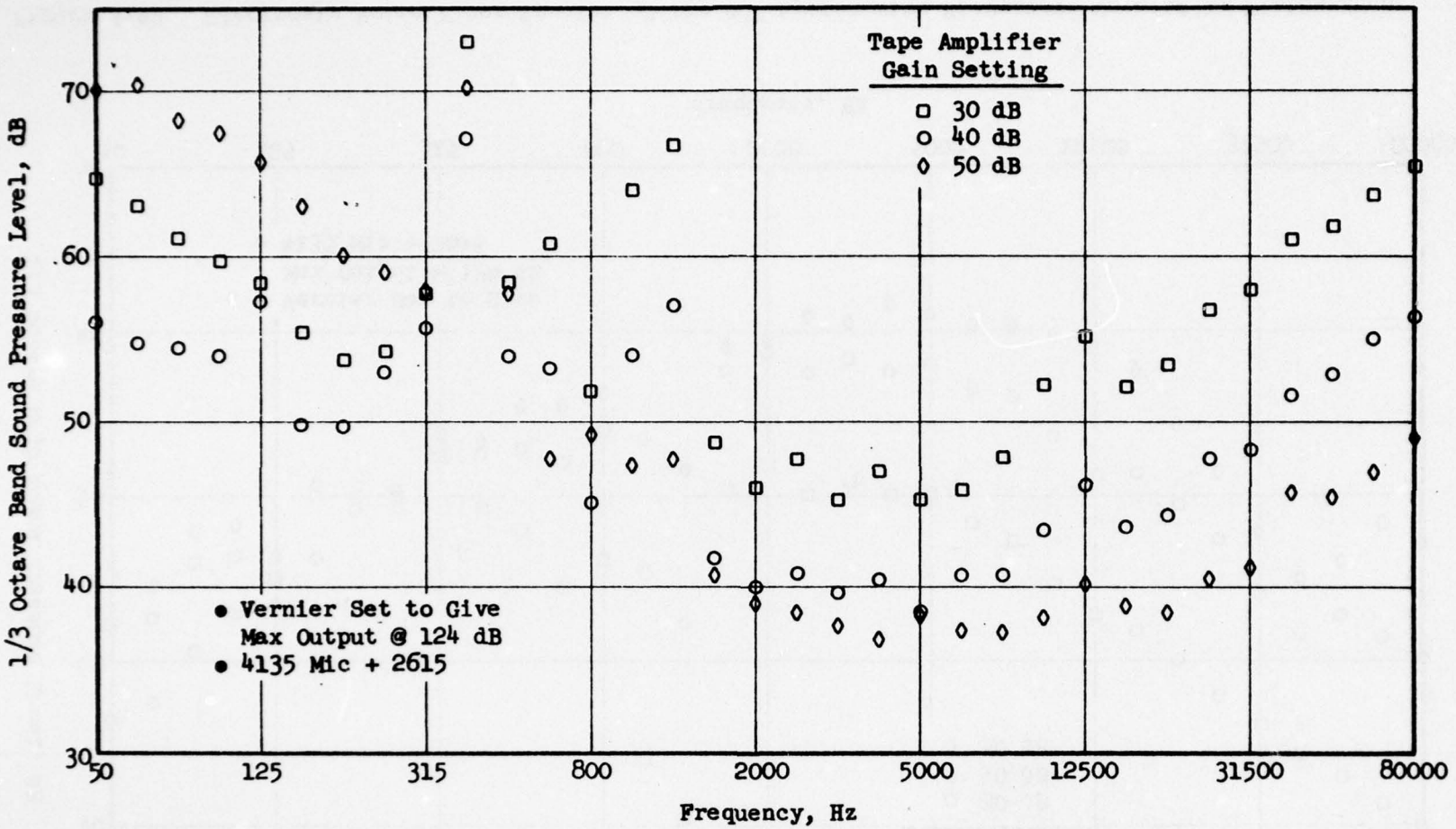


Figure 4-41. Electronic Noise Floor Spectra of the 120° System with Microphone Covered by Piston Phone.

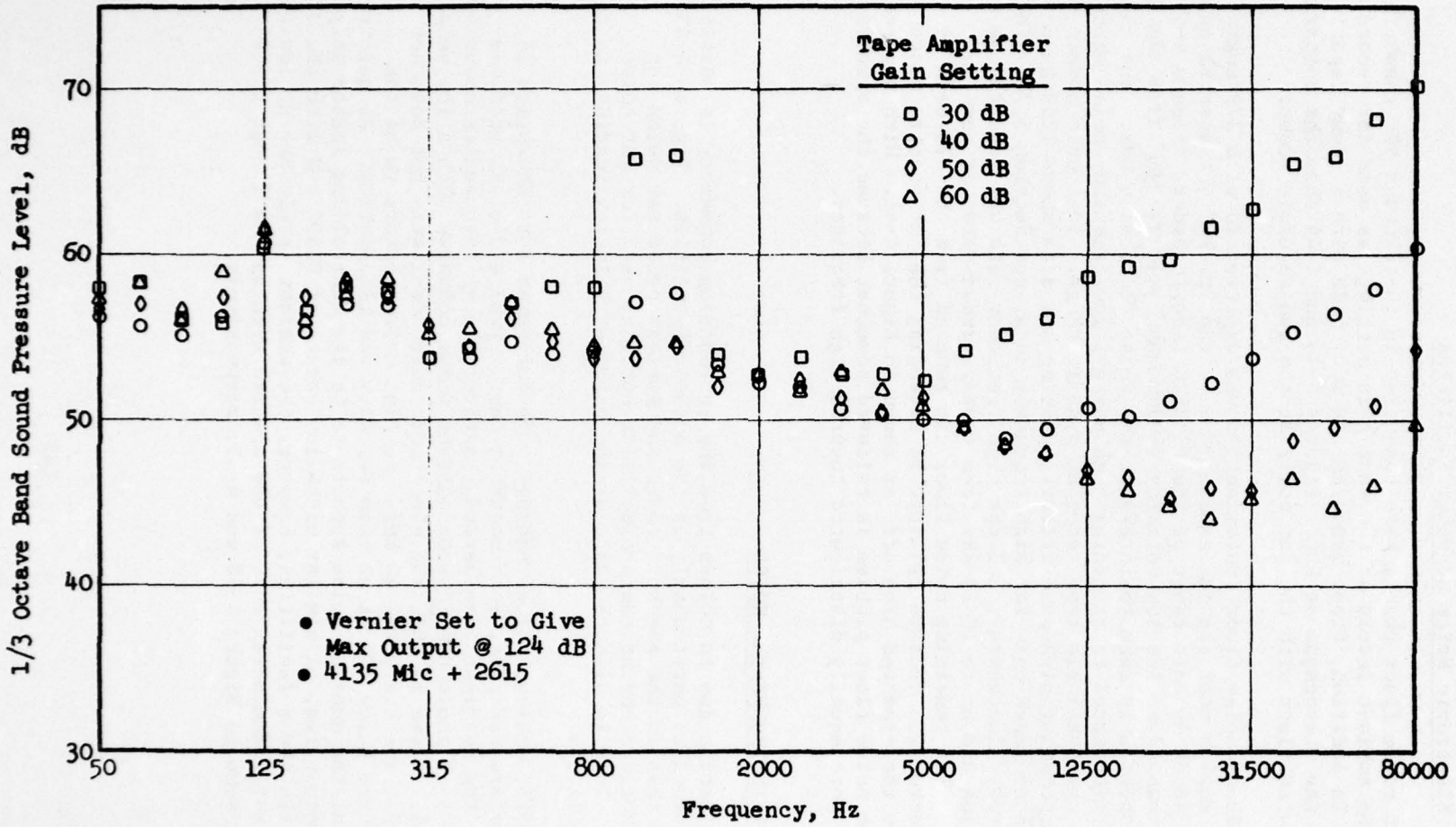


Figure 4-42. Electronic Noise Floor Spectra of the 150° System with Microphone Covered by Piston Phone.

4.6.4 Electronic Noise at Other Facilities

Similar noise floor checks were conducted in the USC and UBC chambers by recording the ambient levels at the same gain settings as used for recording jet noise. In addition, floor measurements were made with a dummy capacitance to simulate the microphone at UBC. Figures 4-43 and 4-44 show the comparison of the measured floor with the jet noise at the two anechoic rooms.

Significant noise floor contamination was experienced with J79 engine facility at angles near the jet exhaust due to the "peaky" jet spectra and the limited 46 dB dynamic range of the GE/EFTC tape recorder. Figure 4-45 shows a narrowband of the low velocity (500 ft/sec) spectra 160° from the inlet axis. The spectra is seen to intersect the noise floor at 4 kHz. The cause of this was pinpointed to recording high energy, low frequency noise which used up all the available tape recorder dynamic range. The conic nozzle was rerun, incorporating high pass filters, passing all data above 1250 Hz on the high microphone (used only for high frequency data, see Section 5.7). The technique proved successful, and the high frequency data was resolved up to 15 kHz on line and up to 10-12 kHz from tape-recorded data, as seen in Figure 4-45. The remaining noise floor was removed from the J79 data by utilizing correction factors obtained by extending the jet spectra slope according to the expected drop off, as shown in Figure 4-46. With suppressor nozzles, the noise floor problem is relieved somewhat because the spectra is flatter and more equally distributed towards high frequency.

4.7 AMBIENT ENVIRONMENTAL NOISE

Contamination due to noises from the surrounding community is possible at low frequencies, particularly in the outdoor facilities. Figures 4-43 and 4-44 showed that in the anechoic rooms the ambient noise was below the electronic noise floor at the preamplifier settings used for jet noise recordings. This is also the case at the high jet velocity readings in the outdoor facilities.

At JENOTS, ambient noise readings were collected for the entire 24 hours and before and after each acoustic test. Twelve o'clock noon was found to be the noisiest time period, particularly at frequencies above 400 Hz. Figure 4-47 shows the 12 noon ambient noise compared with a low velocity jet spectrum. Above 10 kHz, the electronic noise dominates but does not affect the jet spectra until 40 kHz. Ambient noise appears to be the dominant source below 200 Hz at this velocity and time period. At quieter time periods, the ambient noise appears to be the controlling factor only at very low frequencies. A similar situation occurs at CR&DC and with the J79 at EFTC. With these facilities, however, the ambient levels are so low that electronic noise dominates most of the spectra even at the lowest power setting, as seen in Figure 4-48 and 4-49, respectively.

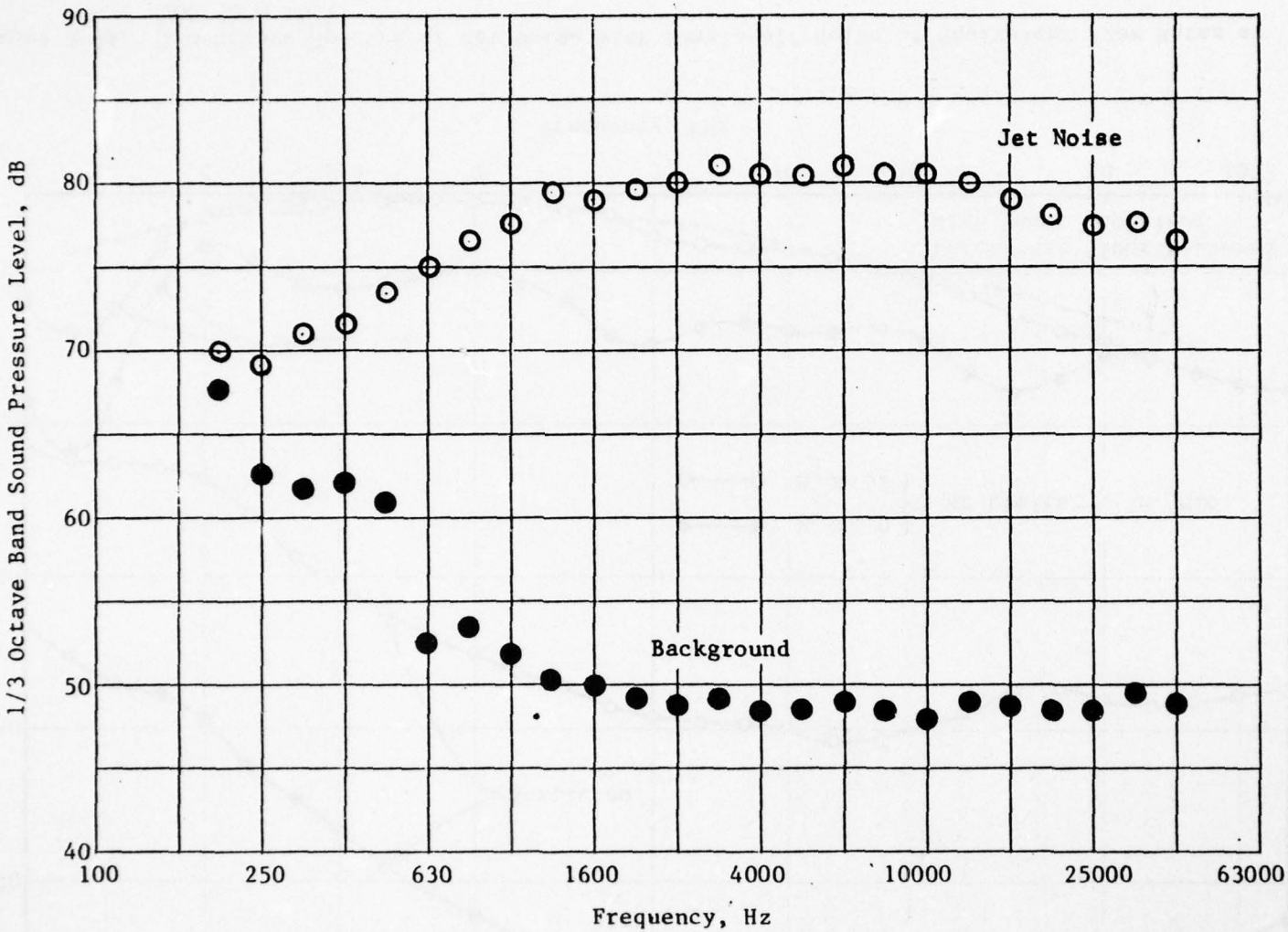
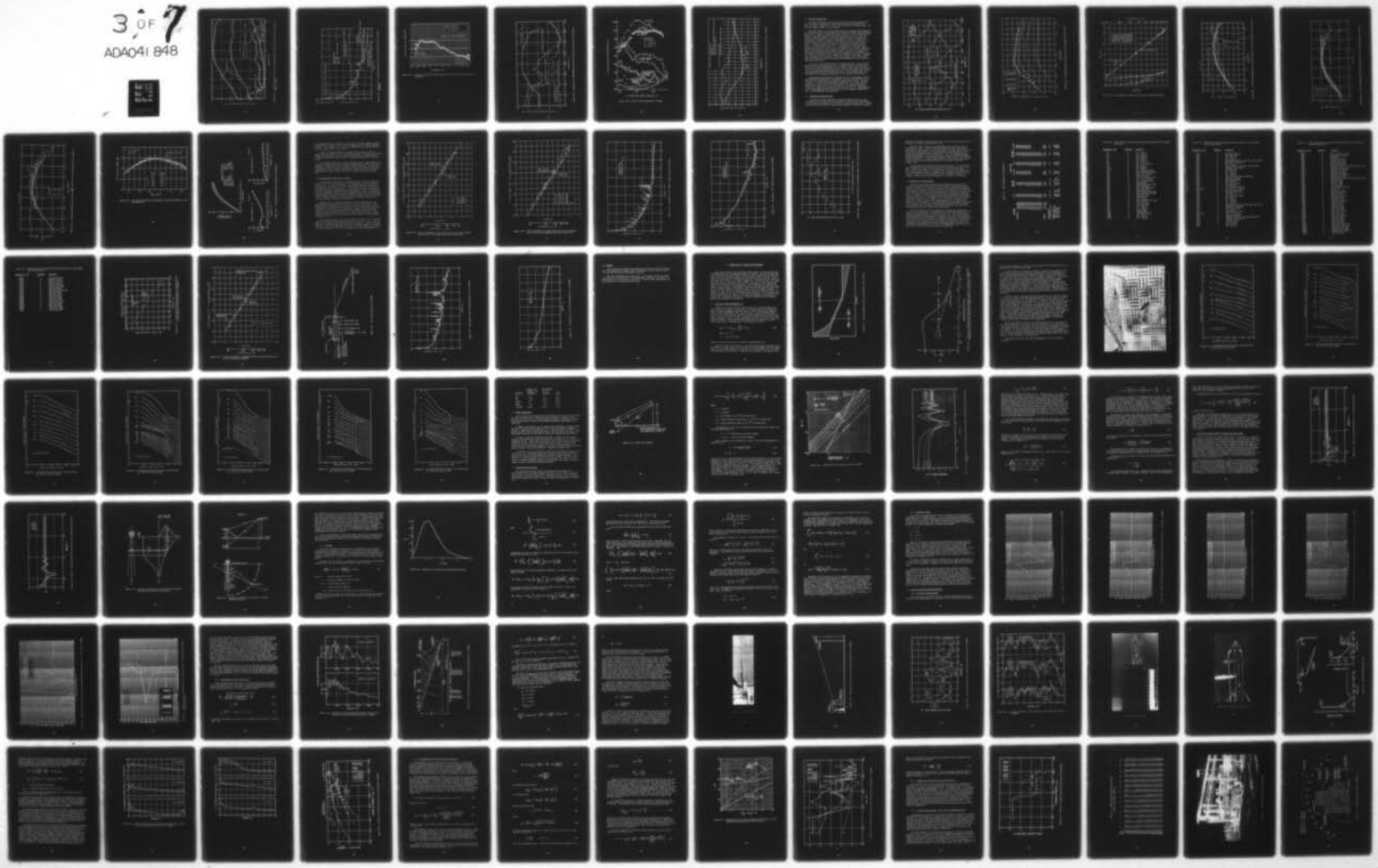


Figure 4-43. Comparison of the Jet Noise of a 2-inch Jet at $M_j = 0.69$ and $\theta = 90°$ with Electronic and Acoustic Background Noise at USC.

AD-A041 848 GENERAL ELECTRIC CO CINCINNATI OHIO AIRCRAFT ENGINE GROUP F/G 14/2
HIGH VELOCITY JET NOISE SOURCE LOCATION AND REDUCTION. TASK 1. --ETC(U)
FEB 77 C T SAVELL, E J STRINGAS DOT-OS-30034
UNCLASSIFIED R77AEG187 FAA-RD-76-79-1 NL

3 OF 7
ADA041 848



3 OF 7

ADA041 848

1.0 1.1 1.25 1.4 1.6 2.8 2.5 3.2 2.2 3.6 2.0 4.0 1.8 4.5 5.0 5.6

MICROCOPY RESOLUTION TEST CHART
NATIONAL BUREAU OF STANDARDS-1963-A

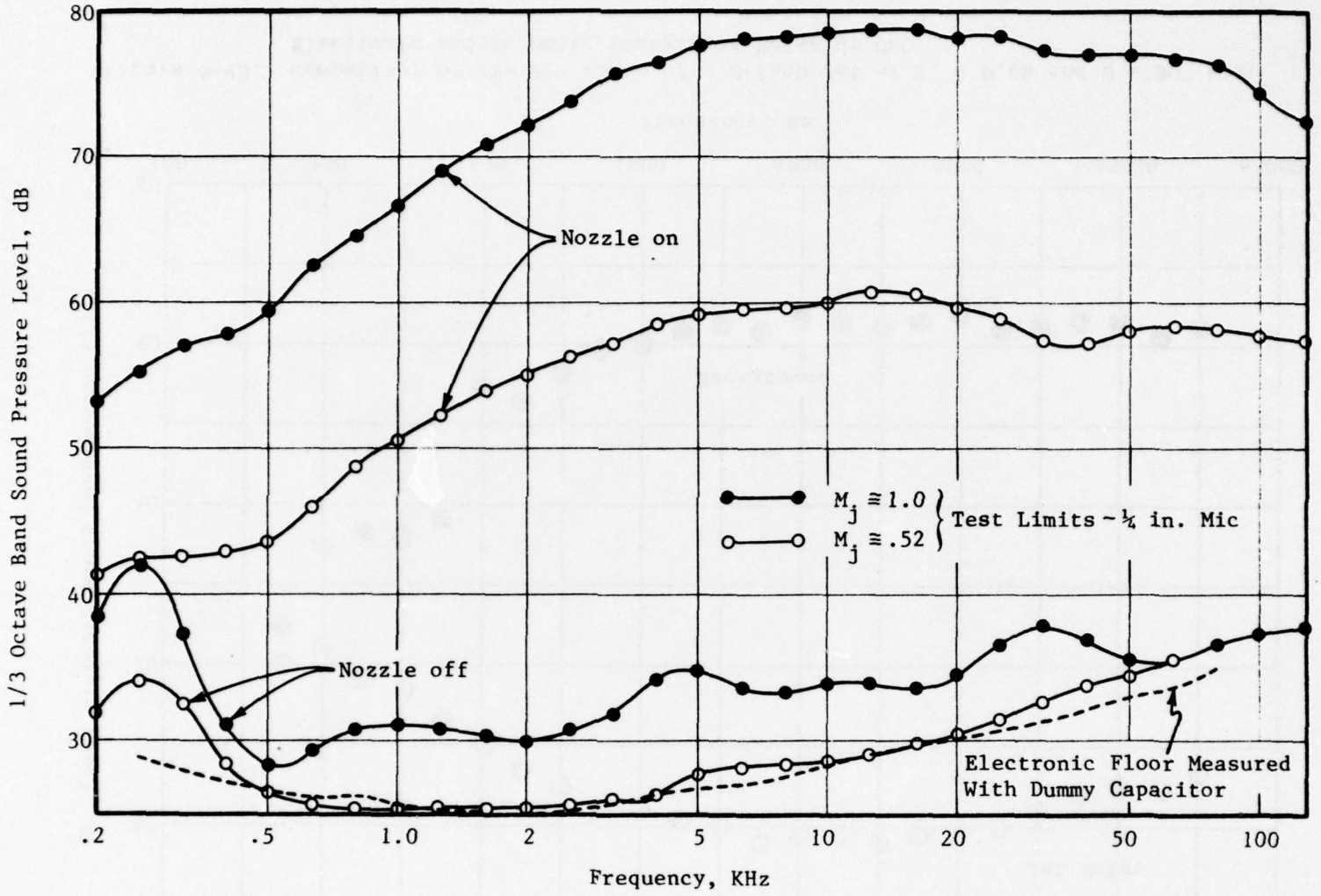


Figure 4-44. 1/3-Octave Spectra of Jet Noise with Nozzle-off Noise at Equivalent Flow Rates at UBC (θ = 90°).

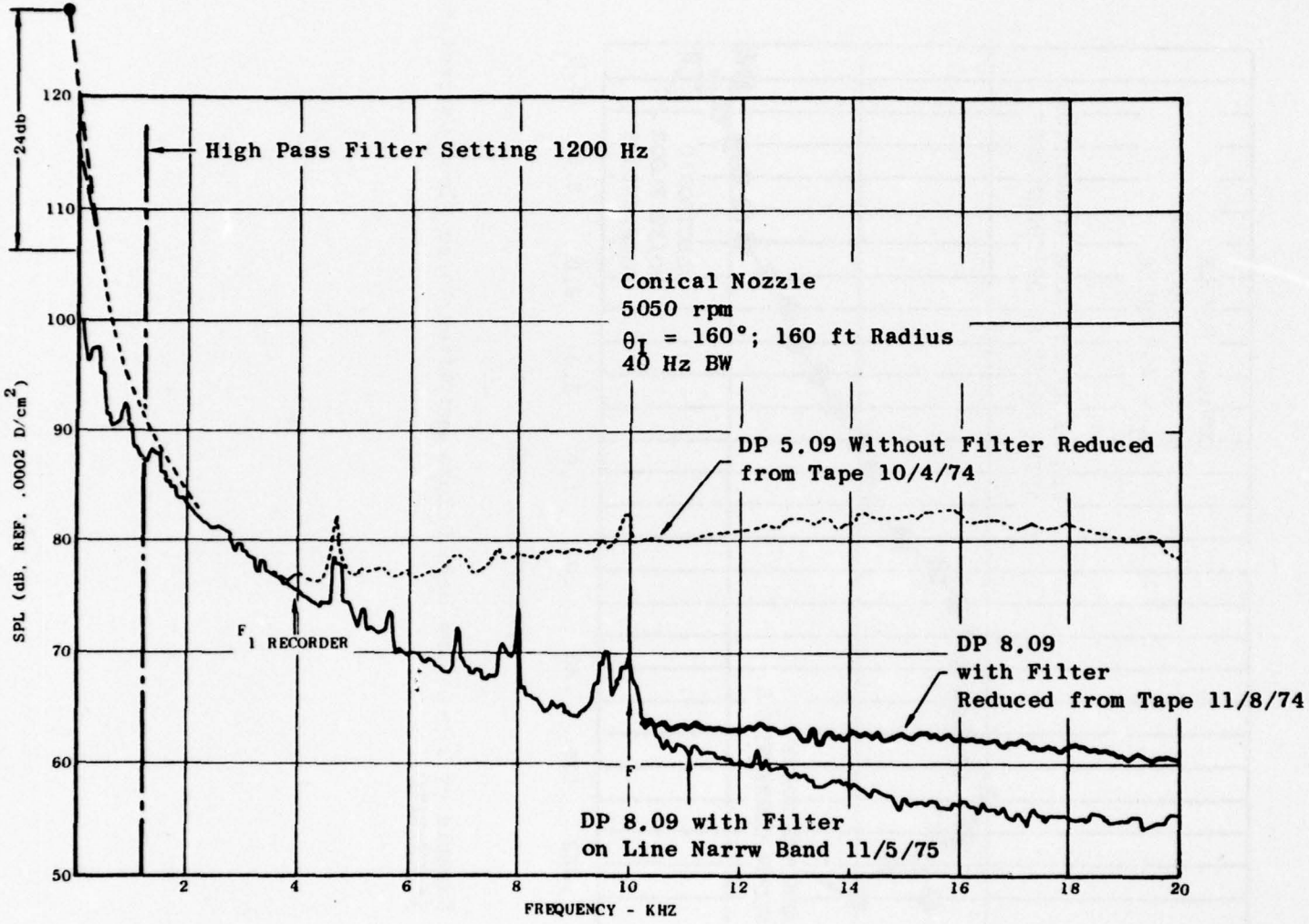


Figure 4-45. Comparison of Narrowband Spectra With and Without On-Line Filters at GE/EFTC.

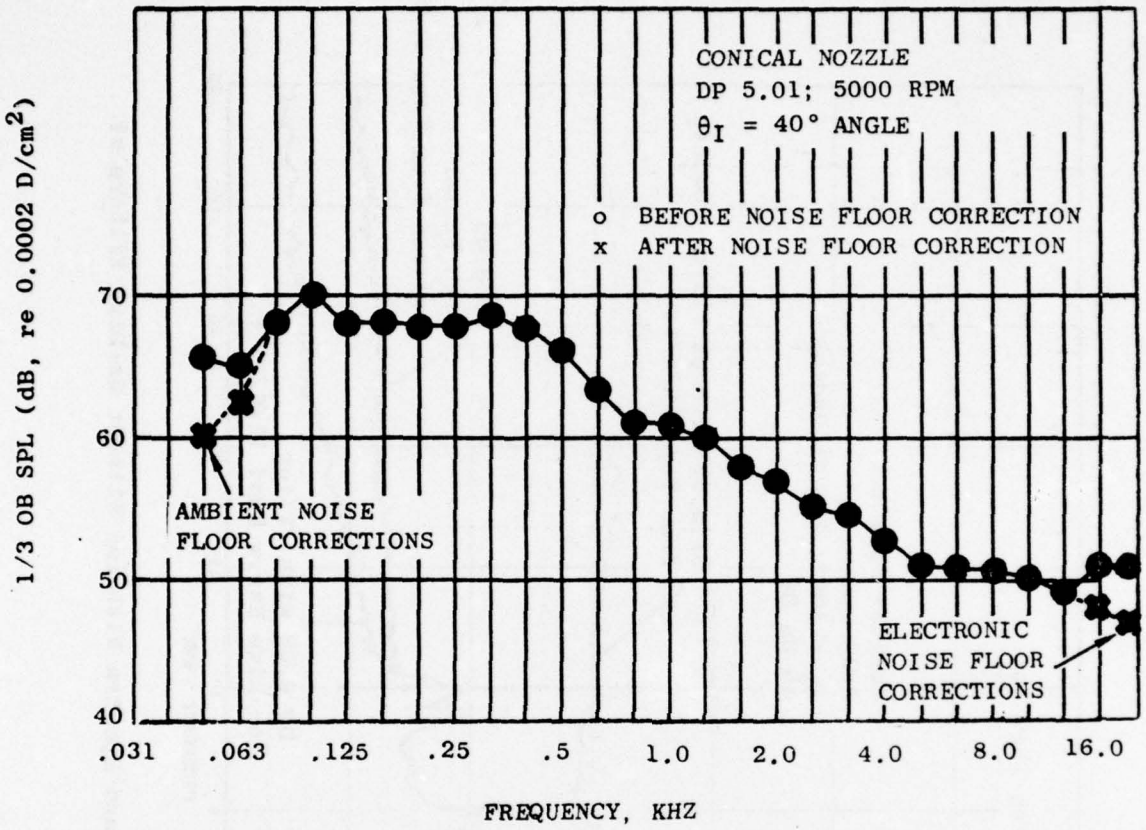


Figure 4-46. Example of 1/3-Octave Data Before and After Noise Floor Corrections at GE/EFTC.

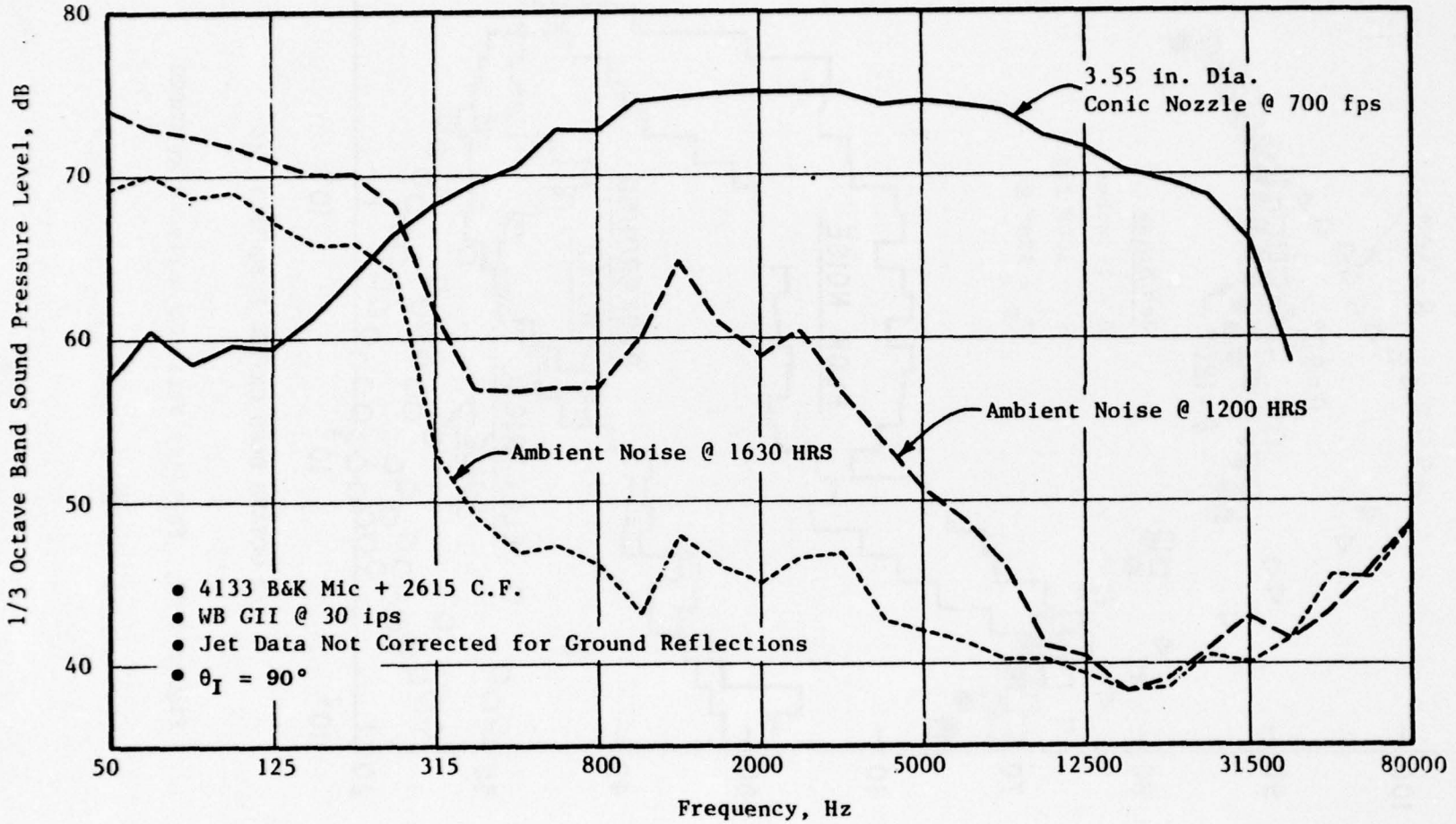


Figure 4-47. Comparison of JENOTS Ambient Noise Levels with Low Velocity Jet Spectra.

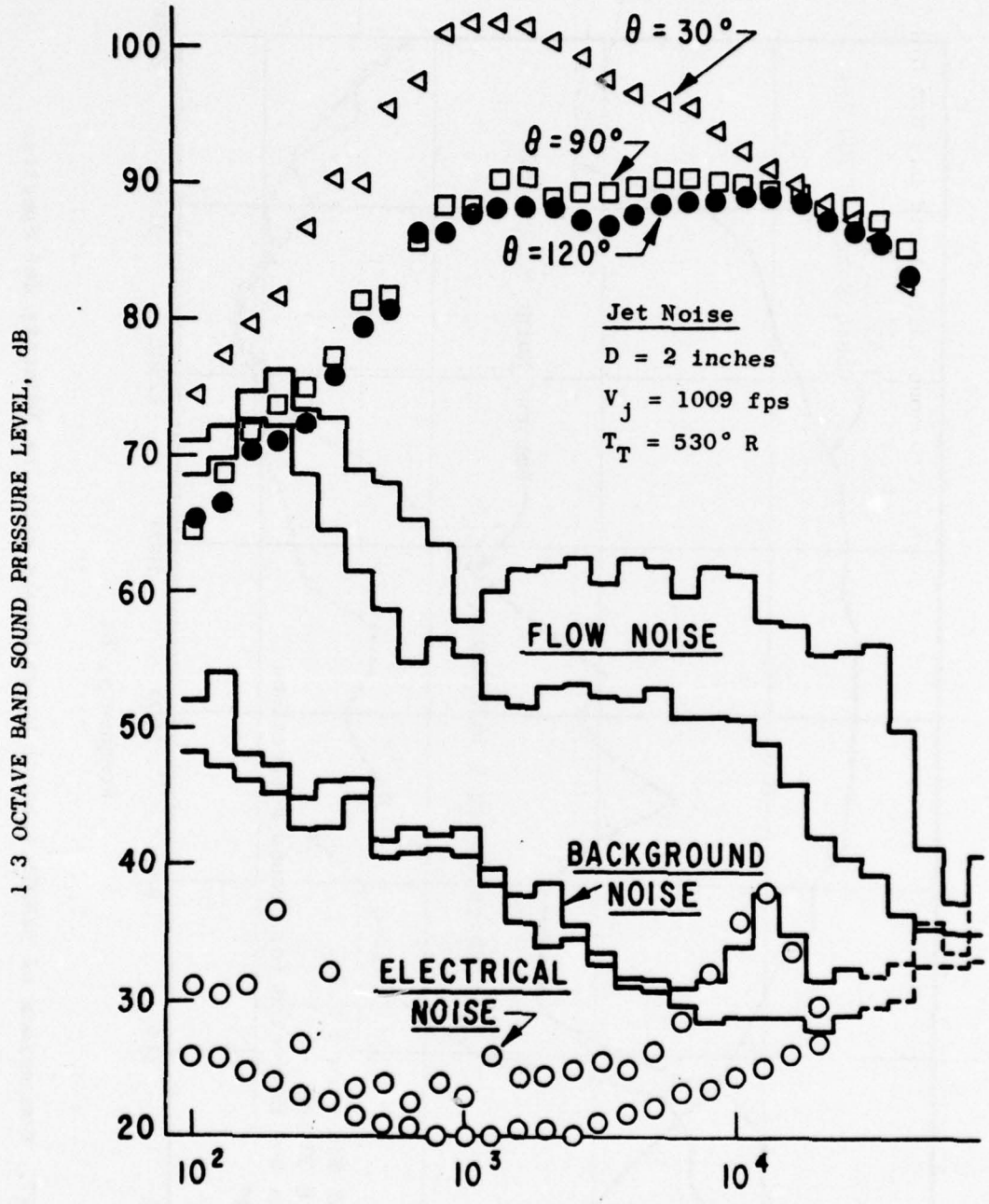


Figure 4-48. Facility Noise Comparisons at CR&DC.

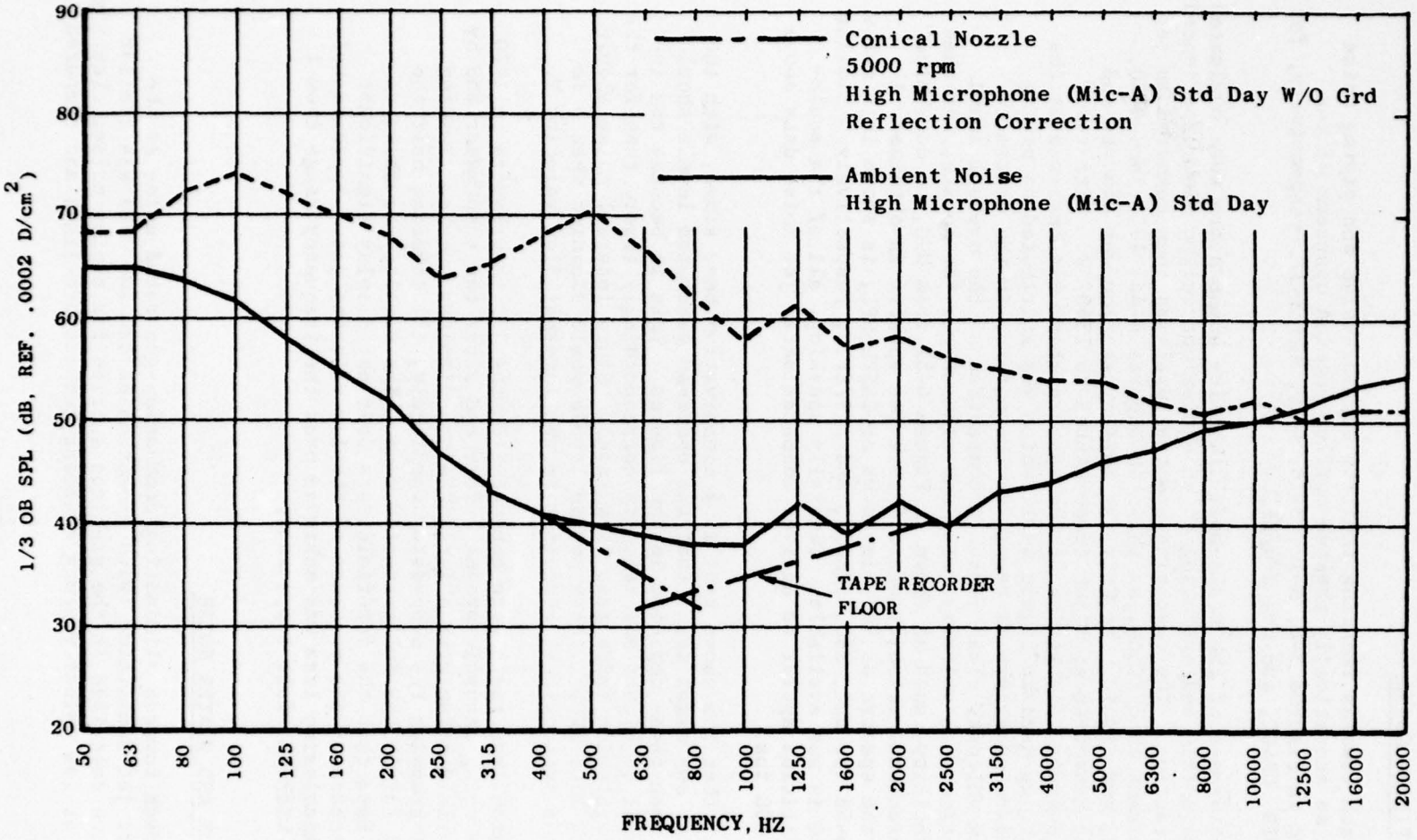


Figure 4-49. Comparison of the Ambient Noise Level with Recorded Jet Noise at GE/EFTC.

4.8 FACILITY PIPING NOISE

The approach towards reducing facility control valve and piping noise was to install an acoustically treated muffler section upstream of the nozzle as shown in Figures 3-6, 3-12, 3-16, 3-26, and 3-37, respectively, for USC, UBC, JENOTS, CR&DC, and the J79/EFTC.

The effectiveness of the scale-model facility suppressors were evaluated by removing the nozzle and operating at an equivalent weight flow experienced during actual testing. The resulting spectra level was then compared to jet spectra at the same conditions, as shown in Figures 4-44, 4-48, and 4-50, for UBC, CR&DC, and JENOTS. At USC, the muffler section was removed and replaced by the heater to give jet temperatures to 1360° R. With this modification, however, distortion of the spectra shape was observed at low jet Mach number, as seen in Figure 4-51, which was attributed to piping noise. It appears necessary to resort to the muffler in the system to obtain very low velocity clean jets. A comparison of the overall sound pressure variation with velocity, with and without the jet nozzle, was then made at each facility, such as shown in Figure 4-52 from UBC, to determine the lowest operational velocity where a pure jet spectra is obtained. A comparison of the spectra at 90°, in terms of OASPL-SPL, is shown in Figures 4-53 through 4-56 for USC, UBC, JENOTS, and J79/EFTC, respectively. Similar data from CR&DC is not available. Generally speaking, all of the scale-model test facilities appear to deliver uncontaminated jet noise data above approximately 600 fps.

It is felt that the above test is a conservative one, since, with the nozzle in place, one might argue that the upstream generated levels should be even lower than those depicted in the figures. This is because the in-duct density will be higher and velocity correspondingly lower, than for the no-nozzle configuration (same mass flow rate). Since internal noise should scale something like $\rho V^6 D^2$, these source levels would diminish when ρ is increased with a proportional reduction in the internal flow velocity V.

Transmission loss tests were conducted on the J79 suppressors in 1970 (Reference 28) using acoustic probes before and after the suppressor and by recording far-field noise with a large 28-inch-diameter nozzle. Testing included: (1) removing the suppressor completely, (2) covering half the treatment, and (3) in the fully treated mode. The results are shown in Figure 4-57. Note that the far-field data does not display significant attenuation because of the presence of the low velocity jet. Approximately 6 to 17 dB transmission loss was achieved over the frequency range from 1 kHz to 10 kHz with the full suppressor.

4.9 COMBUSTION AND HEATER NOISE

The approach towards eliminating combustion-generated noise at the scale-model hot jet facilities (with exception of UBC and J79) was similar to the technique described in the previous section for piping noise. Testing was conducted at low velocity along constant temperature lines and compared

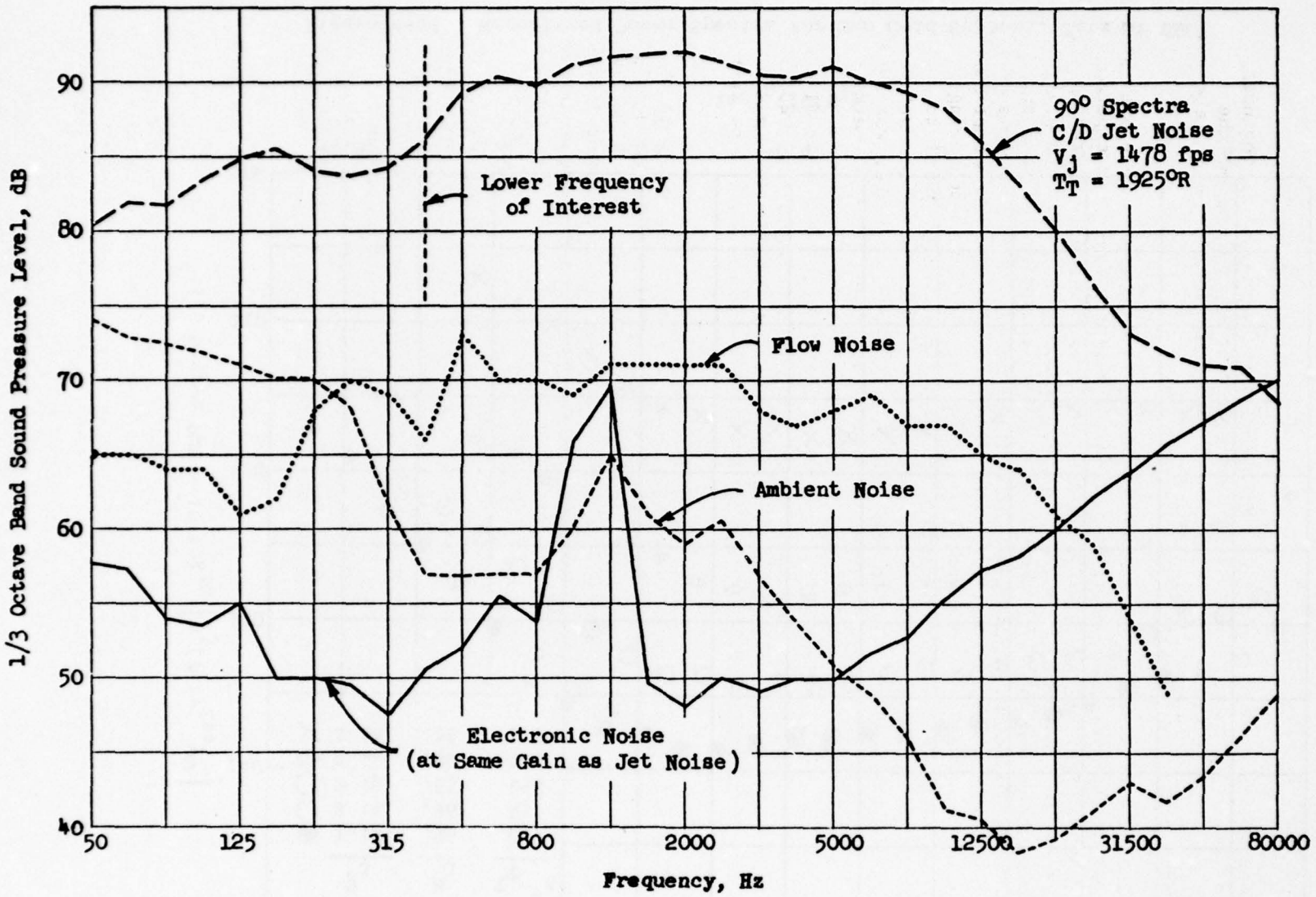


Figure 4-50. Comparison of JENOTS Potential Noise Contaminates with Jet Noise Level.

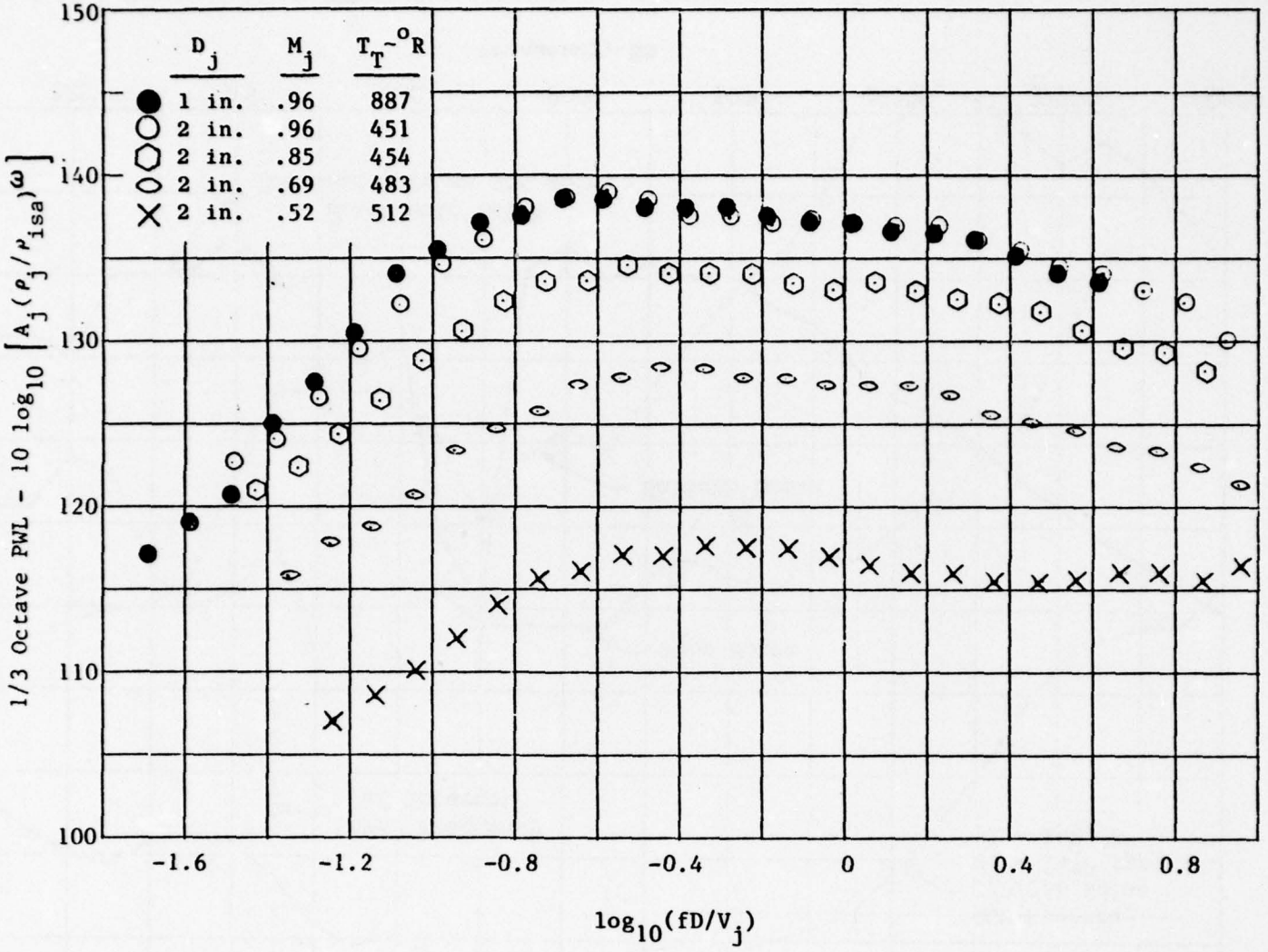


Figure 4-51. Normalized Power Spectra for Two Cold Subsonic Jets at USC.

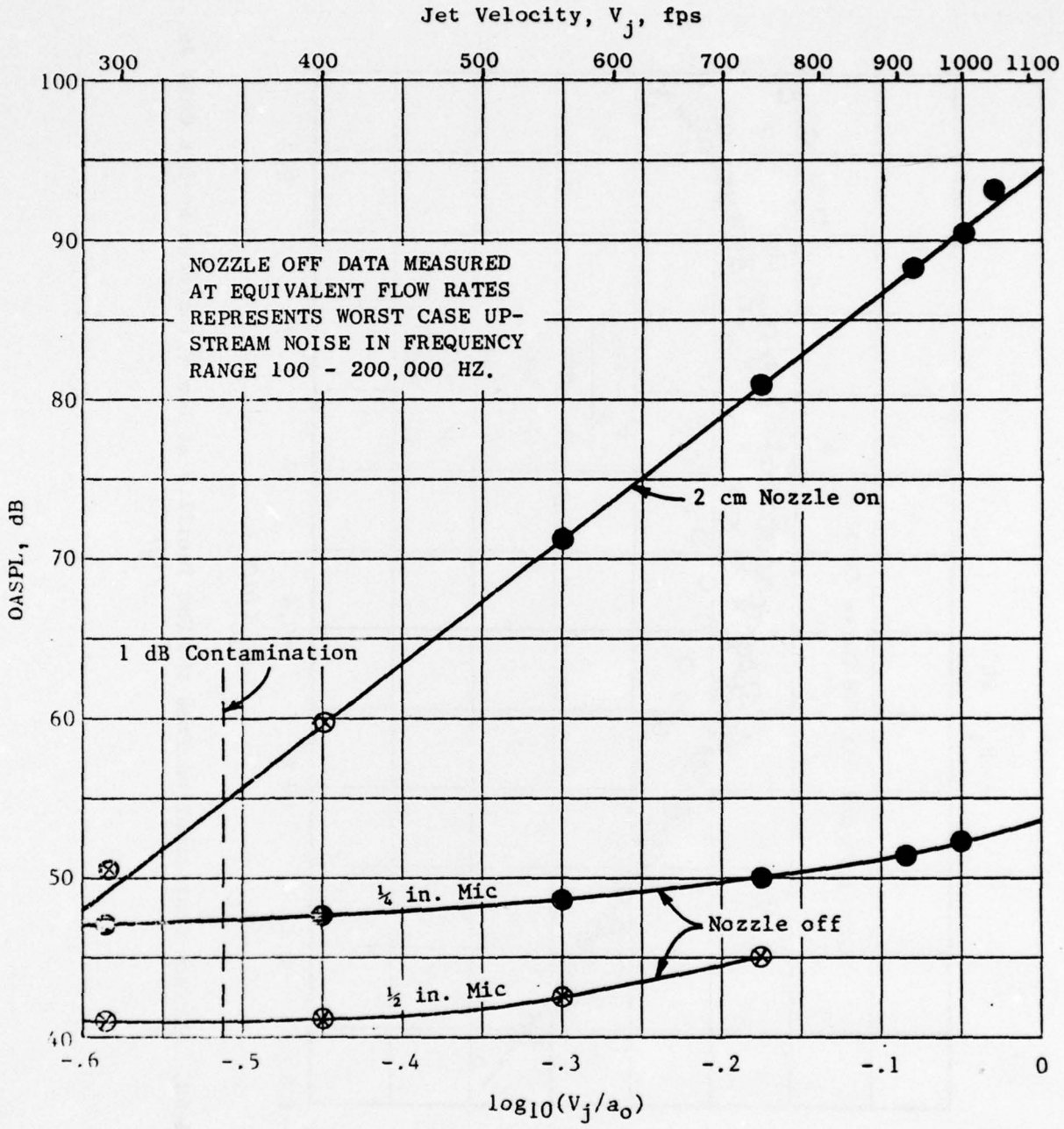


Figure 4-52. UBC Comparison of OASPL at 90° for Jet Nozzle On and Off.

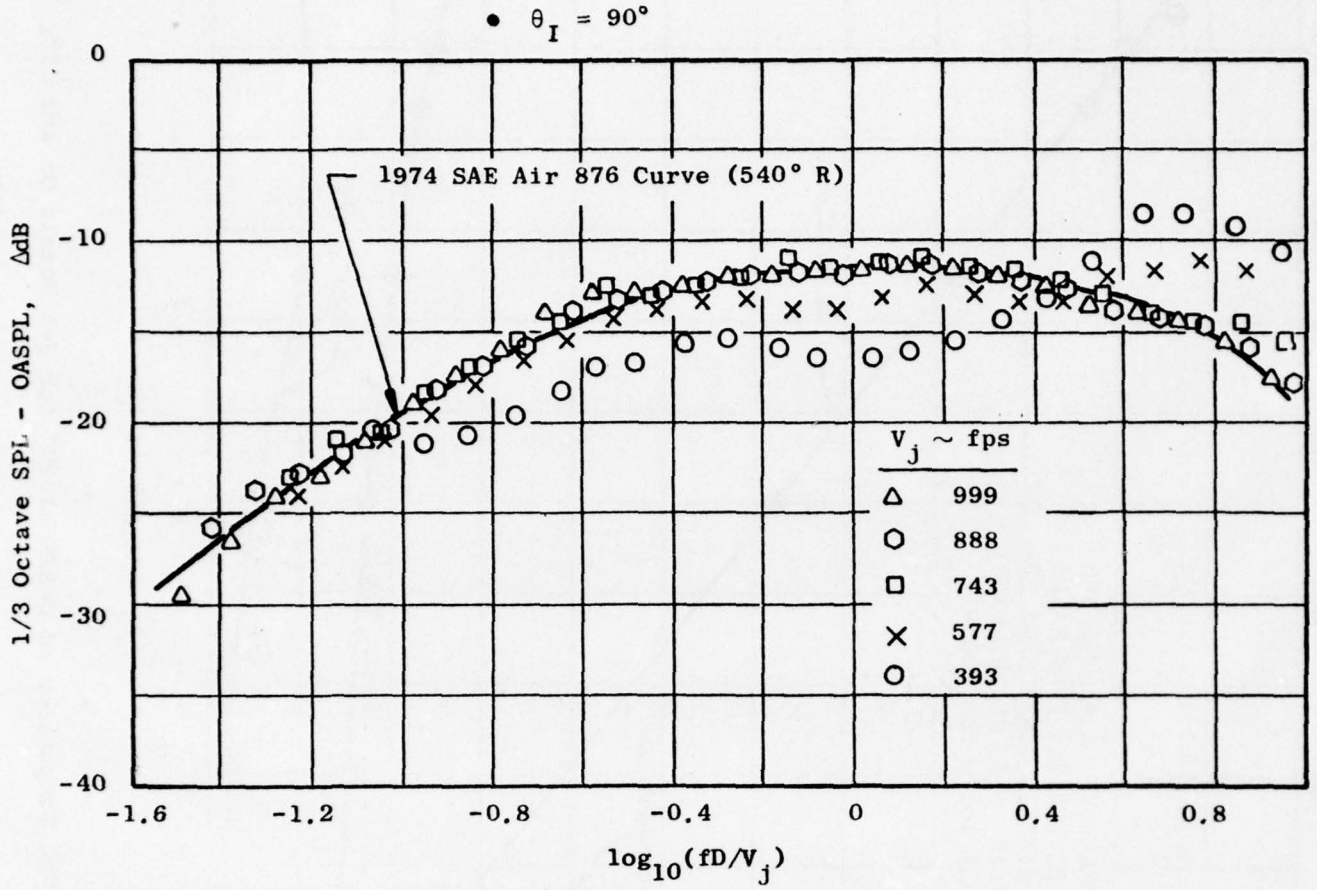


Figure 4-53. Airflow Contamination from the USC Facility at Low Velocities with a Cold Jet.

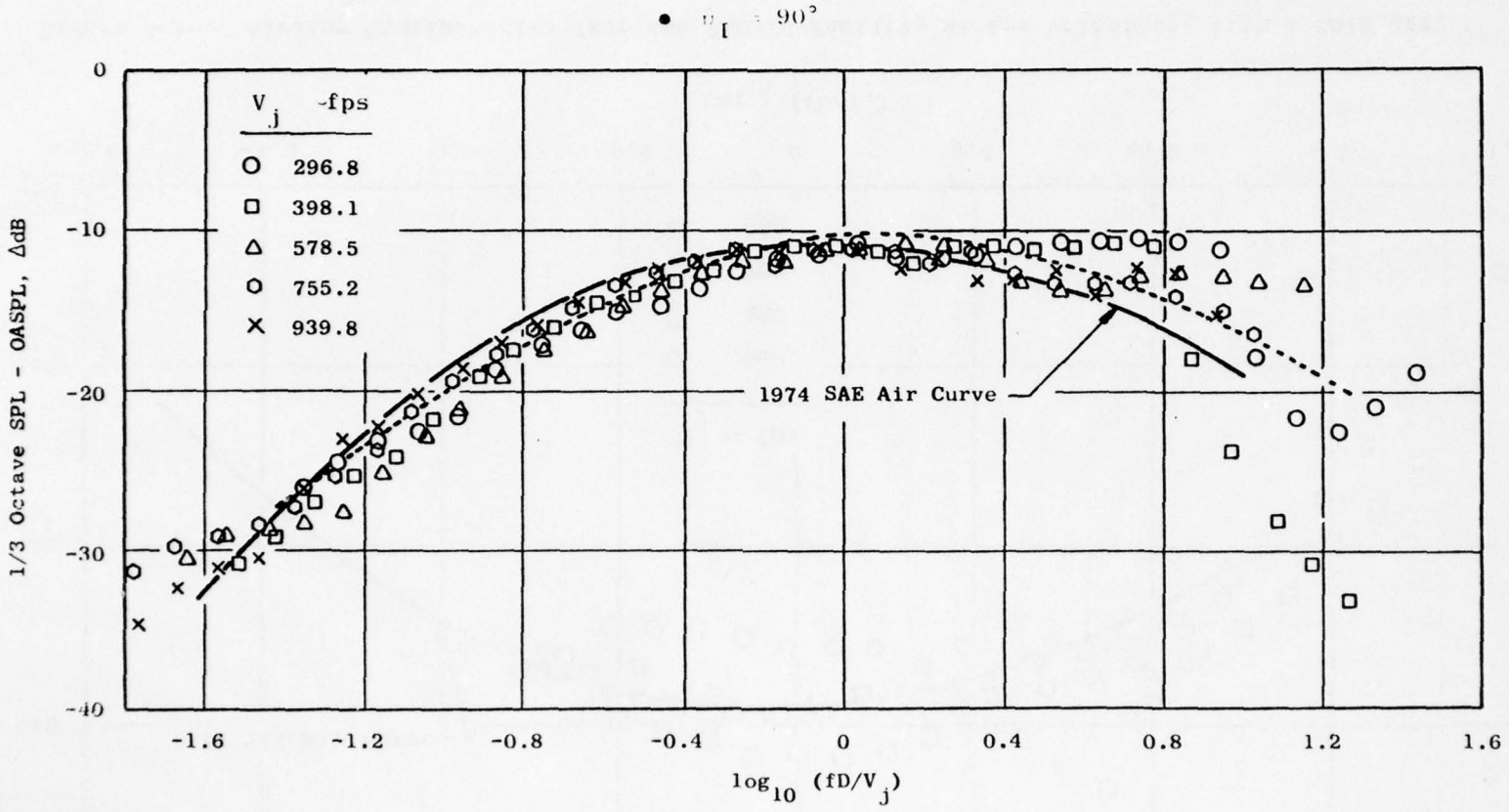


Figure 4-54. Airflow Contamination from the UBC Facility at Low Velocities with a Cold Jet.

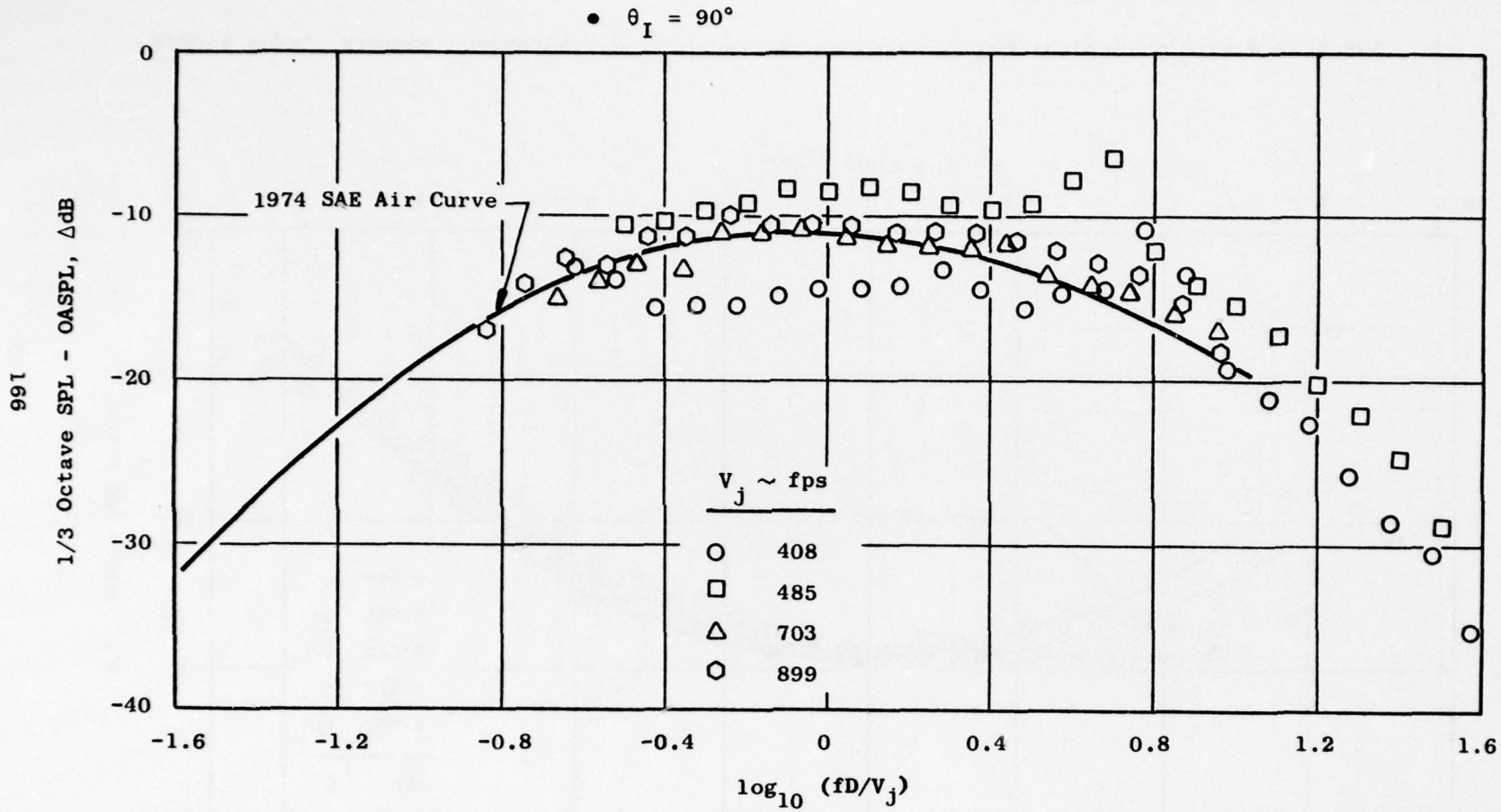


Figure 4-55. Airflow Contamination from the JENOTS Facility at Low Velocities with a Cold Jet.

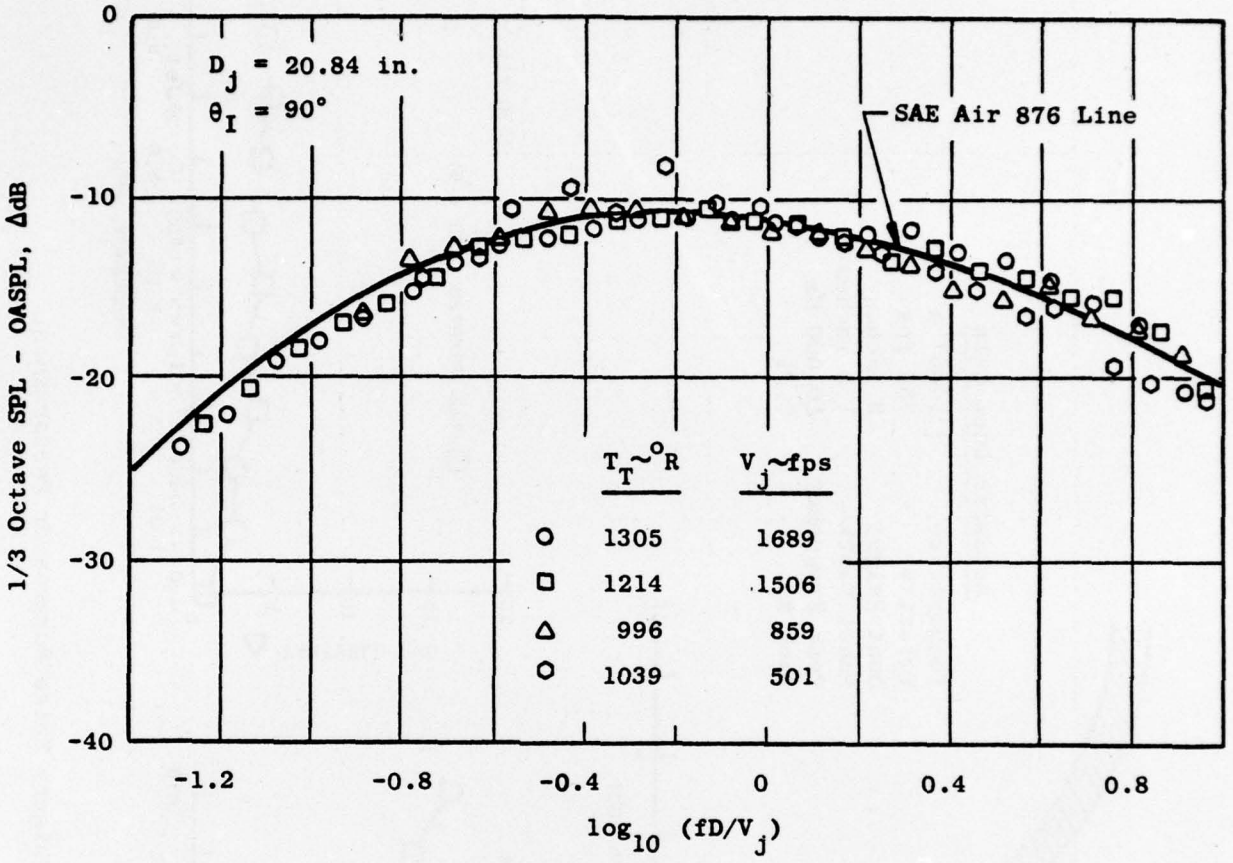
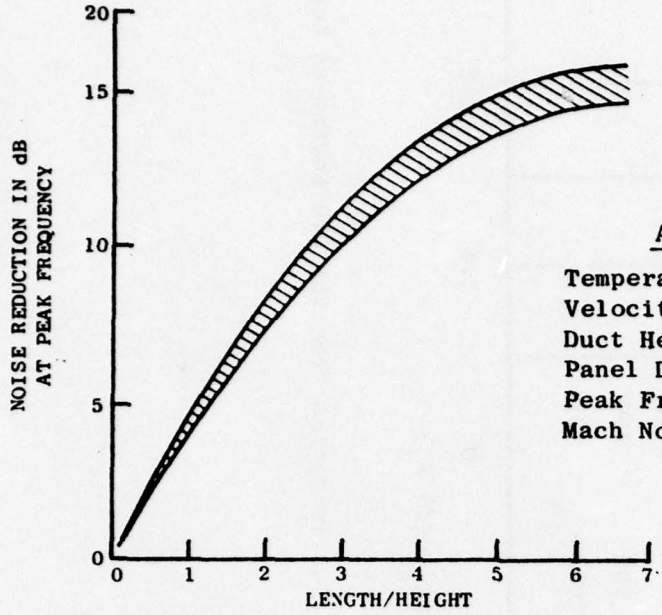
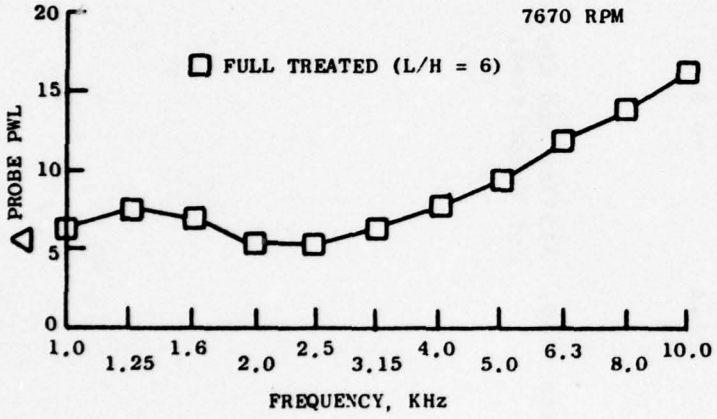


Figure 4-56. Airflow and Core Noise Contamination from the J79 Engine at Low Jet Velocities.



Acoustic Duct Data

Temperature	1460° R
Velocity	750 fps
Duct Height	8 inches
Panel Depth	1.5 inches
Peak Frequency	10,000 Hz
Mach No.	0.41



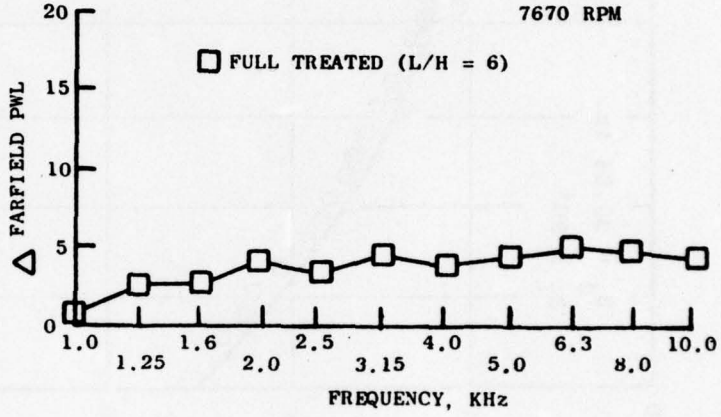


Figure 4-57. J79 Turbomachinery Noise Suppressor Performance.

to the eight-power law. Variations of less than 1 dB were accepted as uncontaminated data. Figure 4-58 is a typical example from the JENOTS coannular facility. In all cases, the variation at temperature achieved the same low velocity limits as the cold jet case.

At USC, the maximum stagnation temperature was limited to 1050° R rather than the design 1350° R of the heater, because of unforseen instability problems in the system. This problem is probably due to a Rijke thermo-acoustic phenomenon (Reference 29) and is being investigated for corrective action.

At the JENOTS single-flow facility, the acoustically treated muffler is removed at temperatures above the muffler design limit of 1600° R, and often testing is conducted to as low as 1000° R without a muffler. To check the cleanliness of this no-muffler configuration, constant temperature runs were repeated resulting in the data line shown in Figure 4-59. The no-muffler configuration is seen to give clean jet noise down to 600 fps jet velocity.

4.10 TURBOMACHINERY NOISE FROM J79 ENGINE

The J79 engine installation at GE/EFTC provides a jet noise source for future studies in jet mixing noise, jet noise source locations, suppressor effects, etc. In order to accurately study these phenomena, the source of jet noise must be essentially free of other engine noise sources, such as turbomachinery and obstruction noise. There are three primary transmission paths for such noise contamination from the engine: (1) out the inlet, (2) out the jet exhaust, and (3) through the engine casing walls. The approach towards eliminating the engine noise contamination was to suppress the sound from the engine using massive inlet and exhaust suppressors on the installation, as shown in Figures 3-34 through 3-37, and encasing the engine in a lead box, as shown in Figures 3-40 and 3-41.

Analysis of the J79 engine far-field 1/3-octave band data with the suppressors in place showed the possibility of some turbomachinery tones still present, although their effect for the most part was small. It was determined that correction factors applied to the 1/3-octave band data would be adequate to eliminate this contamination. Figures 4-60 and 4-61 are typical 40 Hz and 4 Hz narrowband plots, respectively, showing the turbomachinery noise (which was limited to the lowest three rpm's run). Figure 4-60 also shows the electronic noise floor from 11,000 Hz, up as discussed in Section 4.6.4.

The following criteria was used to eliminate the tones. It was assumed that in a given 1/3-octave band an addition of less than 1 dB due to turbomachinery noise meets the "essentially free" requirement. Figure 4-62 shows the amount a given turbomachinery noise pure tone must exceed the broadband noise in a given 1/3-octave band, as shown on a 40 Hz bandwidth plot, before the limit is exceeded. The J79 rotating parts and their fundamental and

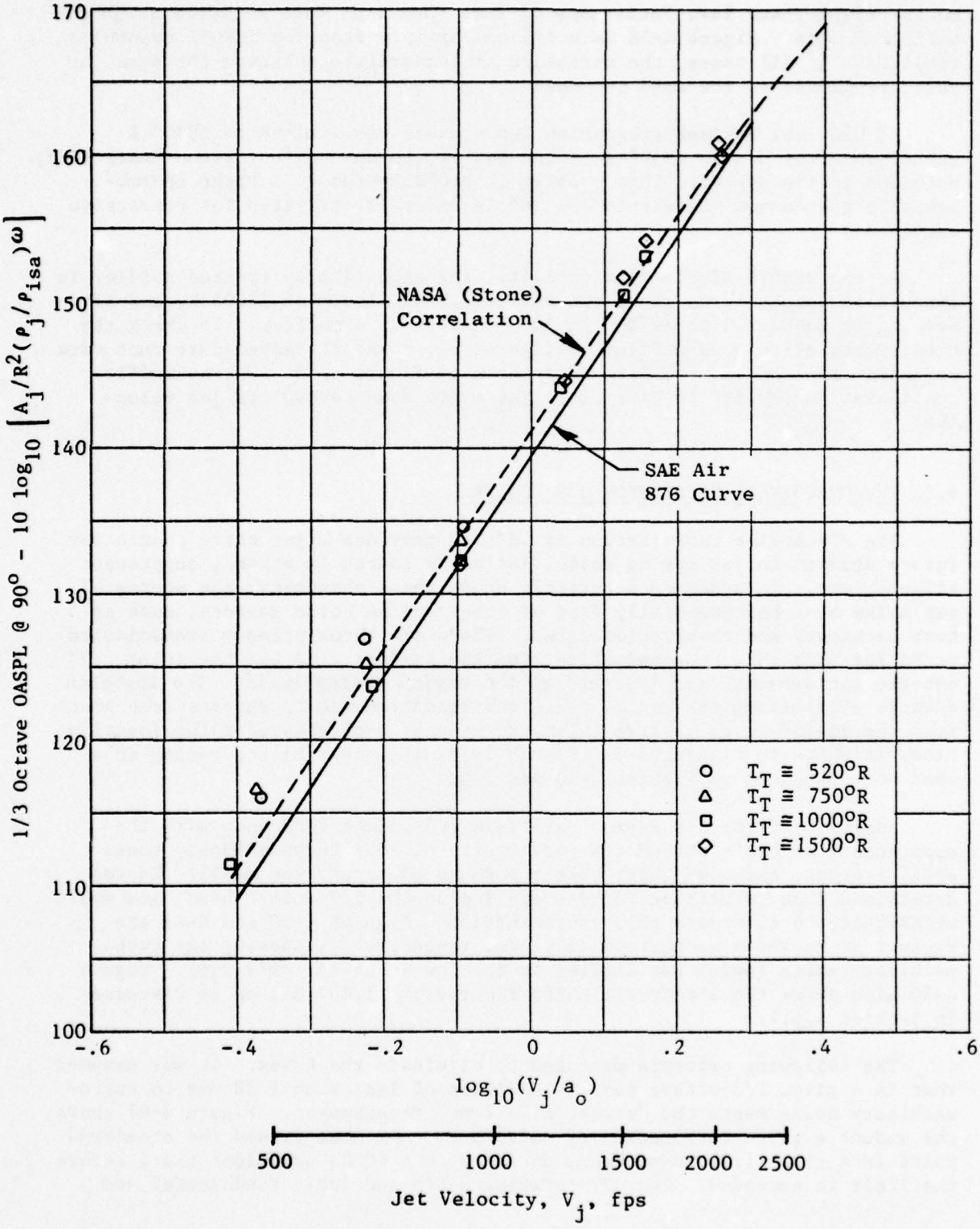


Figure 4-58. Velocity Dependence of the Normalized Overall Sound Pressure Level at 90° for the JENOTS Dual-Flow Installation.

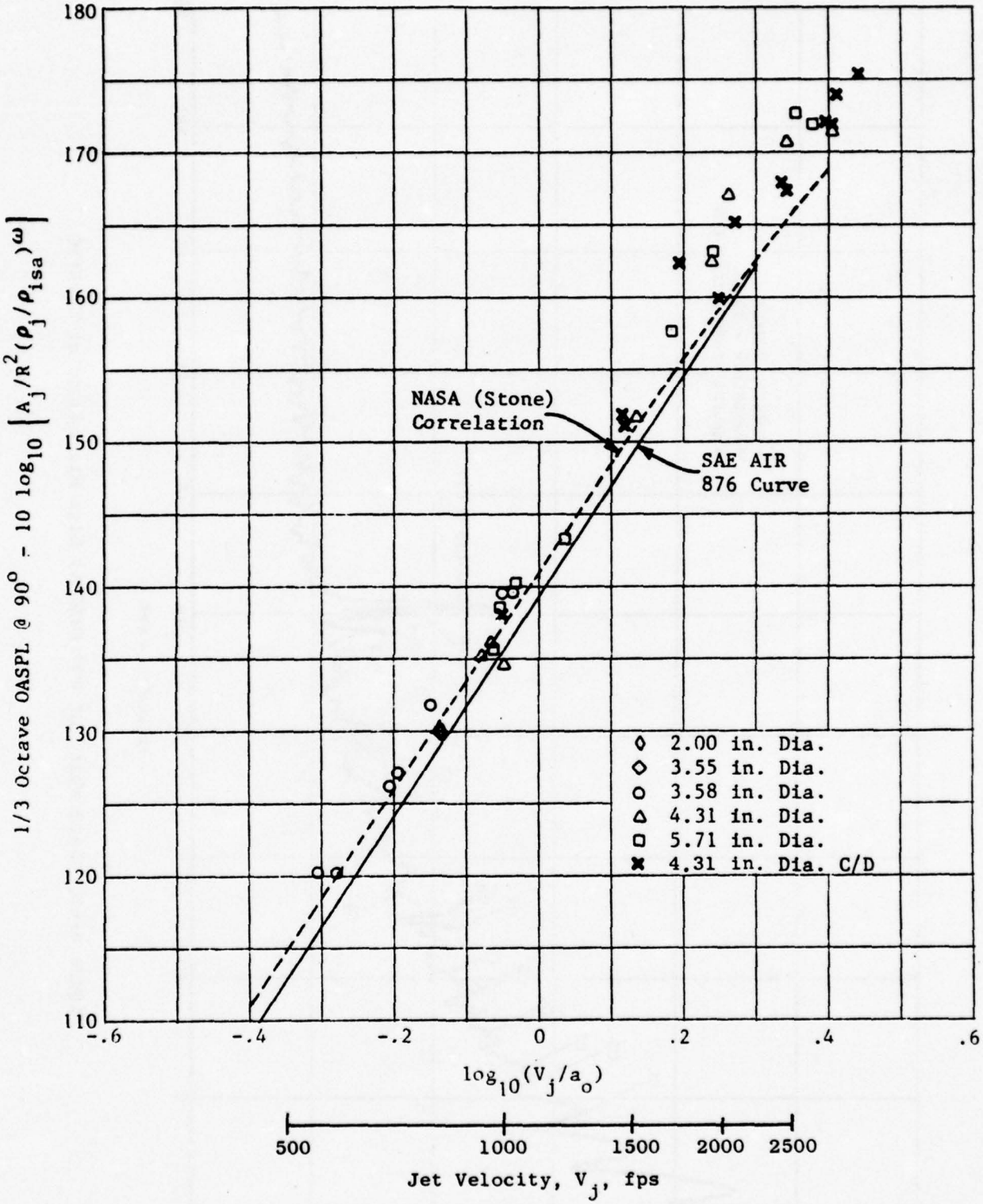


Figure 4-59. Velocity Dependence of Normalized Overall Sound Pressure Level at 90° for the JENOTS Single-Flow Installation.

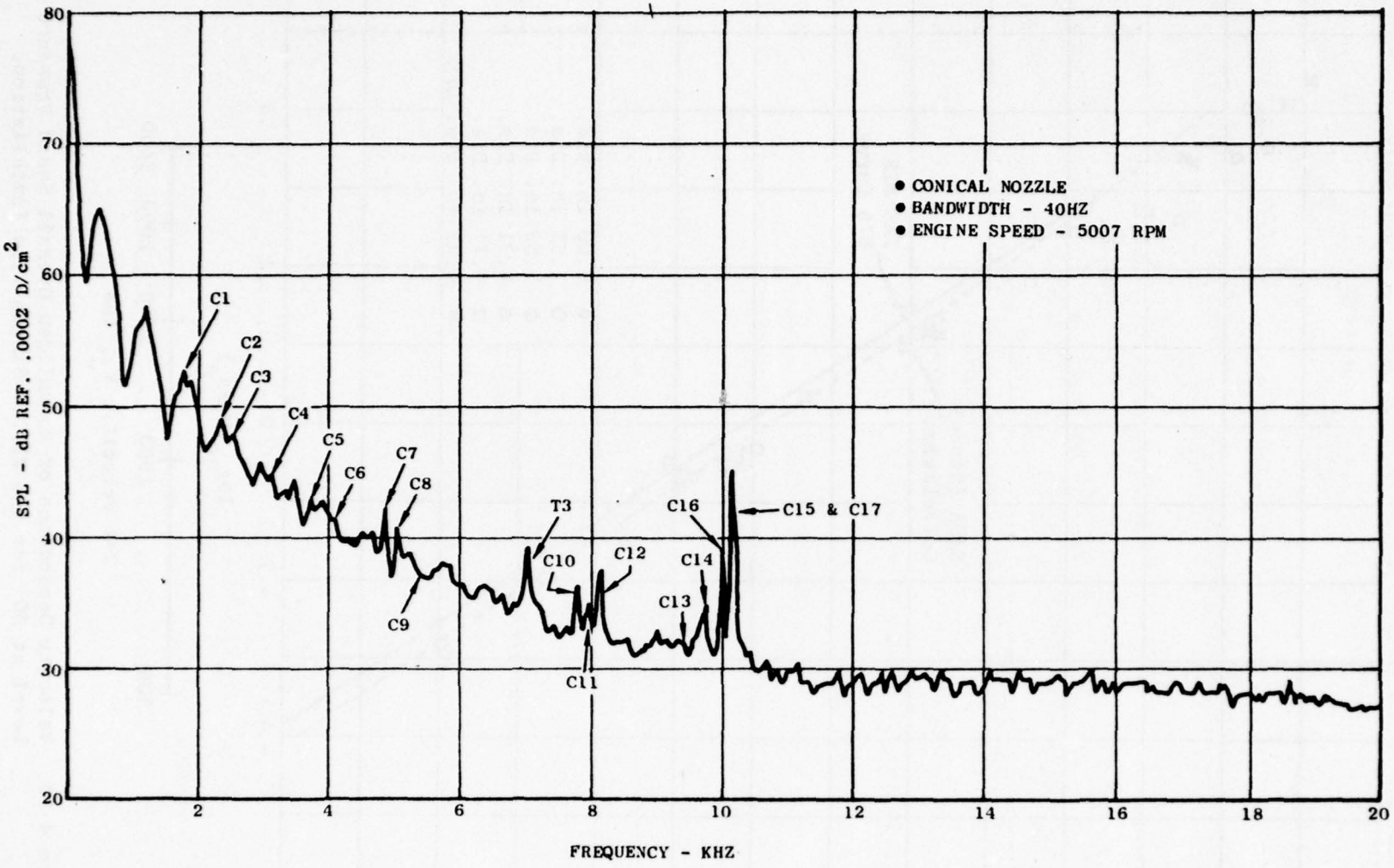


Figure 4-60. Narrowband of 60° (MIC-A) High Microphone at GE/EFTC.

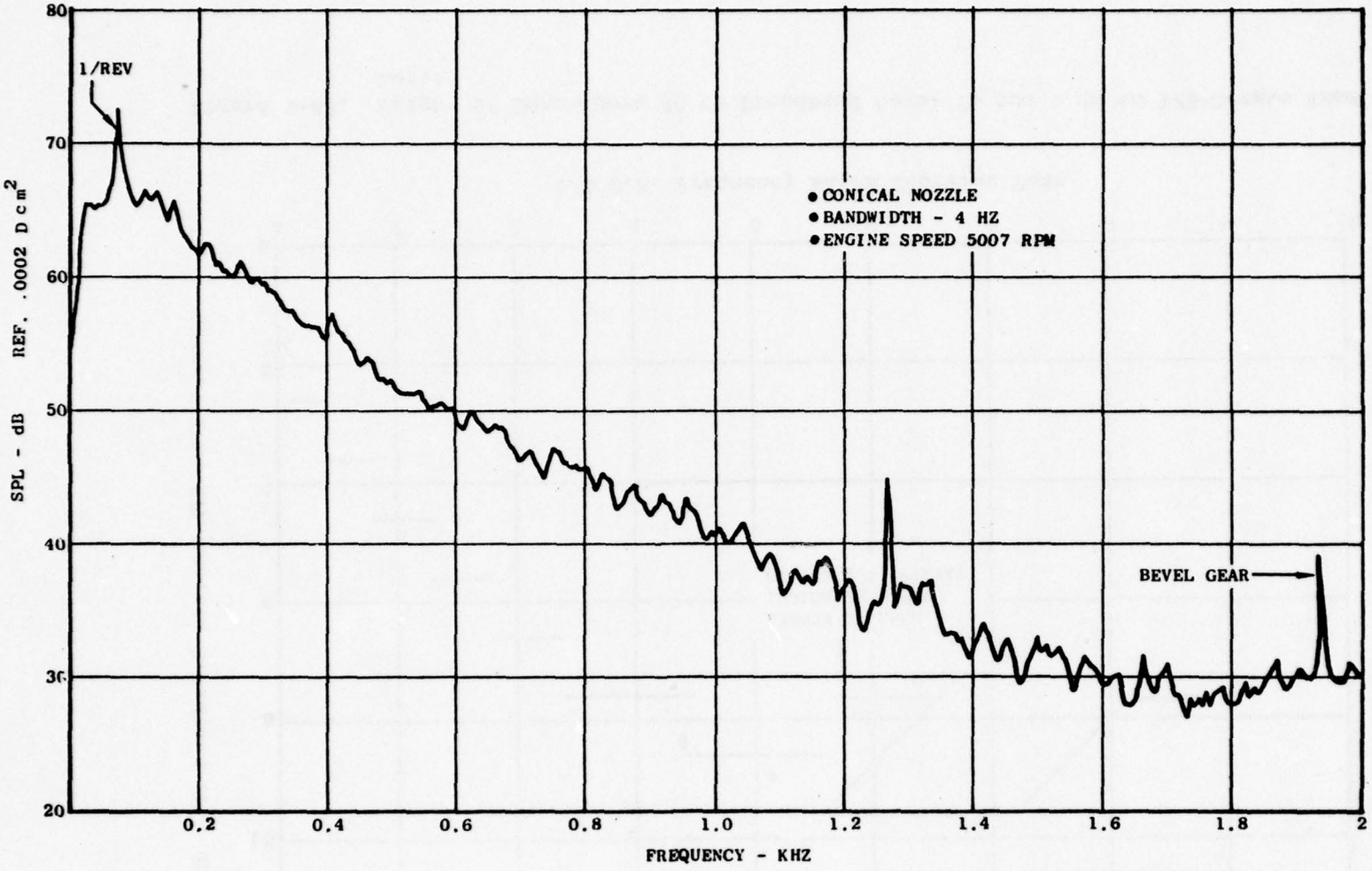


Figure 4-61. Narrowband of 60° (MIC-B) Low Microphone at GE/EFTC.

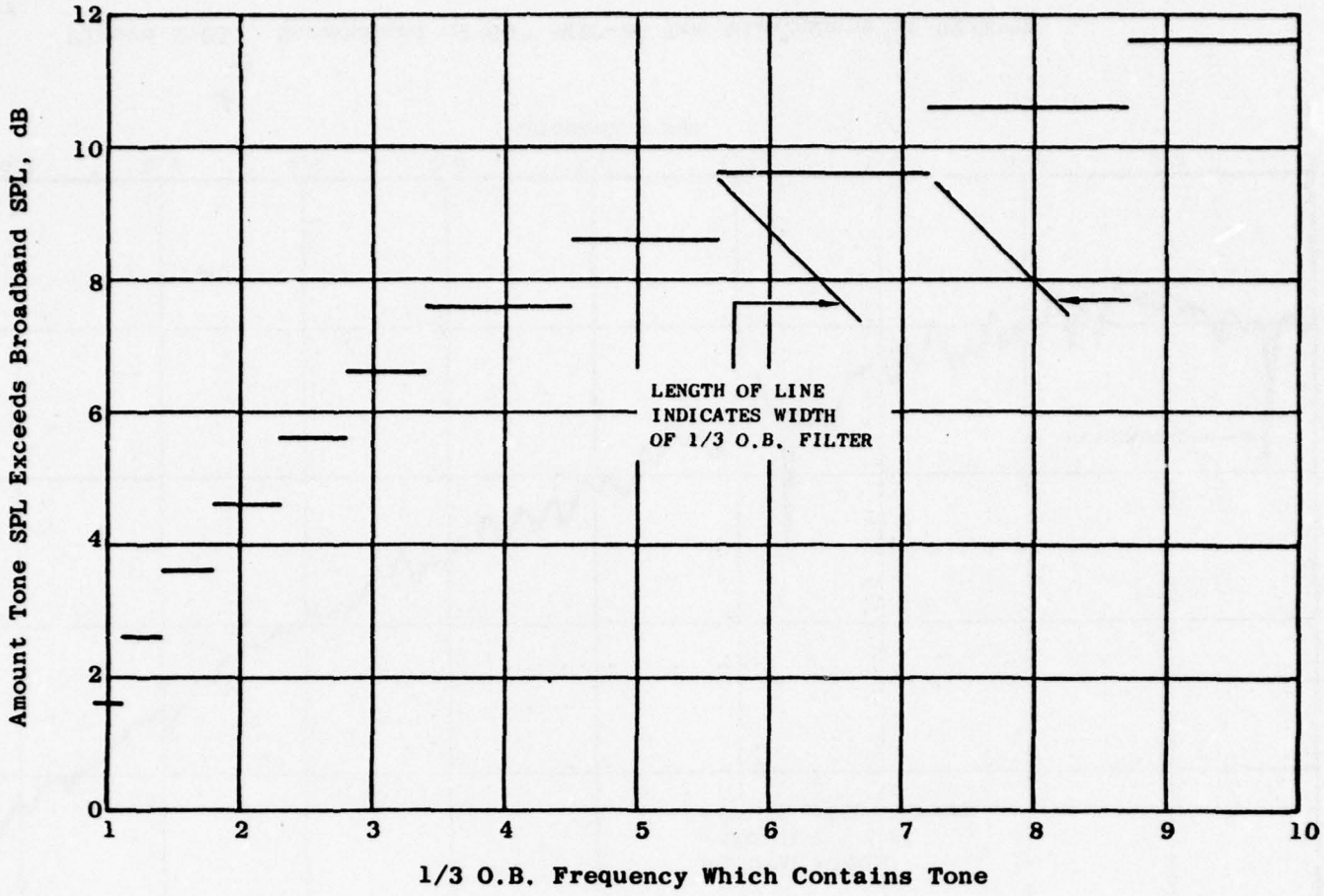


Figure 4-62. Height of Tone Above 40 Hz Broadband Level to Add 1 dB to 1/3-Octave Band Level.

harmonic frequencies, given in Tables 4-I and 4-II, provide the location (in frequency) of possible turbomachinery tones.

Using the above criteria, 40 Hz narrowband plots were inspected for turbomachinery tones. The most noticeable tones occurred at low speeds where the jet noise was low. The conical nozzle run showed tones at 2000 Hz and 10,000 Hz which appear to be from the radial bevel gear and the 13th through 15th compressor stages, respectively. The 4 Hz narrowband plots showed the presence of 1/rev and 2/rev tones, with these tones also affecting surrounding bands. Some unidentifiable tones were found in the 5000 rpm conical nozzle run: (V_j = 500 fps) at 630 Hz. These were corrected where it was felt they would severely compromise the accuracy of the PWL (Figure 4-63).

This procedure was performed on all the J79 spectra. As a final check for contamination, a plot of the J79 overall level versus jet velocity was made. Figure 4-64 shows that the 5000 rpm (V_j = 500 fps point falls well above classical theory. It appears that this point is contaminated by both turbomachinery tones and broadband noise. Combustor noise may also be present. Useable jet noise spectra from the J79 engine, therefore, is limited to points above idle which began at a jet velocity of 750 fps.

4.11 MECHANICALLY RADIATED NOISE

The mufflers previously described are effective in eliminating the noise which propagates with the flow out the exhaust nozzle (and inlet on the J79). However, noise within the piping may be transmitted through the casing walls and radiate to the sound field. The anechoic rooms at USC and UBC have the valving and lead-in piping external to the room. Except for the inlet plenum walls, there exists no possibility for mechancially radiated noise. At JENOTS, all the air supply lines were wrapped with acoustically absorbing lead material to eliminate the possibility of pipe noise escaping through the walls of the air supply lines. All elbows in the air supply lines were packed with acoustically absorbing material to minimize the generation of turning noise. The effectiveness of these design modifications were discussed in Section 4.8 where the nozzle was removed and the nozzle-on weight flows were simulated. Under these conditions, any mechanically radiated noise would have showed up in the spectra.

On the J79 engine, a casing suppressor was especially designed and installed for this program. It consisted of a lead-lined plywood box fitted around the engine, as shown in Figures 3-40 and 3-41. Near-field casing microphones were located as shown in Figure 4-65 in order to determine the effectiveness of the lead casing box. Figures 4-66 and 4-67 are narrowband plots of the front (2) and back (3) microphone, respectively. These plots are typical of all engine speeds run and show that the box is effectively attenuating the turbomachinery tones propagating through the casing. The resulting broadband level is believed to be propagating around the box, i.e., jet noise or core noise from the exhaust or inlet ducts.

Table 4-I. J79-15 Engine Noise Components.

COMPONENT		ENGINE SPEED 5040 RPM Fund		5040 RPM 2nd Harm		5040 RPM 3rd Harm	6550 RPM Fund	6550 RPM 2nd Harm	6550 RPM 3rd Harm
Compressor	1st Stage	1765		3540		5295	2295	4590	6885
	2nd Stage	2270		4540		6810	2950	5900	8850
	3rd Stage	2520		5040		7560	3270	6540	9810
	4th Stage	3275		6550		9825	4260	8520	12780
	5th Stage	3570		7740		11610	5030	10060	15090
	6th Stage	4120		8240		12360	5350	10700	16050
	7th Stage	4860		9720		14580	6320	12640	18960
	8th Stage	5120		10240		15360	6650	13300	19950
	9th Stage	5290		10580		15870	6870	13740	20610
	10th Stage	7810		15620		23430	10150	20300	30450
	11th Stage	7980		15960			10370	20740	
	12th Stage	8140		16280			10580	21160	
	13th Stage	9650		19280			12530	25060	
	14th Stage	9740		19480			12660	25320	
	15th Stage	10150		20300			13190	26380	
	16th Stage	10000		20000			13000	26000	
	17th Stage	10150		20300			13190	26380	
Turbine	1st Stage	6220		12440		18660	8070	16140	24210
	2nd Stage	4790		9580		14370	6230	12460	18690
Inlet Gear Box									
Radial Bevel Gear		1930	23	3860	46	5790	2510	5020	7530
Transfer Gear Box									
Radial Bevel Gear		1930	23	3860	46	5790	2510	5020	7530
Tach. Gen Gear		1750	20.3	3410	40.6	5115	2220	4440	6660
Fuel Pump Gear		1705	20.3	3410	40.6	5115	2220	4440	6660
Cont. Alt. Gear		4080	48.15	8160	97	12240	5300	10600	15900

Table 4-II. J79-15 Engine Noise Component Frequency Spectrum for Idle Speed, 5040 rpm.

Frequency - cps	Harmonic	Component
37	F	No. 1 Brg f_t
37	F	No. 2 Brg f_t
38.2	F	No. 3 Brg f_t
74	2	No. 1 Brg f_t
74	2	No. 2 Brg f_t
76.4	2	No. 3 Brg f_t
84	F	No. 1, 2, 3 Brg f_r
111	3	No. 1 Brg f_t
111	3	No. 2 Brg f_t
114.6	3	No. 3 Brg f_t
134	F	No. 3 Brg Scav Pump
167	F	Rear Gearbox Scav Pump
168	2	No. 1, 2, 3 Brg f_r
172	F	Main Lube Pump
250	F	Tran Gearbox Scav Pump
252	3	No. 1, 2, 3 Brg f_r
268	2	No. 3 Brg Scav Pump
318	F	Nozzle Pump
334	2	Rear Gearbox Scav Pump
344	2	Main Lube Pump
402	3	No. 3 Brg Scav Pump
415	F	Main Fuel Pump
500	2	Tran Gearbox Scav Pump
501	3	Rear Gearbox Scav Pump
516	3	Main Lube Pump
636	2	Nozzle Pump
695	F	No. 2 Brg f_b
750	3	Trans Gearbox Scav Pump
788	F	No. 1 Brg f_b
830	2	Main Fuel Pump
851	F	No. 2 Brg f_2
902	F	No. 1 Brg f_2
910	F	No. 3 Brg f_b
954	3	Nozzle Pump
1055	F	RGB Tach Gen Gear
1070	F	No. 3 Brg f_2
1081	F	No. 2 Brg f_1
1115	F	No. 1 Brg f_1

Table 4-II. J79-15 Engine Noise Component Frequency Spectrum for Idle Speed, 5040 rpm (Continued).

Frequency - cps	Harmonic	Component
1120	F	TGB Scav Pump Gear
1245	3	Main Fuel Pump
1285	F	No. 3 Brg f_1
1390	2	No. 2 Brg f_b
1460	F	RGB Gear-Hor Shaft, Lube Pump, Fuel Control
1545	F	RGB Noz Act Pump Gear
1576	2	No. 1 Brg f_b
1705	F	TGB Hor Shaft, Fuel Pump, Tach Gen Gear
1765	F	Compressor 1st Stage
1800	F	A/B Fuel Pump
1702	2	No. 2 Brg f_2
1804	2	No. 1 Brg f_2
1820	2	No. 3 Brg f_b
1930	F	Inlet GB & TGB Radial Bevel Gear
2020	F	Main Fuel Control
2085	F	RGB Scav Pump Gear
2085	3	No. 2 Brg f_b
2110	2	RGB Tach Gen Gear
2140	2	No. 3 Brg f_2
2185	F	TGB Main Drive Gear #1
2230,2162	2	No. 1 and No. 2 Brg f_1
2240	2	TGB Scav Pump Gear
2270	F	Compressor 2nd Stage
2364	3	No. 1 Brg f_b
2520	F	Compressor 3rd Stage
2570	2	No. 3 Brg f_1
2553	3	No. 2 Brg f_2
2706	3	No. 1 Brg f_2
2730	3	No. 3 Brg f_b
2920	2	RGB Gears Hor Shaft, Lube Pump, Fuel Cont.
3090	2	RGB Noz Act Pump Gear
3165	3	RGB Tach Gen Gear
3210	3	No. 3 Brg f_2
3275	F	Compressor 4th Stage
3345,3243	3	No. 1 & 2 Brg f_1
3360	3	TGB Scav Pump Gear
3410	2	TGB-Gear Tach Gen, Fuel Pump, Hor Shaft
3445	F	TGB-Main Drive Gear #2
3530	F	Turbine 3 Stage
3530	2	Comp 1 Stage
3600	2	AB, Fuel Pump
3855	3	No. 3 Brg f_1

Table 4-II. J79-15 Engine Noise Component Frequency Spectrum for Idle Speed, 5040 rpm (Continued).

Frequency - cps	Harmonic	Component
3860	2	TGB & IGB Rad Bev Gear
3865	F	Compressor 5th Stage
4040	2	MF Control
4080	F	TGB Cont Alt Gear
4115	F	Compress 6th Stage
4170	2	RGB Scav Pump Gear
4370	2	Main Drive Gear #1
4380	3	RGB Gear Hor Shaft, Lube Pump, Fuel Cont.
4540	2	Compressor 2nd Stage
4635	3	RGB Noz Act Pump Gear
4790	F	Turbine 2nd Stage
4872	F	Compress 7th Stage
4945	F	TGB A/B Fuel Pump Gear
5040	2	Compress 3rd Stage
5115	3	TGB Gear-Tach Gear, Fuel P and Hor Shaft
5125	F	Comp 8th Stage
5290	F	Comp 9th Stage
5295	3	Comp 1st Stage
5400	3	A/B Fuel Pump
5790	3	IGB & TGB Rad Bev Gear
6060	3	MF Control
6220	F	Turbine 1st Stage
6255	3	RGB Scav Pump Gear
6550	2	Comp 4th Stage
6555	3	TGB Main Dr Gear #1
6810	3	Comp 2nd Stage
6890	2	TGB Main Dr Gear #2
7060	2	Turbine 3rd Stage
7560	3	Comp 3rd Stage
7730	2	Comp 5th Stage
7810	F	Comp 10th Stage
7980	F	Comp 11th Stage
8140	F	Comp 12th Stage
8160	2	TGB, Cont Alt Gear
8230	2	Comp 6th Stage
9580	2	Turbine 2nd Stage
9660	F	Comp 13th Stage
9744	2	Comp 7th Stage
9745	F	Comp 14th Stage
9825	3	Comp 4th Stage
9890	2	TGB AB Fuel Pump Gear
10000	F	Compressor 16th Stage
10165	F	15th and 17th Stage
10250	2	Compressor 8th Stage
10335	3	TGB Main Drive Gear #2
10580	2	Comp 9th Stage

Table 4-II. J79-15 Engine Noise Component Frequency Spectrum for Idle Speed, 5040 rpm (Concluded).

Frequency - cps	Harmonic	Component
10590	3	Turbine 3rd Stage
11595	3	Comp 5th Stage
12240	3	TGB Cont Alt Gear
12345	3	Comp 6th Stage
12440	2	Turbine 1st Stage
14370	3	Turbine 2nd Stage
14580	3	Comp 7th Stage
14835	3	TGB A/B Fuel Pump Gear
15360	3	Comp 8th Stage
15620	2	Comp 10th Stage
15870	3	Comp 9th Stage
15960	2	Comp 11th Stage
16280	2	Comp 12th Stage
18660	3	Turbine 1st Stage
19280	2	Comp 13th Stage
19480	2	Comp 14th Stage
20000	2	Comp 16th Stage
20300	2	15 and 17th Stage
23430	3	Comp 10th Stage

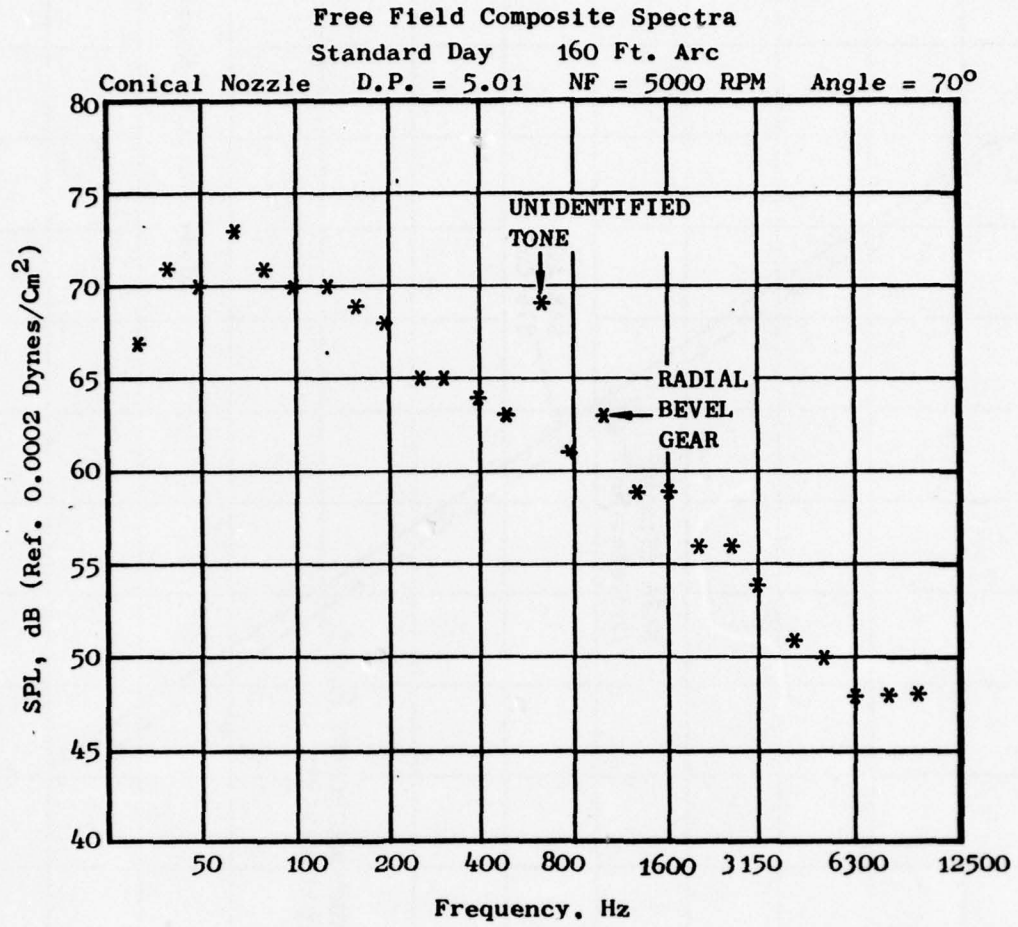


Figure 4-63. 1/3-Octave Band Composite Spectra of the 70° Station at Idle Speed for a Conical Nozzle at GE/EFTC.

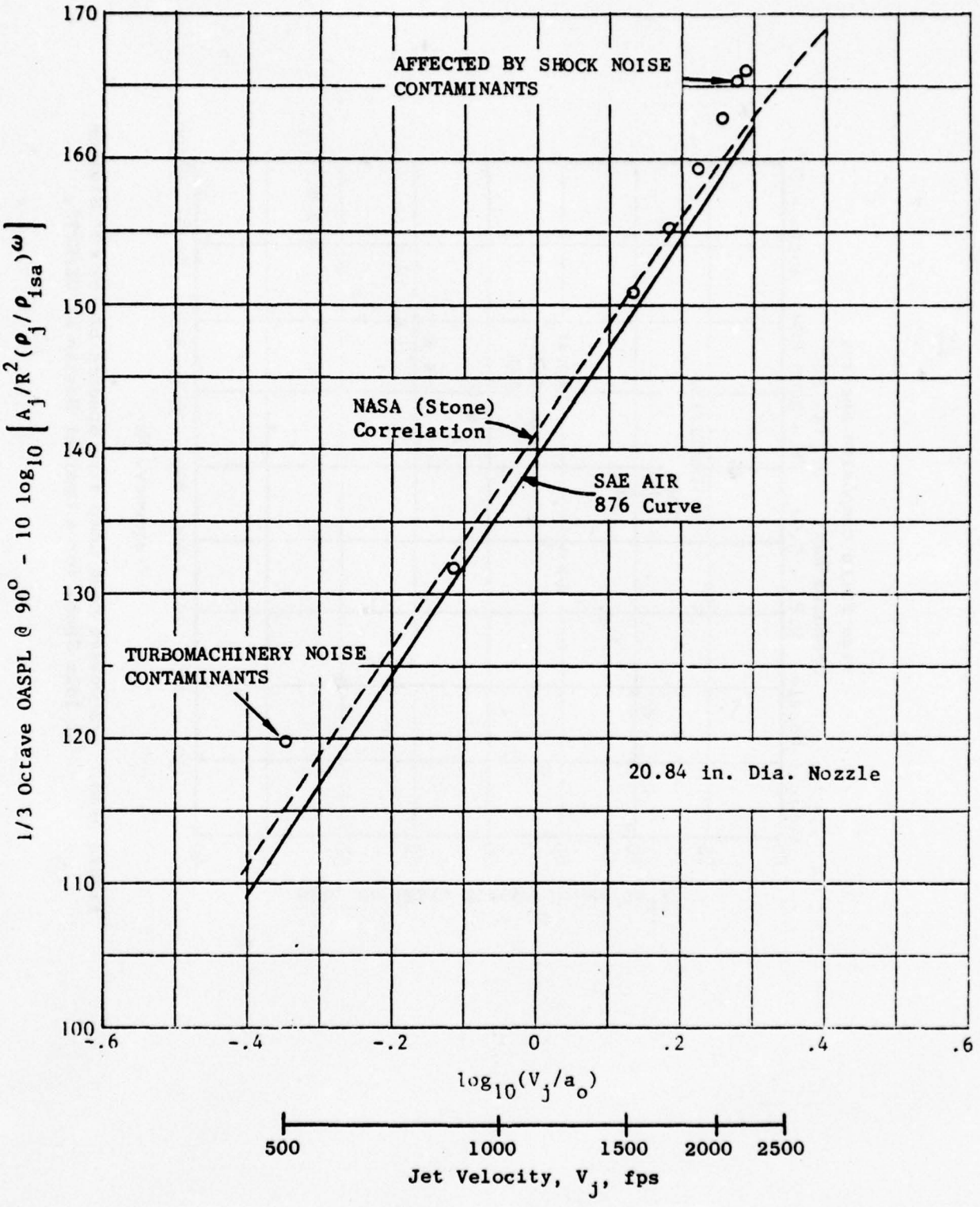


Figure 4-64. Velocity Dependence of Normalized Overall Sound Pressure Level at 90° for the J79 at GE/EFTC.

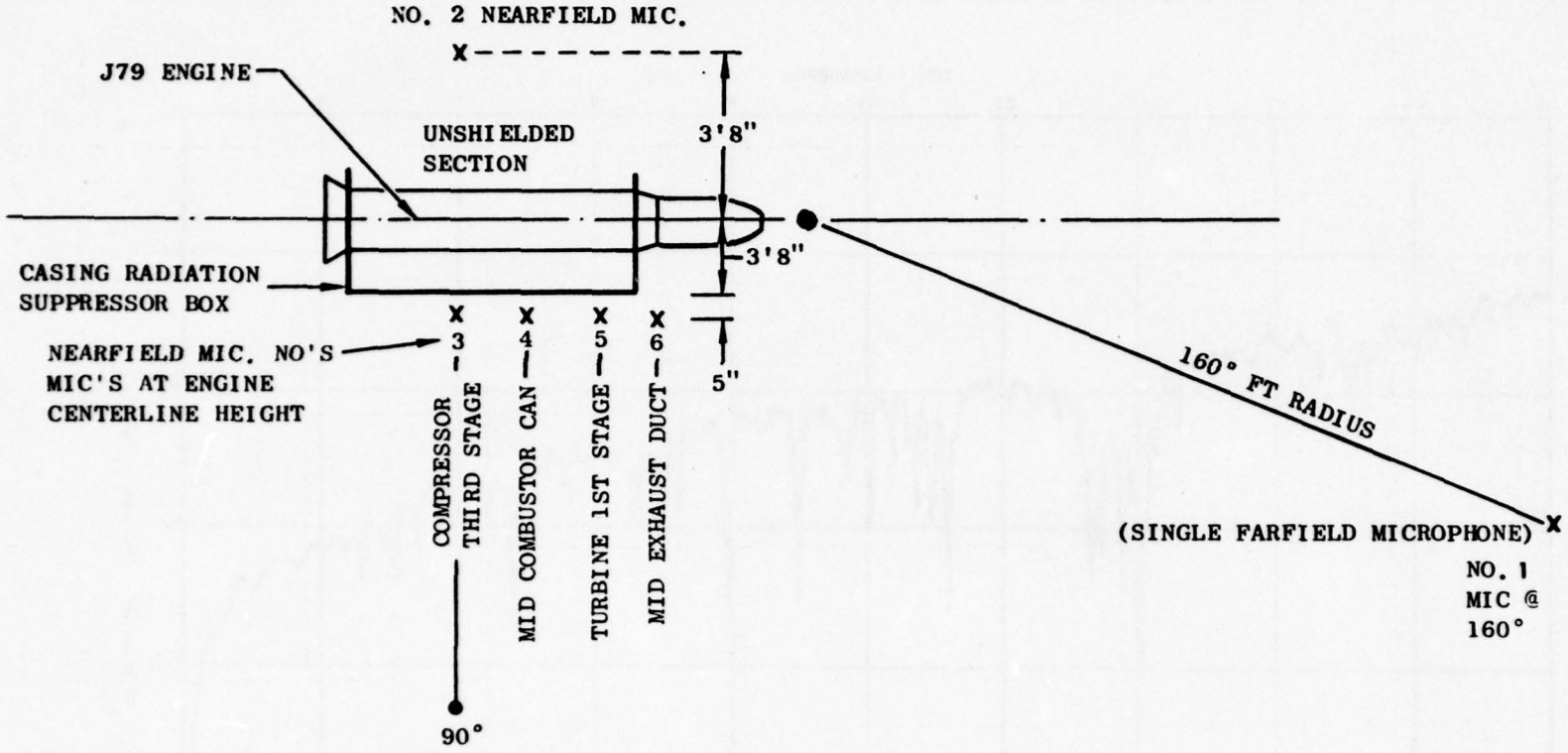


Figure 4-65. Near Field MIC Setup at GE/EFTC.

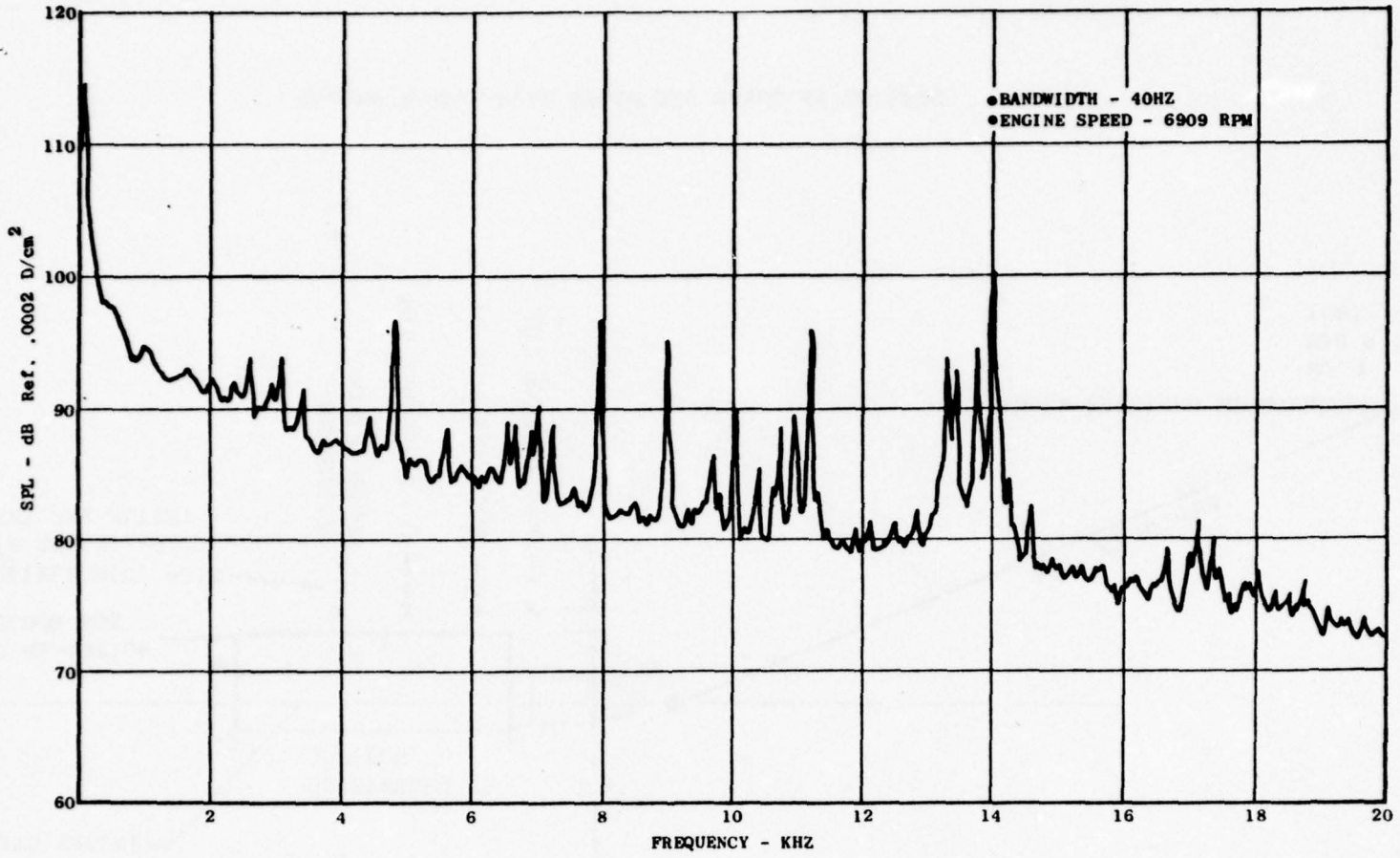


Figure 4-66. Narrowband of Near Field Microphone No. 2 at GE/EFTC.

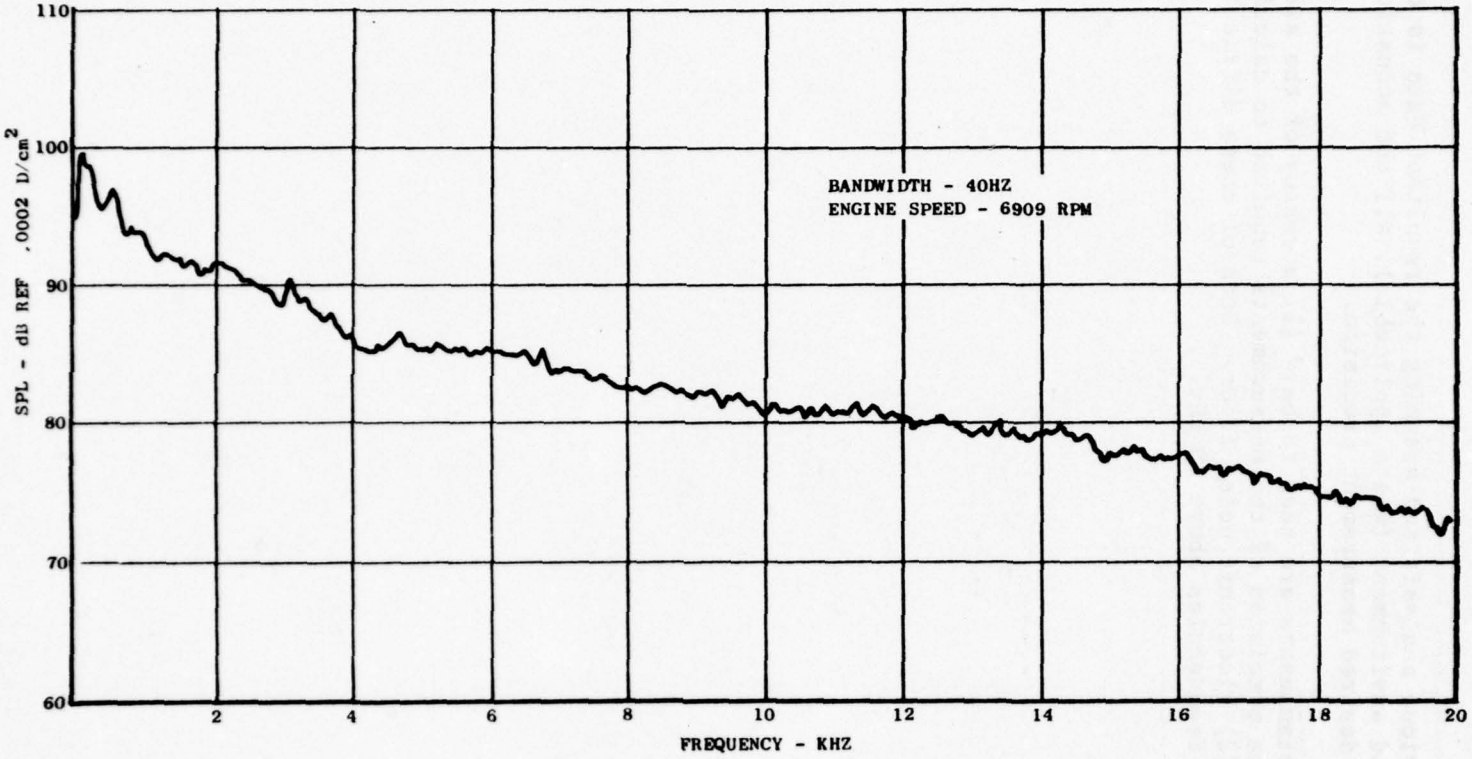


Figure 4-67. Narrowband of Near Field Microphone No. 3 at GE/EFTC.

4.12 SUMMARY

From the previous analysis and assuming the resultant data is corrected for a non-freefield environment (where applicable), all the acoustic facilities can meet the desired measurement precision.

The chief contaminants are seen to be: (1) accuracy of the air attenuation model and the precision of the measurements required to calculate air attenuation; and (2) electronic noise floor. Both of these difficulties are most important at frequencies above 20 kHz.

5.0 CORRECTIONS TO A FREEFIELD ENVIRONMENT

Each of the acoustic test facilities were required to deliver effective free-field data over the frequency range of interest. That is, the data must be free of ground and obstruction reflections and reverberations so that the sound decays as an inverse square law with distance from the source. Generally, one can divide the variation of sound in a room into the near field and far field of the source, as shown in Figure 5-1. Near the source, the sound level may vary in any fashion, but, ideally far away, the level should drop off 6 dB for every doubling of distance. In the presence of a significant number of reflections, a reverberant field may be encountered where the sound energy remains constant with distance from the source (as seen in Figure 5-1) due to the large number of reflection modes. The more common situation, however, is that only a few significant reflections occur and the sound field generally decays as $1/r^2$, but in an oscillatory fashion. In an anechoic room such as the USC and UBC chambers, the wedges are designed to eliminate any reflections. Therefore, when one is in the far field of the jet, inverse square law variation can be expected.

5.1 LOCATION OF THE MEASUREMENT ARC

Studies as to where the near field ends and the far field begins have been conducted on numerous type sources. Point and compact, low intensity sources, such as speakers, generally begin to follow the inverse square law after a quarter wavelength ($\lambda/4$) from the source. The distributed, high intensity, jet source does not give point source behavior until much further away. Testing with high velocity jets since the early 1950's has lead to the general criteria of five to eight wavelengths from the jet nozzle to the far-field measurement. Requiring the lowest frequency of interest to be one octave below the jet Strouhal peak on a Mach one jet leads to:

$$R_{FF} = N\lambda = 2N\lambda_{peak} = \frac{2ND_j}{M_j S_j} = 10\ ND_j \qquad (38)$$

where $N = 5 \rightarrow 8$

or $R_{FF} = 50 - 80\ D_j$

which is the often quoted rule of thumb for a measurement arc.

Figure 5-2 shows the variation of the OASPL with distance recorded in the UBC chamber at right angles of the jet axis. It would appear from this figure that, at least along the 90° ray, the near field (or initiation of far field) is experienced by 10 diameters. Assuming that the OASPL is controlled by the

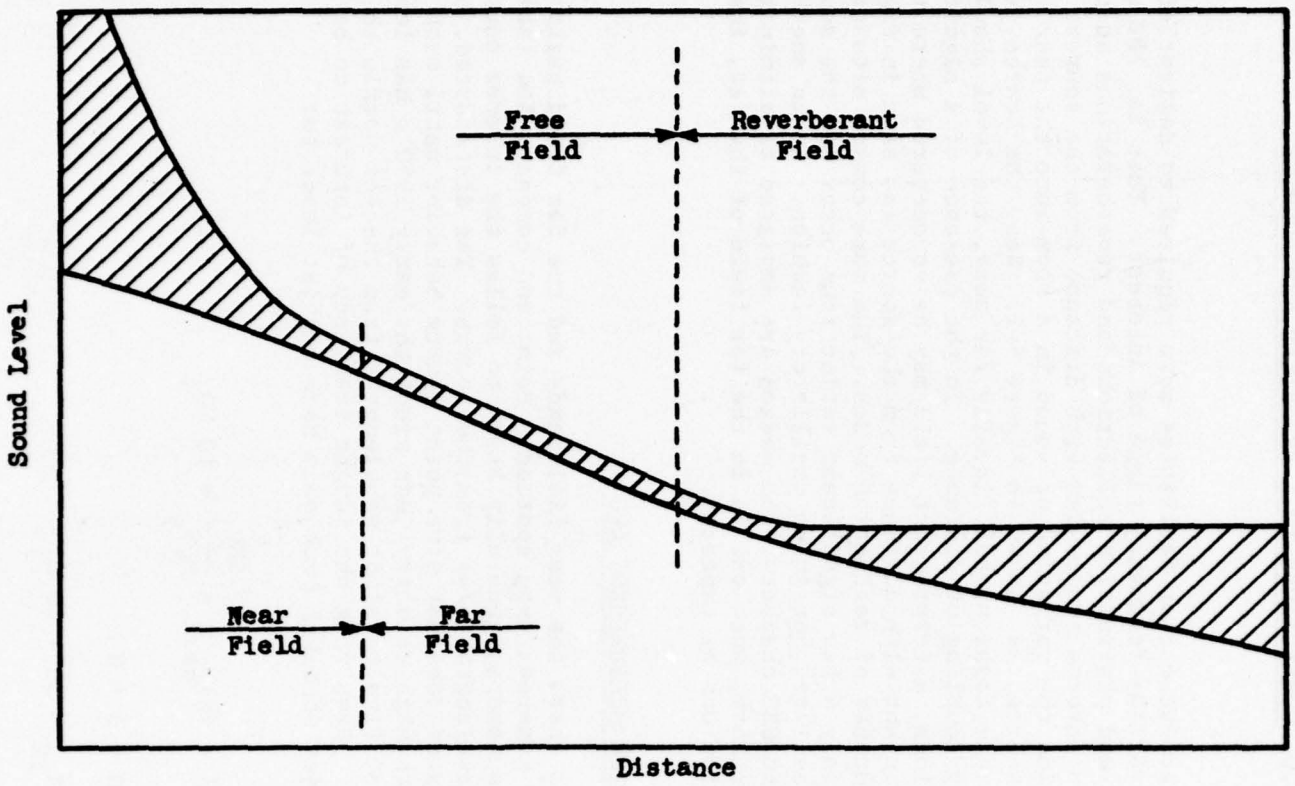


Figure 5-1. General Behavior of Sound with Distance from a Source.

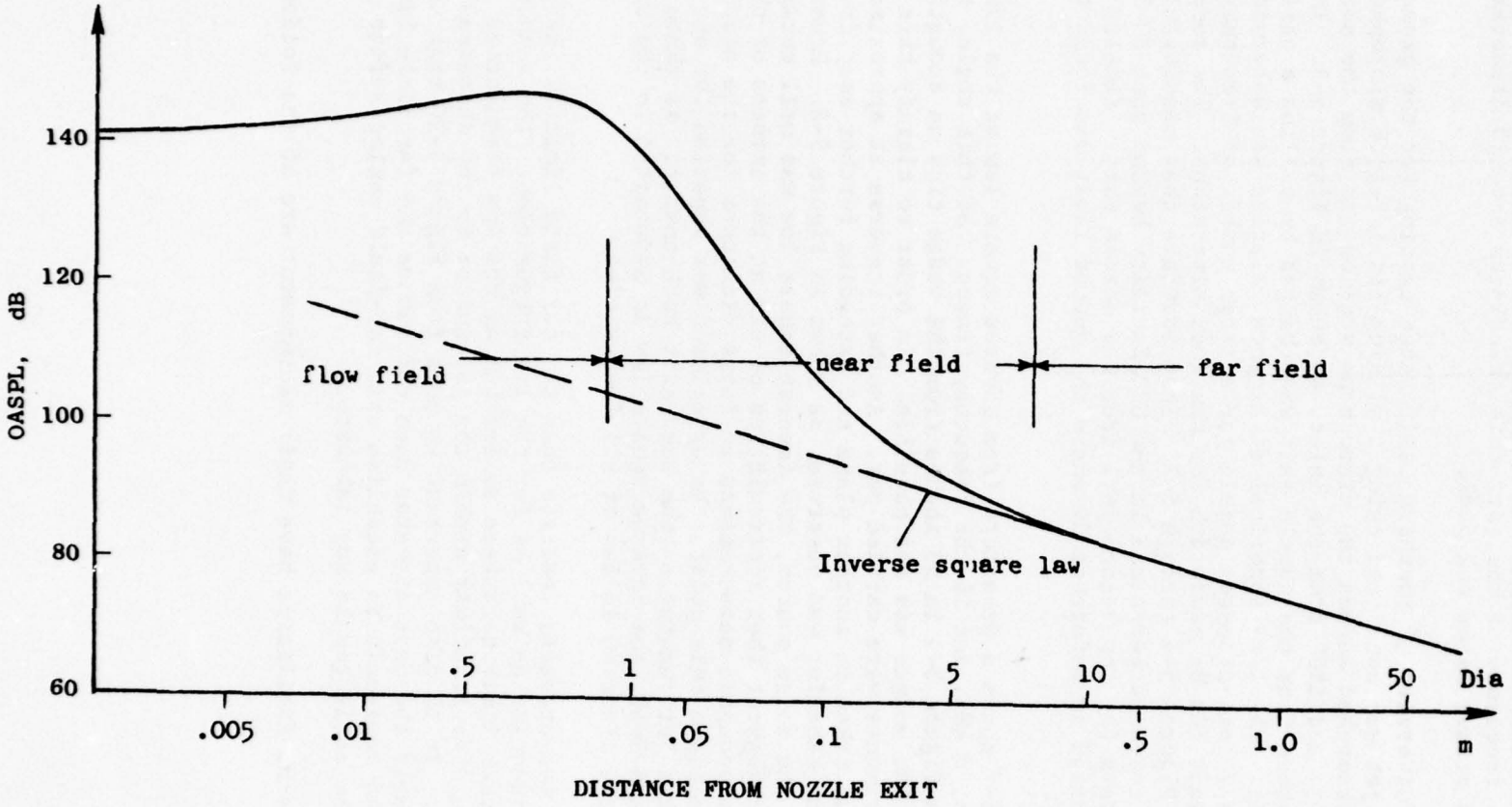


Figure 5-2. Variation of Pressure Fluctuation with Distance from Jet, Starting at 4 Diameters Downstream in the Jet and Proceeding at Right Angles to the Jet Axis at UBC.

peak Strouhal frequency of the jet, this translates into 20 diameters for the frequency one octave below the peak.

At the University of Southern California, testing for the geometric far field of the jet was conducted using a sliding B&K 1/2-inch microphone on a steel cable stretched across the microphone station ray from the nozzle at 70°, 90°, 120°, and 150° from the inlet, as shown in Figure 5-3. The distance of the microphone from the nozzle exit was changed by pulling a string attached to it. The $1/r^2$ spherical divergence relation was determined utilizing the 2-inch-diameter nozzle for a large number of frequency bands using a constant 100 Hz bandwidth for the four directions. The results are presented in Figures 5-4 through 5-7. They indicate that meaningful jet noise measurements could be performed in the USC facility beyond some 80-inches (or 40 diameters for the 2-inch jet) from the nozzle exit. Similar experiment has been reported in Reference 30 where the quoted limit was found to be 54 diameters.

Figure 5-7 shows a departure from inverse square law at the 150° station for the 5 kHz, 8 kHz, and 16 kHz frequency traces. At this angle, the fixed microphone on Figure 3-3 is 59 inches from the wedge tips so acoustic influence from the wedges was not possible. In order to clarify this discrepancy, further experiments were carried out. Another traverse at approximately the same angle was taken in another plane and extending further away from the jet exit. Similar behavior was observed, as shown in Figure 5-8. However, using a speaker as the noise source, the inverse square law was well established. These results suggest that recirculation of air at the corners of the room was affecting the acoustic measurements at large distances for the acute angle cases. To validate this point, the experiment was repeated for one case using a smaller jet running at the same exit Mach number. As shown in Figures 5-9 and 5-10, the inverse square law is maintained to the extent of the traverse after 80 inches at all frequencies.

The USC measurements indicate that the far field limit is the same for the high frequencies as well as for the low frequencies. The reason for the high frequencies limit to extend as far out as the low frequencies is because of refraction effects either within the jet and/or by the entrained air at the jet boundary. It is also important to note from Figure 5-10 that using a nozzle with half the exit diameter does not reduce the far field limit by two. Thus, it seems advisable to establish this far-field region before jet noise data are to be collected in any laboratory.

The present facilities have their measurement arc at the following locations:

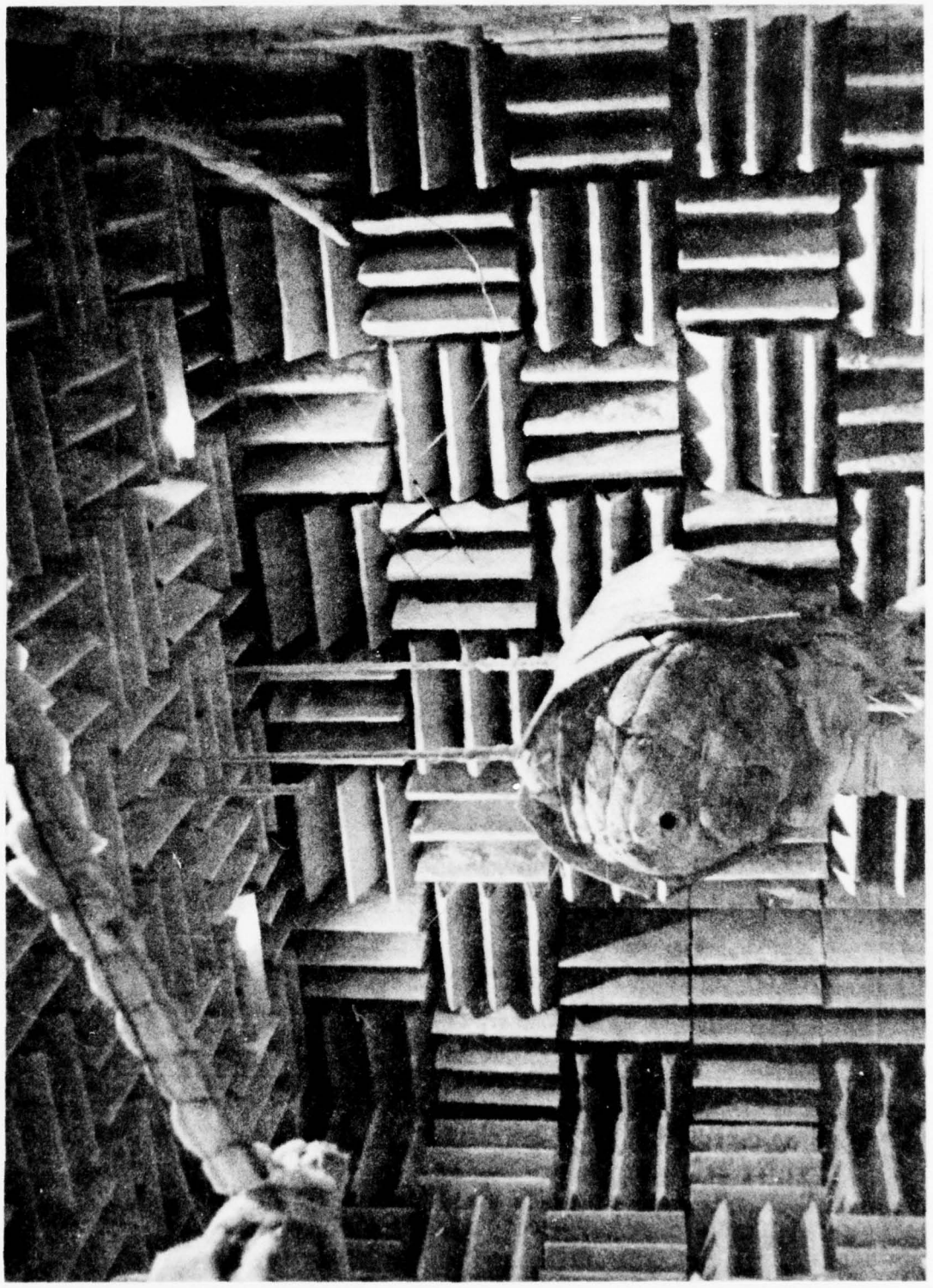


Figure 5-3. Arrangement of Cable and Microphone for Spherical Divergence Test at USC.

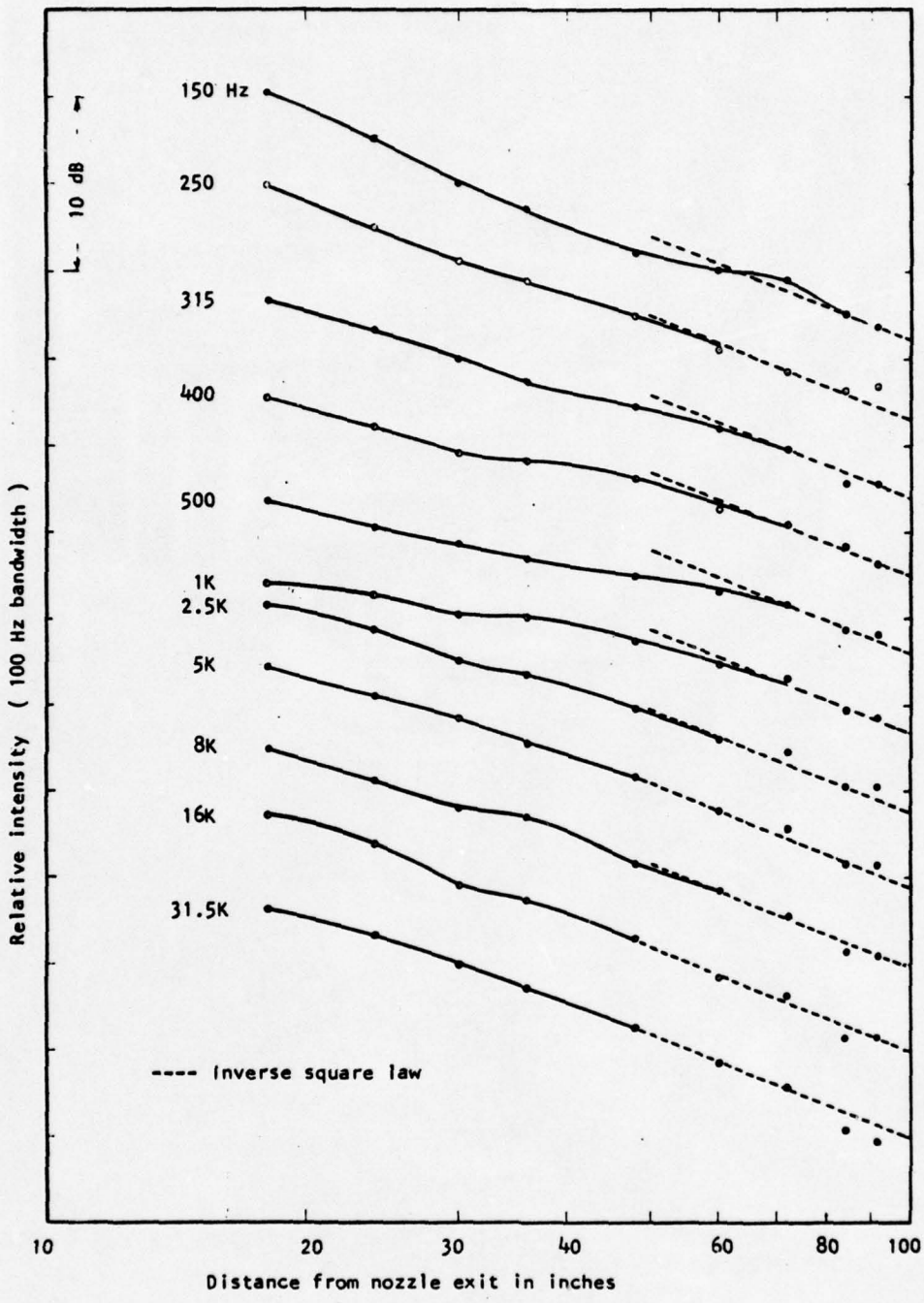


Figure 5-4. Intensity-Distance Plots with a 2-inch Cold Jet, $M_j = 0.85$, $\theta_I = 70°$ at USC.

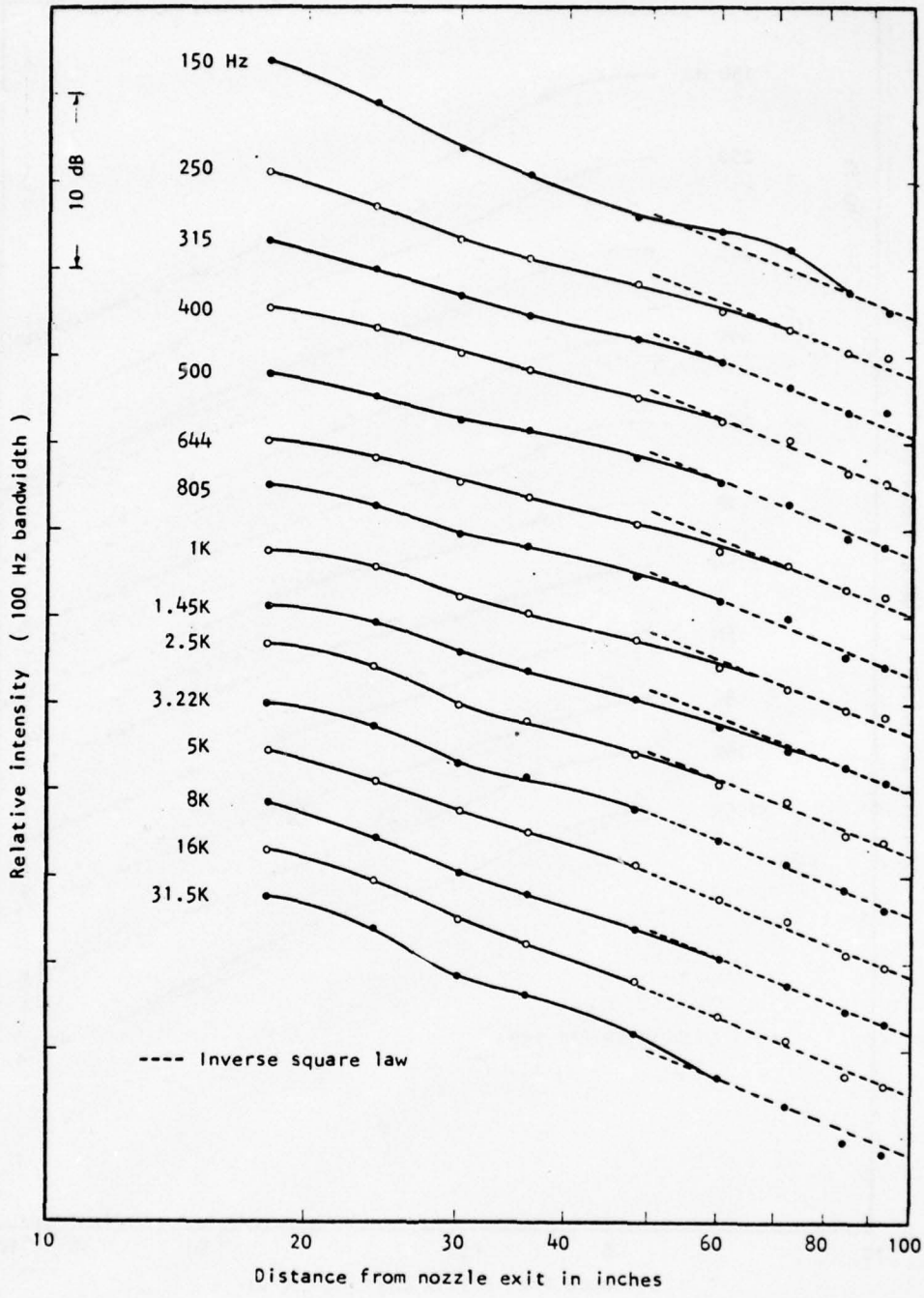


Figure 5-5. Intensity-Distance Plots with a 2-inch Cold Jet, $M_j = 0.85$, $\theta_I = 90°$ at USC.

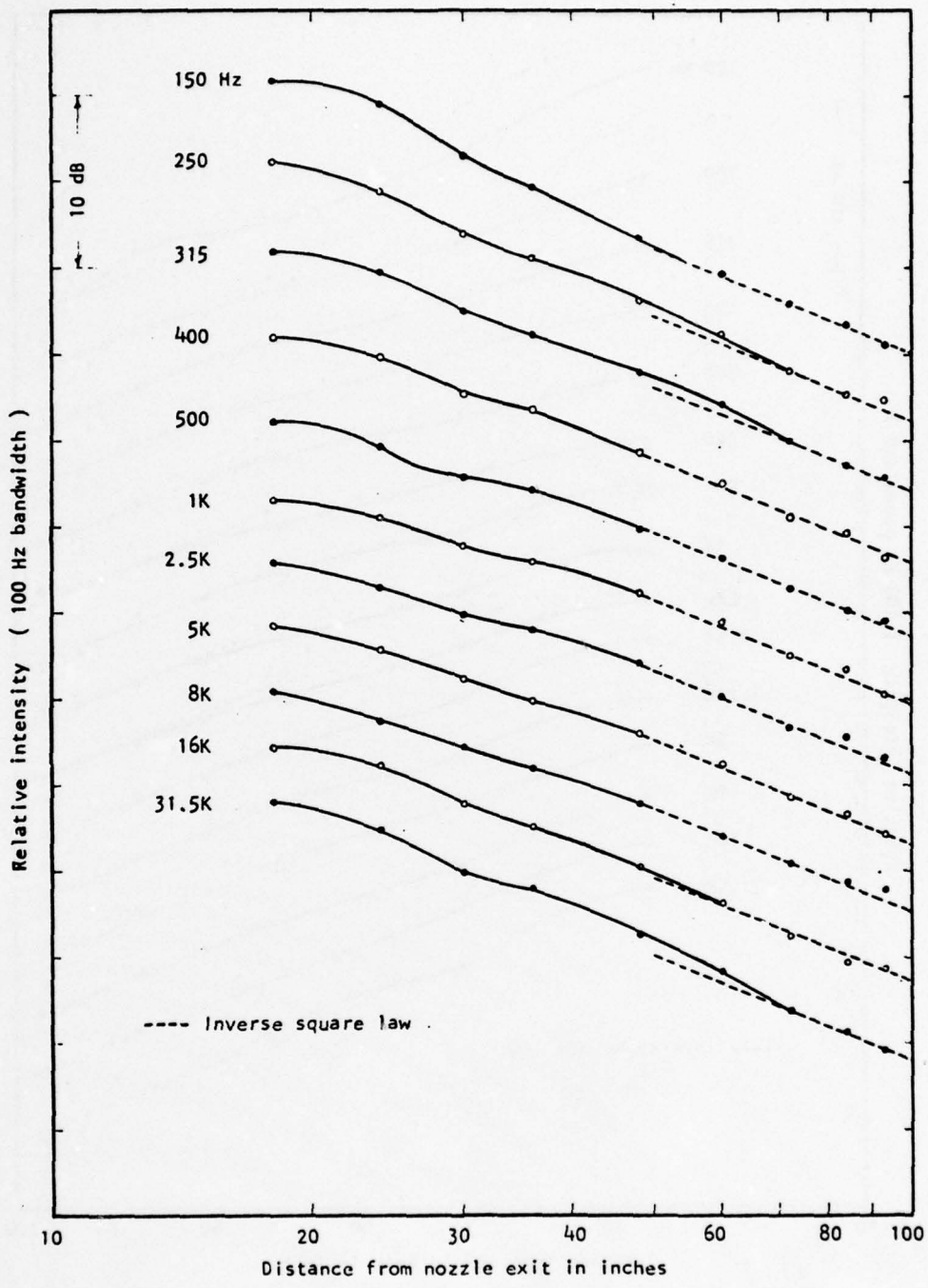


Figure 5-6. Intensity-Distance Plots with a 2-inch Cold Jet, $M_j = 0.85$, $\theta_I = 120°$ at USC.

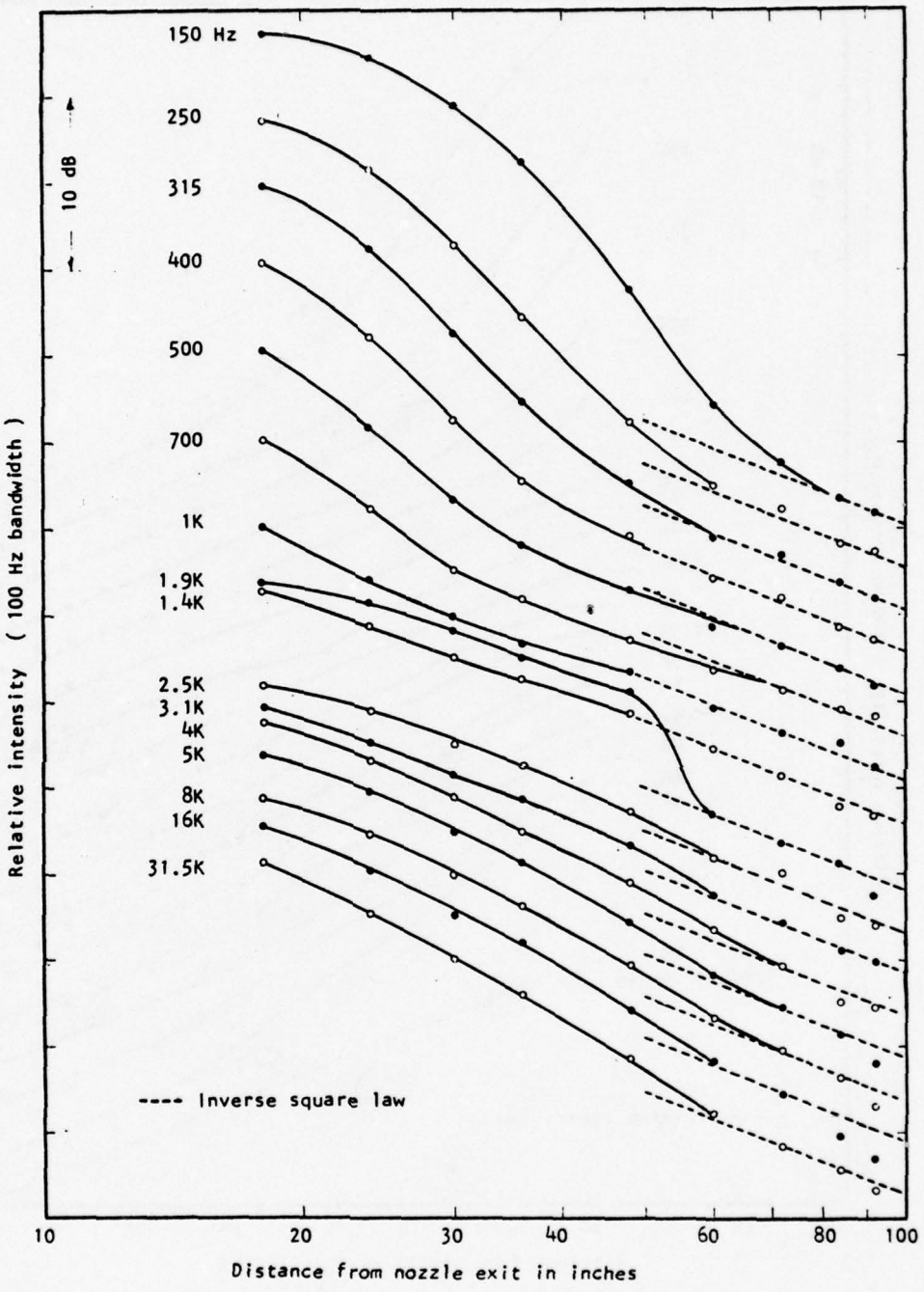


Figure 5-7. Intensity-Distance Plots with a 2-inch Cold Jet, $M_j = 0,85$, $\theta_I = 150°$ at USC.

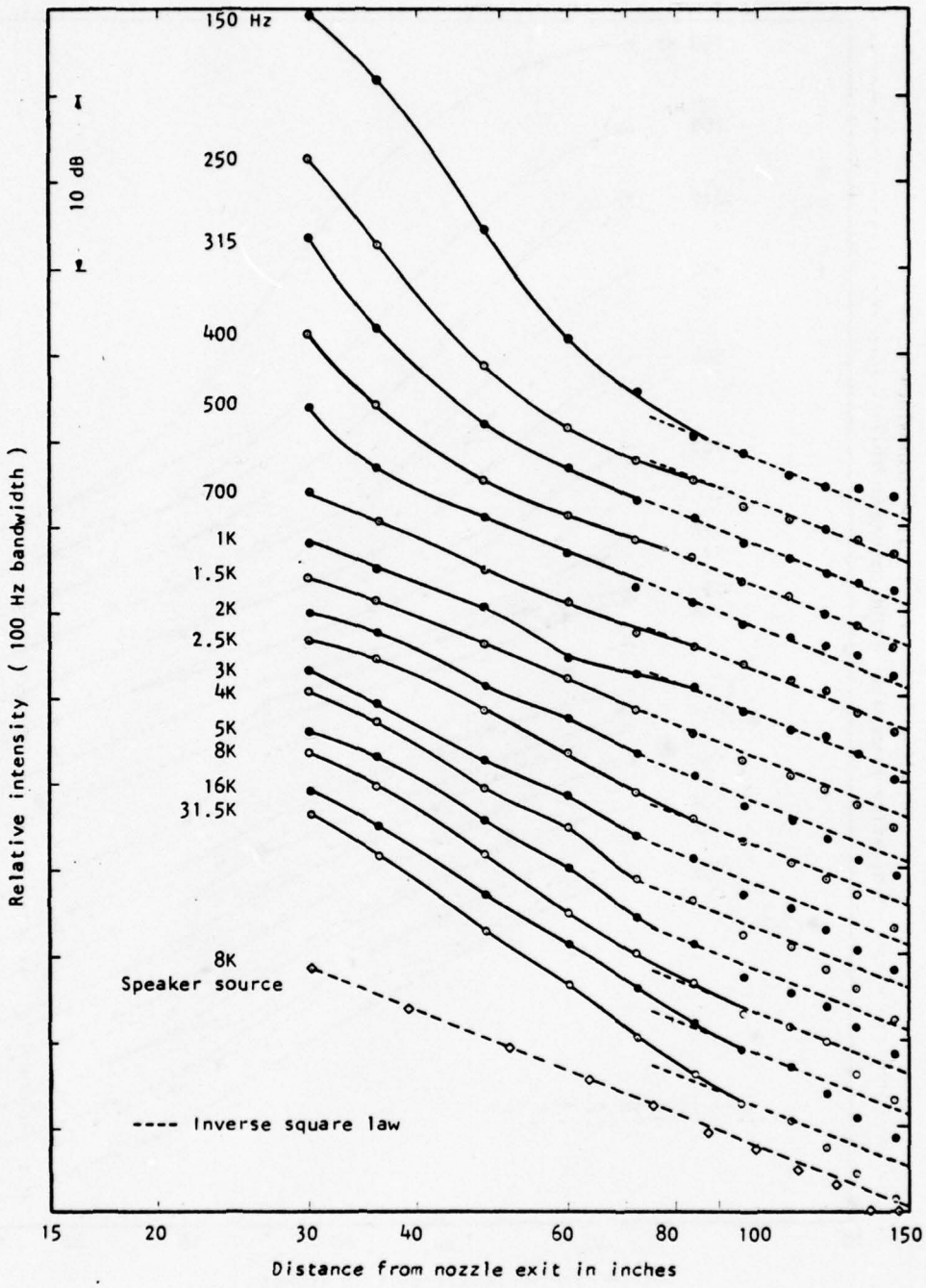


Figure 5-8. Intensity-Distance Plots with a 2-inch Cold Jet, $M_j = 0.85$, $\theta_I = 152°$ at USC.

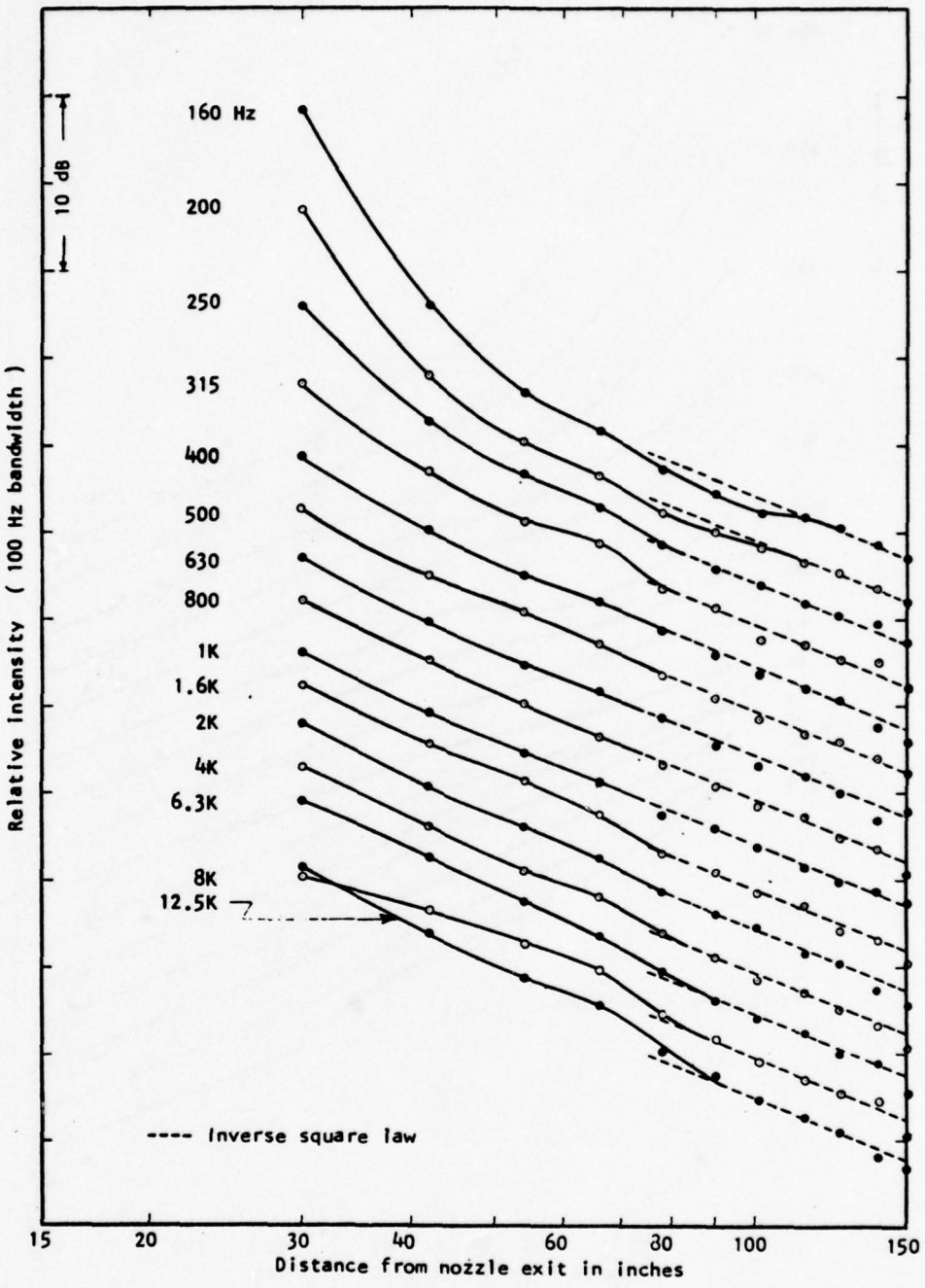


Figure 5-9. Intensity-Distance Plots with a 2-inch Cold Jet, $M_j = 0.85$, $\theta_I = 153°$ at USC.

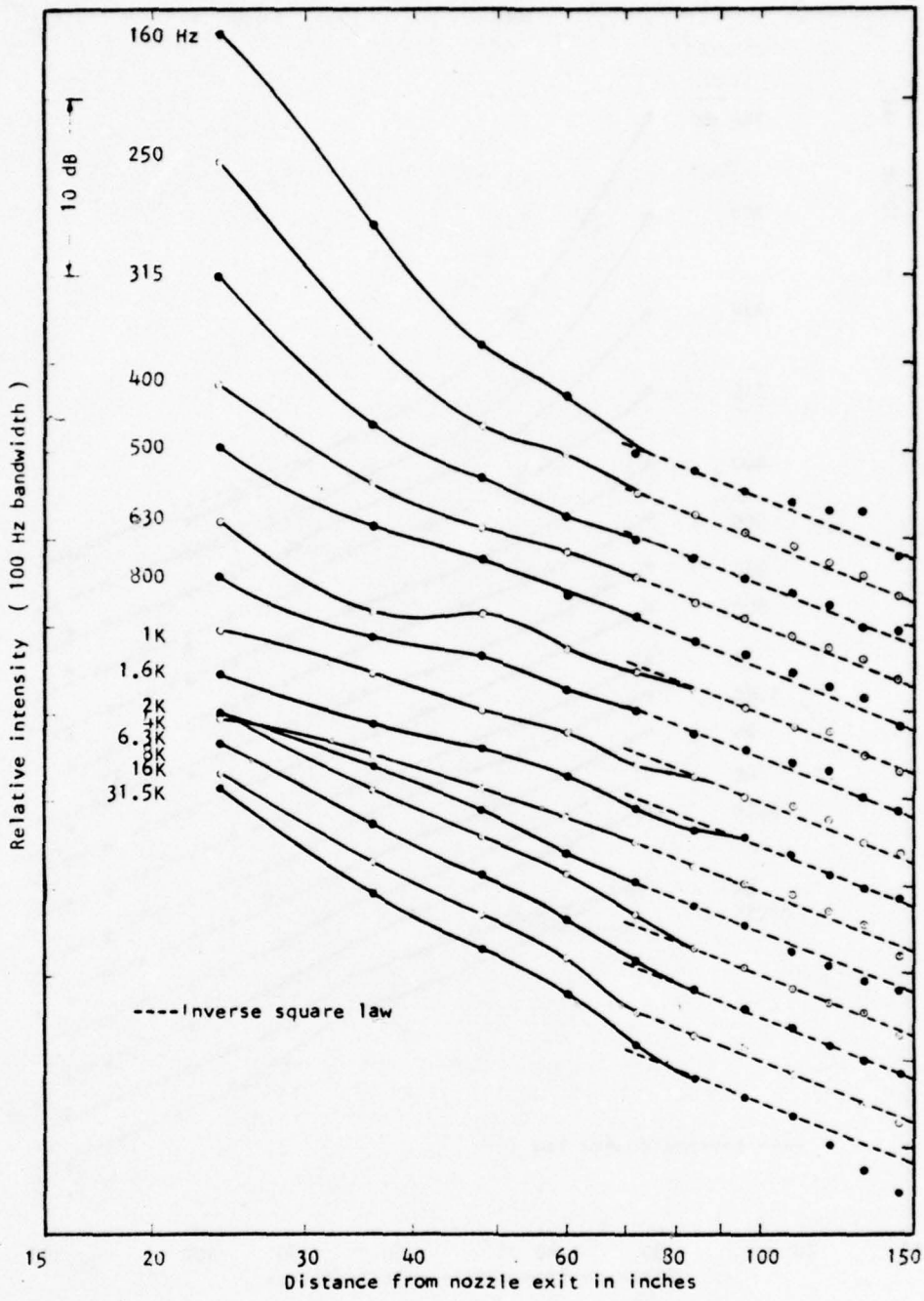


Figure 5-10. Intensity-Distance Plots with a 1-inch Cold Jet, $M_j = 0.85$, $\theta_I = 153°$ at USC.

Facility	Largest Jet Diameter (D) (inches)	Measurement Arc (R) (feet)	R/D
USC	2.0	7.5	45.0
UBC	0.787	10.0	152.5
JENOTS	6.0	40.0	80.0
CR&DC	2.0	9.0	54.0
J79/EFTC	20.84	160.0	92.1

5.2 GROUND REFLECTIONS

The two anechoic facilities have the advantage of an anechoic environment for their jet noise work. The three outdoor facilities, however, have a ground plane which is an efficient reflection surface. The approach towards converting the facility data to free field was different with each of the facilities.

At JENOTS, the approach was to elevate the microphones to a height above the ground so that the first ground null was below the lowest frequency of interest. Semiempirical correction factors, which included the effect of the ground impedance, jet scattering phenomenon, and distributed jet source, were determined and applied to the data to remove the remaining ground effects.

At CR&DC, a rotating microphone boom shown in Figure 3-25 for use in measuring nonaxisymmetric nozzle configurations is rotated to its directly overhead position. Eight inches of acoustic foam is then placed on the ground underneath the jet and in the surrounding acoustic arena. The resulting reflection pattern is found to have a less than 1 dB contribution to the spectra and can be effectively ignored. Microphone boom and support structure saddle potential reflection problems are examined in Section 5.11.

At GE/EFTC, the J79 installation utilized two microphones, placed at the same radius, but at different distances from the ground, giving reflection patterns of nulls and reinforcements in different frequency ranges. The two spectra were corrected using the equations for the effect of ground reflections for a finite impedance ground on a distributed jet source. The most accurate frequencies ranges from the two microphones were combined to give a single, accurate, free-field composite spectrum.

5.3 GROUND REFLECTION THEORY

The mean square pressure which is measured in the presence of a reflecting plane is the time average of the square of the sum of the direct wave and the reflected wave which simultaneously arrive at the microphone. The geometry is shown in Figure 5-11. The reflection index from a broadband point source under 1/3-octave filtering is given by (References 31 through 34).

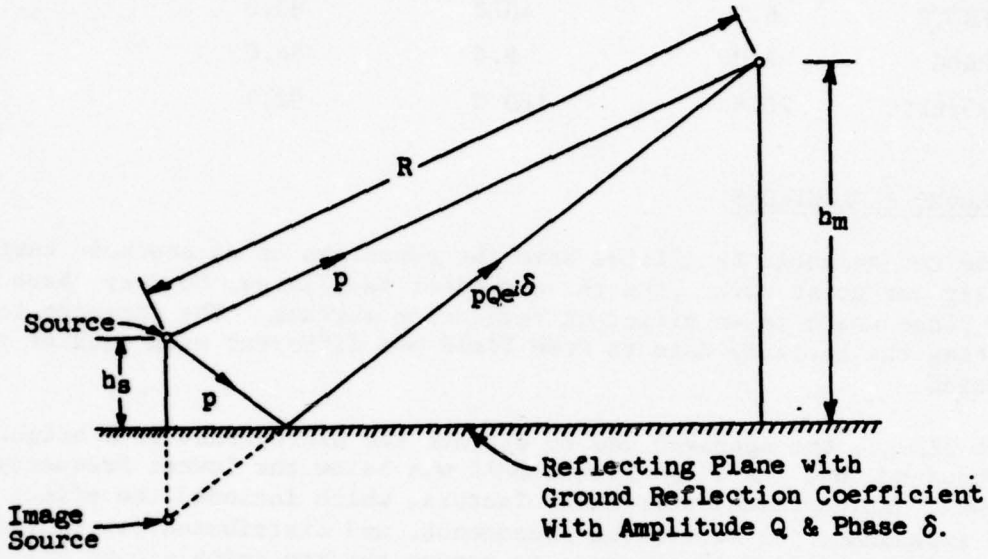


Figure 5-11. Sound Field Geometry.

$$\Delta N = 10 \log_{10} \left[1 + \frac{Q_i^2}{Z^2} + 2 \frac{Q_i}{Z} \frac{\sin\left(\alpha \frac{\Delta r}{\lambda_i}\right)}{\left(\alpha \frac{\Delta r}{\lambda_i}\right)} \cos\left(\frac{\beta \Delta r}{\lambda_i} - \delta_i\right) \right] \qquad (39)$$

where

α = 0.7257079

β = 6.3249559

λ_i = Wave length of the ith 1/3-octave band

Q_i = Ground reflection coefficient in the ith 1/3-octave band

δ_i = Ground reflection phase in the ith 1/3-octave band

The parameters Δr and z are calculated from the direct path length R and reflected path length as:

$\Delta r = r - R$ = difference in the path lengths

$Z = r/R$ = ratio of the path lengths

These relations can be expressed in terms of the sound field geometry of Figure 5-11 as:

$$Z = \sqrt{1 + 4(h_m/R)\ (h_s/R)} \qquad (40)$$

$$\Delta r = R(Z - 1) \qquad (41)$$

Figure 5-12 is a convenient working curve for rapid estimates of Z and Δr given the direct acoustic path length, R, the microphone height, h_m, and the source heights, h_s. The theoretical reflection indices calculated from Equation (39) for perfectly hard reflector ($Q_i = 1$ & $\delta_i = 0$) are shown in Figure 5-13. These curves have a number of important features. The low frequencies below the first cancellation null is characterized by a smooth almost constant reinforcement. With $Z \simeq 1.0$ one obtains the ideal 6 dB doubling expected with the summing of two identical sources. The cancellation nulls are seen to occur at odd integer multiples of $\Delta r/\lambda_i = 0.5$. So, for example, the frequency of the first null is calculated from:

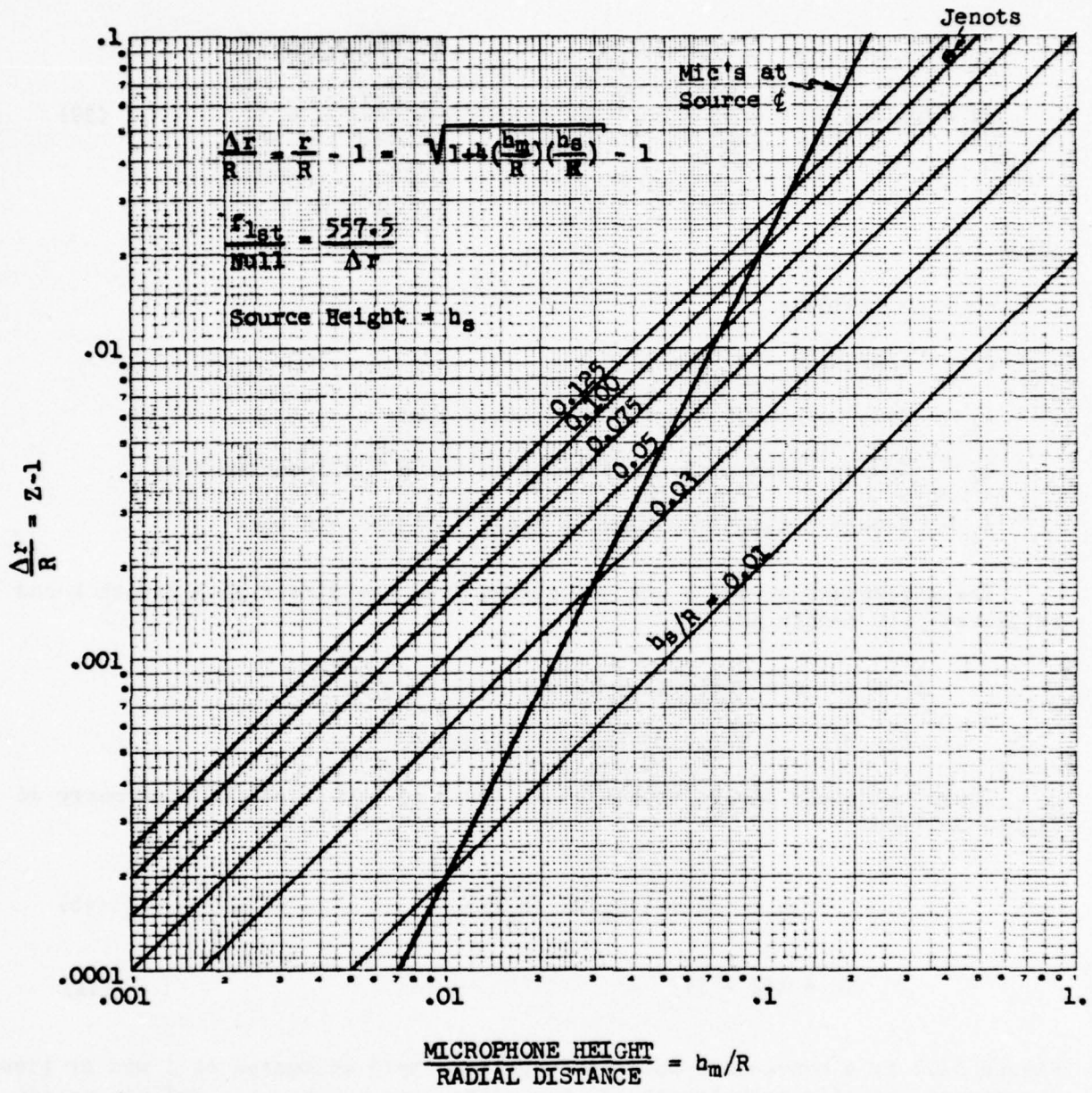


Figure 5-12. Working Curve for Calculating Null Frequency.

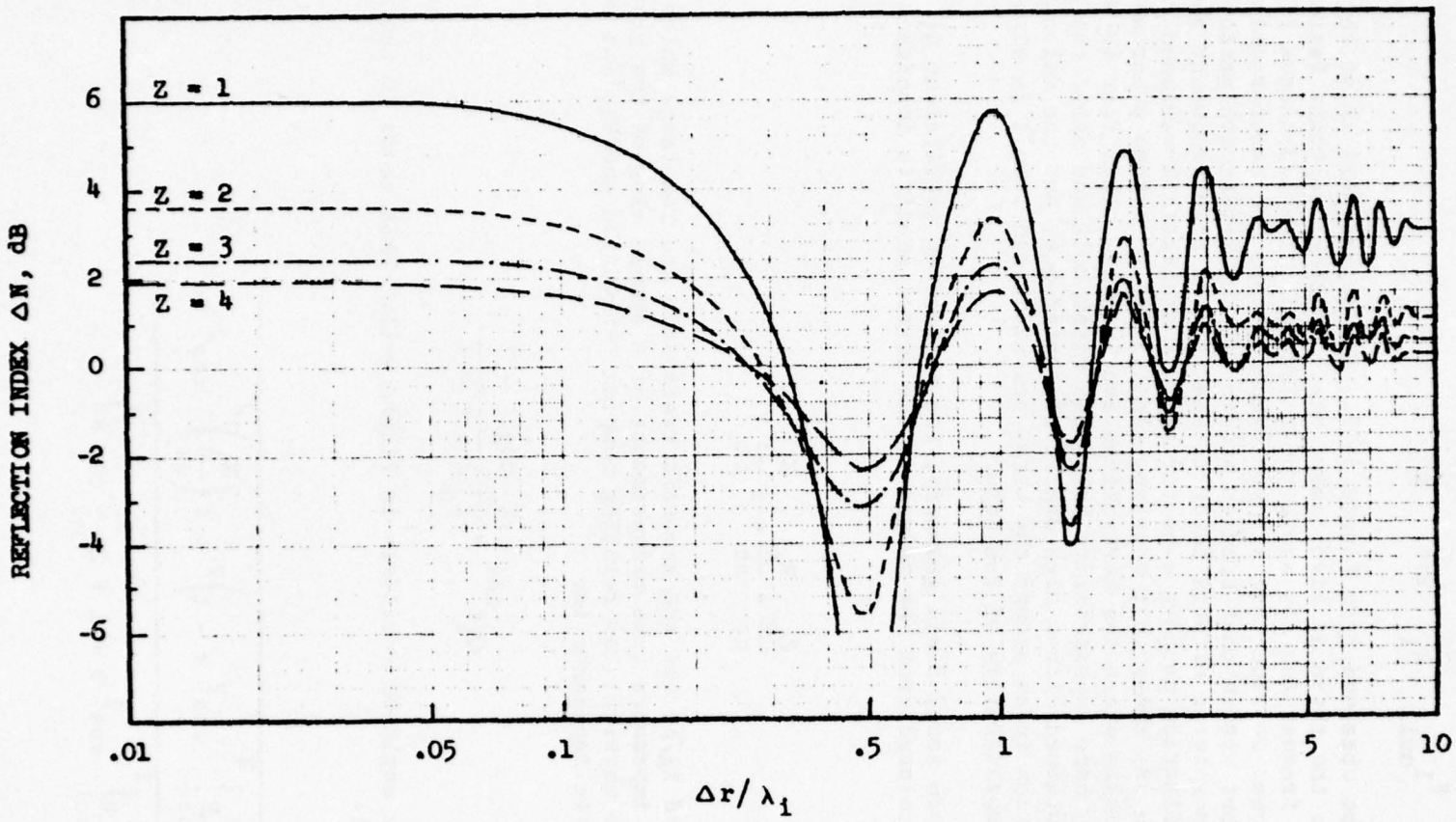


Figure 5-13. Theoretical Reflection Indices (1/3-Octave Bands) (Point Source over a Reflecting Surface).

$$f_{1_{null}} = \frac{C}{\lambda_i} = \frac{C}{2\Delta r} = \frac{557.5}{\Delta r} \tag{42}$$

where Δr can be obtained from Figure 5-12. The second null is at three times the frequency: the third at five times, etc. Another important feature is that, at high frequencies say above the third null, the 1/3-octave filter bandwidth becomes so wide that all the cancellations and reinforcements average together within that band to smooth out the reflection pattern. In practice, atmospheric effects tends to scatter the high frequency sound and smooth the reflection pattern even further. A statistical variance calculation (Equation 39) shows that greatest sensitivity to errors occur near the cancellation nulls where the derivatives are largest. This fact is borne out by experiment where repeatability below the first null and above the third null can be obtained with a high degree of confidence, but the calculation of the reflection index around the first few nulls can result in significant error and unrepeatability of the data.

For a given sound field geometry, the reflection coefficient Q_i and phase δ_i can be calculated from the values of the normal specific impedance ratio of the surface:

$$\frac{Z_n}{\rho c} = \frac{R_A}{\rho c} + i\,\frac{X_A}{\rho c} \tag{43}$$

where $R_A/\rho c$ and $X_A/\rho c$ are the acoustic resistance and reactance which can be obtained from impedance tube measurements of a sample slug of the ground material. The physical law relating complex reflection coefficient and complex specific impedance is:

$$Q_i e^{i\delta i} = \frac{Z_n \cos\theta - 1}{Z_n \cos\theta + 1} \tag{44}$$

where θ is the angle of incidence in Figure 5-11. This leads to the relations (Reference 34):

$$Q_i = \frac{\sqrt{\left(\left|\frac{Z_n}{\rho c}\right|^2 \cos^2\theta - 1\right)^2 + 4\left(\frac{X_A}{\rho c}\right)^2 \cos^2\theta}}{\left(\left|\frac{Z_n}{\rho c}\right|^2 \cos^2\theta + 1 + 2\,\frac{R_A}{\rho c}\cos\theta\right)} \tag{45}$$

$$\delta_i = \text{Tan}^{-1}\left[\left(2\,\frac{X_A}{\rho c}\cos\theta\right) / \left(\frac{Z_n^2}{\rho c}\cos^2\theta - 1\right)\right] \qquad (46)$$

The ground plane is assumed to be homogeneous so that the values of R_{A_i} and X_{A_i} are constant with position in the sound field. Further, an average constant value is used for each 1/3-octave band. Physically the acoustic resistance, R_A, is analogous to a damping constant or stiffness of a spring-damper-mass system. The acoustic reactance, X_A, is equivalent to the difference between the inertial and the spring resistance or compliance of the mechanical, analog. With a perfectly "hard" reflector, the acoustic resistance is infinite and the acoustic reactance is minus infinity. This gives, in the limit Equations (45) and (46), that $Q_i \to 1$ and $\delta_i \to 0$.

Unfortunately, in most cases impedance tube measurements of the ground material are not possible and another approach must be taken to obtain the reflection coefficient. The phase of the reflection coefficient, δ_i, should have the effect of delaying the wave train which would tend to create an effective path length differential, $\Delta r'$, greater than the geometric difference, Δr. Defining a phase factor, ϕ, to be the ratio of the effective path length difference to the geometric difference, i.e.:

$$\phi = \frac{\Delta r}{\Delta r'}, \qquad (47)$$

and using the relation for the frequency location of the cancellation nulls, one obtains:

$$\phi = \frac{f_{measured}}{f_{calculated}} = \frac{2\Delta r\, f_{measured}}{(2n+1)C} \qquad (48)$$

This parameter can be easily calculated with the use of a narrowband of the measured reflection pattern by simply picking off the measured frequency of the nulls and dividing by the calculated value from Equation (42).

The phase factor is related to the phase of the reflection coefficient by (Reference 34)..

$$\phi = \frac{1}{1 - \frac{\delta\lambda_i}{2\pi\Delta r}} \qquad (49)$$

This relation reveals that ϕ is a function of the ground impedance and incidence angle (through δ), frequency (through δ and λ_i), and the geometric

path length difference Δr if one restricts the analyses to always consider the first null under different geometric configurations (so $\Delta r/\lambda_i = 0.5$), ϕ should only be a function of Z_n and θ.

Using Equation (49) in the derivation of the reflection index, one obtains:

$$\Delta N = 10 \log_{10} \left[1 + \left(\frac{|Q_i|}{Z} \right)^2 + \frac{2|Q_i|}{Z} \frac{\sin\left(\frac{\alpha \Delta r}{\phi \lambda_i}\right) \cos\left(\frac{\beta \Delta r}{\phi \lambda_i}\right)}{\left(\frac{\alpha \Delta r}{\phi \lambda_i}\right)} \right] \qquad (50)$$

instead of Equation (39).

The effect of decreasing the phase factor, ϕ, is to shift the nulls to lower frequency and to reduce the amplitude of the reflection index (as shown in Figure 5-14). A reduction in the reflection coefficient, Q, with fixed phase factor is simply a reduction in the reflection index (as seen in Figure 5-15). Both the reflection coefficient amplitude and phase factor will vary with frequency. In general, therefore, the calculation of the reflection index, ΔN, for a typical sound field will be different from that predicted with an idealized hard surface (shown in Figure 5-13) by an amount that varies with frequency.

5.4 DISTRIBUTED SOURCE EFFECTS ON GROUND REFLECTION INDEX

The jet is not really a "point source", but is comprised of a volumetric distribution of sources throughout the jet plume. It is also known that the high frequency noise from a jet comes from compact regions close to the nozzle exit, while low frequency noise emanates from widely distributed regions further downstream in the plume. In fact, models have been postulated, and to some extent experimentally verified, which consider the jet as a continuous streamwise distribution of acoustic sources whose amplitudes and frequencies vary monotonically along the jet axis. Figure 5-16 illustrates this conceptual model. A ramification of recognizing this situation is that the radiation paths, both direct and reflected, will vary with the position of the sources, and will, therefore, be different for different frequencies and associated locations along the jet.

Even without ground reflections, the decay of sound from a distributed source, as measured from the geometric origin of the sound field, would show a deviation from the inverse square law simply because the true acoustic distance, r, differs from the measurement length, r_m, as shown in Figure 5-17. The acoustic distance is a minimum when r and r_m are perpendicular ($R_m = x \cos \theta$). One would, therefore, expect the sound to increase with increasing distance, R_m, in Figure 5-17 until $R_m = x \cos \theta$ and decrease thereafter since the receiver is actually getting closer to the incremental point source

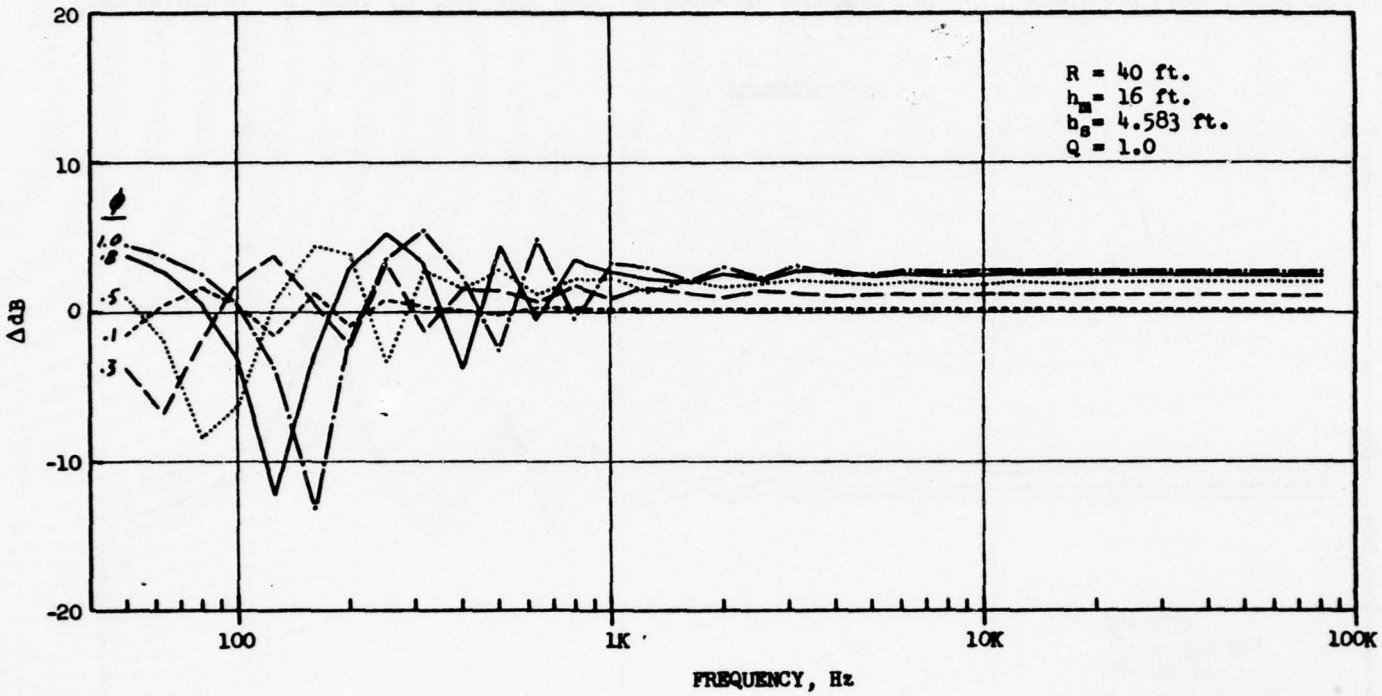


Figure 5-14. Effect of Varying Phase Factor on the Reflection Pattern.

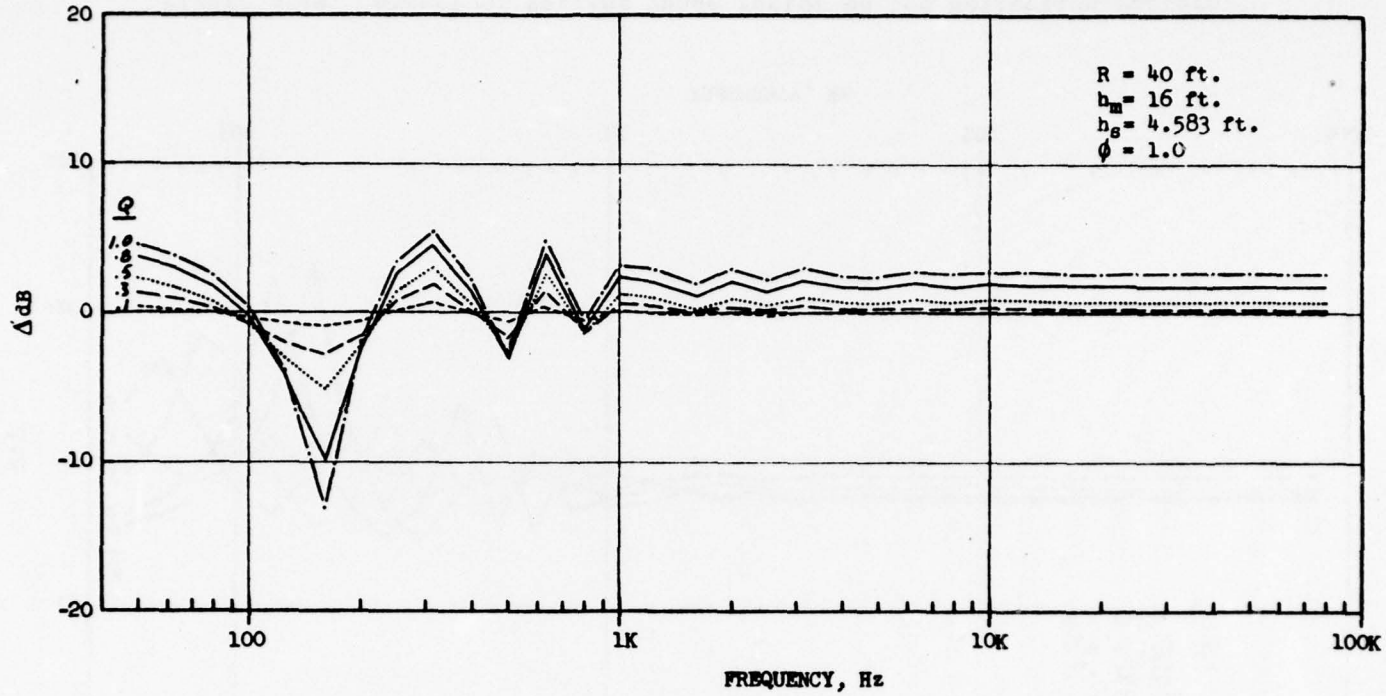


Figure 5-15. Effect of Varying Coefficient of Reflection on the Reflection Pattern.

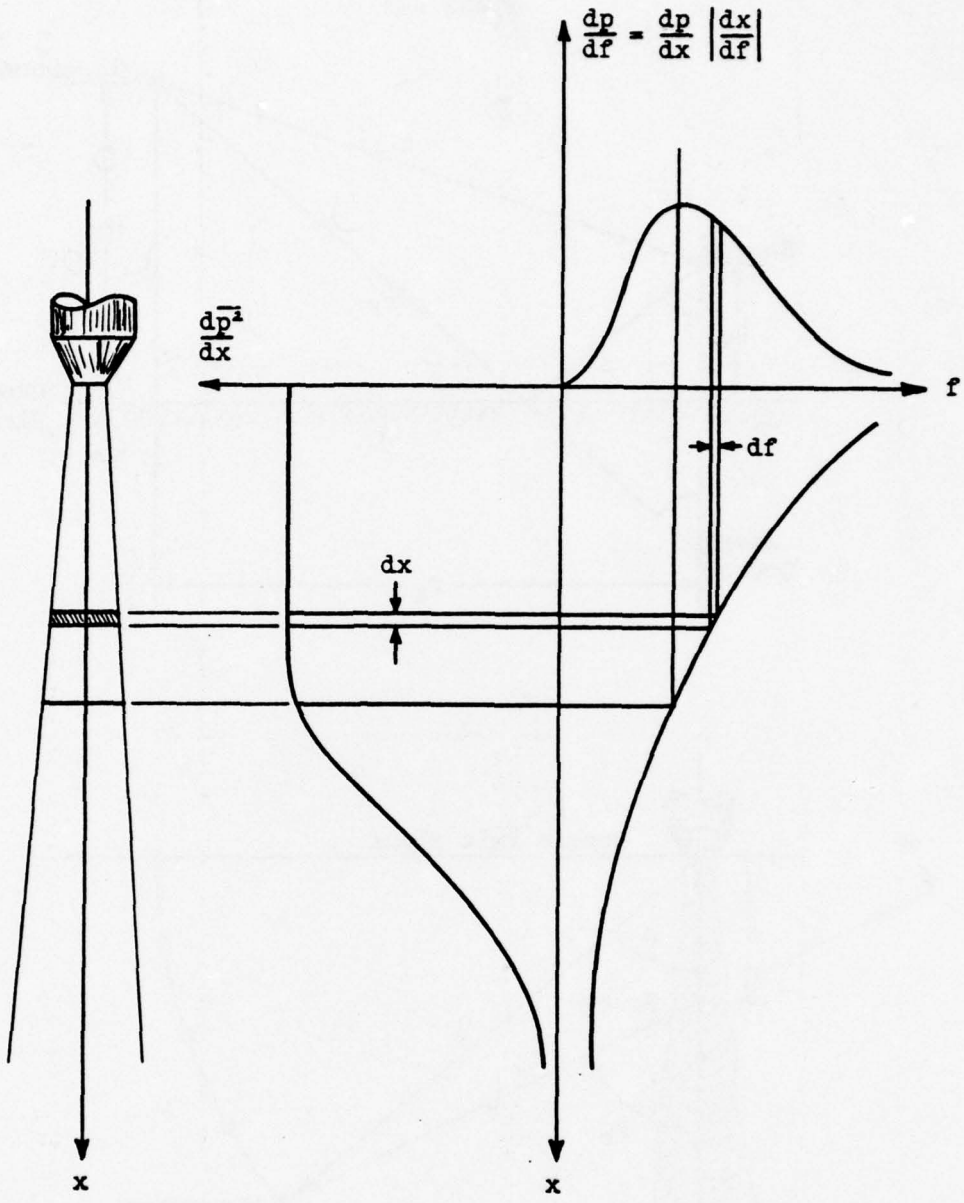


Figure 5-16. Schematic of Typical Jet Plume Source Distribution and Associated Frequency Distribution.

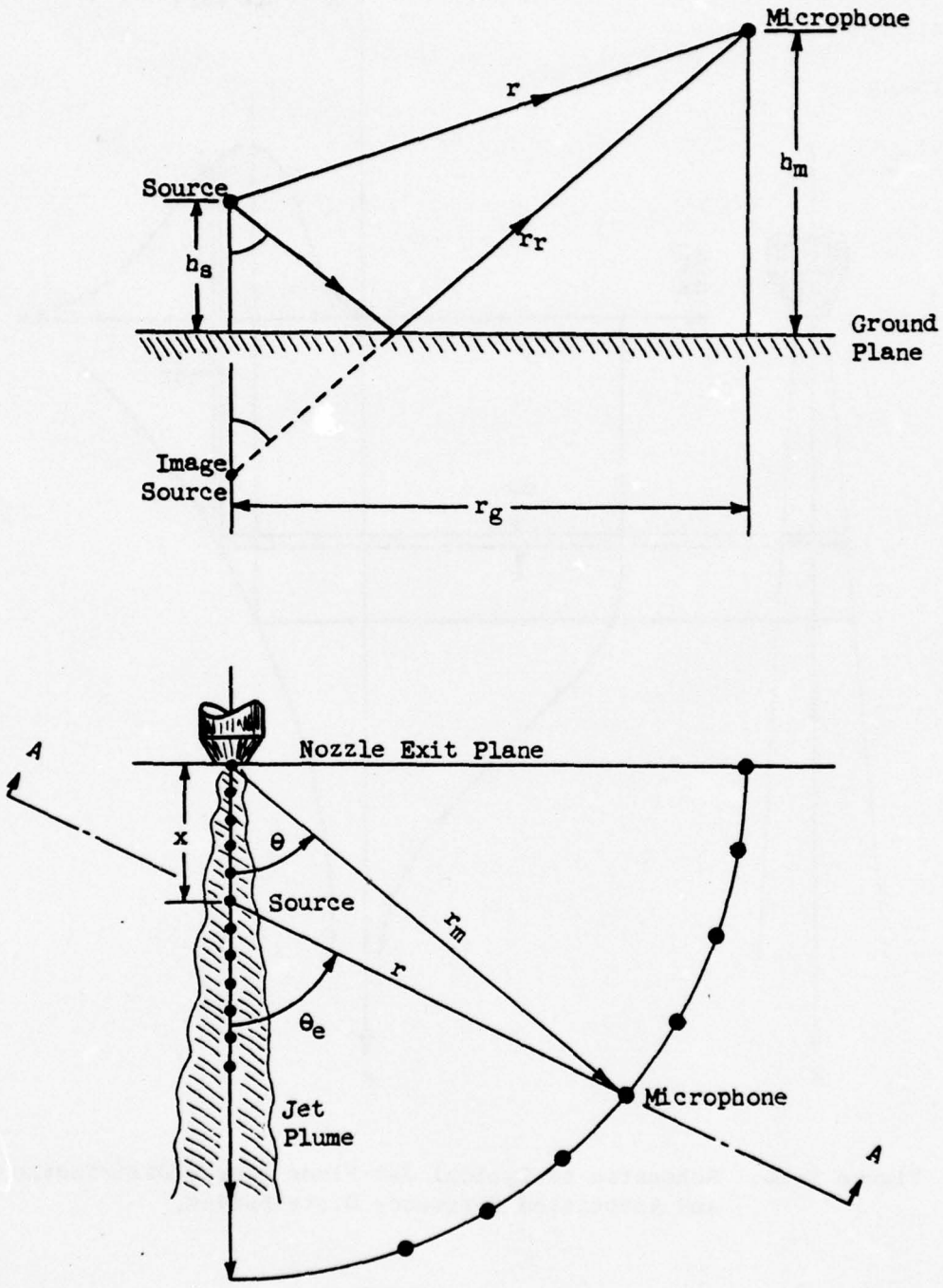


Figure 5-17. Geometry and Notation for Analysis of Ground Reflection Effects.

illustrated on the figure until after this minimum approach distance is passed by. With a distributed line source, such as the jet exhaust, the sound levels would remain relatively constant until the receiver is sufficiently far from the jet, because of these geometric considerations. Figures 5-2 through 5-10 show this effect with anechoic room jet noise measurements at 90° to 150° from the inlet axis. Significant deviation from the inverse square law is observed at low frequency for small angles, near the jet axis. Far away from the jet, the difference between R and R_m is significant and the expected inverse square law is achieved. When a ground plane is present, however, the resulting ground reflection pattern will be drastically changed by small differences in the source location.

A study was undertaken to assess the degree to which the distribution of the source strengths along the jet affects the ground reflection corrections. The following paragraphs summarize the development of and results obtained from this study.

5.4.1 Analysis

The effect of ground reflections will be considered in the following discussion with the geometry of Figure 5-11, and with the previous point source analysis extended to include a distribution of point sources along the jet axis. Figure 5-18 illustrates a typical distribution of acoustic source strength and frequency of the source as a function of distance along the jet plume.

Motsinger (35) has derived a correlation for the line source distribution exhibited by a jet in a form (shown in Figure 5-18) as follows:

$$\frac{dSPL}{d(x/D)} = F(x/D,f) = \left[\frac{dSPL}{d(x/D)}\right]_p + H(x/x_p) \qquad (51)$$

where x - distance along the jet axis

D - effective diameter of the jet nozzle

SPL - sound pressure level, dB

f - 1/3-octave band frequency

[ ]p - denotes values at the peak of the correlation curve

Consider each "slice-of-jet" as a point source. The far field sound pressure at a given observation point due to one slice-of-jet on the axis is, from Reference 32.

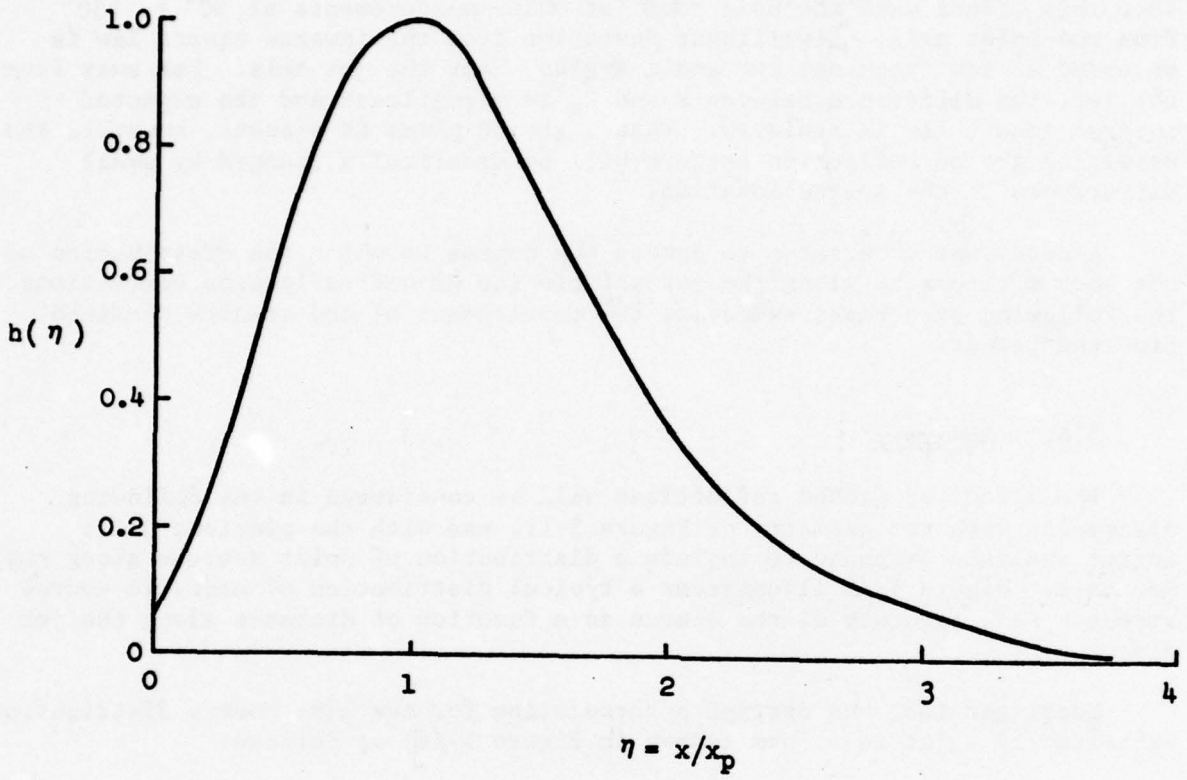


Figure 5-18. Normalized Jet Plume Source Strength Distribution.

$$\frac{\overline{p^2}}{p_{ff}^2} = 1 + \frac{1}{z^2} + \frac{2}{z}\, C(\tau) \tag{52}$$

where

$$C(\tau) = \frac{\int_{fa}^{fb} w(f)\, \cos(2\pi f \tau)\, df}{\int_{fa}^{fb} w(f)\, df} \tag{53}$$

$$\Delta\overline{p^2} = \left[\frac{d\overline{p^2}}{d(x/D)}\right]_{ff} \left[1 + \frac{1}{z^2} + \frac{2}{z}\, C(\tau)\right] d(x/D) \tag{54}$$

Integrating the above to obtain the contribution from all the "slices-of-jet" distributed along the jet axis,

$$\overline{p^2} = \left[\overline{p^2}\right]_{ff} + \int_0^{\infty} \left[\frac{d\,\overline{p^2}}{d(x/D)}\right]_{ff} \left[\frac{1}{z^2} + \frac{2}{z}\, C(\tau)\right] d\left(\frac{x}{d}\right) \tag{55}$$

where subscript "ff" denotes free-field conditions. In terms of SPL, this equation becomes

$$SPL = SPL_{ff} + 10 \log_{10} \left\{1 + \frac{1}{p_{ff}^2} \int_0^{\infty} \left[\frac{1}{z^2} + \frac{2}{z}\, C(\tau)\right] \left[\frac{d\,\overline{p^2}}{d(x/D)}\right]_{ff} d\left(\frac{x}{d}\right)\right\} \tag{56}$$

If the source length is assumed to be very small such that z and $C(\tau)$ are independent of x, Equation (61) reduces to

$$SPL = SPL_{ff} + 10 \log_{10} \left\{1 + \left[\frac{1}{z^2} + \frac{2}{z}\, C(\tau)\right] \frac{1}{p_{ff}^2} \int_0^{\infty} \left[\frac{d\,\overline{p^2}}{d(x/D)}\right]_{ff} d\left(\frac{x}{D}\right)\right\} \tag{57}$$

or

$$SPL = SPL_{ff} + 10 \log_{10} \left\{ 1 + \frac{1}{z^2} + \frac{2}{z} C(\tau) \right\} \tag{58}$$

just as before for a point source (Equation 52). The difference between Equations (54) and (55) gives the "line source distribution" effect.

Let the source distribution be expressed in the following normalized form:

$$\frac{d\overline{p^2}}{d(x/D)} = \left[\frac{d\overline{p^2}}{d(x/D)} \right]_p h\,(x/x_p) \tag{59}$$

where subscript p denotes peak pressure level values. Motsinger (38) has found that $h(x/x_p)$ is a relatively "universal" curve in that distributions in any 1/3-octave band seem to possess the same distribution when normalized in this form. The values of x_p and $[d\overline{p^2}/d(x/D)]p$ are, of course, a function of frequency. Thus

$$\left(\overline{p^2}\right)_{ff} = \int_0^\infty \left[\frac{d\overline{p^2}}{d(x/D)} \right] \left(d\,\frac{x}{D} \right) = \left[\frac{d\overline{p^2}}{d(x/D)} \right]_p \left[\frac{x}{D} \right]_p \int_0^\infty h(\eta)\, d\eta \tag{60}$$

where $\eta = x/x_p$. Similarly,

$$\int_0^\infty \left[\frac{1}{z^2} + \frac{2}{z} C(\tau) \right] \left[\frac{d\overline{p^2}}{d(x/D)} \right] d\left(\frac{x}{d}\right) = \left[\frac{d\overline{p^2}}{d(x/D)} \right]_p \left[\frac{x}{D} \right]_p \int_0^\infty \left[\frac{1}{z^2} + \frac{2}{z} C(\tau) \right] h(\eta)\, d\eta \tag{61}$$

so that, when substituting Equations (60, 61) into (56), we obtain the final result

$$SPL = SPL_{ff} + 10 \log_{10} (1 + K) \tag{62}$$

where

$$K = \frac{\int_0^\infty \left[\frac{1}{z^2} + \frac{2}{z} C(\tau)\right] h(\eta)\, d\eta}{\int_0^\infty h(\eta)\, d\eta} \tag{63}$$

The function $h(\eta)$, obtained from Motsinger's correlation, (Reference 35), is shown in Figure 5-18. For the case of a point source, Equation (63) reduces to $K = 1/z^2 + 2C(\tau)/z$.

From geometry of Figures 5-11 and 5-17, the reflected wave path length is given by

$$r_r = r + \sqrt{r_g^2 + (h_s + h_m)^2} - \sqrt{r_g^2 + (h_s - h_m)^2} \tag{64}$$

where r_g is the projected distance along the ground between source and microphone. The distance r_g can be found from r_m and θ by the following formulas,

$$r_g = r\sqrt{1 - (h_m - h_s)^2/r^2} \tag{65}$$

$$r = r_m\sqrt{1 + (x/r_m)^2 - 2(x/r_m)\cos\theta} \tag{66}$$

Using the distributed source model we can relate frequency to distance along the jet axis. Again drawing upon Motsinger's correlation of jet noise apparent source distributions, an empirical relation between frequency and the location of the peak noise source is proposed as follows:

$$\frac{fD}{V_j} = \left(1.25\,\frac{x - x_p}{D}\right)^{-1.22} \tag{67}$$

where x_p is the beginning of peak noise generation region (also end of potential core). Motsinger gives an empirical relation for x_p as a function of jet Mach number, as follows:

$$\begin{aligned} &M_j < 1, \quad x_p/D = 4 \\ &M_j > 1, \quad x_p/D = 4\, M_j^{\,1.153} \end{aligned} \tag{68}$$

Given a 1/3-octave band frequency of interest, the axial location x can be found from Equations (67,68).

The remaining parameter which needs to be determined is $C(\tau)$ given by Equation (53). For typical jet noise spectra, the evaluation of $C(\tau)$ over a constant percent bandwidth (such as 1/3 octave) is simplified with little loss in accuracy by assuming w(f) is essentially "white noise" over the integration interval. Thus, for w(f) = constant = w_o,

$$\int_{f_a}^{f_b} w(f) \cos(2\pi f\tau)\, df \tilde{=} \frac{w_o}{2\pi\tau} \left[\sin(2\pi\tau f_b) - \sin(2\pi\tau f_a)\right] \tag{69}$$

$$\tilde{=} \frac{w_o}{\pi\tau} \sin\left[\pi\tau(f_b - f_a)\right] \cos\left[\pi\tau(f_b + f_a)\right]$$

and

$$\int_{f_a}^{f_b} w(f)\, df = (f_b - f_a)\, w_o \tag{70}$$

so

$$C(\tau) \tilde{=} \frac{\sin\left[\pi\tau(f_b - f_a)\right]}{\pi\tau(f_b - f_a)} \cos\left[\pi\tau(f_b + f_a)\right] \tag{71}$$

Equations (64-71) provide all of the ingredients necessary to estimate the correction to observed sound pressure level for ground reflection effects. Given a jet velocity V_j, Mach number M_j, and jet diameter D, Equations (67) and (68) can be used to compute the peak-noise location x as a function of frequency f. Given the geometry of the problem, i.e., microphone height, h_m, source height, h_s, microphone arc radius, r_m, and angles, θ, Equations (62) and (63) can be used to evaluate the ground reflection correction. The function h (η) is given by Figure 5-18, and the integration can be performed numerically using Equations (69-71) to evaluate r, r_r, and $z = r_r/r$. Equation (71) is used to evaluate $C(\tau)$, and the value of x at any value of η (the variable of integration) is obtained from $x = h\, x_p$.

5.4.2 Parametric Study

The procedure just described was used to estimate the ground reflection corrections for the JENOTS facility. To avoid the question of ground impedance effects, all results were plotted as ground reflection index relative to the point source value. This assumes that the ground impedance effect is the same for a point source and a line distribution of sources. The following values of the facility geometric variables were assigned:

$D = 4$ in.

$r_m = 40$ ft.

$h_m = 15.93$ ft.

$h_s = 55$ in.

Figures 5-19 through 5-23 show the ground reflection index corrections computed for the case $V_j = 1000$ fps and $M_j = 1.0$. It can be seen that the error incurred in assuming a point source for ground reflection index estimates is very large at angles close to the axis (as much as 8 dB). At right angles ($\theta_I \sim 90°$) to the jet axis, the distributed source effect is very small. This trend is primarily a result of the difference between the reflected and direct paths being close to that for a point source near 90°. This difference departs from the point source value as angle of observation is increased or decreased from 90°.

The lower frequencies, by virtue of Equation (67), have larger values of x, and, therefore, larger deviations from point source behavior as frequency is reduced can be expected. Figures 5-19 through 5-23 show that this is the case.

Calculations were also done for several other operating conditions representative of the JENOTS facility certification points. Figure 5-24 summarizes the results of these calculations as a limit line in the (θ_I, f) domain. This limit line represents the boundary of the region where the difference between distributed line source and concentrated point source is greater than 1 dB. In general, the line source distribution effect is not very sensitive to operating condition. From Figure 5-24, it appears that good JENOTS facility measurement accuracy could easily be consumed by erroneous ground reflection corrections between $400 \leq f \leq 1200$ Hz, for $\theta_I \geq 110°$ and $\theta_I \leq 60°$ if the corrections were derived strictly from point considerations.

5.5 JENOTS GROUND REFLECTION CORRECTIONS

5.5.1 Microphone Height Change

Early testing at the JENOTS facility utilized microphones distributed around a 40-foot measurement arc which were at the nozzle centerline height of

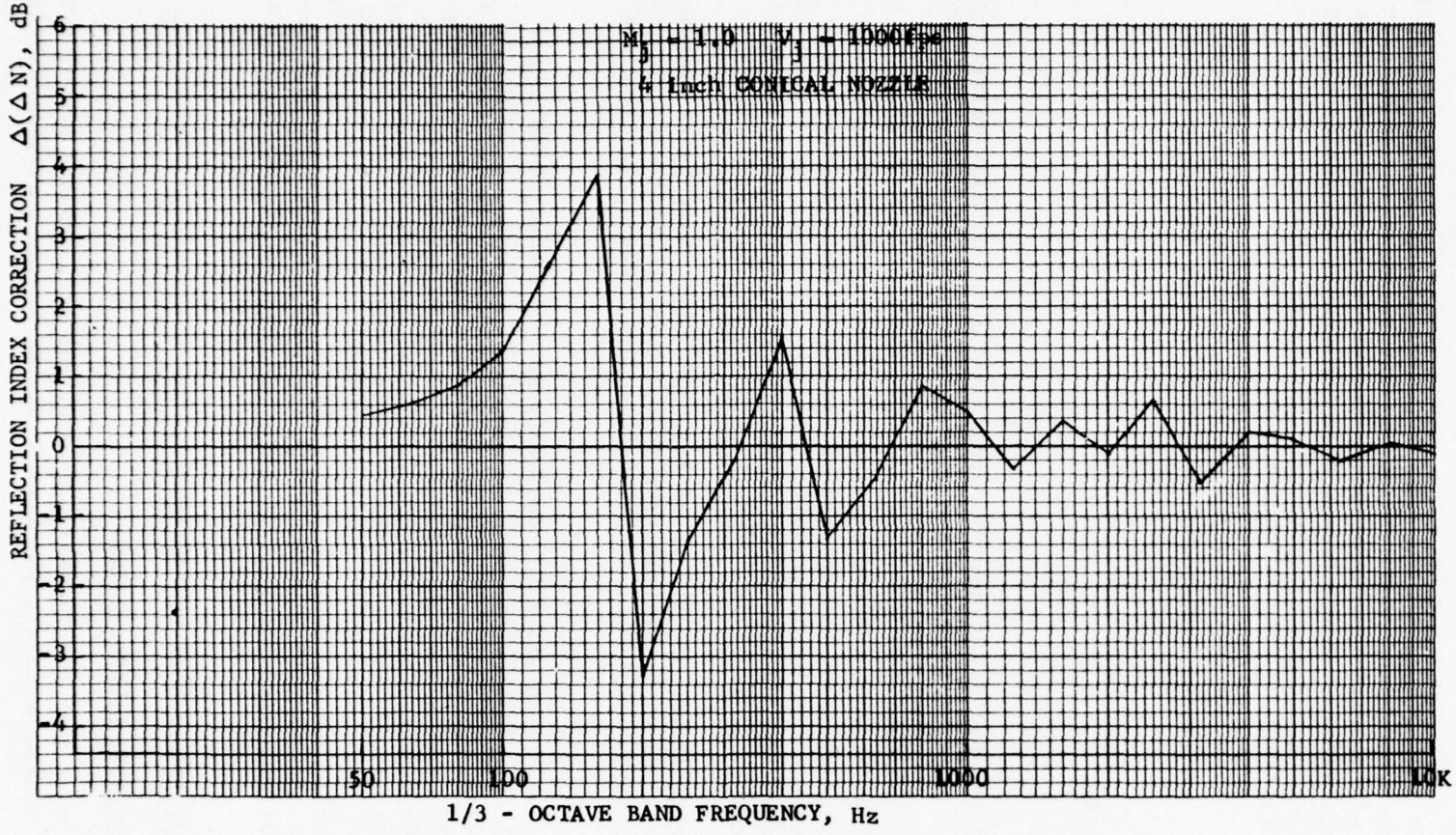


Figure 5-19. Reflection Index Correction Due to Distributed Source Location for θ_I = 30° Angle at JENOTS.

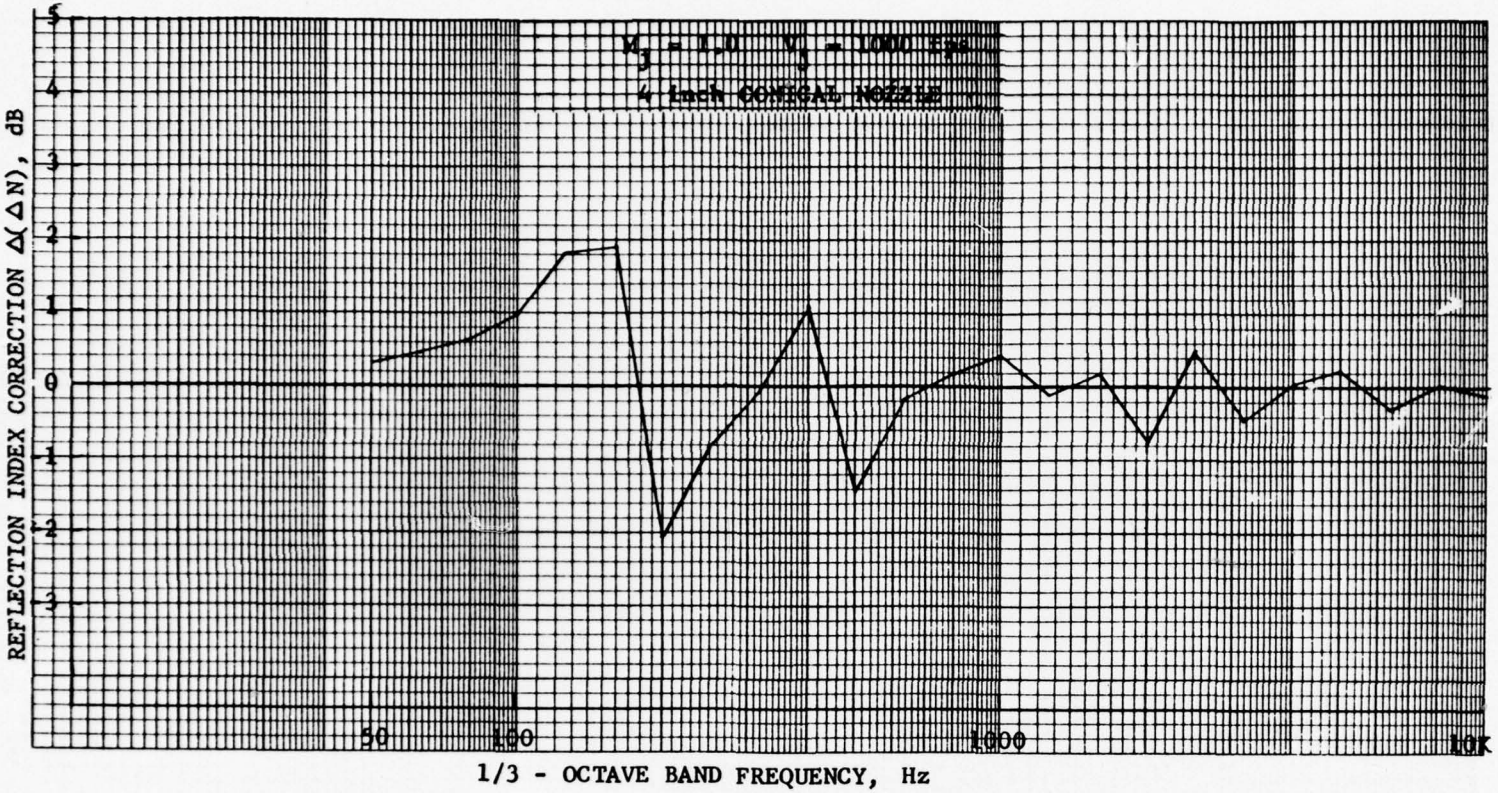


Figure 5-20. Reflection Index Correction Due to Distributed Source Location for θ_I = 60° Angle at JENOTS.

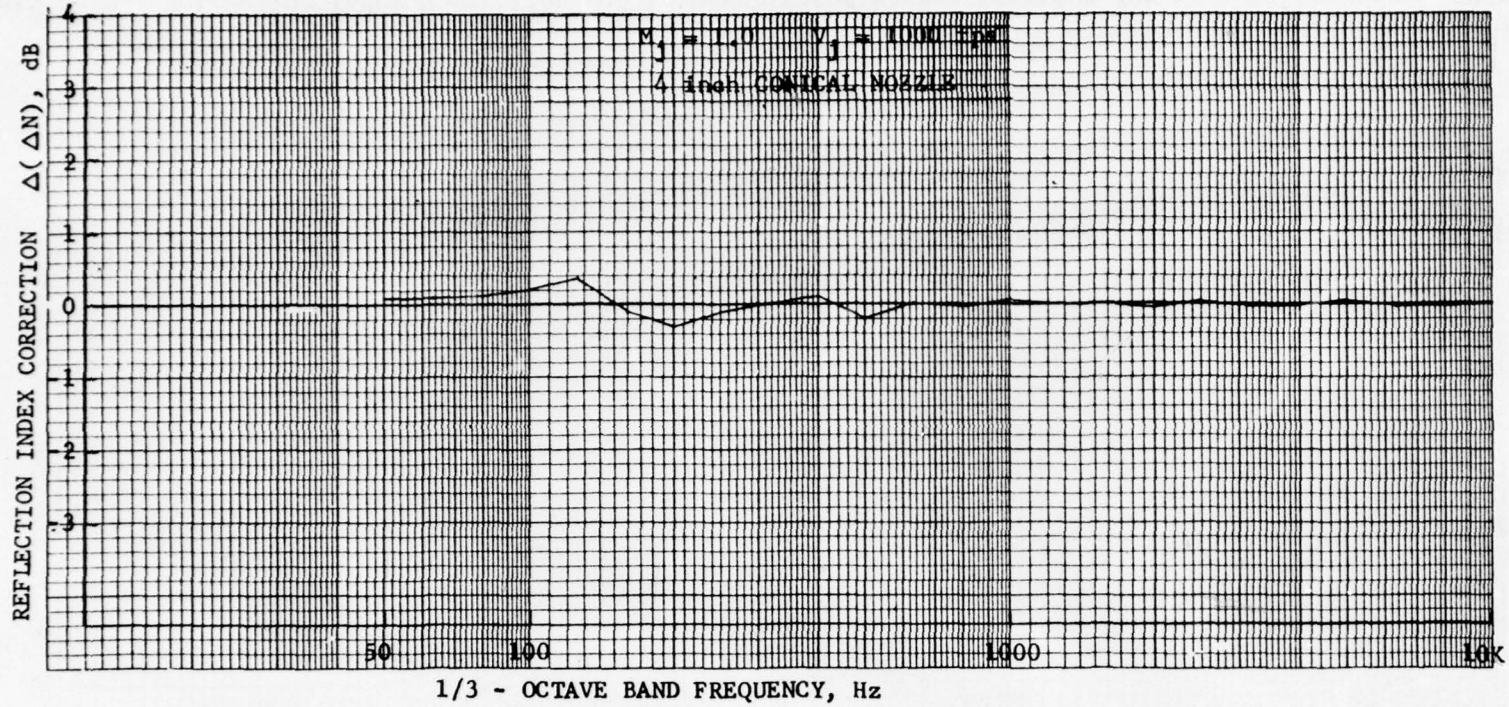


Figure 5-21. Reflection Index Correction Due to Distributed Source Location for $\theta_I = 90°$ Angle at JENOTS.

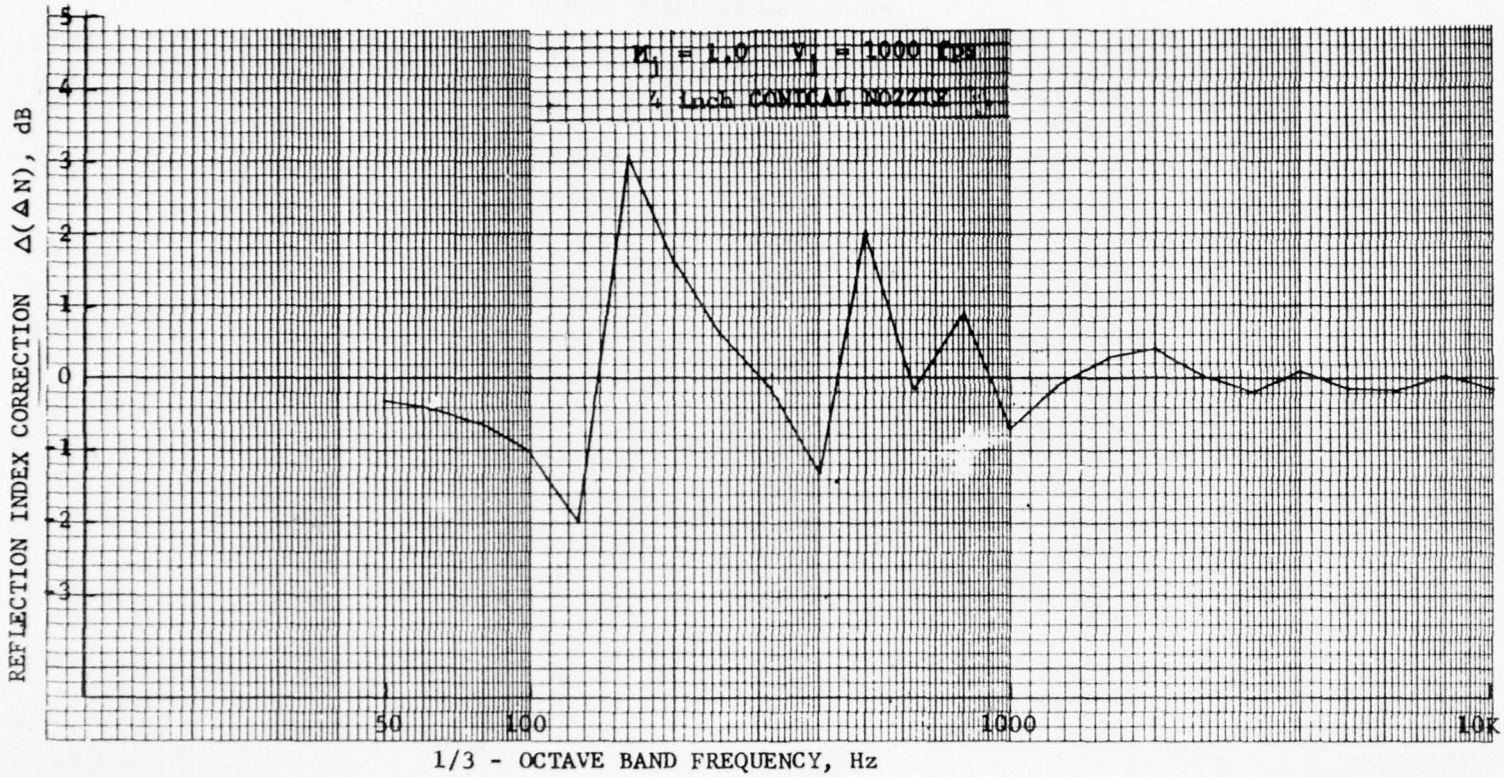


Figure 5-22. Reflection Index Correction Due to Distributed Source Location for θ_I = 120° Angle at JENOTS.

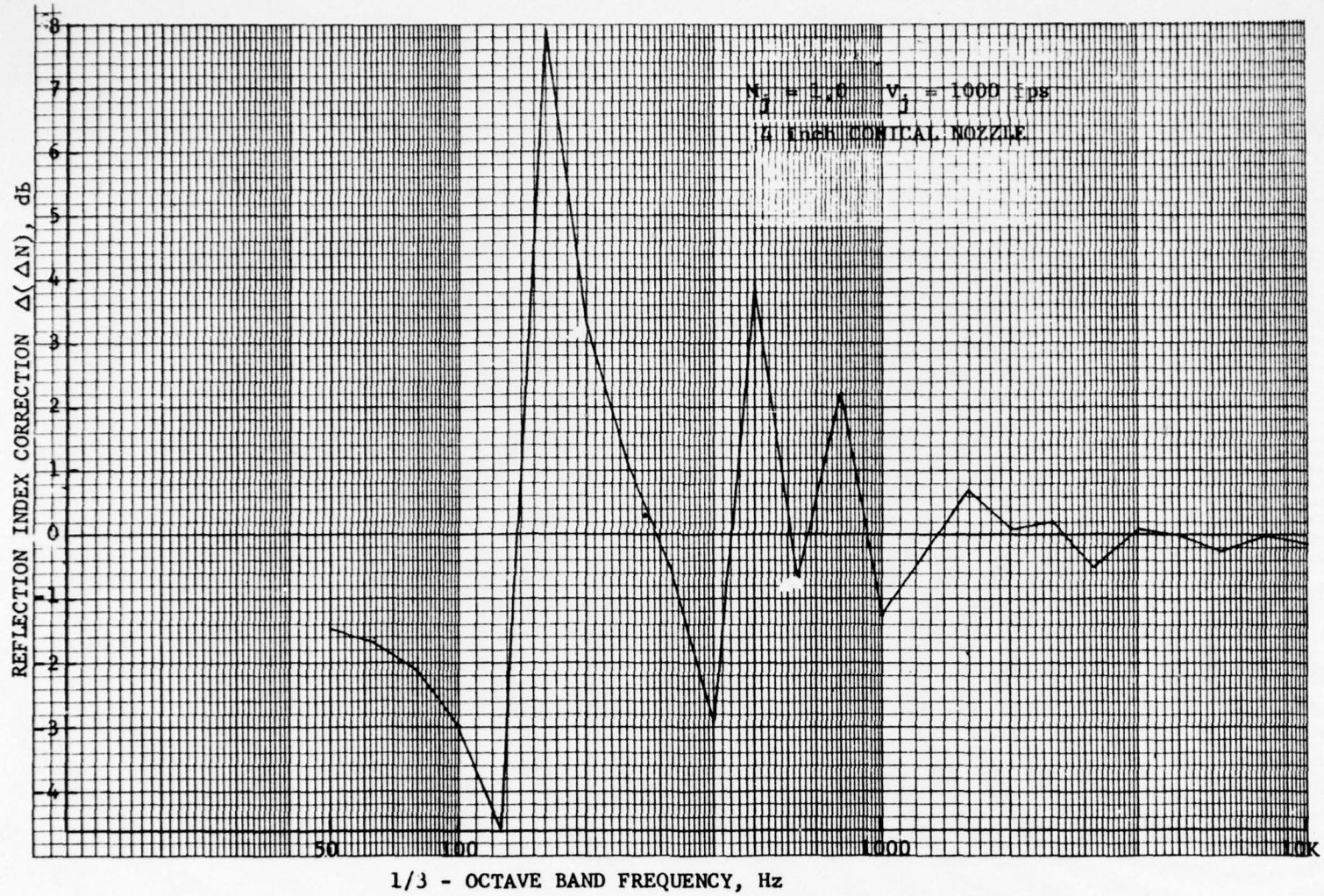


Figure 5-23. Reflection Index Correction Due to Distributed Source Location for θ_I = 160° Angle at JENOTS.

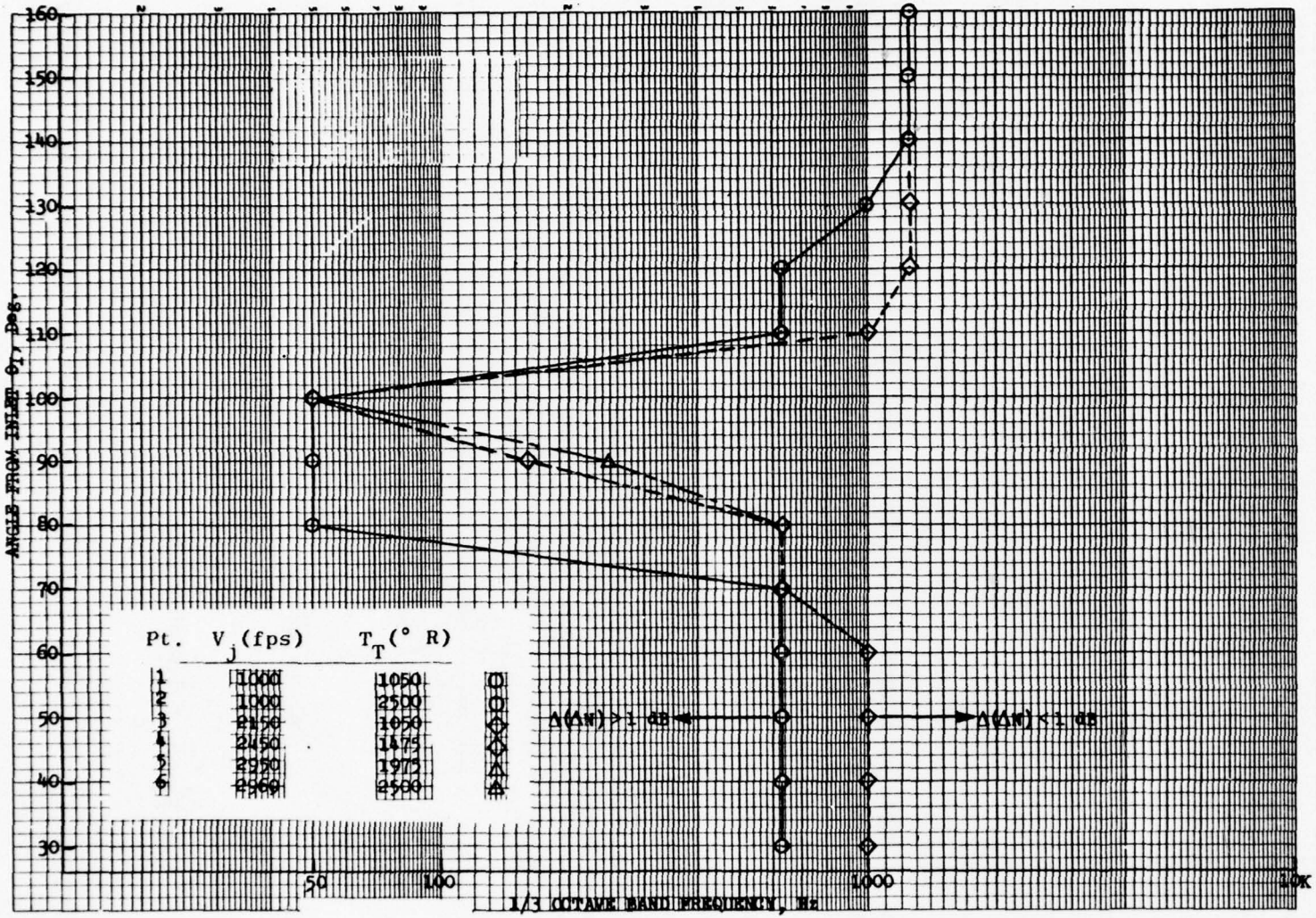


Figure 5-24. JENOTS Facility Operational Limit Lines for Less than 1 dB Correction to Ground Reflection Index.

55 inches above the ground. This gave a ground reflection interface pattern which was quite severe, as shown in Figure 5-25(a), particularly in the 500 Hz first null region. To cure this, the microphones were evaluated to a height of 15.93 feet above the ground and moved in slightly to give an acoustic radius of 40 feet from the nozzle centerline to the microphone. This change shifted the first null into the 160 Hz 1/3-octave band and the second null into the 400 Hz band, etc., as shown by the spectra in Figure 5-25(b). One consideration of this design change is the fact that with the microphones at the 15.93-foot elevation each microphone station is in a different azimuthal plane of the nozzle symmetry, as illustrated by Figure 5-26. Care must, therefore, be taken in interpreting data from significantly nonsymmetrical nozzles, such as a 2D or rectangular shape. Even with these designs, however, the major portion of the planar differences occurs between the 0 and 40° microphone stations (relative to the jet axis) as seen in the table on Figure 5-26.

With an improved ground reflection pattern, the next task is to obtain the necessary correction factors to the data to make it effective free-field spectra. This requires the determination of the ground impedance phase factor and reflection coefficient (ϕ and Q in Equations 46 and 49), an estimate of the scattering phenomenon, and a correction for the distributed source effects of the jet.

5.5.2 Determination of the Phase Factor

Before discussing the test results for the determination of the phase factor using Equation (48), the expected variation in phase factor due to measurement errors must be determined. Taking the differential of Equation (48) relating phase factor to test measurements yields:

$$\frac{\sigma_\phi}{\phi} = \pm\sqrt{\left(\frac{\sigma_{\Delta r}}{\Delta r}\right)^2 + \left(\frac{\sigma_{f_{measured}}}{f_{measured}}\right)^2 + \left(\frac{\sigma_a}{a}\right)^2} \qquad (72)$$

$$a_o = \sqrt{\gamma RT} \qquad (73)$$

$$\sigma_{a_o} = \frac{a_o\,\sigma_T}{2T} = 1.0886\ \sigma_T \ @\ T = 513°\ R \qquad (74)$$

considering the geometry of Figure 5-11 and Equations (40) and (41) it can be shown that:

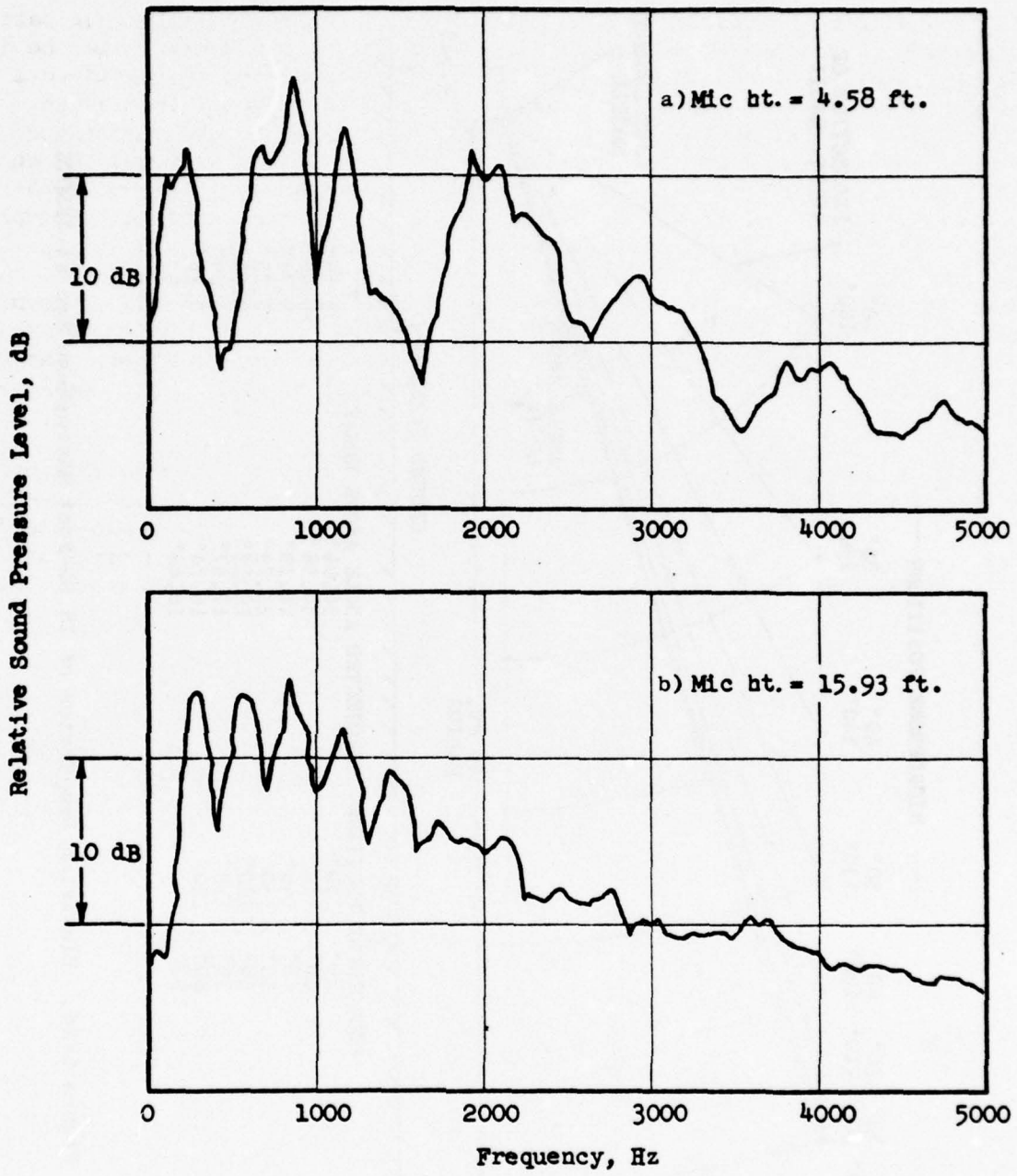
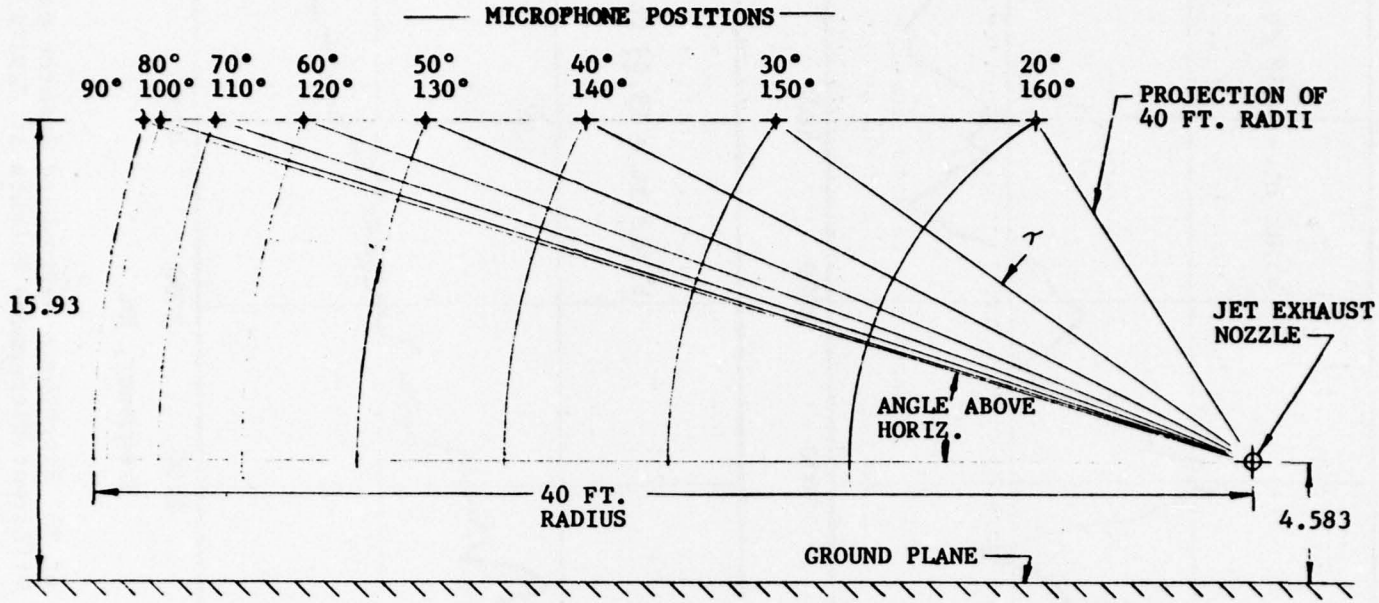


Figure 5-25. Comparison of 90° Microphone Narrowband Spectra of Jet Noise with Different Microphone Heights at JENOTS.



MICROPHONE POSITION	PROJECTED ANGLE ABOVE HORIZ.	τ
20° , 160°	56.04°	39.56°
30° , 150°	34.56°	18.08°
40° , 140°	26.19°	9.71°
50° , 130°	21.73°	5.25°
60° , 120°	19.12°	2.64°
70° , 110°	17.57°	1.09°
80° , 100°	16.74°	0.26°
90°	16.48°	-

Figure 5-26. Elevation Projection of 15.93-Foot Microphone Arc at JENOTS.

$$\sigma_{\Delta r}^2 = \left(\frac{Z-1}{Z}\right)^2 \sigma_R^2 + \left(\frac{4h_m}{RZ}\right)^2 \sigma_{h_s}^2 + \left(\frac{4h_s}{RZ}\right)^2 \sigma_{h_m}^2 \qquad (75)$$

At JENOTS, $h_m = 15.93'$, $h_s = 55''$, $R = 40'$, from Figure 5-17, $Z = 1.087$ so:

$$\left(\frac{\sigma_{\Delta r}}{\Delta}\right)^2 = 3.667 \times 10^{-5} \sigma_R^2 + 1.242 \times 10^{-3} \sigma_{h_s}^2 + 1.0197^{-4} \sigma_{h_m} \qquad (76)$$

Thus, we have five types of possible measurement errors to contend with: σh_s, σh_m, σ_R, σ_T, and σ_f measured.

The values of σh_s and σh_m indicate, in addition to measurement error, the uncertainty with which we know the exact location of the sound source and receiver, respectively. The value σ_R reflects a physical measurement error. The error in T, σ_T, is also a measurement error.

The value of $\sigma_{f_{measured}}$ is not only a function of the measurement system but also the resolution of the frequency scale for reading $f_{measured}$. This is, to a large part, a random error and should be cancelled through the averaging procedure. For any given sweep, $\sigma_{fmeasured}/f_{measured}$ should be significant only for the lower frequencies (i.e. in comparing repeats one would expect more scatter at low frequencies in the value of ϕ due to measurement error and in reading the null frequency).

If we use the estimated values:

σ_R = 12 inches

σh_s = 2 inches

σh_m = 1 inch

σ_T = 1 degree

$\sigma f_{measured} = 0$

Then

$$\left(\frac{\sigma_{a_o}}{a_o}\right)^2 = 0.009 \times 10^{-4}; \quad \left(\frac{\sigma f}{f}\right)^2 = 0; \quad \left(\frac{\sigma \Delta r}{\Delta r}\right)^2 = 30.26 \times 10^{-4} \qquad (77)$$

So

$$\frac{\sigma_\phi}{\phi} = \pm 0.055$$

That is, the expected error in obtaining ϕ is 5.5% over the frequency range where the null can accurately be calculated. At the low frequency, the expected error and scatter in ϕ should be larger.

Three experimental techniques were attempted in the study of the JENOTS phase factor. First, an Altec driver with a drawn tube to give a point source output shown in Figure 5-27 was installed at the JENOTS facility with the tube located at the nozzle center exit plane as shown in Figure 5-28. Various signal inputs were introduced to the Altec driver; namely, a sweep sine wave up to 9000 Hz, a constant level white noise with frequency, and discrete steady-state frequency sine waves. All the data suffered from the same problem of severe lobing resulting from standing waves in the speaker tube. Figure 5-29 shows a narrowband of the white noise data from three microphones. Lobes appear about every 200 Hz which wash out the cancellations and reinforcements from the ground reflections. Figure 5-30 shows similar results experienced with the sweep oscillator. Because of the speaker lobes, the task of locating the ground nulls by this approach was not considered practical.

The second technique utilized a specially designed capacitor bank which would generate a symmetric spark discharge as shown in Figures 5-31 and 5-32. The spherical wave from the spark would travel to a far-field microphone along the direct and reflected paths. The measured waveform would give both the phase information (from the time delay between the waves) and the reflection coefficient from the amplitude ratio of the waves viz:

$$\phi^{OA} = \frac{\Delta r \; \Delta t_{measured}}{C} \tag{78}$$

$$Q_{OA} = \frac{A_{reflected}}{A_{direct}} \tag{79}$$

Figure 5-33 shows the waveforms from a laboratory setup with a reflective surface. The Q, and ϕ, which are measured from the wave form characteristics, are overall values averaged over all frequencies. In order to determine the frequency distribution, 1/3-octave filters were introduced after the microphones. The result however was that the spark impulse caused the filters to ring and the data was confused by a decaying sine wave corresponding to the frequency response of the filter. The next approach to obtaining a frequency distribution was to capture the waveforms on a biomation digital transient

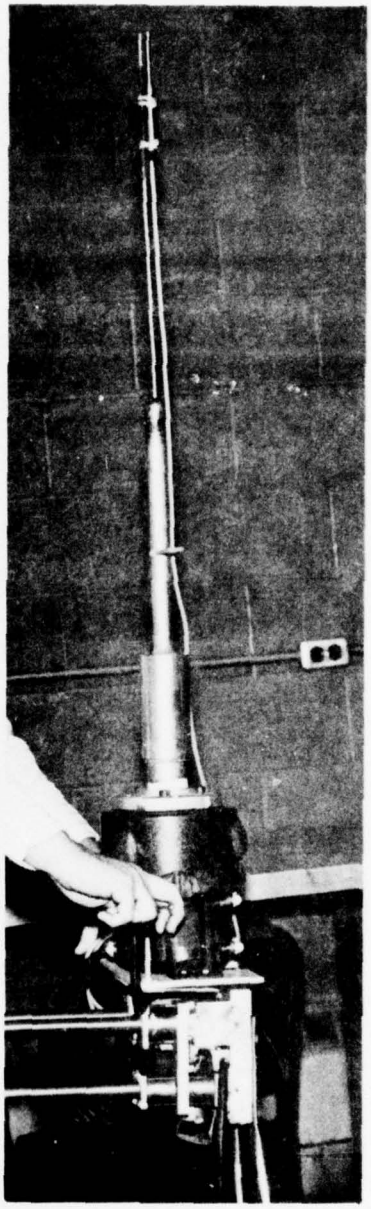


Figure 5-27. Altec Driver.

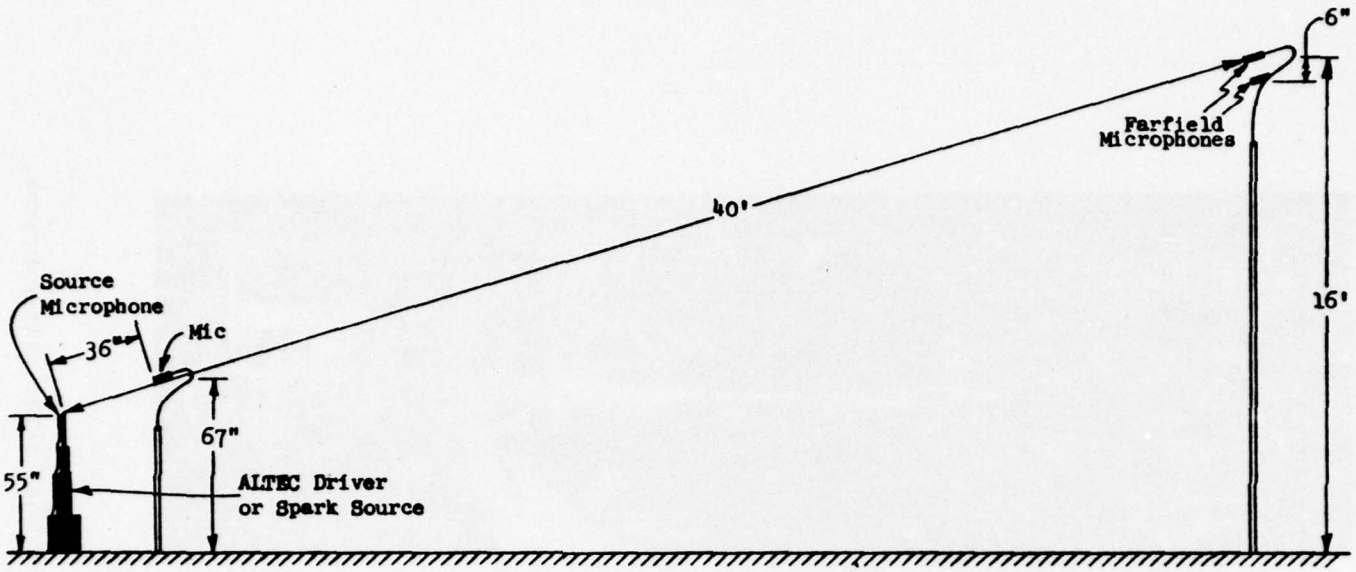


Figure 5-28. Sound Field Set Up for Altec Driver and Spark Test at JENOTS.

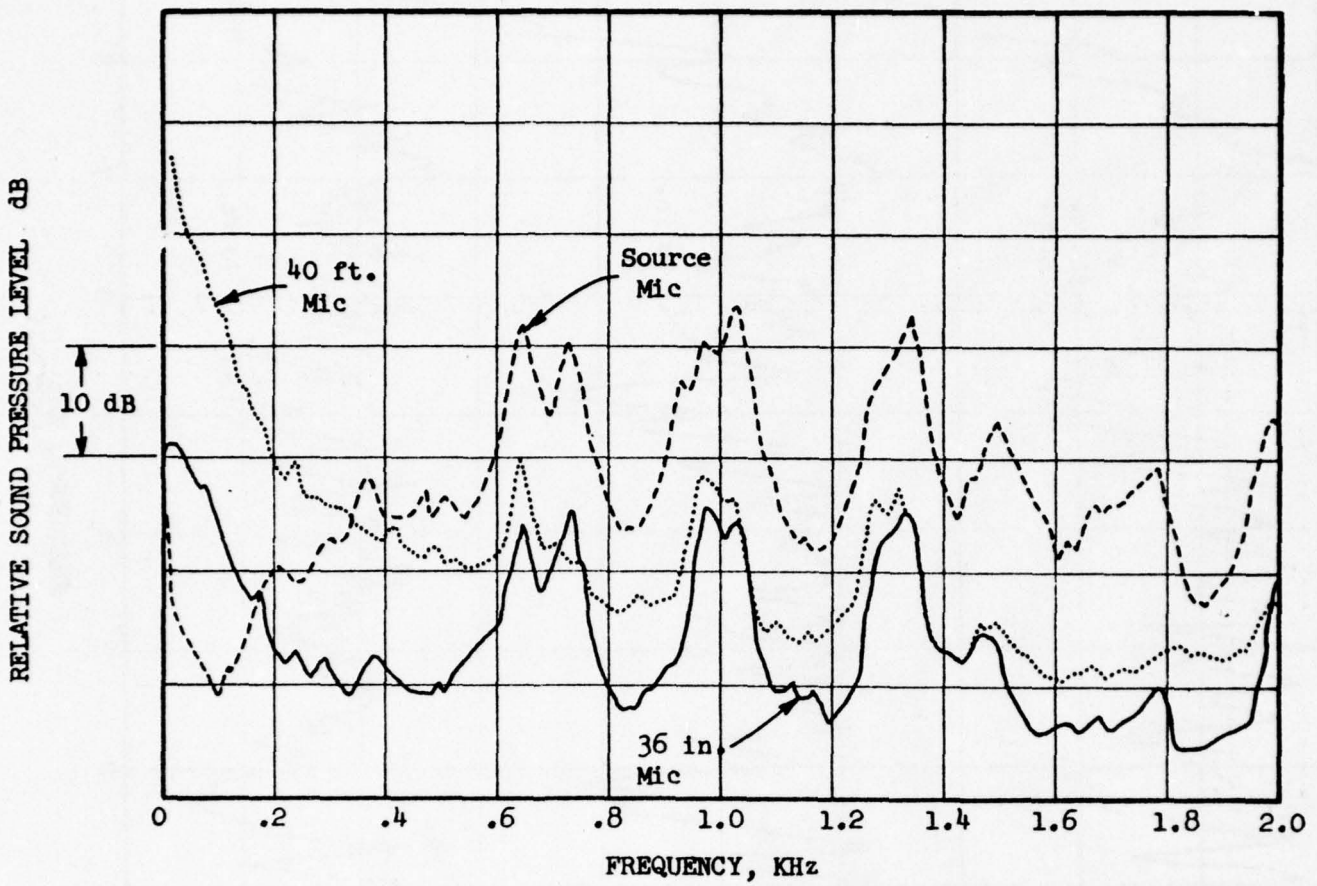


Figure 5-29. 10-Hz Narrowband of White Noise Signal from Altec Driver at JENOTS.

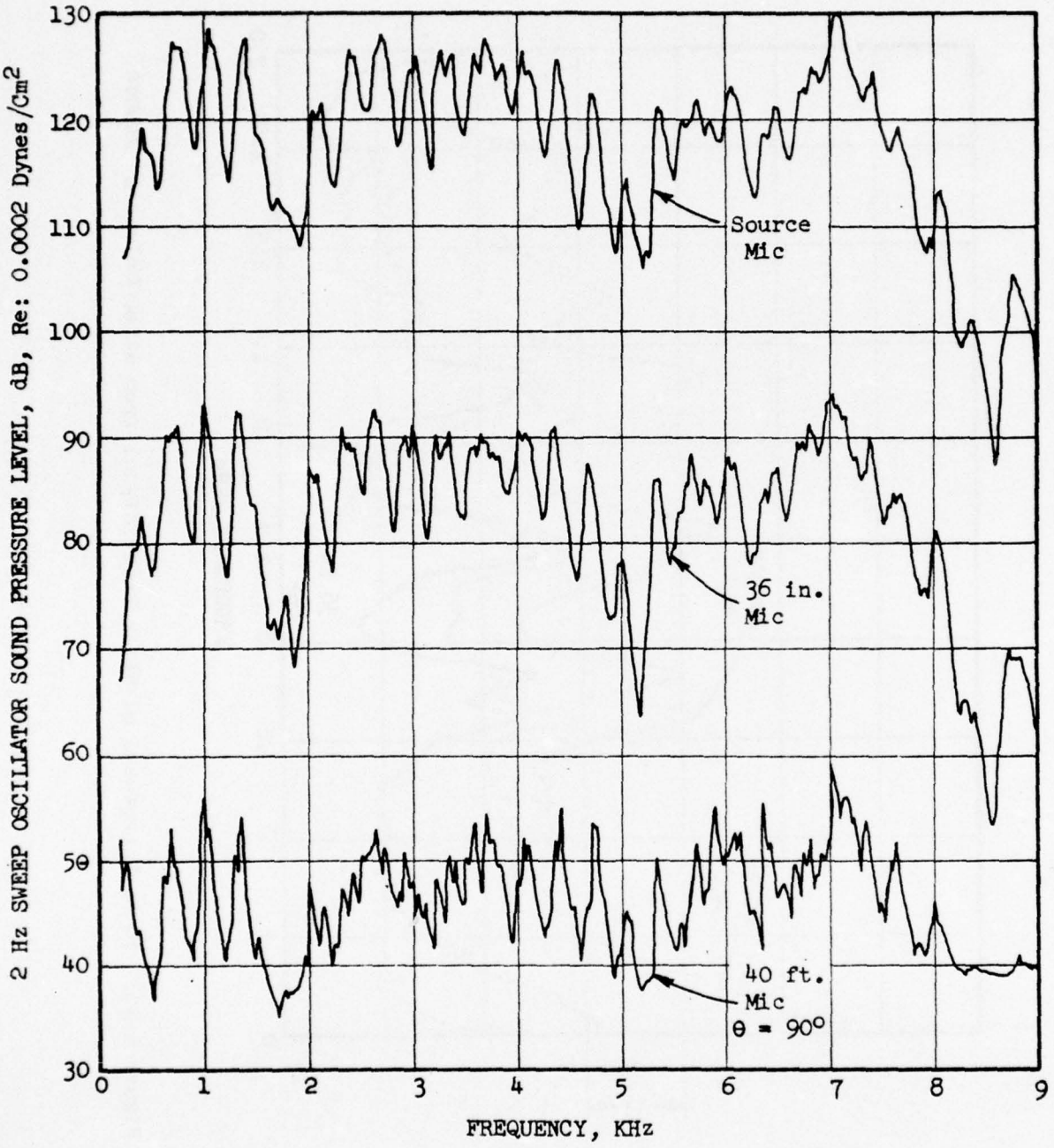


Figure 5-30. Two-Hz Narrowband of Sweep Oscillator Signal from Altec Driver at JENOTS.

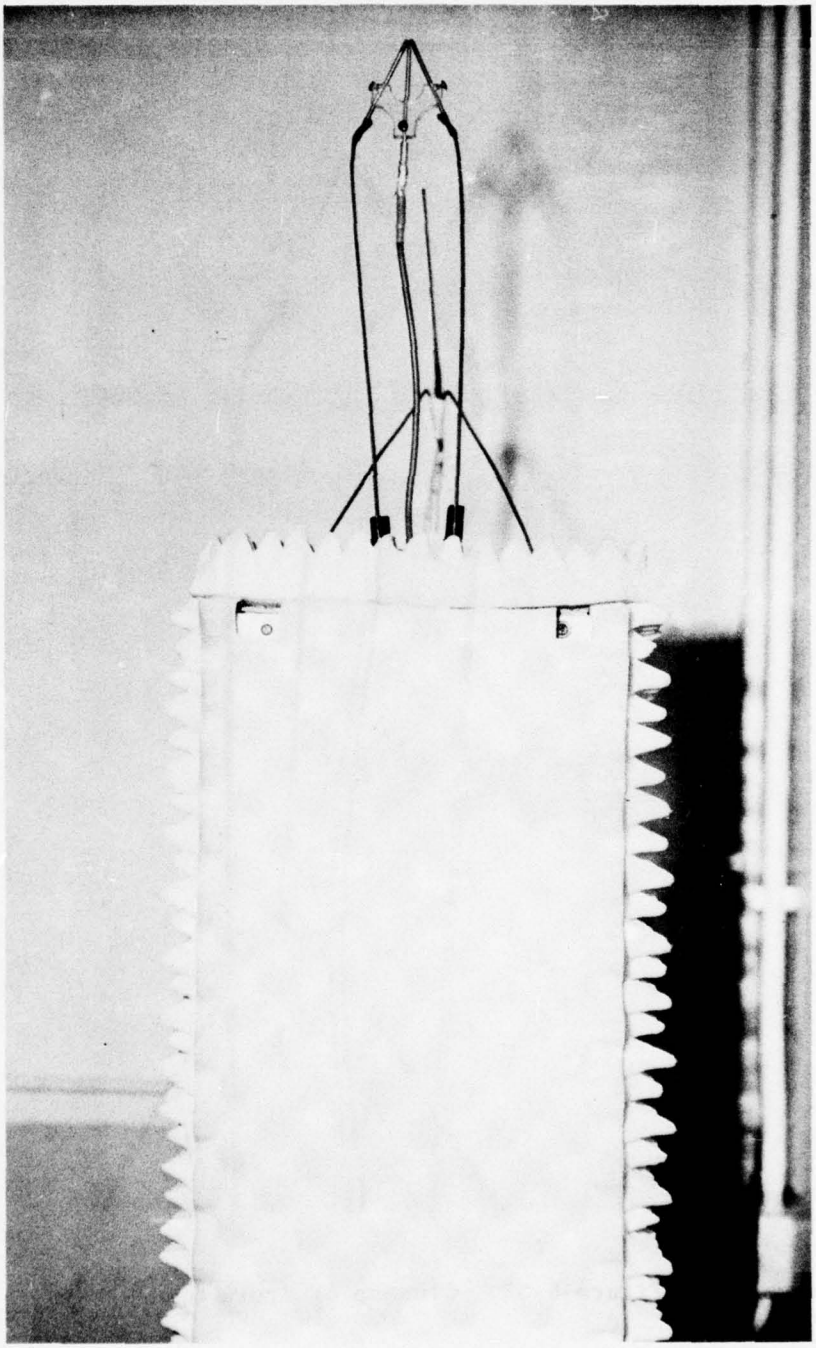


Figure 5-31. Spark Source.

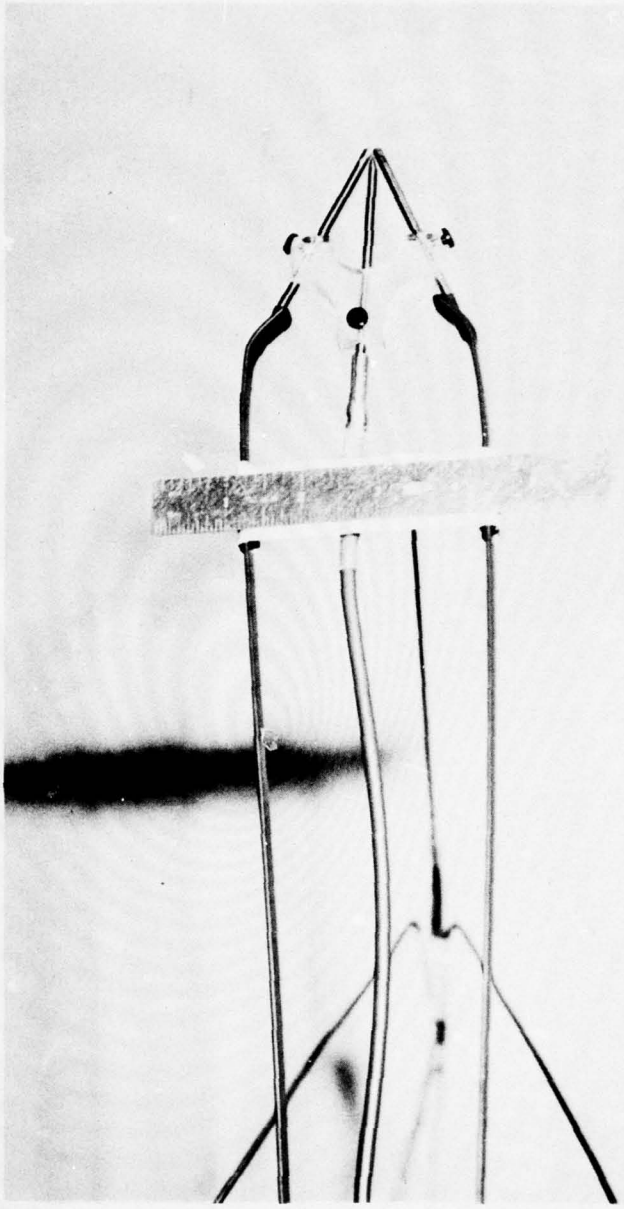


Figure 5-32. Closeup of Spark Gap.

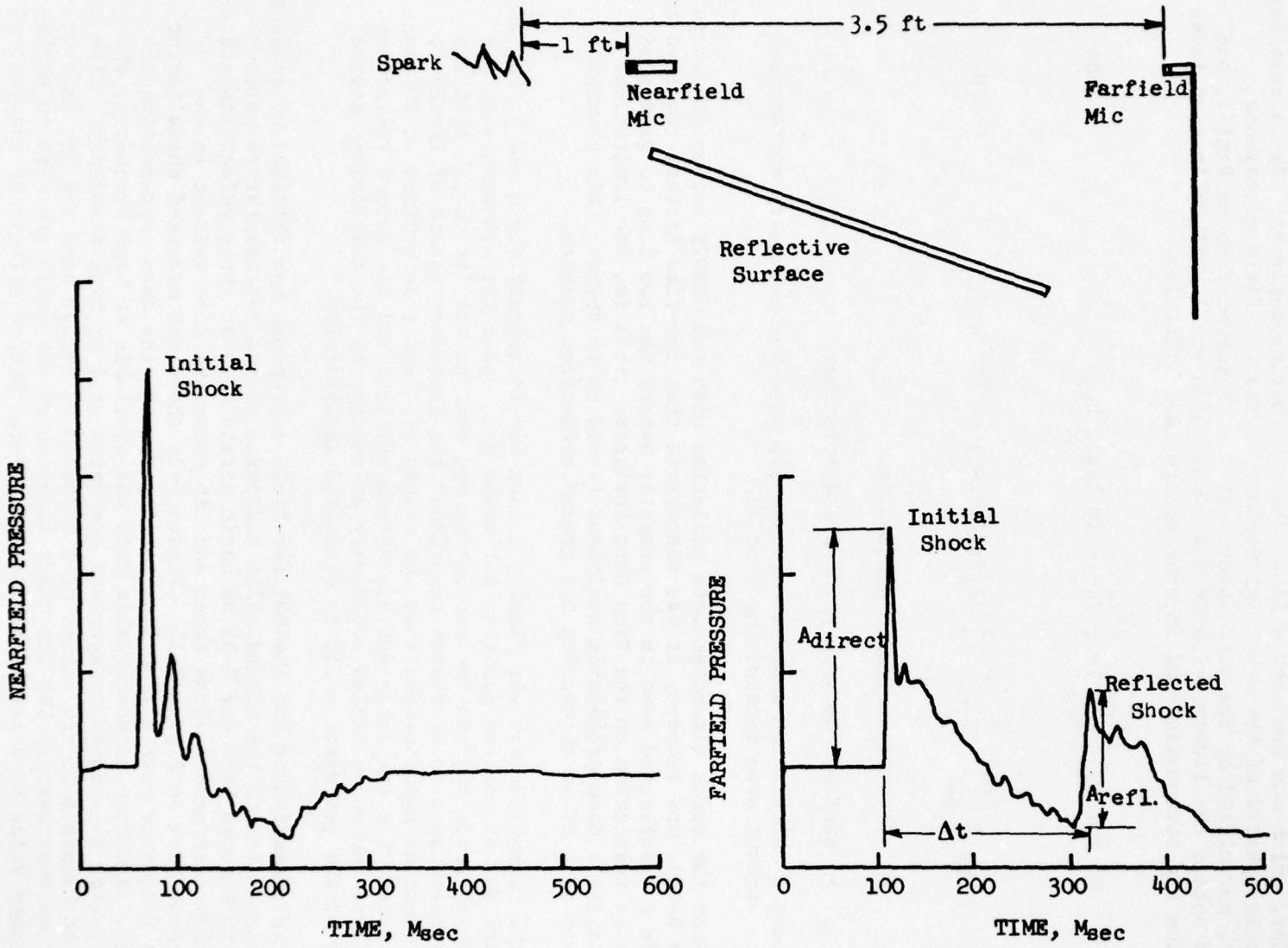


Figure 5-33. Spark Waveforms from Lab Test.

recorder, which was fed into a Time Data 100 Fourier analyzer. By calculating the cross spectra of the source microphone to the far-field microphone, $S_{SF}(f)$, normalized by the auto spectra of the source microphone $S_{SS}(f)$, one should obtain the linear transfer function, which equals the reflection index plus the air attenuation and inverse square law. That is:

$$\Delta N = \log_{10}\left(\frac{S_{SF}}{S_{SS}}\right) - \frac{\alpha R_{SF}}{1000} - 20 \log_{10} R_{SF} \tag{80}$$

$$S_{SF} = \underset{T\to\infty}{\text{Limit}} \frac{1}{T} \int_0^{\infty} \int_0^{T} P_S(t) P_F(t-\tau)\, e^{i2nf\tau}\, dt\, d\tau \tag{81}$$

α = air attenuation in dB/1000 ft

R_{SF} = distance between point S and F in feet

Such a calculation would theorectically give the necessary correction factors without even determining Q or ϕ.

When the spark discharge data collected with the JENOTS set up (shown in Figure 5-28), was reduced, it was discovered that the time history required to include the reflected wave in the computer memory was too long to give good frequency resolution on the Time Data Analyzer. That is, the limitations of the available data processing equipment caused us to abandon this promising approach as a means of solving the ground reflection problem.

The technique that was finally chosen was to extract the Q and ϕ from the standard 90° microphone position jet noise data under the argument that the 40-foot distance between the microphone and the jet was far enough that the jet appeared as a point source throughout the frequency domain of interest. It was further hypothesized that the values of Q and ϕ determined at 90° were also correct for the other arc microphone stations and the ground reflection pattern at the other angles would only be changed by the distributed source effect of the jet which could be estimated analytically.

The phase factor for the 90° far-field microphone was obtained by reading the frequencies of the ground nulls and peaks of the representative narrow-bands in Figures 5-34 and 5-35 of conic nozzle data at three velocities and a dual flow suppressor. Some tones and lip noise are also evident in the suppressor data in Figure 5-35. Figure 5-36 shows the measured phase factor versus frequency with a mean line passing through the data representing the average. Although no measureable data was available at high frequency, the phase factor is assumed to approach the value of 1 at high frequency. Also shown on Figure 5-36 are values of ϕ measured at angles near the jet axis on dual flow suppressor. The frequency location of the nulls are seen to shift to a lower value as a result of the distributed source effects of the jet.

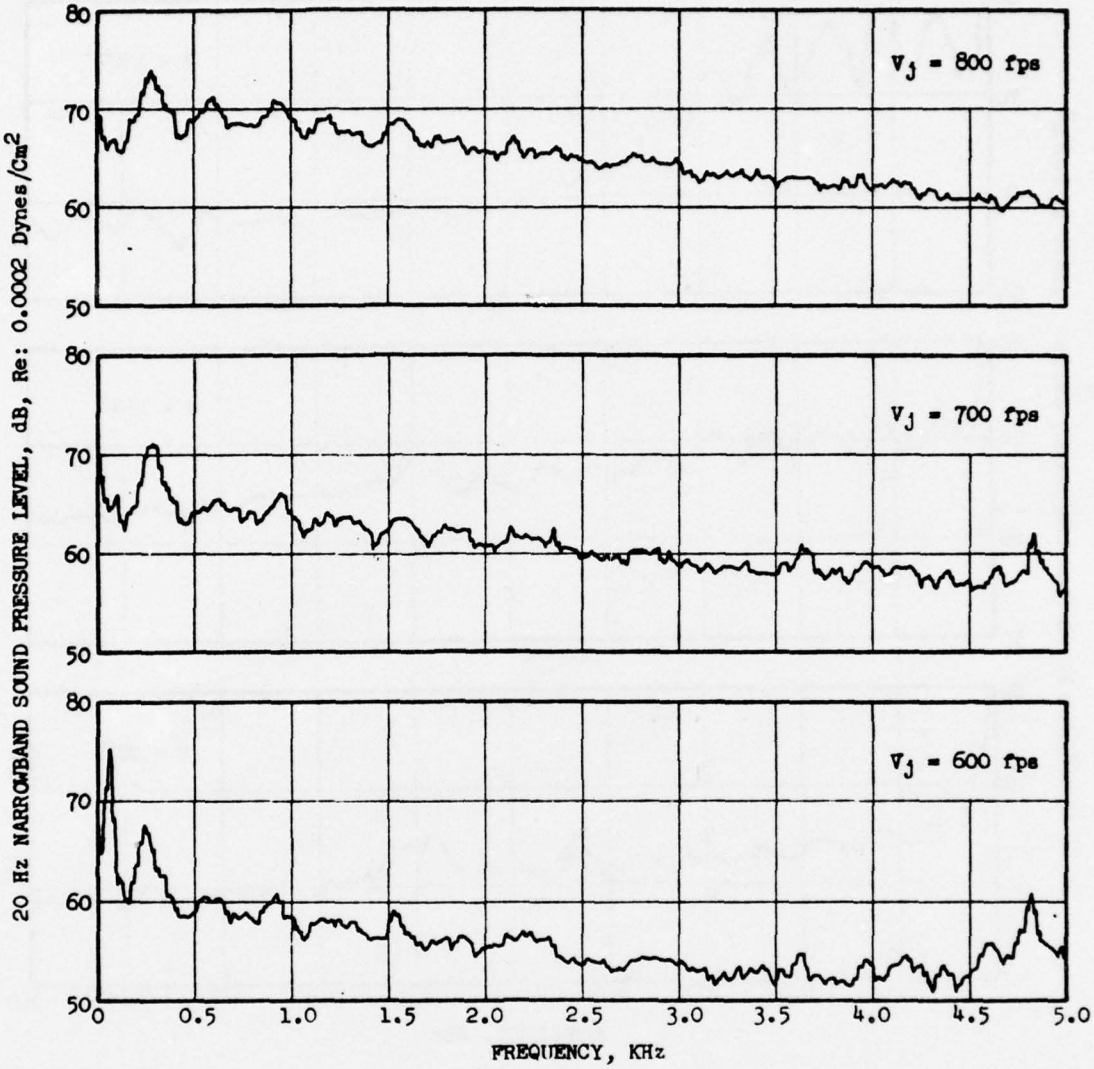
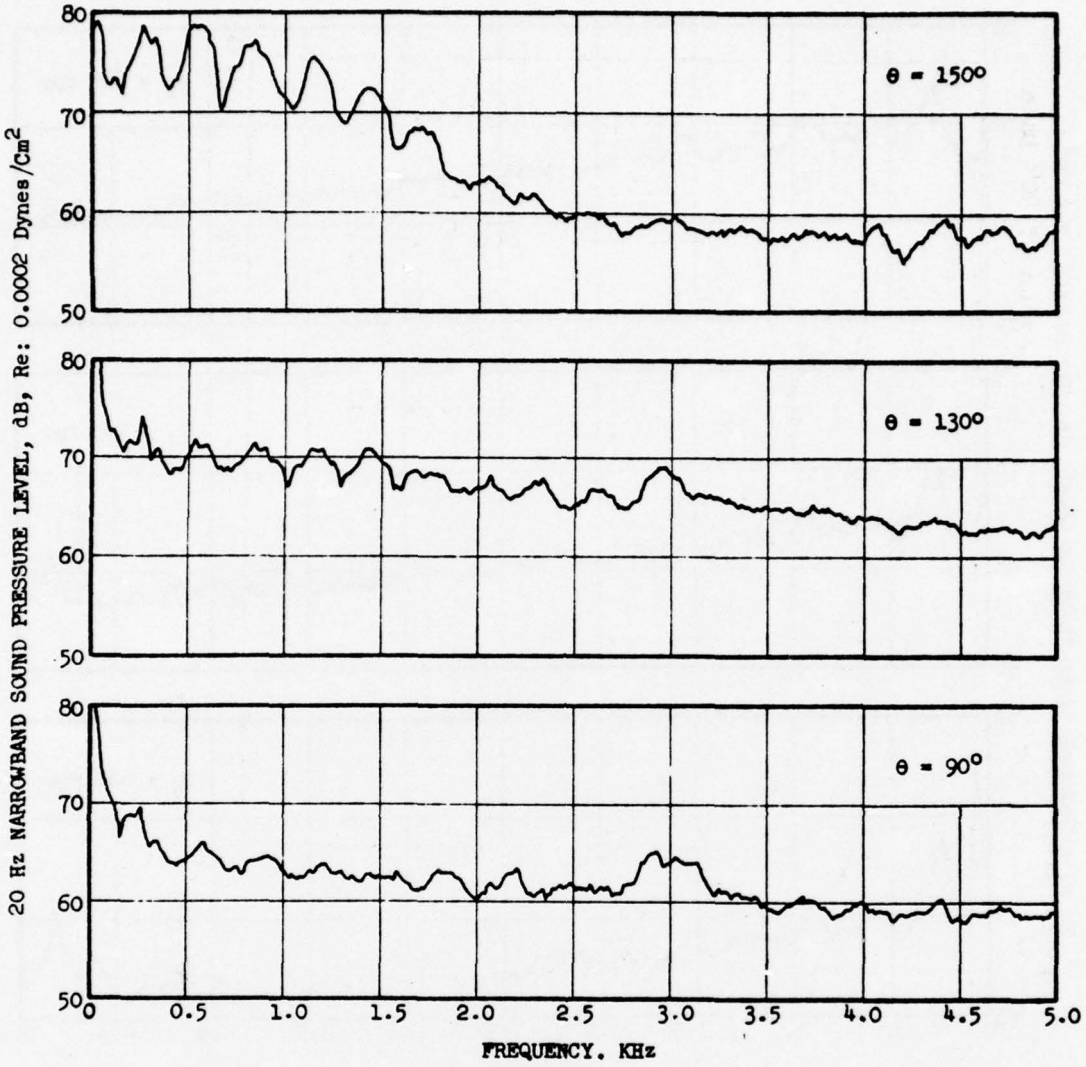


Figure 5-34. 20-Hz Narrowband of 90° Far-field (40 Foot) Conic Nozzle Data (4.64-inch Diameter Cold Jet) at JENOTS.


80
70
60
50
θ = 150°
θ = 130°
θ = 90°
20 Hz NARROWBAND SOUND PRESSURE LEVEL, dB, Re: 0.0002 Dynes/Cm²
0
0.5
1.0
1.5
2.0
2.5
3.0
3.5
4.0
4.5
5.0
FREQUENCY. KHz

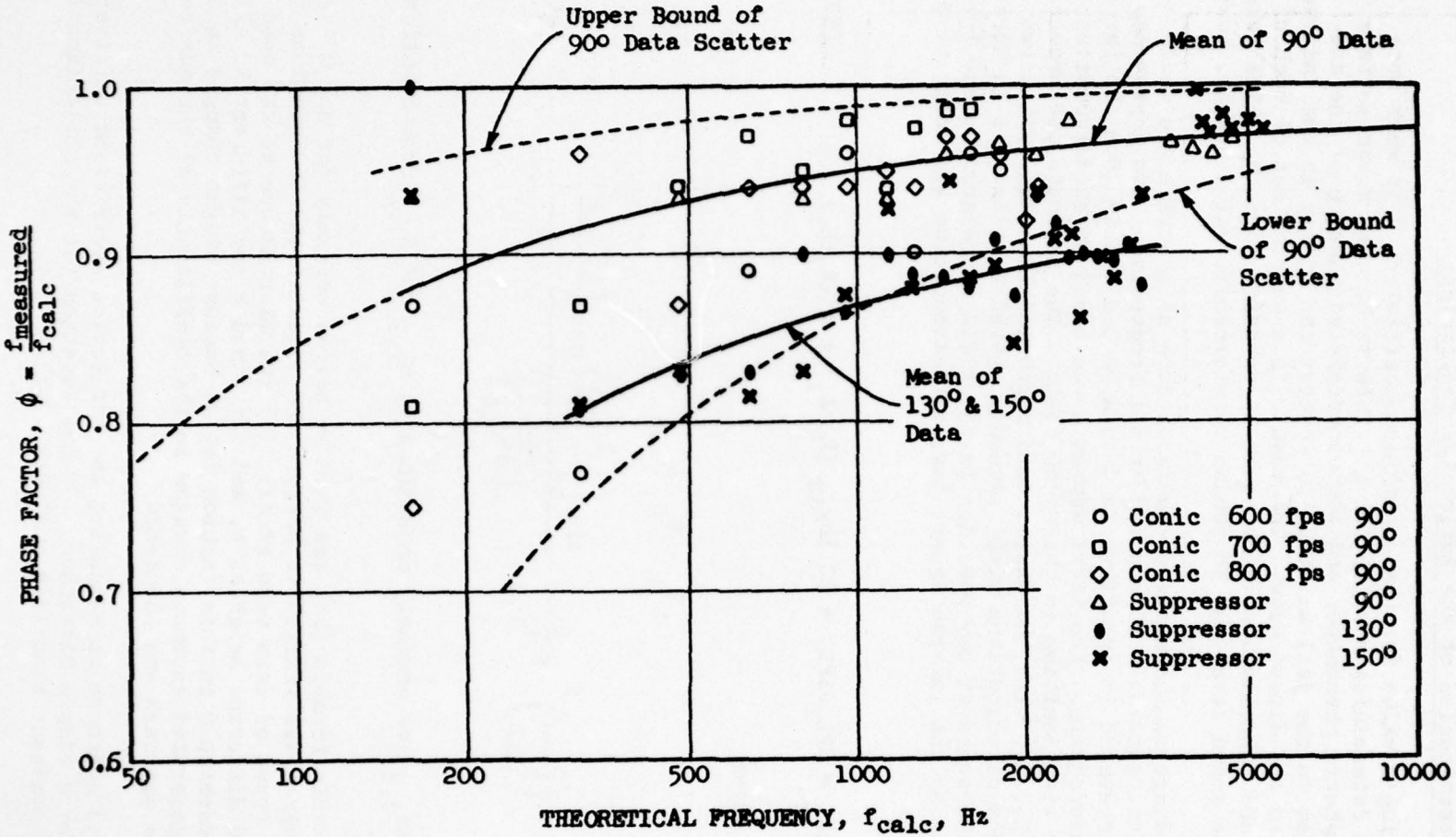


Figure 5-36. Variation of Ground Phase Factor with Frequency at JENOTS.

5.5.3 Determination of the Reflection Coefficient

Establishing a value for the reflection coefficient Q is much more difficult than determining a value for ϕ. This is because gross surface effects (atmospheric phenomenon and the uncorrelated phasing of the distributed sources in the jet) all tend to scatter the energy in the indirect wave relative to the direct wave. The result is a washing out of much of the reinforcement and cancellation which would be expected to occur. The general increase in the sound level due to random reinforcement still occurs, however.

From impedance measurements of surfaces such as concrete one would expect that Q would fall between 0.95 and 1.0 at all freqencies. Two approaches however were attempted in an effort to determine Q directly from the far-field microphone measurements. The first approach was based on the assumption that Q is invariant with position in the sound field. Two separate measurements at (R_1, h_1) and (R_2, h_2) with the source in a fixed location will yield two reflection index distributions with frequency, given a value of ϕ in Equation (50). Since the sound at any position in the field is related to the level at any other point by the inverse square law, air attenuation and reflection index, then:

$$k = \Delta N_2 - \Delta N_1 = SPL_2 - SPL_1 + 20 \log_{10} (R_2/R_1) + \alpha (R_2 - R_1) \tag{82}$$

Equation (12) gives

$$Y_z = Y_1 \, 10^k \tag{83}$$

$$Y_{1,2} = 1 + \left(\frac{Q}{Z_{1,2}}\right)^2 + \frac{2Q}{Z_{1,2}} \; \frac{\sin\left(\frac{\alpha \, \Delta r_{1,2}}{\phi \; \lambda}\right) \cos\left(\frac{\beta \Delta r_{1,2}}{\phi \; \lambda}\right)}{\left(\frac{\alpha \Delta r}{\phi \lambda_{1,2}}\right)} \tag{84}$$

and $Z_{1,2}$ and $\Delta r_{1,2}$ are uniquely determined by $h_{1,2}$ and $R_{1,2}$ from Equations (40) and (41).

The quadratic formula (84) can then be solved uniquely for any Q. A data processing program was written to perform the calculations in Equations (82) to (84). Two types of data were tried: (1) two microphones at the same radius, R, and different heights, h, and (2) fixed h and different R. All efforts to determine Q in this fashion failed because slight changes in the SPL readings generated enormous changes in the coefficients of the quadratic equation. The approach was abandoned.

The second approach at measuring the reflection coefficient utilized the measurements at a single microphone and the equation for the reflection index obtain with a constant bandwidth analysis, viz:

$$\Delta N = 10 \log_{10} \left[1 + \left(\frac{Q}{Z}\right)^2 + \frac{2Q}{Z} \gamma \cos \left(\frac{2\pi \Delta r}{\phi \lambda_1}\right) \right] \tag{85}$$

where

$$\gamma = \frac{\sin \left(\frac{\pi \Delta r \Delta f}{\phi c}\right)}{\frac{\pi \Delta r \Delta f}{\phi c}} \tag{86}$$

at a maximum (reinforcement)

$$\Delta N_{max} = 10 \log_{10} \left[1 + \frac{2Q\gamma}{Z} + \left(\frac{Q}{Z}\right)^2 \right] \tag{87}$$

at a minimum (null)

$$\Delta N_{min} = 10 \log_{10} \left[1 - \frac{2Q\gamma}{Z} + \left(\frac{Q}{Z}\right)^2 \right] \tag{88}$$

subtracting and defining:

$$K = 10^{\left(\Delta N_{max} - \Delta N_{min}\right)/20} \tag{89}$$

gives:

$$\frac{Q}{Z} = \frac{(K^2+1)\,\gamma - \sqrt{(K^2+1)^2\,\gamma^2 - (K^2-1)^2}}{K^2-1} \tag{90}$$

If a small enough band width, Δf, is used to give $\Delta f \ll c/\Delta r$ then $\gamma \sim 1$ and Equation (90) becomes

$$\frac{Q}{K} = \frac{K-1}{K+1} \qquad (\text{as } \gamma \rightarrow 1) \tag{91}$$

Note that the minimum value γ can have for Equation (90) to remain real is

$$\gamma_{min} = \frac{K-1}{K+1} \tag{92}$$

in which case

$$\left(\frac{Q}{Z}\right)_{max} = \frac{K^2+1}{(K+1)^2} \tag{93}$$

Figure 5-37 shows the variation of Q/Z from Equations (91) and (93) with the measured difference in spectral level between the reinforcement and the cancellation null. Using Figure 5-37 with $\gamma \tilde{=} 1.0$, the value of Q was estimated for the narrowband plots (Figures 5-34 and 5-35). Figure 5-38 shows the variation with frequency. The reflection coefficient determined in this fashion is seen to rapidly fall off with increasing frequency. This is a result of the scattering phenomenon mentioned earlier which is not considered in any of the ground reflection equations presented here. As one moves closer to the jet axis, the measured Q increases in value, indicating that uncorrelated phasing between distributed sources in the jet is the chief cause of the energy scattering.

If one uses the value of Q in Figure 5-38 without accounting for the overall pressure increase due to random scattering, an erroneous answer will be obtained. From Equation (45), a total random scattering would give.

$$\Delta N_{\substack{Total \\ Scatter}} = 10 \log_{10} \left[1 + \frac{Q}{Z}\right]^2 \tag{94}$$

where the Q in Equation (94) should be that value obtained from impedance measurements of the surface and not the values on Figure 5-38. Figure 5-38 tells the proper distribution of the amplitude of the ground nulls from the remaining acoustic energy that has not been scattered. In some sense one can establish two reflection coefficients: Q_I, for the surface and Q_s, the reduced value due to scattering.

From this viewpoint the reflection index should be calculated from a modification of Equation (45)

$$\Delta N = 10 \log_{10} \left[1 + \left(\frac{QI}{Z}\right)^2 + \left(\frac{2QsQI}{Z}\right) \frac{\sin\left(\frac{d\Delta r}{\phi\lambda}\right)\cos\left(\frac{\beta\Delta r}{\phi\lambda}\right)}{\left(\frac{\alpha\Delta r}{\phi\lambda}\right)}\right] \tag{95}$$

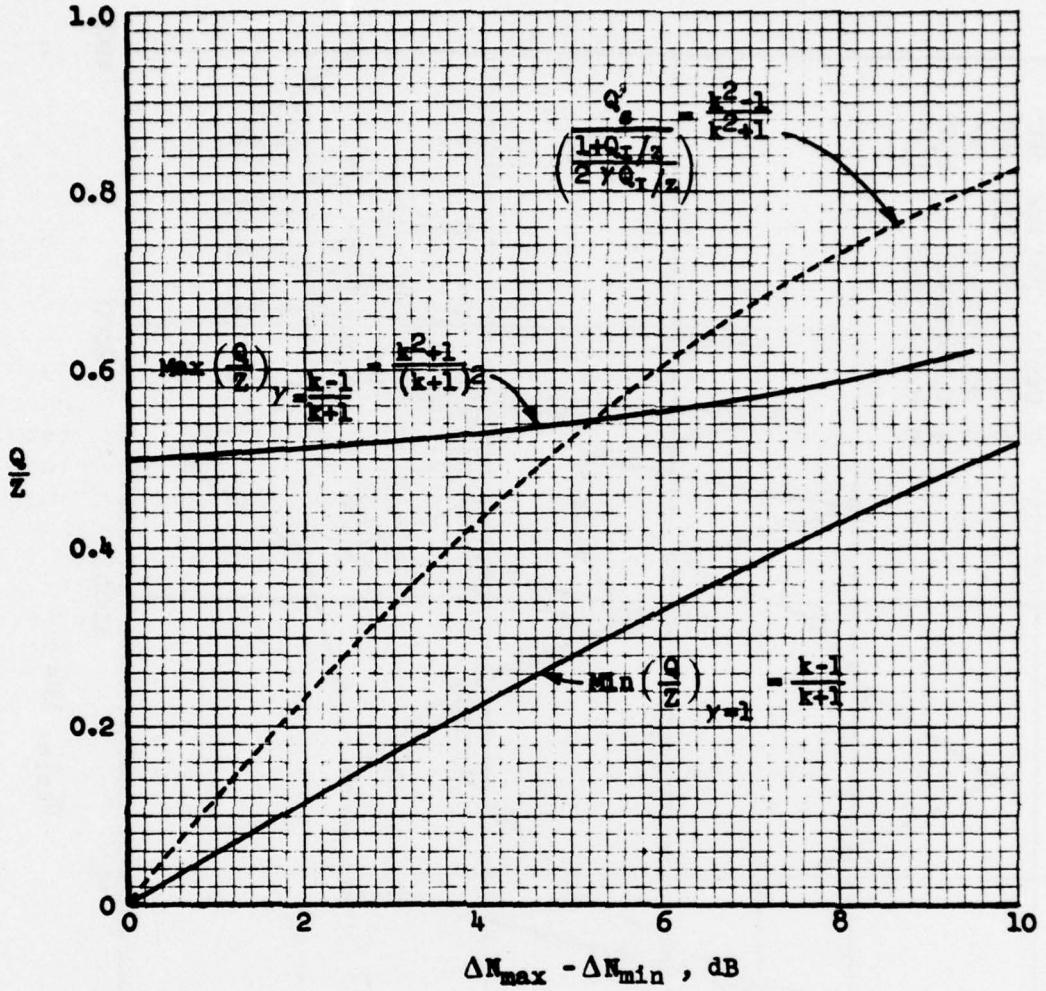


Figure 5-37. Working Curve to Calculate Reflection Coefficient, Q, from Difference Between Adjacent Peaks and Nulls.

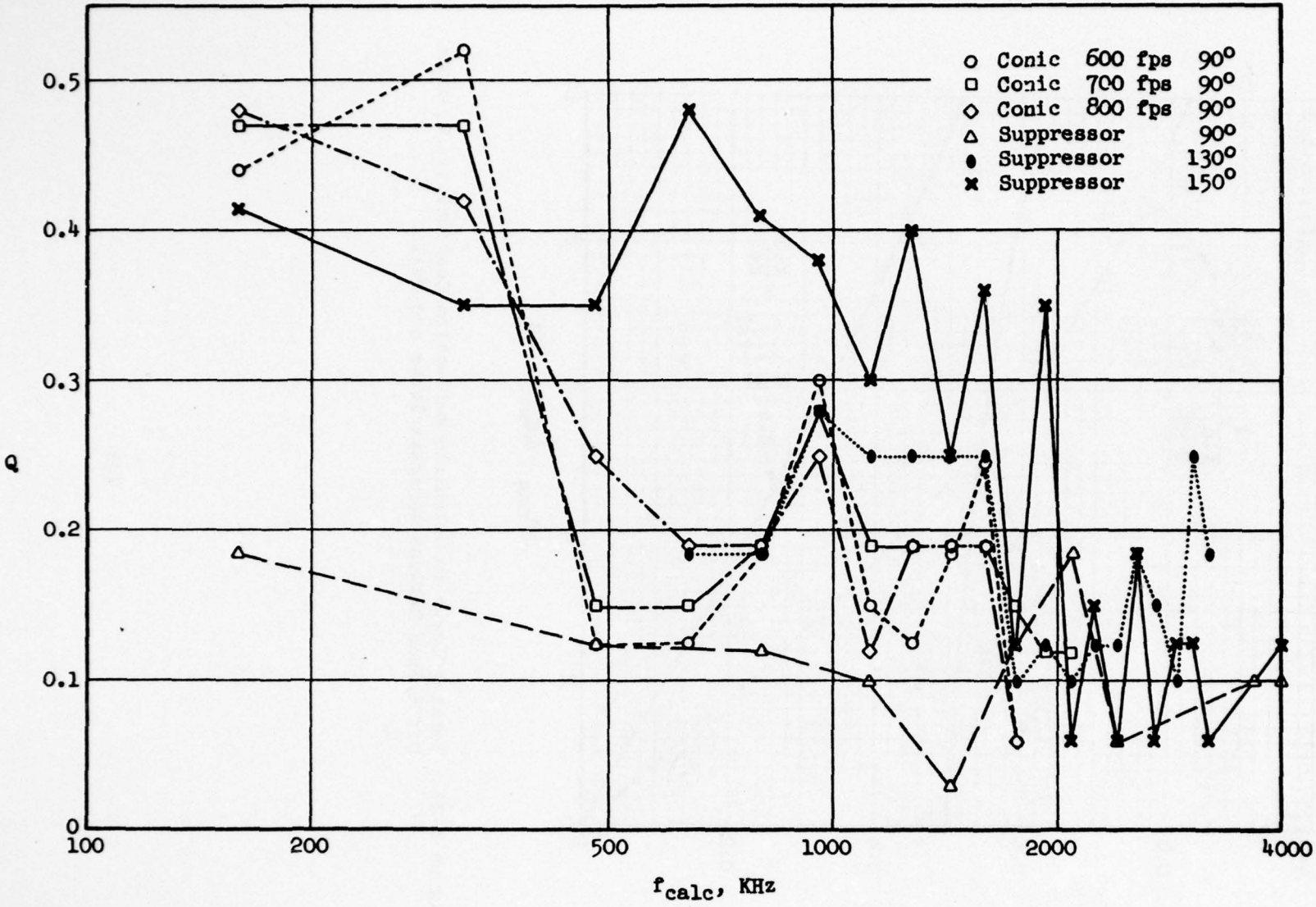


Figure 5-38. Variation of Ground Reflection Coefficient with Frequency at JENOTS.

where Q_I is determined from impedance measurements and Q_s determined from narrowbands using the relation

$$\frac{Q_s}{Z} = \frac{I+Q_I/Z}{2\gamma Q_I} \quad \frac{K^2-1}{K^2+1} \tag{96}$$

derived similarily to Equation (90). This relationship, Equation (96), is plotted on Figure 5-37 and values for Q_s from the JENOTS data are shown in Figure 5-39 for $Q_I = 1.0$.

5.5.4 JENOTS Ground Reflection Correction Factors

Using the value of ϕ and Q_s from Figures 5-36 and 5-39, respectively, with $Q_I = 1.0$, the value of the reflection coefficient correction can be calculated for a point source Equation (95). The choice of $Q_I = 1.0$ has been found, from impedance measurements, to be a good estimate for hard surfaces such as concrete. Figure 5-15 shows that if the true value for concrete is somewhat less than 1.0, say 0.9, the resulting error on the reflection index ΔN is minor. The problem of a distributed source was attacked analytically in Section 5.4 assuming the jet to be a coherent column of sources with specified frequency and amplitude distribution. The analysis of Section 5.4 was modified to include the scattering and ground impedance effects as in Equation (95). The resulting calculations are shown in Table 5-I. These values were incorporated into the data reduction program as standard corrections for JENOTS data.

5.5.5 A Check for Smoothness: Tests with a Fiberglass Ground

To determine the accuracy of the ground reflection corrections, an effort was made to convert JENOTS to a pseudo-anechoic arena by covering the ground with from 6- to 12-inch-thick fiberglass batting such as that typically used in home insulation. This testing was conducted to check the validity of the analytically derived correction factors described in the previous sections. The data was not used to arrive at the final correction factors in Table 5-I. Figure 5-40 shows the JENOTS arena with the fiberglass ground cover. The fiberglass was distributed as shown in Figure 5-41 and 5-42 such that the ideal reflection point had 12 inches of insulation.

The effectiveness of the fiberglass was estimated by using the measured resistance $R/\rho c$ and reactance $X/\rho c$ of the fiberglass supplied by the Corning Company as shown in Figure 5-43. No data is shown beyond 6300 Hz, but the values of the resistance and reactance approach 1 and 0, respectively, for all higher frequencies. In regions of the arena where a double thickness of fiberglass batting was used, the resistance of the surface can be approximated by the values used in Figure 5-43 for a single layer of batting. This is

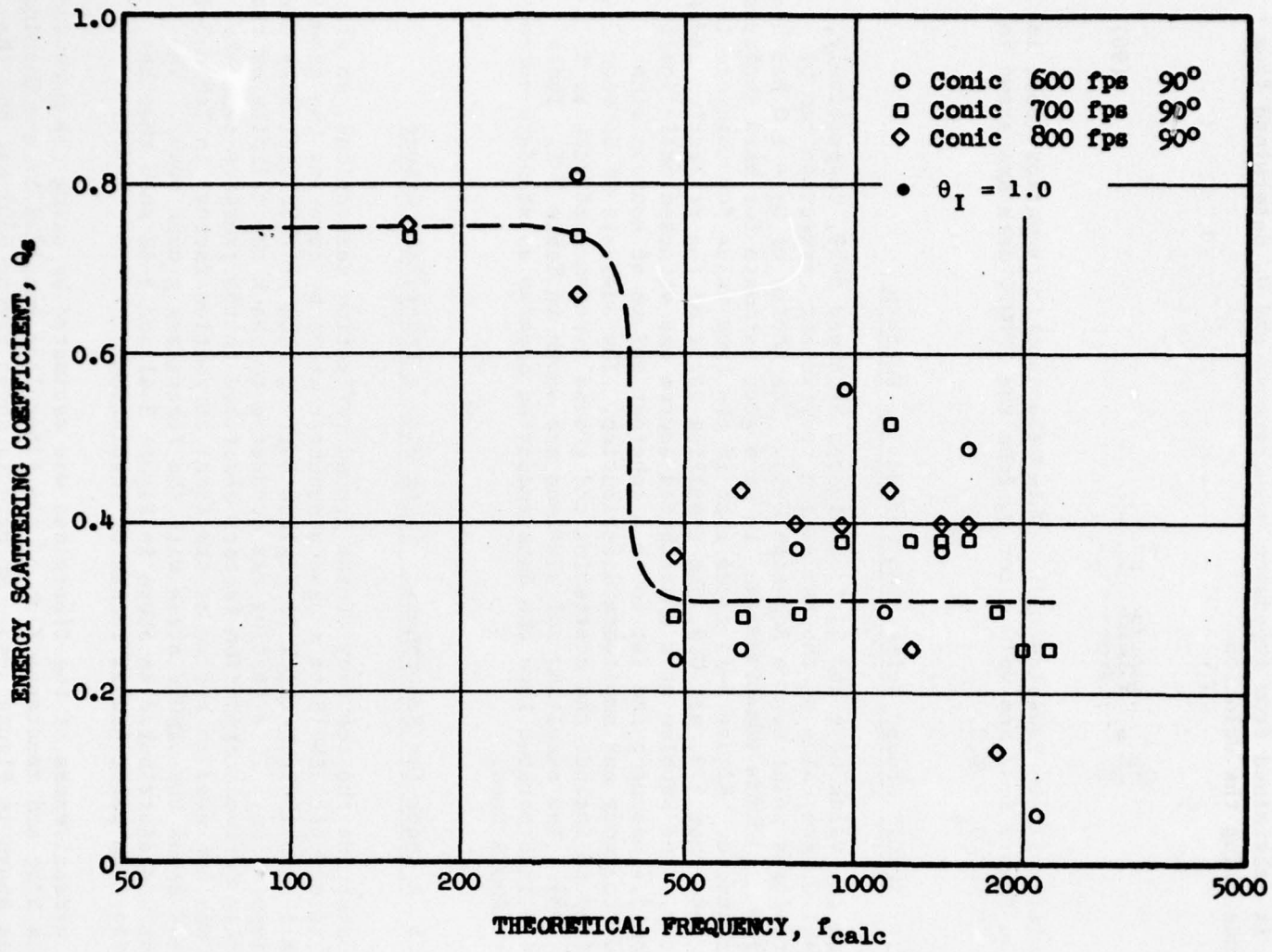


Figure 5-39. Variation of Energy Scattering Coefficient with Frequency.

Table 5-I. JENOTS Ground Reflection Corrections.

(Δ dB's to be added to SPL's)

ANGLES	30	40	50	60	70	80	90	100	110	120	130	140	150	160
FREQUENCY														
50 Hz	-4.99	-4.97	-4.93	-4.88	-4.82	-4.75	-4.66	-4.55	-4.41	-4.24	-4.03	-3.77	-3.46	-3.1
63 Hz	-4.45	-4.41	-4.35	-4.29	-4.21	-4.1	-3.98	-3.82	-3.64	-3.42	-3.16	-2.86	-2.52	-2.19
80 Hz	-4.0	-4.0	-3.34	-3.23	-3.1	-2.95	-2.76	-2.53	-2.27	-1.96	-1.61	-1.22	- .83	- .47
100 Hz	-4.0	-4.0	-3.0	-3.0	-3.0	-2.0	- .7	- .34	- .07	0	0	1.6	2.11	2.54
125 Hz	-3.5	-4.0	-3.5	-2.0	-2.5	- .5	1.7	1.0	1.0	2.0	2.0	2.9	3.8	2.8
160 Hz	0	-1.5	-2.5	- .5	-1.0	1.5	2.7	1.5	3.0	3.0	2.0	3.0	3.2	2.2
200 Hz	-2.0	-1.5	-1.5	-1.0	-1.0	.5	0	0	0.5	1.0	- .17	- .65	-1.03	0
250 Hz	0	0	0	- .5	-1.5	-1.5	-2.5	-2.5	1.5	-1.0	-2.0	-4.48	-4.58	-2.39
315 Hz	1.5	0	-1.5	-1.5	-1.5	-1.8	-4.0	-1.5	-3.0	-3.0	-3.0	-4.9	-5.09	-2.0
400 Hz	-2.0	-4.2	-4.1	-3.5	-2.5	-3.2	-3.1	-2.34	-1.85	-1.34	-4.9	- .37	-0.7	-4.3
500 Hz	-1.0	-1.0	0	-1.3	-1.1	-1.2	-1.1	-1.35	-1.14	-1.87	-2.1	+1.8	- .5	- .5
630 Hz	-1.64	-1.5	-1.0	-2.5	-2.0	-3.2	-2.1	-2.09	-2.03	-3.5	-3.5	-1.64	-1.3	- .9
800 Hz	-1.55	-1.35	-1.12	-1.0	-1.0	-2.0	-2.1	- .88	-1.22	-0.5	-1.05	- .5	- .8	+2.2
1000 Hz	-1.0	-2.44	-1.3	-2.36	-2.3	-2.13	-1.9	-1.72	-1.47	-1.22	-2.1	-1.9	- .71	- .8
1250 Hz	-1.97	-2.03	-2.10	-2.17	-2.24	-2.28	-2.3	-2.28	-2.24	-2.18	-2.12	-2.08	-2.04	-2.2
1600 Hz	-2.17	-1.5	-2.06	-1.98	-1.90	-1.83	-1.8	-1.83	-1.93	-2.07	-2.23	-2.36	-2.45	-2.5
2000 Hz	- .74	-2.0	-2.8	- .92	-1.11	-1.37	-1.7	-1.90	-2.05	-2.10	-2.06	-1.97	-1.88	-1.8
2500 Hz	-1.5	-2.0	-1.8	-2.84	-2.70	-2.52	-2.35	-2.29	-2.31	-2.37	-2.45	-2.51	-2.54	-2.56
3150 Hz	-2.57	-2.57	-2.60	-2.66	-2.78	-2.93	-3.1	-3.14	-3.07	-2.91	-2.75	-2.65	-2.6	-2.59
4000 Hz	-2.80	-2.78	-2.74	-2.66	-2.58	-2.55	-2.60	-2.67	-2.72	-2.72	-2.72	-2.72	-2.72	-2.71
5000 Hz	-2.69	-2.72	-2.77	-2.84	-2.90	-2.85	-2.60	-2.41	-2.36	-2.44	-2.52	-2.56	-2.58	-2.59
6300 Hz	-2.70	-2.68	-2.64	-2.59	-2.56	-2.64	-2.90	-2.97	-2.85	-2.72	-2.68	-2.66	-2.66	-2.66
8000 Hz	-2.76	-2.76	-2.75	-2.73	-2.67	-2.60	-2.70	-2.80	-2.78	-2.74	-2.72	-2.71	-2.7	-2.7
10000 Hz	-2.69	-2.69	-2.68	-2.67	-2.67	-2.71	-2.80	-2.70	-2.60	-2.63	-2.65	-2.65	-2.65	-2.65
12500 Hz	-2.70	-2.70	-2.70	-2.69	-2.69	-2.70	-2.70	-2.70	-2.66	-2.66	-2.66	-2.66	-2.66	-2.66
16000 Hz	-2.61	-2.61	-2.61	-2.60	-2.58	-2.56	-2.70	-2.60	-2.57	-2.57	-2.57	-2.57	-2.57	-2.57
20000 Hz	-2.63	-2.63	-2.63	-2.62	-2.61	-2.61	-2.70	-2.56	-2.60	-2.60	-2.59	-2.59	-2.59	-2.59
25000 Hz	-2.71	-2.71	-2.71	-2.70	-2.70	-2.69	-2.70	-2.68	-2.68	-2.68	-2.67	-2.67	-2.67	-2.66
31500 Hz	-2.74	-2.73	-2.73	-2.73	-2.72	-2.72	-2.70	-2.71	-2.71	-2.70	-2.70	-2.69	-2.69	-2.69
40000 Hz	-2.71	-2.71	-2.71	-2.71	-2.70	-2.70	-2.70	-2.69	-2.68	-2.68	-2.68	-2.67	-2.67	-2.67
50000 Hz	-2.73	-2.73	-2.73	-2.73	-2.72	-2.72	-2.70	-2.71	-2.70	-2.70	-2.70	-2.69	-2.69	-2.69
63000 Hz	-2.70	-2.70	-2.70	-2.69	-2.69	-2.68	-2.70	-2.68	-2.67	-2.67	-2.66	-2.66	-2.66	-2.65
80000 Hz	-2.72	-2.72	-2.72	-2.71	-2.71	-2.71	-2.70	-2.70	-2.69	-2.69	-2.68	-2.68	-2.68	-2.68

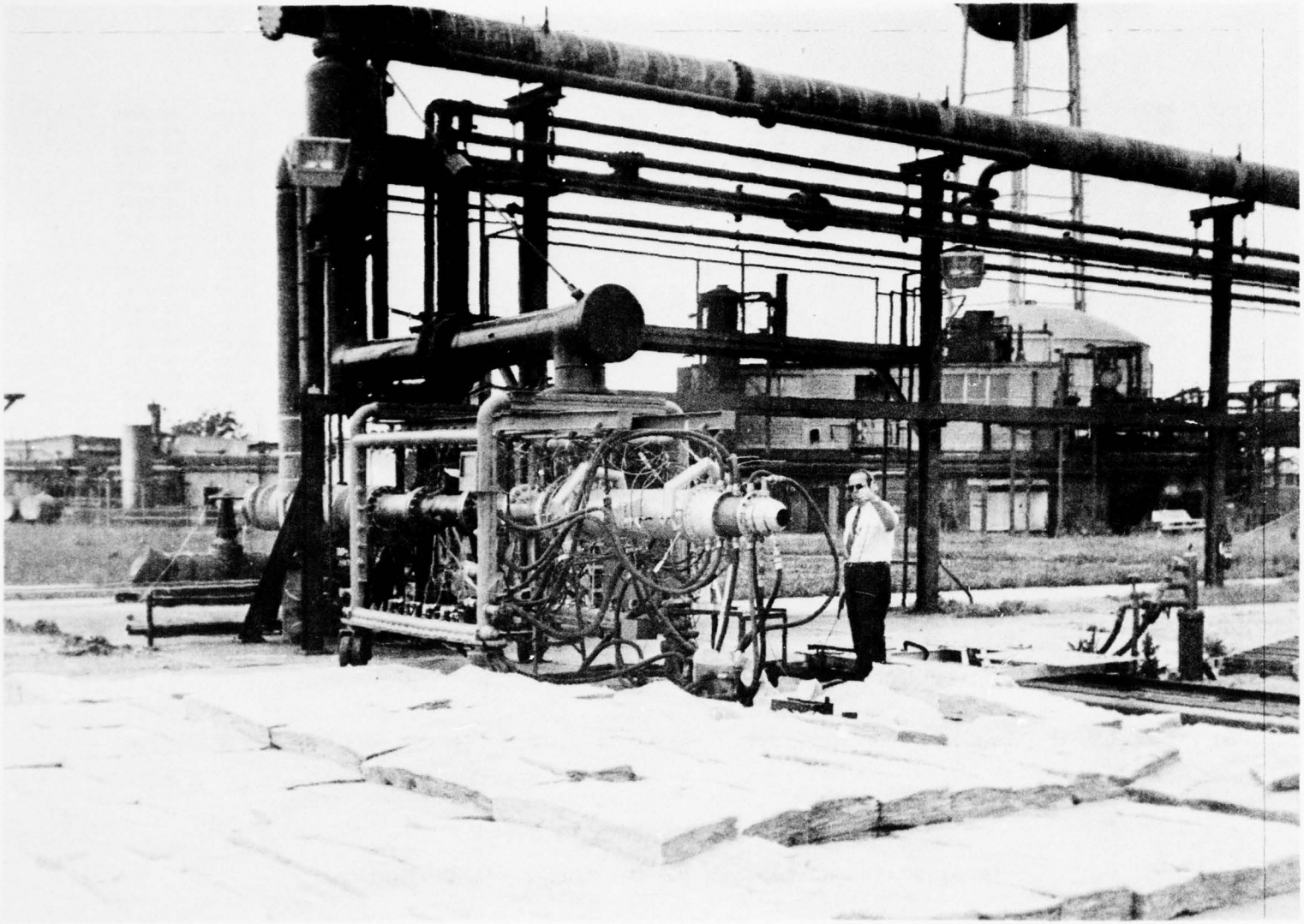


Figure 5-40. JENOTS Test Facility in Evendale, Ohio.

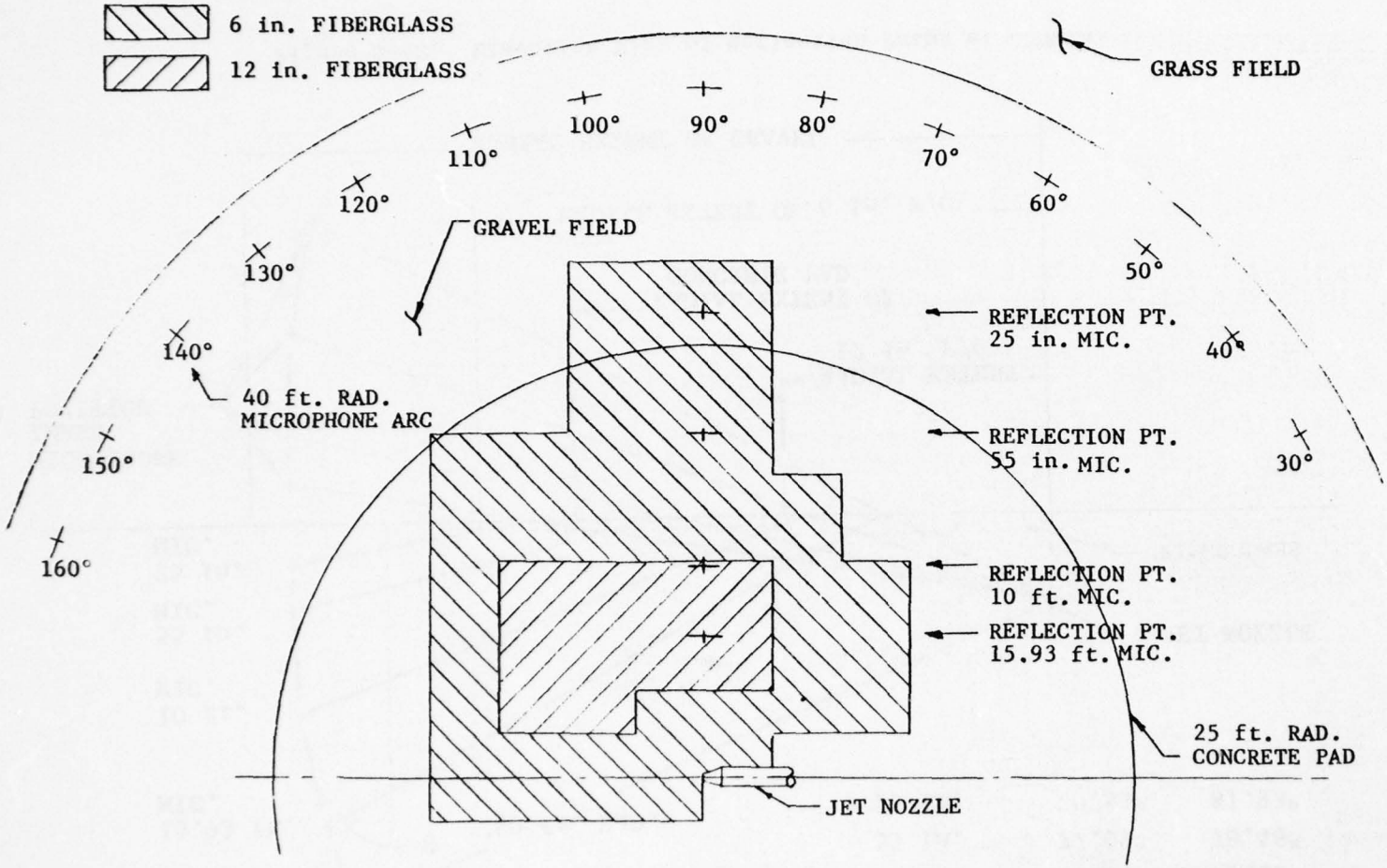
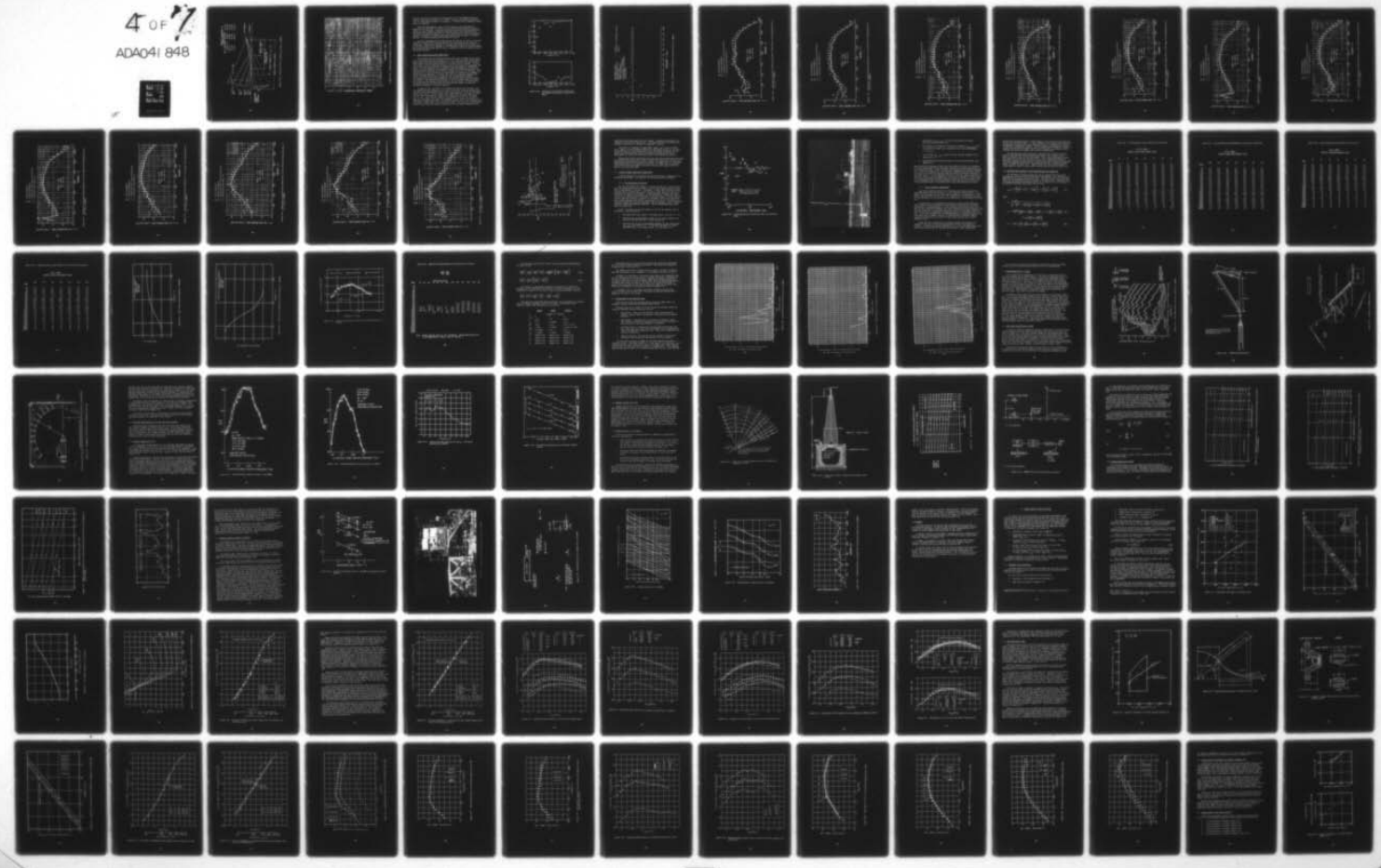
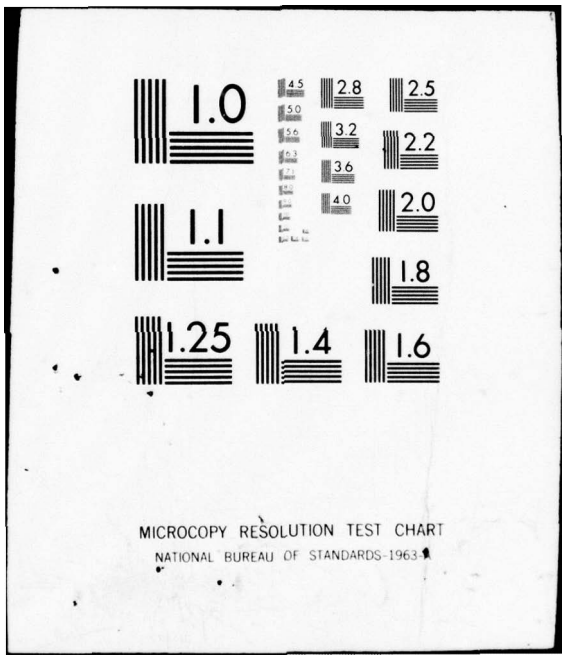


Figure 5-41. Fiberglass Ground Treatment at JENOTS.

AD-A041 848 GENERAL ELECTRIC CO CINCINNATI OHIO AIRCRAFT ENGINE GROUP F/G 14/2
HIGH VELOCITY JET NOISE SOURCE LOCATION AND REDUCTION. TASK 1. --ETC(U)
FEB 77 C T SAVELL, E J STRINGAS DOT-OS-30034
UNCLASSIFIED R77AEG187 FAA-RD-76-79-1 NL

4 OF 7
ADA041 848




1.0
1.1
1.25
1.4
1.6
1.8
2.0
2.2
2.5
2.8
3.2
3.6
4.0
4.5
5.0
5.6
6.3
MICROCOPY RESOLUTION TEST CHART
NATIONAL BUREAU OF STANDARDS-1963-A

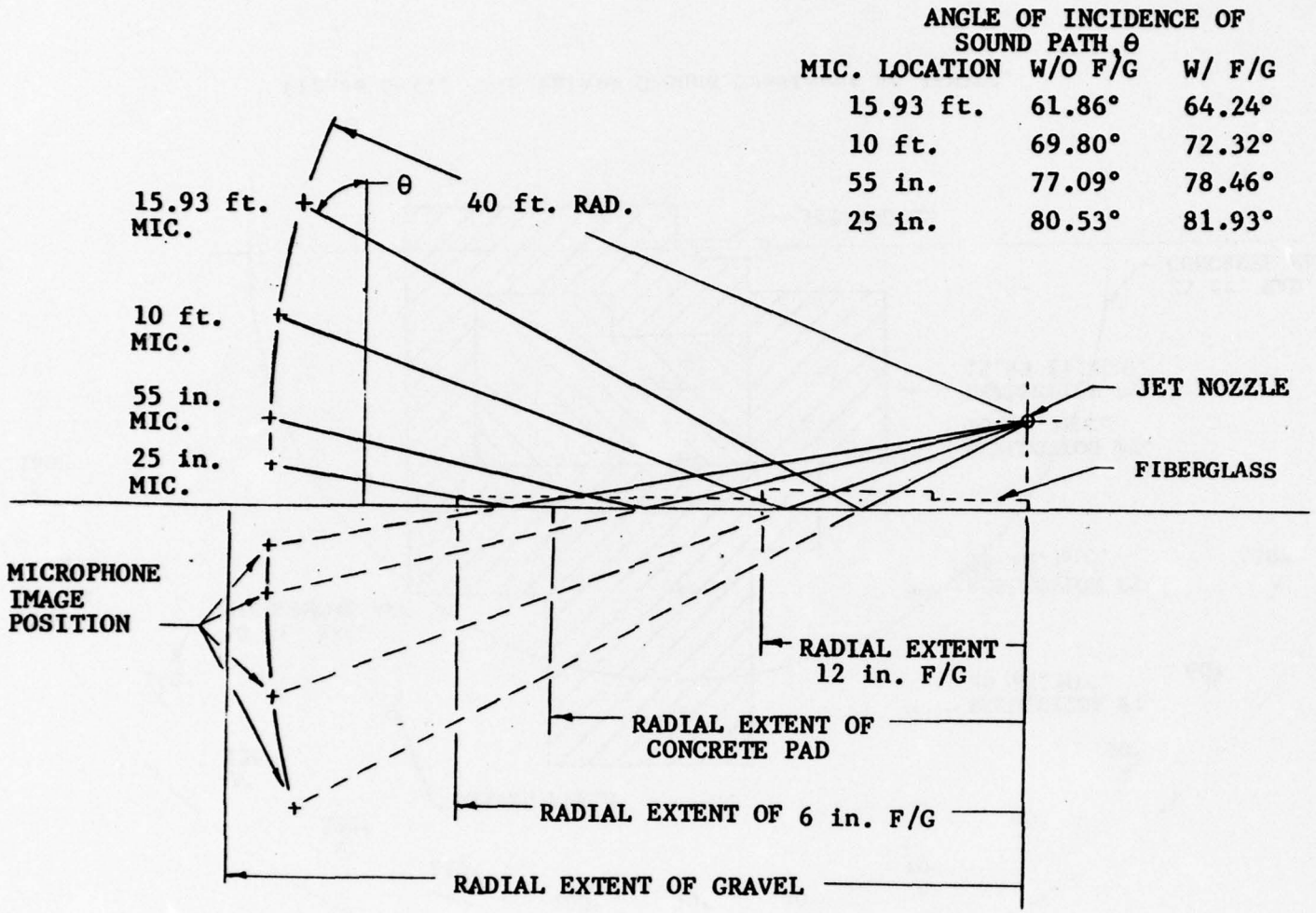


Figure 5-42. Elevation View of Reflection Paths at JENOTS.

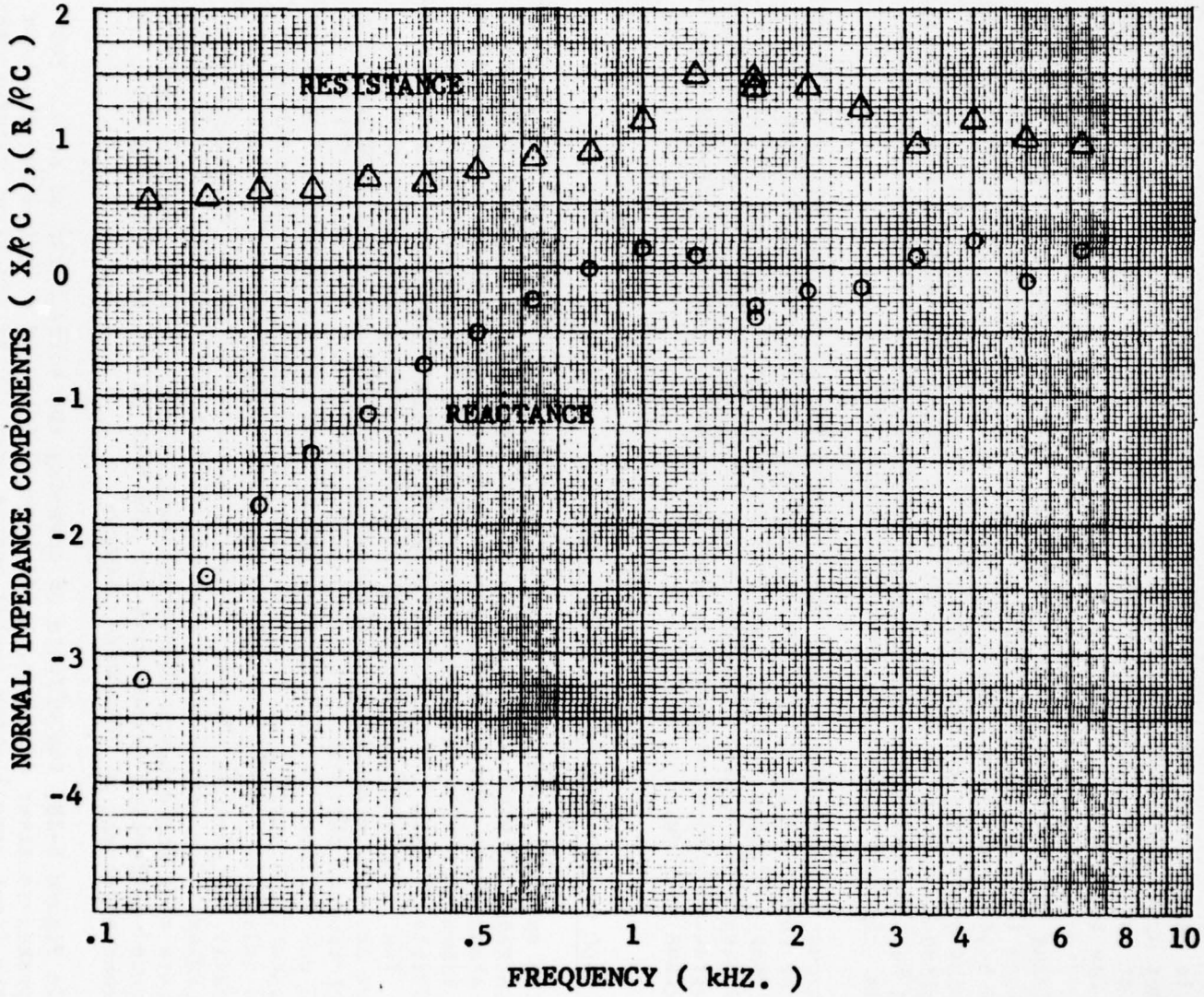


Figure 5-43. Owens-Corning Fiberglass R-19 Nominal 6 inch Thick.

possible because the absorbtive effectiveness of the fiberglass reaches a constant upper limit at about $t/\lambda = 0.086$. In fact, this relation implies that, at the lowest frequency of interest, f = 400 Hz, only 3 inches of fiberglass was required.

Using the experimental values for the reactance and resistance in Equations (45) and (46) for Q and ϕ, the variation with frequency shown in Figure 5-44 is obtained. Ignoring scattering and distributed source effects, the point source reflection index correction factors to be used with the fiberglass are shown in Figure 5-45. This figure implies that the fiberglass should be effective in eliminating ground reflections to within 1 dB above 1000 Hz. At lower frequency some variability occurs.

Acoustic measurements were taken around the 40-foot arc with a 4.31-inch-diameter conical nozzle, with and without the fiberglass at the same jet conditions. Figures 5-46 through 5-57 present the corrections of Table 5-I to the hard surface data compared to the fiberglass results at several angles. The corrected hard ground data is seen to agree with the test results with the fiberglass batting.

5.6 CR&DC GROUND REFLECTION CORRECTIONS

The approach used to eliminate ground reflections at CR&DC was to cover the concrete pad with double layers of 4 x 6 x 4 foot acoustical foam sheets. These sheets were placed on the ground for every acoustic test and stored at other times to prevent deterioration of the foam from the weather. To test the effects of this acoustical covering, the direct radiation loudspeaker was used. The first approach was to calibrate the loudspeaker in an anechoic chamber and then measure the difference between the calibrated spectrum and the spectrum as obtained in the acoustic arena of the Hot Jet Facility. This method was not very satisfactory as the speaker was sensitive to changes in temperature and humidity. To avoid this, the final approach adopted here was to calibrate the speaker during the test by pointing the speaker vertically and placing the microphone at the desired radius directly above the speaker. The near-field microphone (1 foot from the speaker) was used to ensure that the speaker characteristics did not change. In this manner, the ground reflection corrections for the hard pad itself and with two different thickness of foam were measured.

In Figure 5-58, the effects of covering the surface can be seen. For the speaker-receiver distance, R, of both 10 feet and 6 feet above the hard pad, the first cancellation (null) occurs near 100 Hz and first reinforcement (peak) near 200 Hz. Using a point source approximation, the first two nulls and the first two peaks are rather well predicted by Equation (50) using $Q = \phi = 1.0$. Above 400 Hz, however, the prediction is not very accurate. When the foam sheets are used, the impedance of the surface is altered and instead of a simple reflection, the surface absorbs some of the incident sound and causes a phase shift in the reflected sound. This results in a smoothing effect on the first two peaks and nulls, but at the higher frequencies the

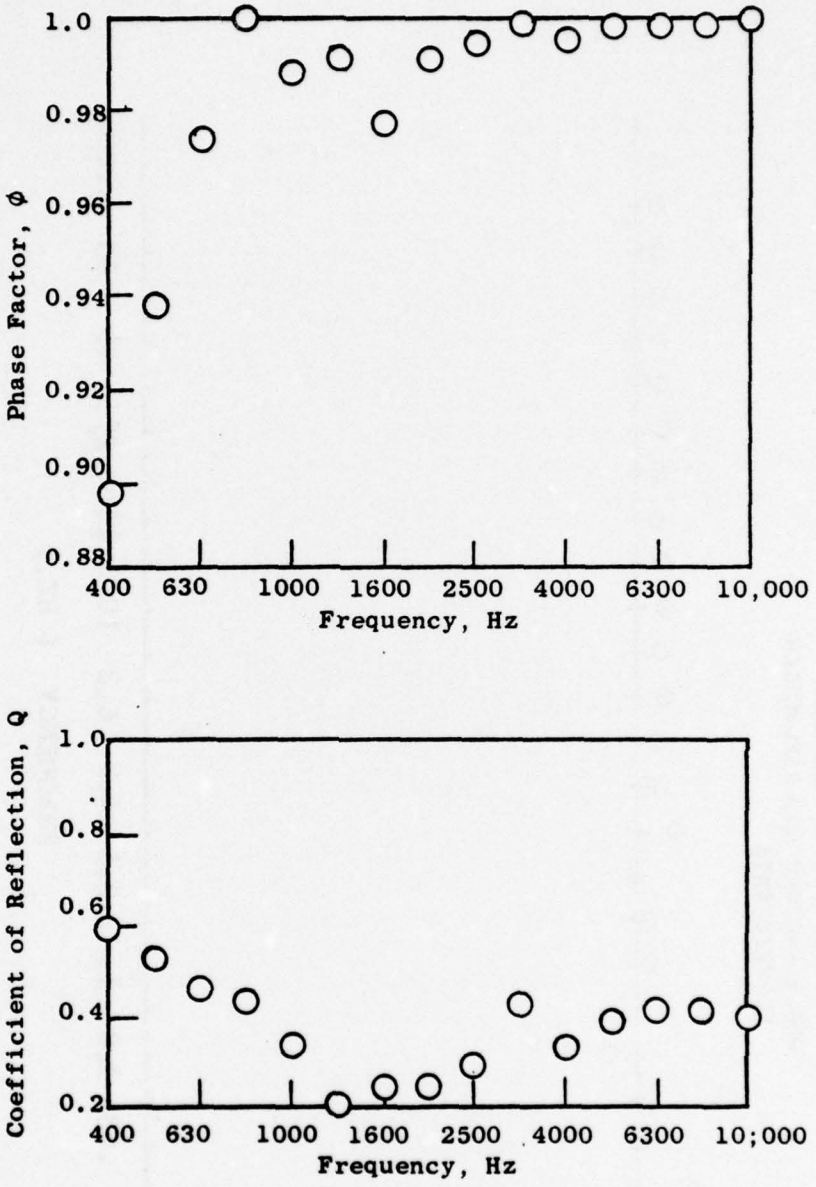


Figure 5-44. Prediction of Reflection Coefficient and Phase Factor Based on Experimental Data.

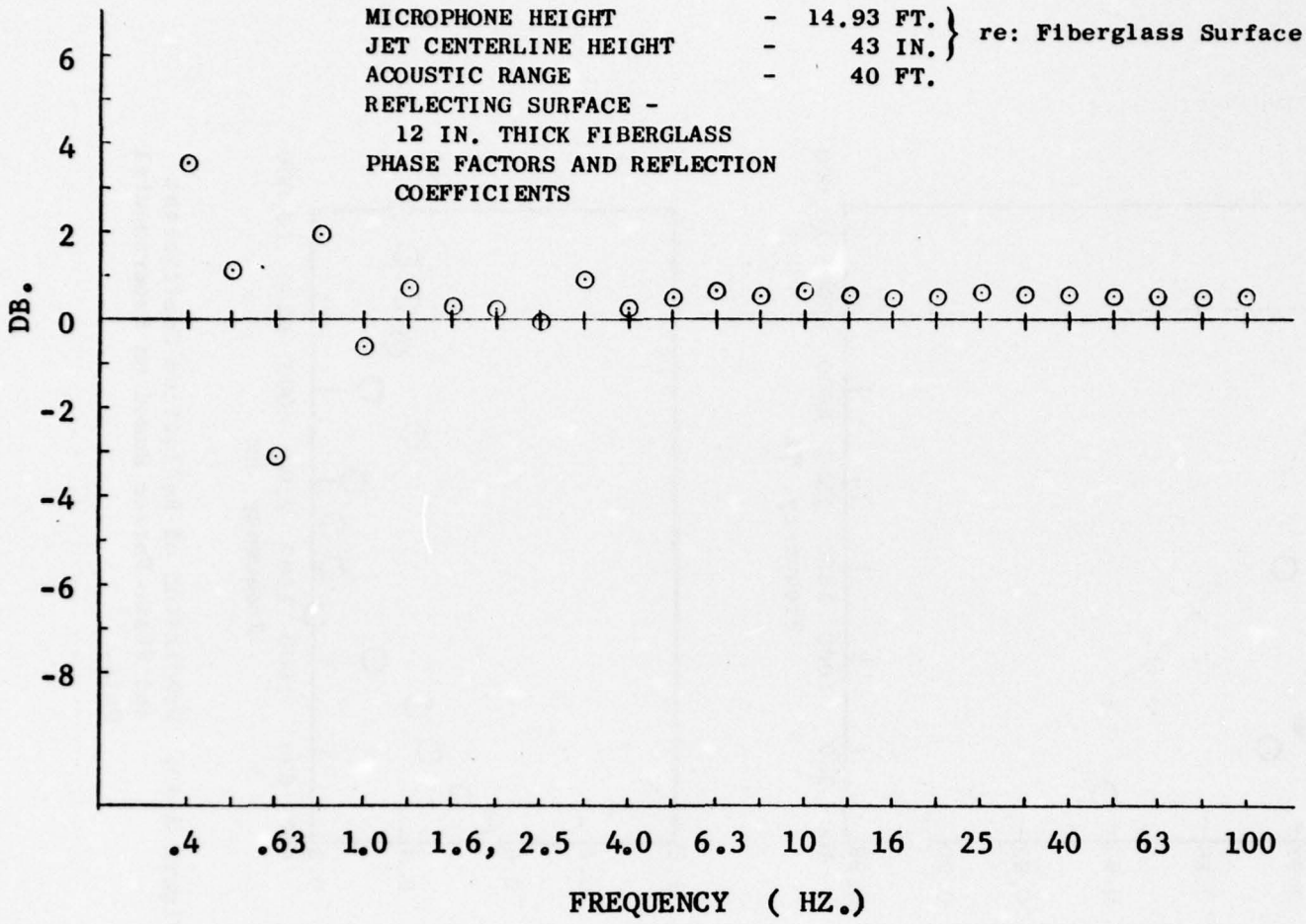


Figure 5-45. Prediction of Reflection Correction Index for JENOTS.

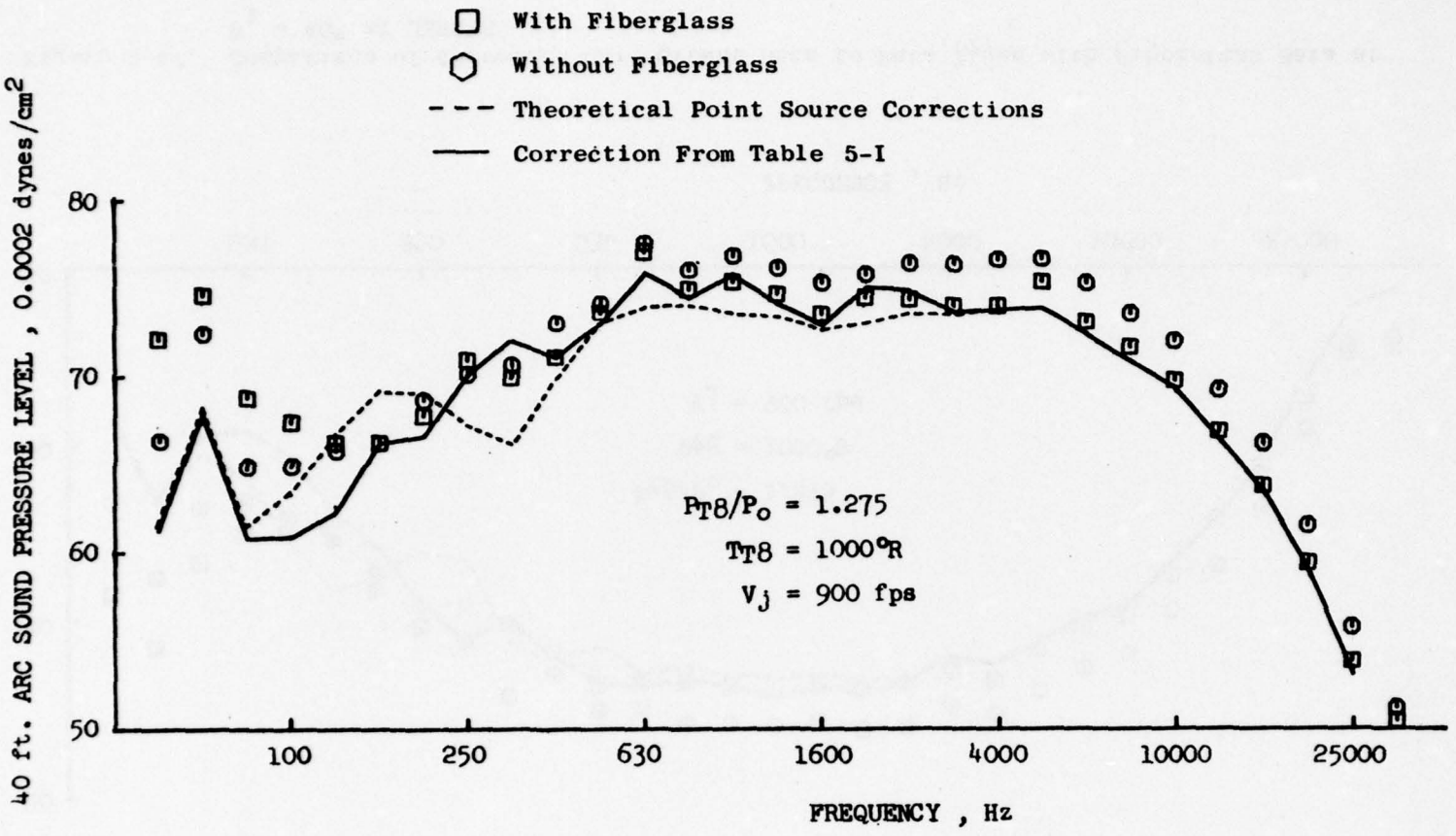


Figure 5-46. Comparison of Corrected Hard Ground Data to Data Taken with Fiberglass Bats at $\theta_I = 30°$ at JENOTS.

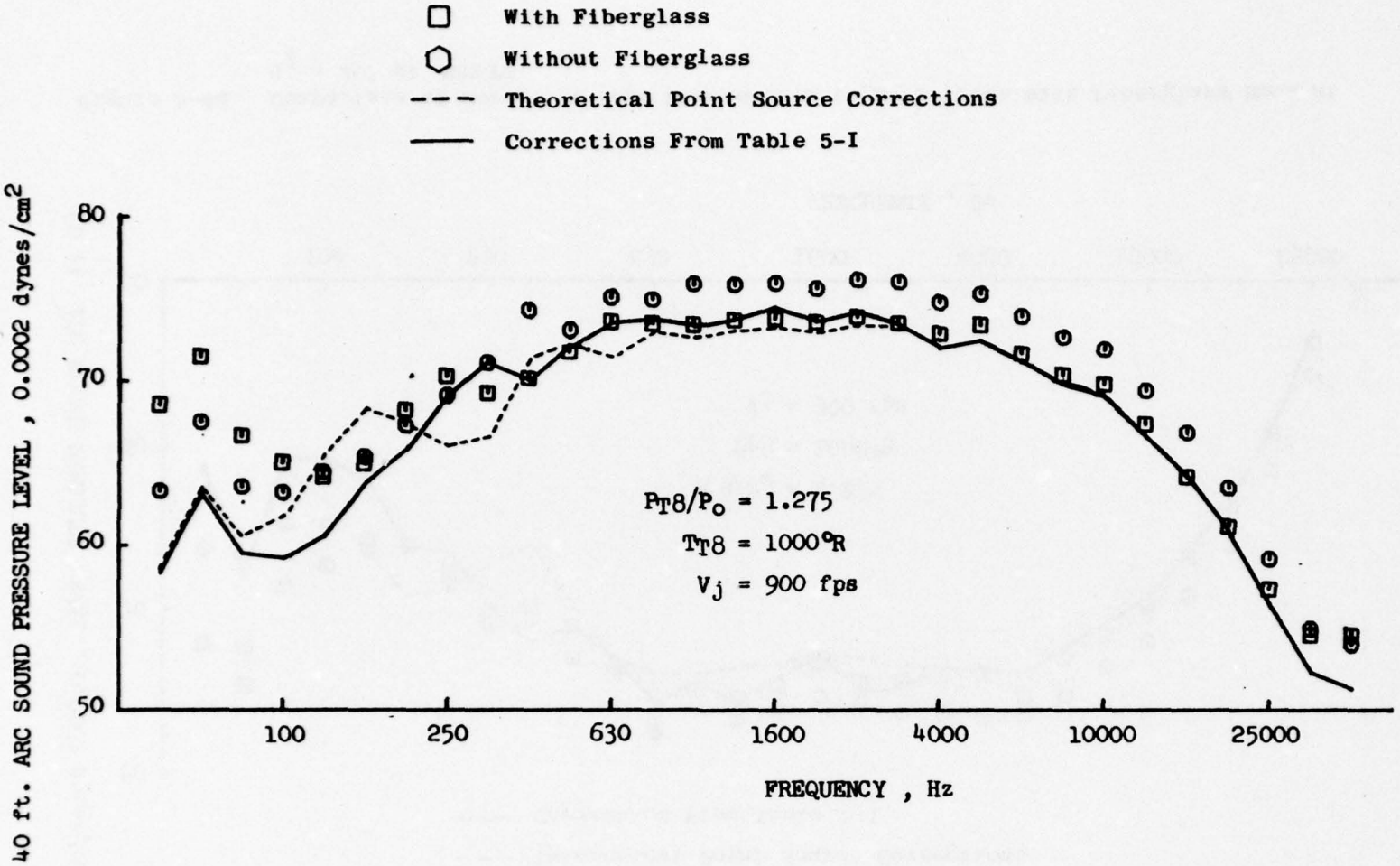


Figure 5-47. Comparison of Corrected Hard Ground Data to Data Taken with Fiberglass Bats at $\theta_I = 40°$ at JENOTS.

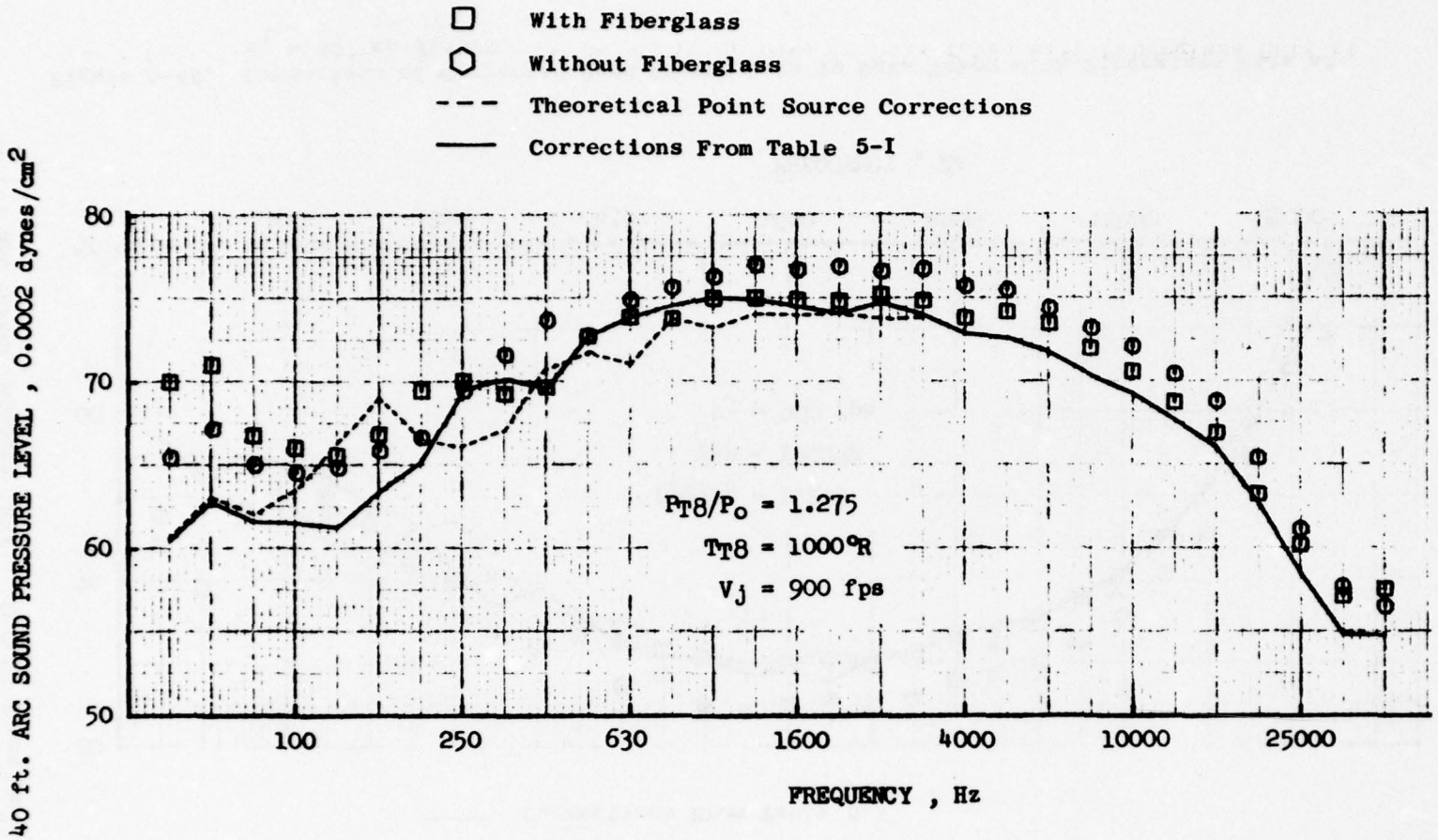


Figure 5-48. Comparison of Corrected Hard Ground Data to Data Taken with Fiberglass Bats at $\theta_I = 50°$ at JENOTS.

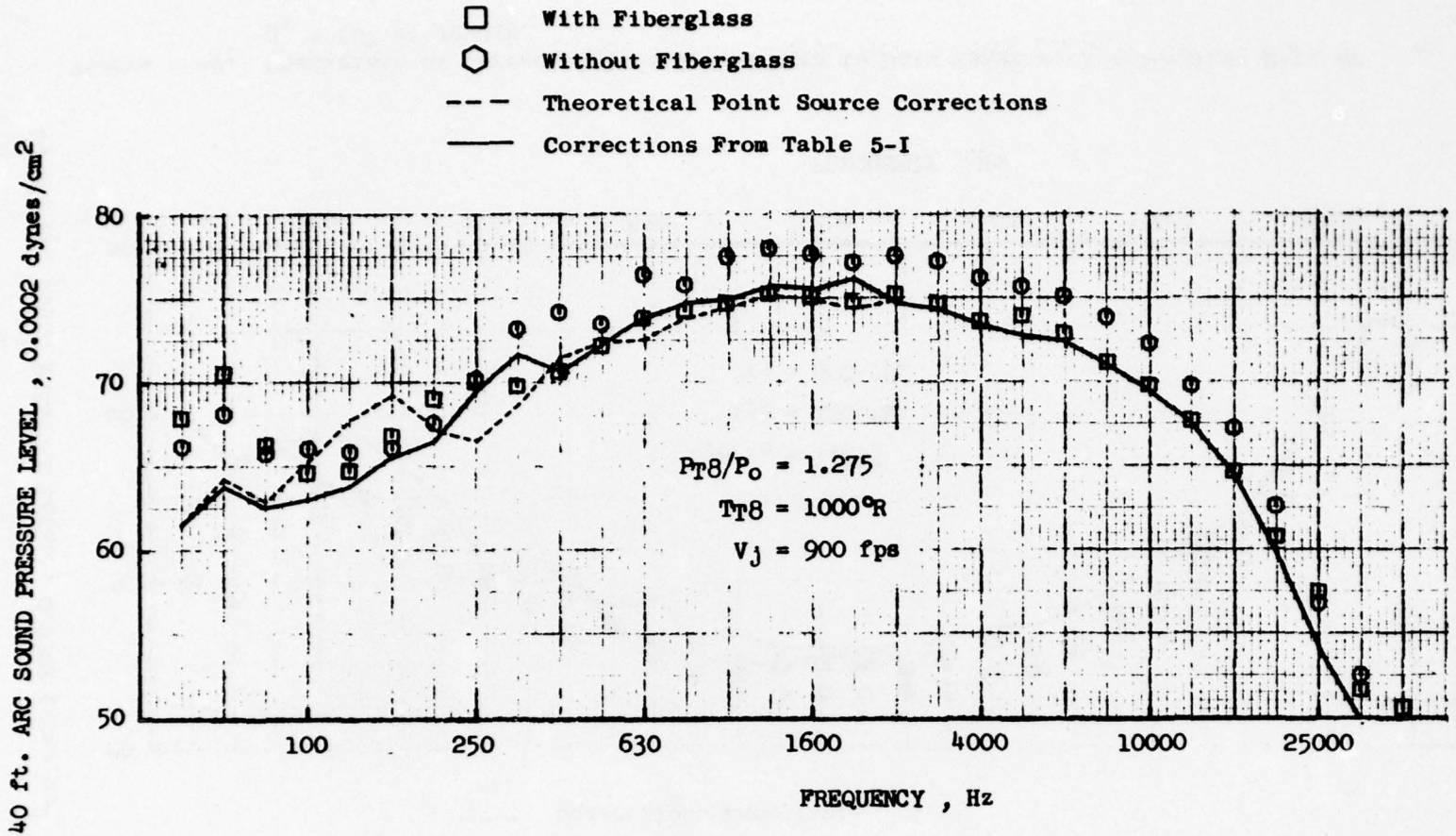


Figure 5-49. Comparison of Corrected Hard Ground Data to Data Taken with Fiberglass Bats at $\theta_I = 60°$ at JENOTS.

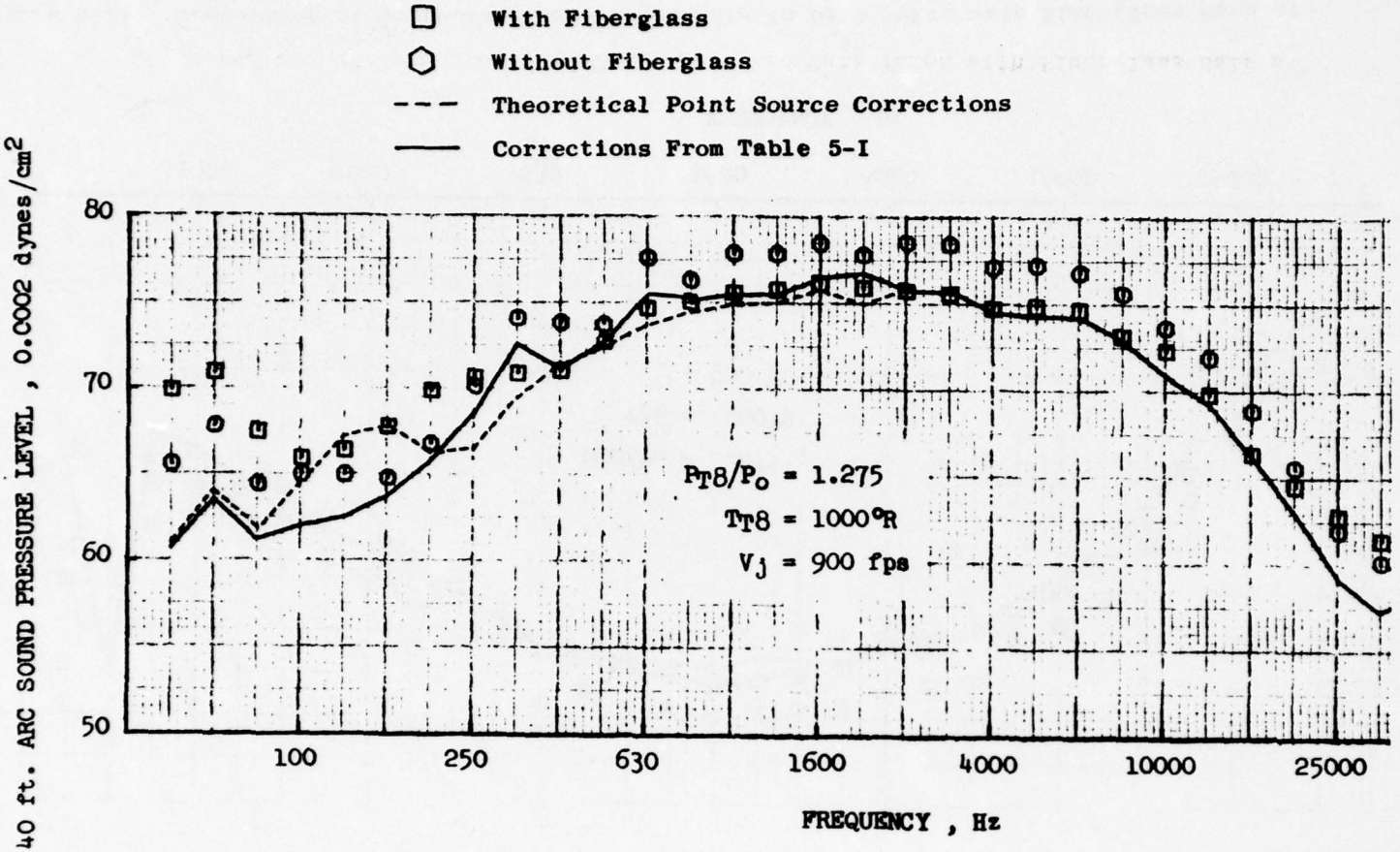


Figure 5-50. Comparison of Corrected Hard Ground Data to Data Taken with Fiberglass Bats at $\theta_I = 70°$ at JENOTS.

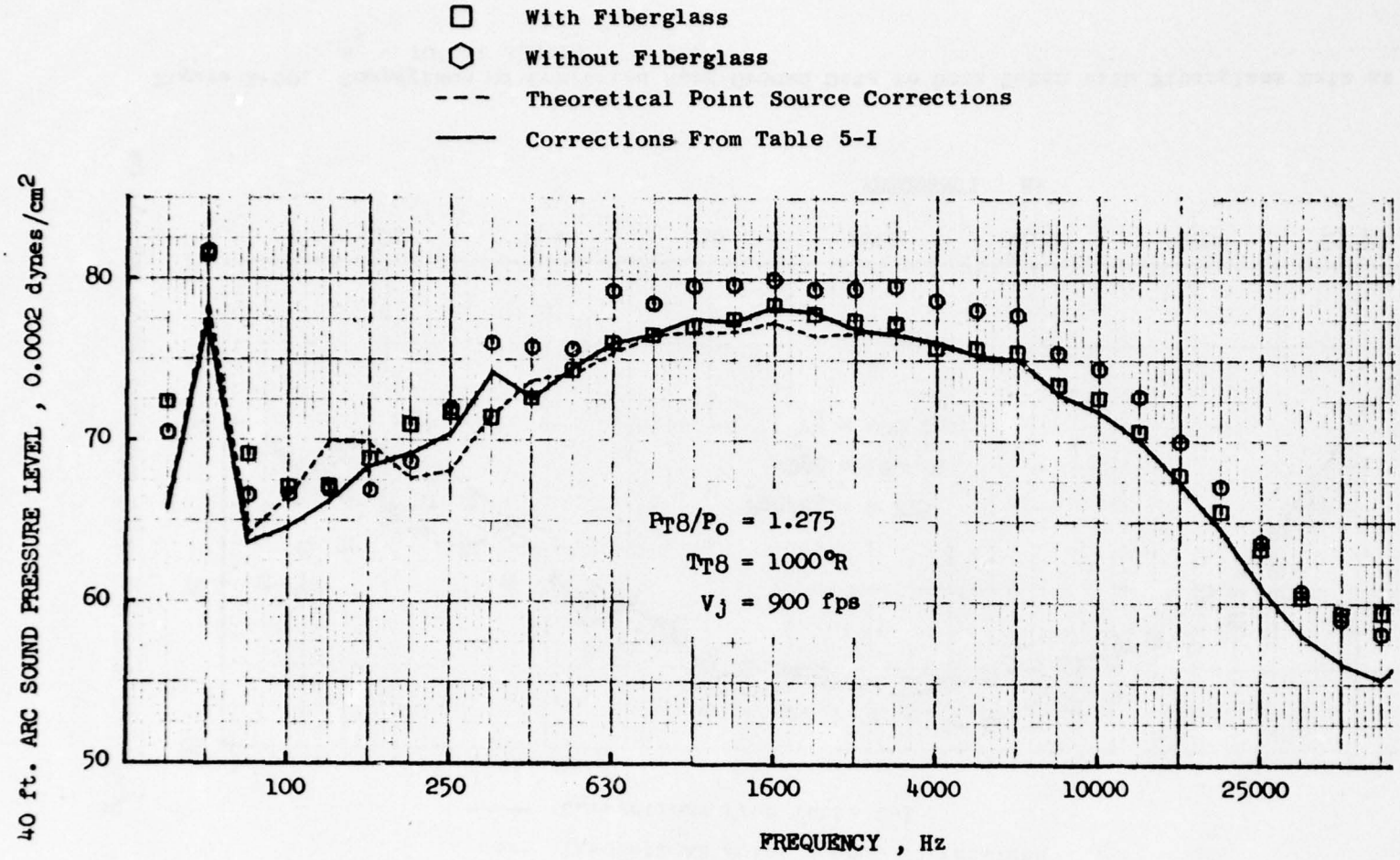


Figure 5-51. Comparison of Corrected Hard Ground Data to Data Taken with Fiberglass Bats at θ_I = 80° at JENOTS.

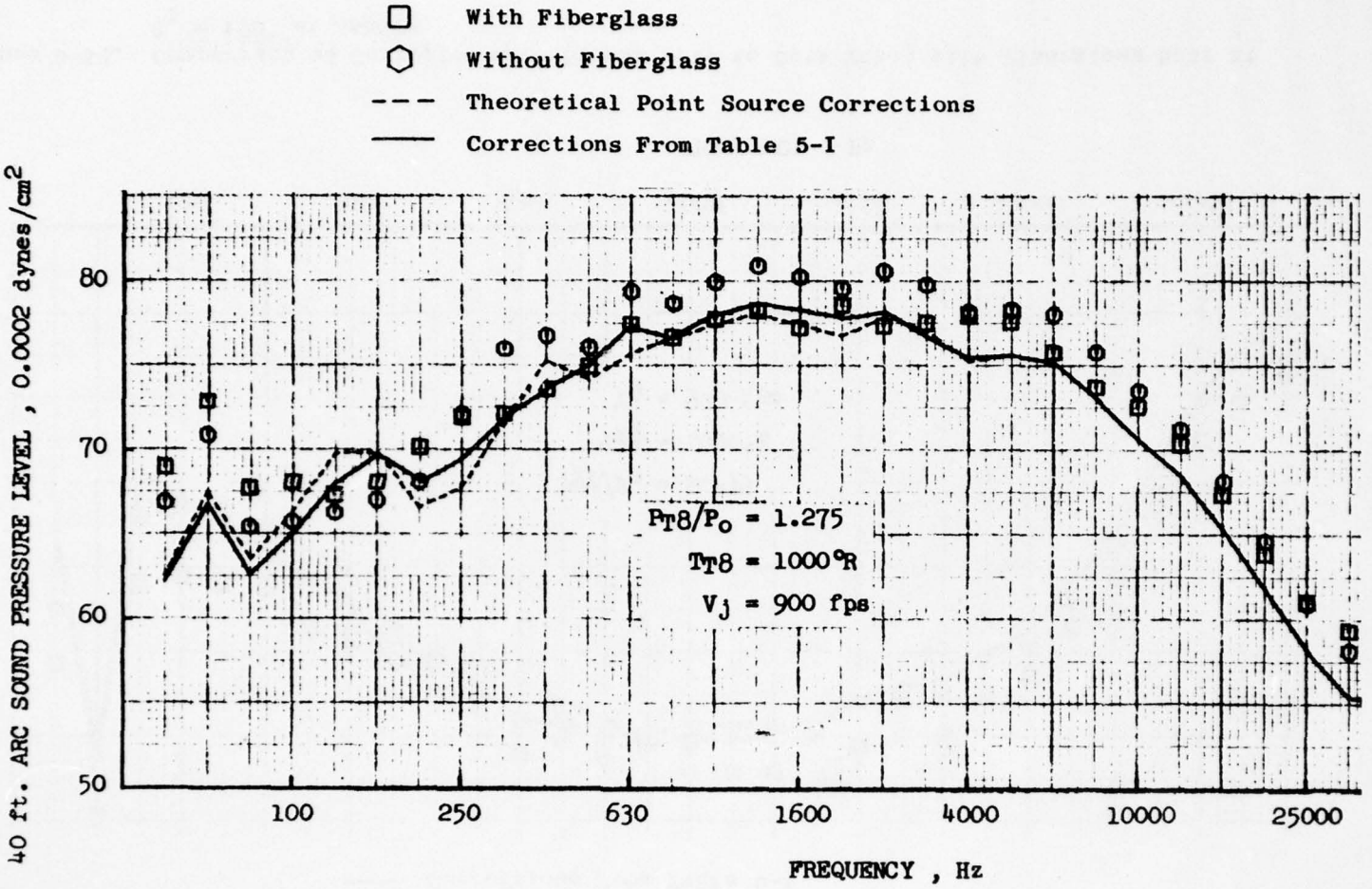


Figure 5-52. Comparison of Corrected Hard Ground Data to Data Taken with Fiberglass Bats at $\theta_I = 90°$ at JENOTS.

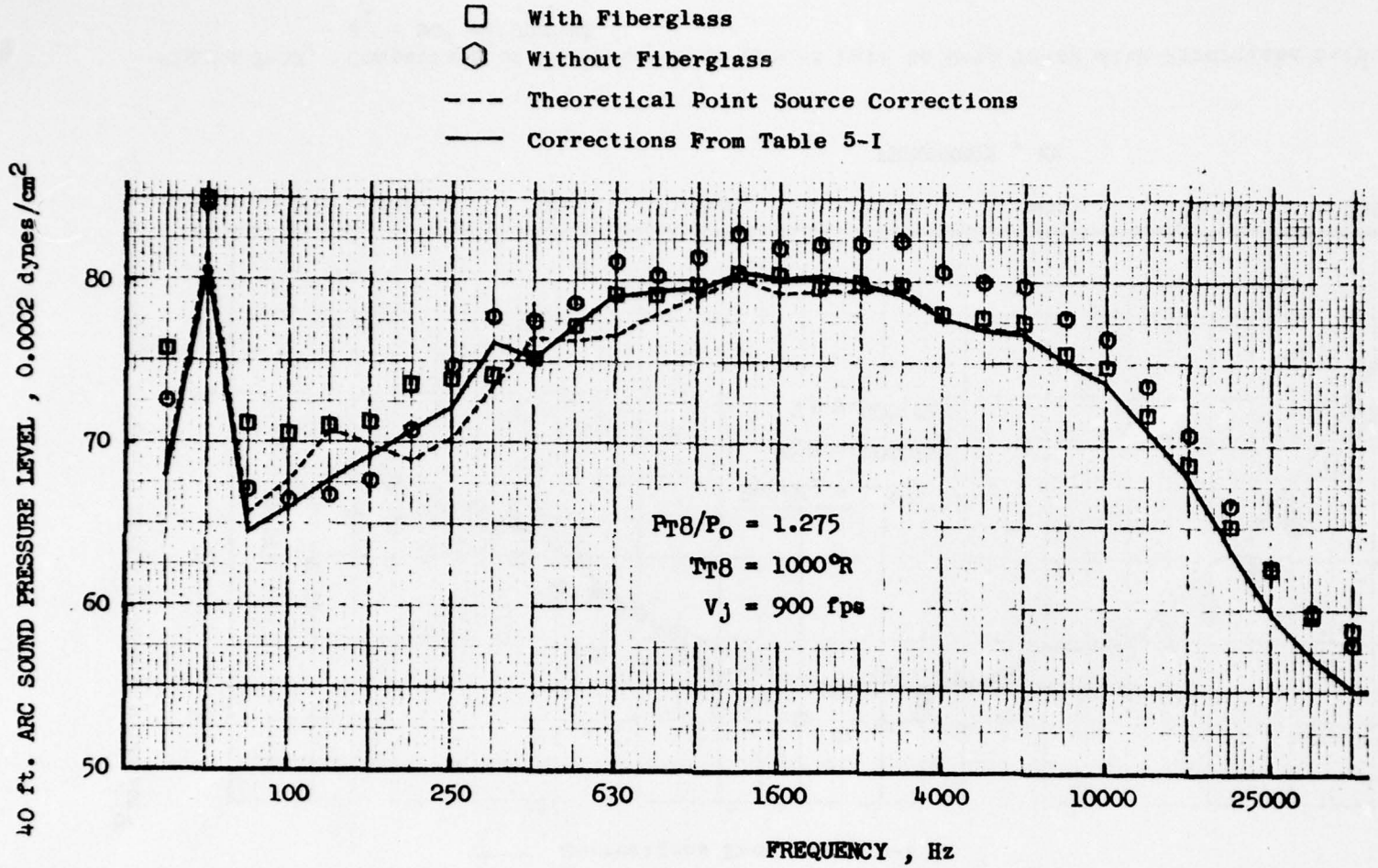


Figure 5-53. Comparison of Corrected Hard Ground Data to Data Taken with Fiberglass Bats at $\theta_I = 100°$ at JENOTS.

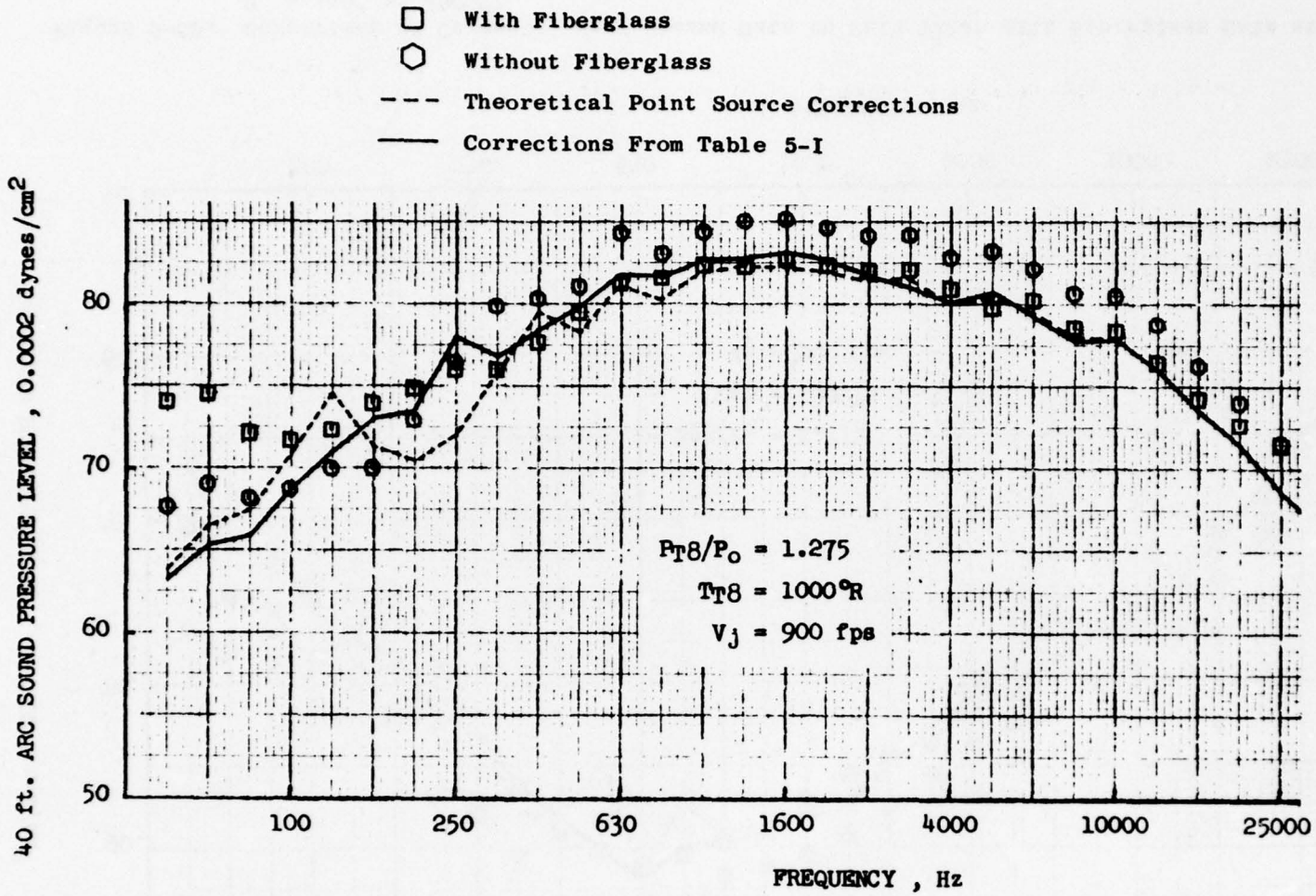


Figure 5-54. Comparison of Corrected Hard Ground Data to Data Taken with Fiberglass Bats at θ_I = 110° at JENOTS.

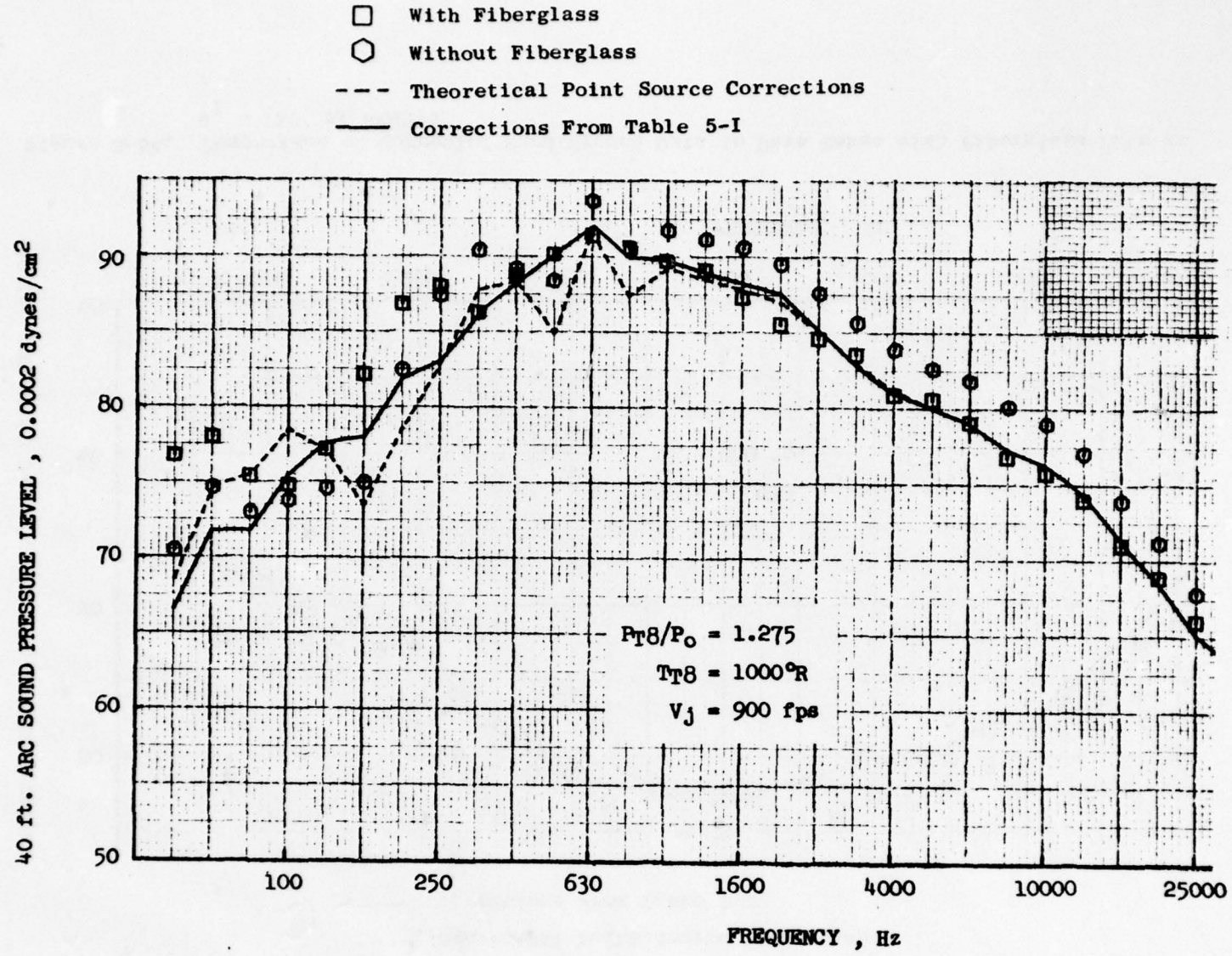


Figure 5-55. Comparison of Corrected Hard Ground Data to Data Taken with Fiberglass Bats at θ_I = 140° at JENOTS.

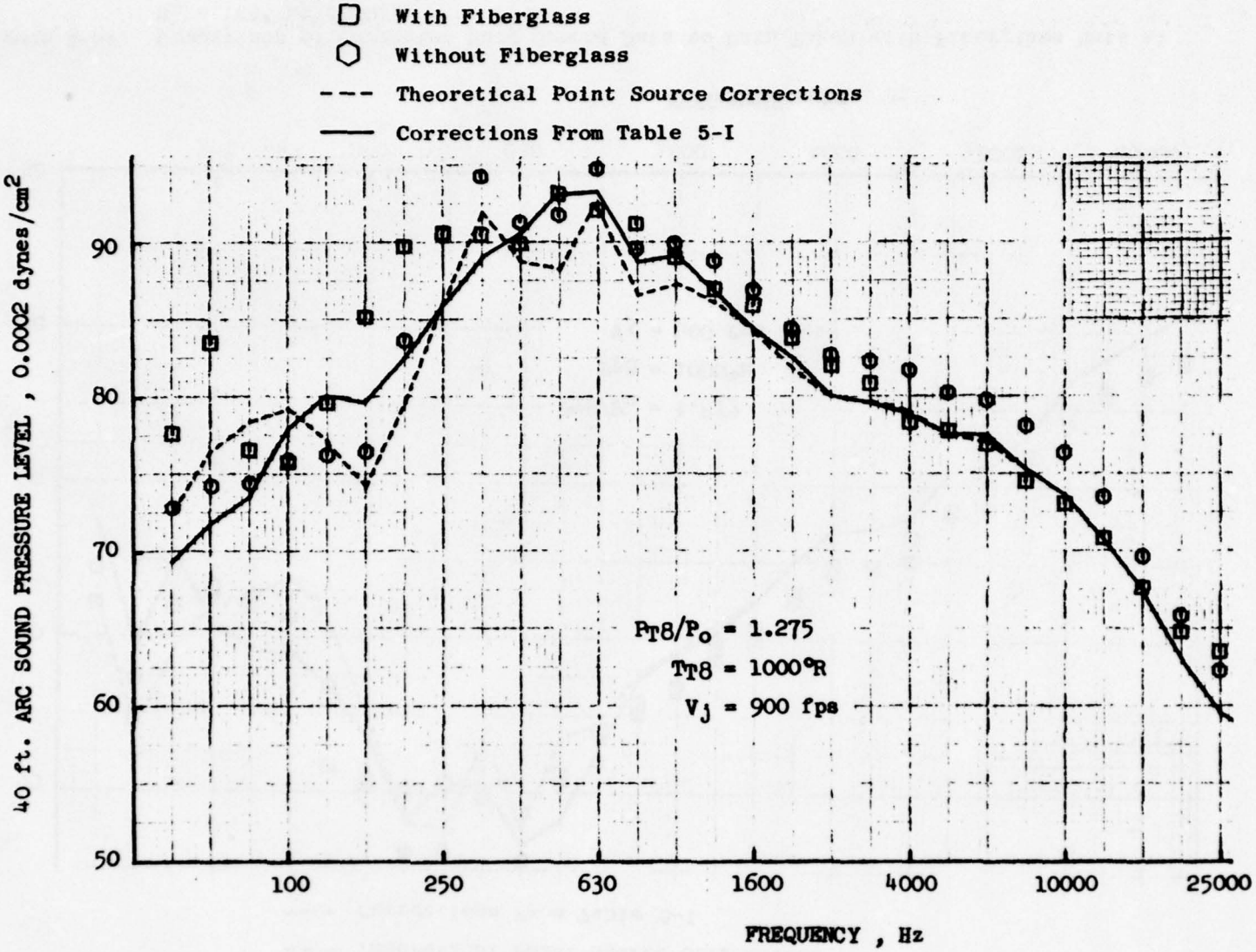


Figure 5-56. Comparison of Corrected Hard Ground Data to Data Taken with Fiberglass Bats at $\theta_I = 150°$ at JENOTS.

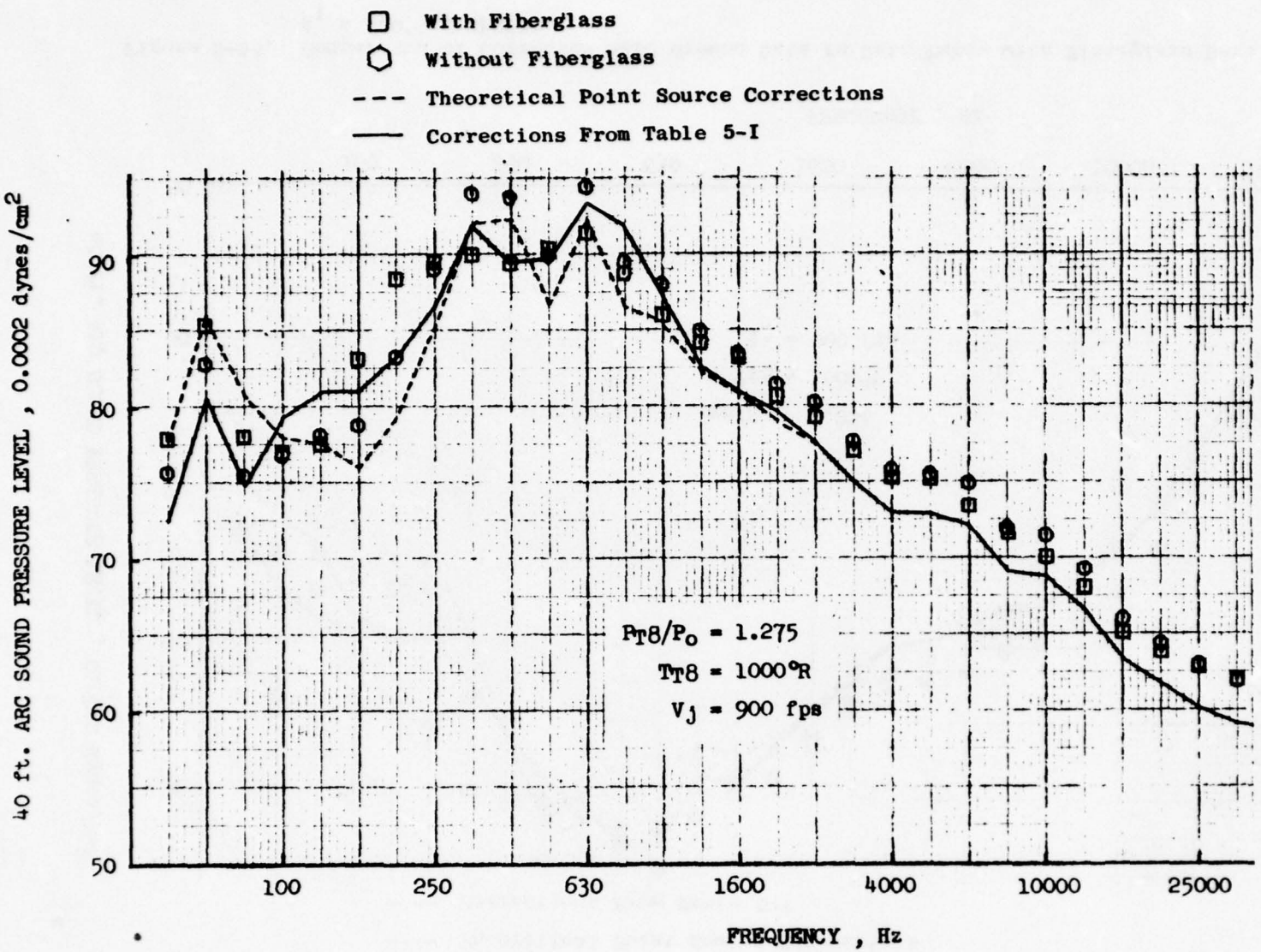


Figure 5-57. Comparison of Corrected Hard Ground Data to Data Taken with Fiberglass Bats at θ_I = 160° at JENOTS.

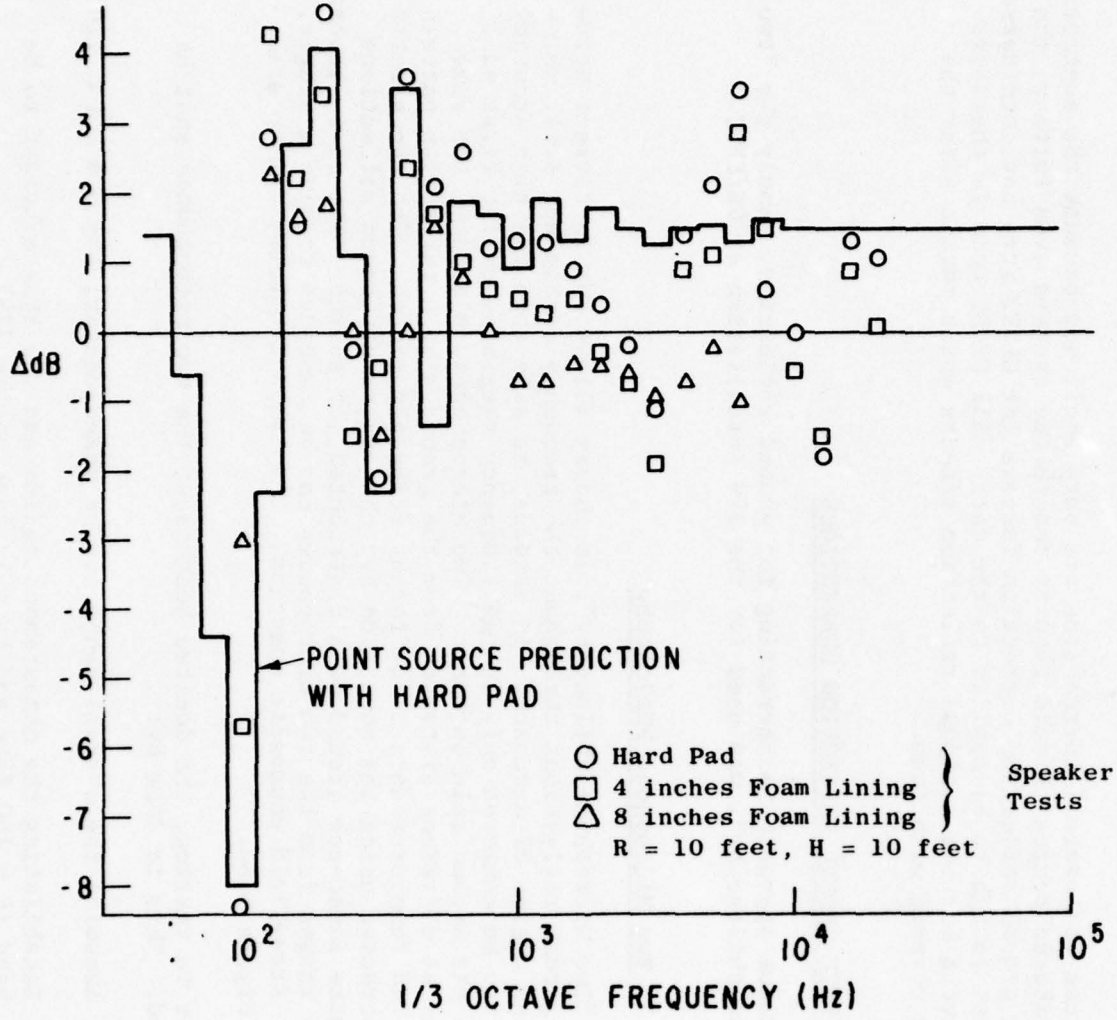


Figure 5-58. Ground Reflection Corrections for Different Ground Treatments at CR&DC.

locations of the peaks and nulls also change. Acceptable performance was achieved with the 8-inch-thick foam. The ground reflection correction was reduced to less than ± 2 dB above a frequency of 200 Hz.

The effect of changing the measurement radius can be seen in Figure 5-59. Again, the low frequency effects are predictable (that is, the peak and nulls occur at lower frequencies due to the larger difference in the direct and reflected paths, but in the middle frequencies the 8-foot measurement arc gives the predictable decay of the reflection pattern).

Because the overall corrections are very small and because the scattering and distributed source effects tend to smooth the spectra even further, the resulting ground reflection correction factors for CR&DC were not considered significant enough to be applied to the data. All CR&DC data is therefore not corrected for the residual reflection effects which remain after the ground is covered with foam.

5.7 J79/EFTC GROUND REFLECTION CORRECTIONS

A unique approach is correcting for ground reflection, namely the "two microphone philosophy", was used for the J79 installation at GE/EFTC.

5.7.1 Two Microphone Philosophy

The "Two Microphone Philosophy", in theory allows one to correct noise data for ground reflections throughout the frequency domain and still maintain a high degree of accuracy. In essence, it says that the high accuracy required can be achieved only in the frequency ranges below the first null and above the second reinforcement. Two microphones, placed at the same radius but at different distances from the ground give a reflection pattern of nulls and reinforcements in different frequency ranges. The two spectra can be corrected using the equations for the effect of ground reflections for a finite impedance ground on a distributed jet source. The most accurate frequency ranges from the two microphones can be combined to give a single, accurate, free-field composite spectrum. The two microphones set up are shown in Figure 5-60.

Prior to testing, the desired heights of the two microphones must be calculated. This is done by:

1. Assuming the overall range of the phase factor, say $0.9 < \phi < 1.0$

2. Establishing the measurement radius and the source height to be used (R = 160 feet and h_s = 12 feet on the J79)

3. Selecting one of the two microphone heights, h_m, and calculating $f_{1st\ null}$ from Figure 5-12. If the high microphone is chosen, the upper value of the phase factor, ϕ, (from step 1) is

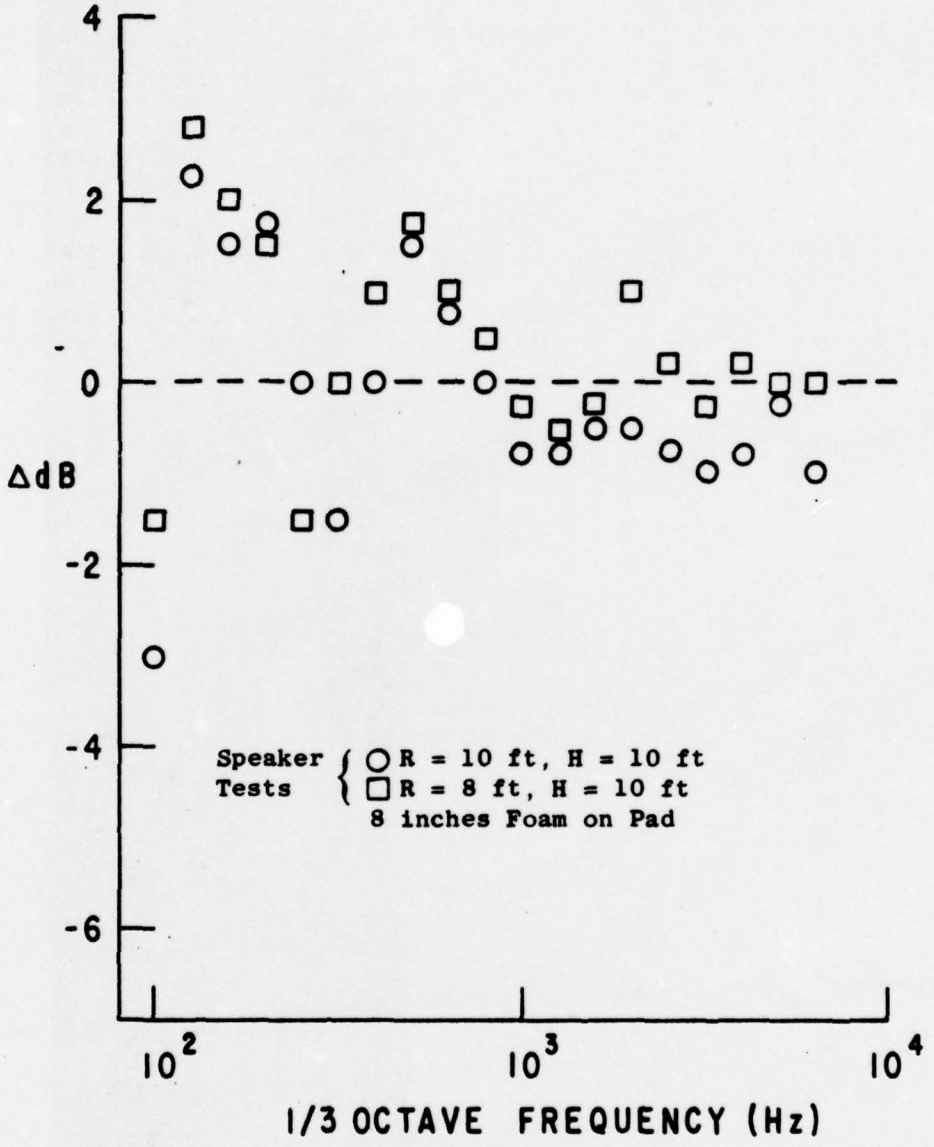


Figure 5-59. Ground Reflection Corrections, ΔdB, for Different Radii.

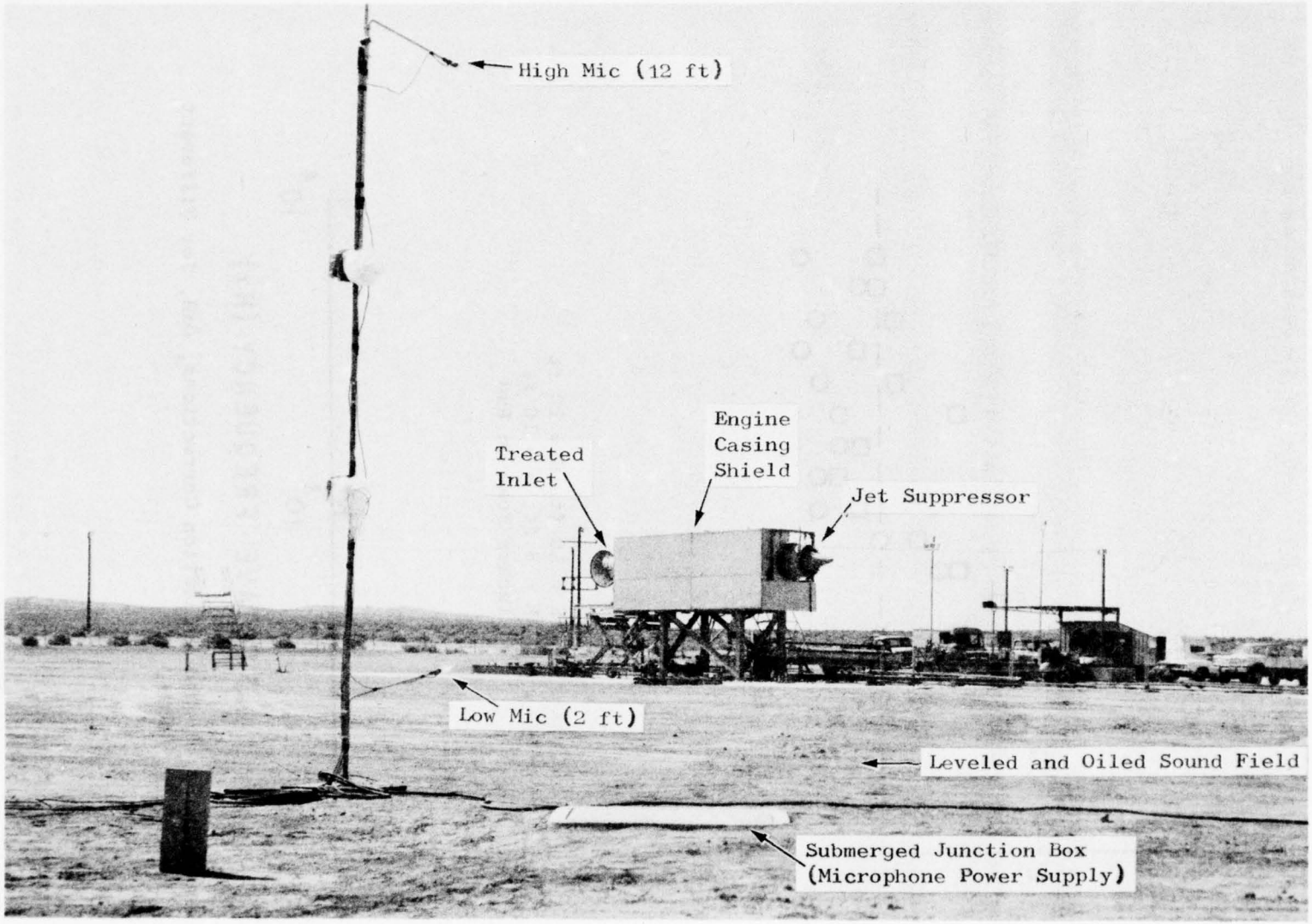


Figure 5-60. Acoustic Arena of the J79 at GE/EFTC Showing Two Microphone Setup.

multiplied by $f_{1st\ null}$; If the low microphone is chosen, the lower value of ϕ is used.

4. Multiplying or dividing the calculated frequency ($f_{1st\ null}\ \phi$) by 5 to obtain the first null frequency of the second microphone, $\phi'\ f_{1st}{}'_{null}$

5. Calculating $f_{1st}{}'_{null}$, using the other extreme estimate of the phase factor, ϕ'

6. Determining the microphone height of the second microphone from Figure 5-12.

Data recorded at frequencies below one-fifth times the first null frequency of the low microphone can be accurately corrected for ground reflections as can frequencies above 5 times the first null frequency of the high microphone (i.e., above the third null). The frequency range between these two limits will have to be carefully matched using an iterative procedure described in the next section. If the flexibility exists in the test setup a separation of the first nulls of the microphones by a factor of 25 instead of five in step (4) above, would permit a smooth spectral combination without matching data. It is recommended that the low microphone not be placed closer than 1 foot from the ground because of boundary layer, wind, and temperature effects.

5.7.2 Ground Impedance Measurement

The present empirical model for correcting the effects of ground reflections employs the phase factor, ϕ, and reflection coefficient, Q. The phase factor accounts for the difference in phase (at the microphone) of the direct and reflected acoustic rays. The coefficient of reflection accounts for the absorption by the ground of the reflected ray, as discussed in Section 5.3.

As mentioned in the discussion of the point source ground reflection model, phase factor and reflection coefficient are difficult to determine analytically or experimentally. It was therefore hypothesized that the ϕ's and Q's were constant throughout the arena (varying only with frequency), and the only variation of the ground reflection pattern at any angle relative to that at 90° was the nonspherical divergence effect, as discussed in Section 5.4. It was also assumed that jet noise generated by a conical nozzle on the J79 engine with an exhaust velocity of 2000 fps has a relatively smooth spectral distribution and is free of other noise sources such as turbomachinery noise.

Using the above assumptions, an iterative method was applied in an attempt to make the 1/3-octave band spectra from the J79 as smooth as possible. By assuming various combinations of ϕ and Q and using them in the point source model, the 90° spectrum was smoothed. Then, applying the

nonspherical divergence model to other angles of the conical nozzle signature the ϕ's and Q's were refined. A third assumption, that ground reflections and nonspherical divergence are weak functions of nozzle configuration, allowed corrections to suppressor nozzles. The correction factors appear in Tables 5-II and 5-III and plots of phase factor and coefficient of reflection versus frequency are given in Figures 5-61 and 5-62, respectively.

For the most part these corrections appeared good, however, some mismatch of the high and low microphones was present, but, because of the spectral shape, it was not very noticeable. Also, since the mismatch varied with angle it was felt the ϕ's and Q's were still sufficiently accurate. Empirical corrections were applied by forcing the corrected data from the high and low microphones to match for all angles in the 400 to 1600 Hz frequency range, as shown in Figure 5-63. These corrections were checked against a large number of cases to ensure their accuracy and are given in Table 5-IV.

5.8 PRECISION AND ACCURACY OF THE GROUND REFLECTION CORRECTION

The influence of ground reflections can be removed from the data by applying the correction factors calculated from Equation (50), modified for a distributed jet source with Equation (69). The precision of this correction factor can be determined from an analysis of variance study of Equation (50). Utilizing the methods described in Section 4.1, Equation (5), the variance of the ground reflection corrections have the form:

$$\sigma_{\Delta N}^2 = C^2 \left[\left(\frac{\sigma_\phi}{\phi} \right)^2 + \left(\frac{\sigma_\lambda}{\lambda} \right)^2 + \left(\frac{\sigma_{\Delta r}}{\Delta r} \right)^2 \right] + D^2 \left[\left(\frac{\sigma_Q}{Q} \right)^2 + \left(\frac{\sigma_Z}{Z} \right)^2 \right] \tag{97}$$

where

$$B = \frac{4.3429}{\left[1 + \left(\frac{Q}{Z} \right)^2 + Z \left(\frac{Q}{Z} \right) \left(\frac{\phi\lambda}{\alpha\Delta r} \right) \sin \left(\frac{\alpha\Delta r}{\phi\lambda} \right) \cos \left(\frac{\beta\Delta r}{\phi\lambda} \right) \right]}$$

$$C = \frac{2(Q/Z)B}{\alpha} \left[\left(\frac{\phi\lambda}{\Delta r} \right) \sin \left(\frac{\alpha\Delta r}{\phi\lambda} \right) \cos \left(\frac{\beta\Delta r}{\phi\lambda} \right) - \alpha \cos \left(\frac{\alpha\Delta r}{\phi\lambda} \right) \cos \left(\frac{\beta\Delta r}{\phi\lambda} \right) + \beta \sin \left(\frac{\alpha\Delta r}{\phi\lambda} \right) \sin \left(\frac{\beta\Delta r}{\phi\lambda} \right) \right] \tag{98}$$

$$D = 2(Q/Z)\ \beta \left[\frac{Q}{Z} + \left(\frac{\phi\lambda}{\alpha\Delta r} \right) \sin \left(\frac{\alpha\Delta r}{\phi\lambda} \right) \cos \left(\frac{\beta\Delta r}{\phi\lambda} \right) \right] \tag{99}$$

Table 5-II. Low Microphone Ground Reflection Corrections.

(J79 at EFTC)

ACOUSTIC ANGLE FROM EXHAUST PLANE

FREQ.	30	40	50	60	70	80	90
50	5.1	5.1	5.1	5.1	5.1	5.1	5.1
63	5.1	5.1	5.1	5.1	5.1	5.1	5.1
80	5.0	5.0	5.0	5.0	5.0	5.0	5.0
100	4.9	4.9	4.9	4.9	4.9	4.9	4.9
125	4.8	4.8	4.8	4.8	4.7	4.7	4.7
100	4.8	4.6	4.6	4.6	4.6	4.6	4.6
160	4.6	4.6	4.6	4.6	4.6	4.6	4.6
200	4.4	4.4	4.4	4.4	4.4	4.4	4.4
250	4.1	4.1	4.1	4.1	4.1	4.1	4.1
315	3.8	3.8	3.8	3.8	3.8	3.8	3.8
400	3.4	3.4	3.4	3.4	3.4	3.4	3.4
500	2.9	2.9	2.9	2.9	2.9	2.8	2.8
630	2.3	2.2	2.2	2.2	2.2	2.2	2.1
800	1.5	1.5	1.5	1.4	1.4	1.4	1.3
1000	.3	.3	.3	.2	.2	.1	.1
1250	-1.3	-1.4	-1.4	-1.5	-1.6	-1.7	-1.8
1600	-3.7	-3.8	-3.8	-3.9	-3.9	-4.0	-4.1
2000	-4.0	-3.9	-3.9	-3.8	-3.8	-3.7	-3.6
2500	-.9	-.9	-.8	-.7	-.6	-.4	-.3
3150	2.0	2.0	2.1	2.2	2.2	2.3	2.3
4000	2.5	2.5	2.5	2.4	2.4	2.3	2.2
5000	-1.0	-1.1	-1.3	-1.5	-1.7	-1.9	-2.1
6300	-.3	-.2	-.0	.2	.4	.6	.8
8000	1.6	1.6	1.5	1.4	1.2	1.0	.8
10000	.0	.1	.3	.4	.6	.8	1.0
20000	.0	.1	.3	.4	.6	.8	1.0

Table 5-II. Low Microphone Ground Reflection Corrections (Concluded).

(J79 at EFTC)

ACOUSTIC ANGLE FROM EXHAUST PLANE

FREQ.	100	110	120	130	140	150	160
50	5.1	5.1	5.1	5.1	5.1	5.1	5.1
63	5.1	5.1	5.1	5.1	5.1	5.1	5.1
80	5.0	5.0	5.0	5.0	5.0	5.0	5.0
100	4.9	4.9	4.9	4.9	4.9	4.9	4.9
125	4.7	4.7	4.7	4.7	4.7	4.7	4.7
160	4.6	4.6	4.6	4.5	4.5	4.5	4.5
200	4.4	4.3	4.3	4.3	4.3	4.3	4.3
250	4.1	4.1	4.1	4.1	4.1	4.1	4.1
315	3.8	3.8	3.8	3.8	3.7	3.7	3.7
400	3.4	3.4	3.3	3.3	3.3	3.3	3.3
500	2.8	2.8	2.8	2.7	2.7	2.7	2.7
630	2.1	2.1	2.1	2.0	2.0	2.0	2.0
800	1.3	1.2	1.2	1.1	1.1	1.1	1.1
1000	-.0	-.1	-.1	-.2	-.3	-.3	-.3
1250	-1.9	-2.0	-2.1	-2.2	-2.2	-2.3	-2.4
2000	-3.5	-3.4	-3.2	-3.1	-3.0	-2.9	-2.8
2500	-.1	.0	.1	.3	.4	.5	.5
3150	2.4	2.5	2.5	2.6	2.6	2.6	2.6
4000	2.1	2.0	1.9	1.8	1.7	1.6	1.6
5000	-2.3	-2.5	-2.6	-2.7	-2.7	-2.8	-2.7
6300	1.0	1.2	1.4	1.6	1.7	1.7	1.8
8000	.5	.3	.0	-.2	-.3	-.5	-.5
10000	1.2	1.3	1.4	1.5	1.5	1.5	1.5
20000	1.2	1.3	1.4	1.5	1.5	1.5	1.5

Table 5-III. High Microphone Ground Reflection Corrections.

(J79 at EFTC)

ACOUSTIC ANGLE FROM EXHAUST PLANE

FREQ.	30	40	50	60	70	80	90
50	4.8	4.8	4.8	4.7	4.7	4.7	4.7
63	4.6	4.6	4.6	4.6	4.5	4.5	4.5
80	4.2	4.2	4.2	4.1	4.1	4.1	4.1
100	3.6	3.6	3.6	3.6	3.5	3.5	3.5
125	2.8	2.8	2.7	2.7	2.6	2.6	2.5
160	1.3	1.2	1.2	1.1	1.0	.9	.8
200	-1.0	-1.1	-1.2	-1.3	-1.4	-1.6	-1.7
250	-4.8	-4.9	-5.1	-5.3	-5.5	-5.7	-6.0
315	-7.0	-7.0	-6.9	-6.6	-6.7	-6.5	-6.3
400	-1.4	-1.3	-1.2	-1.0	-.8	-.6	-.4
500	2.2	2.3	2.3	2.4	2.5	2.6	2.7
630	3.2	3.2	3.1	3.1	3.1	3.0	3.0
800	-.1	-.2	-.4	-.6	-.8	-1.1	-1.4
1000	-1.5	-1.4	-1.2	-1.0	-.8	-.5	-.2
1250	2.4	2.4	2.4	2.4	2.3	2.2	2.1
1600	-.3	-.8	-.6	-.5	-.3	-.1	.2
2000	.8	.7	.6	.5	.4	.2	.1
2500	.8	.8	.8	.8	.7	.7	.7
3150	.4	.4	.4	.4	.5	.6	.7
4000	1.0	1.0	1.1	1.1	1.1	1.0	.8
5000	.5	.5	.5	.5	.6	.7	.7
6300	.7	.7	.7	.6	.4	.3	.2
8000	.6	.6	.6	.6	.6	.6	.7
10000	.6	.6	.6	.7	.7	.7	.7
20000	.6	.6	.6	.7	.7	.7	.7

Table 5-III. High Microphone Ground Reflection Corrections (Concluded).

(J79 at EFTC)

ACOUSTIC ANGLE FROM EXHAUST PLANE

FREQ.	100	110	120	130	140	150	160
50	4.7	4.7	4.7	4.7	4.6	4.6	4.6
63	4.5	4.5	4.4	4.4	4.4	4.4	4.4
80	4.0	4.0	4.0	3.9	3.9	3.9	3.9
100	3.4	3.4	3.3	3.3	3.2	3.2	3.2
125	2.5	2.4	2.3	2.3	2.2	2.1	2.1
160	.7	.6	.5	.4	.3	.2	.1
200	-1.9	-2.1	-2.3	-2.5	-2.7	-2.8	-2.9
250	-6.2	-6.5	-6.7	-6.9	-7.1	-7.2	-7.3
315	-6.0	-5.7	-5.5	-5.2	-4.9	-4.7	-4.5
400	-.2	.0	.2	.4	.6	.7	.8
500	2.8	2.9	2.9	3.0	3.1	3.1	3.1
630	2.9	2.9	2.8	2.7	2.6	2.5	2.4
800	-1.7	-2.0	-2.3	-2.5	-2.6	-2.7	-2.8
1000	.1	.4	.7	.9	1.1	1.3	1.4
1250	2.0	1.8	1.6	1.4	1.2	1.0	.9
1600	.5	.7	.9	1.1	1.2	1.3	1.3
2000	-.0	-.1	-.1	-.1	.0	.1	.1
2500	.6	.6	.6	.6	.7	.7	.7
3150	.9	1.0	1.0	1.1	1.0	1.0	1.0
4000	.6	.4	.2	.2	.3	.3	.3
5000	.7	.7	.7	.7	.7	.7	.7
6300	.4	.6	.7	.8	.8	.7	.7
8000	.7	.7	.6	.6	.6	.6	.6
10000	.6	.6	.6	.6	.6	.6	.6
20000	.6	.6	.6	.6	.6	.6	.6

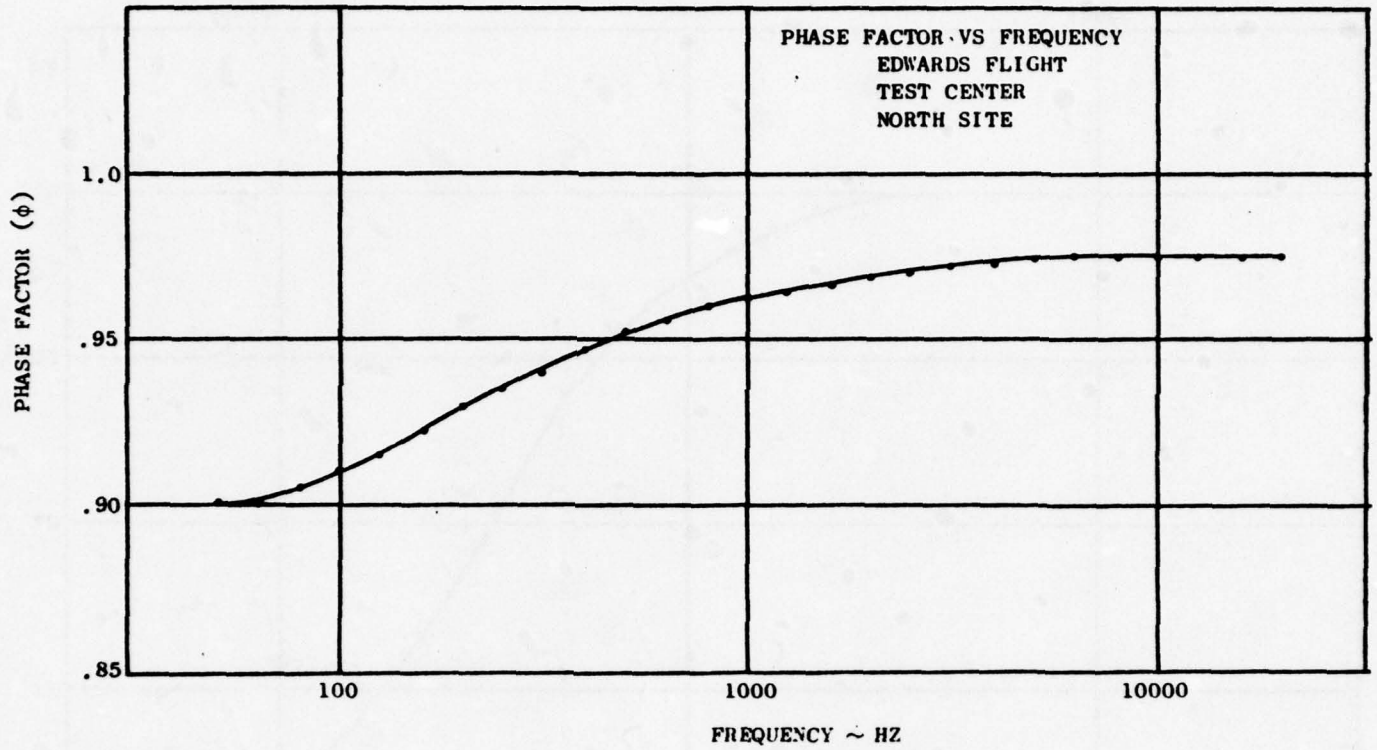


Figure 5-61. Phase Factor Versus Frequency at GE/EFTC.

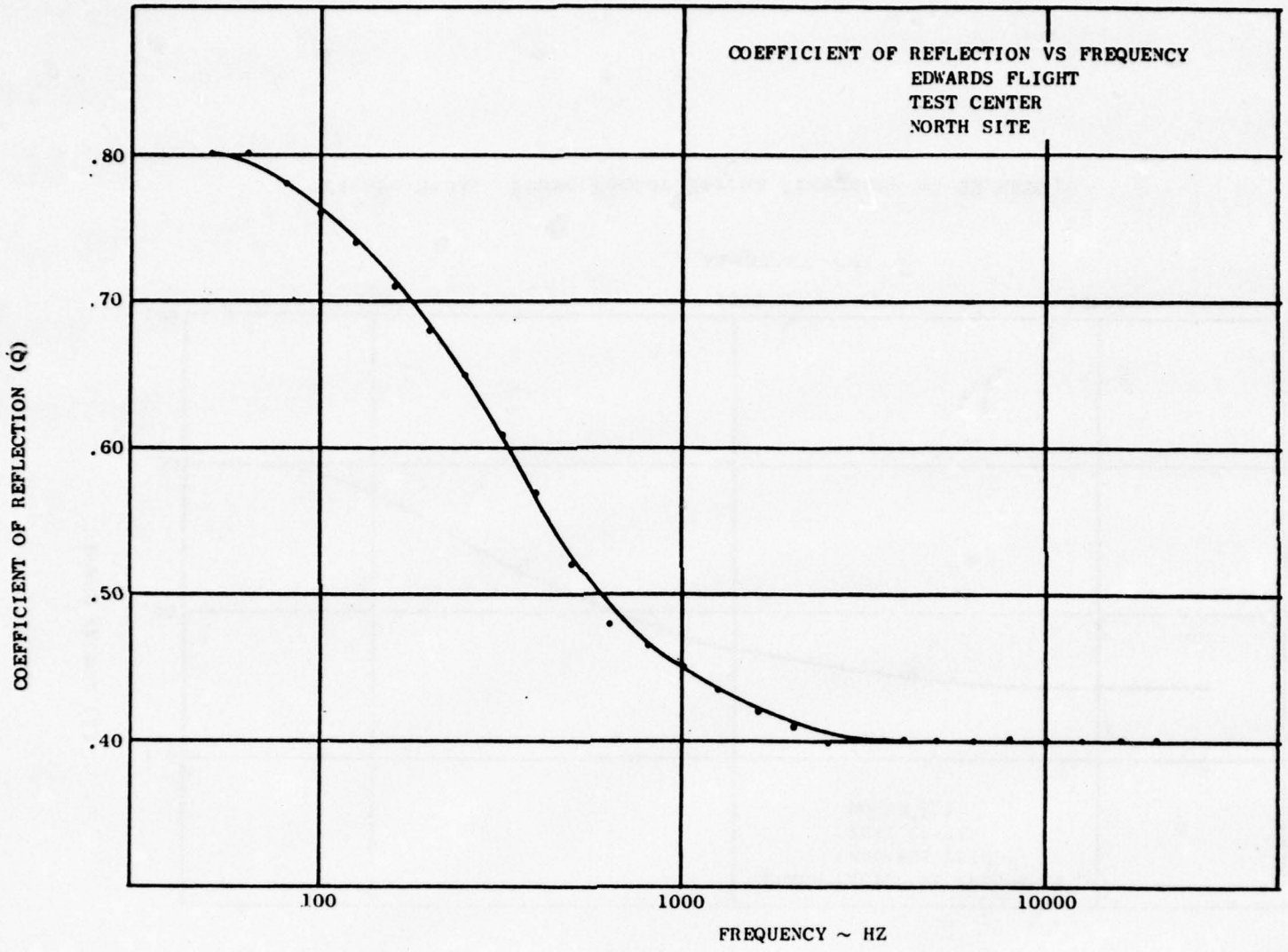


Figure 5-62. Coefficient of Reflection Versus Frequency at GE/EFTC.

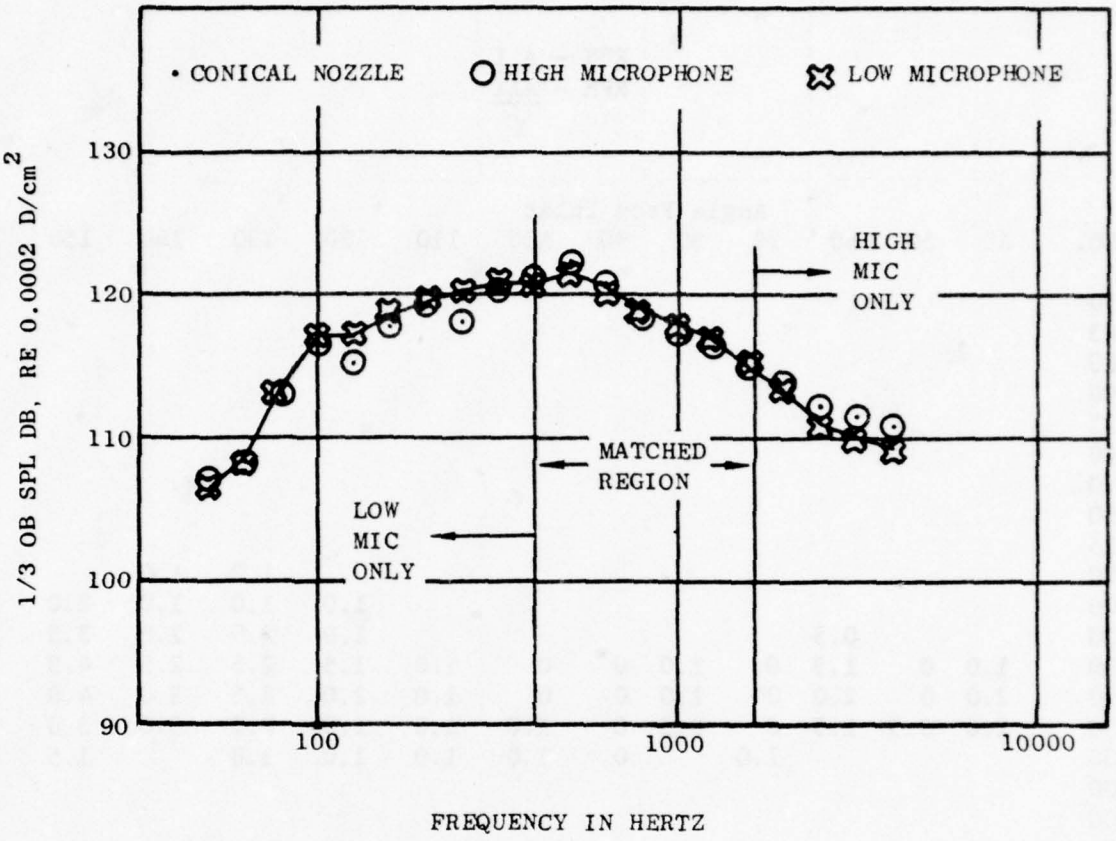


Figure 5-63. Empirical Matching of High and Low Microphone Data at GE/EFTC.

Table 5-IV. Empirical Ground Reflection Corrections to J79 Data.

RUN - A11
RPM - A11

	Angle From Inlet												
FREQ.	40	50	60	70	80	90	100	110	120	130	140	150	160
50													
63													
80													
100													
125													
160													
200													
250													
315													
400										1.0	1.0		
500									1.0	1.0	1.0	2.0	1.0
630			0.5						1.0	2.0	2.0	3.5	1.0
800	1.0	0	1.5	0	1.0	0	0	1.0	1.5	2.5	2.5	4.2	3.5
1000	2.0	0	2.0	0	1.0	0	0	1.0	2.0	2.5	3.0	4.0	2.5
1250	2.0	0.5	1.5	0	0.5	0	1.0	1.0	1.5	2.2	3.0	3.0	2.0
1600				1.0		0	1.0	1.0	1.0	1.0		1.5	2.0
2000													
2500													
3150													
4000													
5000													
6300													
8000													
10000													
12500													
16000													
20000													

Note: Blanks indicate zero (or no) correction. Values given above are to be algebraically added to the 1/3 OB SPL.

The variances $(\sigma\Delta r/\Delta r)^2$ and $(\sigma Z/Z)^2$ can be calculated from Equations (72) and (75) as:

$$\left(\frac{\sigma_{\Delta r}}{\Delta r}\right)^2 = \left(\frac{R}{\Delta r}\right)^2 \left(\frac{Z-1}{Z}\right)^2 \left(\frac{\sigma_R}{R}\right)^2 + \left(\frac{4hmhs}{ZR\Delta r}\right)^2 \left[\left(\frac{\sigma_{hs}}{hs}\right)^2 + \left(\frac{\sigma_{hm}}{hm}\right)^2\right] \quad (100)$$

$$\left(\frac{\sigma_Z}{Z}\right)^2 = \left(\frac{Z-1}{Z}\right)^2 \left[\left(\frac{\sigma_{\Delta r}}{\Delta r}\right)^2 + \left(\frac{\sigma_R}{R}\right)^2\right] \quad (101)$$

The variance in the ground reflection correction as a function of frequency can be calculated from Equation (97) given the geometry of the soundfield in terms of R, h_m, h_{s1}, Q, and ϕ and the measurement variances

$$\left(\frac{\sigma_\phi}{\phi}\right)^2, \left(\frac{\sigma_\lambda}{\lambda}\right)^2, \left(\frac{\sigma_{hm}}{hm}\right)^2, \left(\frac{\sigma_R}{R}\right)^2, \left(\frac{\sigma_{hs}}{hs}\right)^2 \text{ and} \left(\frac{\sigma_Q}{Q}\right)^2$$

The three test facilities which record data in the presence of a ground plane are JENOTS, GE/CR&DC, and GE J79 at EFTC. The estimated input values for these three facilities are as follows:

	JENOTS	CR&DC	GE/EFTC
f	variable 1/3 octaves		
$\sigma_{\lambda/\lambda}$	0	0	0
R	40 ft	9 ft	160 ft
σ_R	1 ft	2 inches	1 ft
hm	16 ft	15 ft	12 ft or 2 ft
σ_{nm}	1 inch	2 inches	3 inch or 2 inch
hs	55 inches	6 ft	12 ft
σ_{ns}	2 inches	2 inches	3 inches
Q	Figure 5-38	Figure 5-44	Figure 5-62
σ_Q	Figure 5-38	Figure 5-38	Figure 5-38
ϕ	Figure 5-36	Figure 5-44	Figure 5-61
σ_ϕ	Figure 5-36	Figure 5-36	Figure 5-36

From these values, the precision of the ground reflection corrections for the three test facilities were calculated. The results are presented in Figures 5-64, 5-65, and 5-66.

The JENOTS corrections in Figure 5-64 are seen to be least accurate at 200, 400, and 800 Hz, with a maximum of 2 dB standard deviation at 400 Hz.

At CR&DC, the precision of the data is very good at all frequencies due to the foam pads on the ground and the "overhead" microphone configurations. The actual-deviation of the data without removing the ground reflections in fact is very small, as seen in Figure 5-59, so no corrections were made to the CR&DC data and bias errors on the order of the corrections shown on Figure 5-59 are present in the data and should be added as the square root of the sum of squares to the precision errors on Figure 5-65.

At GE/EFTC, the two microphone philosophy minimized the precision errors in Figure 5-66 to less than 1 dB except at 1000 and 1600 Hz were a maximum of 1.3 and 2.2 dB occurs.

5.9 REFLECTIONS IN THE ANECHOIC ROOM

Both anechoic rooms utilize high quality acoustic wedges which are designed to give a free-field environment above 150 Hz.

Although there do not appear to be any reflection problems inside the chambers, possible reflecting surfaces include:

- Light Bulbs: There are four 300 watt light bulbs inside the chamber. Removal made no difference to the spherical divergence test data.

- Door handle: microphone boom, jet plenum, jet nozzle: these have all been covered with a minimum of 1-inch-thick fiberglass so that reflection from these elements is minimized.

- Wire mesh floors: Covering both the fine mesh catch-screen and the coarse mesh floor with 1-inch fiberglass did not significantly affect the spherical divergence tests. Thus floor reflections are probably unimportant.

- Nozzle outer wall: The nozzles are not covered by foam during testing so back reflections are possible but not probable.

The wire mesh covering the wedges is the only remaining untested reflecting surface. This mesh consists of 1.5-mm wire on a 1.25-cm grid. It is possible that the wire covering the tips of the wedges could cause unwanted reflections, but there has been no evidence to suggest this. The foregoing general observations apply to a frequency range from 300 Hz to about 100 kHz.

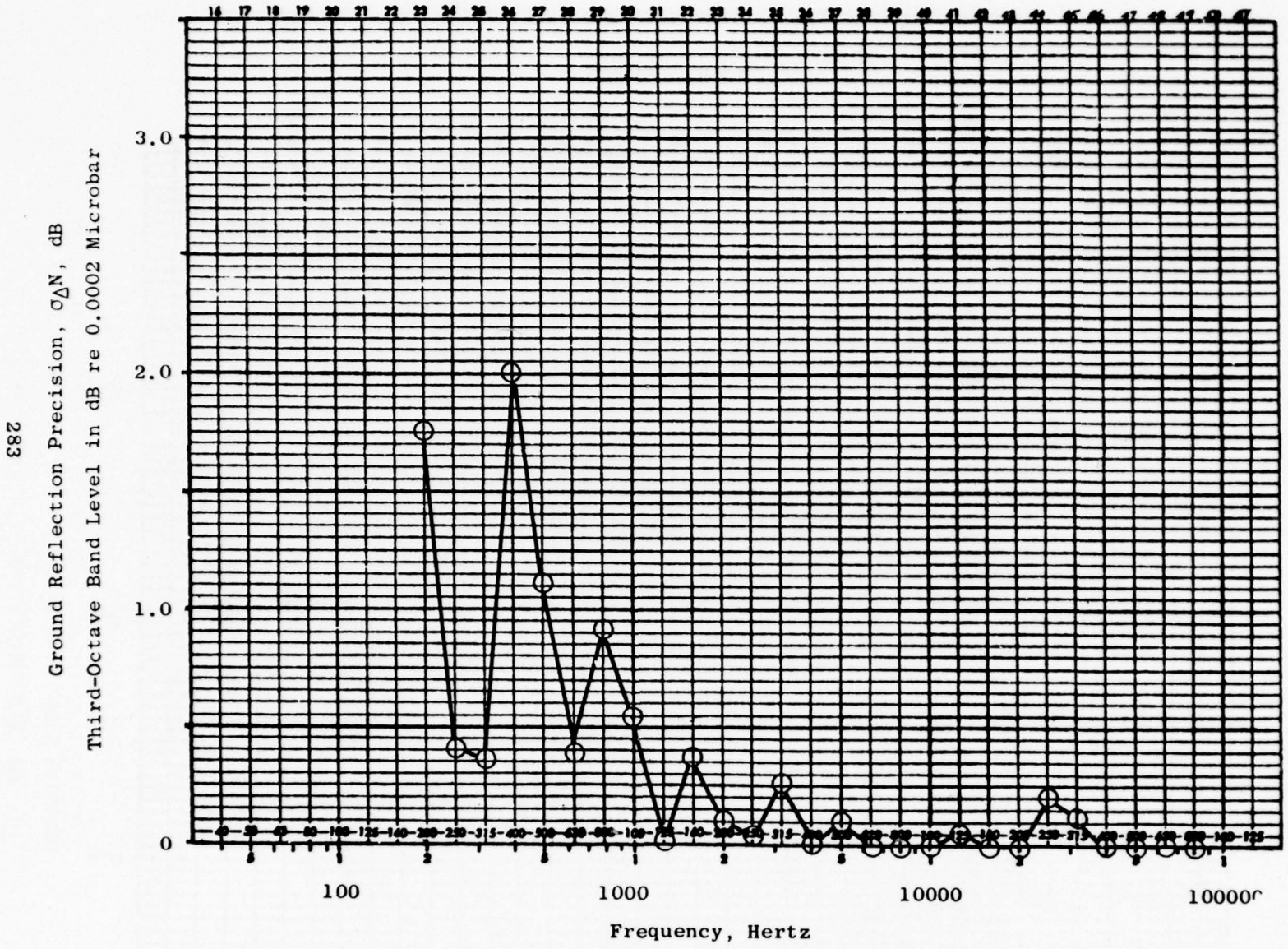


Figure 5-64. Ground Reflection Precision Error at JENOTS.

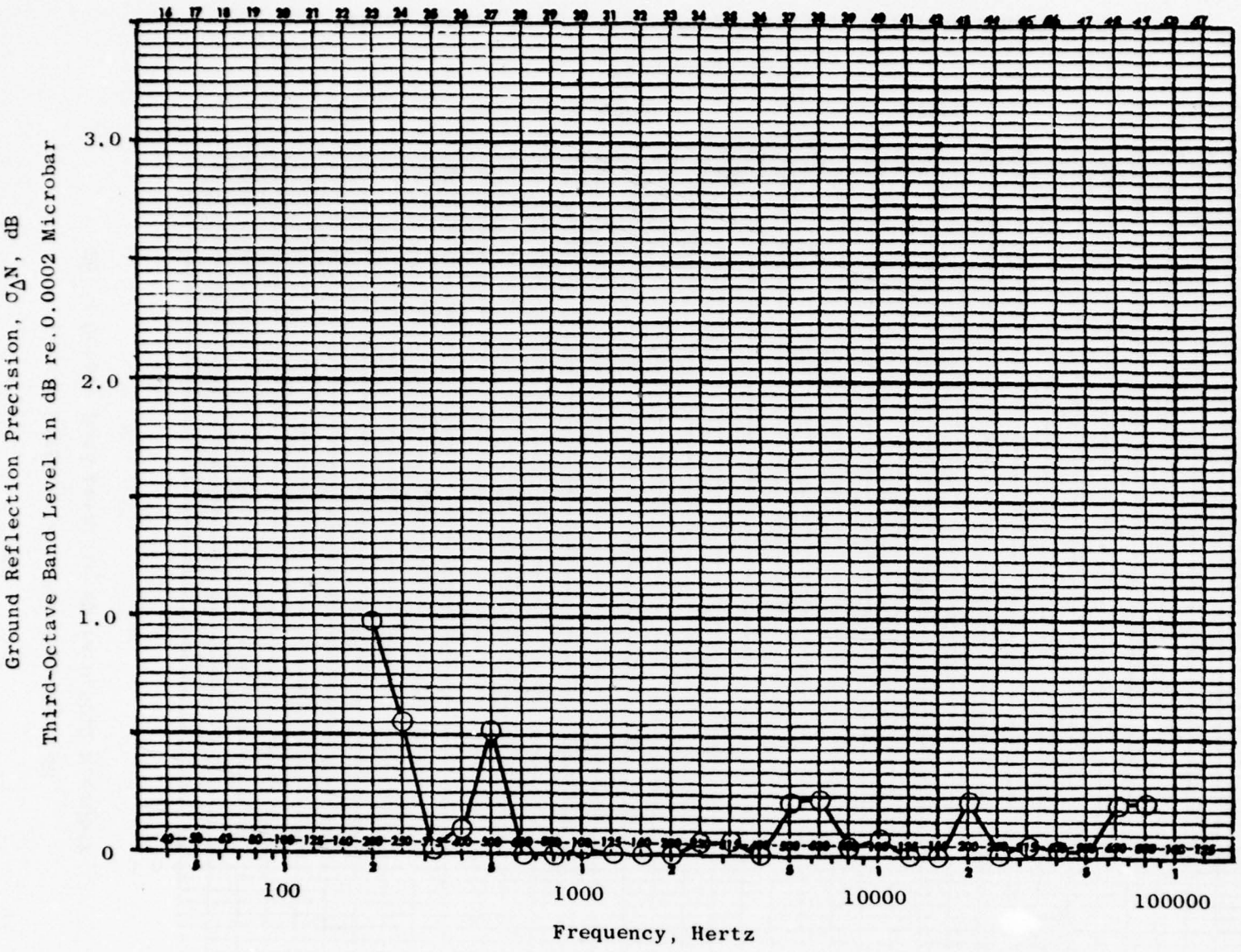


Figure 5-65. Ground Reflection Precision Error at GE/CR&DC.

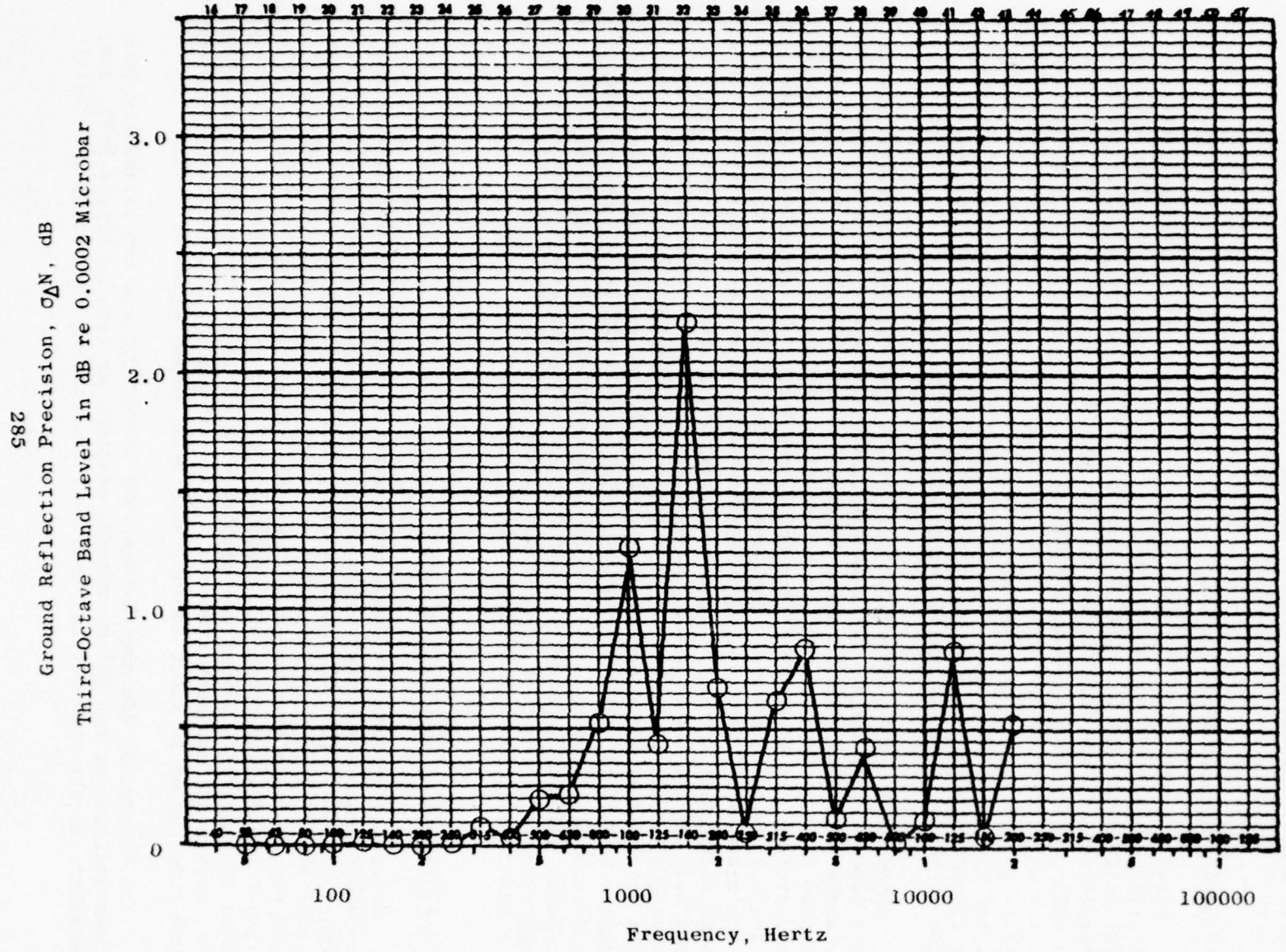


Figure 5-66. Ground Reflection Precision Error at EFTC.

All of these sources were considered as potential reflecting surface. Inverse square law testing however showed them to be insignificant.

5.10 OTHER REFLECTIONS AT JENOTS

After elevating the microphones to 15.93 feet, a reflection pattern was still present in the JENOTS spectra. This pattern appeared to have its first null in the 800 Hz band as shown in Figure 5-67 with higher order cancellations in the 2.5 kHz and 6.3 kHz bands which would be the 2nd and 4th nulls respectively. Such a pattern could only exist if the reflecting surface was close (within 0.35 feet) to either the source or the microphone. Because of the known distributed sources in the jet and the fact the pattern existed in all microphone stations, a reflection off the microphone stand was suspected. New "gooseneck" microphone holders were constructed, as shown in Figure 5-68, which corrected the problem.

Although no other reflection nulls were present in the spectra, there was a concern that the nearby community noise barriers, shown in Figure 5-69, may cause a general reverberation increase in the levels. These walls were oriented in construction such that the reflection angle from the jet source would project the sound away from the sound field. Nevertheless, an analysis of the walls was conducted. The nearest point of the walls to a microphone is on the order of 50 feet, so as an approximation one might estimate the path length difference for any potential reflection to be $\Delta r = 100$ feet for a first null in the 6.3 Hz band. Any higher order band would certainly be washed out by the time the 400 Hz frequency of interest was reached. The extra 100 feet of air attenuation on the reflected wave would have a dramatic effect of quickly producing an effective reflection coefficient $Q \simeq 0$ at high frequency. Even at low frequency, however, the effect of the walls would be negligible. The ratio of the reflected-to-direct path-lengths would be $z = r'/r \sim 3.0$ which, from Figure 5-13, would give only 0.4 dB reinforcement above the third null (30 Hz).

5.11 ADDITIONAL REFLECTIONS AT CR&DC

An area of concern at CR&DC was potential reflections off the microphone boom and support structure saddle (guide plates that ride on the hoop), as shown in Figure 5-70. The main problem, because of the distances and sizes of the obstructions, was suspected to be of a sound scattering nature. This would occur at a higher range of frequency than the ground reflection effects. To cover the desired range of frequencies of 400 Hz and above, an Altec (Model 291-16A) horn driver was coupled to a circular cross section exponential horn, with a 12-inch exit diameter. This combination had an effective frequency range from 200 Hz to about 20 kHz, with peak output at about 2 kHz.

The separation distance between the microphone and the traversing boom is the smallest at the 90° microphone station, as seen in Figure 5-70, and, therefore, is the most crucial location. By varying the microphone radial

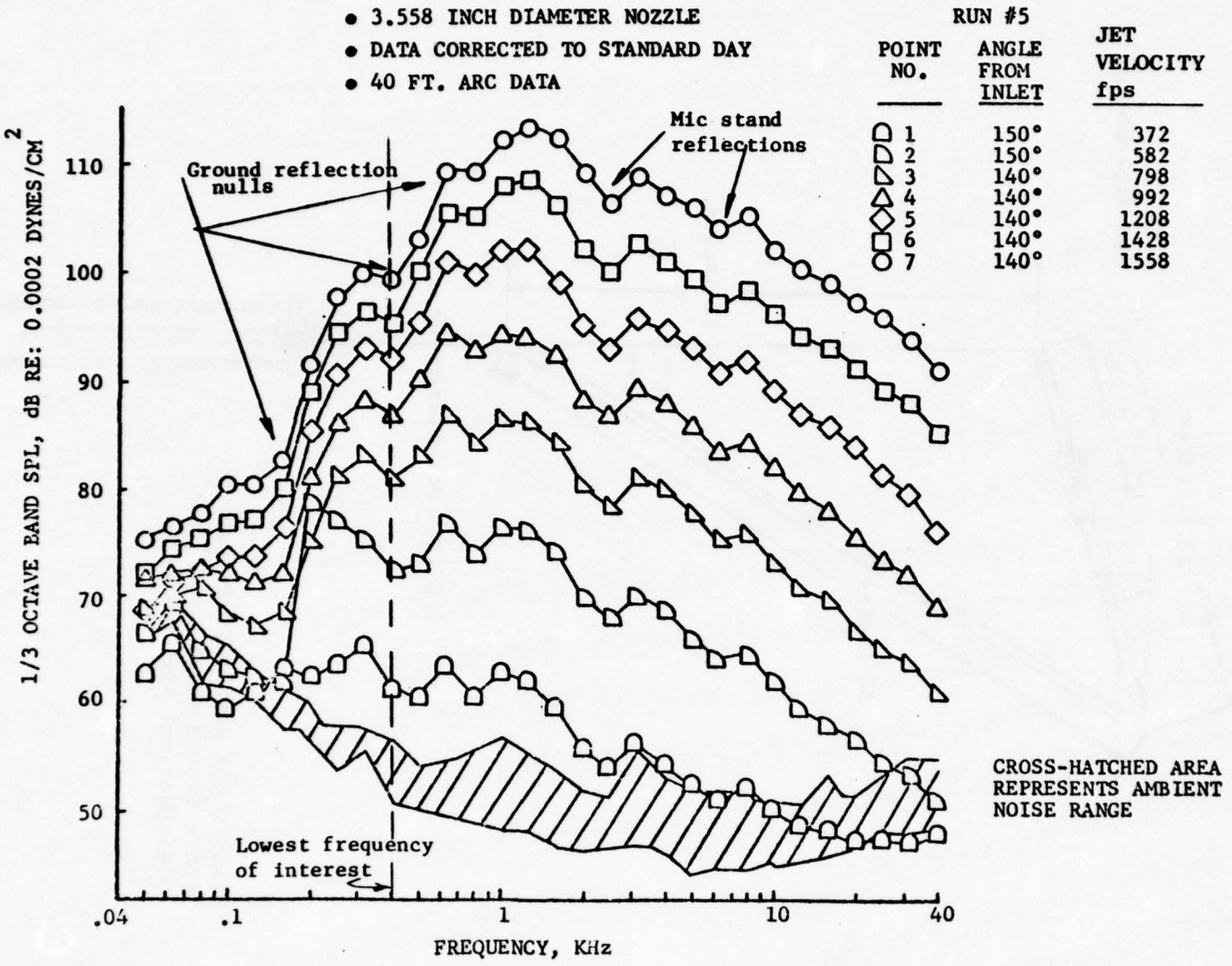


Figure 5-67. Peak OASPL Spectra for Conic Baseline at JENOTS.

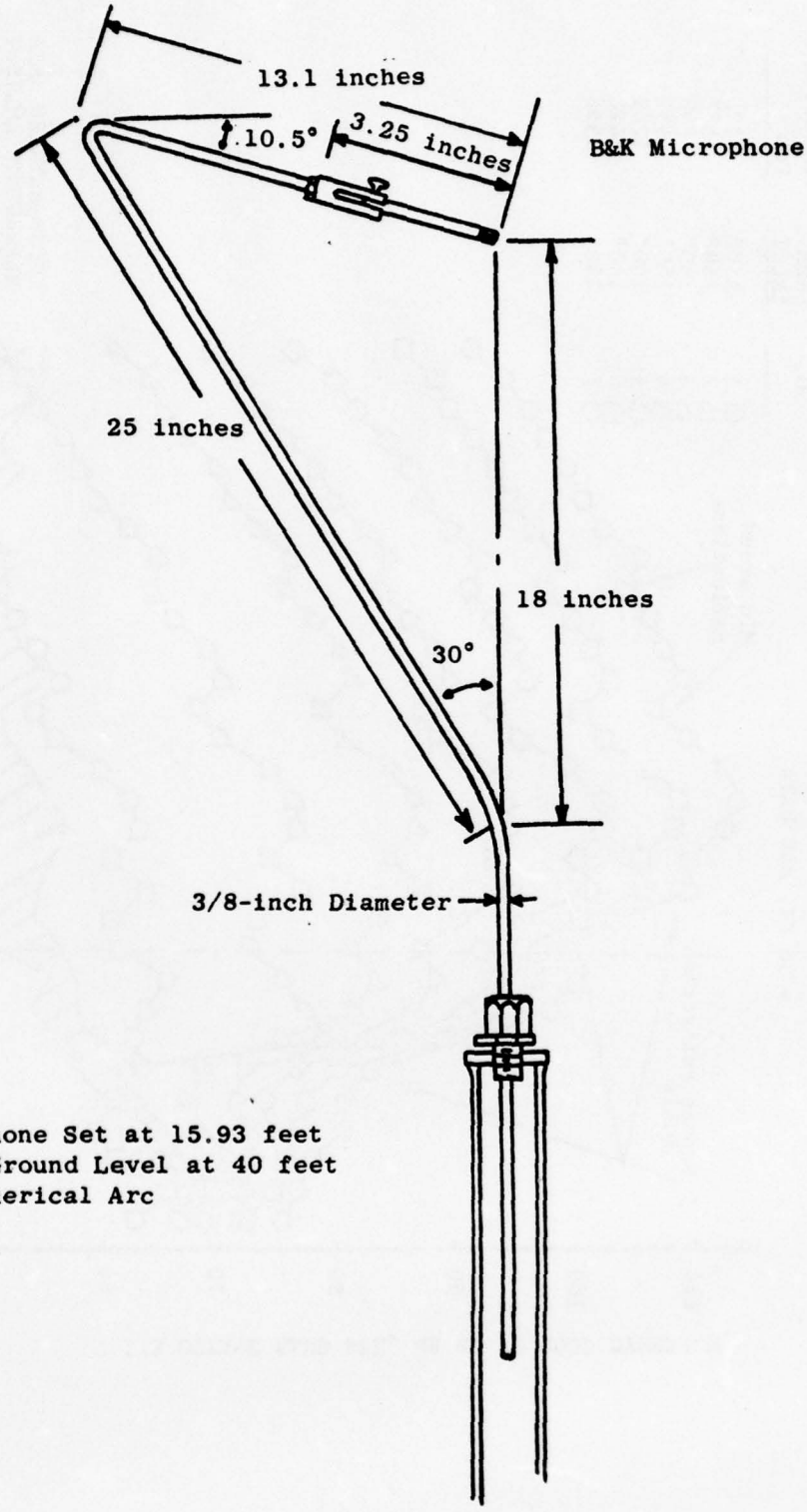


Figure 5-68. JENOTS Microphone Mount.

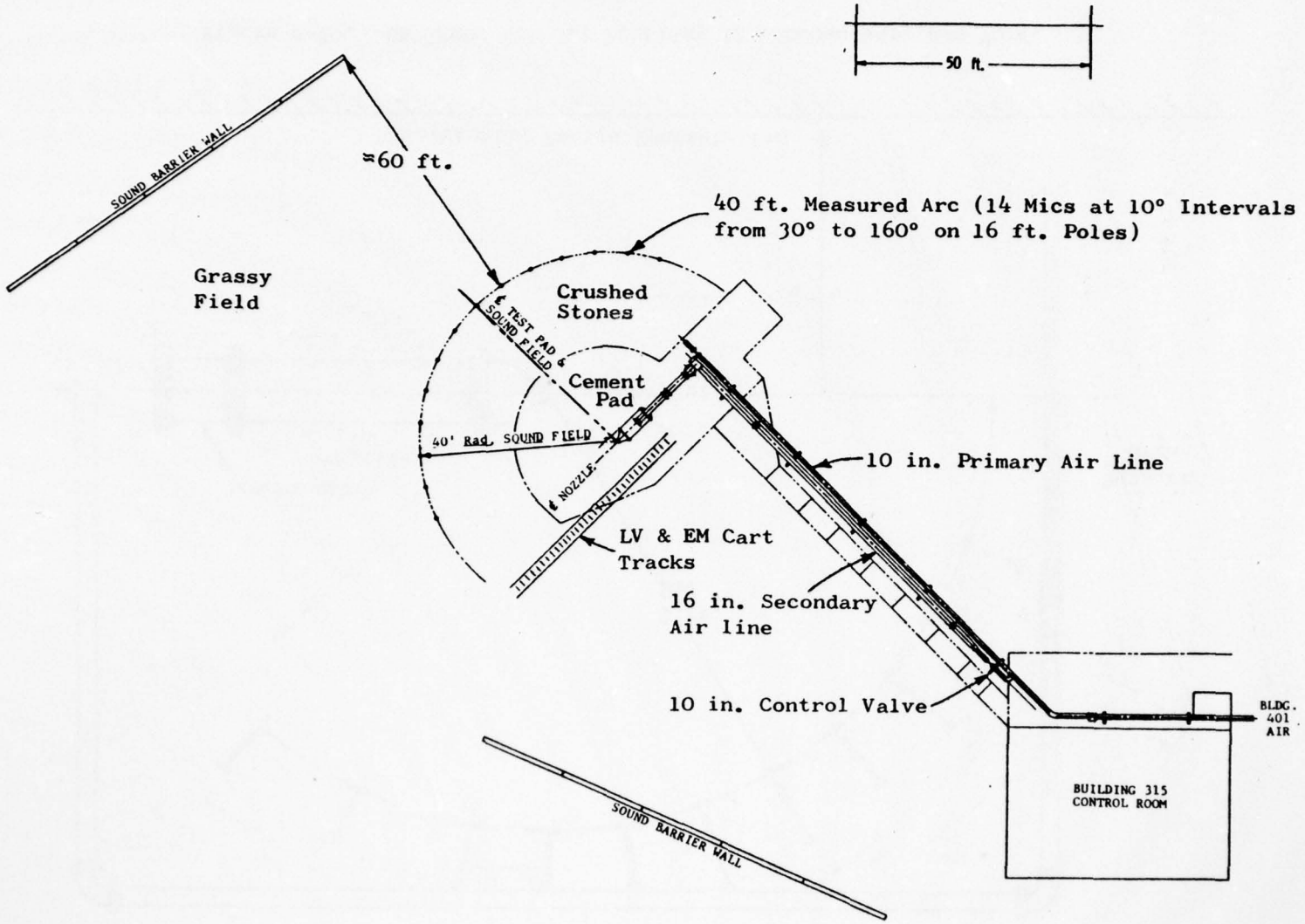


Figure 5-69. Schematic of JENOTS Facility.

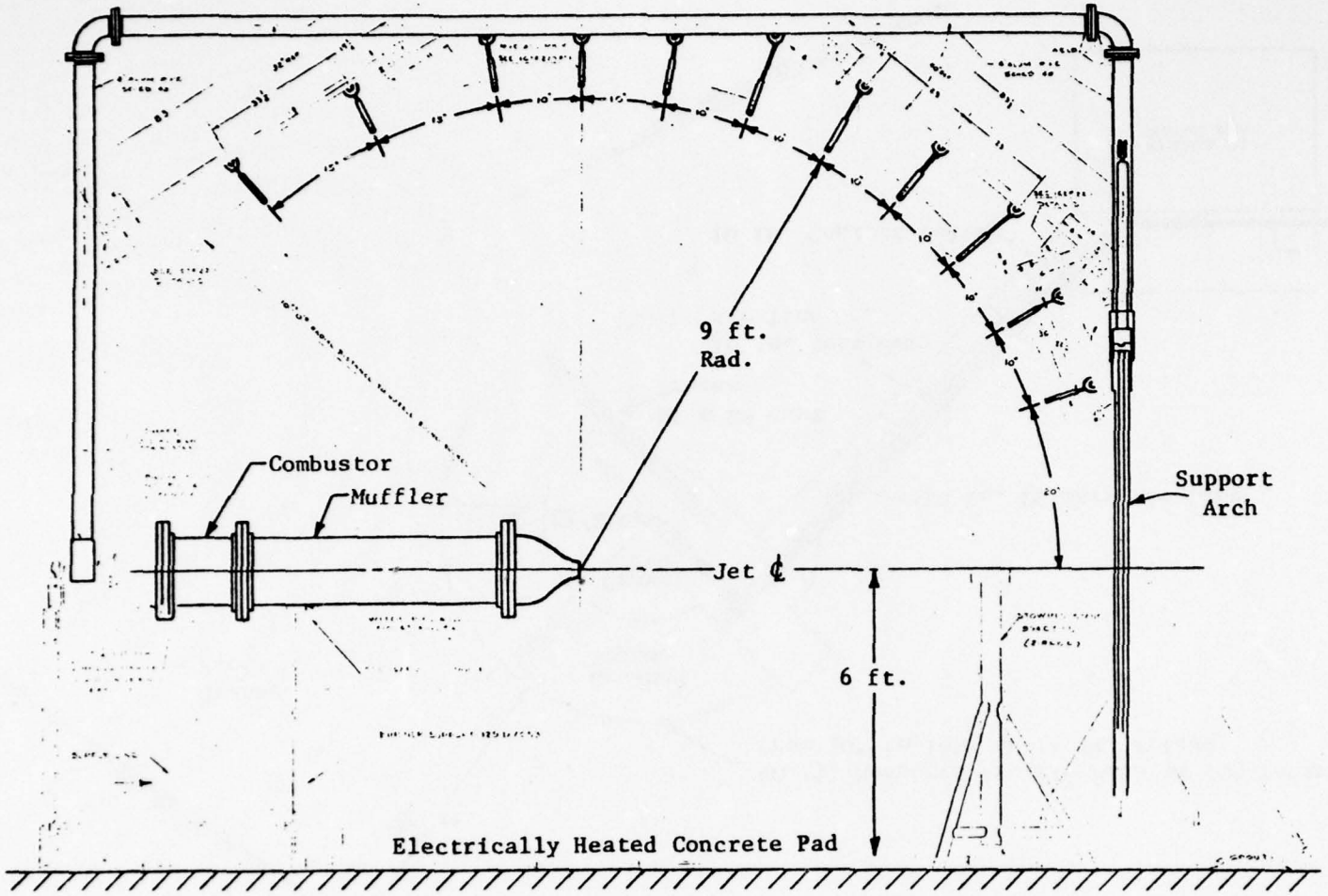


Figure 5-70. GE CR&DC Hot Jet Facility in Schenectady, New York.

location from the jet axis the effect of the boom on the acoustic signals could be seen, as shown in Figure 5-71. With the boom fixed at 11 feet from the jet center line, the microphone was moved from a radius of 9 to 10 feet, the data uniformity decreases as the standoff distance is reduced and the spectrum becomes bumpy in the middle frequencies, indicating the effects of scattering. Scattering is not evident in the high frequency portion of the spectrum due to the 1-inch layer of acoustical foam covering the boom.

The shallow angle microphones are another point of possible contamination by scattering due to the close proximity of the boom to the support ring. To reduce this, the saddle is faced with a two-inch layer of foam. In a test similar to the one described in the preceeding paragraph, it was found that the scattering was insignificant below a radius of 9 feet, as shown by the θ_I = 160° data in Figure 5-72.

As a result of these tests, the maximum acceptable microphone radius was found to be 9 feet. This microphone radius was used for the studies reported throughout the remainder of this report.

5.12 SPURIOUS REFLECTIONS AT 150° AND 160° WITH J79/EFTC

Reflections from something other than the ground were found in the 150° and 160° angles, as shown in Figure 5-73. Since these reflections only affect the 160° angle to any great extent, it was decided to accept the error involved. The casing box around the engine described in Section 3.6.2.3 does seem the most likely candidate for the reflecting surface. However, because of the distributed source nature of the jet, analytical corrections for this are nearly impossible.

5.13 INVERSE SQUARE LAW AT USC

The free-field characteristics of the room were determined by placing a Hi-Fi loudspeaker at one side of the room and measuring the sound field at a number of distances from the speaker with an HP 1-inch microphone. Pure tones were used for this test and the 4 x 4 foot exhaust opening was covered with fiberglass wedges during the test. Results of this test are shown in Figure 5-74.

These tests indicate that the room can provide a satisfactory environment for acoustic measurements. However, the question as to what effect the model jet hardware inside the room and the 4 x 4 foot exhaust opening have on the free-field characteristics of the room had to be answered. After all reflecting surfaces were properly covered with fiberglass, a 1/2-inch-diameter choked jet used as an acoustic source was placed 9-inches from the nozzle exit plane blowing in a direction perpendicular to the plane containing 10 microphones set up for the jet noise experiments. The 10 microphones were on a circular arc centered on the nozzle exit and located 90-inches away. Because of axial symmetry, the 1/2-inch jet is expected to radiate uniformly

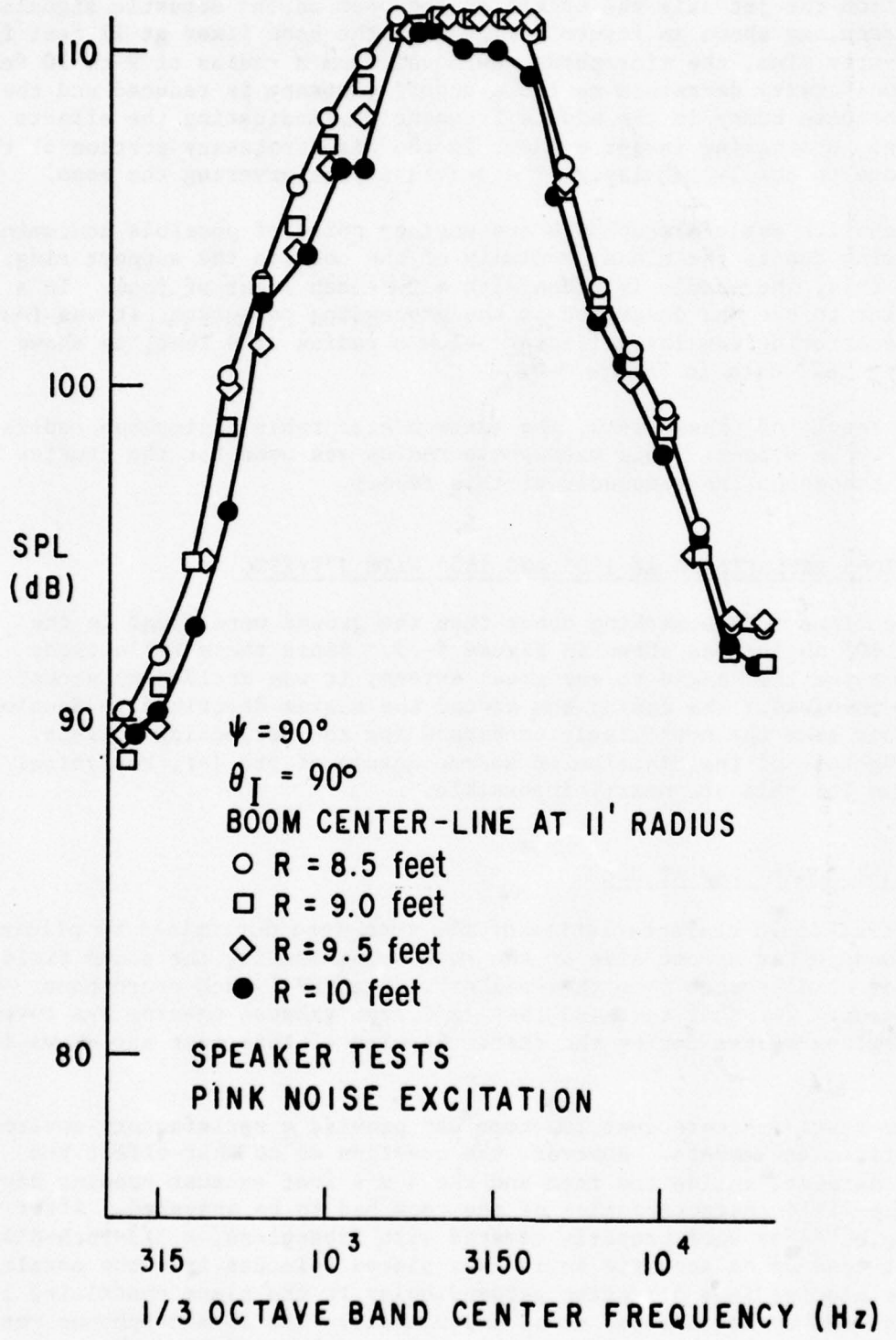


Figure 5-71. Boom-Microphone Separation Effect at GE CR&DC.

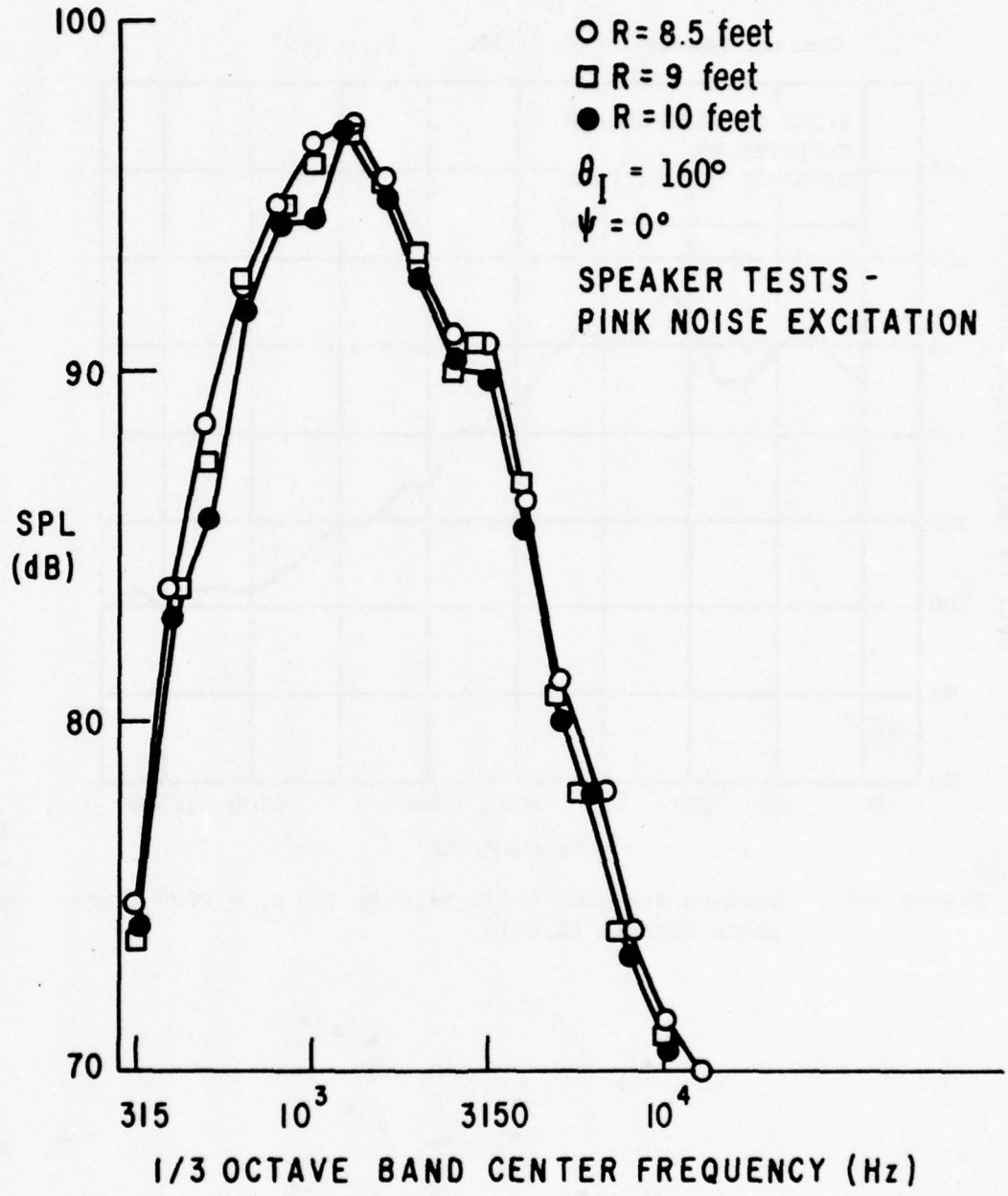


Figure 5-72. Saddle-Microphone Separation Effect at CR&DC.

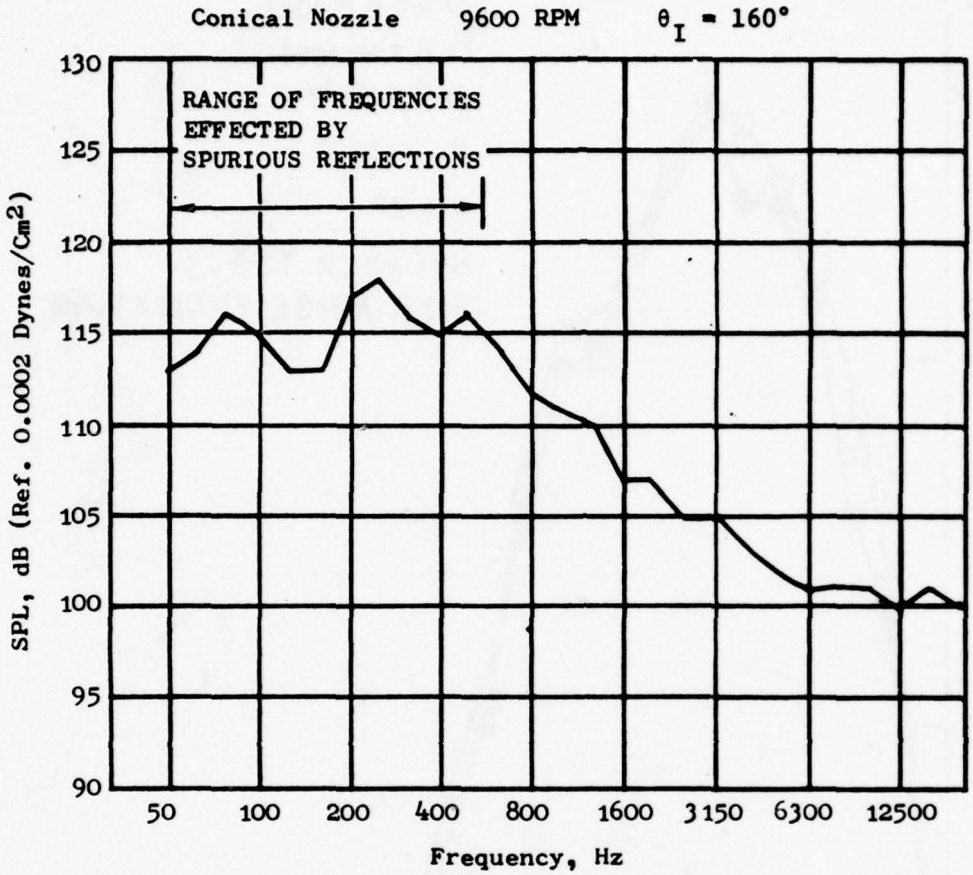


Figure 5-73. Unknown Spurious Reflection in the θ_I = 160° Microphone Data at GE/EFTC.

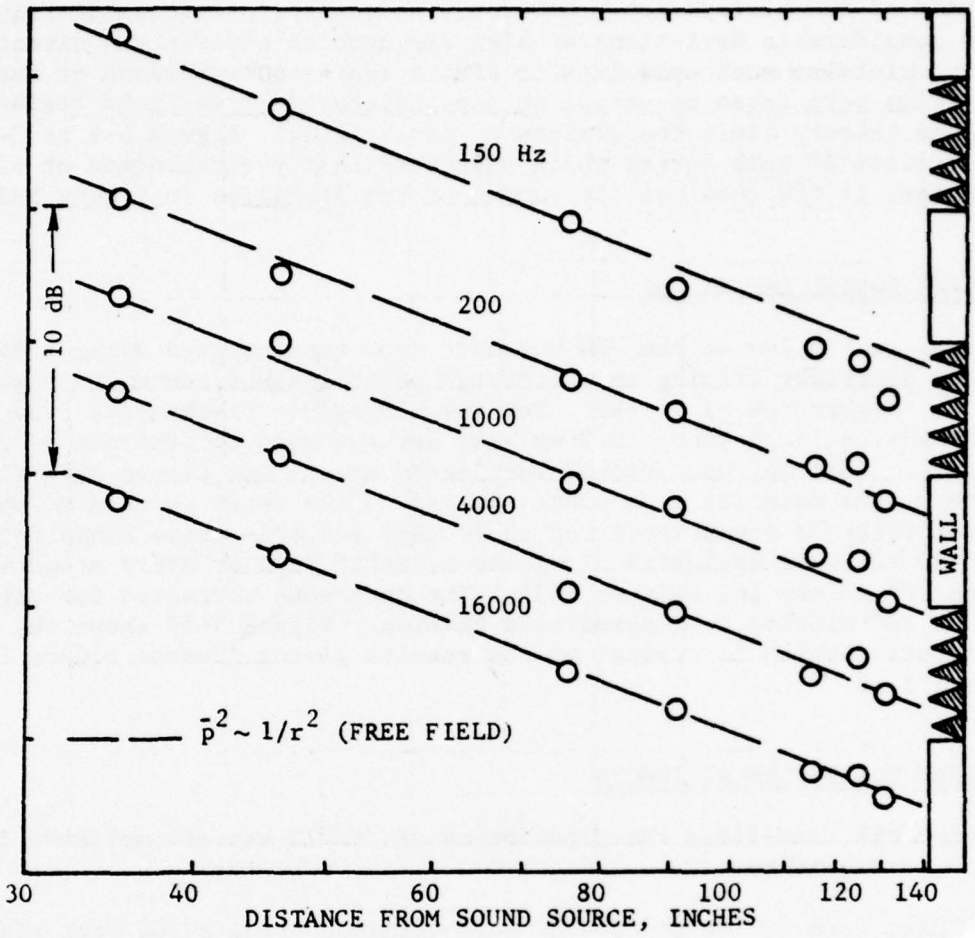


Figure 5-74. Free Field Characteristics of Anechoic Chamber at USC.

in the plane of the microphones. However, the results presented in Figure 5-75 show considerable deviations at high frequencies and certain directions. In order to minimize such anomalies, radial traverse measurements of the radiated noise were taken to establish the undisturbed free-field region in the room and thereby limit the regions of data taking. Figure 5-4 to 5-10 show the results of this survey which suggested that recirculation of air in the corners of the room was the source of the anomalies in Figure 5-75.

5.14 INVERSE SQUARE LAW AT UBC

Inverse square law in the UBC anechoic room was measured using a B&K 1024 random generator driving an artificial point speaker, shown in Figure 5-76, up to frequencies of 20 kHz. For the ultrasonic frequencies from 20 kHz to 100 kHz, a (1/32-inch) (0.8 mm) air jet was used to generate a "point" source noise. This jet was pointed vertically upward and placed slightly downstream of the main jet exit plane similar to the setup as used at USC. Six percent filtered sound level (up to 20 kHz) and 1/3-octave bands from 20 kHz to 80 kHz were evaluated along the acoustic rays at every acoustic angle from 10° to the jet axis to 100°. The data were corrected for air attenuation and plotted in a normalized fashion. Figure 5-77 shows the 90° distribution which is typical of the results giving inverse square law to within ± 1 dB.

5.15 INVERSE SQUARE LAW AT JENOTS

Testing the free-field characteristics at JENOTS was accomplished in three test arrangements.

1. Data from 200 Hz to 1600 Hz were obtained using a 100 watt ElectroVoice speaker and B&K 4133 microphone, both mounted 1 foot above the ground. The microphone was moved to distances of 10, 20, 31.5, 40, 50, and 63 feet from the speaker along the 90° microphone station line from the nozzle, as shown in Figure 5-78.

2. Data from 2 kHz to 10 kHz were obtained by repeating the speaker test with the speaker and microphone both 55 inches above the ground.

3. Data above 10 kHz were obtained using a 2-inch STA nozzle as the source and microphones placed at 8, 16, 32, and 40 feet from the nozzle at the nozzle height of 55 inches above the ground.

The motivation for the geometric setup of the speakers was similar to that for the "two microphone" philosophy at EFTC. At 1 foot above the ground, all data 1600 Hz and lower are below the first ground cancellation null and reliable corrections are available. Similarly at 55-inches, the collected data 2 kHz and above is the second null where reliable data are obtained.

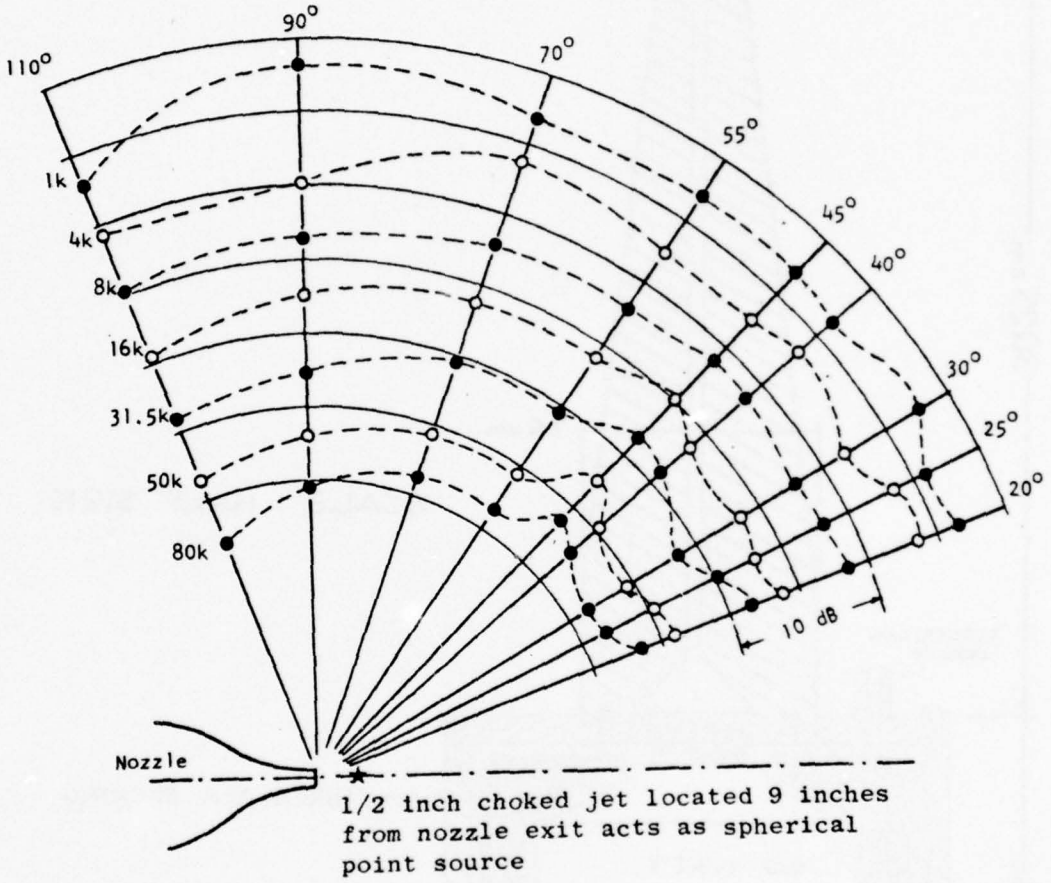


Figure 5-75. Departure of Sound Pressure Levels from Free Field Conditions at USC.

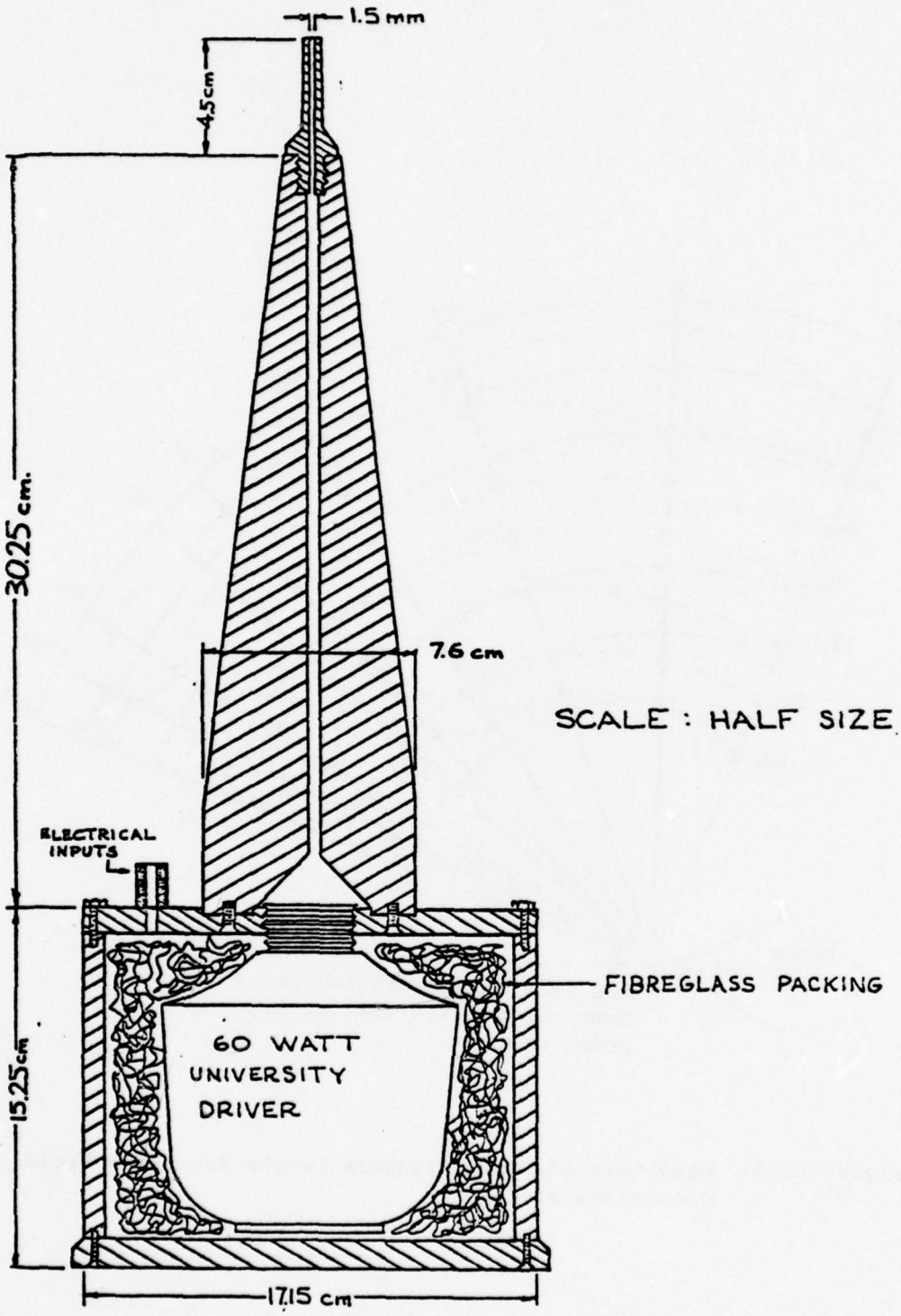


Figure 5-76. Point Source Used for Spherical Divergence Tests at UBC.

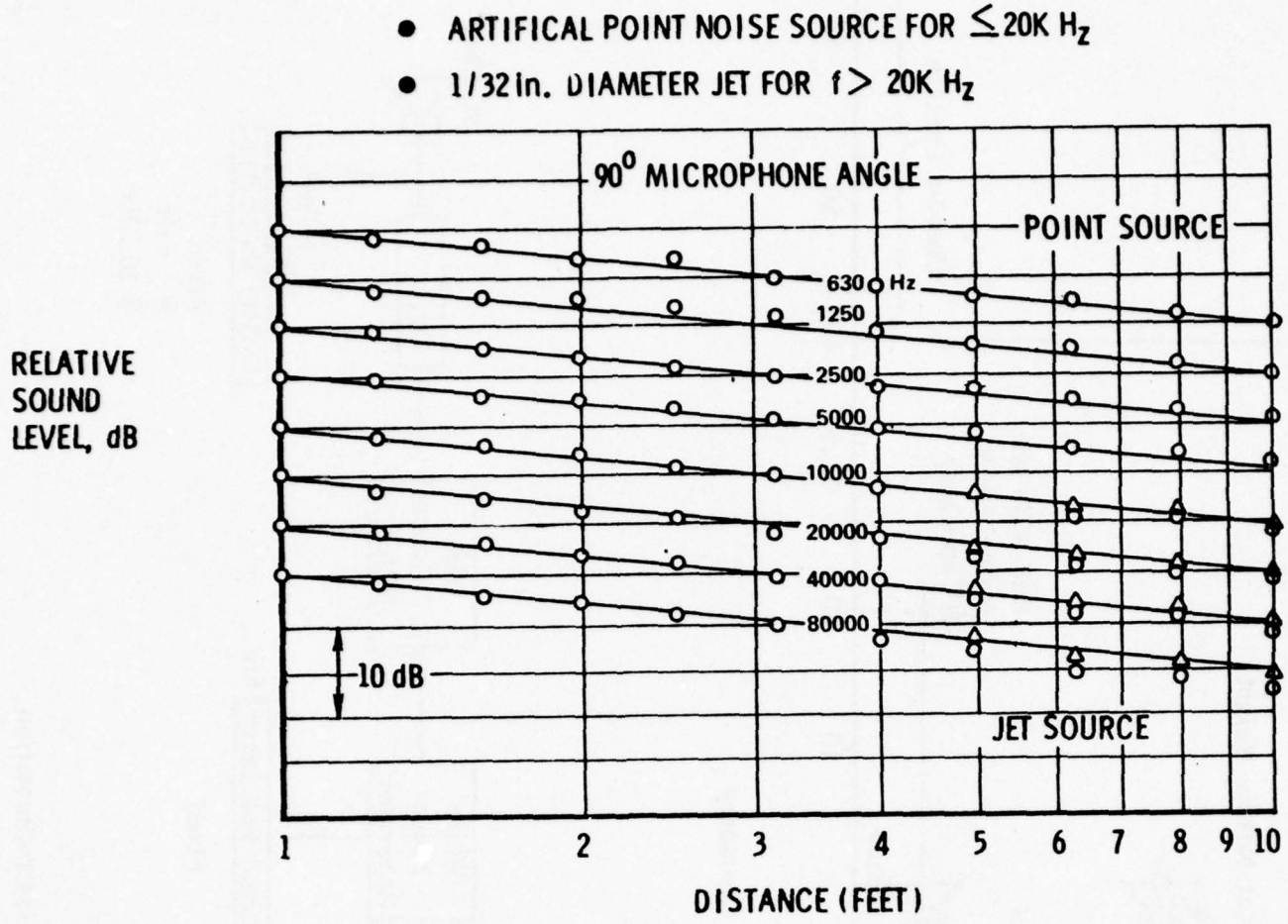
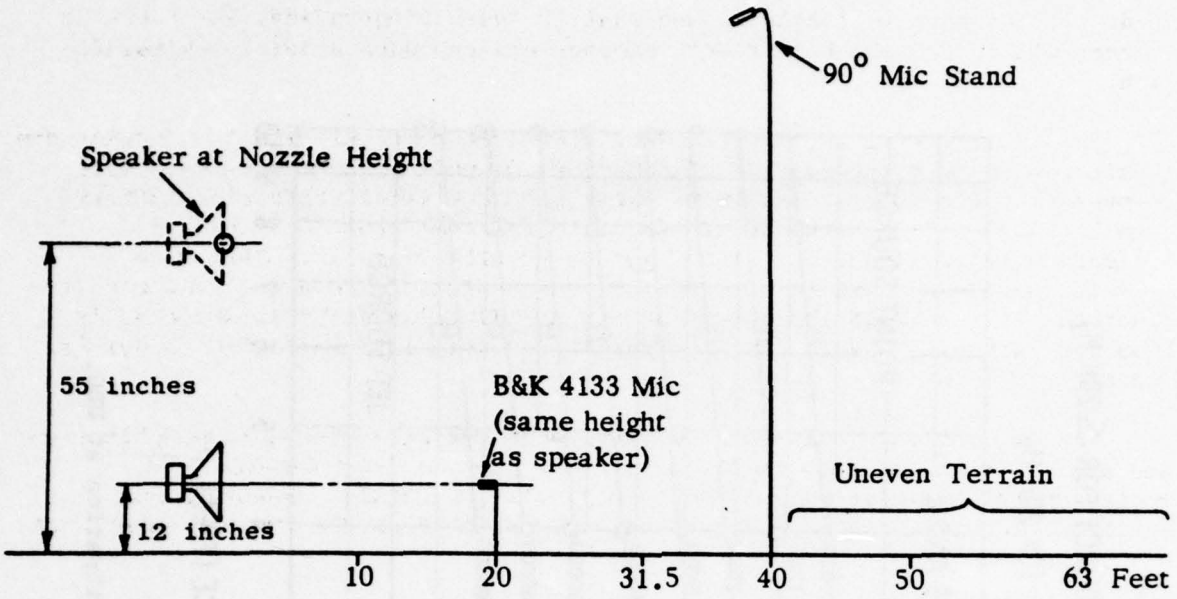
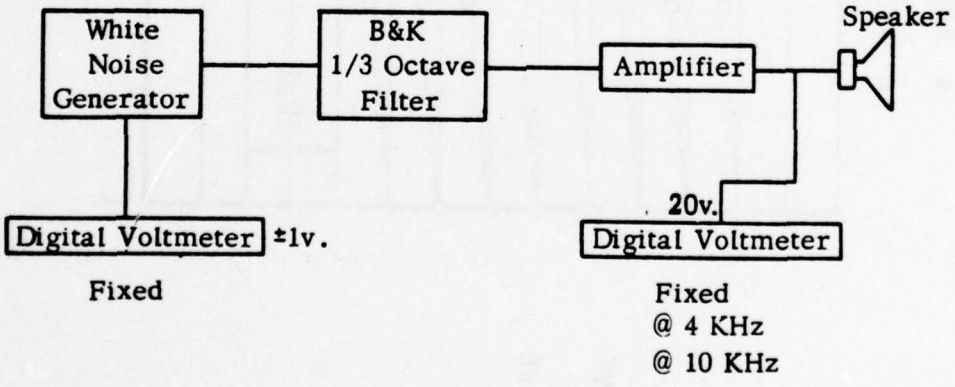


Figure 5-77. UBC Free Field Calibration at UBC.



a) Test Geometry



b) Test Instrumentation

Figure 5-78. JENOTS Setup for Inverse Square Law Test.

At high frequencies, the speakers become insufficient and a small jet is used. It has been well established that at these frequencies, the acoustic sources within the jet become very compact and approach a point representation.

The speaker at low frequcncies and the 2-inch jet at high frequencies are considered to be point sources of sound, so ground reflection effects were removed from the data at each microphone distance using correction factors from Equation (95) and the 90° phase factor ϕ from Figure 5-36 plus a reflection coefficient, Q_S, from Figure 5-39 with $Q_I = 1.0$. The value $Q_I = 1.0$ has been found from impedance measurements to be a good estimate for concrete. Figure 5-15 shows that of the actual value of Q_I is somewhat less than 1.0, say 0.9, the resulting error on the calculate reflection index is minor.

The collected data at each distance were corrected for ground reflection and air attenuation; results are plotted in Figures 5-79 through 5-81. Deviation from inverse square law is minimal. To obtain a quantitative estimate of this variation the standard deviation from the inverse square law was calculated from

$$\sigma^2_{1/R^2} = \sum_{i=1}^{N} \frac{(S_i - S_M)^2}{N} \tag{102}$$

where

$$S_M = \sum_{i=1}^{N} \frac{S_i}{N} \tag{103}$$

and

$$S_i = SPL_i(r) - 20 \log (r/r_o) \tag{104}$$

This variation is shown in Figure 5-82 to be generally less than 1 dB throughout the frequency range.

5.16 INVERSE SQUARE LAW AT CR&DC

To determine whether or not the CR&DC arena exhibited spherical spreading, a closed direct-radiation loudspeaker with an effective output range from 60 Hz to 5000 Hz was used. The speaker was pointed directly at the far-field microphone. In the horizontal position, both were positioned at 6 feet above the concrete pad. An 18 foot by 18 foot area of the concrete pad

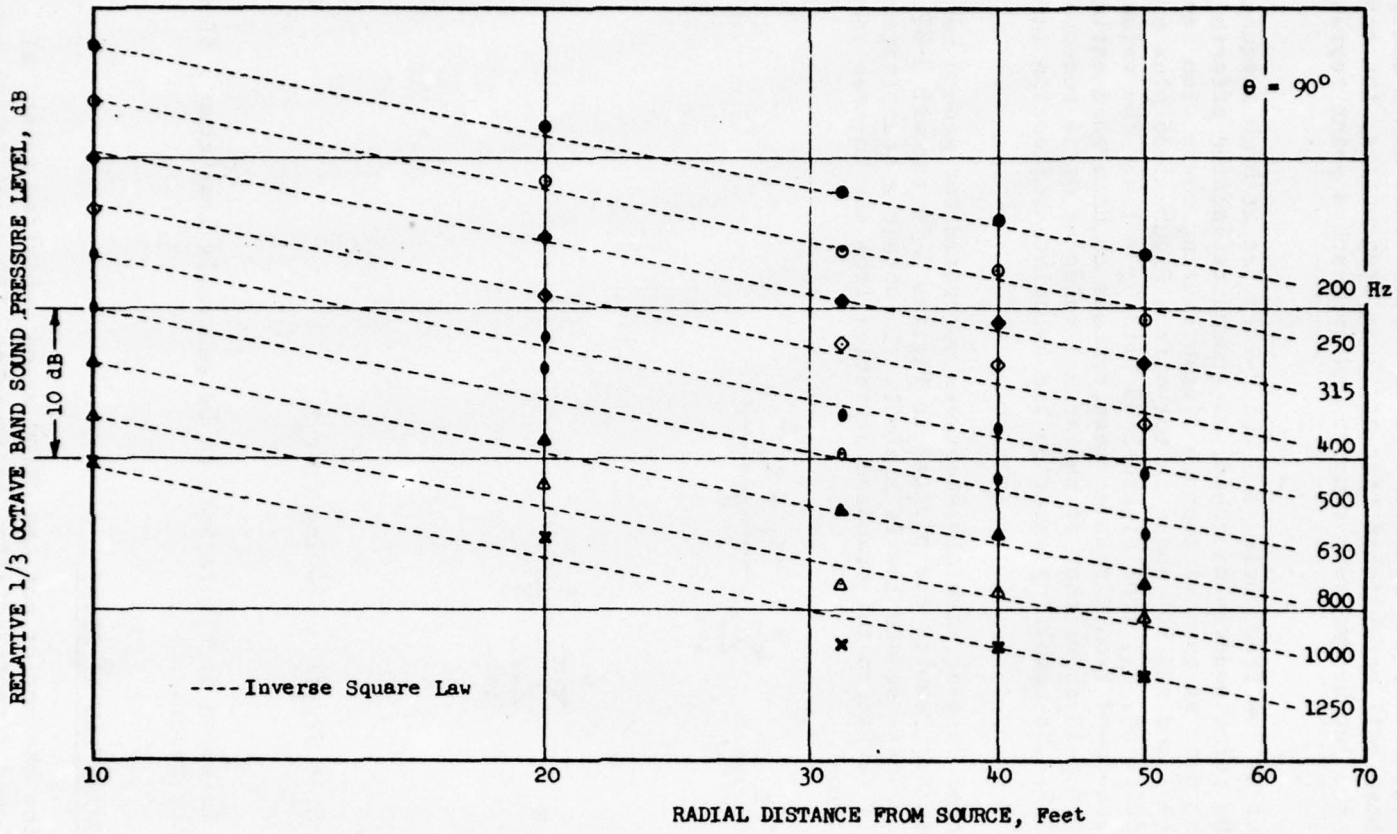


Figure 5-79. JENOTS Inverse Square Law at Low Frequencies Using Microphone and Speaker at 12-inch Height.

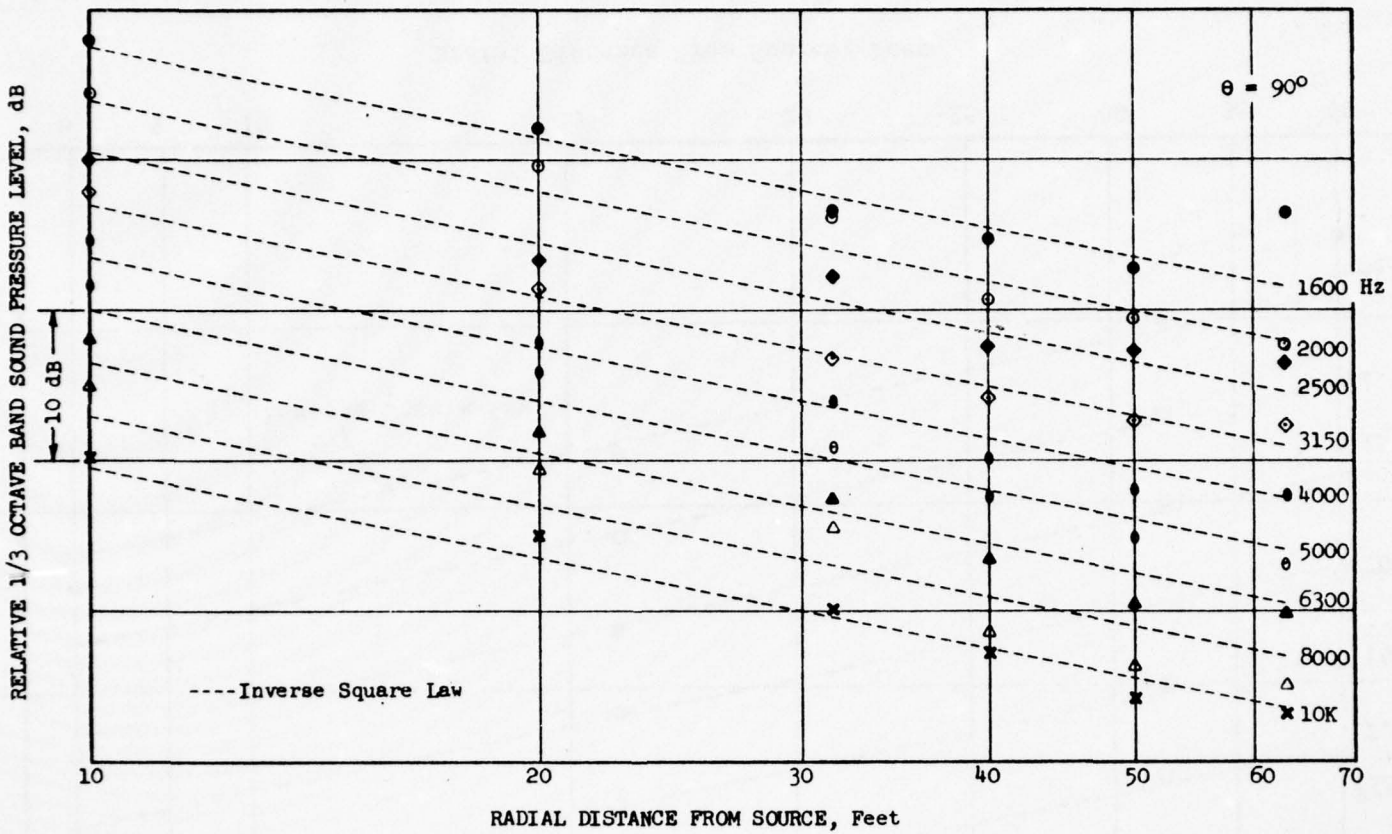


Figure 5-80. JENOTS Inverse Square Law at Intermediate Frequencies Using Microphone and Speaker at 55-inch Height.

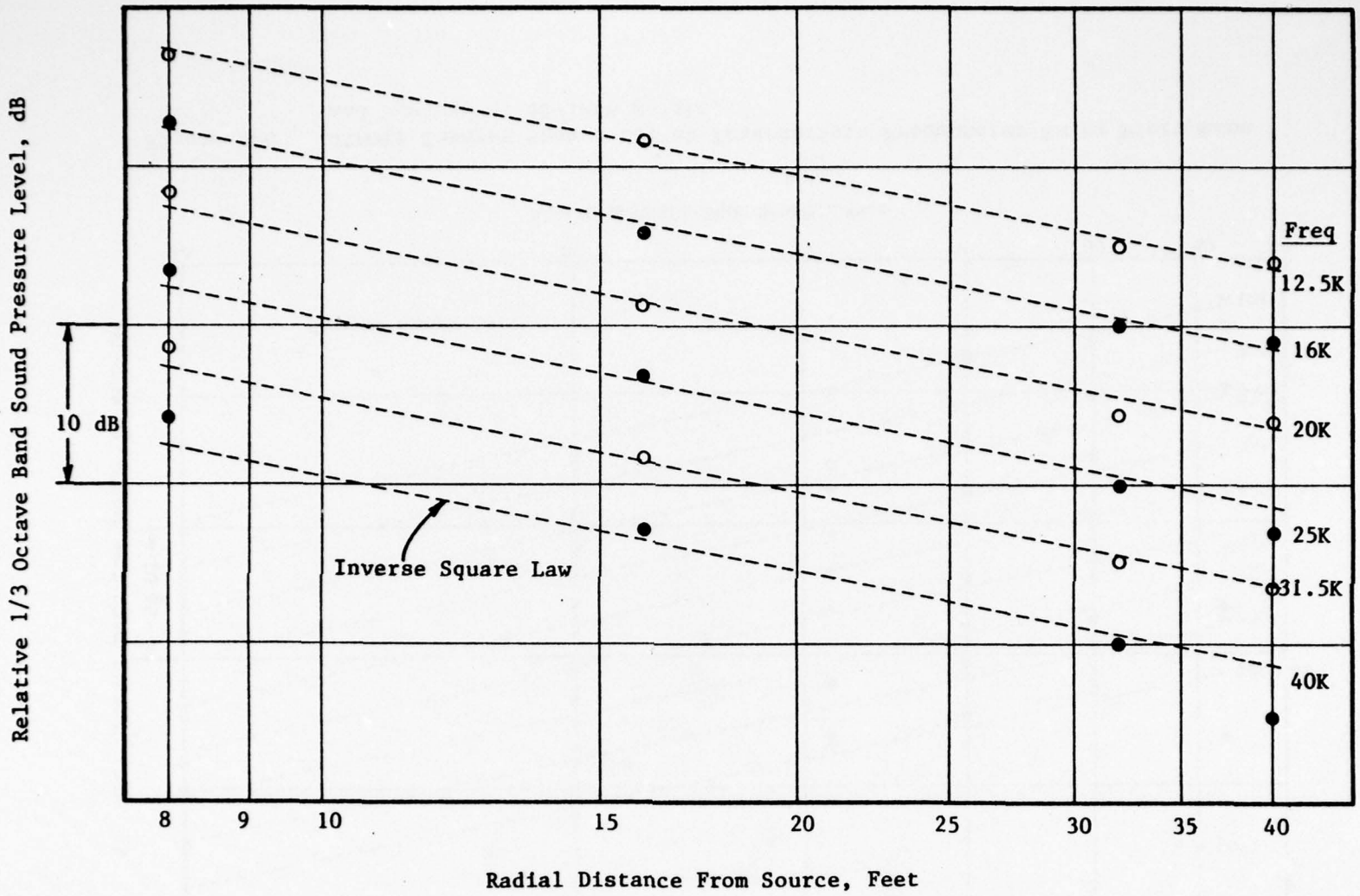


Figure 5-81. JENOTS Inverse Square Law at High Frequencies Using Jet Source and Microphone at 55-inch Height.

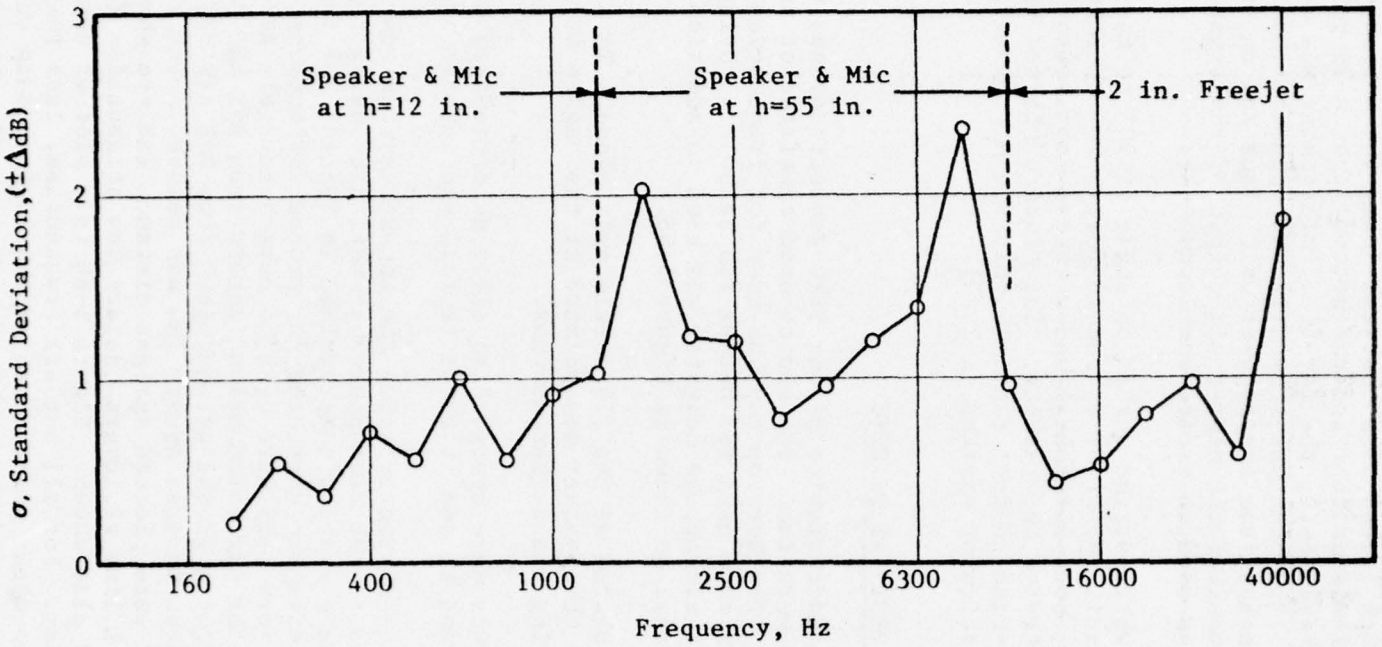


Figure 5-82. Variance in JENOTS Data from Inverse Square Law Line.

was covered with two 4-inch layers of acoustical foam, the top layer a 90 pores per inch (ppi) reticulated foam and the bottom layer a 99 ppi non-reticulated foam. For these tests, the far-field microphone was mounted on a separate tripod and the large boom was stowed in the opposite quadrant. A control microphone (12 inches from the speaker exit plane and on the speaker centerline) was used to monitor the near-field output of the speaker. A random noise generator was used to excite the loudspeaker.

These measurements were carried out at an angle of 90° to the jet axis and at three different radii, R, of 6, 8, and 10 feet. To determine the effect of the boom angle, both horizontal and vertical measurement planes were used. Figure 5-83 illustrates the results. The arena exhibited spherical divergence between the 8- and 10-foot radii, within the experimental repeatability of this particular speaker (± 1 dB).

5.17 INVERSE SQUARE LAW TESTS AT GE/EFTC

To determine the characteristics of the EFTC acoustic arena, tests employing a known source were run. The source used consisted of two speakers, as shown in Figure 5-84. The horn on top was used for frequencies above 800 Hz and the lower speakers were used for 800 Hz and below. A roving microphone setup (12-foot and 2-foot microphone heights) was used in addition to the standard 160-foot arc array, as shown in Figure 5-85.

The speakers were located at the J79 nozzle exit plane. To avoid directionality problems, the speaker was pointed at the angles of interest (60°, 90°, and 160°) during the different runs.

The various tests runs were designed to allow determination of ground reflection coefficients and to see if the site followed inverse square law.

To determine the site characteristics the speaker system was used as the source while the distance to the microphone was varied by using the roving microphone. Applying the ϕ's and Q's determined in Section 5.7 in the point source model, the data was corrected for ground reflections. The two microphone heights of Figure 5-85 were used to more accurately determine the free-field data. Using the air attenuation factors from SAE ARP 866 (Reference 16) and the "extra ground attenuation" from SAE AIR 923 (Reference 11), attenuation other than inverse square law was removed. The resultant SPL's for each frequency were plotted against distance and are shown in Figures 5-86 and 5-87. A line of inverse square law attenuation (6 dB per doubling of distance) is also shown. Figure 5-88 is a plot of standard deviation versus frequency. For all but six frequencies, less than 1 dB error is present. At 50 Hz the upper point contains the 20-foot data which, for this frequency, is in the near field. The lower point omits these data. The points above 10 kHz had to be obtained by filtering the input signal to the speaker to give the required frequency of interest. This approach was used in an effort to avoid contamination by ambient noise. Data 10 kHz and below were obtained by running a pink noise signal through the speaker system. Because of this difference, it is felt that the 12,500, 16,000, and 20,000 points do not accurately represent the site. At 315 and 4000 Hz, a

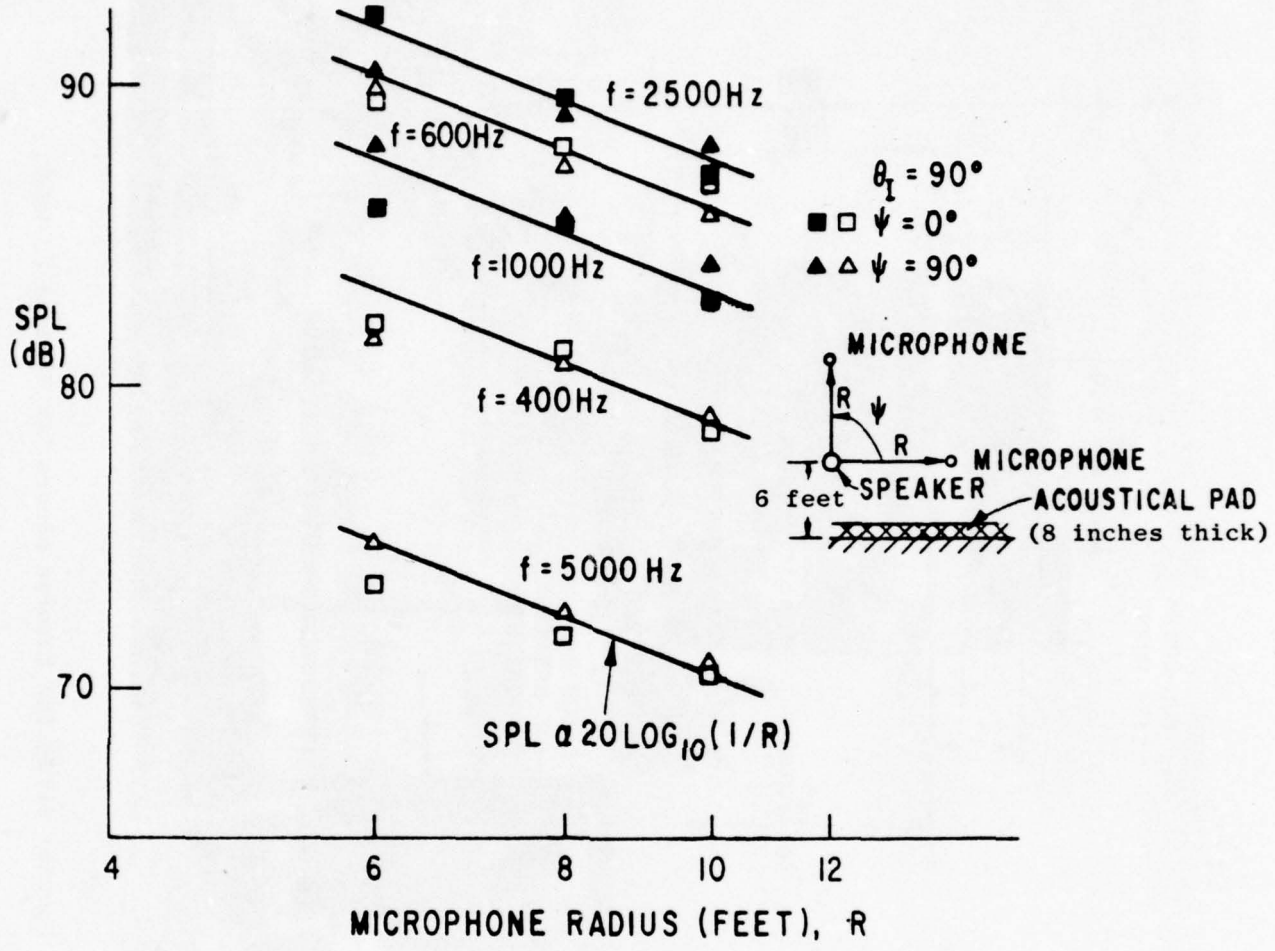


Figure 5-83. Spherical Divergence Tests at GE/CR&DC (Loudspeaker Acoustic Source).

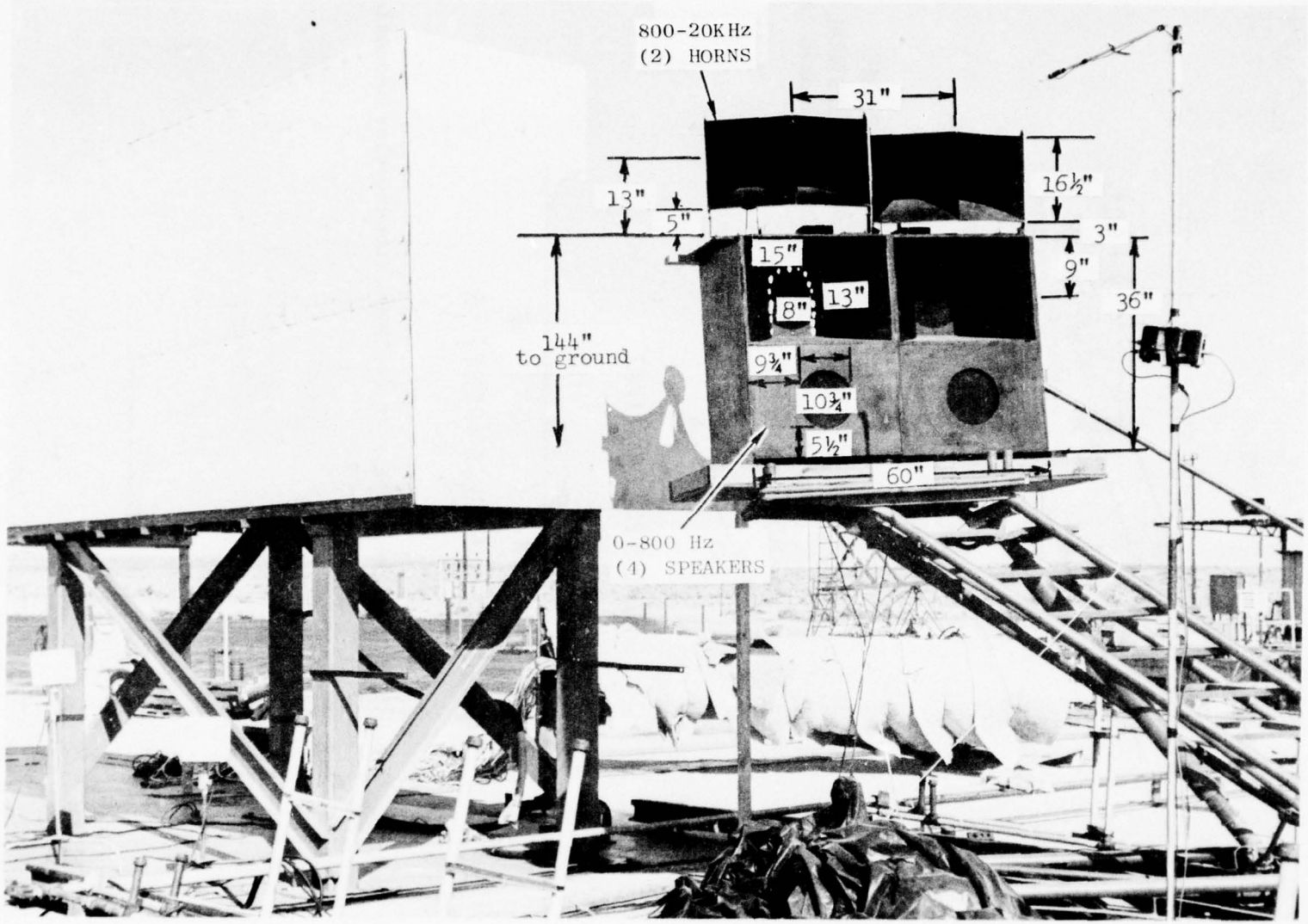


Figure 5-84. Speaker Setup for Inverse Square Law Test at GE/EFTC.

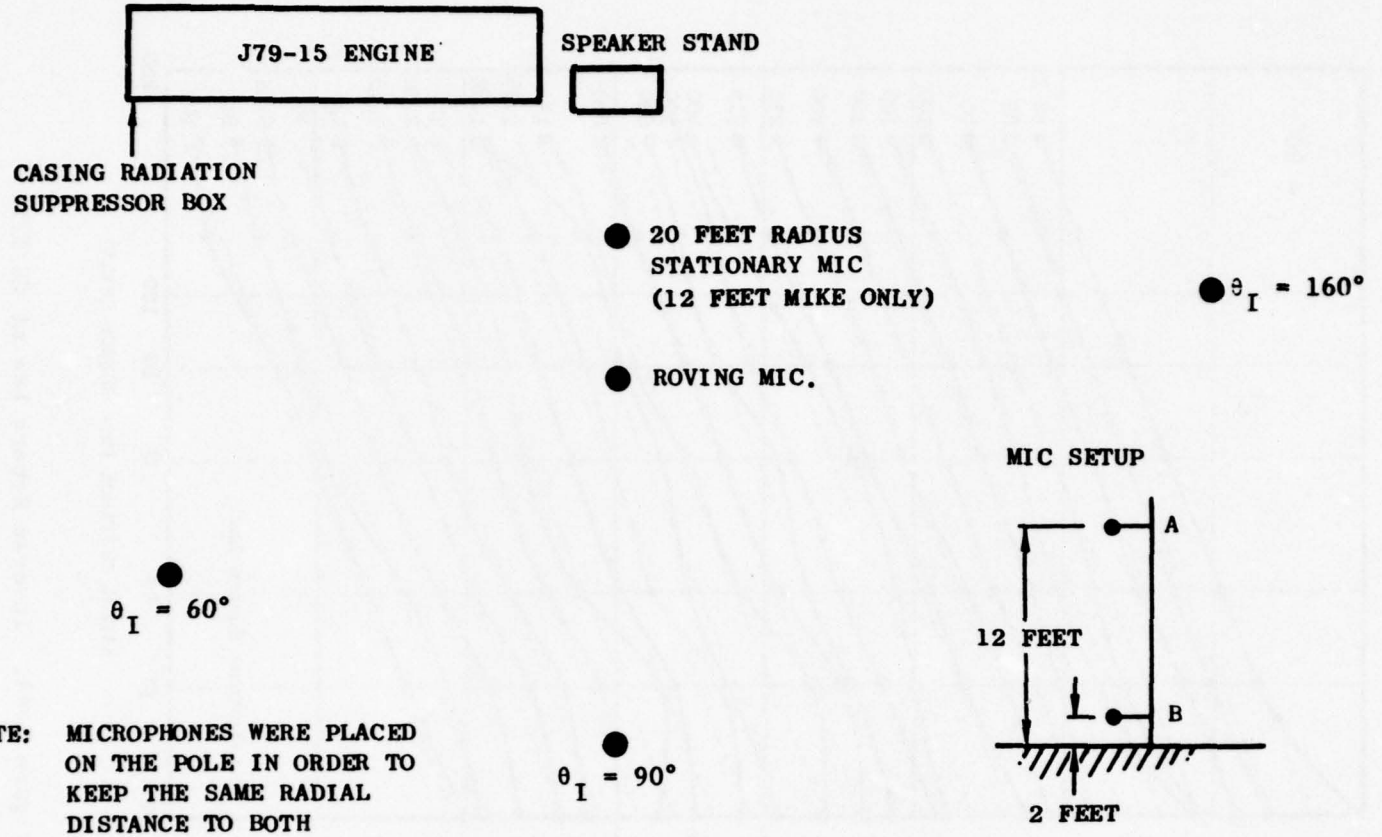


Figure 5-85. Microphone Setup for Speaker Test at GE/EFTC.

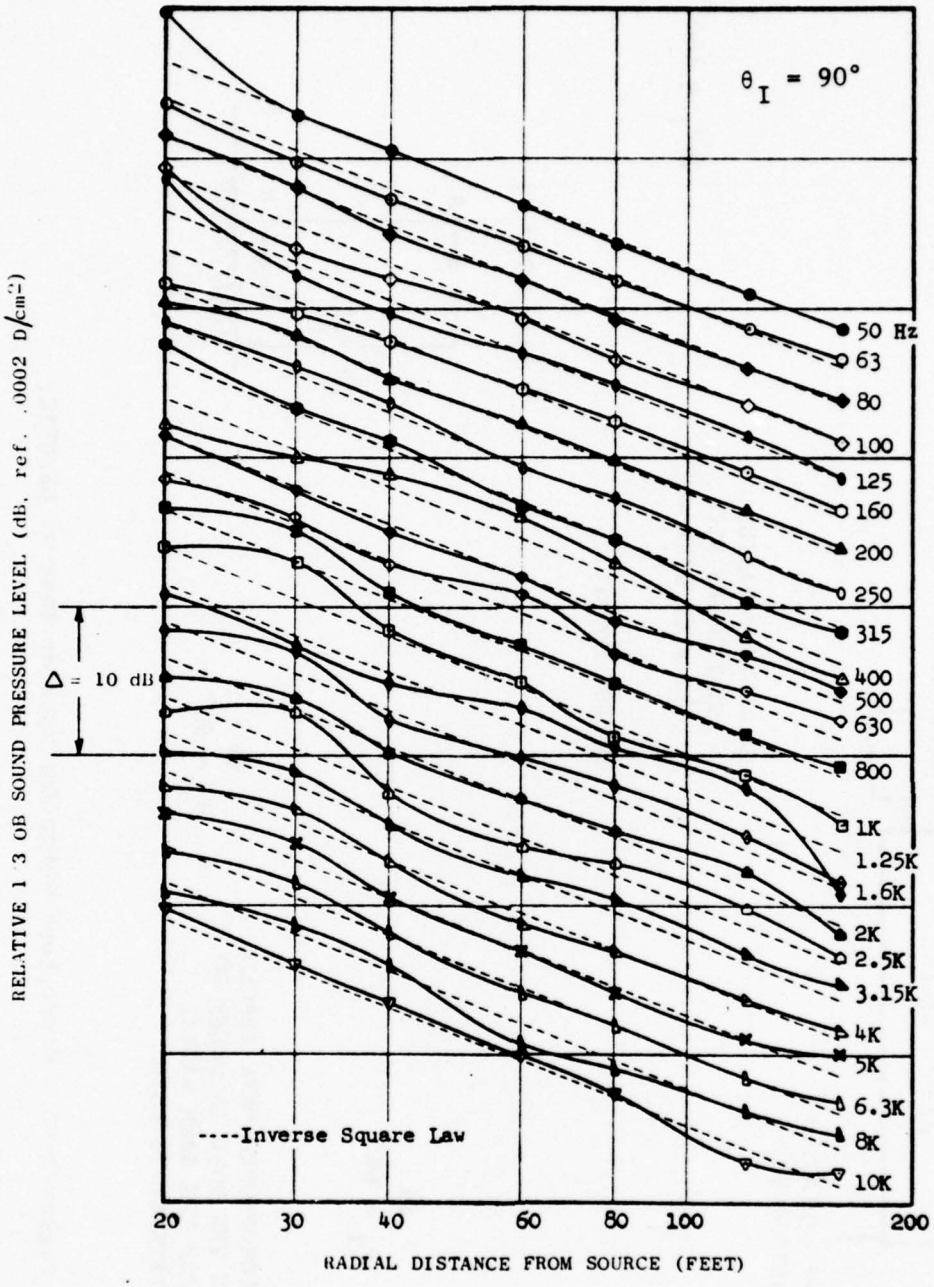


Figure 5-86. Inverse Square Law at GE/EFTC.

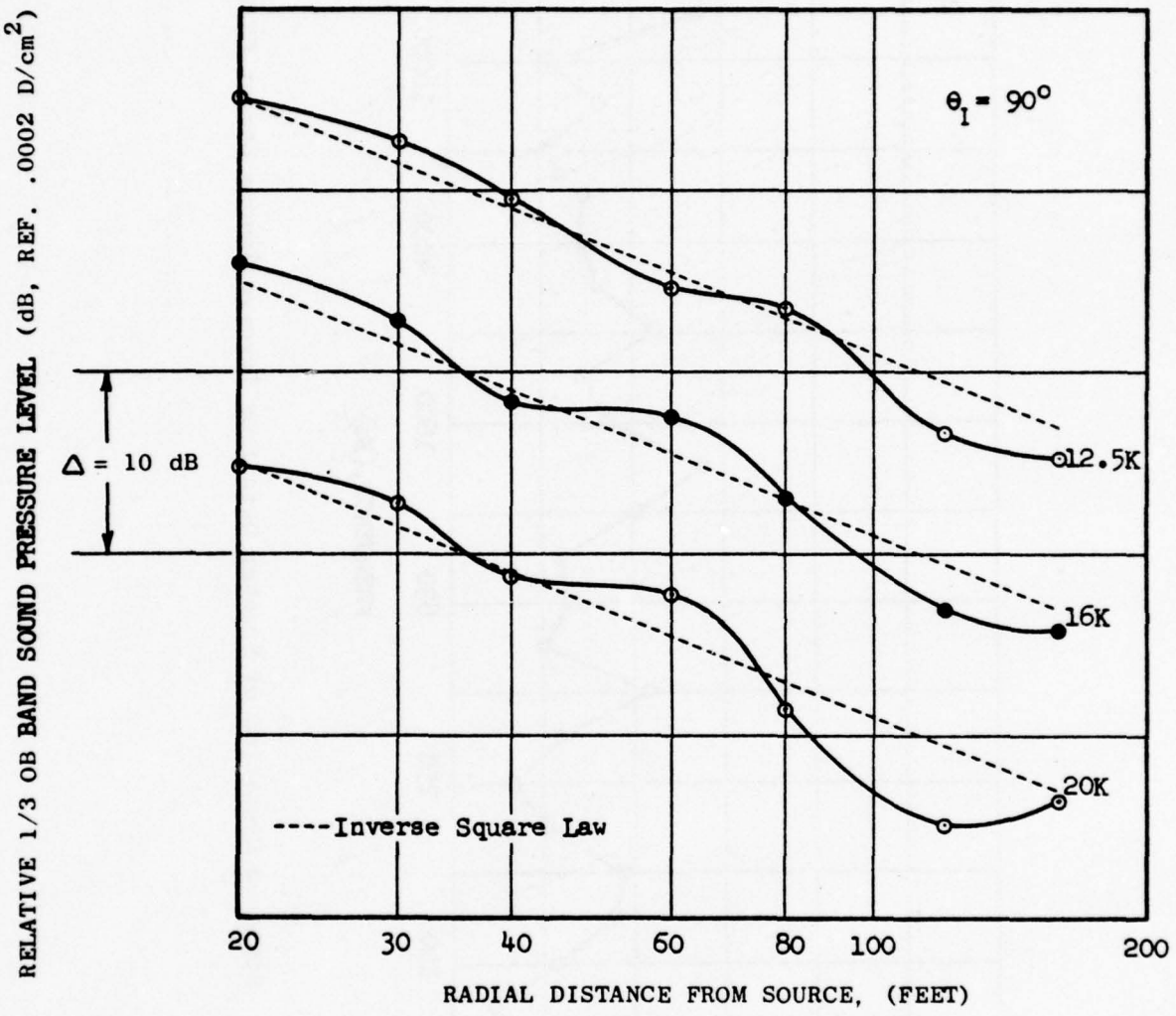


Figure 5-87. High Frequency Speaker Results at GE/EFTC.

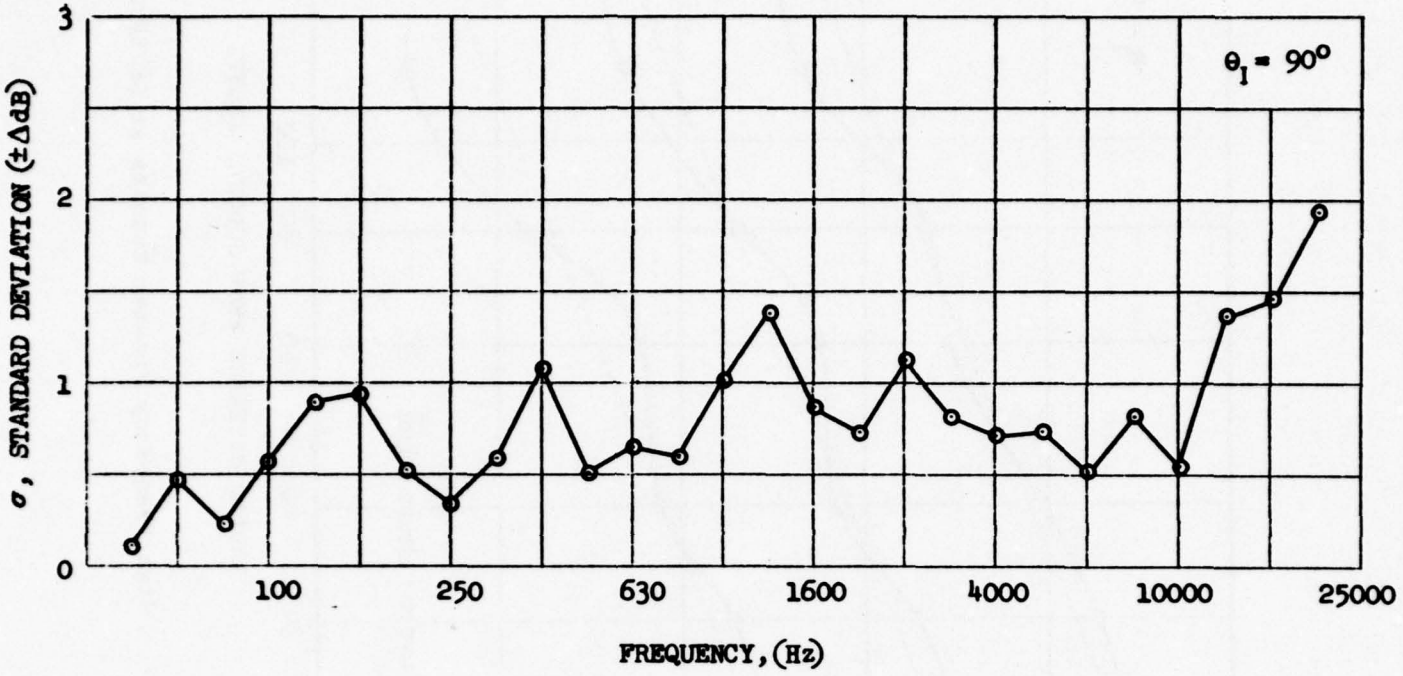


Figure 5-88. Standard Deviation of Speaker Data from Inverse Square Law at GE/EFTC.

speaker "hole" was present in the basic speaker spectra. This is the probable cause of the high variance at 4000 Hz. As noted earlier, the system changed from the speakers to the horn at 1000 Hz, therefore, the limited frequency range of the horn is the probable cause of the higher error at 1000 Hz. With these exceptions the data follows the inverse square law.

5.18 SUMMARY

A thorough study of the acoustic arena characteristics at the test facilities was conducted. At USC and UBC, the anechoic environment provided a free-field environment accurate to within ± 1 dB. Recirculation in the corners of the USC chamber cause deviations at some angles.

At JENOTS, elevating the microphone, changing the stand, determining the ground impedance, scattering phenomenon, and distributed source effects gave free-field variation to within ± 1 dB.

At CR&DC, the placing of 8 inches of foam over the pad while testing reduces the ground effects to less than 1 dB in the frequency range of interest; inverse square law is achieved to within ±1 dB.

At Edwards Flight Test Center, the J79 arena utilized the best portions of the spectra from two microphones each at different heights above the ground. Utilizing the measured ground impedance and distributed source effects inverse square law is achieved within ± 1 dB. A reflection occurs in the 150° and 160° spectra from an unknown source with the casing radiation suppressor box being suspect.

6.0 CERTIFICATION OF THE FACILITIES

As a final test of the cleanliness and free-field environment of the test facilities, recorded and processed acoustic data from round conical nozzles were compared to "classical referee" data at similar aero conditions. This "classical" data consisted of previously published data which made the same claims to cleanliness and free-field properties. The comparisons are made in terms of the semiempirical scaling laws which have been proposed by Hoch, et al. (Reference 23), that include the jet temperature effects. In particular, all data are compared with respect to:

- Lighthills's Parameter: OAPWL versus $\rho_o V_j^8 A_j / a_o^5$
- SNECMA/NGTE Power* relation: OAPWL $-10 \log_{10}(A_j[\rho_j/\rho_{isa}]^{\omega})$ versus $\log_{10} V_j/a_o$
- Overall 90° level variation with velocity: $OASPL_{90°} - 10 \log_{10}([A_j/R^2][\rho_j/\rho_{isa}]^{\omega})$ versus $\log_{10} V_j/a_o$
- Acoustic Power Level* spectral variation: 1/3 octave PWL $- 10 \log_{10}(A_j[\rho_j/\rho_{isa}]^{\omega})$ versus $\log_{10} fD/V_j$
- 90° sound pressure level spectral variation: 1/3-octave $SPL_{90°} - 10 \log_{10}(A_j/R^2)[\rho_j/\rho_{isa}]^{\omega}$ versus $\log_{10} fD/V_j$

Whenever possible, the comparisons are made at points representing the aerodynamic boundaries or operating limits of the facilities. The maximum variations of the data are expected at these points.

6.1 "REFEREE" DATA PRESENTATION

A detailed search of the literature revealed that there was very little available data that satisfied both the cleanliness and free-field requirements of this program.

Only six sets of external data were found suitable:

- University of South Hampton [Lush, Reference 36]
- NGTE [Ahuja and Bushell, Reference 37]

*Reference Area used to calculate PWL is implied in the normalization factor.

- NASA Lewis (Olsen, Gutierrez and Dorsch, Reference 41)
- SNECMA (Hoch and Duponchell, Reference 23)
- NGTE (Cocking and Bryce, References 23 and 39)
- Lockheed* (Tanna, et al., Reference 40)

The first three data sets were run with a cold jet while the last three were with heated jets (up to 1700° R). Figure 6-1 shows the aerodynamic points (in terms of V_j and T_T) at which acoustic data were available.

In addition to the above data, the September 1974 edition of the SAE A21 Committee proposed AIR 876 "Jet Exhaust Noise Prediction" (Reference 41) was used as representing a bench mark for data comparison.

Figure 6-2 shows the referee data in terms of Lighthill's parameter with various values of the K parameter.

As postulated by Lighthill, the subsonic round jet in an atmosphere at rest has an acoustic power output of:

$$W = K\rho_o V_j^8 D_j^2 / a_o^5 \qquad (105)$$

Quoting Lighthill (Reference 42), "K is very closely constant in any given series of experiments, being about 0.3×10^{-4} for jets emerging from a nozzle with low turbulence level, 0.6×10^{-4} for jets emerging from straight pipes, and as large as 10^{-4} for jets with a very high level of initial turbulence."

Most of the referee data in Figure 6-2 lies between these limits. A mean value appears to be about $K = 0.5 \times 10^{-4}$.

In jets whose core density differs substantially from that of the ambient (surrounding) air, the acoustic power output becomes dependent on the ratio ρ_j/ρ_{isa}. An empirical correction, in form $-10 \log (\rho_j/\rho_{isa})^{\omega}$ is found to account for this effect quite reliably. The exponent ω, generally ascribed to Hoch (Reference 23), has a complex dependence on velocity as shown by Figure 6-3 (taken from Reference 41). For high speed subsonic jets, it takes values between zero and 1, indicating that for cases where $\rho_j/\rho_{isa} < 1$, heating of the jet leads to reduction of jet noise. Figure 6-4 shows the magnitude of the empirical correction in terms of jet velocity and total temperature.

Figure 6-5 shows the data presented in terms of the SNECMA/NGTE parameter. The line through the data is that found in Reference 23. This curve is high at high velocity, because the line was a fit to supercritical convergent nozzles

---

*The Author is indebted to Dr. Bob Tanna, Mr. Harry Plumblee and the Lockheed Corporation for advanced copies of their data.

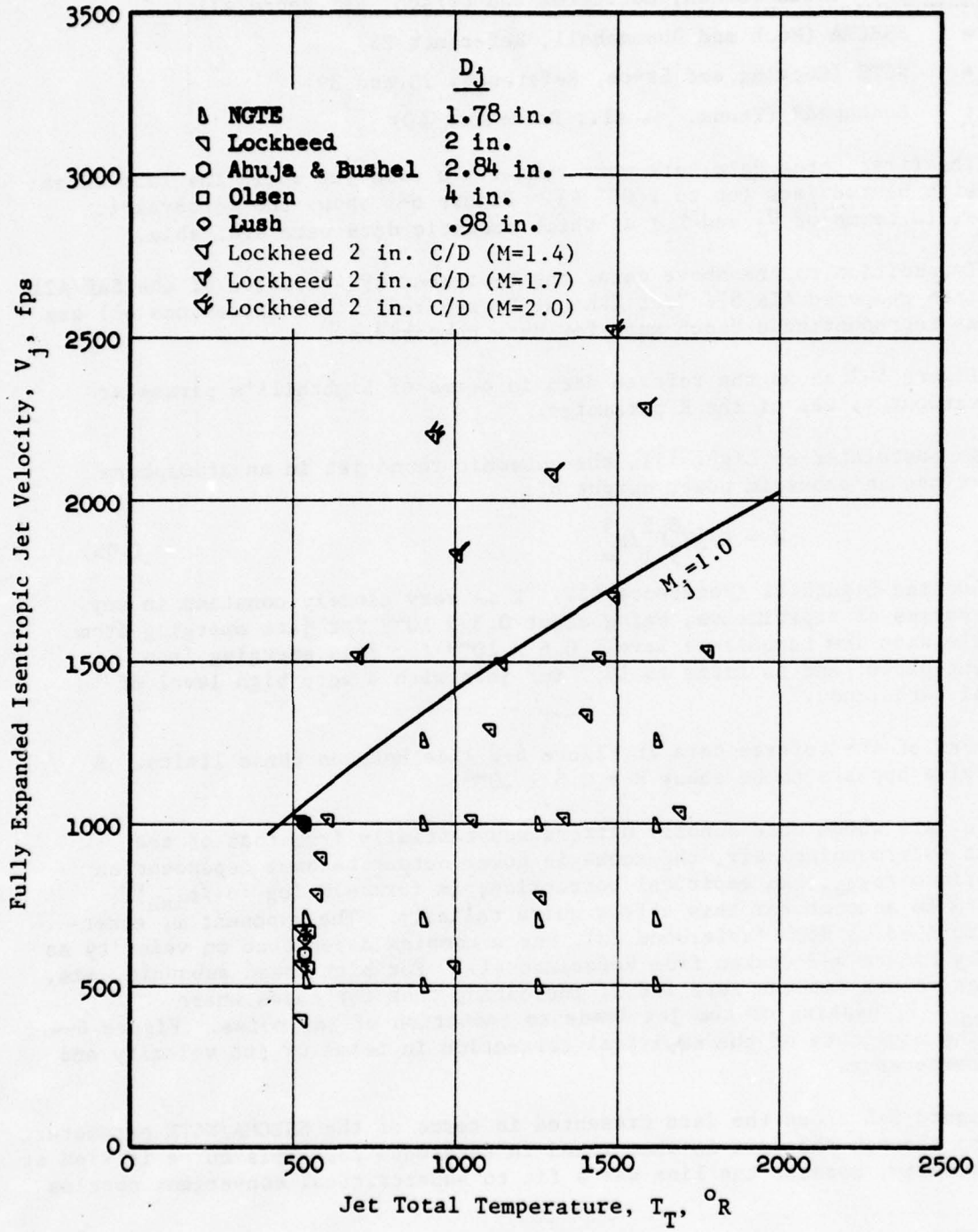


Figure 6-1. Aerodynamic Test Domain for Referee Data.

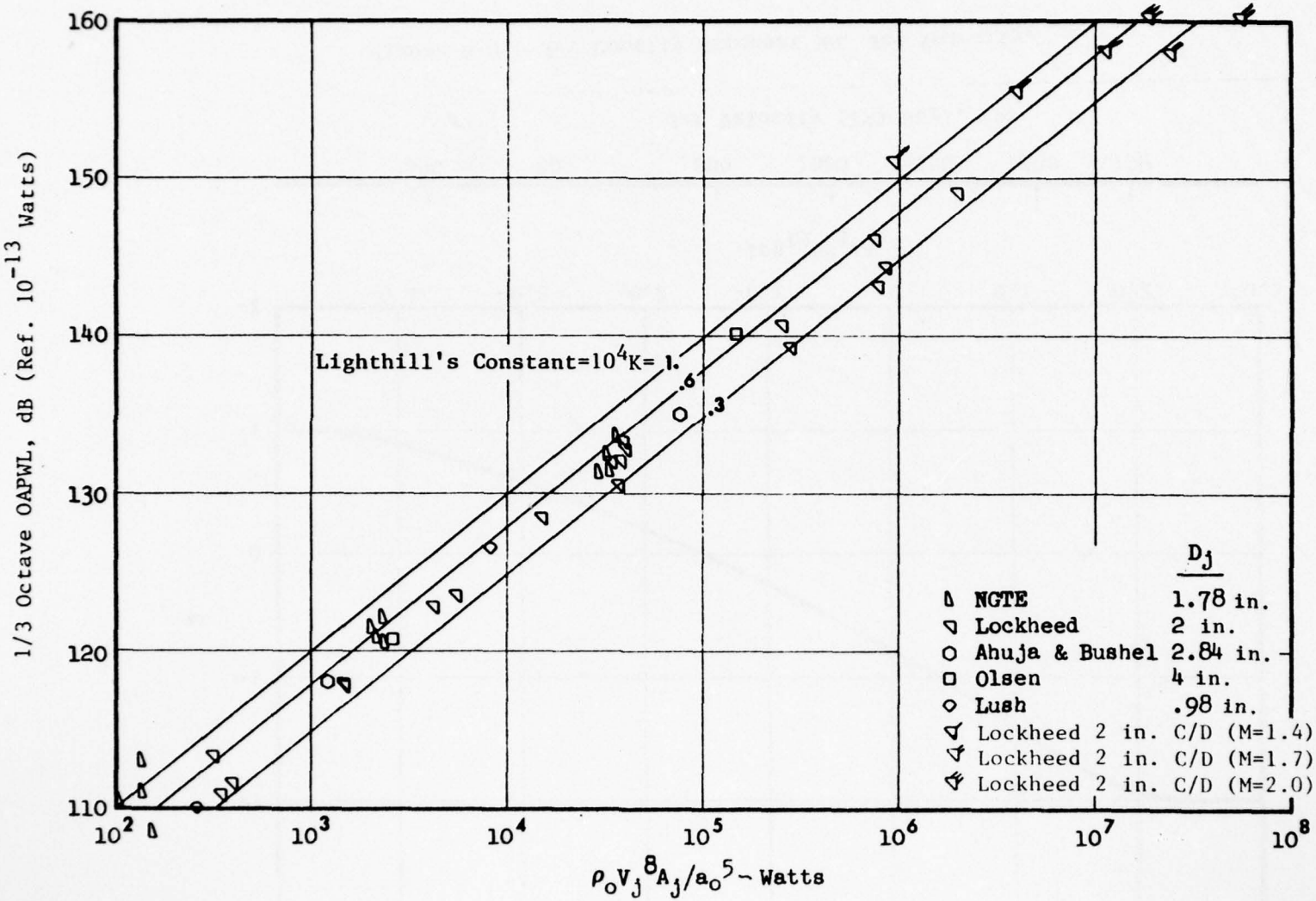


Figure 6-2. Variation of Overall Power with Lighthill's Parameter for Referee Data.

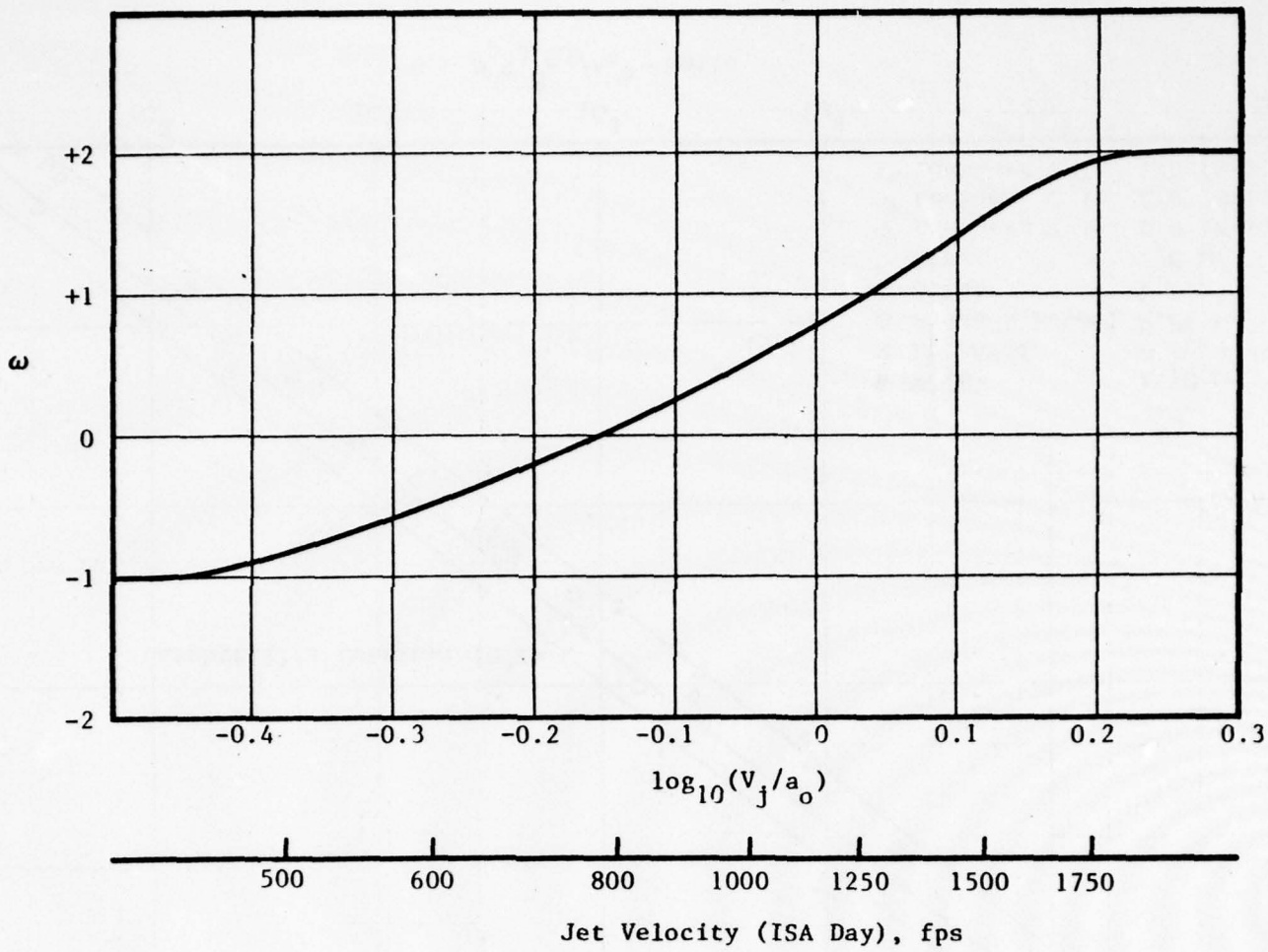


Figure 6-3. Jet Density Exponent Vs. Jet Velocity.

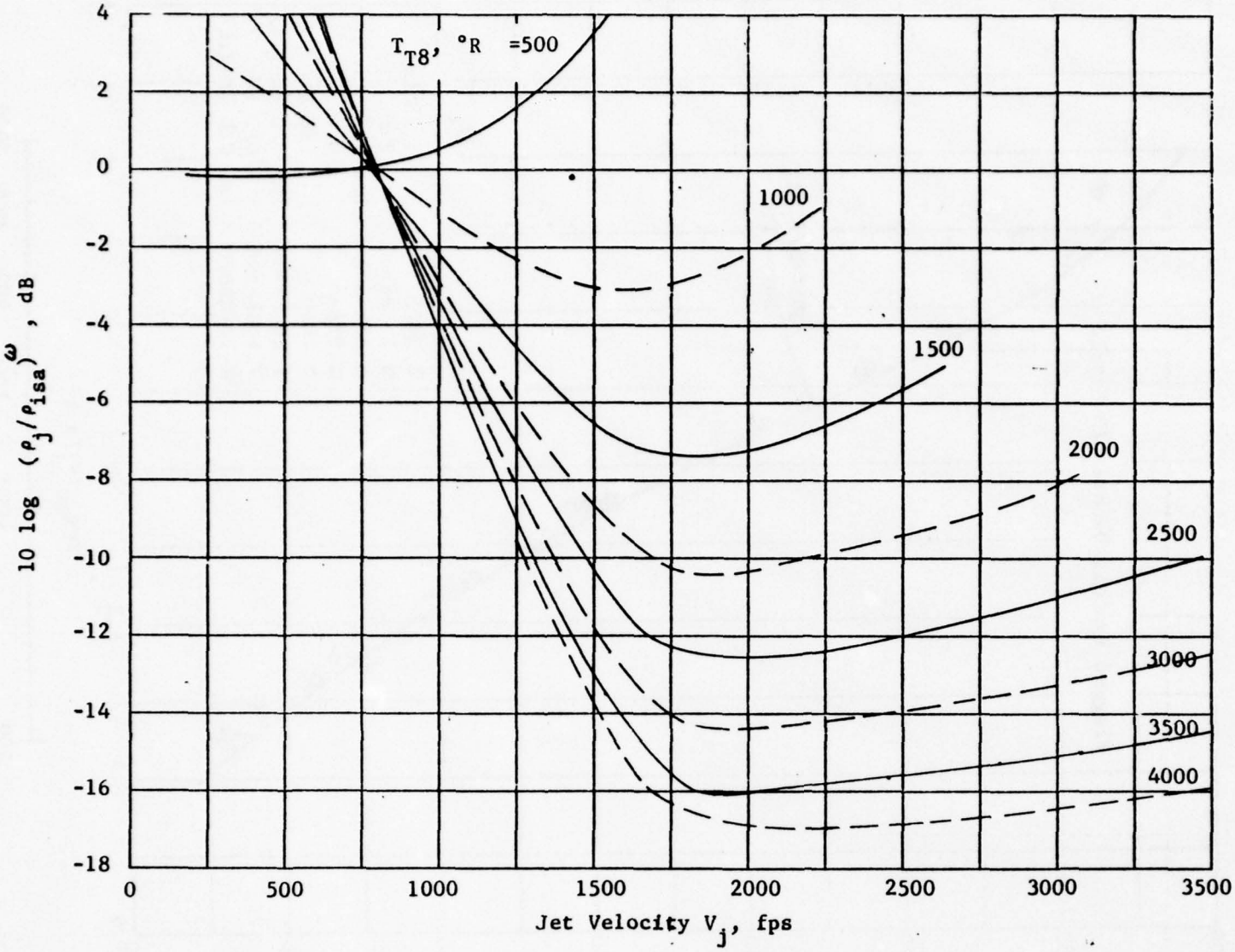


Figure 6-4. Variation of Density Correction Factor with Jet Velocity and Temperature.

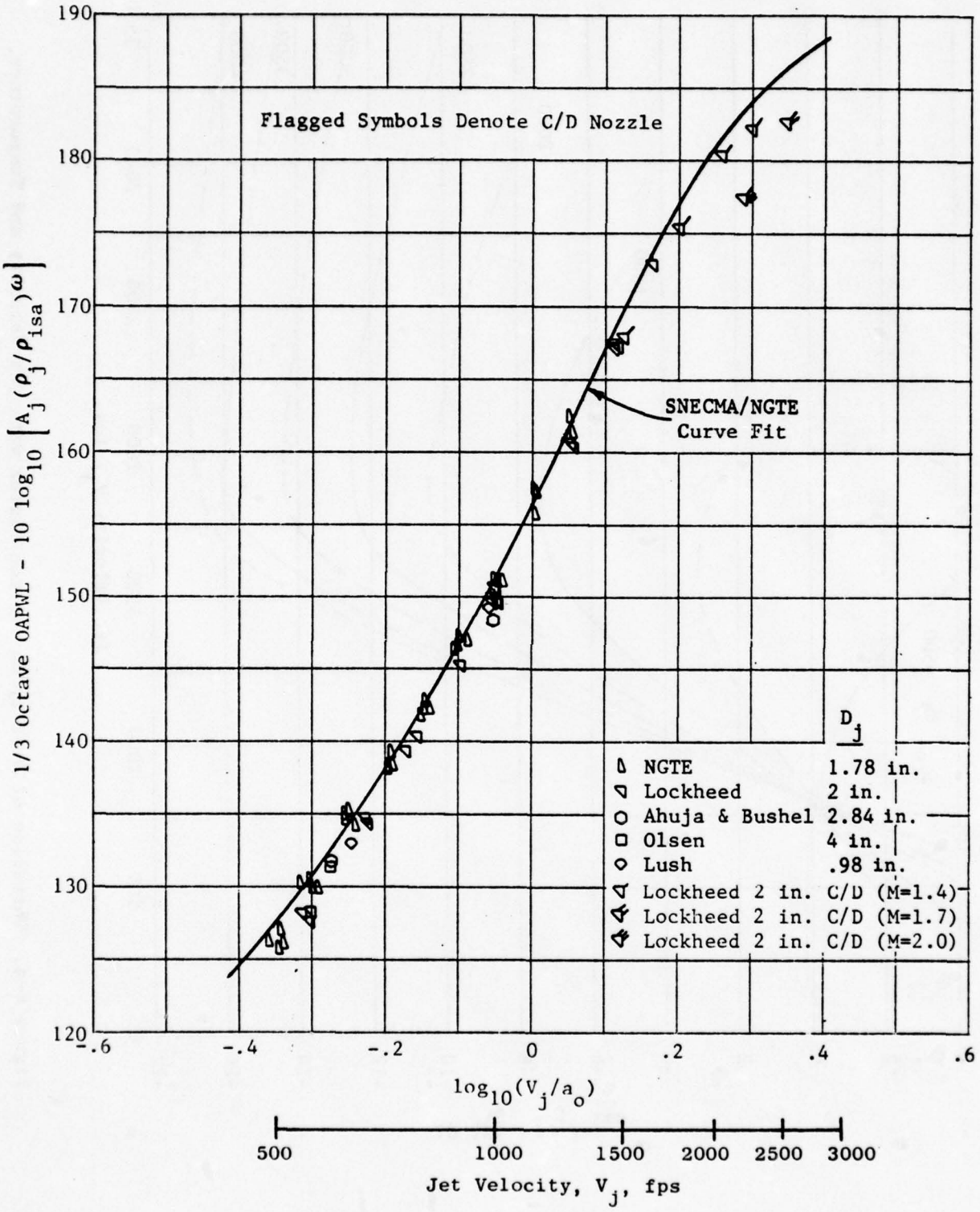


Figure 6-5. Variation of Normalized Overall Power with Jet Velocity for the Referee Data.

with shocks in Reference 23, whereas the Lockheed data are for shock-free C/D nozzles.

Figure 6-6 shows the normalized 90° OASPL variation with velocity. The solid line through the data represents the 1974 SAE A21 Committee curve. The dashed line is a curve fit of numerous data derived by Stone of NASA Lewis (Reference 43). Generally, the SAE curve (Reference 44) underpredicts the data, whereas, Stone's line appears somewhat high at low velocities.

Figures 6-7 and 6-8 show the normalized power spectra shape from the referee facilities. Figure 6-7 shows cold subsonic points. Most of the data disagreement occurs at high frequency, which is probably related to differences in the air attenuation models. In particular, Lockheed uses the Evans (References 20 and 21) technique, whereas the other facilities have been corrected using the SAE ARP 866 (Reference 16) method. A comparison of the two methods was presented in Figure 4-7. The data of Ahuja and Bushell appear to have a spectral abnormality at high frequency, which most likely is related to the facility. Comparison of the normalized PWL spectra from Lockheed and NGTE is presented in Figure 6-8 for subsonic heated jets (T_T = 1260° R). Here, remarkable agreement between the two facilities is found regardless of the fact that different air attenuation models have been used.

Figures 6-9 and 6-10 show the 90° microphone normalized sound pressure spectra for subsonic cold and heated jets, respectively. Figure 6-11 presents the data in terms of the delta level, SPL-OASPL, which is typically used in SAE prediction methods. Also shown is the suggested spectral line from Reference 41. In this form, the data of Lush (Reference 36) are seen to peak at a Strouhal number lower than the other facilities. The distortion of Ahuja and Bushell's data is obvious at high frequency.

All of the data presented in this report have been corrected for air attenuation effects using the SAE ARP 866 (Reference 16) method with a "GE" modification to extend the predictions to 80 kHz as discussed in Section 4.3 and the Appendix. (The Lockheed referee PWL spectra were corrected using the Bass, Bauer, and Evans method of References 20 and 21.) The PWL spectra are corrected by removing all the air attenuation from the data while the presented SPL data at a fixed angle has been corrected for the attenuation experienced for the measured day to a value which would be obtained on a standard day of 59° F and 70% relative humidity over the specified measurement distance.

The normalized sound pressure spectra or the delta level, SPL-OASPL, spectra used for jet noise predictions are more appropriately presented with all air attenuation removed (i.e. "lossless data") rather than with the measurement distance of standard day air attenuation. This "lossless" correction was not attempted in this study because of the unanswered questions on the proper air attenuation model to be used as discussed in Section 4.3. In fact it does not appear that SAE ARP 866 prediction lines were developed from lossless data.

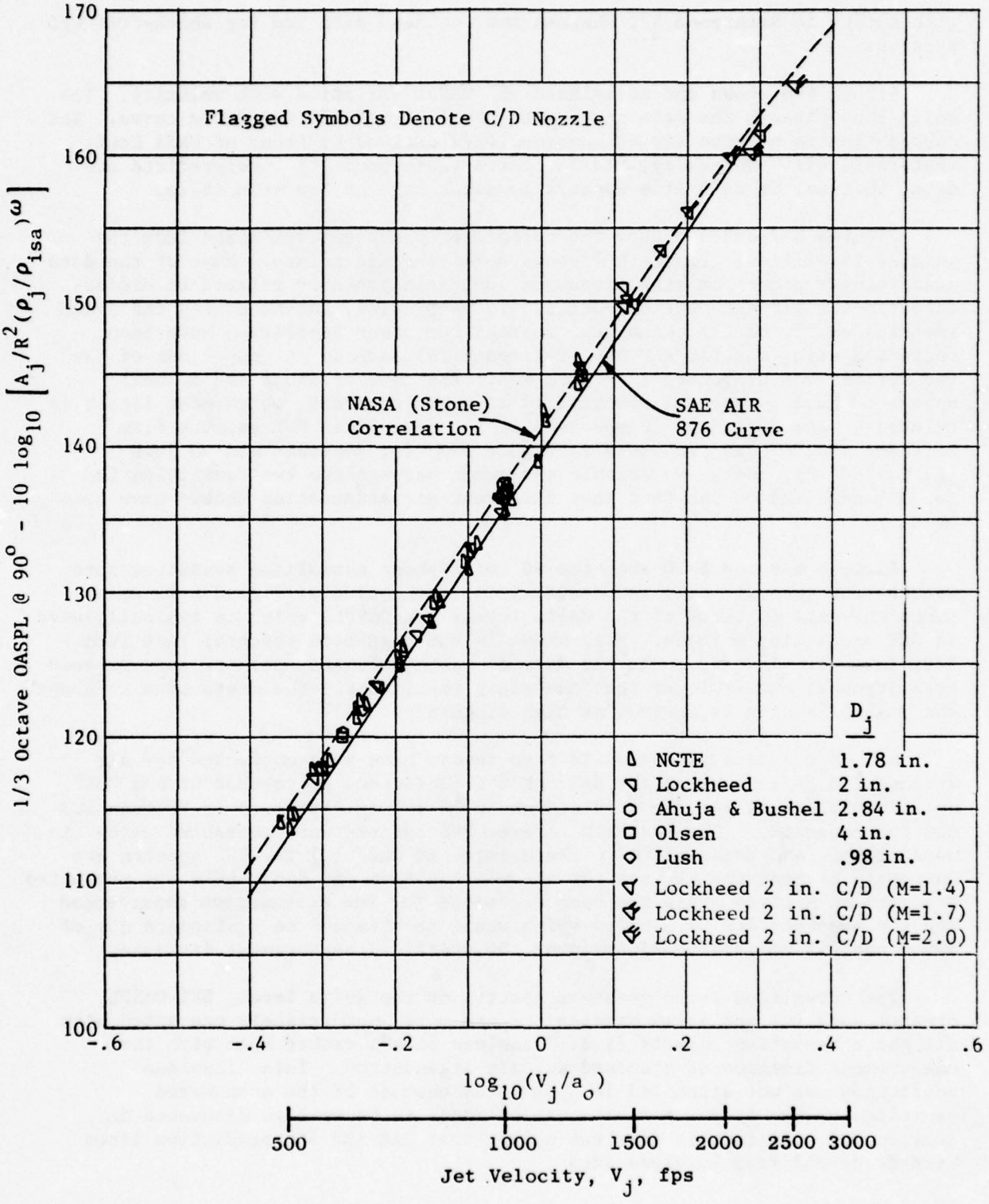


Figure 6-6. Velocity Dependence of Normalized Overall Sound Pressure Level at 90° for the Referee Data.

D_j~in	T_T~^oR	V_j~fps		D_j~in	T_T~^oR	V_j~fps	
◇ 4	amb	600	Olsen	◁ 2	528	562	Lockheed
□ 4	"	994	"	▷ 2	528	674	"
○ 2.84	"	600	Ahuja	△ 2	528	1013	"
○ 2.84	"	1000	"	▷ 2	545	565	"
◇ 0.98	"	640	Lush	△ 2	557	678	"
◇ 0.98	"	984	"	◁ 2	605	1017	"
△ 1.78	"	514	NGTE				
▽ 1.78	"	722	"				
△ 1.78	"	1014	"				

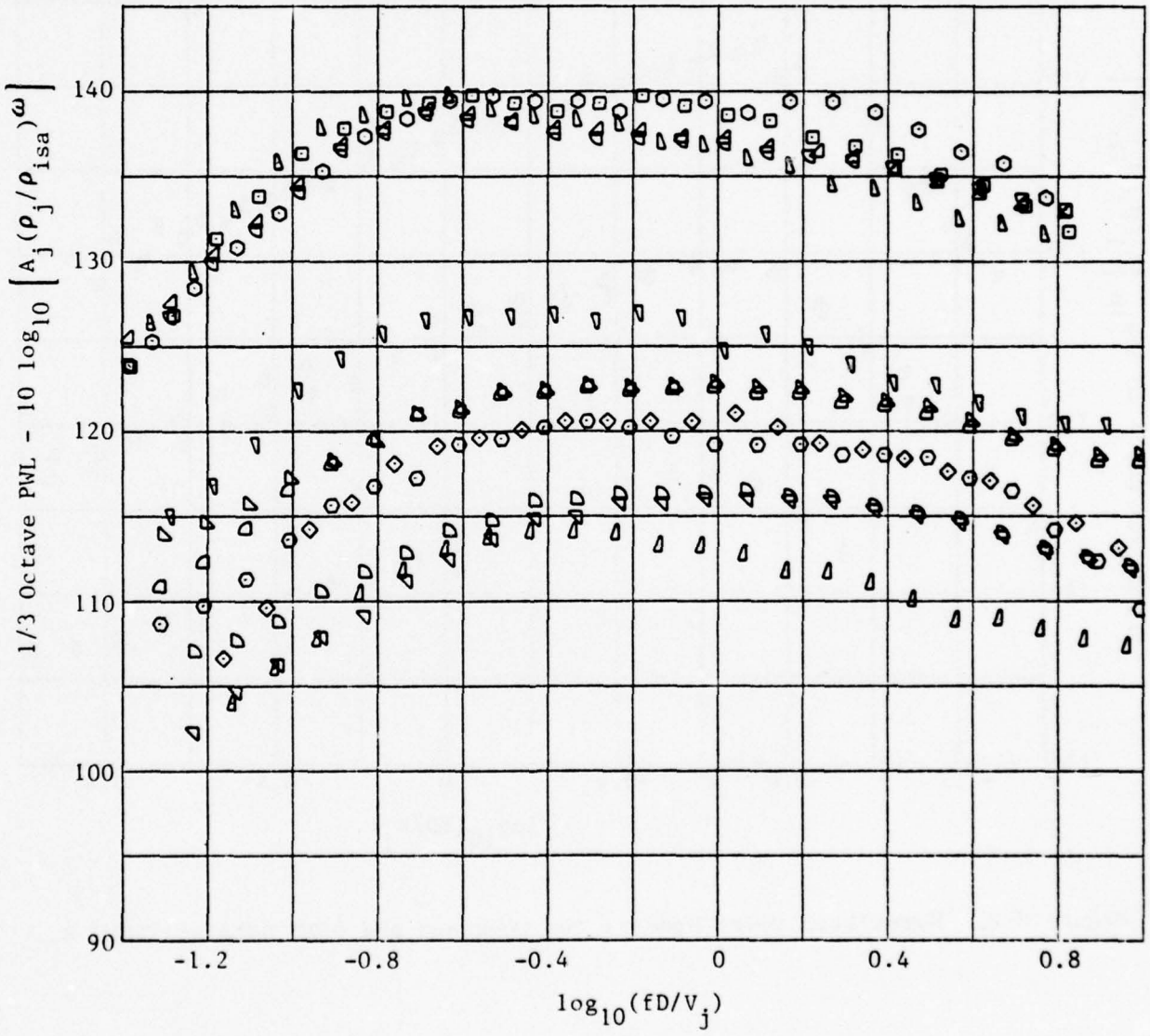


Figure 6-7. Normalized Power Spectra for the Cold Jet Referee Data.

	D_j~in	T_T~^oR	V_j~fps	
▽	2	1342	1024	Lockheed
▽	2	1258	781	"
△	1.78	1260	505	NGTE
▽	1.78	1260	719	"
△	1.78	1260	1005	"

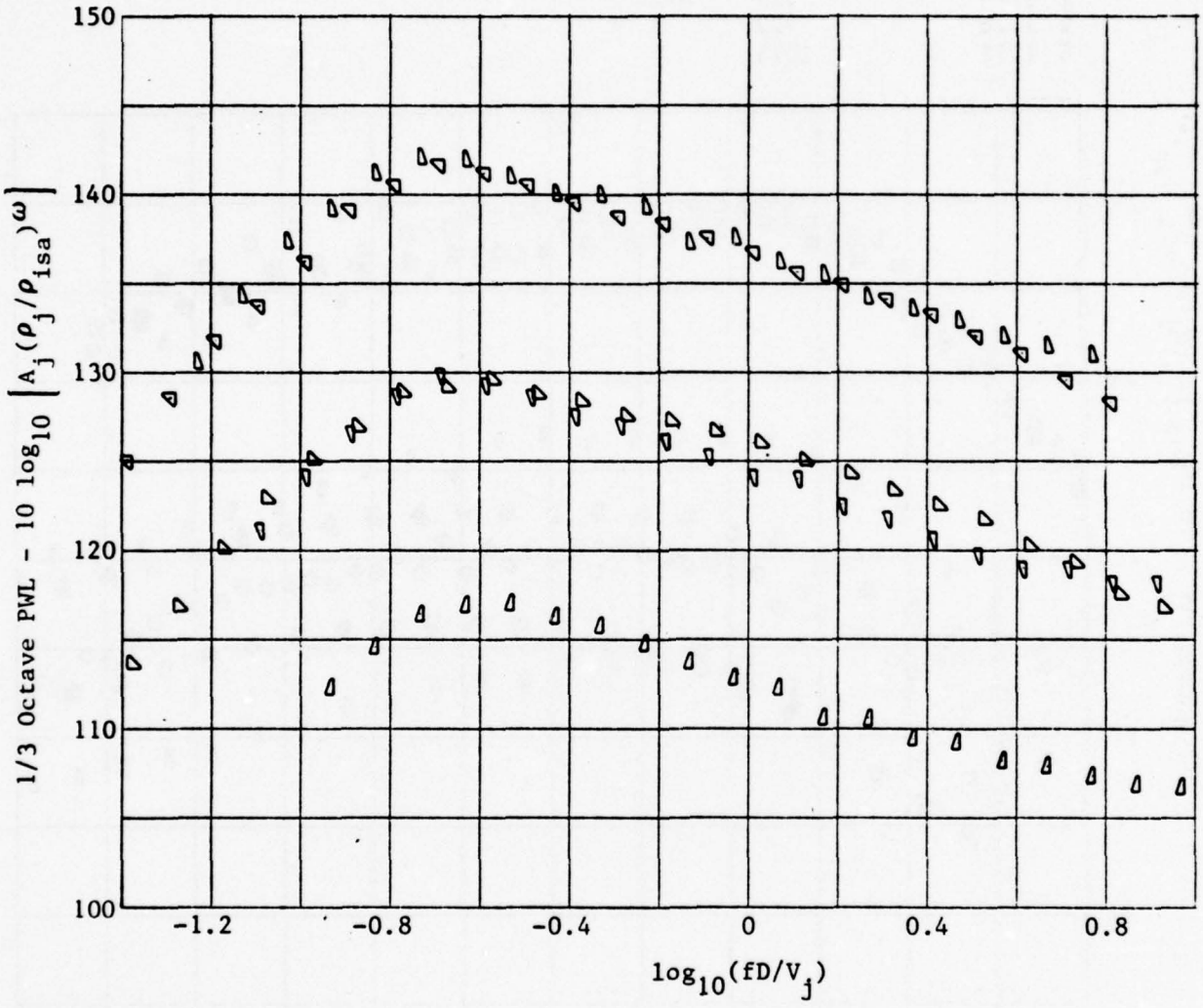


Figure 6-8. Normalized Power Spectra for Lockheed and NGTE Data at 1260° R.

D_j-in	T_T-^oR	V_j-fps		D_j-in	T_T-^oR	V_j-fps	
◇ 4	amb	600	Olsen	◁ 2	528	562	Lockheed
□ 4	"	994	"	▷ 2	528	674	"
○ 2.84	"	600	Ahuja	△ 2	528	1013	"
○ 2.84	"	1000	"	▷ 2	545	565	"
◇ 0.98	"	640	Lush	△ 2	557	678	"
◇ 0.98	"	984	"	▽ 2	605	1017	"
△ 1.78	"	514	NGTE				
▽ 1.78	"	722	"				
△ 1.78	"	1014	"				

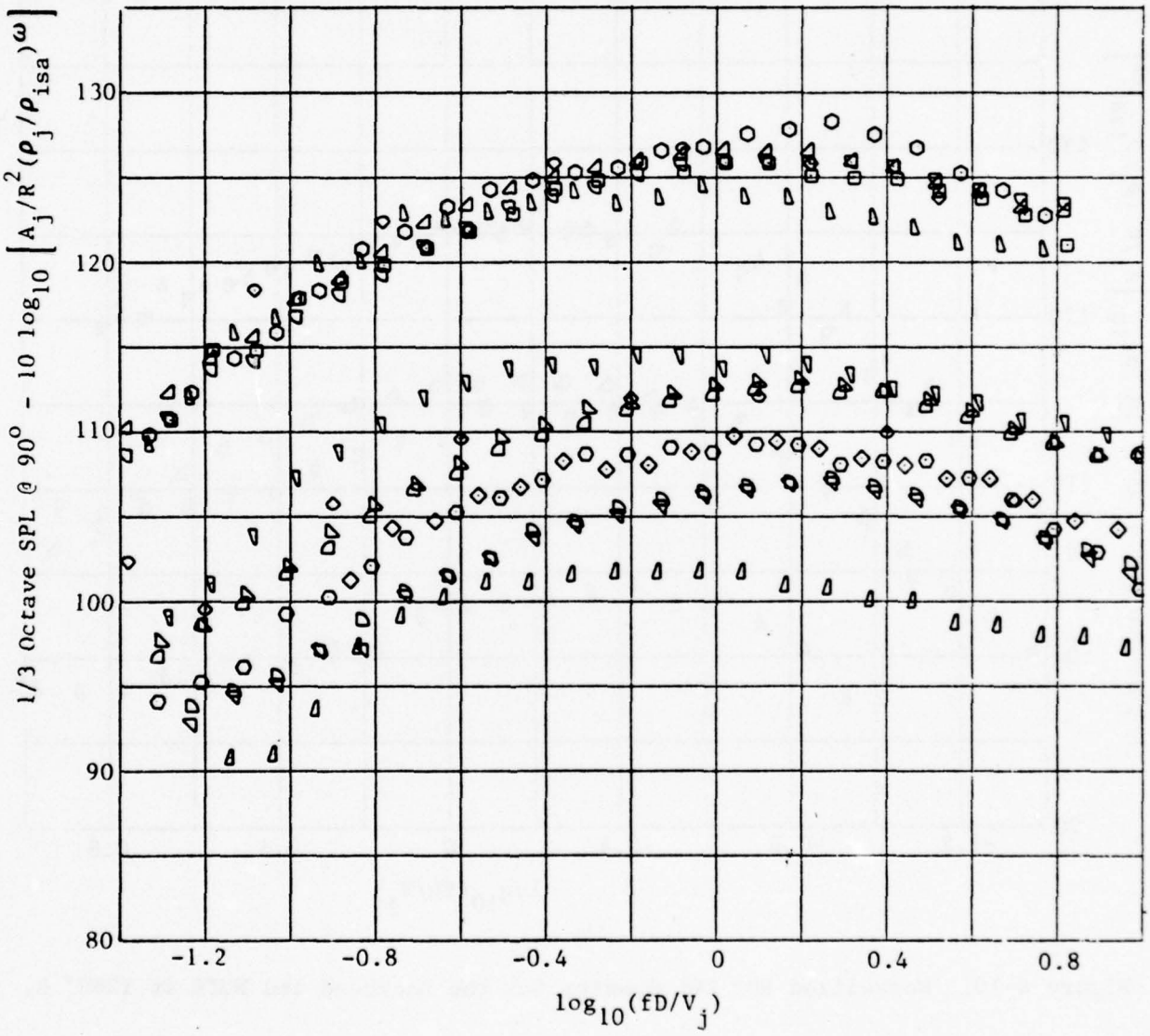


Figure 6-9. Normalized 90° SPL Spectra for the Cold Jet Referee Data.

	D_j-in	T_T-°R	V_j-fps	
◁	2	1342	1024	Lockheed
◁	2	1258	781	"
△	1.78	1260	505	NGTE
◁	1.78	1260	719	"
△	1.78	1260	1005	"

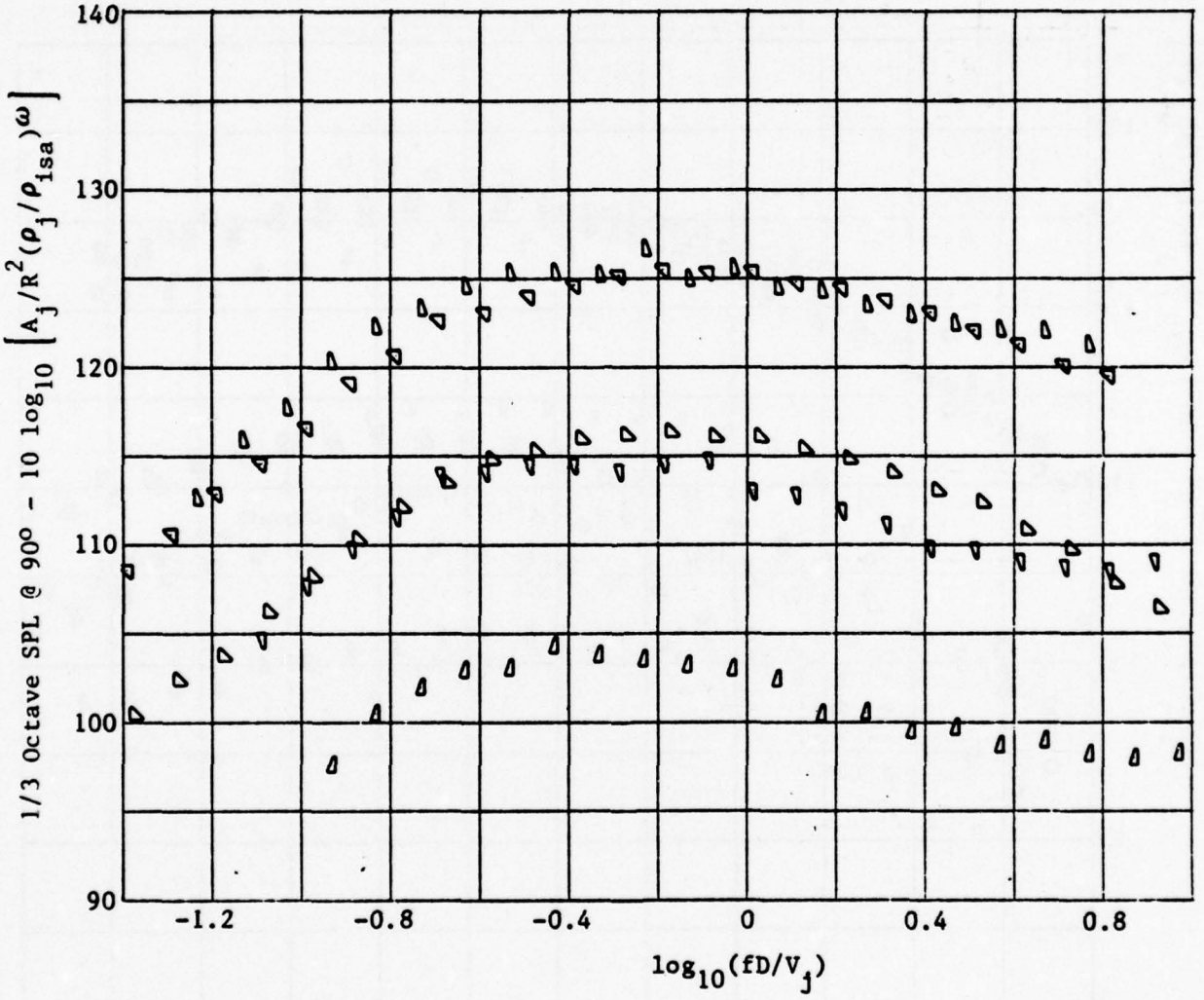
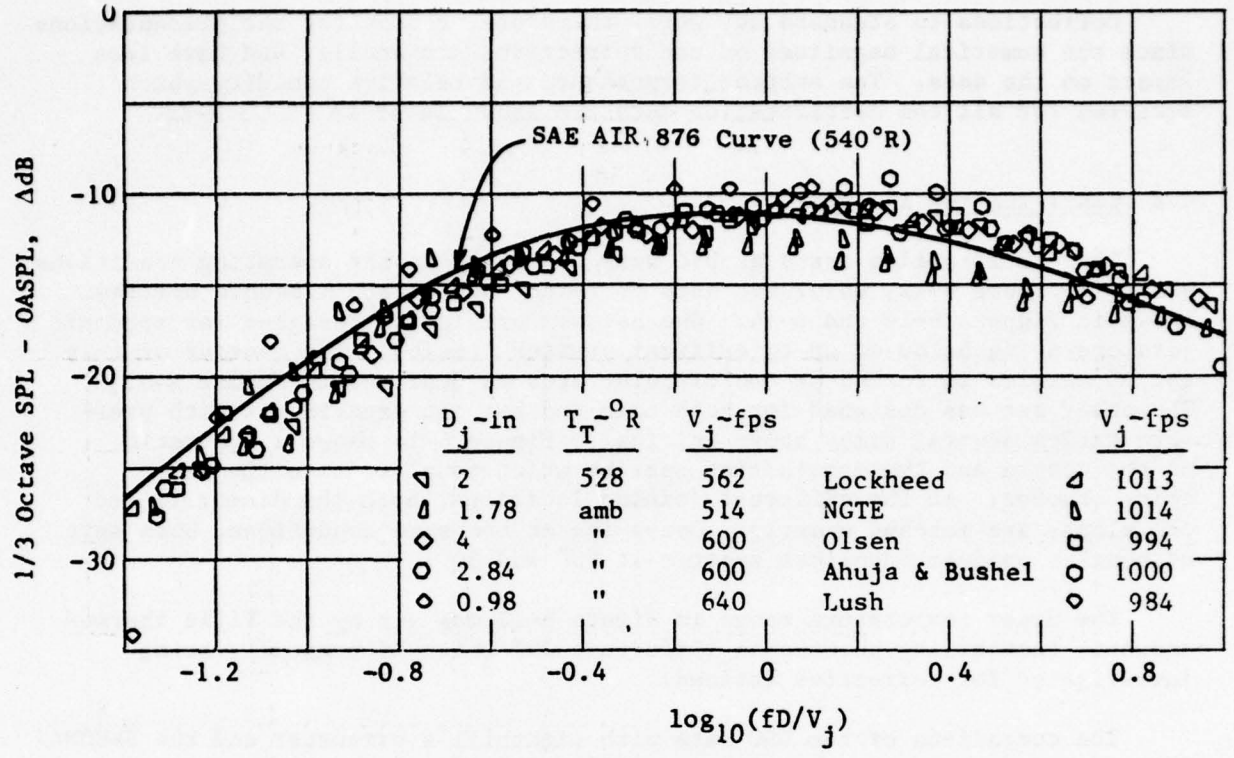


Figure 6-10. Normalized 90° SPL Spectra for the Lockheed and NGTE at 1260° R.



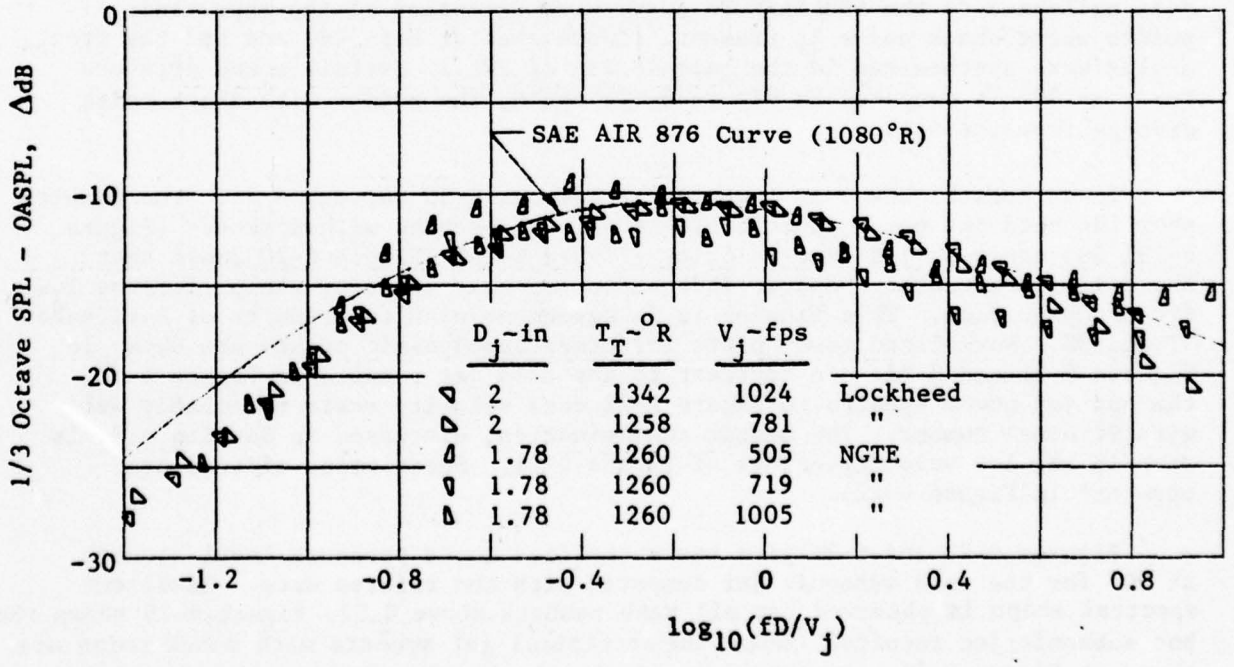


Figure 6-11. SPL Spectra at 90° for Cold and 1260° R Referee Data.

Corrections to standard day were, therefore, chosen for the presentations since the numerical magnitude of the corrections are smaller and have less impact on the data. The ambient temperature and relative humidity which occurred for all the certification data are shown later in Table A-II.

6.2 CERTIFICATION AT (USC)

The certification tests at USC were conducted at the operating conditions shown in Figure 6-12, using two sets of 1-inch and 2-inch subsonic nozzles, shown in Figures 6-13 and 6-14. One set was originally designed for subsonic jets operating below or up to critical pressure ratios. The contour of this set of nozzles is formed by two circular arcs as depicted in Figure 6-13. The other set was designed for both cold and hot jet experiments with pressure ratios several times above critical. Figure 6-14 shows a schematic of the nozzle and the contraction section which couples it to the settling chamber. At the different joining locations, both the diameters and the slopes are matched exactly. Operating at the same conditions, both sets of nozzles produce identical spectra at 90° and 30°.

The upper temperature range in Figure 6-12 was set by the Rijke thermoacoustic instability phenomenon (Reference 29) which is presently being investigated for corrective actions.

The comparison of the USC data with Lighthill's parameter and the SNECMA/NGTE techniques are shown in Figures 6-15 and 6-16. Generally, velocity to the eighth power is followed with some scatter. Both the hot and cold jet data collapses to the SNECMA/NGTE curve with exception of the supersonic points where shock noise is present. (Note that at both USC and UBC the front angles were synthesized in the calculation of PWL.) Overall sound pressure level at 90° is compared in Figure 6-17; again, the points with shock noise diverge from the fit.

Power spectra shape is compared in Figures 6-18 through 6-21. The results show the cold jet power spectra can be Strouhal-scaled with diameter (Figure 6-19) but not with jet exit velocity (Figure 6-20). Figure 6-20 shows that the cold jet spectral shape is independent of exit velocity except for the low frequency portion. This finding is in agreement with the results of References 37 and 38. Normalized power plots for other aerodynamic points are shown in Figures 6-21 and 6-22. In contrast to the cold jet results in Figure 6-20, the hot jet power spectra in Figure 6-21 does velocity scale reasonably well with Strouhal number. The heater contamination, discussed in Section 4.9, is seen in the low velocity points of Figure 6-21. Shock noise effects are apparent in Figure 6-22.

Figures 6-23 and 6-24 give the normalized sound pressure level spectra at 90° for the cold subsonic jet compared with the referee date. Excellent spectral shape is observed for all Mach numbers above 0.52. Figure 6-25 shows the hot subsonic jet results. Choked supercritical jet spectra with shock noise are given in Figure 6-26. A comparison of the shock noise spectra shape at the same jet Mach number but different temperatures in Figure 6-26 shows that it

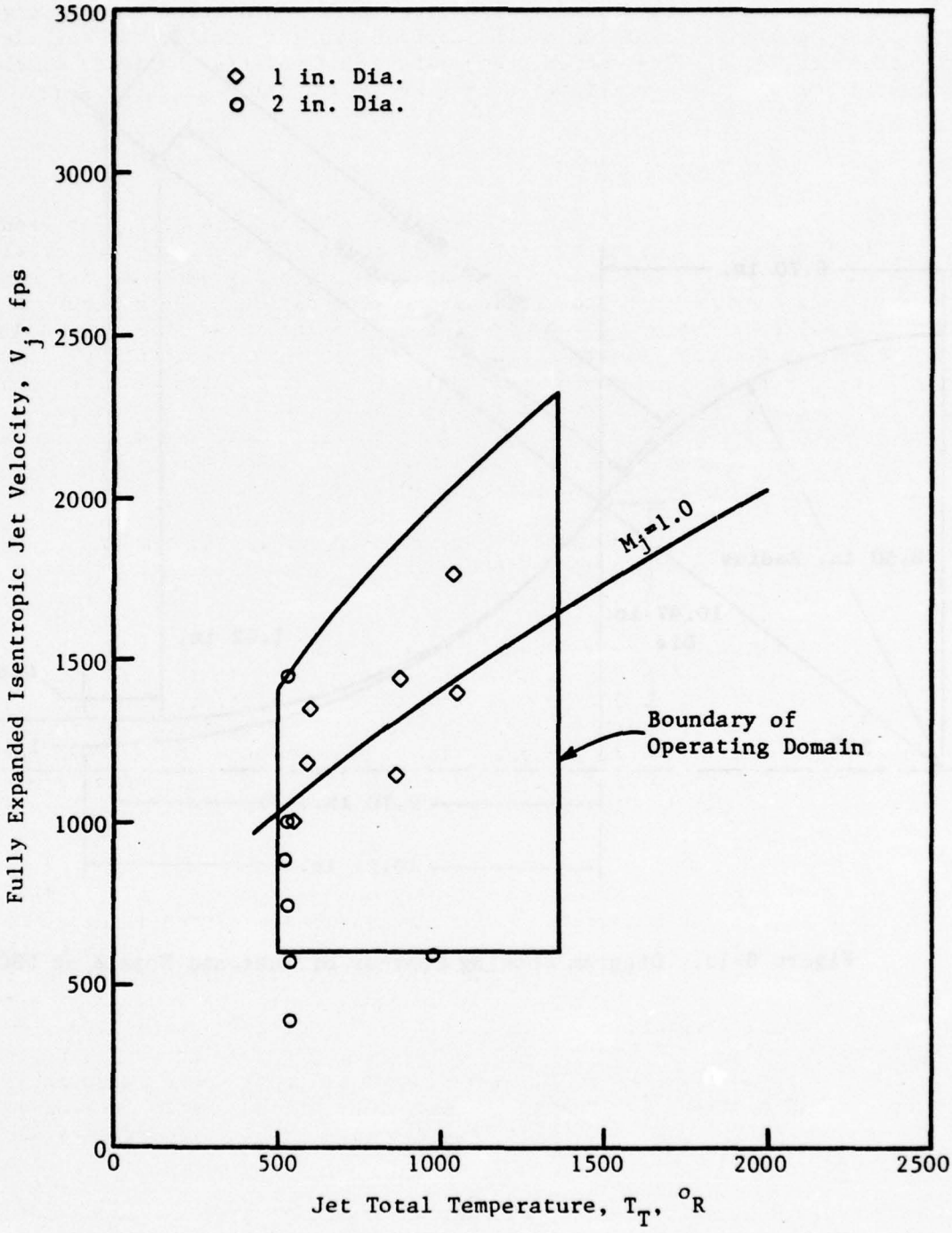


Figure 6-12. Domain of Operation of the USC Anechoic Chamber Jet.

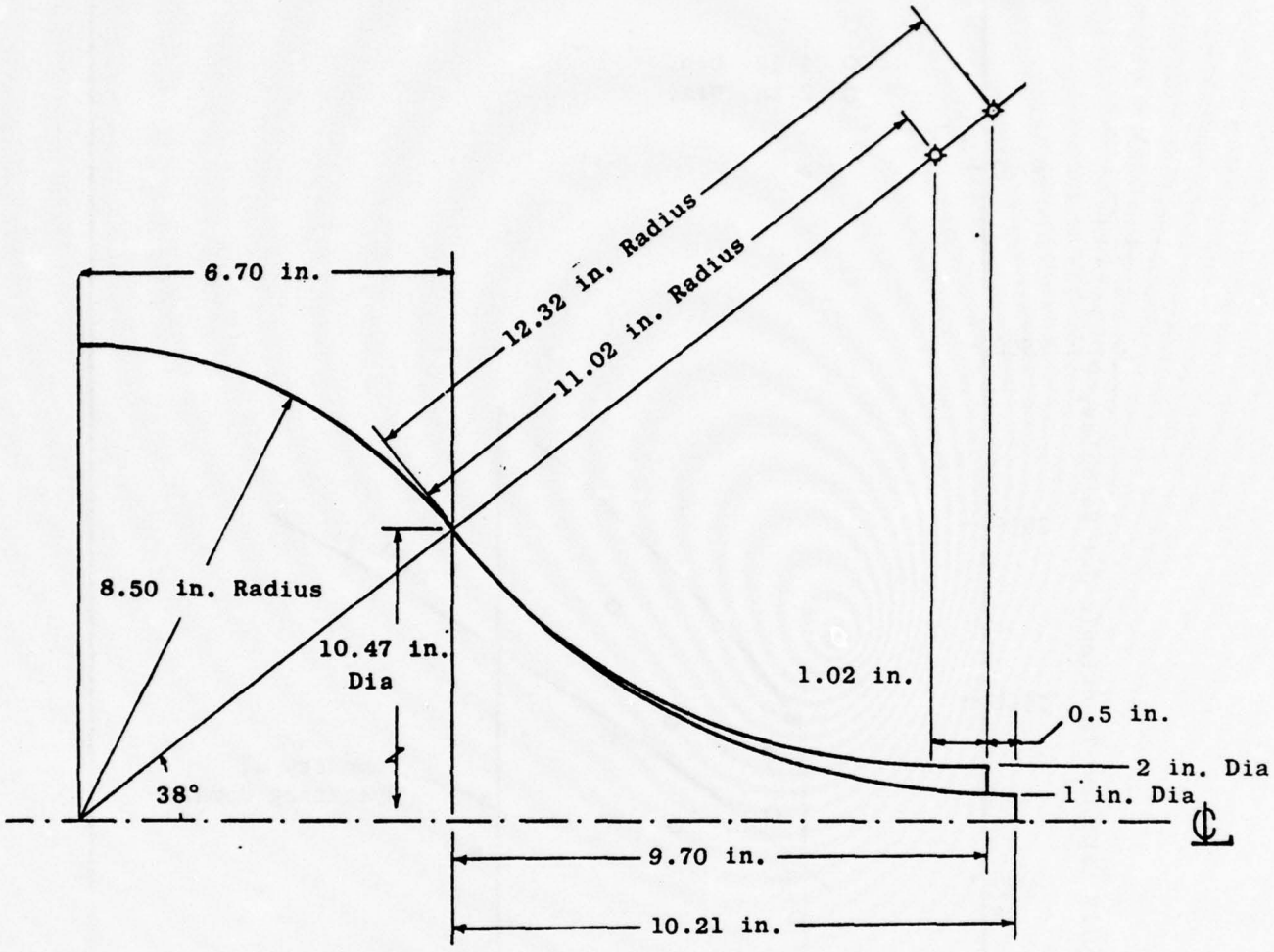


Figure 6-13. Diagram Showing Contour of Subsonic Nozzle at USC.

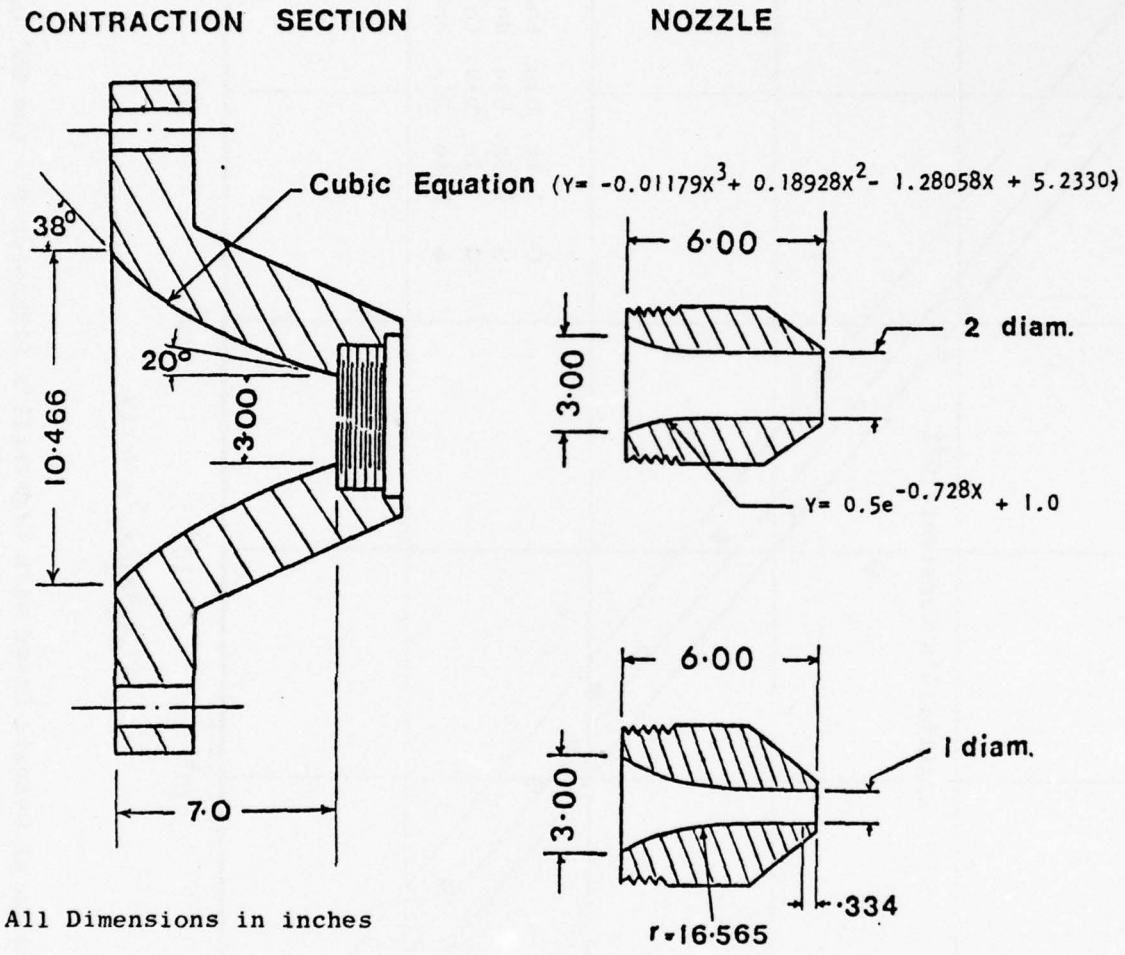


Figure 6-14. Schematic Diagram Showing Contraction Section and Nozzle Contour at USC.

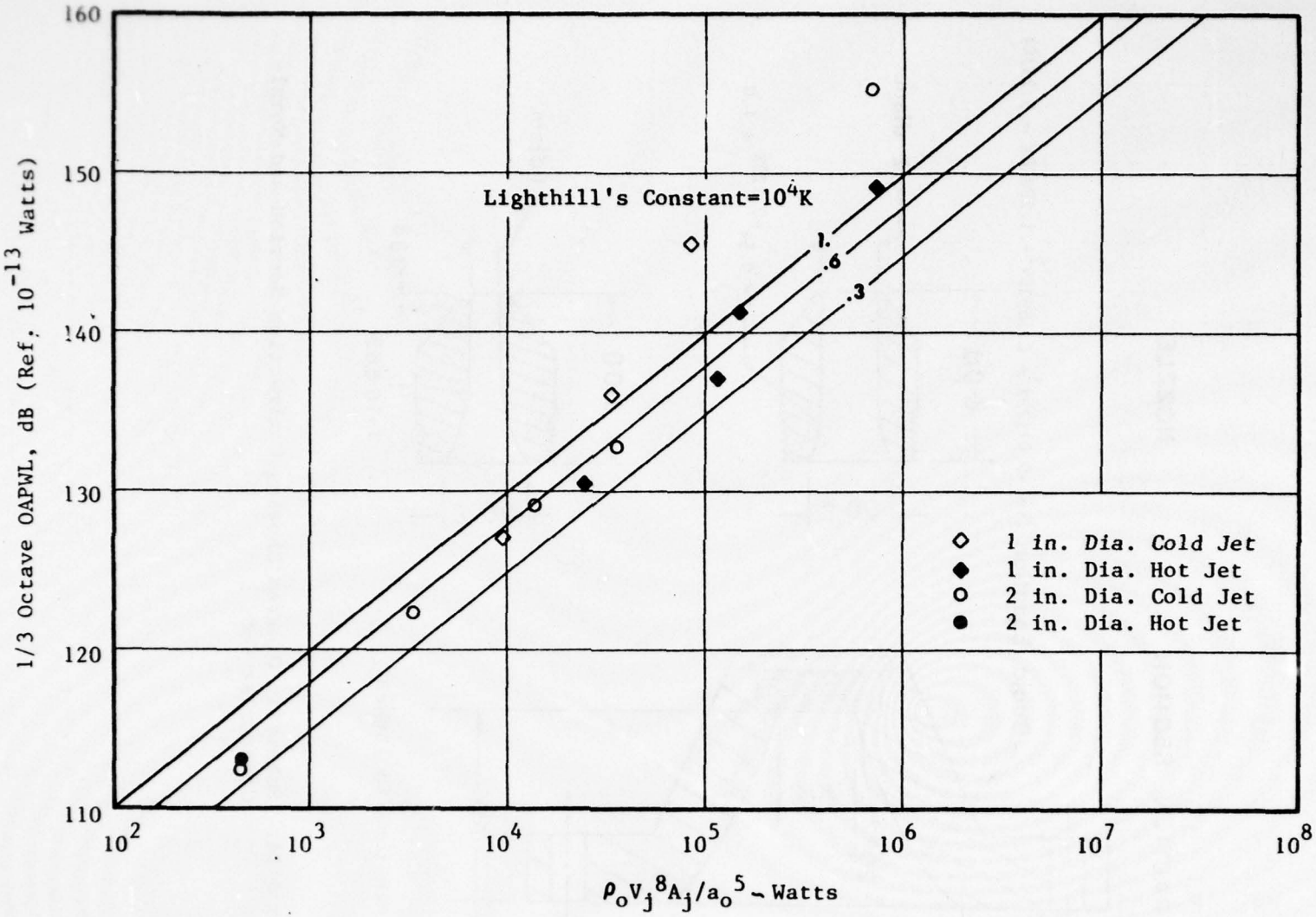


Figure 6-15. Variation of Overall Power with Lighthill's Parameter for the USC Data.

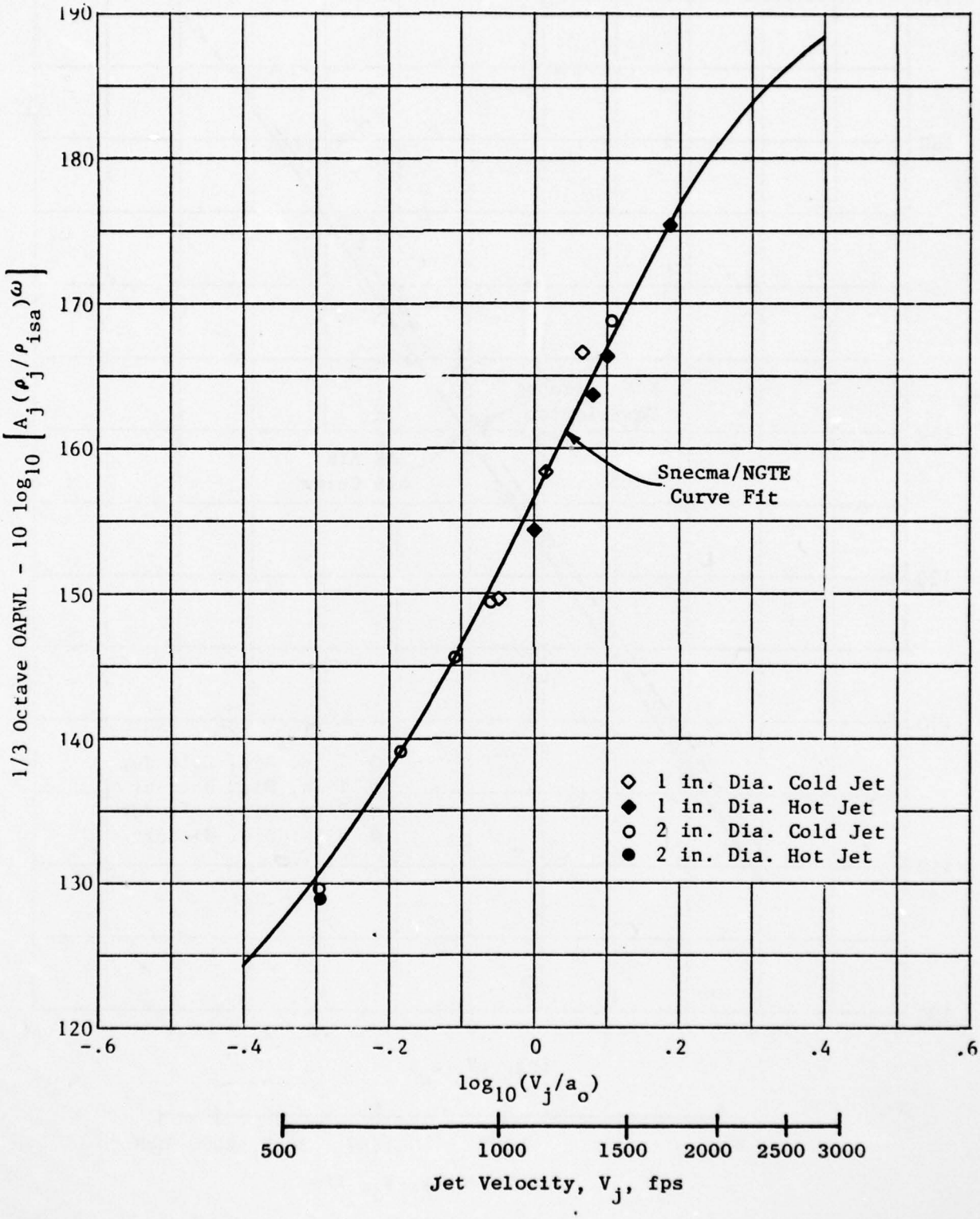


Figure 6-16. Variation of Normalized Overall Power with Jet Velocity at USC.

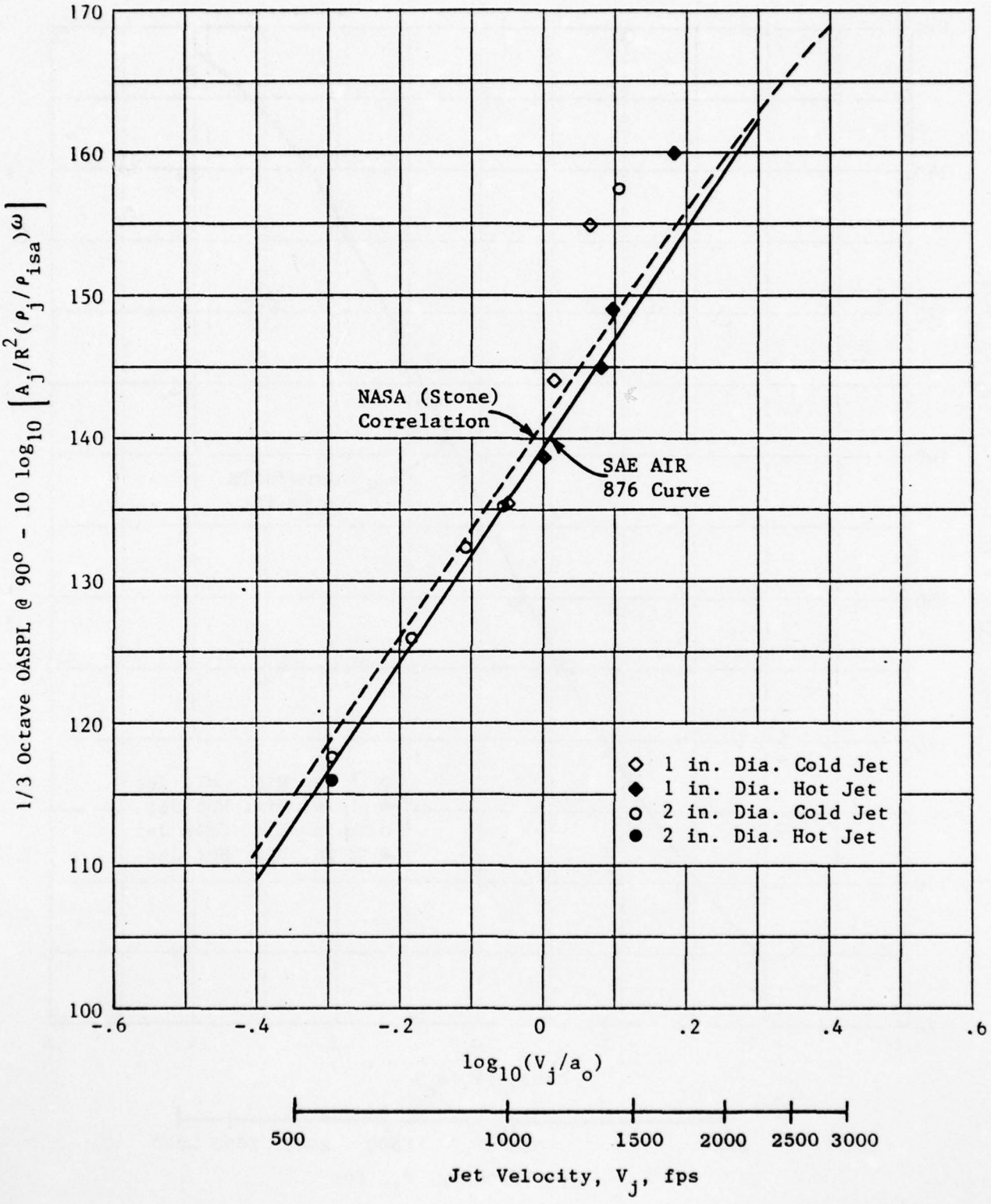


Figure 6-17. Velocity Dependence of Normalized Overall Sound Pressure Level at 90° for the USC Data.

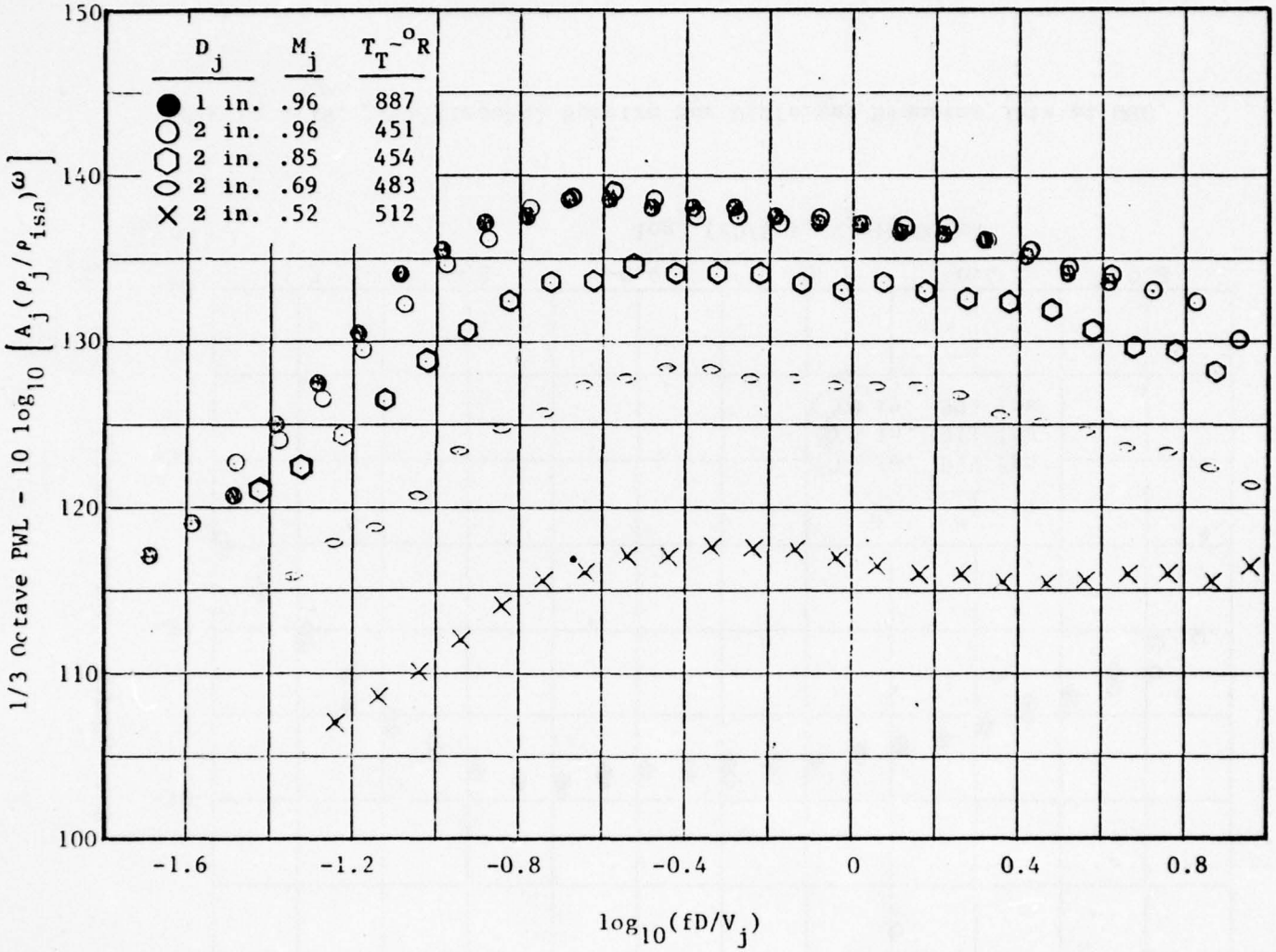


Figure 6-18. Normalized Power Spectra for Two Cold Subsonic Jets at USC.

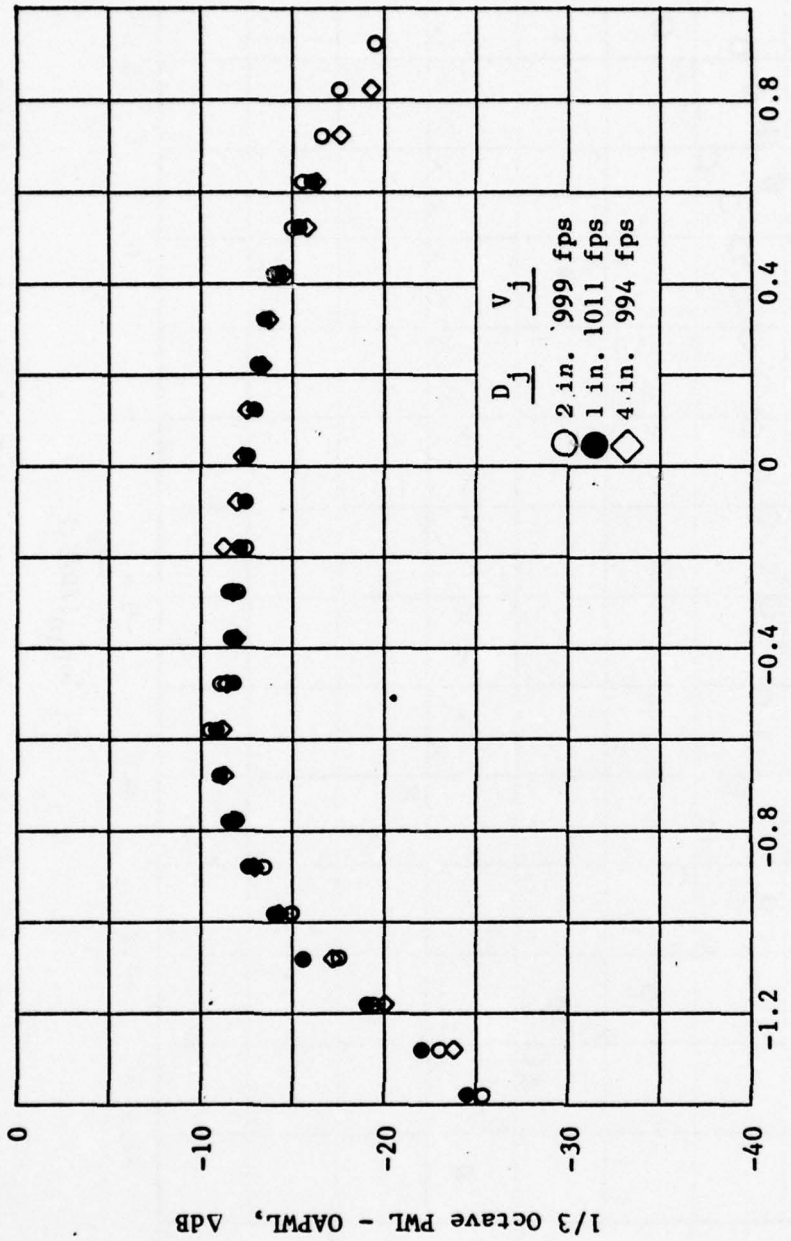


Figure 6-19. PWL Strouhal Spectra for Different Diameter Jets at USC.

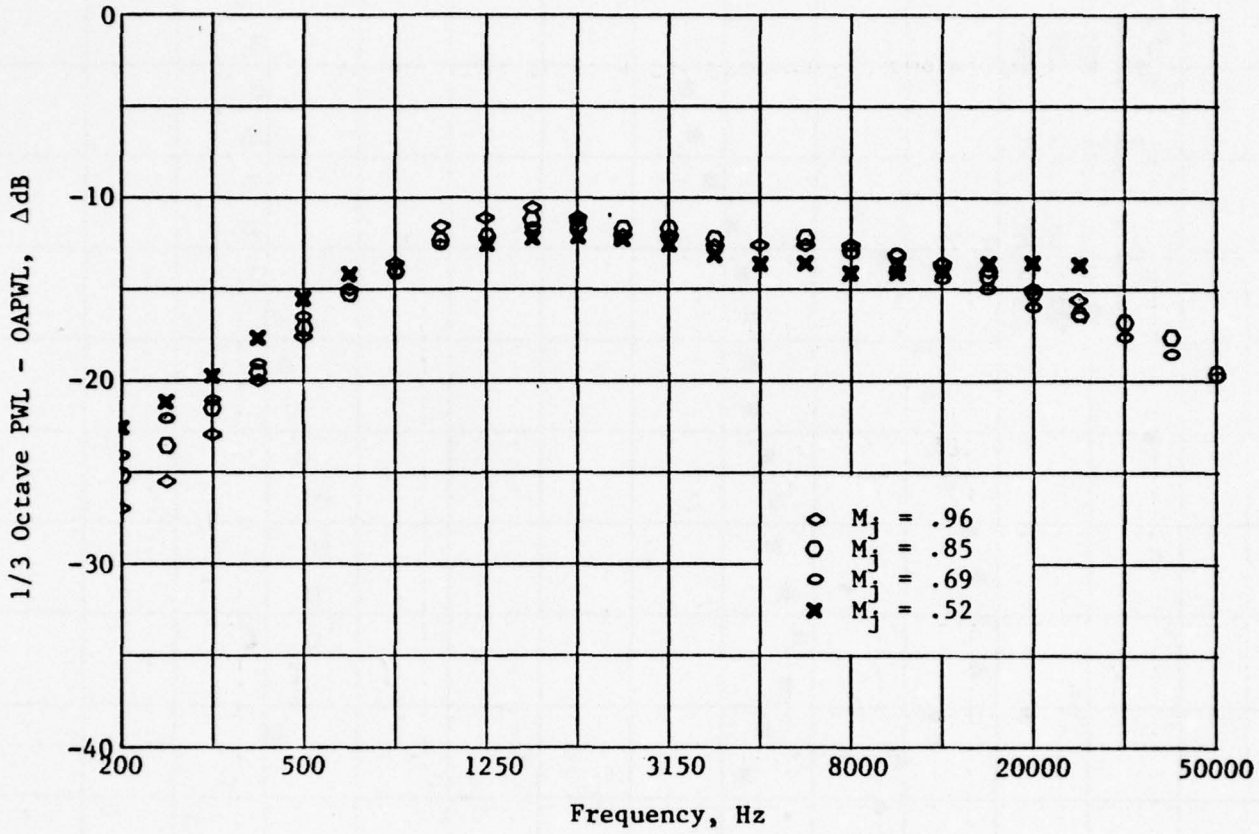


Figure 6-20. PWL Frequency Spectra Variation with Cold Subsonic 2-inch Diameter Jets at USC.

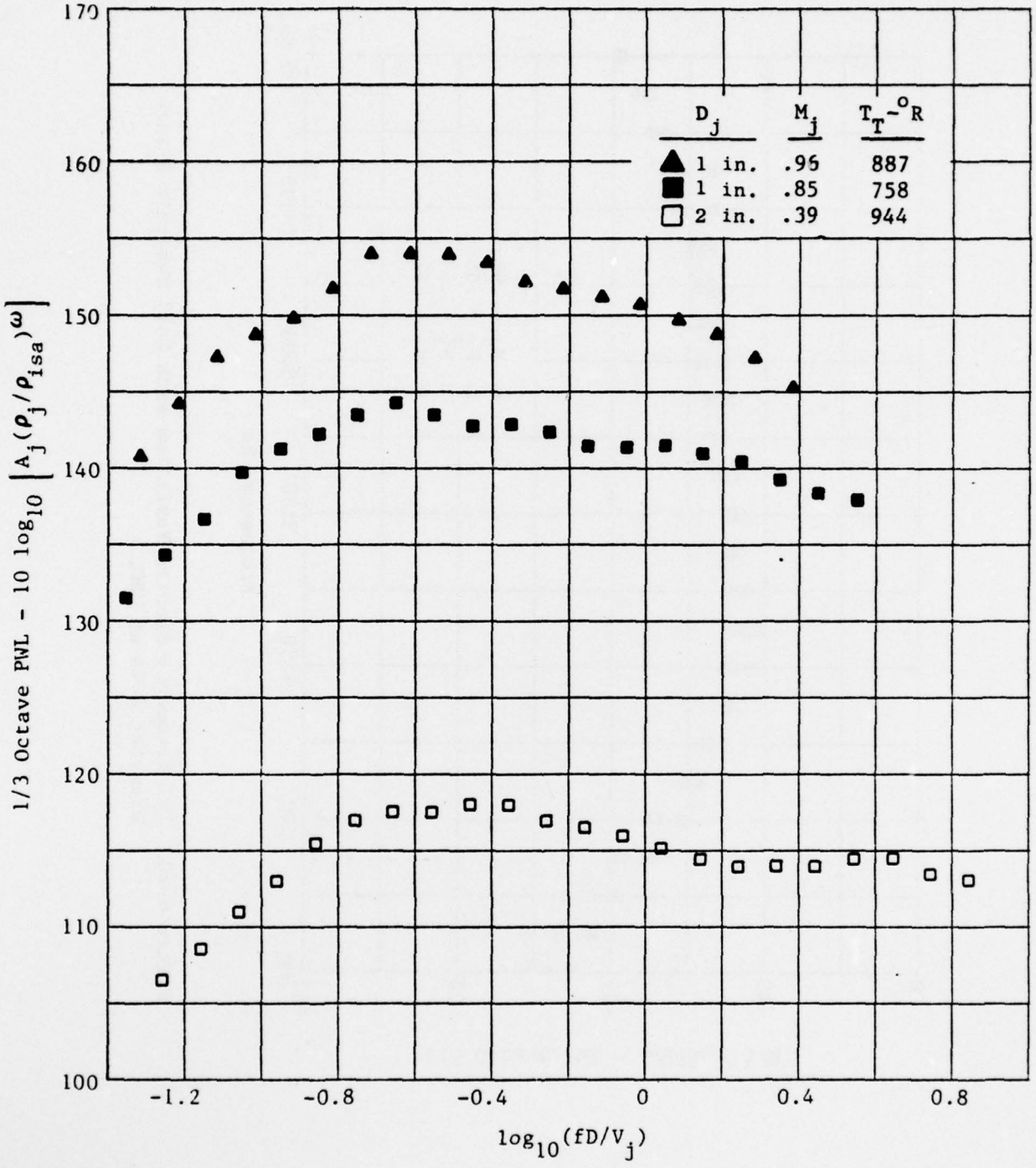


Figure 6-21. Normalized Power Spectra for Subsonic Heated Jets at USC.

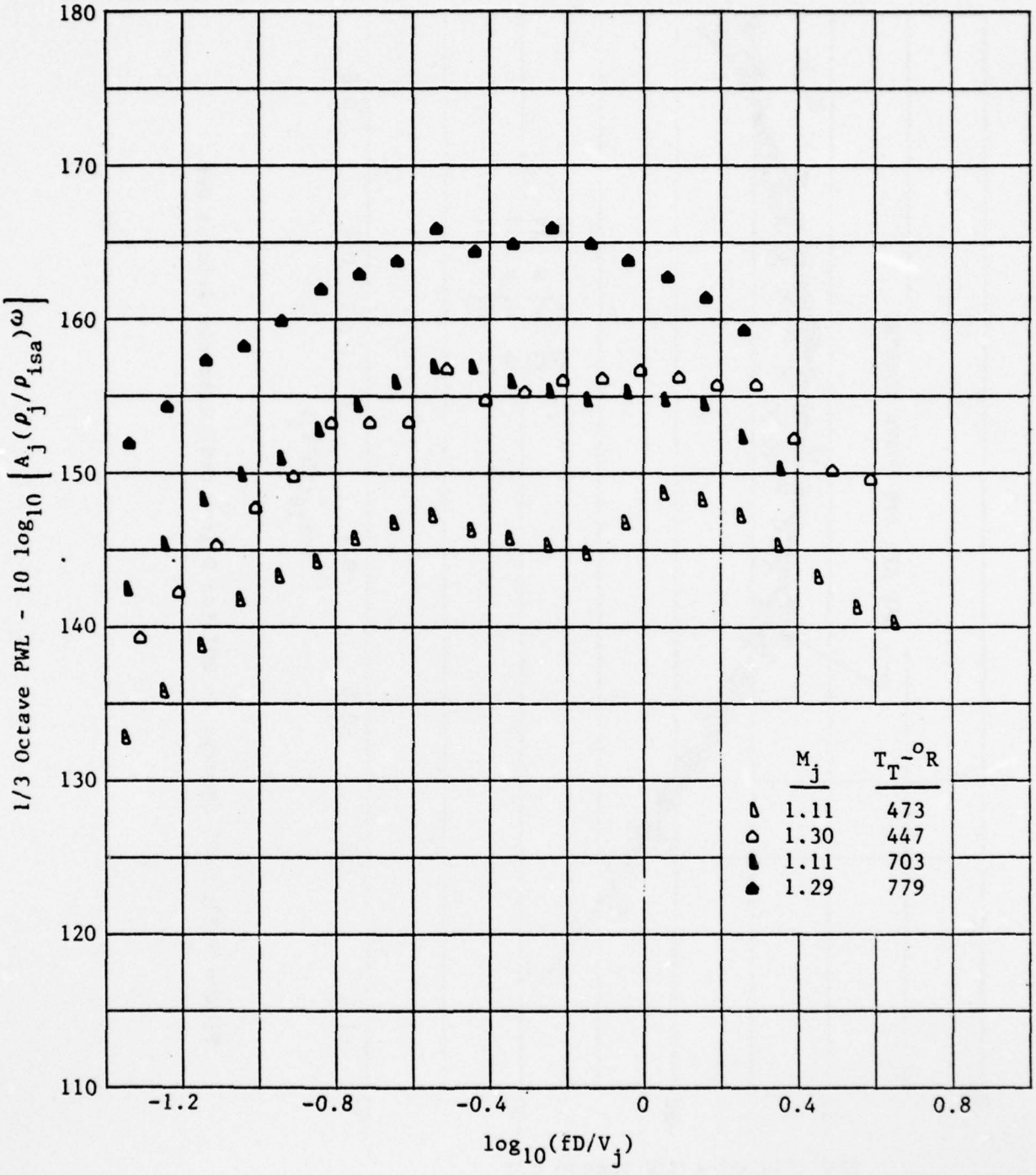


Figure 6-22. Normalized Power Spectra for a 1-inch Cold and Hot Supercritical Jets at USC.

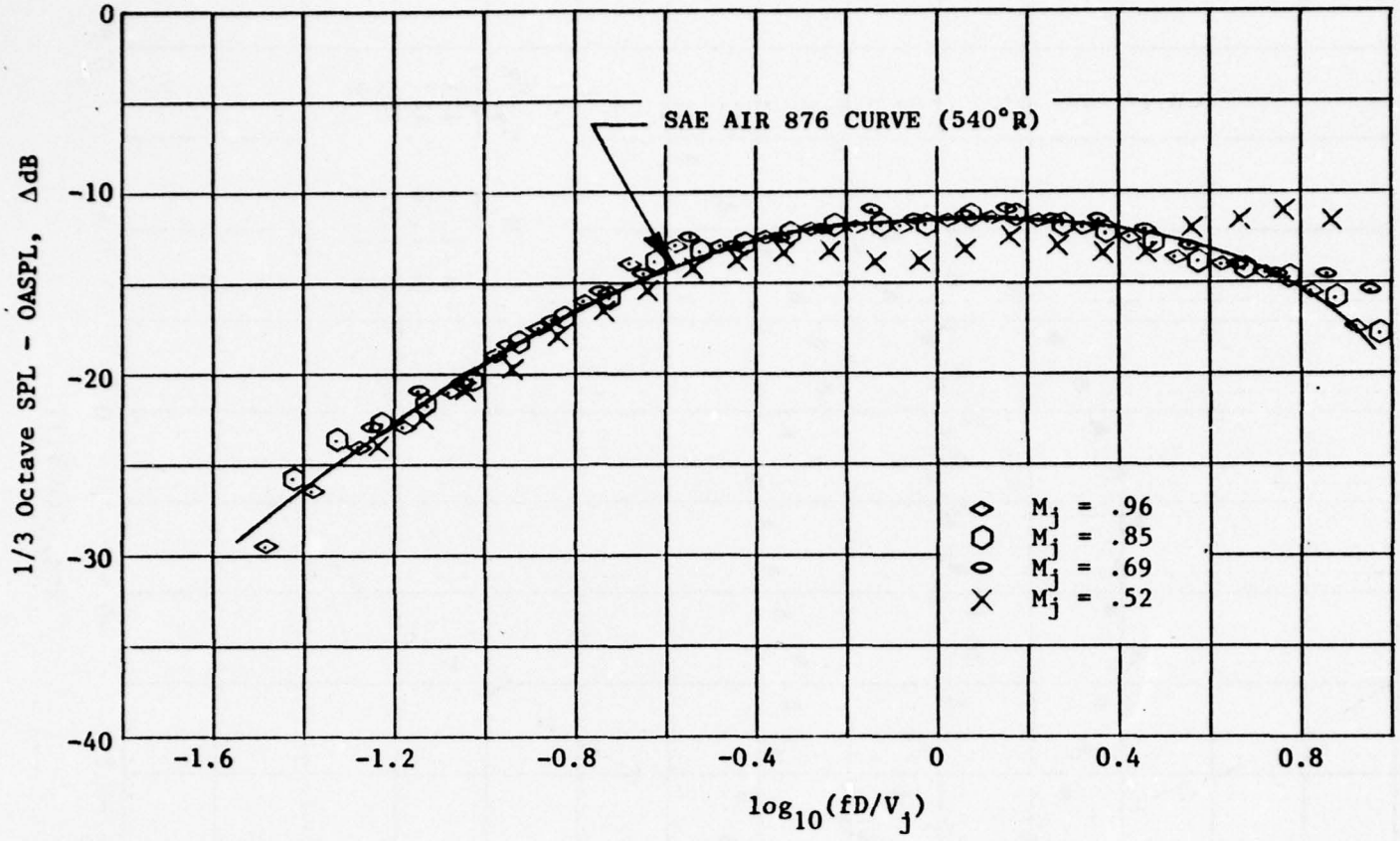


Figure 6-23. SPL Spectra at 90° for 2-inch Cold Subsonic Jets at USC.

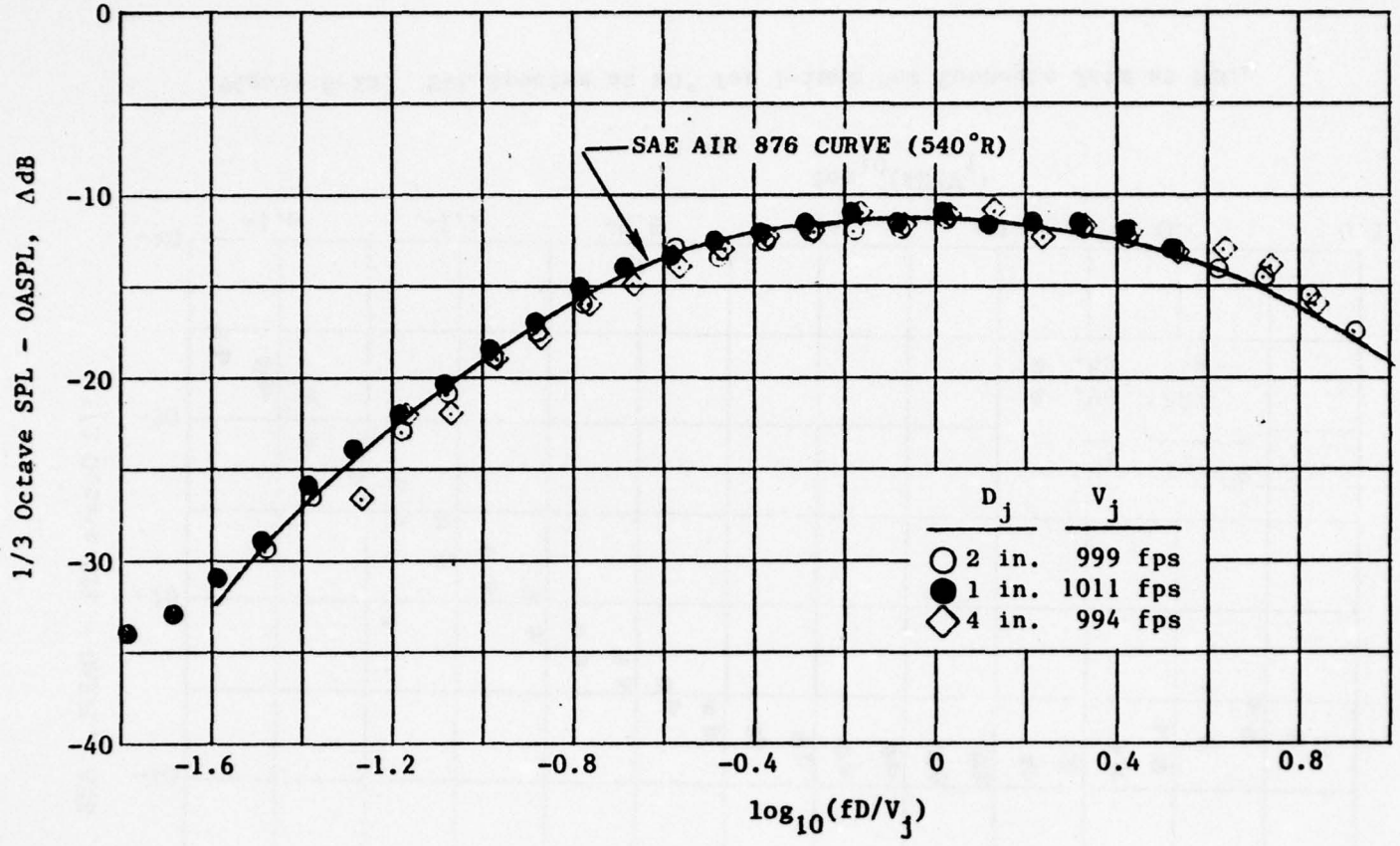


Figure 6-24. SPL Spectra at 90° for Various Diameter Cold Jets at USC.

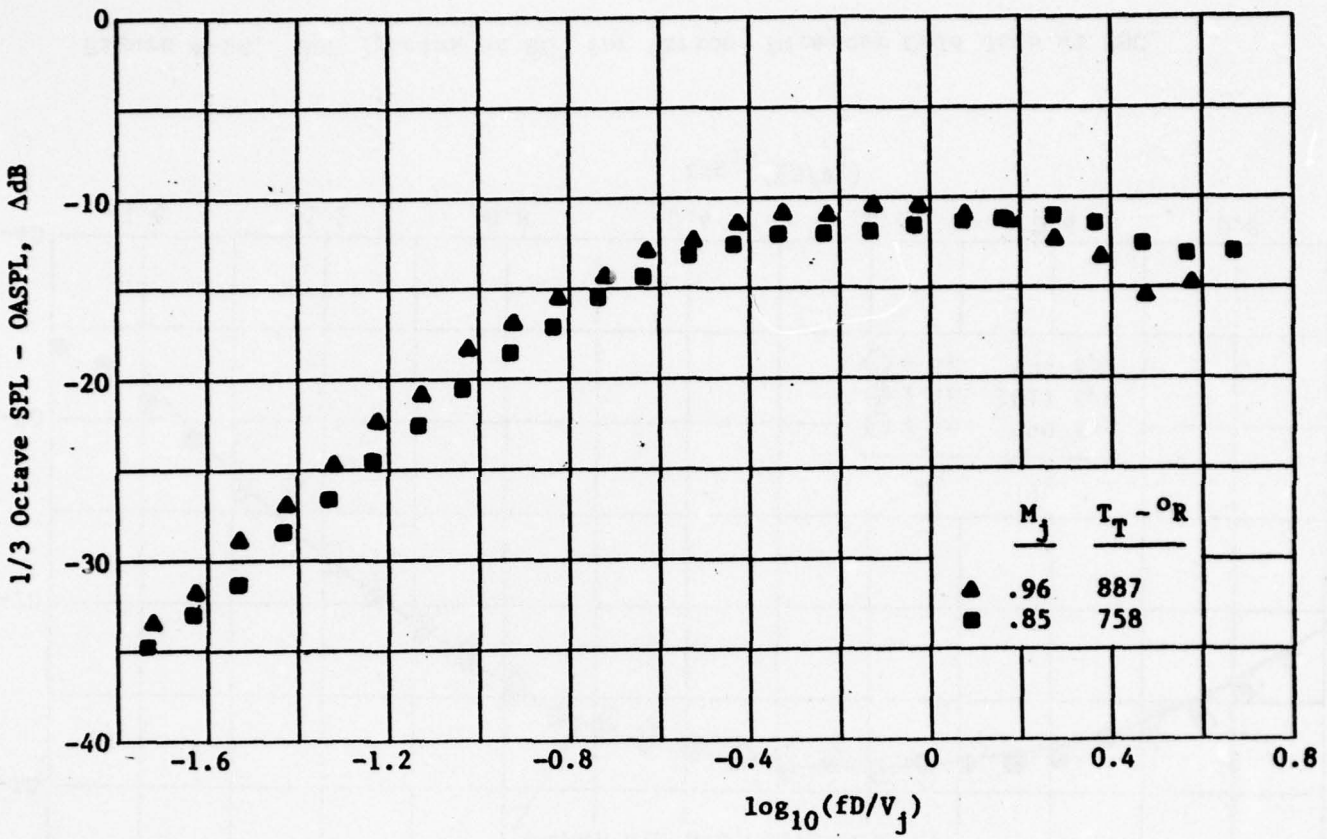


Figure 6-25. SPL Spectra at 90° for 1-inch Hot Subsonic Jets at USC.

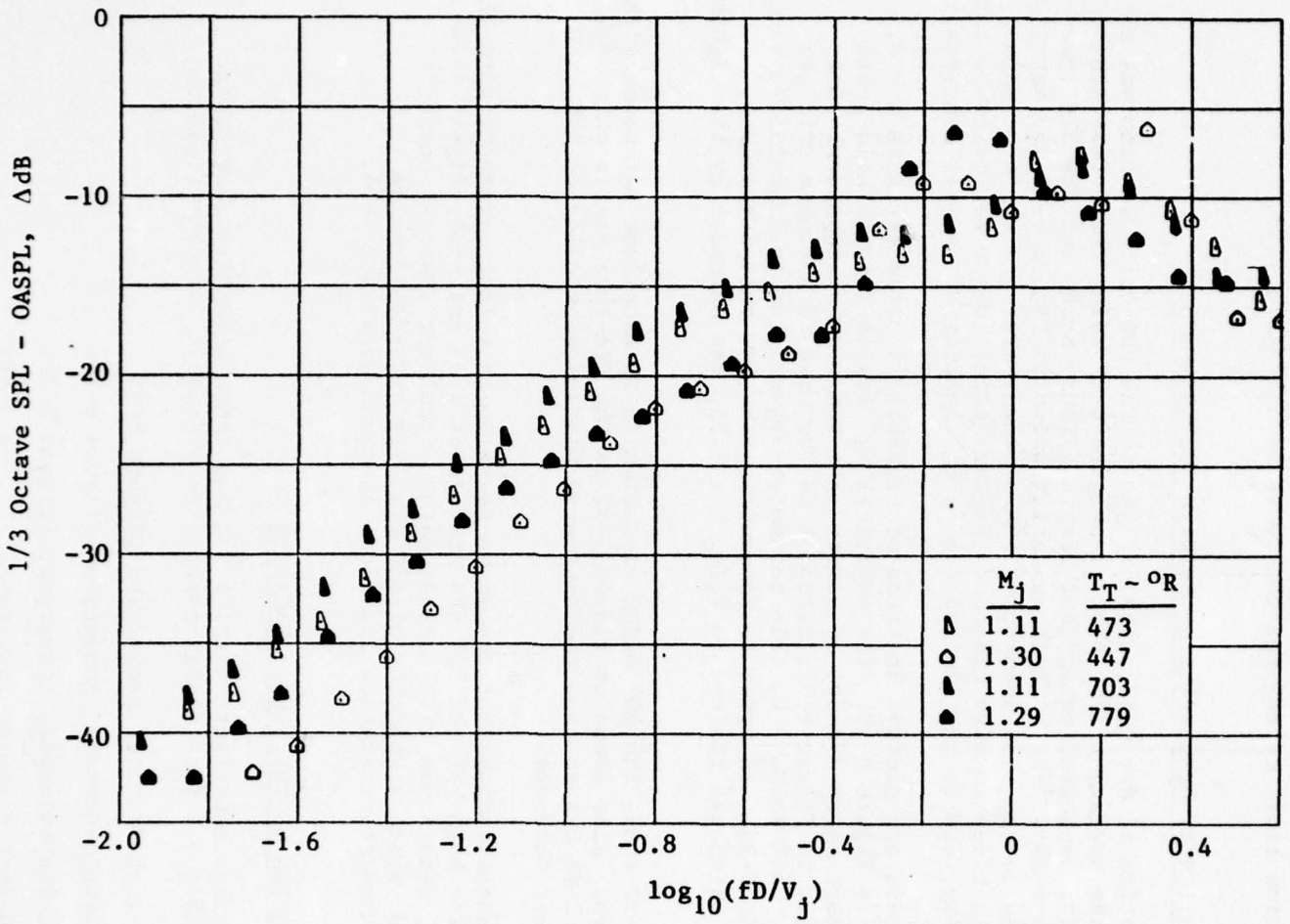


Figure 6-26. SPL Spectra at 90° for 1-inch Supercritical Jets at USC.

is relatively insensitive to heating. Low velocity spectra comparisons below the certification limit of 600 fps can be found in Figure 4-53.

6.3 CERTIFICATION AT UNIVERSITY OF BRITISH COLUMBIA (UBC)

Certification of the cold, subsonic jet in the UBC anechoic room was conducted along the operating line shown in Figure 6-27 using the 0.787-inch (2 cm) diameter, contoured convergent nozzle (Figure 6-28) and the STA type nozzle (Figure 6-29). The highest operating point in Figure 6-27 was obtained while operating in the blow down mode, where steady pressure could be maintained for only three to five minutes. Higher stagnation pressures could not be held steadily, due to the limited (260 cfm) capacity of the air compressor.

The UBC data are plotted in terms of Lighthill's parameter with K = 0.3 to 0.5 x 10^{-4} in Figure 6-30. The empirical V_j^8 law is seen to hold quite well for at least seven decades of power. The temperature dependent parameter is plotted in Figure 6-31; although in the case of subsonic cold jet where $\rho_j/\rho_{isa} \rightarrow 1.0$ as $M_j \rightarrow 0$, this parameter degenerates to Lighthill's law, as shown in Figure 6-31. In order to accommodate the low velocity points, Hoch's curve, which was limited to $V_j/a_o > -0.35$, was extended by the eighth power law.

Figure 6-32 shows the 90° OASPL variation is in excellent agreement with the $V_j^{7.4}$ curve. Also shown on Figure 6-32 is the STA-type nozzle which was approximately 2 dB higher than the contoured nozzles especially at low Mach numbers and near Mach one.

Spectra shape comparisons are shown to be in excellent agreement with the referee data for both PWL and 90° SPL in Figures 6-33 and 6-34. Figure 6-34 shows the ΔSPL comparison with referee data. Excellent spectral shape is obtained at 90° above a velocity of 600 fps. Low velocity spectra below the defined certification limit can be found on Figure 4-54.

6.4 CERTIFICATION OF THE JENOTS FACILITY

Five circular convergent nozzles and one converging/diverging nozzle with a M = 1.55 shock-free design point were available for certification:

- 5.7-inch-diameter convergent (Figure 6-35)
- 4.31-inch-diameter convergent (Figure 6-36)
- 3.56-inch-diameter convergent (Figure 6-37)
- 3.59-inch-diameter convergent (Figure 6-38)
- 4.64-inch-diameter convergent (Figure 6-39)
- 4.31-inch-diameter convergent/divergent (Figure 6-40)

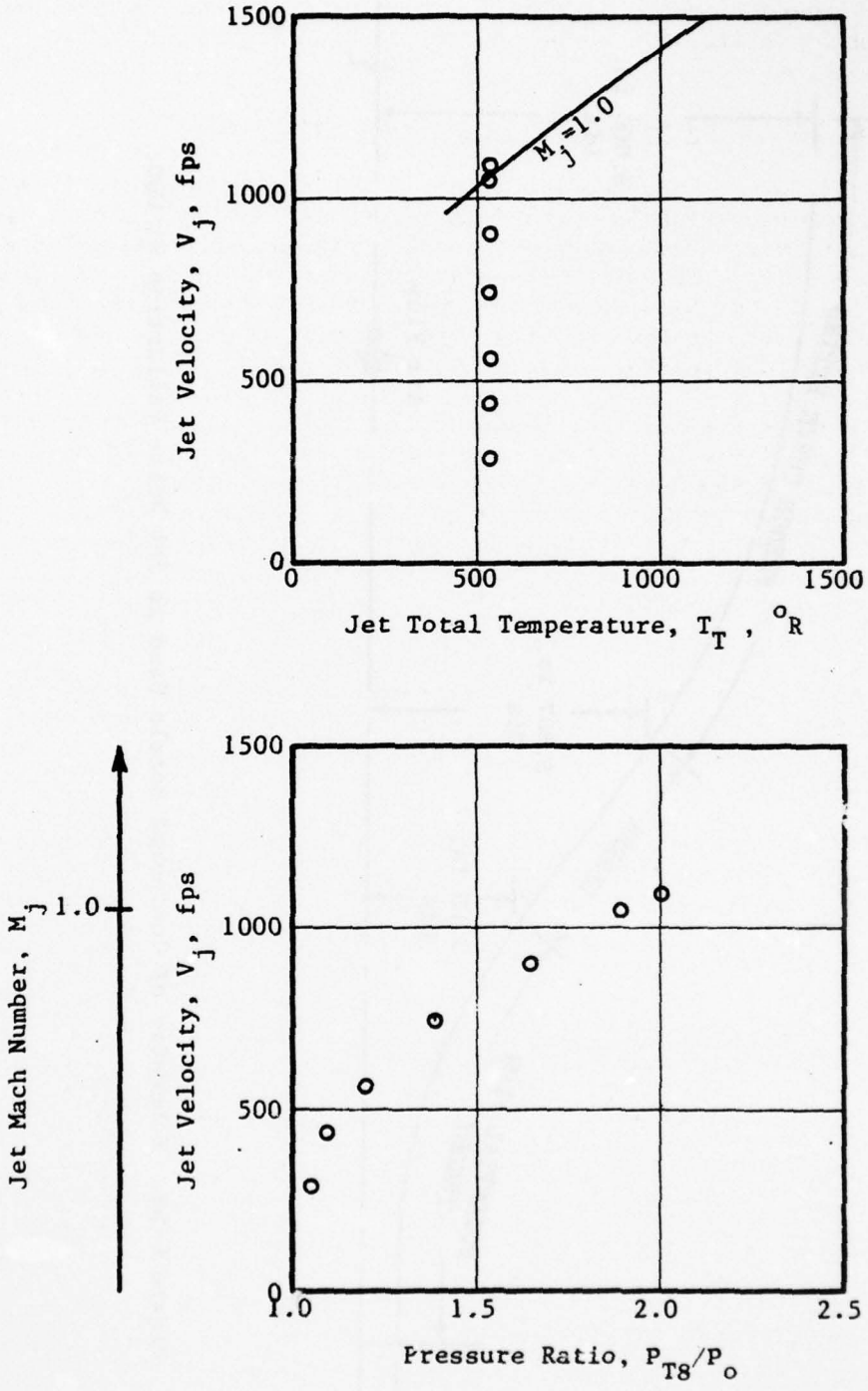
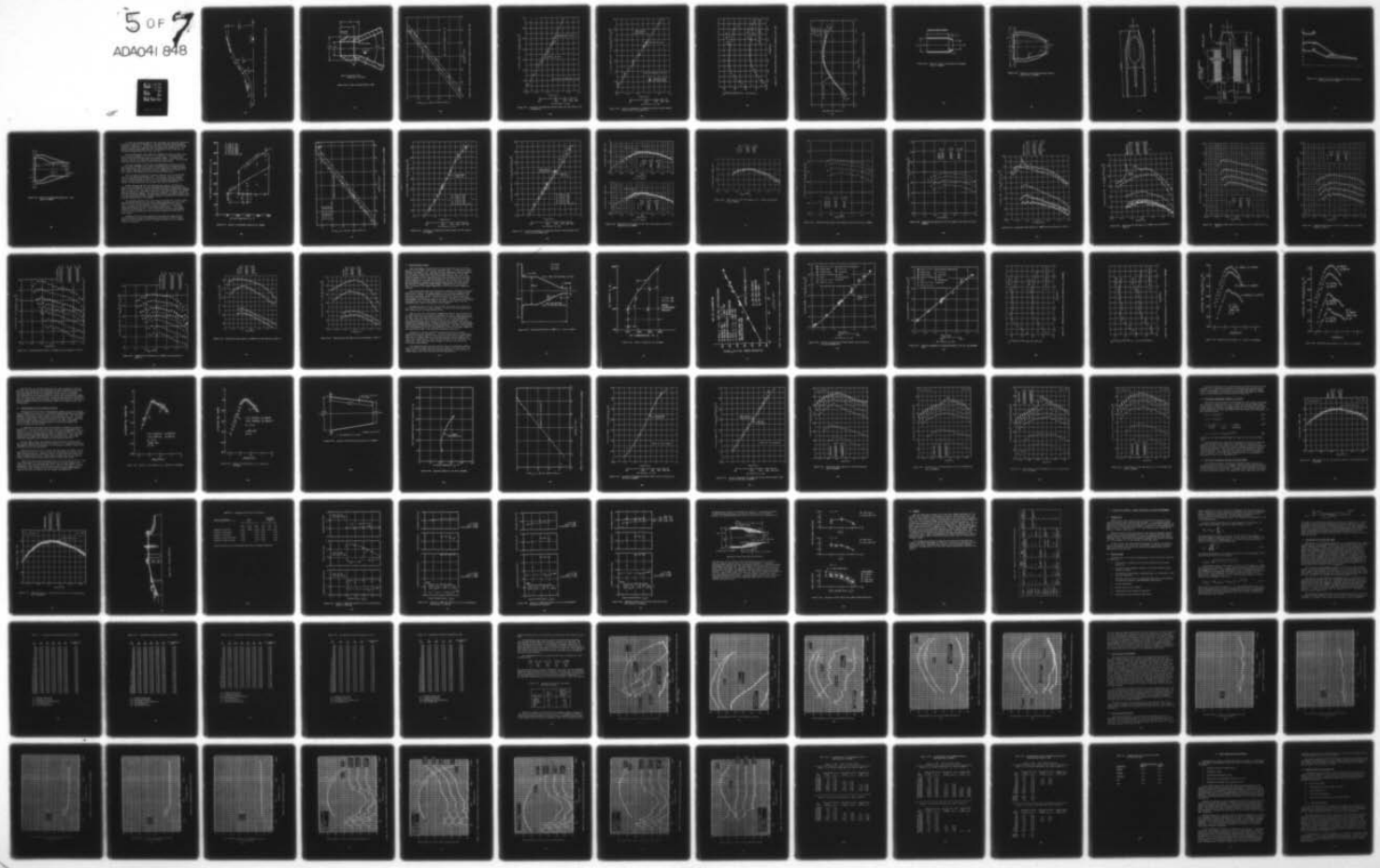


Figure 6-27. Domain of Operation of the UBC Anechoic Chamber Jet.

AD-A041 848 GENERAL ELECTRIC CO CINCINNATI OHIO AIRCRAFT ENGINE GROUP F/G 14/2
HIGH VELOCITY JET NOISE SOURCE LOCATION AND REDUCTION. TASK 1. --ETC(U)
FEB 77 C T SAVELL, E J STRINGAS DOT-OS-30034
UNCLASSIFIED R77AEG187 FAA-RD-76-79-1 NL

5 OF 7
ADA041 848




848

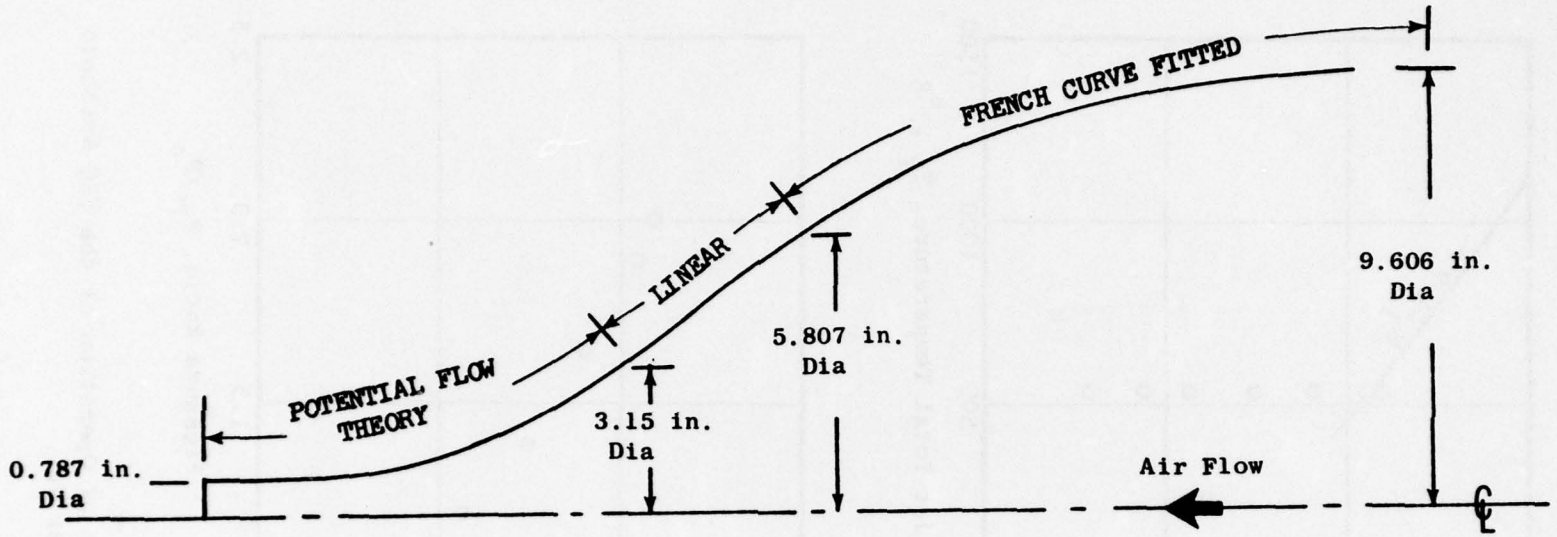
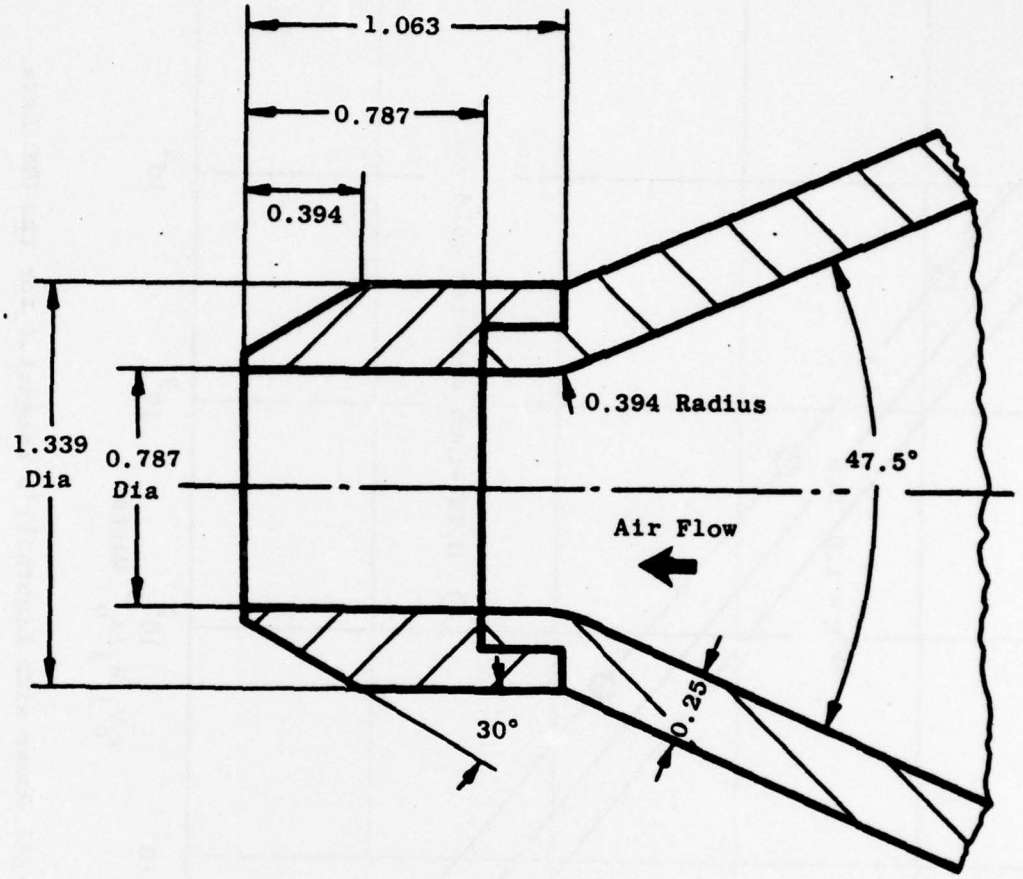


Figure 6-28. Schematic of Contoured Nozzle Used in Jet Noise Validation at UBC.



Scale: Twice Full Size
Dimensions in inches

Figure 6-29. Shape of Nozzle Used at UBC.

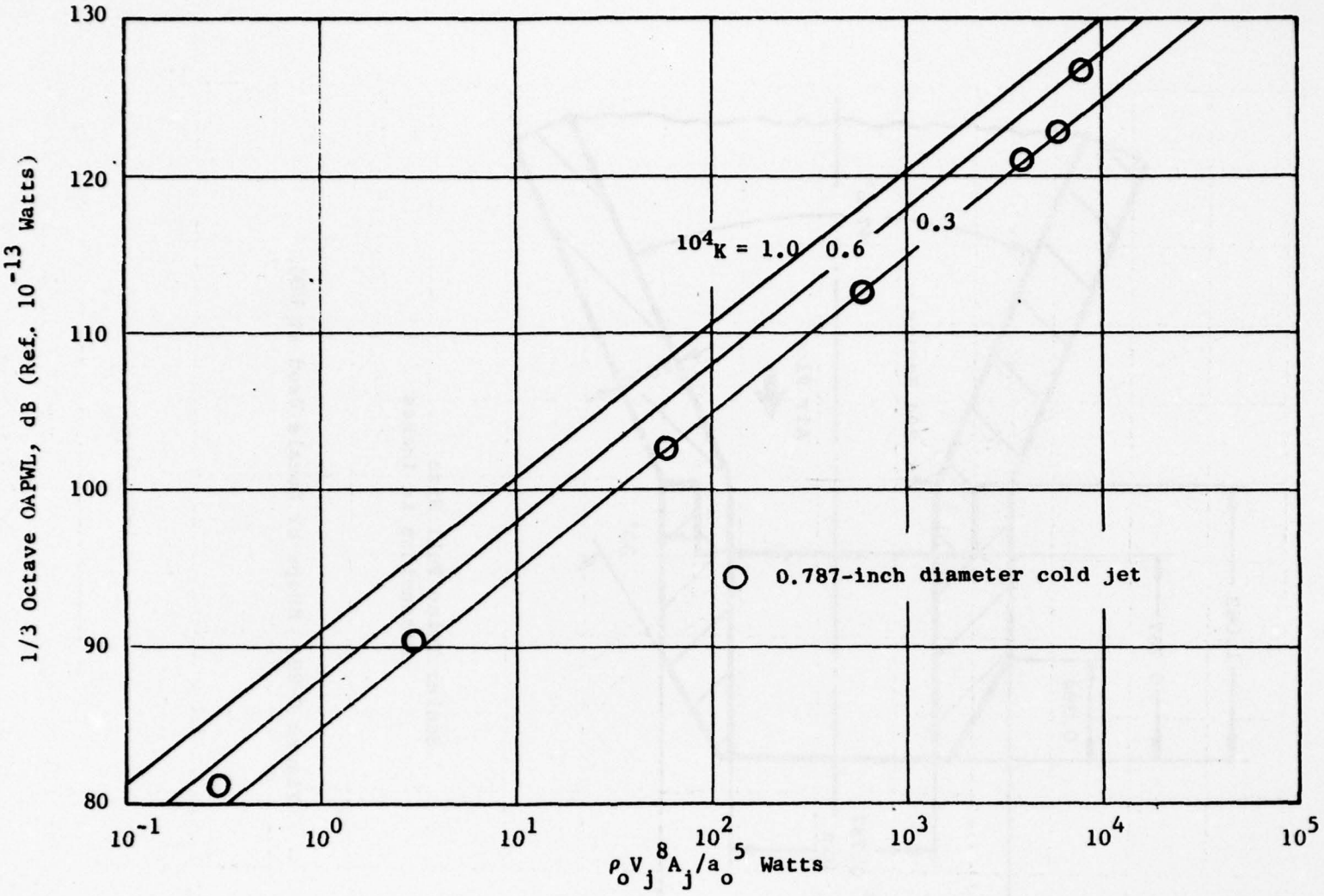


Figure 6-30. Variation of Overall Power with Lighthill's Parameter for the UBC Data.

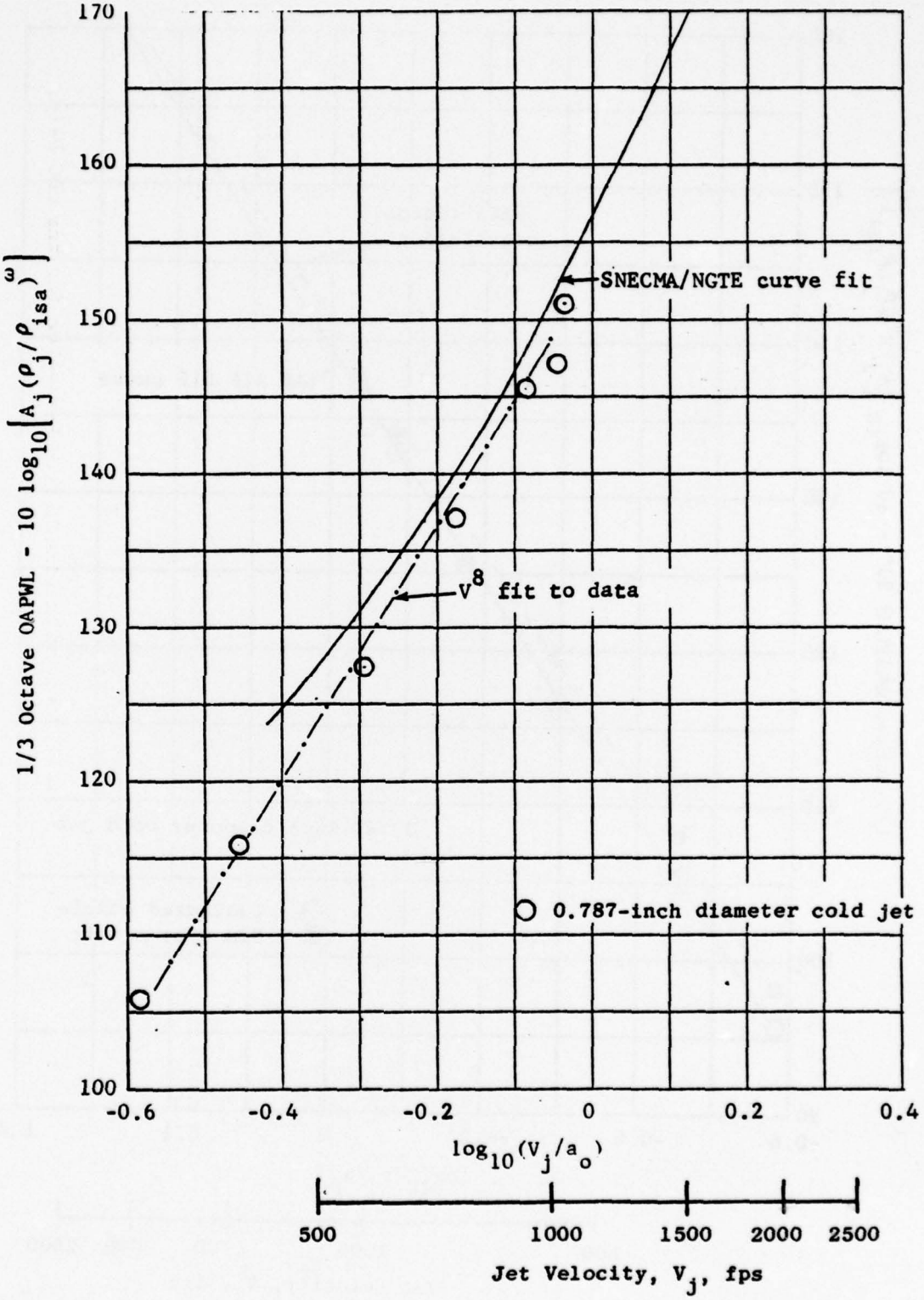


Figure 6-31. Variation of Normalized Overall Power with Jet Velocity for the UBC Data.

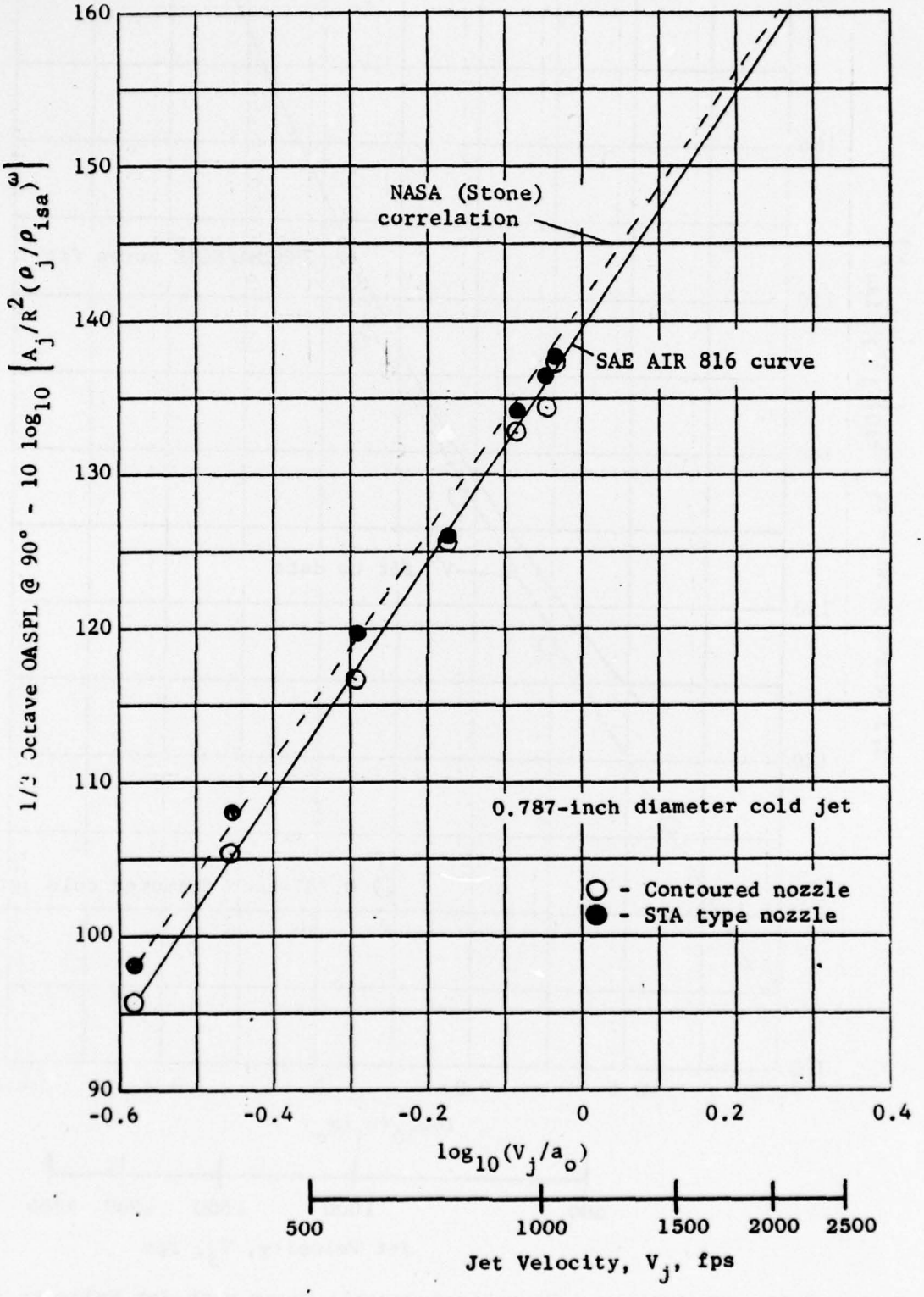


Figure 6-32. Velocity Dependence of Normalized Overall Sound Pressure Level at 90° for the UBC Data.

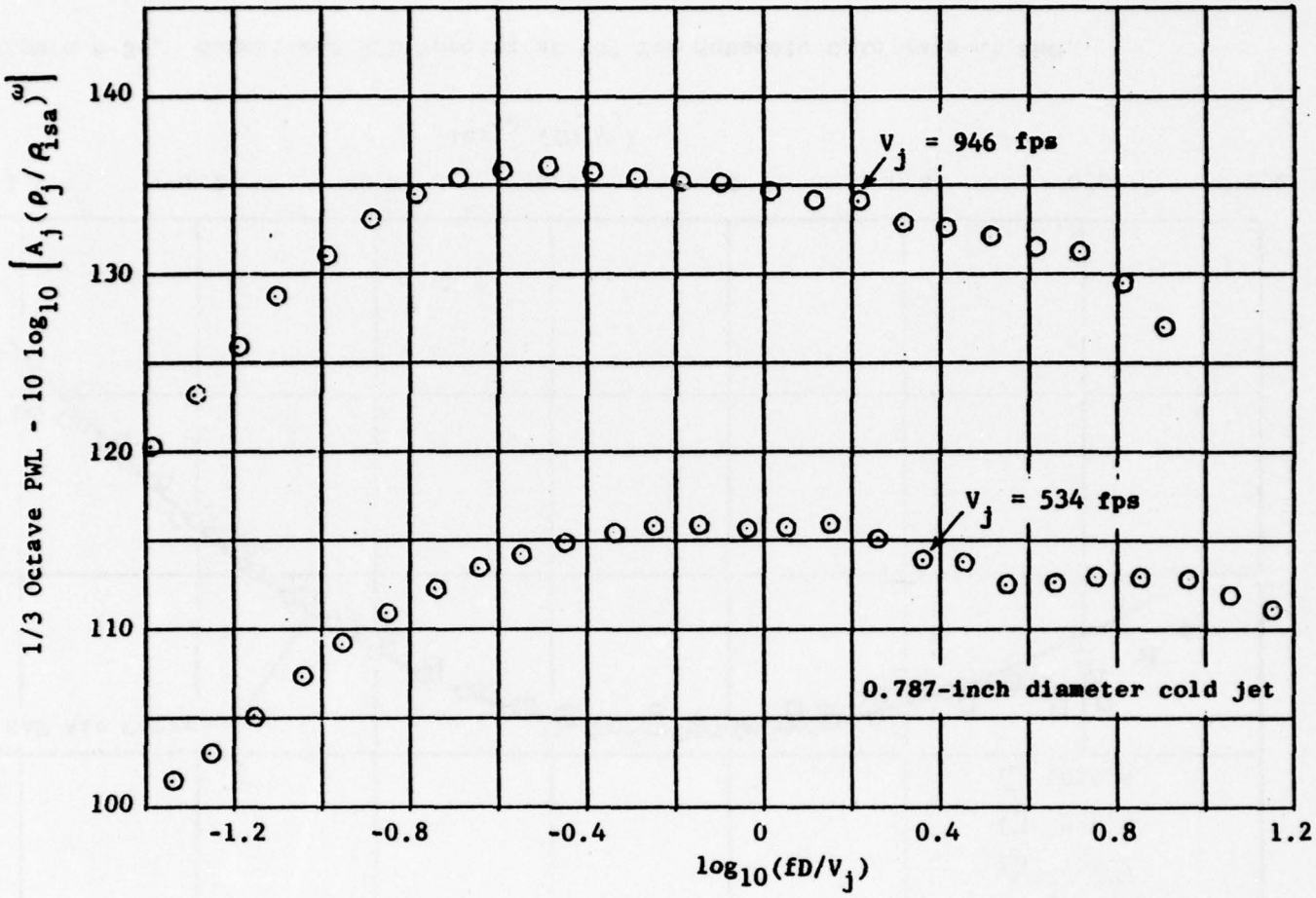


Figure 6-33. Normalized Power Spectra for Cold Subsonic Jets at UBC.

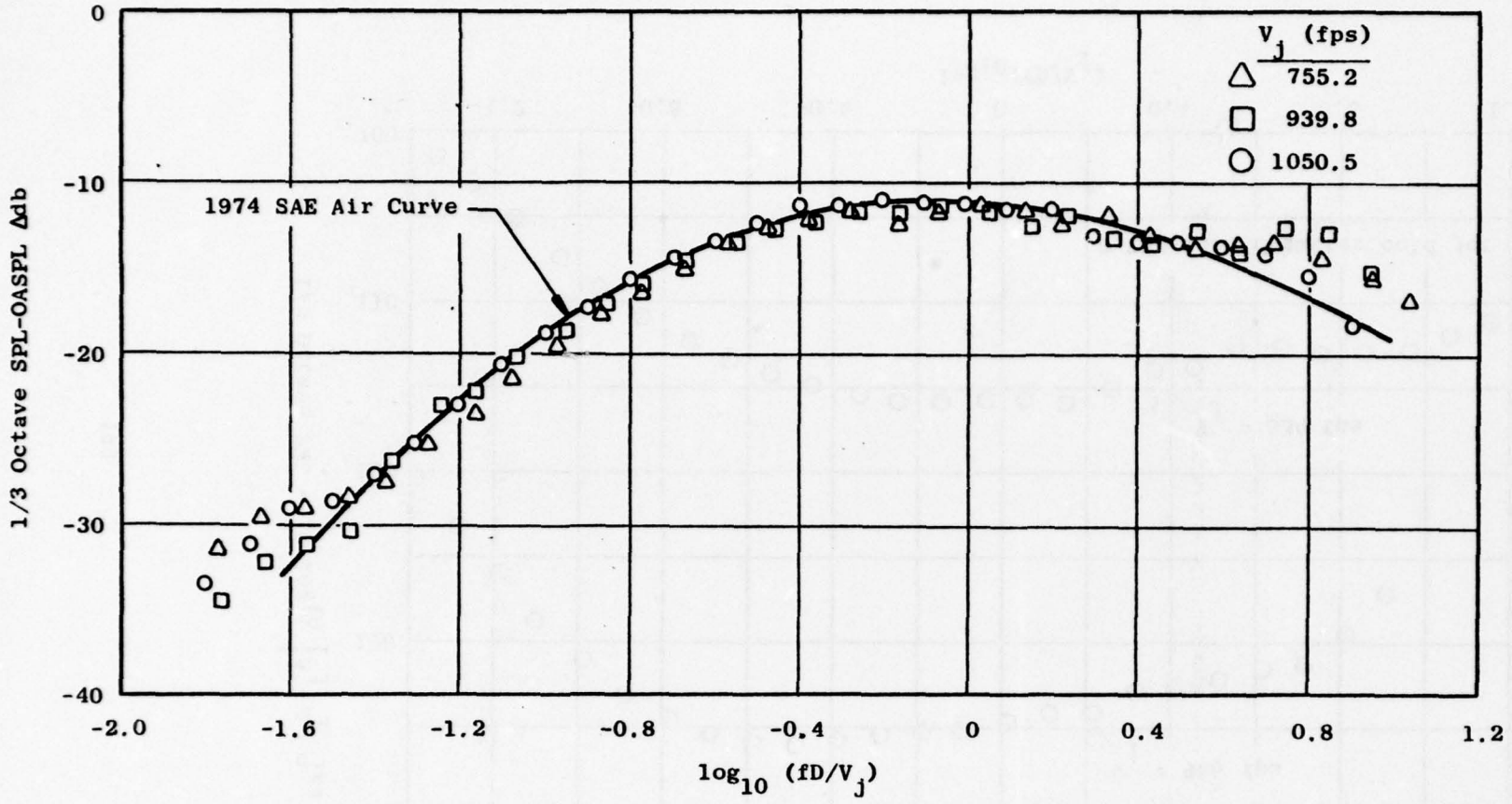


Figure 6-34. Normalized SPL Spectra at 90° for Subsonic Cold Jets at UBC.

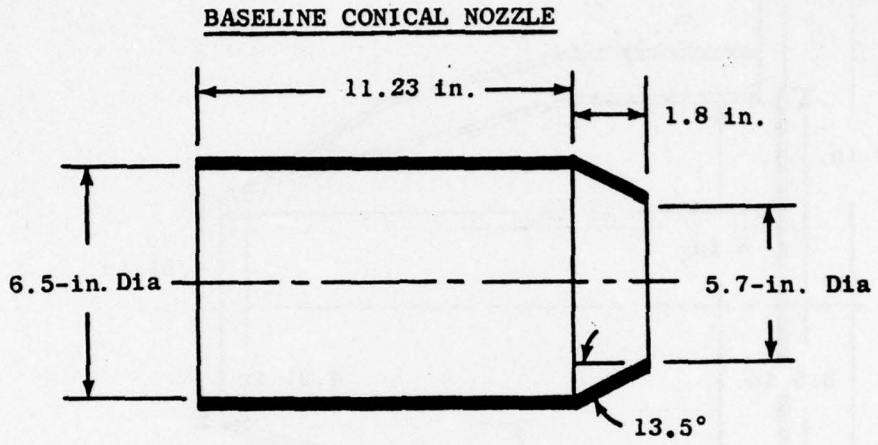


Figure 6-35. Shape of the 5.7-inch-Diameter Convergent Nozzle at JENOTS.

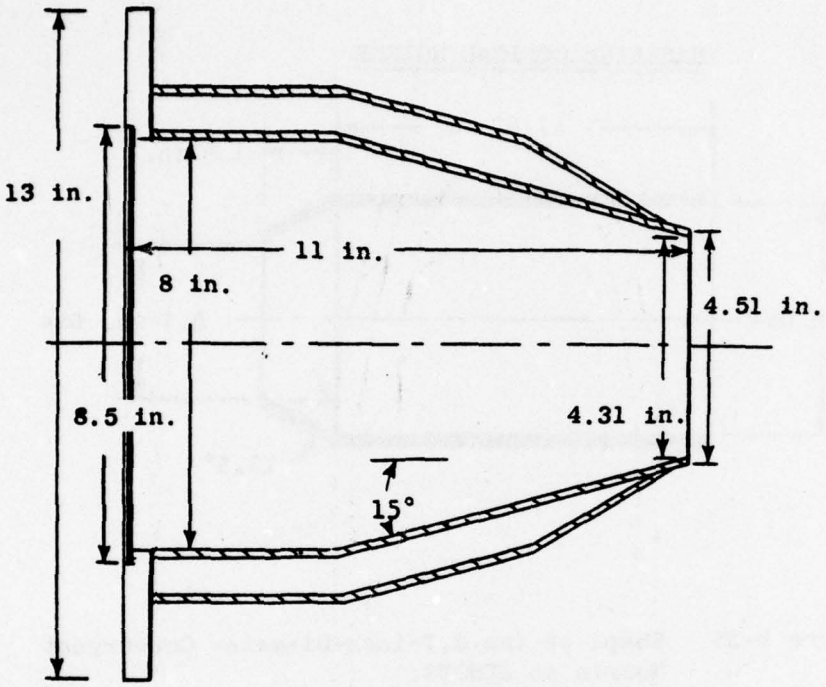


Figure 6-36. Shape of the 4.31-inch-Diameter Convergent Nozzle at JENOTS.

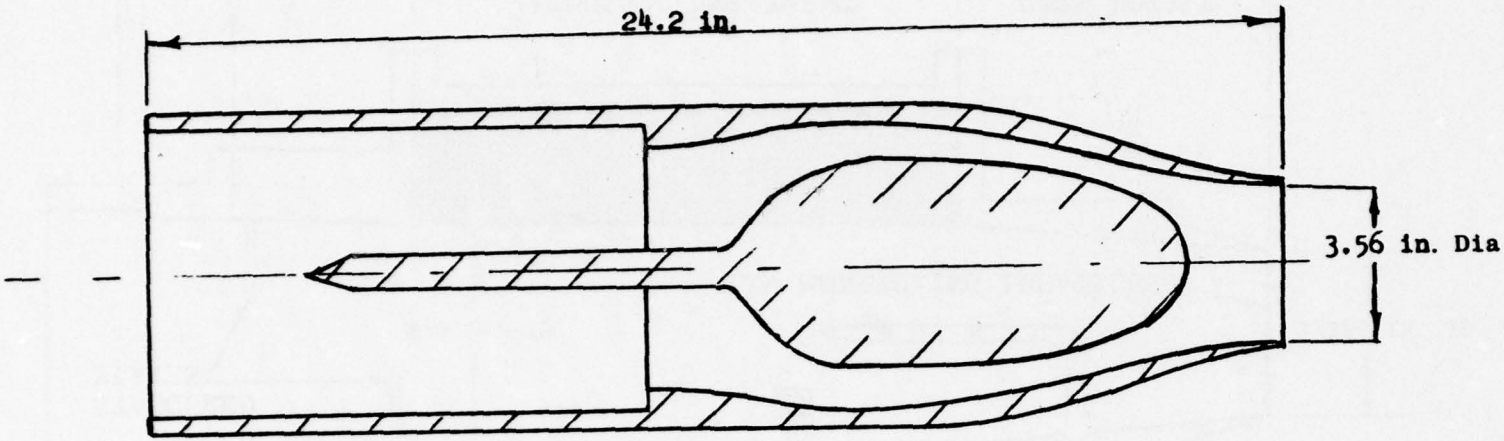


Figure 6-37. Shape of the 3.56-inch-Diameter Convergent Nozzle at JENOTS.

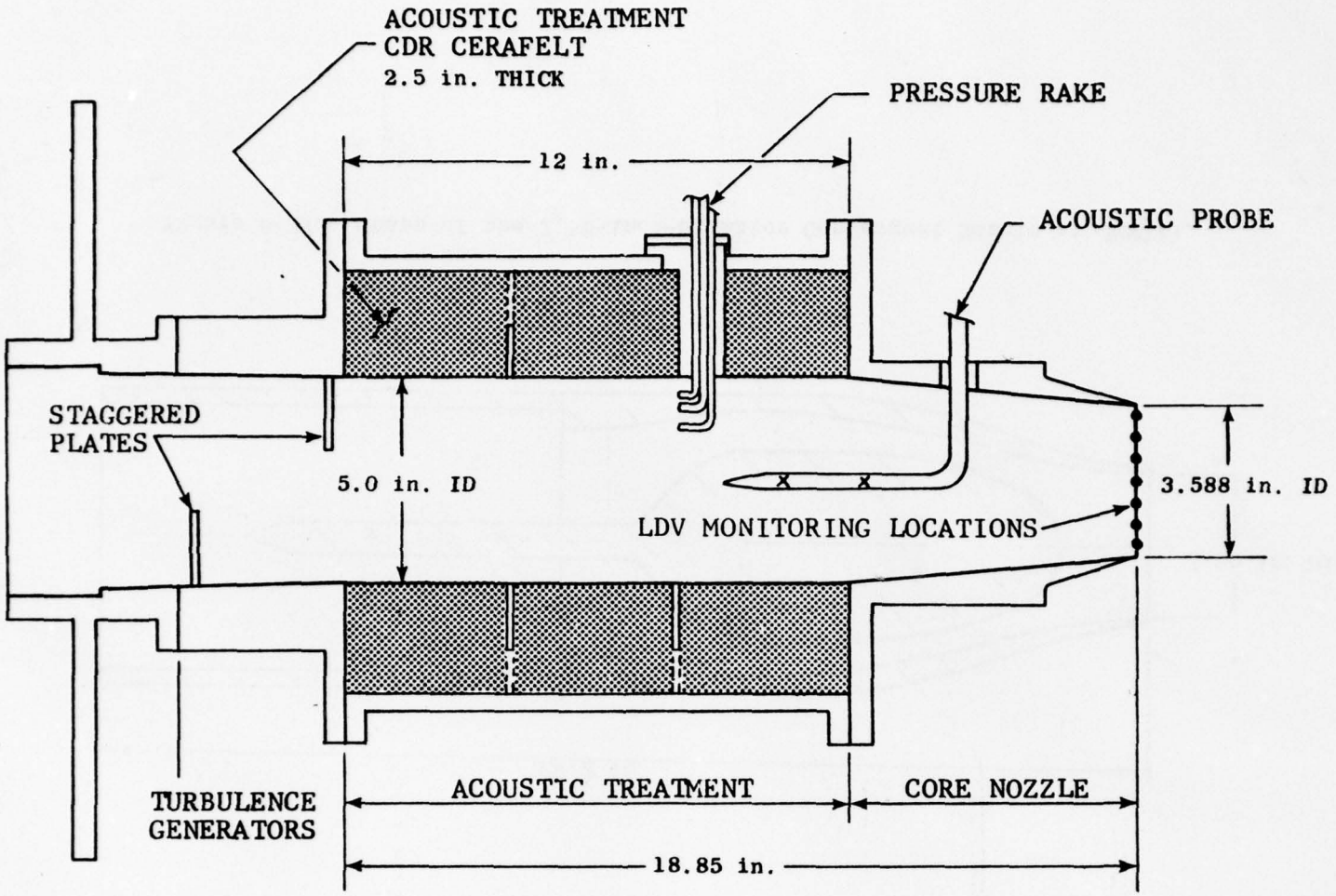


Figure 6-38. Shape of the 3.588-inch-Diameter Nozzle at JENOTS.

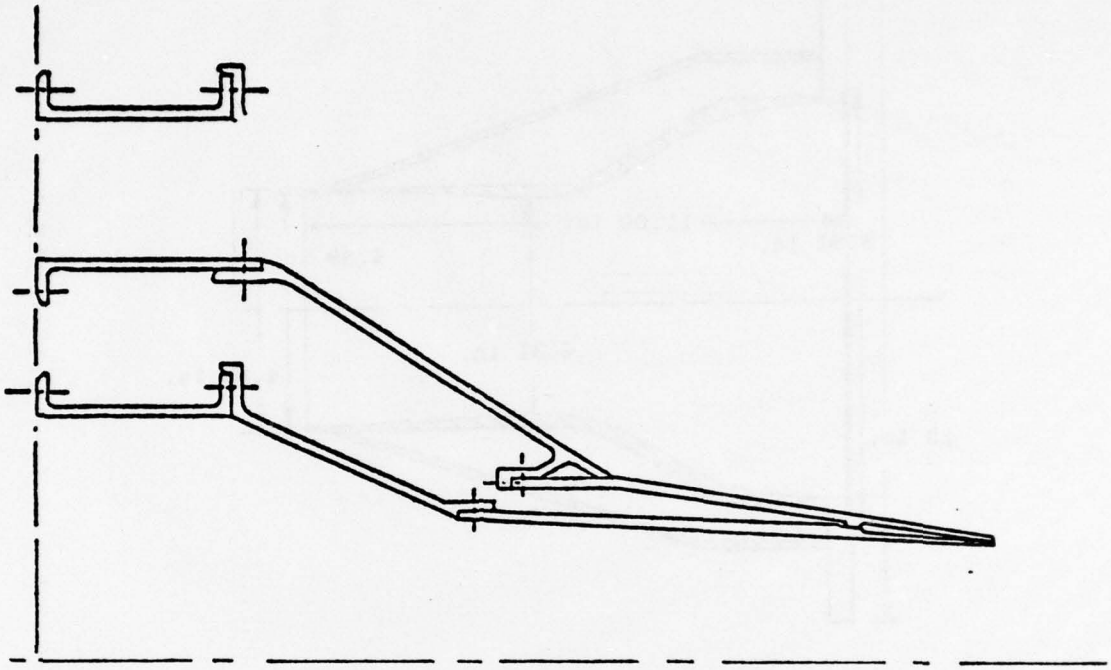


Figure 6-39. Shape of the 4.64-inch-Diameter, Baseline Coannular-Coplanar Nozzle at JENOTS.

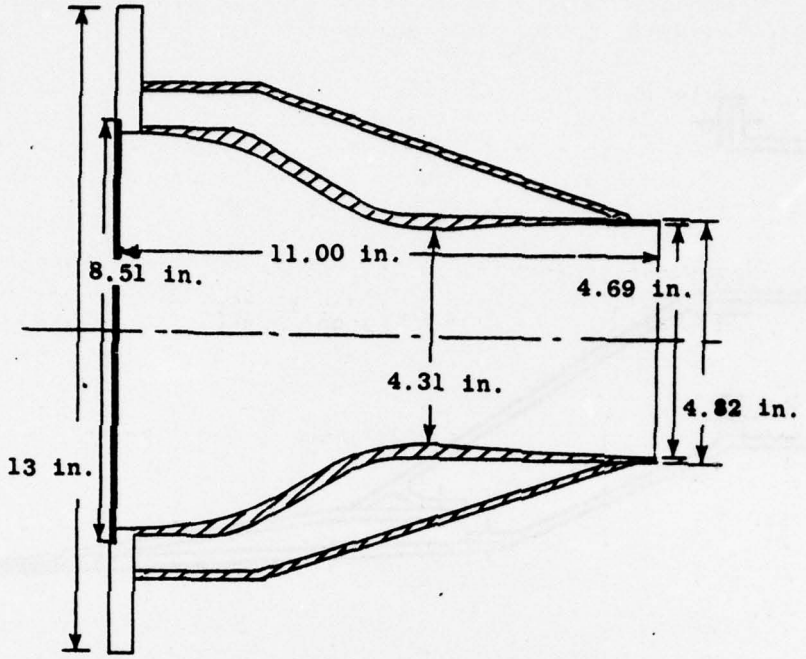


Figure 6-40. Shape of Converging/Diverging (M = 1.55) Nozzle at JENOTS.

To cover the operating range for both the single- and dual-flow facilities, data was collected at the boundary of the defined facility operating limits as shown in Figure 6-41. In addition, selective points within the operating domain were chosen for comparison with the referee data (Reference 5). Low velocity spectra comparisons below the certification limit of 600 fps can be found on Figures 4-55, 6-45, 6-53, and 6-54.

The data correlation with Lighthill's parameter is given in Figure 6-42. Most of the data appears to fit a $K = 0.5 \times 10^{-4}$ line. The points at low velocity from the 3.59-inch nozzle are somewhat higher. At supercritical velocity, the cold jet points are high because of shock noise. The C/D nozzle along the design line is seen to fall below the other points.

Excellent agreement is found with the SNECMA/NGTE correlation line for acoustic power in Figure 6-43. Some of the high velocity converging nozzle data appears high. The correlation of the 90° OASPL data is shown in Figure 6-44. Better agreement is found with Stone's suggested fit to the data. At high velocity, the JENOTS data are above the correlation line.

Spectral shape in Figure 6-45 compares favorably with the SAE AIR 876 line for cold and heated subsonic jets. The spectral shapes at constant velocity (1000 fps) shown in Figure 6-46, also appear to follow the temperature trends observed by Hoch, et al. (e.g., increasing temperature decreases the high frequencies and increases the lows at constant V_j).

Normalized power and 90° sound pressure level spectra are shown in Figures 6-47 through 6-56 for five approximately constant temperature lines (500° R, 1000° R, 1260° R, 1500° R, and 2350° R) within the operational envelope shown in Figure 6-41. The normalized power and SPL characteristics for subsonic jets are depicted in Figures 6-47, 6-48, 6-51, and 6-52. Strouhal scaling is observed for the SPL results. The PWL spectra exhibit the characteristics noted by Olsen (Reference 38) where the peak frequency is invariant with velocity and inversely proportional to jet diameter.

The remaining Figures, 6-49, 6-50, and 6-51 through 6-56, present normalized PWL and SPL spectra for velocities ranging from about 970 fps to 3075 fps. Shock noise is very apparent for the underexpanded conical nozzle plots. Figures 6-49 and 6-50 also include a comparison of a shock-free convergent-divergent nozzle with the aforementioned conical. The dramatic change in spectral shape (e.g., lack of any shock-related tones/broadband, etc.) due to the utilization of the C/D nozzle (Figures 6-49 and 6-50) is quite evident.

Figures 6-55 and 6-56 are included to illustrate that high velocity spectra (>3000 fps) from C/D nozzles appear to conform to what has been reported by Hoch, Cocking, and their colleagues (Reference 23) at somewhat lower jet velocities.

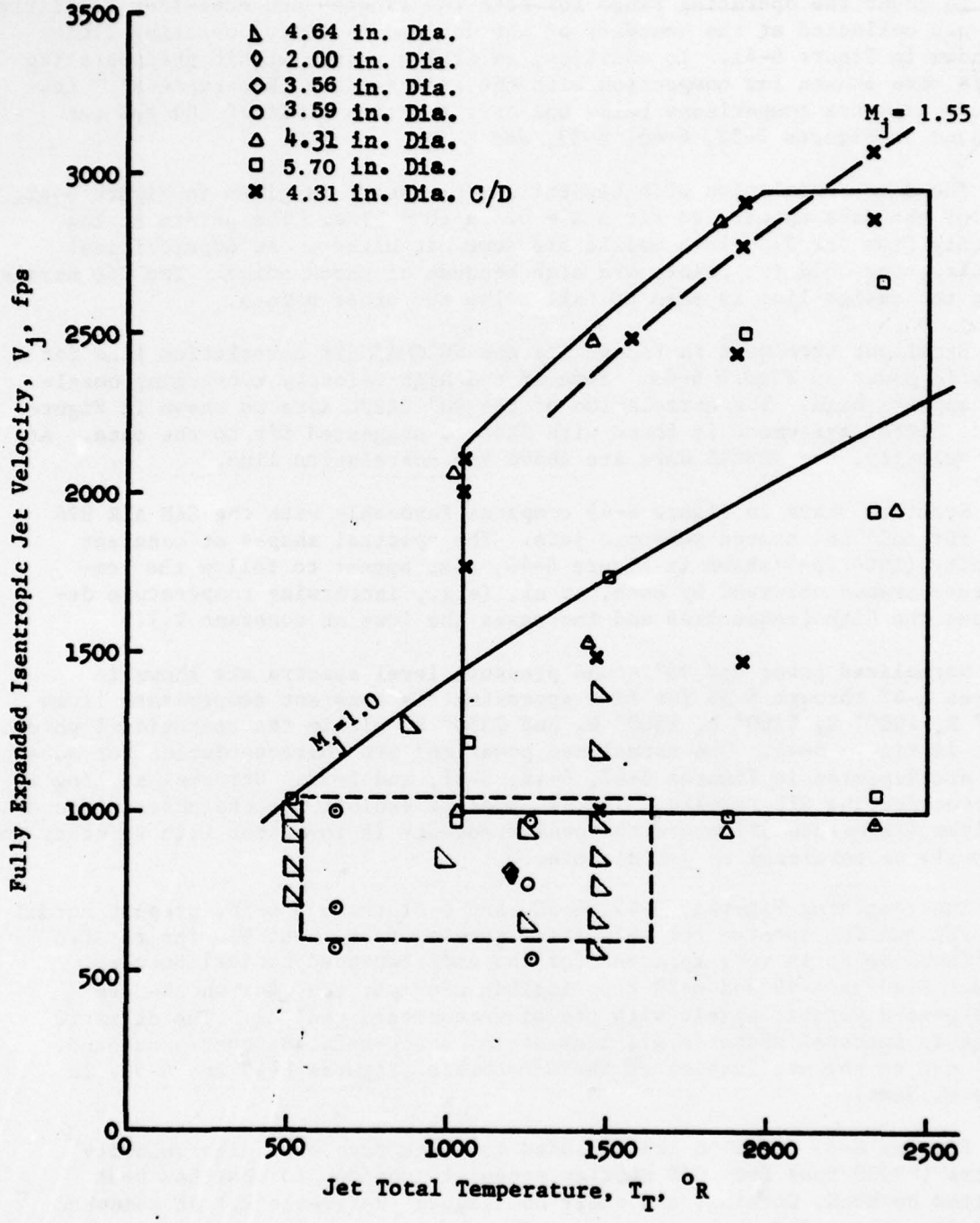


Figure 6-41. Domain of Aerodynamic Operation for JENOTS.

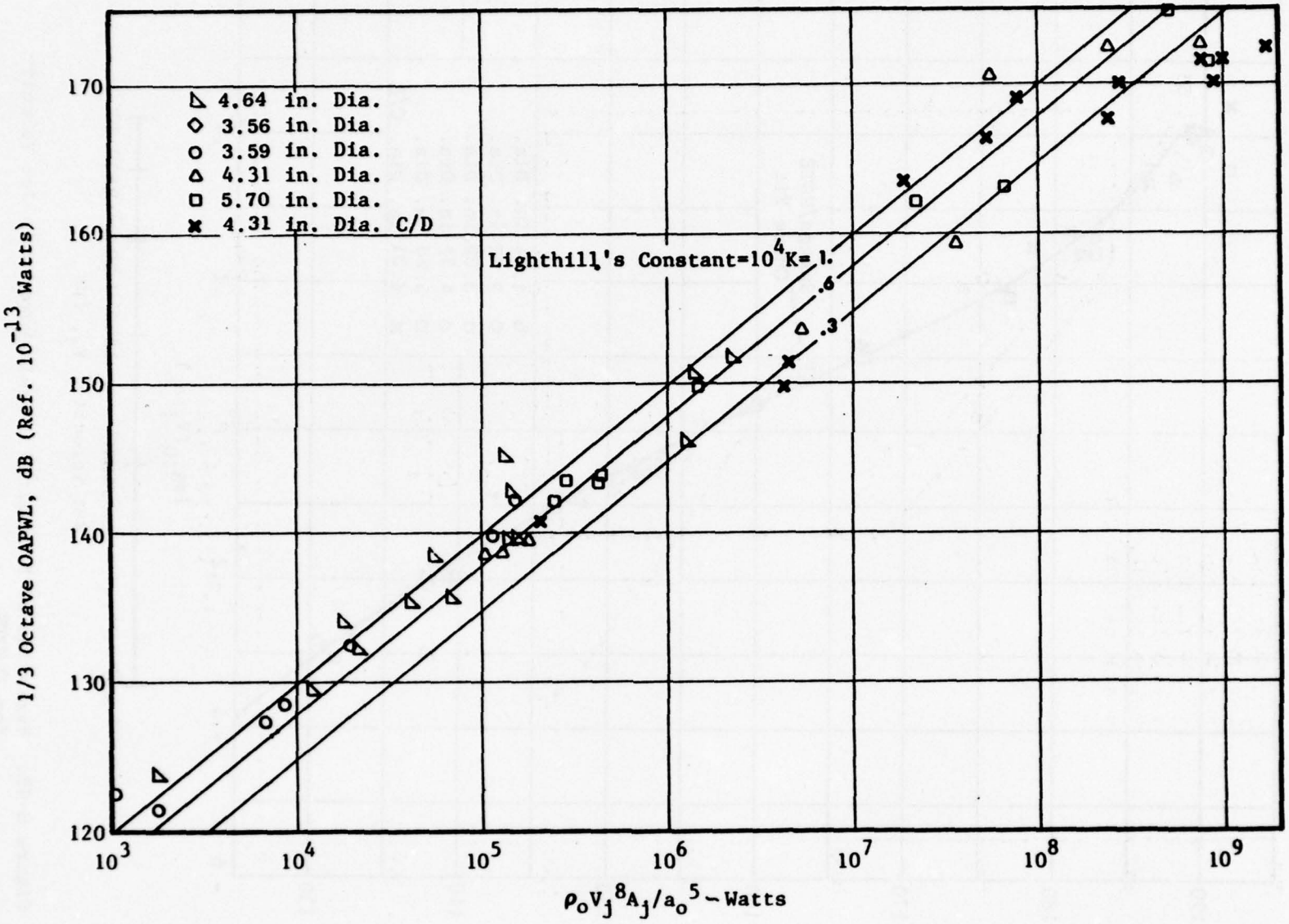


Figure 6-42. Variation of Overall Power Spectra with Lighthill's Parameter for JENOTS.

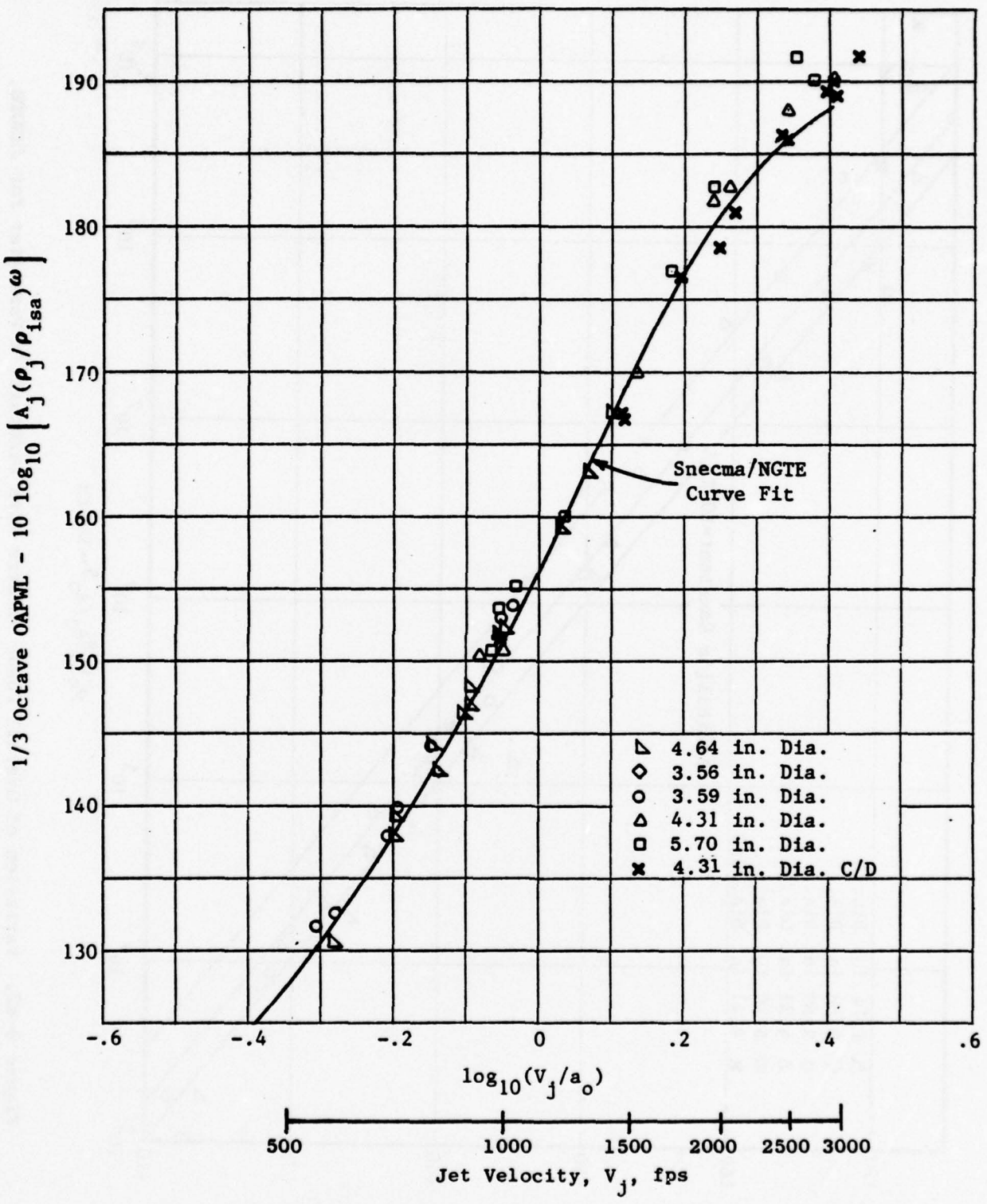


Figure 6-43. Variation of Normalized Overall Power with Jet Velocity for JENOTS.

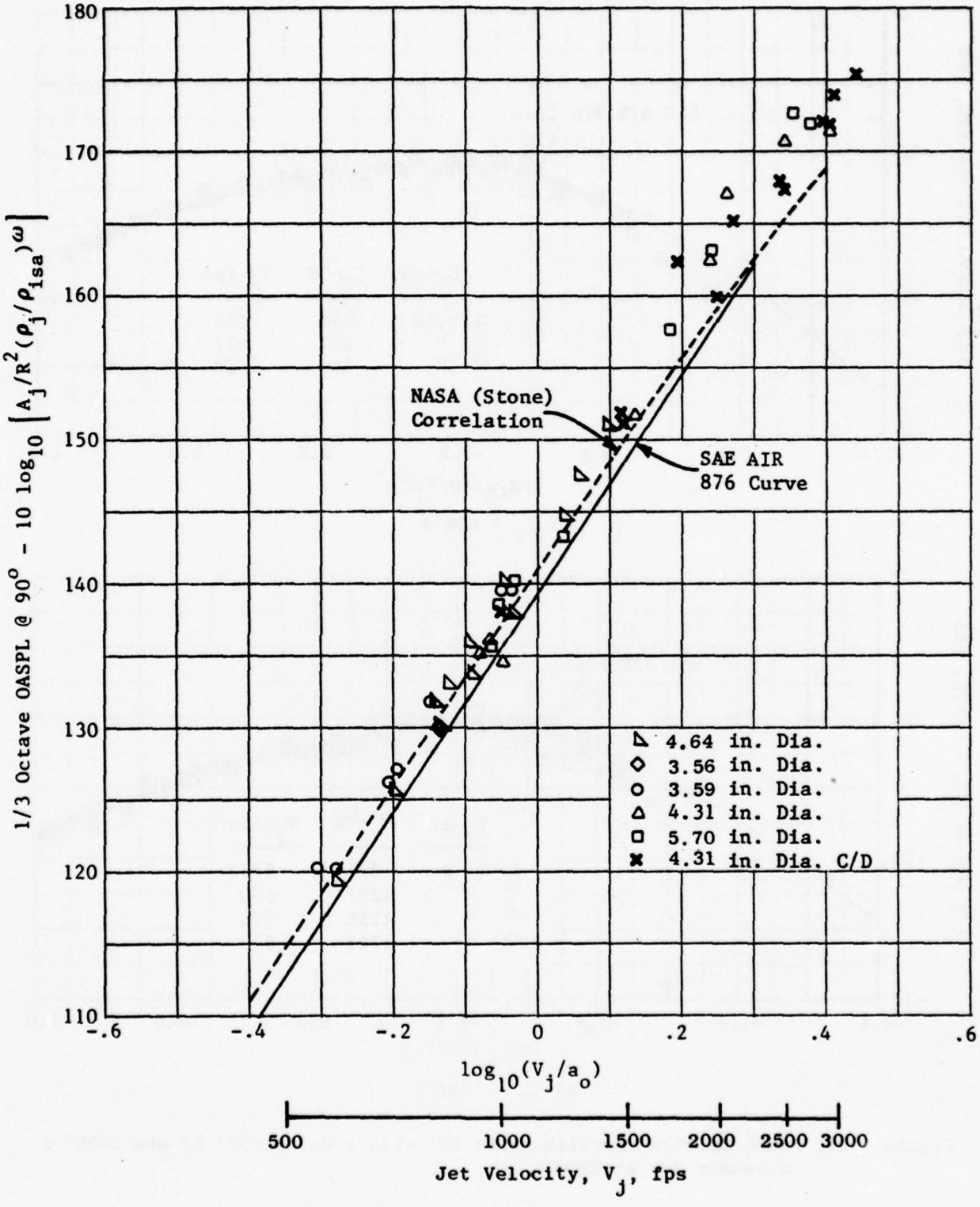
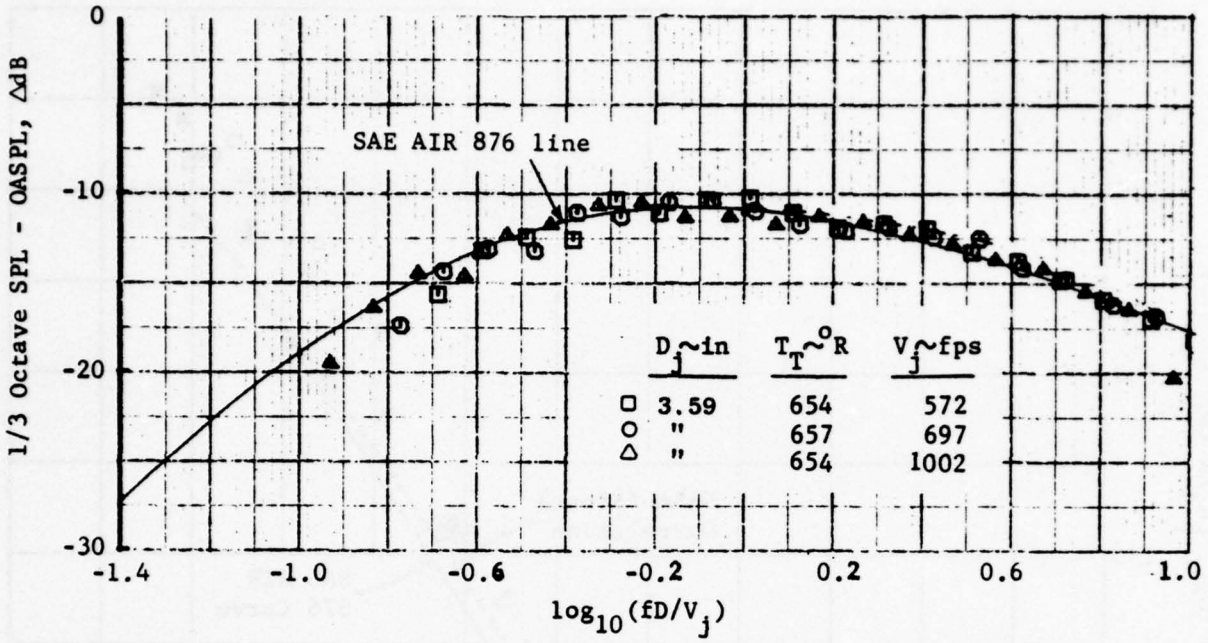
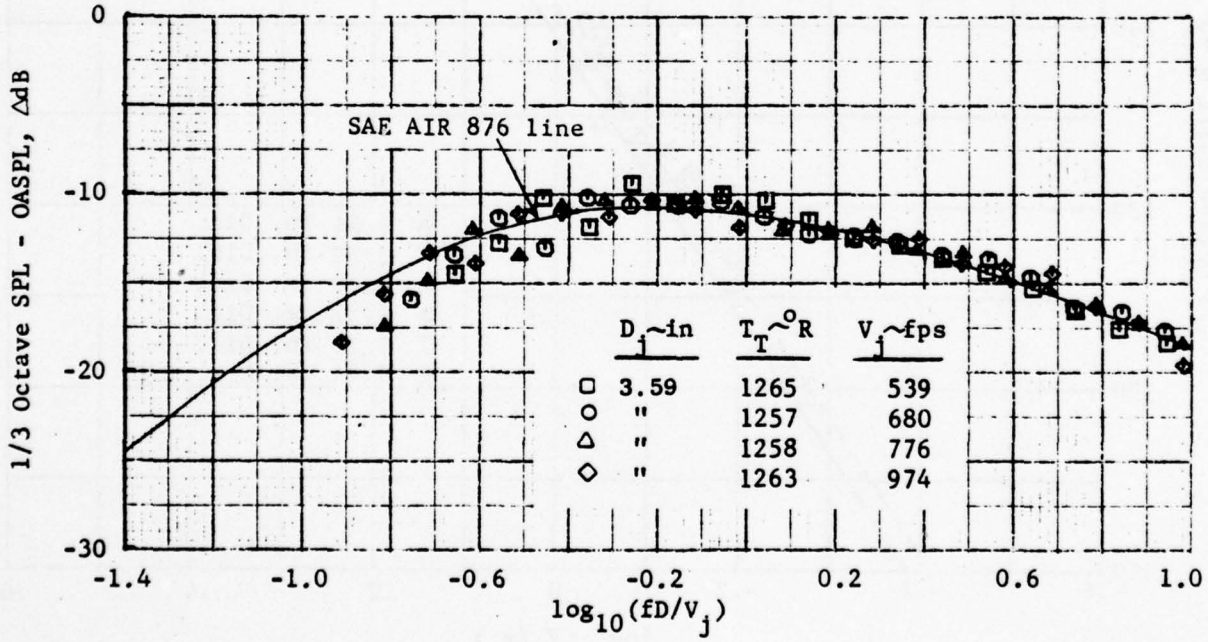


Figure 6-44. Velocity Dependence of Normalized Overall Sound Pressure Level at 90° for the JENOTS Data.



a) T_T = 650°R



b) T_T = 1260°R

Figure 6-45. ΔSPL Spectra Correlation at 90° with a Cold (650° R) and 1260° R Subsonic Jet at JENOTS.

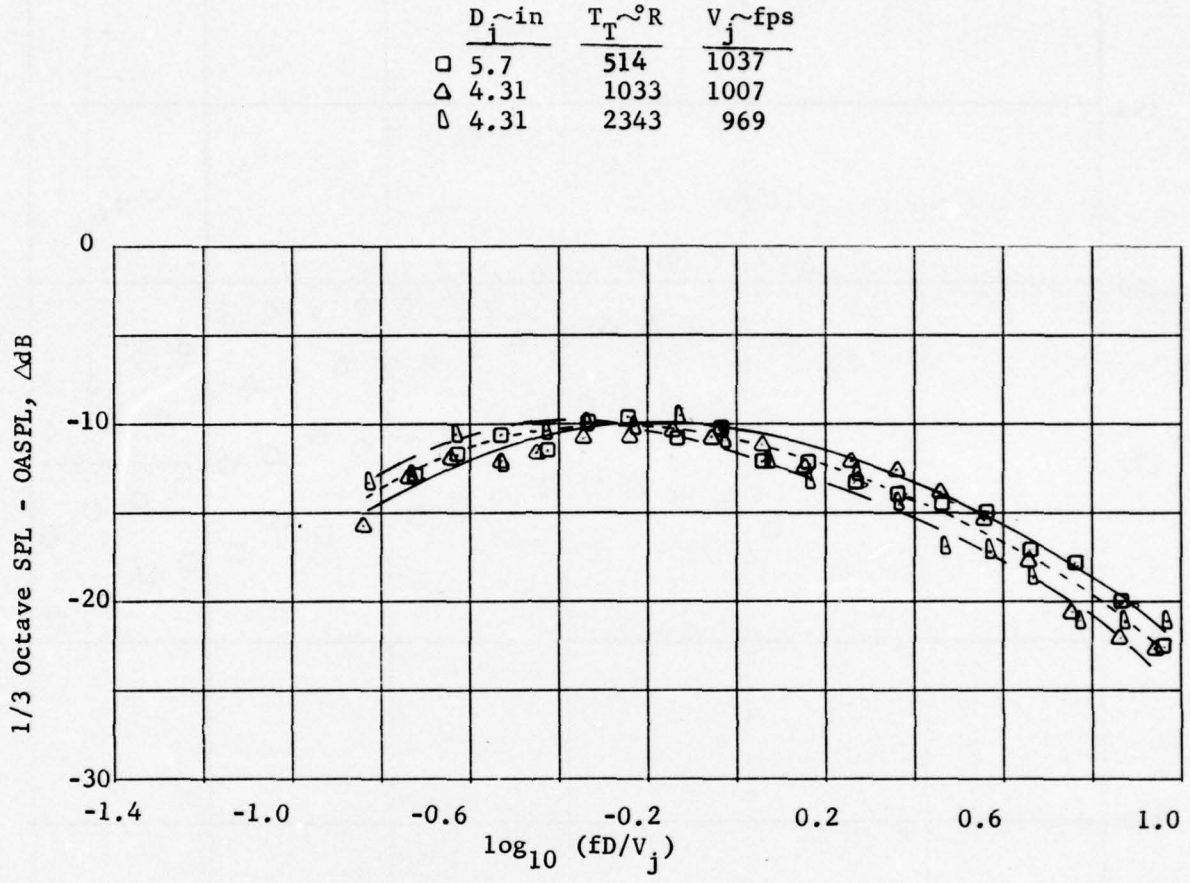


Figure 6-46. ΔSPL Spectra at 90° for Subsonic ($V_j \sim$ 1000 ft/sec) Heated Jets at JENOTS.

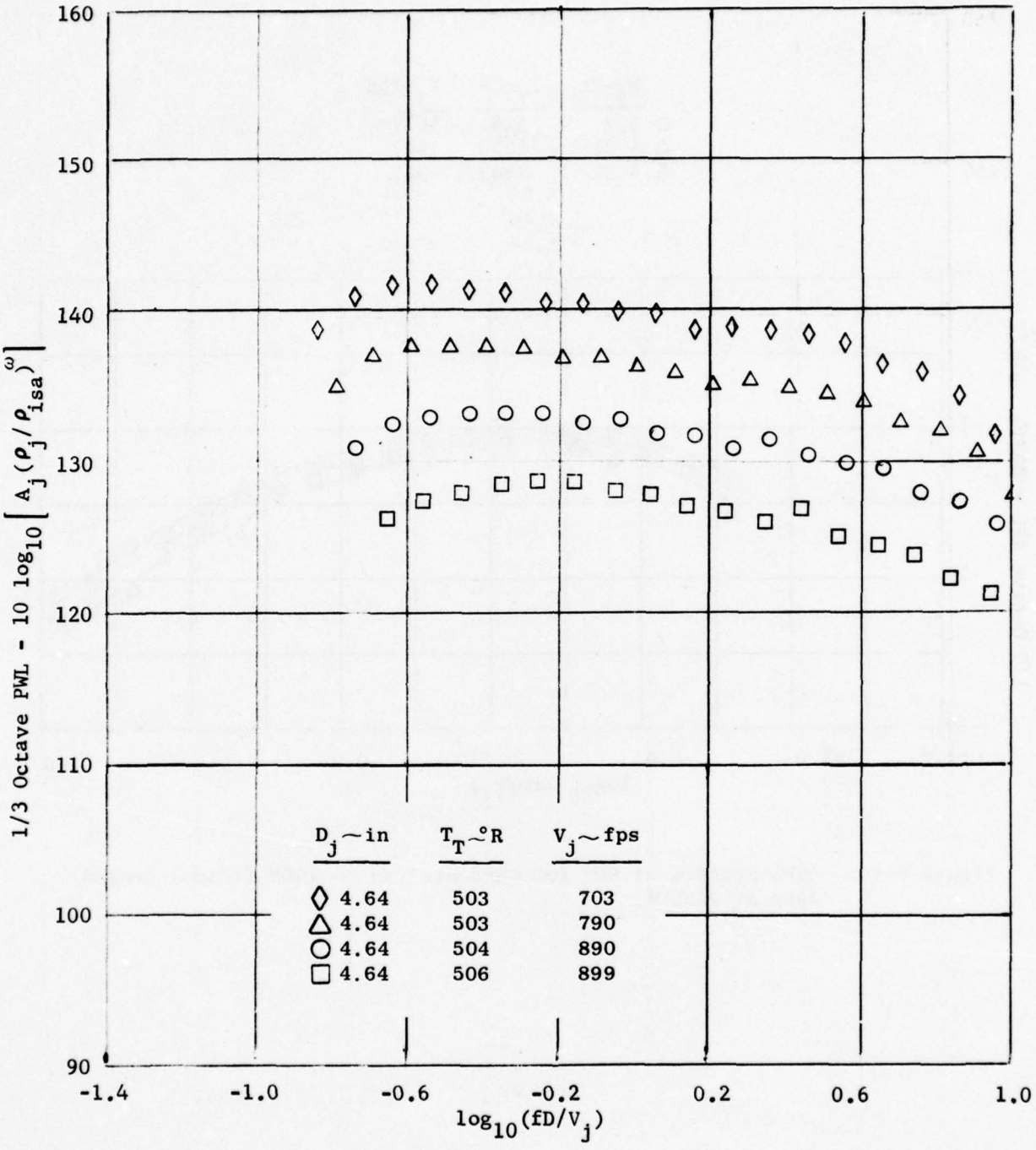


Figure 6-47. Normalized Power Spectra for Subsonic Cold (500° R) Jet at JENOTS.

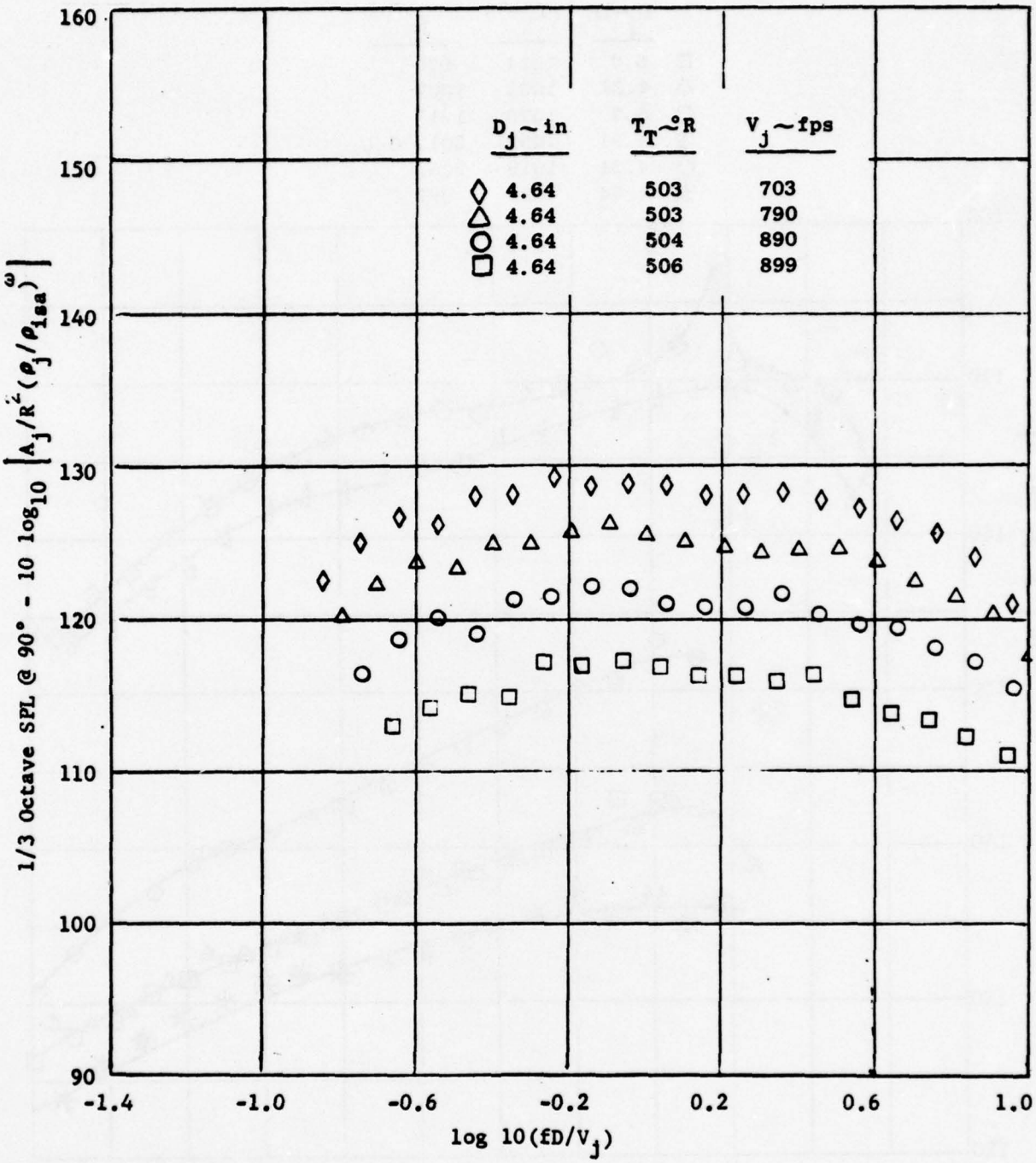


Figure 6-48. Normalized SPL Spectra at 90° for Subsonic Cold (500° R) Jets at JENOTS.

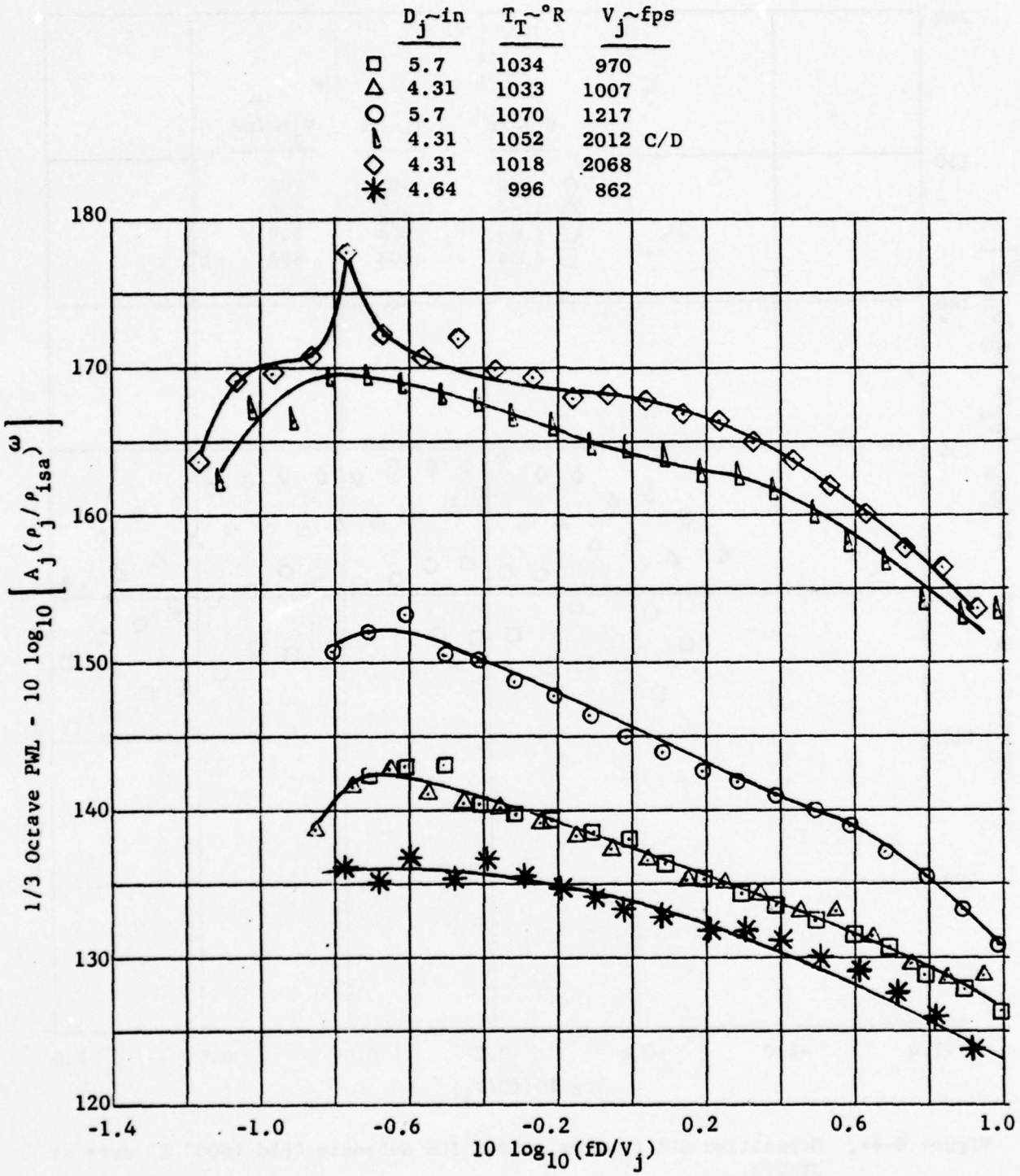


Figure 6-49. Normalized Power Spectra at JENOTS with Jets Heated to 1000° R.

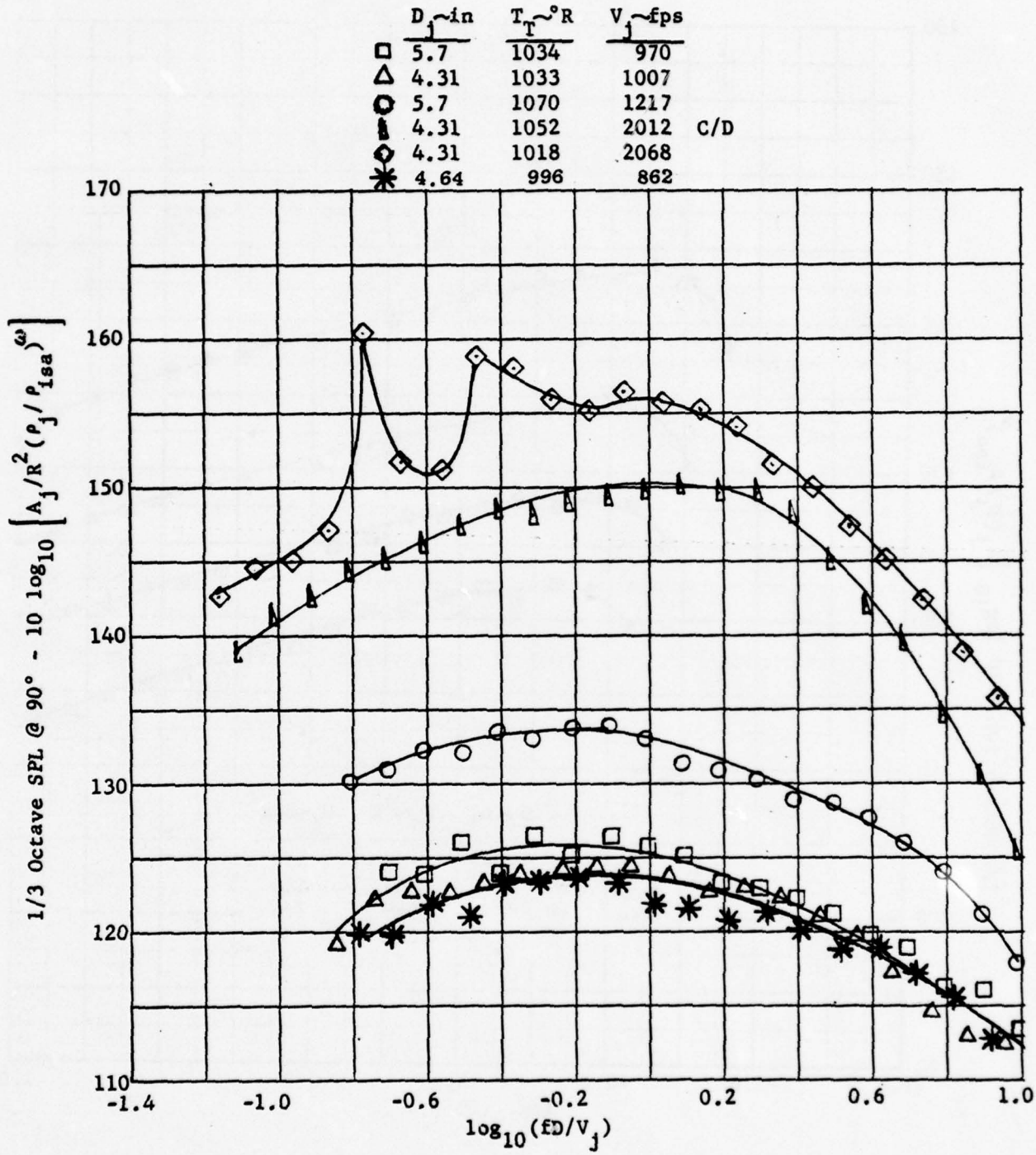


Figure 6-50. Normalized 90° SPL Spectra at JENOTS with Jets Heated to 1000° R.

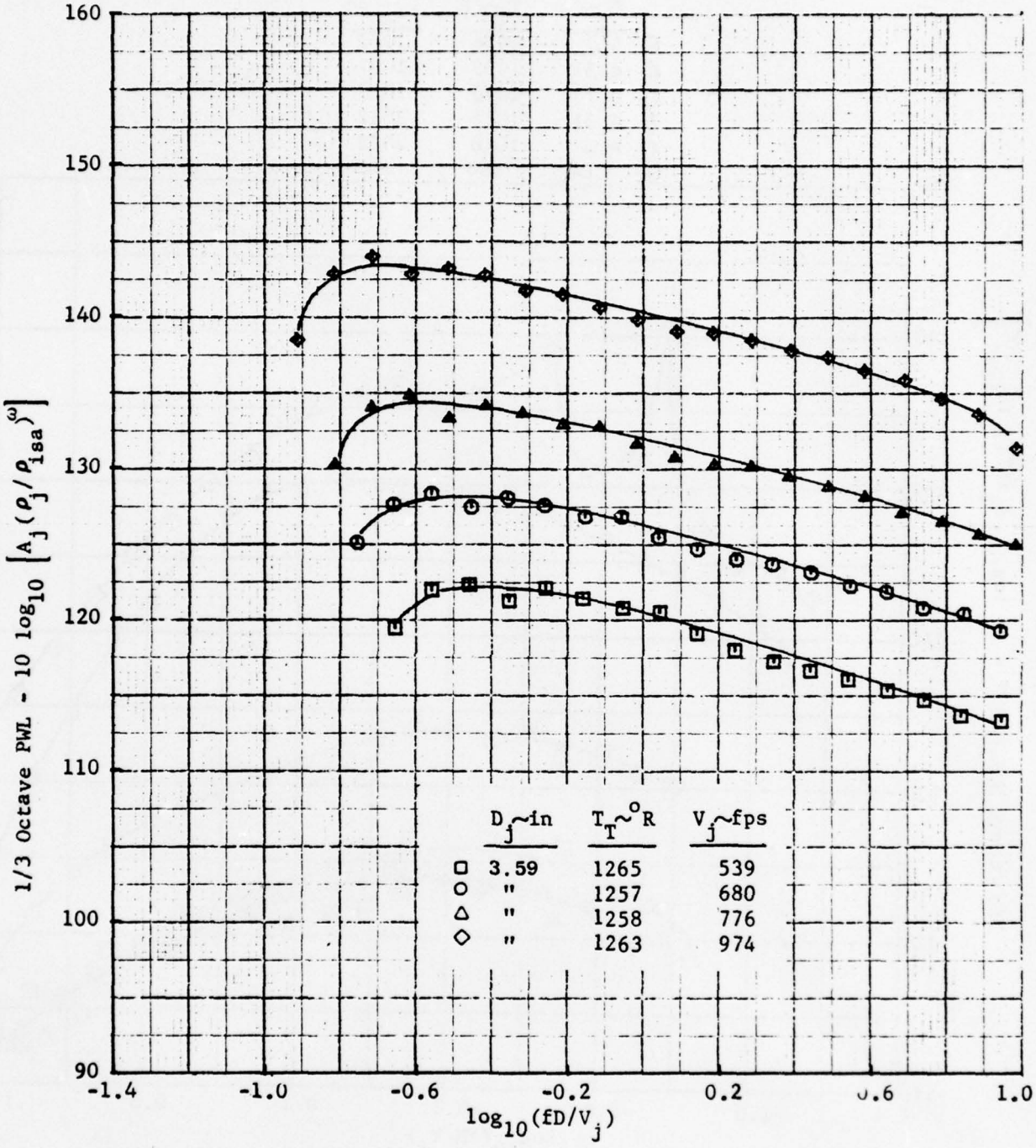


Figure 6-51. Normalized Power Spectra for Subsonic Jets at JENOTS Heated to 1260° R.

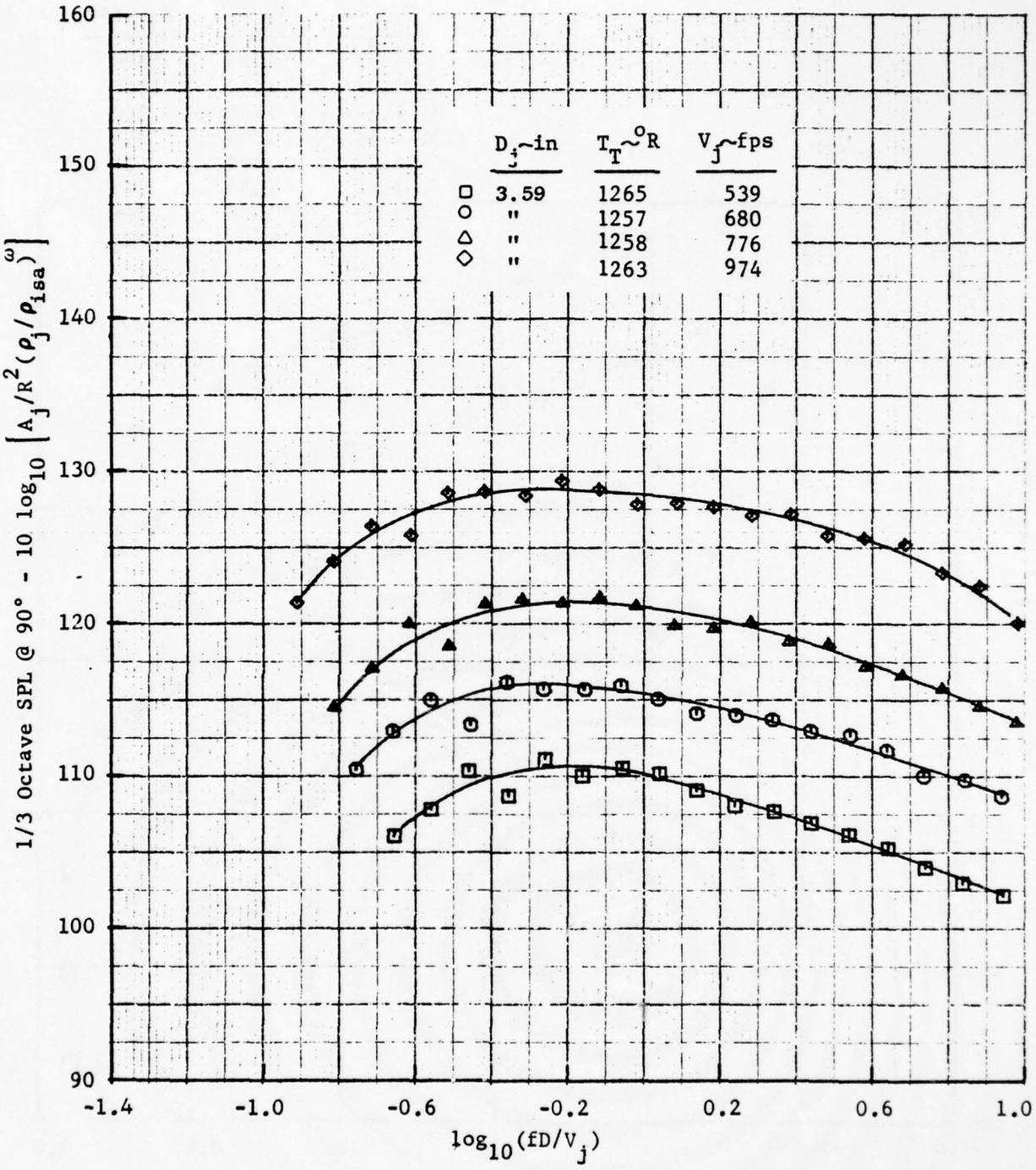


Figure 6-52. Normalized SPL Spectra at 90° for Subsonic Jets at JENOTS Heated to 1260° R.

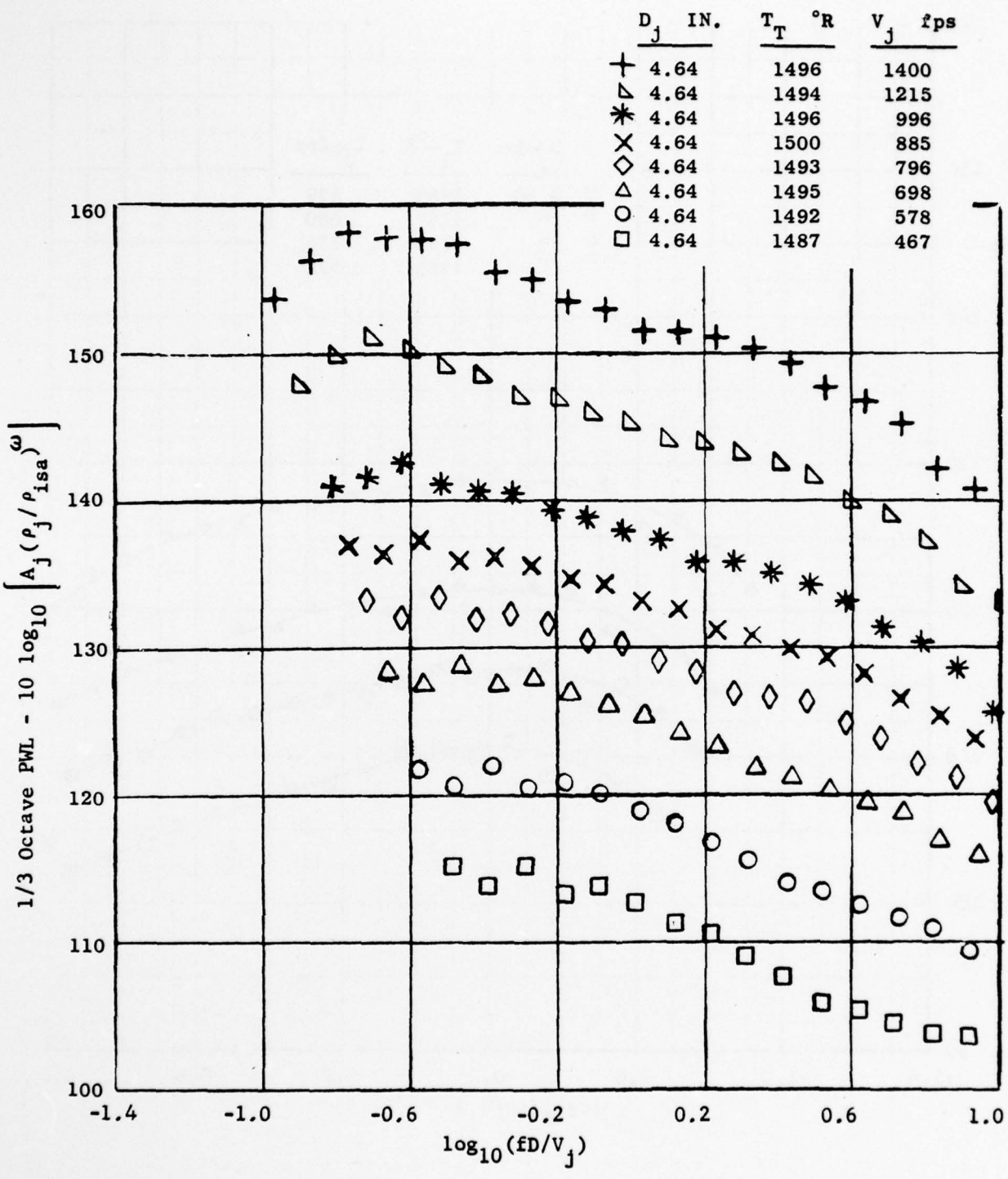


Figure 6-53. Normalized Power Spectra at JENOTS with Jets Heated to 1500° R.

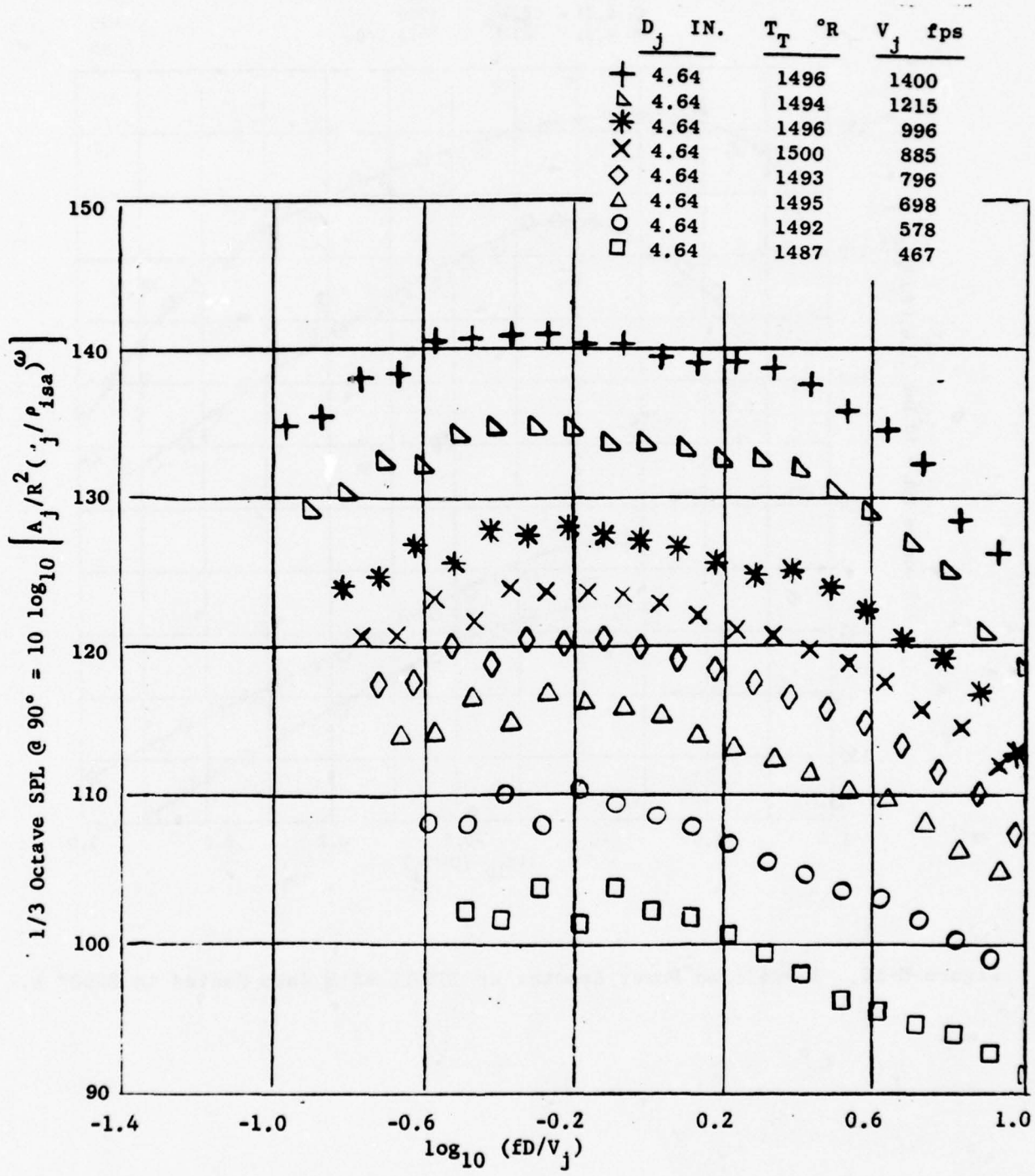


Figure 6-54. Normalized 90° SPL Spectra at JENOTS with Jets Heated to 1500° R.

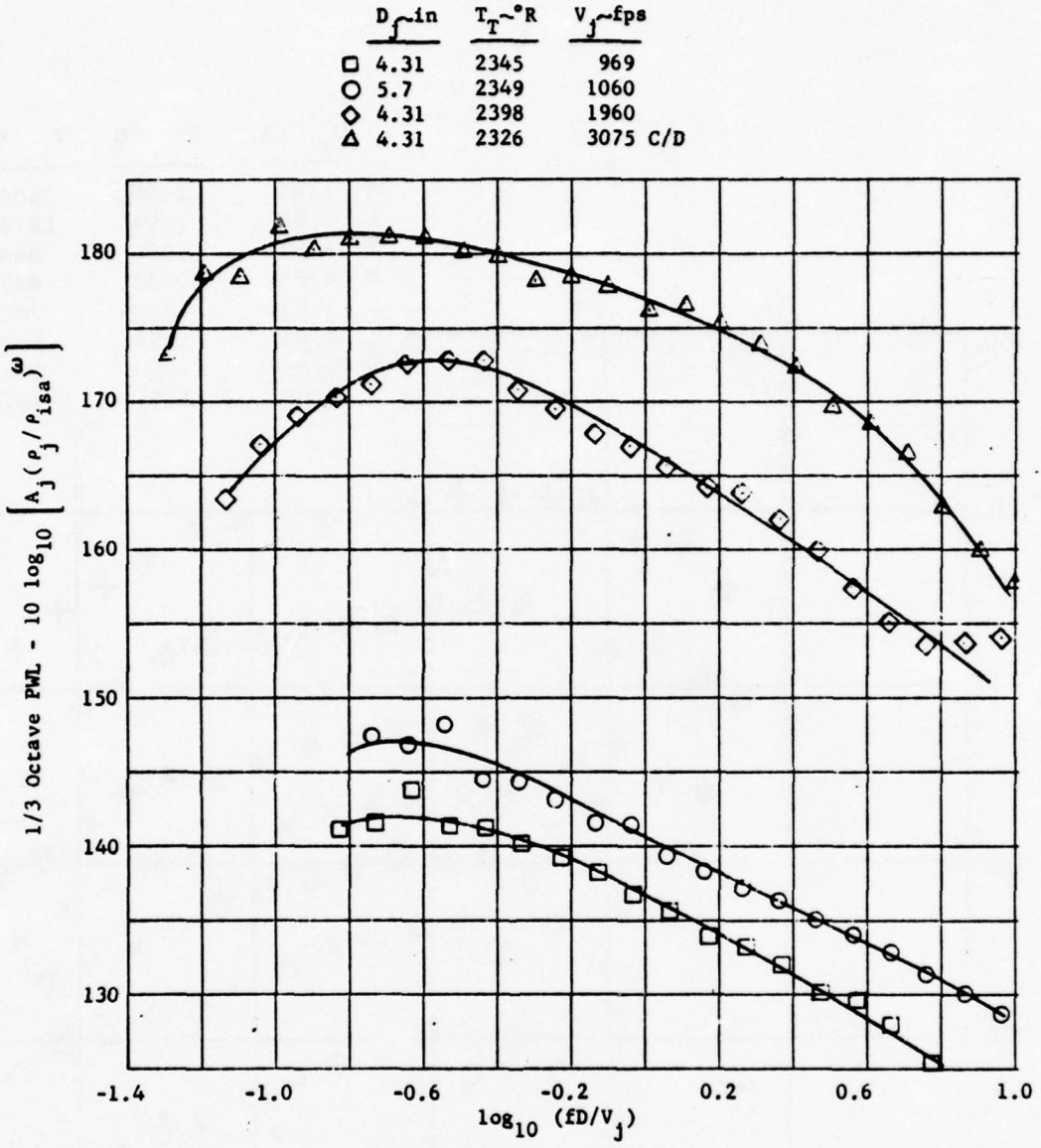


Figure 6-55. Normalized Power Spectra at JENOTS with Jets Heated to 2350° R.

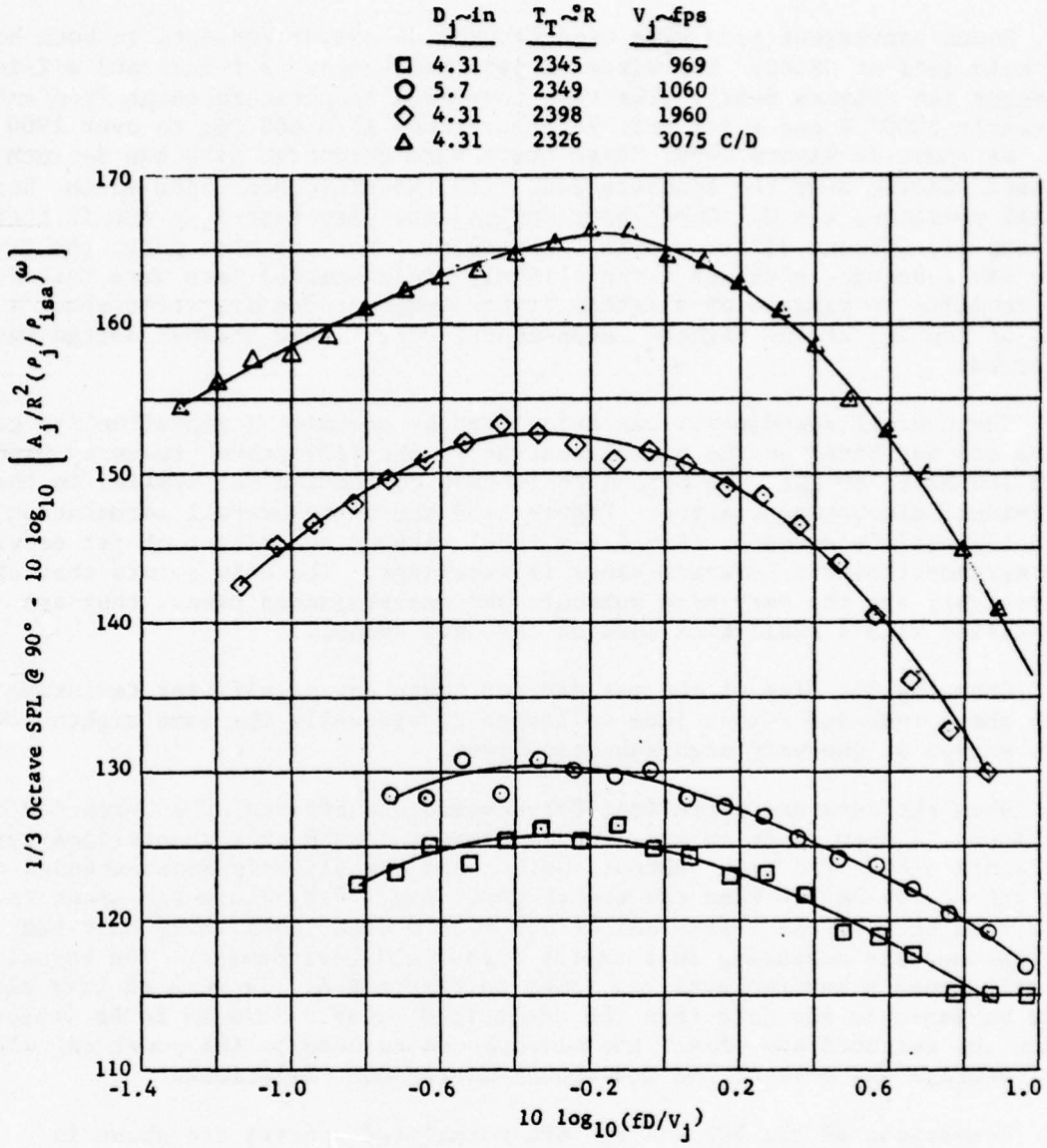


Figure 6-56. Normalized 90° SPL Spectra with Jets Heated to 2350° R.

6.5 CERTIFICATION AT CR&DC

Round convergent jets were used to provide comparison data on both hot and cold jets at CR&DC. Two sizes of jets were used: a 1-inch and a 2-inch-diameter jet (Figure 6-57). The test covered a temperature range from ambient to nearly 2000° R and a jet exit velocity range form 600 fps to over 1900 fps, as shown in Figure 6-58. These tests were conducted with the 8- inch acoustic lining over the concrete pad, with the microphone boom in the horizontal position, $\psi = 0$. Other boom angles were also tested to see if there was any significant difference in the results. For the most part, the jet flow was subsonic, although a few slightly underexpanded jets were tested. The facility is capable of slightly higher temperatures as, after about 1 hour of running at the highest temperature, very little thermal damage was observed.

The overall sound power was calculated by assuming a nonreflective ground plane and was based on the signal content in the 1/3-octave frequency bands from 100 Hz to 40 kHz. No ground reflection correction was applied to the individual microphone spectra. Figure 6-59 shows the overall correlation with Lighthill's equation ($K = 0.6 \times 10^{-4}$) without the effect of jet density. The agreement over a 5-decade range is excellent. The only points that diverge appreciably are the very high subsonic and underexpanded cases, they are identified with a small tick mark on the data symbol.

Changing the size of the jet did not cause any significant deviation as both the 1-inch and 2-inch jets collapsed to virtually the same eighth power law, except at the very high subsonic flows.

When the data are normalized for temperature effects, the corrected overall power is seen to be in excellent agreement with Hoch's generalized curve in Figure 6-60. The high subsonic points and the slightly underexpanded cases fit this curve better than the eighth power law. Very close agreement is also seen between the 1-inch and 2-inch nozzle data, confirming that the microphones are measuring in a nearly free-field environment. The normalized overall sound pressure level, as shown in Figure 6-61, is seen to have slightly more variance in the data than the normalized power. This is to be expected, since the weighted sum of all the microphones as used in the power calculation will average out some of the individual microphone variations.

Comparison of the PWL and 90° SPL normalized spectra are shown in Figures 6-62 and 6-63, respectively. The low velocity data is in good agreement with the others except for some variations below 400 Hz caused by ground reflections. However, the data at the high subsonic velocity exhibit too high a level below 1600 Hz. This could be the result of the near sonic flow conditions. Hoch found substantial changes in the rear arc, as the jet flow became underexpanded.

The normalized power spectrum of heated jets at two different temperatures is shown in Figures 6-64 and 6-65 for a range of jet velocities. The slight shift of the lower spectral peak Strouhal numbers as the velocity is lowered agrees with the hot jet data of Hoch (Reference 2).

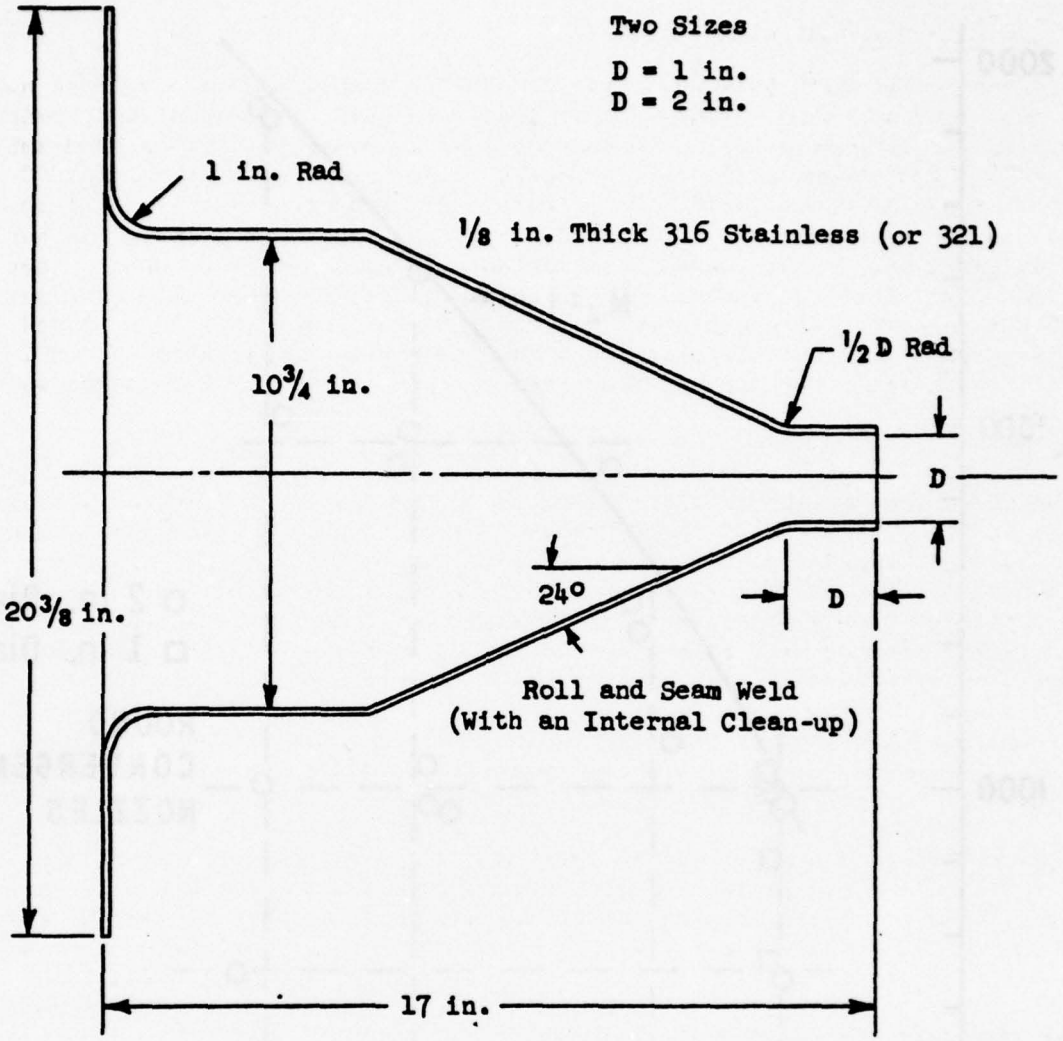


Figure 6-57. Certification Nozzle at CR&DC (D = 1 and 2 inches).

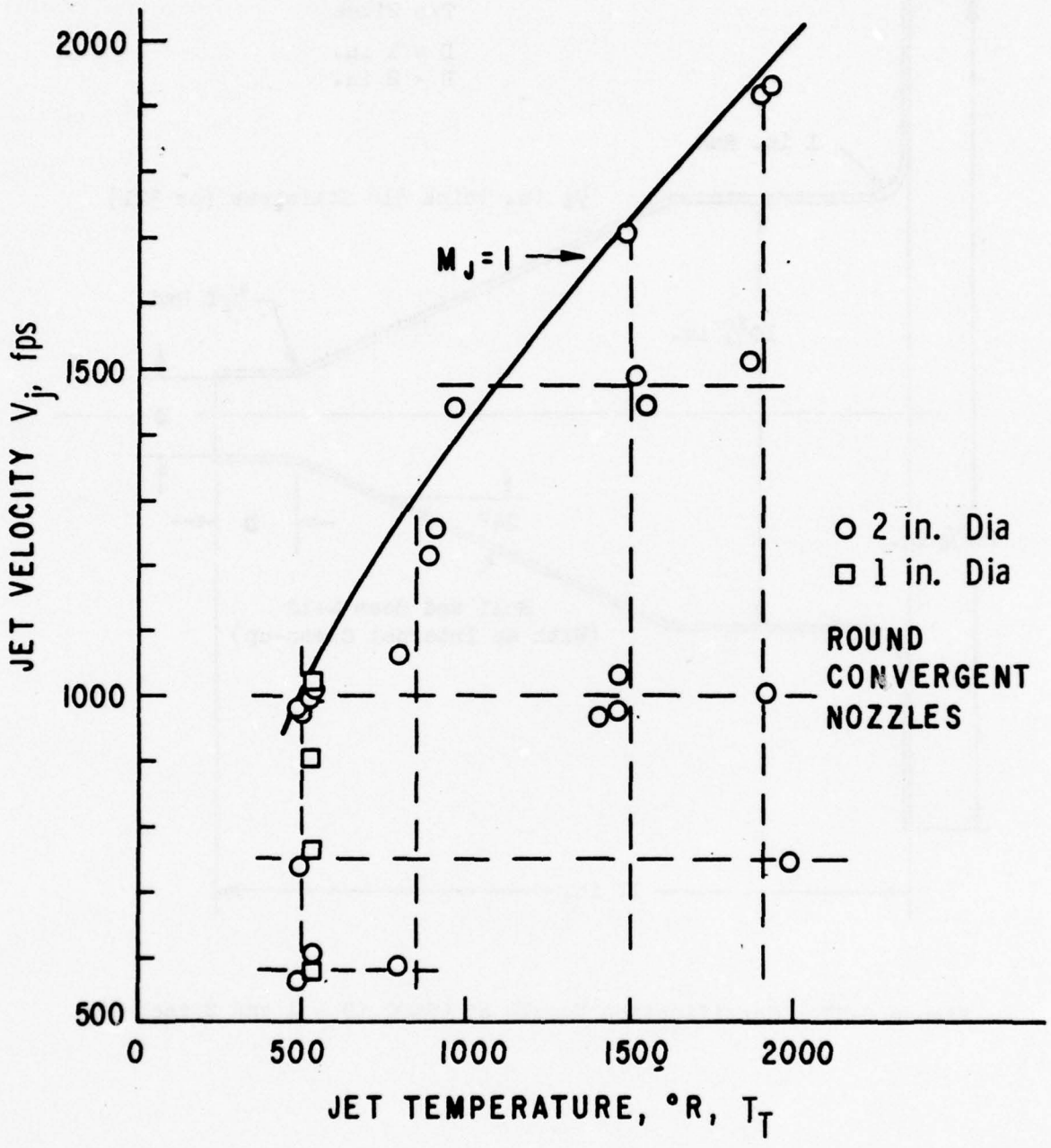


Figure 6-58. Domain of Operation for GE/CR&DC.

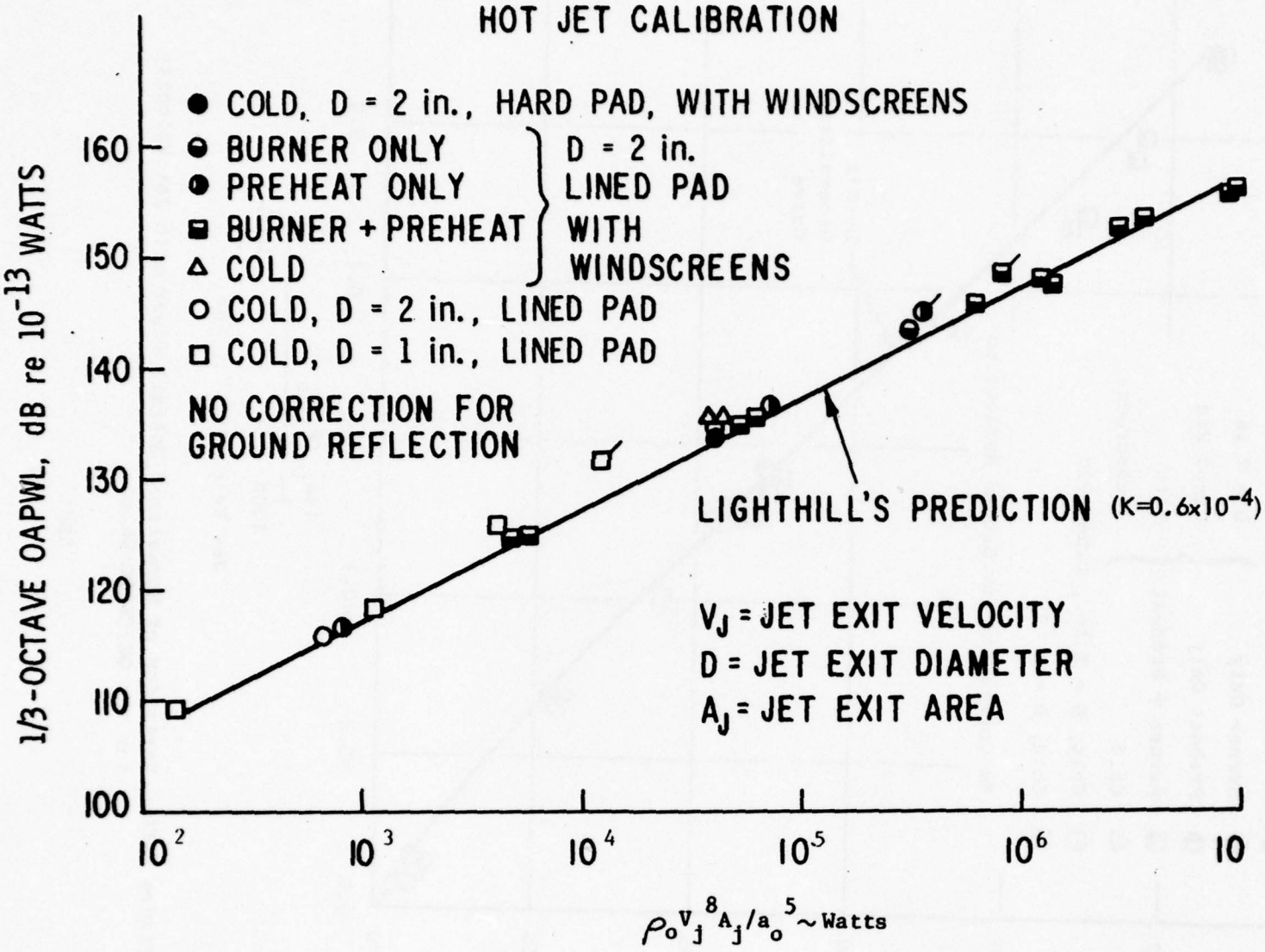


Figure 6-59. Variation of Overall Power with Lighthill's Parameter for the GE/CR&DC Data.

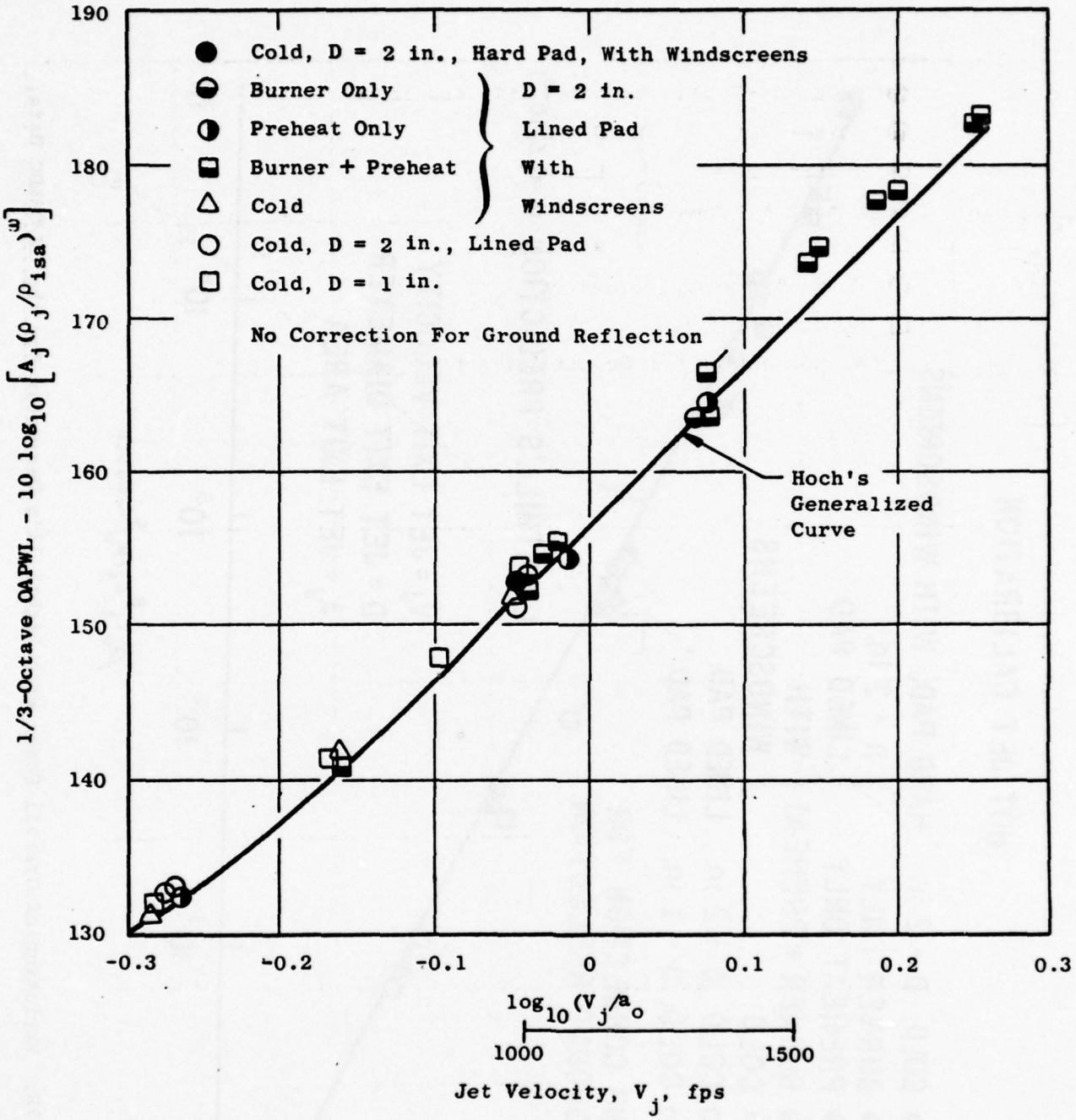


Figure 6-60. Variation of Normalized Overall Power with Jet Velocity for the GE/CR&DC Data.

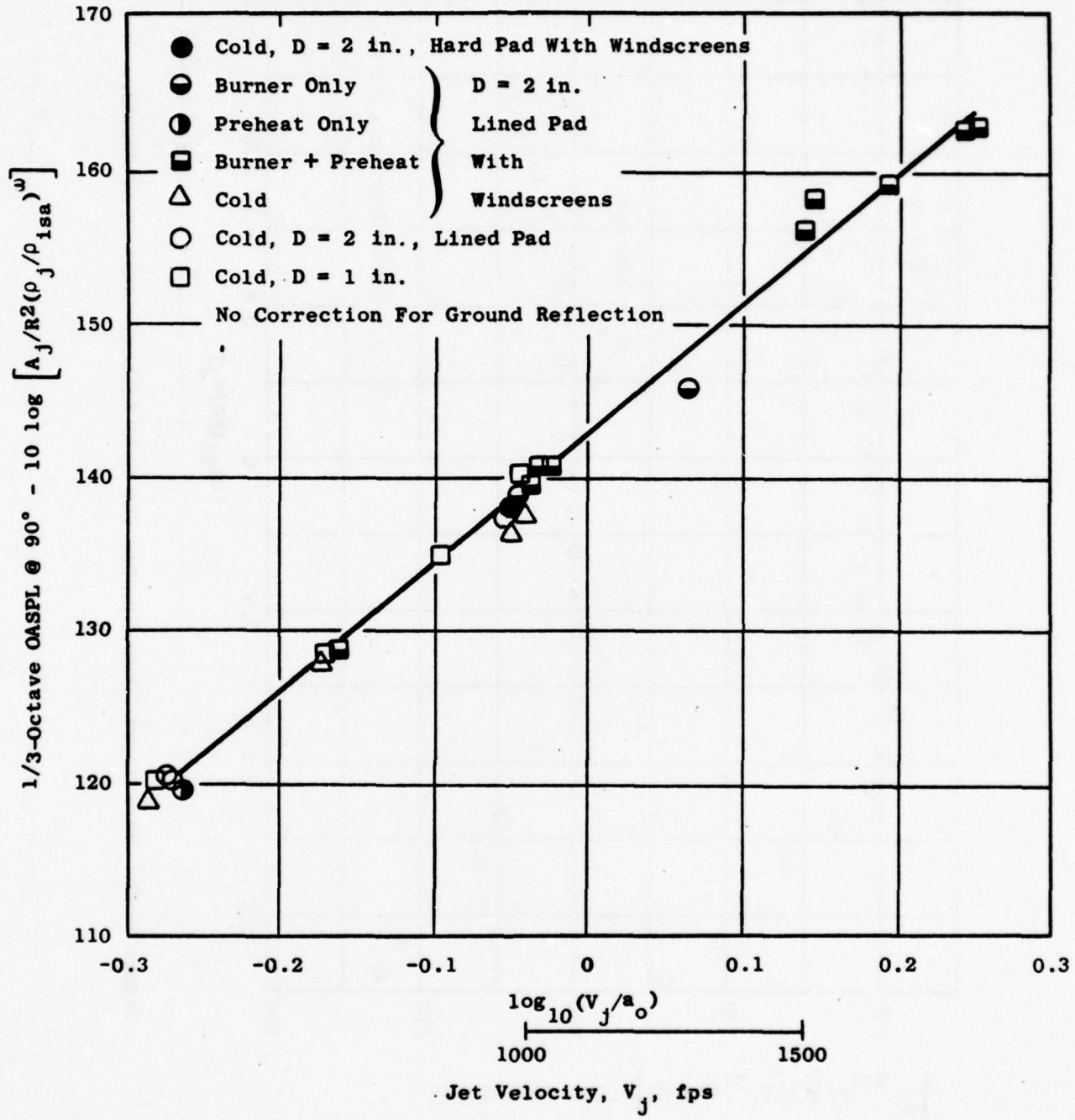


Figure 6-61. Velocity Dependence of Normalized OASPL at 90° for the GE/CR&DC Data.

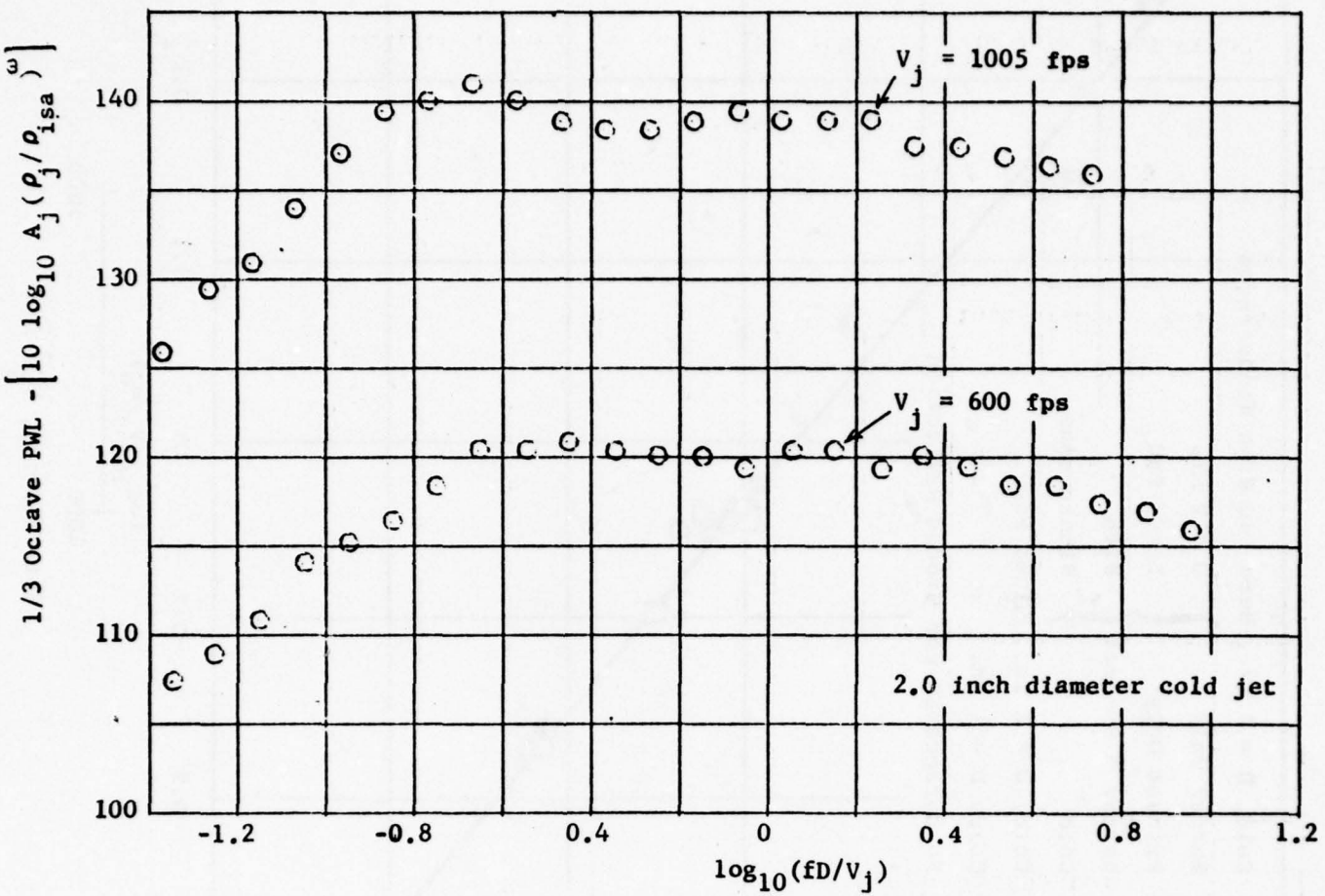


Figure 6-62. Normalized Power Spectra for Cold Subsonic Jets at GE/CR&DC.

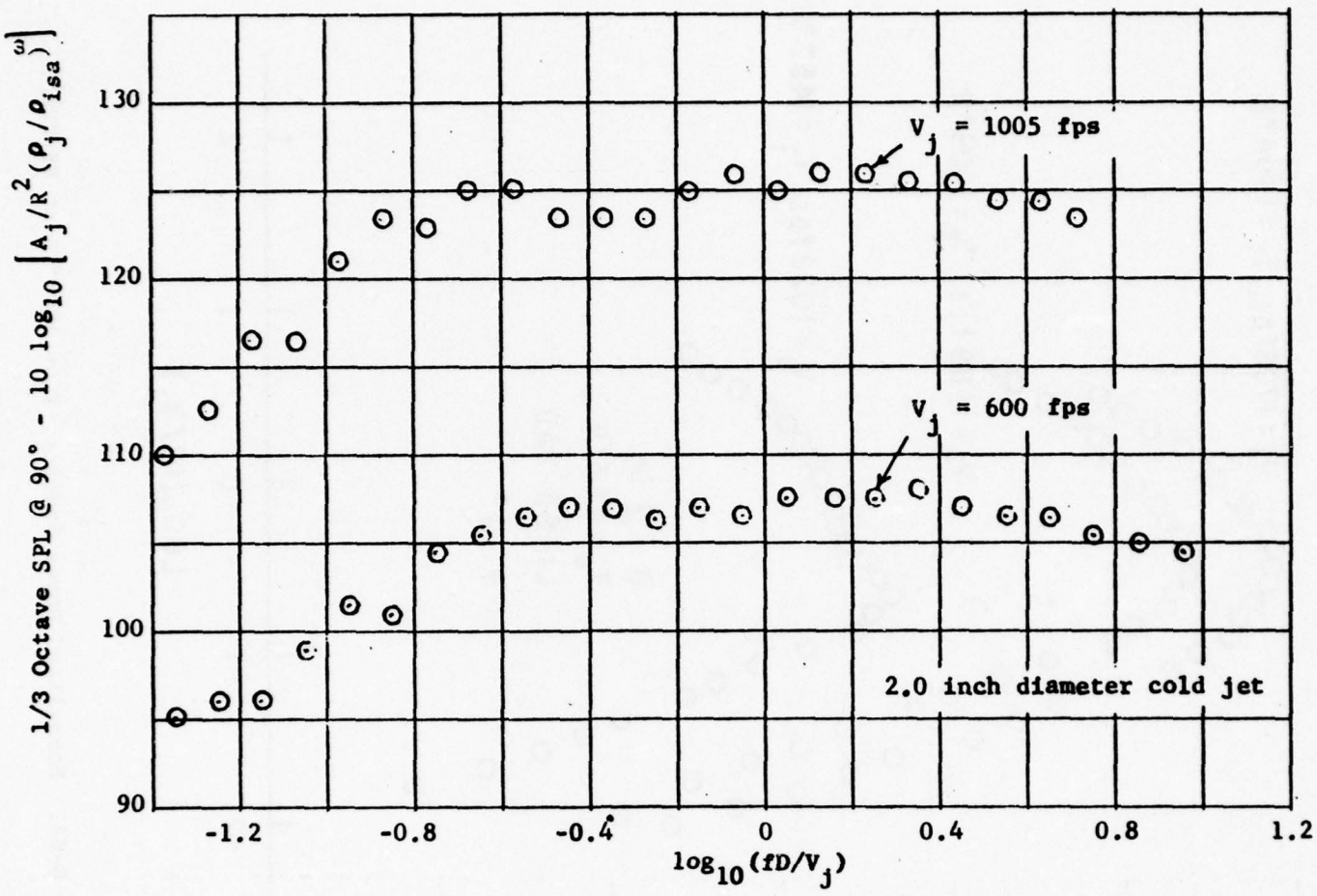


Figure 6-63. Normalized SPL Spectra at 90° for Subsonic Cold Jets at GE/CR&DC.

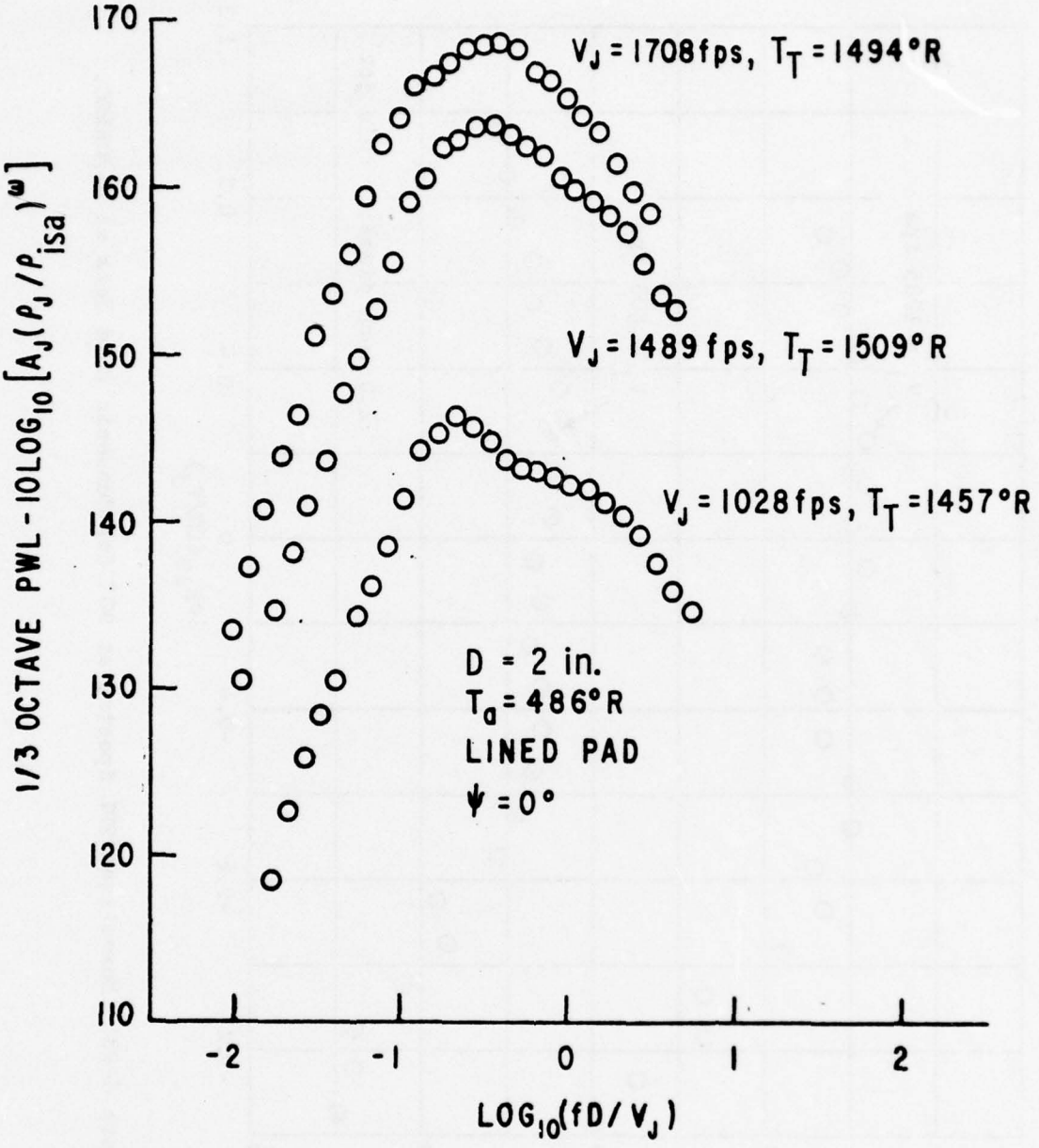


Figure 6-64. Normalized Power Spectra, $T_T \sim 1500°$ R at GE/CR&DC.

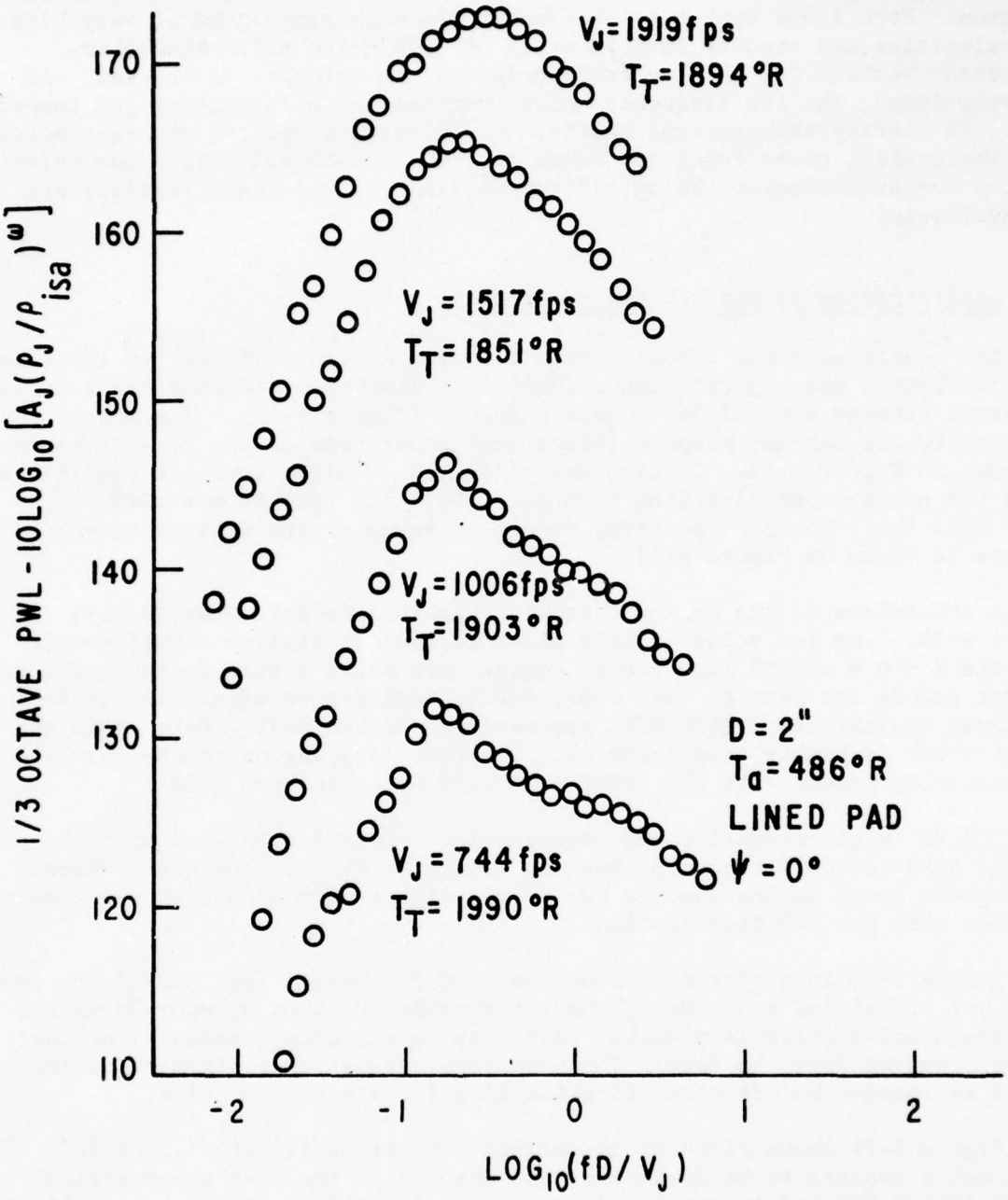


Figure 6-65. Normalized Power Spectra, $T_T \sim 1900°$ R at GE/CR&DC.

Heating a jet at a constant velocity will cause a change in the noise spectrum. Hoch found that this phenomenon was more pronounced at very high jet velocities and results in a lowering of levels for all frequencies. This trend weakens for the low frequencies as the velocity is lowered. At low velocities, the low frequency noise increases with increasing jet temperature. To clarify the spectral shifts, the 1/3-octave spectra are subtracted from the overall power level and shown in Figures 6-66 and 6-67. Low velocity spectra comparison below the certification limit of the CR&DC facility are not available.

6.6 CERTIFICATION OF THE J79 ENGINE AT GE/EFTC

The nozzle used for acoustic certification checkout of the J79 installation at GE/EFTC was conical with a 20.84-inch discharge diameter for a nominal geometric exhaust area of 341.1 square inches (Figure 6-68). The nozzle was attached to the exhaust adapter flange just downstream of the P_T - T_T rakes as shown in Figure 3-32. Testing was conducted at eight throttle conditions along the engine operating line from idle (V_j = 500 fps) to max power (V_j = 2150 fps). The J79 operating domain in terms of the exhaust conditions is shown on Figure 6-69.

A comparison of the engine data with Lighthill's parameter is shown in Figure 6-70. The low velocity idle point is seen to diverge significantly from the $K = 0.6 \times 10^{-4}$ line due to engine core noise contamination. The two highest points are seen to curl over, due to temperature effects. The data are shown against the SNECMA/NGTE parameter in Figure 6-71. Here again the lowest point is higher than expected. The remaining engine points show remarkable agreement with the SNECMA and NGTE anechoic room data.

The 90° angle overall sound pressure level correlation with both the SAE and NASA (Stone) lines are shown in Figure 6-72. At supersonic velocity, the highest speed points diverge due to the significant amount of shock noise obtained with the J79 installation.

Figure 6-73 is a plot of 1/3-octave band PWL versus log (fD/V_j) for the eight jet velocities run. Here, the top five speeds show an up turn in the high frequencies which is probably caused by an electronic noise floor that was not removed from the data. These spectra suggest that air attenuation should be removed before correcting the data for electronic noise.

Figure 6-74 shows plots of normalized SPL versus log (fD/V_j) at 90°. The shock noise appears to be distorting the spectra in the near-supercritical region ($M_j \approx 0.95$) and increasing from there. The 90° angle appears to be an intermediate point between the shock noise dominated front angles, such as the 60° data shown in Figure 6-75, and the pure jet mixing noise spectra near the jet axis, as shown by the 120° spectra in Figure 6-76.

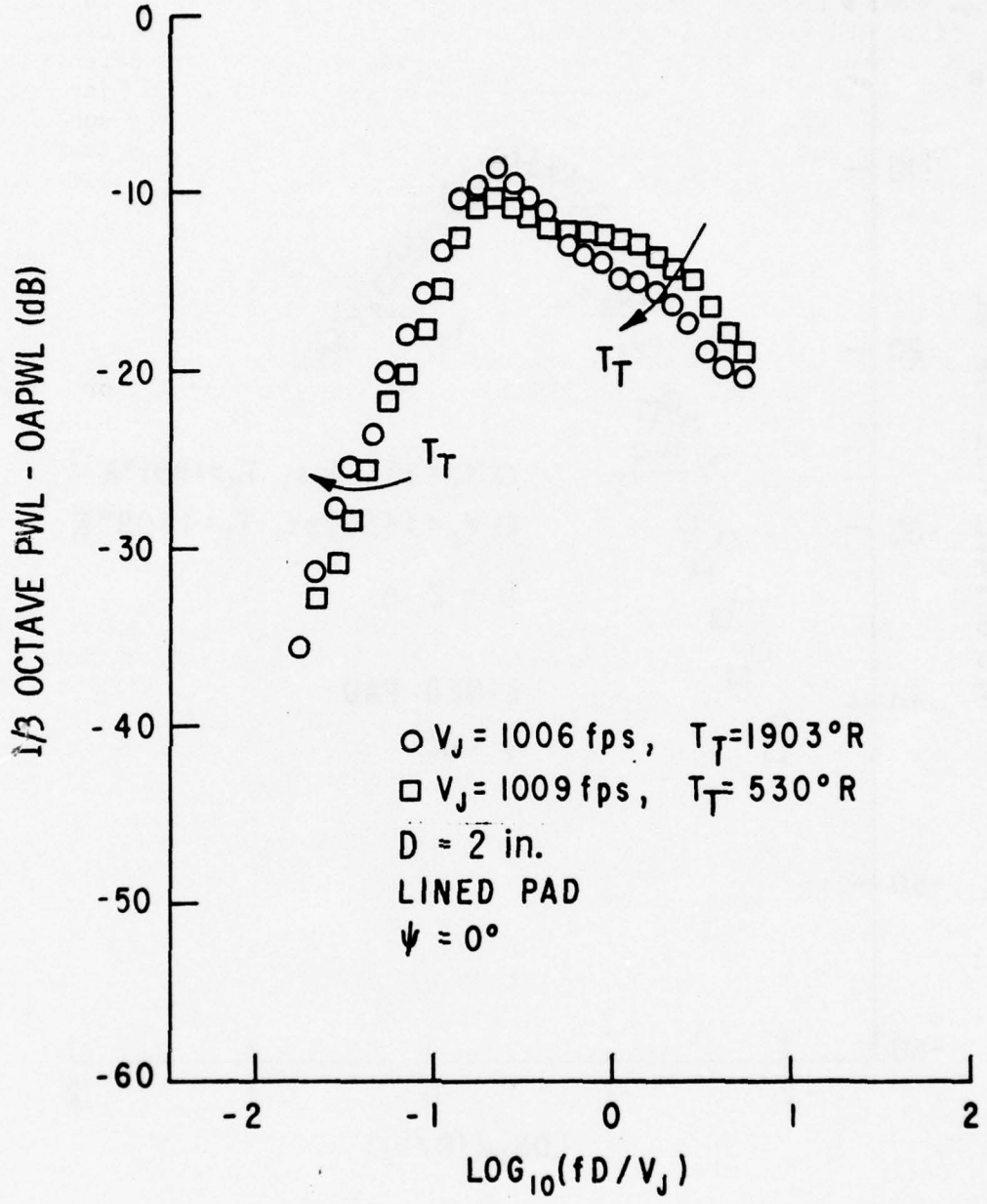


Figure 6-66. Effect of Jet Heating at $V_j \sim 1000$ fps at GE/CR&DC.

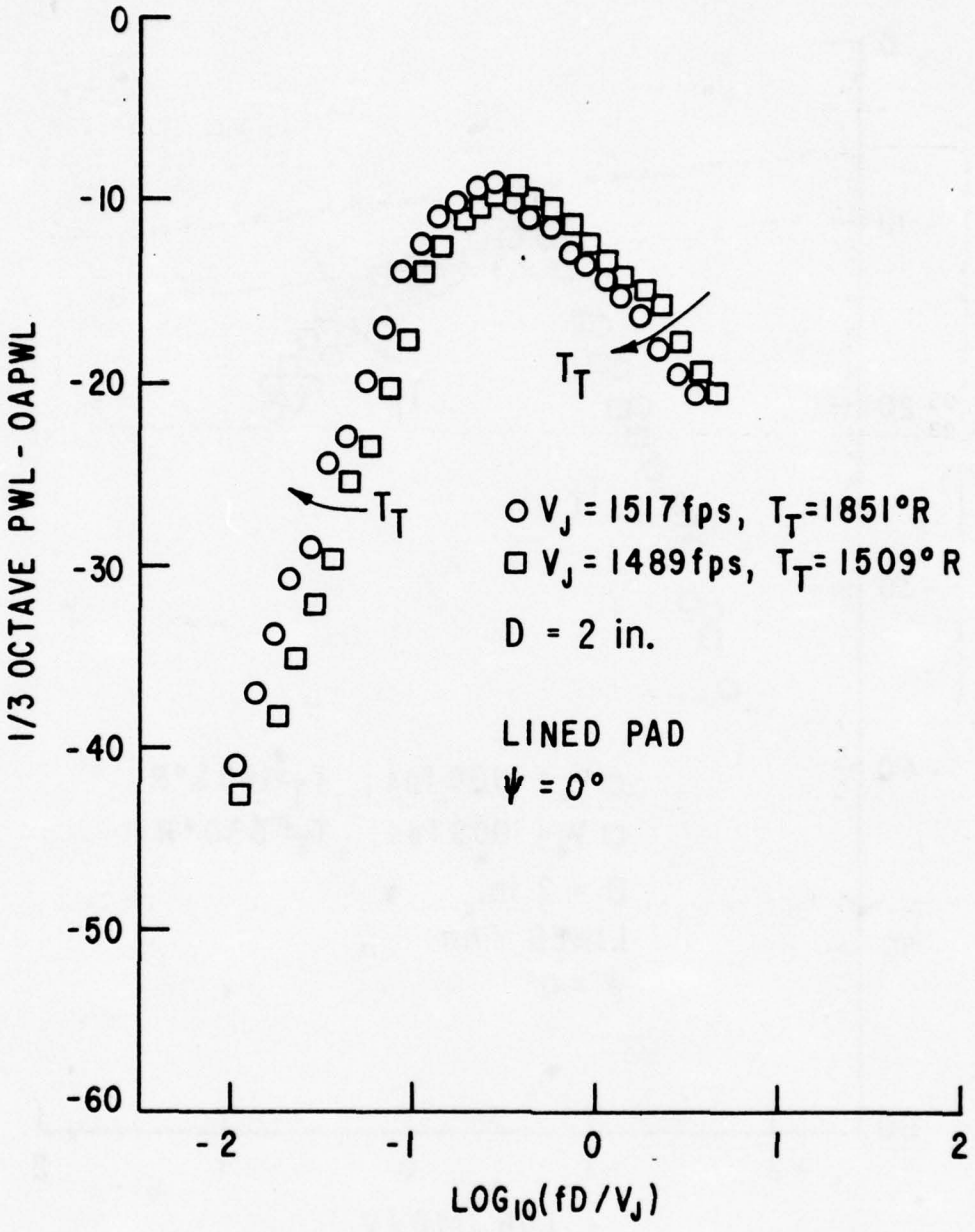


Figure 6-67. Effect of Jet Heating at $V_j \sim 1500$ fps at GE/CR&DC.

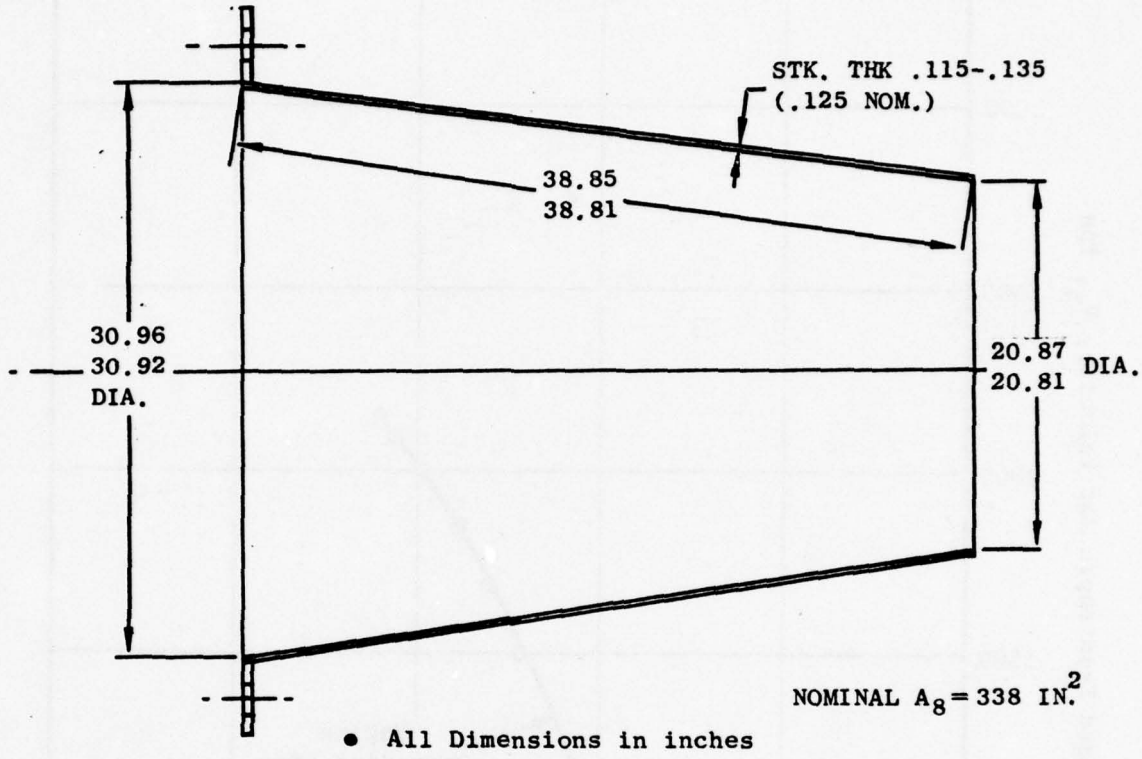


Figure 6-68. Acoustic Certification Conic Nozzle at GE/EFTC.

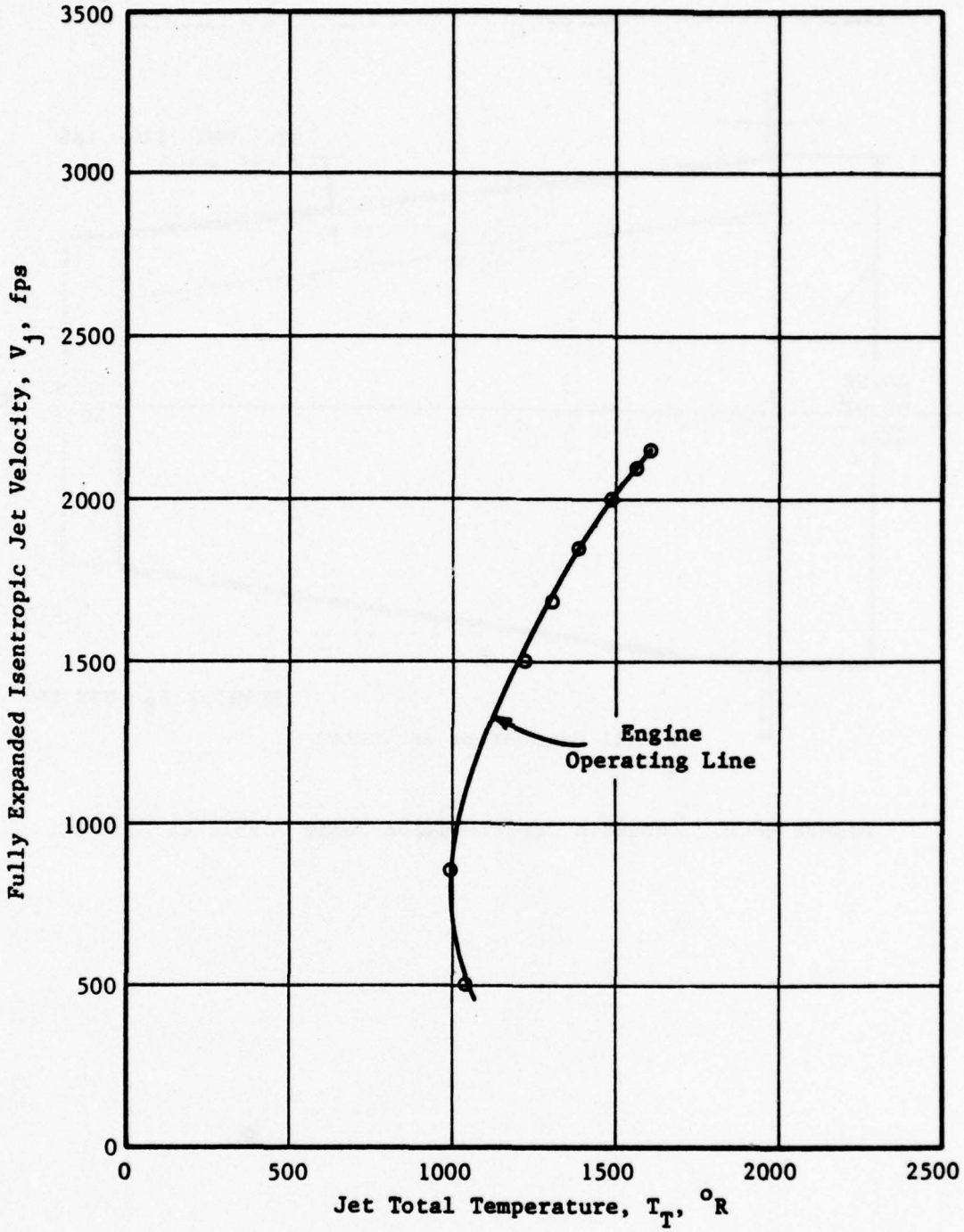


Figure 6-69. Operation Domain of the J79 at GE/EFTC.

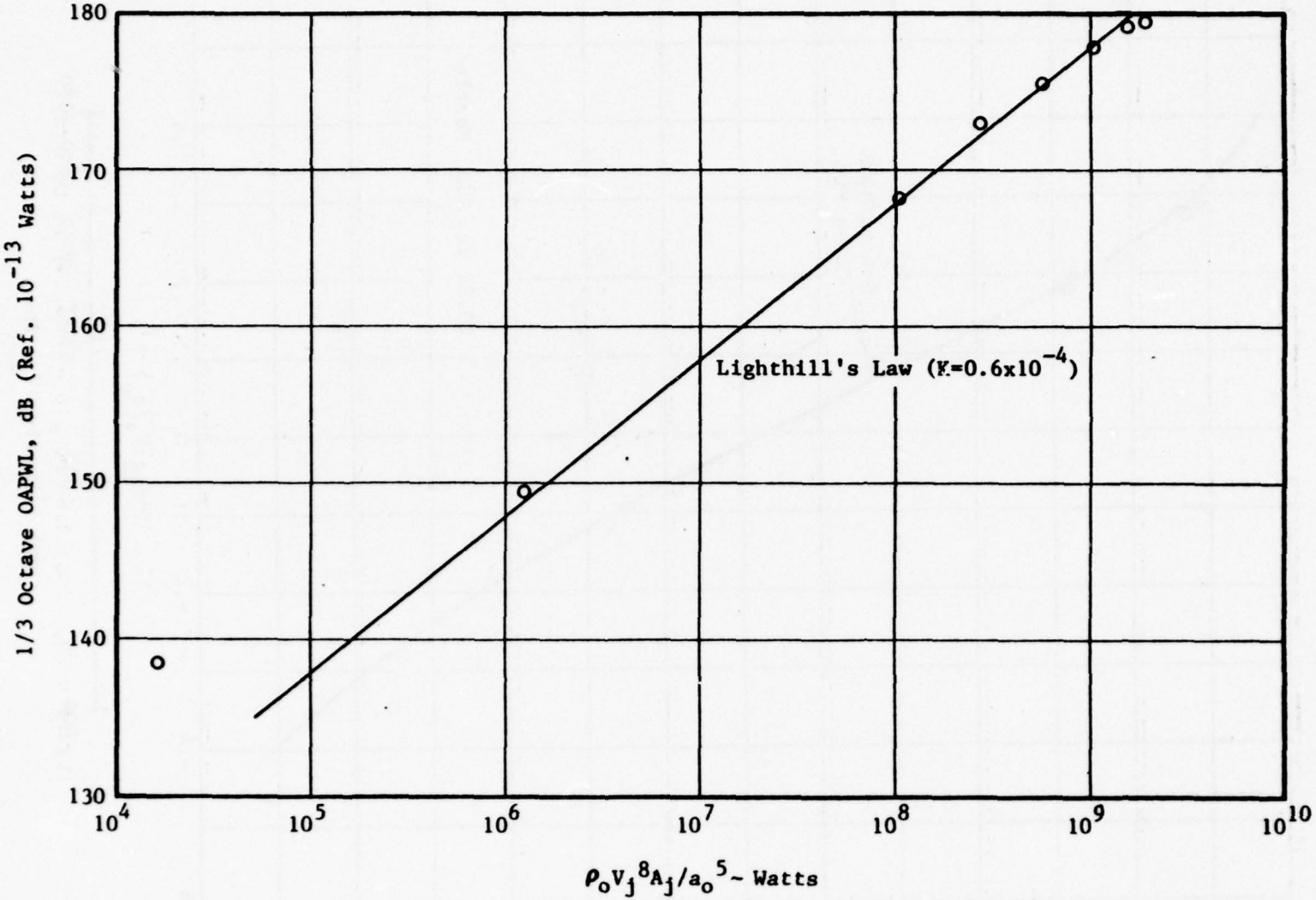


Figure 6-70. Variation of Overall Power with Lighthill's Parameter for the J79 at GE/EFTC.

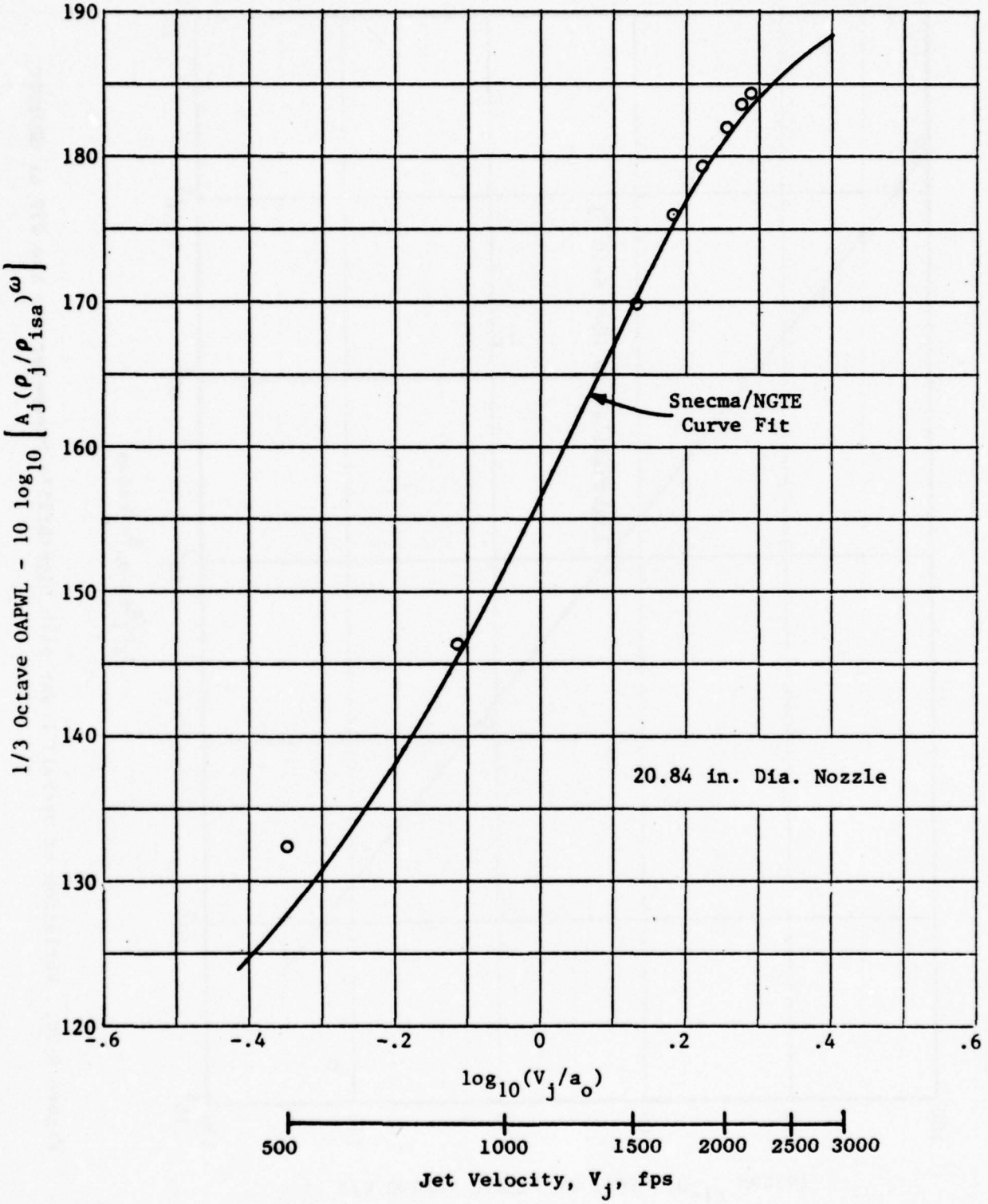


Figure 6-71. Variation of Normalized Overall Power with Jet Velocity for the J79 at GE/EFTC.

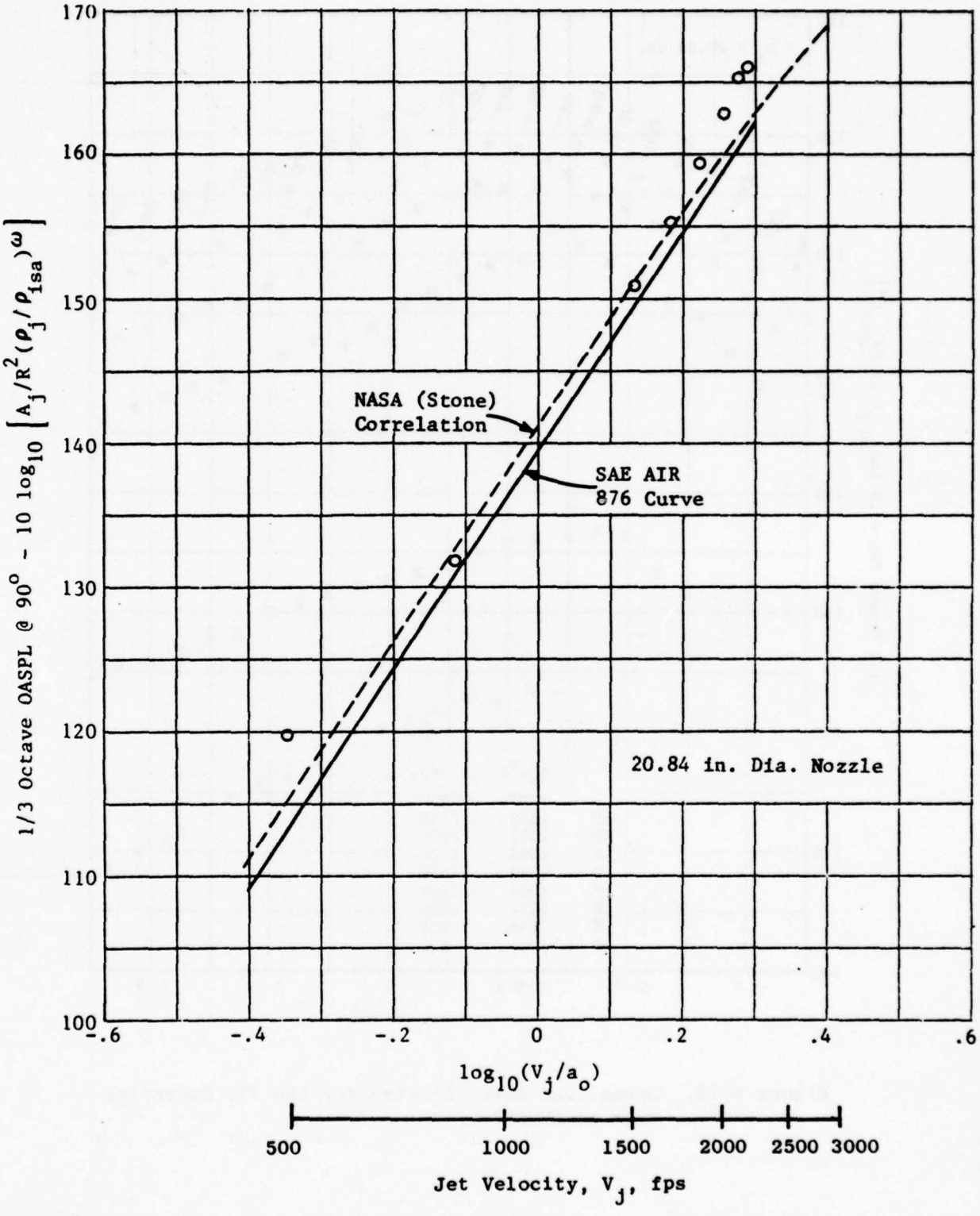


Figure 6-72. Velocity Dependence of Normalized Overall Sound Pressure Level at 90° for the J79 at GE/EFTC.

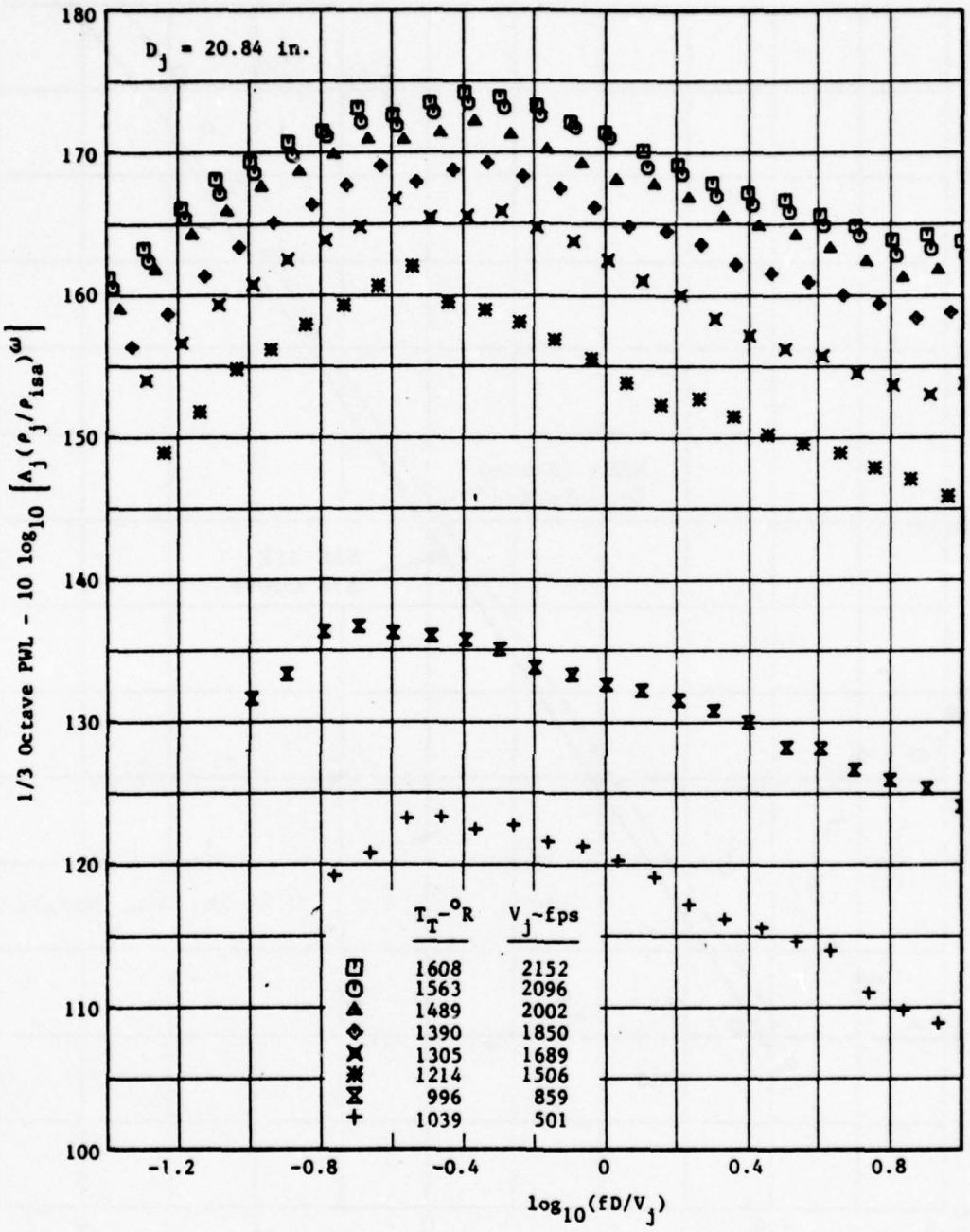


Figure 6-73. Normalized Power Spectra for the J79 Operating Line at GE/EFTC.

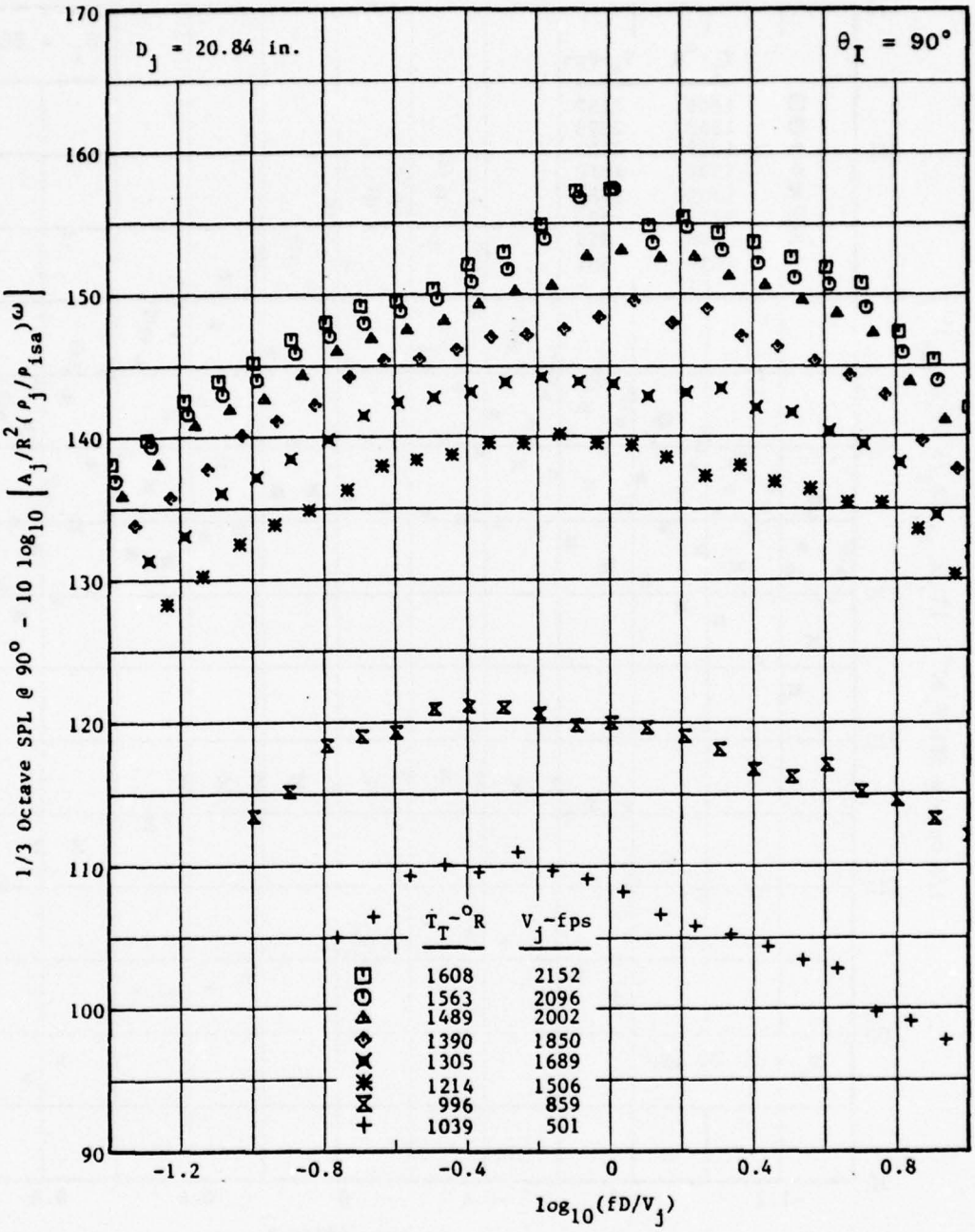


Figure 6-74. Normalized θ_I = 90° SPL Spectra for the J79 Operating Line at GE/EFTC.

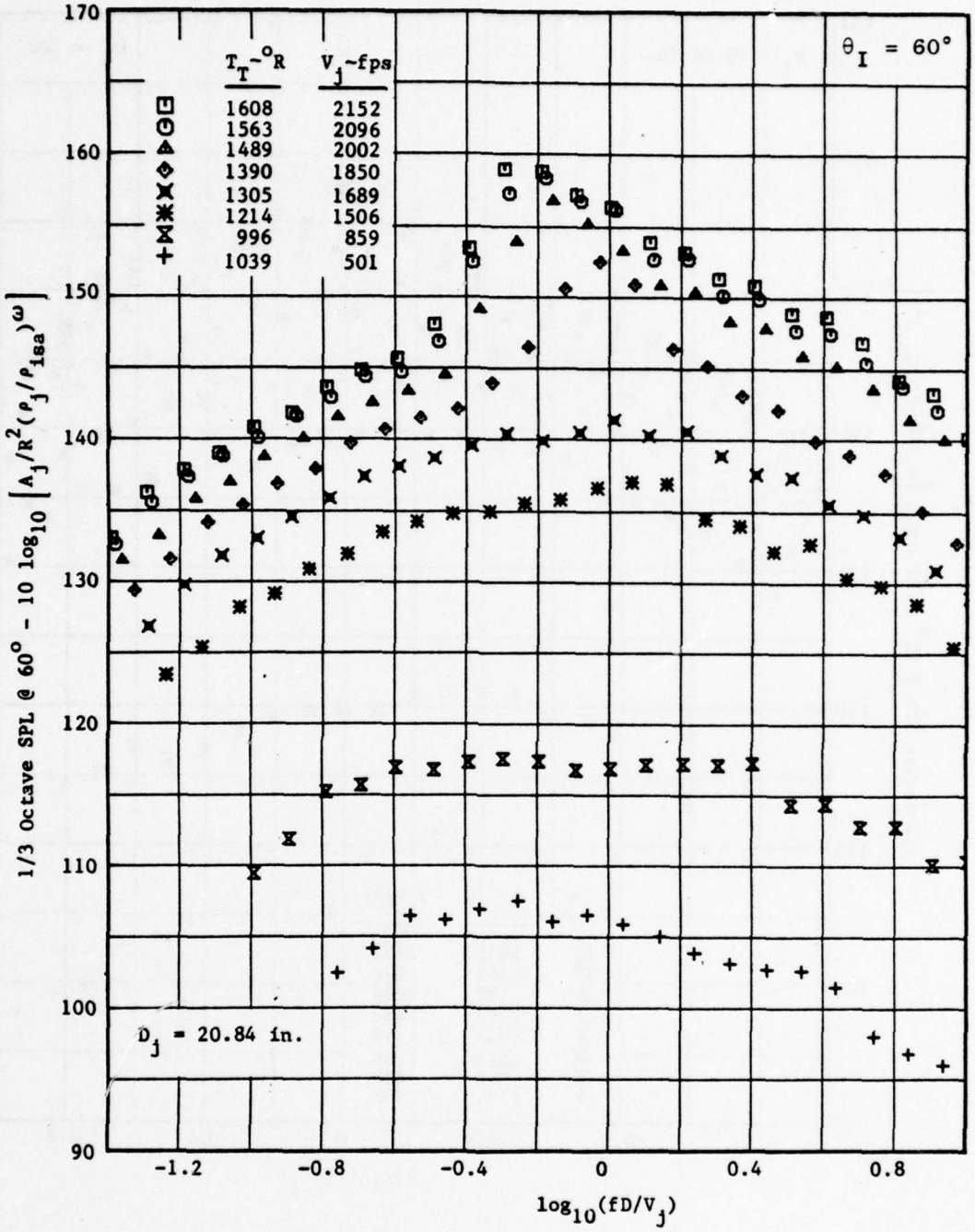


Figure 6-75. Normalized θ_I = 60° SPL Spectra for the J79 Operating Line at GE/EFTC.

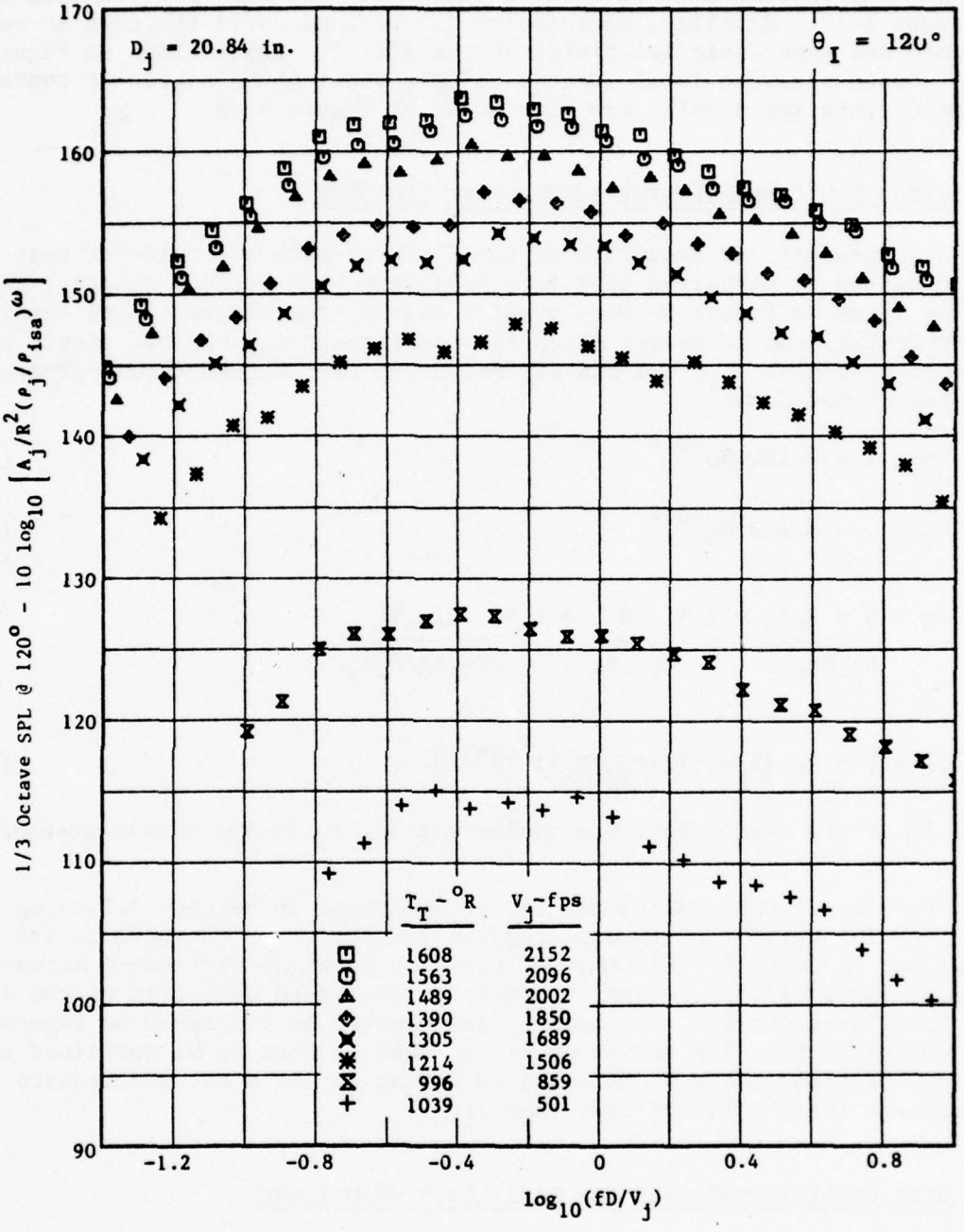


Figure 6-76. Normalized θ_I = 120° SPL Spectra for the J79 Operating Line at GE/EFTC.

The SAE correlation curve is compared with the subsonic jet data at 90° in Figure 6-77. Excellent correlation is obtained as in the case at both subsonic and supersonic velocities at the aft 120° angle shown on Figure 6-78. Sound pressure level spectra at idle showing the degree of contamination of this speed point are also shown on Figure 6-78.

6.7 AERODYNAMIC MEASUREMENT ACCURACY AT FLUIDYNE

The accuracy and precision of the FluiDyne hot- and cold-jet test stands were obtained by comparing test data collected with various diameter ASME nozzles shown in Figure 6-79 to predict values from semiempirical equations. In particular, the flowmeter discharge coefficient C_D, the net static axial thrust coefficient, C_T, and the dimensionless exit stream thrust parameter, f_9, were calculated from:

$$C_D = 1 - 0.184\ R_N^{-0.2} \tag{106}$$

$$C_T = 1 - 0.109\ R_N^{-0.2} \tag{107}$$

$$f_9 = \frac{H + P_a A_9}{A_8\ P_{T_8}} = 1 + \frac{H}{P_{T_8}\ A_8} = 1 + \frac{H/m_a V_i}{P_{T_8} A_8 / P_T A_*} \tag{108}$$

$$f_9 = 1 + C_T\ \left[1 + (1/(P_{T8}/P_o))^{0.2857}\right] \tag{109}$$

where R_N is the throat Reynolds number and P_{T8}/P_o is the nozzle pressure ratio.

The measurements were conducted as described in Section 3.7 using the equations for C_D, C_T and f_9 described in Reference 8. The results are summarized in Table 6-I in terms of the bias (average difference between the measured and predicted values) and scatter (standard deviation of the data from the biased curve). The actual data scatter is displayed on Figures 6-80 through 6-83. The variation of the data is seen to be contained to within 0.3% bias with a 0.25% standard deviation for a net uncertainty of measurement (bias + 2σ) of less than 1/2%.

6.8 DATA QUALITY ASSURANCE FOR NASA LEWIS WIND TUNNEL

Activation and dynamic calibration of the NASA Lewis flow and force measuring system was conducted by GENERAL ELECTRIC and NASA personnel prior to proceeding with the Task 3 scale-model wind tunnel performance testing of suppressed dual-flow plug nozzles. A reference nozzle was used for checking the force measurement system. The Supersonic Tunnel association (STA) has

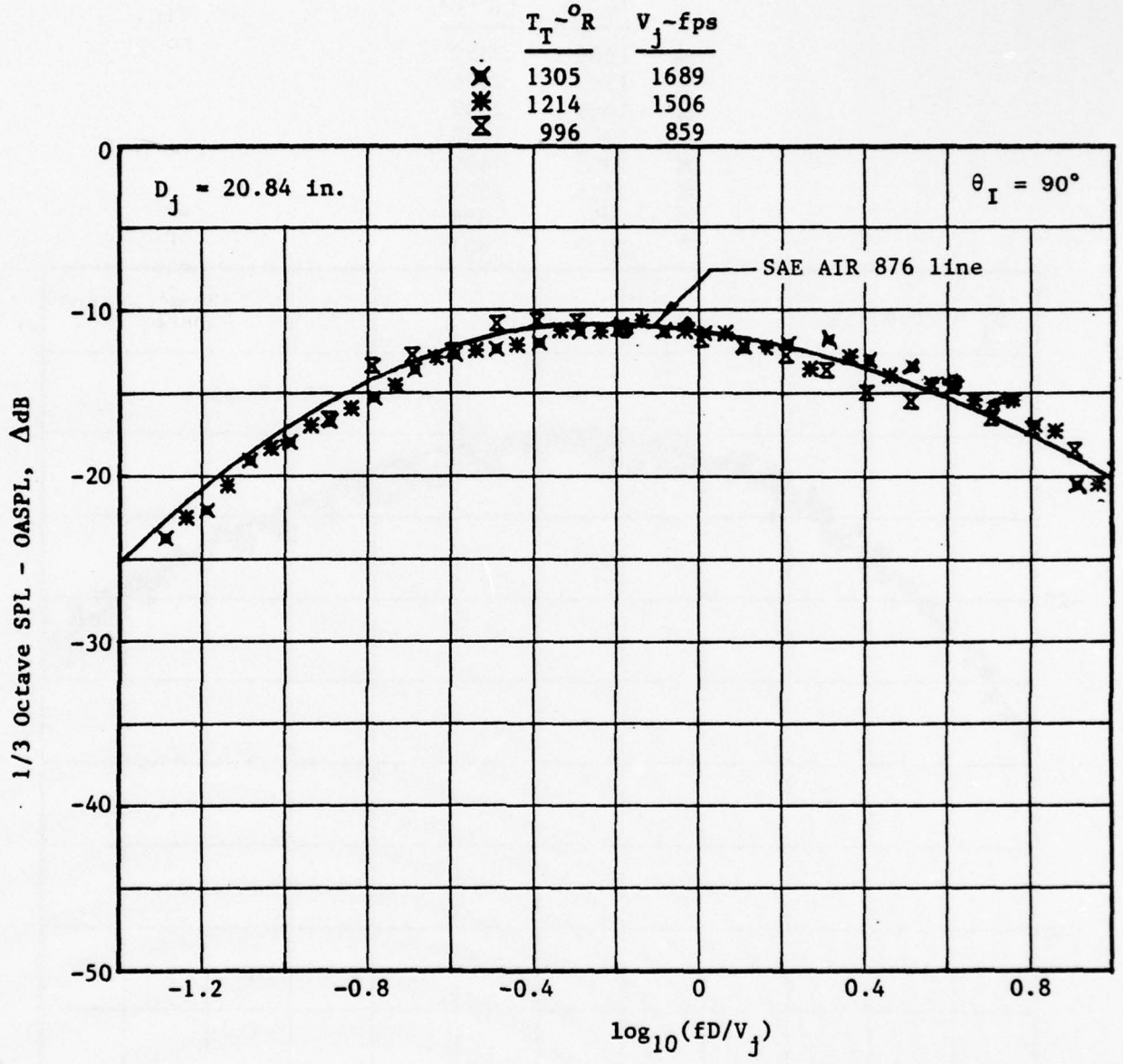


Figure 6-77. ΔSPL Spectra at θ_I = 90° from the Inlet on the J79 Operating Line at GE/EFTC.

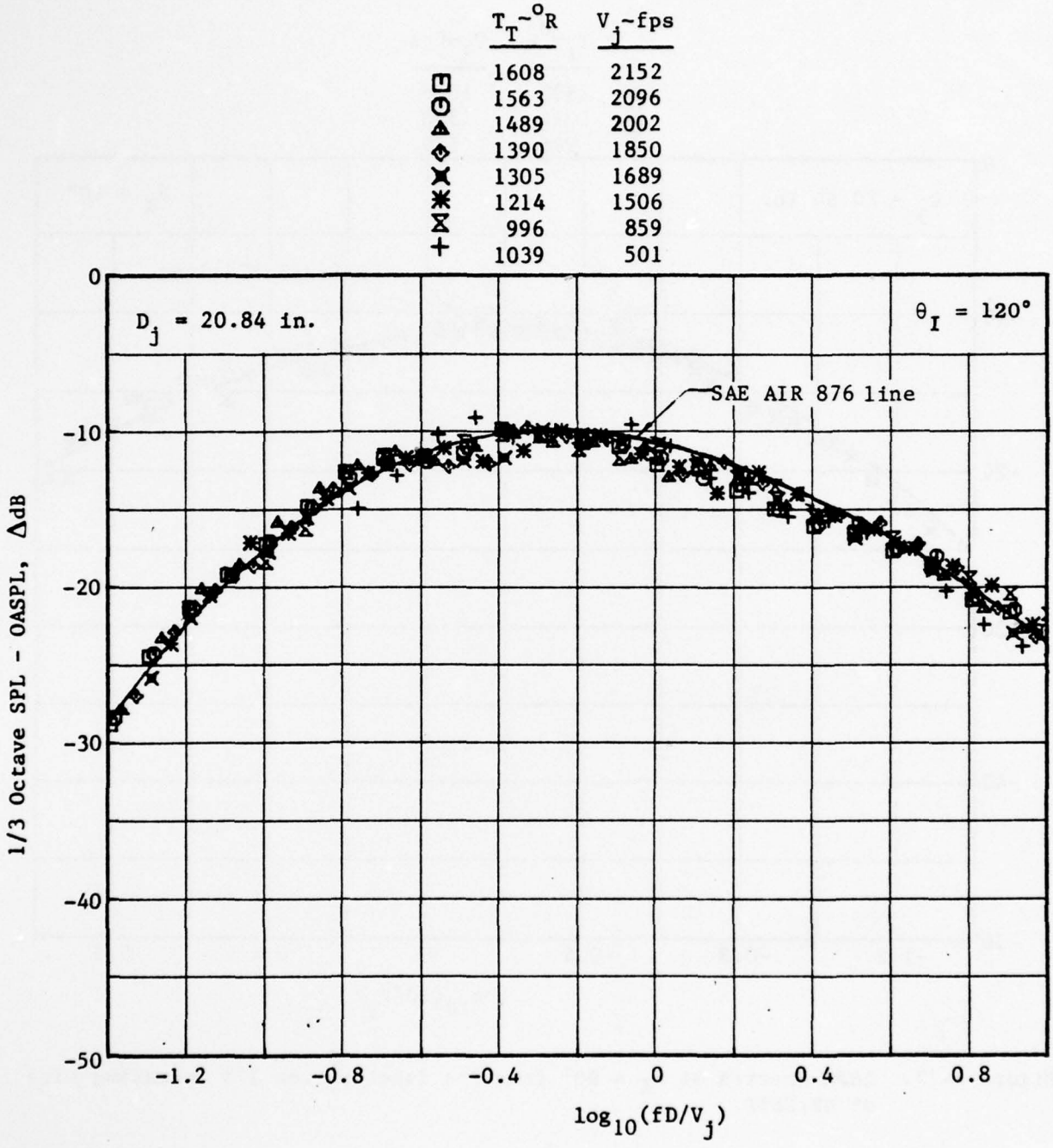


Figure 6-78. ΔSPL Spectra at θ_I = 120° from the Inlet on the J79 Operating Line at GE/EFTC.

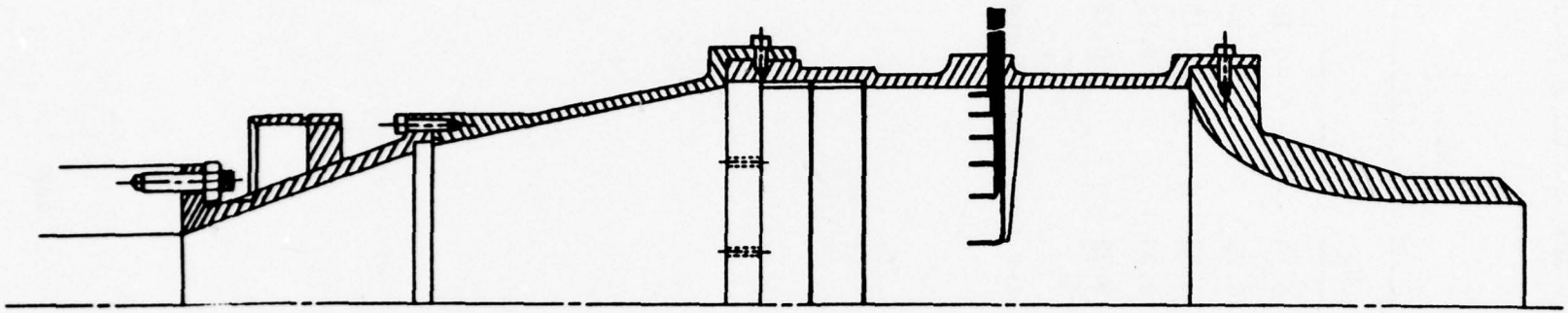


Figure 6-79. FluiDyne ASME Nozzle.

Table 6-I. FluiDyne Aero Facility Accuracies

Facility/Parameter	Bias %			Standard Deviation %		
	C_D	C_T	f_9	C_D	C_T	f_9
Channel 7 Cold Flow	-0.13	-0.08	-0.18	0.06	0.06	0.06
Channel 11 Cold Flow	0.02		0.04	0.02		0.02
Channel 11 Hot Flow	0.25		0.15	0.09		0.10
Channel 11 Dual Flow Cold	0.03		0.12	0.08		0.04
Channel 11 Dual Flow Hot	0.28		0.12	0.05		0.04

(The uncertainty can be calculated from bias +2 standard deviation)

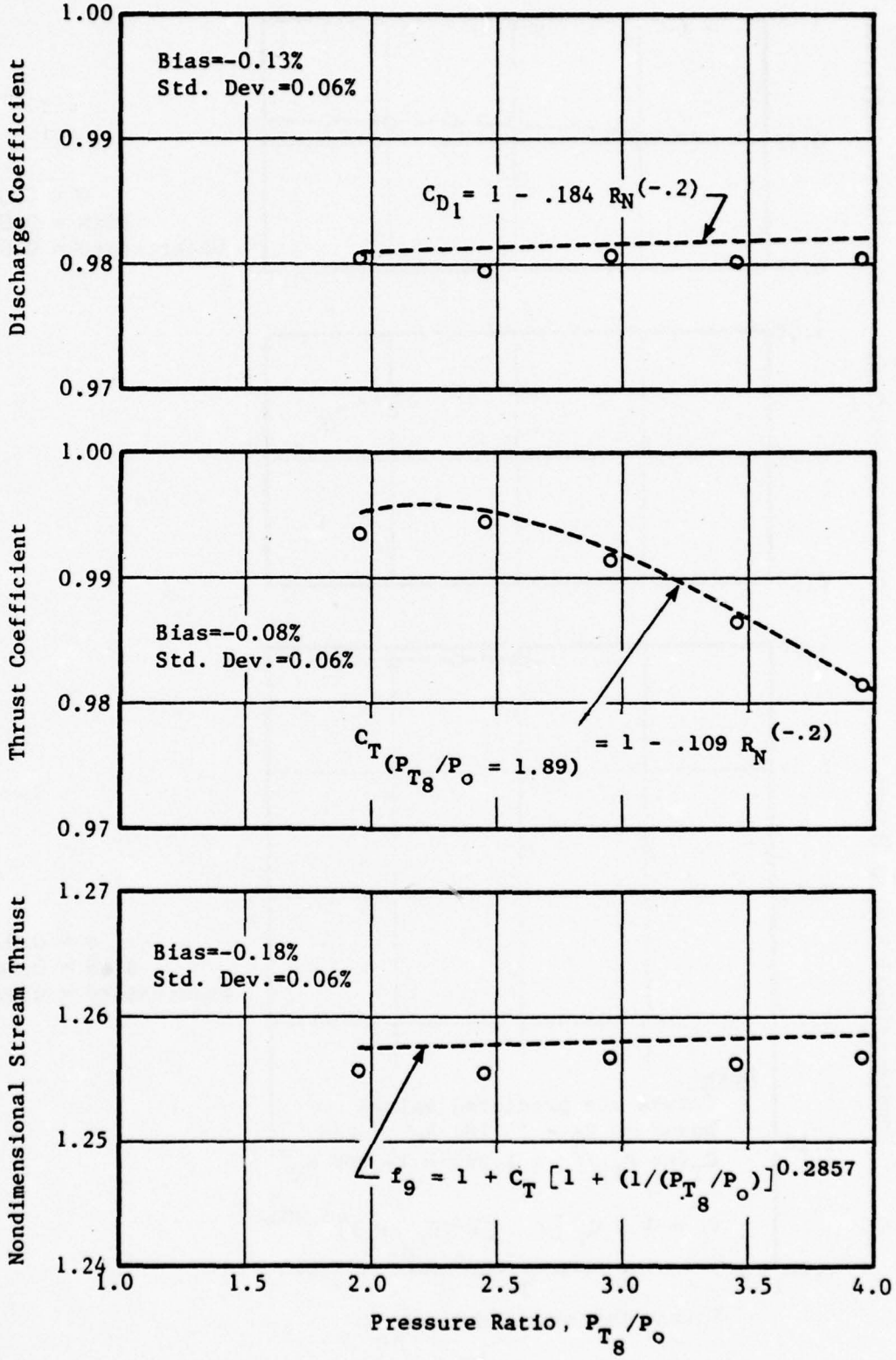


Figure 6-80. Channel 7 ASME Test Results for a 4.5-inch-Diameter Nozzle at FluiDyne.

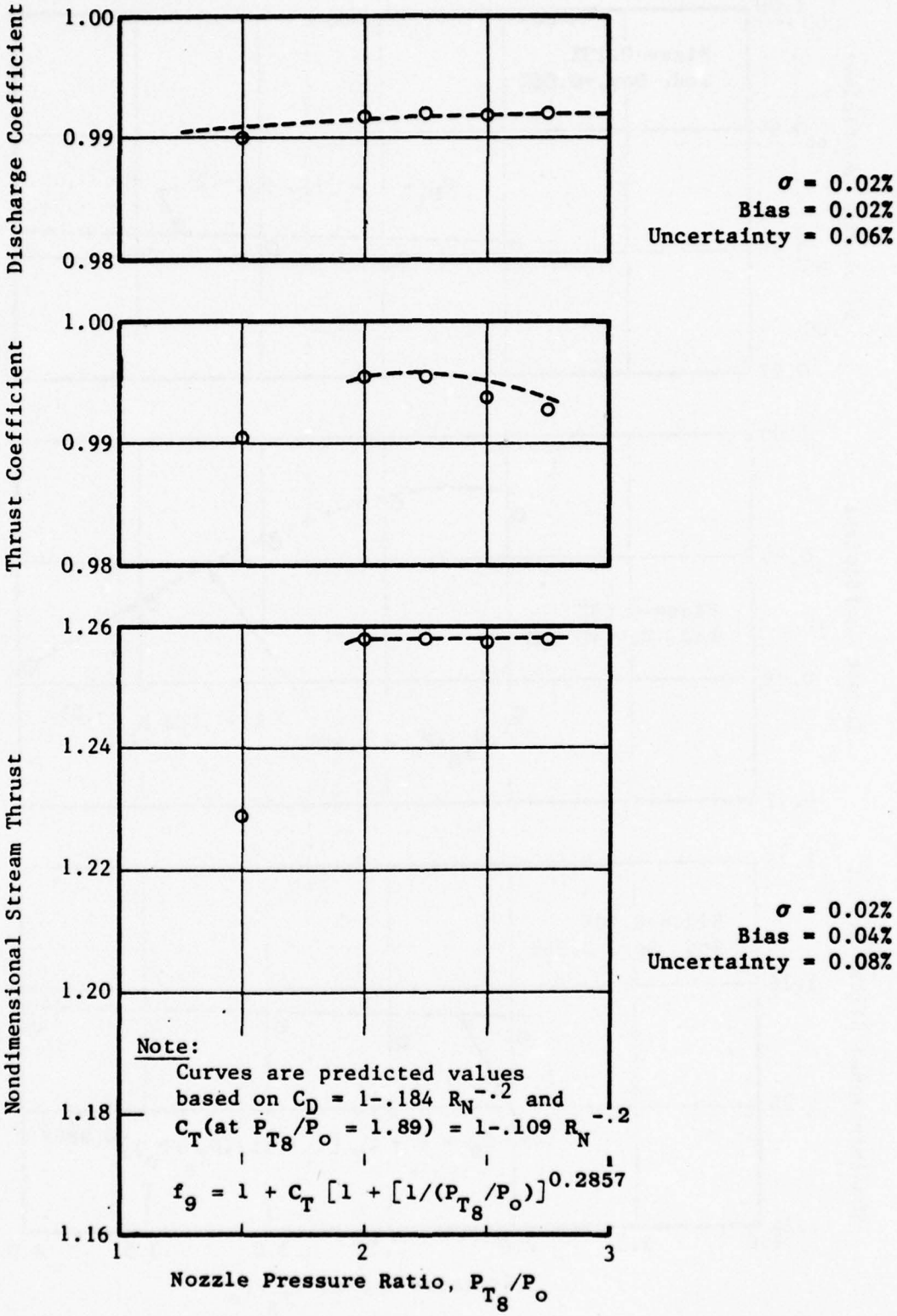


Figure 6-81. Channel 11 ASME Test Results for a 5.5-inch-Diameter Cold Nozzle at FluiDyne.

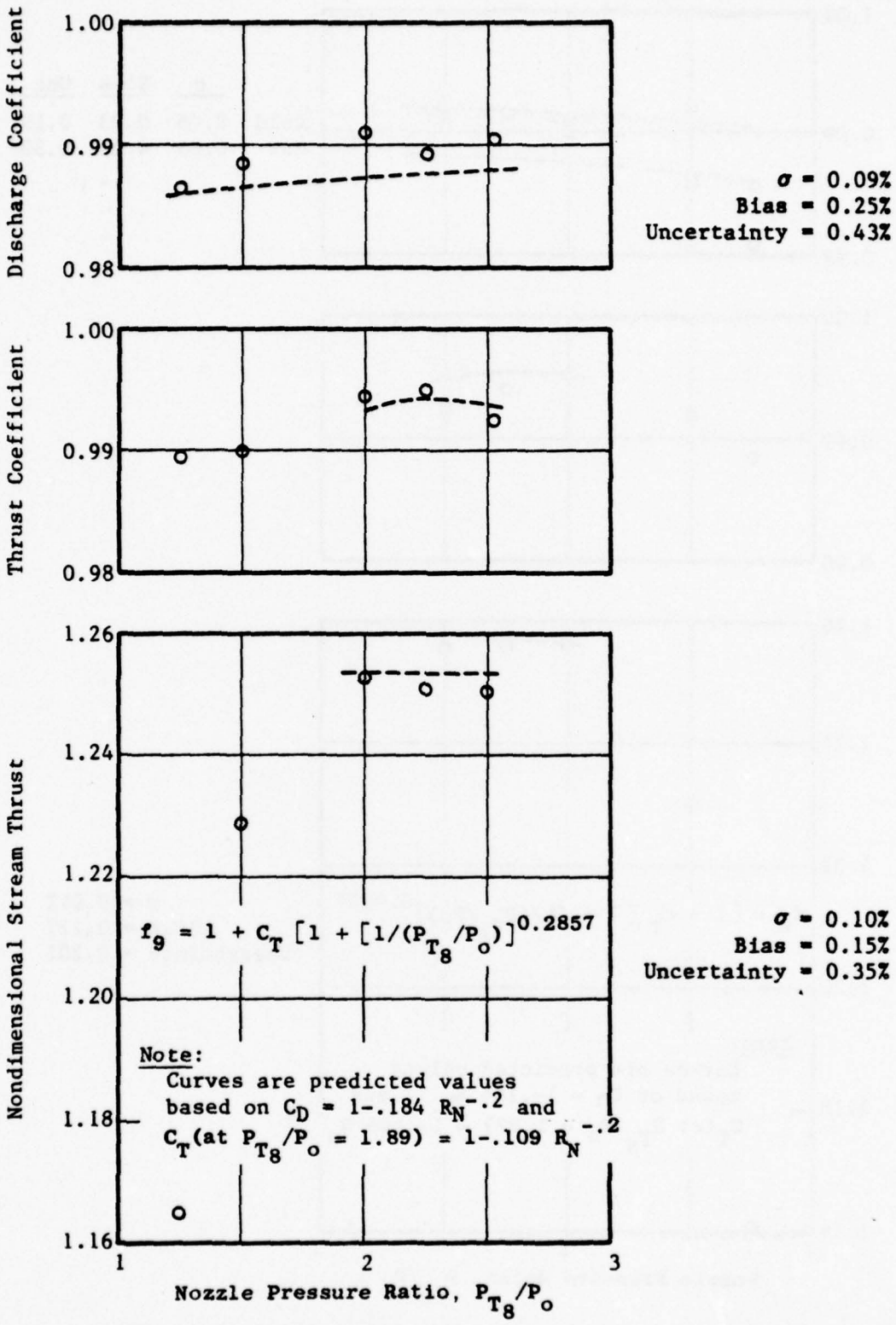
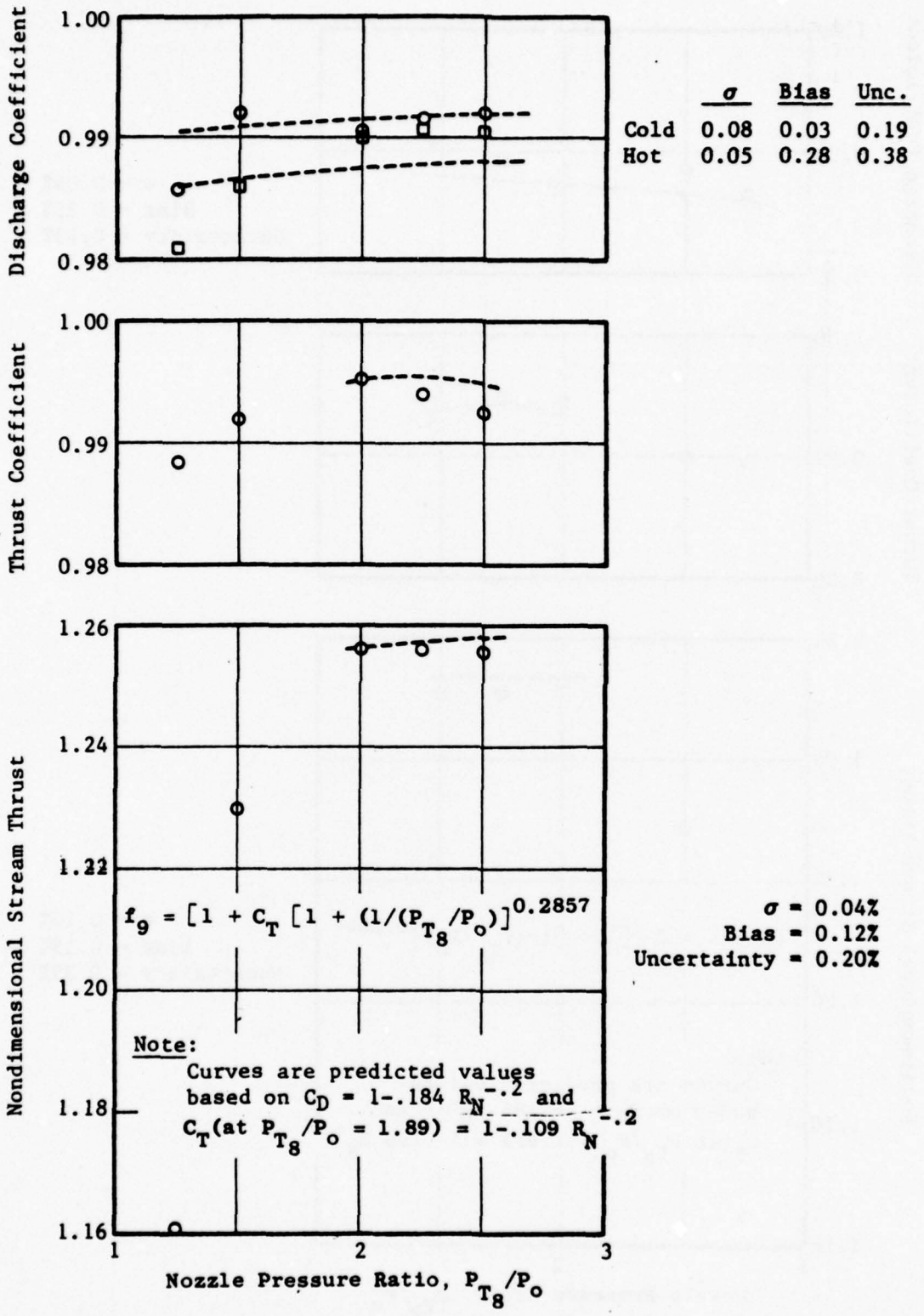


Figure 6-82. Channel 11 ASME Test Results for a 2.5-inch-Diameter Hot Nozzle at FluiDyne.

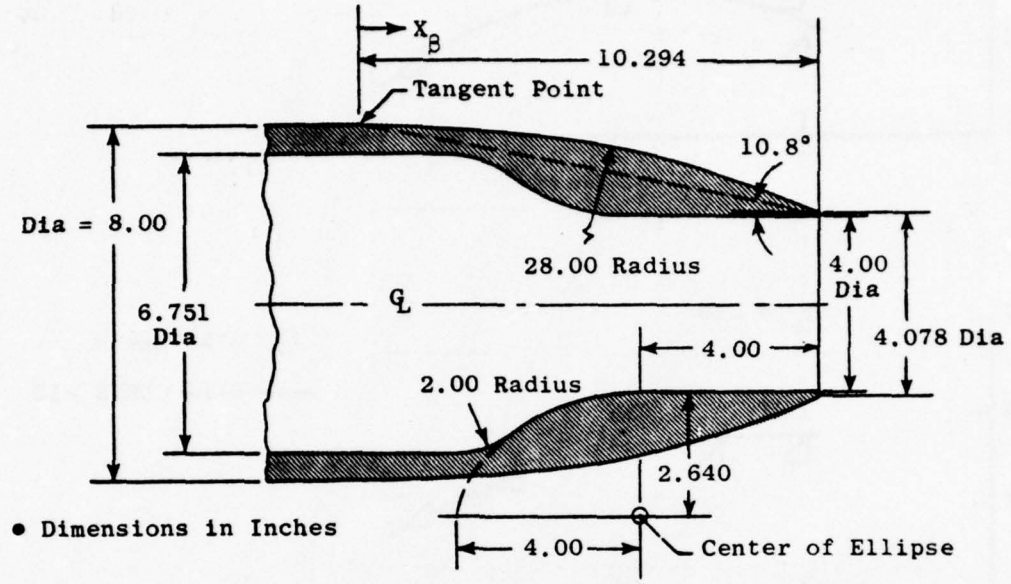


	σ	Bias	Unc.
Cold	0.08	0.03	0.19
Hot	0.05	0.28	0.38

σ = 0.04%
Bias = 0.12%
Uncertainty = 0.20%

Figure 6-83. ASME Test Results for 5.5-inch Cold and 2.5-inch Hot Nozzles at FluiDyne.

recommended this nozzle for verifying data integrity. The external geometry of this reference nozzle is a circular-arc boat-tail and the internal geometry is a modified ASME nozzle contour, as shown in the following sketch:



Supersonic Tunnel Association (STA) Nozzle

The efficiency of this nozzle is well documented and provides an excellent facility checkout for both static and wind-on measurements. Predicted performance and previous test data from several sources at various Mach numbers are presented in Figure 6-84. In this program, the reference nozzle was first tested under static (Mo = 0) conditions. The data fell well within the ±1/2% band shown in the figure, verifying that the force balance system was working properly. As a further check, the nozzle was tested up to tunnel Mach numbers of 0.45 and compared to previous data. All data agreed, therefore the tunnel measurement system (force balance, pressures, temperatures, and data reduction program) was properly functioning; subsequent model data for other configurations had to be correct.

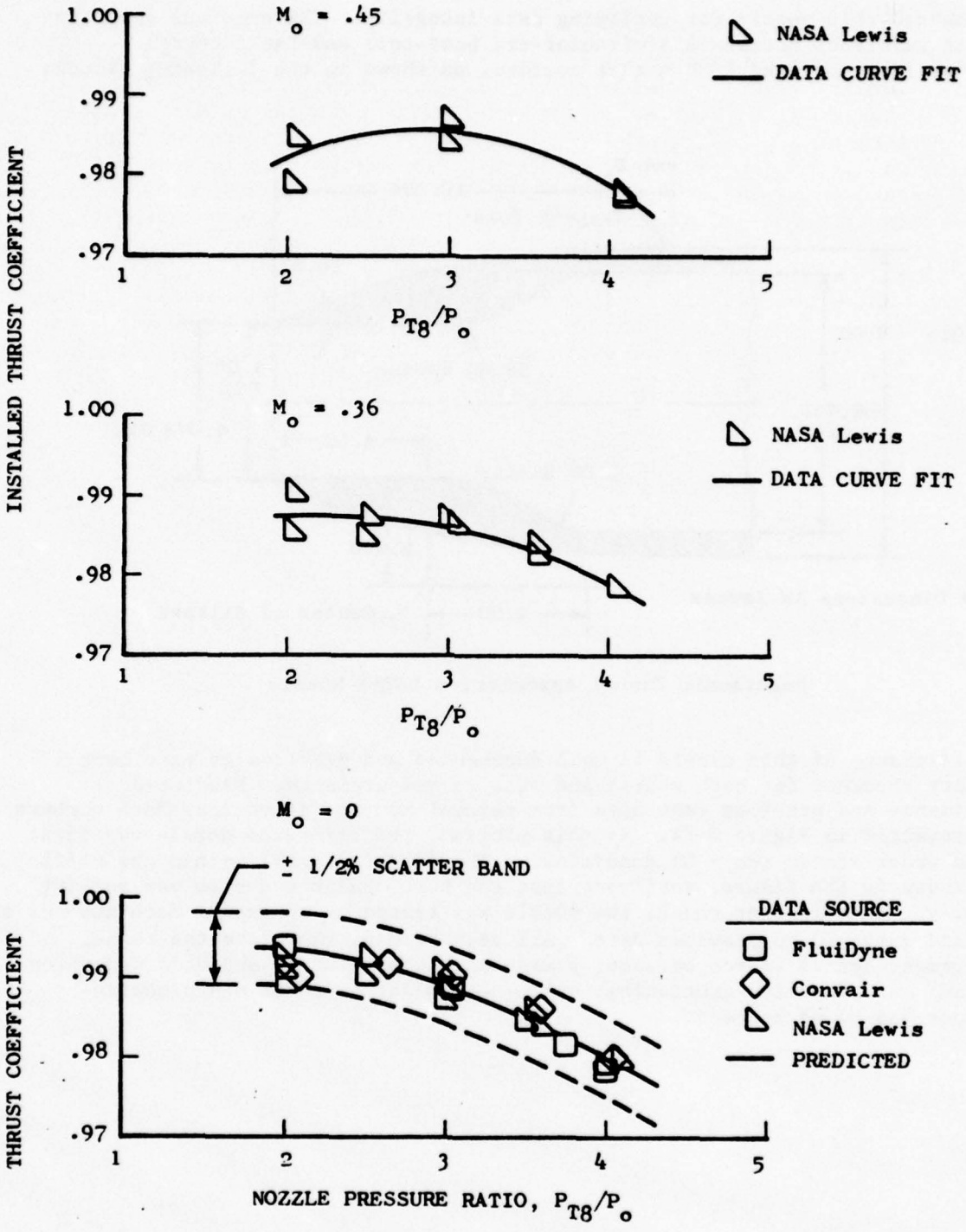


Figure 6-84. Supersonic Tunnel Association (STA) Nozzle Efficiency.

6.9 SUMMARY

The jet noise data recorded at the USC, UBC, JENOTS, GE/CR&DC, and J79 at EFTC, were validated by performing a series of certification tests. The data were taken using circular convergent nozzles over the domain of operation. The results were compared with Lighthill's law and with the SNECMA/NGTE correlation for normalized OAPWL accounting for temperature effects. The overall sound pressure level at the 90° inlet angle was compared with the suggested fits from the SAE A21 Committee and NASA Lewis. Spectral shape was also compared with the A21 committee line. Referee data from highly regarded facilities, such as the Cambridge University (Lush), SNECMA (Hoch), NGTE (Cocking, Ahuja and Bushell) and Lockheed Georgia (Tanna and Dean), were used to establish the correctness and relative accuracy and precision of the correlation lines. Table 6-II summarizes the unique capabilities of each of these facilities as well as their precision/accuracy over the certification frequency range.

The FluiDyne facilities, as expected, are valid for conducting aerodynamic performance experiments in which the resulting data (thrust and flow coefficient) are as controlled and accurate as can be produced anywhere. Similarly, the NASA Lewis 8 x 6 foot wind tunnel demonstrated excellent data quality.

Table 6-II. Summary of Certified Facility Characteristics.

Facility/Item	USC	UBC	GE/JEMOTS (Coannular and Single Flow) Primary	GE/JEMOTS (Coannular) Secondary	GE/CR6DC	GE/EFTC- J79A	FluiDyne - Channels 7, 12, 13, and 11	NASA Lewis 8 ft x 6 ft Wind Tunnel
• Application	Orderly Structure (Task 2)	Laser Shadowgraph (Task 1); Lip Noise (Task 2)	EM Verification (Task 1) Lip Noise (Task 2), Baseline and Suppressed Nozzles (Task 3 and 4)	EM Verification (Task 1) Lip Noise (Task 2), Baseline and Suppressed Nozzles (Task 3 and 4)	Hole-in-the-Wall (Task 1) Basic Experiments in Support of Theoretical Developments (Task 2)	Acoustic Scaling Demonstration (Task 3)	Replaced by NASA Lewis Facility	Thrust and Flow Measurements (Task 3, 4 and 5)
• Nozzle Diameter Range, inches	1 and 2	~3/4	2 to 6	~12	1 and 2	20.84	8	5
• Max. Weight Flow, lbm/sec	~3.5	~0.28	~80	~50	8	160	40	30
• Jet Velocity Range Certified, fps	600 to 1750	600 to 1050	600 to 3000	600 to 1050	600 to 1900	750 to 2150	Velocities Corresponding to Pressure Ratios up to 4.0	Velocities Corresponding to Pressure Ratios in excess of 4.0
• Jet Total Temperature Certified, ° R	540 to 1040	540	540 to 2500	540	540 to 1900	1000 to 1600 per Operating Line	540 to 1700	540
• Thrust Measurement Capability	No	No	No	No	No	Yes	Yes	Yes
• Acoustic Arena	Anechoic	Anechoic	Outdoor Cement Pad to 20 feet, Crushed Rock From 20 ft to 40 ft	Outdoor Cement Pad to 20 feet, Crushed Rock From 20 ft to 40 ft	Outdoor Foam Covered Pad	Outdoor Packed Desert Sand	N/A	N/A
• Microphone Arc Radius, ft	7.5	10	40	40	9	160	N/A	N/A
• Microphone Distributed Angle from Inlet, Degrees	10 Microphones from 70° to 160° Staggered Intervals	1 Moving Microphone from 80° to 180°	14 Microphones Every 10° from 20° to 160°	14 Microphones Every 10° from 20° to 160°	12 Microphones Every 10° From 50° to 160°	26 Microphones (2 per Angle) Every 10° From 40° to 160°.	N/A	N/A
• Microphone Height Above Ground, ft	N/A	N/A	15.91	15.91	6 to 15, Function of Azimuthal Position of Boom	2 and 12	N/A	N/A
• Nozzle Centerline Above Ground, ft	N/A	N/A	4.58	4.58	6	12	N/A	N/A
• Certified 1/3-OB Frequency Range, Hz	315 to 80,000	315 to 80,000	400 to 80,000	400 to 80,000	315 to 40,000	50 to 20,000	N/A	N/A
• Precision OASPL Max./Min. at 90°, σ ± dB	0.32/0.30	0.29/0.27	0.53/0.41	0.53/0.41	0.35/0.32	0.38/0.37	N/A	N/A
• Frequency Range Precision	400 Hz: 3.75 dB 500 Hz: 2.75 dB 6.30 kHz to 10 kHz: 1.25 dB	200 Hz to 1000 Hz: <1 dB 1000 Hz to 63 kHz: 1.25 dB 80 kHz: 1.75 dB	200 Hz to 630 Hz: 3 to 3.75 dB 800 Hz to 63 kHz: <3 dB 80 kHz: 3.75 dB	200 Hz to 630 Hr: 3 to 3.75 dB 800 Hz to 63 kHz: <3 dB 80 kHz: 3.75 dB	400 Hz to 630 Hz: <3 dB 800 Hz to 40 kHz: <3 dB	50 Hz to 1250 Hz: <3 dB 1600 Hz to 10 kHz: <3 dB 12.5 kHz to 20 kHz: 3.75 dB	N/A	N/A

7.0 ANALYSIS OF VARIANCE - OVERALL PRECISION OF ACOUSTIC MEASUREMENTS

7.1 INTRODUCTION

There are two terms which are used to describe the deviation of data from its expected value: precision and accuracy. In a statistical sense, precision is concerned with the random scatter of the data when comparing the mean of the data with a particular sample. Accuracy is a term describing the amount of bias or systematic error in a data population when comparing the mean to a fixed or known value.

Whenever accuracy errors are known to exist they are generally removed from the data utilizing correction factors. The residual precision errors remain with the data and describe the expected repeatability of the results from day to day. The level of precision is stated by the standard deviation, σ, or the variance, σ^2, of the scatter from the mean value.

In this section, the total precision estimate of the data collected at each of the acoustic test facilities is evaluated. Differences in the precision are described in terms of the various contamination error sources which exist in the facility.

7.2 TYPES OF ERROR

The precision of the acoustic measurements at the various test sites can be effected by:

1. Nonanechoic environment and near-field deviations from inverse square law
2. Variation of the frequency response of the data acquisition and reduction systems
3. Inaccuracies in aerodynamic instrumentations or fluctuations in the jet aero conditions
4. Precision errors in the air attenuation model due to environmental fluctuations, gradients, and measurement inaccuracies
5. Ground reflections
6. Ambient levels in the chamber
7. Contamination from piping and combustors
8. Contamination from Electronic Noise Floor

Items 1 through 5 are errors which occur independent of the level being measured. These are a result of changes in parameters which effect the measured acoustic pressure by a multiplier. Whereas, items 6 through 8 are bias errors in that they induce an error in the measured signal due to the presence of a contamination signal and, therefore, are functions of the level being measured.

Accuracy errors which effect the sound pressures as multipliers, influence the sound pressure level by a constant adder, Δ_i, viz:

$$SPL_m = SPL_{jet} + \sum_{j=1}^{k} \Delta_i \tag{110}$$

The measured SPL_m is equal to the actual jet SPL plus all the changes, Δ, from the k number of multiplier errors. In this case for each frequency, the standard deviation of the measurement, σ_m, is just the root mean square of each of the individual standard deviations.

$$\sigma_m = \sqrt{\sum_{j=1}^{k} \sigma_i^2} \tag{111}$$

An intermediate estimate of the precision based on our five multiplier errors can then be obtained for each frequency.

$$\sigma_{interm} = \sqrt{\sigma_1^2 + \sigma_2^2 + \sigma_3^2 + \sigma_4^2 + \sigma_5^2} \tag{112}$$

Contamination accuracy errors which occur due to the presence of a known floor level such as items 6, 7, and 8, each have their own precision estimate and standard deviation. These contamination errors influence the measured SPL depending on the numerical difference in level δ_i between the actual true level without the contaminated floor and the noise floor level viz: $\delta_i = SPL_{no\ floor_i} - SPL_{floor_i}$ where i is the frequency being examined. The magnitued of the adjustment is given by:

$$SPL_{meas_i} = SPL_{no\ floor_i} + 10 \log_{10} \left(1 + 10^{-\delta_i/10}\right) \tag{113}$$

This relation is plotted in Figure 4-2. If the SPL measurement without the noise floor present has a precision standard deviation given by $\sigma_{intermediate}$ and the standard deviation of the floor variation is σ_{floor}, then the standard deviation of the final measurement level with the floor contamination will be given by the equation:

$$\sigma_{m_i} = \frac{\left[\left(10^{-\delta_i/5}\right)\left(\sigma_{\text{intermediate}_i}\right)^2 + \left(\sigma_{\text{floor}_i}\right)^2\right]^{1/2}}{\left(1 + 10^{-\delta_i/10}\right)} \qquad (114)$$

This relation is derived in Section 4.1 and plotted in Figure 4-3. In order to obtain a specific precision statement for acoustic data one must first determine the precision due to multiplier errors as a function of frequency. Once this is done the effect on the total precision due to bias contamination errors can be factored in based on a given uncontaminated spectrum and a given contamination noise floor spectrum using the Equation (114). The result is the precision standard deviation as a function of frequency for the measured spectrum.

7.3 CALCULATION OF THE PRECISION ERROR

The deviation in the inverse square law, σ_1, and deviations due to ground reflections, σ_5, are discussed in Section 5.0 for five test sites; USC, UBC, JENOTS, GE/CR&DC, and GE/EFTC. Each of these errors were determined as a function of frequency. The values of the deviation in inverse square law were in part extrapolated from the available data from USC, UBC, and GE/CR&DC. This made it possible to compare the data from these test sites to other test sites. It should be noted that USC and UBC do not have σ_5 for ground reflections because they are anechoic chambers. In addition to the precision errors, GE/CR&DC has an accuracy error from the ground reflections which they do not remove from their data because of its small magnitude. To account for this ever present accuracy error on the data, the magnitude of the ground reflection bias is treated as an additional precision error, σ_6, and included in the calculation for $\sigma_{\text{intermediate}}$.

The precision of the frequency response of the acoustic data handling system, σ_2, can be determined from Section 4.5.2. The variation in the frequency response was selected to be the same for each of the test sites. However, UBC is slightly less because they reduce their data on-line eliminating the error introduced by recording and playing back magnetic tapes.

The accuracy of the aerodynamic instrumentation, σ_3, can be determined from Figures 4-18 through 4-22. The aerodynamic instrumentation error will depend on the actual test condition. A nominal value of 0.7 dB was selected. The precision of the air attenuation model was calculated from Figures 4-8 through 4-13 for USC, UBC, JENOTS, and CR&DC using the standard day conditions of 59° F and 70% relative humidity and the appropriate measurement distances. At EFTC, the actual test day conditions of 54° F and 80% RH were used, as shown in Figure 4-14.

The resulting standard deviation of these pressure multiplier errors was calculated for each frequency. They can be found listed under $\sigma_{\text{intermediate}}$ in Tables 7-I through 7-V for each of the test sites. This intermediate

Table 7-I. Intermediate Standard Deviations at JENOTS.

f (Hz)	σ_1 (dB)	σ_2 (dB)	σ_3 (dB)	σ_4 (dB)	σ_5 (dB)	$\sigma_{intermediate}$ (dB)
200	0.22	0.83	0.70	0.00	1.75	2.07
250	0.53	0.83	0.70	0.00	0.41	1.28
315	0.36	0.83	0.70	0.00	0.38	1.21
400	0.70	0.83	0.70	0.00	2.01	2.40
500	0.55	0.83	0.70	0.00	1.13	1.66
630	1.00	0.83	0.70	0.00	0.38	1.52
800	0.55	0.83	0.70	0.00	0.90	1.51
1,000	0.91	0.83	0.70	0.00	0.55	1.52
1,250	1.01	0.83	0.70	0.00	0.03	1.48
1,600	2.02	0.83	0.70	0.00	0.39	2.33
2,000	1.23	0.83	0.70	0.00	0.11	1.64
2,500	1.20	0.83	0.70	0.00	0.05	1.62
3,150	0.77	0.83	0.70	0.00	0.25	1.35
4,000	0.96	0.83	0.70	0.00	0.00	1.45
5,000	1.20	0.83	0.70	0.00	0.11	1.62
6,300	1.38	0.83	0.70	0.00	0.00	1.76
8,000	2.35	0.83	0.70	0.00	0.00	2.59
10,000	0.96	0.83	0.70	0.00	0.00	1.45
12,500	0.42	0.94	0.70	0.15	0.08	1.26
16,000	0.51	0.94	0.70	0.30	0.00	1.31
20,000	0.80	0.94	0.70	0.52	0.00	1.51
25,000	0.97	0.94	0.70	0.74	0.21	1.70
31,500	0.60	0.94	0.70	1.04	0.13	1.68
40,000	1.85	0.94	0.70	1.41	0.00	2.60
50,000	1.85	0.94	0.70	1.85	0.00	2.87
63,000	1.85	0.94	0.70	2.37	0.00	3.22
80,000	1.85	0.94	0.70	3.26	0.00	3.93

σ_1 = Inverse Square Law
σ_2 = Frequency Response
σ_3 = Aerodynamic Instrumentation
σ_4 = Air Attenuation
σ_5 = Ground Reflections

Table 7-II. Intermediate Standard Deviations at GE/EFTC.

f (Hz)	σ_1 (dB)	σ_2 (dB)	σ_3 (dB)	σ_4 (dB)	σ_5 (dB)	σintermediate (dB)
50	0.11	0.83	0.70	0.02	0.01	1.09
63	0.47	0.83	0.70	0.04	0.01	1.18
80	0.22	0.83	0.70	0.05	0.01	1.11
100	0.56	0.83	0.70	0.06	0.01	1.22
125	0.90	0.83	0.70	0.08	0.01	1.41
160	0.94	0.83	0.70	0.10	0.01	2.07
200	0.52	0.83	0.70	0.11	0.00	1.21
250	0.33	0.83	0.70	0.12	0.02	1.14
315	0.60	0.83	0.70	0.13	0.08	1.25
400	1.08	0.83	0.70	0.17	0.05	1.54
500	0.51	0.83	0.70	0.25	0.18	1.24
630	0.65	0.83	0.70	0.45	0.23	1.36
800	0.60	0.83	0.70	0.71	0.52	1.52
1,000	1.01	0.83	0.70	0.93	0.13	1.76
1,250	1.38	0.83	0.70	1.06	0.42	2.09
1,600	0.88	0.83	0.70	1.11	2.24	2.86
2,000	0.72	0.83	0.70	1.20	0.66	1.89
2,500	1.12	0.83	0.70	1.30	0.06	2.03
3,150	0.81	0.83	0.70	1.40	0.61	2.04
4,000	0.70	0.83	0.70	1.55	0.90	2.21
5,000	0.73	0.83	0.70	1.75	0.12	2.19
6,300	0.51	0.83	0.70	2.05	0.42	2.41
8,000	0.81	0.83	0.70	2.45	0.02	2.80
10,000	0.55	0.83	0.70	2.75	0.11	3.01
12,500	1.87	0.94	0.70	2.95	0.84	3.78
16,000	1.46	0.94	0.70	3.10	0.04	3.62
20,000	1.95	0.94	0.70	3.20	0.54	3.96

σ_1 = Inverse Square Law
σ_2 = Frequency Response
σ_3 = Aerodynamic Instrumentation
σ_4 = Air Attenuation
σ_5 = Ground Reflections

Table 7-III. Intermediate Standard Deviations at GE/CR&DC.

f (Hz)	σ_1 (dB)	σ_2 (dB)	σ_3 (dB)	σ_4 (dB)	σ_5 (dB)	σ_6 (dB)	$\sigma_{intermediate}$ (dB)
200	0.83	0.83	0.70	0.00	0.96	1.48	2.23
250	0.85	0.83	0.70	0.00	0.56	1.45	2.08
315	0.88	0.83	0.70	0.00	0.02	0.00	1.40
400	0.91	0.83	0.70	0.00	0.12	0.95	1.71
500	0.80	0.83	0.70	0.00	0.53	1.70	2.23
630	0.56	0.83	0.70	0.00	0.00	1.00	1.58
800	0.65	0.83	0.70	0.00	0.01	0.48	1.35
1,000	0.76	0.83	0.70	0.00	0.03	0.29	1.36
1.250	0.75	0.83	0.70	0.00	0.00	0.50	1.41
1,600	0.75	0.83	0.70	0.00	0.00	0.25	1.34
2,000	0.73	0.83	0.70	0.00	0.00	1.00	1.65
2,500	0.71	0.83	0.70	0.00	0.06	0.20	1.30
3,150	0.70	0.83	0.70	0.00	0.06	0.25	1.34
4,000	0.68	0.83	0.70	0.00	0.00	0.20	1.30
5,000	0.65	0.83	0.70	0.00	0.23	0.00	1.29
6,300	0.65	0.83	0.70	0.00	0.24	0.00	1.29
8,000	0.65	0.83	0.70	0.00	0.04	0.00	1.27
10,000	0.65	0.83	0.70	0.00	0.08	0.00	1.27
12,500	0.65	0.94	0.70	0.03	0.00	0.00	1.34
16,000	0.65	0.94	0.70	0.07	0.02	0.00	1.34
20,000	0.65	0.94	0.70	0.12	0.24	0.00	1.37
25,000	0.65	0.94	0.70	0.17	0.01	0.00	1.35
31,500	0.65	0.94	0.70	0.23	0.04	0.00	1.36
40,000	0.65	0.94	0.70	0.32	0.03	0.00	1.38

σ_1 = Inverse Square Law
σ_2 = Frequency Response
σ_3 = Aerodynamic Instrumentation
σ_4 = Air Attenuation
σ_5 = Ground Reflections
σ_6 = Ground Reflection Bias

Table 7-IV. Intermediate Standard Deviation at USC.

f (Hz)	σ_1 (dB)	σ_2 (dB)	σ_3 (dB)	σ_4 (dB)	$\sigma_{intermediate}$ (dB)
200	0.45	0.83	0.70	0.00	1.18
250	0.46	0.83	0.70	0.00	1.18
315	0.48	0.83	0.70	0.00	1.19
400	0.50	0.83	0.70	0.00	1.20
500	0.51	0.83	0.70	0.00	1.20
630	0.55	0.83	0.70	0.00	1.22
800	0.58	0.83	0.70	0.00	1.23
1,000	0.61	0.83	0.70	0.00	1.26
1,250	0.65	0.83	0.70	0.00	1.27
1,600	0.65	0.83	0.70	0.00	1.27
2,000	0.62	0.83	0.70	0.00	1.25
2,500	0.61	0.83	0.70	0.00	1.25
3,150	0.60	0.83	0.70	0.00	1.24
4,000	0.57	0.83	0.70	0.00	1.23
5,000	0.52	0.83	0.70	0.00	1.20
6,300	0.50	0.83	0.70	0.00	1.20
8,000	0.46	0.83	0.70	0.00	1.18
10,000	0.40	0.83	0.70	0.00	1.16
12,500	0.35	0.94	0.70	0.03	1.22
16,000	0.28	0.94	0.70	0.06	1.21
20,000	0.24	0.94	0.70	0.10	1.20
25,000	0.23	0.94	0.70	0.14	1.20
31,500	0.22	0.94	0.70	0.19	1.21
40,000	0.22	0.94	0.70	0.26	1.22
50,000	0.22	0.94	0.70	0.35	1.24
63,000	0.22	0.94	0.70	0.44	1.27
80,000	0.22	0.94	0.70	0.61	1.34

σ_1 = Inverse Square Law
σ_2 = Frequency Response
σ_3 = Aerodynamic Instrumentation
σ_4 = Air Attenuation

Table 7-V. Intermediate Standard Deviation at UBC.

f (Hz)	σ_1 (dB)	σ_2 (dB)	σ_3 (dB)	σ_4 (dB)	$\sigma_{intermediate}$ (dB)
200	0.34	0.43	0.70	0.00	0.89
250	0.34	0.43	0.70	0.00	0.89
315	0.34	0.43	0.70	0.00	0.89
400	0.34	0.43	0.70	0.00	0.89
500	0.34	0.43	0.70	0.00	0.89
630	0.35	0.43	0.70	0.00	0.89
800	0.50	0.43	0.70	0.00	0.96
1,000	0.60	0.43	0.70	0.00	1.02
1,250	0.69	0.43	0.70	0.00	1.07
1,600	0.60	0.43	0.70	0.00	1.02
2,000	0.58	0.43	0.70	0.00	1.01
2,500	0.55	0.43	0.70	0.00	0.99
3,150	0.60	0.43	0.70	0.00	1.02
4,000	0.62	0.43	0.70	0.00	1.03
5,000	0.64	0.43	0.70	0.00	1.04
6,300	0.60	0.43	0.70	0.00	1.02
8,000	0.58	0.43	0.70	0.00	1.01
10,000	0.57	0.43	0.70	0.00	1.00
12,500	0.64	0.63	0.70	0.04	1.14
16,000	0.75	0.63	0.70	0.07	1.21
20,000	0.82	0.63	0.70	0.13	1.26
25,000	0.75	0.63	0.70	0.19	1.22
31,500	0.70	0.63	0.70	0.26	1.20
40,000	0.64	0.63	0.70	0.35	1.19
50,000	0.78	0.63	0.70	0.46	1.31
63,000	0.90	0.63	0.70	0.59	1.43
80,000	1.09	0.63	0.70	0.81	1.65

σ_1 = Inverse Square Law
σ_2 = Frequency Response
σ_3 = Aerodynamic Instrumentation
σ_4 = Air Attenuation

standard deviation must now be modified to reflect bias errors from each test site.

The magnitude of bias error and precison introduced from extraneous noise sources is determined from examining a specific test spectrum. The test spectrum is then compared to the ambient, background, electrical, or other contaminant noise floor. The intermediate standard deviation of the precision error for each test facility is corrected based on the influence of these other noise sources using Equation (114) or Figure 4-3. This influence is a function of the dB level between the test spectrum and the contaminant spectrum at each frequency.

Two representative jet test conditions were used to evaluate the total precision error:

Case	T_T (° K)	T_T (° R)	V_j(m/s)	V_j (fps)
A	600	1080	305	1000
B	300	540	213	700

Each test facility has a different measurement arc radius and can accommodate different nozzle diameters (Table 7-VI) which change the level and shift and modify the spectra of these two test conditions. Accounting for these effects the jet spectra at 90° can be calculated using SAE ARP876 (Reference 41). The measured contamination spectra can then be compared to these test spectra.

Table 7-VI. Comparison of Test Site Arc Radius and Nozzle Diameter.

Test Site	Arc Radius ft	Typical Test Nozzle Diameter inches
JENOTS	40	5.7
GE/EFTC	160	20.84
GE/CR&DC	9	1.0
USC	7.5	1.0
UBC	10	0.79

Figures 7-1 through 7-5 show the known contaminant spectra compared to the two test spectra at each of the test sites. The intermediate standard deviation can now be modified for each test sites contaminant noise sources. It was assumed that flow related contaminant levels had a standard deviation

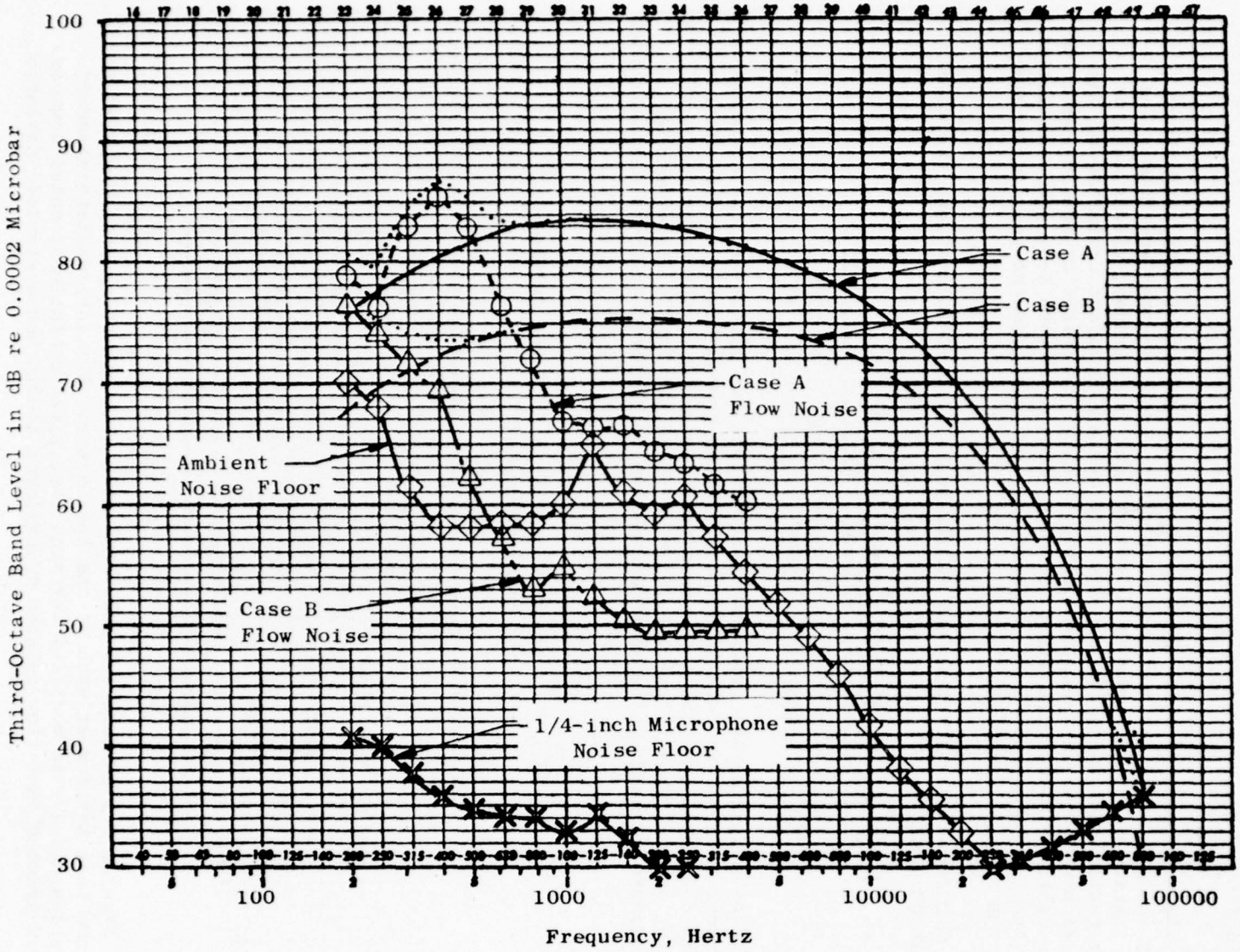


Figure 7-1. Comparisons of Two Test Cases to the Microphone Noise Floor, Ambient Noise and Noise at JENOTS.

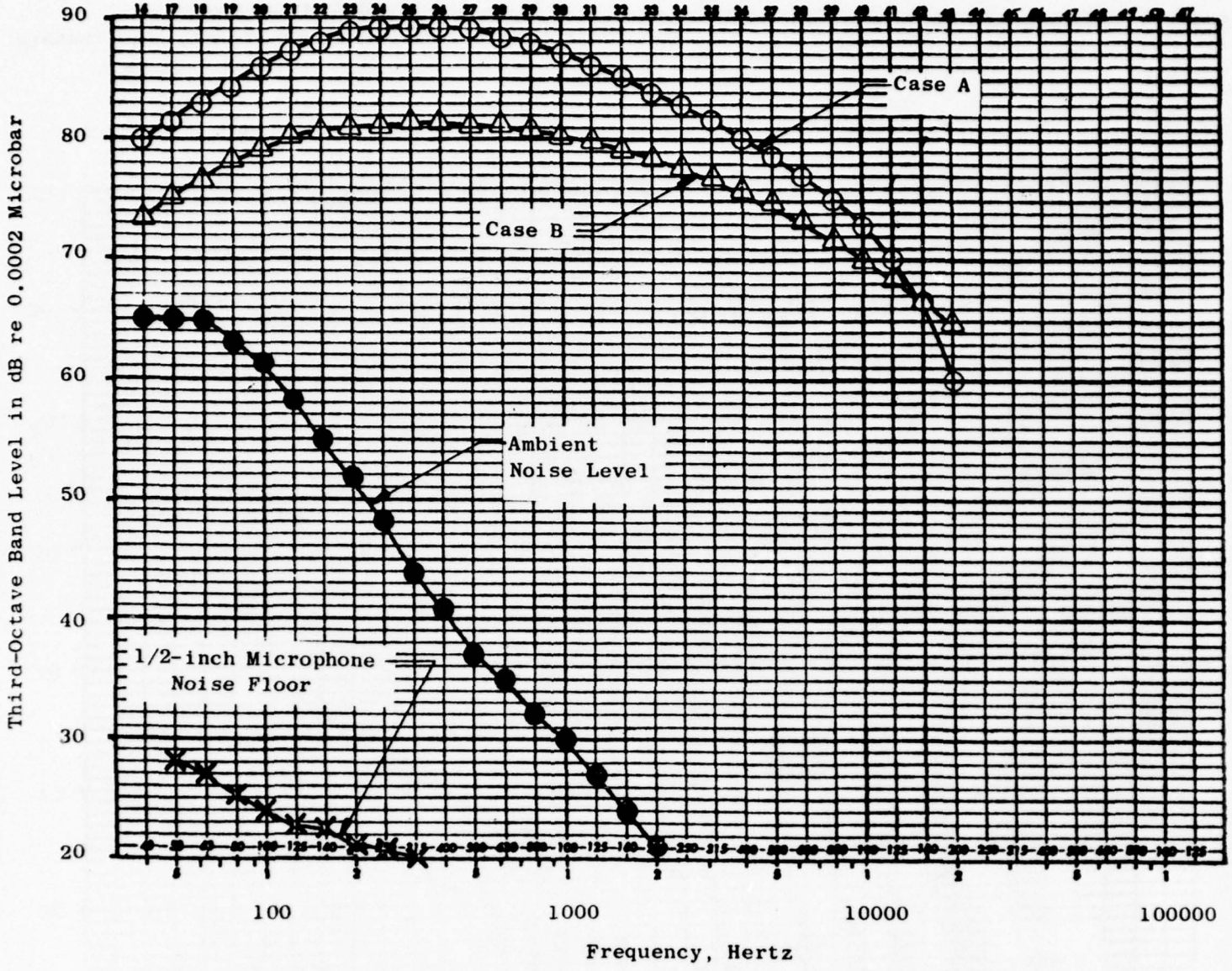


Figure 7-2. Test Spectra at GE/EFTC Compared to Microphone and Ambient Noise Levels.

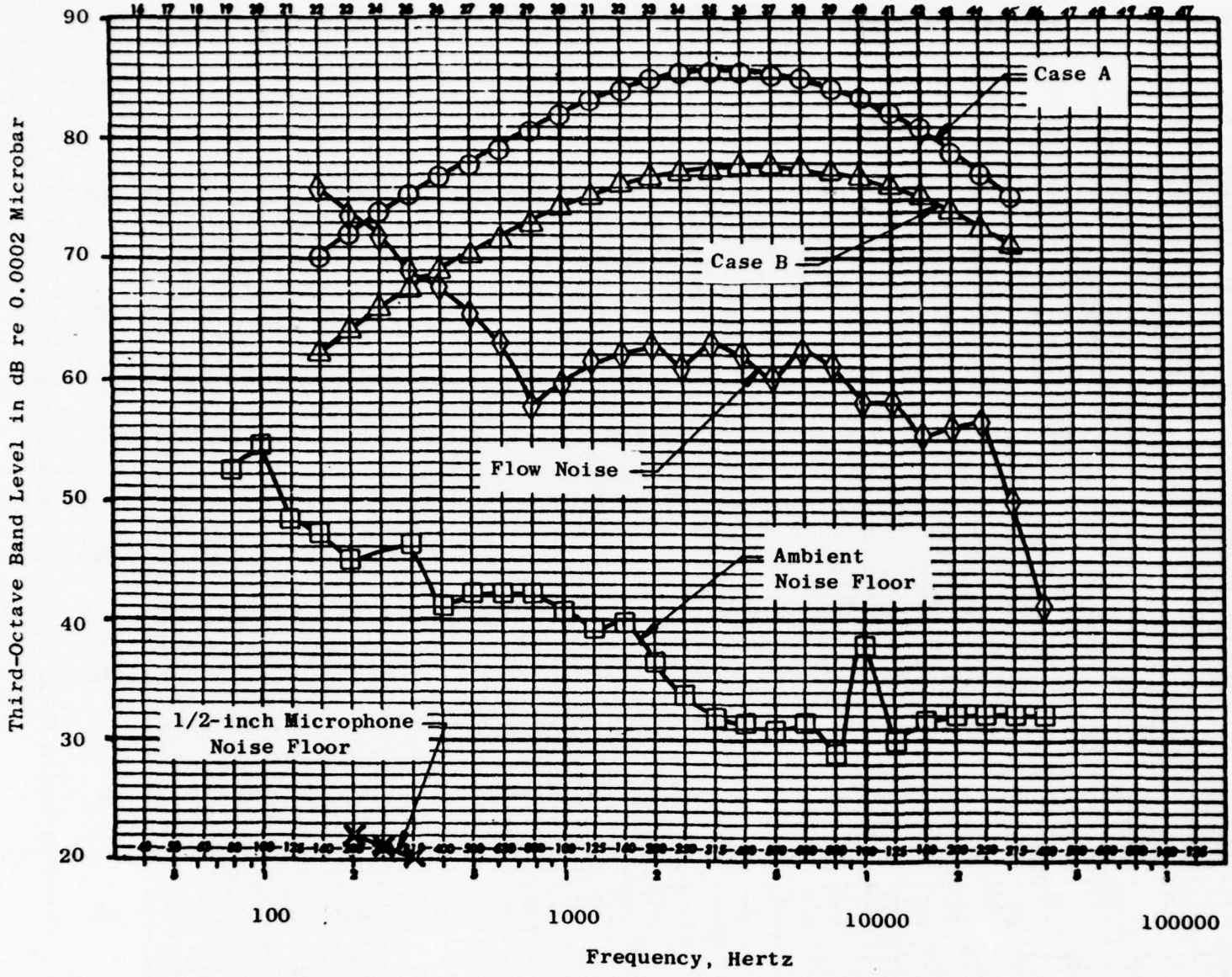


Figure 7-3. Comparison of Two Test Cases to the Flow Noise, Ambient Noise and Microphone Noise Floor at GE/CR&DC.

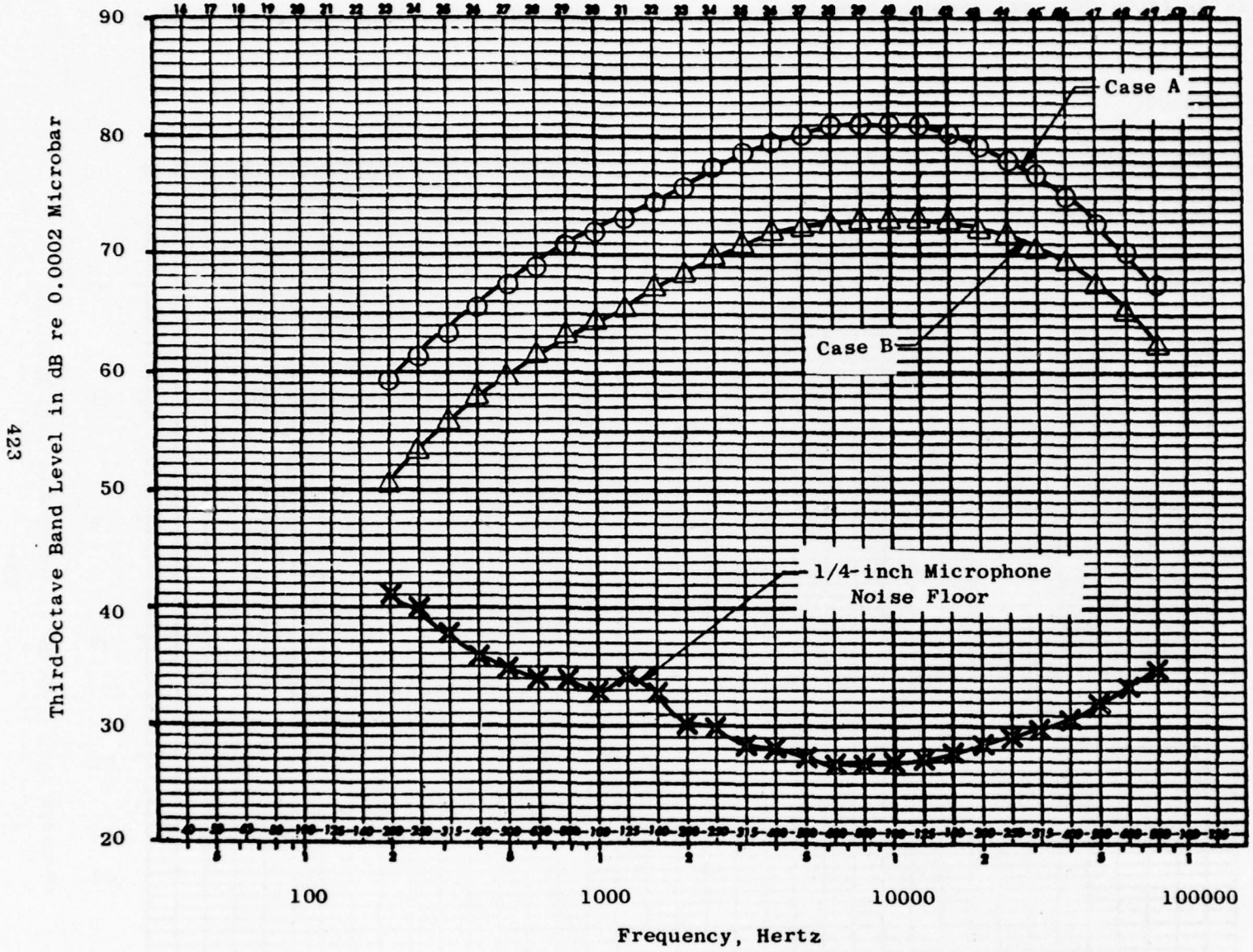


Figure 7-4. Test Spectra at USC Compared to Microphone Noise Floor Level.

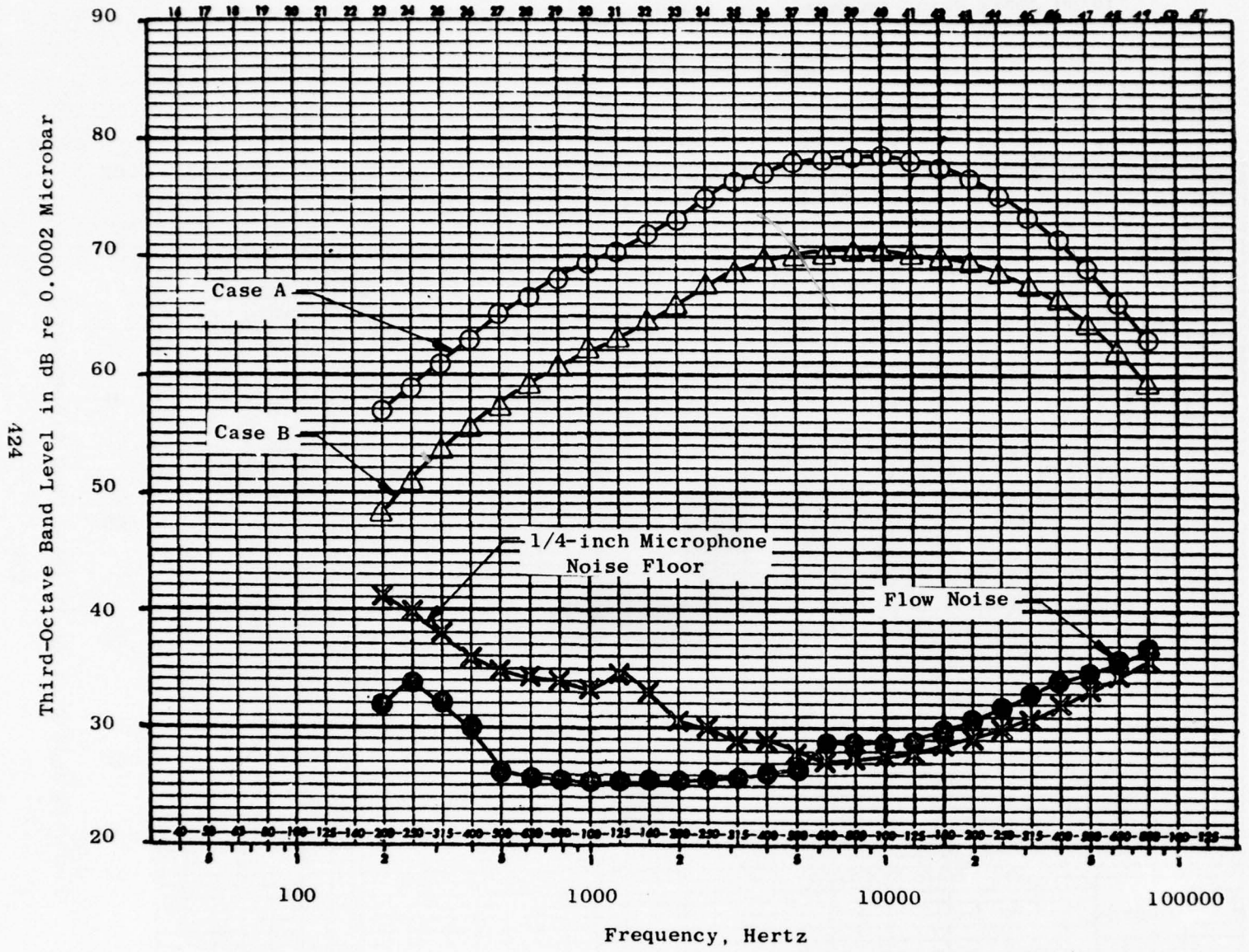


Figure 7-5. Test Spectra at UBC Compared to Flow Noise and the Microphone Noise Floor.

of 5 dB, while microphone and electrical noise floors had a standard deviation of 3 dB. Applying this assumption and the level difference δ_i to Equation (114) the final standard deviations could be determined. The final standard deviations for the two test cases for each of the five test sites are plotted as a function of frequency in Figures 7-6 through 7-10. It can be seen that the standard deviation will be influenced, in part, by the test condition being examined. This is evidenced by the difference in standard deviation levels for the two test cases at some test sites. In general, the higher the test noise level is, the less it will be effected by contaminant levels and the standard deviation will approach the intermediate value level.

7.4 EFFECT OF THE TAPE RECORDER

The best efforts to reduce a test sites standard deviation can be negated if careful attention is not paid of the signal gain into the tape recorder. If not properly set, the tape recorder noise floor will influence the measured spectra. As previously mentioned, UBC reduces their data on line and do not use a tape recorder. However, noise floors of typical tape recorders at the other test sites were compared to the two test spectra in Figures 7-11 through 7-15. In each figure, three noise floors are shown; the optimum gain setting, the gain off by 10 dB, and the gain off by 20 dB. The noise floor at the optimum gain setting is set at the maximum signal to noise ratio. However, in actual practice the optimum gain cannot be exactly set and a good tape recorder operator will keep the gain up as high as possible so that the noise floor will actually be between the optimum level and the level indicated by the gain off by 10 dB. Since amplifiers usually have gain switches in 10 dB steps, if any more gain is applied the signal will be clipped. The gain off by 20 dB noise floor is shown as an example of what can happen if careful attention is not paid to the signal levels going into the tape recorder.

If we assume the standard deviation of the tape recorder noise floor is 3 dB, we can calculate its effect on the test sites standard deviation. The frequencies effected with their standard deviations are listed in Tables 7-VII through 7-IX. Tables were not presented for the intermediate band tape recorder at GE/EFTC, or the wide band Group I tape recorder at GE/CR&DC. Their effect on the test site standard deviation was negligible (<0.05) for the worst case at the highest frequency.

The bias accuracy error introduced by the tape recorder noise floor should always be removed from test data whenever it appears. It is usually evidenced by a curling up of the spectrum at either the very high or very low frequencies.

7.5 OASPL PRECISION ESTIMATE

The standard deviation of the overall sound pressure level can be determined by again employing Equation (114) for each frequency over a test spectrum. The standard deviations of the overall levels for the two test cases and five test sites was calculated and are shown in Table 7-X. UBC had the lowest values at 0.29 and 0.27 dB.

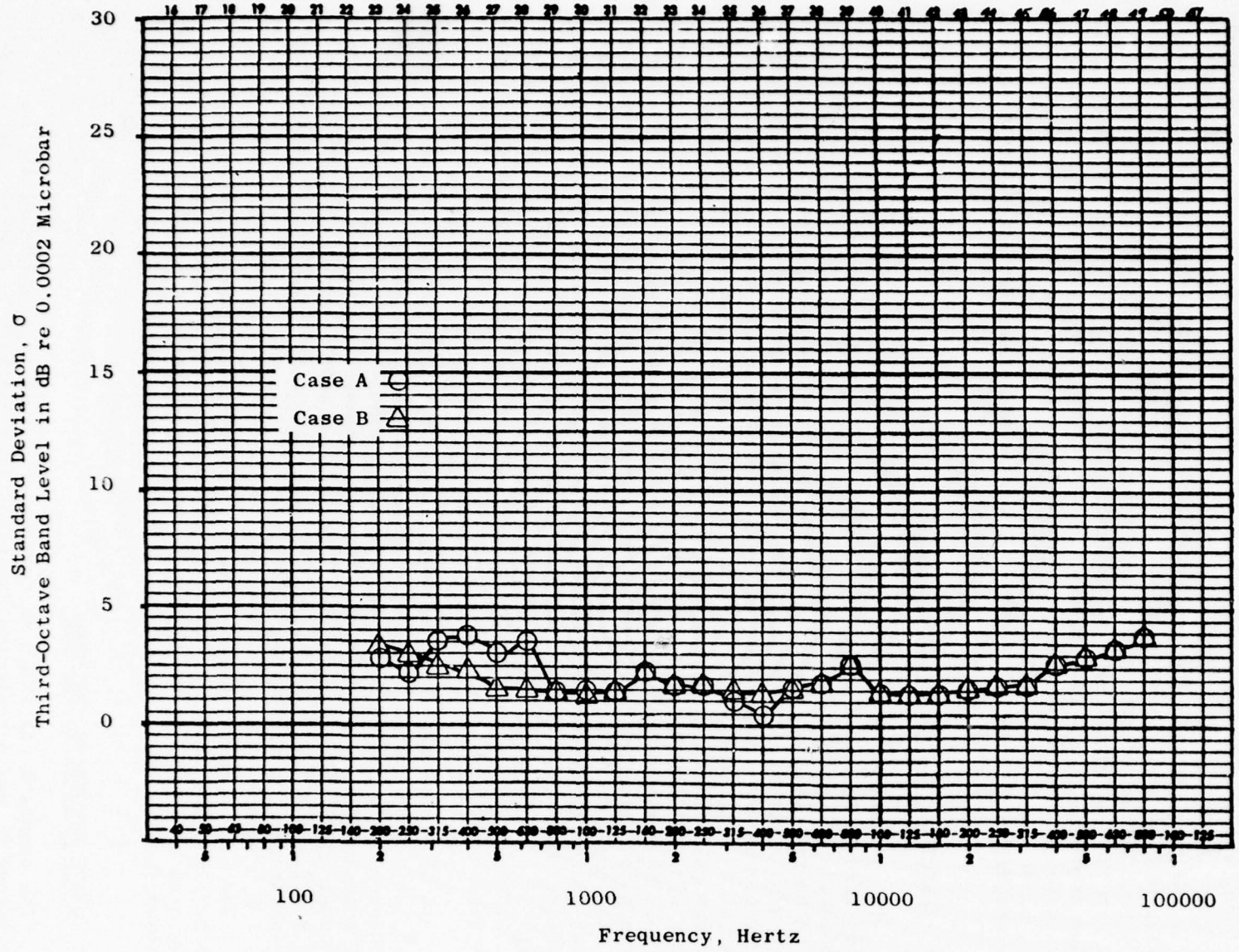


Figure 7-6. Standard Deviation of Data at JENOTS.

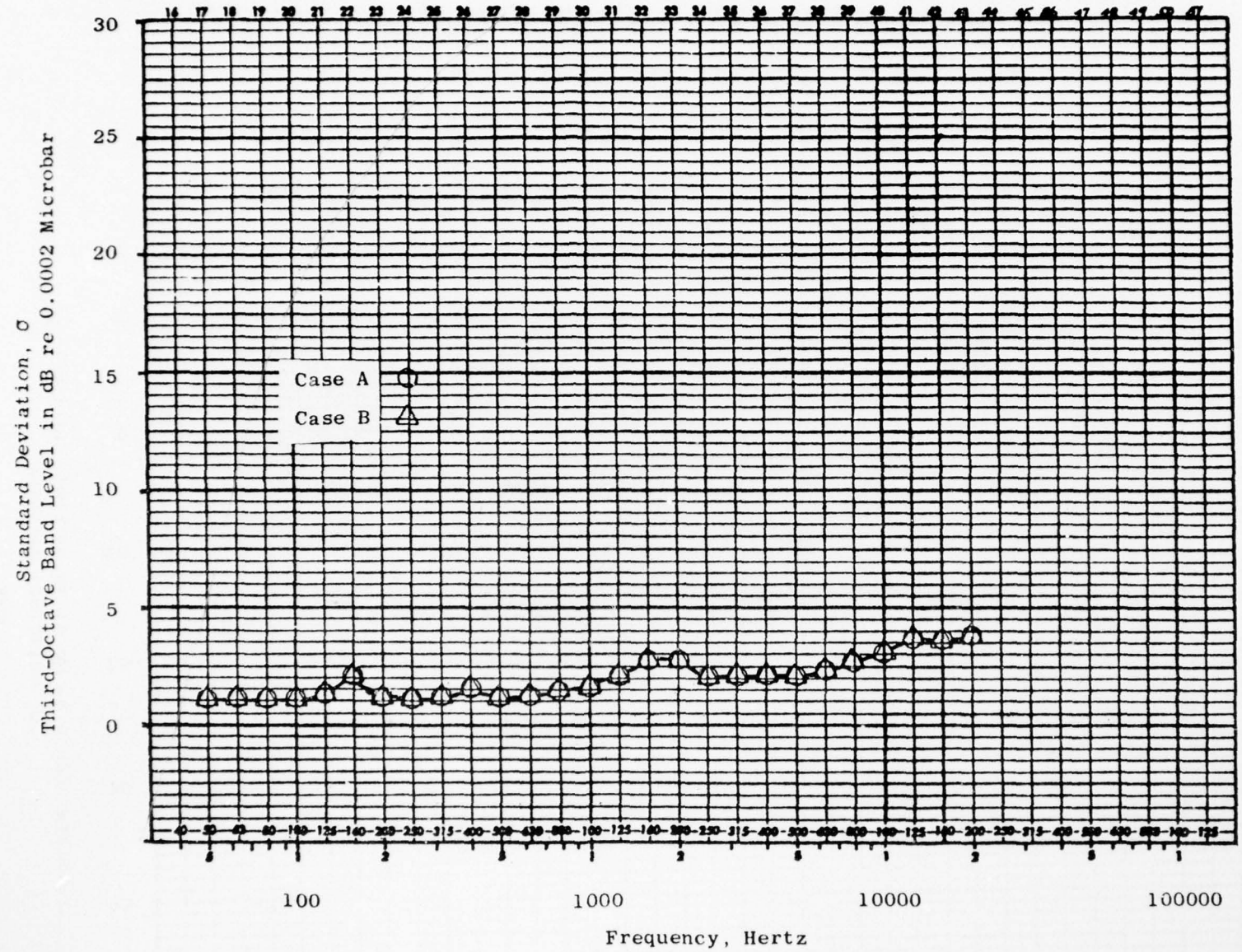


Figure 7-7. Standard Deviation of Data at GE/EFTC.

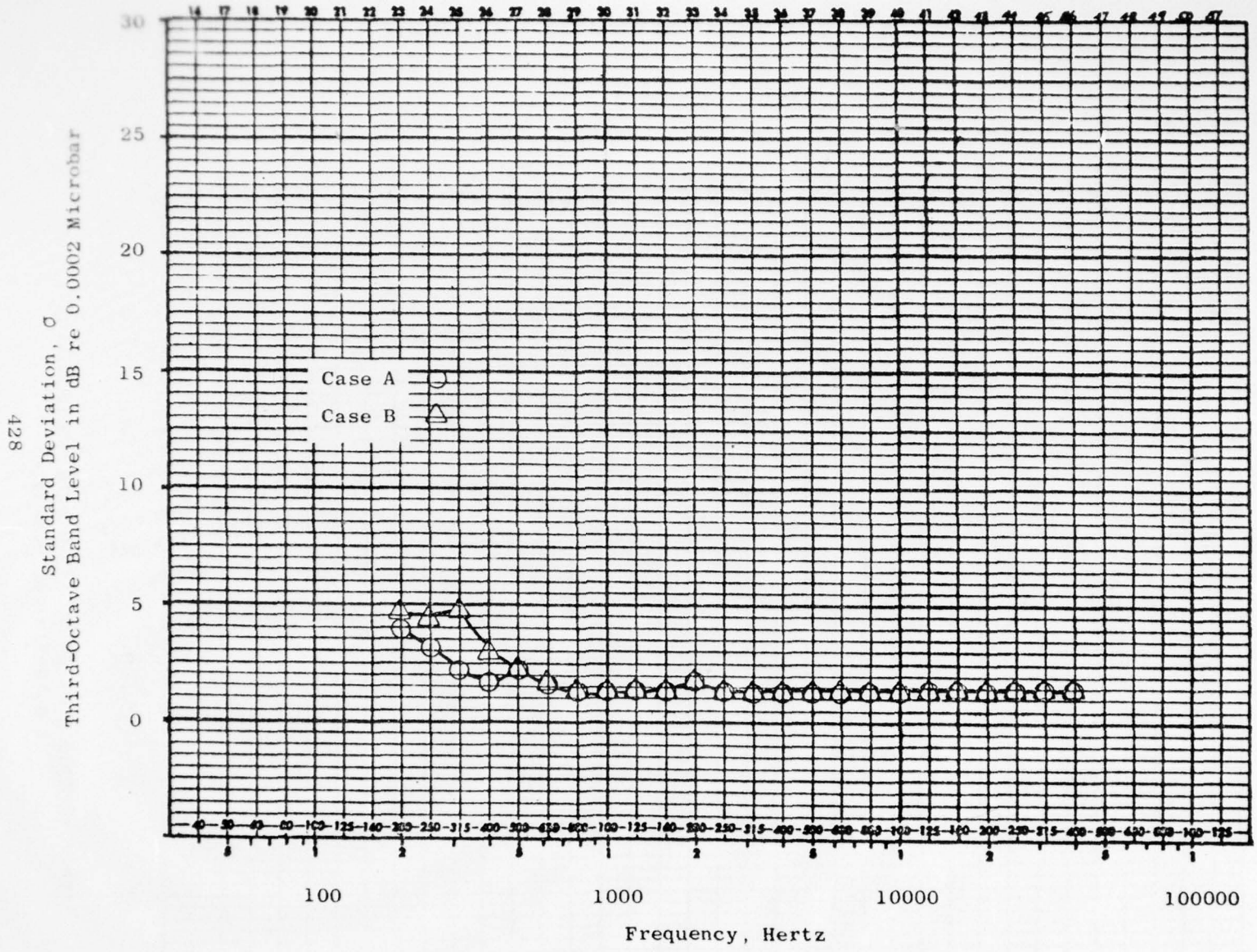


Figure 7-8. Standard Deviation of Data at GE/CR&DC.

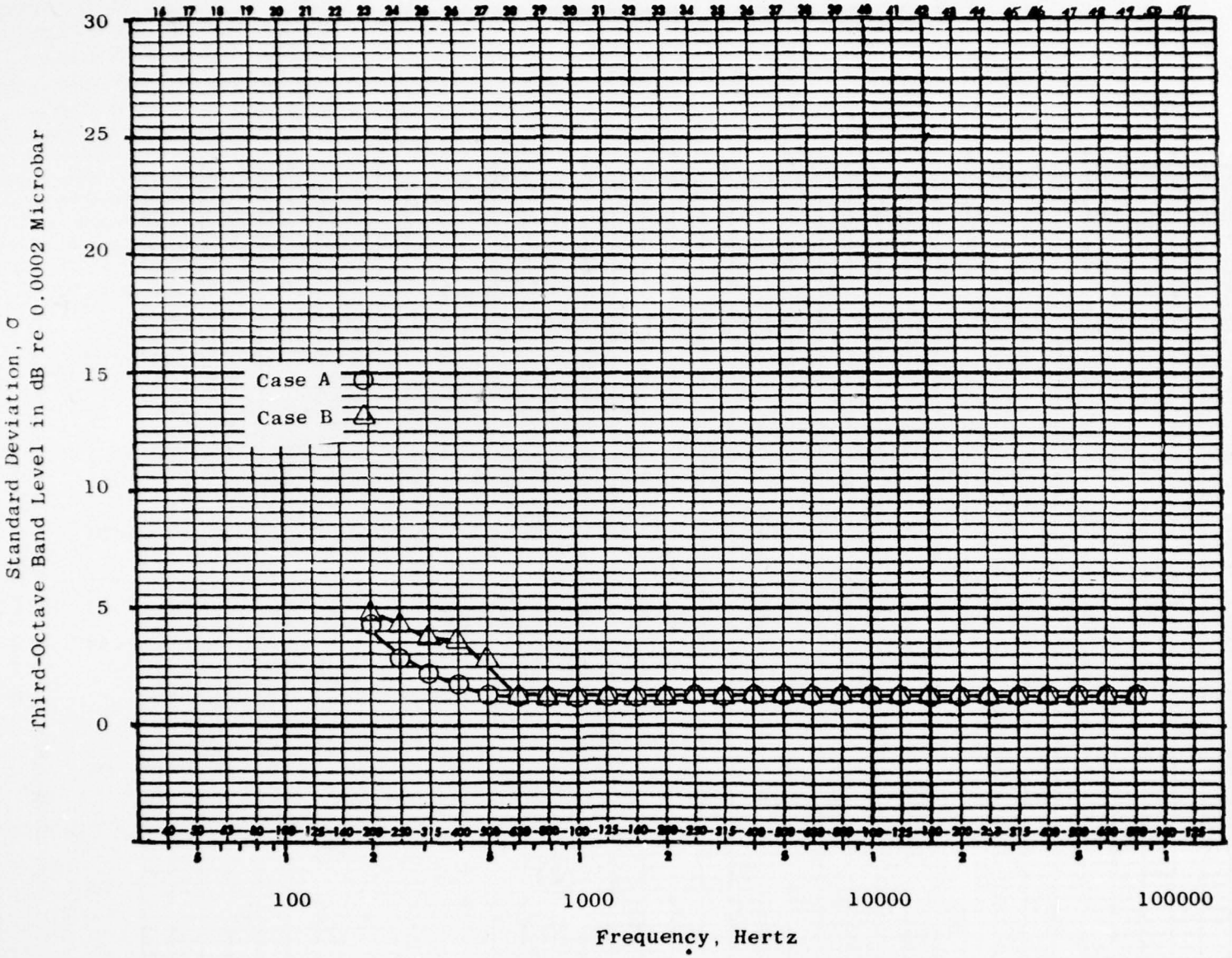


Figure 7-9. Standard Deviation of Data at USC.

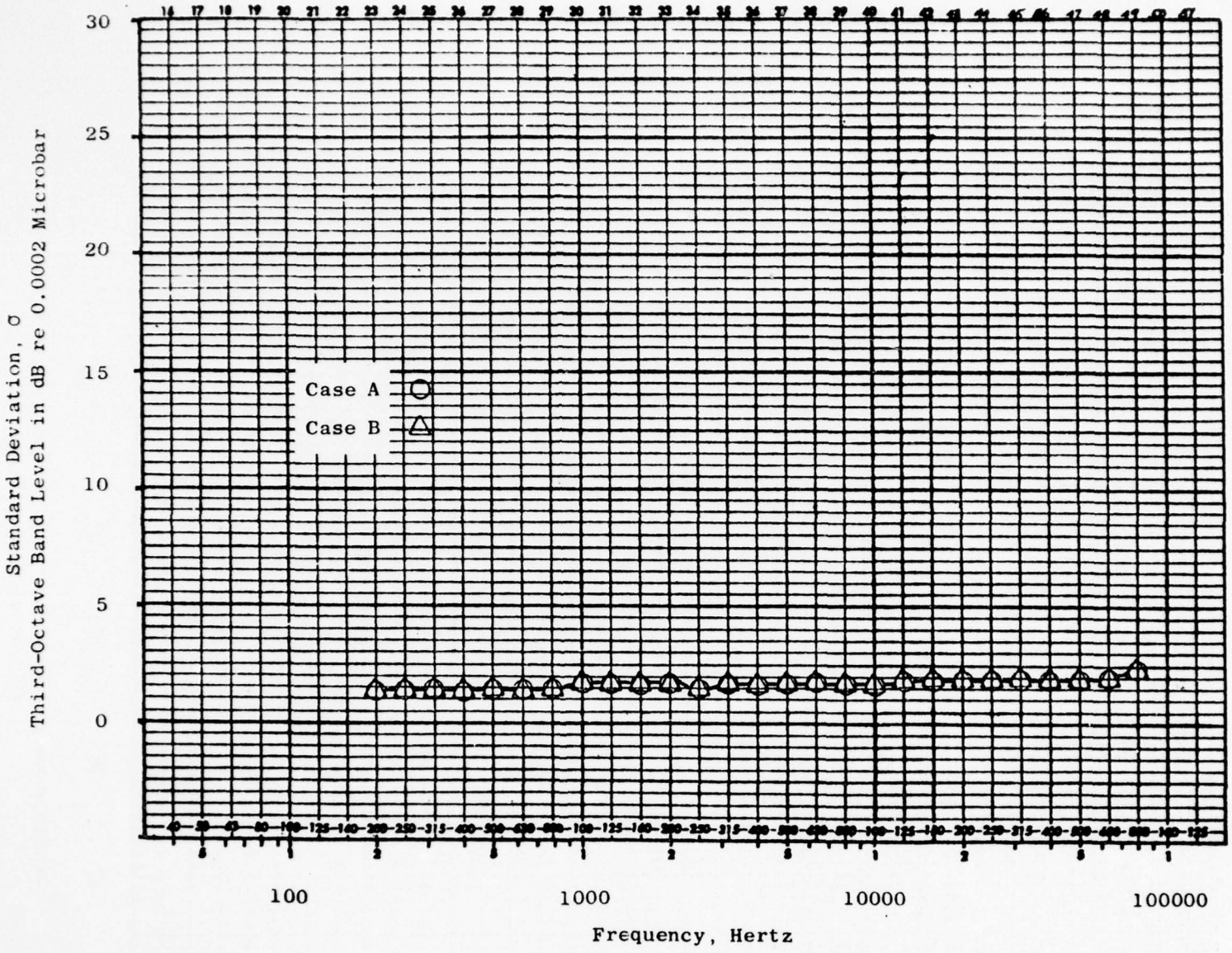


Figure 7-10. Standard Deviation of Data at UBC.

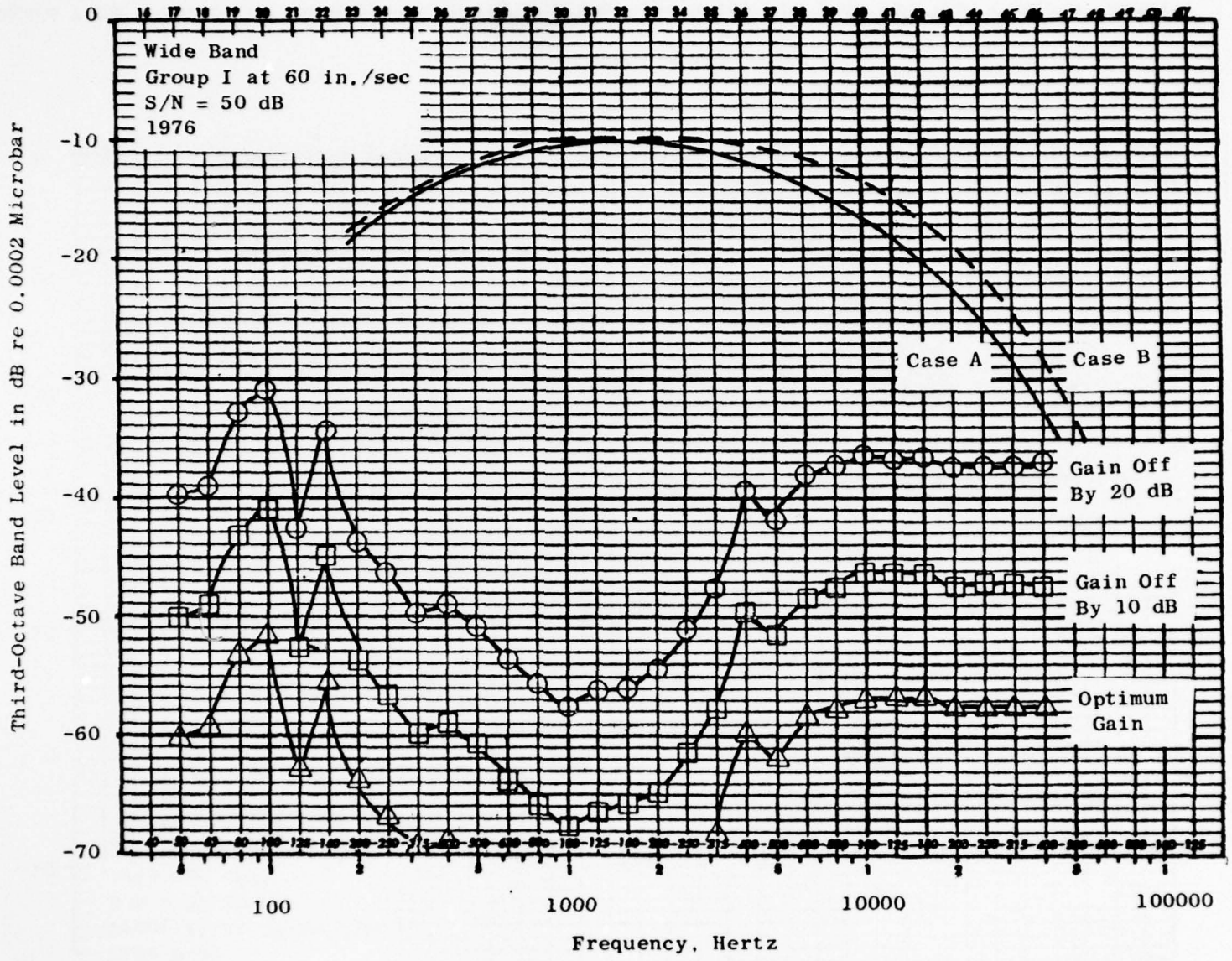


Figure 7-11. Effect of Wideband Group I Tape Recorder Noise Floor on Two Test Cases at JENOTS.

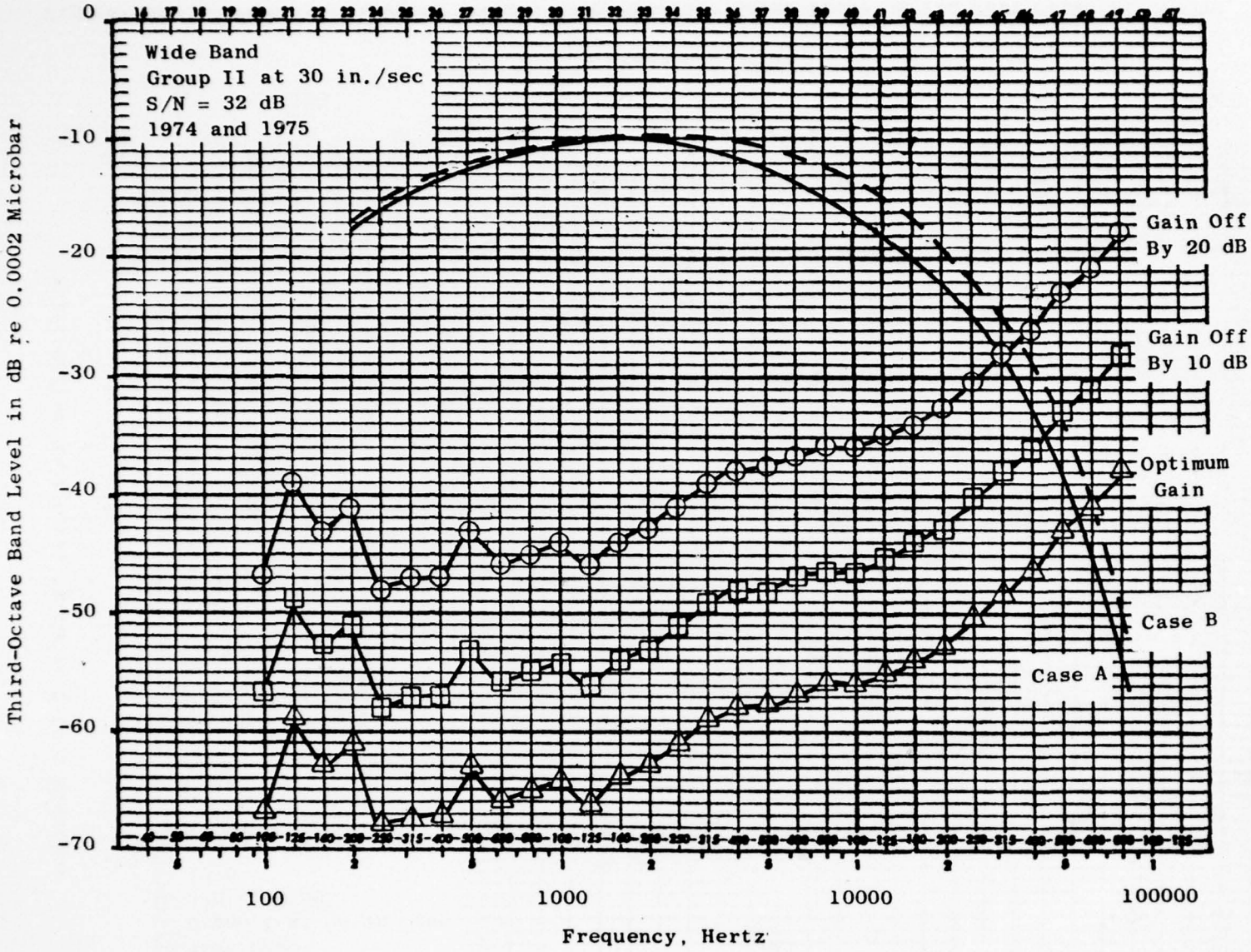


Figure 7-12. Effect of Wideband Group II Tape Recorder Noise Floor on Two Test Cases at JENOTS.

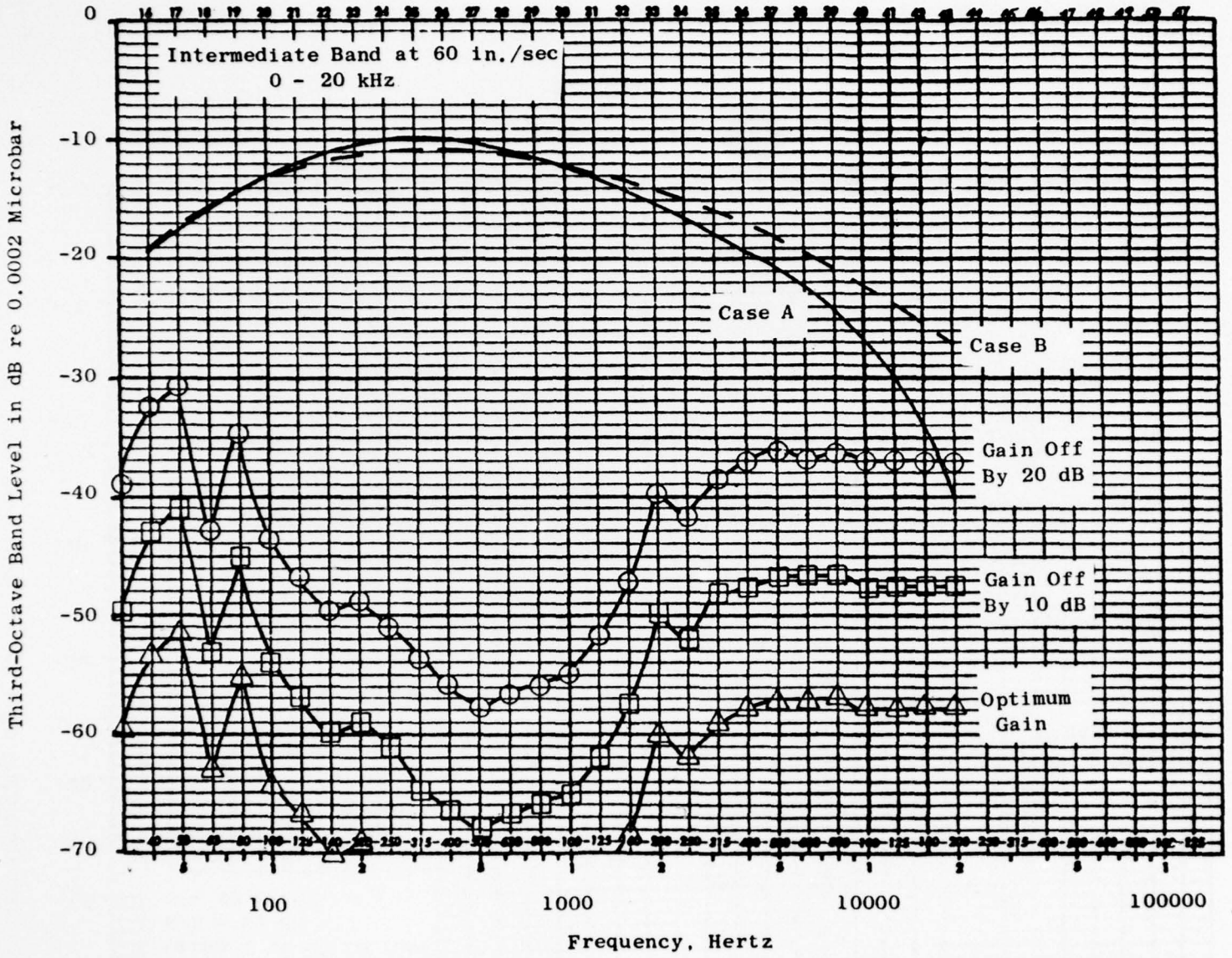


Figure 7-13. Effect of Tape Recorder Noise Floor on Two Test Spectra at GE/EFTC.

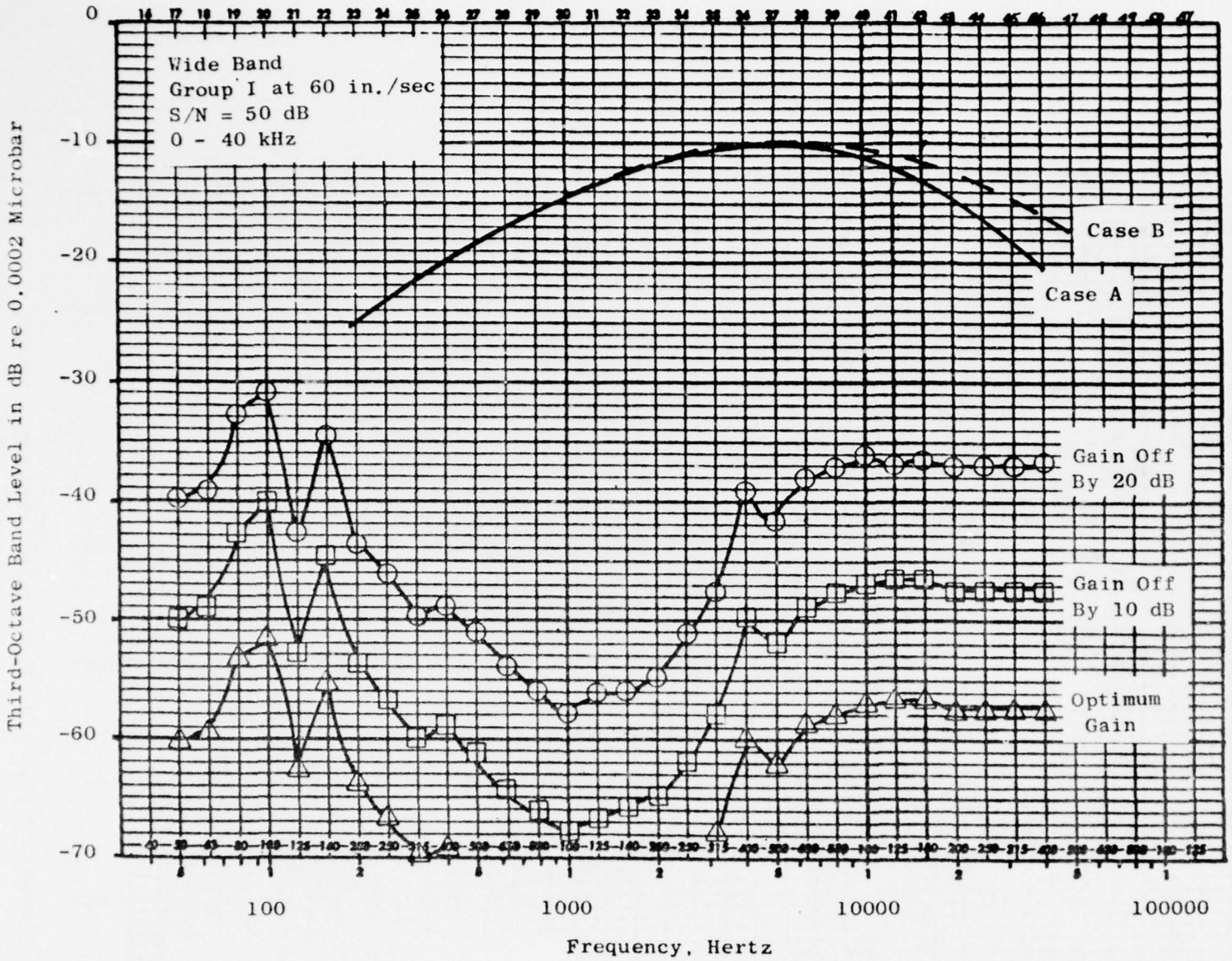


Figure 7-14. Effect of Tape Recorder Noise Floor on Two Test Spectra at GE/CR&DC.

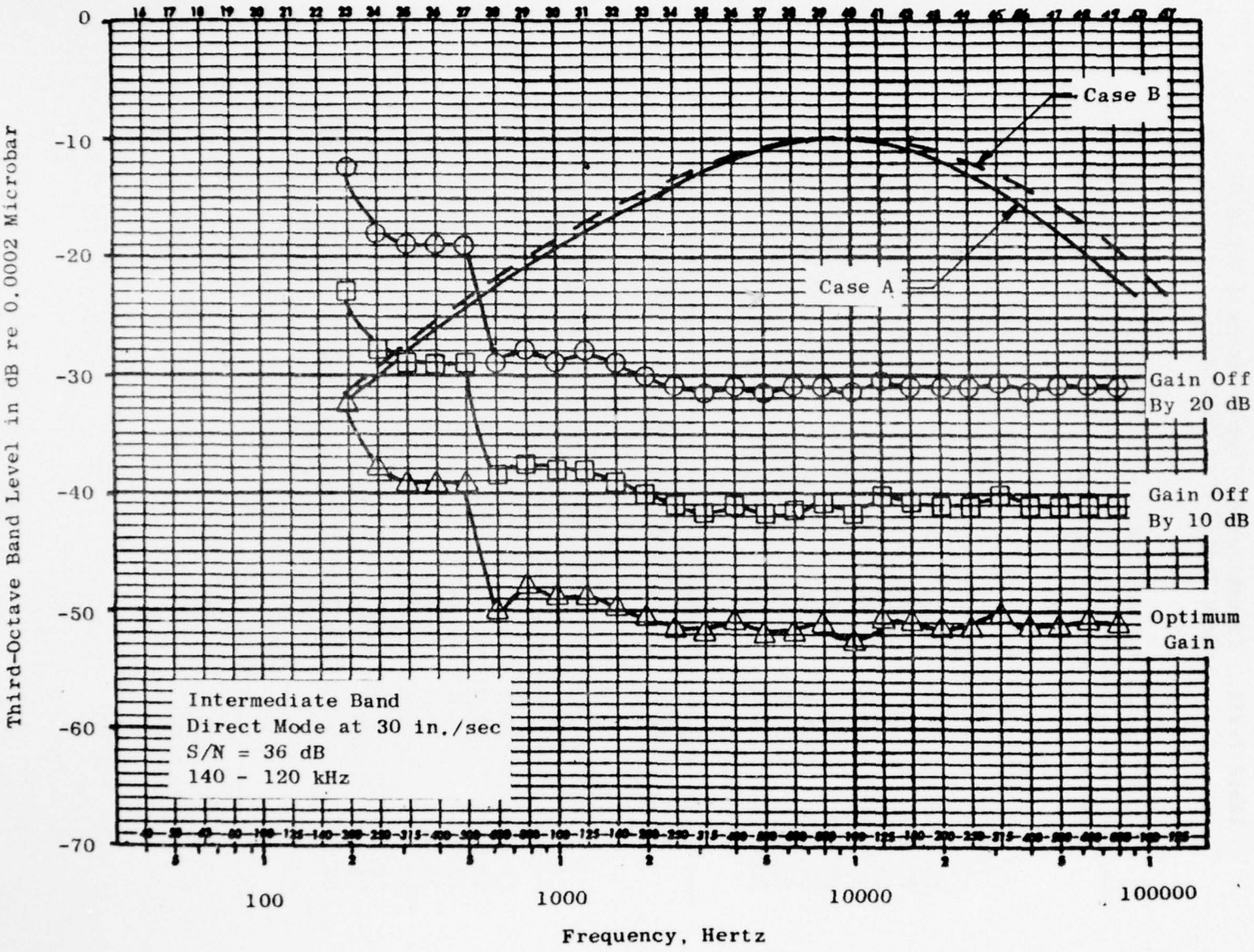


Figure 7-15. Effect of Tape Recorder Noise Floor on Two Test Spectra at USC.

Table 7-VII. Contamination from a Wideband Group II Tape Recorder at JENOTS.

σ_{floor} = 3 dB S/N = 32 dB at 30 ips

Case A: V_j = 305 m/s (1000 fps); T_T = 600° K (1080° R)

f (Hz)	Gain Off By 20 dB δ dB	σ	Gain Off By 10 dB δ dB	σ	Optimum Gain δ dB	σ
16,000	14.0	1.27				
20,000	9.5	1.39				
25,000	5.0	1.48	15.0	1.65		
31,500	0.0	1.72	10.0	1.55		
40,000	-12.0	2.83	- 2.0	2.10	8.0	2.28
50,000	-16.0	2.93	- 6.0	2.47	4.0	2.22
63,000	-26.0	2.99	-16.0	2.93	- 6.0	2.48
80,000	-37.0	3.00	-27.0	3.00	-17.0	2.94

Case B: V_j = 213 m/s (700 fps); T_T = 300° K (540° R)

f (Hz)	Gain Off By 20 dB δ dB	σ	Gain Off By 10 dB δ dB	σ	Optimum Gain δ dB	σ
16,000	17.0	1.29				
20,000	13.0	1.45				
25,000	9.0	1.55				
31,500	3.5	1.49	13.5	1.61		
40,000	- 3.0	2.18	9.0	2.22	19.0	2.55
50,000	-11.0	2.79	- 1.0	2.10	9.0	2.57
63,000	-20.5	2.97	-10.5	2.77	- 0.5	2.20
80,000	-34.0	3.00	-24.0	2.99	-14.0	2.89

Table 7-VIII. Contamination from a Wideband Group I Tape Recorder at JENOTS.

σ_{floor} = 3 dB S/N = 50 dB at 60 ips

Case A: V_j = 305 m/s (1000 fps); T_T = 600° K (1080° R)

f (Hz)	Gain Off By 20 dB δ dB	σ	Gain Off By 10 dB δ dB	σ	Optimum Gain δ dB	σ
6,300	14.5	1.70				
8,000	12.4	2.45				
10,000	10.7	1.36				
12,500	8.5	1.16				
16,000	3.5	1.30	13.5	1.26		
20,000	- 2.5	1.99	7.5	1.36		
25,000	-11.0	2.78	- 1.0	1.83	9.0	1.55
31,500	-28.0	3.00	-18.0	2.95	- 8.0	2.60
40,000	-43.0	3.00	-33.0	3.00	-23.0	3.00
50,000	-53.0	3.00	-43.0	3.00	-33.0	3.00
63,000	-63.0	3.00	-53.0	3.00	-43.0	3.00
80,000	-73.0	3.00	-63.0	3.00	-53.0	3.00

Case B: V_j = 213 m/s (700 fps); T_T = 300° K (540° R)

f (Hz)	Gain Off By 20 dB δ dB	σ	Gain Off By 10 dB δ dB	σ	Optimum Gain δ dB	σ
8,000	15.5	2.52				
10,000	15.3	1.41				
12,500	13.5	1.21				
16,000	12.5	1.25				
20,000	10.0	1.40				
25,000	8.0	1.52				
31,500	5.5	1.47				
40,000	3.5	2.02	13.5	2.49		
50,000	1.0	2.08	11.0	2.67		
63,000	- 1.0	2.20	9.0	2.88		
80,000	- 3.0	2.39	7.0	3.31	17.0	3.85

Table 7-IX. Contamination from an Intermediate Band Tape Recorder Noise Floor at USC.

σ_{floor} = 3 dB S/N = 36 dB at 30 ips

Case A: V_j = 305 m/s (1000 fps); T_T = 600° K (1080° R)

f (Hz)	Gain Off By 20 dB δ dB	σ	Gain Off By 10 dB δ dB	σ	Optimum Gain δ dB	σ
200	- 6.0	2.41				
250	- 3.5	2.11	6.5	1.11		
315	- 1.0	1.75	9.0	1.11		
400	1.2	1.46	11.2	1.14		
500	3.3	1.26	13.3	1.15		
630	5.2	1.17				
800	6.5	1.15				
1,000	8.5	1.16				
1,250	10.0	1.19				
1,600	12.0	1.21				
⋮						
50,000	13.0	1.19				
63,00	10.5	1.19				
80,000	9.0	1.24				

Case B: V_j = 213 m/s (700 fps); T_T = 300° K (540° R)

f (Hz)	Gain Off By 20 dB δ dB	σ	Gain Off By 10 dB δ dB	σ	Optimum Gain δ dB	σ
200	- 6.0	2.41				
250	- 3.3	2.08	6.7	1.11		
315	- 0.9	1.74	9.1	1.11		
400	1.8	1.40	11.8	1.14		
500	3.8	1.22				
630	6.0	1.15				
800	7.5	1.14				
1,000	9.7	1.17				
1,250	11.0	1.20				
1,600	13.0	1.22				
⋮						
63,000	13.5	1.22				
80,000	12.0	1.27				

Table 7-X. Standard Deviation of Test Case OASPL at Five Test Sites.

Test Site	Standard Deviation, σ, dB	
	Case A	Case B
JENOTS	0.53	0.41
GE/EFTC	0.38	0.37
GE/CR&DC	0.35	0.32
USC	0.32	0.30
UBC	0.29	0.27

8.0 NOISE SOURCE LOCATION TECHNIQUES

The search for a single reliable measurement technique for establishing the noise source distributions in the jet plume was conducted in five steps as follows:

1. General survey and classification
2. Feasibility study
3. Controlled experimental study
4. Application of measurement techniques to jets
5. Recommend best method for subsequent tasks

In the recent past, there have been many techniques studied for the location of noise sources in and around flowing jets. There is such considerable variety in the approaches and instrumentation involved with these techniques that it is difficult to succinctly categorize them. Not only are the techniques varied in how the measurements are made but, also, in what is measured. The bulk of the techniques measure pressure fluctuations, but the more exotic techniques measure density, temperature, velocity, and momentum fluctuations.

Significant advances in the instrumentation field have resulted from jet noise source location experiments. Pressure probes have been extensively studied to optimize their usefulness. Far-field listening devices, such as arrays and mirrors, have been considerably improved for jet noise measurements. All sorts of hot wire, hot film, infrared, and laser systems have been developed to implement the more exotic jet noise source location measurement techniques.

The main limitation to all noise source location experiments is the lack of a uniqueness theorem to guarantee that the "source" measured by any one of the techniques is actually the origin of the noise. Unfortunately, several different source distributions are capable of generating a common far-field signature. It is this source position ambiguity, along with the accuracy limitations, that will determine the degree of usefulness of the various noise source location techniques.

As the shortcoming of each of the methods became apparent, it was rated relative to the remaining candidates to see if it was acceptable. Methods which would require extensive research and development time to bring them to the necessary level of acceptance were eliminated from consideration. Three methods (in jet - far field correlation using a laser shadowgraph, hole in the wall, and ellipsoidal mirror microphone) survived the screening process to be applied to jet noise measurements. Of these three, the ellipsoidal mirror microphone was ultimately recommended as the prime source location

technique, along with the laser velocimeter, to be used in subsequent tasks of the DOT High Velocity Jet Noise Program.

The laser velocimeter discussion included in Section 8.4 is based on its development and demonstration as a point source location technique (e.g. in-jet to far field) as carried out under the DOT/USAF Supersonic Jet Exhaust Noise Program, Contract F33615-73-C-2031.

8.1 GENERAL SURVEY AND CLASSIFICATION

A literature survey was made to gather background on the various noise source location techniques. The results of this survey helped guide the selection of the specific techniques further developed under this program. A classification of the techniques was made under five headings for the purposes of this study:

- Near field surveys
- Triangulation and plane image technique
- Hole-in-the-wall
- Directional microphones
- Correlation techniques with in-jet measurements

8.1.1 Near Field Surveys

One of the more obvious techniques for jet noise source location is a simple array of microphones or a traversing microphone that measures sound pressure levels along the boundary of the jet. Several authors (References 44, 45, and 46) have reported results from these type measurements.

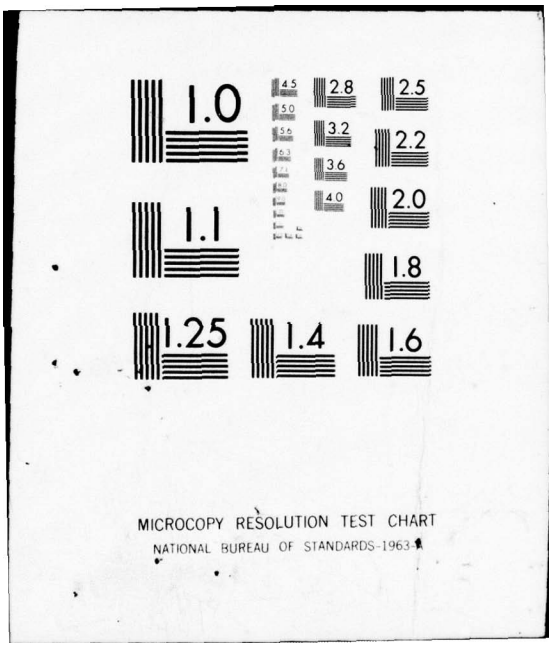
Near-field sound pressure level contours for 1/3-octave bands obtained from noise measurements of a turbofan engine were used for source location determination for a jet under the influence of an outer annular velocity stream. A typical contour from Reference 44 is shown in Figure 8-1. Considering the equal sound pressure level contours to be analogous to altitude contours on a map, and appealing to intuition, a line is drawn up the "spur of the hill," ending at a point in the jet which can be interpreted as being the source location. Obviously, this method is not precise, but it does yield a qualitative description of source location (or apparent source location) in the presence of secondary flow.

An approximation to the contour method is to traverse a microphone along the boundary of a jet as shown in Figure 8-2 (References 47 through 50). The sound pressure at a particular frequency will be a maximum at that location along the jet boundary corresponding to the location of the source of the given frequency.

AD-A041 848 GENERAL ELECTRIC CO CINCINNATI OHIO AIRCRAFT ENGINE GROUP F/G 14/2
HIGH VELOCITY JET NOISE SOURCE LOCATION AND REDUCTION. TASK 1. --ETC(U)
UNCLASSIFIED FEB 77 C T SAVELL, E J STRINGAS DOT-OS-30034
R77AEG187 FAA-RD-76-79-1 NL

6 OF 7
AD A041 848




1.0
1.1
1.25
1.4
1.6
1.8
2.0
2.2
2.5
2.8
3.2
3.6
4.0
4.5
5.0
5.6
6.3
7.1
8
9
10
11
MICROCOPY RESOLUTION TEST CHART
NATIONAL BUREAU OF STANDARDS-1963-A

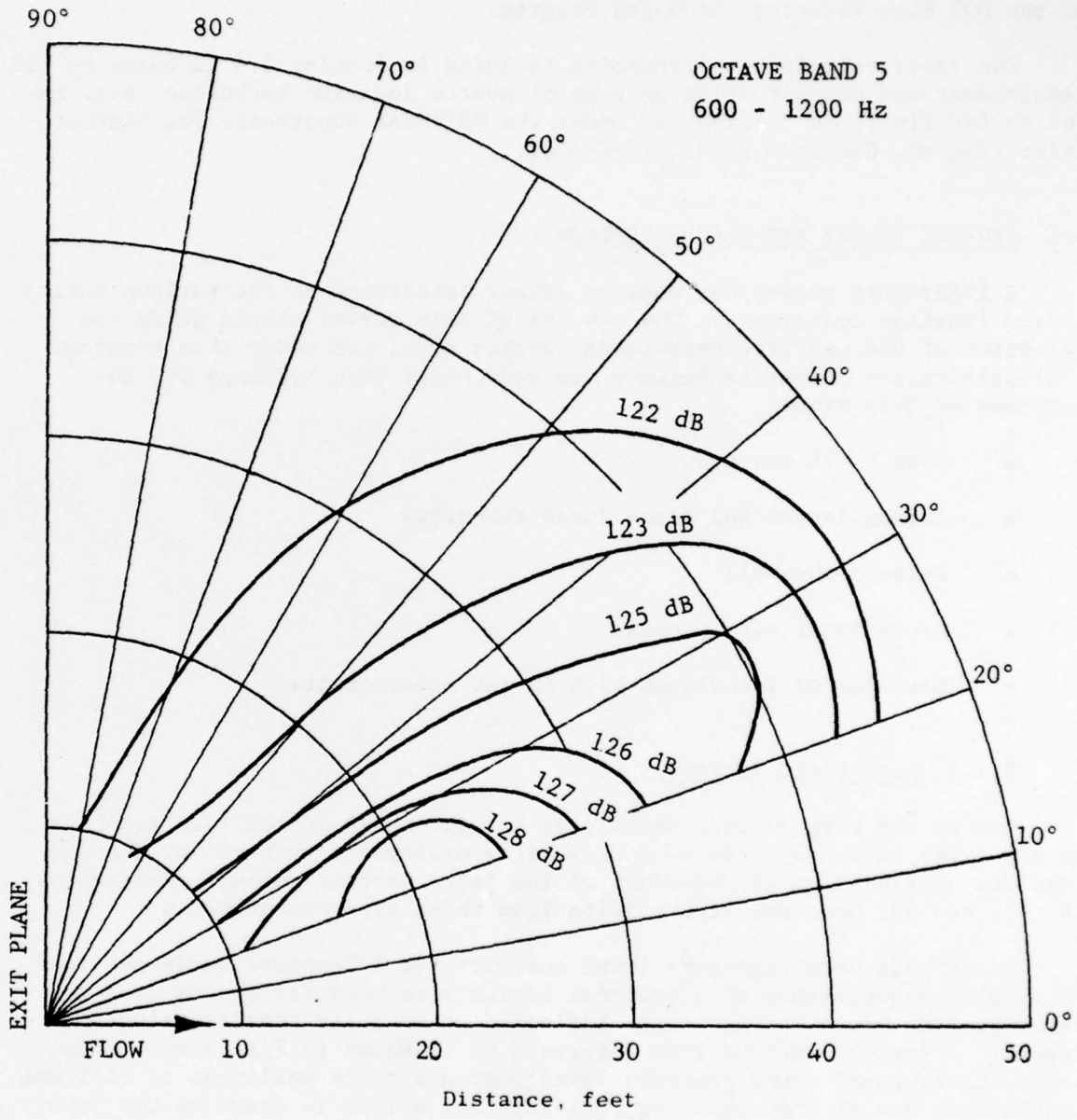


Figure 8-1. Source Location from Sound Pressure Level Contours.

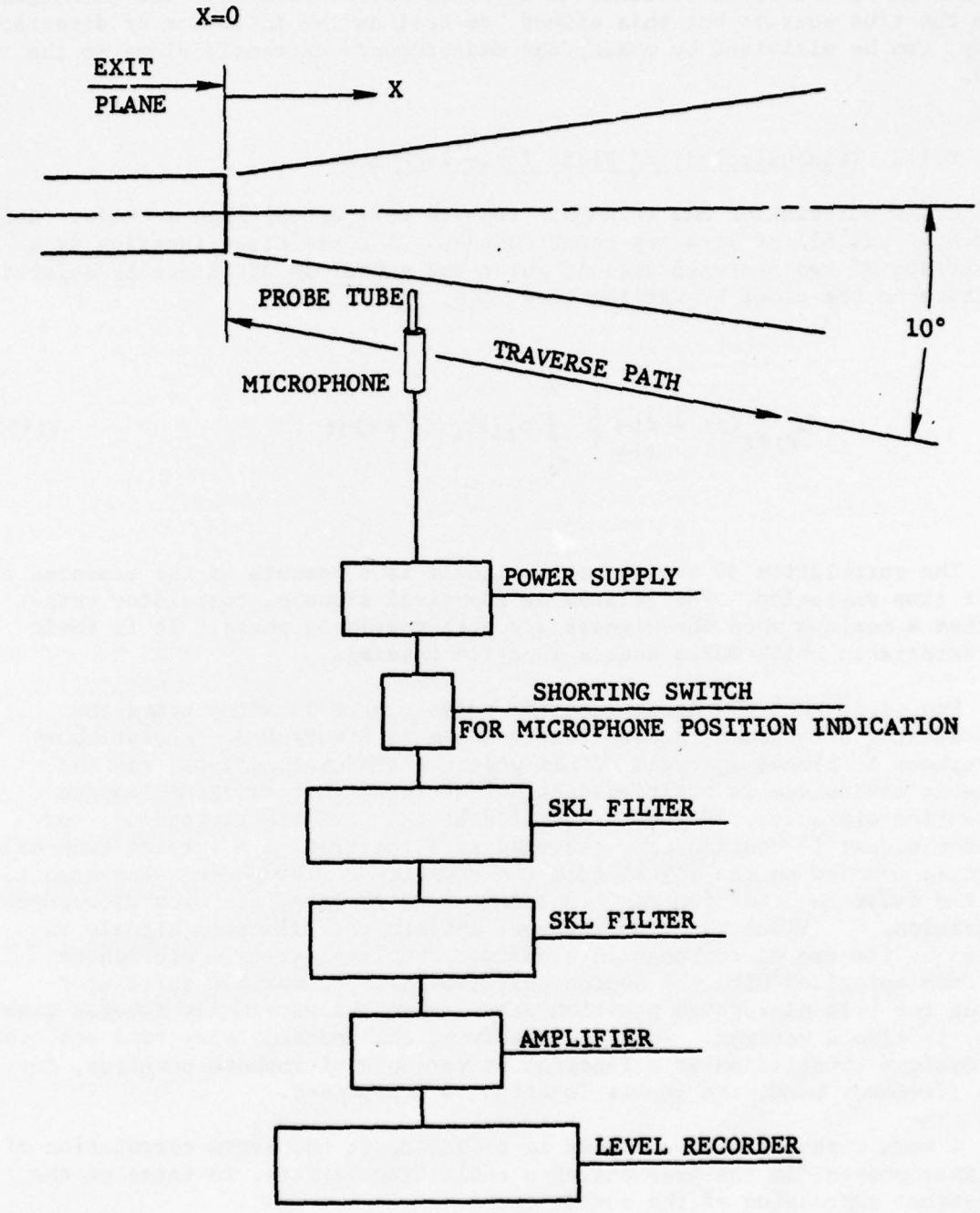


Figure 8-2. Experimental Arrangement for Source Location by Traversing Microphone.

Convection and scattering of the sound emanating from each position in the stream will tend to indicate an apparent source location, not coincident with the true source; but this effect, as well as the influence of directionality, can be minimized by making the measurements extremely close to the flow.

8.1.2 Triangulation and Plane Image Technique

Cross correlation and triangulation are well established methods, (Reference 47 and 51) of locating sound sources. A correlation function is a comparison of two averaged signals where one signal is artificially delayed relative to the other by varying time lags, τ:

$$R_{p_1p_2}(\tau) = \lim_{T\to\infty} \frac{1}{T} \int_0^T p_1(t)p_2(t+\tau)dt \qquad (115)$$

The correlation of the acoustic signals is a measure of the sameness of their time variation. For related or identical signals, correlator output reaches a maximum when the signals are most nearly in phase. It is their characteristic which makes source location possible.

Lee (Reference 47) determined the noise source location using the experimental arrangement schematically shown in Figure 8-3. A stationary microphone is placed upstream of all possible source locations, and the variable microphone is positioned at successively increasing microphone separation distances. For each position of the variable microphone, correlator output is continuously recorded as a function of a varying time delay which is imposed on the signal from the downstream microphone. The magnitude of time delay required for maximum correlation is noted for each microphone separation, S. Since the time interval between the identical signals received by the two microphones is a maximum when the variable microphone position coincides with the source position $(X/D)_{fi}$, maximum correlator output for this microphone position occurs when the externally imposed time delay is also a maximum. Thus, by observing the imposed delay time required for maximum correlation as a function of variable microphone position, for each frequency band, the source location is determined.

A more sophisticated analyses is to interpret the cross correlation of two microphones, in the presence of a reflecting surface, in terms of the analytical expression of the source terms.

The basis of this image technique is the fact that a rigid plane surface near a jet can act as a specular reflector for the sound from the quadrupole source distribution in the jet. In general terms, this can be demonstrated

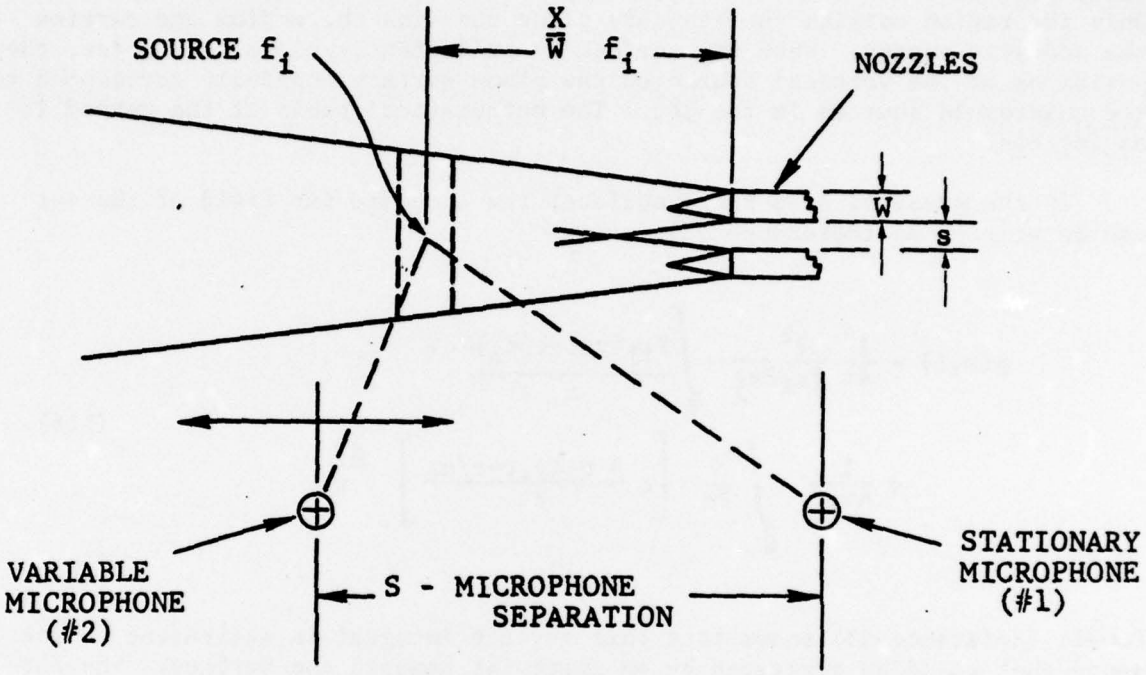


Figure 8-3. Experimental Arrangement for Correlator Sound Source Study.

by considering a rigid surface near a general source point 0 as shown in Figure 8-4. The boundary condition of the rigid surface is that the normal velocity is zero and, thus, the normal gradient of the pressure is zero at the surface. Because of symmetry conditions and boundary conditions, the boundary plane may be replaced by a set of virtual image sources (symmetrically placed) with both source and image radiating into unbounded space. Only the region outside the boundary plane contains the medium and carries the acoustic energy. When the surface is sufficiently close to the jet, the positions of the vertical source on the plane surface hopefully correspond to the quadrupole sources in the jet. The mathematical basis of the method is as follows.

In the presence of a rigid surface, the acoustic far field of the jet can be written as (Reference 52)

$$p(x,t) = \frac{1}{4\pi}\frac{\partial^2}{\partial x_i \partial x_j}\int_V \frac{T_{ij}(y,t-r/a_o)}{r}\,dV + \frac{1}{4\pi a_o}\int_S \frac{\partial}{\partial n}\left[r\,\frac{\partial\, p_s(y,t-r/a_o}{\partial t}\right]\frac{dV}{r} \tag{116}$$

Powell (Reference 53) shows that this surface integral is equivalent to the sound that would be generated by an image jet beneath the surface. The far-field radiation from the surface is

$$p(x,t) = \frac{-1}{4\pi a_o}\int_S \frac{\partial}{\partial n}\left[r\,\frac{\partial\, p_s(y,t-r/a_o)}{\partial t}\right]\frac{dS}{r} \tag{117}$$

Since the pressure on the plate is significant only over a limited region, the following approximation can be used

$$p(x,t) = \frac{-\cos\theta}{4\pi|x|a_o}\int_S \frac{\partial\, p_s\,(y,t-r/a_o)}{\partial t}\,dS \tag{118}$$

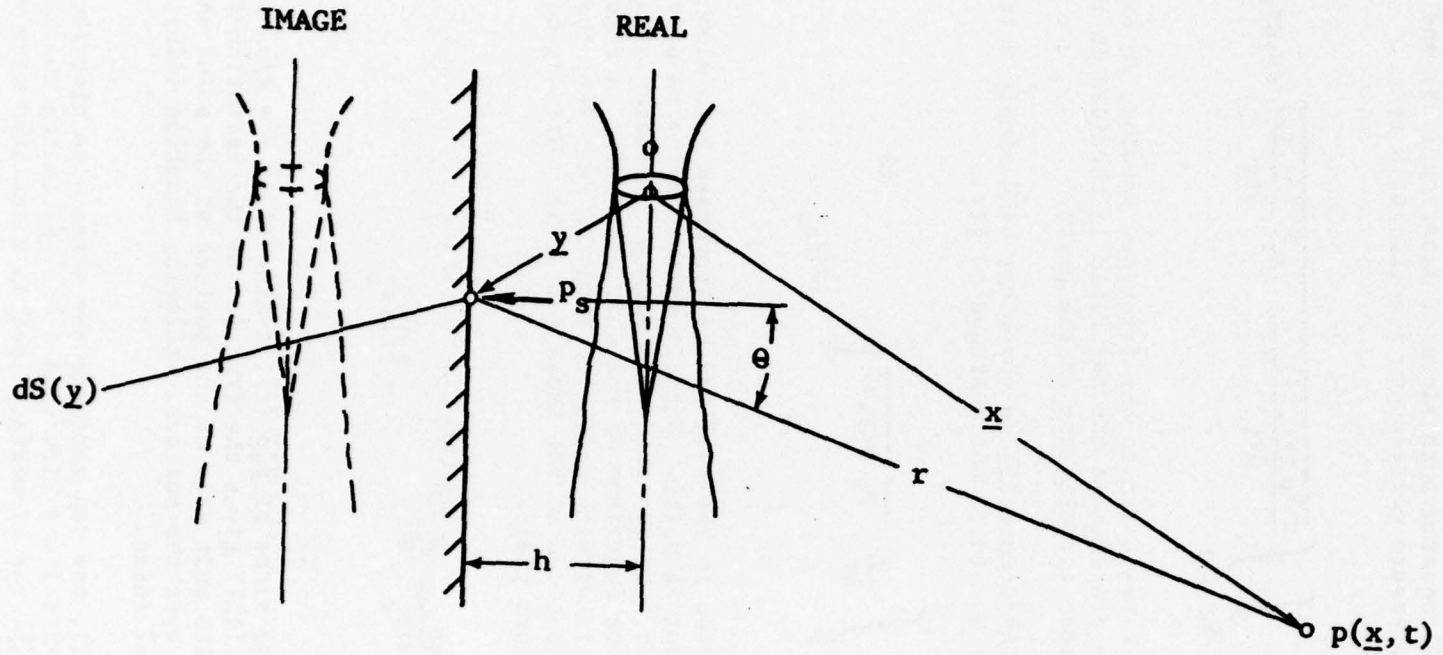


Figure 8-4. Coordinate System for the Image Technique.

Mastrello (Reference 54) squared both sides of Equation (118) and averaged over time to give the pressure correlation function at x as

$$R_{pp}(x,\tau) = \frac{\cos^2\theta}{16\pi^2 a_o^2 |x|^2} \int_{S_2} \int_{S_1} \overline{\frac{\partial p_s(y_1,\tau_1)}{\partial \tau_1} \frac{\partial p_s(y_2,\tau_2)}{\partial \tau_2}} \, dS_1 dS_2 \quad (119)$$

After applying a fourier transform to the frequency domains, an expression for the spectrum of the pressure in the far field is obtained in terms of fourier transform of cross correlations on the plate.

Rackl and Siddon (Reference 55) on the other hand simply multiplied both sides of Equation (108) by p(x,t) and averaged to give

$$\overline{p^2(x)}_{IMAGE} = \frac{-\cos\theta}{4\pi |x| a_o} \int_S \frac{\partial}{\partial \tau} \overline{p_s \, p(y,\tau)} \Big]_{\tau = |x|/a_o} dS \quad (120)$$

A microphone flush mounted in the wall can be traversed both along and across the jet direction, measuring $p_s(t)$. Signals corresponding to $p_s(t)$ and the far-field sound pressure p(t) are processed with a time delay signal correlator, yielding correlation functions of the character shown in Figure 8-5. A precursor wave is associated with radiation from the real jet; the dashed line shows the correlation due to the image jet alone. Writing Equation (120) in differential form yields:

$$\frac{d\,\overline{p^2}}{dS} = \frac{-\cos\theta}{4\pi |x| a_o} \frac{\partial}{\partial \tau} \overline{p_s p(\tau)} \Big]_{\tau = |x|/a_o} \quad (121)$$

It can be shown that the slope of $\overline{p_s p}\,(\tau)$, evaluated at $\tau = r/a_o$ will always be negative. Equation (111) gives the fraction of the radiation from the image jet associated with unit area of the surface at the point where p_s was measured. Integration over the surface, following Equation (120), leads to recovery of the total $\overline{p^2}$ image.

From Equation (121), one can estimate the streamwise distribution of acoustic source strength for any direction θ and, by taking the appropriate Fourier transform of $\overline{p_s p}$, the elementary spectra associated with various parts of the jet flow.

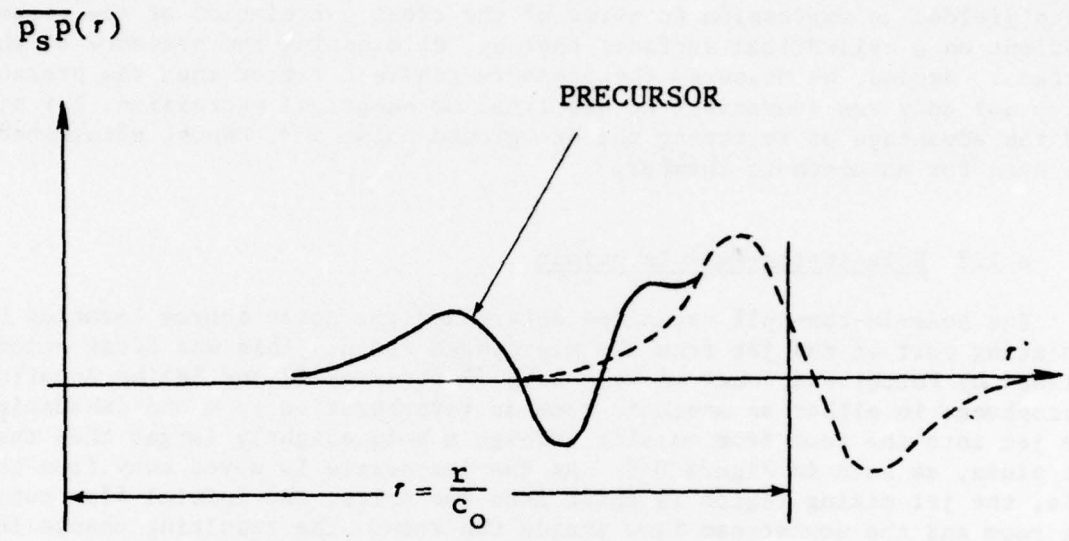


Figure 8-5. Cross-Correlation of the Plane Surface Pressure and Far Field Pressure.

Maestrello (Reference 56) extended his method in two ways. First, he developed an expression for the radial acoustic energy flux

$$I = p\, u_x \tag{122}$$

which yielded an expression in terms of the cross correlation of the pressure gradient on a cylindrical surface; thereby, eliminating the presence of the surface. Second, he measured the pressure gradient rather than the pressure, which not only was convenient to his final mathematical expression, but also had the advantage of rejecting the background noise and, hence, eliminated the need for an anechoic chamber.

8.1.3 Hole-in-the-Wall Technique

The hole-in-the-wall technique determines the noise source location by isolating part of the jet from the microphone field. This was first accomplished by Potter and Jones of Wyle Labs (References 57 and 58) by locating microphones in either an anechoic room or reverberation room and exhausting the jet into the room from outside through a hole slightly larger than the jet plume, as seen in Figure 8-6. As the jet nozzle is moved away from the hole, the jet mixing region is split into two parts; the initial flow outside the room and the downstream flow inside the room. The resulting change in amplitude of the filtering sound signal determines the region of the jet giving the corresponding sound pressure levels. By reversing the experimental setup and locating the nozzle in the room and exhausting the jet through the hole to the outside, the energy loss through the orifice and a better source location can be determined.

The method yields a streamwise estimate of the source strength of a "slice" of the jet rather than of a point in the jet ($d\overline{p^2}/dy$ or dW/dy depending on whether the measurement environment is anechoic or reverberant). Transverse source distribution information which is especially important for asymmetric nozzles is lost. Furthermore, there are serious questions about the acoustic and aerodynamic interference of the hole edge with the developing jet, and of the importance of acoustic "flanking" through the hole at frequencies where λ is on the order of the hole size or greater. Nevertheless, Bishop, Ffowcs-Williams, and Smith (Reference 59) of Rolls Royce; and McGregor and Simcox (Reference 60) of Boeing have successfully obtained significant source distribution information using this approach.

8.1.4 Directional Microphones

Directional microphone systems are popular techniques for resolving a point of sound. Individual microphones, such as the "shotgun" or "end fire array" microphones (Reference 61) or arrays of microphones with proper phase relationships (References 62 and 63), are used. One device, the Acoustic Wattmeter (Reference 64), even records the acoustic intensity flux in one

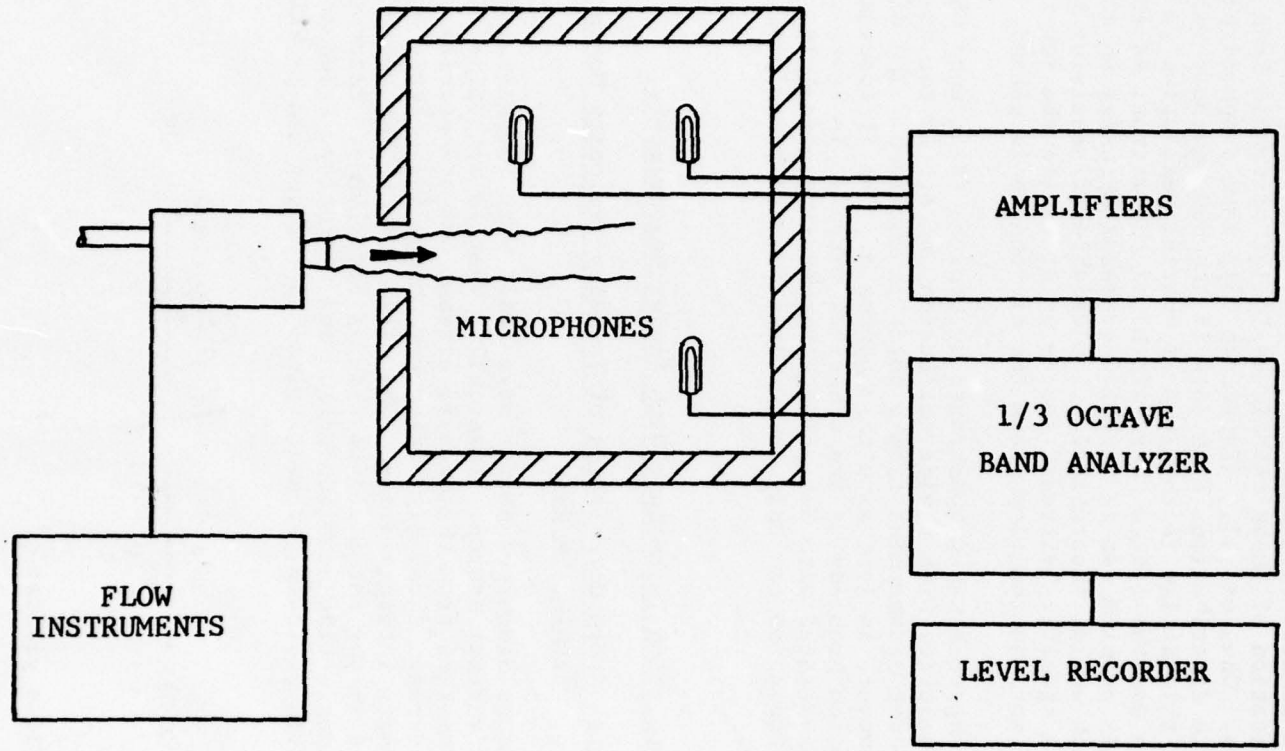


Figure 8-6. Experimental Arrangement for Source Location by the Shielding Method.

direction over a limited frequency range using two microphones. The most successful application of these techniques to jet noise has been with focussed detectors. Chu, et. al., (Reference 65), used a spherical mirror to record the source distributions from jets in the USC anechoic room. The difficulty with this design is the loss of spatial resolution in the cross stream direction and the finite "beam width" of the mirror, as shown in Figure 8-7. This problem can be improved somewhat by using an elliptically shaped dish which would, theoretically, be capable of resolving the acoustic radiation from a specific "virtual" source point inside the jet flow to the listening point outside the flow where the microphone is placed.

The above approcach was demonstrated by Grosche (Reference 66) using an ellipsoid of revolution with a wide collection angle. In two positions of the mirror, a power measurement from a point is obtained. The directive information, however, is lost with this approach. The ellipsoidal mirror has the same resolution problems as the spherical mirror. In fact, there appears to be a limit associated with Heisenbergs uncertainty principle, where localized spatial information can only be resolved down to a scale of about one-half wavelength.

8.1.5 Correlation Techniques With In-Jet Measurements

8.1.5.1 Cross Correlation of Turbulent Velocity Measurements Within the Jet

The techniques discussed so far have dealt with the measurement of the location of the virtual source. Physically, what is determined is where the source finally emerges from the exhaust stream, not necessarily the location of the actual source. Thus, high frequency channeling effects present difficulties with data interpretation. Chu (Reference 67) attempted to directly relate the noise in the far field to the jet turbulence. Returning to Equation (115) and neglecting heat conduction and viscosity, Proudman showed the far-field acoustic pressure per unit volume of the jet can be written as:

$$p(x,t) = \frac{\rho_o}{4\pi a_o^2 |x|} \int_V \frac{\partial^2 u_x^2(y, t-\tau_o)}{\partial t^2} \, dV \qquad (123)$$

Squaring both sides yields:

$$R_{pp}(x_1 t) = \frac{\rho_o^2}{16\pi^2 |x|^2 a_o^4} \int_{V_1} \int_{V_2} \frac{\partial^4 [R_{u_x^2 u_x^2}(y,\tau)]}{\partial \tau^4} \, dV_1 dV_2 \qquad (124)$$

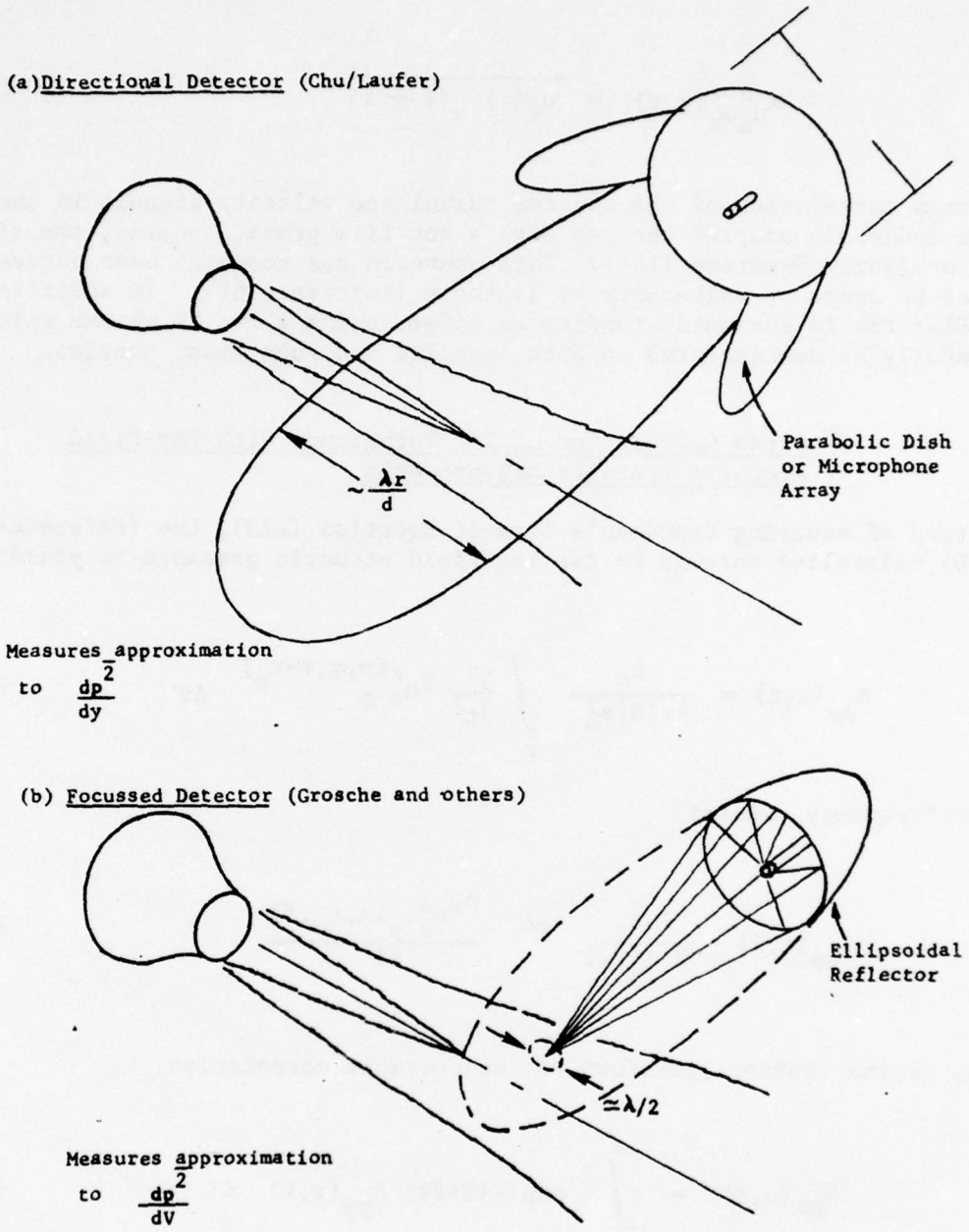


Figure 8-7. Comparison of Parabolic and Ellipsoidal Mirror Desig

where

$$R_{u_x^2 u_x^2}(y,t) = \overline{u_x(\tau) u_x(t+\tau)} \tag{125}$$

is the cross correlation of the squared turbulence velocity signals in the jet. Chu tediously sampled the jet with a hot film probe, squared, the signals and evaluated Equation (114). This approach has recently been successfully used by Jones of University of Illinois (Reference 68). In addition General Electric is currently funding an effort using a Two LV system which will hopefully be demonstrated on both baseline and suppressor nozzles.

8.1.5.2 Cross Correlation of Jet Turbulence With Far-field Acoustic Pressure Measurements

Instead of squaring Proudman's form of Equation (123), Lee (References 69 and 70) multiplied through by the far-field acoustic pressure to yield:

$$R_{pp}(x,t) = \frac{\rho_o}{4\pi |x| a_o^2} \int_V \frac{\partial^2}{\partial t^2} R_{u_x^2 p}(x,y,\tau-\tau_o) \, dV \tag{126}$$

or in the frequency domain:

$$S_{pp}(x,f) = \frac{-\pi \rho_o}{2 a_o^2 |x|} f^2 \frac{\Delta R_{u_x^2 p}(x,\tau_o,f)}{\Delta f} \tag{127}$$

where S_{pp} is the fourier transform of the pressure correlation.

$$S_{pp}(x,f) = \int_{-\infty}^{\infty} \exp(-j2\pi f\tau) \, R_{pp}(x,\tau) \, d\tau \tag{128}$$

He then cross correlated a hot film probe with a far-field microphone and evaluated the pressure correlation with a constant percent frequency band filter. Lee (Reference 69) successfully obtained a picture of the location of the different frequency sources in the jet. Seiner and Reethof repeated the experiment in Reference 71. This was also the basis for the work conducted in the USAF/DOT program using the laser velocimeter, Contract F33615-73-C-2031.

8.1.5.3 Cross Correlation of Jet Pressure and Far-field Pressure Measurements

A measurement of the pressure $p^{(o)}$ or p_s is conceptually attractive, in view of the scalar nature of the varible. An alternate formulation of Equation (123) due to Ribner (Reference 72) or Meecham and Ford (Reference 73) is equally applicable to flow sources:

$$p(x,t) = -\frac{1}{4\pi|x|a_o^2} \int_V \frac{\partial^2 p^o}{\partial t^2} \, dV \tag{129}$$

In this approach, the sound is interpreted as being generated by a distribution of volume sources, which can be represented by the nonacoustic part of the pressure fluctuations $p^{(o)}$ in the source region. Siddon (References 74, 75, and 76) multiplied Equation (129) by the sound pressure and took the time averaged signal to yield:

$$\frac{d\,\overline{p^2}}{dV} = -\frac{1}{4\pi|x|a_o^2} \frac{\partial^2}{\partial\tau^2} R_{p^o p}(\tau)\Big|_{\tau = |x|/a_o} \tag{130}$$

The quantity on the left hand side represents the contribution to the total mean squared sound pressure associated with the region where the turbulent pseudosound $p^{(o)}$ was detected. The term in square brackets establishes the coherence between p^o and p. Experimentally, the procedure is to insert a pressure probe into the source region, as shown in Figure 8-8.

The detected pseudosound $p^{(o)}$ is multiplied instantaneously by the far-field sound pressure p, using a special time-delay computer (correlator). The resulting function $\overline{p^{(o)}\, p(\tau)}$ will vary with the time delay, τ, in the manner depicted on Figure 8-8. The function is observed to peak at a time corresponding with the acoustic travel time between pressure probe and microphone. This "bump" on the function implies that there is something in common between the source fluctuation and the overall radiated sound. From its shape and magnitude, the local source strength may be extracted using Equation 130).

The difficulties inherent in the accurate measurement of "static" pressure fluctuations in turbulent flows are well recognized (e.g., Reference 77). Therefore, to accurately measure the jet pressure, Siddon had to develop a special flat-blade-like probe shown in Figures 8-9 and 8-10.

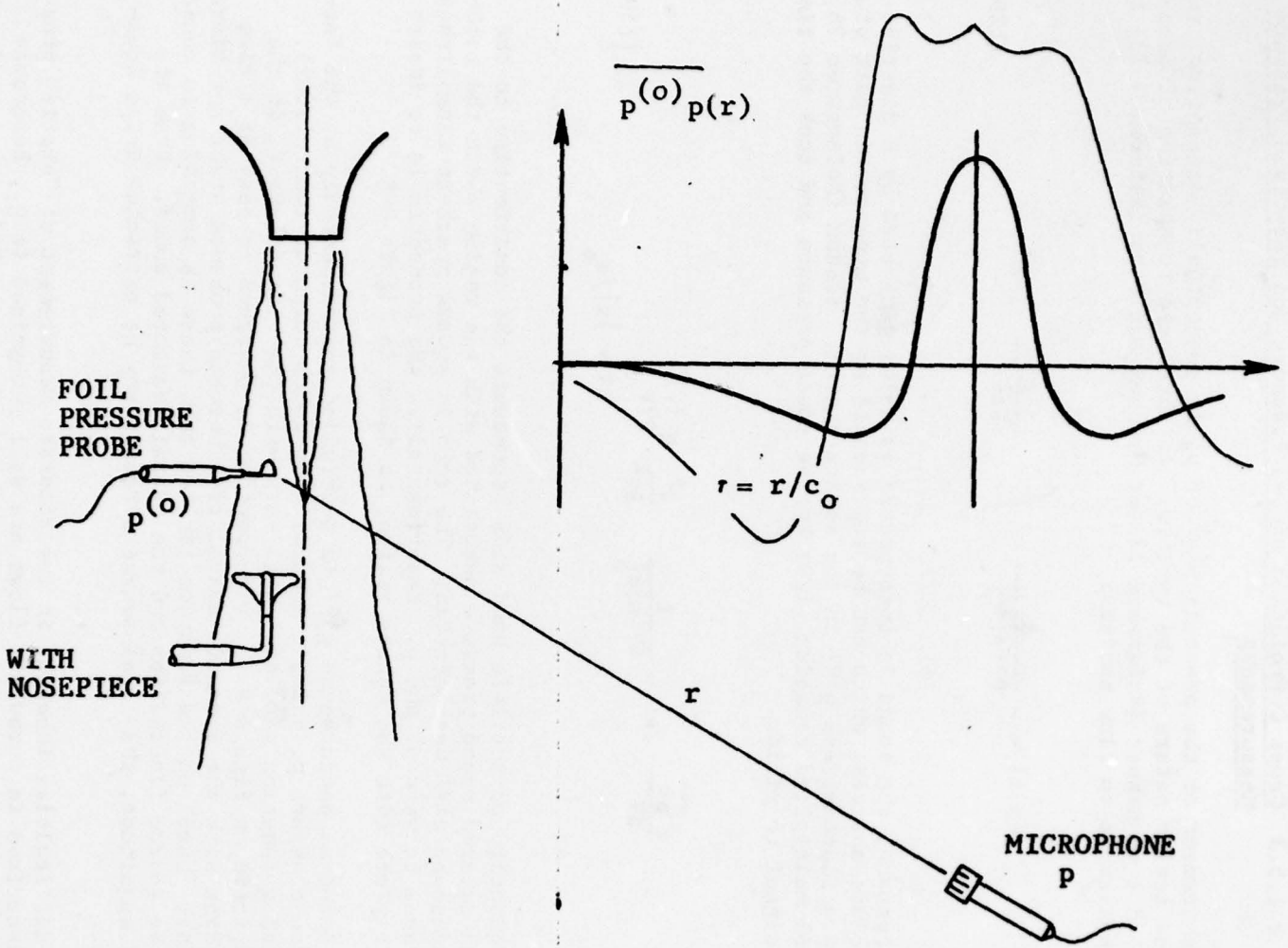


Figure 8-8. Cause Effect Correlation Experiment Showing Contamination Due to Dipole Radiation from Conventional Cylindrical Probe.

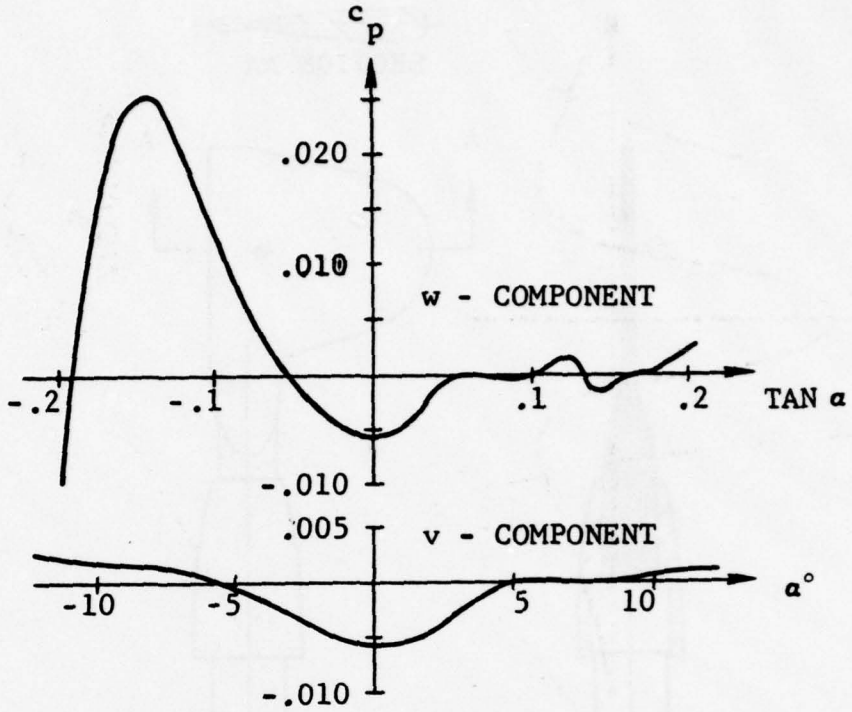


Figure 8-9. C_p Variation for Foil-Type Probe as a Function of Inclination Angle.

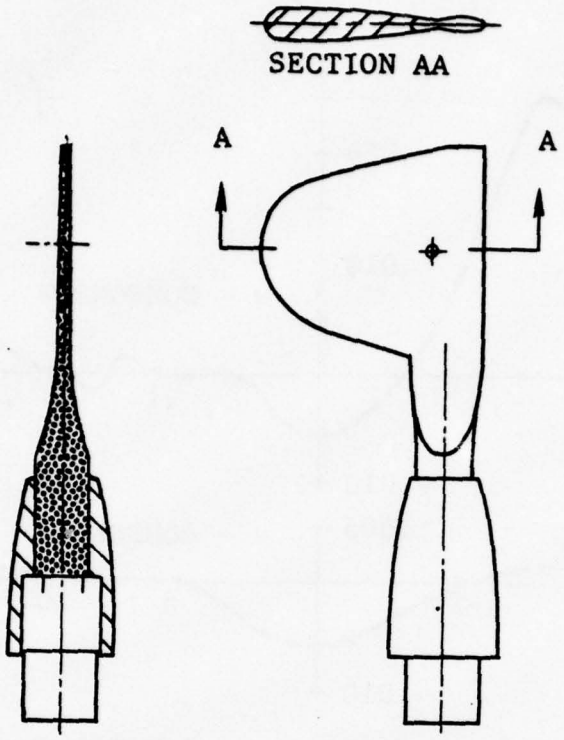


Figure 8-10. Geometry of Foil-Type Pressure Probe which Minimizes Interaction Errors in Plane of Foil.

9.1.5.4 Coherence of Spectral Lines

A method developed in linear transfer functions is the ordinary coherence function. The method approximates propagation of the pressure wave transfer from the near field, P_N, to the far field, P_F, by a linear transfer function

$$p_x(t) = \int \ell(t-\tau) \left[p_o^o(\tau) + \sum_{i=1}^{\infty} p_i^o(\tau) \right] d\tau \tag{131}$$

where $P_i(\tau)$ is the pressure waves arriving at F from other sources in the near field.

If both sides of Equation (131) are multiplied by $P_o^{(o)}(t+\tau)$, time averaged, and fourier transformed to the frequency domain, then:

$$L(f) = \int_{-\infty}^{\infty} e^{i2\pi f\tau}\, \ell(\tau)\, d\tau = \frac{S_{p_o p}^{(f)}}{S_{p_o p_o}^{(f)}} \tag{132}$$

assumed to be where cross term $Sp_o(o)\, P_\tau(o)$ is zero because the source terms are incoherent.

If, now both sides of Equation (131) are squared, time averaged, and a fourier transform is applied, one obtains:

$$S_{pp}(f) = |L(f)|^2 \left[S_{p_o p_o}^{o\ o} + \sum_{i=1}^{\infty} S_{p_i p_i}^{(f)\ o} \right] \tag{133}$$

substituting from Equation (132) into (133) gives the ordinary coherence:

$$\gamma^2 = \frac{|S_{p_o p}^{(f)}|^2}{S_{pp}(f)\, S_{p_o p_o}^{(f)}} = \frac{S_{p_o p_o}^{(f)}}{S_{p_o p_o}^{(f)} + \sum_{i=1}^{\infty} S_{p_i p_i}^{(f)}} \tag{134}$$

One can readily see that the ordinary coherence function γ^2 is a measure of the total spectral content of the near-field measurement found in the far field. If there exist any nonlinearities in the transmission path $\ell\ (t - \tau)$, γ^2 will measure these distortions and interpret them as extraneous noise sources as well. Although developed for stationary uncorrelated mechanical sources, Sharton (Reference 78) used this approach to obtain jet noise source distributions.

8.1.5.5 Noninvasive Measurements

All of the correlation techniques discussed above use either a hot wire or pressure probe which invades the jet stream. The validity of the researchers findings, however, are subject to question because of the inherent probe contamination in their measurements. A noninvasive survey was attempted by Massier (Reference 79) using a laser Schlieren system and the density gradient as the source term. Recently Damkevala (Reference 80) used the cross beam infrared radiometer to conduct two point correlations in the jet. DeBelieval (Reference 81) conducted similar experiments with an infrared radiometer sensitive to temperature fluctuations. Although the IR method is in question because of the difficulty in interpreting the output of the radiometer as strictly pressure (or temperature) fluctuations, there is no question that nonintrusive sensors which monitor static pressure or density fluctuations remotely are the best approach to "in jet" measurements to determine noise sources.

In addition to the infrared radiometer or the laser Schlieren, the laser shadowgraph has the potential of giving pressure fluctuations with time. These methods, together with a photodiode could be used to give quantitative density gradient or density fluctuation readings averaged along the laser beam. The density gradient output obtained with the Schlieren system could be converted to a density reading by the use of a simple integration algorithm. In order to determine which, if any, of these systems could give accurate in jet fluctuating pressure measurements, a feasibility study comparing the various methods was in order.

8.2 THE FEASIBILITY STUDY

In an effort to screen out the methods of lower potential, a feasibility study of the various techniques was conducted.

The feasibility study included detailed quantitative or descriptive values of the pertinent parameters describing the method under investigation. These answers were obtained from established equations, order of magnitude estimates, or experimental established values from test data in the literature. The following parameters were used as the common checklist for comparison among the techniques:

Credibility/Success Factor
Measured Parameter
Inferred Parameter
Operating Principal
Frequency Domain
Spacial Resolution in Three Dimensions
Accuracy in Locating Noise Source Location
Accuracy in Measuring Source Amplitude Level
Operational Limitations (Jet Velocity-Temperature)
Size
Stability
Ease of Operation
Dynamic Range
Noise Floor
Stability of Output With Time (Drift, etc.)
Transfer Function (Gain)
Susceptibility to Noise
Output Characteristics (Linear, Non-Linear)
Development Time and Cost
Operation Time
Data Processing Requirements
Data Processing Time
Data Processing Cost
Math Credibility of Analysis in Data Processing

In terms of these parameters, the ideal method would exhibit the following key characteristics:

Frequency Domain	50 Hz - 80 kHz
Spatial Resolution	point or slice of jet
Accuracy in Locating Source	$\sim$ 100%
Operation Time	< 1 min/pt.
Theoretical Credibility	exact
Development Time	within framework of total program which were used as references in the comparison among the candidates.

8.2.1 Near-field Surveys

A study of the results of the near-field method indicated that its spatial resolution was quite poor. More importantly, there was a real question of the validity of the measurements as indicative of the acoustic source term. It would appear that these measurements are really of the hydrodynamic pseudosound from the jet rather than the true acoustic pressure. Figure 8-11, for example, shows the large disparity of measured source distribution from Lee (Reference 47) compared with other techniques. As indicated earlier,

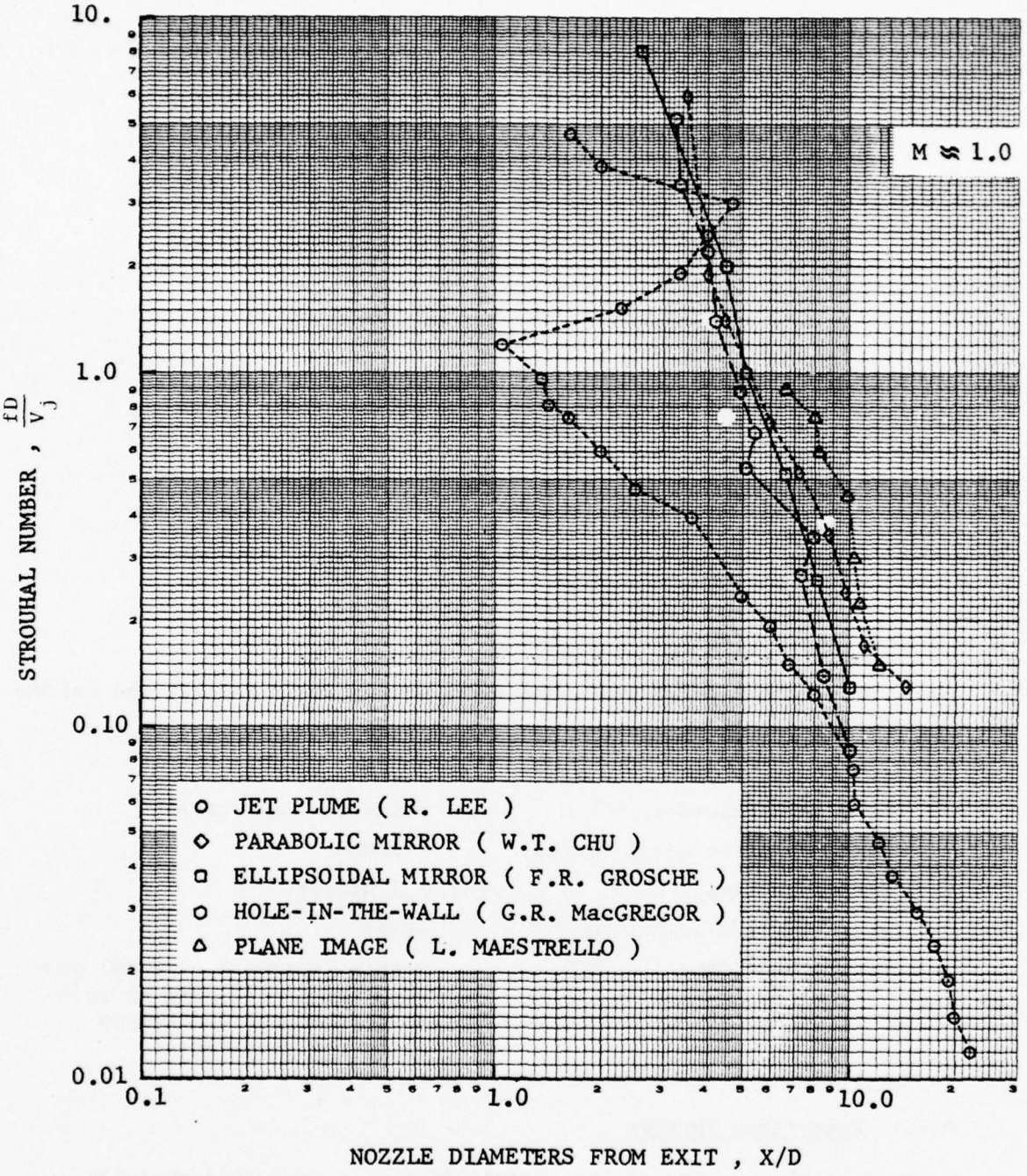


Figure 8-11. Source Frequency Distribution in the Jet.

the time derivative of the pseudosound can be related to the source term. This sophistication is not justified, however, in light of available methods such as the correlation techniques. Based on these arguments, the near-field approach was dropped from further consideration.

8.2.2 Plane Image Versus Hole-In-The-Wall

The plane image and the hole-in-the-wall experiments both produce data which carries essentially equivalent information. Both seem to give a fairly realistic impression of the slice-wise distribution along the axis of a single jet. By their very nature, neither is able to give any information on the transverse (radial) source distribution in the jet. In either case, there is considerable difficulty in defining the volume resolution (i.e., what is the "effective thickness" of a "slice" which contributes to the estimate of dp^2/dy). It is not known to what extent these methods tend to "smear out" the apparent source distribution in the streamwise direction (although this question might be partially answered with the aid of a stationary "point" source, traversed around the regions of anticipated source distributions). For these reasons, neither of these techniques will be of much benefit in resolving the relative importance of mechanisms like shear reduction by interjet ventilation, refractive shielding etc., as they influence the noise reducing capability of multielement suppressor nozzles.

Both methods have been validated by integral closure to recover the total sound power of intensity. Their greatest potential probably lies in applications to high speed (supersonic) and hot jets where direct probing in the flow is difficult and open to much suspicion. Both hole-in-the-wall and image plane methods, however, provoke questions about the degree to which adjacent solid surfaces influence the normal development of jet structure, and whether they radiate additional interaction noise.

The hole-in-the-wall method does offer the advantage of less instrumentation and less data reduction and processing. The technique of obtaining the source distribution from the measured data is fairly straight forward with the hole in the wall. On the other hand, the plane image technique requires cross correlation matrices to be formed and, in the case of Maestrello's method, a very complicated synthesis of the data in terms of complex mathematical representations of the source field.

The fact that the hole in the wall was essentially the only "proven" technique carried a lot of weight regardless of its accuracy and shortcomings. The hole-in-the-wall method was, therefore, selected over the plane-image method to go into the demonstration/application stages.

8.2.3 Directional Microphones

Taken collectively, the various considerations discussed in Section 8.1.4 suggest that an ellipsoidal geometry offers the best prospects for

measuring profiles of noise source strength associated with the apparent (geometrical) source point, coincident with one of the focii of the system. In actual fact, due to the combined effects of convection and refraction, this apparent source location may not coincide exactly with the corresponding point from which actual moving jet sources are emitting. There may be some phase distortion in the received signal because the collected sound will have had to travel by many different ray paths, and may, therefore, be refracted differentially, unless the collection angle $\Delta\theta$ is sufficiently narrow.

Furthermore, the resolution will always be limited to a focal volume with effective dimensions of about one-half wavelength. Nevertheless, it was reasoned that the focussed ellipsoidal detector would be one of our best tools, as has already been evidenced by the work of Grosche (Reference 66). Therefore, the ellipsoidal mirror (EM) was also chosen for further development.

8.2.4 Correlation Techniques

Both the hole in the wall and the ellipsoidal mirror (EM) measure the sound radiation from a virtual source location within the jet. The hole-in-the-wall method, at best, gives slice of jet information. The EM has the promise of much improved resolution but it has a limiting value on the order of a half wavelength which would be quite large at low frequency. The need, therefore, still exists for an instrument which will give point information of the source field within the jet for microscopic mapping of the sources throughout the frequency range. The only techniques which offer such potential are the correlation methods.

8.2.4.1 Two Point or Causality Correlations

The two approaches to correlation location of noise sources in a jet are the two point, "in-jet - in-jet" cross correlation method and the "in-jet - far-field causality" correlation method, both discussed above.

The causality approach eliminates the requirement for a second detector in the fluid stream, but produces essentially the same end information, in source strength distribution and spectral content, as the classical 2-point in-flow method. Both are based on the same classical aerodynamic noise theory, and the approach to stoichastic representation of time average (correlation) properties is equivalent. The causality approach requires many less measurements in the fluid stream and entails the evaluation of only a second derivative with respect to τ rather than a fourth derivative, as in the classical approach. The problems of probe generated noise, hopefully, can be overcome by using sufficiently small probes in large flows, or by the use of a noninvasive probing technique. The question of uncertainty due to a combined convective and refractive effect on the retarded time delay (the time at which correlation or its derivatives is to be evaluated) is not fully resolved, but evidence suggests that the uncertainty will not be significant

in subsonic jets. The causality correlation approach was therefore chosen for future work.

8.2.4.2 Velocity or Pressure?

The answer to the question of the validity of the Ribner dilatation theory was needed to decide whether the in-jet measurement should be a velocity measurement or a pressure measurement. Although answering this question was beyond the scope of Task 1, it was felt appropriate to attempt to develop instrumentation which could answer this question in future work. Under the DOT/USAF Supersonic Jet Noise Program, General Electric had successfully developed the noninvasive laser velocimeter (LV) for measurement of turbulent velocity within the jet plume. As part of that program, a causality correlation (between the LV and a far-field microphone) feasibility demonstration was conducted which yielded encouraging results (see Section 8.4). In light of these facts, it was decided to attempt to develop a parallel instrument in Task 1 which could measure a scalar quantity such as pressure in the jet to compliment the laser velocimeter's capabilities. The combination of these two instruments could then be used to experimentally test the Ribner dilatation hypothesis.

8.2.4.3 Choice of Sensor for In-Jet Measurement

Five different instruments have been identified for measuring unsteady scalar fluctuations in a jet, namely:

1. Acoustic pressure probe
2. Infrared radiometer
3. Infrared laser absorption with radiometer ("cross beam")
4. Laser Schlieren
5. Laser shadowgraph

The acoustic pressure probe is an invasive device which uses a microphone inserted in the jet stream. The infrared radiometer method collects infrared radiation related to temperature fluctuations from a point within the jet using an ellipsoidal mirror and reflects the radiation unto the radiometer. The last three methods all measure the fluctuation which occur within a laser column which is passed through the jet. The column can be conformed to a point by using two lasers, which intersect, and cross correlating the two signals to get the common scalar fluctuations. The sophistication and complexity of these methods called for a study by an expert in the field. The General Electric optics teams, however, was found to be dedicating their full time effort to the development of the laser velocimeter for the DOT/USAF Program, so an outside consultant, Dr. Michael Rudd of BB&N, was retained for the study. In Reference 81, Dr. Rudd compares the five candidate methods using the criteria of Section 8.2. Table 8-I summarizes the results of this in-depth study.

Table 8-I compares various noninvasive point (microscopic) source measurement techniques for probing the jet plume.

Table 8-I. Comparative Merits of Noninvasive Probe Systems.

	INVASIVE	NONINVASIVE			
	Microphone	IR Radiometer	IR Crossed Beam	Laser Schlieren	Laser Shadowgraph
1. Credibility/Success Factor	Reasonable	Fair	Good	Poor	Untried
2. Measured Parameter	Pressure	Temperature	Partial Pressure CO_2	Refractive Index gradient	Second Derivative of Refractive Index
3. Inferred Parameter	Static Pressure	-	Density	Density	Density
4. Operating Principle	Microphone	IR Emission	IR Absorption	Refraction of Light	Focusing of Light
5. Transfer Function	P	$\epsilon\rho T^4$	ρ_{co_2}	$\frac{\partial u}{\partial y}\,dz$	$\frac{\partial^2}{\partial x^2} + \frac{\partial^2}{\partial y^2}\,\mu dz$
6. Noise Floor (dB re .0002 μbar)	80	-	-	106	106
7. Dynamic Range dB	100	100	100	100	100
8. Stability with Time	Good	Good	Good	Fair	Good
9. Susceptibility to Vibration & Noise	Vibration good; dynamic pres. fair	Good	Good	Very Poor	Good
10. Output Characteristics	Linear	$\propto T^4$	Linear	Roughly Linear	Linear
11. Data Processing Requirements	Real Time Correlator	Real Time Correlator plus computer	Real Time Correlator plus computer	Real Time Correlator	Real Time Correlator
12. Data Processing Time	Moderate	Slow	Slow	Moderate	Moderate

Table 8-I. Comparative Merits of Noninvasive Probe Systems (Concluded).

		INVASIVE	NONINVASIVE			
		Microphone	IR Radiometer	IR Crossed Beam	Laser Schlieren	Laser Shadowgraph
13.	Data Processing Cost	Moderate	High	High	Moderate	Moderate
14.	Credibility of Analysis	Good*	Fair	Good	Poor	Good
15.	Operation Time	Moderate	Slow	Slow	Slow	Moderate
16.	Operation Cost	Moderate	Moderate	Moderate	Moderate	Moderate
17.	Ease of Operation	Good	Poor	Poor	Poor	Good
18.	Spatial Resolution ins cubed	$\frac{1}{4} \times \frac{1}{4} \times \frac{1}{4}$	$\frac{1}{10}$ x Ly x Lz	$\frac{1}{10}$ x Ly x Lz	$\frac{1}{20}$ x Ly x Lz	$\frac{1}{20} \times \frac{1}{20}$ x Lz
19.	Frequency Response KHz	80±	50	50	100	100
20.	Jet Velocity Range	<1000 fps	No Limit	No Limit	>500 fps (cold) No Limit (hot)	>500 fps (cold) No Limit (hot)
21.	Temperature Range	<3460°R cooled @ $V_j \approx 300$ f/s <1600°R cooled @ $V_j \approx 1000$ f/s	Only Proved >1200°F	Only Proved -22 to 250°F	No Limit	No Limit
22.	Physical Size (ins)	1 x 1/8 dia.	2 Radiometer 20·5 x 5·5 Dia.	2 Receivers 20 x 5 dia. 2 Transmitters 10 x 5 dia.	2 Receivers 2 x 2 dia. 2 Transmitters 12 x 2 dia.	1 Receiver 6 x 2 dia. 1 Transmitter 24 x 2 dia.

*If spurious pressures can be removed.

In summary, the study showed that the microphone probe has operational limitations in terms of temperature and velocity (subsonic, < 3460° R at $V_J \approx 300$ fps and < 1600° R at $V_J \approx 1000$ fps – both cooled) and can have significant measurement errors because it disturbs the jet stream. However, it was felt that many of these errors could be minimized by proper design. The infrared radiometers which look at the infrared emissions have four major drawbacks: (1) the measured parameter is not clearly understood, (2) it is limited to hot jets above 1200° F, (3) its development cost is very high, (4) the radiation is actually being detected from a virtual point in the jet which is assumed to be the exact location.

The infrared laser absorption method is sensitive only to the partial pressure fluctuations of carbon dioxide which in turn are related to the density, temperature, and concentration fluctuations of the gas. At high temperatures (> 250° F), the absorption of carbon dioxide decreases substantially. Furthermore, the method can not be used in a jet heated by burning a hydrocarbon fuel.

The laser Schlieren method suffers from a calibration difficulty in relating the deflection of the laser beam to any physical parameter in the flow and the system is extremely sensitive to vibration.

The laser shadowgraph has the problem of measuring the partial Laplacian of the refractive index (related to the density) fluctuations along the laser column, $\int (\partial/\partial x^2 + \partial^2/\partial^2 y)\, \mu dy$, which is not directly relatable to an acoustic source term. However, its simplicity, cost, and insensitivity to vibration made it the most attractive technique to pursue. In addition, it appeared that an intensive design program of low noise probe stems might result in an optimum acoustic probe for subsonic jets which could be used to compare with the laser shadowgraph results.

8.2.5 Summary

Based on the feasibility study, laboratory investigations and detailed design efforts were initiated on the following instrumentation techniques:

1. Optimum design of probe stem shape for Causality correlations
2. Laser shadowgraph for Causality correlations
3. Hole in the wall
4. Ellipsoidal mirror microphone

Following completion of the design/development phase, the selected method would be demonstrated on a jet.

8.3 OPTIMUM ACOUSTIC PROBE SHAPE STUDY

Noise source location methods which have used invasive acoustic pressure probes to survey the jet plume have all had to contend with contamination of the measurement. Of course one must ensure that the probe is small compared with the smallest wavelengths of turbulence (proportional to highest frequencies), if meaningful "point" measurements are to result. Two sources of probe contamination can occur: (1) unwanted pressure fluctuations picked up by the in-jet measurement which are not related to the desired hydrodynamic pressure fluctuations, and (2) contamination of the far-field microphones due to dipole radiation from the probe stem in the case of causality correlations.

An in-jet pressure probe can measure signals ($P_{meas.}$) from five contributions as shown in Figure 8-12.

1. Hydrodynamic pseudosound fluctuations ($P^{(o)}$) caused by the turbulent flow
2. Acoustic wave propagation ($P^{(1)}$) within the jet from nearby sources.
3. Probe vibration (P_{vib}) due to the severe shaking that might occur in a highly turbulent jet
4. Surface pressure fluctuations (P_s) due to angle of attack changes on the probe stem
5. Dipole radiation (P_d) back on the sensor from sound generated by the probe stem in the jet stream

The contamination of the far-field microphone (P_{FF}) is merely an extension of (5), above, where the dipole radiation propagates out of the jet into the far field as shown in Figure 8-12.

8.3.1 Desired Measurement

The use of a pressure probe as a source location instrument is based on Ribner's (Reference 72) idea on viewing the turbulent flow as an array of acoustic monopoles generated by a quasi-incompressible isentropic flow. For subsonic flow, Lighthill's wave equation can be written in the approximate form

$$\frac{1}{c_o^2}\frac{\partial^2 p}{\partial t^2} - \nabla^2 p = \frac{\partial^2 \rho u_i u_j}{\partial y_i \partial y_j} \qquad (135)$$

The right hand side of Equation (135) may be regarded as a forcing term of the wave equation for p. Acoustically, it represents a distribution of acoustic quadrupoles embedded in a medium at rest. It can be converted into

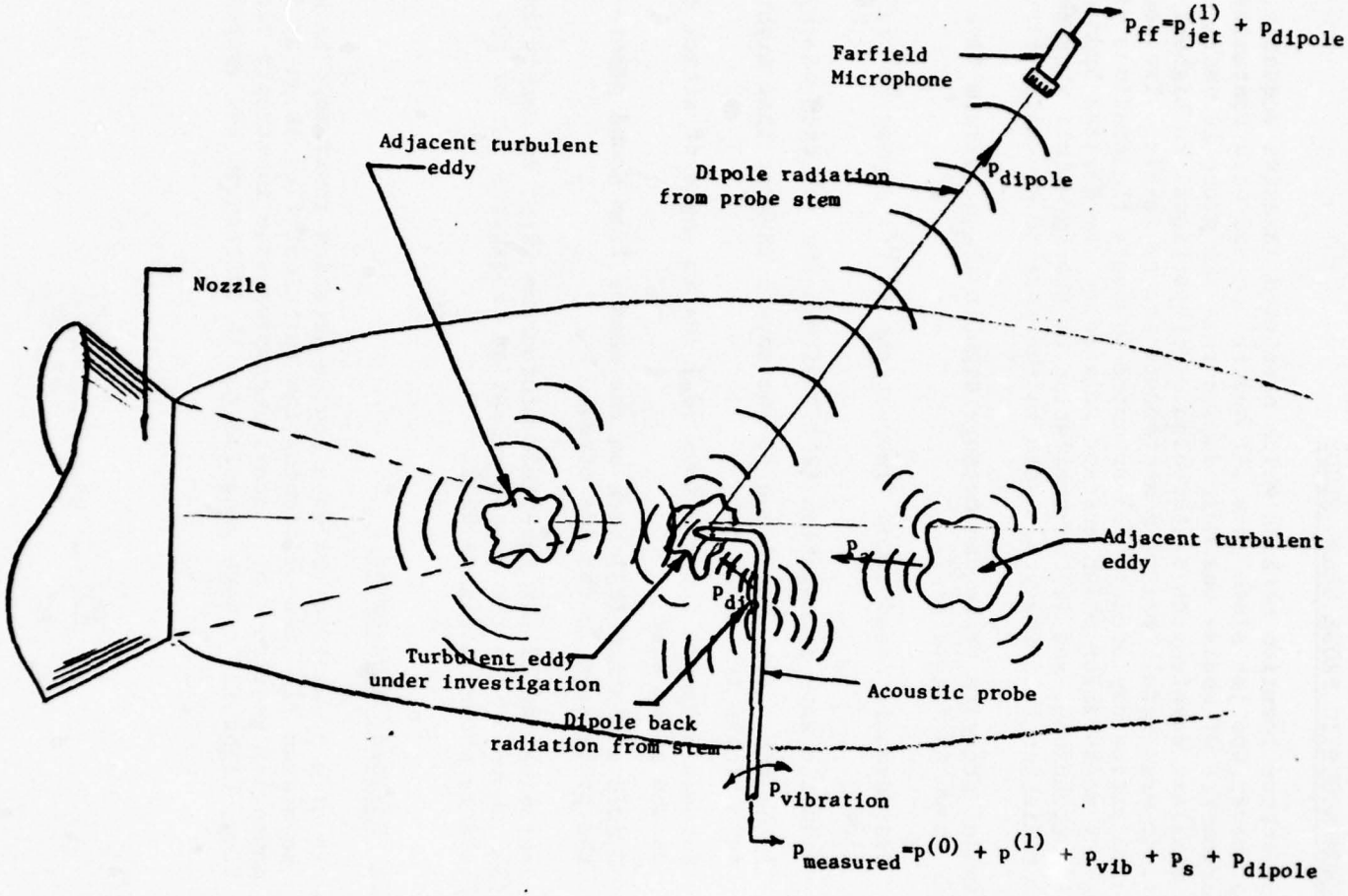


Figure 8-12. Acoustic Probe Contamination.

a corresponding monopole field ("dilatation") by splitting the pressure disturbance into two parts.

$$p - p_o = \left[p^{(0)} + p^{(1)} \right] \tag{136}$$

where:

p = instantaneous static pressure

p_o = local time average static pressure

$p^{(o)}$ = is defined by

$$-\nabla^2 p^{(0)} = \frac{\partial^2 \rho u_i u_j}{\partial y_i \partial y_j} \tag{137}$$

It has been shown that $p^{(o)}$ is the actual perturbation pressure (pseudo-sound) within an exactly incompressible flow and is a good approximation for $M^2 << 1$ (References 72 and 83).

$p^{(1)}$ is the part of the pressure associated with the propagation (not the generation) of acoustic waves. The relationship of $p^{(o)}$ and $p^{(1)}$ is expressed in the "dilatation equation" which results after combining Equation (135), Equation (136), and Equation (137):

$$\frac{1}{c_o^2} \frac{\partial^2 p^{(1)}}{\partial t^2} - \nabla^2 p^{(1)} = - \frac{1}{c_o^2} \frac{\partial^2 p^{(0)}}{\partial t^2} \tag{138}$$

The right hand side of Equation (138) can be regarded as the forcing term of the wave equation for the acoustic pressure $p^{(1)}$. The solution for the radiated sound in terms of Kirchhoff's retarded potentials becomes:

$$p^{(1)}(\underline{x},t) = - \frac{1}{4\pi c_o^2} \int_V \frac{1}{|\underline{x} - \underline{y}|} \left[\frac{\partial^2 p^{(0)}(\underline{y},t)}{\partial t^2} \right]_{\hat{t}} d^3\underline{y} \tag{139}$$

where, again, the brackets indicate evaluation at the earlier time

$$\hat{t} = t - |\underline{x} - \underline{y}|/c_o \tag{140}$$

In the source region, therefore, we want to measure the pseudosound fluctuations $p^{(o)}$ which are related to the acoustic radiation through Equation (139).

8.3.2 Relative Magnitude of Probe Signal Contaminants

The five contributions to the probe measurement can be expressed as

$$p_{measured} = p^{(0)} + p^{(1)} + p_{vib} + p_s + p_d \tag{141}$$

In the acoustic far field (many typical wavelengths away), $p^{(1)}$ approximates the total pressure fluctuation $p(\underline{x},t)$. Figure 8-13 shows the typical variation of the pressure fluctuation with distance from the jet. Starting at a position on the centerline 4 diameters downstream of the nozzle and moving at right angles to the centerline, the far-field condition of a 6 dB drop in the rms pressure per doubling of distance is reached at about 10 diameters (the cross correlation measurements were made about 50 diameters away).

The straight line indicating the 6 dB drop per doubling of distance represents the variation of $p^{(1)}$ alone. If the line is extended backward into the source region, one can estimate the magnitude of an equivalent point source representing the radiation of the whole jet. As shown on Figure 8-13, its pressure field would be about 20 to 40 dB weaker than the actual measured jet pressure, i.e., the approximation of $p^{(o)}$. In fact, the jet is composed of many incoherent sources each of which will of course be weaker than the single equivalent point source. In the source region therefore $p^{(1)}$ is very much smaller than $p^{(o)}$. This means that we do not expect the sound to have any significant back reaction on the flow or to disturb the measurement of $p^{(o)}$ which arises purely from incompressible turbulent momentum exchanges. With the proper transducer mounting, or by the use of a transducer such as a Kulite which is vibration insensitive, the contamination from probe vibration can be eliminated.

The dipole back radiation from the probe stem can be eliminated by proper orientation of the stem and the sensor ports. Dipole noise is known to radiate perpendicular from the surface of the origin of the noise. So, if the probe stem is constructed in such a way that the sensing holes cannot intersect a line normal to the stem surface, the dipole noise contamination will be avoided.

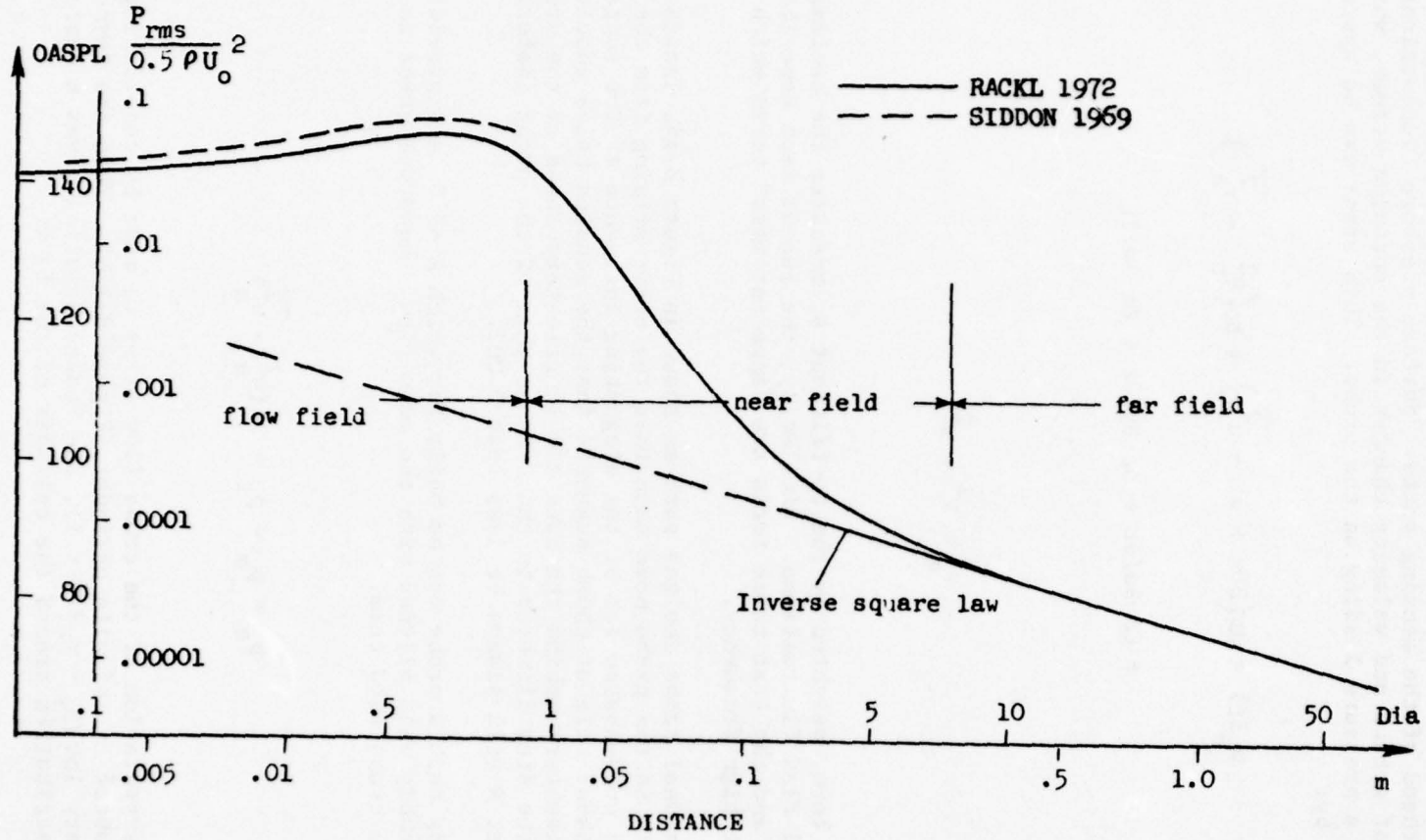


Figure 8-13. Variation of Pressure Fluctuation with Distance from Jet, Starting at 4 Diameters Downstream in the Jet and Proceeding at Right Angles to the Jet Axis.

The remaining contaminant is the surface pressure fluctuation (P_s) in the neighborhood of the sensing ports. Surface pressure fluctuations arise from angle of attack and velocity changes in the oncoming stream, which cause a change in a pressure loading on the probe. This error can be approximated empirically by:

$$p_s(t) \approx A\rho\left(2Uu + u' - \overline{u^2}\right) + B\rho\left(V_n^2 - \overline{v_n^2}\right) \tag{142}$$

$$+ C\rho\ \partial u/\partial t + D\rho\ \partial v/\partial t + E\rho\ \partial w/\partial t$$

where

$$V_n = V^2 + w^2 \tag{143}$$

the leading term, weighted by the coefficient A, measures the contamination due to axial flow fluctuations. Similarily, the second term describes cross flow errors and the last three terms are "apparent mass" terms which are important at high frequency.

Conventional probe designs such as shown in Figure 8-14, locate the sensing holes in the probe nose such that the error arising from the nose curvative is compensated for by the stagnating influence of the supporting stem. The usual rule of thumb suggests that the sensing holes should be located 8 diameters behind the nose and 16 diameters ahead of the stem, provided that the stem diameter is the same as that of the probe (Reference 84). In this case, A will always be less than 0.002.

Assuming that a probe can be built for which A << B, and provided that it is reasonably well aligned with the mean flow, the probe error is dominated by the cross flow term:

$$p_s = p_m - p_t \approx B\rho(v_n^2 - \overline{v_n^2}) \tag{144}$$

A crude interpretation of the cross flow error is made by considering pure cross flow about an infinite cylinder (Figure 8-14b). When the Reynolds number is very low ($R_v \approx v_n d/V < 1$), the Stokes solution gives a surface pressure distribution around the cylinder of the form:

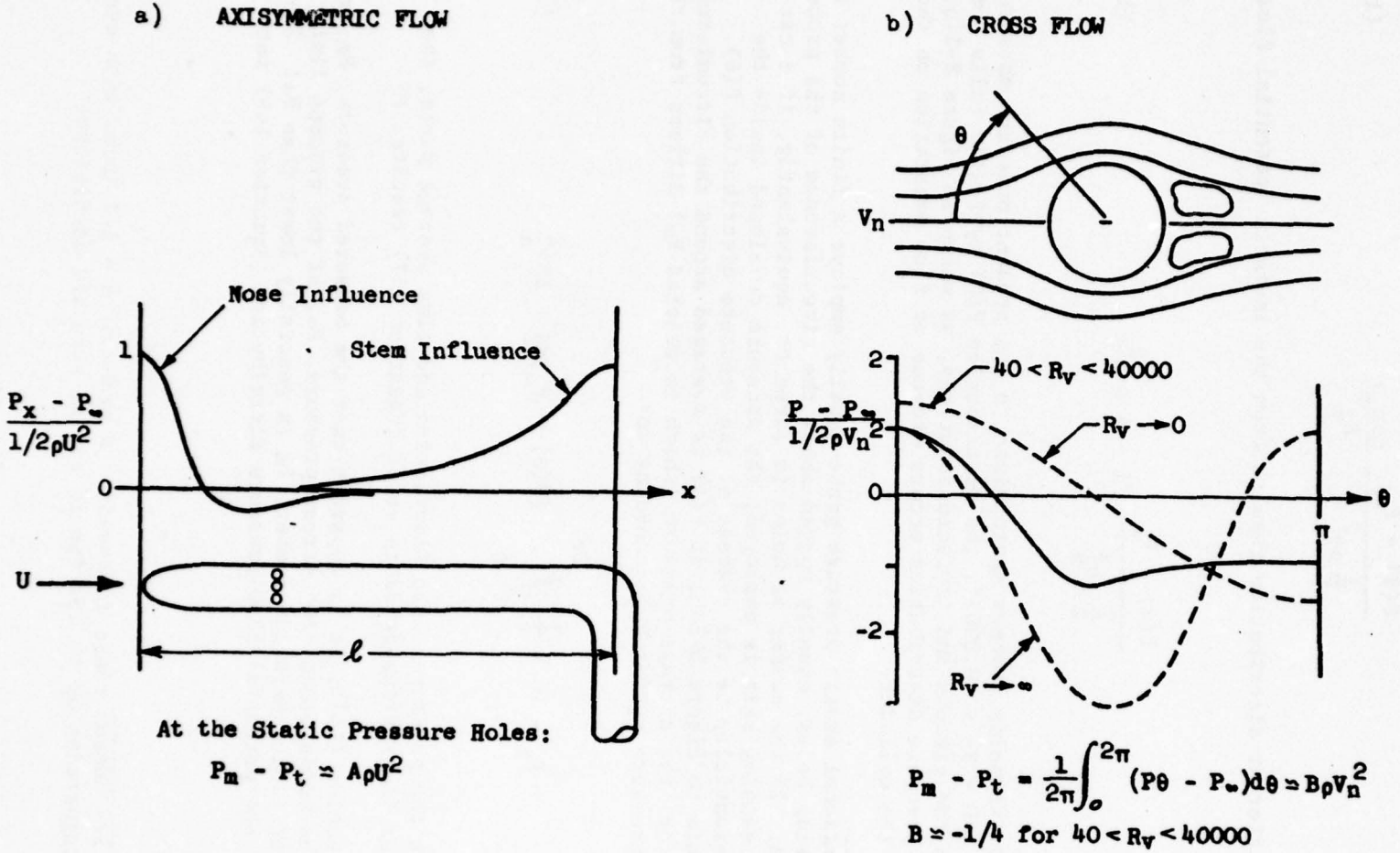


Figure 8-14. Fundamental Error Mechanisms for Conventional Stem Design.

$$\frac{P(\theta) - P_\infty}{\frac{1}{2}\rho v_n^2} \simeq \frac{\cos\theta}{R_v} \tag{145}$$

A somewhat different distribution results from the inviscid (potential flow) solution:

$$\frac{P(\theta) - P_\infty}{\frac{1}{2}\rho v_n^2} \quad 1 - 4\sin^2\theta \tag{146}$$

For cross flow Reynolds numbers appropriate to the present pressure measurement problem ($40 < R_u < 40{,}000$)*, the distribution $P(\theta)$ typically falls somewhere between the viscous and inviscid solutions, as shown in Figure 8-14b. This type of pressure distribution occurs because of flow separation on the back-side of the cylinder.

A conventional static pressure probe usually employs a finite number of pressure sensing holes, equally spaced about the circumference of the probe cross section. If the number of holes is large or, equivalently, if a circumferential sensing slit is employed, the pressure developed inside the probe will essentially be the average of the pressure distribution $P(\theta)$. Referring again to Figure 8-14b, if $P(\theta)$ is averaged around the circumference of the cylinder, the average pressure (which is denoted P_m) differs from the true static pressure P_t (or P_∞) according to:

$$P_m - P_t = \frac{1}{\pi 2}\int_0^{2\pi} [P(\theta) - P_\infty]d\theta \quad B\rho v_n^2 \tag{147}$$

On separating the pressures into fluctuation and time average parts, the expression for fluctuating pressure error (Equation 147) results.

From Equation (147), it is apparent that the measured pressure, P_m, will only equal the undisturbed free stream pressure, P_∞, at the viscous limit ($R_v < 1$). For finite Reynolds number, P_m is generally lower than P_∞. Substitution of the potential flow pressure distribution (Equation 146) into

* This Reynolds number range is based on a probe of d = 1/2 inch, with cross velocity magnitudes up to 160 fps in air at standard conditions.

(147) gives a value $B \simeq -1/2$. However, from experimental pressure distributions such as that shown for $40 < R_v < 40{,}000$, values of B in the range -1/4 to -1/3 are found.

The two-dimensional cross flow model is only a rough approximation to the more complicated case of a probe in an unsteady airflow. The structure of the wake formed in the "dead water" region of the probe must be influenced by the large axial component of velocity $\overline{U}$ and the resulting boundary layer development on the probe. Nevertheless, in a typical unsteady situation with axial flow, the pressure distribution $P(\theta)$ was sampled by Siddon (Reference 85), using a pinhole technique, and was found to behave much like the solid curve in Figure 8-14b.

8.3.3 Design of a Low Noise Probe

Rackl and Siddon (References 75, 86, and 87) developed a low noise, airfoil-shaped probe as shown in Figures 8-9 and 8-10. The sensing holes were located near the trailing edge of the airfoil in a specially designed cusp which gave nearly invariant response to inclination angle changes, as seen in Figure 8-9. The foil was inserted into the jet stream such that the plane of the foil contains the direction of the mean flow and of the radiation to the far-field microphone, as shown in Figure 8-8. The thin structure ensures that dipole radiation in the plane of the foil is virtually eliminated.

The success of Rackl's work prompted a study into additional design philosophies as part of Task 1. It was felt that a multipurpose, low noise probe could be developed from proper placement of holes on straight cylindrical rods. Such a design, it was reasoned, would enjoy a number of advantages; namely:

1. Insensitive to flow angle variations
2. Eliminates dipole back radiation onto the probe sensor
3. By pointing the tip of the cylinder at the far-field microphone, minimum far-field contamination would be obtained.
4. Small size
5. Simple design
6. Potential of an "acoustic rake" for multipoint measurements in the jets.

8.3.3.1 Surface Pressure Distributions

The first step in the design process was to collect information on the surface pressure distribution on cylinders. Although numerous studies have been done in the past, it was necessary to obtain additional data, such as the influence of the probe end, the sensing hole diameter effect, and "yaw" and "pitch" angle variations.

Five 1/8-inch cylinder probes were constructed, as shown in Figure 8-15, for surface pressure measurement. These probes had a single hole of varying diameter drilled at a number of locations from the stem end, as shown in Figure 8-15. The specific values are tabulated below:

Probe	Hole Diameter (inches)	Distance From End (inches)
1	0.042	0.050
2	0.042	0.100
3	0.042	0.150
4	0.042	0.200
5	0.0195	0.150

The inside of the cylinder was vented to a manometer board for reading the surface pressure. The probes were inserted into the potential core of a M = 0.3, 2.5-inch diameter jet and rotated about their axes.

The general distributions described by the solid line in Figure 8-14b were obtained. Figure 8-16 shows typical measurements with yaw angle β at 0° pitch (see Figure 8-16 for nomenclature). The larger 0.042-inch diameter hole is seen to give the proper reading and a distance of 0.15 inch is sufficient to avoid end effects. The end effects are, however, minor so one could move as close as 0.05 inch and experience minor effects. The probe reads stream static pressure at approximately 48° off axis (Point B). The calibration also indicates a fairly constant slope over a range of 30° between points A and B on the figure. This suggests that if two holes were used, equally spaced on both sides of the stagnation point, as shown in Figure 8-17, the probe would read stream static pressure even if the flow angle varied.

8.3.3.2 Two-Hole Probes

Locating two holes on either side of the stagnation point, which dump into a common cavity, will produce a probe which will average together the increase in pressure occurring at one port (when the flow angle is moved closer to the hole) with the decrease in pressure occurring at the second port (because the flow angle has moved further away). The net result is a range of flow angles over which the probe is relatively insensitive to velocity vector changes. Eight two-hole probes were then constructed per the sketch in Figure 8-18, three of which are shown in Figure 8-19. The design and actual fabricated angle spread between the two holes were found to be significantly different upon inspection of the parts, as shown below:

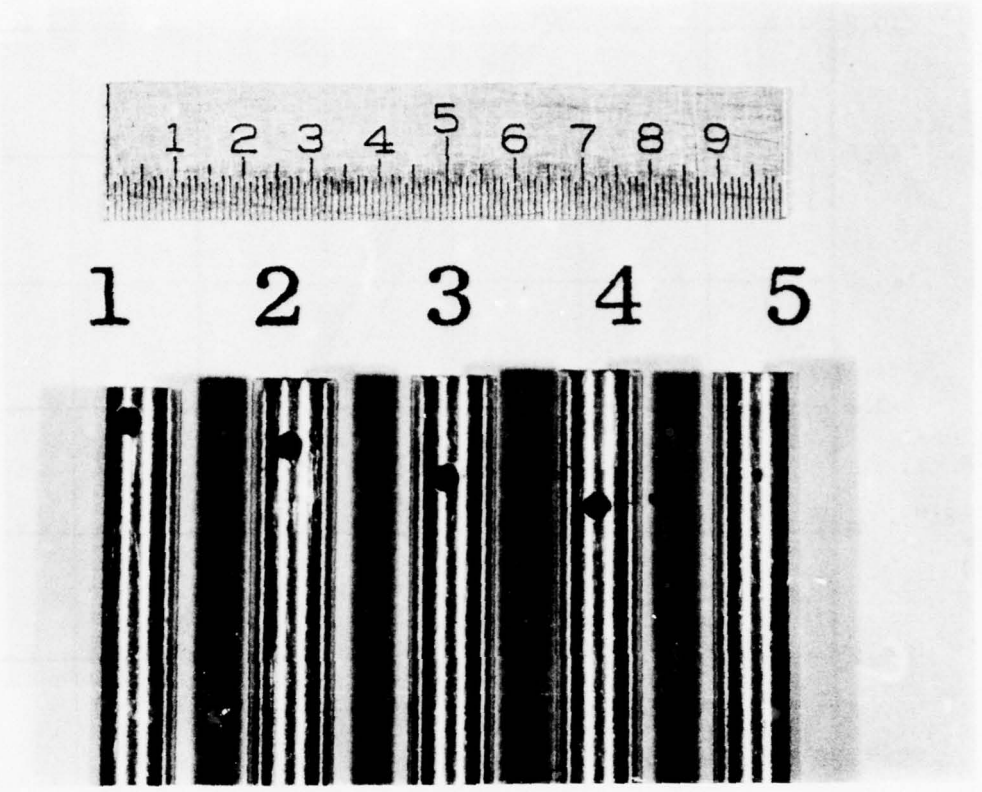


Figure 8-15. Single Hole Cylindrical Probes.

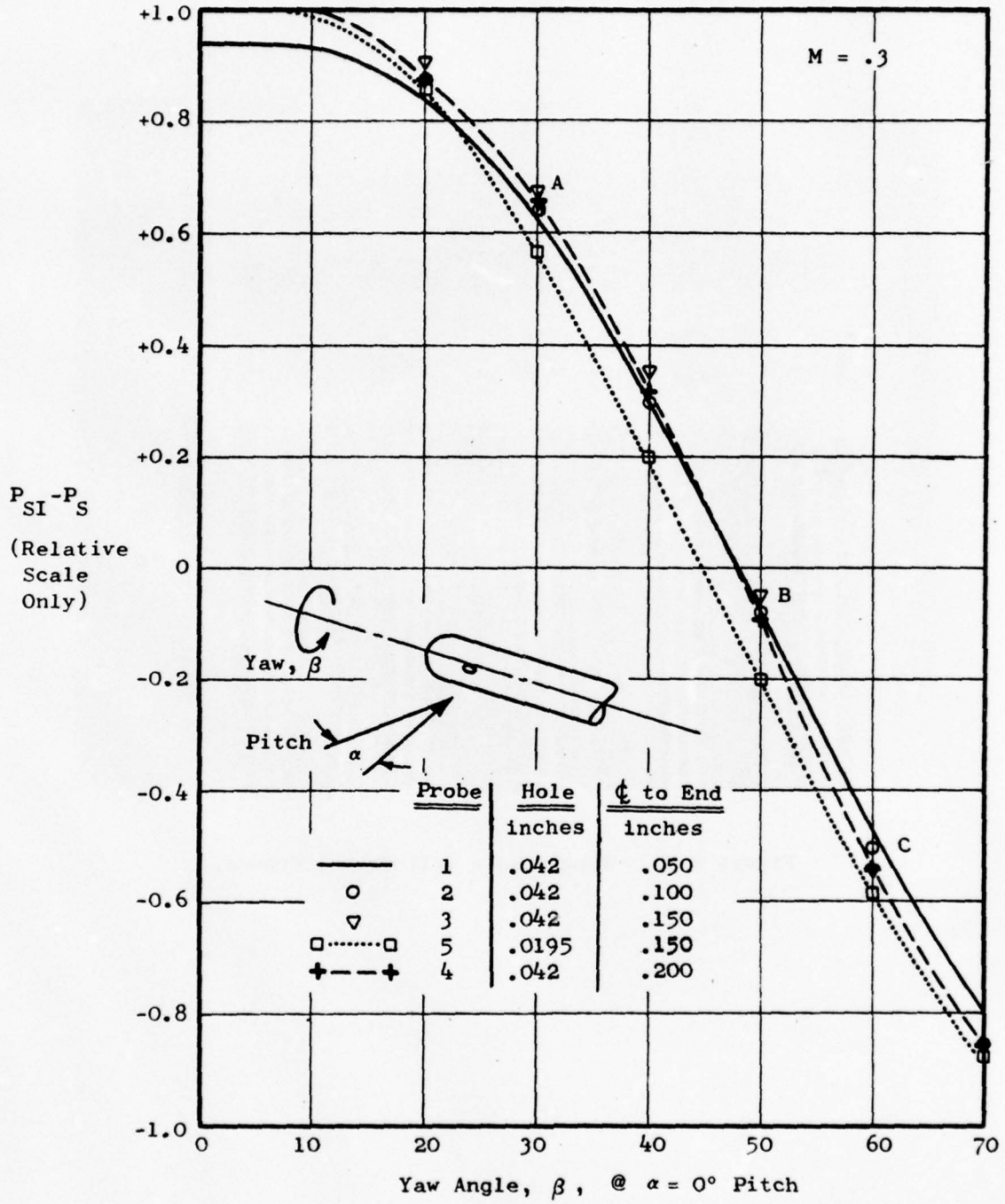


Figure 8-16. Surface Pressure Response at M = 0.3 and Pitch = 0° Angle for Various Single-Hole Cylindrical Probes.

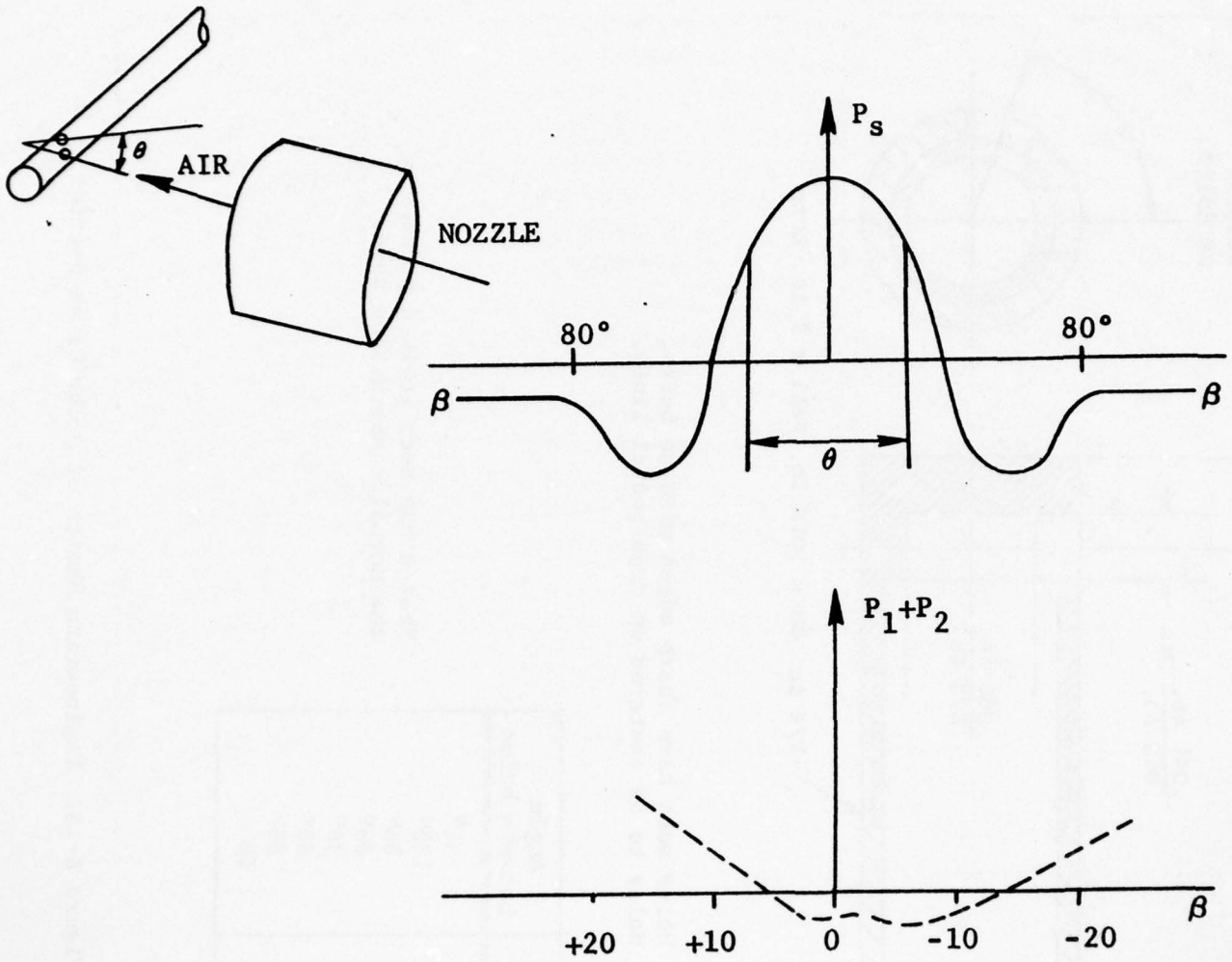
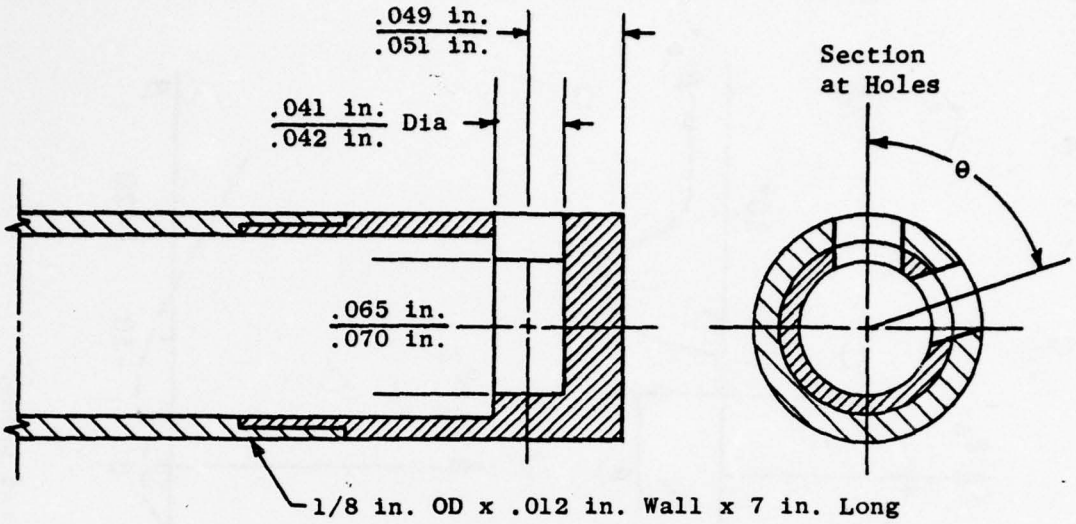


Figure 8-17. Two-Hole Cylindrical Probe.



Note: Holes must have sharp edges with no burrs.
Holes to be centered on true radial lines.

Probe	Angle between holes
6	84°
7	180°
8	86°
9	88°
10	96°
11	86°
12	88°
13	100°

Sketch has been revised to show the actual construction used.

Figure 8-18. Engineering Sketch of Probe Cross Section.

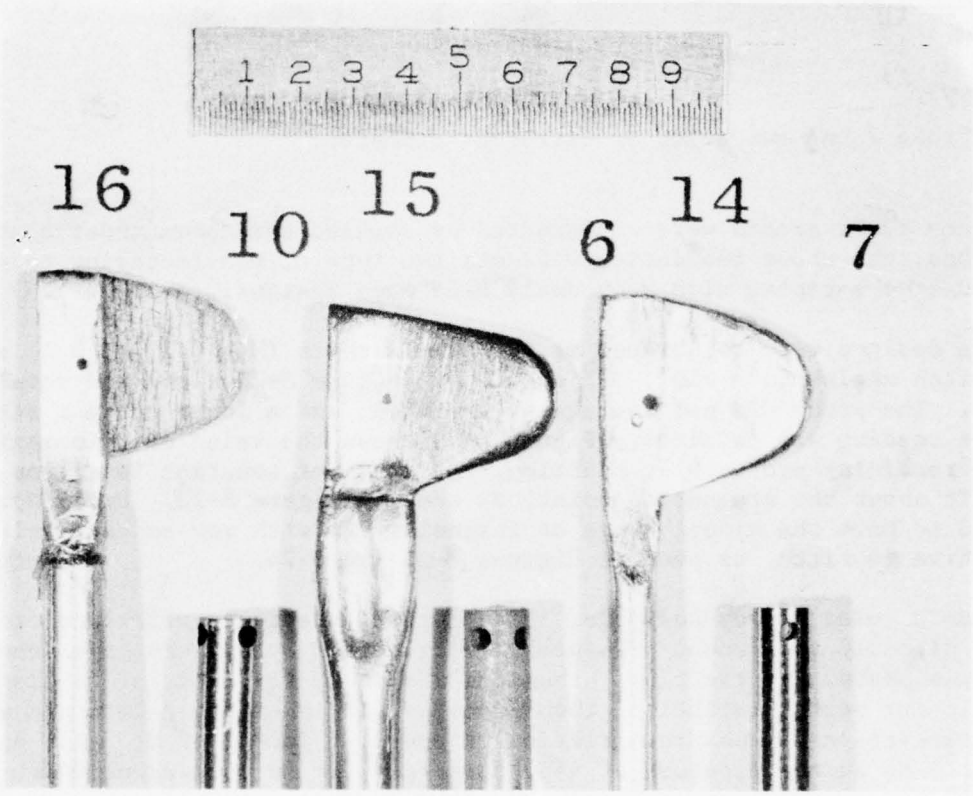


Figure 8-19. Two-Hole Cylindrical and Rackl-Type Probes.

Probe	Angle ( )° Specified	Angle ( )° Measured
6	84	83.5
7*	180	180
8	86	80.5
9	89	80.25
10	96	94.75
11	86	83
12	88	91
13	100	93

* Probe 7 had two holes of different diameter.

Since these probes were constructed by skilled craftsmen under controlled conditions, the above tabulation reflects the type of manufacturing tolerances which must be accepted with such small hand-made designs.

The designs were calibrated at two Mach numbers (M = 0.2 and 0.4) and three pitch angles (α = -10°, 0°, and 10°). Figure 8-20 shows the results of Probe 8. The probe did not average as expected, and a lower maximum static pressure reading was obtained. Figure 8-21 shows the value of this maximum for the remaining probes. In addition, the range of constant level was not symmetric about the stagnation point, as seen in Figure 8-22. Probe No. 10 appeared to have the widest range of insensitivity with yaw and was relatively insensitive to pitch, as seen in Figures 8-23 and 8-24.

From a quasi steady analysis, these surface pressure variations can be related directly to a sound pressure level recorded by a microphone mounted inside the probe. If the flow turbulence was such, for example, to cause a ±15° velocity vector variation, then Probe No. 10 in Figure 8-24 would experience a peak-to-peak pressure variation of around 5 inches of H_2O (12, 454 dynes/cm^2) or an rms pressure of 4440 dynes/cm^2 for an equivalent OASPL of:

$$\text{OASPL} = 20 \log_{10} \left(\frac{P_{rms}}{P_{ref}} \right) = 20 \log_{10} \left(\frac{4440}{.0002} \right) \tag{148}$$

$$\text{OASPL} = 147 \text{ dB}$$

This represents a significant contamination level.

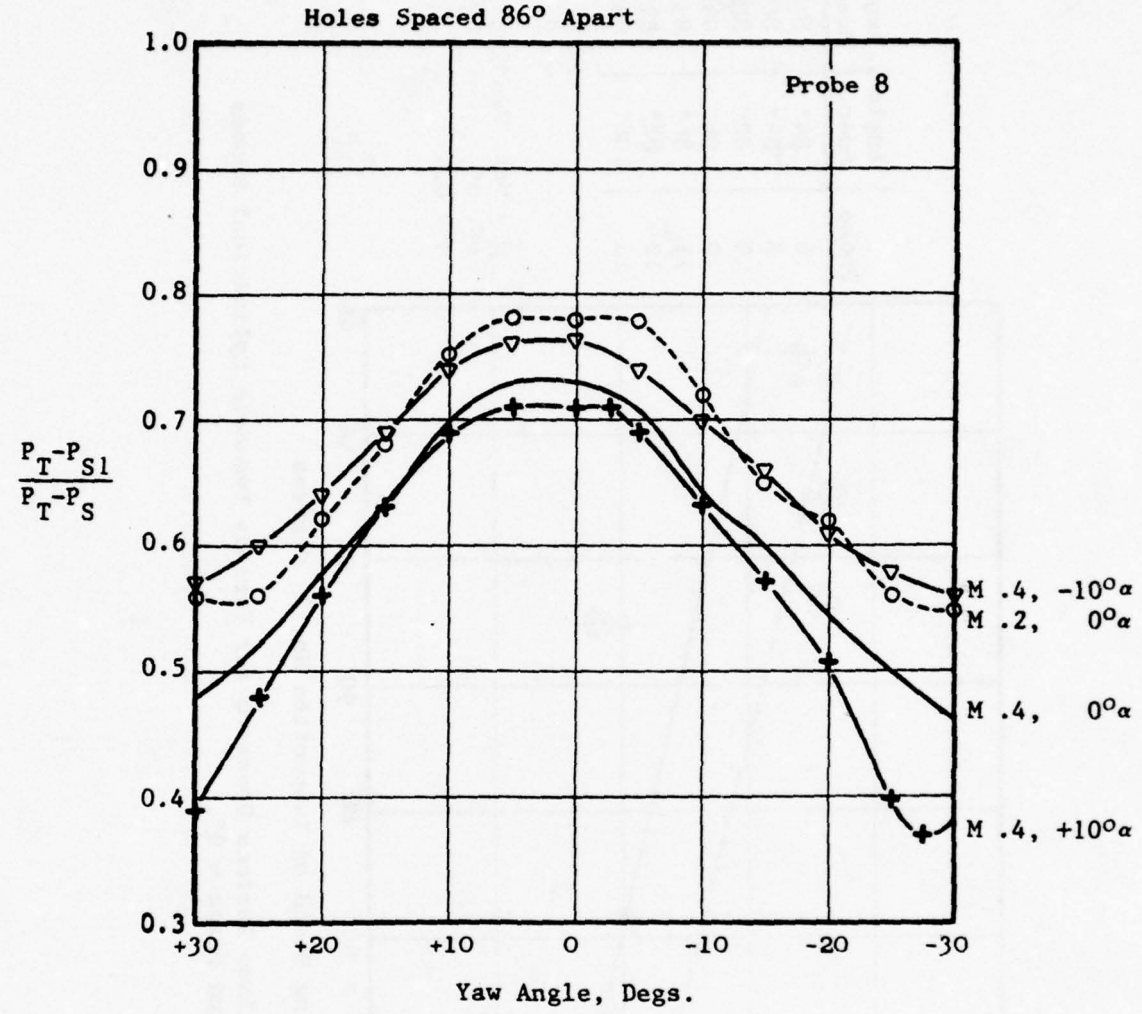
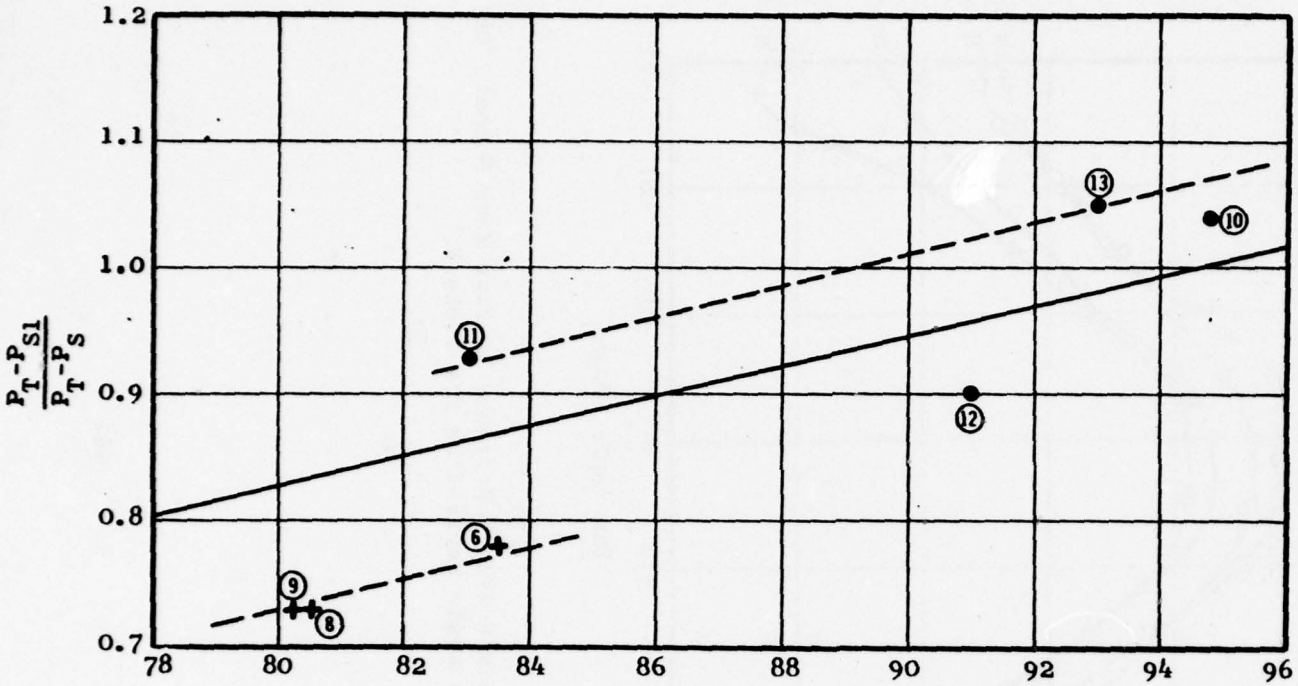


Figure 8-20. Surface Pressure Response to Flow Mach Number, Yaw and Pitch Angle Variations for Probe 8.



Probe	Angle Spec.	Angle Meas.
6	84°	83½°
8	86°	80½°
9	88°	80¼°
10	96°	94¾°
11	86°	83°
12	88°	91°
13	100°	93°

Figure 8-21. Measured Maximum Surface Pressure for Various Two-Hole Cylindrical Probes at M = 0.4 and Pitch = 0°.

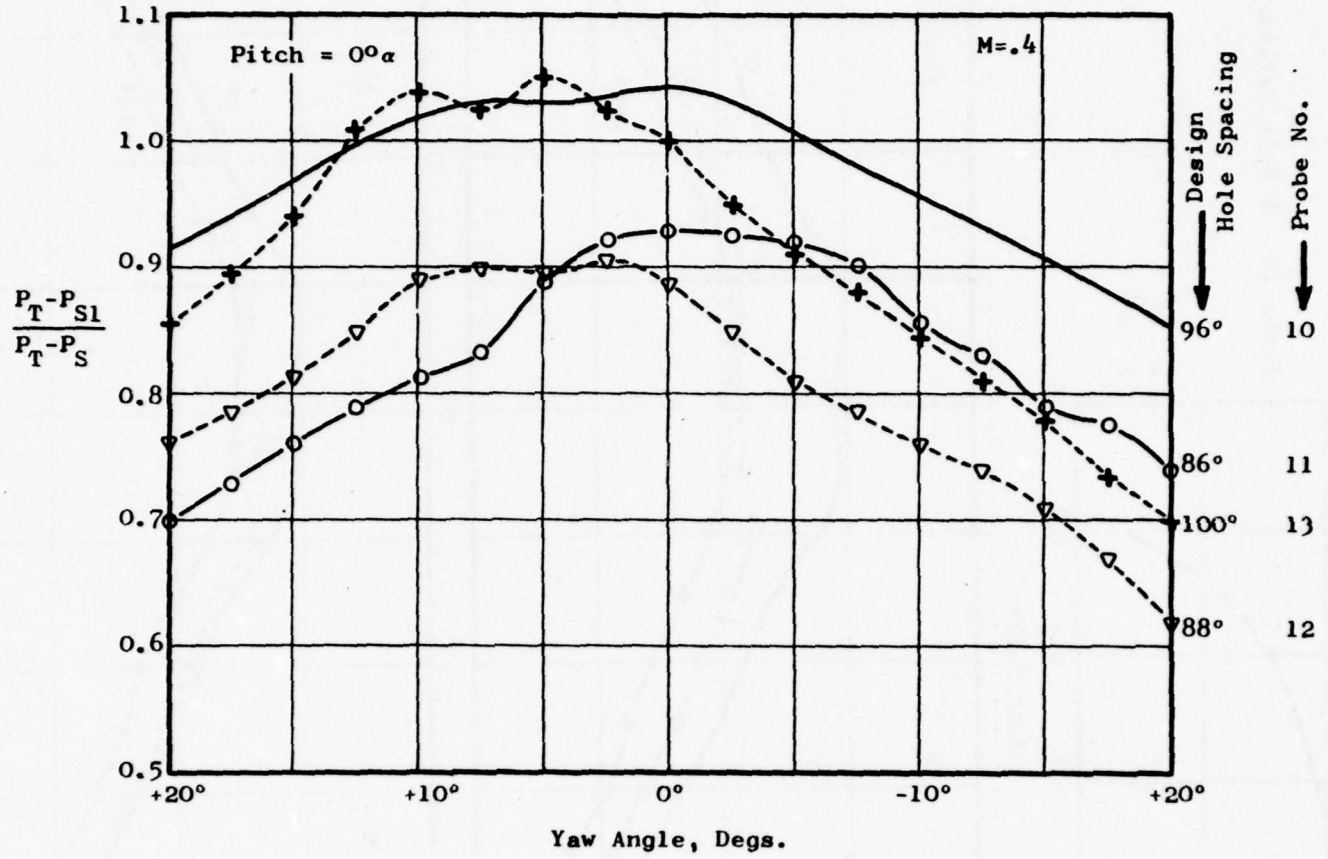


Figure 8-22. Comparison of Surface Pressure Response for Various Two-Hole Cylindrical Probes at M = 0.4 and Pitch = 0.

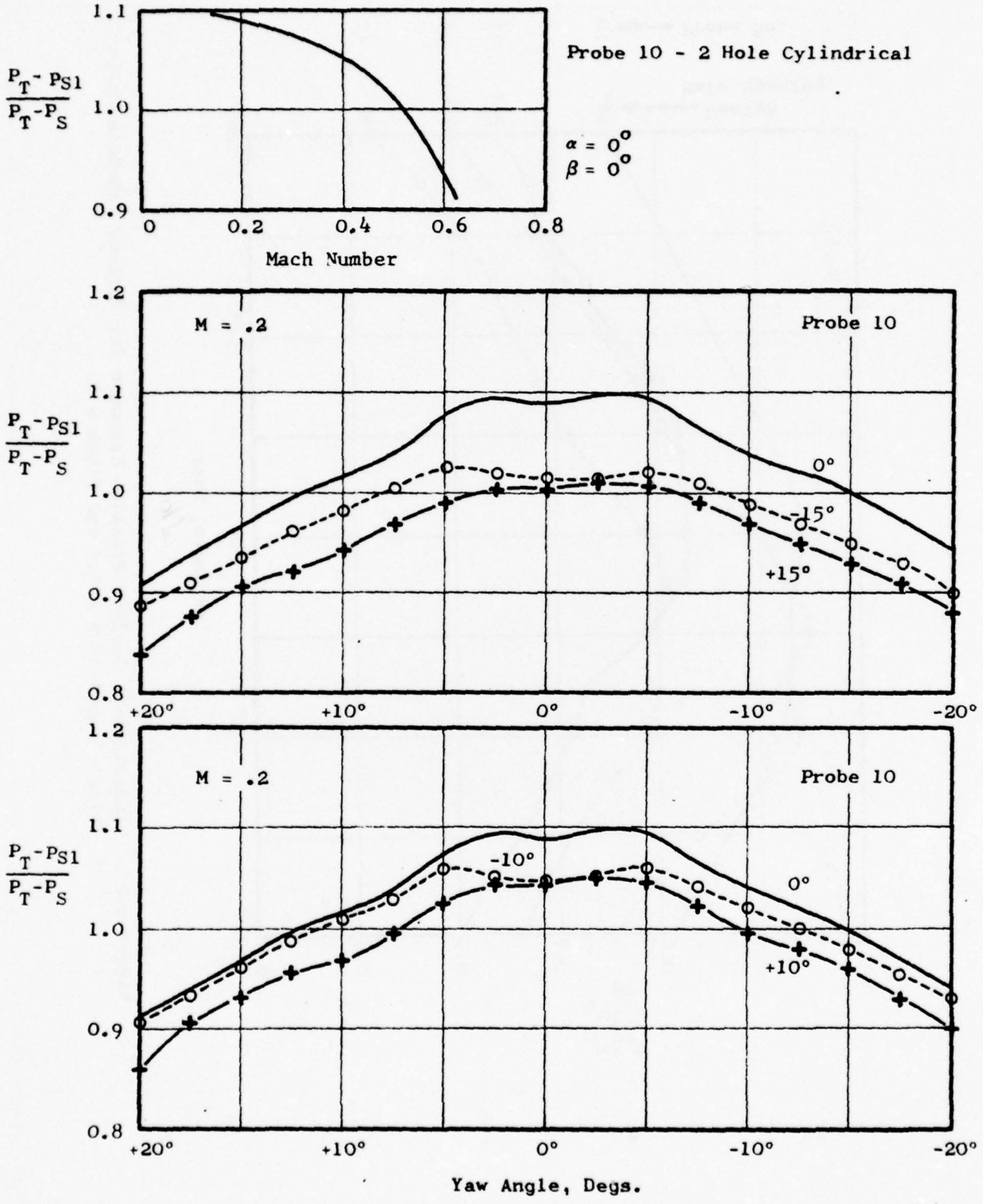


Figure 8-23. Surface Pressure Response to Yaw and Pitch Angle for M = 0.2 for Probe 10.

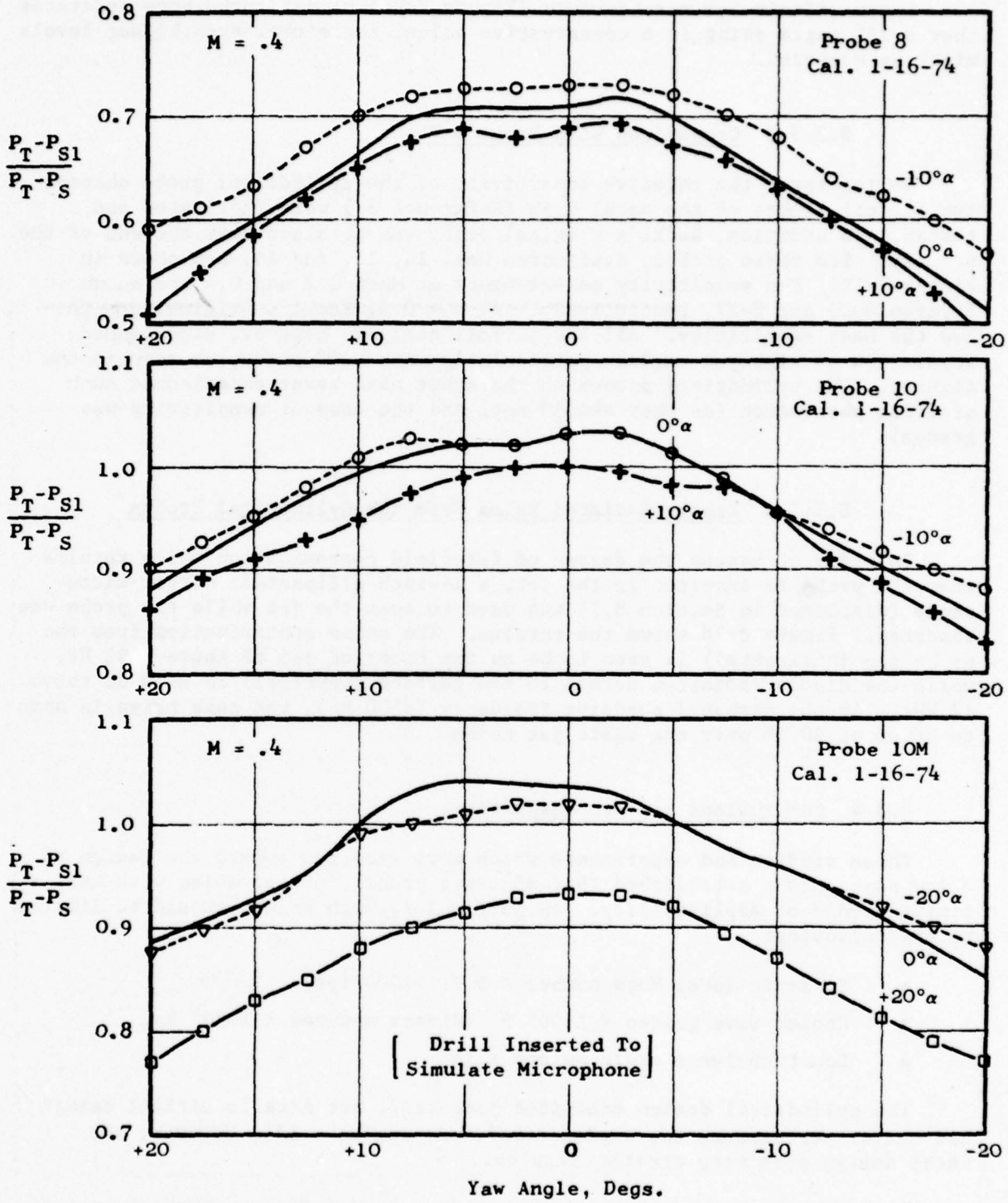


Figure 8-24. Surface Pressure Response to Yaw and Pitch Angles at M = 0.4 for Two-Hole Cylindrical Probes Nos. 8, 10, and 10M.

Laser velocimeter measurements (Figure 8-25) of jet turbulence indicates that a 15° angle swing is a conservative value, therefore, even higher levels might be expected.

8.3.3.3 Comparison With Rackl's Probe

To interpret the relative sensitivity of the cylindrical probe shapes, two airfoil probes of the Rackl type (Reference 87) were fabricated and tested. In addition, Rackl's original probe was obtained near the end of the program. The three probes, designated Nos. 14, 15, and 16, are shown in Figure 8-19. The sensitivity measurements at Mach 0.2 and 0.4 are shown in Figures 8-26 and 8-27, respectively. At M = 0.2, Rackl's original design, had the best sensitivity. All the airfoil designs, however, experienced separation at high yaw angles, particularly with -10° pitch, as seen in the figures. The cylindrical probes on the other hand never experienced such stalling phenomenon (as they should not) and the loss of sensitivity was gradual.

8.3.3.4 Dipole-Radiated Noise From the Cylindrical Probes

In order to assess the degree of far-field contamination which results when the probe is inserted in the jet, a 14-inch ellipsoidal mirror microphone (discussed in Section 8.7) was used to scan the jet while the probe was inserted. Figure 8-28 shows the results. The noise contamination from the probe tip (horizontal) is seen to be on the order of 3-5 dB above 5000 Hz, while the dipole radiation normal to the surface (vertical) is 8-10 dB above 12 kHz. At the Strouhal shedding frequency (6500 Hz), the peak noise is seen to be about 20 dB over the basic jet noise.

8.3.4 Conclusions and Recommendations

These studies and experiments which were directed toward the design of a low noise probe established that acoustic probes for jet noise work have a limited range of applicability. In particular, such probes should be limited to the following:

- Subsonic local Mach number < 0.7 ($\sim$1000 fps)
- Cooled wave guides < 1600° R (direct mounted < 1000° R).
- Low turbulence angle swings < 15°

The cylindrical design exhibited potential, but Rackl's airfoil design had better performance for angles < 15°. At angles > 15°, however, the Rackl design gave very erratic results.

Although the noise source survey of the probe indicated that contamination in the far field can be reduced by properly orienting the cylindrical

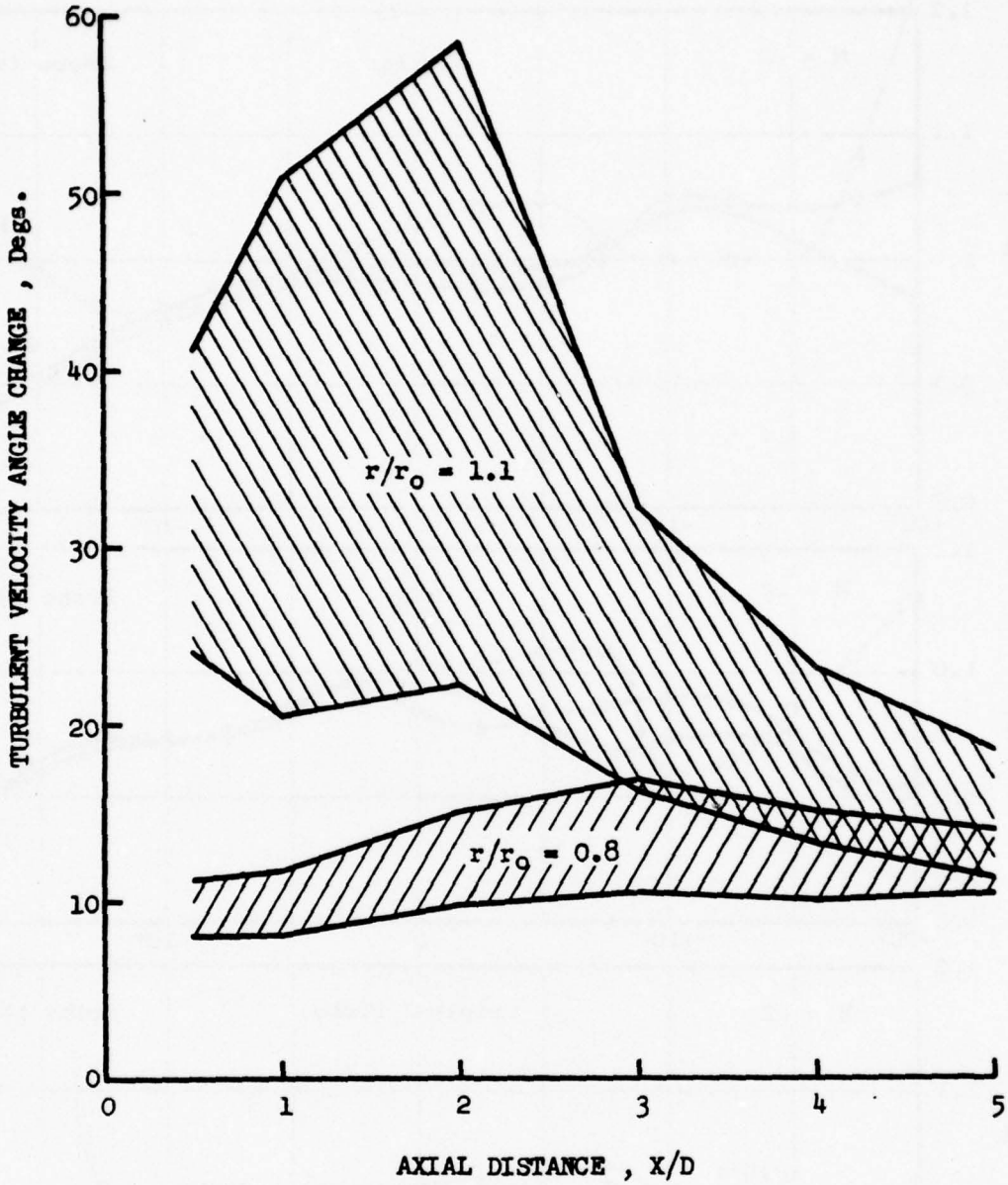


Figure 8-25. Velocity Vector Direction Change in a 40-Chute Nozzle.

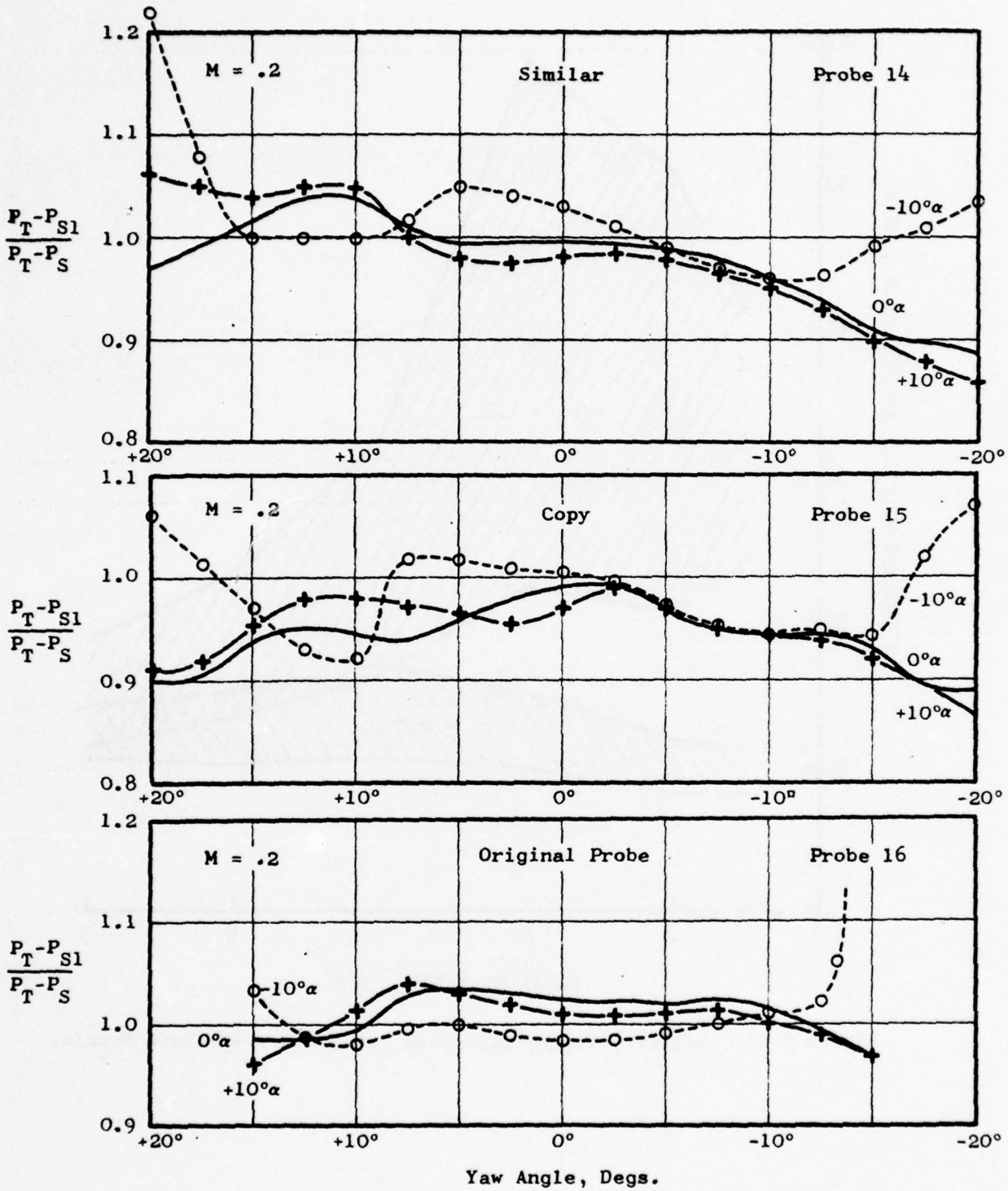


Figure 8-26. Surface Pressure Response to Yaw and Pitch Angles at M = 0.2 for Rackl-Type Probes Nos. 14, 15, and 16.

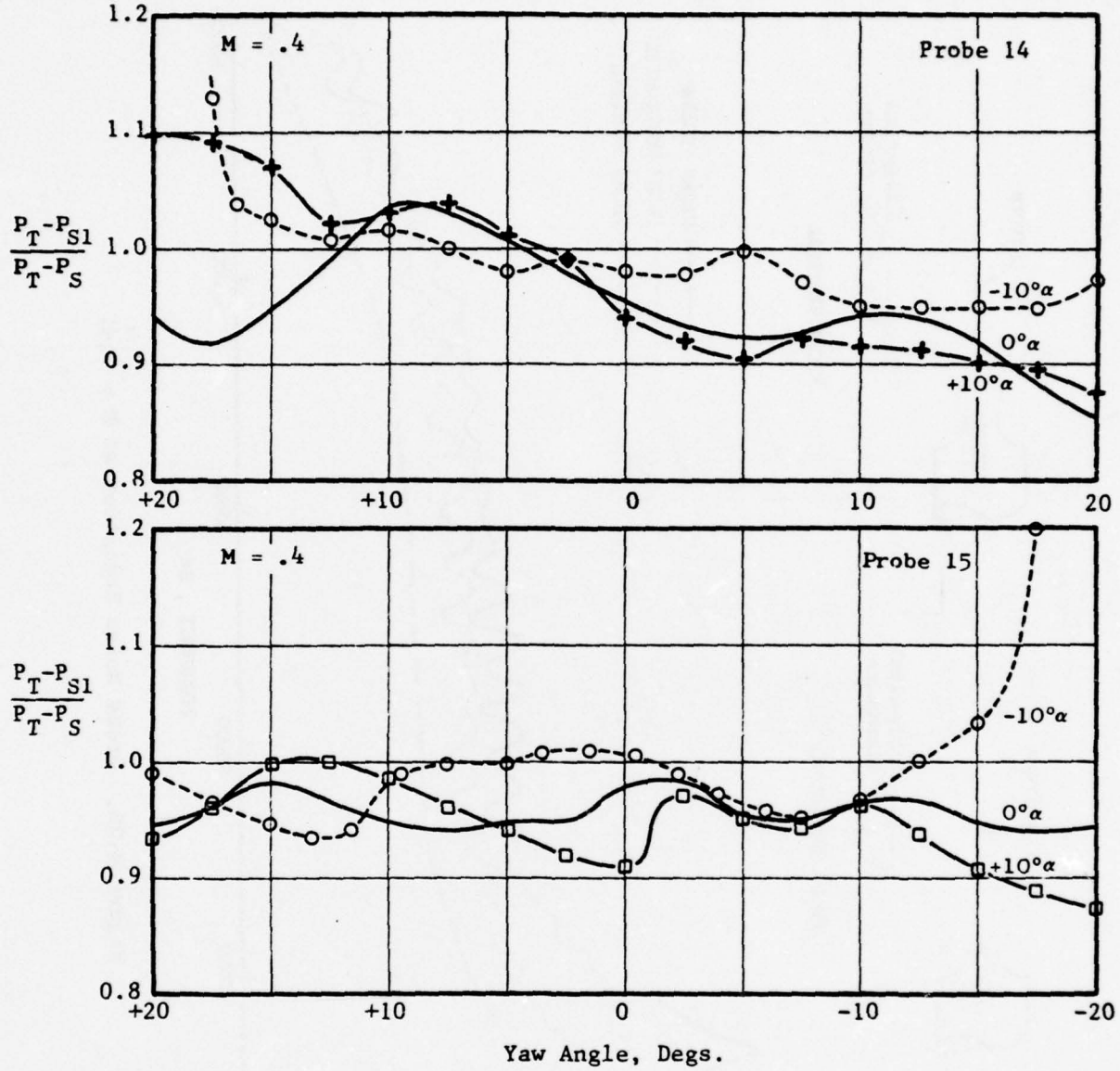


Figure 8-27. Surface Pressure Response to Yaw and Pitch Angles at M = 0.4 for Rackl-Type Probes Nos. 14 and 15.

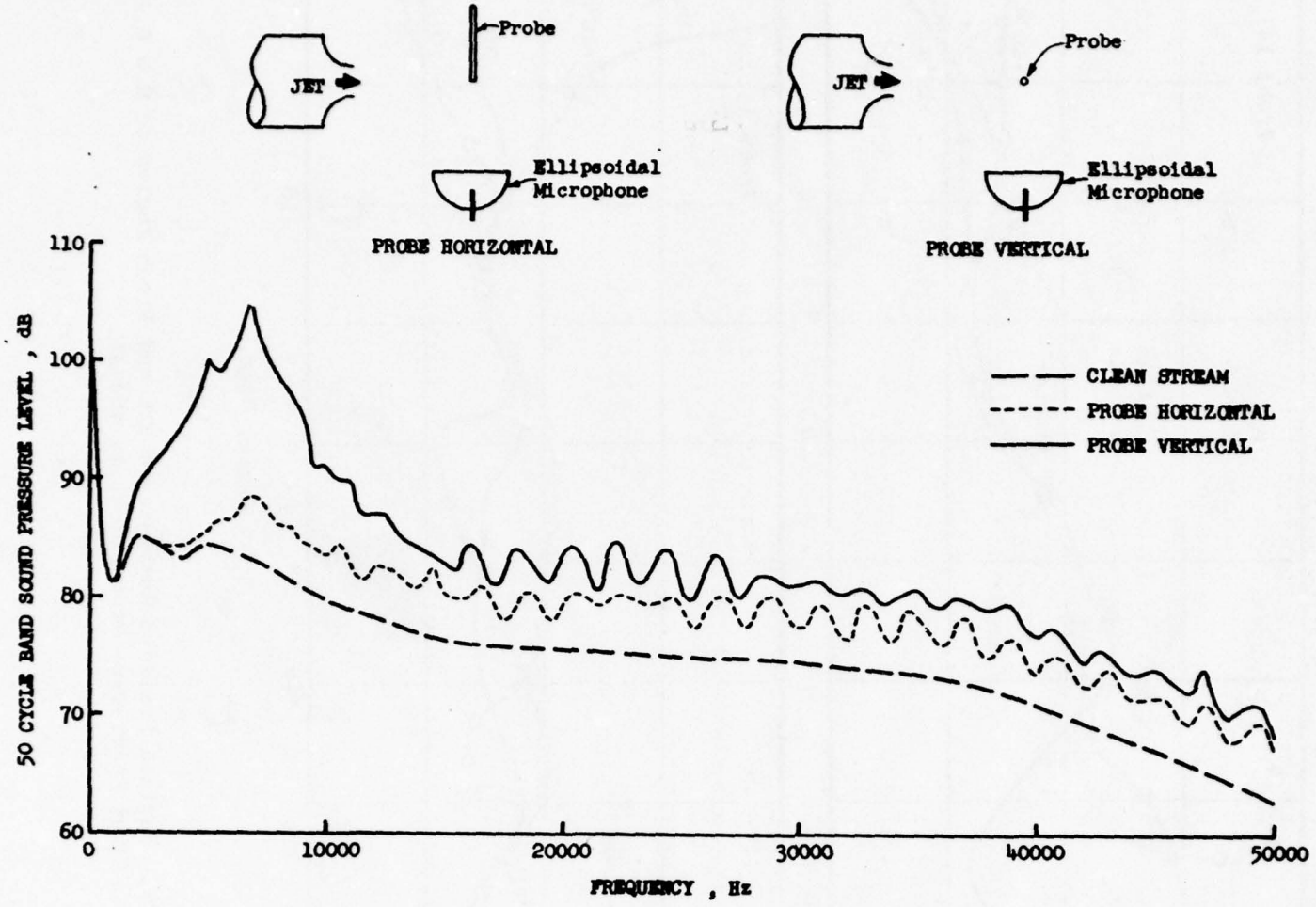


Figure 8-28. Probe Noise Radiation at M = 0.4.

probe, considerable more exploratory work is required. Further investigations directed toward the design of a truly contamination-free probe independent of Mach number and turbulence spectrum are in order. Also, more measurements of the sensitivity of causality correlations to probe generated noise by testing probes of different sizes are needed. However, within the framework of the DOT High Velocity Program, timing considerations (e.g., having a validated technique(s) on hand for use in the remaining tasks) dictated that the in-jet probe not be pursued, at least in this program, as a candidate partner of the causality correlation technique.

8.4 LASER VELOCIMETER DEVELOPMENTS FOR NOISE SOURCE LOCATION

During the course of the DOT/USAF Supersonic Jet Noise Program (Contract F33615-73-C-2031) a considerable amount of energy was directed toward developing instrumentation capable of examining the detailed characteristics of turbulent jet plumes. In the first phase of the study, advanced pressure probe developments were pursued, as were initial demonstrations using a General-Electric-developed laser velocimeter (LV) on heated supersonic jets. It became clear that the laser velocimeter was the measurement tool for the future. The LV offered a means of measuring the flow properties of high velocity/high temperature jets without disturbing the flow. The LV also offered a conceptually easy and accurate method of measurement not only of rms mean velocity and turbulent velocity distributions, but also of spectral and cross-correlation type of information; for direct noise source location type of information the cross-correlation type is very important.

Discussed below are the major results obtained by General Electric and reported in the Final Report (Reference 106).

8.4.1 Basic LV Mean and Turbulent Velocity Measurements

The concept of laser velocimeter measurement for routine mean velocity and turbulent velocity may be described in the following simple fashion. Two beams of monochromatic light intersect at a point in space and set up a fringe pattern of known spacing (see Figure 8-29). The flow is seeded with small particles which pass through the measuring volume. The light scattered from the particles is collected, and the laser signal processor measures the time it takes for the particles to pass through each fringe. Knowing the fringe space and traverse time for each validated particle enables the construction of a histogram (see insert on Figure 8-29). Then, by statistical techniques, the mean values and standard deviations are constructed (the mean velocity and turbulent velocity, respectively). Although the principle of measurement is easy, the practical aspects of designing an electronic processing unit to monitor valid particles is of no small consequence. Investigators have had great difficulty performing measurements in low velocity jets, let alone measurements in heated supersonic jets.

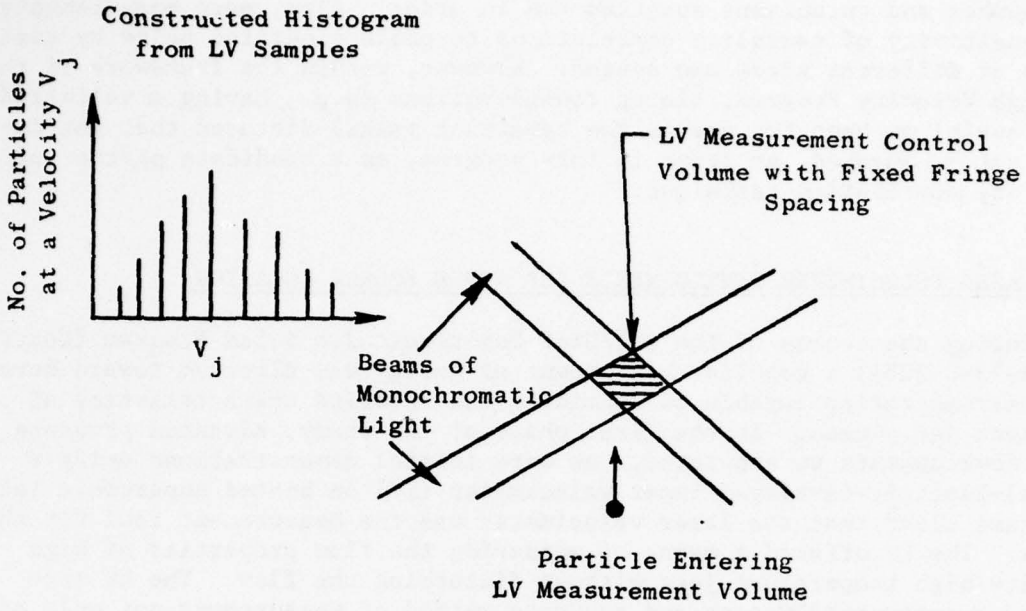


Figure 8-29. Schematic of Laser Velocity Measurements.

Figures 8-30 and 8-31 show typical mean and turbulent velocity measurements for an ambient subsonic and a heated high velocity supersonic shock-free jet. The existence of the extended potential core and the difference in the turbulence distributions between the cases are evident.

Figure 8-32 shows comparisons of LV-measured radial mean velocity profiles between a shock-free nozzle flow and a shocked-nozzle flow, while Figure 8-33 shows LV-measured radial turbulence velocity profiles for the shock-free high temperature test condition. Figure 8-34 shows the influence of jet-exit-plane turbulence over a wide range of velocities (500 - 3000 fps) and temperatures (ambient to 2500° R). Measurements of the type shown are first-of-a-kind type measurements. Of particular note is the last figure. It refutes the argument that turbulence velocity drops off with jet velocity so that lower velocity power laws occur (an argument proposed by Lighthill). Additionally, Figure 8-35 shows measured mean and turbulent velocity measurements along the axis of a high temperature, high velocity, shocked-flow jet. These results show the capability of the LV for defining the shock structure of high velocity jets.

8.4.2 LV-Measured Turbulence Spectra

To construct turbulence spectra from the LV device presents a difficulty not encountered with continuous-type measurement instrumentation. Conventional spectra estimation techniques assume that all values of the input signal are known in the analysis interval. Such knowledge is not available at the LV output. Using the direct time signal to construct the turbulence signal results in excessively high sampling noise levels in the estimated spectra. To overcome this problem, it is necessary to reconstruct the autocorrelation function of the velocity signal, then obtain the spectrum as its Fourier transform.

To illustrate this process, a model for the output of the LV, $y(t)$, may be constructed as the product of a sampling sequence $s(t)$ (consisting of impulses at the particle-arrival times), and $v(t)$, the actual velocity signal as shown in Figure 8-36. For $v(t)$ and $s(t)$ statistically independent:

$$Y(t) = S(t)\, v(t) \tag{149}$$

and:

$$R_{yy}(\tau) = R_{ss}(\tau)\, R_{vv}(\tau) \tag{150}$$

where $R(\tau)$'s are the appropriate autocorrelation functions.

Then, if $R_{ss}(\tau) \neq 0$

$$R_{vv}(\tau) = R_{yy}(\tau)/R_{ss}(\tau) \tag{151}$$

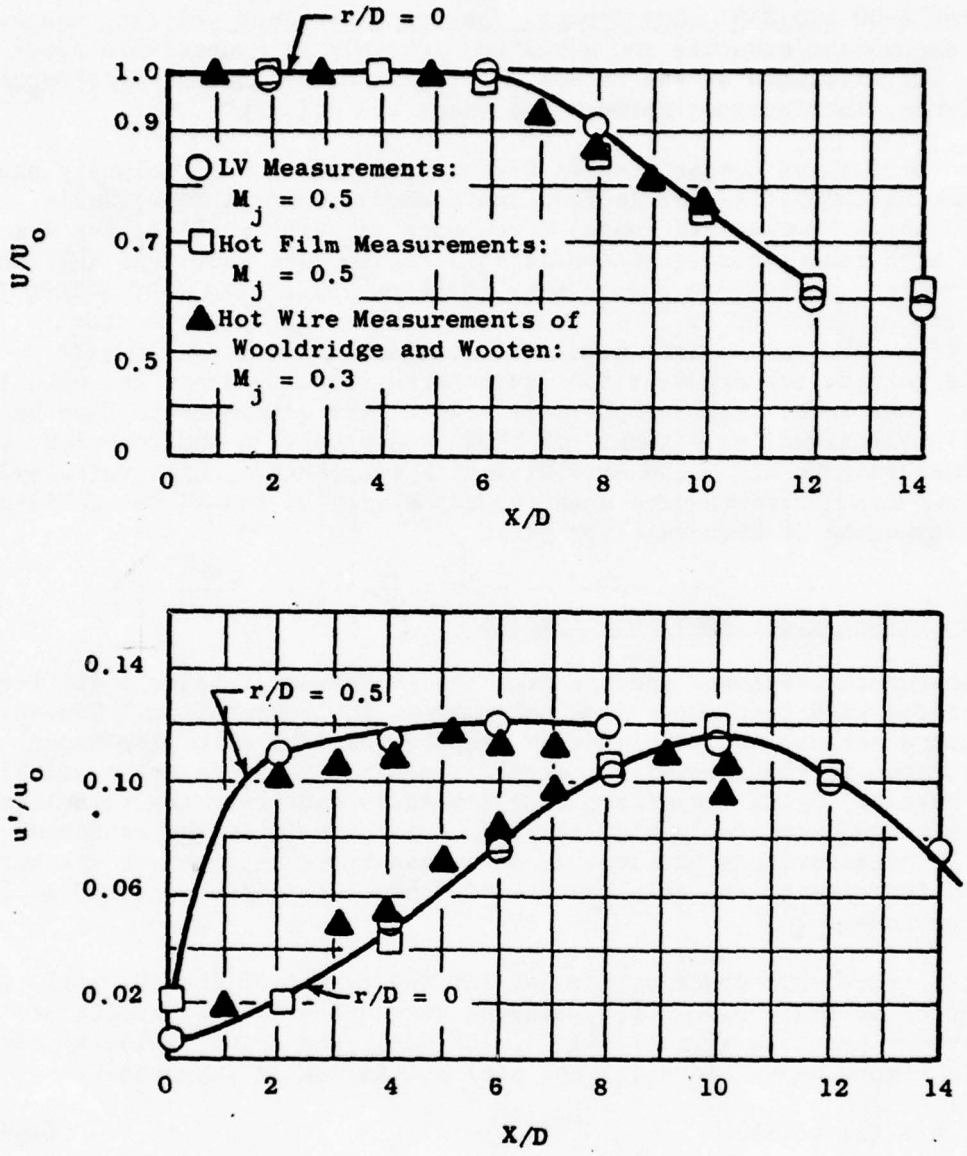


Figure 8-30. Comparisons of LV Measurements with Hot Film/ Hot Wire Measurements for an Ambient Subsonic Jet.

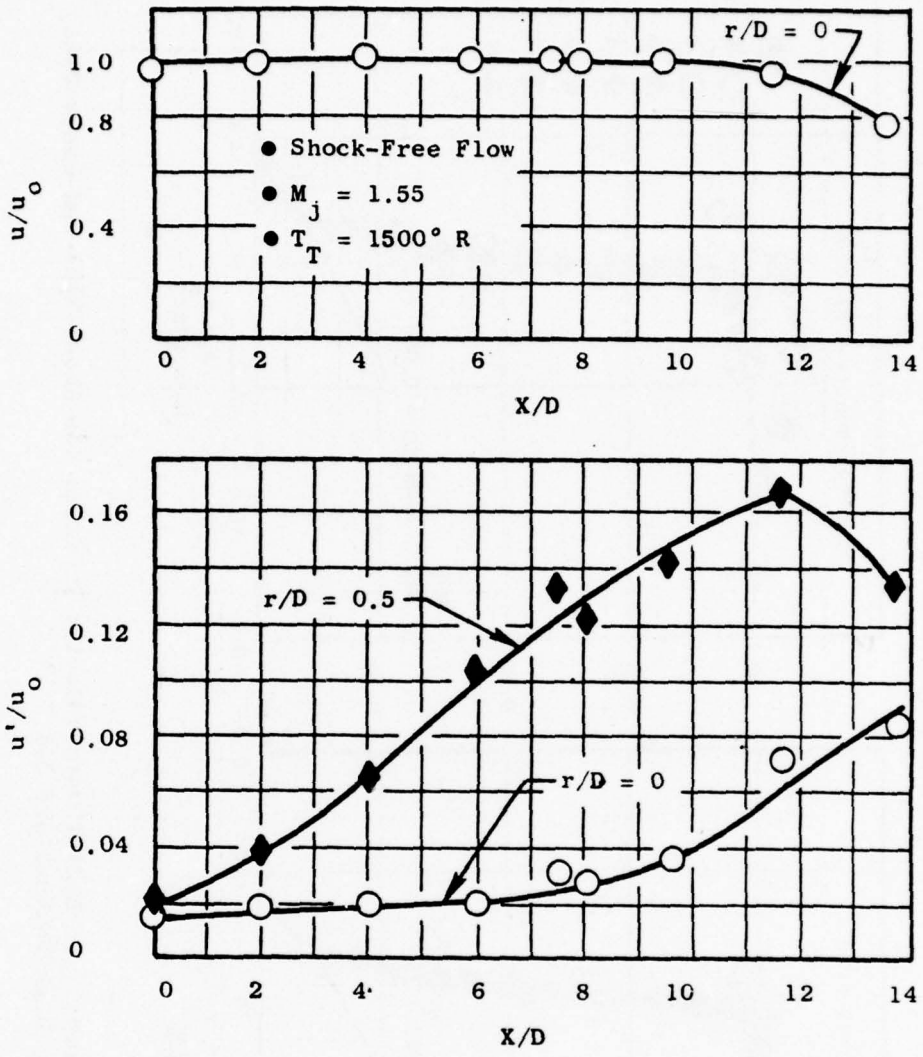


Figure 8-31. LV Measurements of Mean Velocity and Turbulent Velocity Decay for a Shock-Free, High-Velocity, High-Temperature Jet.

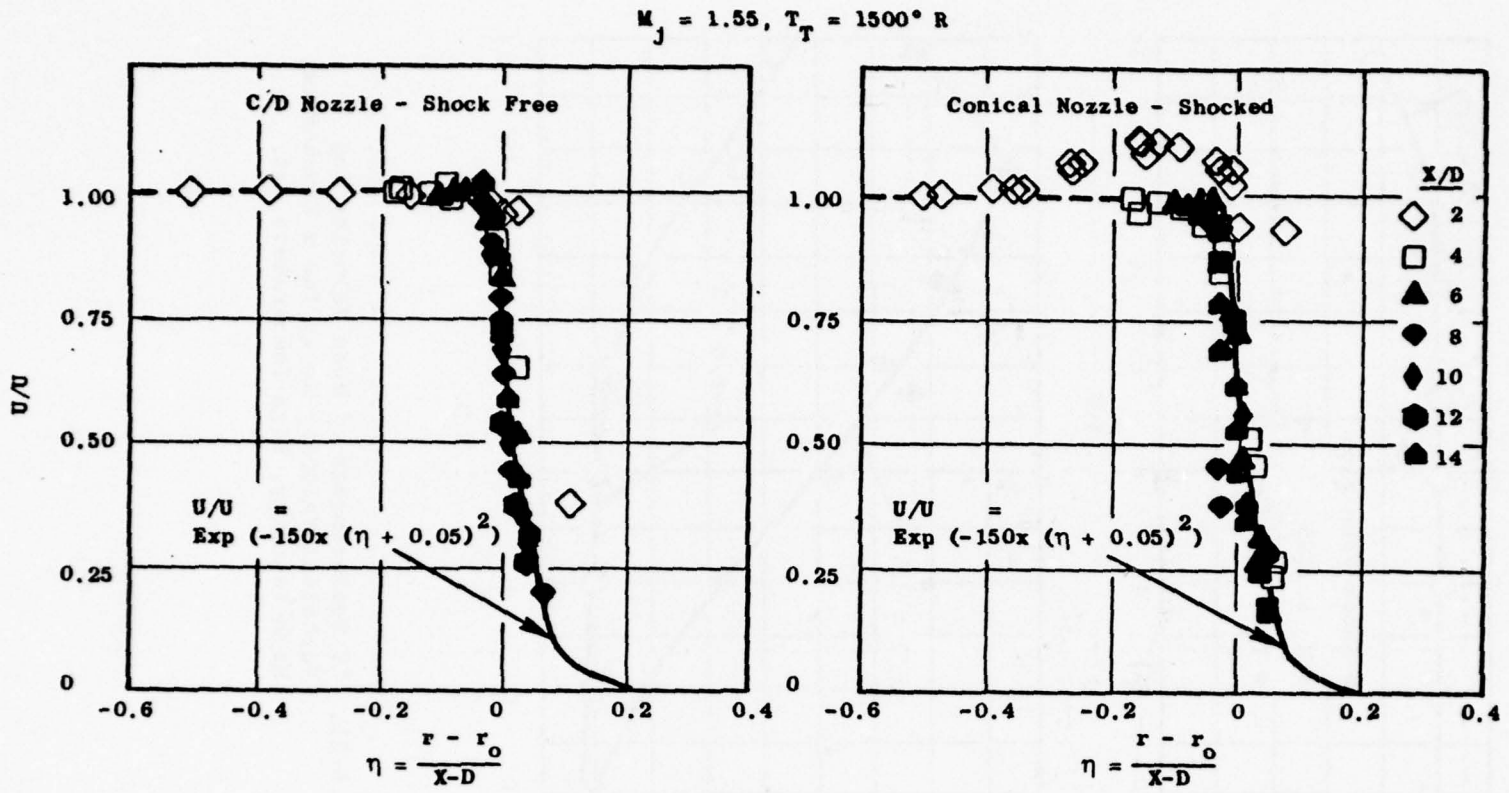


Figure 8-32. LV-Measured Normalized Radial Mean Velocity Profiles for Shock-Free and Shock-Flow, High Velocity, High Temperature Jet.

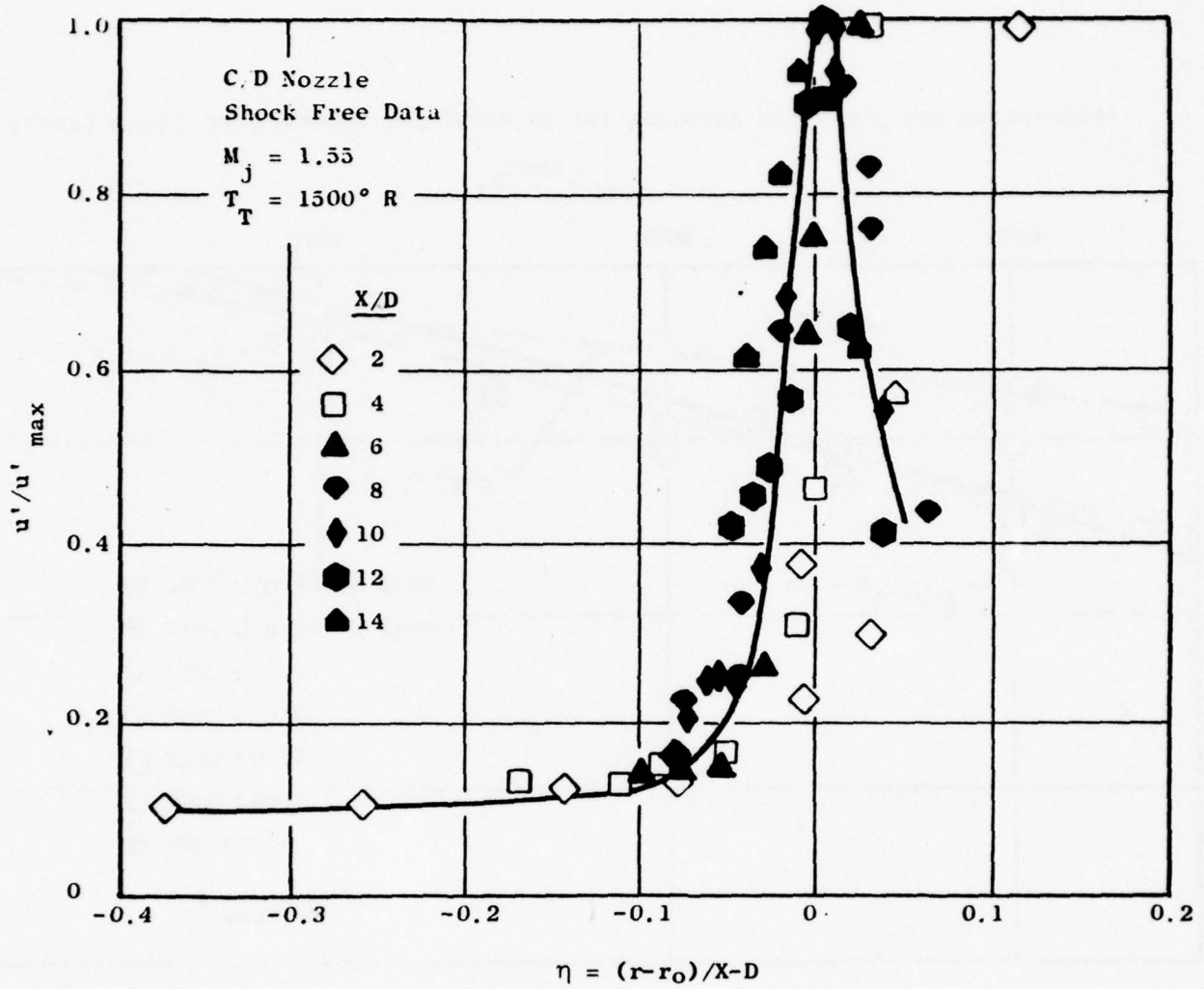


Figure 8-33. LV-Measured Normalized Radial Turbulence Velocity Profiles.

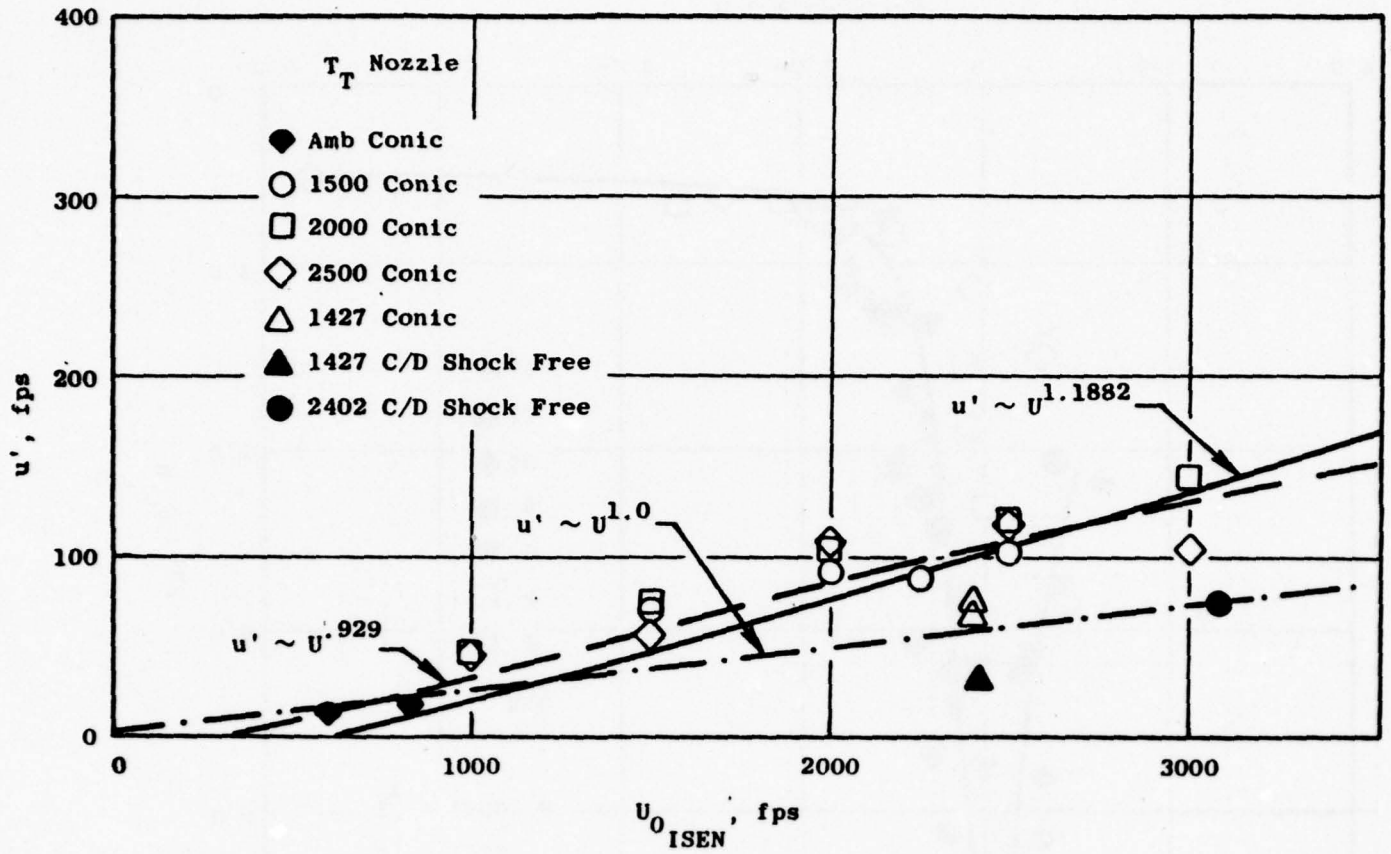


Figure 8-34. LV-Measured Influence of Jet Velocity on Exit Plane Turbulence.

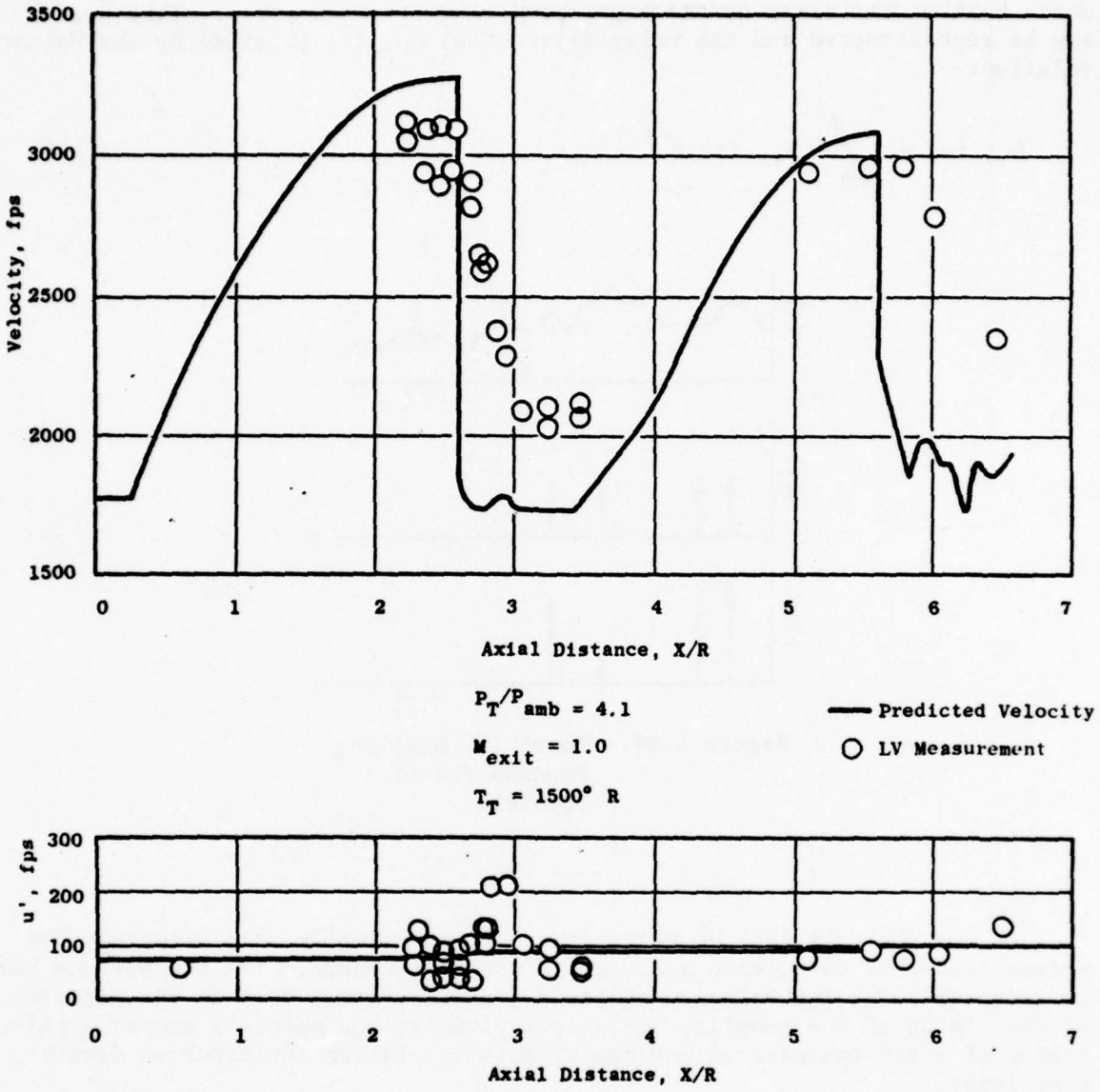


Figure 8-35. LV-Measured Mean Velocity and Turbulence Intensity on Center-Line for a High Velocity, High Temperature Jet.

where both of the terms on the right-hand side are measurable. Thus $R_{VV}(\tau)$ may be reconstructed and the velocity spectrum $S_{VV}(\omega)$ obtained by the Weiner relation:

$$S_{VV}(\omega) = \int_{-\infty}^{\infty} R_{VV}(\tau)\, e^{-i\omega\tau}\, d\tau \qquad (152)$$

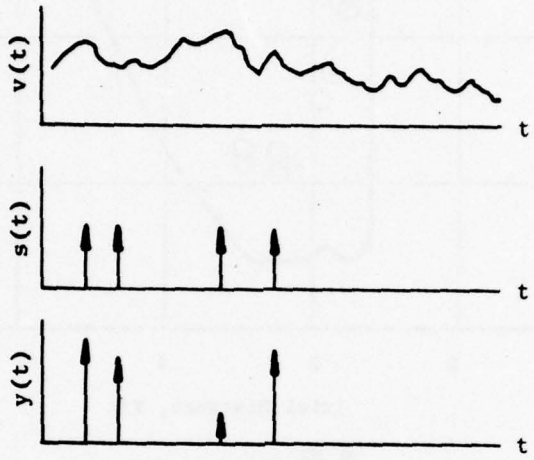
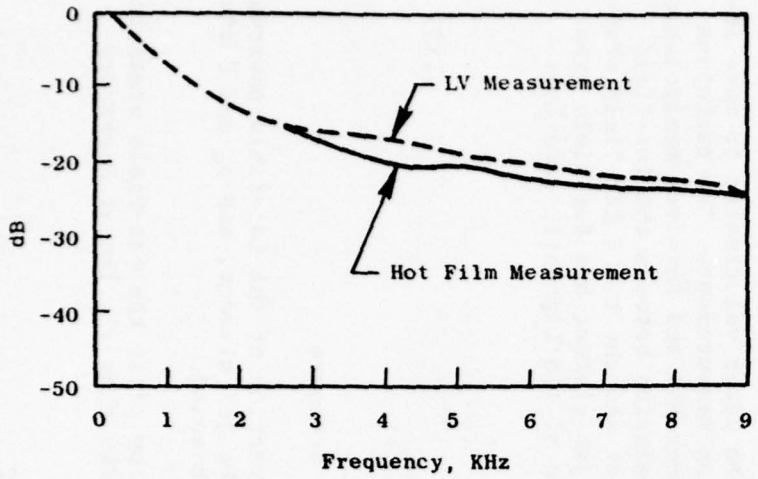


Figure 8-36. Model for Sampling Process for LV Spectra.

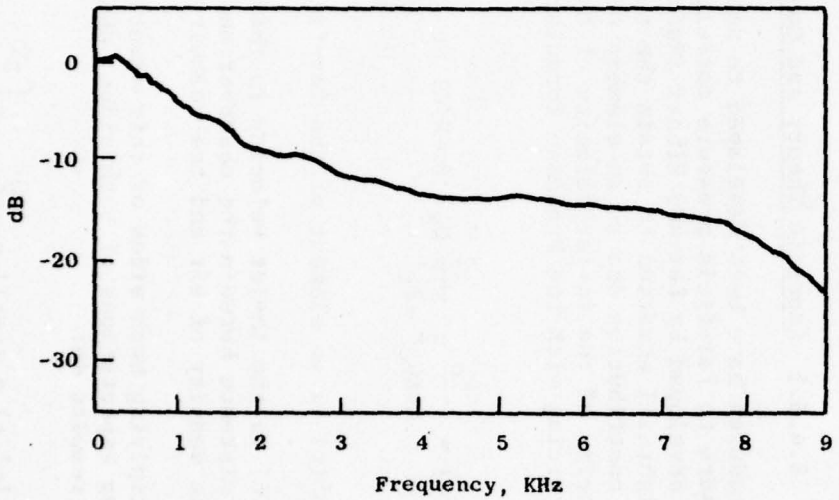
As was the case for the measurement of rms velocity, the principle for estimating an LV turbulence spectrum is straightforward. The success one has in reconstructing the velocity spectrum depends a great deal on the accuracy of the timing of the sampling and output signals, and upon the proper application of error analyses of estimating autocorrelation functions on finite time grids.

Figure 8-37 shows measurements of the axial component of turbulent velocity spectra for an ambient subsonic jet, as well as a sonic heated jet. The reconstruction of these spectra were indeed quite encouraging. Although a great deal of success was obtained from these demonstration spectral experiments, one limiting item which hampered further measurements was the lack of computer speed and LV data rate. In these experiments, the PDP-8 Digital Equipment Corporation mini computer system was used. Performing the necessary arithmetic in a reasonable amount of time with this system was not practical. Any future work in this area should include the use of a much faster system. For future GE work, a PDP 1145 has been selected.



Comparison of Laser Velocimeter and Hot Film Turbulence Spectra

$M_j = 0.5$, $X/D = 6$, $r/r_0 = 1$



Measured Laser Velocimeter Turbulent Spectrum For A Hot Sonic Jet

$M_j = 1.0$, $T_8 = 1500°$ R, $X/D = 10$, $r/r_0 = 0$

Figure 8-37. LV-Measured Axial Turbulent Velocity Spectra for Ambient and Heated Jets.

8.4.3 In-Jet Far-Field Cross-Correlation Measurements

In-jet jet noise source location has been of interest for a number of years. Particular emphasis has been placed on this area due to the Government's and industries' revived interest in developing understanding and technology associated with noise source definition and reduction for high and low velocity exhaust jets. In addition to many theoretical considerations (such as selection of the proper noise source terms), the selection of the proper instrumentation to perform such measurements is of importance if the developed techniques are to be used in more than the most ideal laboratory conditions.

Discussed below is the General Electric study which was aimed at demonstrating the feasibility of the technology for utilizing the laser velocimeter for noise source correlation. The study indicates the additional analytical complications necessary when treating a signal of discrete character as opposed to continuous-type signals. The results show that the laser velocimeter can indeed be used for such measurements, but it must be pointed out that success is highly dependent on the type of signal processor used.

8.4.3.1 Acoustic Theory and General Approach

Procedures have been developed to use the laser velocimeter to make in-jet pressure to far-field pressure correlation measurements. The technique used was developed by Lee and Ribner (Reference 69) and involves manipulation of the Lighthill equation to obtain the correlation between the far-field pressure contribution due to an element of jet and the total far-field pressure in terms of the in-jet velocity of the jet element and far-field pressure. Starting with the Proudman formulation of the Lighthill equation:

$$dp'(t) = \frac{\rho_o}{4\pi X C_o^2} \frac{\partial^2}{\partial t^2} U_x^2 \, (t-X/C) \, dv \qquad (153)$$

where, $dp'(t)$ is an element of the far-field pressure

U_x (t) is the in-jet velocity in the direction of the far-field observer, x is the distance between the observer and the jet element, and ρ_o and C are the static density of air and the velocity of sound.

Multiplying both sides of this equation by $p(t)$, the far-field pressure, and taking expectations of both sides; assuming that all linear operators commute, results in:

$$d\,E\,[p'(t)\;p\;(t+\tau)] = \frac{\rho_o}{4\pi X C^2} E\left[\frac{\partial^2}{\partial t^2} U_x^2 \, (t-X/C)\; p\;(t+\tau)\right] dv \qquad (154)$$

By the linear operation theorem of probability (Reference 88), one can commute the derivative and expectation operators to obtain:

$$d\,E\,[p'(t)\;p\;(t+\tau)] = \frac{\rho_o}{4\pi XC^2}\;\frac{\partial^2}{\partial_\tau{}^2}\;E\left[U_x{}^2\;(t-X/C)\;p\;(t+\tau)\right]\;dv \qquad (155)$$

Finally, if all processes are stationary and ergodic, one may replace the ensemble averages with time averages, so that:

$$\overline{dp'p}(\tau) = -\frac{\rho_o}{4\pi XC^2}\frac{\partial^2}{\partial_\tau{}^2}\;\overline{U_x{}^2 p}\;(\tau+X/C)\;dv \qquad (156)$$

In other words, the contribution to the far-field pressure autocorrelation function from an element of jet volume is proportional to the second derivative with respect to lag of the cross correlation between the in-jet velocity squared and the far-field pressure evaluation at the retarded time, x/c.

In the General Electric experiments, an attempt was made to determine the quantity of the LHS of Equation (156) by computing the quantity of the RHS. Because the laser velocimeter (LV) is to be used to measure the in-jet velocity, a special cross-correlation estimator is developed to cope with the random arrival of velocity information at the LV output. The required computations are realized on a PDP 11/45 mini-computer, which also controls the taking of the data and the intersample timing.

The sections that follow deal with a theoretical development of the random sample correlation estimator and an explanation of the sampling scheme used. The method selected for estimating the second derivative in Equation (156) is discussed together with the special window function developed to reduce the variance of the statistic. Results of a simulation performed to test the computer programs and demonstrate the convergence of the estimator are given. The last section describes the demonstration experiments.

8.4.3.2 The Random Sample Correlation Estimator

Because the operation of the LV is based on the random arrival of particles at the probe volume, velocity information is available only as point estimates at random times. Thus, a special estimator is required to construct the cross correlation between the square of the LV output and the far-field microphone data. The approach used is based on interpreting "expectation" as a discrete time average, as may be done for stationary, ergodic processes. The random arrival of an LV point can be used to trigger the sampling of an equispaced far-field pressure record, square the velocity

value, and form the product with the points in the microphone data record. This gives us one ensemble of lag values. Successive ensembles are then averaged to obtain the required amount of statistic stability. Thus, the equation for the cross-correlation estimator is:

$$\widehat{\overline{U_x^2 p(nT)}} = \frac{1}{N} \sum_{i=1}^{N} U_x^2 (t_i)\ p\ (t_i + nT) \tag{157}$$

where the t_i are n random times at which velocity samples are available at the LV output. If the retarded time, X/C, is longer than the retarded time minus the largest lag value of interest, the arrival of a velocity sample may be used to trigger the pressure record sampling. This is illustrated in Figure 8-38. It is easy to show that $\widehat{U_x^2 p(nT)}$ is in an unbiased estimate of $\widehat{E[U_x^2 p(nT)]}$, since it results in:

$$\begin{aligned} E\left[\widehat{U_x^2 p(nt)}\right] &= \frac{1}{N} \sum_{i=1}^{N} E\left[U_x^2 (t_i)\ p\ (t_i + nT)\right] \\ &= E\left[U_x^2 p\ (nT)\right] \end{aligned} \tag{158}$$

The variance of the estimator may be determined assuming U_x^2, and p(t) are jointly normal random variables and E[p(t)]=o. This gives:

$$VAR\left[\widehat{U_x^2 p(nT)}\right] = \frac{\sigma^2_{U_x^2}\ \sigma^2_p}{N}\left[1 + \rho^2\ U_x^2 p(nT)\right] \tag{159}$$

where:

$$\sigma^2_{U_x^2} = VAR\ (U_x^2)$$

$$\sigma_{p2} = VAR\ (p^2)$$

and, $\rho U_x^2 p$ is the correlation coefficient as a function of lag value between U_x^2 and p.

Thus, the variance of the estimator is finite and the estimate converges to the true value as $1/\sqrt{N}$. If we assume the N is large enough to invoke the Central Limit Theorem, one may write a confidence statement for $\overline{U_x^2}\ p(nt)$ as:

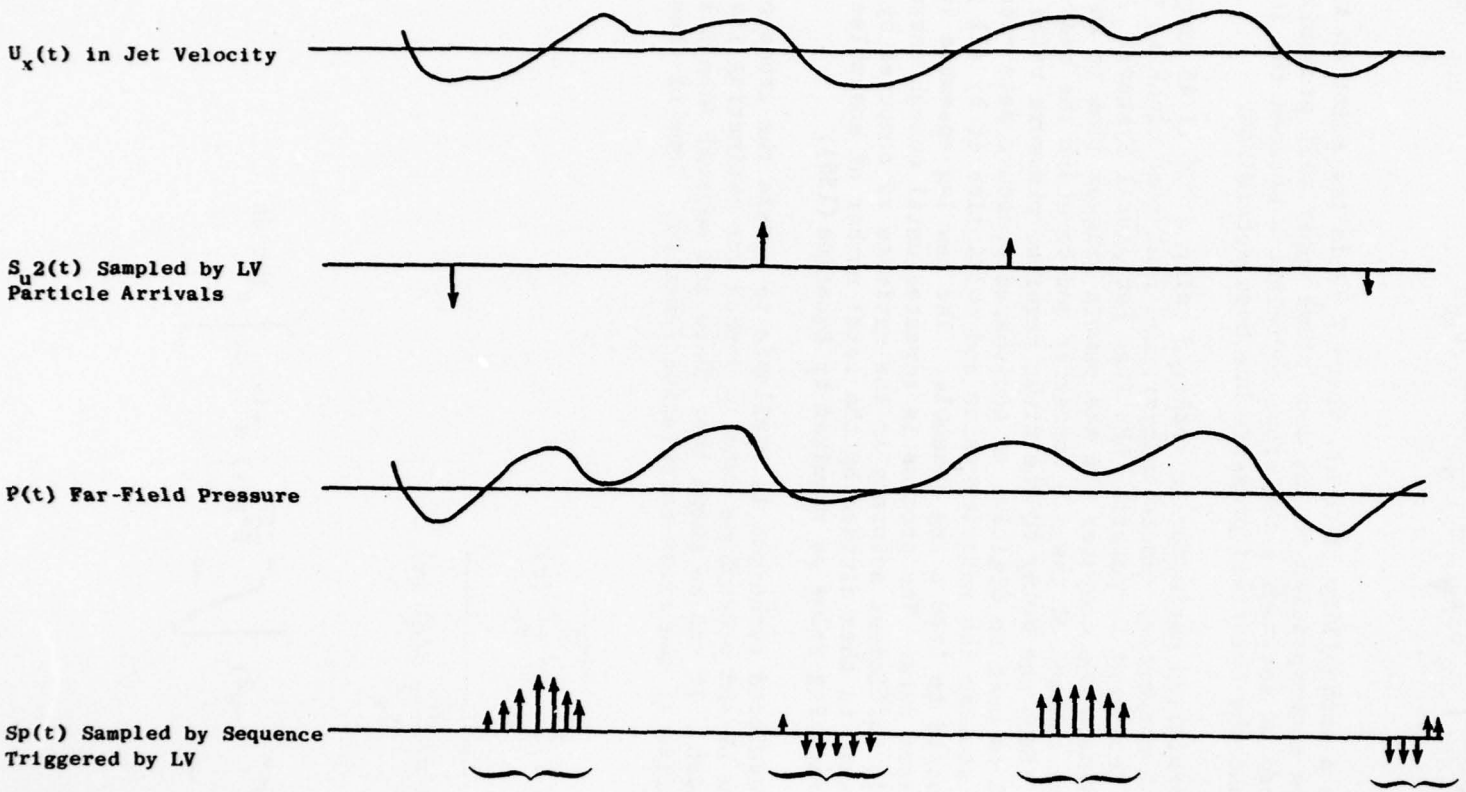


Figure 8-38. Schematic of Sampling Scheme.

$$\left| \widehat{\overline{U_x^2 p(nt)}} - U_x^2 p(nt) \right| \leq Z_{\alpha/z} \sqrt{\frac{1 - \rho(nt)_{U_x^2 p}}{N}} \sigma_{U_x^2} \sigma_p \qquad (160)$$

which is true with a probability of $(1-\alpha)$, where $Z_{\alpha}/2$ is the point on the unit normal distribution corresponding to the cumulative upper tail probability of $\alpha/2$. Thus, a method of estimating the cross correlation between the in-jet velocity squared and the far-field pressure has been determined.

The cross-correlation estimator is realized using a PDP 11/45 computer equipped with an AD converter, remote trigger, and real time clock in the form of a Digital Equipment Corporation LPS (Lap Peripheral System). Arrival of an LV output signals the computer via the remote trigger line to read the LV output using one channel of the A/D converter and to start the real-time clock. The clock times the delay to the first required pressure value and a second A/D channel is used to digitize an equispaced pressure data record. The computer then squares the velocity value and multiplies it by all points in the pressure record to form a lag ensemble. The new lag ensemble is then added to the previous data. The process is repeated until enough ensembles are added to obtain sufficient accuracy in the estimate as computed by Equation (160). The result is then divided by the total number of ensembles added to obtain the average lag value as required by Equation (158).

Now that a developed technique is available to obtain the cross-correlation function from LV and microphone data, a method for estimating its second derivative is needed. It can be shown that there are several identities for the second derivative of the cross-correlation function. Some of these are:

$$\frac{\partial^2}{\partial_\tau{}^2} \overline{U^2 p}(\tau) = - \frac{\partial}{\partial_\tau} \overline{U^2 \frac{\partial_p}{\partial_t}} (\tau) \qquad (161)$$

$$= \overline{U^2 \frac{\partial^2}{\partial_\tau{}^2} p(t)} (\tau) \qquad (162)$$

$$= - \frac{1}{2\pi} \int_{-\infty}^{\infty} (-\omega^2) \left[\int_{-\infty}^{\infty} \overline{U^2 p}(\tau) \, e^{-i\omega\tau} d\tau \right] e^{i\omega\tau} \, dw \qquad (163)$$

Equations 161 and 162 suggest we may take one or two derivatives of the pressure, before it is sampled, if one is sure these quantitites are sufficiently band-limited for our analysis. Equation 163 suggests that the differentiation may be performed in the frequency domain by multiplying the associated cross spectrum by ω^2. A modification of this approach is to operate on the sampled version of the cross correlation with a set of weights which can be derived using Shannon's sampling theorem (Reference 89). Under the assumption that the cross spectra satisfies

$$S_{U_x^2 p}(\omega) = 0 \text{ for } |\omega| > \frac{\pi}{T} \tag{164}$$

where T is the spacing of the cross-correlation samples, $U_x^2 p(\tau)$ is related to its sampled version by:

$$U_x^2 p(\tau) = \sum_{n=-\infty}^{\infty} U_x^2 p(nT) \frac{\text{Sin}\left(\frac{\pi\tau}{T} - n\pi\right)}{\left(\frac{\pi\tau}{T} - n\pi\right)} \tag{165}$$

Directly differentiating both sides, results in:

$$\left.\frac{\partial^2 \overline{U_x^2 p(\tau)}}{\partial \tau^2}\right|_{\tau=kT} = -\frac{\pi^2}{3T^2} \overline{U^2 p(kT)} + \sum_{\substack{n=-\infty \\ n\neq k}}^{\infty} -\frac{(-1)^n}{T^2 n^2} 2 \overline{U^2 p\,[(k-n)T]} \tag{166}$$

This is an unbiased estimate of the second derivative under the band-limited assumption. It also gives a smaller error, when $S_{U_x^2 p}(\omega)$ is not exactly band-limited, than other derivative estimates based on weights. Take, for example, the "standard" three-point estimate of the second derivative:

$$\frac{\partial^2}{\partial \tau^2} \overline{U_x^2 p(nT)} = \frac{1}{T^2}\left\{U_x^2 p\left[(n-1)\,T - 2\,\overline{U_x^2 p(nT)} + U_x^2 p\,(n+1)T\right]\right\} \tag{167}$$

Figure 8-39 shows the comparison between the "Shannon theorem" estimate: and the "three-point" estimate of the second derivative of the cross-correlation function whose cross spectrum is also shown. From Figure 8-40, two things are observed. First, the Shannon estimate has an associated bias error about half of the three-point estimate. Second, for the bias error to be reduced to 10%, $T = \pi/\omega_c$ must be about 30 times the three dB point of the cross

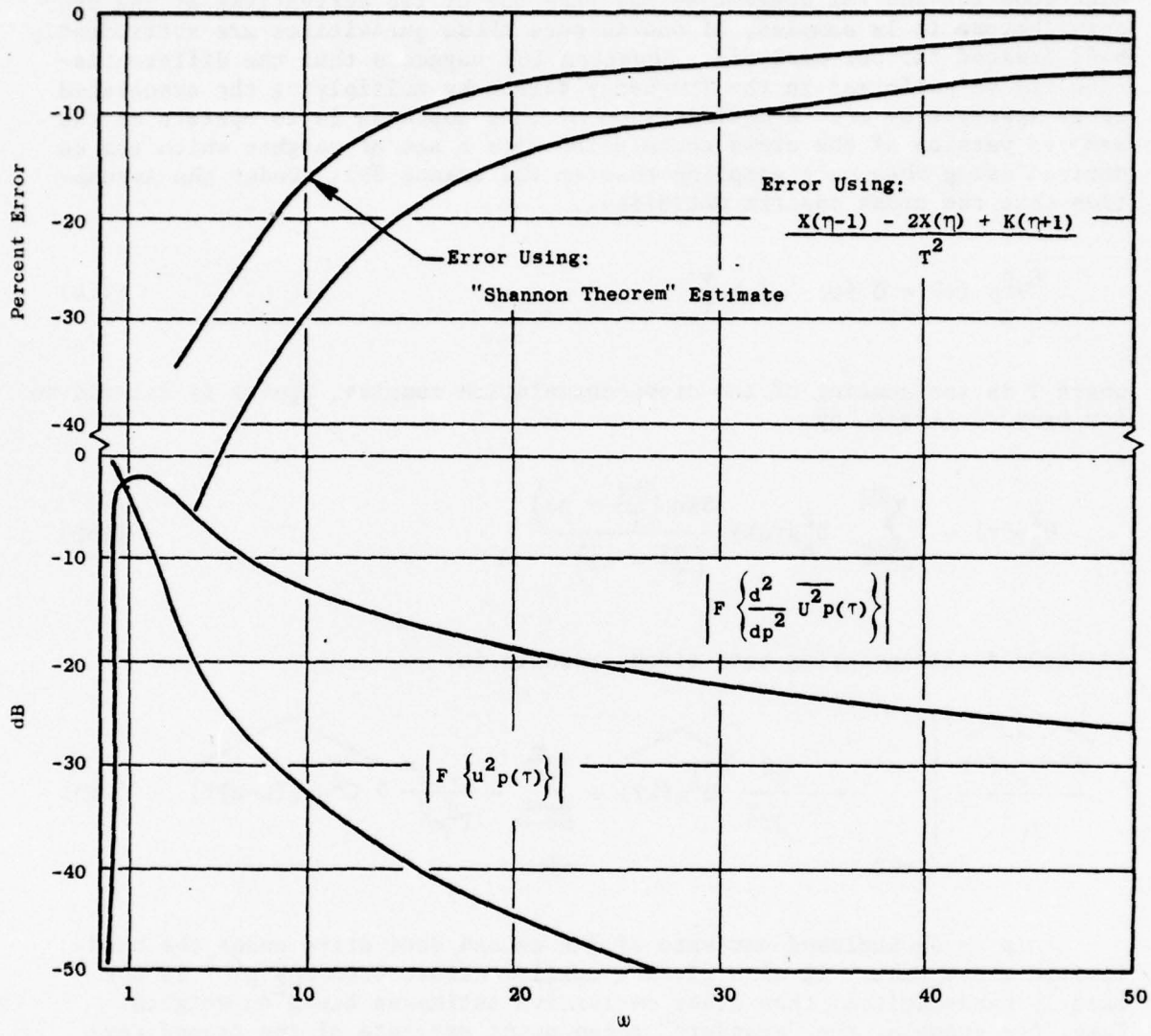


Figure 8-39. Bias Error in Derivative Estimate as a Function of Cutoff Frequency.

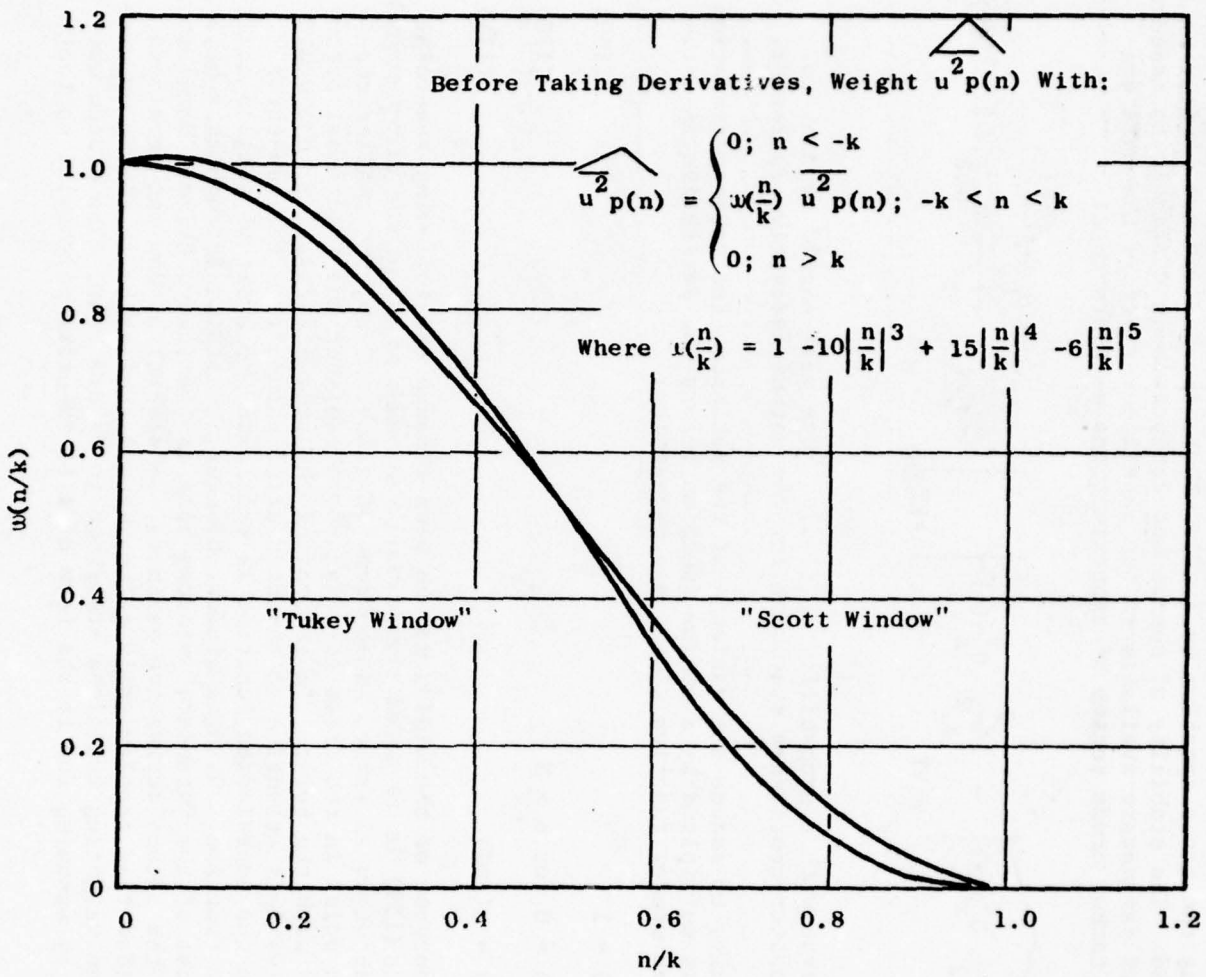


Figure 8-40. Influence of Window Function to Improve Stability of Second Derivative.

spectrum. This is because taking the second derivative is equivalent to multiplying the cross spectrum by $(-\omega^2)$. Thus, the "tails" are greatly accentuated. The stability of the second derivative is difficult to measure in terms of parameters available to the experimenter before the data are taken. A rather crude series of approximations suggests that:

$$\left| \widehat{\frac{\partial^2}{\partial_\tau^2} U_x^2 p(\tau)} - \left. \frac{\partial^2}{\partial_\tau^2} U_x^2 p(\tau) \right|_{\tau=kT} \right|_{\tau=kT} \leq \sqrt{\frac{40}{N}} \frac{\sigma_{U_x}^{2\sigma p}}{T^2} Z_{\alpha/2} \qquad (168)$$

might be true with a probability of $(1-\alpha)$. More work should be done to obtain a better confidence statement for the second derivative estimator.

Finally, to reduce the variance of the estimate, the cross-correlation function is multiplied by a window function before the derivative is estimated. The window function $\omega(nt)$, has properties:

$$\omega(OT) = 1 \qquad (169)$$

$$\omega(nT) = 0 \text{ for } n \geq N \qquad (170)$$

$$\text{and, } \omega(nT) = \omega(-nT) \qquad (171)$$

The purpose of the window may be seen through the following reasoning. By Equation (159) it is noted the variance of each point in the cross correlation has about equal error, independent of value. Thus, the smaller the value of a point in the cross correlation, the higher the fractional error associated with the point. In estimating the second derivative, one would like to give less attention to the high-error points than the low-error points, so the correlation function is multiplied by a set of weights called the window function. Using a window, however, generally introduces a bias error. Most of the "standard" windows such as the Tukey, Parzen, Hann, etc., will bias the second derivative estimate. A special window was developed which avoided this problem while maintaining a similarity to the Tukey window. These weighting functions are shown in Figure 8-40. The window was developed by assuming for it the form of a fifth-order polynomial so that:

$$\omega(n/k) = a_o + a_1 \left|\frac{n}{k}\right| + a_2 \left|\frac{n}{k}\right|^2 + a_3 \left|\frac{n}{k}\right|^3 + a_4 \left|\frac{n}{k}\right|^4 + a_5 \left|\frac{n}{k}\right|^5 \qquad (172)$$

where k is the adjustable window length. Six conditions were then established on the coefficients, so that the constants could be determined. These conditions were:

1. $a_o = 1$, window should preserve the amount of power in the signal.

2. $a_1 = 0a$; $a_2 = 0$; the window shouldn't bias the estimate of the second derivative.

3. $\omega(n/k)\big|_{n=k} = 0$: $\partial/\partial n\ (n/k)\big|_{n=k} = 0$; and $\omega(n/k)\big|n = k/2 = 0.5$

which preserve some of the properties of the Tukey window.

The coefficients are determined to give

$$\omega(n/k) = 1 - 10\left|\frac{n}{k}\right|^3 + 15\left|\frac{n}{k}\right|^4 - 6\left|\frac{n}{k}\right|^5 \qquad (173)$$

8.4.3.3 Simulation Experiments

To establish confidence in the computer programs and procedures developed for in-jet to far-field cross correlation, a simulation device was built to provide signals representing LV and microphone outputs. A block diagram of the simulation hardware is shown in Figure 8-41. Two white noise generators were used to supply uncorrelated Gaussian noise sources. These sources were then filtered to give them spectra like those expected in the actual experiment to be conducted. These are shown in Figure 8-42. A constant value was added to the velocity channel to represent the mean velocity and this signal was then sent through an analog squaring circuit and added to the pressure channel. The pressure signal thus was correlated to the velocity squared. The simulator was used to obtain estimates of

$$\overline{U_x^2 p(\tau)} \text{ and } \frac{\partial^2}{\partial \tau^2}\ U_x^2 p(\tau)$$

for cases where the correlation coefficient between U_x^2 and $p(t)$ was 0.1, 0.3, and 1. The number of data ensembles averaged in each case was 20,000, 100,000, and 500,000.

The 500,000 ensemble average represents a definite practical upper limit on data processed, since it represents about 4 hours of test data. The results show that for these conditions, it is easy to resolve when $\rho = 1$ and fairly easy when $\rho = 0.3$. However, when $\rho = 0.1$, difficulty was encountered

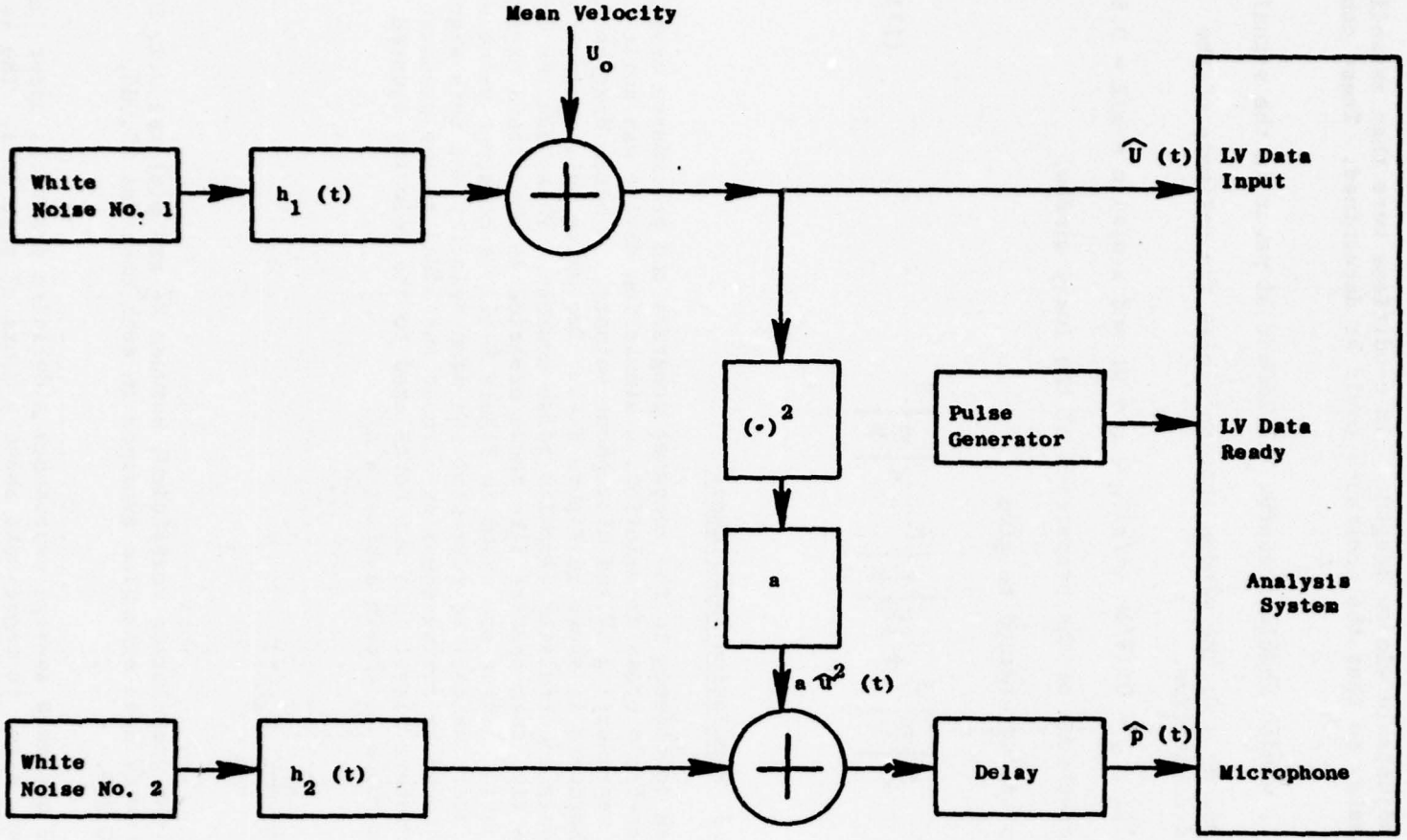


Figure 8-41. Schematic of System Used to Generate Simulated Data.

Expected Jet and Far Field Conditions: $u/U = 0.2$, $M_j = 0.8$, $X/D = 4$, $R/R = 1$

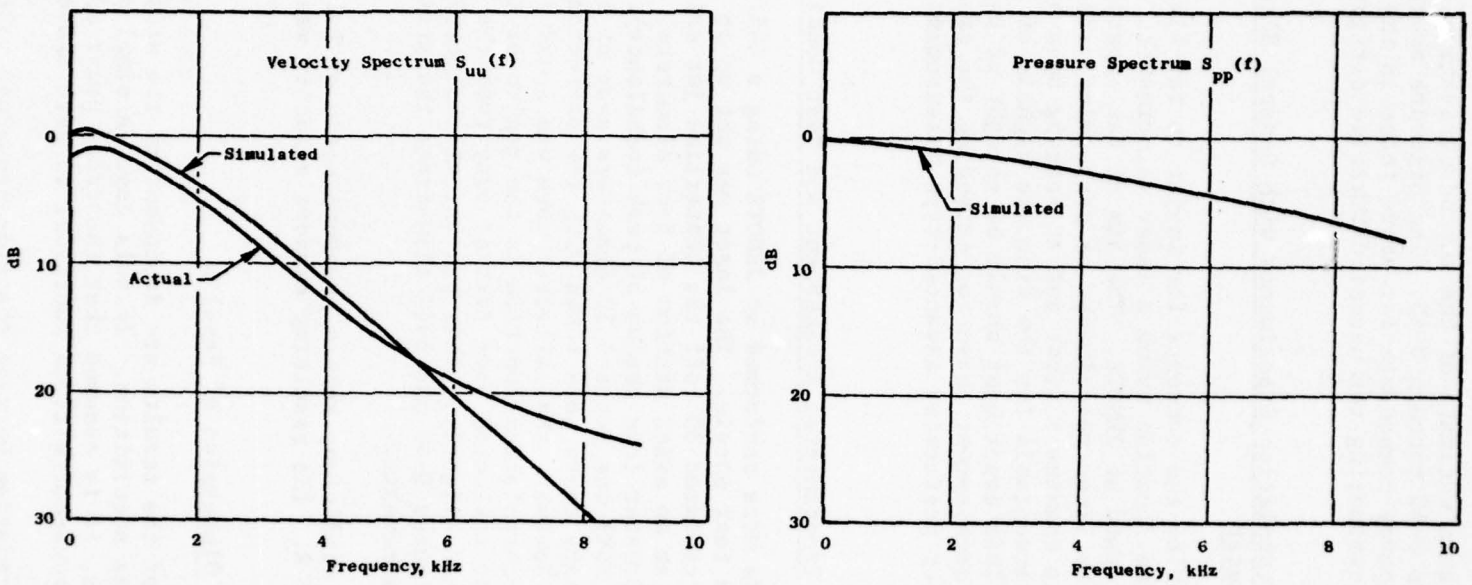


Figure 8-42. Simulation Specifications.

in obtaining a reliable estimate of the second derivative. This may be seen by examining Figures 8-43 through 8-45. The pressure spectrum in the simulation contained frequency components far above those in the velocity squared, and this fact made estimating the second derivative difficult.

8.4.4 Cross-Correlation Experiments with General Electric's Laser Velocimeter

In order to verify the concepts for in-jet to far-field cross correlation and noise source location using a laser velocimeter, a demonstration experiment was performed at JENOTS. The aim of the experiment was to assess the capability of the laser velocimeter on performing cross-correlation-type measurements, and to examine a first cut at setting up a proper random data and error analysis acceptable for the discrete signals of the laser velocimeter instrument. This experiment should be thought of as only a first try in the complicated development chain for extending the capability of the laser velocimeter for performing advanced-type measurements in realistic exhaust jets.

8.4.4.1 Experimental Arrangement and Test Conditions

The experiments were performed at JENOTS using a 4-5/8 inch-diameter conic nozzle as the test nozzle. The laser was set up so that the measuring control volume was centered 30° off the centerline jet axis. The measuring volume was located at an axial station of four diameters, and a radial location of one-half diameter (the region of peak turbulence). The far-field microphone (a 4136 B&K) was located 50 diameters away at the 30° jet angle position. Preliminary tests were taken with the microphone in the horizontal plane of the jet. However, the reflected wave was found to influence the shape of the cross-correlation function in the region of the retarded time. In order to move the reflected wave farther away from the retarded time, the microphone was raised slightly. This put the microphone 7° out of the plane of measurement. Figures 8-46 and 8-47 illustrate the arrangement used for performing the measurements.

The flow test conditions were a pressure ratio of 1.175 and a total temperature of 670° R. The resulting exhaust velocity was 600 fps.

8.4.4.2 Discussion of Results

The validity of the results are dependent on the sampling frequency used in the pressure data acquisition. In this case, a sampling interval of 40 μ sec was used. Thus, it is assumed that the cross power spectrum (Fourier transform of the cross-correlation function) is zero above 12.5 kHz.

The cross correlation between the time-dependent velocity and the far-field acoustic pressure signal was constructed from six records of 20,000 product pair ensembles which were considered suitable for processing (120,000

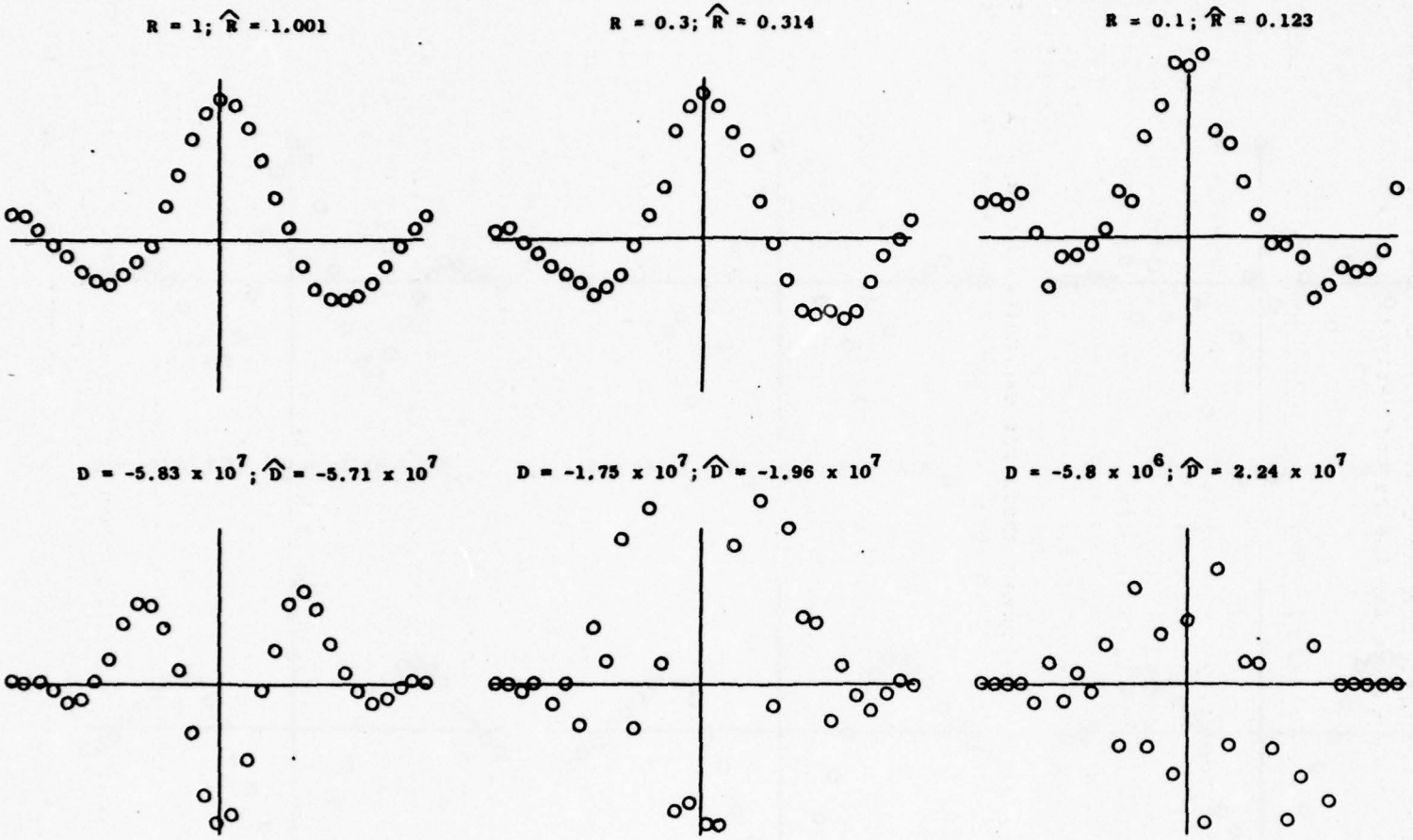


Figure 8-43. Analysis of Simulated Data, N = 20,000 Samples.

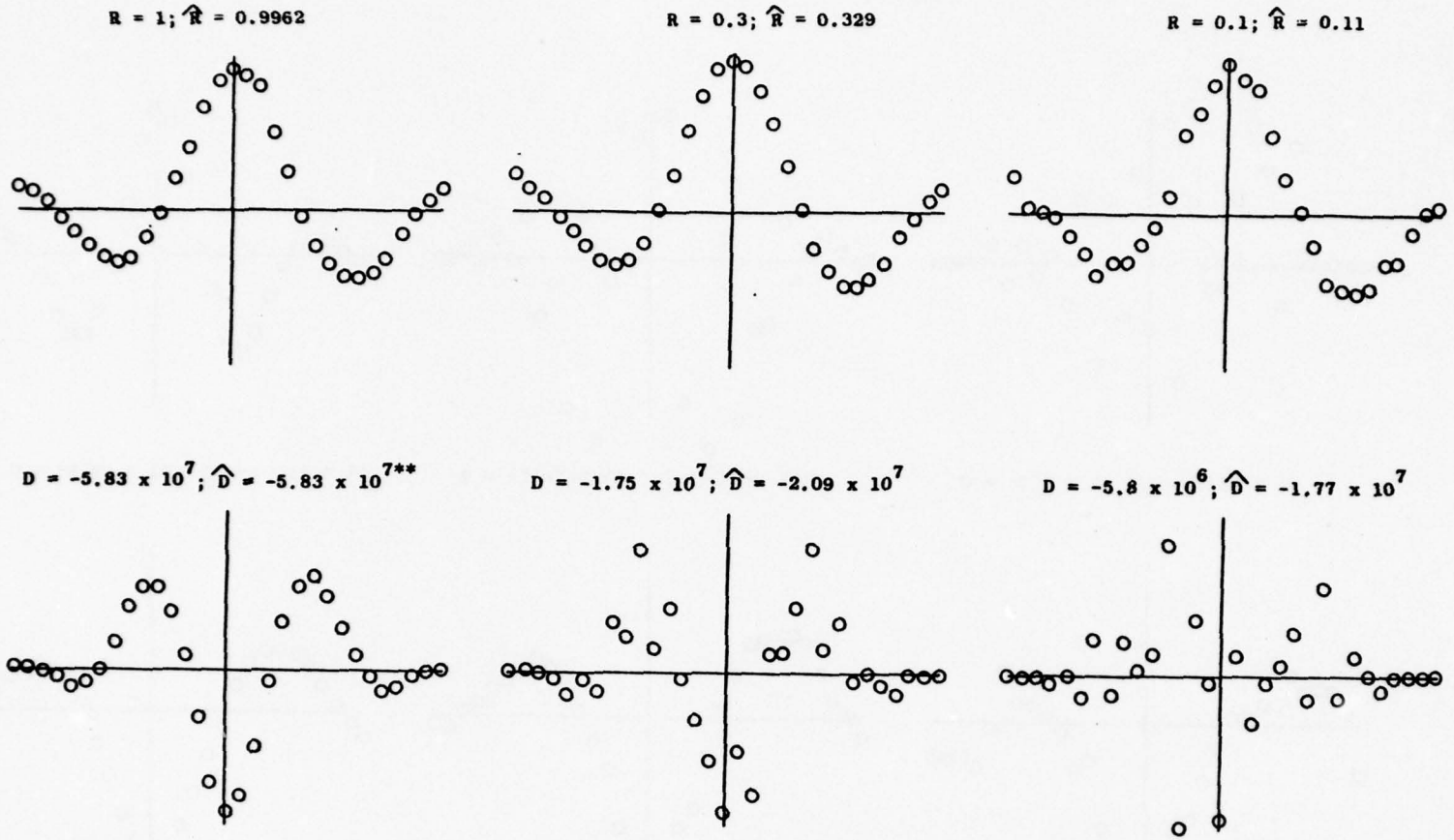


Figure 8-44. Analytis of Simulated Data, N = 100,000 Samples.

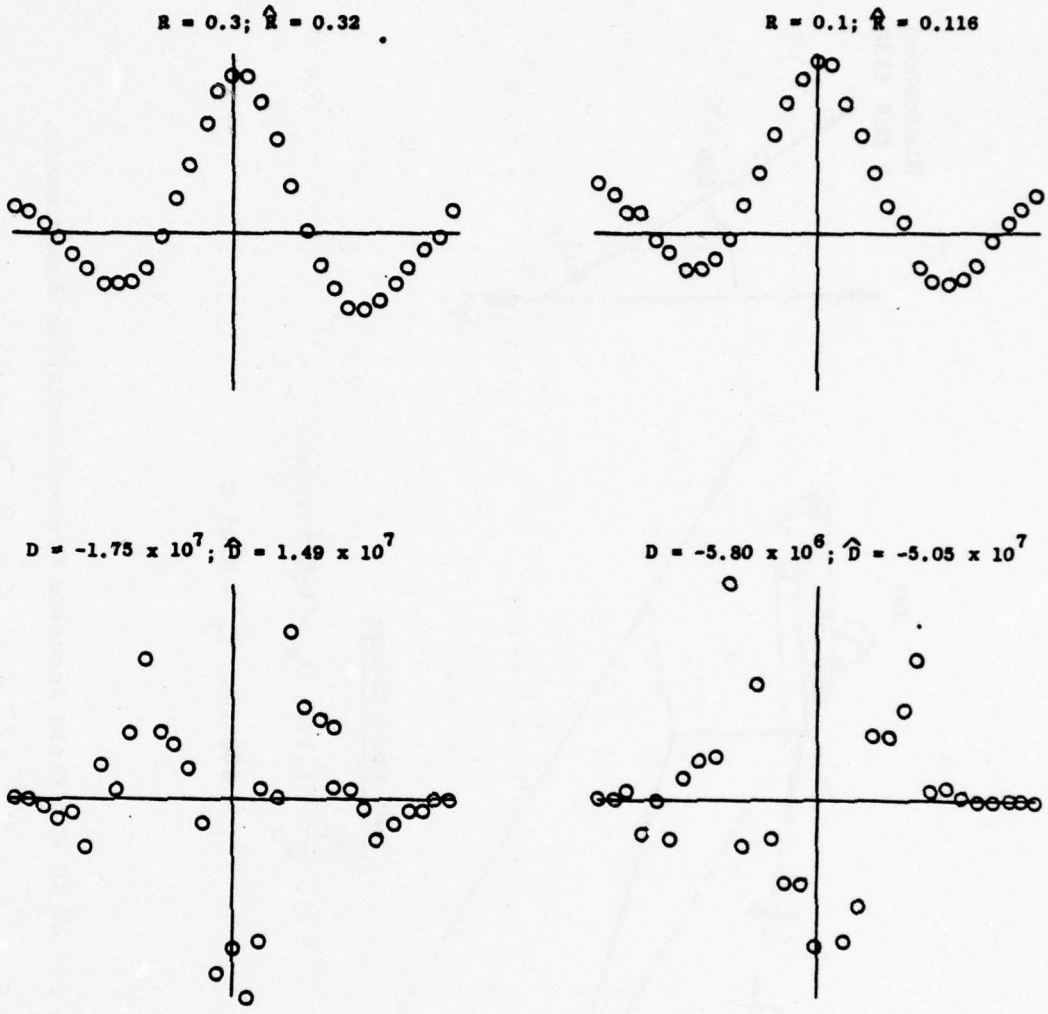
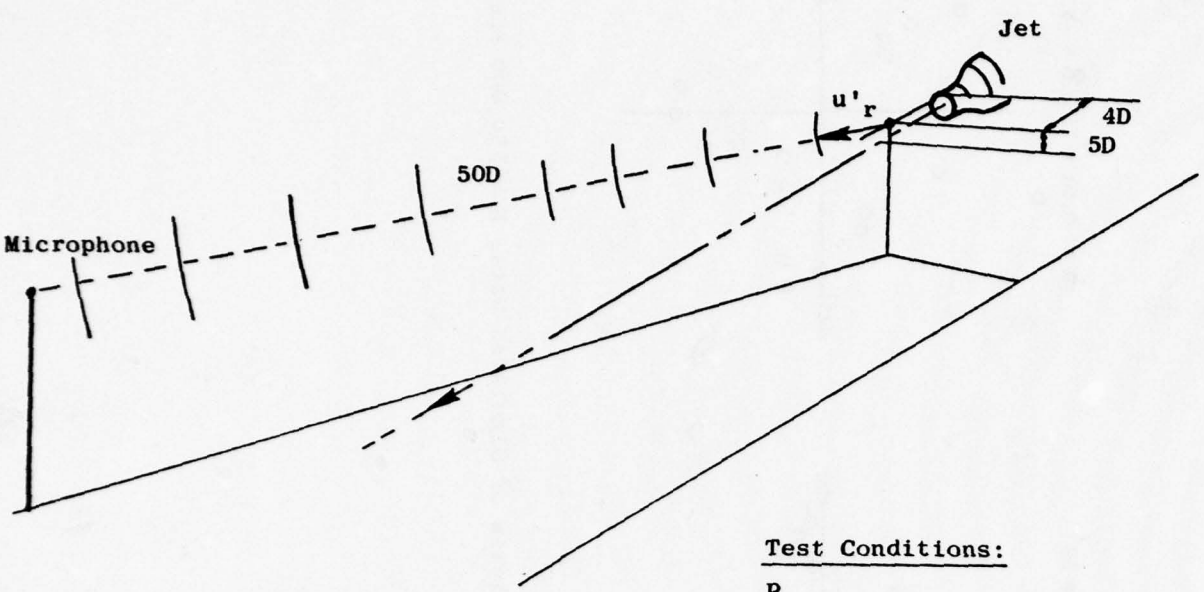
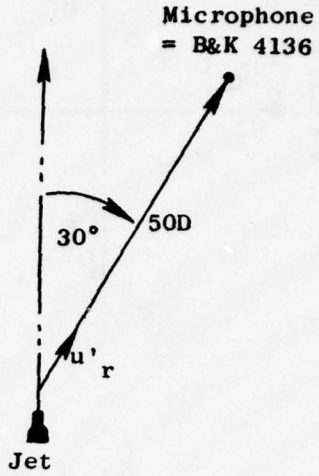


Figure 8-45. Analysis of Simulated Data, N = 500,000 Samples.





Test Conditions:

$\frac{P_T}{P_o} = 1.175$, $D_8 = 4\text{-}5/8$ inches

$V_j = 600$ fps, $T_T = 670°$ R

Figure 8-46. General Arrangement for LV to Far-Field Acoustic Cross-Correlation Experiments.

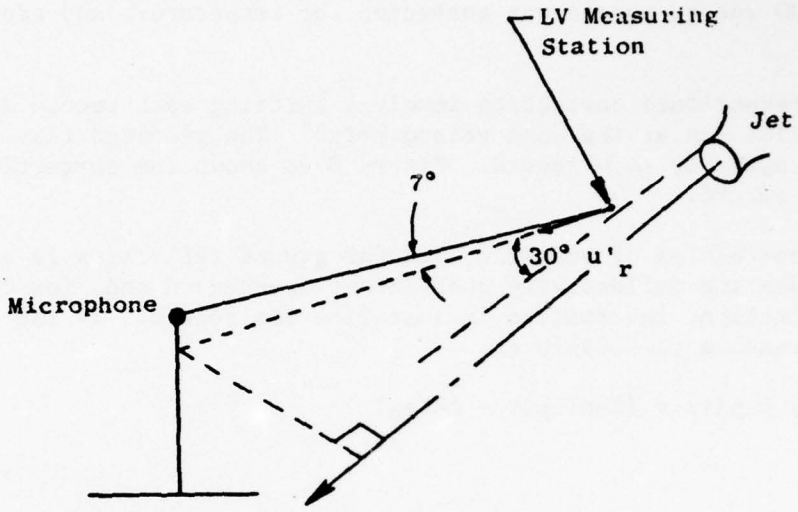


Figure 8-47. Test Arrangement Showing Microphone Slightly Out of Plane for LV Far-Field Acoustic Cross-Correlation Experiments.

average product pairs). Because the experiments were performed outdoors, there existed ambient temperature changes as well as ground reflections. Each 20,000 record sample was corrected for temperature and ground reflections.

The temperature correction involved shifting each record so that the retarded time was at the same record point. The retarded time was calculated from $\tau_r = a_o/R$ for each record. Figure 8-48 shows the correction applied to a typical record.

The correction of acoustic data for ground reflection is at best approximate because the reflectivity coefficient is unknown and, for the case of ideal reflection, information is lost from the record. If the ground reflection in pressure is modeled as:

$$p'(t) = p(t) + (1-\varepsilon)\, p(t - \Delta R/a_o) \tag{174}$$

where,

$p'(t)$ is the measured acoustic pressure

$p(t)$ is the actual acoustic pressure

ε is the absorption coefficient of the reflected surface

It is found that the result of cross correlating $p'(t)$ with $v^2(t)$, the in-jet velocity squared, is:

$$R_{v^2p'}(\tau) = R_{v^2p}(\tau) + (1-\varepsilon)\, R_{v^2p}(\tau-\Delta R/a_o) \tag{175}$$

It may be shown that, to recover $R_{v^2p}(\tau)$, one must provide the operation:

$$R_{v^2p}(\tau) = \sum_{k=0}^{\infty} (1-\varepsilon)^k\, R_{v^2p'}(\tau-\tau_o k) \tag{176}$$

From this it can be seen that the absorption coefficient also determines the effective number of values of $R_{v^2p'}(\tau)$ necessary for the reconstruction and that the uncertainty in $R_{v^2p}(\tau)$ will increase as $\varepsilon \to 0$. Thus the choice of ε depends on:

1. The level of uncertainty in the data
2. The length of $R_{v^2p'}(\tau)$ available
3. The actual value of ε.

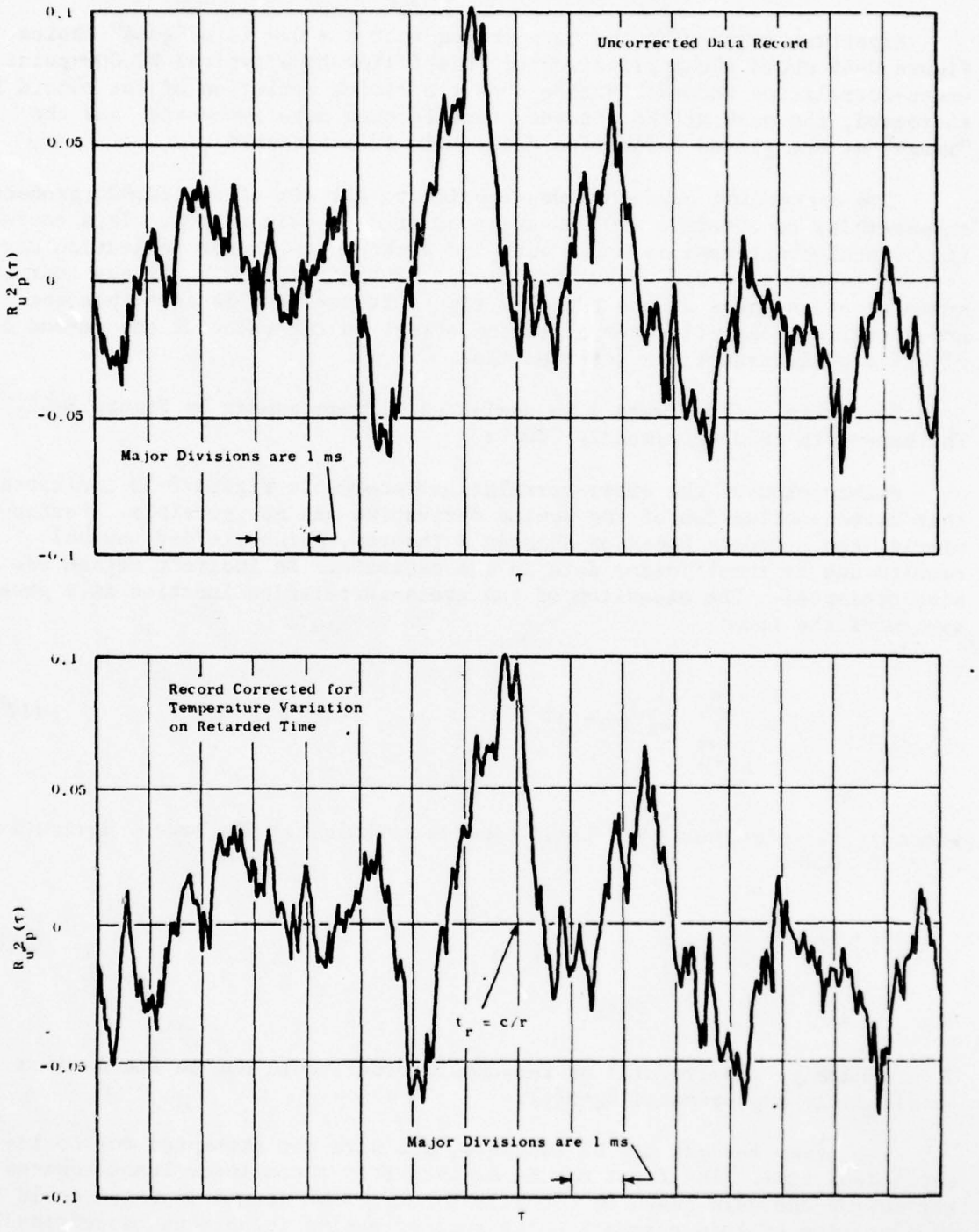


Figure 8-48. LV-Measured Normalized Cross Correlation of In-Jet Velocity to Far-Field Acoustic (180,000 Samples).

Experimentation with the data showed that $\epsilon = 0.4$ is a "good" choice. Figure 8-49 shows the application of this filter to a typical 20,000-point cross-correlation record. Notice that the random variation of the record is increased, the peak at the retarded time becomes more symmetric, and the "image" at the ground reflection delay time is suppressed.

The correction procedure was applied to all six of the 20,000 product subensembles to obtain a 120,000 averaged product pair record. This correlation function estimate is shown with and without the ground reflection correction in Figure 8-50. Note the removal of the image peak and the improved symmetry of the peak at the retarded time. It may also be seen that the ground reflections will have a serious effect on the value of the second derivative evaluated at the retarded time.

The cross spectra were also evaluated. These appear as Figure 8-51. The bandwidth is approximately 200 Hz.

Examination of the cross-correlation records in Figure 8-50 indicated that direct estimation of the second derivative was not possible. Particularly, the approach based on Shannon's Theorem, which yielded unusable results due to insufficient data in the estimate. An indirect method was also attempted. The expansion of the cross-correlation function in a power series of the form:

$$R_{v^2p}(\tau) \simeq \sum_{i=0}^{\infty} a_i (\tau-\tau_r)^i \tag{177}$$

where a_i is determined by a least squares technique. The second derivative at τ_r is then:

$$\left[\frac{\partial^2}{\partial \tau^2} R_{v^2p}(\tau)\right]_{\tau=\tau_r} = Z\, a_2 \tag{178}$$

Unfortunately, a polynomial of reasonable order could not be found which sufficiently approximated $R_v{}^2p(\tau)$.

Two other methods may be suitable, but were not attempted due to insufficient time. The first may be derived from a nonlinear least squares regression analysis based on acoustic theory. The second approach could be a modification of this approach using autoregressive techniques, specifically, a new technique called Linear Predictive Filtering. Both of these techniques should be evaluated in the future. The Shannon procedure, however, would be sufficient and would provide the most accurate estimate of the second derivative if enough product pairs were used in the cross-correlation estimate.

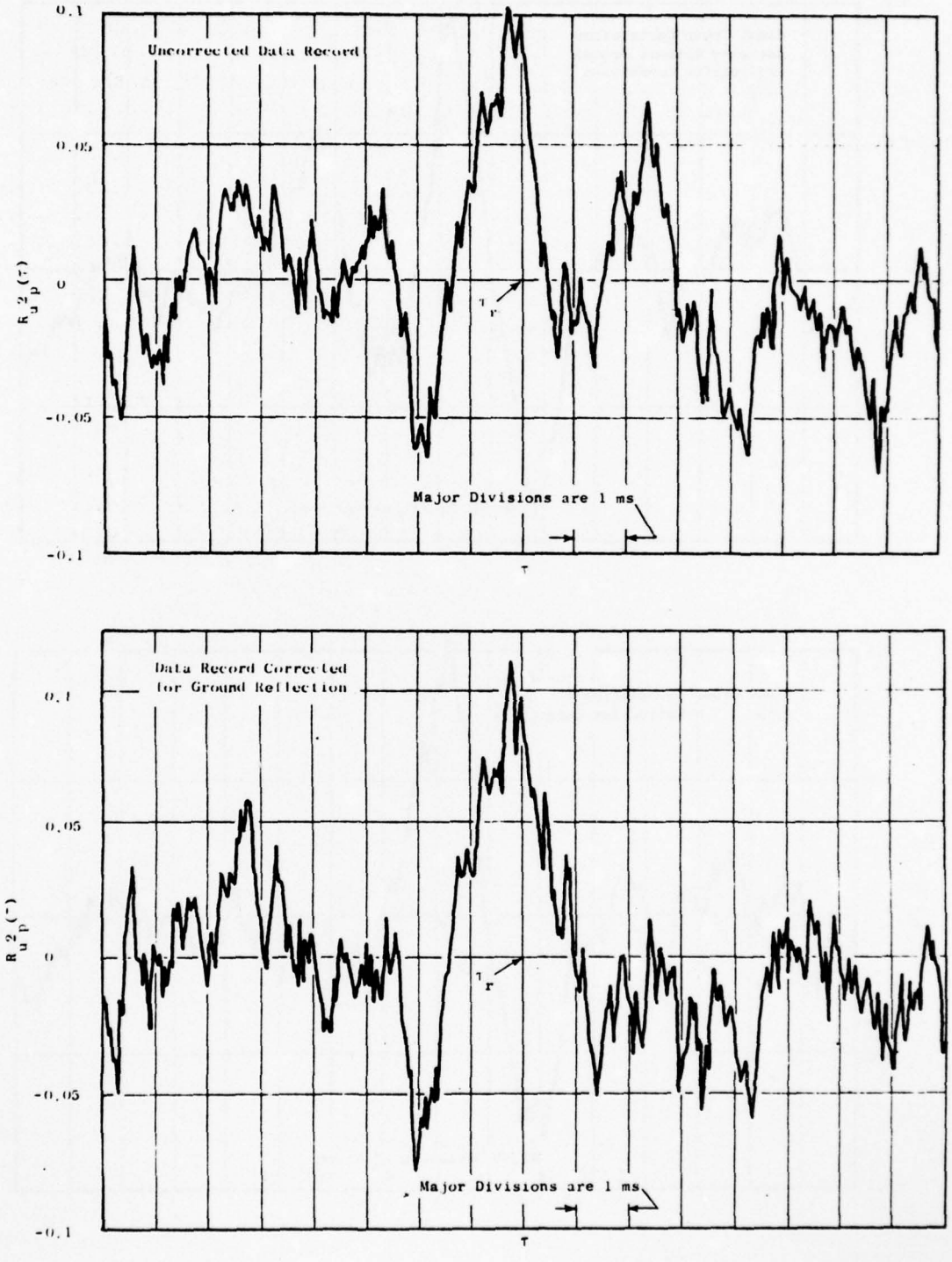


Figure 8-49. LV-Measured Cross-Power Spectrum.

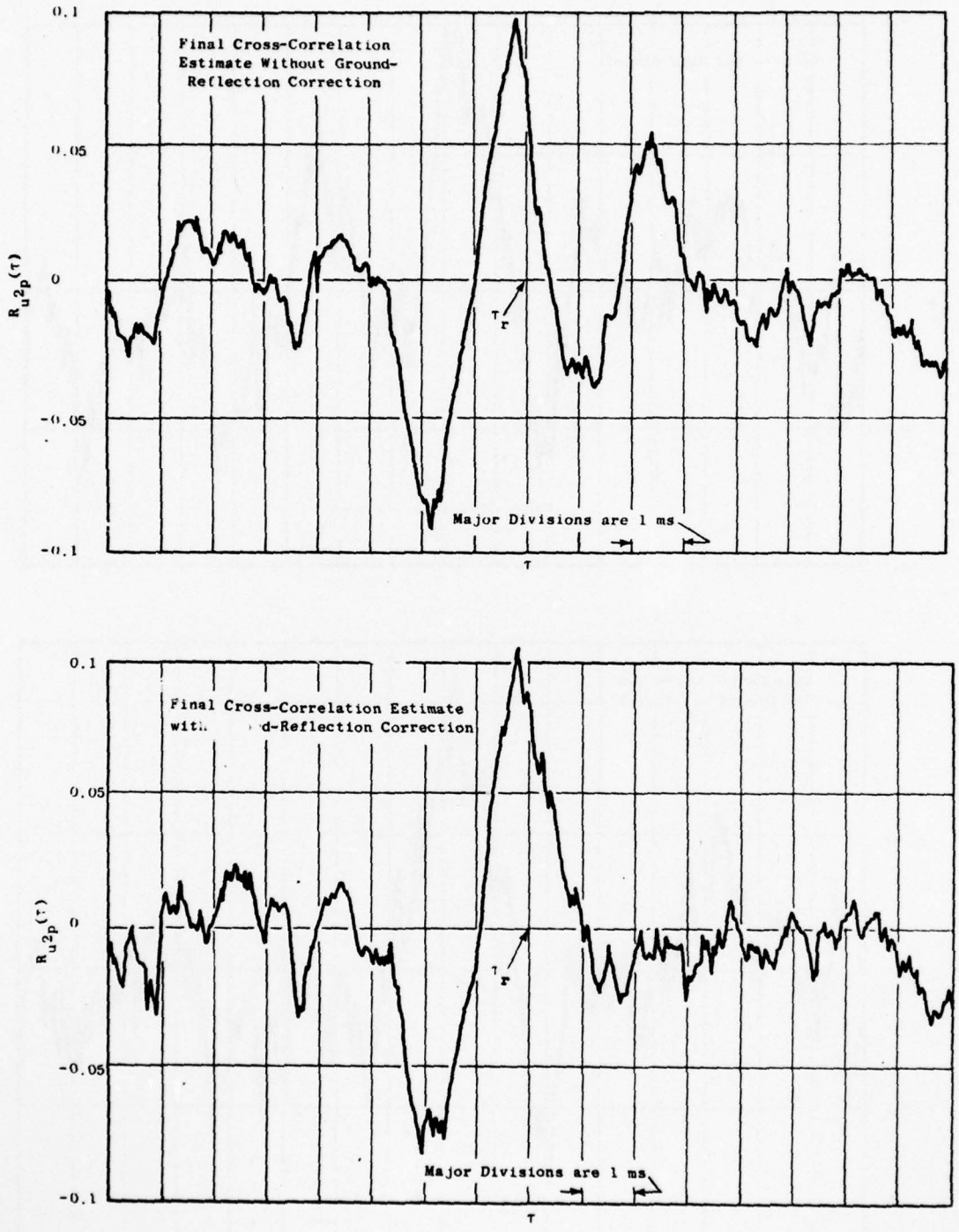


Figure 8-50. Expected Shape of Cross Correlation and Cross-Power Spectrum without Ground Reflection.

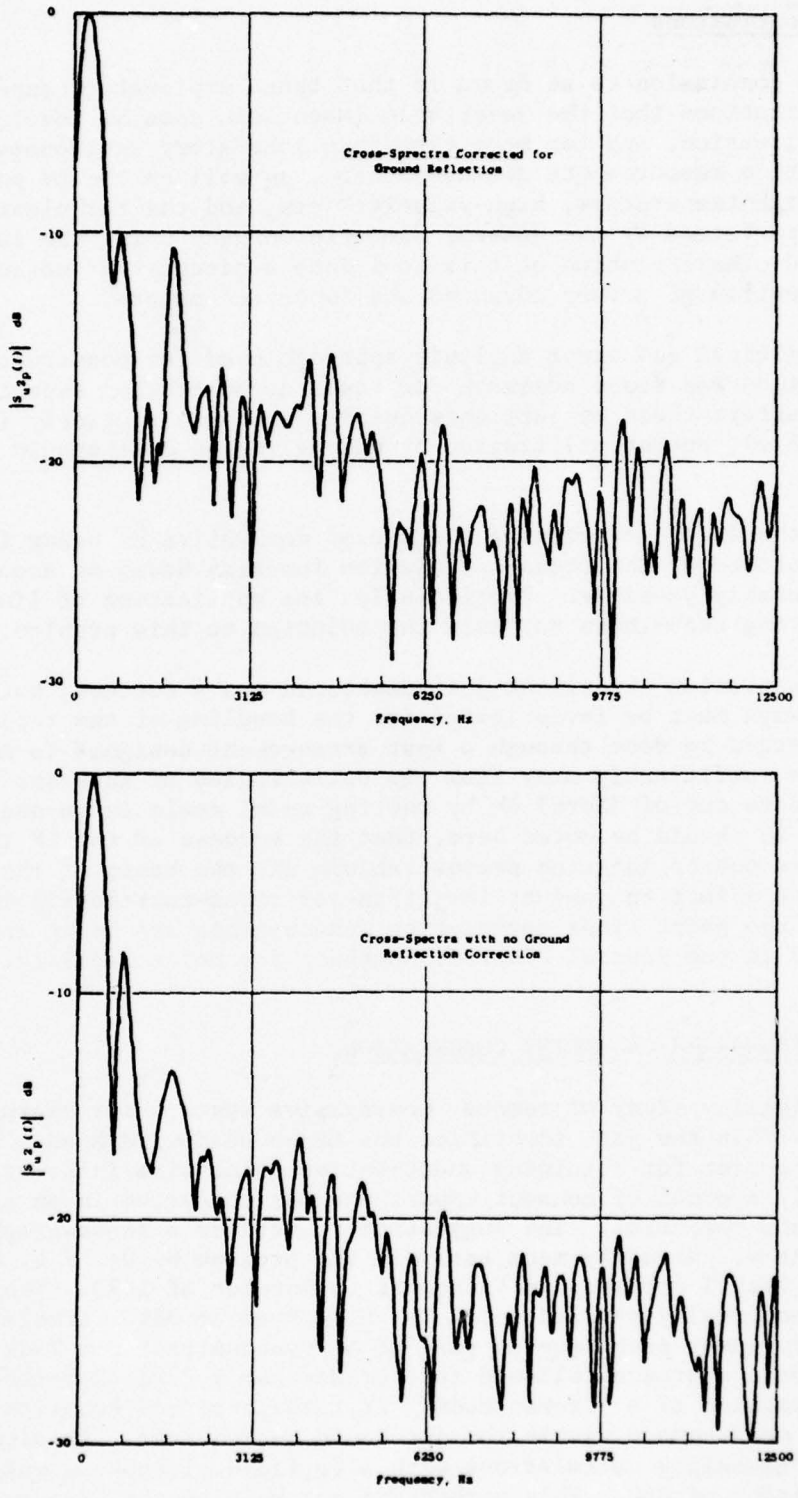


Figure 8-51. Cross Spectra of Final Correlation Files.

8.4.5 Conclusions

The main conclusion to be drawn is that these exploratory experiments gave good indications that the laser velocimeter can soon be developed for noise source location, and for more than just laboratory environments. The cross correlation measurements discussed here, as well as the LV parametric studies for high-temperature, high-velocity jets, and the turbulent spectrum measurements performed by the General Electric Company using the laser velocimeter lift the classification of this tool into a category of noncontact-type measurement devices of a very advanced and important nature.

The statistical and error analysis approach used for construction of the cross correlation was found adequate for these demonstration experiments. However, to perform these measurements quicker and more routinely (which is highly desirable), better utilization of the validated data should and can be implemented.

Better methods of determining the second derivative by using information about the structure of the cross-correlation function based on acoustic theory are probably possible. Particularly, the application of linear predictive filtering techniques may hold the solution to this problem.

The demonstration experiment just described was a success, but it is evident that ways must be investigated for the handling of the reflected waves. This could be done through a test arrangement designed to move the reflected wave sufficiently away from the prime region of interest (as far as testing full-size out of doors) or by testing model scale in an anechoic environment. It should be noted here, that the success of the LV in these series of noise source location demonstrations was the basis of the General Electric funded effort to conduct in-jet/in-jet cross-correlation measurements. These two point cross correlation measurements are being conducted as part of Task 3 in the General Electric Anechoic Jet Noise Facility.

8.5 LASER SHADOWGRAPH CAUSALITY CORRELATION

The feasibility study of remote, noninvasive systems for measuring fluctuations within the jet identified the Laser shadowgraph as a high potential instrument for obtaining quantitative point wise information. As part of Task 1, a proof of concept experiment was conducted in an attempt to demonstrate this potential. The suggestion to utilize a shadowgraph as the jet measurement was actually made early in the program by Dr. F.D. Grosche of DVMR during a Task 1 workshop in Vancouver in October of 1973. The idea, however, was not really studied until Dr. M.J. Rudd of BB&N formulated a suggested measurement technique as part of his subcontract for Task 1 (Reference 82). Rudd's approach followed that of Meecham & Ford (Reference 73) using the assumption of a "frozen model" of turbulence and Equation (129) so only a single measurement within the jet would be required. An alternative method, using causality correlations with a farfield microphone was suggested by Dr. T.E. Siddon of UBC. This method did not rely on the "frozen model" of turbulence. The causality approach was selected for development and demonstration on a subsonic jet in the UBC anechoic room (Reference 90).

8.5.1 The Density Laplacian as a Source Term

Lighthill's solution for the jet noise problem is given by

$$\rho(\underline{x},t) = \frac{p(\underline{x},t)}{c_o^2} = \frac{1}{4\pi c_o^2} \int_{V_{eff}} \left[\frac{\partial^2 T_{ij}}{\partial y_i \partial y_j} \right]_{\hat{t}} \frac{dV(\underline{y})}{r} \tag{179}$$

where

$$r = |\underline{x} - \underline{y}|, \quad t - \hat{t} = t_{tr} = \text{acoustic travel time from } \underline{y} \text{ to } \underline{x} \tag{180}$$

and

$$T_{ij} = \rho u_i u_j + (p - c_o^2 \rho)\delta_{ij} + \tau_{ij} \tag{181}$$

For incompressible inviscid turbulence (approximated by an unheated low speed jet) the equation

$$\nabla^2 p = - \frac{\partial^2 \rho_a u_i u_j}{\partial y_i \partial y_j} \tag{182}$$

describes the flow field; ρ_a is the total density. Note that T_{ij} from Equation (182) reduces to $\rho_a u_i u_j$ for this case. For a quasi-incompressible gas, we have the isentropic relation:

$$c_o^2 \nabla^2 \rho = \nabla^2 p \tag{183}$$

Therefore, in this limit, where $u_i/c_o << 1$. Equation (183) becomes:

$$p(\underline{x},t) = - \frac{c_o^2}{4\pi} \int_{V_{eff}} [\, \nabla^2 \rho \,]_{\hat{t}} \frac{dV(\underline{y})}{r} \tag{184}$$

Arguments are presented in Reference 90 to support the use of this relation at high Mach number.

Multiplying both sides to Equation (184) by the far-field pressure at some earlier time $t' = t - \tau$ and time averaging gives

$$pp(\underline{x},\tau) = -\frac{c_o^2}{4\pi} \int_{V_{eff}} \left[\overline{\nabla^2 \rho p}\right]_{\tau}^{\wedge} \frac{dV(\underline{y})}{r} \tag{185}$$

or in the frequency domain:

$$\Phi(\underline{x},\nu) = 2 \text{ Re } F\{\overline{pp}(\underline{x},t)\} = \tag{186}$$

$$= -\frac{c_o^2}{4\pi} \int_{V_{eff}} \text{Re } F\{[\overline{\nabla^2 \rho p}]_{\tau}^{\wedge}\} \frac{dV(\underline{y})}{r} \tag{187}$$

where F is the Fourier transform given by:

$$F\{f(\tau)\} = \int_{-\infty}^{\infty} e^{-i2\pi\nu\tau} f(\tau)\, d\tau \tag{188}$$

The distribution of source strength per unit volume is obtained by differentiating Equations (185) and (187) with respect to Volume with $\tau = 0$.

$$\frac{\overline{\partial p^2}(\underline{x})}{\partial V} = -\frac{c_o^2}{4\pi r} [\overline{\nabla^2 \rho p}]_{\tau}^{\wedge} \tag{189}$$

$$\frac{\partial \phi(\underline{x}, \nu)}{\partial V} = - \frac{c_o^2}{2\pi r} \text{ Re } F\left[\overline{\nabla^2 \rho p}\right]_{\hat{\tau}} \tag{190}$$

Note that the causality products in Equation (189) and Equation (190) favor only those residual fractions of the source disturbance which show up as part of the far-field sound. Passive, nonradiative disturbances, even of corresponding frequency, will not correlate on time average because they bear no unique phase relationship with the far-field component of equivalent frequency. If they do correlate it is due to radiation from a nearby point and the correlation function will not "peak" at the correct time delay. It is important therefore to not merely take the maximum value of correlation as indicative of the local source strength, unless this occurs at the correct time delay. Further discussion along these lines, including a consideration of circumstances which lead to regions of apparent "negative source strength", is included in References 91 and 92.

8.5.2 Laser Shadowgraph

The Shadowgraph was first proposed as a quantitative instrument for the measurement of turbulence by Roe (Reference 93) and later, with the Laser as a light source, by Rudd (Reference 94). The shadowgraph has been used as an instrument for flow visualization for very many years but has only been used as a qualitative instrument for visualizing shock waves or a turbulent wake. The instrument consists of an arc lamp or a spark light source whose light is collimated to produce a parallel beam of light which is passed through the flow region and falls on a screen, or photographic plate, on the other side. A silhouette of any solid object in the flow is produced and also the light will be refracted by density variations in the flow to produce light and dark bands. Astronomers have also found these "shadow bands" to exist when starlight is refracted by atmospheric turbulence. As the light and dark bands are convected by the wind passed the observer, so the brightness of the star appears to fluctuate. This is the cause of the twinkling, or scintillation, of stars at night. Shadow bands are responsible for the "poor viewing" of stars when they appear to quiver when viewed through a telescope.

The fluctuations of received light intensity, i, are proportional to the second refractive index gradient perpendicular to the light path (Reference 95).

$$\frac{i}{I_o} = - \frac{1}{n_o} \int_L \left(\frac{\partial^2 n}{\partial x^2} - \frac{\partial^2 n}{\partial y^2} \right) dz \tag{191}$$

where l = distance from refracting medium to receiver, n = refractive index, n_o = ambient refractive index, L = thickness of refracting medium, I_o = ambient light intensity.

For gases where the refractive index n_o is only slightly greater than 1, it is related to the local density through (see for instance Reference 96, p. 258):

$$\frac{n_\alpha - 1}{n_o - 1} = \frac{\rho_\alpha}{\rho_o} \tag{192}$$

where $n_\alpha = n_o + n$ and $\rho_\alpha = \rho_o + \rho$. Or, Equation (192) can be rewritten:

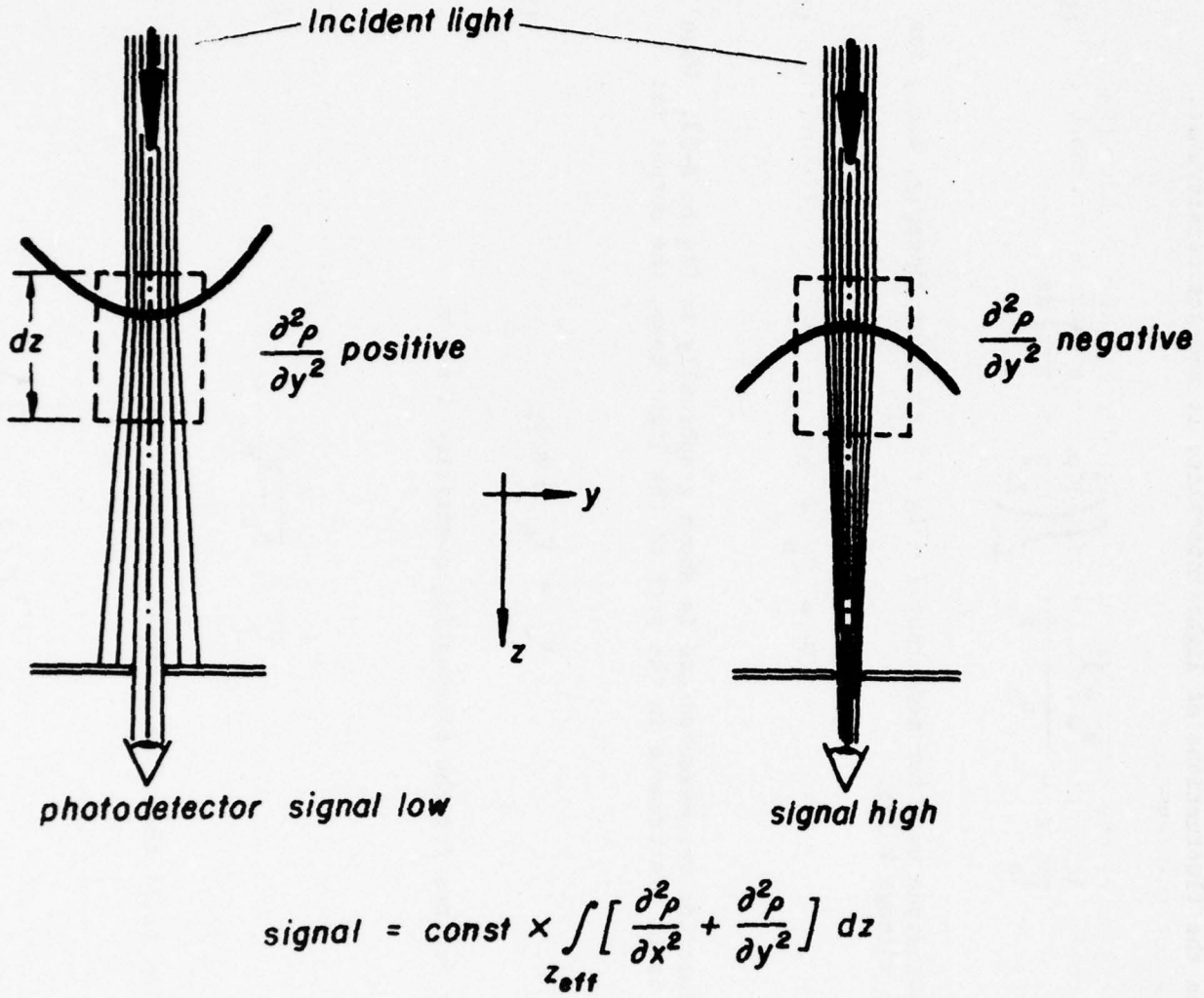
$$n_\alpha = 1 + \frac{n_o - 1}{\rho_o} \rho_\alpha \tag{193}$$

For small disturbances of n and ρ we get:

$$n = \frac{n_o - 1}{\rho_o} \rho \tag{194}$$

A simple physical illustration of the shadowgraph behavior is given in Figure 8-52. A cylindrical element of the disturbed flow merely acts as a time dependent lens which refracts the light beam, causing it to disperse and concentrate at the photodiode*.

*The center portion of the light beam is skimmed off by a tiny aperture, in order to ensure a relatively uniform light intensity distribution falling on the diode. In fact, if the undisturbed light beam is characterized by a rather nonuniform intensity distribution at the plane of the photodiode, then first order refractive gradients can lead to unwanted diode signals. This Schlieren-like behavior was a source of considerable difficulty in this set of experiments, and was not fully eliminated. This question was examined further in the section on calibration.



$$\text{signal} = \text{const} \times \int_{z_{eff}} \left[\frac{\partial^2 \rho}{\partial x^2} + \frac{\partial^2 \rho}{\partial y^2} \right] dz$$

Figure 8-52. Principle of Shadowgraph Detection.

Combining Equation (191) and Equation (194) we obtain the relation between the fluctuations of light intensity, i, and gas density, ρ:

$$\frac{i}{I_o} = - \frac{n_o - 1}{n_o} \frac{1}{\rho_o} \int_L \left(\frac{\partial^2 p}{\partial x^2} + \frac{\partial^2 p}{\partial y^2} \right) dz \tag{195}$$

The photodiode used for measuring $I = I_o + i$ responds linearly, i.e., its output voltage V is:

$$V = V_n + h\, I \tag{196}$$

This function was measured and is shown graphically in Figure 8-53. When there is no disturbance in the path of the light beam, the output is:

$$V_o = V_n + h\, I_o \tag{197}$$

and it follows for the fluctuating quantities i and v:

$$\frac{i}{I_o} = \frac{v}{V_o - V_n} \tag{198}$$

Equation (195) therefore becomes:

$$v = S \int_L \left(\frac{\partial^2 p}{\partial x^2} + \frac{\partial^2 \rho}{\partial y^2} \right) dz \tag{199}$$

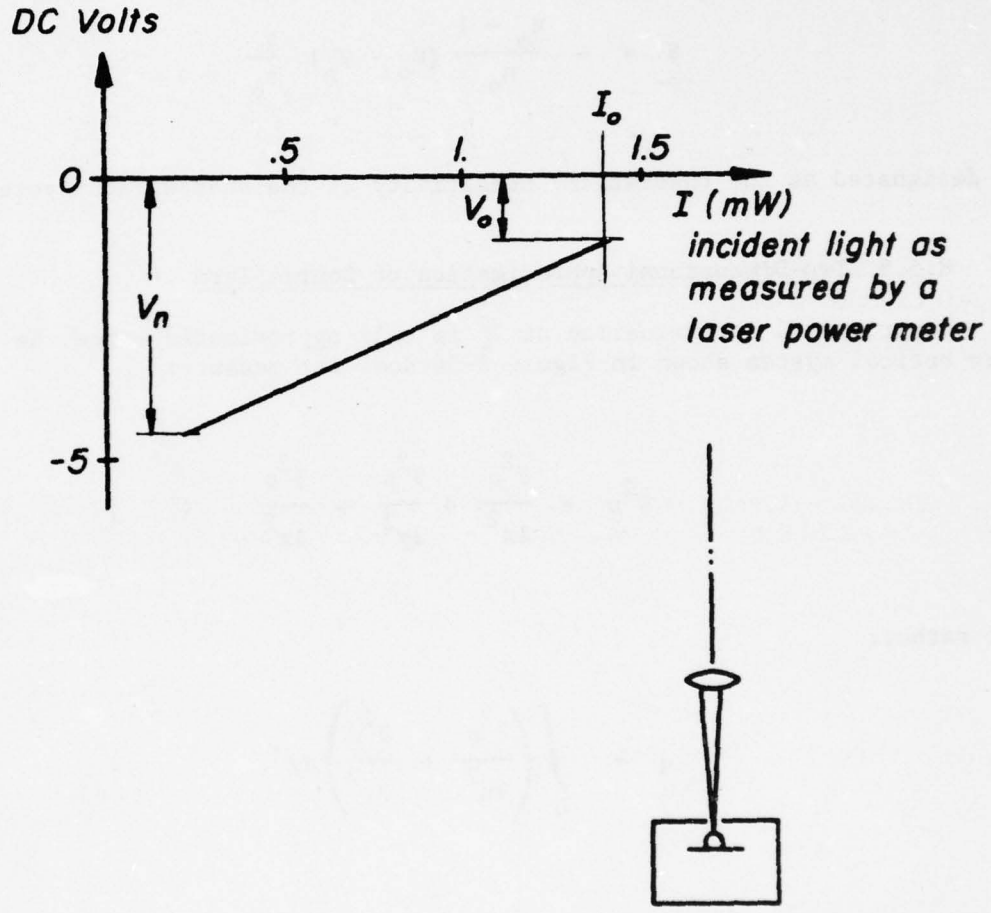
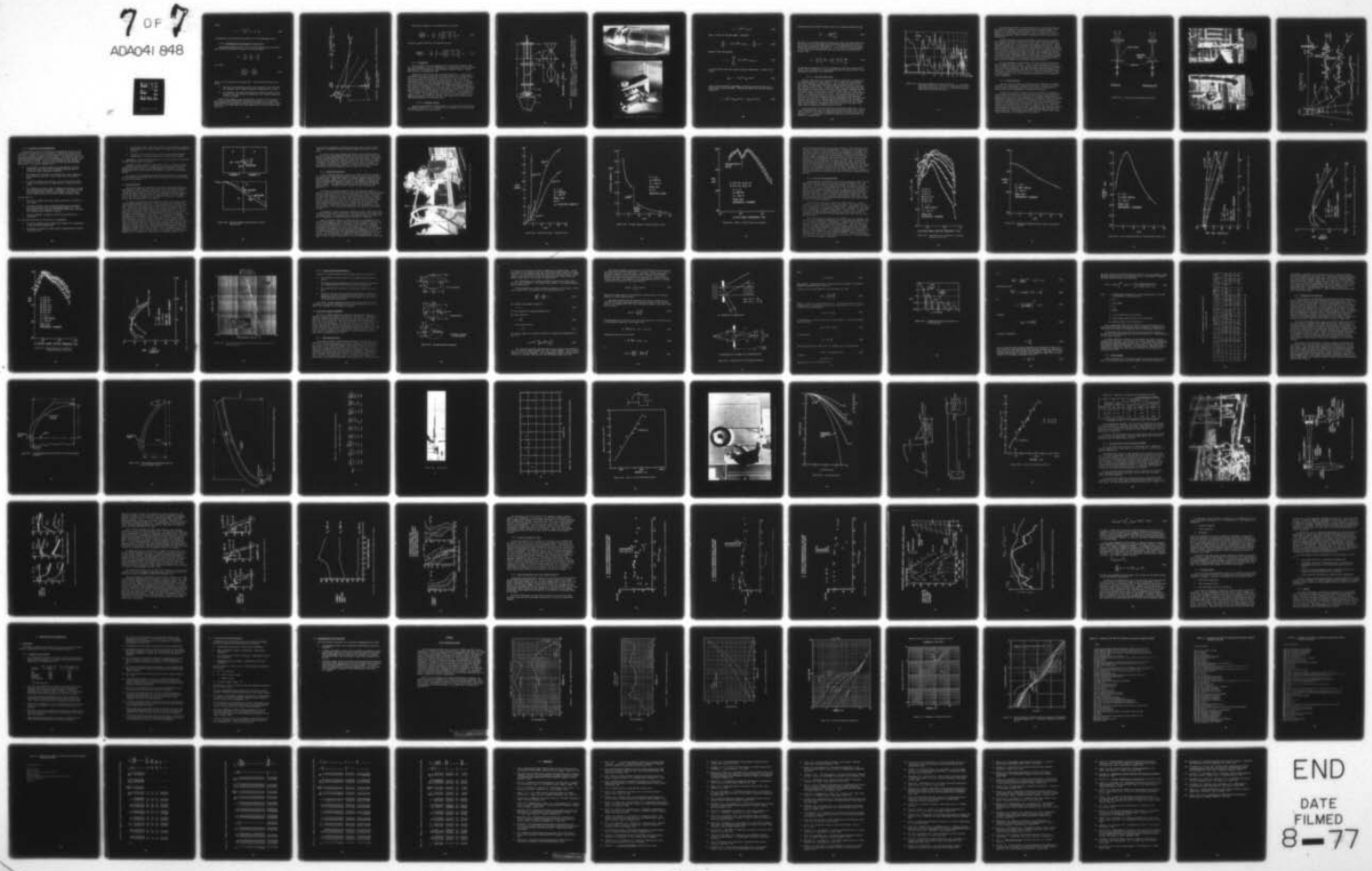


Figure 8-53. DC Voltage at Photodetector Output as a Function of Incident Light Intensity.

AD-A041 848 GENERAL ELECTRIC CO CINCINNATI OHIO AIRCRAFT ENGINE GROUP F/G 14/2
HIGH VELOCITY JET NOISE SOURCE LOCATION AND REDUCTION. TASK 1. --ETC(U)
FEB 77 C T SAVELL, E J STRINGAS DOT-OS-30034
UNCLASSIFIED R77AEG187 FAA-RD-76-79-1 NL

7 OF 7
AD A041 848



END
DATE FILMED
8-77


1.0
1.1
1.25
1.4
1.6
1.8
2.0
2.2
2.5
2.8
3.2
3.6
4.0
4.5
5.0
5.6
MICROCOPY RESOLUTION TEST CHART
NATIONAL BUREAU OF STANDARDS-1963-A

where:

$$S = - \frac{n_o - 1}{n_o} (V_o - V_n) \frac{1}{\rho_o} \tag{200}$$

is designated as the theoretical sensitivity of the shadowgraph system.

8.5.3 Two-Dimensional Approximation of Source Term

Experimental determination of ∇_ρ^2 is only approximated since the single-beam optical system shown in Figure 8-54 does not measure:

$$\nabla^2 \rho = \frac{\partial^2 \rho}{\partial x^2} + \frac{\partial^2 \rho}{\partial y^2} + \frac{\partial^2 \rho}{\partial z^2} \tag{201}$$

but rather:

$$q = \int_L \left(\frac{\partial^2 \rho}{\partial x^2} + \frac{\partial^2 \rho}{\partial y^2} \right) dz \tag{202}$$

where z is the direction of the light beam. The differences between q and ∇_ρ^2 are:

1. One term of the Laplacian operator ∇_ρ^2 is neglected since the light beam responds only to density gradients perpendicular to itself.

2. By its nature, the light beam integrates conditions along its path. Therefore, we cannot obtain pointwise but only linewise resolution of source strength.

Despite this somewhat crude approximation it should still be possible to obtain more detailed information on source distribution in a jet than has been available, in particular in cases where the insertion of probes is made difficult by very high speed flow, high temperature, or too much probe generated noise.

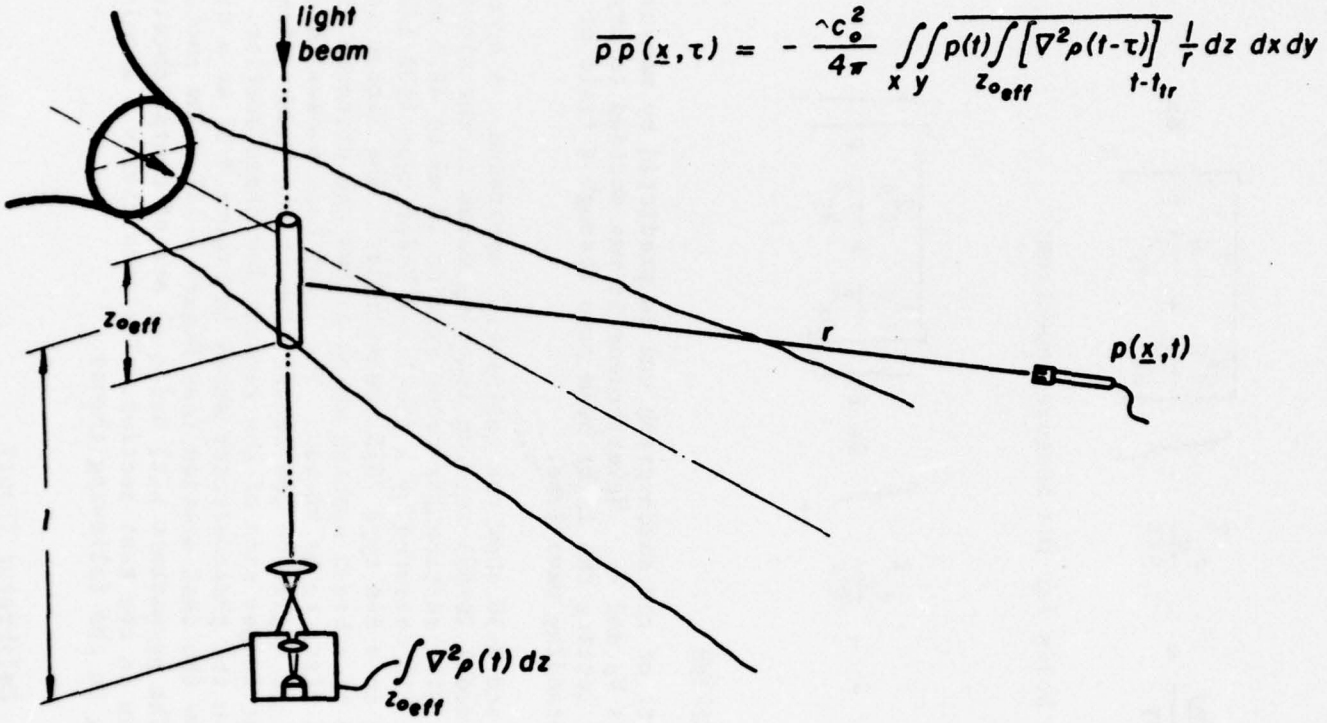


Figure 8-54. Sketch of Shadowgraph System. Sizes and Distances not Proportionate. (see Figure 8-60).

The quantity measured in the experiments is therefore:

$$\frac{\partial \overline{p_m^2(x)}}{\partial x\, \partial y} = -\frac{c_o^2}{4\pi r} \int_L \left[\overline{\frac{\partial^2 \rho}{\partial x^2} + \frac{\partial^2 \rho}{\partial y^2}\, p} \right]_{\hat{\tau}} dz \qquad (203)$$

A similar equation holds for the measured spectrum:

$$\frac{\partial \phi_m(x,\nu)}{\partial x\, \partial y} = -\frac{c_o^2}{2\pi r} \int_L \mathrm{Re}\, F \left\{ \left[\overline{\frac{\partial^2 \rho}{\partial x^2} + \frac{\partial^2 \rho}{\partial y^2}\, p} \right]_{\tau} \right\} dz \qquad (204)$$

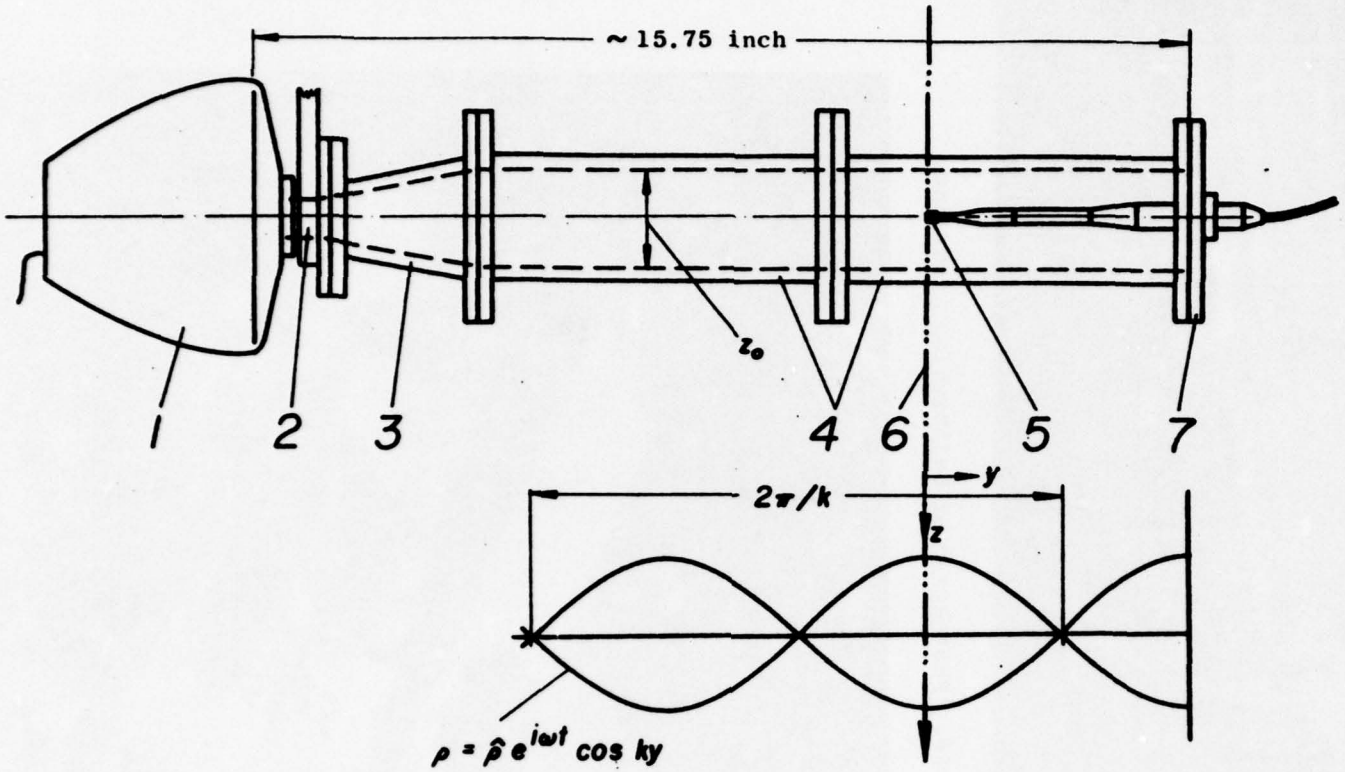
8.5.4 Calibration

The sensitivity of the shadowgraph can be predicted by measuring only the two dc voltages V_o and V_n. Nevertheless it was decided to try to measure the sensitivity by letting the light beam pass through a field of intense sound waves in a standing wave tube.

Figures 8-55 and 8-56 show the calibration apparatus. A horn driver (University Sound model ID-60) sets up standing waves in the plexiglass test section of a tube (with rectangular cross section 17 mm by 44.5 mm). The sound pressure p(t) is measured by a Bruel and Kjaer type 4138 1/8-inch microphone mounted on a B&K type 2618 preamplifier. The latter is mounted into the end plate by a brass bushing which allows the distance of the microphone from the end plate to be varied. The light beam passes through the test section at right angles to the center line of the calibration apparatus and parallel to the longer side of the rectangular cross section. The light beam is incident on the photodetector shown in Figure 8-57 at a distance of l = 0.65 meters below the test section (see Figure 8-54). The photodetector signal is q(t). The parameters p(t) and q(t) are of course obtained at the same axial position in the test section. The sensitivity S should then be obtained according to the following theory.

8.5.4.1 Calibrator Theory

Assuming plane harmonic standing waves in the test section we can write the density fluctuation ρ as a function of the coordinate y in the direction of the centerline of the test section:



$$\text{light intensity} \;\alpha\; -\int_{z_o} \nabla^2 \rho \, dz \;=\; z_o k^2 \rho$$

Figure 8-55. Calibration Apparatus: 1 - Horndriver, 2 - Throat with Circular Cross Section, 3 - Transition Piece, 4 - Plexiglass Test Sections with Rectangular Cross Section, 5 - 1/8-inch Microphone Mounted on Preamplifier, 6 - Light Beam, 7 - End Plate.

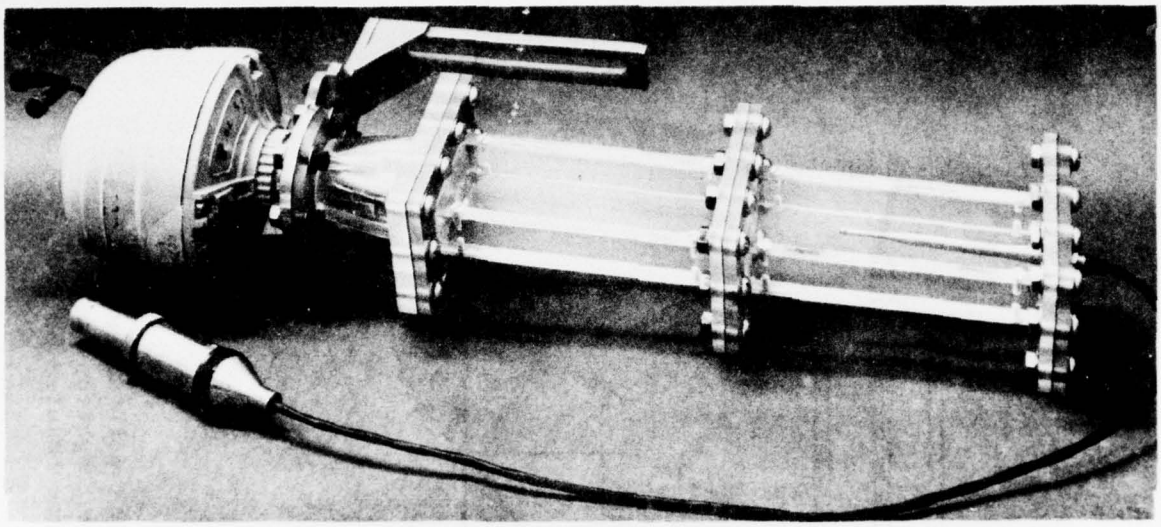


Figure 8-56. Photograph of Calibration Apparatus.

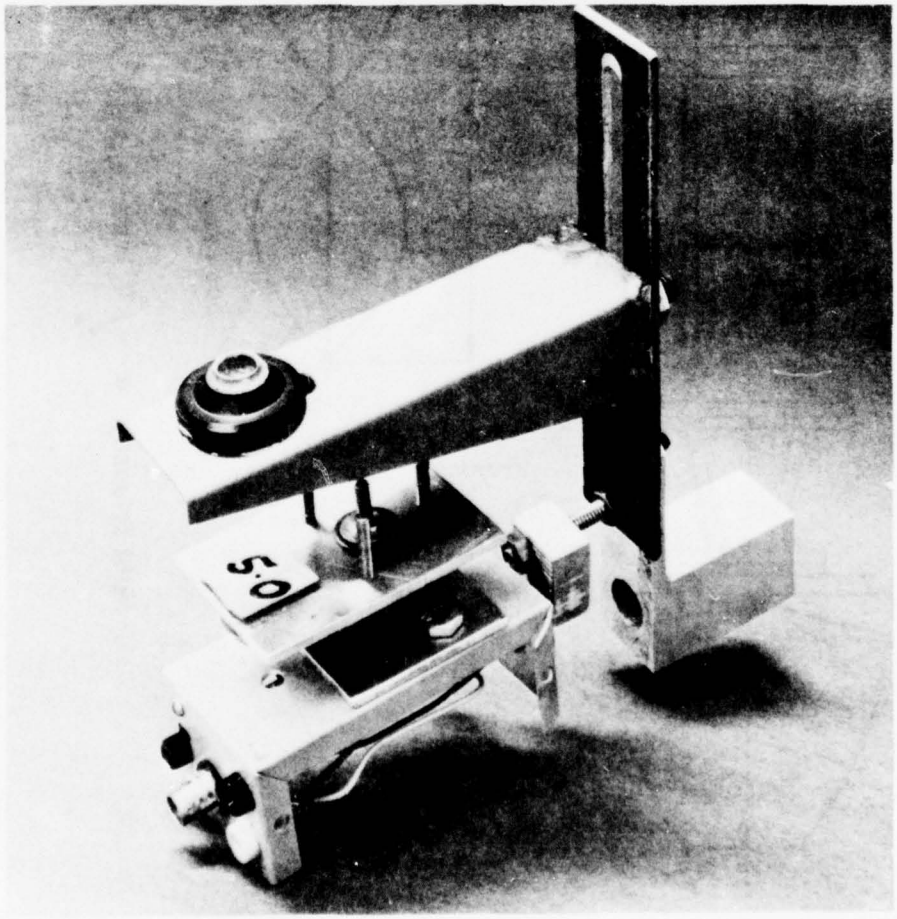


Figure 8-57. Photograph of Photodetector and Optics.

$$\rho = \hat{\rho}\, e^{i2\pi\nu t} \cos ky \tag{205}$$

Here $k = 2\pi\nu/Co$ is the wave number. Therefore:

$$\frac{\partial^2 \rho}{\partial y^2} = - k^2 \hat{\rho}\, e^{i2\pi\nu t} \cos ky \quad , \quad \frac{\partial^2 \rho}{\partial x^2} \approx 0 \tag{206}$$

Equation (199) then becomes:

$$v = S \int_{-z_o/2}^{z_o/2} -k^2 \hat{\rho}\, e^{i2\pi\nu t} \cos ky \, dz \tag{207}$$

z_o is the width of the test section along the light beam. In terms of rms values:

$$v_{rms} = - S z_o k^2 \rho_{rms} \cos ky \tag{208}$$

Linear acoustics should be applicable in the test section as long as the sound field is not too intense. Pressure and density are then in phase and related by:

$$p = c_o^2 \rho \longrightarrow p_{rms} \cos k_y = p_{rms} \cos ky/c_o^2 \tag{209}$$

Combining Equations (208) and (209) results in the measured sensitivity S_m^1:

$$S_m^1 = - \frac{v_{rms} c_o^2}{k^2 z_o p_{rms}} \tag{210}$$

S_m^1 needs to be corrected slightly because some of the light gets reflected at the surfaces of the calibration tube thereby decreasing the sensitivity, as can be seen from Equation (200) where $V_o - V_n$ is proportional to the light intensity incident on the photodetector. Let V_o^1 be the dc voltage measured at the output of the photodetector with the light beam crossing the test section, then:

$$S_m = \frac{V_o - V_n}{V_o^1 - V_n} S_m^1 = - \frac{c_o^2}{k^2 z_o} \frac{V_o - V_n}{V_o^1 - V_n} \frac{v_{rms}}{p_{rms}} \tag{211}$$

If voltages are measured in Volts (V), pressure in Newtons per square meter (N/m^2), time in seconds (sec), and length in meters (m), then the unit of the shadowgraph sensitivity S is ($Vm^5/(Nsec^2)$).

8.5.4.2 Practical Difficulties

Equation (208) shows that V_{rms} increases with the square of frequency if the pressure amplitude is held constant. It is, therefore, advantageous to use a high frequency for measuring S_m as long as plane wave motion in the test section is maintained. The lowest order cross mode occurs at about 3.8 kHz, the next one at 7.6 kHz. Figure 8-58 shows, for a microphone and light beam distance of 50 mm from the end plate, three frequency responses obtained by driving the horn driver with a sine signal swept from 1 to 10 kHz (the horn driver cannot be used beyond 11 kHz). Curve A represents the microphone signal: its peaks and valleys are close to the expected standing wave pattern except at the high frequency end where cross modes become important. Curve B is the trace of the signal from the photodetector with the light beam crossing the test section. The microphone was retracted a few millimeters from the light beam so that acoustic and optical interferences were reduced. Curve C was obtained by turning the calibrator just out of the way of the light beam but leaving everything else for curve B.

Curve C should be flat and indicates the electronic noise level. But at the low frequency end, there are some ripples which are probaly due to structural conduction of vibrations originating from the horn driver (all instrumentation, i.e., light source, calibration apparatus, and photodetector, are mounted on a common beam).

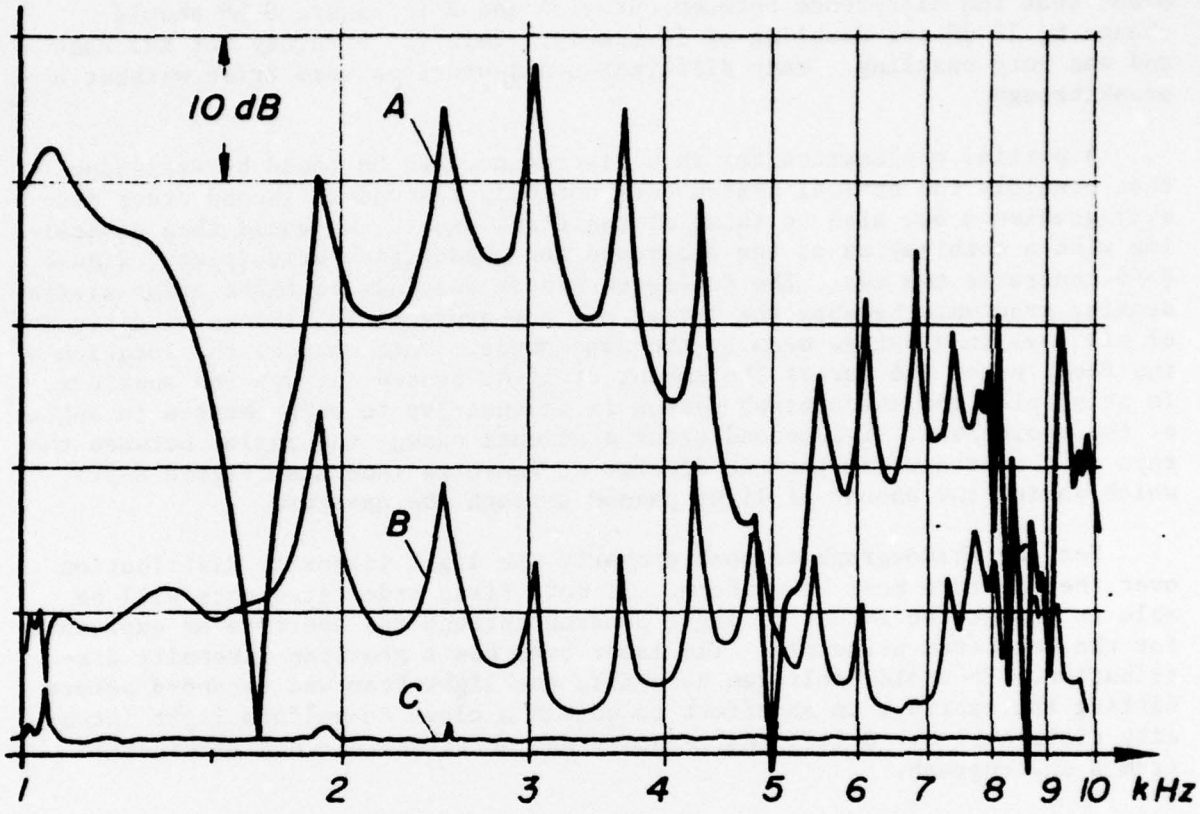


Figure 8-58. Calibration Apparatus Frequency Responses. A: Microphone (Distance to End Plate is 50 mm); B: Photodetector Output, Light Beam Crosses Test Section; C: Photodetector Output, Light Beam Just Misses Test Section.

As already stated above, the photodetector output should increase with the square of frequency if the pressure amplitude is held constant. This means that the difference between curves A and B in Figure 8-58 should change by 12 dB per doubling of frequency. This is certainly not the case and was very puzzling. Many different configurations were tried without a breakthrough.

A partial explanation for this discrepancy can be found by realizing that possibly the optical system does not only respond to second order density gradients but also to those of the first order. We would then be dealing with a combination of the Schlieren and shadowgraph principles. Figure 8-59 contrasts the two. The Schlieren system responds to first order spatial density gradients because the latter are a measure of the change of direction of all rays in a narrow beam by the same angle. This changes the location of the focal point and varies the amount of light passed through the aperture. In principle, the shadowgraph system is insensitive to such changes in angle of the whole beam. The second order gradients change the angles between the rays of a beam causing them to diverge or converge (see also Figure 8-52) which varies the amount of light passed through the aperture.

For the shadowgraph to work properly the light intensity distribution over the aperture must be uniform. If not, first order gradients will be able to change the amount of light passing through the aperture as explained for the Schlieren principle. The laser beam has a gaussian intensity distribution. To avoid Schlieren behavior, the light beam was expanded before hitting the aperture in an effort to obtain a close to uniform light intensity distribution. Still, the response was unfortunately not as expected from a shadowgraph.

8.5.5 Jet Noise Surveys

A partial jet noise survey was completed in the UBC anechoic chamber using the test setup shown in Figures 8-60 and 8-61. However, this was conducted prior to discovering that the optical system was responding to a hybrid combination of shadowgraph and Schlieren principles.

Reference 90 includes an indepth review of the results including 1/3-octave spectra from both the far-field microphone and from the photodetector signal as well as typical cross correlations. Although contamination was subsequently found, the cross correlation records shown in Figure 8-62 present some initial evidence of causality correlations using the remote sensing instrument described herein and in all probability bear some degree of resemblance to a legitimate source distribution. The typical cross correlation records shown on Figure 8-62 for a far-field angle to the jet of 60° were hand smoothed from the original record. As expected, their frequency content tends toward lower frequencies with accompanying amplitude decreases when going downstream. Nevertheless these results must be regarded with a skeptical eye because of the inadequacy of the detector.

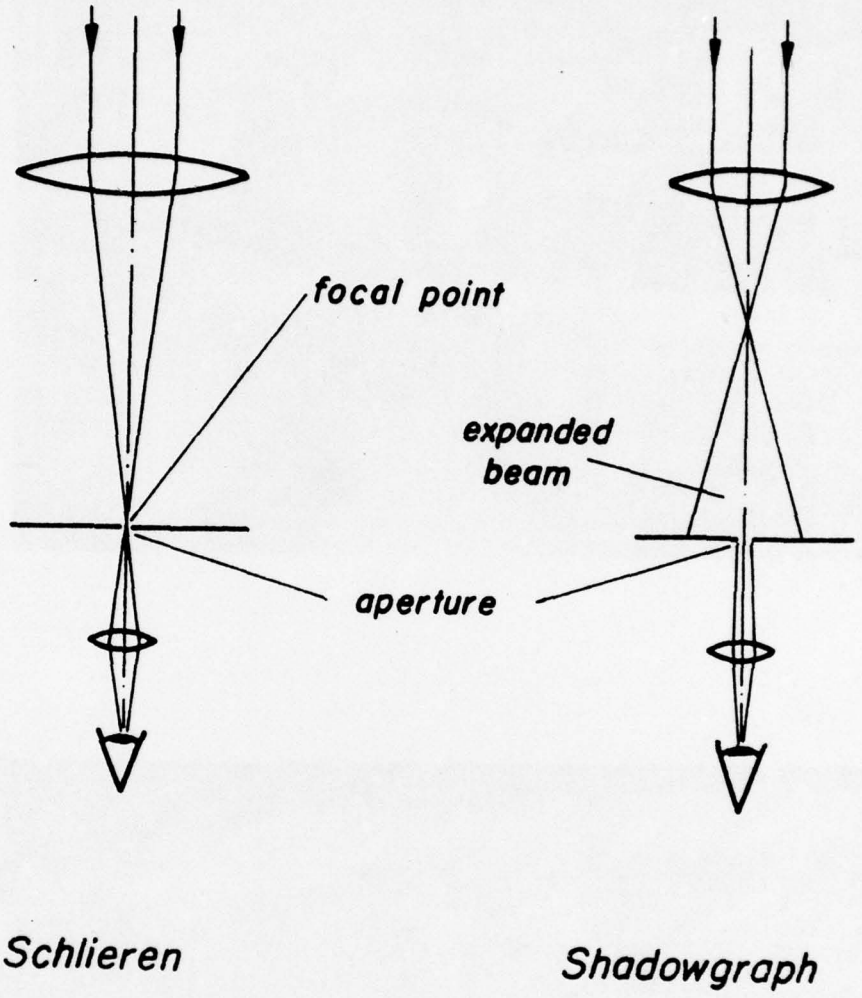


Figure 8-59. Schlieren and Shadowgraph Principles.

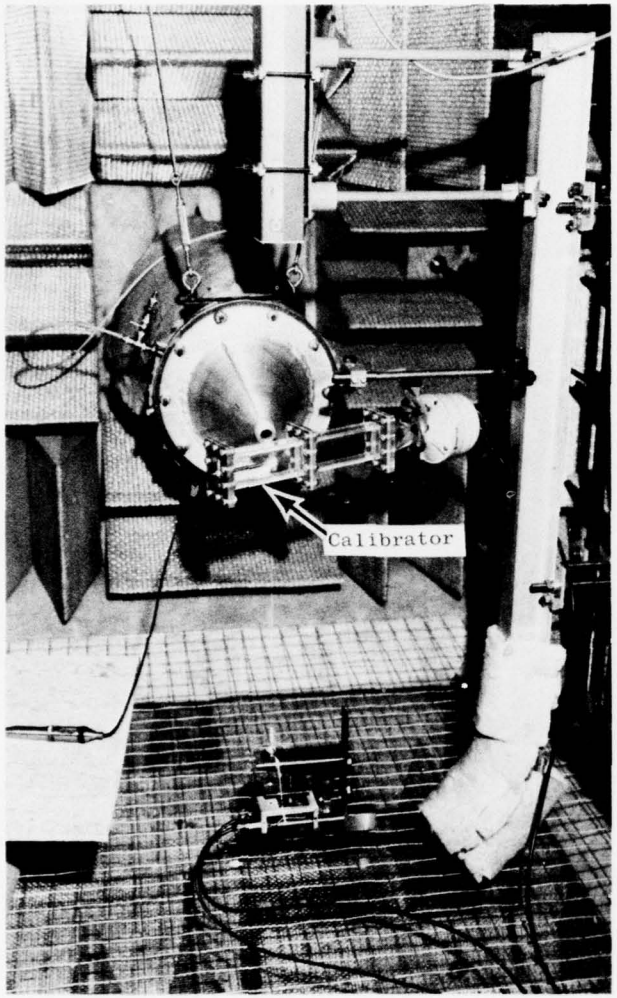


Figure 8-60. Photograph of Shadowgraph System with Calibration Apparatus Mounted.

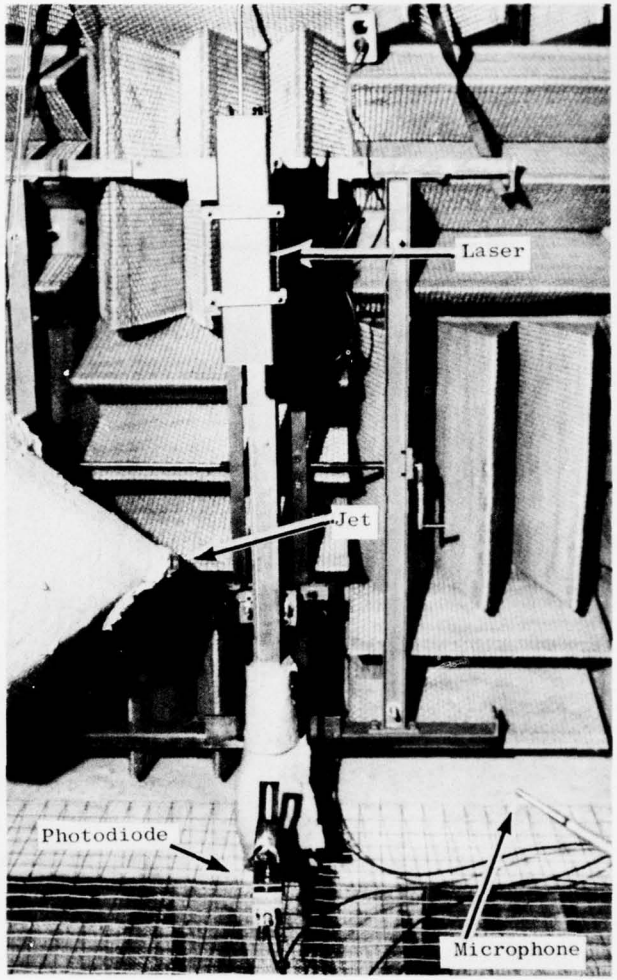


Figure 8-61. Photograph of Shadowgraph System Mounted on Traversing Gear. Also Shown are the Jet Nozzle, and in the Foreground, the Far-Field Microphone.

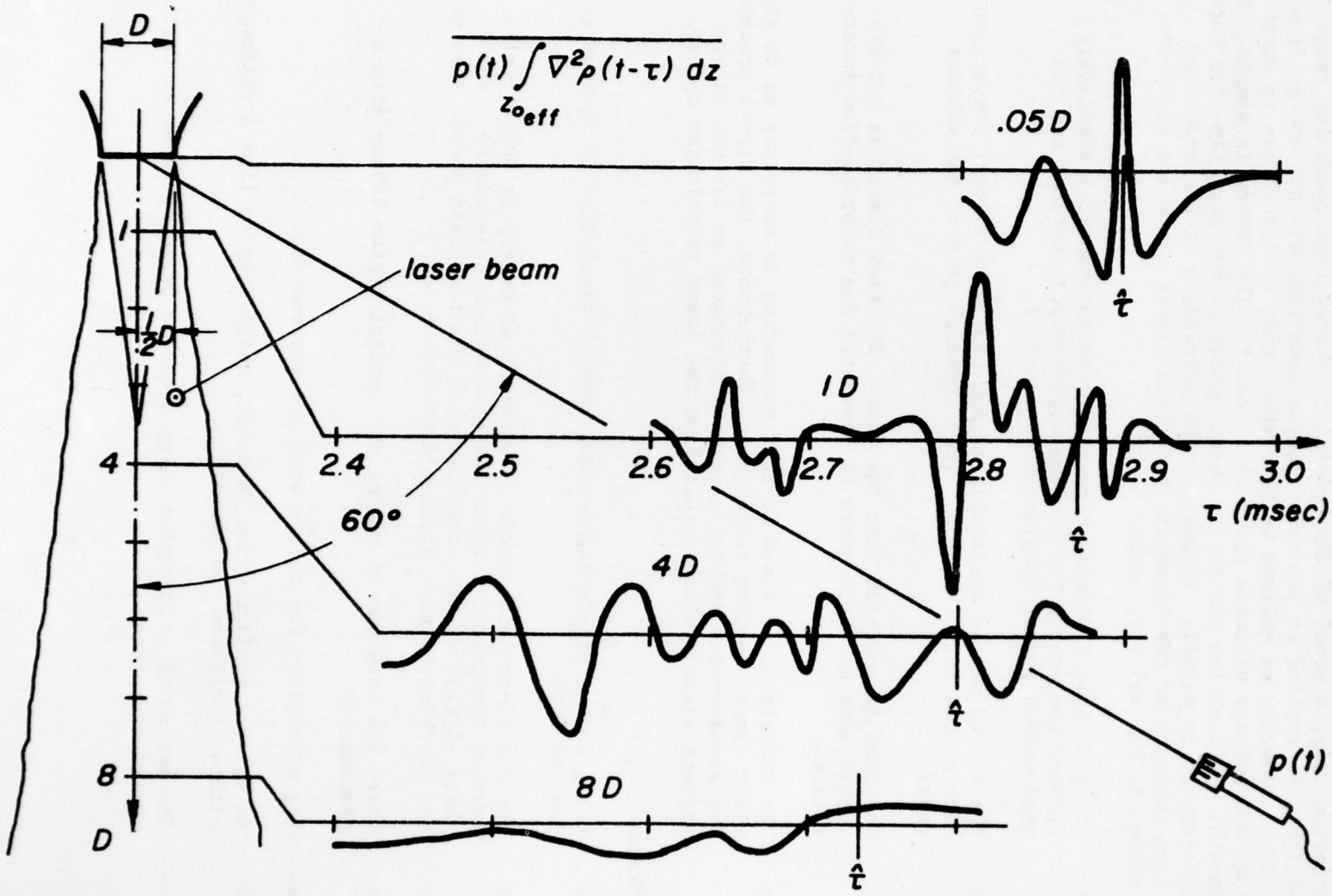


Figure 8-62. Typical Cross Correlation Records.

8.5.6 Conclusions and Recommendations

Unfortunately, a proof of the concept of shadowgraph causality cross correlations, as applied to jet noise source location, did not emerge from this study. However, we believe we have shown that the technique is worth pursuing, and perhaps ultimate proof will result. The theory is simple. The experimental difficulties may not be unsurmountable, but more time for hardware development is needed. To sum up, the advantages of the technique, apart from the ones of the causality principle proper expounded elsewhere (References 74, 91, and 94), appear to be:

- The principle is simple because of the mathematical similarity between the source term in the aerodynamic equations and the shadowgraph output (Laplacian of density).
- The method may be applicable to any flow with a local convection Mach number less than one. That includes jets of hot exhaust gases.
- No probe is inserted into the flow: The flow itself is not disturbed, and no extra noise is generated due to probe-flow interaction.
- The experiment is clean in that no seeding is necessary as in some other remote sensing techniques. Furthermore, the signal processing requirements are not nearly as stringent as for the intermittent signals which result from the laser velocimeter system.

Disadvantages are:

- Using only a single light beam, spatial resolution is limited to a line element.
- The signal-to-noise ratio is affected adversely by acoustically passive disturbances which the shadowgraph responds to. While these signals do not correlate with the far-field sound, they make the correlation more difficult to detect.
- There are problems of making the optical system behave like a shadowgraph.

The following priorities for future work are recommended:

- An optical configuration be sought which behaves like a shadowgraph without Schlieren contamination.
- The method of calibration using acoustic standing waves be further tested and proven.

- The acoustic travel time from the source to the receiver be measured using a strut with a force transducer in place of the laser beam in the flow.

- The whole jet be surveyed with a view of achieving the integral closure test. This would constitute the proof of the concept.

Subsequently, methods should be explored for recovering the 3-D Laplacian and improving the spatial resolution.

Perhaps an ultimate benefit of this method lies in its power as a tool, in conjunction with the laser velocimeter system, of being used to measure directly the various terms in the inhomogeneous wave equation. Thus, an experimental check could be made on the validity of various source approximations.

As a result of the experimental difficulties encountered in this study, it was decided that no further work would be pursued on the Laser Shadowgraph as part of this program.

8.6 HOLE IN THE WALL

The "hole-in-the-wall" experiment is a means of determining the axial distribution of noise sources in a jet plume. There are several versions of this method, but their common feature is that the jet is caused to flow through an aperture that is made as small as possible without affecting the jet or producing an additional noise through buffeting or toroidal edge - tones. The idea is to separate the jet noise into two parts: upstream of the aperture and downstream of the aperture.

Of course, the aperture cannot completely separate the noise as there is noise leakage through the aperture in both directions, with preference for contributions from upstream sources to appear downstream of the hole in the wall. Potter and Jones (References 57 and 58) in the original version of this method used a reverberant chamber and a movable jet nozzle. They claim to be able to establish closure on the noise distribution by first determining the distribution by upstream measurements and then by reversing the experiment and determining the distribution by downstream measurements. This contention must be examined in more detail. In Figure 8-63, a schematic representation of a hole-in-the-wall experiment is shown using two back-to-back reverberant or anechoic chambers (A and B) with an aperture between them. In this experiment, the acoustic power in both A and B will be simultaneously measured. The sum of the acoustic power must be a constant, P_t, if there is no interaction noise. Suppose that the aperture could completely separate the noise; then as the jet was withdrawn into Chamber A, the power measured in Chamber B, P_B, would decrease. Due to leakage, however, the measured value of P_B will be larger than the true value. The acoustic power measured in A will likewise be decreased by an identical amount so that

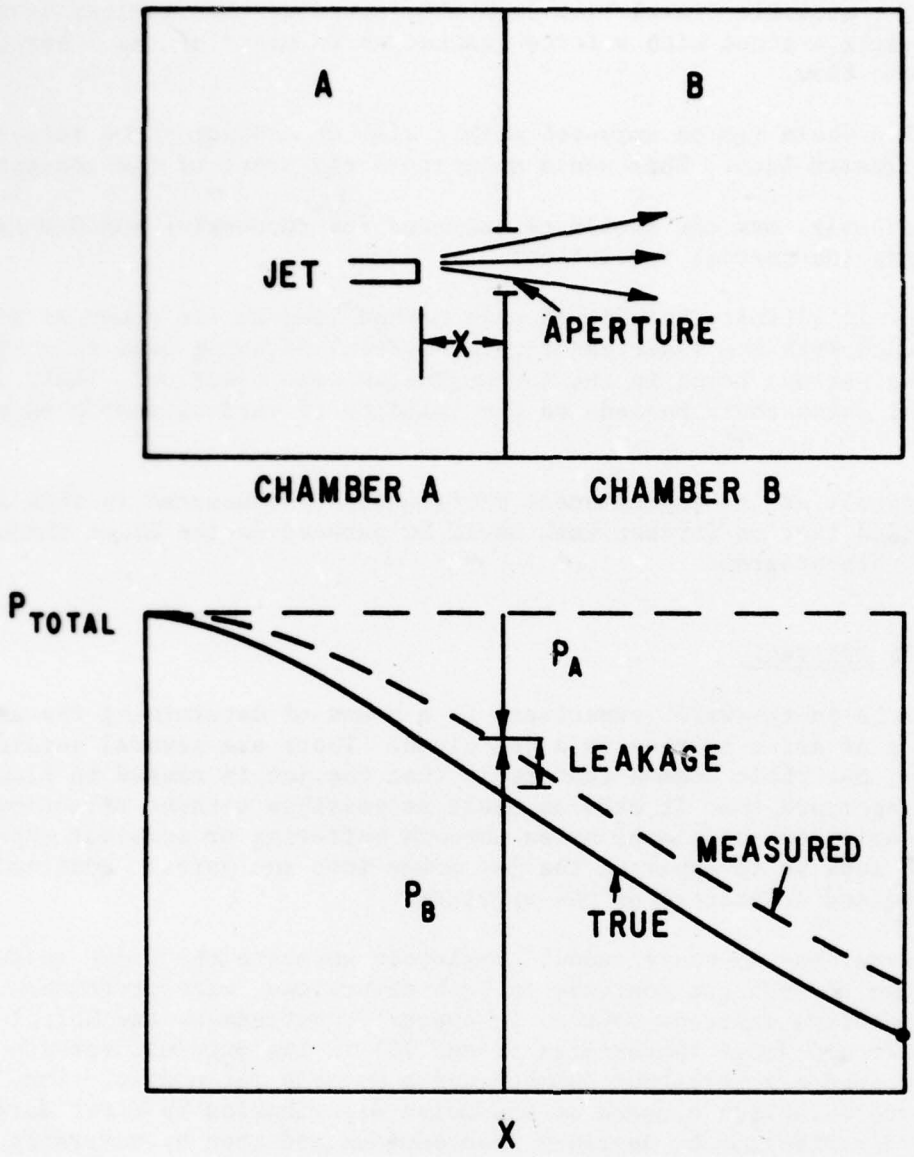


Figure 8-63. Acoustic Leakage and Nonclosure of Source Distribution.

"reversing" the experiment (as done by Potter and Jones) does not provide closure as it reproduces the same cumulative power distribution in both cases.

In a more recent study, McGregor and Simcox (Reference 60) have used a movable jet and a fixed absorbent chamber to absorb the upstream noise, and measured the downstream noise with an outdoor microphone array. This method is more attractive in that it does not require that the reverberant characteristics of the chamber be calibrated and the jet itself is not as subject to possible excitation due to high acoustic level inside the chamber. In this method, it is necessary, however, to calibrate the aperture diameter versus axial distance to maintain closure on the total jet power.

8.6.1 Design and Calibration

A third, slightly different, version of the hole in the wall is used in this study with a translating absorbent chamber and a fixed jet nozzle and microphone array. Figure 8-64 shows the absorbent chamber mounted on a cart that can traverse axially on a set of rails. The chamber is constructed of 1/2-inch transite and lined with 2 inches of high temperature acoustic material, Kaowool. Two industrial mufflers are used to silence the entrainment air inlets. A series of orifice plates are used to provide the aperature.

To determine the minimum aperture size for a given axial station, a series of tests without the absorbent chamber were conducted. The total acoustic power was measured for a series of axial positions for a given orifice plate. In Figure 8-65, the results, using a two-inch convergent nozzle, are shown. The ΔdB is the increase in jet noise power over the case without any orifice plates. Close to the jet exit plane, the incremental noise increased sharpl with increased distance, usually with a vigorous toroidal edge tone that would dramatically disappear with a very slight upstream movement of the orifice plate. Without this toroidal edge tone, the incremental jet noise was quite small. At the larger axial distances, the edge tone was less well defined.

The frequency of peak interaction component decreases rapidly with axial distance as can be seen in Figure 8-66. Also, there seems to be a sharp drop in frequency after 6 to 8 diameters with a change from nearly pure edge tones below 7 diameters to broadband buffeting noise above 10 diameters.

When the absorbent chamber is placed over the jet, the measured interaction noise changes as some of the acoustic power is absorbed, and only the acoustic power downstream of the aperture, plus any leakage, is measured. As can be seen from Figure 8-65, it is virtually impossible not to generate interaction noise, except very close to the nozzle exit. The question as to the degree of contamination on the farfield noise measurement can be answered by investigating hole in the wall measurements far downstream in the jet ($x/D>6$). At these stations, the interaction spectral peak and the jet noise spectral peak are separated in frequency and can be distinguished. An example of this is shown in Figure 8-67 for a 1-inch-diameter nozzle, where two

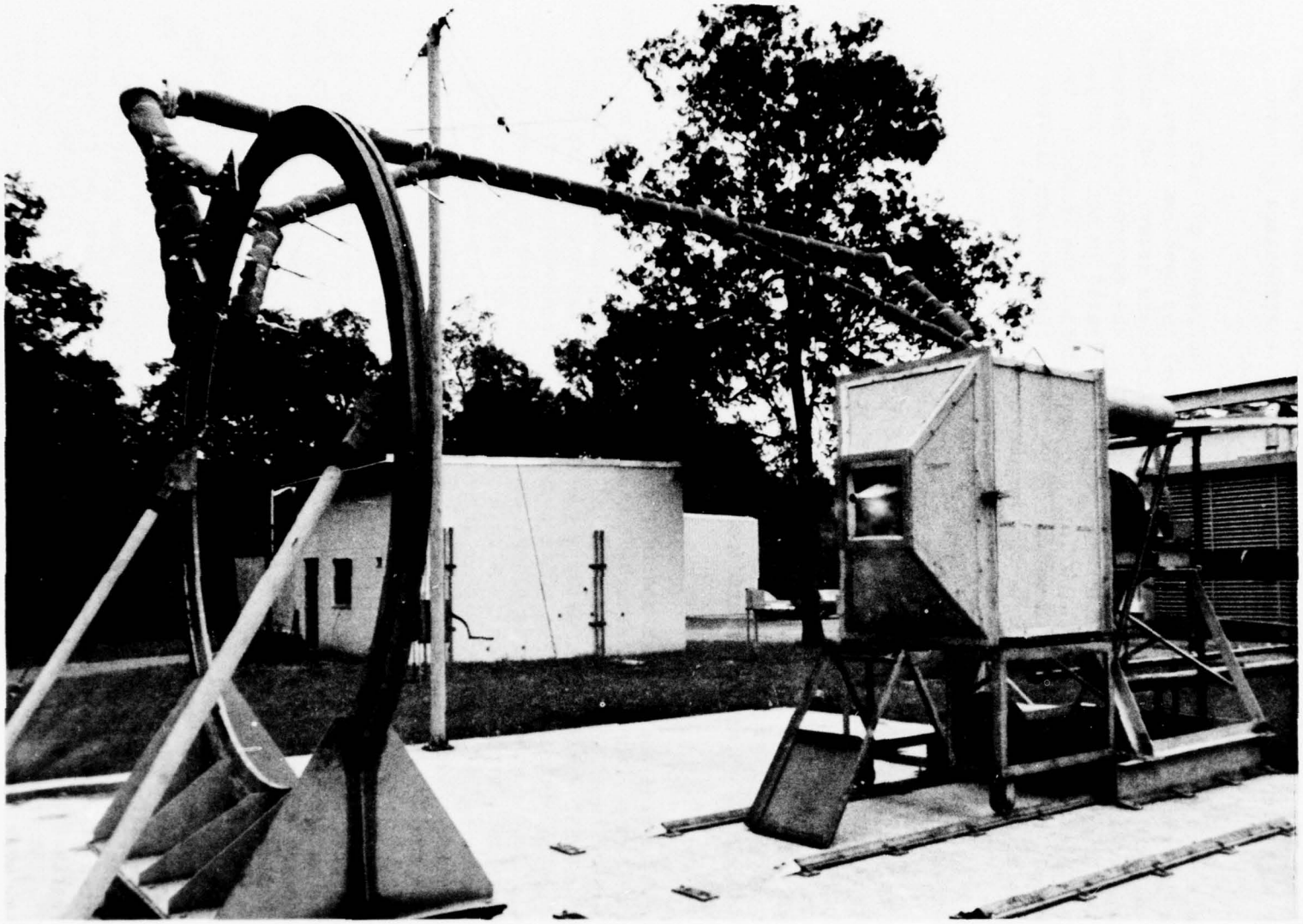


Figure 8-64. "Hole-in-the-Wall" Experimental Apparatus.

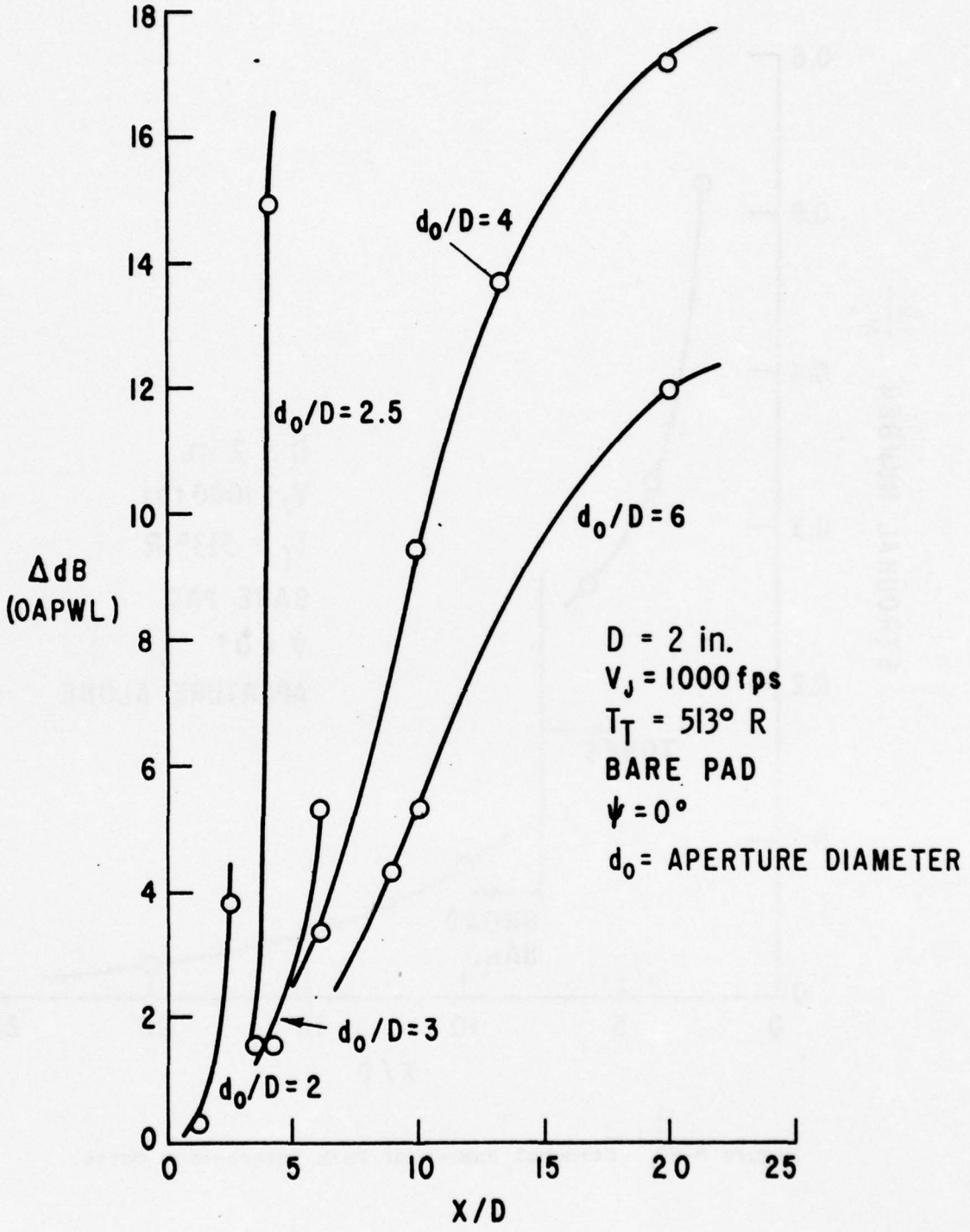


Figure 8-65. Interaction Noise - Aperture Alone.

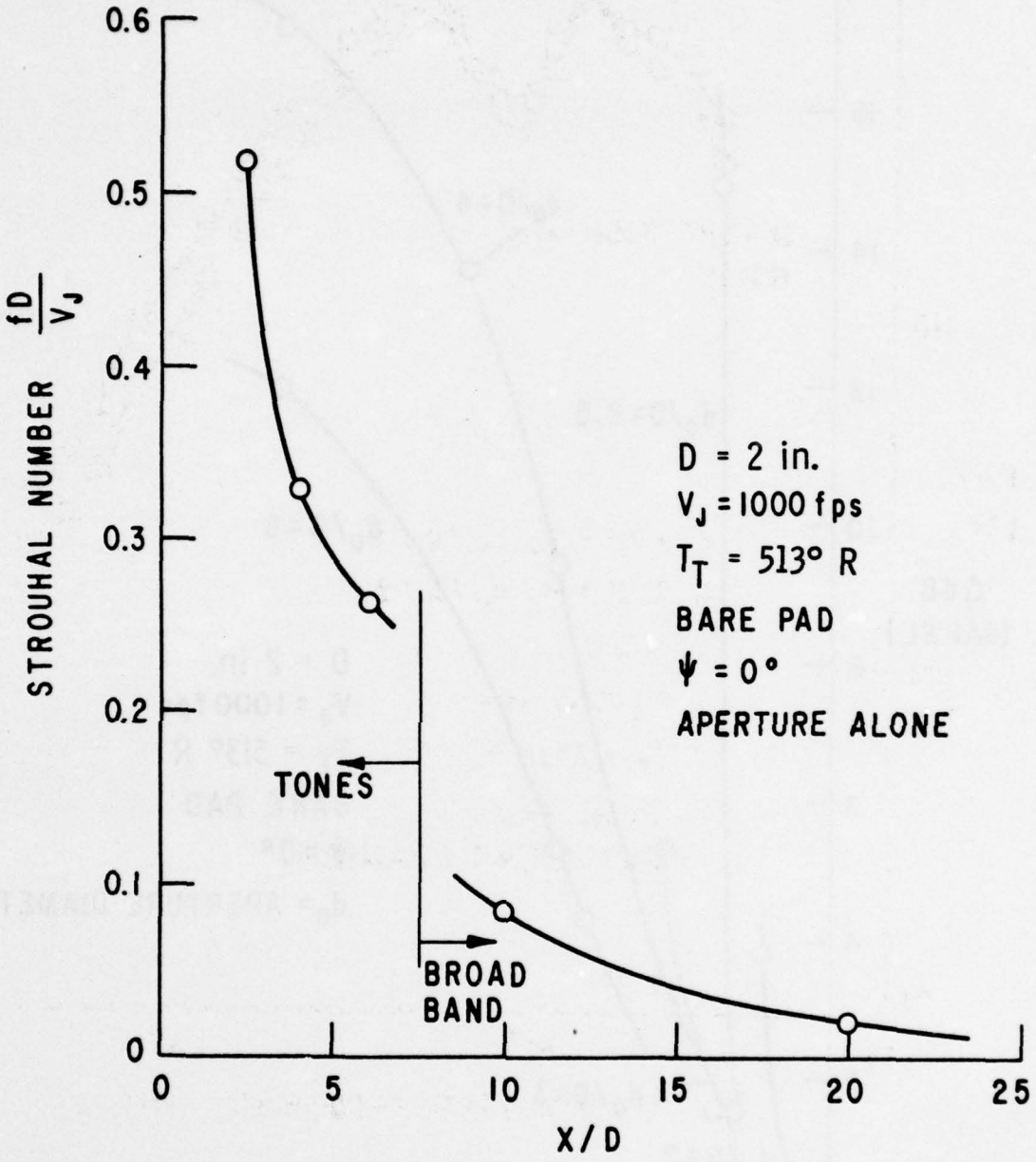


Figure 8-66. Strouhal Number of Peak Interaction Noise.

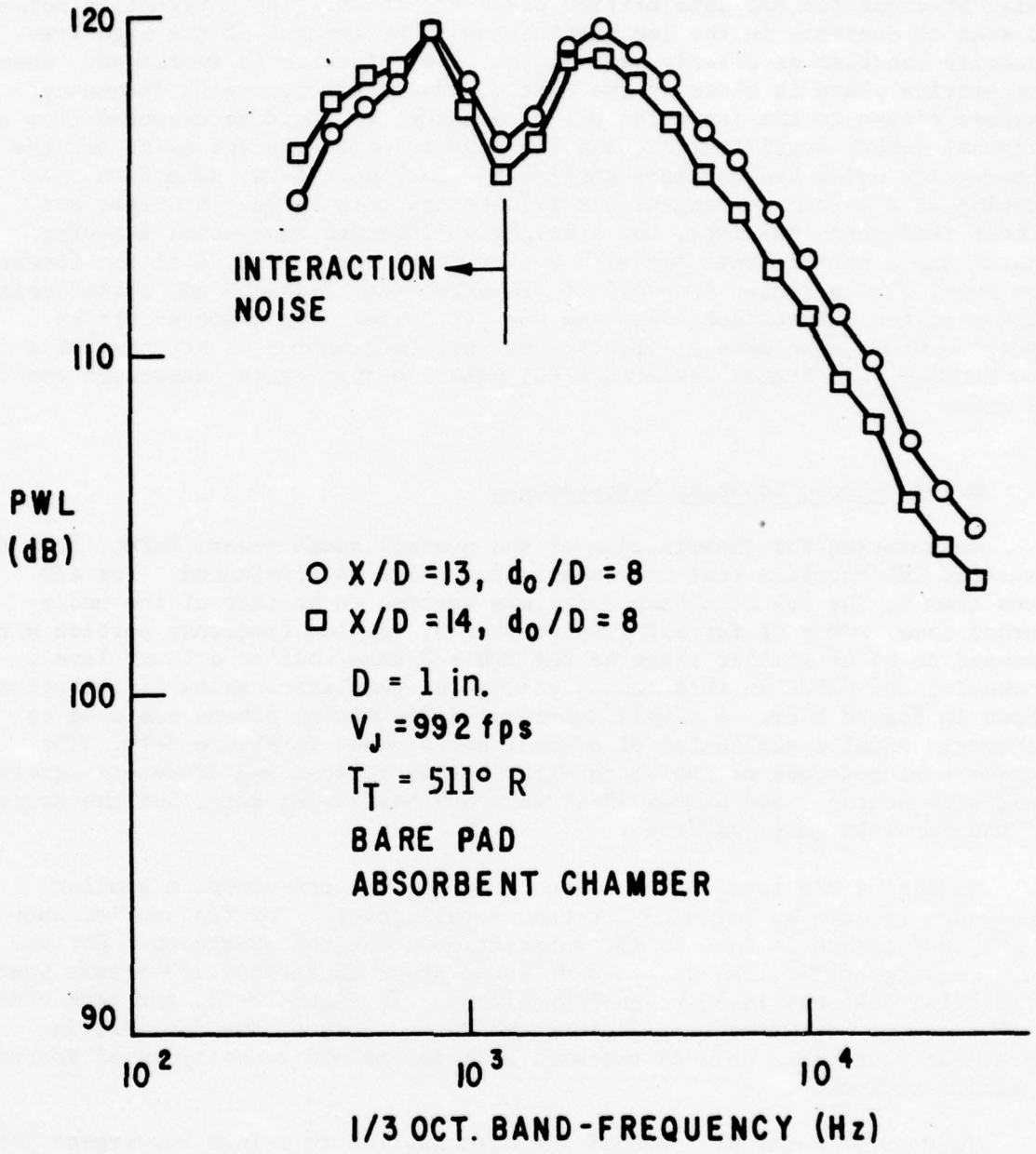


Figure 8-67. Effect of Axial Location of Aperture.

axial stations for the same orifice plate are shown. The interaction noise is seen to dominate in the low frequencies. The removal of the high frequencies can also be clearly seen as the axial distance is increased. When the orifice plate is close to the nozzle, the interaction peak frequency becomes closer to the jet noise peak frequency, as would be expected from a Strouhal number consideration, and the separation of the jet noise and the interaction noise becomes more difficult. In Figure 8-68, data from the mapping of a 1-inch convergent jet illustrates this trend. McGregor and Simcox (Reference 60) data, for a slightly different case using a moving nozzle and a heated sonic jet with a microphone array limited to the forward arc only, show a larger drop off of PWL with axial distance and better separation of the interaction noise and the jet noise. The diameter of the aperture would also have an effect, but this information is not available in the McGregor and Simcox (Reference 60) paper so that exact comparison cannot be made.

8.6.2 Source Location Measurements

Calculating the distribution of the overall sound power, OAPWL, from the measured PWL requires that the interaction noise be eliminated. For x/D less than 6, the low frequency noise was assumed to be that of the undisturbed case, x/D = 0; for x/D greater than 6, the low frequency portion were assumed to be of similar shape as the x/D = 0 case, but at a lower level. Computing the OAPWL in this manner yields the cumulative axial distribution shown in Figure 8-69. A simple numerical differencing scheme was used to determine axial distribution of overall sound shown in Figure 8-70. The location of the peak of the sound distribution between 6-8 diameters agrees well with McGregor and Simcox (Reference 60) heated-jet data, but the shape of the curve is quite different.

To define the location of a source of a given frequency, a similar procedure is used as followed for the overall power. For frequencies above 5 kHz, the method is free of the interaction noise contamination. For the 1-inch convergent jet, the decrease of sound power in various 1/3-octave bands with axial distance is shown in Figure 8-71. In Figure 8-72, the peak contributions at high frequencies are found to be close to the jet exit in agreement with other hole-in-the-wall experiments and other types of source location methods.

This hole-in-the-wall method was also applied to 2-inch convergent jets, but due to the limitation on physical size of the chamber and aperture, the jet could only be surveyed to 10 diameters. Similar trends as those in the one inch jet were observed, as shown in Figure 8-73. Since the data were limited, the source distribution of overall acoustic power was not carried out. For the higher frequencies, the source distributions were calculated and are shown in Figure 8-74. The trends observed with this two-inch jet are similar to the one-inch jet, with reasonable agreement on the location of peaks and shape when the Strouhal number is matched. Figure 8-75 shows the distribution of the peaks at each frequency with the jet. Excellent agreement with the other techniques is observed.

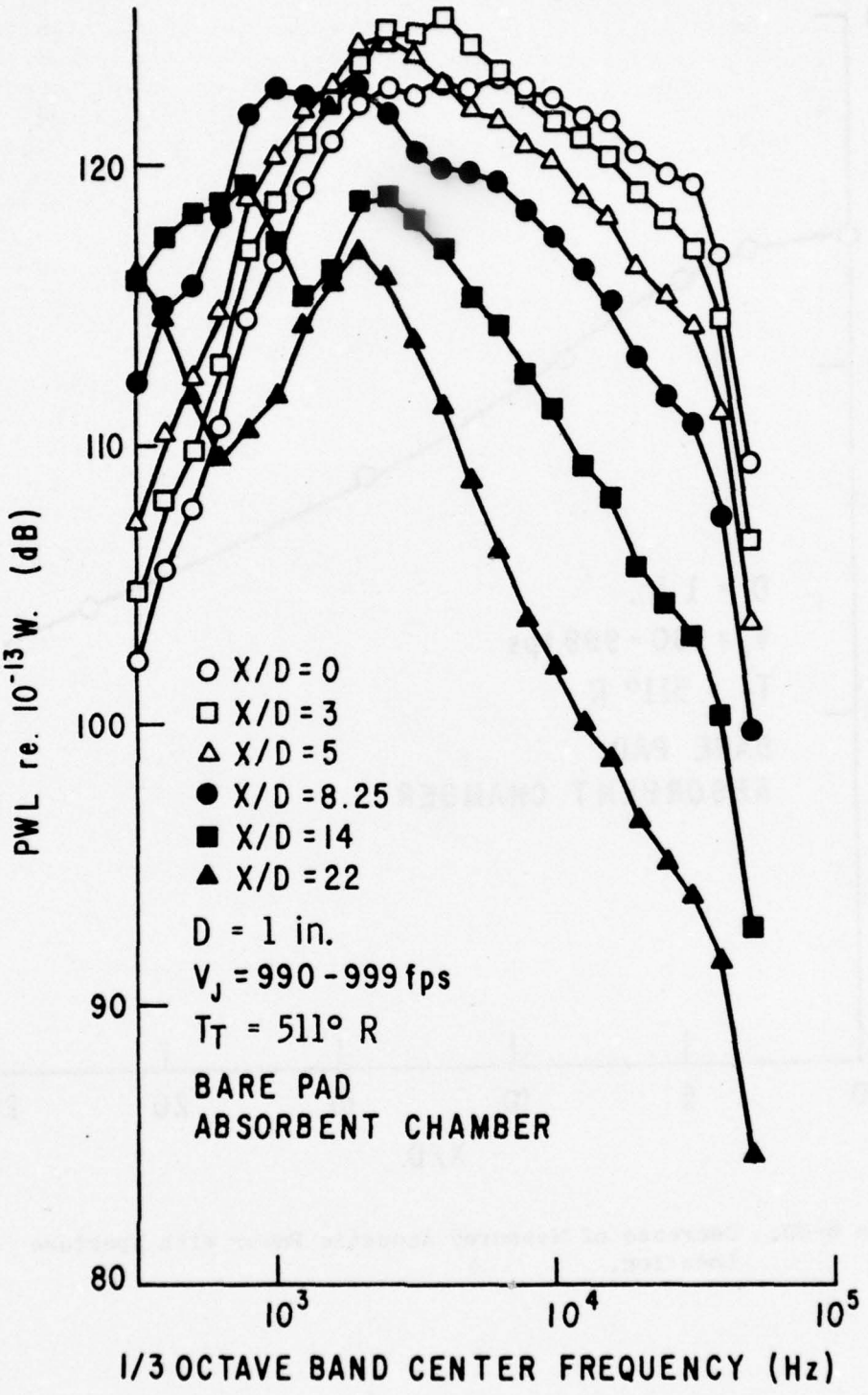


Figure 8-68. Power Spectra as a Function of Aperture Location, 1-inch Jet.

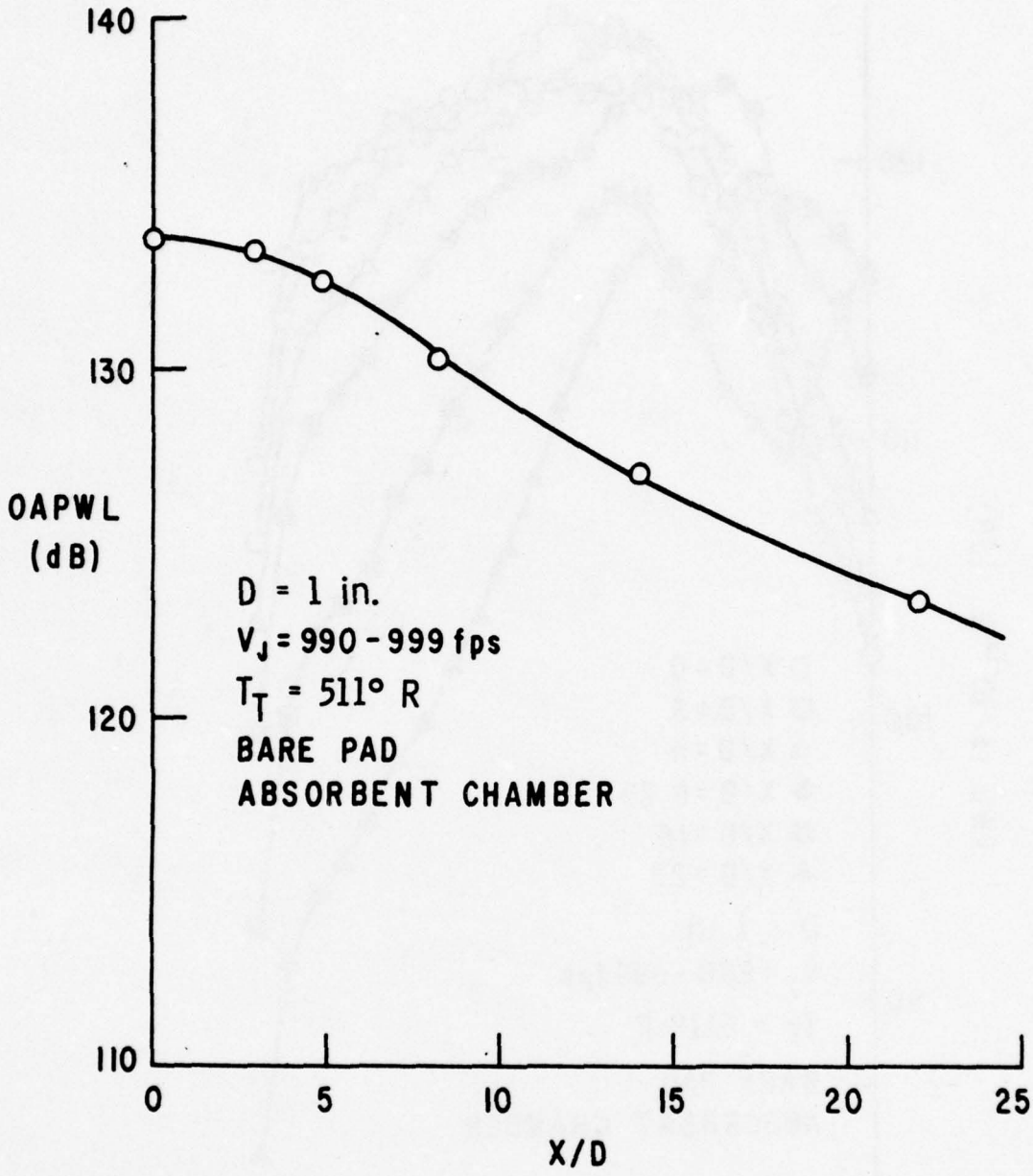


Figure 8-69. Decrease of Measured Acoustic Power with Aperture Location.

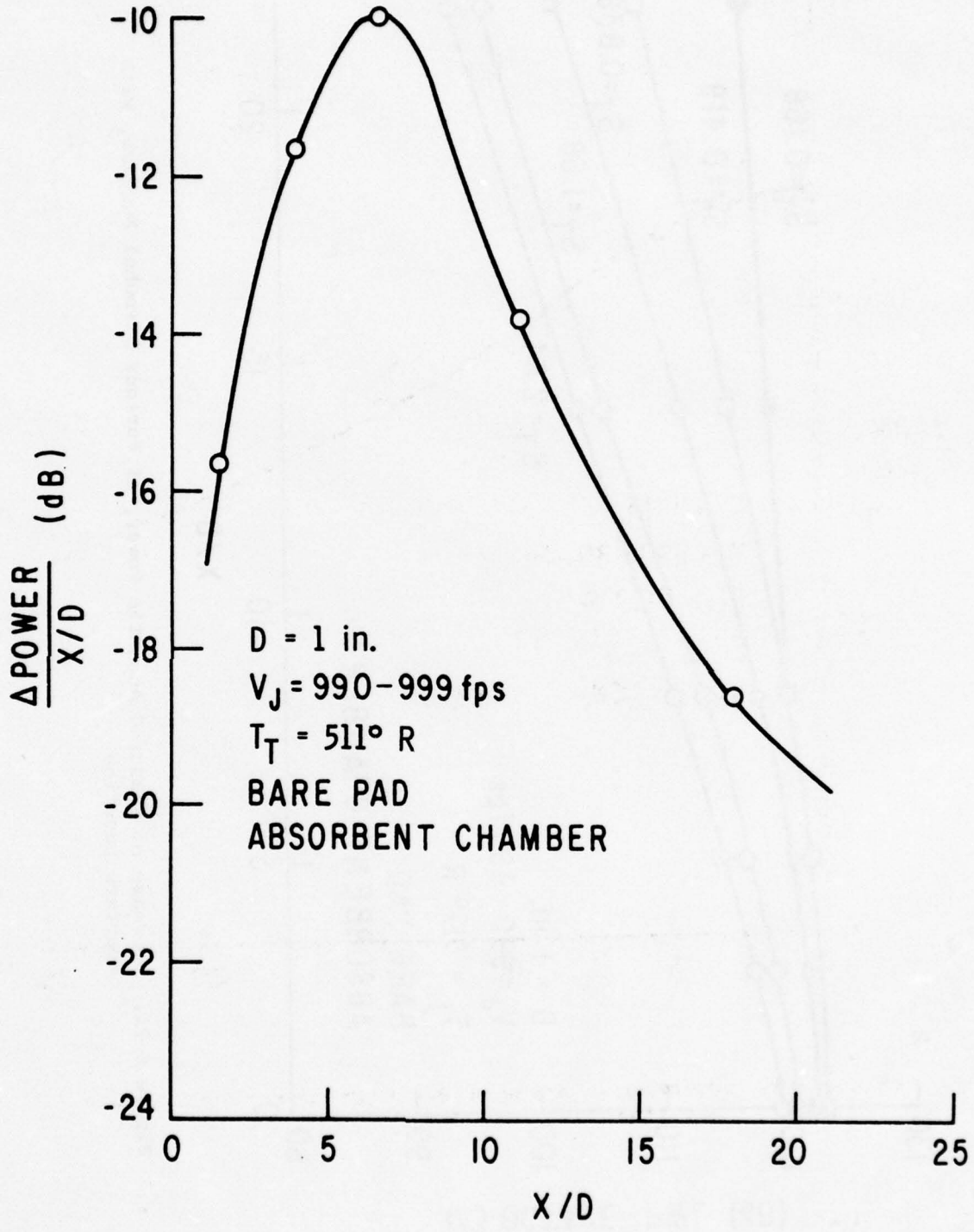


Figure 8-70. Axial Source Distribution (Percent OAPWL Versus X/D).

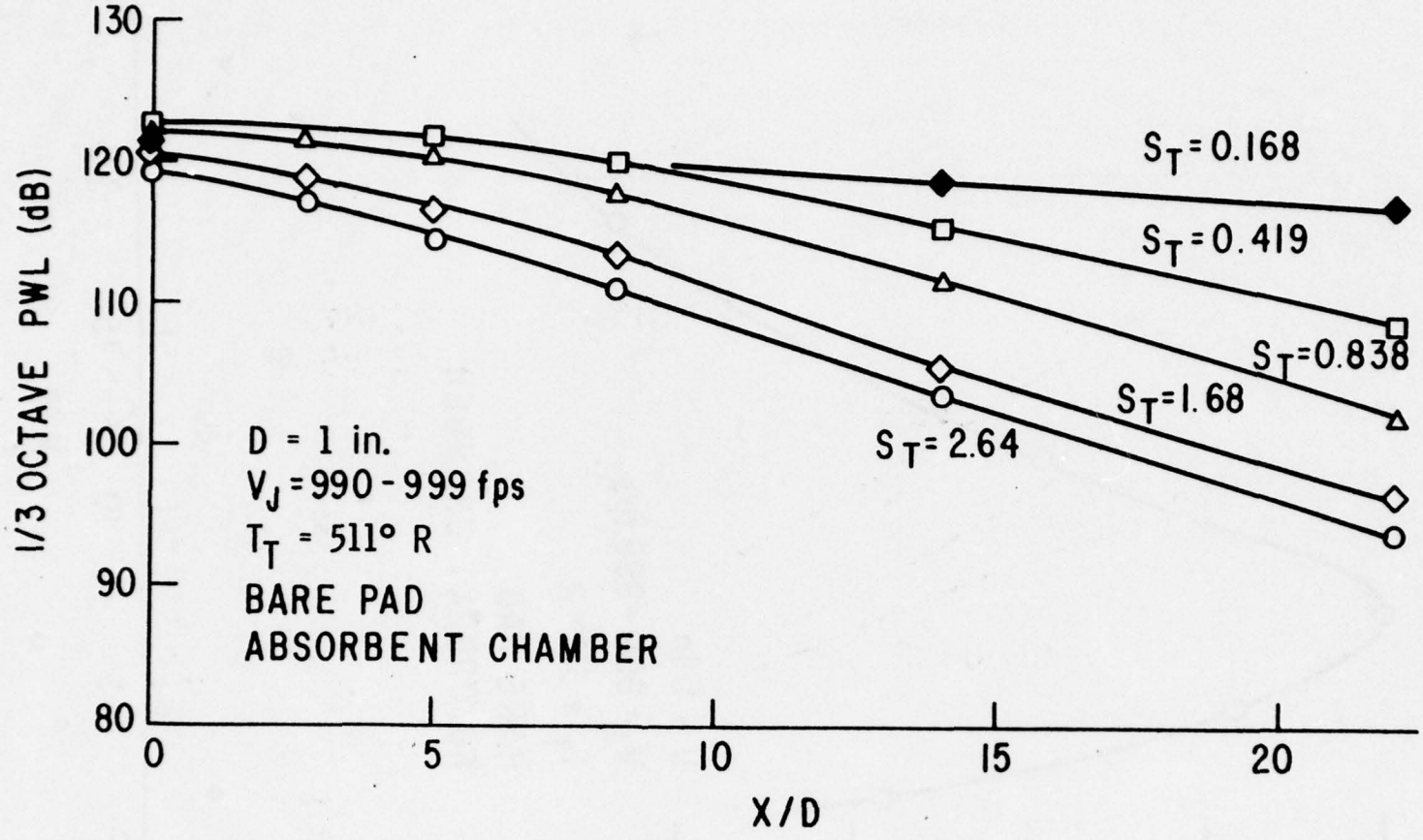


Figure 8-71. Decrease of Measured Acoustic Power, at Various Strouhal Numbers, with Aperture Location

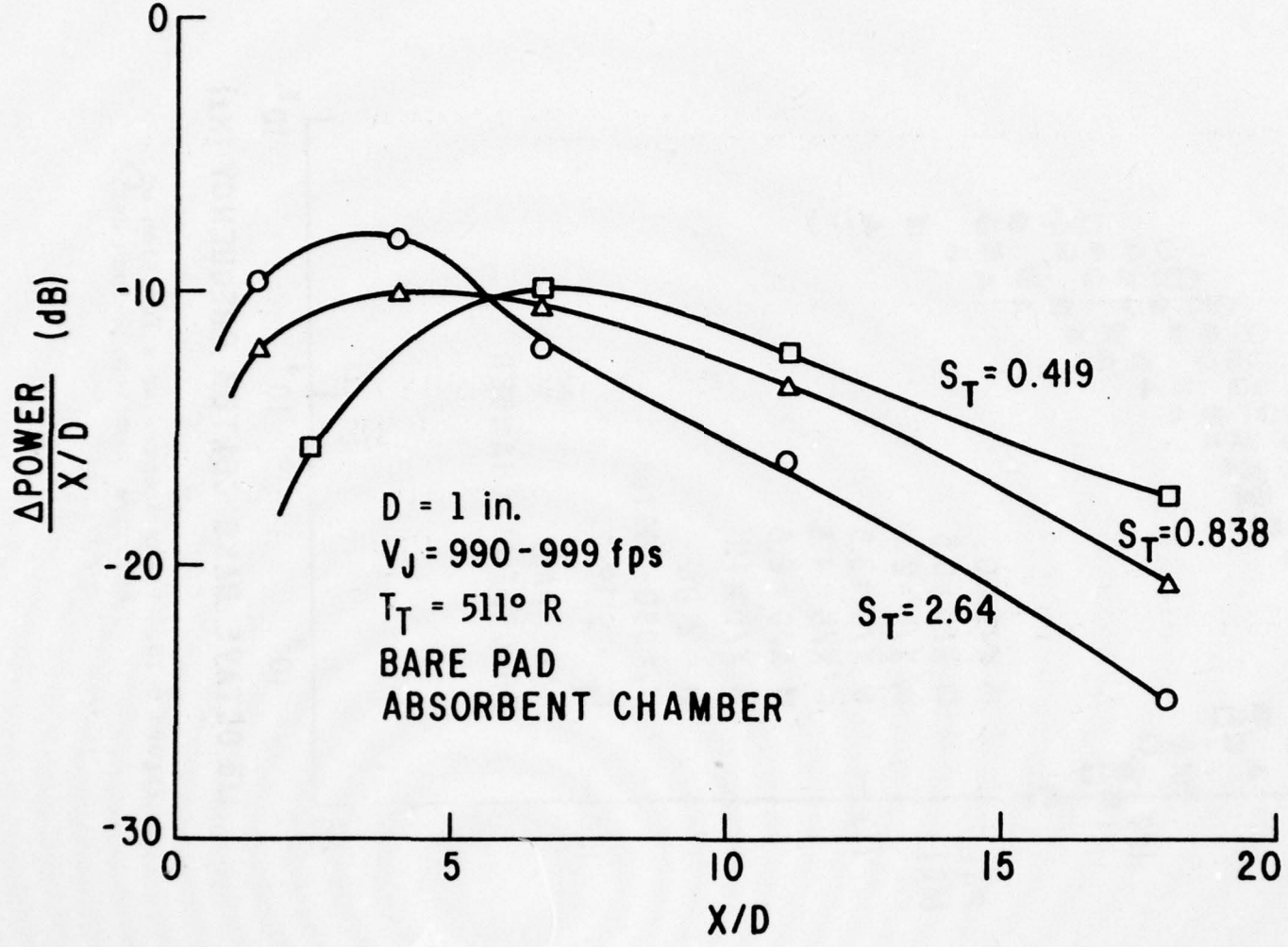


Figure 8-72. Axial Source Distribution at Various Strouhal Numbers, 1-inch Jet.

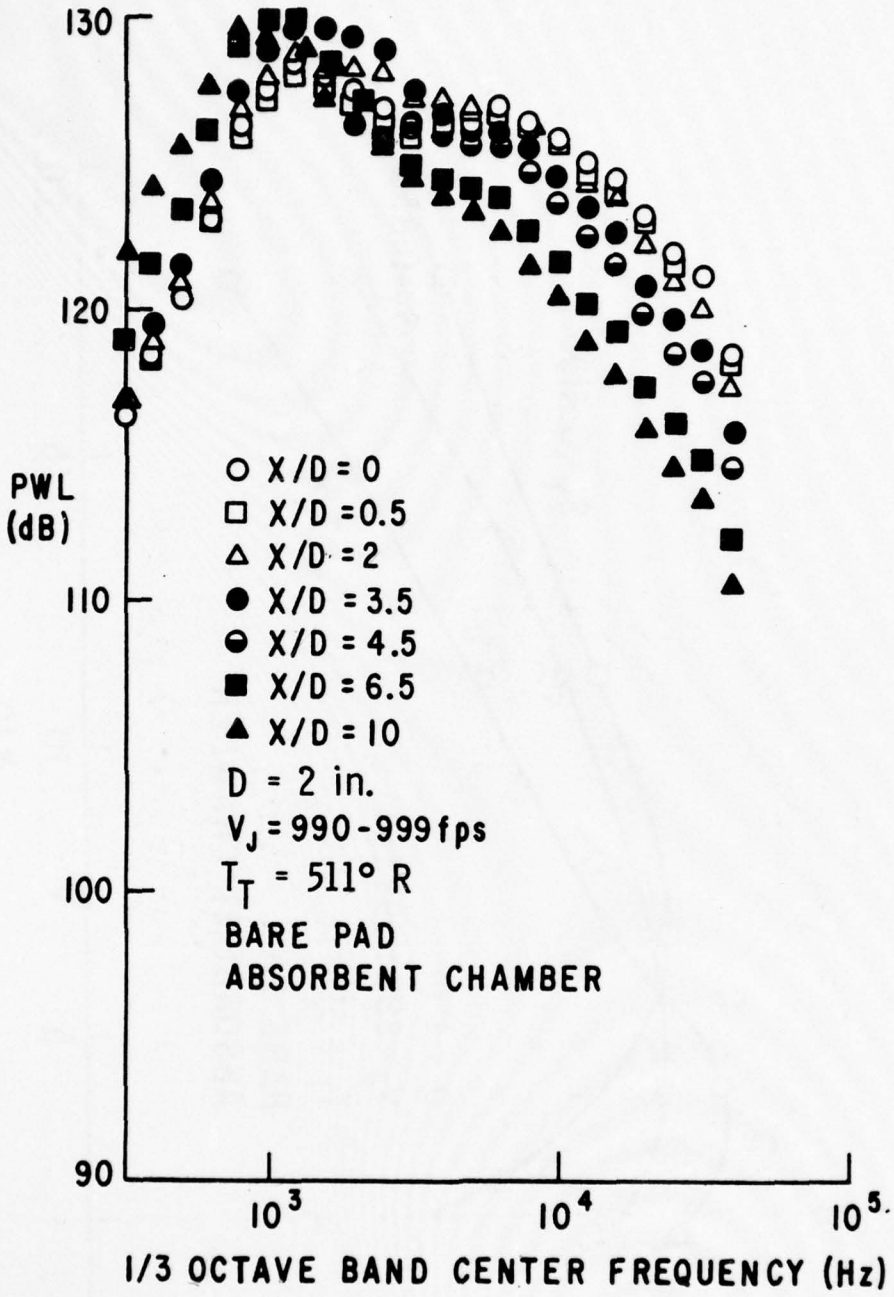


Figure 8-73. Power Spectra as a Function of Aperture Location, 2-inch Jet.

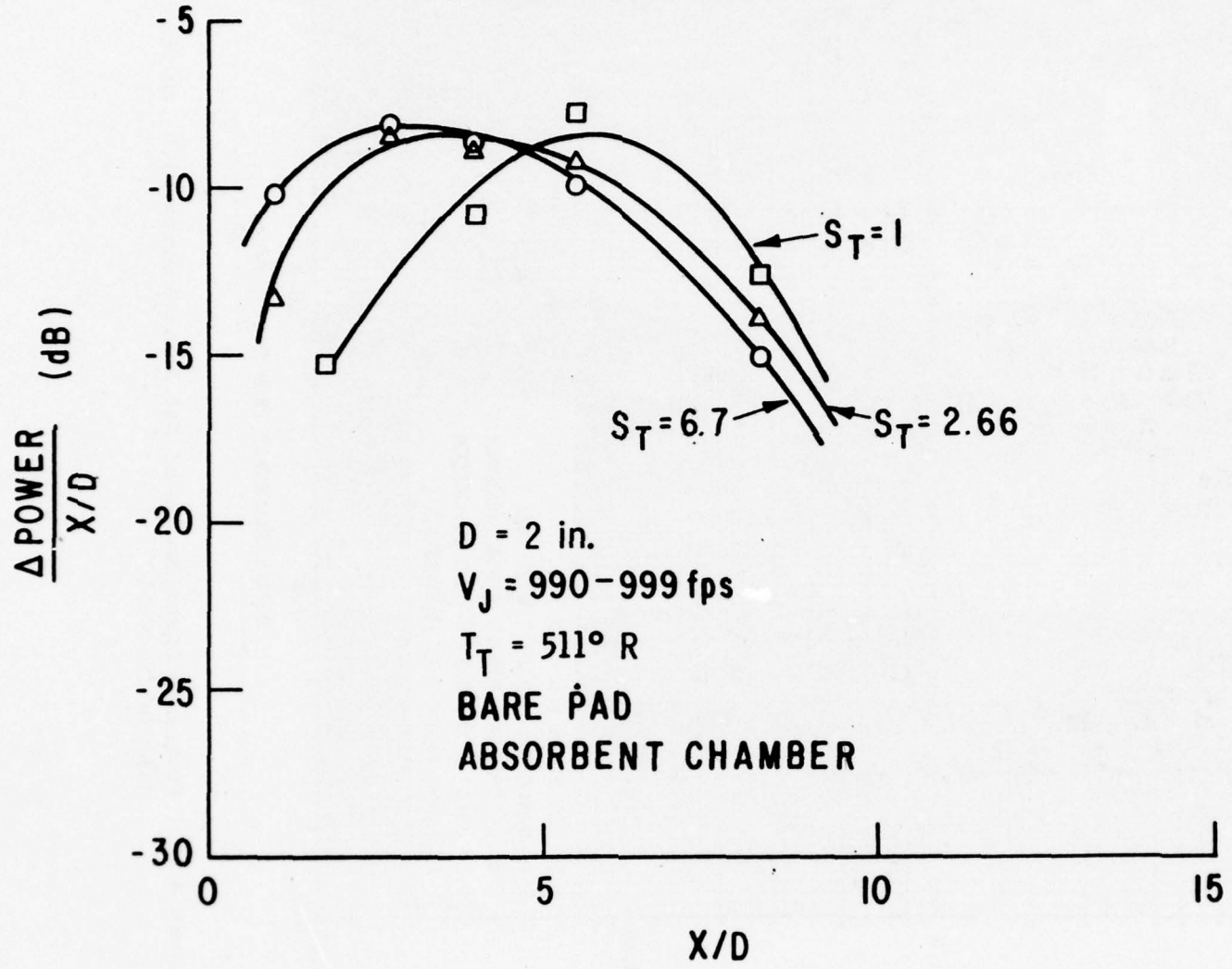


Figure 8-74. Axial Source Distribution at Various Strouhal Numbers, 2-inch Jet.

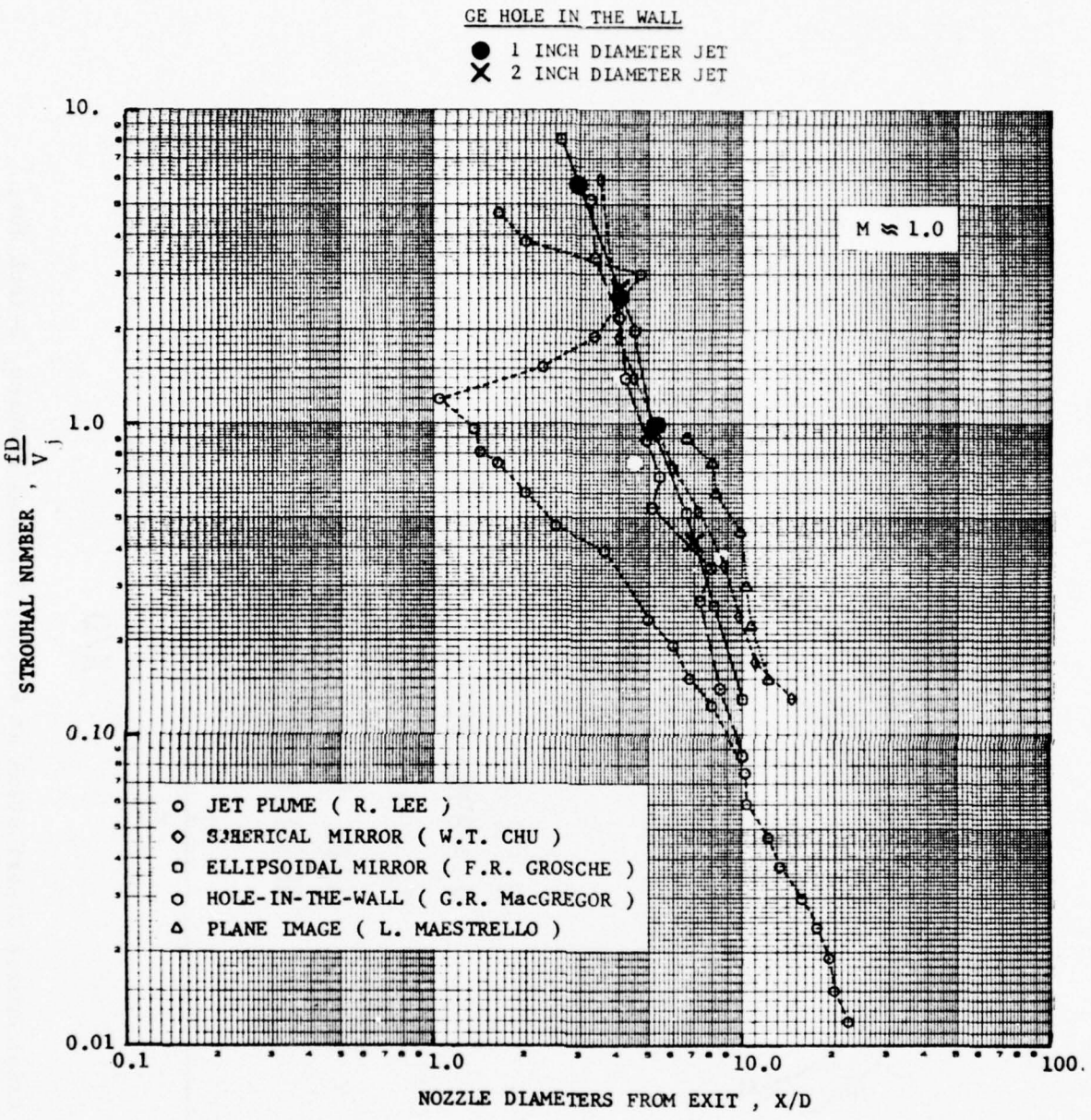


Figure 8-75. Frequency Distribution of Jet Noise Sources with the GE Hole in the Wall.

8.6.3 Conclusions and Recommendations

Based on the previous analysis the following conclusions are drawn:

- The technique is better suited for the higher frequency measurements.
- Jet suppressors with geometries other than circular or rectangular will cause problems with the construction of the aperture.
- The technique does not require any additional measurement equipment.
- The source location results using this method are in reasonable agreement with data of McGregor and Simcox (Reference 60) and the trends exhibited follow currently held opinions on the nature of the axial source distribution.

As a result of these experimental studies the "hole in the wall" was considered an acceptable alternative source location technique and could be used in the remainder of the program as required.

8.7 ELLIPSOIDAL MIRROR MICROPHONES

The use of curved surfaces to concentrate sound has been known and applied in architectural design since the early renaissance. Development of reflector designs incorporating a microphone at the focus was initiated in World War I for anti-aircraft location and extended into Hollywood sound booms and radio broadcasting. The first application of the technique for jet noise source location appears to be the work of Grosche of DFVLR in West Germany (Reference 97) who used a spherical dish to map the sound field. Chu of USC (Reference 65) developed the technique further with a spherical design. Recently, Grosche (Reference 66) incorporated a large ellipsoidal design which needed to be swung to two positions to collect the total power radiating from the neighborhood of a point.

8.7.1 Operating Principles

The purpose of using an ellipsoidal-shaped dish as the direction microphone was to theoretically resolve a "point" of noise on to the microphone. The ellipse has the remarkable property that the tangent at any point makes equal angles to the focal radii drawn to that point, so that if the focal radii were straight line acoustic rays and the tangent line were a mirror, the angle of incidence would equal the angle of reflection, and the law of reflection would be satisfied at all points on the ellipse. Therefore, all rays of Figure 8-76a from a point source at F_1 would be reflected to the focal point F_2, and conversely all rays in the plane of the figure from a point source at F_2 would be collected at the focal point F_1. These statements

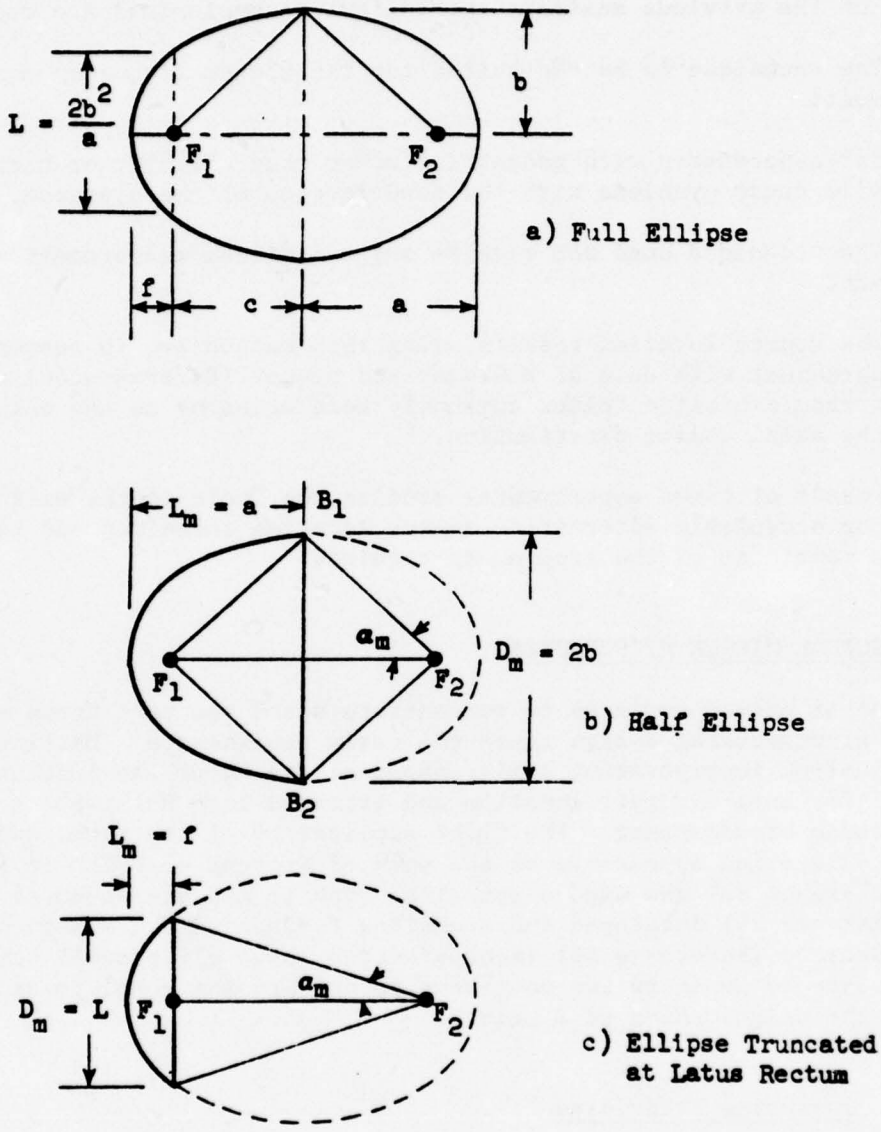


Figure 8-76. Ellipsoidal Mirror Geometry.

are true only if the entire ellipse is employed as in Figure 8-76a. If only the segment of the ellipse to the left of the minor axis is used as in Figure 8-76b all the rays from F_2 outside the angle B_1 F_1 B_2 ($2\alpha_m$) are lost. If the segment of the ellipse left of the latus rectum is used, sound outside the aperture angle $2\alpha_m$ is lost as shown in Figure 8-76c.

The configuration of a prolate ellipsoidal reflector is, thus, determined by three parameters: the primary focal length, f, the working distance, and the aperture, α_m.

These parameters are related through the geometry of the ellipse. Referring to Figure 8-76, the equation for an ellipse is given by:

$$\left(\frac{x}{a}\right)^2 + \left(\frac{y}{b}\right)^2 = 1 \tag{212}$$

The primary focal length is given by:

$$f = a - c \tag{213}$$

for an ellipse with a working distance of 2c.

The latus rectum by:

$$L = \frac{2b^2}{a} \tag{214}$$

The eccentricity by:

$$e = \frac{c}{a} \tag{215}$$

The aperture angle of a truncated ellipsoid of length L_m and diameter D_m is given by:

$$\alpha_m = \text{Tan}^{-1}\left[\frac{D_m}{2(C + a - L_m)}\right] \tag{216}$$

The idealized principles discussed above are all based on the assumption that sound travels along straight line rays in small bundles. This is approximately true at high frequency. At low frequencies, however, the wave characteristics of acoustics take over and wave diffraction comes into play.

The precise mathematical description of the diffraction pattern from an ellipsoidal dish is quite complicated. An analogy, however, can be drawn to the simple problem of the diffraction of plane waves at two-dimensional aperture of width D as shown in Figure 8-77a. In Figure 8-77b, angle θ indicates the angular distribution of the intensity at a distance from the center of the slit. The response Q of an omni-direction source of strength I_o dominated by diffraction can be described by:

$$Q(r,\theta) = \frac{I_o}{4\pi r^2} G H(r,\theta) \tag{217}$$

where G is the gain and H is the directional characteristic of the system referred to as the window function.

The window function for the diffraction by a slit in Figure 8-77a is obtained from the net integrated mean square displacement at the far-field point (r, θ), Figure 8-77b, due to the variation in phase of the sound across the slit width.

$$H(r,\theta) = \left[\frac{r}{D}\,\overline{y}\right]^2 \tag{218}$$

The displacement y at a point P will vary with position S in the slit because of these phase differences. From Figure 8-77b,

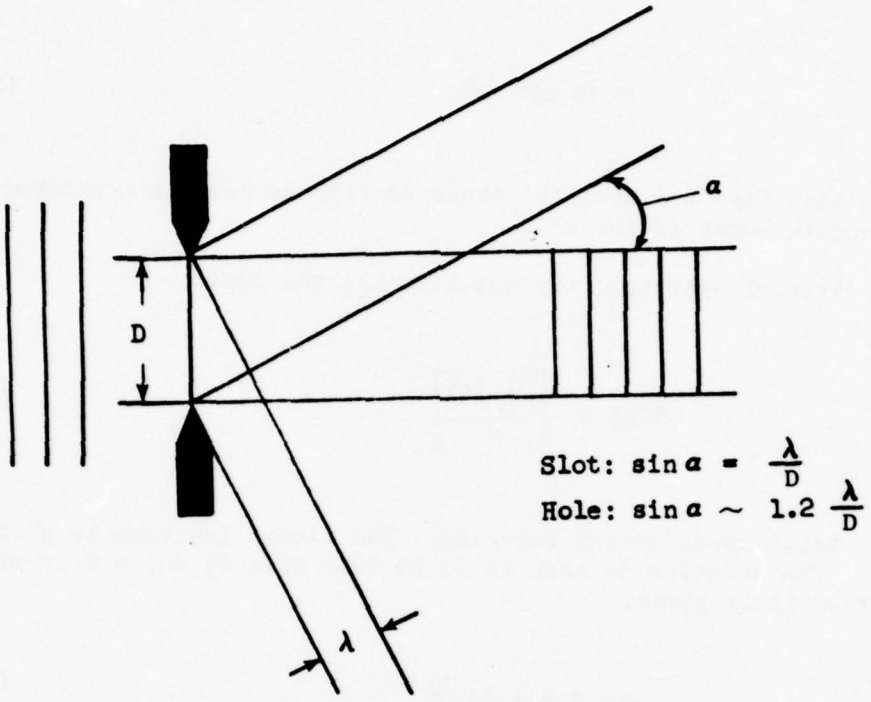
$$dy = \frac{ds}{r} \sin\left[\omega t - k(r - s \sin\theta)\right] \tag{219}$$

Integrating across the slit yields

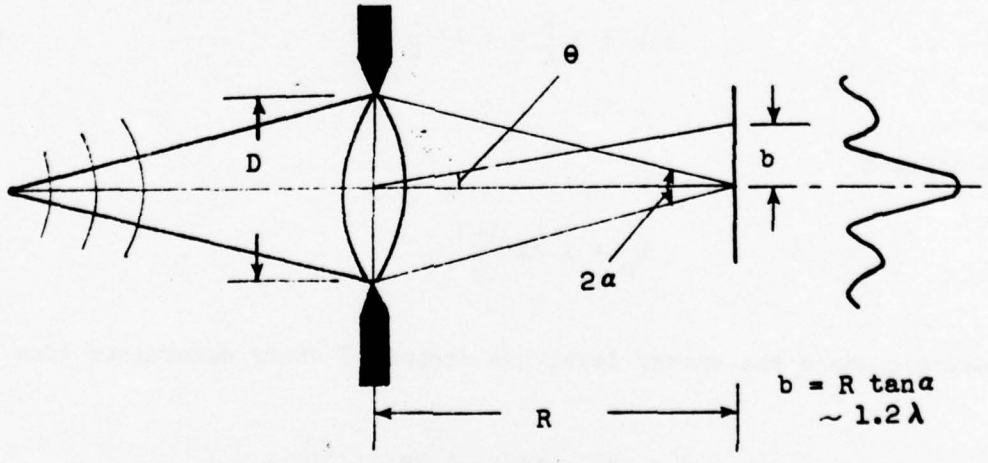
$$y = \frac{D}{r} \frac{\sin\eta}{\eta} \sin(\omega t - kr) \tag{220}$$

so

$$H(r,\theta) \left[\frac{\overline{ry}}{D}\right]^2 = \left[\frac{\sin\eta}{\eta}\right]^2 \tag{221}$$



a) Diffraction of plane waves



b) Diffraction at the edges of a focussing device

Figure 8-77. Diffraction of the Ellipsoidal Mirror.

where

$$\eta = \pi D \sin \theta / \lambda \tag{222}$$

The parameter η signifies one half the phase difference between contributions coming from opposite edges of the slit.

In the case of circular aperture, the solution has the form:

$$H(\eta) = \left[\frac{2J_1(\eta)}{\eta}\right]^2 \tag{223}$$

where J_1 is the first order Bessel function. The window function is plotted in Figure 8-78. The solution is seen to go to zero when $J_1(\eta) = 0$ or at $\eta = 3.8317$ so Equation (222) gives:

$$\sin \theta = 1.22 \frac{\lambda}{D} \tag{224}$$

At some distance r from the aperture, the displacement h to the first minimum can be obtained.

$$\sin \theta \simeq \frac{h}{r} = 1.22 \frac{\lambda}{D} \tag{225}$$

so one expects

$$h_o = 1.22 \frac{\lambda r}{D} \tag{226}$$

The location where the energy level has dropped 3 dB is determined from

$$\Delta = 3\text{dB} = 10 \log_{10}(H(\eta)/H(0)) \tag{227}$$

or where

$$H(\eta)/H(0) = 0.5$$

Note that $H(0) = 1.0$ from Figure 8-78.

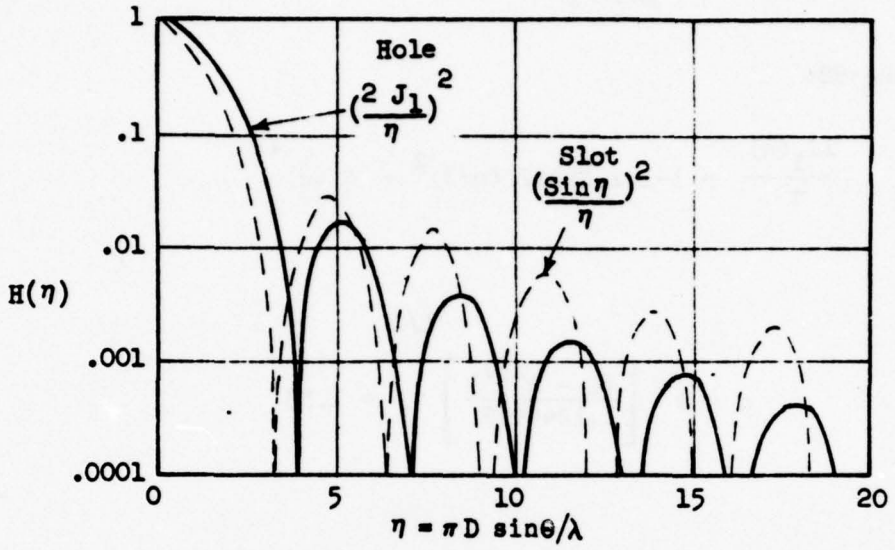


Figure 8-78. Fraunhaufer Diffraction Patterns for a Slot and Hole.

so

$$\frac{2J(\eta)}{\eta} = \left[\frac{H(\eta)}{H(0)}\right]^{1/2} = \sqrt{0.5} = 0.7071 \tag{228}$$

From Reference 98:

$$\frac{2J_1(\eta)}{\eta} = 1-1.1249997\ (\eta/3)^2 + \sigma\ (\frac{\eta}{3})^4 \tag{229}$$

so

$$\eta = 3\ \left[\frac{(1 - H^{1/2})}{1.1249999}\right]^{1/2} = 1.53 \tag{230}$$

therefore

$$h_{3dB} = 0.487\ \left(\frac{\lambda r}{D}\right) \tag{231}$$

The gain is defined by

$$G = \frac{I_M}{I_{FF}} \tag{232}$$

with I_m being the sound intensity measured by the diffraction image of the point source of sound and I_{FF} being the intensity measured by a microphone in the free field at the same distance from the source. One expects G to vary inversely proportional to the area of the diffraction image which is proportional to λ^2, according to Equation (221) for H

$$G \sim \frac{1}{\lambda^2} \sim f_n^2 \tag{233}$$

The exact solution to the sound pressure created in the focal plane by a wave reflected from the walls of an ellipsoidal mirror is determined according to Rosenberg (Reference 99) by the expression

$$p(y,f) = P_o kFE \int_0^{\alpha m} I_o(kg \sin\alpha) \left[\frac{1 + \tan^2(\alpha/2) \sin\alpha}{1 + E^2 \tan^2(\alpha/2)} \right] d\alpha \qquad (234)$$

where y = instantaneous coordinate in a plane perpendicular to the axis of revolution of the concentrator.

$k = 2\pi/\lambda$

λ = wave length

$F = a - c$

$E = \frac{1 + e}{1 - e}$

$e = c/a$ = eccentricity of the ellipse

J_o = zeroth order Bessel function of the first kind

α_m = aperture angle of the concentrator

This relation shows that both the window function and the gain of an ellipsoidal mirror have a complicated frequency dependence through the term "kFE" beyond the simple "ky" dependence found for Fraunhaufer diffraction.

In References 100 and 101, Williams has devised numerical prediction procedures for the three-dimensional collection volume (i.e., window function) for any shape reflector.

All these theoretical analyses only approximate the values of actual window function and gain. In Reference 102, Borisov and Gynkina compared the experimentally measured window and gain from 13 ellipsoidal mirror designs to the predicted values using Rosenberg's equation above. Their results are reproduced in Table 8-II. Generally, the experimentally measured window was significantly narrower than the theoretical prediction, particularly for eccentricities >0.85.

8.7.2 Mirror Designs

Three ellipsoidal mirror microphone designs were constructed as part of Task 1 of the High Velocity Jet Noise Program. The first was a small, 14-

Table 8-II. Experimental Study of Ellipsoidal Mirrors.

(from Reference 102)

e	a	b	c	F = a-c	α°	f = 19.5 KHz							f = 14 KHz								
	mm					F/λ	G_{P_T}	G_{P_E}	$\frac{G_{P_T}}{G_{P_E}}$	h_T	h_E	h_T/h_E	F/λ	G_{P_T}	G_{P_E}	$\frac{G_{P_T}}{G_{P_E}}$	h_T	h_E	h_T/h_E	P_{max_T}	P_{max_E}
										mm							mm			dB	
0.2	100	98	20	80	90	4.7	17.6	14.3	1.23	17.8	18.1	0.08	3.15	12.5	11.1	1.12	25.6	26.1	0.98	183.1	180
					180		29.8	20.5	1.45	17.6	16	1.1									
					60		20.3	22.2	0.93	24.8	24.6	1.01		14.3	17.8	0.8	35	33.2	1.09	180	179.5
0.5	66	57.2	33	33	90	1.7	29.8	28.4	1.05	20.4	21.3	0.96	1.43	21.2	28.6	0.9	28.8	29.1	0.99	183.4	181.5
					180		40.6	34.4	1.18	19.6	16.6	1.18		29	27.5	1.05	27.6	26	1.06	186	183.5
					43.6		21.2	17.2	1.23	40	38.4	1.04		15.2	16.8	0.09		*		177.3	176.5
0.72	65.3	55	47.3	18	90	1.01	35	31.4	1.12	30	21.8	1.38	0.78	24.7	18.8	1.47	42	44	0.96	181.7	176.5
					180		42.4	41.5	1.02	28.8	20.4	1.41		30.5	28.4	1.07				183.3	181.3
					31.6		51.2	18.3	2.86	36	*	1.38		36.2	8	4.5				173.5	166
0.85	100	105	170	30	180	1.66	104.2	61.4	1.7		26		1.29	74.2	27	2.75				180	176.5
					22		29.6	20.3	1.45		*			20.4	17	1.2		*		170	167
0.92	162	80	149	13	90	0.72	53	64	0.83	32	18	1.78	0.56	37.9	53	0.72	44	*		175	177
					180		59.2	84	0.71	32	15.3	2.1		42.5	75	0.57	40	30	1.33	176.5	180

* The diameter of the focal spot cannot be determined, due to the absence of a distinct minimum on the experimental curves.

inch-diameter, deep-dish cut at the minor axis with a 10.66-inch working distance for laboratory work, Figure 8-79. The second was an 18-inch-diameter, shallow-dish cut at the latus rectum with a 9-foot working distance for jet noise testing at JENOTS, Figure 8-80. The last was a 36-inch-diameter, deep-dish cut with a 15-foot working distance, Figure 8-81 for future noise source location work in the subsequent tasks of the Program. At the time of this report, the 36-inch-diameter mirror had been fabricated and was undergoing calibration. The calibration was done in Task 3 and will be reported as part of the Task 3 effort. Table 8-III shows the design parameters for the three dishes.

8.7.3 Calibration of the Mirrors

The first mirror to be fabricated and tested was the small laboratory model. Calibration was conducted using an Altec 100 W horn driver with tubes and couplers to reduce the output to 1/4-inch tube representing a point source, as shown in Figure 8-82. The mirror was mounted on a track system to translate past the point source. The Altec output was located at one focus and the mirror was oriented with its face parallel to the tracks for a mapping of the window function in a plane passing through the focus. The experiment was repeated with the source off the focus to measure the axial depth of the three-dimensional collection volume. Measurements were taken over a range of frequencies to 20 kHz. The result was a tear-shape collection volume with a 3 dB down diameter approximately 0.8λ, as shown in Figure 8-83. The gain increased at nearly 6 dB per octave, as shown in Figure 8-84.

With these encouraging results, the second 18-inch-diameter shallow dish was constructed for testing on the JENOTS jet facility. Calibration was conducted outdoors because of the 9-foot working distance of the mirror and to ensure that there would be no reflection in the plane of measurement. The Altec driver source and the microphone were mounted 6 feet 4 inches above the ground with the mirror on a rotary actuator, as shown in Figure 8-85, with the microphone at the pivot point. Window function mapping was then obtained by sweeping the mirror face past the point source and plotting the data versus angle. A reference microphone for gain calibration was located an equal distance from the source as the mirror microphone out of the field of rotation.

The results of the calibration are shown in Figures 8-86 through 8-88. The shallow mirror was found to have a much wider window function than the first mirror. The 3 dB down width ($2h_{3dB}$) was on the order of 6.7λ, which was somewhat larger than the 5.844λ estimated from the Fraunhaufer Equation (231). The estimated and measured values from the two mirrors are shown in Table 8-IV. From the Table, we see that a slight reduction in the window width is expected with the new deep-dish design. Significant deviation from the Fraunhaufer shape of the window occurred with the 18-inch reflector, as seen in Figure 8-86. The frequency dependent windows expected from Rosenberg's equation were measured.

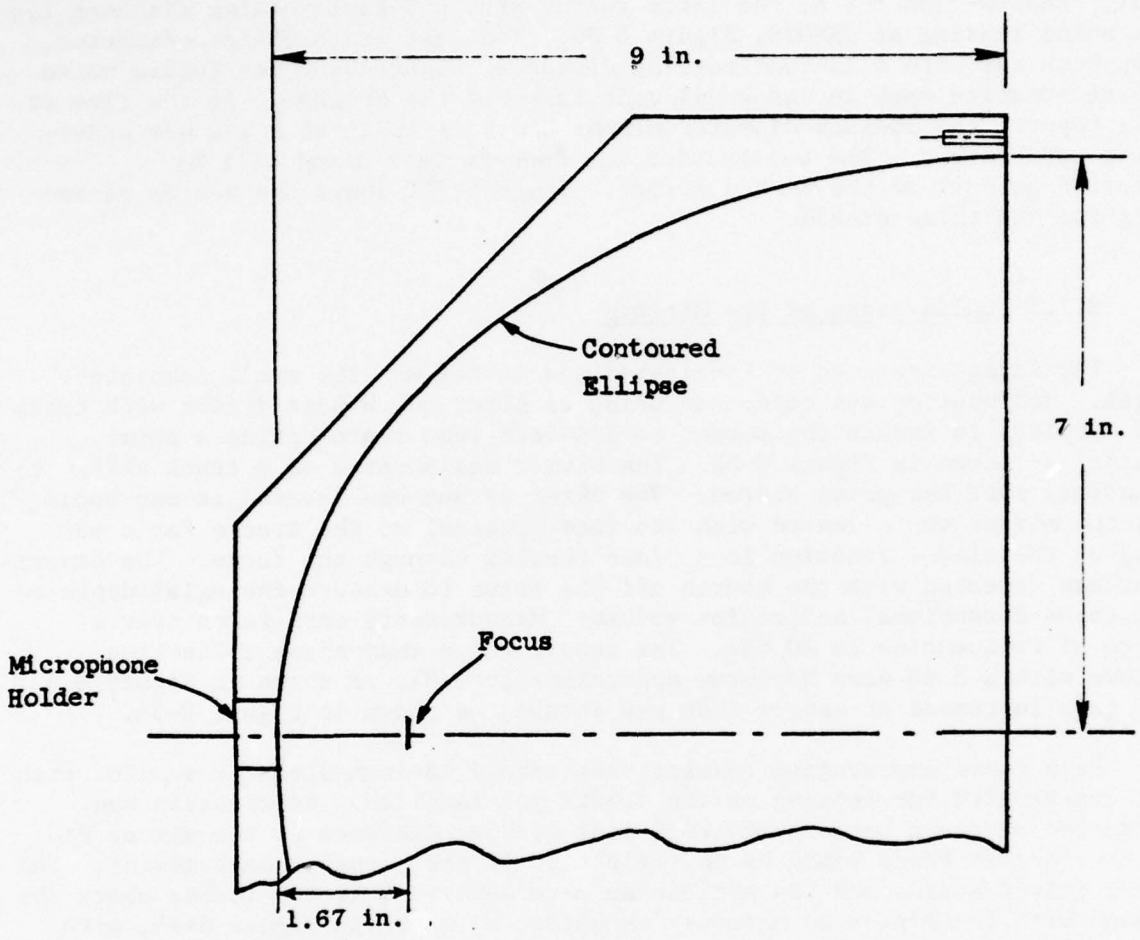


Figure 8-79. 14-inch-Diameter Deep-Dish EM with 10.66-inch Working Distance.

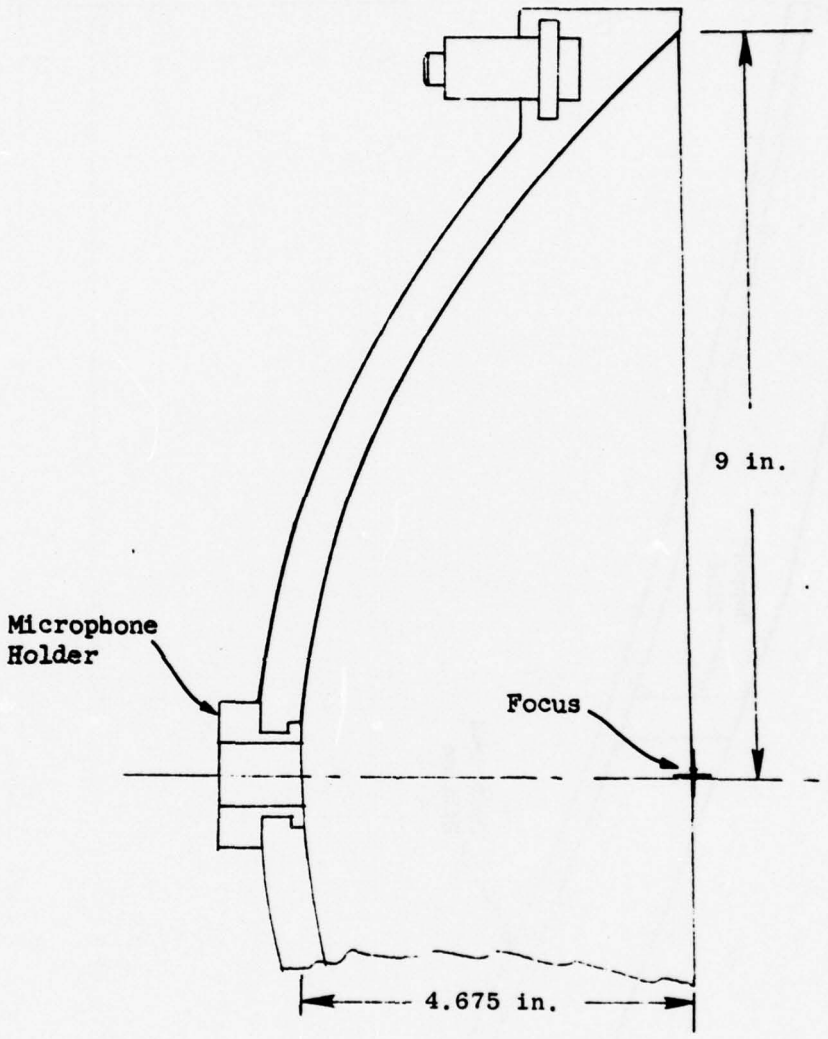


Figure 8-80. 18-inch-Diameter Shallow-Dish EM with 9-foot Working Distance.

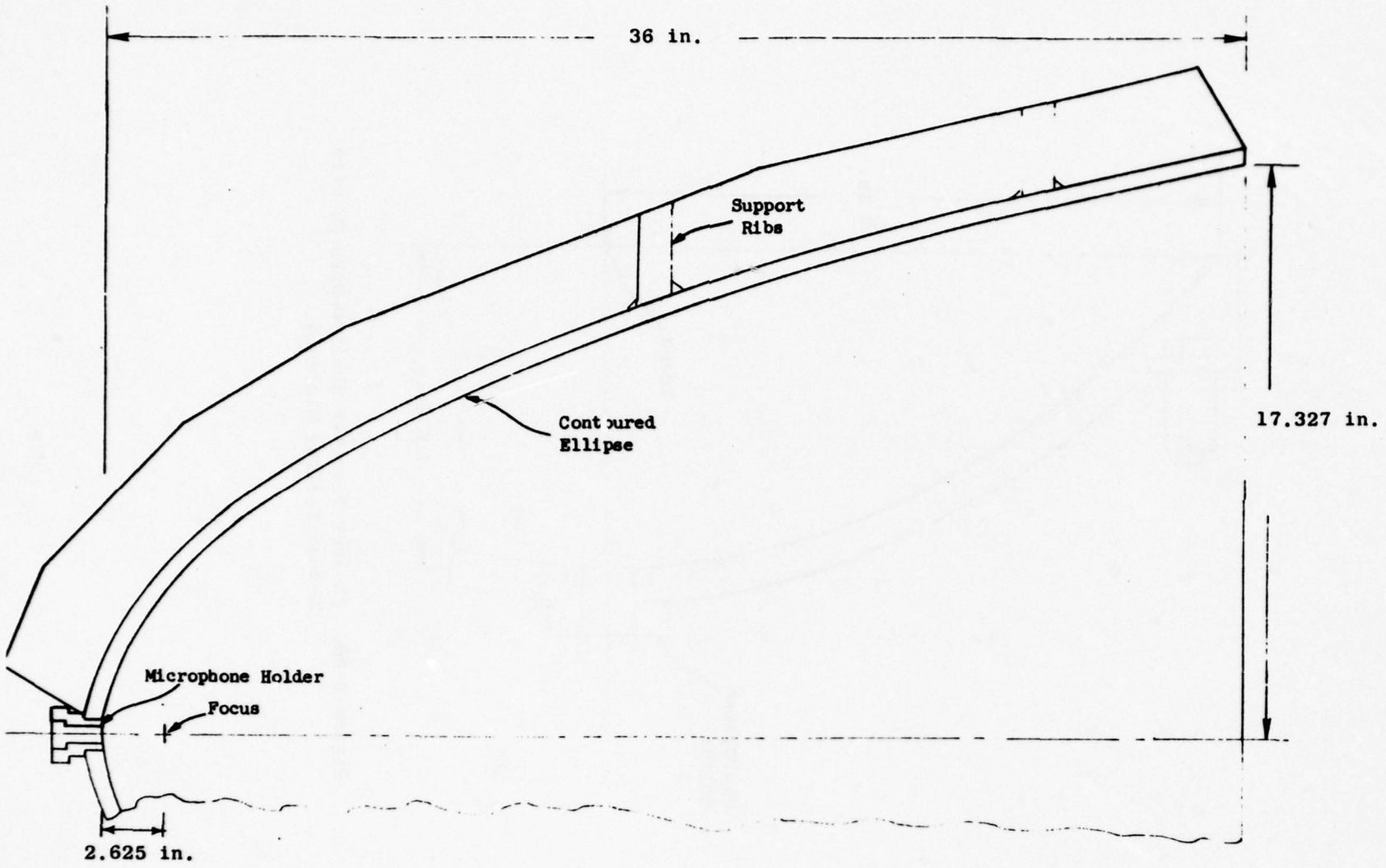


Figure 8-81. 36-inch-Diameter Deep-Dish EM with 15-foot Working Distance.

Table 8-III. Design Parameters of Ellipsoidal Mirrors.

- Air Length Dimensions in Inches

Mirror	Major Semi-Axis a	Minor Semi-Axis b	Half Working Distance c	Focal Length F	Eccentricity e	Latus Rectum L	Mirror Diameter D_m	Mirror Length L_m	Mirror Aperture α_m
1	9.0	7.0	5.33	1.67	0.592	5.444	14.0	9.0	52°42'
2	58.675	22.983	54.0	4.675	0.92	18.0	18.0	4.675	4°46'
3	92.625	21.895	90.0	2.625	0.971	10.35	34.654	36.0	6°44'

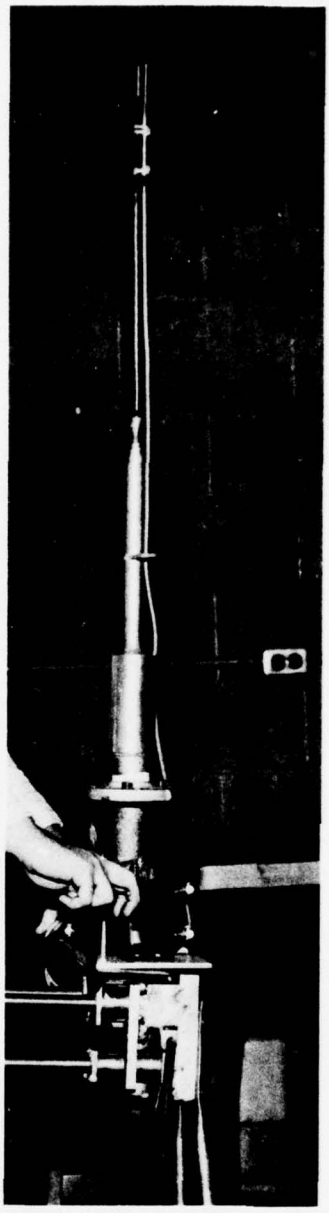


Figure 8-82. Altec Driver.

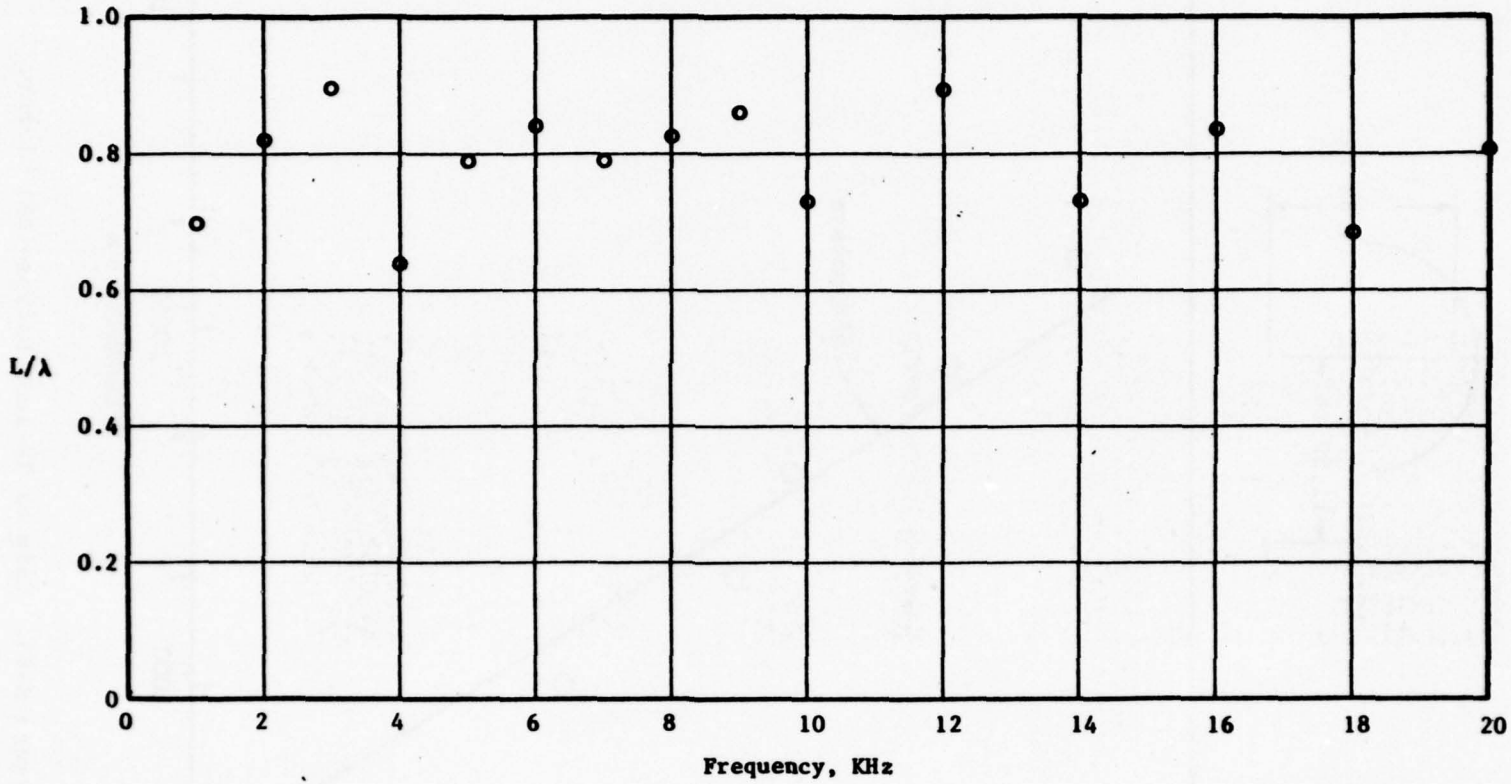


Figure 8-83. Resolution Window Width (3 dB Down) for 14-inch Ellipsoidal Mirror.

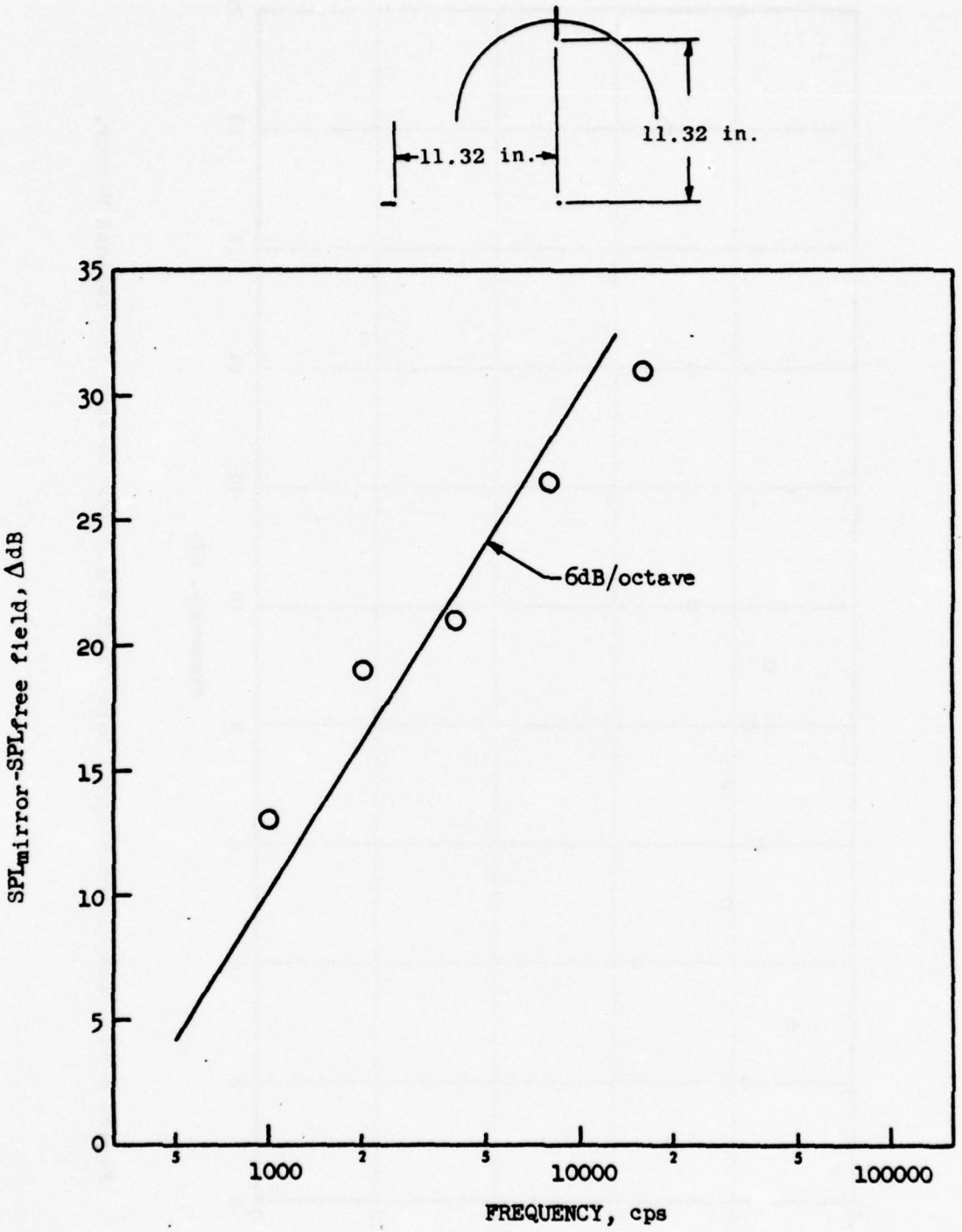


Figure 8-84. Gain of 14-inch Ellipsoidal Mirror.

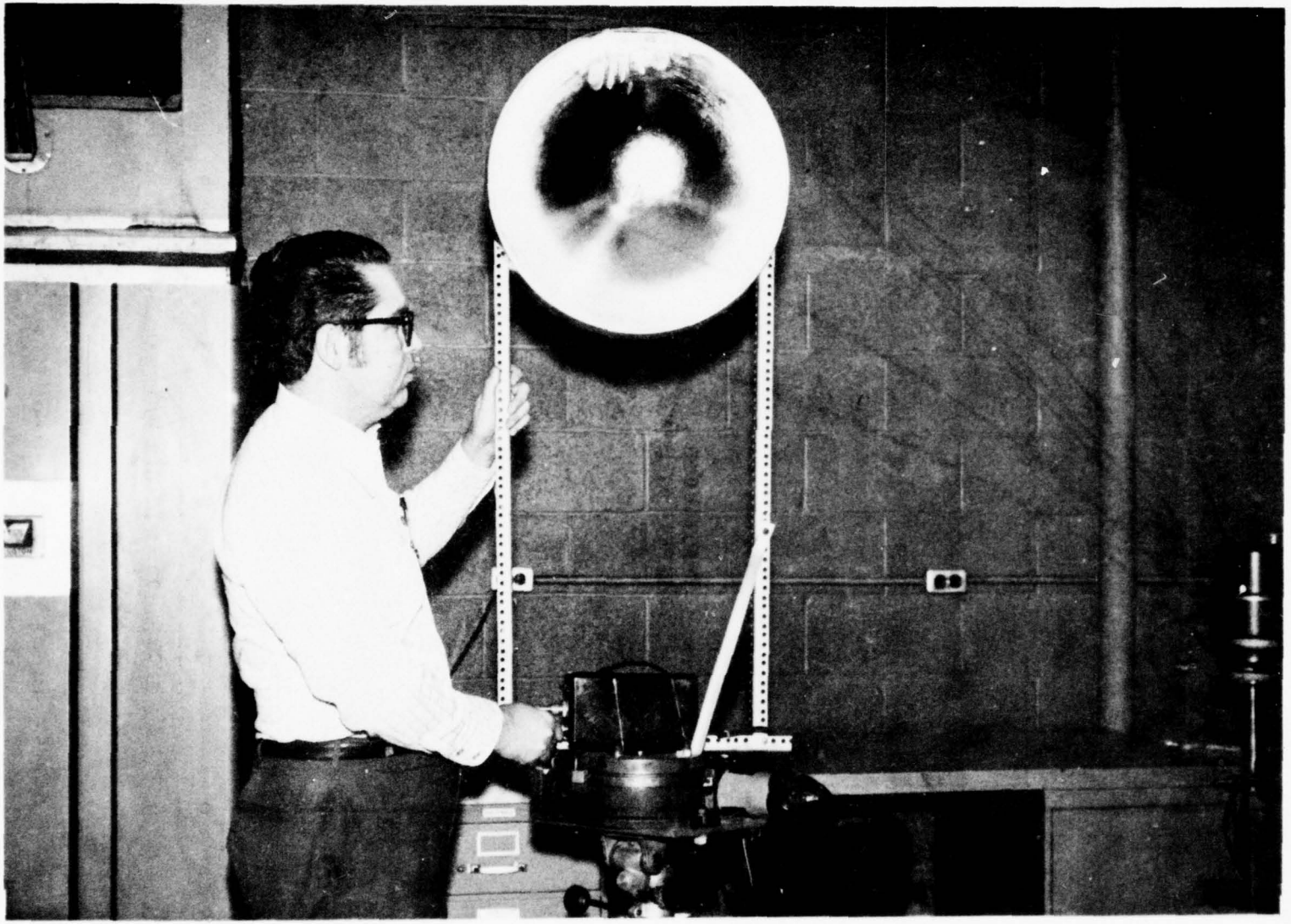


Figure 8-85. 18-inch Ellipsoidal Mirrow Mounted on Rotary Actuator.

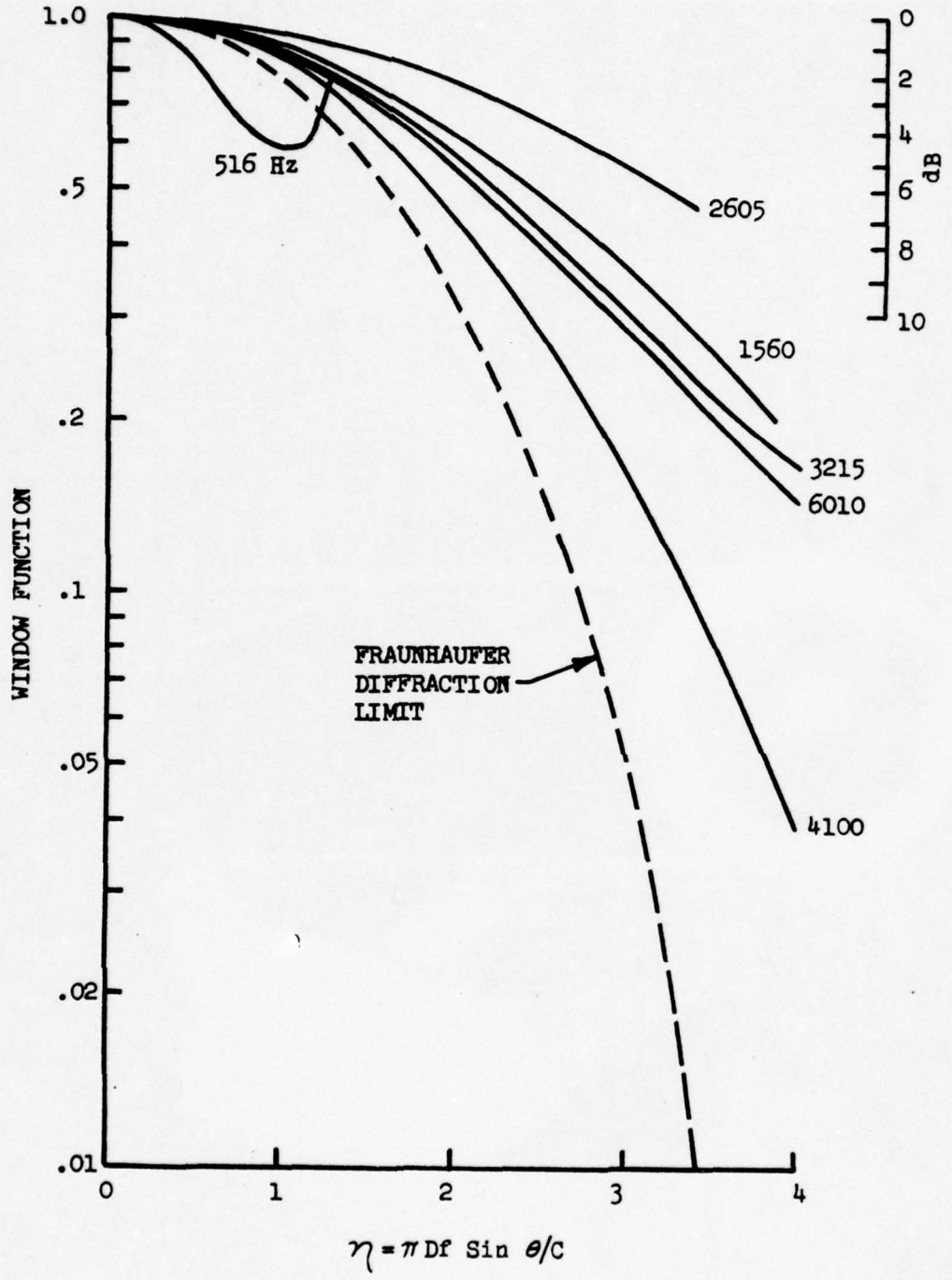


Figure 8-86. 18-inch Reflector.

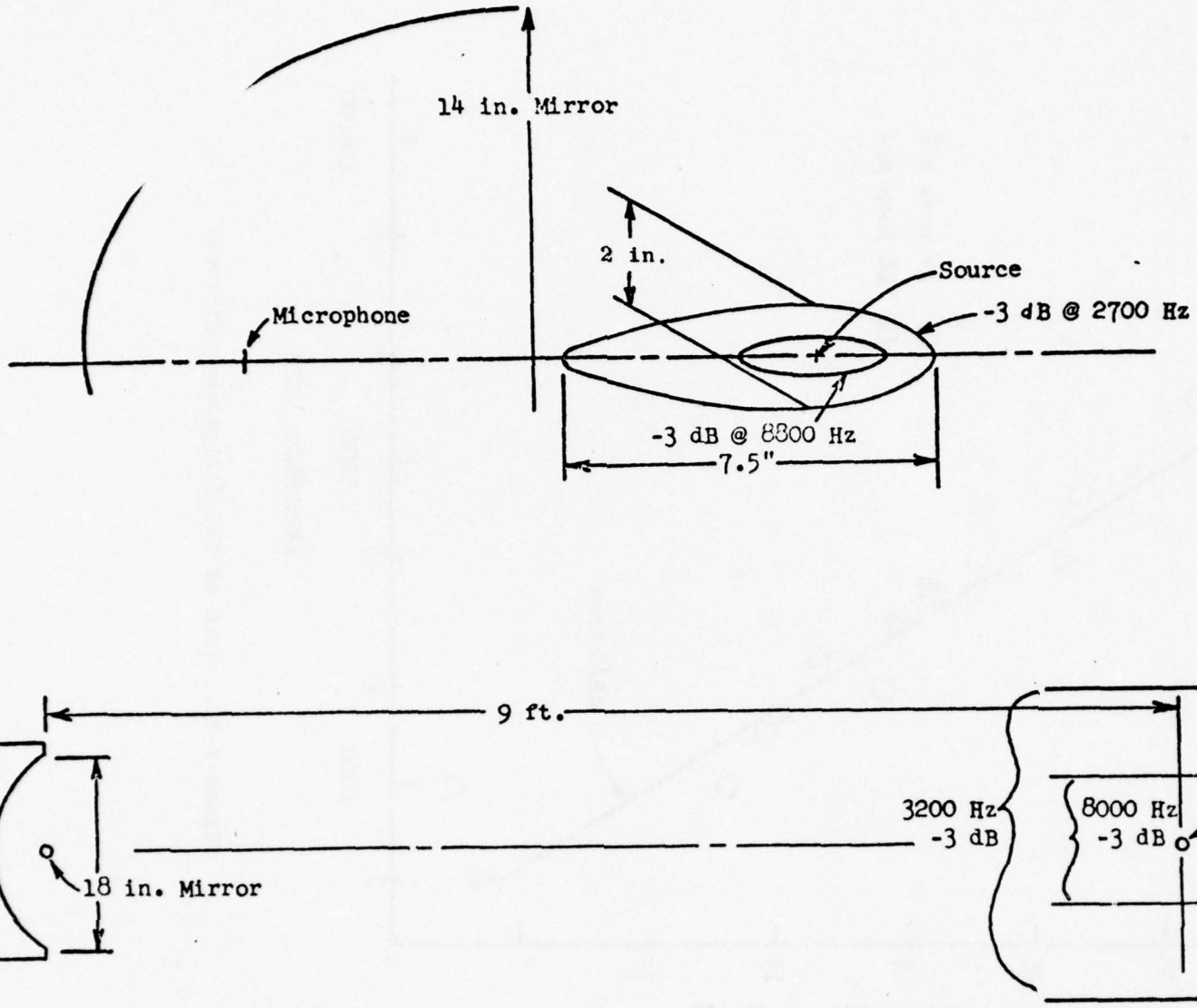


Figure 8-87. Resolution Volume of the Mirrors.

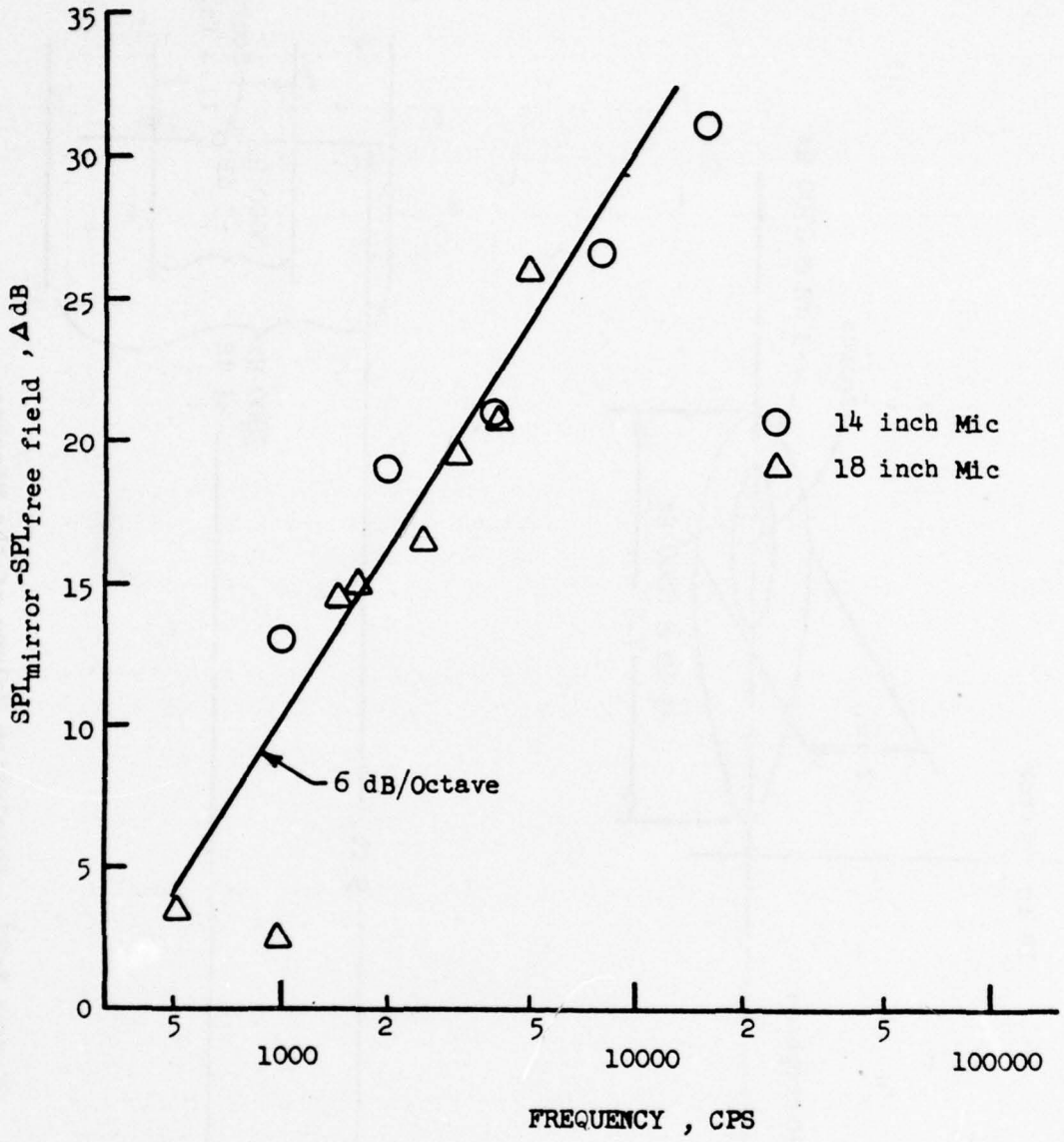


Figure 8-88. Gain of the Ellipsoidal Mirrors.

Table 8-IV. Comparison of Measured and Estimated Window Size.

(All Dimensions in Inches)

Mirror	Working Distance 2c	Mirror Diameter D_m	Calculation		Measurement at 8 kHz of h_{3dB}/λ
			1.22 (r/D_m) $h_o/8\lambda$	0.487 (r/D_m) h_{3dB}/λ	
1	10.66	14.0	0.9289	0.371	0.4
2	108.0	18.0	7.32	2.922	3.35
3	180.0	34.654	6.336	2.529	TBD*

* Calibrated in Task 3; to be Reported in Task 3 Final Report

A three-dimensional mapping of the collection volumes from both mirrors is shown in Figure 8-87. The small tear-shape volume found with the 14-inch mirror could not be reproduced with the 18-inch design because only limited axial data were recorded. The same general shape, however, appears to be developing in Figure 8-87.

The gain of the 18-inch mirror had the same 6 dB per octave slope as the 14-inch, as seen in Figure 8-88. Even more surprising is that both mirrors apparently have the same intercept as well.

8.7.4 Jet Noise Source Location Mapping at JENOTS

The 18-inch mirror was installed on a traversing cart at JENOTS for detailed mapping of the noise sources in the jet plume of a conic nozzle, as shown in Figure 8-89.

Measurements were taken by slowly moving the cart parallel to the jet axis, as shown in Figure 8-90. A 1/8-inch B&K 4138 microphone was installed in the mirrors elliptic focus with the second focus at the center of the jet. The output of the microphone was recorded on tape together with the cart position signal. In data reduction, the microphone signal was filtered at each 1/3-octave center frequency, adjusted for the gain of the mirror, and plotted versus the calibrated axial position of the cart representing the location of the focal spot within the jet. No processing of the data to correct for the window function weighting was conducted.

Figure 8-91 shows typical traverses at the three cold jet conditions tested representing subsonic (597 fps), critical (1047 fps) and supersonic (1411 fps) conditions.

All the traverses exhibited a similar peaking at characteristic distances within the jet plume; higher frequencies peaking closer to the jet exit plane. The lower frequencies were also much more gently changing. The

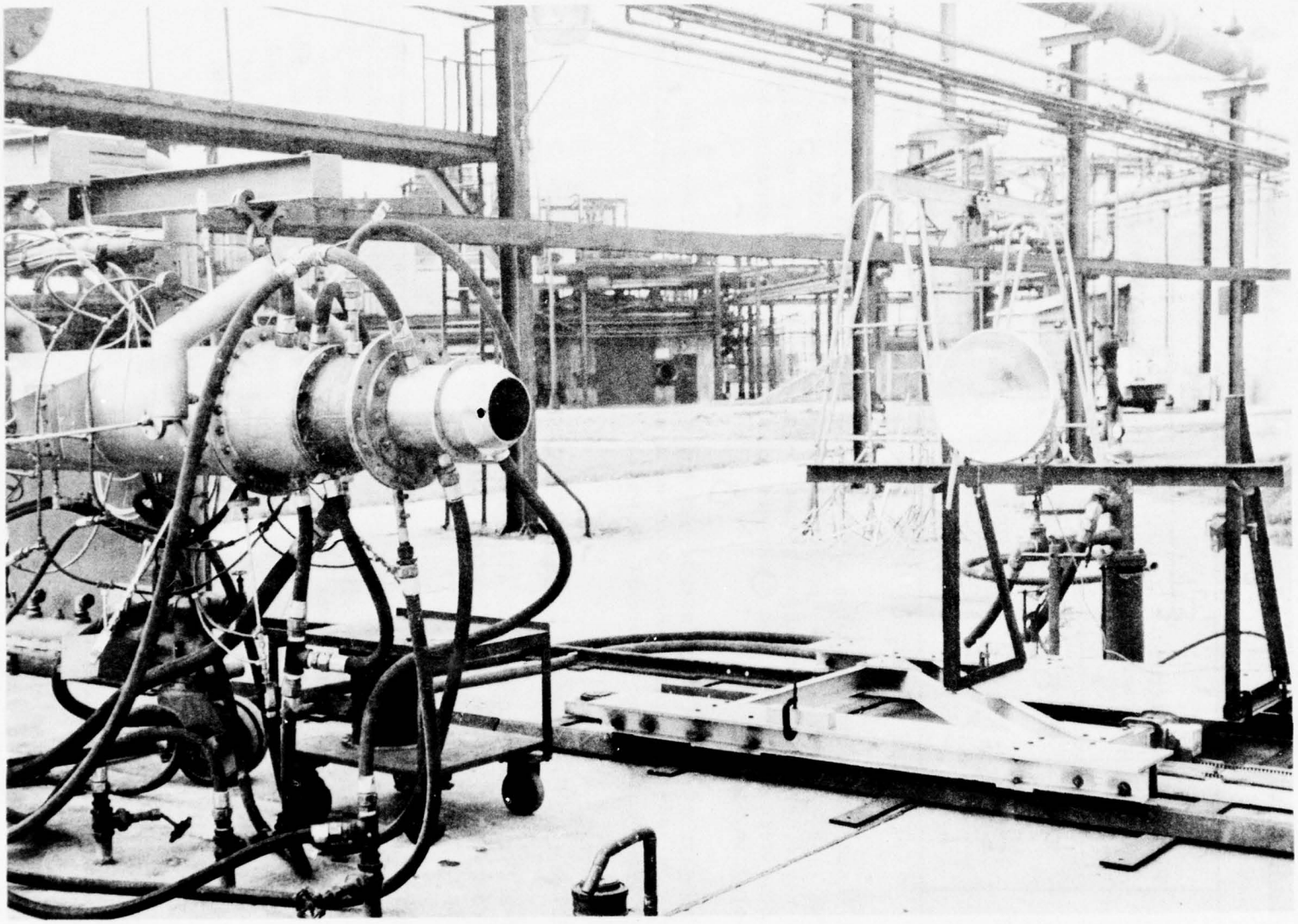


Figure 8-89. Ellipsoidal Microphone Installation at JENOTS.

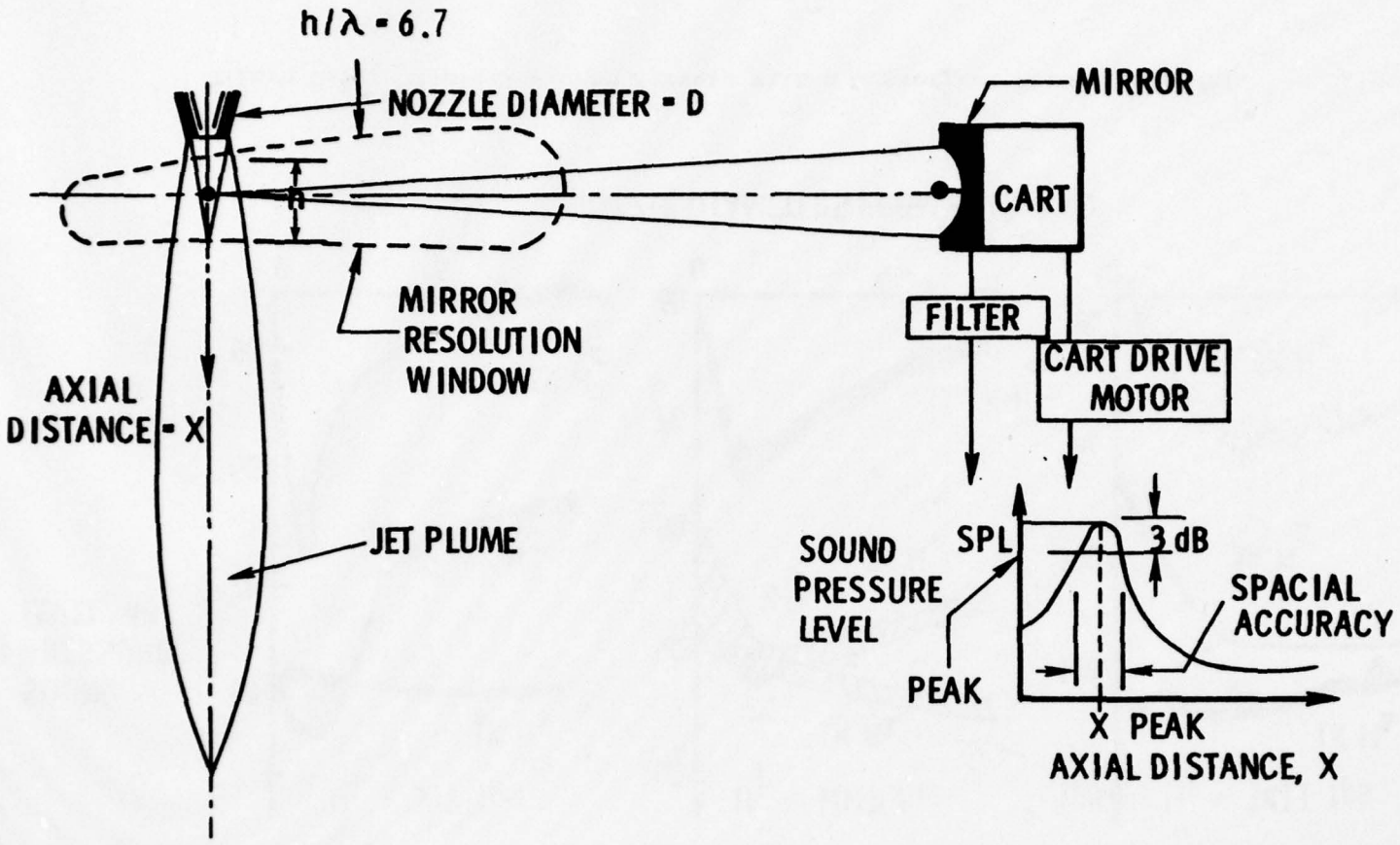


Figure 8-90. Test Setup for Ellipsoidal Surveys.

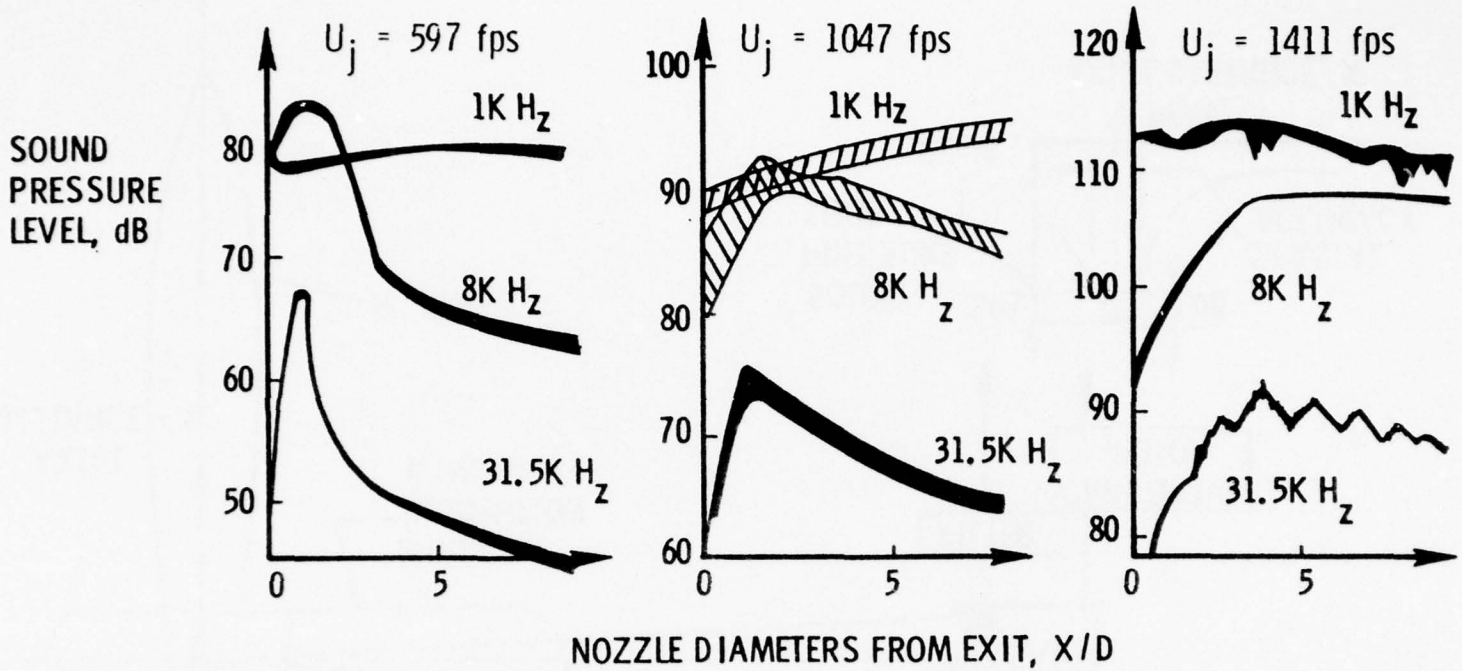


Figure 8-91. Typical Mirror Surveys with a Convergent Nozzle Cold Jet.

width of the lines in Figure 8-91 represent the levels experienced from repeated traverses (at least six) which were used to represent an assembly average of the data (since continuous traverses were used). One observes that the transonic point ($U_j \simeq 1047$ fps) has the most variability, and high repeatability is experienced at other conditions. Even at Mach one, the variability is generally within 3 dB. At high frequency in the supersonic case, a definite "zig-zag" pattern is observed, most likely the result of shock cell oscillation within the plume.

Each of the xy traverse plots were cross-plotted to give frequency spectra per slice of jet shown in Figure 8-92. The spectra has a characteristic two-hump shape at all but the supersonic exit plane station. The first hump is the result of pseudosound oscillations being picked up by the mirror, indicating the system is in the near field of the jet. From the spectra shape, it appears that all data below 1000 Hz are affected (although only every third 1/3-octave is plotted). The second hump is the jet Strouhal peak. To solve this problem, the third EM was designed. This mirror has a working distance of 15 feet which will hopefully provide far-field measurements down to about 400 Hz. The design was fabricated at the end of the Task 1 effort for calibration and use in subsequent tasks of the program.

By summing the levels at each station in spectra of Figure 8-92, the overall energy distribution in the jet is obtained, as shown in Figure 8-93. At subsonic and transonic velocities, the nearly constant distribution of acoustic energy is found. The data, however, fail to drop off beyond 10 diameters as would be predicted (Reference 42) because the data in Figure 8-93 have not been corrected for the window function. That is to say, the mirror measurements beyond 10 diameters can still "hear" the high level signals earlier in the jet which tend to hold up the overall level. This difficulty is being corrected by proper computer processing of the data which is presently being programmed for Task 3 work.

The supersonic velocity point in Figure 8-93 displays the characteristic upswing in the source strength at eight diameters which has been previously observed with laser velocimeter measurements (Reference 103).

The popular method of presenting jet noise source locations is in terms of the frequency distribution of the sources, as shown in Figure 8-94. Here, each 1/3-octave frequency is used to calculate a Strouhal number. The axial traverse plots in Figure 8-91 are then used to determine the axial location of the peak level within the jet and that 1/3-octave frequency. This peak position in terms of nozzle diameters is shown by the centerline of the cross hatch in Figure 8-94. The cross-hatching is used to represent the measured invariance of the level in the jet. The lines bounding the hatching are the axial positions where the mirror sound level has fallen to 3 dB below the peak value (see Figure 8-90). A number of authors have measured the source distribution within a Mach one jet by other means. Their data are shown, in Figure 8-94, to be within 3 dB of the peak level recorded with the ellipsoidal mirror microphone.

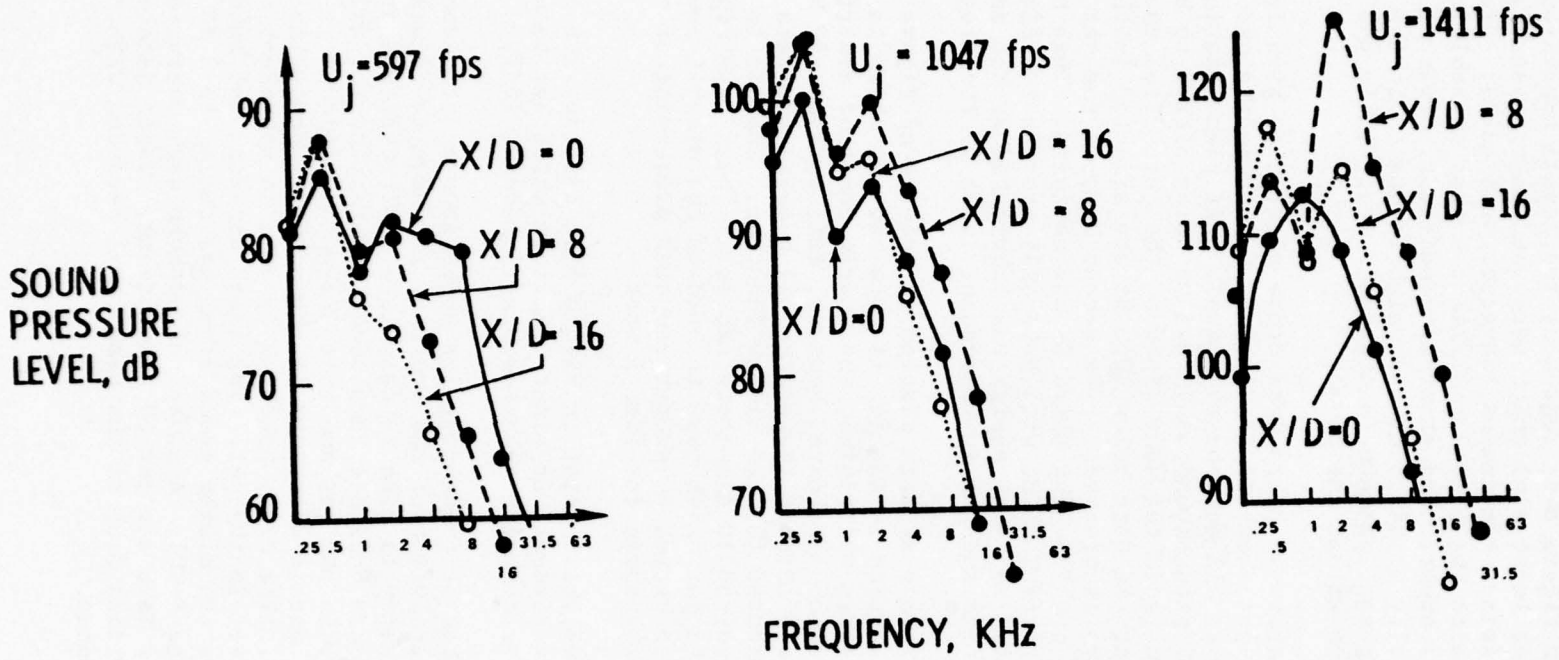


Figure 8-92. Ellipsoidal Mirror Frequency Spectra.

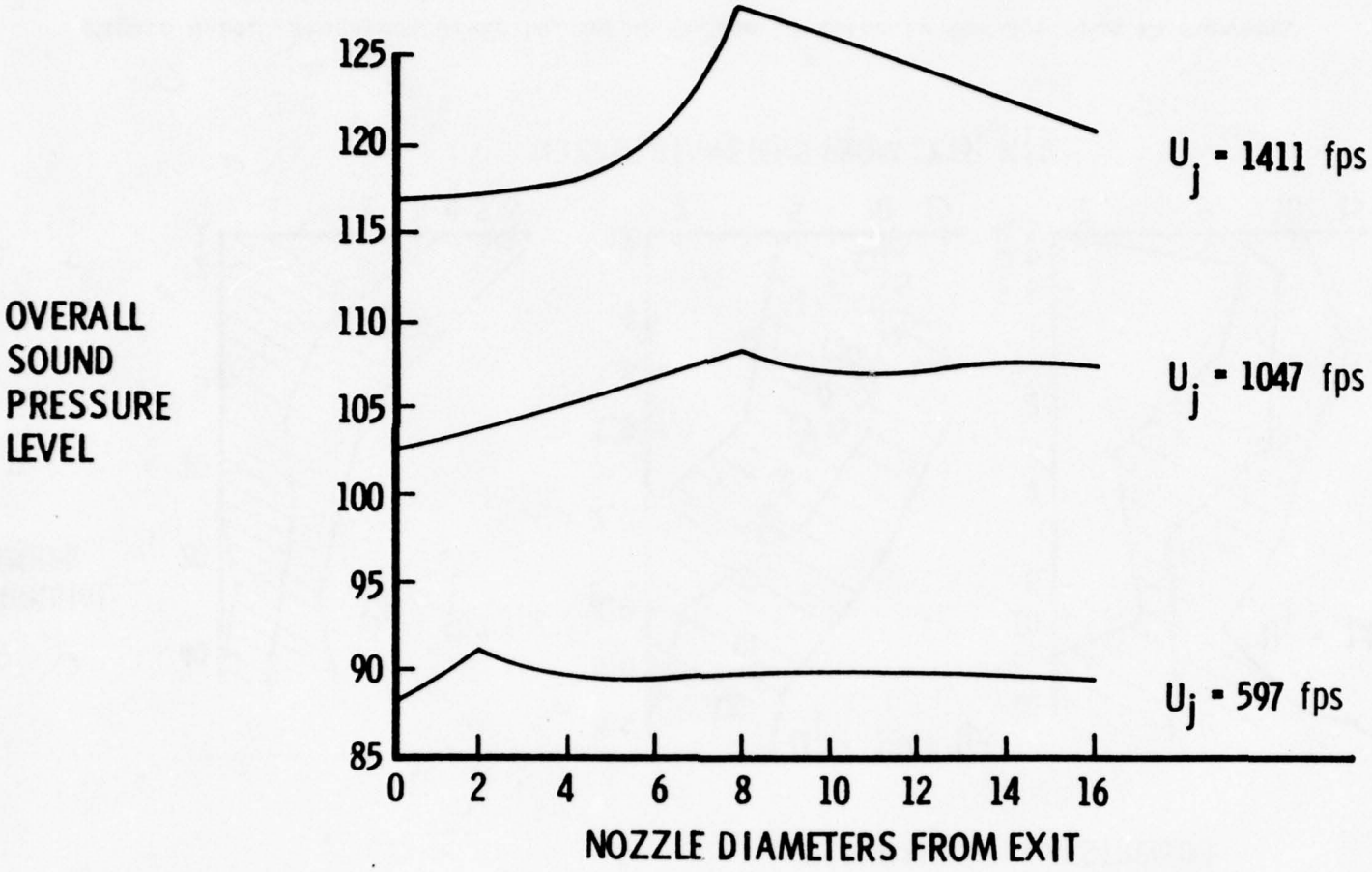


Figure 8-93. Energy Distribution in the Jet from Ellipsoidal Mirror Surveys.

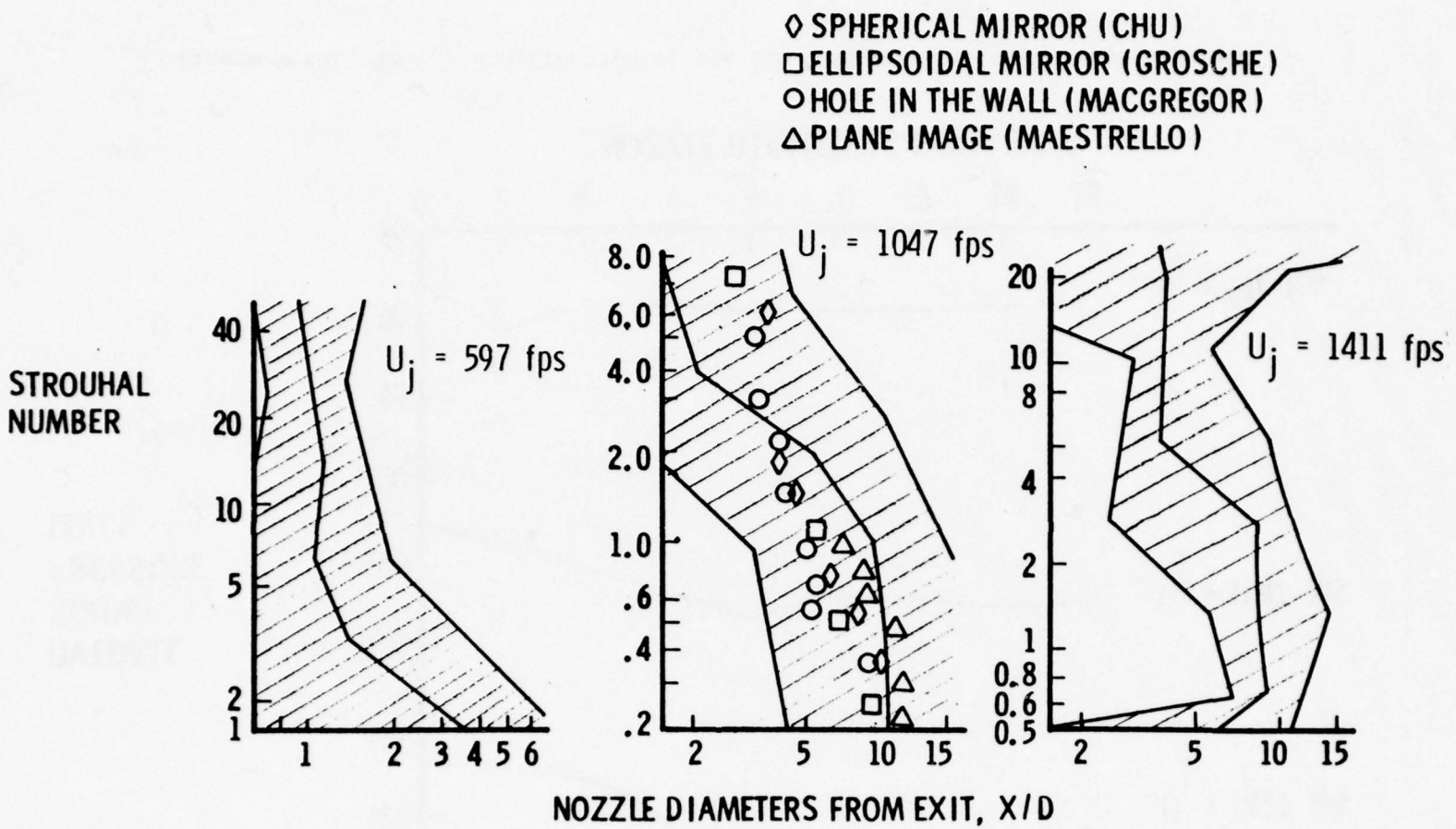


Figure 8-94. Frequency Distribution of Source Location in the Jet from EM Surveys.

The variation of the level within the jet appeared to have a similar shape at all frequencies. To check this, the data were normalized by the method suggested by Motsinger and Sieckman (Reference 35) of simply adjusting the level and axial location to the peak value. This mode of data presentation for various frequencies is shown for the three velocity conditions in Figures 8-95 through 8-97. There is general collapse of the data at the sonic point in Figure 8-96, but with the high and low velocity data show considerable scatter inconsistent with frequency. Again, this can probably be attributed to the fact that the data is not corrected for the window function.

8.7.5 A Test for Integral Closure

An important check for the accuracy of the method is the integral closure check. This test is one to see that all the energy being picked up in the far field is accounted for by the ellipsoidal mirror. Testing was conducted by situating a far-field microphone 40 feet from the jet along the 90° station while surveying the plume with the EM. The mirror data was then processed by logarithmically summing the SPLs at each axial station along the jet at each frequency. The resulting spectra shown in Figure 8-98 represents the total acoustic flux from the jet in 90° direction and can be compared with the far-field microphone measurements after inverse square law and air attenuation adjustments are made. The comparison in Figure 8-98 shows excellent agreement at high frequency. At intermediate frequency, 1000 to 4000 Hz, the mirror measurements are higher because of the double accounting (e.g., overlap) at each axial station with the wide window function. At high frequency, of course, the window is narrow enough that it is essentially a differential increment of jet and an accurate distribution is obtained. Below 1000 Hz, the pseudosound fluctuations of the jet are included in the mirror measurements because of the closeness of the EM to the plume.

8.7.6 Loss of Resolution Due to the "Window Function"

The previous data presentation suffers from the double accounting produced by the diffraction window function. The mirror can be thought of as a wide spatial filter which sweeps the jet, as shown schematically in Figure 8-99. The actual "narrowband" (in space) acoustic power distribution, P^2_{actual}, may be quite erratic in shape. However, since adjacent points are averaged into each reading, the measured distribution, $P^2_{measured}$, is smoothed and the overall level is increased. This increase in level is not to be confused with the inherent mirror gain, which results from the ability of the mirror to concentrate sound at the focus.

The mirror measurement of power spectral density at an arbitrary axial position in the jet can be described analytically in terms of a convolution integral.

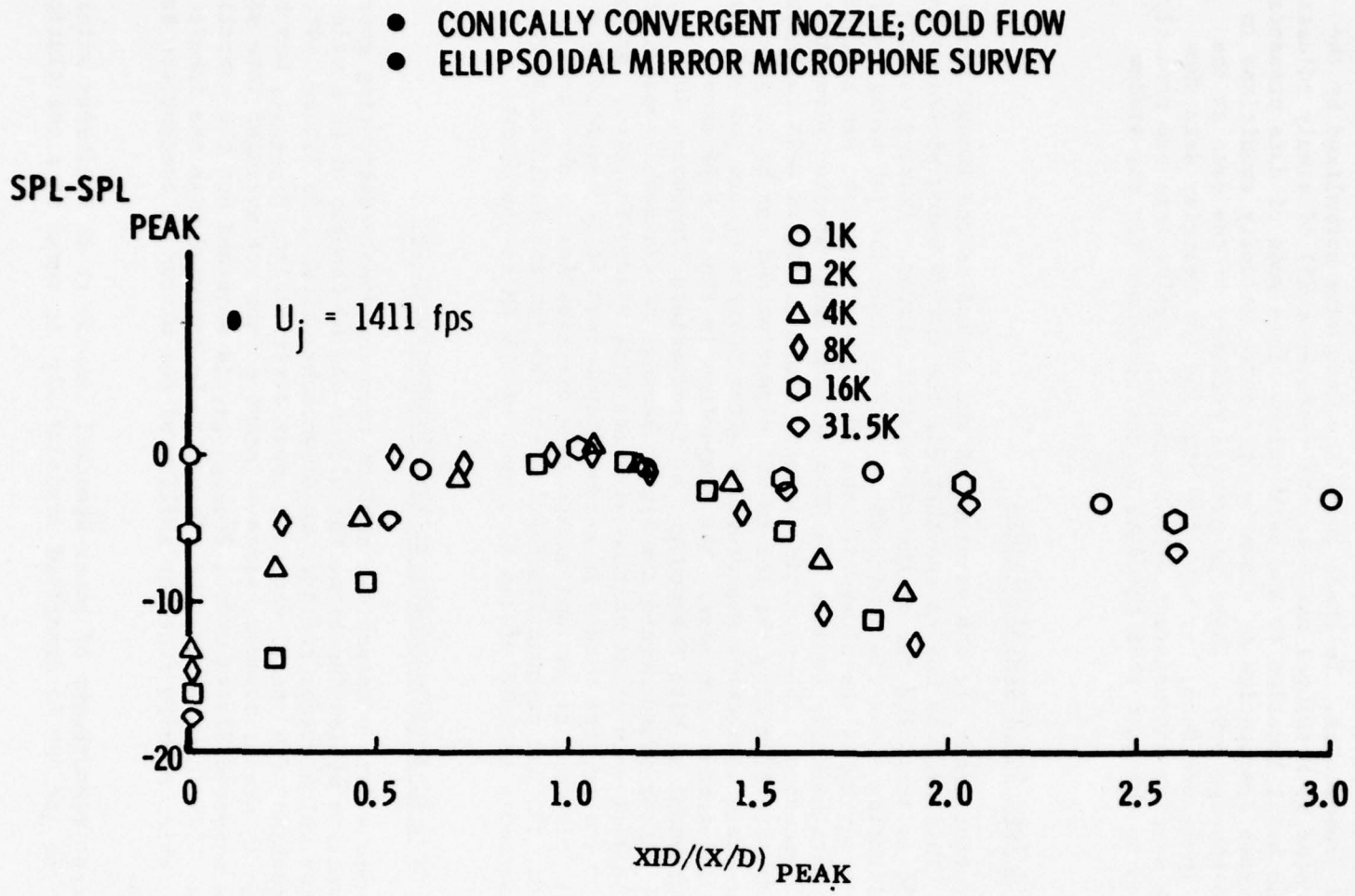


Figure 8-95. Generalized Source Distribution in a Supersonic Cold Jet from EM Survey.

- CONICALLY CONVERGENT NOZZLE; COLD FLOW
- ELLIPSOIDAL MIRROR MICROPHONE SURVEY

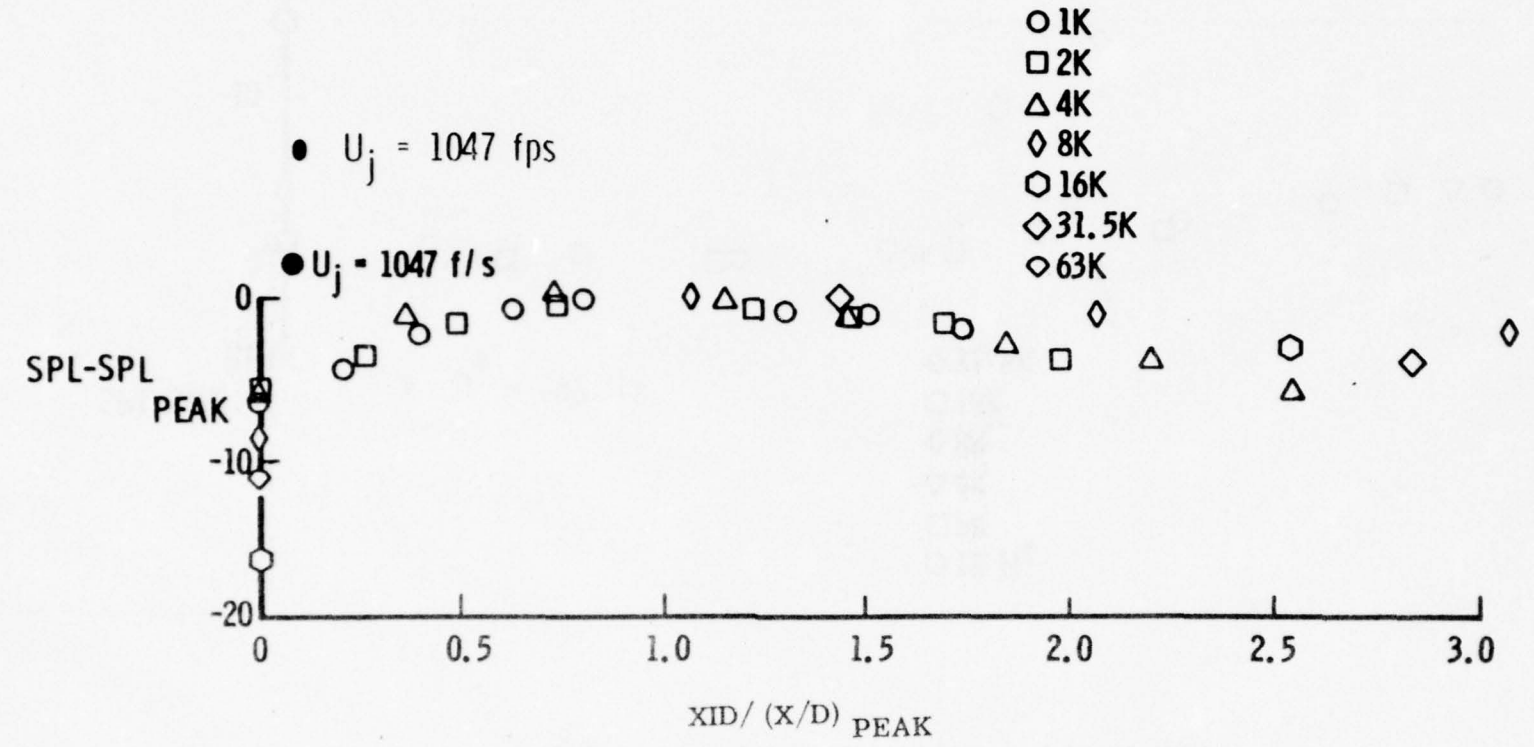


Figure 8-96. Generalized Source Distribution in a Sonic Jet from EM Surveys.

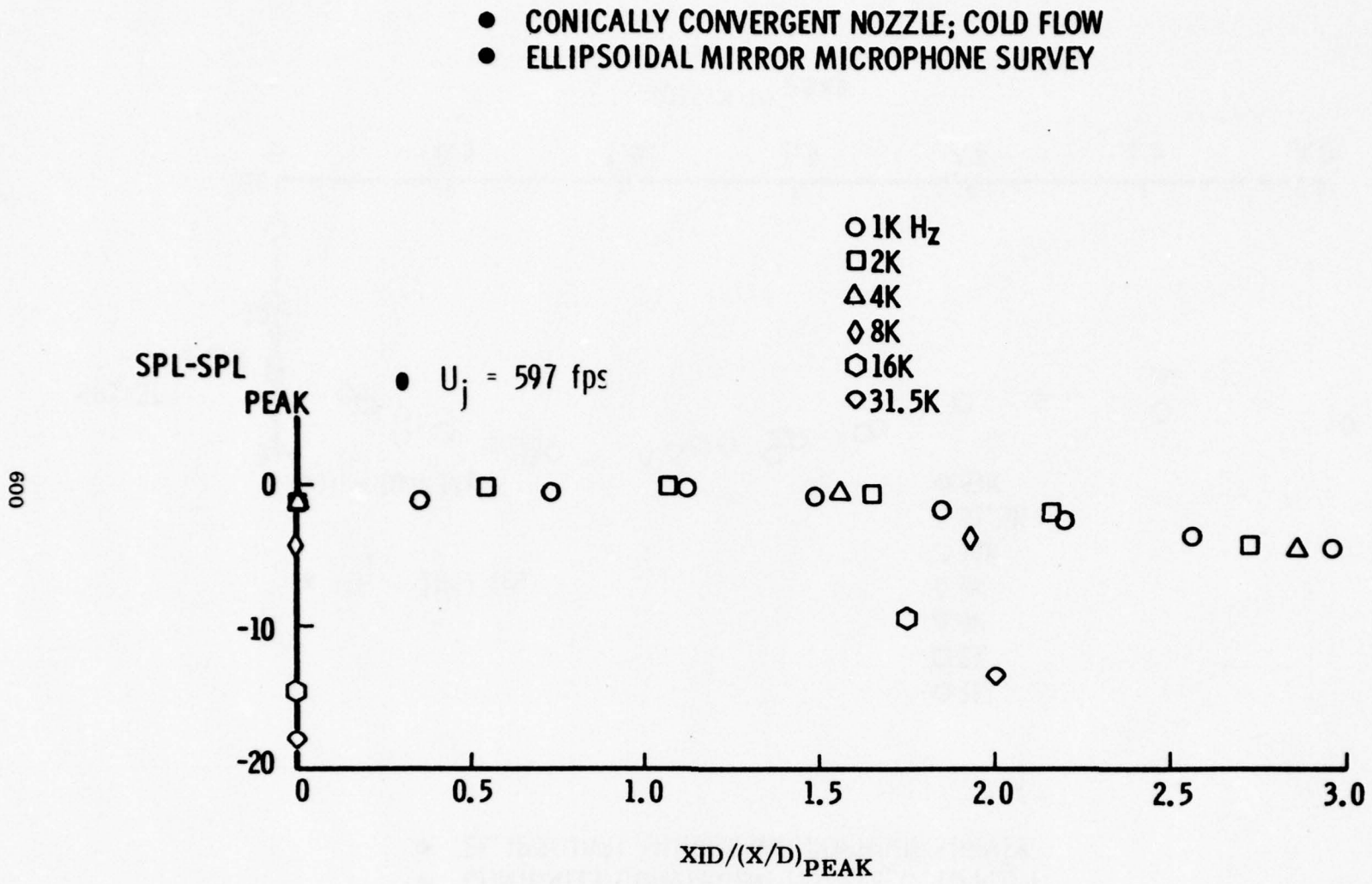


Figure 8-97. Generalized Source Distribution in a Subsonic Cold Jet from EM Surveys.

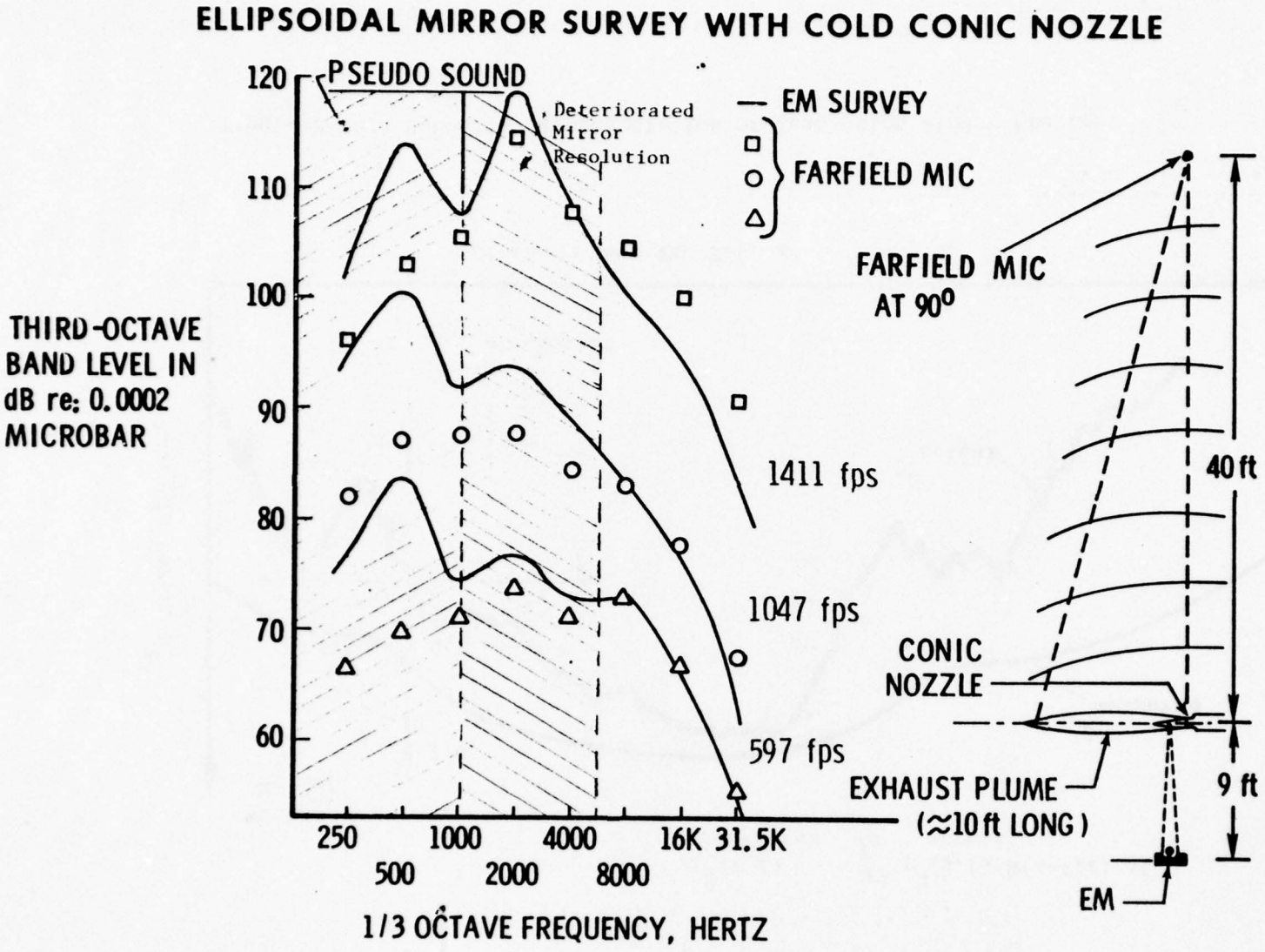


Figure 8-98. Integral Closure Test of the Ellipsoidal Mirror.

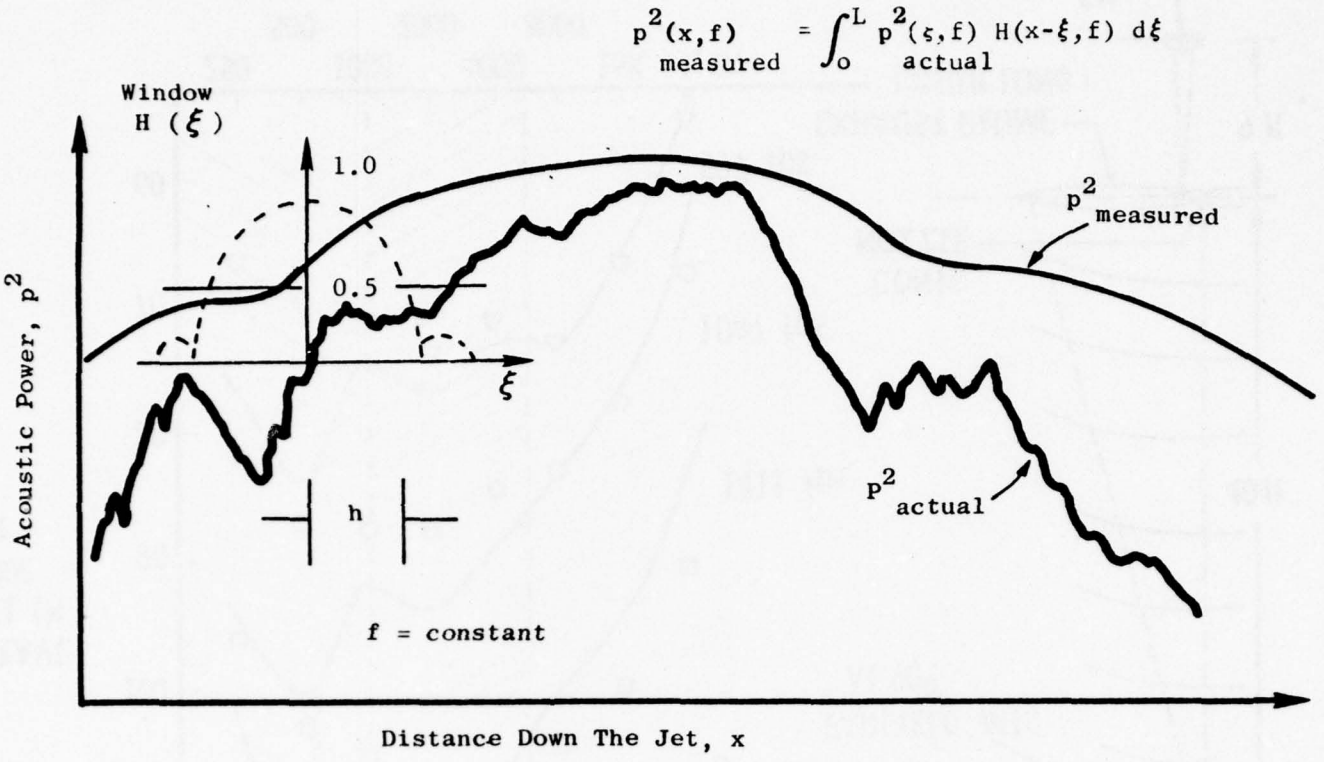


Figure 8-99. Schematic Representation of Resolution Window Problem.

$$P_{measured}(x,f) = \int_0^L p_{actual}(\xi,f) H(x - \xi,f) d\xi \qquad (235)$$

In order to obtain the true acoustic power distribution in the jet, it is necessary to solve (deconvolve) the integral equation for the excitation signal at each axial station, given knowledge of the system (mirror) characteristics and the response signal. Note that this must be done separately for each frequency of interest. In practice, the data is generally analyzed in 1/3-octave bands.

Due to the complexity of the problem, a numerical solution of Equation (235) is mandatory. This reduces the continuous physical problem to a system with a finite number of degrees-of-freedom. In a numerical evaluation of the equation, the definite integral is expressed as the summation of integrals between discrete points within the continuous domain. The integrand is then approximated by a polynomial over each individual sub-range (e.g., trapezoidal rule). This leads to a system of simultaneous linear algebraic equations in place of the original integral equations:

$$\left[P^2_{measured}(f)\right]_i = \sum_{j=1}^{n} H_{ij}(f)\, \alpha_j(f) \left[P^2_{actual}(f)\right]_j \qquad (236)$$

The term $\alpha_j(f)$ includes the mirror gain G (f), as well as any factors introduced by the numerical integration.

Deconvolution problems which occur in practice are often quite difficult to solve because the systems of equations are ill-conditioned. This is particularly true, in the present case, at lower frequencies where the window functions are broad and relatively "flat". Because of ill-conditioning, arbitrarily small errors in response can result in large errors in the deconvolved excitation, depending on the characteristics of the convolution and the solution technique that is used. Since the response and the mirror system characteristics (window function) are obtained by physical measurement, the presence of errors (noise) is unavoidable. Therefore, great care must be exercised in the choice and implementation of a solution technique if the variance of the deconvolved data is to be kept within reasonable bounds.

A comparative study of numerical techniques for accomplishing the deconvolution was made by Schlinker, et. al. (Reference 104). Three methods were considered:

1. Integral transform

2. Matrix inversion

3. Relaxation

Based on an evaluation in terms of resolution, sensitivity to noise, and amount of computation, the relaxation procedure was found to be superior to the others for use in processing source location data from the USC spherical mirror. Following a review of the results and recommendations of this study, the relaxation technique, which is actually an adaptation of the classical point Jacobi iterative method for solution of simultaneous linear algebraic equations, was chosen for incorporation into the standard EM data reduction computer program. Additional solution techniques, not included in the USC study, are currently being evaluated in order to determine if further improvements can be made.

A measure of the improvement in mirror resolution achieved by deconvolution of Equation (236) can be obtained from "before and after" comparisons of data from measurements on point sources. A point source experiment utilizing a 1/2-inch-diameter jet (small broadband noise source) was done under Task 3. The data is currently being reduced and therefore no calculations have been made. This information will appear in the Task 3 Final Report.

8.7.7 Sources of Error

As in the case of any measurement system, it is necessary that potential limitations and sources of error in the application of the ellipsoidal mirror technique be assessed. These can be separated into three distinct areas:

1. Theoretical limitations

2. Data acquisition errors

3. Data processing errors and limitations

In the realm of theoretical limitations, there are several items to be considered. The most fundamental limitation is that, since it senses far-field acoustic radiation, the EM can only define an "apparent" source distribution, which includes the effects of factors such as refraction in the jet. In addition, there are limitations to the range of frequencies over which the EM provides useful data. These are dependent on the exact physical characteristics of the system in use. There are two potential limits at low frequency. One is the point at which the mirror is no longer operating in the acoustic far field. This occurs when the ratio of working distance to wavelength falls too low. The other limit is the point at which the reflected

acoustic waves become completely dominated by diffraction. This occurs when the ratio of aperture diameter to wavelength falls too low and the mirror is no longer able to focus the incoming waves. At high frequencies, the system is limited by microphone frequency response/directivity and by the dimensional tolerances of the mirror. The latter limit is reached when deviations from theoretical mirror contour or focal point location become appreciable fractions of wavelength.

In addition to real or potential problems generally associated with the acquisition of acoustic data, there are particular sources of error associated with the mode of operation of the EM. As was described in Section 8.7.4, measurements are taken while the mirror is slowly traversed parallel to the jet axis. In data reduction, the signal is resolved into 1/3-octave bands and averaged over discrete time steps, then digitized. Since the mirror is moving during these time steps, the digitized spectra represent averages over some distance. This fact limits the resolution capability of the mirror to the width of an individual time step. Since the averaging time must be long enough to allow for extraction of a statistically valid sample, resolution can only be improved by decreasing the traverse speed (i.e., covering less distance during a fixed time interval).

The major sources of error encountered in data processing of EM data are:

1. Statistical error due to insufficient averaging time.

2. Enhancement of ambient or electronic noise, or of statistical measurement error, due to an ill-conditioned window function matrix.

3. Limits on achievable resolution due to numerical instability in solution of an ill-conditioned set of equations.

4. Errors induced by uncertainty in window function measurements.

In order to gain a better understanding of these phenomena and to further establish the reliability of the EM, an analytical error analysis is currently underway as part of Task 3 of this program and will be included in the Task 3 Final Report.

8.7.8 Summary

The design, development, calibration, and application of ellipsoidal mirror technology has resulted in a successful method for obtaining macroscopic noise source location information for jets. Two problem areas, namely, location of the mirror in the near field of the jet and the processing of the data to remove the diffraction window function, have hopefully been solved by the design of a new EM with a longer working distance from the jet axis, and by the development of an EM data processing program to remove the window function. These improvements will be utilized in future measurements in subsequent tasks of the High Velocity program.

9.0 CONCLUSIONS AND RECOMMENDATIONS

9.1 CONCLUSIONS

The previous analyses of the various test facilities and noise source location techniques have resulted in the following conclusions.

9.1.1 Activation of Facilities

1. All of the acoustic test facilities are capable of attaining the desired domain of operation. In terms of jet velocity and total temperature, the maximum values are:

Facility	Max. Jet Velocity (fps)	Max. Total Temperature (° R)
USC	1750	1040
UBC	1050	540
GE/JENOTS	3000	2500
GE/CR&DC	1900	1900
J79 @ GE/EFTC	2150*	1600*

*Per Operating Line

2. All of the scale model test facilities can deliver "pure" uncontaminated jet noise over the velocity (600 - 3000 fps) and frequency (400 - 80,000 Hz) range of interest. Table 6-II summarizes the key characteristics of these anechoic scale model and outdoor scale model and large scale acoustic facilities.

3. The two most serious contaminants are the lack of proper air attenuation corrections at high frequency and electronic noise floor. Both of these effects can be significant above 20 kHz.

4. The exact relationships for the air attenuation model at high frequency are yet unknown so a bias in the correction factors is possible.

5. Electronic noise floor problems occurring with the "peaky" spectra near the jet axis can be improved by utilizing high pass filters and two microphones.

6. When correcting for electronic noise floor, the final spectral shape should be analyzed with air attenuation removed.

7. The accuracy of the aerodynamic instrumentation systems at the facilities were excellent. A statistical study of the variance showed that a large variability is only possible at low velocity, high temperature conditions.

8. Contamination from the ambient background noise was insignificant.

9. Contamination from facility type noise such as from the flow piping and valves, combustor or heater, and turbomachinery (on the J79) was effectively eliminated - through the use of acoustically-treated mufflers.

10. The scale model test facilities delivered uncontaminated jet noise above a velocity of 600 fps. The lowest J79 engine speed where pure jet noise was attained corresponded to a jet velocity of 750 fps.

11. All of the test facilities have measurement arc radii greater than the 50 nozzle diameters considered a minimum based on experimental results to date.

12. All the facilities gave inverse square law with a nominal variance of ± 1 dB.

13. Classical ground reflection theory was modified to account for finite impedance surface, jet scattering, and distributed source effects. The resulting corrections successfully produced effective free-field results at GE/JENOTS.

14. The use of an overhead microphone array and ground treatment produced an effective free-field environment at GE/CR&DC.

15. The use of two microphones with the J79 at GE/EFTC produced an effective free-field "composite" spectra after ground reflection corrections were made which included the effects of a finite impedance surface and distributed sources.

16. A spurious reflection from an unknown source (the casing radiation box is suspected) distorted the spectra at 150° and 160° from the inlet during GE/EFTC J79 tests.

17. Round nozzle spectra obtained from the facilities was found to be in substantial agreement with the referee data of Lush, Ahuja and Bushell, Olsen, Hoch, Cocking, Tanna, and the SAE A21 Committee.

18. The Fluidyne Engineering Corporation and NASA Lewis 6 × 8-foot wind tunnel facilities can provide aerodynamic performance data that are as controlled and accurate as can be produced anywhere.

9.1.2 Noise Source Location Techniques

1. A screening study of potential noise source location techniques resulted in experimental investigations of four areas:

   - Optimum-shaped probe stems - point source information
   - Laser shadowgraph causality correlations - point source information
   - "Hole-in-the-wall" isolation technique - essentially slice of jet information
   - Ellipsoidal Mirror Microphone - essentially slice of jet information

2. Acoustic probes were found to have a limited domain of operation; specifically:

   - M_j < 0.7 (1000 fps)
   - T_T < 1000° R direct mounted
     < 1600° R cooled
   - Turbulence angle swings < 15°

3. The design of a two-hole cylinder probe gave comparable accuracy to Rackl's airfoil probe.

4. The laser shadowgraph method produced only qualitative results because of unwanted Schlieren-type behavior in the optical system.

5. The hole in the wall gave reasonable results, but its applicability is limited by the need for asymmetric apertures when using non-circular nozzles (2-D), suppressors, etc.

6. The ellipsoidal mirror microphone was found to be superior to the hole in the wall in obtaining macroscopic noise source distributions in the jet plume (e.g., faster and more flexible).

7. The mirror designed for JENOTS testing was found to be in the near field below 1000 Hz so a new "deep-dish" mirror with a longer working distance has been fabricated for operation in subsequent program tasks.

8. A loss of resolution due to the diffraction "window function" of the mirror was found. Numerical methods in data reduction are being implemented for future use of the mirror.

9.2 RECOMMENDATIONS FOR FUTURE WORK

From the previous conclusions, the following recommendations are drawn:

1. An experimental study of air attenuation characteristics should be conducted.

2. A remote, noninvasive, sensor which can measure an unsteady, scalar, thermodynamic quantity at a point in the fluid should be developed. Such an instrument could be used with the causality (or 2 point) correlation method to give microscopic noise source mapping within the jet.

3. Additional effort should be directed toward assessing the apparently successful AF/DOT single-point in-jet-to-far-field acoustic pressure cross correlation demonstration in future programs. (A General Electric funded effort is currently underway to do just this along with "injet-injet" turbulent velocity measurements utilizing a 2 LV system.)

APPENDIX

GE AIR ATTENUATION MODEL

The air attenuation model used for the USC, JENOTS, and EFTC data was developed in 1973 by R.G. Fogg of General Electric (Reference 105). Mr. Fogg noticed that a linear extrapolation of the SAE ARP866 curves (Reference 16) or the predictions of Harris (Reference 22) tended to distort the spectral shape for frequencies above 20 kHz when the data was scaled or PWL was calculated as seen in Figures A-1 and A-2. He hypothesized that this distortion was the result of applying excessive air attenuation at the high frequencies. From Harris' data it was clear that the molecular absorption diminished in percent of the total absorption as the frequency increased leaving the classical absorption as the dominant attenuator. By curve fitting the trends of the classical and molecular absorption with frequency at various humidities and a temperature such as in Figure A-3, a family of prediction curves as shown in Figure A-4 were developed. For comparison, similar presentation from Harris (Reference 22) and Evans (Reference 20) are given in Figures A-5 and A-6, respectively.

Table A-I is a listing of the computer program used to generate the correction factors, and Table A-II, a listing of ambient temperature, barometric pressure, and relative humidity for the data displayed in the certification plots. With Tables A-I and A-II, one can calculate the value of the air attenuation corrections applied to the JENOTS data in Figures 6-42 through 6-56.

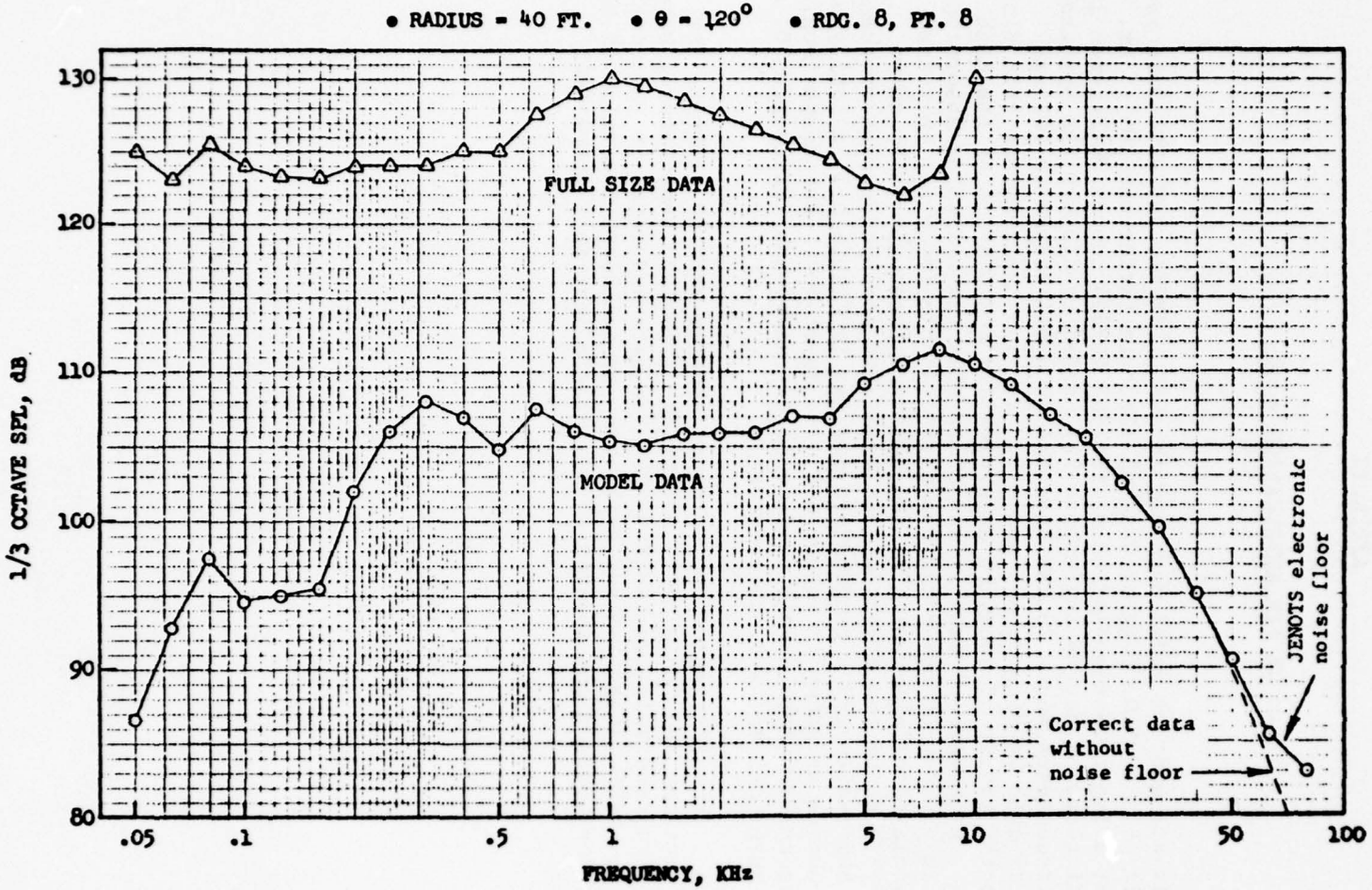


Figure A-1. JENOTS Data - SPL Spectra FSDR Program Calculation.

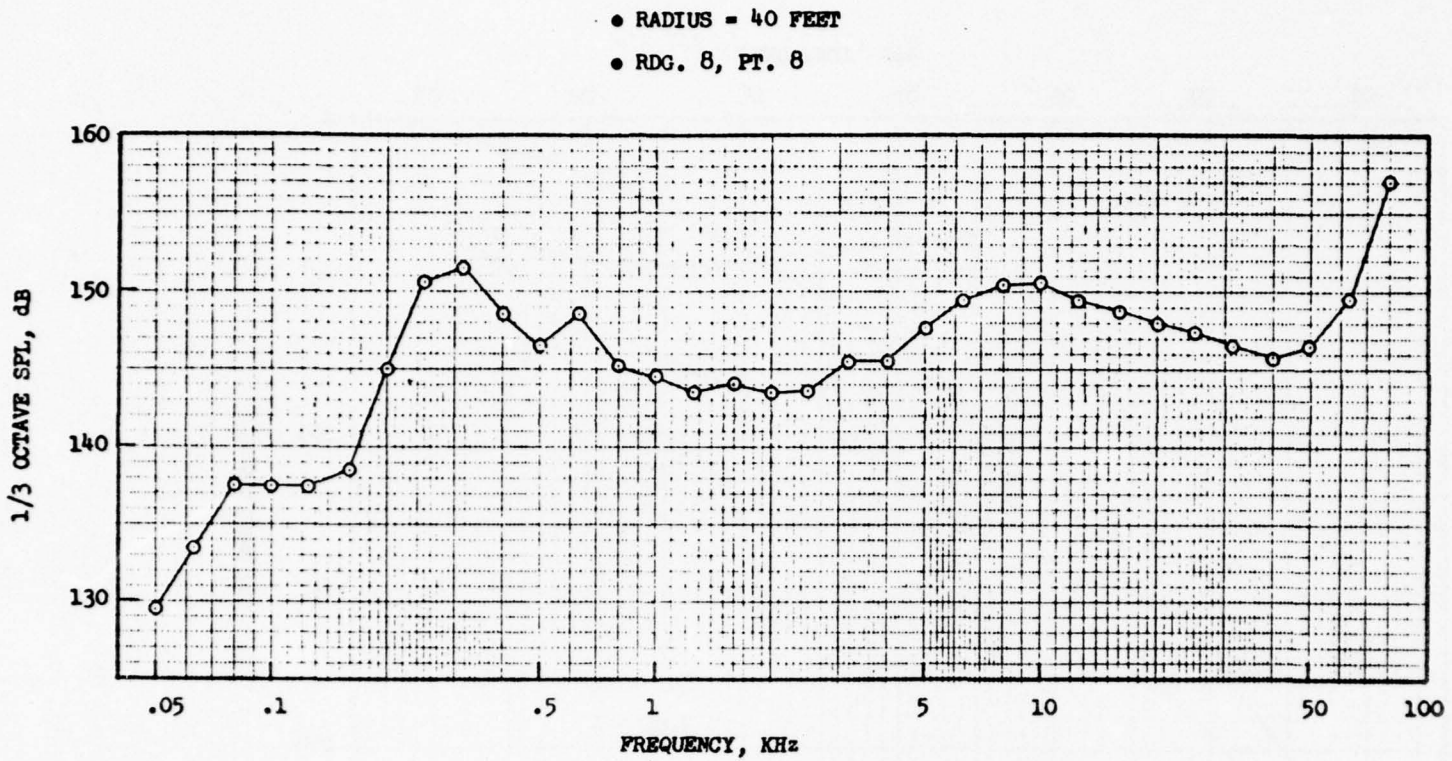


Figure A-2. JENOTS Data, PWL Spectra FSDR Program Calculation.

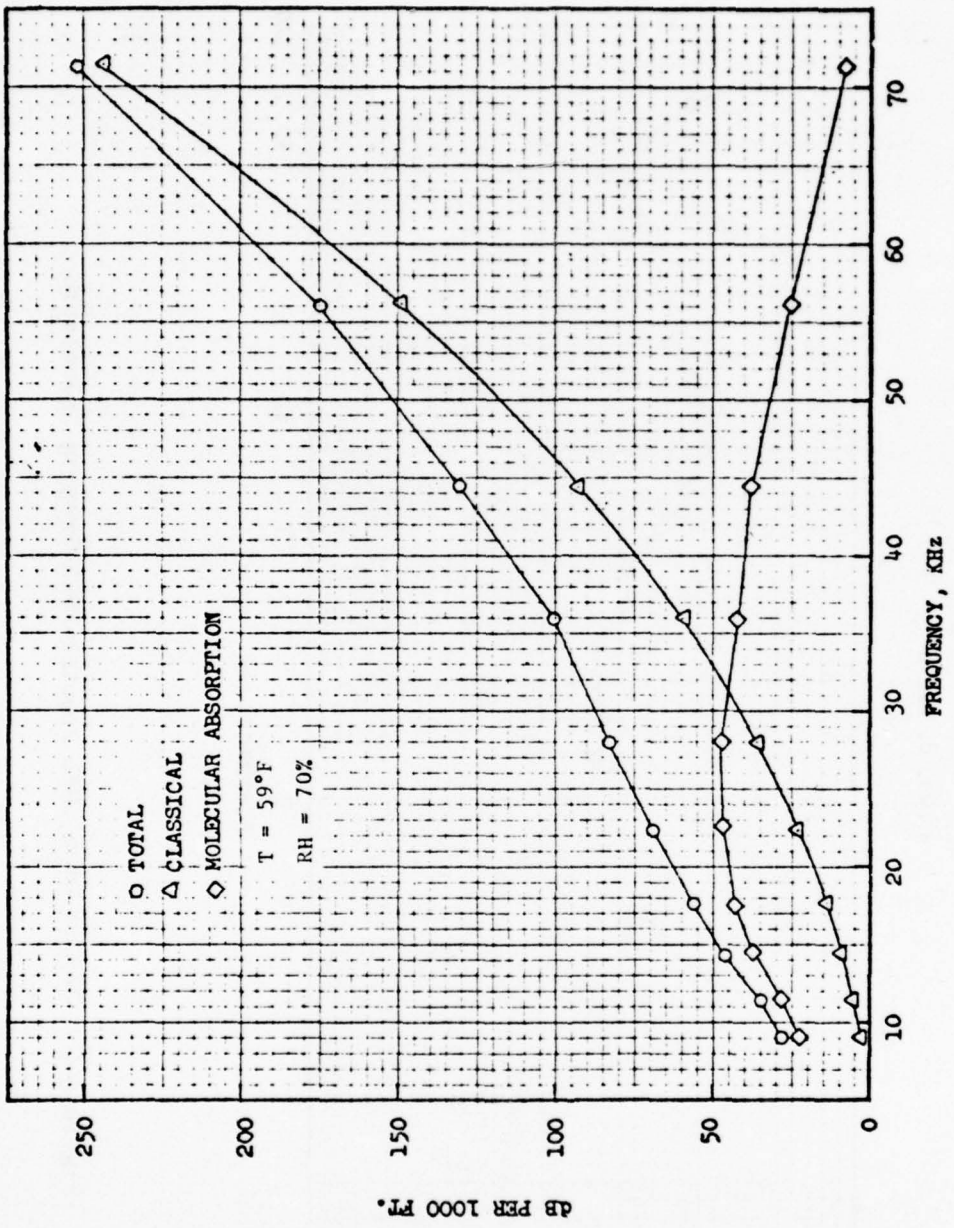


Figure A-3. Revised Atmospheric Correction Factors.

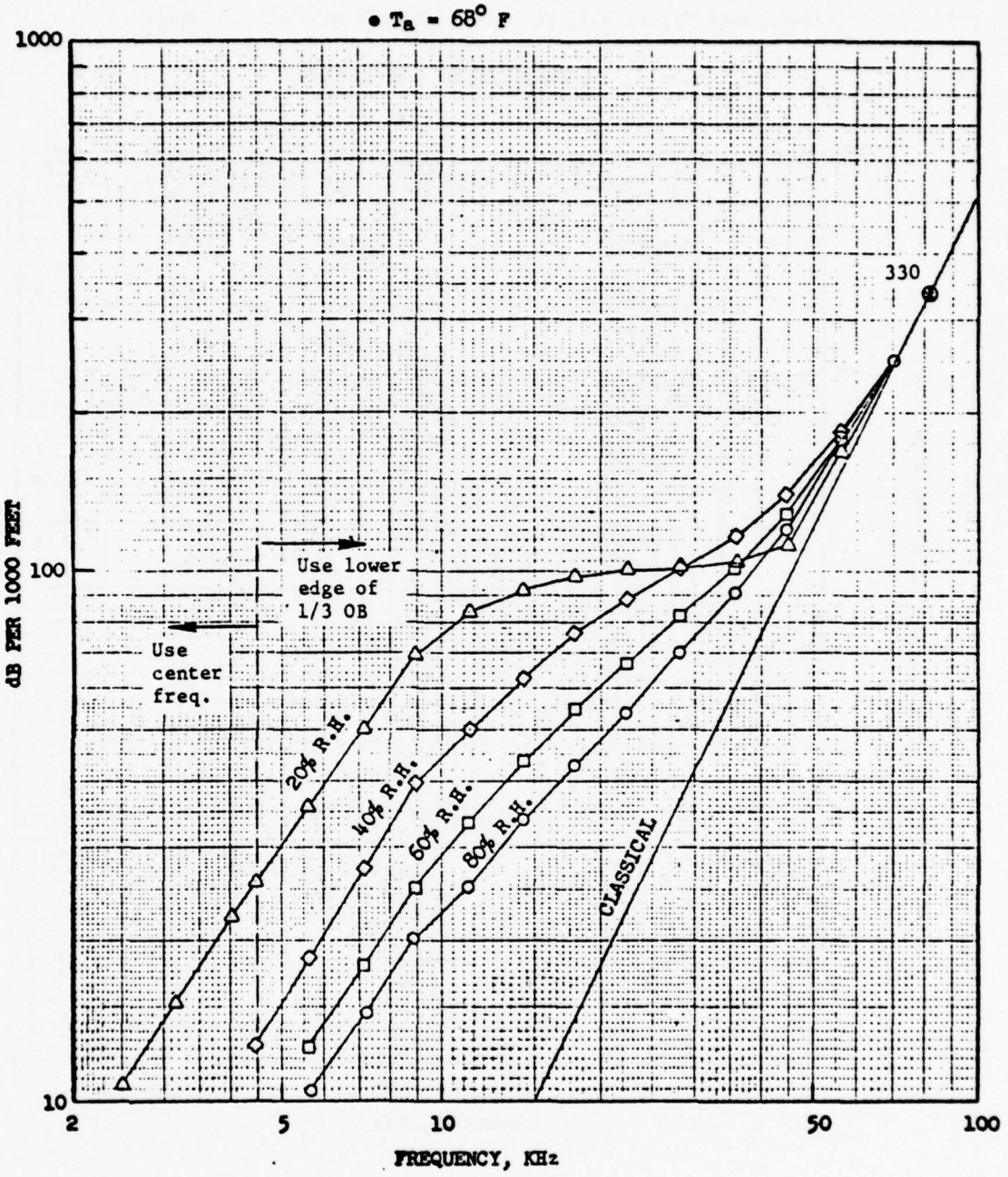


Figure A-4. Revised Atmospheric Absorption.

(Reference Figure 3.2, Page 3-3, "Harris Handbook of Noise"

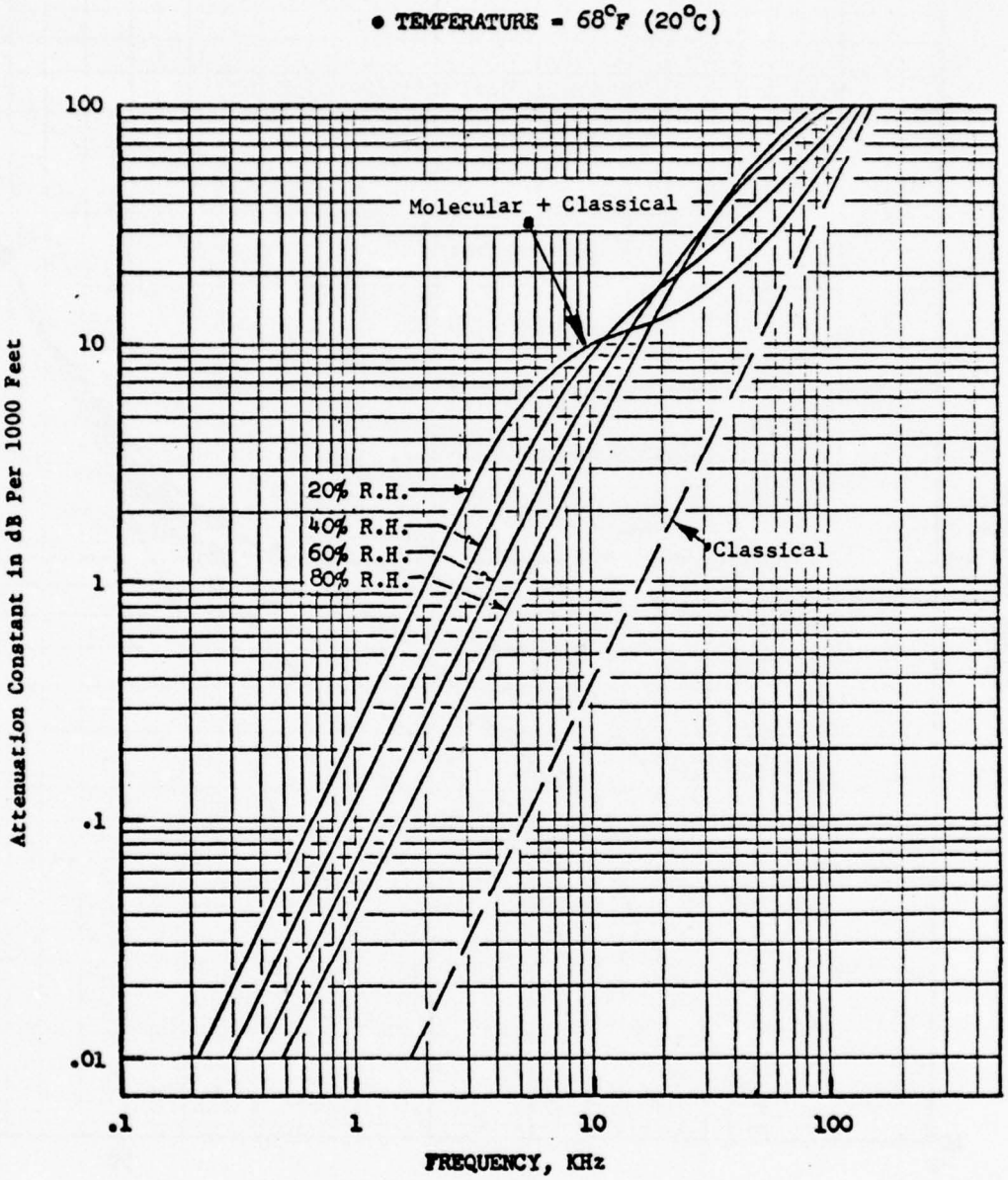


Figure A-5. Atmospheric Attenuation Factors.

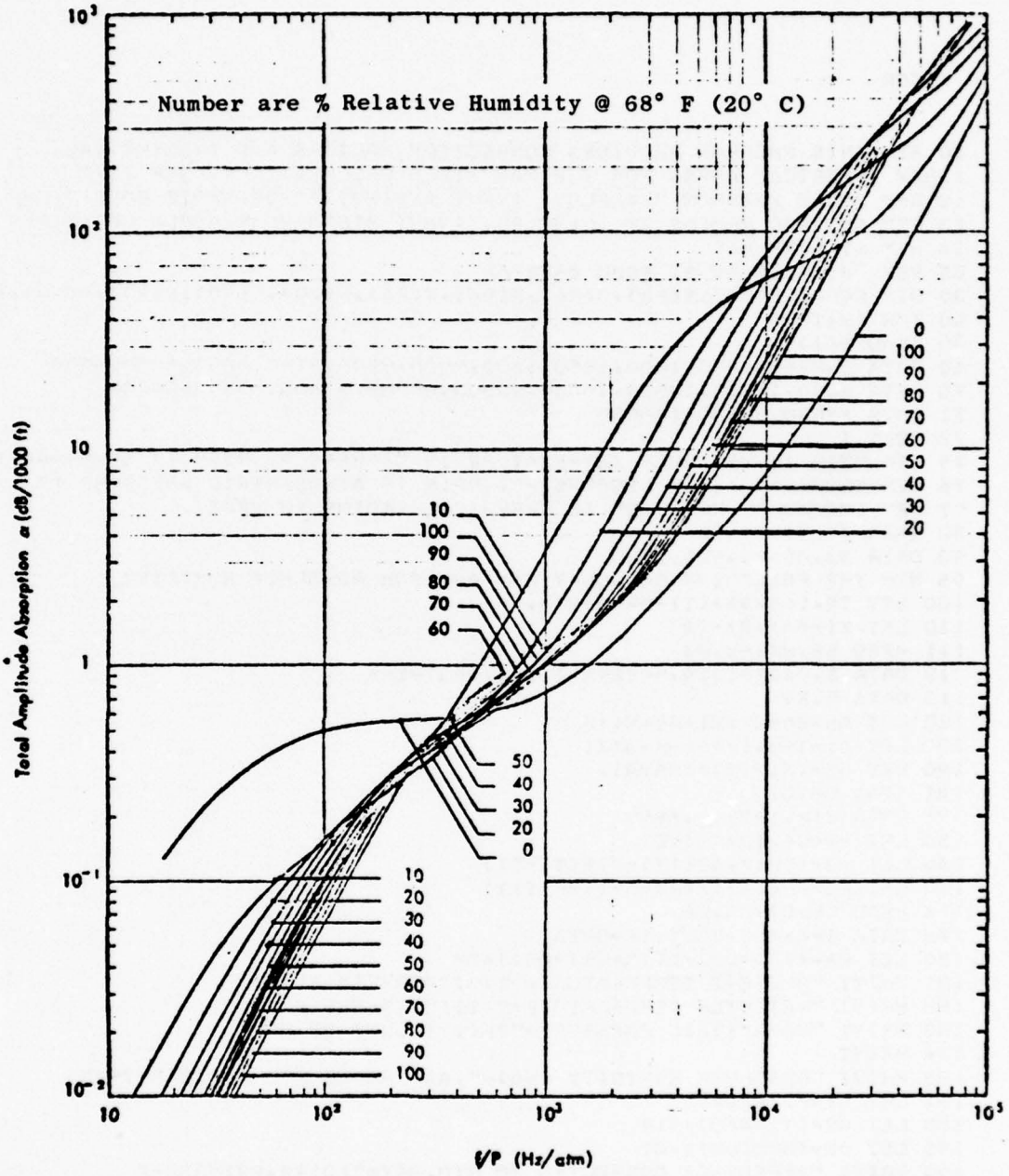


Figure A-6. Total Absorption of Sound in Air as a Function of Frequency. The Curves Range from 0 - 100% Relative Humidity and are for 20° C.

Table A-I. Listing of the "GE" Air Attenuation Correction Computer Program.

```
 FICOR

10 REM THIS PROGRAM PROVIDES CORRECTION FACTORS AND INCREMENTAL
11REM SPHERICAL AREAS FOR THE FAR FIELD CALCULATIONS. SEE TIME
12 REM SHARE PROGRAM "FARFLD". INPUT AMBIENT ATMOSPHERIC CONDITIONS
13 REM AND ARC RADIUS AT  LINE 90. INPUT MICROPHONE ANGLE LOCATIONS
14 REM AT LINE 940
25 REM PREPARED BY R. FOGG 4-28-66
30 DIM C(24),F(24),F(24),G(24),H(24),K(24),M(20),N(20),P(20),S(20),Z(24)
40 FOR I=1TO24
50 READ F(I)
60 DATA 500,630,800,1000,1250,1600,2000,2500,3150,4000,5000,6300
70 DATA 8000,10000,12500,16000,20000,25000,31500,40000,50000
71 DATA 63000,80000,100000
72 NEXT I
75 REM "T1" IS WET BULB TEMPERATURE IN DEGREES F. "T3" IS ATMOSPHERIC
76 REM TEMPERATURE IN DEGREES F . "P1" IS ATMOSPHERIC PRESSURE IN
77 REM INCHES OF HG ."R2" IS SPHERICAL RADIUS IN FEET .
80 READ T1,T3,P1,R2
90 DATA 33,40,29.921,1000
95 REM THE FOLLOWING CALCULATIONS ARE FOR ABSOLUTE HUMIDITY
100 LET T2=((5/9)*(T1-32))+273.16
110 LET X1=647.27-T2
111 READ B6,B7,B8,B9
112 DATA 3.2437814,5.868826E-3,1.1702379E-8
113 DATA 0.69
120 LET A5=B6+B7*X1+B8*X1↑3
130 LET A1=1+B9*1.1967946E-3*X1
140 LET A2=(X1/T2)*(A5/A1)
141 READ C6,C7
142 DATA 218.167,14.6959
150 LET P=(C6/10↑A2)*C7
160 LET A3=((P1*.49115)-P)*(T3-T1)
170 LET P2=P-((A3)/(2755-1.28*T1))
171 READ C8,C9,D5,D6
172 DATA 144,460,85.7,16.02E3
180 LET A4=((P2*C8)/((T3+C9)*D5))*D6
181 PRINT "AMBIENT TEMPERATURE=";T3;"DEGREES F"
182 PRINT "WET BULB TEMPERATURE=";T1;"DEGREES F"
183 PRINT "BAROMETRIC PRESSURE=";P1;"INCHES OF HG"
184 PRINT
185 PRINT "ABSOLUTE HUMIDITY (HA)=";A4;"GRAMS PER CUBIC METER"
187 LET D1=P1/29.921
188 LET D2=(T3+460)/519
189 LET D3=(SQR(D2))/D1
190 PRINT "IMPEDENCE CORRECTED TO STD.DAY=";D3*2.227525E-6
191 PRINT
192 PRINT
193 REM THE FOLLOWING CALCULATIONS ARE FOR ALPHA MOL MAX
200 REM H MOL MAX
205 READ F1,F2,F3,F4,F5,F6
210 FOR I=1TO24
```

Table A-I. Listing of the "GE" Air Attenuation Correction Computer Program (Continued).

```
/FICOR CONTINUED


220 IF F(I)> 4000 THEN 227
225 LET A6=F(I)
226 GO TO 230
227 LET A6=89*F(I)
230 LET H(I)=.028961*A6↑.51093
235 IF F(I)>4000 THEN 250
240 LET A6=F(I)
245 GO TO 260
250 LET A6=89*F(I)
260 LET C(I)=A6*.00357451*EXP(.0117537*T3)
261 IF A6<=5900 THEN 266
263 DATA .15023777E02,.93707731E-02,-.36541712E-06,.56857640E-11
264 DATA -.31243496E-16,.0117537
265 LET C(I)=(F1+F2*A6+F3*A6↑2+F4*A6↑3+F5*A6↑4)*EXP(F6*(T3-59))
266 IF F(I) >4000 THEN269
267 LET A6=F(I)
268 GO TO 270
269 LET A6=89*F(I)
270 LET Y4=.279189E-7*A6↑2.05403
280 LET Y5=.261933E-7*A6↑2.050881
290 LET X(I)=Y5+(Y4-Y5)*(T3-32)/68
300REM THE FOLLOWING CALCULATIONS ARE FOR ALPHA MOL OVER ALPHA MOL AI
 05 LET A7=A4/H(I)
310 IF A7> 6.5 THEN 440
320 IF A7<1.0 THEN 380
330 LET Y1=(.16955546E-2*A7)-.35055924E-1
340 LET Y2=(Y1*A7)+.28070773
350 LET Y3=(Y2*A7)-.10521673E1
360 LET Z(I)=(Y3*A7)+.18209020E1
370 GO TO 450
380 LET Y1=(.74335316E1*A7)-.171860E2
390 LET Y2=(Y1*A7)+.11814166E2
400 LET Y3=(Y2*A7)-.23792759E1
410 LET Y4=(Y3*A7)+.13220157E1
420 LET Z(I)=(Y4*A7)+.5230581E-3
430 GO TO 450
440 LET Z(I)=.2
450 LET Z(I)=.001*INT(1000*Z(I)+.5)
460 LET E(I)=Z(I)*C(I)
470 REM THE FOLLOWING CALCULATIONS ARE FOR THE EGA CORRECTION
480 LET R1=R2
510 LET C1=(.20411435E-20*R1)-.66703093E-16
520 LET C2=(C1*R1)+.72854603E-12
530 LET C3=(C2*R1)-.32650913E-8
540 LET C4=(C3*R1)+.49614255E-5
550 LET C5=(C4*R1)+.44663072E-2
560 LET G1=(C5*R1)+.59387702
570 LET F1=(.16573369E-24*R1)-.46152934E-20
580 LET E2=(E1*R1)+.32361609E-16
590 LET E3=(E2*R1)+.39118972E-13
```

Table A-I. Listing of the "GE" Air Attenuation Correction Computer Program (Continued).

```
)F1COR CONTINUED


600 LET E4=(E3*R1)-.104^4995E-8
610 LET E5=(E4*R1)+.29126338E-5
620 LET E6=(E5*R1)-.54370996E-3
630 LET G2=(E6*R1)+.59506112
650 IF R1<=4000 THEN 680
660 LET G1=5.010264
670 LET G2= 15.44041+.0001*(R1-4000)
680 IF F(I)=63 THEN 720
690 IF F(I)>=2000 THEN 740
700 LET Z1=.2*((LOG(F(I)/62.5))/LOG(2))
710 GO TO 750
720 LET Z1=0
730 GO TO 750
740 LET Z1=1.0
750 LET G(I)=(Z1*(G1-G2))+G2
760 NEXT I
765 PRINT "CORRECTION FACTORS IN DB AT ARC RADIUS=";R2;"FEET"
770 PRINT "FREQUENCY";TAB(11);"CLASSICAL";TAB(22);"VOL.ABSORP.";TAB(36);
771 PRINT "TOTAL ABSORP";TAB(51);"EGA";TAB(63);"TOTAL CORR"
790 FOR I= 1 TO 24
800 PRINT F(I);TAB(8);K(I)*R2/1000;TAB(22);E(I)*R2/1000;
801 PRINT TAB(36);(K(I)+E(I))*R2/1000;TAB(51);G(I);TAB(63);
802 PRINT ((K(I)+E(I))*R2/1000)+G(I)
810 NEXT I
820 REM THE FOLLOWING CALCULATIONS ARE FOR STRIP AREA
821 PRINT
822 PRINT
825 PRINT "ANGLE LOCATION","STRIP AREA FOR";R2;"FOOT SPHERICAL RADIUS"
826 PRINT "(DEGREES)","(SQ. FT.)"
830 REM "M(I)" AND "N(I)" ARE ANGLES WHICH DEFINE THE ARC ASSIGNED
840 REM TO EACH MICROPHONE. "P(I)" IS THE MICROPHONE LOCATION ANGLE.
845 READ F1,F2,F3,F4
846 DATA 1.5,3.1416,2,.0174533
850 READ N
855 DATA 17
860 FOR I= 1 TO N
870 READ P(I)
875 NEXT I
880 DATA 0,10,20,30,40,50,60,70,80,90,100,110,120,130,140,150,160
895 FOR I= 1 TO N
900 LET M(I)=P(I)-(P(I)-P(I-1))/F3
910 LET N(I)=(P(I+1)-P(I))/F3+P(I)
915  IF I=1 THEN 917
916 GO TO 920
917 LET M(I)=P(I)-(P(I+1)-P(I))/F3
920 IF M(I)< 0 THEN 940
930 GO TO 950
940  LET M(I)= 0
950 IF N(I) > 180 THEN 970
954 IF I=N THEN962
```

Table A-I. Listing of the "GE" Air Attenuation Correction Computer Program (Concluded).

```
*F1CCR CONTINUED

958 GO TO 980
960 GO TO 980
962 LET N(I)=P(I)+(P(I)-P(I-1))/P3
966 GO TO 960
970 LET N(I)=180
980 LET S(I)=F1*F2*F2+F3*(COS(N(I)*F4)-COS(N(I)*F4))
990 PRINT P(I),S(I)
995 NEXT I
1000 END
```

Table A-II. Summary of Ambient Conditions During Certification Testing of the Facilities.

Pt.	P_o, psia	P_8, psia	P_8/P_o	T_o, °R	T_8, °R	V_j, ft/sec	M_j	Amb. Temp., °F	Wet Bulb Temp., °F	Bar. Press., in. Hg	Rel. Hum., %	D_j inch	Ref.
	14.18	16.96	1.196	532.0	528.0	562.0	0.512	72.0	63.3	28.87	61.0	2.0	Lockheed Georgia
	14.18	18.39	1.297	532.0	528.0	674.0	0.621	72.0	63.3	28.87	61.0		
	14.18	26.28	1.853	531.0	528.0	1013.0	0.982	71.0	62.5	28.87	61.0		
	14.20	16.92	1.192	530.0	545.0	565.0	0.507	70.0	62.8	28.91	66.0		
	14.20	18.22	1.283	530.5	557.0	678.0	0.608	70.5	62.5	28.91	63.0		
	14.20	24.30	1.211	532.0	605.0	1017.0	0.911	72.0	62.6	28.91	58.0		
	14.22	17.98	1.264	554.0	1342.0	1024.0	0.598	94.0	71.5	28.95	32.0		
	14.20	16.40	1.155	557.0	1258.0	781.0	0.465	97.0	71.0	28.91	26.0		
	14.7	18.06	1.229	537.0	537.0	600.0	0.55	77.0	-	-	-	4.0	NASA-Lewis
	14.7	26.7	1.816	537.0	537.0	994.0	0.96	77.0	-	-	-	4.0	Olsen
	14.7	18.06	1.229	537.0	537.0	600.0	0.55	77.0	-	-	-	2.84	AHUJA/
	14.7	26.7	1.816	537.0	537.0	1000.0	0.96	77.0	-	-	-	2.84	Bushell
	14.7	18.61	1.266	537.0	537.0	640.0	0.59	77.0	-	-	-	0.98	LUSH
	14.7	26.3	1.789	537.0	537.0	985.0	0.95	77.0	-	-	-	0.98	LUSH
	14.7	17.0	1.156	519.0	540.0	514.0	0.46	59.0	-	-	-	1.78	NGTE
	14.7	19.7	1.240	519.0	540.0	722.0	0.66	59.0	-	-	-		
	14.7	26.9	1.830	519.0	540.0	1014.0	0.97	59.0	-	-	-		
	14.7	15.6	1.061	519.0	1260.0	505.0	0.30	59.0	-	-	-		
	14.7	16.6	1.129	519.0	1260.0	719.0	0.43	59.0	-	-	-		
	14.7	18.7	1.272	519.0	1260.0	1005.0	0.60	59.0	-	-	-		

Table A-II. Summary of Ambient Conditions During Certification Testing of the Facilities (Continued).

Pt.	P_o, psia	P_8, psia	P_8/P_o	T_o, °R	T_8, °R	V_j, ft/sec	M_j	Amb. Temp., °F	Wet Bulb Temp. °F	Bar. Press., in. Hg	Rel. Hum., %	D_j inch	Ref.
3	14.509	15.960	1.100	512.0	498.9	401.3	0.372	33.5	31.5	29.540	81.0	4.64	NASA-Lewis
4	14.510	16.687	1.150	↓	500.4	485.2	0.451	33.5	31.5	29.542	81.0	↓	DBTF Prog,
6	14.509	19.558	1.348		502.9	702.9	0.667	33.5	31.5	29.540	81.0		JENOTS
7	14.509	21.241	1.464		503.0	789.7	0.758	34.5	32.0	29.540	76.0		Model 8
8	14.509	23.679	1.632		504.1	889.4	0.867	34.5	32.0	29.540	76.0		↓
9	14.509	26.885	1.853		506.0	991.0	0.982	35.0	32.5	29.540	76.5		
23	14.465	15.101	1.044		1487.6	467.4	0.254	38.5	35.0	29.451	70.0		
24	14.465	15.449	1.068		1492.0	578.2	0.314	38.5	35.0	29.451	70.0		
25	14.462	15.923	1.101		1494.6	698.4	0.381	38.5	35.0	29.444	70.0		
26	14.462	16.4	1.134		1492.6	796.4	0.436	38.0	35 0	29.444	74.5		
27	14.462	16.892	1.168		1500.4	885.7	0.486	38.0	35.0	29.444	74.5		
28	14.462	17.629	1.219		1496.2	996.1	0.550	38.0	35.0	29.444	74.5		
29	14.462	19.509	1.349		1493.9	1215.5	0.680	39.0	35.5	29.444	70.0		
30	14.462	21.621	1.495		1495.8	1400.4	0.793	39.0	35.5	29.444	70.0		
117	14.460	15.299	1.058		895.6	414.8	0.286	38.0	35.5	29.441	79.0		
120	14.450	15.664	1.084		1258.4	587.2	0.347	38.0	35.5	29.420	79.0		
121	14.450	16.092	1.114		1243.3	673.9	0.401	38.0	35.5	29.420	79.0		
122	14.460	18.205	1.259		1255.0	981.4	0.591	38.0	35.5	29.441	79.0		
118	14.460	26.173	1.810	↓	892.3	1292.9	0.961	38.0	35.5	29.441	79.0	↓	↓
18	13.541	14.54	1.077	515.0	1039.0	510.0	0.322	55.0	51.0	27.57	77.0	20.84	FAA
17	13.541	16.91	1.252	515.0	996.0	863.0	0.578	55.0	51.5	27.57	80.0	↓	SST Phase II,
3	13.536	24.4	1.807	514.0	1214.0	1510.0	0.967	54.0	51.0	27.56	82.0		J79 @ EPTC
15	13.541	27.22	2.016	514.5	1305.0	1693.0	1.058	54.5	51.0	27.57	79.0		↓
5	13.536	30.0	2.222	514.0	1390.0	1855.0	1.146	54.0	51.5	27.56	85.0		
13	13.536	32.58	2.413	513.5	1489.0	2008.0	1.208	53.5	51.0	27.56	85.0		
12	13.536	34.04	2.521	513.5	1563.0	2103.0	1.245	53.5	51.0	27.56	85.0		
11	13.536	34.9	3.585	513.5	1608.0	2159.0	1.269	53.5	51.0	27.56	85.0	↓	↓

Table A-II. Summary of Ambient Conditions During Certification Testing of the Facilities (Continued).

Pt.	P_o, psia	P_8 psia	P_8/P_o	T_o, °R	T_8, °R	V_j, ft/sec	M_j	Amb. Temp., °F	Wet Bulb Temp., °F	Bar. Press., in. Hg	Rel. Hum. %	D_j inch	Ref.
0	14.773	16.088	1.089	539.0	539.0	393.0	0.35	79.0	68.0	30.08	55.0	2	USC
1	14.773	17.758	1.202	540.0	540.0	577.0	0.52	70.0	59.5	30.08	53.0	2	
2	14.802	20.353	1.375	539.5	529.0	743.0	0.69	79.5	67.8	30.14	53.0	2	
3	14.793	23.654	1.599	537.0	519.0	888.0	0.85	77.0	66.5	30.12	56.0	1	
4	14.793	26.701	1.805	539.0	534.0	999.0	0.96	79.0	68.0	30.12	55.0	2	
5	14.793	60.679	4.108	539.5	524.0	1448.0	1.58	79.5	67.5	30.12	52.0	2	
6	14.763	16.398	1.111	559.0	973.0	587.0	0.39	99.0	85.0	30.06	55.0	2	
7	14.763	26.515	1.796	538.0	553.0	1011.0	0.96	78.0	66.7	30.06	53.5	1	
8	14.763	32.067	2.172	536.0	590.0	1184.0	1.11	76.0	65.7	30.06	56.0	1	
9	14.763	40.852	2.767	536.0	598.0	1347.0	1.30	76.0	65.7	30.06	56.0	1	
10	14.763	23.614	1.599	546.0	867.0	1147.0	0.85	86.0	74.2	30.06	56.0	1	
11	14.763	26.707	1.809	560.0	1050.0	1401.0	0.96	100.0	86.0	30.06	56.0	1	
12	14.763	31.970	2.165	550.0	876.0	1442.0	1.11	90.0	77.6	30.06	56.0	1	
13	14.763	40.323	2.731	558.0	1038.0	1764.0	1.29	98.0	81.5	30.06	48.5	1	
1	14.484	15.210	1.050	532.0	539.5	297.0	0.265	72.0	60.5	29.49	50.0	0.787	UBC
2	14.484	15.813	1.092	538.0	531.0	398.0	0.357	73.0	62.0	29.49	53.0		
3	14.637	17.615	1.204	542.0	541.0	579.0	0.521	82.0	69.0	29.80	50.0		
4	14.637	20.323	1.389	539.5	545.0	765.0	0.700	79.5	67.3	29.80	51.0		
5	14.637	24.149	1.65	542.0	552.0	940.0	0.876	82.0	70.9	29.80	56.0		
6	14.637	26.724	1.826	542.0	551.0	1022.0	0.968	82.0	70.0	29.80	53.0		
7	14.637	29.391	2.008	544.0	551.0	1051.0	1.000	84.0	66.2	29.80	37.0		
2	14.611	26.885	1.840	529.8	530.4	1009.0	0.976	70.5	61.4	29.75	59.0	2	R&DC
4	14.610	17.974	1.230	529.4	530.1	605.0	0.552	69.7	61.4	29.75	62.0	2	
6	14.617	27.132	1.856	528.6	528.4	1014.0	0.983	67.6	60.3	29.76	65.5	1	
8	14.618	20.582	1.408	528.4	523.1	769.0	0.717	67.2	60.2	29.76	67.0	1	
6	14.674	18.250	1.344	486.5	1457.2	1028.0	0.567	26.5	26.6	29.88	100.0	2	
8	14.678	17.196	1.172	486.0	1903.1	1005.0	0.481	26.1	26.2	29.88	100.0	2	
9	14.679	21.514	1.466	486.1	1851.1	1517.0	0.760	26.1	26.2	29.89	100.0	2	
10	14.681	27.245	1.856	486.0	1893.8	1919.0	0.983	25.9	26.1	29.89	100.0	2	
12	14.686	27.334	1.861	485.6	1493.9	1708.0	0.986	25.6	25.8	29.90	100.0	2	
13	14.686	23.198	1.580	485.5	1508.7	1489.0	0.835	25.6	25.8	29.90	100.0		

Table A-II. Summary of Ambient Conditions During Certification Testing of the Facilities (Concluded).

Pt.	P_o, psia	P_8, psia	P_8/P_o	T_o, °R	T_8, °R	V_jk ft/sec	M_j	Amb. Temp., °F	Wet Bulb Temp., °F	Bar. Press., in. Hg	Rel. Hum. %	D_j inch	Ref.
116	14.539	16.877	1.161	493.5	654.0	572.0	0.467	33.5	31.5	29.610	81.0	3.59	FAA
117	14.548	18.170	1.249	493.5	657.0	697.0	0.573	33.5	31.5	29.618	81.0		Core
120	14.546	23.467	1.613	493.5	654.0	1002.0	0.856	33.5	31.5	29.620	81.0		Engine
173	14.533	15.55	1.070	495.0	1265.0	539.0	0.317	33.0	30.5	29.590	75.0		Prog.
174	14.533	16.2	1.114	497.0	1257.0	680.0	0.403	33.0	30.5	29.590	75.0		Ph. II
175	14.533	16.75	1.152	497.0	1258.0	776.0	0.461	33.0	30.0	29.592	69.5		
177	14.546	18.22	1.253	500.0	1263.0	974.0	0.584	33.0	30.0	29.615	69.5		
29	14.470	16.289	1.126	531.4	2342.9	969.0	0.430	67.0	55.0	29.46	46.0	4.31	AF/DOT
1	14.478	19.503	1.347	525.6	1033.1	1007.0	0.670	64.0	57.0	29.48	65.0		Program
13	14.477	65.289	4.510	534.1	1018.0	2068.0	1.640	68.0	59.0	29.47	58.0		
3	14.479	240.56	1.661	528.7	1441.4	1534.0	0.395	64.0	57.0	29.48	65.0		
12	14.479	65.326	4.512	531.4	1453.3	2480.0	1.645	68.0	59.0	29.47	58.0		
27	14.465	23.704	1.639	533.6	2398.2	1960.0	0.896	65.0	55.0	29.44	52.5		
45	14.387	58.475	4.064	519.3	2326.1	3075.0	1.588	63.0	59.0	29.29	79.5	4.31	
70	14.273	55.124	3.862	535.0	1051.7	2012.0	1.535	75.5	65.5	29.07	57.0		
88	14.524	28.34	1.951	521.3	514.8	1037.0	1.026	-	-	29.57	-	5.7	FAA SST
83	14.516	19.118	1.317	523.8	1033.9	970.0	0.644	66.0	51.0	29.55	33.5		Phase II
84	14.516	16.652	1.147	524.2	2342.8	1060.0	0.464	66.0	51.0	29.55	33.5		
94	14.521	22.259	1.833	523.3	1070.2	1217.0	0.810	61.0	50.0	29.56	46.0		
172	14.446	27.287	1.889	546.6	1506.8	1741.0	1.011	79.0	67.0	29.32	51.5		

10.0 REFERENCES

1. "Task 1 Detailed Work Plan," High Velocity Jet Noise Source Location and Reduction (DOT OS-30034), General Electric Company, August 30, 1973.

2. "High Velocity Jet Noise Source Location and Reduction; Part I Technical Proposal," Volumes I and II, submitted in response to RFP DOT OS-30034 for Department of Transportation, General Electric Company, P72-166, February 1, 1973.

3. Chu, W.T.; "General Jet Noise Experiments in the USC Anechoic Chamber," USC subcontractor report to the General Electric Company, August 1974.

4. Chu, W.T., Petersen, R., and Kao, K.; "Directivity of Jet Noise," J. of Acoustic Soc. of Am., Volume 51, No. 3, pp. 830-832, 1972.

5. Savell, C.T., et al.; "Test Facility Validation Memos for JENOTS," AEG TM 74-144. General Electric Company, Cincinnati, Ohio, June 1974.

6. Kantola, R.A.; "CR&DC Hot Jet Acoustic Facility," GE CR&DC subcontractor report to GE AEG, February 1975.

7. Claes, H.P., Sieckman, A.R., Savell, C.T., and Schumate, C.L.; "Certification of the J79 at GE/EFTC as a Jet Noise Source," R75AEG165, General Electric Company, January 1975.

8. Whittaker, R.W.; "Validation of FluiDyne Static Thrust Facilities for High Velocity Jet Noise Source Location and Reduction Program." AEG TM 73-893, General Electric Company, November 1973.

9. Berrettoni, J.N.; "Tolerancing by the Statistical or Differential Method," Automotive Technical Committee of the American Society for Quality Control, Automotive Supplement No. 1, May, 1954.

10. Berrettoni, J.N.; "Mathematical Formulation of Tolerancing by the Statistical or Differential Method: Mean and Variances of Functions of One or More Variables," ACQC LCS Codes 120: 60:000; 400:00:000; Unpublished.

11. Anon, "Method for Calculating the Attenuation of Aircraft Ground to Ground Noise Propagation during Takeoff and Landing." SAE AIR 923, 1966.

12. Buell, C.E.; "Variability of Sound Propagation Prediction Due to Atmospheric Variability," NASA CR 61160, January, 1967.

PRECEDING PAGE BLANK-NOT FILMED

13. Anon, "A Pr[illegible] to Study the Effects of Motion on Jet Exhaust Noise from Airc[illegible], Volume I, Technical Proposal," submitted in response to RFP-3-5[illegible]880-Q for Nasa Lewis, P74-32, April, 1974.

14. Anon, "Revised Uniform Summary of Surface Weather Observations EAFB California," WBA No. 23114, USA FTAC, Data Processing Division, (Air Weather Service CMAC), 1972.

15. Anon, "Tables of Surface Weather Conditions for Albany Airport and Greater Cincinnati Airport," U.S. Weather Bureau, Ashland, N.C., 1973

16. Anon, "Standard Values of Atmospheric Absorption as a Function of Temperature and Humidity for Use in Evaluating Aircraft Flyover Noise," SAE ARP 866, 1964.

17. Ibid., Proposed revision to SAE ARP 866, October, 1973.

18. Harris, C.M.; "Absorption of Sound in Air in the Audio-Frequency Range," JASA, Volume 35, 1963.

19. Knesner, H.O., "Interpretation of the Anomalous Sound Absorption in Air and Oxygen in Terms of Molecular Collisions," JASA, Volume 5, 1933.

20. Evans, L.B., Bass, H.E., and Sutherland, L.C.; "Atmospheric Absorption of Sound: Theoretical Predictions," Journal of Acoustic Society of America, Volume 51, 5 (Part 2), 1972.

21. Bass, H.R., Bauer, H.J., and Evans, L.B.; "Atmospheric Absorption of Sound: Analytical Expression," Journal of Acoustic Society of America, Volume 52, 5 (Part 2), 1972.

22. Siddon, T.E., Hoglund, L., and Davis, B.; "Validation Report - UBC Anechoic Chamber and Jet Noise Facility," UBC subcontractor report to General Electric Company, November, 1974.

23. Hoch, R.G., Duponchel, J.P., Cocking, B.J., and Bryce, W.D.; "Studies of the Influence of Density on Jet Noise," Journal of Sound and Vibration, 28(4), pp. 649-668, 1973.

24. Bruel and Kjaer Company, "Measurement Microphones," selected reprints from the Technical Review, pp. 62-112, September 1972.

25. Schottky,; "On Spontaneous Current Fluctuations in Various Electric Conductors," Annd Physik, 57, pp. 541-569, 1918 (in German).

26. Johnson, J.B., and Llewellyn, F.B.; "Limits to Amplification," Bell System Technical Journal 14," pp. 15-96, 1935.

27. Beranek, L.L.; Acoustic Measurements, page 189, Wiley, 1949.

28. Eckels, R.E.; "J79 Turbomachinery Noise Testing," General Electric Company, AEG, October 20, 1970.

29. Feldman, Jr., K.T.; "Review of the Literature on Rijke Thermoacoustic Phenomena," J. Sound Vibration, 7(1), 1968.

30. Burrin, R.H., Dean, P.D., and Tanna, H.K.; "A New Anechoic Facility for Supersonic Hot Jet Noise Research at Lockheed-Georgia," paper presented at the 86th Meeting of the Acoustical Society of America, Los Angeles, California, October, 1973.

31. Franken, P.A.; "A Theoretical Analysis of the Field of a Random Noise Source Above an Infinite Plane," NACA TN 3557, 1955.

32. Howes, W.L.; "Ground Reflection of Jet Noise," NACA TN 4260, 1958, (NASA TR 1253, 1959).

33. Hoch, R., and Thomas, P.; "Influence des Reflections sur les Spectres de Pression Acoustique des Jets." Ler Colloque d Acoustique Aeronatique Toulouse, 1968.

34. Anon, "Acoustic Reflections Produced by a Reflecting Plane," AIR 1327 Proposed SAE A21 Committee document, October 1973.

35. Motsinger, R.E., and Sieckman, A.R.; "Prediction of Supersonic Jet Noise Reduction using Multitube Nozzle Suppressors," R73AEG156, General Electric, March 6, 1973.

36. Lush, P.A.; "Measurements of Subsonic Jet Noise and Comparison with Theory," J. Fluid Mech., Volume 46, pt. 3, pp. 477-500, 1971.

37. Ahuja, K.K., and Bushell, K.W.; "An Experimental Study of Subsonic Jet Noise and Comparison with Theory," Journal of Sound and Vibration, 30(3), pp. 317-341, 1973.

38. Olson, W.A., Gutierrez, O.A., and Dorsch, R.G.; "The Effect of Nozzle Inlet Shape, Lip Thickness and Exit Shape on Subsonic Jet Noise," NASA TMX 68182. Lewis Research Center, 1973.

39. Cocking, B.J.; "The Effect of Temperature on Subsonic Jet Noise," NGTE Report No. R331, May 1974.

40. Tanna, H.K., and Dean, P.D.; "Results for the AFAPL/DOT Contract," Lockheed, Georgia Company. To be published in Journal of Sound and Vibration.

41. Anon, "Jet Exhaust Noise Predictions," Proposed AIR 876, SAE A21 Committee, September, 1974.

42. Lighthill, M.J.; "Sound Generated Aerodynamically," the Bakerian Lecture, 1961, Proc. Roy. Soc. Volume 267A, p. 172, May 1962.

43. Stone, J.R.; "Interim Prediction Method for Jet Noise," NASA TMX 71618, NASA Lewis Research Center, 1974.

44. Smith, E.B., and Semrau, W.R.; "Second Noise Measurement of the GEX200 (CJ805-23) Engine," General Electric Company Report DF59FPD394, June 1959.

45. Gerrard, J. II, "An Investigation of the Noise Produced by a Subsonic Air Jet," Journal of the Aeronautical Sciences, 23, pp. 855-866, 1956.

46. Yu, J.C., and Dosanjh, D.S.; "Noise Field of Co-axial Interacting Supersonic Jet Flows," AIAA Paper No. 71-152, 1971.

47. Lee, B., et al.; "Research Investigation of the Generation and Suppression of Jet Noise," General Electric Company, Flight Propulsion Laboratory Department, Cincinnati, Ohio, prepared under Navy Bureau of Weapons Contract No. as 59-6160-C, 1961.

48. Howes, W.L., Calagham, E.E., Coles, W.D., and Mull, H.R.; "Near Noise-Field of a Jet Engine Exhaust," NASA Report 1338, 1957.

49. Lassiter, L.W., and Hubbard, H.H.; "The Near Noise Field of Static Jets and Some Model Studies of Devices for Noise Reduction," NASA Technical Note 3187, 1954.

50. Nagamatsu, H.T., and Sheer, R.E., Jr.; "Flow and Acoustic Characteristics of Subsonic and Supersonic Jets from Convergent Nozzle," AIAA Paper No. 70-802, 1970.

51. Parthasarathy, S.P.; "Evaluation of the Noise Autocorrelation Function of Stationary and Moving Noise Sources by a Cross Correlation Method," AIAA Paper No. 73-186.

52. Curle, N.; "The Influence of Solid Boundaries upon Aerodynamic Sound," Proc. Roy Soc. A231, pp. 505-514, 1955.

53. Powell, A.; "Aerodynamic Noise and the Plane Boundary," JASA 31, No. 8, 1960.

54. Maestrello, L., and McDaid, E.; "Acoustical Characteristics of a High Subsonic Jet," AIAA Paper No. 70-234, 1970.

55. Rackl, R., and Siddon, T.E.; "Jet Noise Study Using Image Technique," Proc. of Canadian Congress of Applied Mechanics, 1971.

56. Maestrello, L., and McDaid, E.; "Near-Field Characteristics of a High Subsonic Jet," AIAA Paper No. 71-155, 1971.

57. Potter, R.C., and Jones, J.H.; "An Experiment to Locate the Acoustic Sources in a High Speed Jet Exhaust System," Acoustic Society of America, 1967.

58. Potter, R.C.; "An Investigation to Locate the Acoustic Sources in a High Speed Exhaust Stream," Research Staff Report WR 68-4, Wyle Laboratories, 1968.

59. Bishop, K.A., Ffowcs-Williams, J.E., and Smith, W.; "On the Noise Sources of the Unsuppressed High-Speed Jet," J. Fluid Mech. Volume 50, Part 1, pp. 21-31, 1971.

60. MacGregor, W.A., and Simcox, C.D.; "The Location of Acoustic Sources in Jet Flows by Means of the Wall Isolation Technique," AIAA Paper 73-1041, 1973.

61. Mason, W.P., and Marshall, R.N.; "A Tubular Directional Microphone," JASA Volume 10, pp. 206-215, January 1939.

62. Radecki, K.P., "Design, Description and Operational Procedure for a Broadside Directional Acoustic Array in Jet Engine Noise Analysis," TM AEG 75-222, General Electric Aircraft Engine Group, Cincinnati, Ohio, 1975.

63. Tatge, R.B.; "Directive Acoustic Arrays for Jet Engine Noise Source Location," GE TIS 70-c-052, General Electric Company CR&DC Schenectady, New York, January 1970.

64. Schultz, T.J.; "Acoustic Wattmeter,: JASA Volume 28, No. 4, 693-699, July 1956.

65. Chu, W.T., Laufer, J., and Kao, K.; "Noise Source Distribution in Subsonic Jets," Internoise 72 Proceeding, October 1972.

66. Grosche, F.R.; "Distribution of Sound Source Intensities in Subsonic and Supersonic Jets," AGARD CPP 131, Noise Mechanisms, Brussels, September 1973.

67. Chu, W.T.; "Turbulence Measurements Relevant to Jet Noise," UTIAS Report No. 119, November 1966.

68. Jones, B.G., Planchon, H.P., and Hammersley, R.J.; "Turbulent Velocity Space Time Correlation Measurements in a Plane Two Stream Mixing Layer at Velocity Ratio of 0.3," AIAA Paper 73-225, January 1973.

69. Lee, H.K., and Ribner, H.S.; "Direct Correlation of Noise and Flow of a Jet," AIAA Paper No. 72-640, June 1972.

70. Lee, H.K.; "Correlation of Noise and Flow of a Jet," University of Toronto, Institute for Aerospace Studies UTIAS Report No. 168 (AFOSR-TR-71-2572), 1971.

71. Seiner, J.M., and Reethof, G.; "On the Distribution of Source Coherency in Subsonic Jets," AIAA Paper 74-4, January 1974.

72. Ribner, H.S.; "Aerodynamic Sound from Fluid Dilations - A Theory of Sound from Jets and Other Flows," UTIA, p. 86, 1962.

73. Meecham, W.C., and Ford, G.W.; "Acoustic Radiation from Isotropic Turbulence," JASA 30, 318, 1958.

74. Siddon, T.E.; "New Correlation Method for Study of Flow Noise," Proceedings of 7th International Congress on Acoustics, Budapest, August 1971.

75. Siddon, T.E., and Rackl, R.; "Cross Correlation Analysis of Flow Noise with Fluid Dilations as Source Fluctuation," Presented at 82nd Meeting of the Acoustical Society of America, Denver, October 1971.

76. Siddon, T.E.; "Jet Noise Research - Progress and Prognosis," Internoise 72 Proceedings, October 1972.

77. Ginoux, J.J. (ed.), "Round Table Discussion at Specialists Meeting on the Mechanism of Noise Generation in Turbulent Flow," Sponsored by AGARD Fluid Mechanics Panel. Rhode-Saint-Genese, Belgium, 1-5 April, 1963.

78. Scharton, T.D., and White, P.H.; "Simple Pressure Source Model of Jet Noise," ASA Journal Volume 52, Part 2, 399, July 1972.

79. Massier, P.F., Parthasarathy, S.P., and Cuffel, R.F.; "Experimental Evaluation of Fluctuating Density and Radiated Noise from a High Temperature Jet," JPL TM 33-643, Jet Propulsion Lab., Cal Tech., October 1973.

80. Damkevala, R.J., Grosche, F.R., and Guest, S.H.; "Direct Measurement of Sound Sources in Air Jets Using the Crossed Beam Correlation Technique," AGARD Conference on Noise Mechanisms, AGARD cpp-131, pp. 3-1 - 3-15, 1973.

81. DeBelleval, J.F., Randon, J., Perulli, M., and Taillefesse, C.; "Influence of Refraction Effects on the Interpretation of a Hot Jet Acoustic Radiation," AIAA Paper No. 73-990, 1973.

82. Rudd, M.J., and Barakat, R.G.; "A Feasibility Study of Remote Sensing Techniques for Jet Noise Source Locations," BBN Report 2799 to the General Electric Company, April 12, 1974.

83. Kraichnan, R.H.; "Pressure Field Within Homogeneous Anisotropic Turbulence," J. Acoustic Soc. Am., 28 (1), pp. 64-72, January 1956.

84. Pope, A.; Wind Tunnel Testing, John Wiley and Sons, Ltd. (Second edition).

85. Siddon, T.E.; "On the Response of Pressure Measuring Instrumentation in Unsteady Flow," University of Toronto Institute for Aerospace Studies Report No. 136, also condensed in NASA SP-207, January 1969.

86. Rackl, R.; "Further Studies on Cross-Correlations Between Fluid Dialations and Flow Noise," Paper XX-3, presented at 84th Meeting of Acoustic Soc. Amer., Miami Beach, November 1972.

87. Rackl, R.; "Two Causality Correlation Techniques Applied to Jet Noise,: PhD Thesis, U. of Brit. Col., April 1973.

88. Papoulis, A.; Probability, Randoni Variables and Stochastic Processes, McGraw-Hill, 1965.

89. Papoulis, A.; Fourier Transform and its Application, McGraw-Hill, 1962.

90. Rackl, R., and Siddon, T.E.; "Shadowgraph Causality Correlation for Jet Noise Diagnostics," UBC subcontractor report to the General Electric Company, November 29, 1974.

91. Siddon, T.E.; "Noise Source Diagnostics Using Causality Correlations," Proc. of AGARD CPP-131, pp. 7-1 to 7-12; See also Panel Discussion, pp. A1 - A4.

92. Siddon, T.E.; "'Causality' Corrections as a Quantitative Tool in Acoustic Diagnostics," paper B4 at 86th Meeting of Acoust. Soc. Amer., Los Angeles, Cct. Abstract published in J. Acoust. Soc. Amer., 55(2), 1974, p. 387, 1973.

93. Roe, G.E.; "An Optical Study of Turbulence," J. Fluid Mech. 43, pp. 607-635, 1970.

94. Rudd, M.J., "The Velocity Measurement of Phase Objects," Proceedings of Electro-Optic Systems in Flow Measurement - University of Southhampton, 25-26 September, 1972.

95. Holder, D.W., and North, R.J.; "Schlieren Methods," Nat. Phys. Lab., Notes on Appl. Science No. 31, Her Majesty's Stationery Office, London, 1963.

96. Jenkins, F.A., and White, H.E.; "Fundamentals of Optics," 3rd Edition, McGraw Hill, 1957.

97. Grosche, F.R.; "Measurements of the Noise of Air Jets from Slot Nozzles with and without Shields," 6th Congress of the International Congress of the International Council of the Aeronautical Sciencies; Munchen, Germany, ICAS Paper No. 68-33, September 1968.

98. Abramowitz, Milton and Stegun, Irene A.; "Handbook of Mathematical Functions," Dover Publications, Inc., New York, page 370, Equation 9.4.4, 1965.

99. Rosenberg, L.D.; "Sound Focusing Systems," [in Russian] Izd., ANSSR, Moscow, 1949.

100. Williams, W.F.; "Contoured Patterns from Reflector Systems: A Spherical Wave Expansion Solution," AIAA Paper No. 74-487, 1974.

101. Williams, W.F., et al.; "FY '72 Final Report Communication Satellite Antenna Research," NASA Work Unit 164-21-54, JPL 362-10601-0-3330, Jet Propulsion Lab., Cal. Tech., Pasadena, California, 1972.

102. Borisov, Y.Y., and Gynkina, N.M.; "Elliptical Sound Focusing Elements," Soc. Phys. Acoust., Volume 19, No. 4, January-February, 1974.

103. Benzakein, M.J., Chen, C.Y., and Knott, P.R.; A Computation Technique for Jet Aerodynamic Noise," AIAA paper No. 71-583, 1971.

104. Schlinker, R.H., Petersen, R.A., and Kaplan, R.E., "Enhancement of Directional Microphone Measurements," AIAA paper 73-1040, 1973.

105. Fogg, R.G., "Internal Memorandum," General Electric Company, Aircraft Engine Group, Cincinnati, Ohio, December, 1973.

106. Knott, P.R., et al., "Supersonic Jet Exhaust Noise Investigation," General Electric Company, R74AEG452, July 1976.